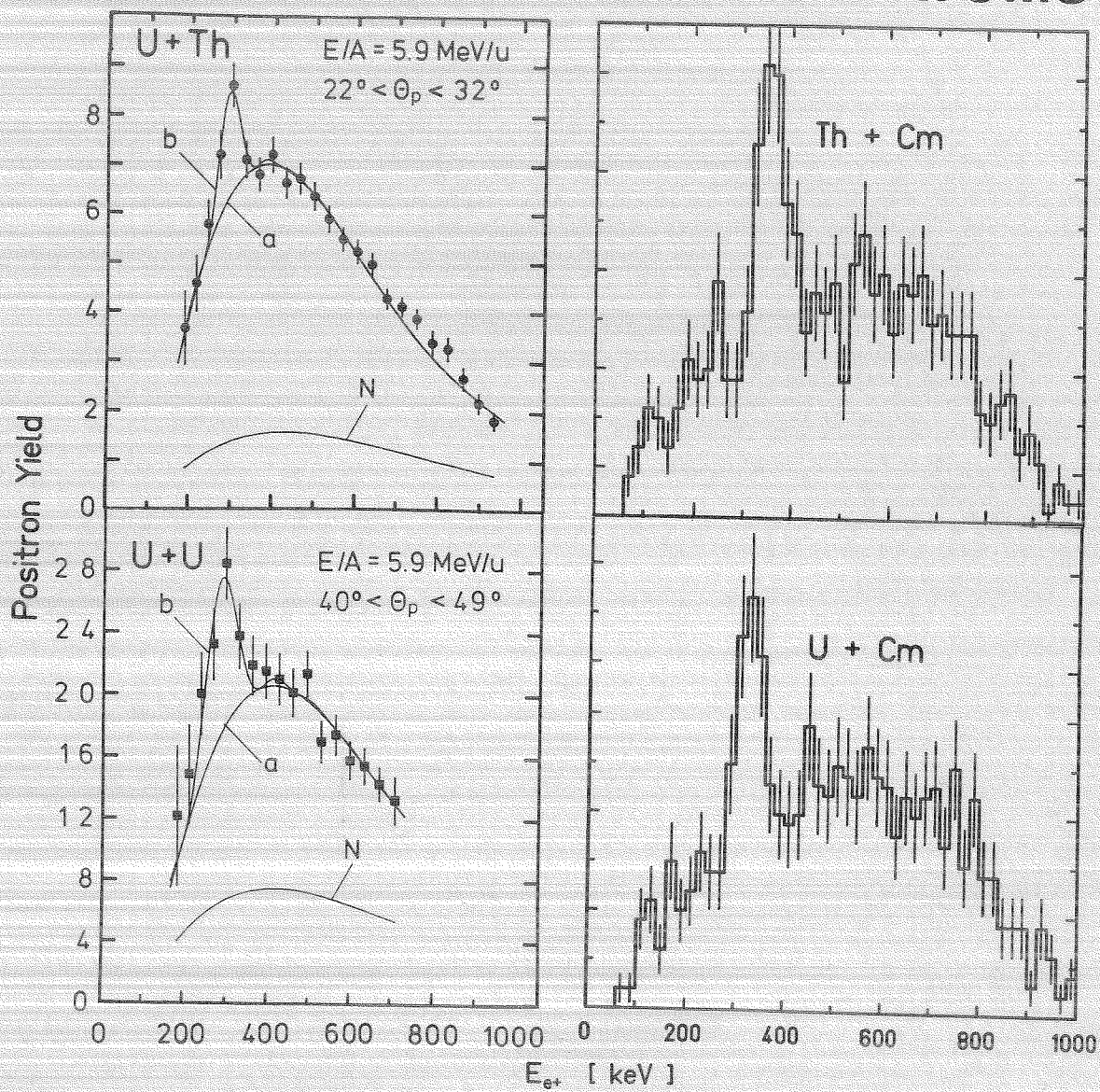
GSI

GSI 84-1
MARCH 1984
ISSN 0174-0814

SCIENTIFIC REPORT 1983

POSITRONS FROM QUASIATOMS



GSI GESELLSCHAFT FÜR SCHWERIONENFORSCHUNG
DARMSTADT
MITGLIED DER AGF

Positrons from Quasiatoms

The cover shows positron spectra recorded with the orange-β-spectrometer (left) and the EPOS positron spectrometer system (right). In all four collision systems narrow lines have been detected. The result can be explained by spontaneous electron-positron creation in overcritical Coulomb fields, where the binding energy of the innermost electrons exceeds twice the electron mass. Positrons of atomic origin according to theory are indicated by curve "a" and in case of prolonged nuclear contact with "b". The letter "N" denotes the nuclear background already substracted. Corresponding experiments are described in this report starting at page 148.

SCIENTIFIC REPORT 1983

Herausgeber: Gesellschaft für Schwerionenforschung mbH
Postfach 11 05 41
6100 Darmstadt

Redaktion: G. Siegert

Druck: G. Scheid, Darmstadt-Arheilgen

ISSN 0174-0814

The Scientific Report 1983 of the GSI shows a considerable increase in the number of contributions (about 15 %), particularly in areas like reaction studies, exotic nuclei, applications of heavy ions in biology and to solid state devices, experimental techniques and accelerator developments. In context with a revision of the plans for future accelerators, a synchrotron (SIS 18) connected with an experimental storage ring (ESR) was studied and proposed to provide the basis for a unique and broad research program in medium energy heavy ion physics in the late eighties. This proposal was presented to the scientific council and an international group of experts on April 5/6, 1984, who recommended its speedy realisation.

Considerable progress was achieved in the study of subbarrier fusion of heavy ions. The enhancement of the fusion cross-section due to collective excitations and open transfer channels with positive Q-values was observed in accordance with theoretical suggestions. For the fusion of symmetric heavy systems dynamical inhibitions were found experimentally. A large number of experiments investigating transfer and deep inelastic reactions showed new results on the mass drift mode, the equilibration of the neutron to proton ratio, and on pairing and shell effects in multi nucleon transfer.

At medium energies elaborate experiments for the study of the fragmentation process as well as the investigation of cooperative effects in the subthreshold π^0-production are reported. The reaction studies at high energies in Berkeley could be extended to heavy collision systems for which collective nuclear matter flow has been observed and explained in the framework of a hydrodynamical model.

A broad γ-spectroscopy program gives evidence of double γ-decay of 0^+-states, γ-deexcitation of giant resonances built on excited states, magnetic moments of rotational states, shape transitions and back bending in plutonium nuclei.

Collinear laser spectroscopy was successfully carried out on neutron deficient indium and tin nuclei, separated with an on-line mass

separator, which was also used for nuclear decay studies of neutron rich and neutron deficient isotopes far off stability. A search for further proton radioactive isotopes was successfully carried out with SHIP, whereas new efforts to produce superheavy nuclei via the fusion of ^{48}Ca with ^{248}Cm remained unsuccessful.

The investigation of positron production in heavy ion-atom collisions was continued to understand the origin of the observed positron lines in the heaviest collision systems. Dopplershift measurements indicate that the positron lines originate from a composite system moving with the center of mass velocity, which supports the suggestion of spontaneous emission as an origin of the lines. Many interesting investigations of atomic processes are reported like the positron creation in deep inelastic collisions, the interference in quasi-molecular X-ray production, the pumping of infrared lasers with heavy ions, and the measurement of production of "cold" highly charged recoil ions. High resolution spectroscopy on highly ionized ions starts to give interesting results on the fine structure splitting and on the Lambshift.

An impressively large program was carried through to study various biological effects of heavy ions on phages, DNA strands, bacilli, spores and cells with many new and unexpected results. The production of microfilters was increased.

New developments in target technologies, detector design and construction, electronics and experimental methods are reported. The UNILAC operation reached the highest efficiency during the past years with interesting improvements of ion sources and beam handling devices. Large efforts went into the planning for SIS 18/ESR and in prototype component developments.

The results presented in this Scientific Report have been obtained by a cooperative effort between GSI and scientists from universities and research institutes in Germany and in many other countries.

P. Kienle

Some of the results included here are progress reports of research projects and therefore should be considered preliminary communications.

Several University projects were funded by the BMFT (Federal Ministry for Research and Technology); they are marked with a "B" after the title. In addition GSI supported external groups with certain resources for development of methods and facilities which are of general interest, this is indicated by a "G" in the title.

CONTENTS PAGE

Survey of Experiments at GSI in 1983 XXXI

1. Nuclear Physics/Nuclear Chemistry

1.1 Nuclear Reactions

1.1.1 Reactions near the Coulomb-Barrier

^{90}Zr Induced Subbarrier Fusion Reactions 2
(J.G. Keller, K.-H. Schmidt, W. Reisdorf, F.P. Heßberger, G. Münzenberg, H. Stelzer, H.-G. Clerc, C.-C. Sahm)

Radiative Fusion Observed in ^{90}Zr Induced Reactions 3
(J.G. Keller, H.-G. Clerc, F.P. Heßberger, G. Münzenberg, W. Reisdorf, C.-C. Sahm, K.-H. Schmidt)

Fusion Probability of Symmetric Heavy Systems 4
(C.-C. Sahm, H.-G. Clerc, K.-H. Schmidt, F.P. Heßberger, J.G. Keller, G. Münzenberg, W. Reisdorf, D. Vermeulen)

Production Cross Sections for Neutron Deficient Th-Isotopes in the Reactions ^{48}Ca+^{172,173,176}Yb 5
(C.-C. Sahm, H.-G. Clerc, K.-H. Schmidt, Y.K. Agarwal, P. Armbruster, F.P. Heßberger, S. Hofmann, G. Münzenberg, W. Reisdorf, D. Vermeulen)

Entrance Channel Differences in Heavy Ion Fusion 6
(W. Kühn, V. Metag, H. Gröger, T.L. Khoo, R. Repnow, R.V.F. Janssens, D. Freeman, B. Haas, F. Haas, D. Habs, S. Hlavac, R.S. Simon)

Neutron and Gamma Emission in the Fusion Reaction ^{86}Kr + ^{64}Ni 7
(U. Arlt, H. Dittmar, B. Lohmüller, Th. Kratz, K. Sapotta, K. Stelzer)

Fission Following Quasi-Elastic Scattering in the Reaction ^{238}U + ^{238}U 8
(J. Schukraft, P. Glässel, D. Habs, D. Harrach v., H.J. Specht)

Time-Scale of Sequential Fission in the Reaction ^{238}U + ^{248}Cm at 8.43 MeV/u 9
(P. Glässel, D. Harrach v., H.J. Specht)

Angular Distributions of Sequential Fission in the Reactions ^{208}Pb, ^{238}U + ^{90}Zr at 7.5 MeV/u 10
(P. Glässel, D. Harrach v., H.J. Specht)

PAGE

Quasi Fission - The Mass Drift Mode in Heavy Ion Reactions 11
(J. Toke, R. Bock, G.X. Dai, A. Gobbi, S. Gralla, K.D. Hildenbrand, W.F.J. Müller, A. Olmi, H. Stelzer, B.B. Back, S. Bjoernholm)

Features of the Sequential Fission Processes Observed in ^{238}U Induced Reactions at 6 MeV/u 12
(G.X. Dai, A. Gobbi, S. Gralla, K.D. Hildenbrand, J. Kuzminski, W.F.J. Müller, A. Olmi, H. Stelzer, J. Toke)

Potential-Energy Surfaces Guiding Fusion and Binary Decay of Heavy Composite Systems 13
(N. Carjan, A. Gobbi)

Study of the ^{84}Kr on ^{27}Al Reaction Mechanism at 490 MeV 14
(B. Heusch, H. Freiesleben, W.F.W. Schneider, B. Kohlmeyer, H. Stege, F. Pühlhofer)

Transfer Cross Sections from the Reaction of ^{48}Ca + ^{254}Es 15
(J.F. Wild, E.K. Hulet, R.W. Lougheed, J.H. Landrum, R.J. Dougan, A.D. Dougan, H. Gäggeler, M. Schädel, K.J. Moody, G.T. Seaborg)

Is ^{197}Au + ^{63}Cu the Dynamic Twin of ^{238}U + ^{56}Fe? 16
(B. Jäckel, A. Rox, W. Westmeier, R.A. Esterlund, H. Schulte, P. Patzelt)

Dynamic Inhibition of Fusion in the System ^{238}U + ^{nat}Fe 17
(A. Rox, B. Jäckel, R.A. Esterlund, W. Westmeier, U. Reus, H. Schulte, P. Patzelt)

Charge and Mass Transport in the Reaction ^{70}Ge + ^{238}U at 8 MeV/u 18
(M. Marinescu, D. Bangert, B. Kohlmeyer, F. Pühlhofer, W.F.W. Schneider, D. Schüll, H. Freiesleben, H. Sohlbach)

Pairing Effects in the Quasi-Elastic Neutron Transfer between Tin Isotopes 19
(W. Oertzen v., R. Künkel, B. Gebauer, A. Gamp, H.G. Bohlen, A. Miczaika, D. Schüll, W.F.W. Schneider)

Quasi-Elastic Mass-Flow and Few Nucleon Transfer Reactions for ^{48}Ti Incident on ^{42}Ca and ^{26}Mg 20
(C. Brendel, J. Carter, A. Richter, G. Schrieder, F. Beck, D. Schüll)

PAGE

Quasi-Elastic Neutron Transfer in the Reactions $^{208}Pb + ^{58}Ni$ and $^{208}Pb + ^{64}Ni$ 21
(K. Sapotta, R. Bass, V. Hartmann, H. Noll, K. Stelzer)

Strong Dominance of Closed Shells on the Diffusive Phase in ^{238}U Induced Reactions 22
(G. Beier, J. Friese, P. Kienle, H.J. Körner, W. Mayer, W.A. Mayer, L. Müller, W. Wagner, W. Henning)

1.1.2 Reactions above the Coulomb-Barrier

Empirical Description of the Element Production in Dissipative Heavy-Ion Collisions 23
(H.J. Wollersheim)

Equilibration of the Neutron to Proton Ratio for Heavy Asymmetric Systems in Heavy Ion Collisions 24
(R. Lucas, C. Gregoire, C. Ngo, J. Poitou, E. Tomasi, A. Gobbi, A. Olmi, H. Sann, G. Wirth, J.V. Kratz, U. Lynen)

Angular Distributions for Symmetric Fragmentation in $^{50}Ti + ^{208}Pb$ Collisions 25
(K. Lützenkirchen, J.V. Kratz, L. Dörr, G. Wirth, C. Gregoire, R. Lucas)

Light-Particle Emission in the Fusion Reaction $^{48}Ti+^{45}Sc$ at 16 MeV/u 26
(H.-J. Keim, B. Kohlmeyer, H. Stege, H.-A. Bösser, F. Pühlhofer, W.F.W. Schneider)

Alpha Particle Associated Collisions of ^{208}Pb with ^{56}Fe 27
(P.J. Brülls, H.P. Hollenbach, M. Mutterer, J. Pannicke, J.P. Theobald, K. Weingärtner)

Evolution of Charge and Mass Transfer in the Reaction ^{92}Mo on ^{154}Sm at 14.8 MeV/u 28
(M. Petrovici, R. Bock, A. Gobbi, S. Gralla, G. Guarino, K.D. Hildenbrand, U. Lynen, W.F.J. Müller, A. Olmi, H. Sann, H. Stelzer, J. Toke, H.J. Wollersheim)

Product Distributions at High Excitation Energies in Heavy Ion Collisions at 8 to 20 MeV/u 29
(S. Gralla, R. Bock, G.X. Dai, A. Gobbi, K.D. Hildenbrand, J. Kuzminski, W.F.J. Müller, U. Lynen, A. Olmi, M. Petrovici, H. Sann, H. Stelzer, J. Toke, H.J. Wollersheim)

PAGE

Emission of Light Charged Particles in Reactions between ^{92}Mo and ^{92}Mo at 18 MeV/u 30
(N. Herrmann, A. Gobbi, S. Gralla, K.D. Hildenbrand, J. Kuzminski, W.F.J. Müller, A. Olmi, M. Petrovici, H. Sann, H. Stelzer, J. Toke, P. Maurenzig, A. Stefanini)

Search for High-Energy γ-Rays in the System ^{100}Mo + ^{100}Mo at 14.7 MeV/u 31
(J. Kuzminski, A. Gobbi, S. Gralla, N. Herrmann, K.D. Hildenbrand, W.F.J. Müller, A. Olmi, M. Petrovici, H. Sann, R.S. Simon, H. Stelzer, J. Toke, P. Maurenzig, A. Stefanini)

Evidence for Reaction-Channel Dependent Excitation-Energy Sharing in Quasi-Elastic Reactions of ^{86}Kr with ^{208}Pb 32
(H. Sohlbach, H. Freiesleben, B. Kohlmeyer, M. Marinescu, F. Pühlhofer, W.F.W. Schneider, D. Schüll, P. Braun-Munzinger)

"Fragmentation" in the System ^{197}Au + ^{197}Au at Energies ≤ 15 MeV/u 33
(Th. Blaich, J.V. Kratz, G. Wirth, K. Sümmerer)

Sequential Fission in the Reaction 10 MeV/u U + U 34
(G. Breitbach, P. Crombach, G. Fiedler, E. Koglin, E. Reichwein)

Determination of Reaction Parameters from Elastic Scattering Studies 35
(H.A. Khan, K. Jamil, N.A. Khan, M.A. Sial, R. Brandt)

The Reaction ^{238}U + ^{nat}U + at 16.7 MeV/N (From Sequential Fission Process to Light Particle Emission) 36
(E.U. Khan, P. Vater, R. Brandt)

Reactions of 10 and 16.7 MeV/Nucleon on ^{238}U, ^{208}Pb and ^{197}U 37
(M. Debeauvais, J. Ralarosy, J. Tripier, S. Jokic)

1.1.3 Nuclear Reactions at High Energies

Fragmentation of ^{12}C at 84 MeV/u 38
(R. Wada, A. Gobbi, K.D. Hildenbrand, W.F.J. Müller, H. Sann, H. Stelzer, U. Lynen, D. Pelte, R. Trockel)

Azimuthal Angular Correlations between Heavy Projectile Fragments and Light Particles in ^{18}O Induced Reactions at 84 MeV/u 39
(W.F.J. Müller, A. Gobbi, K.D. Hildenbrand, H. Rabe, H. Sann, H. Stelzer, R. Wada, R. Glasow, K.H. Kampert, R. Santo, R. Trockel, D. Pelte, U. Winkler, I. Bock, U. Lynen)

PAGE

Low Energetic Alpha Spectra in ^{12}C Induced Reactions at 84 MeV/u 40
(R. Trockel, R. Glasow, K.H. Kampert, R. Santo, A. Gobbi, K.D. Hildenbrand, W. Müller, H. Rabe, H. Sann, H. Stelzer, R. Wada, D. Pelte, U. Lynen

Multiplicity Selected Light Particle Detection in Reactions with 84 MeV/u ^{12}C Projectiles 41
(R. Glasow, K.H. Kampert, R. Santo, D. Pelte, U. Winkler, A. Gobbi, K.D. Hildenbrand, W.F.J. Müller, A. Olmi, H. Sann, H. Stelzer, I. Bock, U. Lynen)

Emission of Fragmentation Products ($5 \leq Z_L \leq 26$) in the Interaction of 84 MeV/u ^{12}C with ^{208}Pb Targets 42
(B. Grabez, R. Beckmann, P. Vater, R. Brandt)

Cooperative Production of Pions and Photons as a Probe for the Dynamics of Nucleus-Nucleus Collisions 43
(H. Noll, E. Grosse, H. Dabrowski, H. Heckwolf, O. Klepper, Ch. Michel, W.F.J. Müller, H. Stelzer, C. Brendel, W. Rösch, P. Braun-Munzinger)

Pion Production in Nucleus-Nucleus Collisions at Energies far below the NN-Threshold 44
(H. Heckwolf, G. Bizard, P. Braun-Munzinger, C. Brendel, H. Dabrowski, E. Grosse, J. Julien, O. Klepper, J.L. Laville, Ch. Michel, A.C. Mueller, W.F.J. Müller, H. Noll, F.E. Obenshain, G. Pappalardo, P. Paul, J. Peter, L. Ricken, W. Rösch, J. Stachel, H. Stelzer, G.R. Young, P.H. Zhang)

Pion Production as a Probe of the Nuclear Matter Equation of State 45
(J.W. Harris, R. Stock, R. Bock, R. Brockmann, A. Sandoval, H. Ströbele, G. Odyniec, H.G. Pugh, L.S. Schroeder, R.E. Renfordt, D. Schall, D. Bangert, W. Rauch, K.L. Wolf)

Momentum Flow in the 800 Mev/u Ar + Pb Reaction 46
(R.E. Renfordt, D. Schall, K. Tittel, R. Brockmann, J.W. Harris, M. Maier, A. Sandoval, R. Stock, H. Ströbele, H.G. Pugh, L.S. Schroeder, K.L. Wolf)

Relativistic Nuclear Collision Studies with the Plastic Ball 47
(M. Doss, H.-A. Gustafsson, H.H. Gutbrod, K.H. Kampert, B.W. Kolb, H. Löhner, B. Ludewigt, A.M. Poskanzer, T. Renner, H. Riedesel, H.G. Ritter, A. Warwick, H. Wieman)

PAGE

Thermalization in High Energy Nuclear Collisions 48
(H.-A. Gustafsson, H.H. Gutbrod, B.W. Kolb, H. Löhner, B. Ludewigt, A.M. Poskanzer, T. Renner, H. Riedesel, H.G. Ritter, A. Warwick, H. Wieman)

Radii of the Participant Region in Relativistic Nuclear Collisions Measured from Proton-Proton Correlations 49
(H.-A. Gustafsson, H.H. Gutbrod, B.W. Kolb, H. Löhner, B. Ludewigt, A.M. Poskanzer, T. Renner, H. Riedesel, H.G. Ritter, A. Warwick, F. Weik, H. Wieman)

Observation of Strong Azimuthal Asymmetry between Slow and Fast Secondaries in High Energy Nuclear Collisions in the Plastic Ball 50
(H.H. Gutbrod, H. Löhner, A.M. Poskanzer, T. Renner, H. Riedesel, H.G. Ritter, T. Siemiarczuk, J. Stepaniak, A. Warwick, F. Weik, H. Wieman)

Collective Flow Observed in Relativistic Nuclear Collisions 51
(H.-A. Gustafsson, H.H. Gutbrod, B.W. Kolb, H. Löhner, B. Ludewigt, A.M. Poskanzer, T. Renner, H. Riedesel, H.G. Ritter, A. Warwick, F. Weik, H. Wieman)

Participant-Spectator Identification in Plastic-Ball Events 52
(H.-A. Gustafsson, H.H. Gutbrod, B.W. Kolb, H. Löhner, B. Ludewigt, A.M. Poskanzer, T. Renner, H. Riedesel, H.G. Ritter, A. Warwick, F. Weik, H. Wieman)

Reactions of U at 3.97 GeV/Nucleon on ^{12}C with SSNTD 53
(M. Debeauvais, J. Ralarosy, J. Tripier, S. Jokic)

Radiochemical Search for Anomalons 54
(G. Dersch, R. Beckmann, R. Brandt, T. Lund, K. Aleklett, E.M. Friedlander, P. Mc Gaughey, G.T. Seaborg, W. Loveland, N. Porile)

About the Anomalous Behaviour of Projectile Fragments of Charge Two 55
(E. Ganßauge, U. Bieschke, H. Kallies, F. Killinger, N. Klein, R. Kretschmer, A. Laschek, W. Weidner)

Is There an Energy Dependence in the Anomalon Effect at Charge Two? 56
(F. Killinger, E. Ganßauge, U. Bieschke, H. Kallies, N. Klein, R. Kretschmer, A. Laschek, W. Weidner)

PAGE

1.2 Nuclear Structure

Search for Quasimolecular γ Transitions in the $^{12}C + ^{12}C$ System at $E_{CM} = 14.6$ MeV 57
(G. Koch, R.D. Fischer, W. Kühn, V. Metag, R. Mühlhans, R. Novotny, H. Ströher, H.J. Hennrich, D. Habs, R. Kroth, D. Schwalm, A. Lazzarini, R.S. Simon)

Double γ Decay in ^{40}Ca 58
(R. Kroth, D. Habs, N. Kwong, J. Schirmer, D. Schwalm, M. Zirnbauer, C. Broude)

Double γ Decay 59
(D. Habs, R. Kroth, N. Kwong, J. Schirmer, D. Schwalm, M. Zirnbauer, C. Broude)

Gamma Decay of Giant Resonances Built on Excited Nuclear States 60
(W. Hennerici, H.J. Hennrich, G. Himmele, R. Repnow, W. Wahl, D. Habs, U. Helmolt v., H.W. Heyng, R. Kroth, D. Schwalm, A. Lazzarini, V. Metag, R.S. Simon)

Measurement of Magnetic Moments in ^{156}Dy 61
(G. Seiler-Clark, D. Pelte, D. Schwalm, H. Emling, H. Grein, E. Grosse, R. Kulessa, Ch. Michel, H.J. Wollersheim, M. Hass, G.J. Kumbartzki, K.-H. Speidel)

Transfer and Simultaneous Coulomb Excitation in Heavy Ion Collisions 62
(Ch. Lauterbach, F. Azgui, J. Barette, C.R. Bingham, H. Emling, E. Grosse, M.W. Guidry, G. Seiler-Clark, W. Spreng, J. Stachel, H.J. Wollersheim)

Search for Shape Transitions in ^{156}Er 63
(F. Azgui, H. Emling, W. Spreng, H.J. Wollersheim, R. Kulessa, T. Byrski, F.A. Beck, G.J. Costa, B. Haas, C. Gehringer, J.C. Merdinger, J.P. Vivien)

The γ-Soft Triaxial Nucleus ^{196}Pt 64
(A. Mauthofer, H. Ower, K. Stelzer, Th. W. Elze, J. Idzko, H.J. Wollersheim, H. Emling, E. Grosse, P. Fuchs, D. Schwalm)

Electromagnetic Properties of High Spin States in ^{242}Pu and ^{244}Pu 65
(W. Spreng, F. Azgui, H. Emling, E. Grosse, R. Kulessa, Ch. Michel, R.S. Simon, H.J. Wollersheim, M. Mutterer, J.P. Theobald, D. Schwalm, N. Trautmann, M.S. Moore)

PAGE

γ-γ-Coincidence Measurement on ^{242}Pu 66
(W. Spreng, F. Azgui, H. Emling, E. Grosse, Ch. Michel, R.S. Simon, H.J. Wollersheim, M. Mutterer, J.P. Theobald, D. Schwalm, G. Seiler-Clark, N. Trautmann, M.S. Moore

1.3 Exotic Nuclides

Collinear Laser Spectroscopy of Fusion Produced ^{107} - ^{111}Indium 67
(G. Ulm, J. Eberz, G. Huber, H. Lochmann, R. Menges, R. Kirchner, O. Klepper, T.U. Kühl, P.O. Larsson, D. Marx, D. Schardt)

On the Nuclear Mean-Square Charge Radii of Tin Isotopes in the Mass Range 104 ≤ A ≤ 124 68
(D. Berdichevsky, G. Ulm)

High Yield Production of Neutron-Deficient Indium and Tin Isotopes 69
(R. Kirchner, O. Klepper, P.O. Larsson, D. Marx, E. Roeckl, D. Schardt)

Production of Very Neutron-Rich Isotopes in the Manganese-to-Nickel Region at the GSI On-Line Mass Separator 70
(E. Runte, K.-L. Gippert, W.-D. Schmidt-Ott, P. Tidemand-Petersson, R. Kirchner, O. Klepper, P.O. Larsson, E. Roeckl, K. Rykaczewski, D. Schardt, N. Kaffrell, P. Peuser, M. Bernas, P. Dessagne, M. Langevin)

Coincidence Measurements of β-Delayed Protons and γ-Rays from the Precursor ^{117}Ba 71
(P. Tidemand-Petersson, R. Kirchner, O. Klepper, W. Kurcewicz, P.O. Larsson, E. Roeckl, D. Schardt, A. Plochocki, J. Zylicz, G. Nyman, I.S. Grant)

Studies on Short-Lived Praseodymium Isotopes at the HELIOS Facility 72
(T. Karlewski, N. Hildebrand, N. Kaffrell, N. Trautmann, G. Herrmann, M. Brügger)

Search for Proton Radioactivity in Fusion Reactions with ^{58}Ni Projectiles 73
(S. Hofmann, Y.K. Agarwal, P. Armbruster, F.P. Heßberger, P.O. Larsson, G. Münzenberg, K. Poppensieker, W. Reisdorf, J.R.H. Schneider, H.-J. Schött)

PAGE

Identification of New Neutron Rich Isotopes of Heavy Lanthanides at the GSI On-Line Mass Separator 74
(K. Rykaczewski, P.O. Larsson, R. Kirchner, O. Klepper, E. Roeckl, D. Schardt, K.-L. Gippert, E. Runte, W.-D. Schmidt-Ott, P. Tidemand-Petersson, N. Kaffrell, P. Peuser, W. Kurcewicz, J. Zylicz)

The β-Decay Branching ^{180}Lu -> ^{180}Hf^{m} and the Nucleosynthesis of ^{180}Ta^{m} 75
(W. Eschner, W.-D. Schmidt-Ott, K.-L. Gippert, E. Runte, H. Beer, G. Walter, R. Kirchner, O. Klepper, E. Roeckl, D. Schardt)

Accelerator Mass Spectrometry on ^{205}Pb 76
(H. Ernst, G. Korschinek, P. Kubik, W. Mayer, H. Morinaga, E. Nolte, U. Ratzinger, W. Henning, W. Kutschera, M. Müller, D. Schüll)

Evaporation Residue Production in Fusion Reactions ^{48}Ca+^{206},^{208}Pb 77
(F.P. Heßberger, Y.K. Agarwal, P. Armbruster, A. Ghiorso, S. Hofmann, M. Leino, G. Münzenberg, K. Poppensieker, W. Reisdorf, K.-H. Schmidt, J.R.H. Schneider, W.F.W. Schneider, D. Vermeulen)

A Search for New Isotopes from Reactions of ^{16},^{18}O and ^{22}Ne with ^{254}Es 78
(M. Schädel, W. Brüchle, M. Brügger, H. Gäggeler, D. Schardt, K. Sümmerer, R.W. Lougheed, J.H. Landrum, J.F. Wild, R.J. Dougan, A.D. Dougan, E.K. Hulet, G.D. O'Kelley)

Search for Superheavy Nuclei from Fusion of ^{48}Ca with ^{248}Cm at SHIP 79
(Y.K. Agarwal, P. Armbruster, S. Hofmann, F.P. Heßberger, G. Münzenberg, K. Poppensieker, W. Reisdorf, K.-H. Schmidt, J.R.H. Schneider, W.F.W. Schneider, D. Vermeulen, A. Ghiorso, M. Leino, K.J. Moody)

Error Analysis in the Case of Poor Statistics 80
(K.-H. Schmidt, C.-C. Sahm, K. Pielenz, H.-G. Clerc)

Fragmentation of the Intermediate Complex in the (^{48}Ca+^{248}Cm) Reaction at the Coulomb Barrier 81
(P. Armbruster, Y.K. Agarwal, A. Ghiorso, S. Hofmann, F.P. Heßberger, M. Leino, K.J. Moody, G. Münzenberg, K. Poppensieker, W. Reisdorf, K.-H. Schmidt, J.R.H. Schneider, W.F.W. Schneider, D. Vermeulen)

PAGE

Attempts to Produce Superheavy Elements in the ^{48}Ca $+^{248}Cm$ Reaction Applying On-Line Chemical Techniques 82
(H. Gäggeler, W. Brüchle, M. Brügger, M. Schädel, K. Sümmerer, G. Wirth, C. Frink, N. Greulich, G. Herrmann, U. Hickmann, N. Hildebrand, J.V. Kratz, N. Trautmann, K.J. Moody, G.T. Seaborg, H. Dornhöfer)

A Search for Superheavy Elements Using the ^{48}Ca + ^{254}Es Reaction 83
(R.W. Lougheed, J.H. Landrum, E.K. Hulet, J.F. Wild, R.J. Dougan, A.D. Dougan, H. Gäggeler, M. Schädel, K.J. Moody, G.T. Seaborg)

Search for Volatile Reaction Products in the Reaction ^{48}Ca + ^{248}Cm 84
(N. Hildebrand, C. Frink, N. Greulich, U. Hickmann, W. Kieling, N. Trautmann, G. Herrmann, H. Gäggeler, K. Sümmerer, G. Wirth)

Excitation Functions for Heavy Actinides from the Reaction of ^{48}Ca with ^{248}Cm 85
(W.R. Daniels, M.M. Fowler, D.C. Hoffman, W. Brüchle, M. Brügger, H. Gäggeler, M. Schädel, K. Sümmerer, G. Wirth, Th. Blaich, G. Herrmann, J.V. Kratz, M. Lerch, N. Trautmann, D. Lee, K.J. Moody, G.T. Seaborg, H.R. Gunten v.)

Gamma-Ray Catalog 86
(U. Reus, W. Westmeier)

1.4 Theory

1.4.1 Nuclear Structure and Decay

What Do We Know about the Surface of Nuclear Charge and Mass Densities? 87
(D. Berdichevsky, U. Mosel)

Influence of Deformation on Mono- and Quadrupole Pairfields 88
(K. Mühlhans, U. Mosel)

Study of the Coriolis Attenuation for Odd-A-Nuclei 89
(E. Müller, U. Mosel)

Yrast Spectra of ^{158}Dy and ^{168}Yb in the Spin Projected Cranked HFB Approach 90
(A. Ansari, U. Mosel, E. Wüst)

Low-Spin Structure of the S-Band 91
(A. Ansari, U. Mosel, E. Wüst)

PAGE

Effect of Number Projection on the Cranked HFB Results 92
(A. Ansari, K. Mühlhans, E. Wüst)

New Terms in the Nuclear Hamiltonian at High Spins 93
(U. Post, E. Wüst, U. Mosel)

Confrontation of Different Collective Models 94
(M. Seiwert, P.O. Hess, J.A. Maruhn)

Separation of Collective and Statistical Components for Average Transition Probabilities in HFB Model 95
(A. Baran, K. Dietrich, P. Ring)

1.4.2 Nuclear Reactions at Low Energies

Renormalisation of the Double Folding Model 96
(M. Seiwert, W. Greiner, W.T. Pinkston)

The Nucleus-Nucleus Potential in Molecular Resonances 97
(A. Faessler, M. Ismail, M. Rashdan, L. Satpathy, W. Wadia)

The Volume Contribution of the Ion-Ion Optical Potential from Realistic Complex Nucleon-Nucleon Interaction 98
(A. Faessler, M. Ismail)

Studies of Heavy-Ion Direct Reactions to the Continuum Using the Nearside-Farside Technique 99
(D.R. Dean, U. Mosel, H. Lenske, H.H. Wolter)

Exact First- and Second-Order Distorted Wave Methods 100
(O. Tanimura, R. Kaps, U. Mosel, R. Wolf)

Polarization Effects on CC and DWBA Potentials 101
(R. Wolf, O. Tanimura, U. Mosel)

Coupling Effects on Fusion and Reaction Cross Sections 102
(J. Makowka, U. Mosel, R. Wolf)

Coupled Channel Calculations for the Scattering of ^{28}Si on ^{28}Si 103
(A. Thiel, W. Greiner)

The Momentum Diffusion Tensor For The Particle Exchange Model 104
(H. Feldmeier, H. Spangenberger)

Exchange of Particles, Momentum and Entropy between Two Colliding Nuclei 105
(H. Feldmeier)

PAGE

The RPA Description of Quantal Brownian Motion 106
(C. Yannouleas)

Closed Irreversible Equations of Motion for the One-Body Density 107
(P. Buck, H. Feldmeier, F. Beck)

Explicit Treatment of N-Body Correlations within a Density-Matrix Formalism 108
(S.J. Wang, W. Cassing)

On Thermal Blocking Mechanism of the Mass Drift in Dissipative Heavy Ion Collisions 109
(T. Matulewicz, A. Gobbi, J. Toke)

Time-Dependent Study of Shell Effects in Mass Transfer - The $^{136}Xe + ^{209}Bi$ (1130 MeV) Reaction - 110
(B. Strack)

Non-Adiabatic Effects in the Time Dependent Level Crossing Problem 111
(A. Gozdz, E. Werner, M. Brack)

On the Dynamical Single-Particle Basis in Large-Amplitude Nuclear Motion 112
(W. Cassing, S.J. Wang, W. Nörenberg)

Traces of Landau-Zener Transitions in the Fusion Cross Section of Heavy Nuclei? 113
(W. Cassing)

Diabatic Interaction Potential for Nucleus-Nucleus Collisions 114
(A. Lukasiak, W. Nörenberg)

Scaling Property and Cranking Mass Tensor in the Diabatic Approach 115
(A. Lukasiak, W. Cassing, W. Nörenberg)

Block Diagonalization for an Improved Diabatic Basis with Full Spin-Orbit Coupling 116
(A. Lukasiak, W. Nörenberg)

Elastoplasticity Tensor for Nucleus-Nucleus Collisions 117
(A. Lukasiak, W. Nörenberg)

On a Fluid-Dynamical Description of Elastoplastic Fermi Systems 118
(B. Morgenstern, W. Nörenberg)

PAGE

Relaxation Times for Distorted Fermi Distributions in Intermediate Energy Nucleus-Nucleus Collisions 119
(W. Cassing, M. Malvetti, H.J. Simonis)

Nonequilibrium Light Particle Emission in Heavy-Ion Collisions: A Two Step Process! 120
(W. Cassing)

Butterfly- and Belly-Dancer-Model for Nuclear Molecules 121
(P.O. Hess, W. Greiner, W.T. Pinkston)

Study of Fusion-Fission Potentials in Superheavy Systems 122
(K. Depta, R. Herrmann, V. Schneider, X.-Z. Wu, K.H. Ziegenhain, J.A. Maruhn, W. Greiner)

Hartree-Fock and Shell Model Calculations for the U-U Compound System 123
(L. Neise, J.A. Maruhn, W. Greiner)

Investigation of Ternary Fission for the System ^{238}U-^{238}U 124
(X.-Z. Wu, J.A. Maruhn, W. Greiner)

1.4.3 Nuclear Reactions at High Energies

The Heavy-Ion Potential at Intermediate Energy 125
(M. Trefz, A. Faessler, W.H. Dickhoff, L. Rikus, S.B. Khadkikar)

Cold Break-Up of Spectator Nuclei in Nucleus-Nucleus Collisions at High Energy 126
(J. Aichelin, J. Hüfner, R. Ibarra)

Expansion and Disassembly Phase of Energetic Nuclear Reactions: - A Problem of Dynamical Instabilities? - 127
(B. Strack, J. Knoll)

Equilibration of a Three Component Nuclear System in Heavy-Ion Collisions 128
(A. Rosenhauer, L.P. Csernai, J.A. Maruhn, W. Greiner)

Flow Analysis of Relativistic Nuclear Collisions - Influence of Self-Consistent Interaction - 129
(J. Theis, H. Stöcker, G. Graebner, G. Buchwald, J.A. Maruhn, W. Greiner)

Nuclear Compression in High Multiplicity Selected Collisions of $^{93}Nb(E_{lab}=0,4$ GeV/n) + ^{93}Nb in View of Recent Data 130
(G. Buchwald, G. Graebner, D. Barthel, J.A. Maruhn, W. Greiner, H. Stöcker)

PAGE

Deformed Nuclei in the 3D-Nuclear Fluid Dynamical Model 131
(D. Barthel, G. Buchwald, G. Graebner, M. Seiwert, J.A. Maruhn, W. Greiner)

Comparison of Intermediate Energy Fluid Dynamical Calculations with Recent MSU $^{40}Ar(137\ MeV/n)+^{197}Au$ Data 132
(G. Buchwald, G. Graebner, T. Rentzsch, J.A. Maruhn, W. Greiner, H. Stöcker)

Dynamical Correlations in Intermediate Energy Nucleus - Nucleus Collisions 133
(W. Cassing)

On the Influence of a Time - Dependent Mean Field on Subthreshold Pion Production in Nucleus - Nucleus Collisions 134
(W. Cassing)

Pion Production at Subthreshold Energies Nucleon-Nucleon Single Collision Vs. Co-Operative Mechanisms 135
(R. Shyam, J. Knoll)

Mean Field Approach to Pion Production in Intermediate Energy Heavy Ion Collisions 136
(M. Tohyama, R. Kaps, D. Masak, U. Mosel)

Antisymmetrization and π-Production 137
(D. Masak, R. Kaps, U. Mosel, M. Tohyama)

Pion Bremsstrahlung far Below the Single N-N Threshold 138
(D. Vasak, B. Müller, W. Greiner)

Isospin Statistics 139
(M. Uhlig, D. Vasak, C.S. Warke, J.A. Maruhn, W. Greiner)

Pion Bremsstrahlung Coupled to Hydrodynamics 140
(M. Uhlig, D. Vasak, G. Buchwald, J.A. Maruhn, W. Greiner)

Phase Transition of the Baryon-Antibaryon Plasma in a Nonlinear Relativistic Mean Field Theory 141
(J. Theis, H. Stöcker, J.A. Maruhn, W. Greiner)

Instability of High Temperature Baryonic Matter in a Relativistic Mean Field Theory 142
(J. Theis, T. Biro, W. Greiner)

PAGE

Simulation of Dynamical Instabilities in the Deconfinement Phase Transition 143
(J. Theis, H. Stöcker, G. Graebner, J.A. Maruhn, W. Greiner)

Color-Singlet Droplets at Finite Baryon Number Density 144
(H. Th. Elze, W. Greiner, J. Rafelski)

Fission of Bags in Spontaneous Quark-Antiquark Pair-Production in Supercritical Colour Fields 145
(D. Vasak, K.-H. Wietschorke, B. Müller, W. Greiner)

2. Atomic Physics

2.1 Superheavy Quasi-Atoms and Inner Shell Excitation Mechanism

Studies of the Positron Structure in (U*U)-Collisions via Determination of the Source Velocity 148
(E. Berdermann, J. Kemmer, P. Kienle, H. Tsertos, W. Wagner, F. Bosch, C. Kozhuharov, W. Koenig)

On the Origin of the Structure in Positron Spectra from U + Cm Collisions 149
(H. Bokemeyer, H. Folger, H. Grein, Y. Kido, T. Cowan, J.S. Greenberg, J. Schweppe, K. Bethge, A. Gruppe, K.E. Stiebing, D. Schwalm, P. Vincent, R. Fonte, H. Backe, M. Begemann, M. Klüver, N. Trautmann)

Positron Production in Elastic and Dissipative Heavy Ion Reactions 150
(E. Bozek, U. Gollerthan, E. Kankeleit, G. Klotz, M. Krämer, R. Krieg, U. Meyer, H. Oeschler, P. Senger)

High Energy δ-Rays from Pb-Pb and Pb-Cm Collisions 151
(P. Armbruster, F. Bosch, C. Kozhuharov, E. Berdermann, P. Kienle, H. Tsertos, W. Wagner, J.B. Wilhelmy)

Strong Differences between K-Shell Excitation Probabilities in Solid and Gas Targets for Very Heavy Collision Systems 152
(B. Liu, D. Liesen, A. Warczak)

Structures in the Sn-K and Ag-K Vacancy Production at 1.4 MeV/u Projectile Energy 153
(A. Warczak, D. Liesen, B. Liu)

Quasimolecular L -> K and M -> K Vacancy Transfer in 3.6 MeV/u Sm^{q+} - Xe Collisions 154
(P.H. Mokler, D.H.H. Hoffmann, W.A. Schönfeldt, A. Warczak)

PAGE

Interferences in Quasimolecular X-Rays from 2,7 MeV/u Ge^{31+} - Kr Collisions 155
(R. Schuch, A. Oppenländer, J. Konrad, M. Schulz, P.H. Mokler, W. Schadt, H. Schmidt-Böcking)

2.2 Few Electron Systems, Recoil Ions and Capture Processes

Heavy Ion Beam Pumped Gas Lasers 156
(A. Ulrich, P. Kienle, D.E. Murnick, D.H.H. Hoffmann, H.F. Beyer)

Anomalous L X-Ray Transitions of Highly Ionized, Fast Projectiles 157
(W.A. Schönfeldt, D.H.H. Hoffmann, P.H. Mokler, A. Warczak)

X-Ray Emission after Multielectron Capture into Highly Charged Sm^{q+}-Projectiles 158
(W.A. Schönfeldt, D.H.H. Hoffmann, P.H. Mokler, A. Warczak)

A New Method for a Precision Measurement of the 1s-Binding Energy in Few Electron High Z-Atoms 159
(W. Koenig, B. Martin, J. Soltani, F. Bosch, C. Kozhuharov, R. Mann)

High Precision Spectroscopic Studies in H- and He-like Kr Ions 160
(J.P. Briand, P. Indelicato, M. Tavernier, H.F. Beyer, D. Liesen, B. Liu, A. Warczak)

Lamb Shift Measurements in High Z Hydrogenic Ions 161
(J.S. Brown, B.P. Duval, H.A. Klein, J. Laursen, A.F. McClelland, P.H. Mokler, J.D. Silver)

Recoil Ion Production Cross Sections for 3.6 - 15.5 MeV/amu Uranium Bombardment of Rare Gas Targets 162
(S. Kelbch, R. Mann, P. Richard, H. Schmidt-Böcking, T. Ullrich)

Observation of Highly Charged-Recoil Ions for High Resolution Spectroscopy 163
(S. Chen, H.A. Schüssler, U. Trebus, J. Zhang, W. Becker, R. Mann)

Soft X-Ray Spectroscopy of Ion-Induced Ne Recoils 164
(F. Folkmann, N. Eisum, P.H. Mokler)

Q-Value Spectroscopy of Recoil Ions Colliding with Rare Gas Atoms 165
(R. Mann, S. Bayerbach, S. Hagmann, B. Warczak)

Charge Transfer Involving Multiply Charged Ions 166
(A. Müller, B. Schuch, W. Groh, P.C. Kester, I. Wirkner-Bott, E. Salzborn)

PAGE

Collinear Laser Spectroscopy on Fast Atomic Beams of Tin and Germanium 167
(H. Lochmann, J. Eberz, G. Huber, R. Menges, G. Ulm, T.U. Kühl)

2.3 Theory

Lamb-Shift Corrections in Hydrogen-Like Atoms 168
(W.R. Johnson, G. Soff)

Electron Excitations in Asymmetric Heavy Ion Collisions 169
(G. Mehler, T. Reus de, J. Reinhardt, B. Müller, W. Greiner, G. Soff, U. Müller)

Charge Transfer in the Presence of a Nuclear Resonance 170
(D.H. Jakubaßa-Amundsen, P.A. Amundsen)

Inner Shell Vacancy Formation in Deep-Inelastic Heavy-Ion Collisions 171
(U. Müller, G. Soff, J. Reinhardt, T. Reus de, B. Müller, W. Greiner)

Atomic Excitations and the Time Structure of Nuclear Reactions 172
(J. Reinhardt, B. Müller, W. Greiner, U. Müller, U. Heinz)

Beam Energy Dependence of Spontaneous Positron Production in Delayed Nuclear Collisions 173
(U. Heinz, U. Müller, J. Reinhardt, B. Müller, W. Greiner)

On the Evidence for Spontaneous Positron Production in Heavy Ion Collisions 174
(T. Reus de, J. Reinhardt, B. Müller, W. Greiner, U. Müller, G. Soff)

Spectra of δ-Electrons and Positrons Emitted in Deep-Inelastic Heavy-Ion Reactions 175
(U. Müller, G. Soff, J. Reinhardt, T. Reus de, B. Müller, W. Greiner)

Delta Electron Spectra in I-U and Au-U Collisions 176
(G. Mehler, T. Reus de, J. Reinhardt, B. Müller, W. Greiner, G. Soff, U. Müller)

Relativistic Wave Packets and Delta-Electron Emission 177
(H.-J. Bär, G. Soff)

δ-Electron Emission in Strong Projectile Fields 178
(D.H. Jakubaßa-Amundsen)

PAGE

Atomic Excitation Processes in Nuclear Reactions with Three-Body Break-Up 179
(U. Müller, J. Reinhardt, T. Reus de, B. Müller, W. Greiner)

K-Shell Ionization in Relativistic Heavy-Ion Collisions 180
(U. Becker, S.R. Valluri, N. Grün, W. Scheid)

Relativistic Bound State Wavefunctions in Momentum Space 181
(G. Soff, U. Müller, P. Schlüter, K.-H. Wietschorke, T. Reus de, G. Mehler, J. Reinhardt, B. Müller, W. Greiner)

The Zero-Point Energy in Quantum Electrodynamics 182
(G. Plunien, B. Müller, W. Greiner)

Bound Electron States in Critical Magnetic Fields 183
(K.-H. Wietschorke, P. Schlüter, W. Greiner, G. Soff)

Molecular Ring Currents from Magnetic Monopoles 184
(M. Kleber)

Relativistic Many-Body Approach to the Photoionization of Cesium 185
(W.R. Johnson, G. Soff)

Screening Effects in Relativistic Many Body Systems 186
(R.M. Dreizler, E. Engel, E.K.U. Groß, P. Malzacher)

Volume Isotope Shift Calculations for IIa- and IIb-Elements 187
(G. Torbohm, B. Fricke, A. Rosen)

Search for an Optimal Basis-Set for Relativistic Molecular Calculations. I.: The H_2^+-Problem 188
(H. Hartung, B. Fricke, W.-D. Sepp, D. Kolb)

Advantages and Problems of Higher Order Finite-Element-Methods 189
(W. Schulze, D. Kolb, B. Fricke)

A Fast Solution of the Two-Dimensional Poisson-Equation for Di-Atomic Molecules 190
(W. Sengler, D. Kolb, B. Fricke)

Exact HF-Calculations of Symmetry Violation in Heavy Atoms 191
(A. Schäfer, B. Müller, W. Greiner)

Bound State Solutions of the Klein-Gordon Equation for Strong Potentials 192
(W. Fleischer, G. Soff)

PAGE

3. Radiation Effects

3.1 Radiation Effects in Biological Systems

The Effects of Heavy Ions on PM2 Phages 194
(A.M. Kellerer, M. Laßmann, H. Roos, W.-H. Thomas, A. Wenning, F. Zilker)

Induction of DNA Strand Breaks by High LET Irradiations 195
(M. Larsson, L. Hieber)

DNA Strand Breaks in Mammalian Cells Exposed to Low-Energetic Heavy Ions 196
(B. Rydberg)

Inactivation Cross Sections for Spores of Bacillus Subtilis 197
(M. Schäfer, R. Facius, H. Bücker)

Heavy Ion Effects on B. Subtilis Spores: Inactivation, Repair and Mutation Induction 198
(K. Baltschukat, H. Bücker, R. Facius, G. Horneck, M. Schäfer)

The Inactivation of Dry Yeast Cells by Protons in the Energy Range Below 2 MeV 199
(M. Kost, E. Schneider, J. Kiefer, J. Günzl, E. Huttel, P. Keiner)

Recovery from Transcription Inhibition in Yeast Cells Exposed to Charged Particles 200
(K.J. Weber, E. Schneider, J. Kiefer)

Interpretation of Heavy Ion Survival Data: Influence of Energy Density 201
(J. Kiefer)

Chromosome Aberrations in V 79 Chinese Hamster Cells Produced by Heavy Charged Particles 202
(W. Müller, H.G. Miltenburger, G. Kraft)

Heavy Ion Induced Alterations in Proliferation Kinetics of Mammalian Cells 203
(L. Hieber, M. Larsson, D. Pollet, G. Kraft)

Proliferation Kinetics of Irradiated Cell Populations Determined by the Bromodeoxyuridine-33258H Technique 204
(E. Kuchinka, L. Hieber, G. Kraft)

Inactivation of Mammalian Multicell Spheroids by Heavy Charged Particles 205
(M. Schuber, G. Kraft)

PAGE

Application of the Texture Analyse System (T.A.S.) for Colony Counting 206
(B. Warczak, W. Kraft-Weyrather, G. Kraft)

Search for Critical Target Sites of the Cell Nucleus Experiments with Heavy Ions in the keV Regime 207
(G. Kraft, W. Kraft-Weyrather, H.G. Miltenburger, W. Müller, M. Schuber)

Biological Effects of Uranium Ions- Experiments with Heavy Ions at Relativistic Energies 208
(G. Kraft, E.A. Blakely, W. Kraft-Weyrather, W. Müller, H.G. Miltenburger, R. Roots, W. Schimmerling, C.A. Tobias, M. Wong, T.C. Yang)

Heavy Ion Experiments with Plant Seeds and Spores 209
(U. Bork, K. Koller-Lampert, M.E. Starke, A.R. Kranz)

3.2 Radiation Effects in Solids

Investigation of Ion Induced Defects in Insulators by Small Angle Scattering 210
(D. Albrecht, P. Armbruster, R. Spohr, M. Roth, K. Schaupert, H. Stuhrmann)

Structure Determination of Nuclear Tracks Using H_2O/D_2O Contrast Variation 211
(K. Schaupert, G. Fiedler, D. Albrecht, P. Armbruster, R. Spohr, M. Roth, H. Stuhrmann)

An Approach to Simulate Solar Wind Erosion of Extraterrestrial Surfaces 212
(K. Thiel, U. Saßmannshausen)

Ion-Induced Sputtering of Selected Selenides and Tellurides 213
(G. Freisem-Broda, K. Thiel, B. Wolf)

Sputtering and Implant Behaviour of LiF:U-Single Crystals under Heavy Ion Bombardment 214
(K. Thiel, U. Saßmannshausen, U. Bangert, D.E. Arafah, K. Recker, B. Wolf)

Influence of Heavy Ion Induced Radiation Damage on the Piezoelectric Properties of PVDF 215
(B. Hahn, B.E. Fischer)

Graded Index Antireflecting Surfaces (continued) 216
(B.E. Fischer, K.-D. Hummel)

Manufacture of Single-Pore Membranes 217
(H. Gaiser, H.-R. Kiesewetter, K. Poppensieker, R. Spohr, K. Schaupert)

PAGE

Heavy Ion Track Etching in Olivine 218
(C. Perron, M. Maury, P. Pellas, V.P. Perelygin, S.G. Stetsenko)

Modification of the CR-39 Microfilter Pores 219
(M. Berndt, J. Krause, G. Siegmon, R. Beaujean, W. Enge)

Nuclear Track Filters Made of Quartz Crystals, to be Used in Environmental Protection 220
(M. Plachky, G. Tress, E.U. Khan, P. Vater, R. Brandt, W. Holländer)

The Gas Flow through Mica Nuclear Track Microfilters: Experiments and Calculations Using a Capillary Model 221
(G. Tress, P. Vater, R. Brandt)

Secondary Ion Emission from Amino-Acids as Function of Projectile Velocity 222
(O. Becker, W. Knippelberg, K. Wien)

A Research Program for Studying the Use of Ion Beam Techniques for Corrosion Protection 223
(H. Ferber, W. Ensinger, A. Meger, Ph. Munn, G.K. Wolf, H. Folger)

Hydrogen Trapping in Ion-Bombarded Iron Studied by the $^{1}H(^{15}N,\alpha\gamma)^{12}C$-Reaction 224
(G. Frech, G. Reiss, G.K. Wolf)

Improved Mechanical Properties of Ion Bombarded Press Tools 225
(G.K. Wolf, B. Traving)

4. Developments

4.1 Target and Stripper Technology, Chemical Procedures

Preparations of Heavy-Ion Targets 228
(H. Folger, W. Hartmann, J. Klemm, W. Thalheimer)

The Medium-Current Mass Separator 229
(K.H. Behr, A. Brünle, C. Bruske, K. Burkhard, M. Chen, W. Hüller, R. Kirchner, F. Nickel, E. Roeckl)

Continuous Gaschemical Separations of Nuclear Reaction Products with Fluorinating Agents 230
(U. Hickmann, N. Trautmann, G. Herrmann)

Preparation and Gaschromatographic Separation of Actinide Hexafluoracetylacetonates 231
(N. Greulich, N. Trautmann, G. Herrmann)

PAGE

Determination of Adsorption Enthalpies for Polonium on Metal Surfaces by On-Line Isothermal Gaschromatography 232
(H. Gäggeler, B. Eichler, N. Greulich, H. Dornhöfer)

Chemical Separation of Astatine from Bi/Pb-Targets 233
(S. Zauner, J.V. Kratz, E. Kuchinka, W. Brüchle, H. Gäggeler)

Solubility of Calcium Acetylacetonate in Methyl-tert.-butyl Ether (MTB) 234
(A. Knöchel, H. Röhl)

Further Investigations on Hydrogenated Carbon Foils 235
(H. Baumann, K. Bethge, F. Rauch, W. Reeh, H. Wirth)

4.2 Experimental Set-Ups

A Position-Sensitive Twin Ionization Chamber for Experiments at High Incident Energies 236
(G. Augustinski, H.J. Beeskow, H.W. Daues, A. Gobbi, S. Gralla, K.D. Hildenbrand, J. Kuzminski, M. Ludwig, W.F.J. Müller, A. Olmi, W. Quick, H. Sann, H. Stelzer, J. Toke)

Position-Sensitive Scintillation Detectors for Light Charged Particles 237
(N. Herrmann, A. Gobbi, S. Gralla, K.D. Hildenbrand, J. Kuzminski, M. Ludwig, W.F.J. Müller, A. Olmi, W. Quick, H. Stelzer, J. Toke)

A New Heavy Ion Lanterne 238
(G. Augustinski, H.J. Beeskow, H.W. Daues, U. Lynen, H. Stelzer, R. Wada)

A Set-Up for Coincidence Measurements between π^0s and Forward Going Charged Particles from Intermediate Energy Nuclear Collisions 239
(A. Oskarsson, P. Grimm, E. Grosse, H. Heckwolf, Ch. Michel, H. Noll)

Calibration Measurements and Monte Carlo Calculations for a Lead Glass Cerenkov Detector 240
(H. Noll, Ch. Michel, C. Brendel, E. Grosse, O. Klepper, W.F.J. Müller, W. Rösch, H. Stelzer)

A Forward Scintillator Hodoscope for the Streamer Chamber Facility 241
(R. Brockmann, J.W. Harris, M. Maier, A. Sandoval, R. Stock, H. Ströbele, R.E. Renfordt, D. Schall, D. Bangert, W. Rauch, P. Eitner, G. Odyniec, H.G. Pugh, A. Dacal, M. Ortiz)

PAGE

Automatic Track Measurement on Streamer Chamber Pictures with High Multiplicity Events 242
(D. Schall, K. Tittel, H. Ströbele)

A New High Precision Recoil Distance Plunger Apparatus 243
(H. Emling, F. Azgui, H. Grein, G. Seiler-Clark, H. Sitta)

Design of a High Performance Compton Suppression Spectrometer 244
(Ch. Michel, F. Azgui, H. Emling, H. Grein, E. Grosse, H.J. Wollersheim)

An Electrostatic Separator Designed for the NaI Crystal Ball Spectrometer 245
(W. Bonin, M. Dahlinger, D. Habs, B. Schwartz, H. Grösch, R.S. Simon)

ROMA - A Rotating Wheel Multidetector Apparatus used in Experiments with ^{254}Es as a Target 246
(K. Sümmerer, M. Brügger, W. Brüchle, H. Gäggeler, E. Jäger, M. Schädel, D. Schardt, E. Schimpf)

The Status of ARCA - Automated Rapid Chemistry Apparatus 247
(W. Brüchle, M. Brügger, B. Haefner, M. Schädel, E. Schimpf)

High Resolution Detection System for Positron Studies with the "Orange"-β-Spectrometer 248
(E. Berdermann, J. Kemmer, P. Kienle, H. Tsertos, W. Wagner, F. Bosch, C. Kozhuharov, W. Koenig)

An Alkali Atomic Beam for Charge Exchange in Collinear Laser Spectroscopy 249
(G. Berthes, G. Huber, R. Menges, H. Lochmann, G. Ulm)

The Scanning Ion Microscope - A Progess Report 250
(B.E. Fischer, H. Bräuer)

4.3 Detectors

Further Developments on Gas-Filled Heavy Ion Detectors 253
(N. Shenhav, H. Stelzer)

Tests of an Ionization Chamber Designed for Bragg-Curve Spectroscopy 254
(U. Helm, C. Schmitt, C.-C. Sahm, H.-G. Clerc)

PAGE

Luminescence Processes in Heavy-Ion Excited Scintillation Gases and Bragg-Curve Spectrometry with a Scintillation Drift Chamber 255
(F.-J. Hambsch, P. Grimm, M. Mutterer, J. Pannicke, J.P. Theobald)

Light Particle Detection by BGO-Scintillators with Photodiode Readout 256
(R. Glasow, K.H. Kampert, H. Löhner, G. Gaul)

A Low Mass Multistep Zero Degree Detector for Studies of the Multifragmentation of Relativistic Nuclei 257
(R. Albrecht, H.W. Daues, M. Doss, H.-A. Gustafsson, H.H. Gutbrod, K.H. Kampert, B.W. Kolb, H. Löhner, B. Ludewigt, A.M. Poskanzer, H.G. Ritter, H. Stelzer, H. Wieman)

Time-Of-Flight Measurements with Plastic-Ball Modules 258
(H.-A. Gustafsson, H.H. Gutbrod, B.W. Kolb, B. Ludewigt, A.M. Poskanzer, H.G. Ritter, H. Wieman, R. Glasow, K.H. Kampert, H. Löhner)

Investigation of the ^{238}U Ion Tracks Registered in ChaoYang No. 1 Polycarbonate 259
(T.-S. Kang, P.-J. Zhai)

Etching Rates along Heavy Ion Latent Damage Trails 260
(H.A. Khan, N.A. Khan)

Studies of Etched Channels in Hostaphan and CR-39 Plastic Track Detectors 261
(H.A. Khan, N.A. Khan, R. Brandt)

Limitation of Conventional Geometry Factor Formulae when Used for "Source-Solid State Track Detector" Systems 262
(H.A. Khan, N.A. Khan)

A Result of Stochastic Geometry for Track-Etching Dosimetry 263
(A.M. Kellerer, H. Roos)

Are Long Tracks in Meteoric Olivines Possibly Due to SHE in Cosmic Rays? 264
(R. Dersch, E.U. Khan, P. Vater, E.M. Friedlander, V.P. Perelygin, R. Brandt)

Tracks of Heavy Ions in Evaporated Selenium-Films 265
(B. Pischel, F. Granzer)

Radiochromic Detectors as a Tool to Monitor Heavy Ion Particle Fluence 266
(E. Schneider, G. Döll, M. Kost, G. Lenz)

PAGE

4.4 Electronics, Computing Center and Workshops

Experimental Electronics Department
(Elektronik/Experimente) 267
(R. Albrecht, J. Dengler, G. Eidmann, H.-G. Essel, A. Fehres, H. Hammal, H. Hardel, J. Hoffmann, H.P. Liebold, H.-G. Martens, W. Meufels, K. Mömerzheim, K. Poppensieker, A. Przybyla, D. Quis, M. Richter, H.-G. Schmidt, G. Schneider, R. Schulze, K. Senft, E. Sturm)

Development of an Hybrid Current Sensitive Preamplifier VT130 for the 0°-Multiwire Detector of the Plastic Ball 269
(R. Albrecht, R. Schulze)

Performance of the GSI Constant Fraction Discriminators CF4000 and CF8000 270
(R. Albrecht, O. Althoff, A. Höhler, R. Schulze)

A Programmable Pulse Distributor for 32 Detectors 271
(W. Brüchle)

Determination of Matrix Elements from Multiple Coulomb Excitation Experiments 272
(H. Grein, H. Emling, J. Stachel)

MONA, A Data Acquisition System for VAX Computers 273
(B.W. Kolb)

GOOSY, A New Acquisition and Analysis System for Experiment Data 274
(F. Busch, H.-G. Essel, H. Göringer, H. Grein, V. Hartmann, J. Hoffmann, J. Lowsky, D.C. Marinescu, W.F.J. Müller, M. Richter, G. Schneider, K. Winkelmann)

Computing Center 275
(H. Egger, S. Glückert, H. Hultzsch, J. Lowsky, O. Siart)

Experiment Data Processing 281
(F. Busch, D. Croome, H. Göringer, V. Hartmann, J. Lowsky, D. Marinescu, K. Winkelmann, G. Zaidman)

An Inter-Address Space Communication Sub-System for MVS 282
(D.C. Marinescu, H. Hultzsch, J. Lowsky)

The Free Form Conditions in SATAN 283
(H. Göringer)

PAGE

The Concept of Common Data Structures in SATAN 284
(V. Hartmann, G. Zaidman)

Enhancements to the SIMPLE Preprocessor 285
(D. Croome, K. Winkelmann)

Foil Generator 286
(W. Kynast)

Graphics and Numeric Operating Method (GNOM) 287
(I. Giese, W. Kynast, M. Feyerabend, H. Chytrek)

AGF Plotfile Interpreter 288
(I. Giese, K. Schwinn)

Data Management 289
(C. Besthorn, G. Schuette, O. Siart)

Enhancements in Telecommunications 290
(F. Busch)

User and System Interfaces for Communication 291
(U. Ernst)

Engineering and Technology 292
(E. Malwitz, K. Blasche, W. Bleuel, H. Gaiser, C. Hoffmann, K. Illert, H.-R. Kiesewetter, U. Kopf, W. Schmidt)

Electroplating Workshop 295
(H. Gaiser, H. Eckhardt, K. Blasche)

5. Accelerator

5.1 UNILAC Performance and Ameliorations

Unilac Operation 298
(N. Angert, G. Hutter, J. Klabunde, M. Müller, P. Strehl, D. Wilms)

Unilac Injector 299
(M. Müller, W. Jacoby, M.M. Khaouli, J. Bossler, H. Emig, N. Hofmann, K.-D. Leible, M. Stork, H. Krichbaum, H.-P. Kurz, R. Rulfs, K. Schneider)

The PIG Source "Sputtershort" Circuit 300
(M. Müller, M.M. Khaouli, R. Rulfs)

Improvements to the Unilac RF System 301
(G. Hutter, W. Gutowski, W. Hartmann, G. Kube, A. Morhardt, H. Valter, W. Vinzenz)

Tests of a New 1.6 MW/108 MHz Amplifier-Powertube Combination 302
(G. Hutter, K.H. Knobbe, I. Beling, J. Denteler)

PAGE

1.5 MHz / 4.5 MHz RF-Chopper for the Unilac 303
(W. Gutowski, G. Hutter)

Longitudinal Emittance Measurements 304
(P. Strehl)

Unilac Beam Diagnostics with Particle Detectors 305
(A. Ziem, P. Borisch)

Capacitive Pick-Up Versus Inductive Loop Monitor 306
(H. Vilhjalmsson, M. Witzky)

The Beam Structure Demodulator - A Nondestructive Current Monitoring System - 307
(N. Schneider)

A Control System for the Unilac Injector 308
(W. Jacoby, M.M. Khaouli, M. Müller)

Development of a Pulsed Power-Supply 309
(G. Breitenberger, R. Steiner)

An ECR Source for Highly Stripped Ions 310
(H. Schulte)

5.2 Accelerator Projects

SIS - The Synchrotron Facility for Heavy Ions 311
(K. Blasche, D. Böhne, B. Franzke, H. Prange, R. Steiner)

Multiturn-Injection for High Currents 312
(H. Eickhoff)

A Novel Method of Bunching Slowly Extracted Synchrotron Beams 313
(B. Franzke)

On the Ion Optical Transfer Matrix of Dipole Magnets as Given by the Shape of Their End Fields 314
(B. Langenbeck)

MIRKO - An Interactive Program for Beam Lines and Synchrotrons 316
(B. Franczak)

Energy, Luminosity and Current Limits for a Heavy Ion Collider 318
(K. Blasche)

Status of the SIS 18 Injection System 320
(W. Bourgeois, H. Eickhoff, B. Franzke)

Design of the Electrostatic Injection Septum for SIS 18 321
(W. Bourgeois, H. Eickhoff, B. Franzke)

PAGE

Activities on the SIS Prototype Accelerating Station 322
(M. Emmerling, K. Kaspar, A. Gasper)

Beam Loading and Beam-Cavity Interactions in the SIS Cavities 323
(K. Kaspar)

New Configuration of the Bias Windings in the SIS Prototype Cavity 324
(K. Kaspar, M. Emmerling)

Tests of the Control Loops of the SIS Prototype Accelerating Station 325
(M. Emmerling, K. Kaspar)

Report of the Ultra High Vacuum Activities 326
(P. Finke, A. Kritzer, H. Prange)

SIS-Controlsystem 327
(H. Brandis, R. Kühn, E. Schaffner)

Finite-Element Calculations in Accelerator Design 330
(C. Riedel)

6. Inertial Confinement Fusion

A Revision of the HIBALL Driver Accelerator 332
(I. Hofmann, R.W. Müller)

Study on the SITAR-Storage Ring Experiment 333
(I. Hofmann, K. Beckert, D. Böhne, B. Franzke, R.W. Müller)

An Improved Criterion for Stability of Coherent Motion in Circular Accelerators 334
(K. Beckert, H. Eickhoff, V.G. Vaccaro)

Nonlinear Phenomena in Computer Simulation of the Microwave Instability 335
(I. Hofmann, I. Bozsik)

High-Current Ion Sources Development 336
(R. Keller, P. Spädtke)

Computer Simulation of High-Current DC Beam Transport 337
(P. Spädtke)

Pre-Acceleration of High-Current DC Ion Beams 338
(P. Spädtke, H. Emig, R. Keller, J. Klabunde, K.-D. Leible, D. Vogt, B. Wolf)

Developments in the High-Current Hollow Beam Test Experiment 339
(P. Kreijcik, R. Keller, P. Spädtke)

PAGE

Heavy Ion RFQ Accelerator "MAXILAC" 340
(R.W. Müller, U. Kopf, J. Bolle, S. Arai, P. Spädtke)

Development of Split Coaxial RFQ-Resonators 341
(H. Klein, W. Neumann, H. Deitinghoff, P. Junior, K. Langbein, P. Leipe, G. Riehl, A. Schempp, R.W. Müller)

Drift-Tube Geometry Optimization 342
(J. Ungrin)

K-V and Gauss Distributions at Increasing Intensities 343
(J. Struckmeier, J. Klabunde, M. Reiser)

Emittance Growth Due to a Change of the Particle Distribution 344
(J. Struckmeier, J. Klabunde, M. Reiser)

Transport of Intense Ion Beams in a Quadrupole Doublet 345
(A. Schönlein, J. Klabunde)

Experimental Results of the Beam Transport Experiment at GSI 346
(J. Klabunde, A. Schönlein, J. Struckmeier, P. Spädtke)

X-Ray Production in Collisons of Relativistic Heavy Ions and Atoms 347
(R. Anholt, W.E. Meyerhof, J.D. Molitoris, C. Stoller, H. Bowman, J. Rasmussen, J.-S. Xu, D.H.H. Hoffmann)

Radiative Electron Capture by Relativistic Heavy Ions 348
(R. Anholt, W.E. Meyerhof, C. Stoller, J.D. Molitoris, H. Bowman, J. Rasmussen, J.-S. Xu, D.H.H. Hoffmann)

Precision X-Ray Wavelength Measurements in Few-Electron Argon Recoil Ions 349
(H.F. Beyer, R.D. Deslattes, R.E. LaVilla, P.H. Mokler, F. Folkmann, K.-H. Schartner)

Position-Sensitive Proportional Counter for X-Ray Spectroscopy 350
(H.F. Beyer, R.D. Deslattes)

Growth of Foil Distortions in Rayleigh-Taylor Instable Configurations 351
(G. Buchwald, D. Barthel, J. Cieza, J.A. Maruhn)

Critical Thickness of Foils in Raleigh-Taylor Instable Configurations 352
(G. Buchwald, D. Barthel, J. Cieza, J.A. Maruhn)

7. Annex

		PAGE
7.1	Scientific Activities outside GSI	
7.1.1	Publications	354
7.1.2	Conference Contributions	366
7.1.3	Seminars at other Institutes	382
7.1.4	Lectures and Courses	391
7.2	Scientific Activities within GSI	
7.2.1	Conferences and Seminars on Research Proposals	392
7.2.2	Seminars at GSI	393
7.2.3	GSI-Preprints	396
7.2.4	GSI-Reports	398
7.2.5	Visiting Groups at GSI	399
7.3	Scientific Committees, Directorate and Personal	400
7.4	Scientific Cooperation	403
7.5	Author Index	408

SURVEY

OF EXPERIMENTS AT GSI

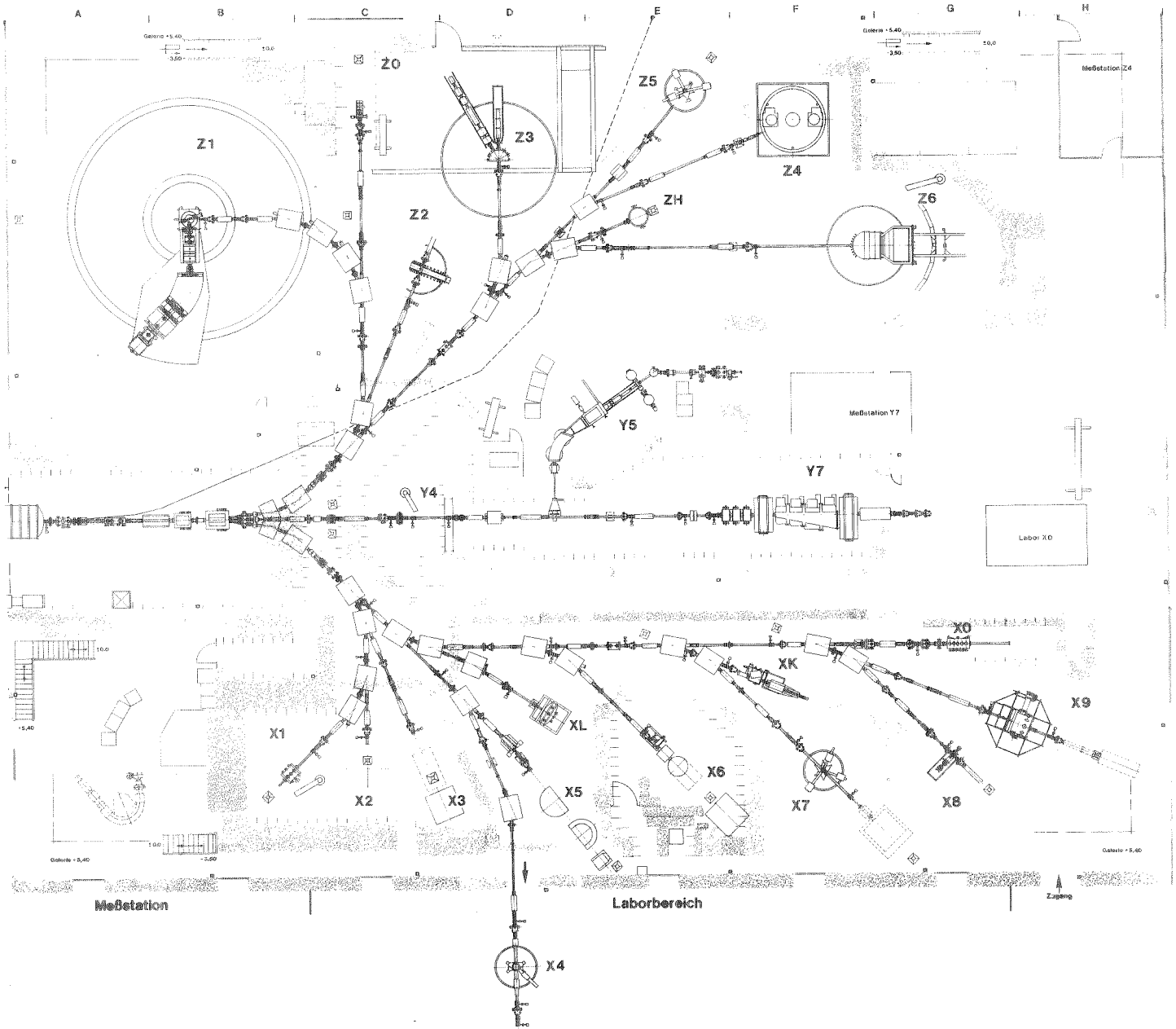
IN 1983

	Exp. Nr.	Authors	Affiliation	Title	Beam-time (d)	Ions	Corresp. Article on Page
Nuclear Physics/ Nuclear Chemistry	4	Gäggeler et al.	GSI, Univ. Mainz	Search for Superheavy Elements	1.0	^{40}Ar	84
	35	Heusch, Schneider, Freiesleben, Stege, Kohlmeyer, Pühlhofer	GSI, Univ. Bochum, Univ. Marburg, CRN Strasbourg	Quasifission in the System $^{84}Kr + ^{27}Al$	1.3	^{84}Kr	14
	141	Hildenbrand, Bock, Schneider, Schüll, Busch, Freiesleben	GSI, Univ. Bochum, Univ. Marburg	Diffusion of Nucleons near Closed Shells	1.4	$^{144, 154}Sm$	-
	183	Theobald, Brülls, Gobbi, Hollenbach, Mutterer, Pannicke, Weingärtner	GSI, TH Darmstadt	Heavy-Ion Collisions Accompanied by Particles	2.1	^{208}Pb	27
	201	Huber, Lochmann, Ulm, Kirchner, Marx, Klepper, Kühl	GSI, Univ. Mainz	Laser-Spectroscopy of Fusion Products	3.9	^{16}O, ^{14}N	67
	205	Kleinheinz, Kirchner, Klepper, Larsson, Roeckl, Schardt, Zuber	GSI, KFA Jülich	Investigation of Very Neutron-Deficient Isotopes of Lanthanum	3.8	^{58}Ni	-
	208	Clerc, Sahm, Keller, Münzenberg, Reisdorf, Schmidt	GSI, TH Darmstadt	Cold Fusion	1.9	^{90}Zr	2, 3, 4
	216	Beier, Friese, Henning, Kienle, Körner, Mayer, Wagner	TU München	Multi-Nucleon Transfer as a Function of Incident Energy	3.8	^{238}U	22
	218	Spreng, Azgui, Emling, Grosse, Kulessa, Michel, Simon, Wollersheim, Mutterer, Theobald, Schwalm, Moore	GSI, TH Darmstadt	Investigation of the Back-bending in ^{242}Pu and ^{244}Pu by γ-γ -Coincidence Measurements	3.6	^{208}Pb	65, 66
	221	von Oertzen, Gebauer, Bohlen, Miczaika, Schüll	GSI, HMI Berlin	Neutron Transfer	2.8	^{120}Sn	19
	234	Schmidt-Ott, Klepper, Kirchner, Kurcewicz, Schardt, Gippert, Runte, Tidemand-Petersson, Kaffrell, Peuser, Bernas, Dessagne, Langevin, Rykaczewski	GSI, Univ. Mainz, Univ. Göttingen, IPN Orsay, Univ. Warsaw	Investigation of Neutron-rich Isotopes of Elements Mn to Cu at the GSI On-Line Mass Separator	3.6	^{82}Se, ^{238}U	70
	241	Schädel, Brüchle, Gäggeler, Kratz, Sümmerer, Wirth, Gehmecker, Trautmann	GSI, Univ. Mainz	Effects of the Entrance Channel on the Production of Heavy-Isotopes of Actinides in Damped Heavy-Ion Collisions	1.3	^{197}Au	85

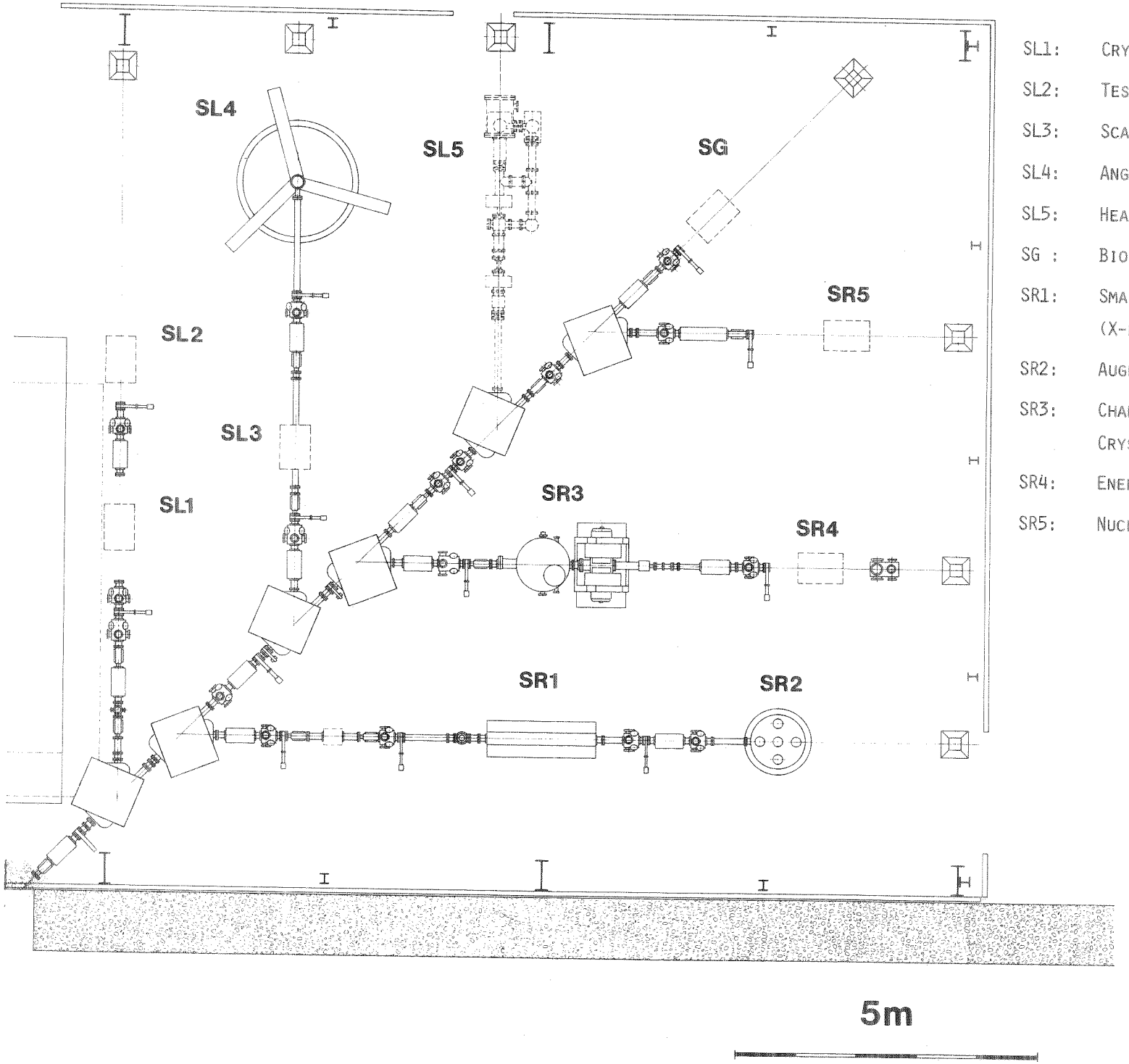
	Exp. Nr.	Authors	Affiliation	Title	Beam-time (d)	Ions	Corresp. Article on Page
Nuclear Physics/ Nuclear Chemistry	259	Pühlhofer, Keim, Kohlmeyer, Stege, Bösser, Schneider	GSI, Univ. Marburg	Fusion Reactions at Energies between 10 and 20 MeV/u	3.2	^{48}Ti	26
	261	Hildenbrand, Gobbi, Gralla, Kuzminski, Lynen, Müller, Olmi, Sann, Stelzer, Toke, Wollersheim, Maurenzig, Stefanini, Petrovici, Santo	GSI, Univ. Florenz, IPNE Bucharest, Univ. Münster	Fast Dissipative Collisions	2.9	$^{92,100}Mo$	28, 29, 30, 31
	263	Emling, Grosse, Michel, Wollersheim, Schwalm, Kulessa	GSI, Univ. Heidelberg, Univ. Krakau	Shape Transitions in Nuclei in the Light Rare Earth Region	1.3	^{132}Xe	63
	276	Hofmann, Armbruster, Heßberger, Reisdorf, Münzenberg, Schneider	GSI	Search for Further Proton Emitters in the Region of Neutron-deficient Isotopes of the Rare Earth Elements	4.6	^{40}Ca, ^{58}Ni	73
	280	Klepper, Kirchner, Kurcewicz, Larsson, Roeckl, Komninos, Nolte, Zganjar	GSI, TU München, Univ. Louisiana	Spectroscopy of Palladium to Indium Isotopes Close to the Doubly-Magic Nucleus ^{100}Sn	1.3	^{40}Ca	69
	292	Beer, Walter, Kirchner, Klepper, Kurcewicz, Roeckl, Schardt, Gippert, Schmidt-Ott	GSI, KfK Karlsruhe, Univ. Göttingen	Measurement of the Decay-Chain $^{180}Lu \rightarrow {}^{180}Hf^{m}$ to Investigate the Formation of $^{180}Ta^{m}$	0.9	^{136}Xe	75
	293	Lützenkirchen, Kratz, Brüchle, Brügger, Gäggeler, Sümmerer, Wirth, Lucas, Poitou	GSI, Univ. Mainz, CEN Saclay	Angle-Dependence of the Symmetric Fragmentation of $^{54}Cr + {}^{208}Pb$	1.1	^{50}Ti	25
	294	Guidry, Barette, Riedinger, Bingham, Baktash, Lee, Stachel, Emling, Grosse, Wollersheim	GSI, CEN Saclay, Univ. Tennessee, Oak Ridge, Univ. Mainz	Simultaneous Nucleon Transfer and Coulomb-Excitation	1.9	^{161}Dy	62
	295	Lazzarini, Vandenbosch, Metag, Olmi, Gobbi, Hildenbrand, Müller	GSI, Univ. Gießen, Univ. Washington	Spin-Spin Correlations in Deeply Inelastic Collisions	4.0	^{238}U, ^{132}Xe	-
	296	Harrach, Glässel, Specht, Wallenwein	Univ. Heidelberg	Investigation of Fast Multi-Body Processes	3.9	^{129}Xe	8, 9, 10
	297	Münzenberg, Agarwal, Armbruster, Heßberger, Hofmann, Poppensieker, Sahm, Reisdorf, Schneider, W. Schneider, Schmidt, Vermeulen, Ghiorso, Moody	GSI, TH Darmstadt, LBL Berkeley	Formation of Superheavy Elements by Fusion	16.3	^{48}Ti, ^{48}Ca	79

	Exp. Nr.	Authors	Affiliation	Title	Beam-time (d)	Ions	Corresp. Article on Page
Nuclear Physics/ Nuclear Chemistry	298	Gäggeler, Brüchle, Brügger, Schädel, Sümmerer, Wirth, Frink, Greulich, Hickmann, Hildebrand, Kratz, Trautmann, Herrmann, Dornhöfer, Gunten v., Hoffman, Daniels, Ghiorso, Lee, Moody, Seaborg	GSI, Univ. Mainz, Univ. Göttingen, Univ. Bern, LANL, LBL Berkeley	Production of Heavy and Superheavy Elements in the $^{48}Ca + ^{248}Cm$ Reaction	10.2	$^{40,48}Ca$	82, 85
	300	Ernst, Morinaga, Nolte, Korschinek, Kubik, Henning, Roecki, Schüll	GSI, TU München, Argonne NL	Accelerator Based Mass-Spectrometry	1.0	^{205}Tl	76
	302	Esterlund, Jäckel, Rox, Westmeier, Schulte, Patzelt	Univ. Marburg	Is $^{63}Cu + ^{197}Au$ the Dynamic Twin of $^{56}Fe + ^{238}U$?	1.1	^{197}Au	16
	304	Emling, Björnholm, Borggreen, Pedersen, Sletten, Azgui, Wollersheim	GSI, NBI Kopenhagen	Search for Yrast Traps in Prolate Hf- W- and Os-Isotopes	2.8	^{136}Xe	-
	305	Schädel, Gäggeler, Schardt, Sümmerer, A. Dougan, R. Dougan, Hulet, Landum, Lougheed, Wild	GSI, LLNL	Exploration of Actinide and Transactinide Nuclei in Heavy-Ion Reactions with ^{254}Es	7.7	$^{16,18}O$, ^{22}Ne	15, 78
	308	Pühlhofer, Bangert, Kohlmeyer, Schüll, Schneider, Freiesleben	GSI, Univ. Marburg, Univ. Bochum	Mass-and Charge- Transfer in the Reaction of $^{70}Ge + ^{232}Th$	5.1	^{70}Ge	18
Atomic Physics	15	Kienle, Berdermann, Bosch, Clemente, Kozhuharov, König, Tsertos, Wagner	GSI, TU München, Univ. Heidelberg	Positron-Spectroscopy	4.8	^{238}U	148
	184	Beyer, Mann, Folkmann, Mokler, Scharmann, Schartner	GSI, Aarhus, Univ. Gießen	High Resolution X-Ray Spectroscopy	1.0	U	349
	245	Silver, Moscatelli, Duval, Klein	Univ. Oxford	Lamb Shift Measurements in High Z Hydrogenic Ions	1.0	Fe,Kr	161
	247	Kozhuharov, Bosch, Armbruster, Clemente, Kienle, Koenig, Martin, Tsertos, Wagner	GSI, TU München, MPI Heidelberg	Spectroscopy of High-Energetic δ-Electrons Emitted in Collisions of Pb with U- and Th-Targets	2.8	Pb	151
	260	Beyer, Bosch, Dohmann, Deslattes, Liesen, Mokler, Schartner	GSI, Univ. Gießen, NBS	Direct Measurements of 2s1/2-2p1/2 Lambshift in Hydrogen-Like Krypton	2.0	Kr	160

	Exp. Nr.	Authors	Affiliation	Title	Beam-time (d)	Ions	Corresp. Article on Page
Atomic Physics	281	Oeschler, Bozek, Gollerthan, Klotz, Kankeleit, Krämer, Krieg, Meyer, Senger	TH Darmstadt, Univ. Krakau	Positron- and Electronspectroscopy after Heavy-Ion Interaction at the TORI-Spectrometer	4.9	^{238}U	150
	285	Schuch, Konrad, Schulz, Mokler, Schadt, Schmidt-Böcking, Hoffmann, Justiniano	GSI, Univ. Heidelberg	Experiments of Slow-Down Hydrogen-Like Ge-Ions	2.1	Ge	155
	288	Koenig, Martin, Soltani, Kozhuharov, Mann, Mokler	GSI, MPI Heidelberg	1s-Atomic Binding Energies of Few Electron Projectiles Determined by Conversion Electron Spectroscopy	2.4	Gd	159
	290	Schönfeldt, Hoffmann, Mokler	GSI	Electron-Capture into Excited Levels of Highly-Ionized Heavy Ions at Low Velocity	2.6	Sm	157
	299	Greenberg, Bokemeyer, Folger, Grein, Kido, Cowan, Schweppe, Bethge, Gruppe, Stiebing, Schwalm, Vincent, Backe, Begemann, Klüver, Trautmann	GSI, Univ. Yale, Univ. Frankfurt, Univ. Heidelberg, Univ. Mainz, Rutgers Univ.	Study of e^+-Creation in Superheavy Quasiatomic Systems	7.6	^{238}U	149
	Test	Ulrich, Kienle, Murnick, Hoffmann, Perlow	GSI, TU München, Bell Lab., Argonne NL	Heavy Ion Beam Pumped Laser	1.0	Xe	156
Solid State Physics/ Biology and Applied Heavy Ion Research	var.	Coordinator: Kraft	GSI	Biology	1.6	various	194-209
	var.	Coordinator: Spohr	GSI	Nuclear Tracks	2.7	various	210-221
	214	Kiesewetter, Spohr, Roggenkamp	GSI, RWTH Aachen	Single Pore Membrane	3.3	Xe, U	217



X1	Irradiation Experiments
X2	Variing Equipment
X3/4	Set-ups for Atomic Physics
X5/L	Set-ups for Atomic Physics
X6	Variing Equipment
X7	γ-γ-Correlation Measurements
X8/9	$e^{\pm}$- Spectrometers
XK	Charge Changing Processes
X0	Irradiation Facility
Y4	Irradiation Experiments
Y5	On-line Isotope Separator
Y7	Velocity Separator 'SHIP'
Z0	Irradiation Experiments
Z1	Magnetic Spectrograph
Z2	$e^{\pm}$- Spectrometer
Z3	TOF Telescope
Z4	Many Particle Telescope
Z5	Variing Equipment
Z6	Kinematic Coincidence Telescope
ZH	Facility for Polarized γ's



SL1: CRYSTAL SPECTROMETER

SL2: TEST POSITION

SL3: SCATTERING CHAMBER

SL4: ANGULAR CORRELATION

SL5: HEAVY ION MICROPROBE

SG : BIOLOGICAL EXPERIMENTS

SR1: SMALL ANGLE SCATTERING (X-RAY PARTICLE COINCIDENCE)

SR2: AUGER SPECTROMETER

SR3: CHARGE CHANGING COLLISIONS, CRYSTAL SPECTROMETER

SR4: ENERGYLOSS EXPERIMENTS

SR5: NUCLEAR TRACK EXPERIMENTS

1. Nuclear Physics/Nuclear Chemistry	PAGE
1.1 Nuclear Reactions	2
1.1.1 Reactions near the Coulomb-Barrier	2
1.1.2 Reactions above the Coulomb-Barrier	23
1.1.3 Nuclear Reactions at High Energies	38
1.2 Nuclear Structure	57
1.3 Exotic Nuclides	67
1.4 Theory	87
1.4.1 Nuclear Structure and Decay	87
1.4.2 Nuclear Reactions at Low Energies	96
1.4.3 Nuclear Reactions at High Energies	125

^{90}ZR INDUCED SUBBARRIER FUSION REACTIONS [B]

J.G.Keller, K.-H. Schmidt, W. Reisdorf, F.P. Heßberger, G. Münzenberg, H. Stelzer
Gesellschaft für Schwerionenforschung,GSI, Darmstadt
H.-G. Clerc, C.-C. Sahm
Institut für Kernphysik, Technische Hochschule, Darmstadt

The fusion of ^{90}Zr with ^{90}Zr, ^{92}Zr and ^{96}Zr was investigated by using the velocity filter SHIP in combination with time-of-flight-ΔE-E methods. Experimental details have been given previously.[1] The evaporation residue excitation functions are shown in fig. 1. The data are not yet corrected for the acceptance of the velocity filter. This correction will increase the cross sections by a factor varying from 2 to 4. The results for the three systems differ considerably. For energies above the barrier, the cross sections reflect the variation of the fission barrier which increases with increasing mass of the Hg isotopes. The observed evaporation residue cross sections saturate at those angular momentum values, where the fission barrier is about equal to the neutron binding energy. For energies below the barrier, however, the influence of the different fission barriers is expected to be rather weak. The subbarrier fusion cross section increases drastically with the distance of the target isotopes from the N=50 shell.

The influence of the collective properties of the different target isotopes on the fusion cross section was estimated by use of a coupled channel calculation for inelastic excitations as proposed by Broglia et al.[3] (see fig. 2) . The first 2^+ state and the first 3^- state were included. The inelastic excitations can account for the relative enhancement of the subbarrier fusion in the system ^{90}Zr + ^{92}Zr, but the further enhancement for the system ^{90}Zr + ^{96}Zr cannot be explained in this way. Fig. 3 demonstrates that the Q-values for some selected particle transfer reactions between projectile and target increase with increasing neutron number of the target isotope. In particular, the positive Q-value transfer reactions available in the ^{90}Zr + ^{96}Zr system may couple to the fusion process enhancing its subbarrier probability[4].

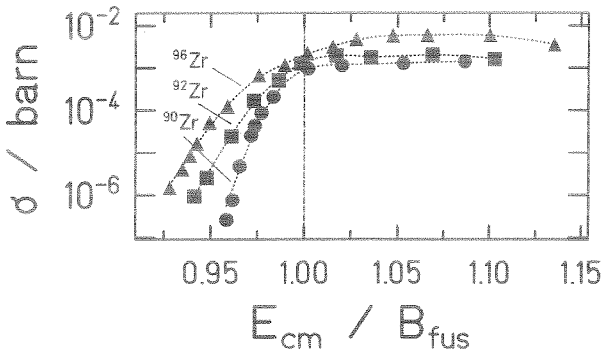


Fig. 1: Measured evaporation residue cross sections for the fusion of ^{90}Zr with ^{90}Zr, ^{92}Zr and ^{96}Zr. The data are not corrected for the acceptance of SHIP. B_{fus} is the fusion barrier esimated from the Bass potential[2].

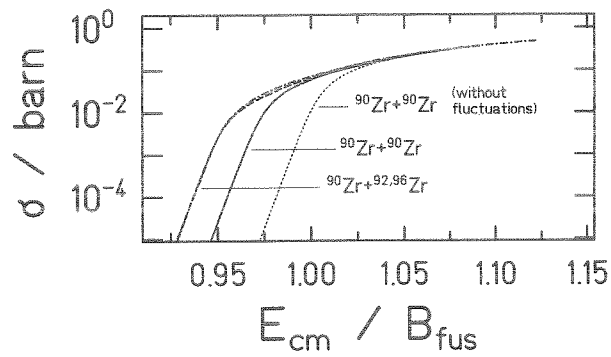


Fig. 2: Calculated fusion cross sections for the systems shown in fig. 1.

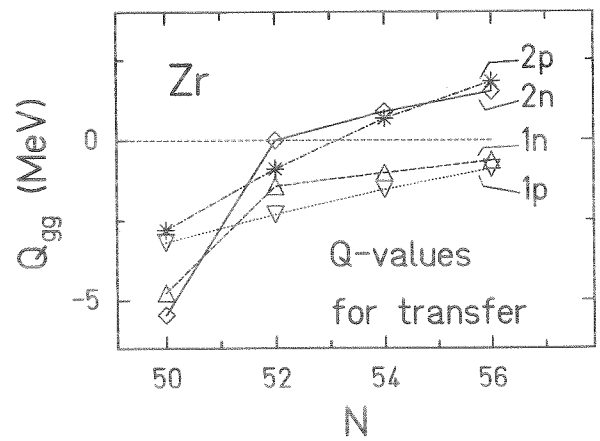


Fig. 3: Q-values for particle transfer between the ^{90}Zr projectile and the ^{90}Zr, ^{92}Zr, ^{94}Zr and ^{96}Zr target nuclei as a function of the neutron number in the target nucleus.

1. J.G. Keller, K.-H. Schmidt, H. Stelzer, W. Reisdorf, Y.K. Agarwal, F.P. Hessberger, G. Münzenberg, H.-G.Clerc, C.-C. Sahm: GSI preprint 84-4 (1984) and submitted to Phys. Rev. C
2. R. Bass: in Lecture Notes in Physics 117(1979)281, Berlin 1979
3. R.A. Broglia, C.H. Dasso, S. Landowne, G. Pollarolo: Phys. Lett. 133B(1983)34
4. R.A. Broglia, C.H. Dasso, S. Landowne, A. Winther: Phys. Rev. C27(1983)2433

RADIATIVE FUSION OBSERVED IN ^{90}ZR INDUCED REACTIONS [B]

J.G. Keller*, H.-G. Clerc+, F.P. Heßberger*, G. Münzenberg*, W. Reisdorf*,
C.-C. Sahm+, K.-H. Schmidt*
*GSI Darmstadt, +Institut für Kernphysik, TH Darmstadt

After the observation[1] of the radiative fusion process in the reaction $^{90}Zr + ^{90}Zr \rightarrow ^{180}Hg$, that is the deexcitation of the compound nucleus ^{180}Hg only by γ-radiation, the search for this cold fusion process was continued at the velocity filter SHIP. In two other cases, $^{90}Zr + ^{92}Zr \rightarrow ^{182}Hg$ and $^{90}Zr + ^{94}Mo \rightarrow ^{184}Pb$, the γ-channel could be unambiguously identified. In fig. 1, excitation functions for the three radiative fusion reactions, observed until now, are shown. In all three cases, the γ-channel was identified by the observation of the α-decay of the compound nucleus.

An interesting characteristic of the excitation functions is the shift to lower energies in the system $^{90}Zr + ^{94}Mo$ if compared to the lighter systems. Qualitatively this may be explained by the lowering of the fission barrier when passing from the Hg-isotopes to ^{184}Pb, an effect which also lowers the angular momentum range contributing to the evaporation residue cross section. The shift of about 7 MeV would just be explained by the different values of the rotational energy associated with an average angular momentum of $\ell \approx 40$ for the two lighter systems and an average value of $\ell \approx 15$ for ^{184}Pb.

In the case of $^{90}Zr + ^{90}Zr$, the cross section of the γ-channel could be reproduced by an evaporation calculation. The fusion cross section as well as the fission barriers were fixed by the requirement that he measured[2] total evaporation residue cross section must be reproduced. The γ-strength used for E1 transitions was given by 0.02 Weißkopf units × (2J+1) . This relatively strong γ-competition was not fitted to this specific case, but was also found necessary to reproduce the shape of particle evaporation channels in other systems (e.g. ref.[3]).

We conclude that the measured radiative-fusion excitation-functions may be explained in the statistical model without the need for a specific direct process. The γ-strength, however, generally needed for the reproduction of measured excitation functions for evaporation residues is much higher than generally observed in discrete E1-transitions between levels of low spin.

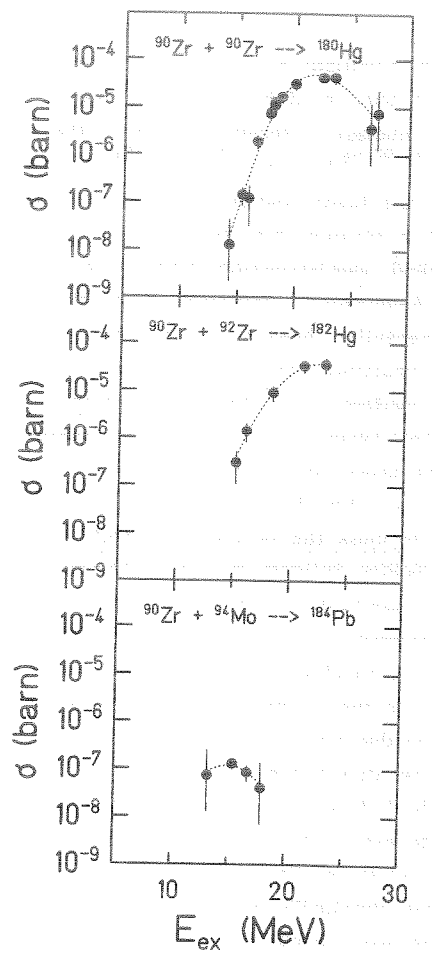


Fig.1: Measured excitation functions of the radiative fusion reaction for three different systems.

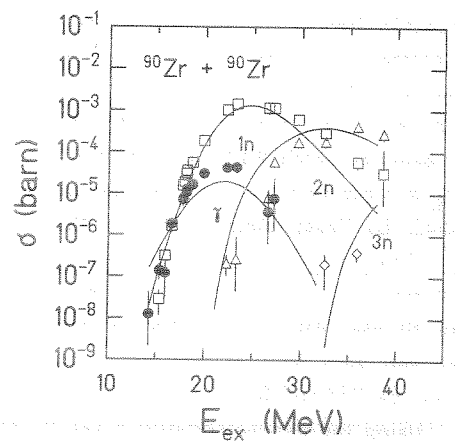


Fig.2: Data points: Measured excitation functions of the reaction $^{90}Zr(^{90}Zr,xn)^{180-x}Hg$. Lines: Result of an evaporation calculation.

1. J.G. Keller, H.-G. Clerc, K.-H. Schmidt, Y.K. Agarwal, F.P. Heßberger, R. Hingmann, G. Münzenberg, W. Reisdorf, C.-C. Sahm, Z. Phys. A 311 (1983) 243
2. J.G. Keller, K.-H. Schmidt, H. Stelzer, W. Reisdorf, Y.K. Agarwal, F.P. Hessberger, G. Münzenberg, H.-G.Clerc, C.-C. Sahm: GSI preprint 84-4 (1984)
3. W. Kühn, P. Chowdhury, R.V.F. Janssens, T.L. Khoo, F. Haas, J. Kasagi, R.M. Ronningen, Phys. Rev. Lett. 51 (1983) 1858

FUSION PROBABILITY OF SYMMETRIC HEAVY SYSTEMS [B]

C.-C. Sahm, H.-G. Clerc
Institut für Kernphysik, Technische Hochschule Darmstadt
K.-H. Schmidt, F.P. Heßberger, J. Keller, G. Münzenberg, W. Reisdorf,
D. Vermeulen
Gesellschaft für Schwerionenforschung, GSI, Darmstadt

Excitation functions for evaporation residue formation have been used to determine the probability for compound nucleus formation in the reactions $^{124}Sn + ^{92,94,96}Zr$ and $^{86}Kr + ^{123}Sb$. As reported earlier[1], the fusion barrier can be extracted from the evaporation residue cross sections, if certain conditions are fulfilled. One assumption made in ref.[1] was that the barrier penetration coefficient is of the Hill-Wheeler type. Recently, however, experimental evidence has been accumulating that this assumption is not valid for massive systems[2,3]. Therefore we tried to determine the fusion probability in a more model independent way. Since the cross section for evaporation residue formation is only a tiny fraction of the fusion cross section, one has to know the survival probability of the evaporation residues in order to extract the fusion probability. The survival probability has been measured using more asymmetric projectile-target combinations with ^{40}Ar as projectile leading to the same compound nuclei[4]. In the asymmetric reactions, both the evaporation residue cross section and the fusion cross section were determined. As the survival probability should be independent of the entrance channel, we can use it to extract the fusion probability in the case of the symmetric reactions. Since the survival probability decreases drastically with increasing angular momentum, the fusion probability determined here is valid for head-on collisions.

Fig. 1 shows the resulting fusion probability for the reactions $^{86}Kr + ^{123}Sb$ and $^{124}Sn + ^{96}Zr$. The fusion probabilities saturate at energies significantly higher than expected from a conventional barrier penetration model (dotted curves). Following the ideas of Esbensen[5] and Reisdorf[2], we describe the fusion probability by means of fluctuations of the fusion barrier with a gaussian probability distribution. The mean value V_B and the variance σ^2 of the fusion barrier were determined by least square fits to the data (full curves). The shift of the barrier (with reference to a potential reproducing the Ar induced reactions) necessary to fit the data is 9±2 MeV for the Kr-induced reaction and 26±4 MeV in the Sn-induced reaction. This may be interpreted in terms of the extra push model[6]. Using the parameterization given in ref.[7], one would expect an extra push of 3 and 11 MeV for the Kr and the Sn induced reaction, respectively.

The finding of an extra push for the systems investigated here indicates that the measured fusion probability may not be interpreted as the transmission of the fusion barrier, but the fusion probability may rather be determined by the dynamical evolution from the contact figuration to the compound nucleus.

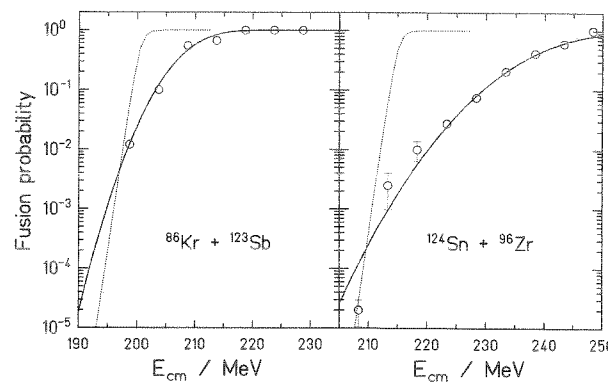


Fig. 1: Open circles: experimental fusion probability for head-on collisions.
Dotted curves: conventional barrier penetration model.
Full curves: fitted fusion probability parametrized with the barrier V_B and barrier fluctuations σ with gaussian distributions.
$^{86}Kr+^{123}Sb$: V_B=209±3 MeV, σ/V_B=2.2%
$^{124}Sn+^{96}Zr$: V_B=241±4 MeV, σ/V_B=3.7%

1. K.-H. Schmidt et al.: Z. Phys. A301,21(1981)
2. W. Reisdorf et al.: Phys. Rev. Lett. 49,1811(1982)
3. M. Beckerman et al.: Phys. Rev. C25,837(1982)
4. H.-G. Clerc et al.: Nucl. Phys. A, (1984) (in press) and D. Vermeulen et al.: to be published
5. H. Esbensen: Nucl. Phys. A352,147(1981)
6. S. Bjørnholm, W.J. Swiatecki: Nucl. Phys. A391,471(1982)
7. R. Bock et al.: Nucl. Phys. A388,334(1982)

Production Cross Sections for Neutron Deficient Th-Isotopes in the Reactions $^{48}Ca+^{172,173,176}Yb$

C.-C. Sahm, H.-G. Clerc
Institut für Kernphysik, Technische Hochschule Darmstadt
K.-H. Schmidt, Y.K. Agarwal*, P. Armbruster, F.P. Heßberger, S. Hofmann, G. Münzenberg, W. Reisdorf, D. Vermeulen
Gesellschaft für Schwerionenforschung, GSI, Darmstadt

Recently an intense ^{48}Ca-beam has become available at the UNILAC. This allowed an extension of our previous systematic study[1] of production cross sections for neutron deficient thorium isotopes in ^{40}Ar-induced fusion reactions to ^{48}Ca-induced fusion reactions.
In the reactions $^{48}Ca+^{172,173,176}Yb$ the nuclei $^{216,217,220}Th$ were produced as residues after the evaporation of 4 neutrons from the compound nuclei. The results are shown in Fig. 1. In order to compare cross sections for different projectile - target combinations, the cross sections $\sigma_{residue}$ are divided by $(\pi\lambda\!\!\!^{-2}\ 15^2)$, with $\lambda\!\!\!^{-}$ being the de Broglie-wavelength corresponding to the entrance channel, and 15 being the effective angular momentum cut-off caused by the ℓ-dependent fission probability in the evaporation cascade. The quantity plotted on the ordinate axis of Fig. 1 is equal to the survival probability of the compound nucleus at zero angular momentum[2], provided the incoming energy is large enough to neglect the influence of the fusion barrier on the evaporation residue cross section. For the ^{48}Ca-induced fusion reactions, the peak of the 4n-excitation function occurs well above the fusion barrier. The deviation (about a factor of 3) of the ^{48}Ca-data from the ^{40}Ar-data at $N_{residue} = 126$ in Fig. 1 is probably caused by the fact that for the ^{40}Ar-induced reactions the maximum of the 4n-excitation function is reduced due to the influence of the fusion barrier.
Neglecting for the purpose of this report the fine details in Fig. 1, the new data support the conclusions drawn previously: The measured production cross sections for neutron deficient thorium-isotopes are some orders of magnitude smaller than predicted by an evaporation calculation which takes into account shell effects. Thus, the influence of the spherical N = 126-shell is much smaller than expected. A possible explanation of this effect is a temperature-induced deformation of the excited Th-nuclei in the evaporation cascade[3].

*Permanent Address: Tata Institute of Fundamental Research, Bombay, INDIA

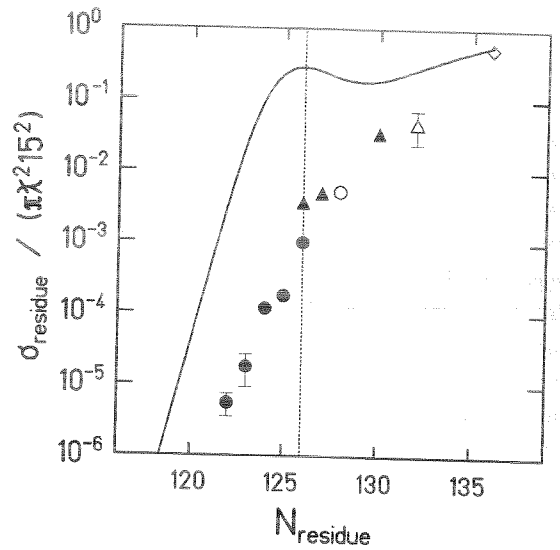


Fig. 1: Cross section for the production of thorium isotopes as residues after the evaporation of 4 neutrons as a function of the neutron number in the residual nucleus.
▲ this work
● $^{40}Ar+Hf$, Ref. 1
○ $^{16}O+^{206}Pb$, Ref. 5
△ $^{18}O+^{209}Pb$, Ref. 6
◇ $\alpha+^{226}Ra$, Ref. 7
Full curve: Survival probability calculated with the HIVAP-code[4].

[1] D. Vermeulen et al., to be published
[2] K.-H. Schmidt, W. Faust, G. Münzenberg, W. Reisdorf, H.-G. Clerc, D. Vermeulen, W. Lang, Proc. Conf. Phys. Chem. of Fission, Jülich 1979, IAEA Vienna 1980, vol. 1, p. 409
[3] K.-H. Schmidt, J.G. Keller, D. Vermeulen, Z. Phys. A315 (1984) 159
[4] W. Reisdorf, GSI Rep. 81-2 (1981) 73 and W. Reisdorf, Z. Phys. A300 (1981) 227
[5] O. Häusser, W. Witthahn, T.K. Alexander, A.B. McDonald, J.C.D. Milton, A. Olin, Phys. Rev. Lett. 31 (1973) 323
[6] W. Bonin, private communication (1982)
[7] R. Vandenbosch, G.T. Seaborg, Phys. Rev. 110 (1958) 507

Entrance Channel Differences in Heavy Ion Fusion

W. Kühn, V. Metag, II. Physikalisches Institut, Universität Gießen
H. Gröger, T.L. Khoo, R. Repnow, Max-Planck-Institut für Kernphysik, Heidelberg
R.V.F. Janssens, Argonne National Laboratory, Argonne, Illinois, USA
D. Freeman, B. Haas, F. Haas, CRN Strasbourg, France
D. Habs, Physikalisches Institut, Universität Heidelberg
S. Hlavač, R.S. Simon, GSI Darmstadt

It was recently found[1] that in the fusion of ^{64}Ni and ^{92}Zr there was a suppression of neutron emission. One possible reason is that in the relaxation from the initially highly distorted shape the compound nucleus is trapped in a superdeformed minimum. In this event the energy available for neutron emission is reduced, leading to a suppression of neutron emission. One consequence of this hypothesis is that there should be an entrance channel dependence in neutron emission: with the use of mass asymmetric reaction partners, corresponding to a smaller initial deformation, there should be less suppression.

It is crucial, however, to compare corresponding reactions as a function of the incident ℓ-values. To this end experiments have been performed with the Darmstadt-Heidelberg crystal ball using the reactions $^{12}C + ^{144}Sm \rightarrow ^{156}Er^*$ and $^{64}Ni + ^{92}Zr \rightarrow ^{156}Er^*$ at several beam energies, including those where the compound nucleus is formed at the same excitation energies with both projectiles. In coincidence with the ball, γ-ray spectra using a Ge detector and neutron energy spectra using time-of-flight techniques were measured. The following information may be obtained as a function of ℓ: (a) the γ-ray energy and multiplicity distribution; (b) the neutron energy and multiplicity distribution; (c) the entry line. In fact the goal is to completely characterize the decay of the compound nucleus so that all parameters entering into statistical model calculations are simultaneously constrained.

The analysis is still preliminary but the following tentative observations may be made. In reactions with 62.5 MeV ^{12}C and 225 MeV ^{64}Ni, which form the compound nucleus at the same excitation energy (E* = 39 MeV) and with similar maximum angular momentum, the entry line for the Ni-induced reaction lies higher. This reflects the fact that γ-emission removes more energy in this reaction, a consequence of suppressed neutron emission. Comparison of the Ge spectra between the two reactions in the case where E* = 47.5 MeV shows that, for given multiplicity interval, less neutrons are emitted with Ni as the projectile (see Fig. 1). Furthermore, the population of the near-yrast states is very different: in the Ni-induced reaction mainly the aligned-particle states are populated while in the ^{12}C-induced reaction a positive parity band-like structure receives significant population as well (see the $14^+ \rightarrow 12^+$ and $12^+ \rightarrow 10^+$ transitions in ^{154}Er marked (a) and (b)). A similar difference in the population pattern is also observed at E* = 39 MeV. Thus it appears that indeed there are pronounced entrance effects in these fusion reactions. However, it is too early to state that the Bohr independence hypothesis does not apply, since the γ-ray angular distributions have not yet been analysed to establish that the same multiplicity windows imply the same spin windows in both reactions.

[1] W. Kühn, P. Chowdhury, R.V.F. Janssens, T.L. Khoo, F. Haas, J. Kasagi and R.M. Ronningen, Phys.Rev.Lett. 51 (1983) 1858.

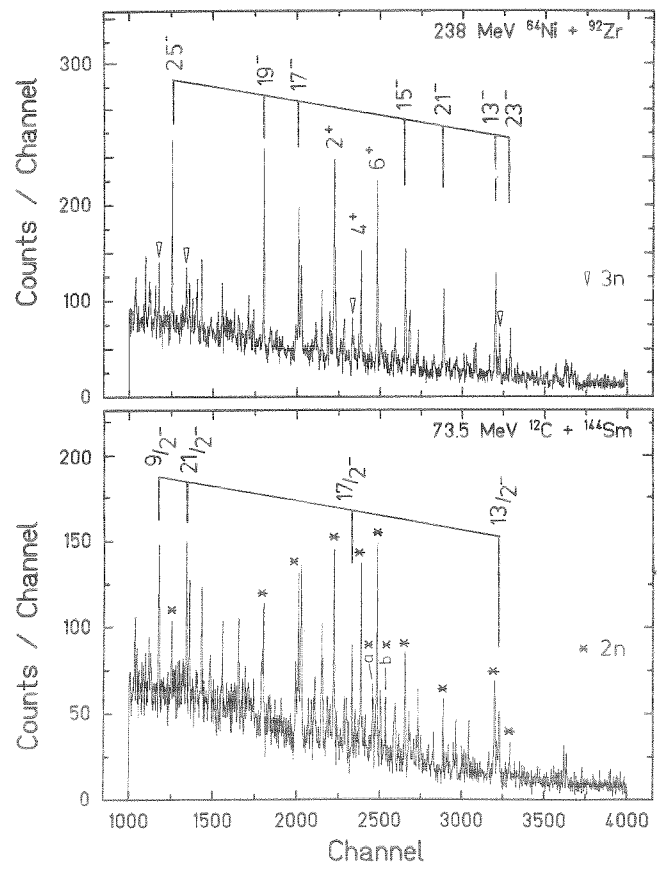


Fig. 1: Ge spectra of ^{64}Ni- and ^{12}C-induced reactions leading to ^{156}Er at E* = 47.5 MeV, as observed for identical multiplicity windows $20 < N_\gamma < 25$. Transitions after emission of 2 (3) neutrons are labelled by their integer (halfinteger) spins of the initial state. In the Ni-induced reaction the lines marked 2^+ and 6^+ in ^{154}Er contain additional contributions from higher transitions.

Neutron and Gamma Emission in the Fusion Reaction $^{86}Kr + ^{64}Ni$ B

U. Arlt, H. Dittmar+, B. Lohmüller, Th. Kratz, K. Sapotta*, K. Stelzer
Institut für Kernphysik der J.W. Goethe-Universität Frankfurt am Main

In order to study the decay of heavy compound nuclei (A=150) at high excitation energies and high angular momenta an experiment with the system $^{86}Kr + ^{64}Ni$ (ε=3.8MeV/u) was performed in Dec. 82 which was analysed in the period of this report.

Previos studies of the systems $^{86}Kr + ^{76}Ge$ and $^{86}Kr + ^{64}Ni$ had shown that the C.M. neutron angular distributions are highly anisotropic and strongly depend on the energy of the emitted neutrons[1].

The angular distributions can be explained and anlysed in the framework of the statistical model[2] in which the anisotropies are closely correlated to the compound nucleus spin and moment of inertia and the angular momentum of the emitted neutrons.

The accuracy of the earlier experiments had been impaired by contaminations with light elements (C and O) which necessitated considerable corrections for background neutrons.

For the new experiment targets essentially free from contaminations with light nuclei could be obtained by rolling 500µg/cm² ^{64}Ni foils on a Pb/Cu backing (preparation by the target laboratory of GSI). A ^{3}He activation analysis performed at the Institut für Kernphysik Frankfurt[3] showed a contamination of < 2µg/cm² as compared to > 30µg/cm² for the earlier targets, which had been produced by the sputtering technique.

The set-up of the multi-detector experiment was similar to the one described earlier[4]. An additional NE213 detector at -30° was used as a multiplicity filter in order to increase the number of neutron-neutron coincidences, because the anisotropy and the center of mass motion results in a concentration of neutrons at foreward angles.

In a second part of the experiment neutron spectra in coincidence with characteristic gamma-rays were recorded to determine neutron spectra for individual xn-channels. For this purpose a large Ge(Li) detector (150cm³) at -90° and two large NE213 scintillators (4.5" diam. x 2" th.) at 0° and 30° and flight paths of 50cm were used.

The analysis of the neutron angular distributions and energy spectra essentially confirmes the results found for the $^{86}Kr + ^{76}Ge$ reaction[5].

The energy dependence of the anisotropy parameter A_2 (A_2=0.289 for E_n=1.95MeV to A_2=0.96 for E_n=11.75MeV) could be fitted by a linear function of energy.

The neutron energy spectra, corrected for the angular distributions have the shape of a Maxwellian energy distribution and yield identical temperatures for all observation angles.

The temperature parameter is T=1.46 ± 0.09MeV in the case of the $^{64}Ni + ^{86}Kr$ system and T=1.60 ± 0.04MeV for the $^{12}C + ^{86}Kr$ system.

The analysis of the reaction $^{12}C + ^{86}Kr$ confirmed the significant anisotropy in the angular distribution as observed in an earlier survey experiment with ^{86}Kr-ions of 4.2MeV/u[6]. In contrast to the heavier systems the magnitude of the anisotropy in this system cannot be reproduced by the statistical model.

[1] U. Arlt et al., GSI Scientific Report 1982, p.5
[2] T. Ericson, V. Strutinsky, Nucl. Phys. 8 (1958) 284
[3] R. Bass et al., IKF-Jahresbericht 1980, p.94
[4] U. Arlt et al., GSI Scientific Report 1980, p.13
[5] H. Dittmar, Dissertation, Frankfurt am Main 1983
[6] U. Arlt et al., GSI Scientific Report 1978, p.7

+ Now at Herder Gymnasium, Frankfurt am Main
* Now at Siemens AG, München

Fission following quasi-elastic scattering in the reaction $^{238}U + ^{238}U$ B

J. Schukraft, P. Glässel, D. Habs, D. v. Harrach, H.J. Specht
Physikalisches Institut, Universität Heidelberg

The reaction $^{238}U + ^{238}U$ at 7.5 MeV/u was investigated for fission following quasi-elastic scattering, i.e. Coulomb-fission-like events. The experimental set-up[1], consisting of large area gas counters, allowed a complete kinematical reconstruction of the 2- and 3-body coincidences with a Q-value resolution of ≈ 45 MeV (fwhm). The kinematic mass resolution was not sufficient to discriminate few-nucleon transfers.

The normalized binary differential cross section (dots in Fig.1a) exhibits a dependence on scattering angle equivalent to an excitation function (solid line)[2], if compared at the same distance of closest approach (upper scale). In this sense, a quasi-elastic scattering forward of the grazing angle (87° CM) can be compared to sub-Coulomb scattering. The Wilczynski-plot (Fig.2) shows that at forward lab angles quasi-elastic distant collisions and the deep-inelastic close collisions are separable in Q-value, thus resolving the ambiguity of identical target and projectile for the former.

The fission probability for the quasi-elastic ridge is plotted in Fig.1b. From the shape of the asymmetric fission fragment mass distribution, $|Q|<11$ MeV is inferred for $\theta_{CM}<70°$. For comparison, Coulomb-fission data from $^{184}W + ^{238}U$ [2], scaled according to the experimentally confirmed Z_p^7-dependence, are plotted vs. r_{int}/r_{min} (solid line). The qualitative agreement suggests Coulomb fission to be the dominant mechanism for $\theta_{CM}<70°$ ($r_{int}/r_{min} < 90°$).

From the absence of Coulomb final state interactions which would have caused a variation of the fission fragment separation velocity with orientation[3], a lower limit of $1 \cdot 10^{-20}$s is established for the time-scale of the fission process, excluding a fast three-body break-up.

Strong in-plane anisotropies (Fig.3) indicate anisotropic spin-alignment of the fissioning nucleus with in-plane spin components oriented perpendicular to the semisector axis ($\phi_{ss} = 0$) of the projectile trajectory. Fits with theoretical distributions yield alignment parameters $P_{xx} = \langle I_x^2 \rangle / I^2 = 0.56 - 0.65$, $P_{yy} = 0 - 0.05$, $P_{zz} = 0.37 - 0.51$ (z normal to the scattering plane, y semisector) rather independent of θ_{CM}, except near 90°, where the contributions of projectile- and target-fission are equal and cancel in anisotropy (to first order).

A comparison with the alignment predicted by Coulomb excitation calculations suggests that dominantly high spins $I \approx 14 - 28$ ħ contribute to fission, as expected from the spin-dependence of Γ_n/Γ_f. The data are thus consistent with a slow fission process induced by the Coulomb interaction.

[1] P. Glässel et al., Phys. Rev. Lett. 43, 1483 (1979)
[2] G. Himmele et al., Nucl. Phys. A391, 191 (1982)
[3] P. Glässel, D. v. Harrach et al., Phys. Rev. Lett. 48, 1089 and 1093 (1982); Z. Physik A310, 189 (1983)

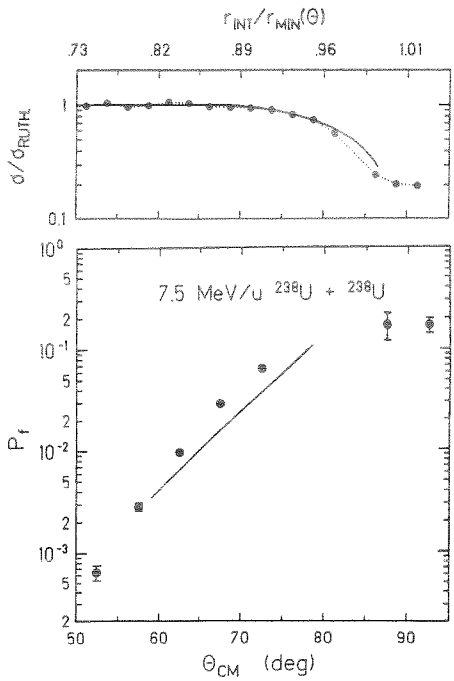


Fig. 1 Binary cross section (a) and fission probability (b) bs. scattering angle.

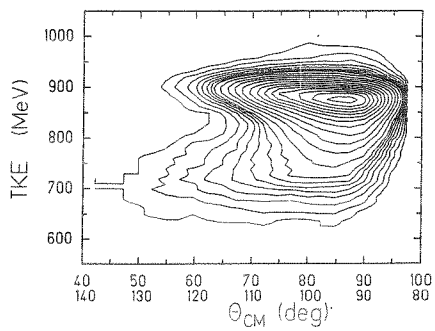


Fig. 2 Wilczynski-plot of the first reaction step of 3-body events.

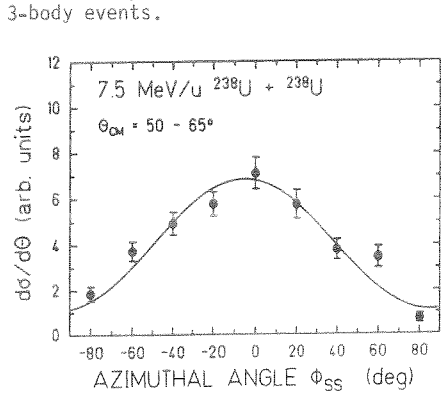


Fig. 3 Azimuthal distribution of fission fragments for quasi-elastic events integrated over polar angle.

Time-scale of sequential fission in the reaction $^{238}U + ^{248}Cm$ at 8.43 MeV/u

P. Glässel, D. v. Harrach, H.J. Specht
Physikalisches Institut, Universität Heidelberg

The investigations of sequential fission following deep-inelastic collisions of heavy systems like U + Cm have been continued and extended to higher bombarding energy. Compared to previous results at 7.5 MeV/u[1], substantially increased yields were found for large mass transfers, i.e. for very heavy intermediate fissioning systems (Z= 100-120), in agreement with radiochemical data[2]. In addition, a clear separation is observed between quasi-elastic ternary events with small mass transfer and deep-inelastic events with large mass transfer, possibly due to the competition of 4-body events from double sequential fission which were not recorded. The deep-inelastic three-body data are centered at total kinetic energy losses of 280 MeV and nuclear charges of the intermediate fissioning systems of Z = 108 (Fig.1).

The significant increase in statistics allows to improve the previously deduced lower time-limit on the life-time of the intermediate system and to extend the study up to Z = 120. For a time-interval $\tau_{ss} < 10^{-20}$s between scission of the deep-inelastic complex and scission of the intermediate system, a detectable modulation should result of the separation velocity of the fission fragments vs. orientation, with a minimum for fission collinear with the recoil ($\Phi_f = 0$ in Fig.2), due to the Coulomb final state interaction with the third particle. Such modulations with amplitudes up to ±10% have previously been observed for lighter systems[3]. The U + Cm data, however, exhibit only very weak modulations of < 1%, consistent with zero effect, regardless of the Z of the intermediate system (Fig.2). This leads to a lower limit $\tau_{ss} > 1.0\text{-}1.5 \cdot 10^{-20}$s, equivalent to a separation of the primary collision partners greater than 250 - 400 fm at scission.

In view of the excitation energies, deformations and spins involved, τ_{ss} may be identified with the dynamical evolution time of the fission process for the heavier nuclei with vanishing barrier (Z > 105). Theoretical saddle-to-scission-times in the framework of one-body-dissipation[4] seem to be compatible with our limit, whereas two-body-viscosity models, preferred recently on the basis of fusion data[5], but also TDHF-calculations predict too short time-scales of $3\text{-}4 \cdot 10^{-21}$s.

In the angular correlations of fission, no indications exist for fission from an intermediate state not equilibrated with respect to orientation and mass-asymmetry as observed in the system Xe + Sn[3]. The rather long life-times and associated large, spin-dependent rotation angles of the fissioning system do, on the other hand, not allow to completely exclude this possibility.

[1] P. Glässel et al., Phys. Rev. Lett. 43, 1483 (1979)
[2] H. Gäggler et al., Proc.IV Int. Conf. Nuclei far from Stability, June 81, Helsingor, p.763, CERN Report 81-09
[3] P. Glässel et al., Phys. Rev. Lett. 48, 1089 and 1093 (1982); Z. Physik A310, 189 (1983)
[4] J.W. Negele et al., Phys. Rev. C17, 1098 (1978)
[5] K. Thomas et al., to appear in Phys. Rev. C (1983); J.R. Nix, to appear in Com. Nucl. Part. Phys. (1983)

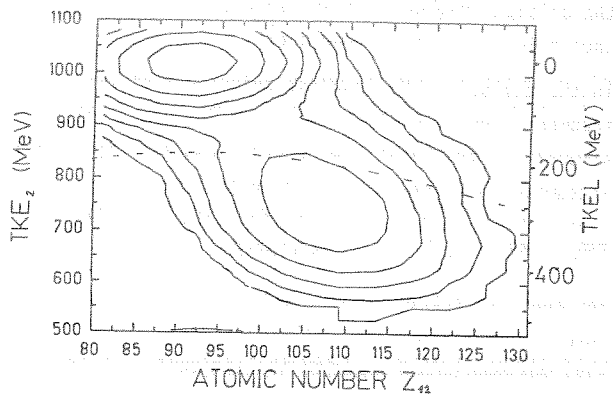


Fig. 1 Total kinetic energy of first reaction step vs. atomic number of intermediate system for 3-body events in $^{238}U + ^{248}Cm$ at 8.43 MeV/u (contours spaced a factor of 2). The dashed line indicates the Coulomb energy of touching spheres.

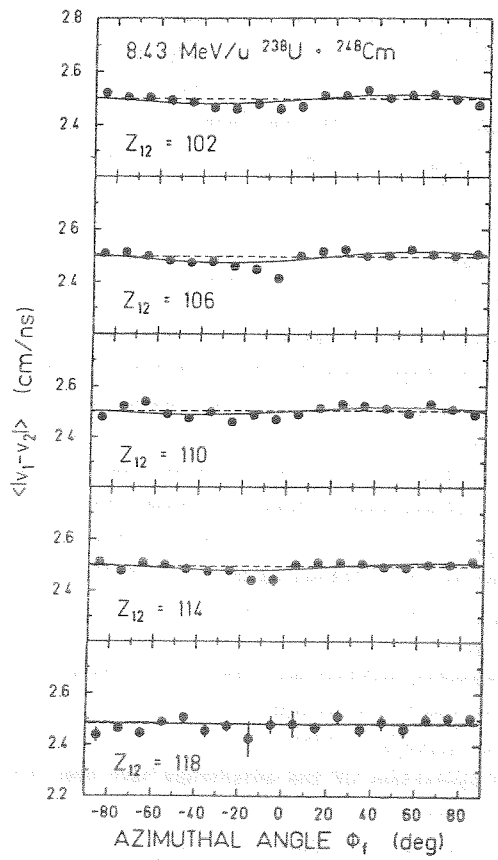


Fig. 2 Fission fragment separation velocity vs. azimuthal angle for several Z-bins.

B

Angular distributions of sequential fission in the reactions ^{208}Pb, ^{238}U + ^{90}Zr at 7.5 MeV/u

P. Glässel, D. v. Harrach, H.J. Specht
Physikalisches Institut, Universität Heidelberg

The controversial question of sequential fission anisotropies[1,2] has been reinvestigated. Three-body events from the reaction ^{208}Pb + ^{90}Zr at 7.5 MeV/u were recorded with an improved set-up. Compared to a previous measurement[1], redesigned windows of both the large area PPAC and the ionization chamber allowed a better coverage of the critical region in phase space, thus reducing the uncertainties of Monte-Carlo efficiency corrections.

In the analysis, the in-plane anisotropy of the fission fragment angular distributions was found to depend strongly on the first step energy loss such that data integrated over energy loss lead to erroneous conclusions. Under this new aspect, the data from the reaction ^{238}U + ^{90}Zr [1] were also reevaluated.

For moderate energy losses, both systems exhibit a strong in-plane anisotropy of ≈ 1:2 (see Fig.1), with the intensity maximum coinciding with the semisector of the in- and outgoing trajectory of the fissioning nucleus (ϕ_f^{ss} = 0). This anisotropy indicates different components of the transferred spin in the two orthogonal directions within the scattering plane; the observed orientation is consistent with expectations in a statistical nucleon-exchange model, which generates only small spin components in the direction of the mean nucleon flux. With K_0 = 12,15 and under the (extreme) assumption M_y=0 for the smaller in-plane component along the semisector axis, lower limits for the average spin perpendicular to the scattering plane $\langle I_Z \rangle$ and for the other rms-spin-component M_x are obtained: $\langle I_Z \rangle = 48^{+11}_{-6}$, 36 ±3 and $M_x = 17^{+7}_{-5}$, 16^{+4}_{-3} for Pb and U resp. Qualitatively similar, even larger anisotropies were found for quasi-elastic events in U+U[3].

For increasing energy losses, the anisotropy decreases without, at first, changing its orientation (Fig.2). This is to be expected in a nucleon-exchange picture, as for larger energy losses the increasing contact angle of the complex will wash out the anisotropy. For the largest observed energy losses, however, the anisotropy rises again, associated simultaneously with a sudden change of its orientation by 60 - 90° which in the case of Pb+Zr corresponds to a reversal of the effect. For both systems, energy-loss-integrated angular distributions therefore exhibit much smaller anisotropies, with different sampled phase-spaces possibly responsible for previous discrepancies[1,2].

Similar variations of the anisotropy have been observed in other systems[4].

[1]D.v. Harrach et al., Phys. Rev. Lett. 42, 1728 (1979)
[2]P. Dyer et al., Nucl. Phys. A322, 205 (1979)
C. Le Brun et al., Phys. Rev. C25, 3112 (1982)
[3]J. Schukraft et al., this report
[4]D.J. Morrissey et al., Z. Phys. A305, 131 (1981)

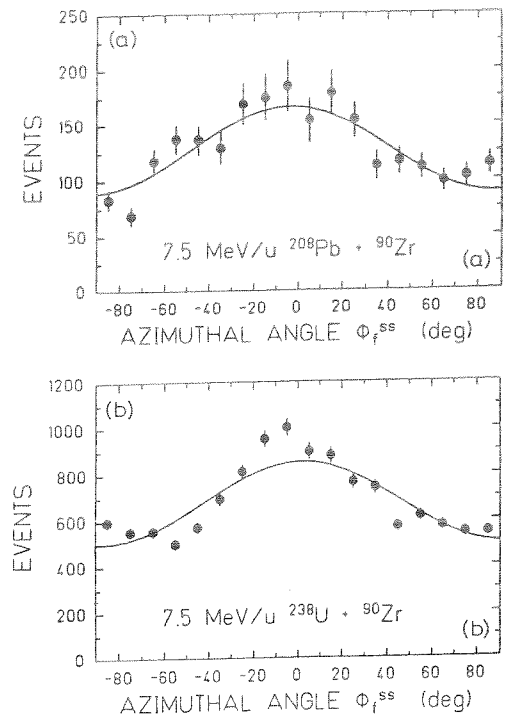


Fig. 1 Fission fragment angular distribution in the scattering plane of the first reaction step, in the rest-frame of the fissioning nucleus, for TKEL = 70 - 170 MeV (Pb) and 40 - 140 MeV (U).

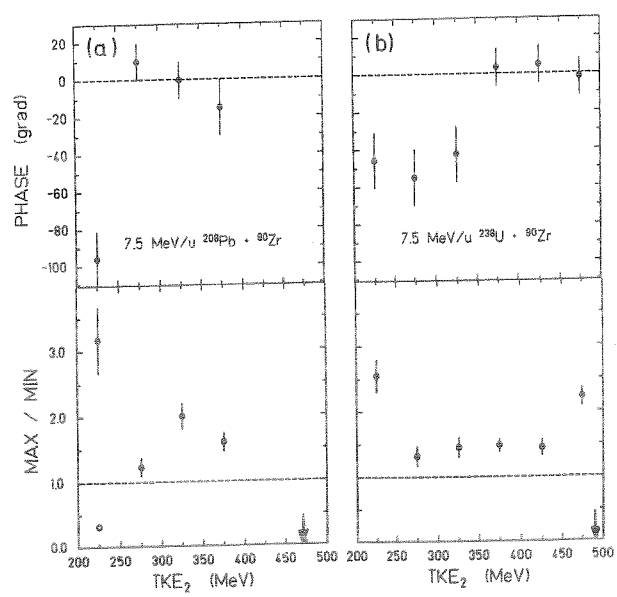


Fig. 2 Orientation of the maximum (top) and anisotropy of the fission fragment in-plane distribution vs. TKE of the primary fragments. Positive ϕ_{ss} are counted from the semisector towards the outgoing trajectory of the fissioning system. The arrows indicate TKEL = 0.

Quasi Fission - the Mass Drift Mode in Heavy Ion Reactions

J. Tõke,* R. Bock, G.X. Dai,** A. Gobbi, S. Gralla, K.D. Hildenbrand
W.F.J. Müller, A. Olmi*** and H. Stelzer, GSI Darmstadt
B.B. Back+ and S. Bjørnholm, NBI Copenhagen, Denmark

The quasi- or fast- fission reaction has emerged in recent years as a route intermediate between deep inelastic scattering and (compound) fusion - fission[1,2]. In order to explore in detail the phenomenology of this reaction we have studied ^{238}U-induced reactions on ^{16}O, ^{27}Al, ^{48}Ca, ^{48}Sc, ^{48}Ti, ^{58}Fe, ^{64}Ni and ^{89}Y targets at 5.4 and 6.0 MeV/u. The disruptive Coulomb forces shift these systems away from compound fusion limits, but on the other hand they are not large enough to prevent the capture altogether. With a setup of four 30 x 20 cm^2 position-sensitive avalanche detectors[3] operated in binary and ternary coincidences we have measured the triple differential cross sections $d^3\sigma/(dA \cdot d\theta \cdot dTKE)$ for the binary exit channels in full range of encountered fragment masses and total kinetic energies (TKE) and almost full range of C.M. angles. In addition, in somewhat more restricted range, we were able to reconstruct also the binary steps preceeding the sequential fission seen in ternary exit channels[4]. This allowed us to gain a virtually complete control over the (primary) binary collision phenomenology in the reactions studied. Fig.1 shows the fragment mass spectra projected out of the measured triple differential cross sections. Dotted lines represent the yield when the sequential-fission component is added. Dashed lines are drawn based on the correlations observed in the double differential cross sections $d^2\sigma/(dA \cdot d\theta)$ and $d^2\sigma/(dA \cdot dTKE)$ and represent schematically spectra of projectile- and target- like fragments of fully relaxed TKE which we ascribe to quasi fission reaction. This reaction is clearly seen to explore the entire configuration space between contact and fully relaxed (both in TKE and mass asymmetry) configurations. Depending on the target Z-value and center of mass energy the drift of the system towards symmetry finds itself in a stronger or weaker competition with the tendency to reseparate into two fragments. As a result the observed fragment mass spectra vary from a nice peak centered at symmetry (^{16}O and ^{27}Al targets) through essentially flat distributions (^{48}Ca, ^{48}Sc and ^{48}Ti targets) to branches from the two target- and projectile-like peaks with a broad minimum inbetween (^{58}Fe, ^{64}Ni and ^{89}Y targets). With exception of the ^{16}O and ^{27}Al cases where the captured systems perform a number of revolutions before reseparating into exit channels the reaction times estimated from angular distributions are in the range of 2-8x10^{-21} s.

* A.v.Humboldt-Fellow, IMP, Lanzhou, P.R. of China
** now at INFN, Florence, Italy
+ on leave from Argonne Nat. Lab, USA

1) W. Swiatecki, Nucl.Phys. A376 (1982) 275
2) R. Bock et al., Nucl. Phys. A388 (1982) 334
3) J. Tõke et al., GSI Annual Report 1982, p.10
and G.X. Dai et al. GSI Annual Report 1982, p.225
4) G.X. Dai et al., following contribution

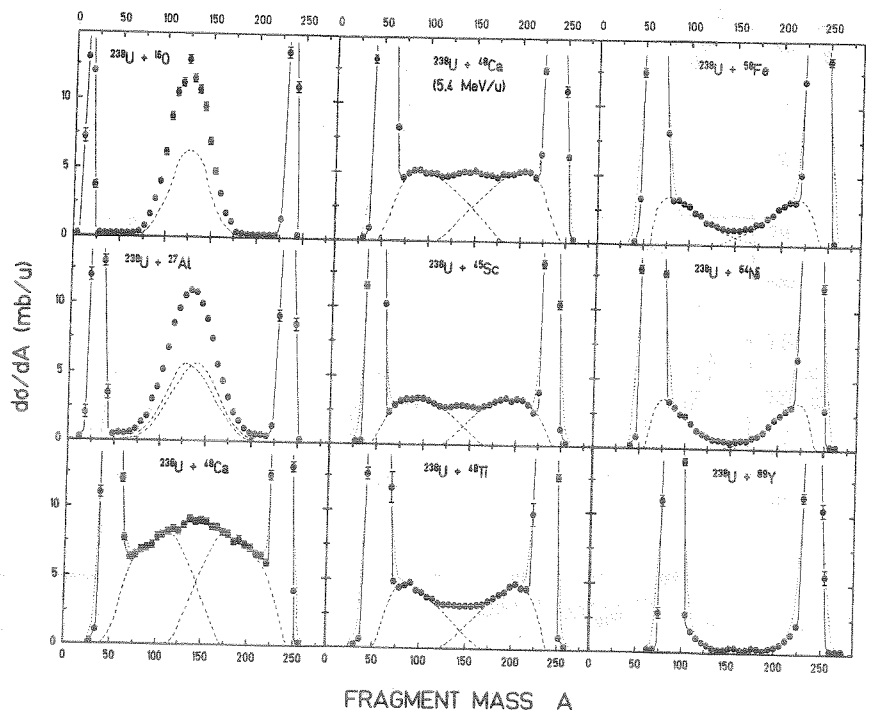


Fig. 1. Fragment mass spectra and their schematic decomposition.

Features of the Sequential Fission Processes Observed in ^{238}U Induced Reactions at 6 MeV/u

G.X. Dai,* A. Gobbi, S. Gralla, K.D. Hildenbrand, J. Kuzminski,** W.F.J. Müller, A. Olmi,*** H. Stelzer and J. Toke, GSI Darmstadt

In our recent experimental studies of fusion dynamics involving ^{238}U projectiles and ^{16}O, ^{27}Al, ^{48}Ca, ^{48}Sc, ^{48}Ti, ^{58}Fe, ^{64}Ni and ^{89}Y targets, most of the fusion - fission and quasi - fission yield is found in the binary exit channel [1]. There exists, however, a region of fragment masses A > 200, corresponding to short interaction time limit, where the excited heavy products may undergo (sequential) fission, and where therefore the reconstruction of the binary yield alone will miss a part of the reaction cross section.

In order to gain a more complete control over the reaction yield, triple coincidences of three heavy fragments were recorded as well. This allowed, by using the pulsed UNILAC beam and the timing and position sensitive features of the four 30 x 20 cm^2 avalanche counters [2], to measure all three velocity vectors for each ternary event and thus to determine subsequently the three fragment masses and corresponding CM angles and kinetic energies. Sharp correlations observed in relative velocities of the fragments confirm that at our low incident energies most if not all ternary events result from the sequential fission process; following a reseparation of the composite system into a binary (quasi - elastic, deep - inelastic and also strongly asymmetric quasi - fission) channel the heavy partner fissions sequentially. Kinematical reconstruction of the initial binary step of the observed ternary events completes our analysis of the binary exit channels [1]; in addition, the sequential fission is interesting in itself. Fig. 1a shows as an example mass vs. CM angle correlations of the binary yield reconstructed from ternary events. This yield has been normalized (with an accuracy of 30 %) to absolute units by using a procedure based on Monte Carlo simulations. As expected, the sequential fission affects fragment masses at A > 200 and an angular region in the vicinity of the grazing angle. The corresponding complete yield for the binary processes including that observed directly in binary channels (elastic and quasi- elastic scattering, however, excluded) is shown in Fig. 1b.

Fig. 2 shows two examples of mass spectra observed in ternary exit channels. For the lighter system there are clearly two peaks in the (sequential) fission fragment spectrum, whereas for the heavier one there is only one maximum. This might be a reflection of the difference in the excitation energies of the fissioning U-like products and of washing out of the shell effects at higher exitations.

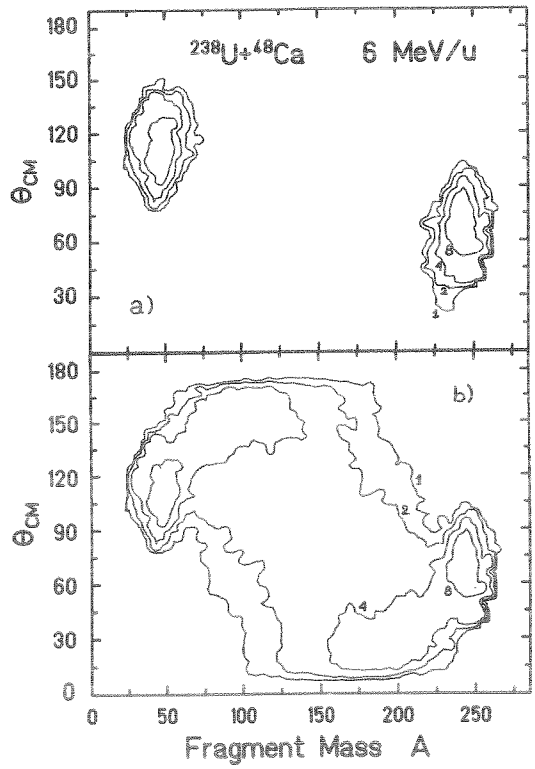


Fig. 1. Double differential cross sections $d^2\sigma/(dA \cdot d\theta_{CM})$ (mb/u·rad) reconstructed from ternary events alone (a) and from all events (b).

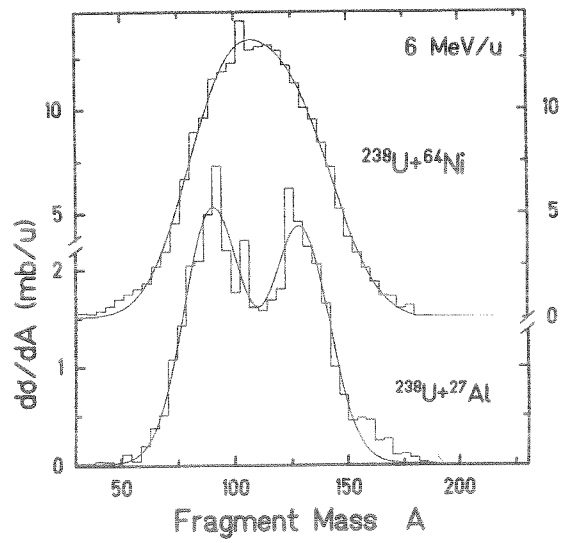


Fig. 2. Fragment mass spectra from sequential fission of U-like primary products.

* A.v.Humboldt-Fellow, IMP, Lanzhou, P. R. of China
** on leave from Silesian University, Katowice, Poland
*** now at INFN, Florence, Italy

1) J. Toke et al., GSI Annual Report 1982, p.10 and previous contribution
2) G.X. Dai et al., GSI Annual Report 1982, p.225

Potential-energy surfaces guiding fusion and binary decay of heavy composite systems

N. Carjan (CEN Gradignan), A. Gobbi (GSI Darmstadt)

A large amount of recent experimental data seems to indicate that the relation between the properties (shapes and heights) of the interaction barrier (tangent configuration) and of the conditional saddle plays an important role in explaining the gross properties of the various types of heavy-ion reactions.

In the frame of an elegant algebraic model (1) Swiatecki found that the properties of the conditional saddle depend only on the effective fissility parameter χ. To test this static scaling rule numerical calculations were performed in this work: the change of the conditional saddle with the asymmetry $\eta = (A_1 - A_2)/(A_1 + A_2)$ for two different systems (total charge and mass Z, A = 94, 232 and 108, 264) was studied in detail. These systems correspond to $^{24}Mg + ^{208}Pb$ and $^{56}Fe + ^{208}Pb$ reactions which have been extensively measured (Fig. 1).

To describe the nuclear shapes involved, two spheres connected by a quadratic surface of revolution (2) have been used. Before scission the system was split into fragments 1 and 2 by the plane $Z = Z_o$, Z_o being the intersection of the internal tangents at the two spheres. In this way the following three quantities could be chosen here to define the shapes: the distance between mass centers D (in units of $R_o = 1.225\ A^{1/3}$ fm), the mass asymmetry η and the 'neck' parameter λ. This choice allows a direct comparison with other shape parametrisations (3,4) and a simple relation with known nuclear characteristics.

For each shape the macroscopic deformation energy is given by the sum of Coulomb and sharp surface terms. Assuming that the mass asymmetry η is the slowest changing degree of freedom, we have first searched for the energetically most favourable path in the (λ, D). Such paths derived for all η's form an energy surface in (λ, D)-plane. An adequate way to study the evolution in mass-asymmetry of the system is to represent it in polar coordinates (Fig. 2), where the radial coordinate is the distance D and the polar angle is the asymmetry η. Therefore the central part (where a shallow pocket is present) represents rather compact mono nucleus configurations whereas the outermost parts represent separated fragments.

One easily notices the strong difference between the two systems. The lighter system displays the expected continuous variation of the properties of the conditional saddle with the asymmetry. Increasing the total charge a rupture of this conditional saddle line occurs at intermediate asymmetries such that a $\lambda = 0.6$, for instance, the macroscopic barrier is double-humped. This rather sudden change of the barrier properties is evidently in variance with the above mentioned scaling rule. The first minimum represents the real ground state while the second is unstable towards decreasing mass asymmetry. The particular nuclear shape in the second minimum (the neck connecting the two spherical nuclei takes the shape of an extended truncated cone) is probably responsible for its appearance.

The interaction barrier in the incoming channel is given by the open dot line. For $^{24}Mg + ^{208}Pb$ reaction this barrier is located inside the conditional-saddle line and therefore the system is driven towards a compact compound-nucleus which will subsequently decay by fission ($\eta \simeq 0$) or by evaporation ($\eta \simeq 1$). For the $^{56}Fe + ^{208}Pb$ reaction, on the contrary, the interaction barrier lying (in the second minimum) between the two conditional-saddle lines, the formation of the compound nucleus is hindered. The system will change the mass asymmetry and decay over a broad range of fragment masses in qualitative agreement with Fig. 1.

1. Swiatecki, W.J., Physica Scripta 24 (1981) 113
2. Blocki, J. and Swiatecki, W.J., LBL reprint 12811
3. Möller, P. and Nix, J.R., Nucl. Phys. A281 (1977) 354
4. Paskevich, V.V, Nucl. Phys. A169 (1971) 275

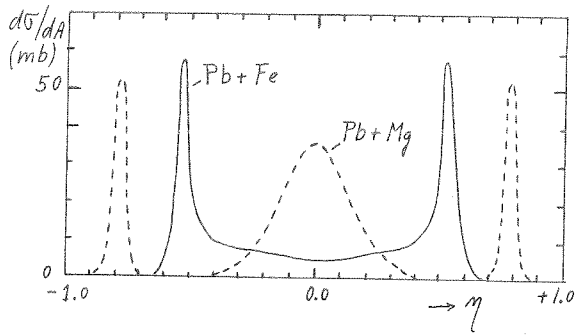


Fig. 1: Mass distribution for the total reaction cross section.

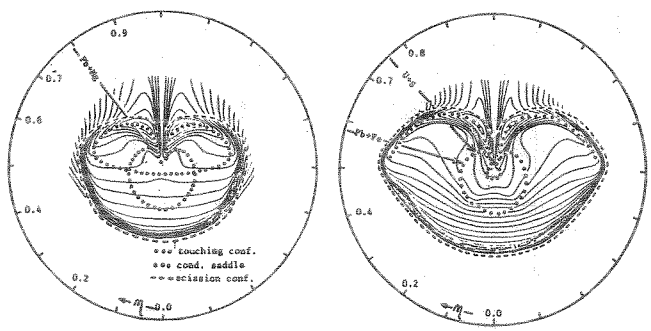


Fig. 2: Polar-coordinate representation of the potential energy corresponding to $^{24}Mg + ^{208}Pb$ (left) and $^{56}Mg + ^{208}Pb$ (right) composite systems. The radius D/R_o varies from 1.1 to 3.0.

Study of the ^{84}Kr on ^{27}Al reaction mechanism at 490 MeV [BG]

B. Heusch
Centre de Recherches Nucléaires and Université Louis Pasteur - Strasbourg (France)

H. Freiesleben
Institut für Experimentalphysik, Ruhr - Universität Bochum

W.F.W. Schneider
G.S.I. - Darmstadt

B. Kohlmeyer, H. Stege and F. Pühlhofer
Fachbereich Physik der Philipps-Universität Marburg

This study was undertaken in order to complete earlier detailed measurements of the fusion-evaporation-residue cross section (FE) [1] by determining the fusion-fission (FF), the deep-inelastic (DI) and quasi-elastic (QE) components of the reaction.

Self supporting ^{27}Al-targets (290 and 510 µg/cm^2 thick) were bombarded by a 490 MeV ^{84}Kr-beam from the UNILAC. Two ionization chambers of broad dynamic range allowing for unit Z resolution were used to determine the angular distributions of projectile-like as well as target-like fragments in the laboratory angle range of 3° to 60°.

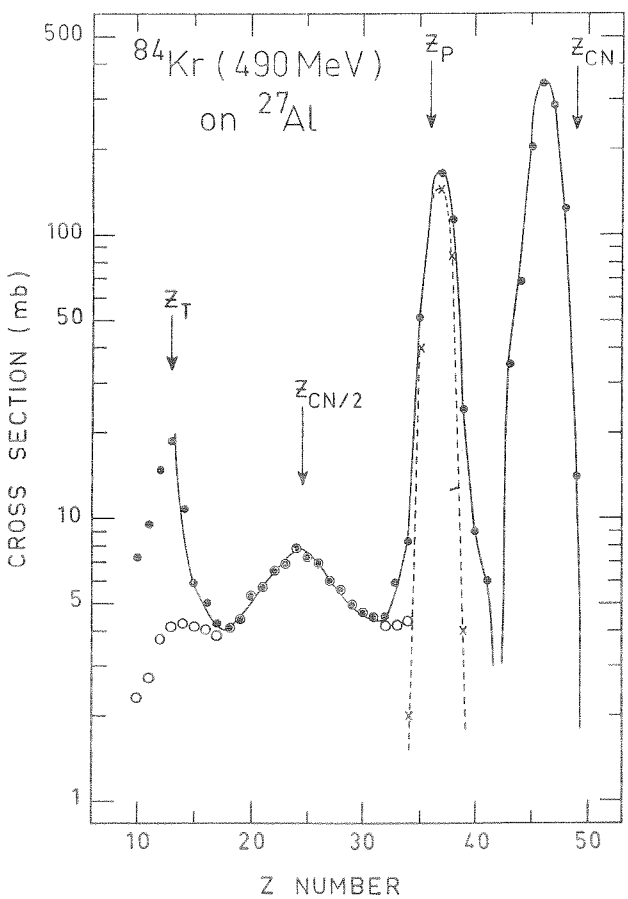


Fig. 1

Special care was taken of the gas pressure to adjust the dynamic range according to Z and E_{lab} of the reaction products. Fig. 1 displays by a solid line the measured total reaction cross section for the observed elements. The FE-component from ref. 1 is added for completeness.

A decomposition of the total cross section is tentatively indicated. The dashed line about the projectile Z number (Z = 36) refects the cross section of quasi-elastic events defined operationally by Q ≥ - 25 MeV. These events exhibit a bell-shaped angular distribution with a maximum forward of the grazing angle. The remaining cross section which show a forward peaked angular distribution corresponds to Di-events. Centered at $Z_{CN}/2$ a fully relaxed component is observed which is attributed to FF by its $1/\sin \theta_{cm}$-angular distribution. For fully relaxed target-like fragments the angular distribution of each element can be decomposed in a $1/\sin \theta_{cm}$ and a backward peaked distribution. The cross-section of the former is indicated by open circles ; it suggests a long living, however not mass-equilibrated intermediate system. The latter component could only be evaluated for Z ≥ 13 ; the energy spectra of the lightest elements do not allow for a cross section determination as they are seriously cut by the energy threshold of the ΔE - E-ionization chamber.

The integrated cross sections of σ_{FE} = (1075 ± 100) mb, σ_{FF} = (50 ± 10) mb, $\sigma_{QE} + \sigma_{DI} \simeq$ (530 ± 100) mb compare well with a reaction cross section of σ_R = 1730 mb as obtained from an optical model analysis of the "elastic-scattering" angular distribution.

1) W.F.W. Schneider et al., Nucl. Phys. A371, 493 (1981).

Transfer Cross Sections from the Reaction of ^{48}Ca + ^{254}Es

J. F. Wild, E. K. Hulet, R. W. Lougheed, J. H. Landrum, R. J. Dougan, A. D. Dougan
Lawrence Livermore National Laboratory
H. Gäggeler, M. Schädel
GSI Darmstadt
K. J. Moody, G. T. Seaborg
Lawrence Berkeley Laboratory

We bombarded a 4.8-μg/cm² ^{254}Es target, electroplated on a thin beryllium foil, with 266-MeV ^{48}Ca ions from the SuperHILAC at the Lawrence Berkeley Laboratory. This energy is about 11% above the Coulomb barrier, which generally provides the maximum tranfer cross sections for heavy actinides.

The reaction products recoiling from the einsteinium target were collected on a 6.3 mg/cm² thick copper catcher foil. Following each of two short (~2 h) bombardments, the catcher foil was transported to a laboratory for separation of the actinide products before isotopic analysis by alpha spectroscopy with surface-barrier detectors. Figure 1 shows the measured cross sections for the actinide products.

The steady decrease in cross section for each transferred proton resembles the results from heavier systems like ^{238}U + ^{248}Cm[1], and it does not show the relative enhanced yields for two proton transfer products as observed with lighter projectiles like ^{18}O and ^{22}Ne[2].

Fig.2 shows a comparison of cross sections for the production of (a) Fm isotopes (ΔZ=1), and (b) Md(ΔZ=2) and No (ΔZ=3) isotopes in the bombardment of ^{254}Es with 98 MeV ^{18}O, 121 and 126 MeV ^{22}Ne, and 266 MeV ^{48}Ca. Although the Fm cross sections from all the irradiations are comparable, the Md cross sections are more than one order of magnitude lower for the ^{48}Ca bombardment. We may gain a better qualitative understandig for this from considerations where the level density of the final system is related to the product excitation energy, E*, as do Hoffman and Hoffman[3]. They described the cross section as being roughly proportional to exp (c E*). However, differences in transfer probabilities and the kind of transfer mechanism for projectiles like ^{18}O, ^{22}Ne and ^{48}Ca may also play an important role.

1. M. Schädel et al., Phys. Rev. Letter 48, 852 (1982)
2. M. Schädel et al., GSI Scientific Report 1982, p. 67 (1983), and contribution to this report
3. D. C. Hoffman and M. M. Hoffman, Report LA-UR-82-824 (1983)

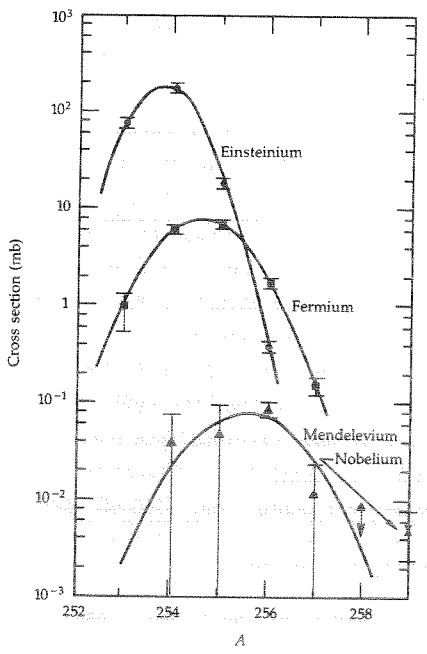


Fig.1: Measured cross sections for isotopes of Es, Fm, Md and No produced in the bombardment of ^{254}Es with 266-MeV ^{48}Ca ions.

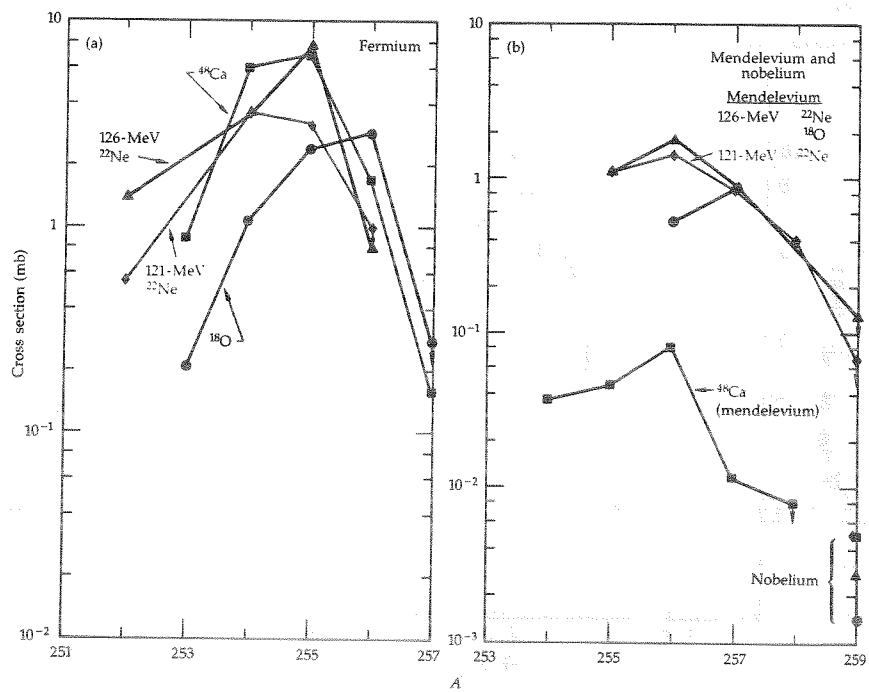


Fig.2: (a) Comparison of cross sections for the production of Fm isotopes in the bombardment of ^{254}Es with 98-MeV ^{18}O (dot), 121-MeV ^{22}Ne (diamond), 126-MeV ^{22}Ne (triangle), and266-MeV ^{48}Ca (square). (b) Production of Md and No isotopes.

B

Is $^{197}Au + ^{63}Cu$ the *Dynamic Twin* of $^{238}U + ^{56}Fe$?

B. Jäckel, A. Rox, W. Westmeier, R.A. Esterlund, H. Schulte and P. Patzelt
Institut für Kernchemie, Universität Marburg

The purpose of this experiment is to further test the Dynamic Fusion Model of Bjørnholm and Swiatecki[1] in three respects: a) the general validity of the scaling parameters a, f and $(Z^2/A)_{th}$; b) to determine an important point on the s-wave extra push curve[2] at $X_{eff} = 0.84$; and c) to further examine the hypothesis of dynamic equivalence of systems with similar $(Z^2/A)_{eff}$. In addition, we wish to deduce information on saddle-point configurations of fissioning capture nuclei via a K_0 analysis of the angular distribution anisotropy $W(\Theta)/W(90°)$. To accomplish this, we intend to measure the excitation function and angular distributions for symmetric fragmentation.

The Dynamic Fusion Model is formulated in terms of an effective fissility $(Z^2/A)_{eff} = 4Z_pZ_t/A_p^{1/3}A_t^{1/3}(A_p^{1/3}+A_t^{1/3})$, which implies that systems with comparable effective fissilities should exhibit similar amounts of extra push with increasing orbital energy i.e., that they should be *Dynamic Twins*. Such a pair of systems exists in $^{238}U + ^{56}Fe$ $(Z^2/A)_{eff} = 40.3$ and $^{197}Au + ^{63}Cu$ $(Z^2/A)_{eff} = 40.4$. This hypothesis can be tested via the construction of a rectilinear cross-section plot[1], which is based on experimental data only, and thus is *model-parameter independent*.

We report here preliminary values from the first of our measurements of reaction component yields for $^{197}Au + ^{63}Cu$. Thin (0.9 mg/cm²) metallic targets of separated[3] ^{63}Cu were irradiated with 7.1 MeV/u ^{197}Au ions from the GSI UNILAC. Reaction products were scattered into circular Al (or Be) catcher foils subtending the lab angles: a) 0° - 2.24° (Be); b) 2.24° - 16.4° (lab grazing angle, projectile); c) 16.4° - 29.7° (lab recoil angle, target); d) 29.7° - 56.3° (maximum kinematic angle for fully-damped symmetric). Foil a) is a simple velocity filter, catching reaction products emitted near 180° c.m. and letting other products through. Foils b) and d) collect primarily Au-like and Cu-like deep-inelastic products, and foil c) constitutes a "window" for symmetric fragmentation products. Some yields for the mass region near symmetry are shown in Fig. 1. In all, a total of 271 cross sections for nuclides in the ranges $24 \leq A \leq 206$ and $11 \leq Z \leq 84$ were determined.

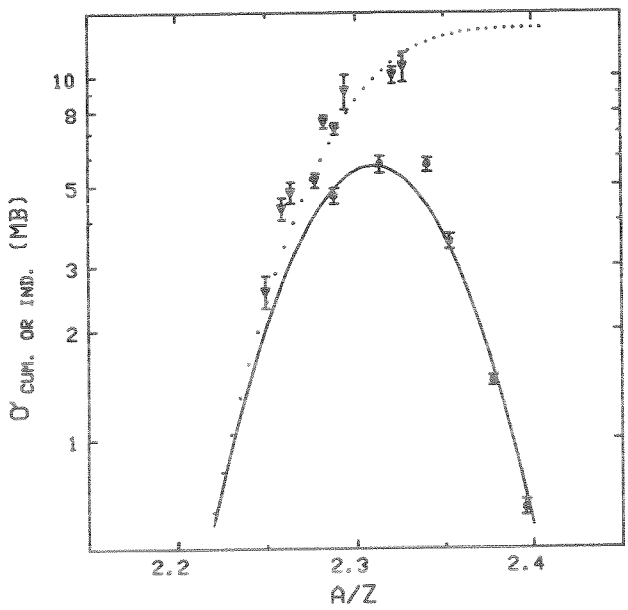


Fig. 1: Independent (circles) and cumulative (triangles) cross sections vs. A/Z for $115 \leq A \leq 125$.

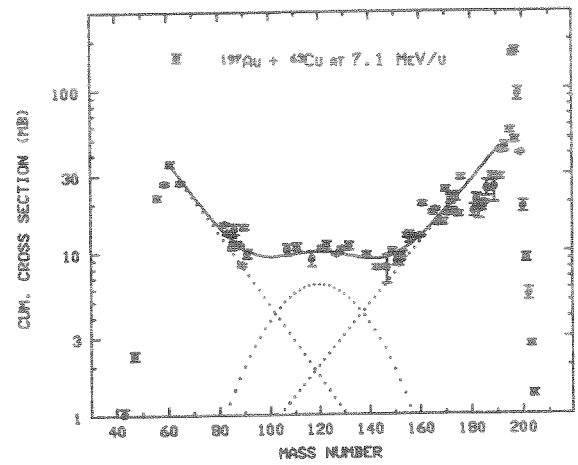


Fig. 2: Cumulative cross sections as zeroth approximation to mass-yield curve. See text for details.

As a zeroth approximation to the true integrated mass-yield curve (not yet finished), we display in Fig. 2 cumulative yields near beta-stability. If Z_p is sufficiently far from stability, such cross sections integrate physically via beta decay over practically the entire mass-yield chain, thus constituting fairly good approximations to the actual mass yields.

Assuming that the deep-inelastic yields follow an exponential dependence on A, and that the symmetric component is gaussian, we have resolved this curve into separate components: a) quasielastic transfer, ca. 440 mb; b) deep-inelastic transfer, ca. 1150 mb; symmetric fragmentation, ca. 150 mb. From the Dynamic Fusion Model, we expect 189 mb for the last.

[1] S. Bjørnholm and W.J. Swiatecki, Nucl. Phys. A391, 471 (1982).

[2] H. Gäggeler et al., Preprint GSI-83-38a (Dec. 1983).

[3] Provided by H. Folger and the GSI target laboratory.

Dynamic Inhibition of Fusion in the System $^{238}U + ^{nat}Fe$

B

A. Rox, B. Jäckel, R.A. Esterlund, W. Westmeier, U. Reus, H. Schulte and P. Patzelt

Institut für Kernchemie, Universität Marburg

In Fig. 1, we display a part of the yield surface for this system at 7.6 MeV/u. Starting from the top of the figure and moving downwards, we observe initially the "goldfinger" (survivors of sequential fission following deep-inelastic transfer), moving with an abrupt shift in the N/Z ratio into the symmetric component and thence with another shift in N/Z into the sequential fission component. The lone peak positioned on the neutron-rich side is the heavy partner of the low-energy quasielastic transfer induced fission component. Due to the fact that the lower-mass partner crosses over the beta-stability line, and is heavily fed by cumulative decay of sequential fission products, it cannot be unambiguously separated from sequential fission.

In order to further refine our measurement of the s-wave fusion-barrier shift for this system, previously[1] given as 35 ± 8 MeV, we have determined another point at higher energy (7.6 MeV/u) on the excitation function for symmetric fragmentation. Additionally, a counter[2] experiment on this system at 8.4 MeV/u has been performed for the same purpose, using the fission-fragment angular correlation method. Fig. 2 displays these results

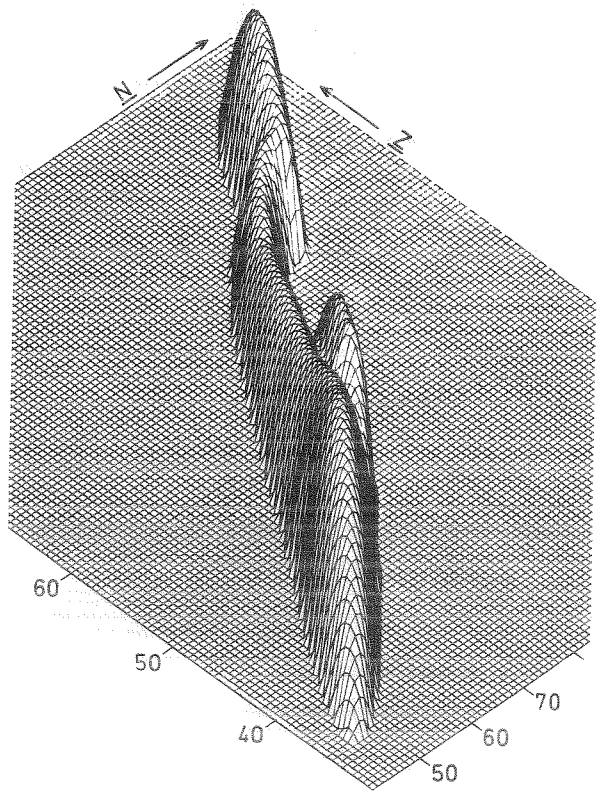


Fig. 1: Yield-surface plot (N vs. Z vs. log σ) for the system $^{238}U + ^{nat}Fe$. Discussion in text.

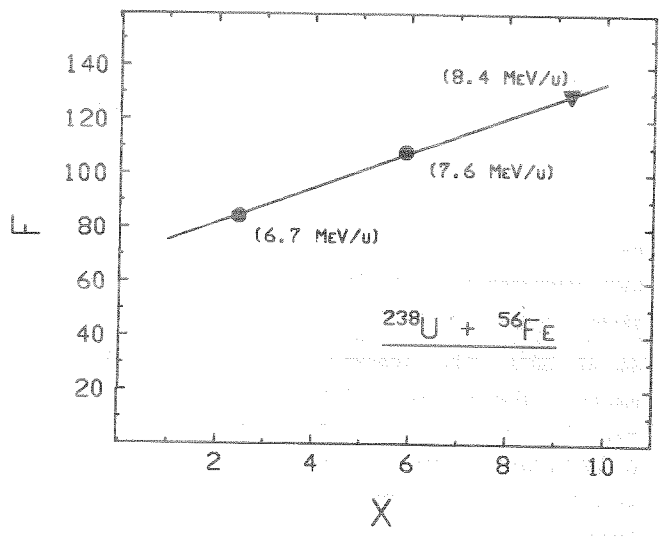


Fig. 2: Modified rectilinear cross-section plot for symmetric fragmentation. For details, see text.

as well as a previous[1] value in the form of a modified[3] rectilinear cross-section plot. The axes in such a plot are normally the root of the cross-section defect vs. the energy-weighted reduced fusion cross section i.e., $\sqrt{E - B - E\sigma/\pi R_c^2}$ vs. $E\sigma/\pi R_c^2$. In the above case, these axes have been modified[3] such that the slope of the plot is af^2 with intercept $a((Z^2/A)_{eff} - (Z^2/A)_{th})$. The Dynamic Fusion Model[3] predicts that in such a plot, the fusion data points should follow a straight line. Both the radiochemical data and the counter[2] datum appear to verify this hypothesis.

Since three model parameters are to be derived from two data (slope and intercept), it is necessary to assume a value for one of the scaling parameters. We deem it reasonable to adopt a value of 5/7 for the friction form factor f, corresponding to rolling in the entrance channel. We thus obtain a thud-wall slope coefficient a = 12.8 and an extra-push threshold $(Z^2/A)_{th}$ = 34.9 (X_{th} = 0.74). For comparison, if we adopt the value f = 3/4 from Ref. 3, we obtain a = 11.6 and $(Z^2/A)_{th}$ = 34.3 (X_{th} = 0.72). Both sets are in reasonable agreement with those of Ref. 3 i.e., a = 12 ± 2 and $(Z^2/A)_{th}$ = 33 ± 1 (X_{th} = 0.70 ± 0.02). The new value for the s-wave fusion-barrier shift, which is independent of the value assumed for f, amounts to 29 ± 5 MeV.

[1] A. Rox et al., GSI 83-1, 12 (1983).

[2] M. Kaplan, private communication (1983).

[3] W.J. Swiatecki, Nucl. Phys. A376, 275 (1982).

CHARGE AND MASS TRANSPORT IN THE REACTION $^{70}Ge + ^{238}U$ AT 8 MeV/u [B]

M. Marinescu, D. Bangert, B. Kohlmeyer, F. Pühlhofer
Fachbereich Physik der Universität Marburg
W.F.W. Schneider, D. Schüll
GSI, Darmstadt
H. Freiesleben, H. Sohlbach
Institut für Experimentalphysik, Ruhr Universität, Bochum

Projectile like fragments from the reaction $^{70}Ge + ^{238}U$ were measured at an incident energy of 8 MeV/u and at several angles around the grazing angle (θ_{lab} = 35, 38, 44, 47, 50°). The experiment was performed at the GSI magnetic spectrometer, which enabled a simultaneous mass (A) and charge (Z) identification of the reaction products with a resolution better than one unit, as well as a low background measurement even at small energy losses. We used a uranium target of 200 µg/cm^2, sandwiched between two carbon layers of 30 and 20 µg/cm^2, respectively. The energy resolution at 7° was approximately $\Delta E/E < 8 \times 10^{-3}$.

The goal of this experiment is to obtain the mass and Z - distributions of the products from quasielastic and deep-inelastic collisions and to determine the charge and mass drift and the respective variances , σ_Z^2, σ_N^2, σ_A^2, as a function of energy-loss and scattering angle. Due to the mass asymmetry in the entrance channel and the difference in N/Z ratios of the target and projectile the system is expected to show a N/Z equilibration and a mass drift to symmetry during the collision. For this reason it was chosen as a test case for models of dissipative heavy ion collisions, in particular the stochastical nucleon exchange model presented earlier [1].

The data for one angle, 44°, which we estimated to be around the maximum of the angular distribution are completely processed. The TKEL spectra for all identified isotopes were produced up to 120 Mev and the N - Z drift of the nuclide distribution centroids was determined for 5 MeV energy bins from 0.0 up to 60 MeV. Mass numbers A between 65 and 74 and atomic numbers Z between 28 and 34 were identified at this angle. The mass distributions for different elements are rather narrow, the FWHM being smaller than 5 mass units.

The drift of the centroids of the nuclide distributions are shown in Fig.1 as a function of the dissipated energy.

A preliminary and only approximate correction for sequential neutron and proton emission was applied to the data. For comparison, results from a model calculation for stochastical nucleon exchange based on single particle transitions are given also in Fig. 1. In order to fit the data, a relatively large contribution of mutual inelastic excitations to the dissipated energy would be required (50% instead of the 30% used in the figure). This is consistent with previous results. A more detailed interpretation will be made as soon as all data have been analyzed.

1) D.Bangert et al., GSI Scientific Report 1982,p.89)

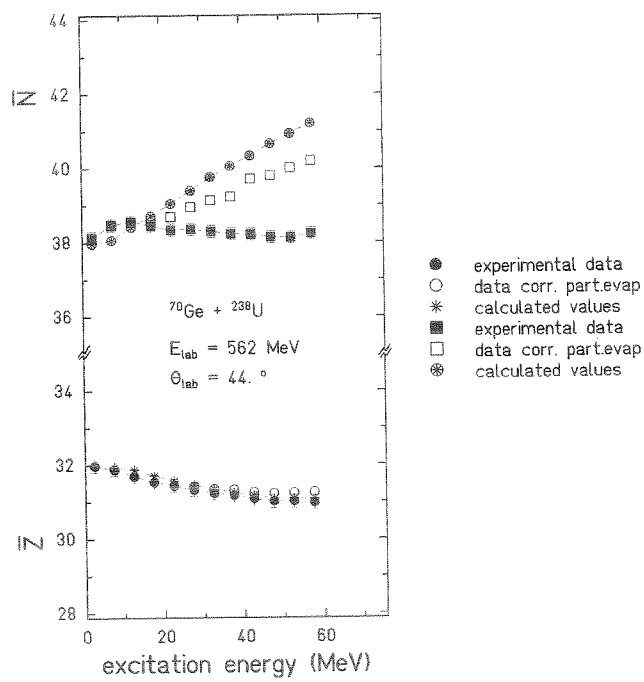


Fig. 1. The drift of the nuclide distribution centroids vs. excitation energy.

Pairing Effects in the Quasi-Elastic Neutron Transfer Between Tin Isotopes

W. von Oertzen, R. Künkel, B. Gebauer, A. Gamp, H.G. Bohlen, A. Miczaika, HMI Berlin
D. Schüll, W. Schneider, GSI Darmstadt

The investigation of pairing effects in the transfer of neutrons between low-lying states at energies close to and below the Coulomb barrier has been continued with the system $^{120}Sn + ^{112}Sn$. At the GSI magnetic spectrometer in December 83 a third run was performed in order to complete the data of the previous experiments which had been obtained with targets of insufficient homogeneity .

Targets of high isotopic purity produced by direct deposition onto a Carbon backing in the focal plane of the GSI isotope separator[1] were used because the elastic scattering on impurities competes with the multiple n-transfer with relative yields down to three orders of magnitude. In the previous run the energy resolution obtained was limited to 3.5-4 MeV (FWHM) due to the inhomogeneity of the targets. Some spectra for separated masses are shown in fig. 1. With the new targets the resolution was clearly improved.

For the masses 110, 111 as well as for 113, 114, 115 and 116 the yield is extended approximately within the same Q-value window of about 20 MeV width (which was therefore used for integration of cross sections) as for the mass 112 (elastic recoils: large angle scattering was measured by observing recoils at small angles). The concentration of the yield at the lowest excitation energies and the slopes of the transfer probabilities (see below) indicate that the low-lying states contribute most.

The differential cross sections of the different masses $\sigma_t(\theta)$ were transformed into probabilities $P_t(\theta)$ by means of the first-order perturbation approach $\sigma_t(\theta) = \sigma_e(\theta) \cdot P_t(\theta)$ and the angles were transformed to reduced distances of closest approach d_0 using Coulomb orbits. For definition of $\sigma_e(\theta)$ the elastic and inelastic cross section of mass 112 was taken according to the approach in ref. 2.

The results of both experiments are combined in fig.2. The experimental slopes of $P_t(d_0)$ agree well with the calculated radial dependence of the formfactors for the transfer reactions to the ground states: in fig. 2 α_1 and α_2 are the decay constants for the bound state wave functions of a single neutron and two neutrons, respectively, with the average binding energy between target and projectile. Using a definition of the enhancement which is described in more detail in refs. 2 and 3 we find that the two-neutron transfer is significantly enhanced. In addition, the probabilities reach values close to 0.5 at small distances d_0.

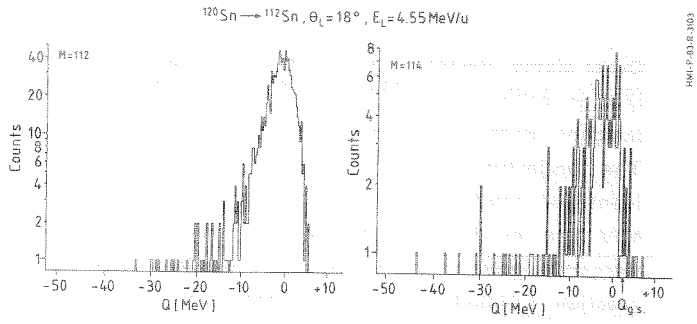


Fig. 1 Spectra of elastic recoils (M=112) and two-neutron transfer (M=114) as function of Q-value. The energy resolution is 3.5-4 MeV (FWHM).

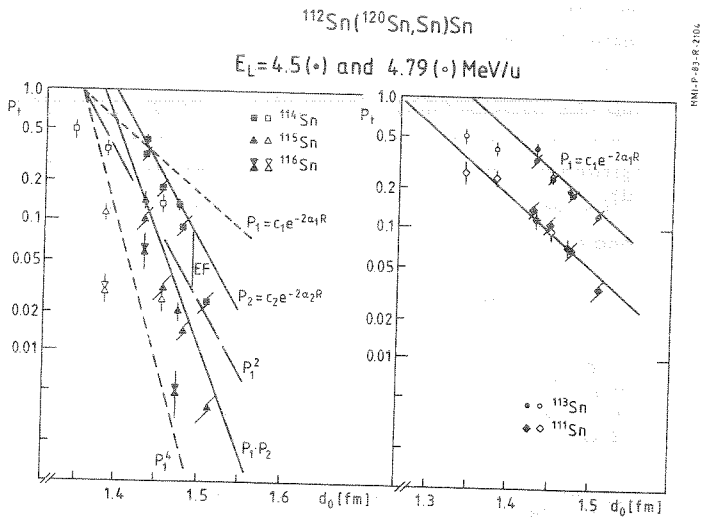


Fig. 2 Experimental transfer probabilities P_t (as defined in the text) for single- and multi-neutron transfer as function of the reduced minimum distance $d_0 = R_{min}/(A_1^{1/3} + A_2^{1/3})$. If corrected for the Q-value dependence of the cross sections, the data for ^{111}Sn (Q=-4.5 MeV) and ^{112}Sn (Q=-1.4 MeV) fall on the same curve. The straight lines give the slopes of the form factors for neutron transfer in the semiclassical approximation (see text). EF represents the enhancement factor of the two-neutron transfer due to the coherence of shell model states in the sequential 2-n transfer as compared to a successive independent single neutron transfer. If phase space factors are taken into account approximately the value EF ≈ 30 is obtained.

[1] K.H. Behr et al., GSI Scientific Report 1982, p. 218
[2] H. Siekmann et al., Z. Physik A307 (1982) 113
[3] W. von Oertzen et al., Z. Physik A313 (1983) 189

Quasi-Elastic Mass-Flow and Few Nucleon Transfer Reactions for ^{48}Ti Incident on ^{42}Ca and ^{26}Mg B,G

C. BRENDEL, J. CARTER*, A. RICHTER, G. SCHRIEDER, F. BECK
Institut für Kernphysik, Technische Hochschule Darmstadt
and D. SCHÜLL, GSI Darmstadt

Quasi-elastic nucleon transfer reactions have been studied in collisions of ^{48}Ti onto ^{42}Ca and ^{26}Mg at high incident energies at the GSI magnetic spectrometer[1]. The projectile-like final reaction products could be identified unambigously and energy spectra upto $E_x \approx 80$ MeV total excitation energy were extracted. Since the measured spectra may contain contributions from other reaction products with succeeding particle decay the shape of the measured spectra may be different from the primary distributions. In the reported measurements preferentially one and two nucleon decay occurs, thus, using the particle seperation energies and reaction kinematics, regions in the spectra can be marked which are particle stable or which are contaminated by one or two particle decay from reaction channels one, respectively two mass units above. Adding up the corresponding contributions, energy integrated cross sections for each final reaction product can be estimated. Figure 1 displays these results for ^{48}Ti + ^{42}Ca and ^{48}Ti + ^{26}Mg at the corresponding grazing angle (9.75° and 7°, resp.) measured at 385 MeV. The

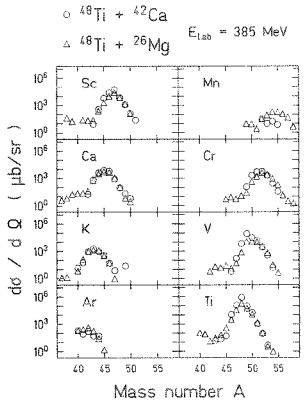


Fig.1: Energy integrated cross sections as a function of mass for each Z measured in the reactions ^{48}Ti + ^{42}Ca (θ_{Lab} = 9.75°) and ^{48}Ti + ^{26}Mg (θ_{Lab} = 7°).

mass and the Z distributions for both systems are similar, however, in the ^{48}Ti + ^{26}Mg case more final products have been measured. The primary cross section of the reaction products far from the injection channel is essentially built up by the different contributions produced by sequential particle decay and the stable part in these energy spectra is neglegible. Contrary to this the cross section for the few nucleon transfer channels is mainly covered by the stable part of the measured energy spectrum which in general is below E_x=15 MeV. These directly produced parts of the spectra show a gross structure specific to each reaction channel which persists as a function of scattering angle and for each incident energy measured. For low excitation energies (< 15 MeV) the single nucleon transfer channels in the ^{48}Ti + ^{42}Ca system could be described by a core-excitation model involving single particle states in both of the outgoing nuclei [1,2].

The two neutron transfer channel ^{50}Ti + ^{40}Ca has been described in the frame of this model as a two-step process by multiplying the probability functions for each transfer step. The result in the upper part of fig. 2 shows a broad distribution located at $E_x \approx 12$ MeV and approximately 10 MeV wide underlying the structure of the experimental spectrum. By subtracting this distribution from the experimental spectrum one obtaines a

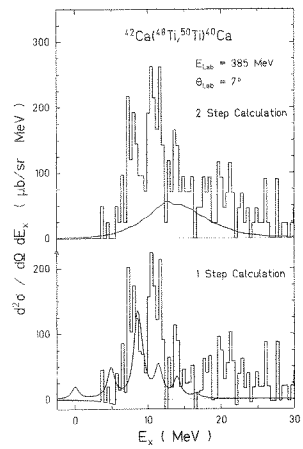


Fig.2: Two neutron transfer $^{42}Ca(^{48}Ti,^{50}Ti)^{40}Ca$. Upper part: 2-step calculation. Lower part: 1-step calculation and subtracted spectrum.

distribution as shown in the lower part of fig. 2 which still contains the specific structure. Using the core excitation model the strength for 1-step transfer of two neutrons as a pair was calculated including also deep-lying hole-states of the donor nucleus and is shown as a smooth curve. The correspondence of the localization of the peaks at excitation energies below 15 MeV is quite gratifying, although the strength of the calculated cross section is somewhat different from the experimental one.

Similar results can be obtained for the corresponding reaction channels in the system ^{48}Ti + ^{26}Mg which can be described satisfactorily for all angles measured. At present the single charge exchange channels are being studied in the same framework using a coupled-channels DWBA code which adds up the amplitudes of the two steps coherently.

---

* Present address: Department of Physics, University of the Witwatersrand, Johannesburg, South Africa

[1] C. Brendel, J. Carter, F. Beck, G. Delic, R.H. Lemmer, A. Richter, G. Schrieder and D. Schüll, GSI-Report 83-1 (1983) 15

[2] C. Brendel, J. Carter, F. Beck, A. Richter, G. Schrieder, D. Schüll, G. Delic and R.H. Lemmer, Phys. Lett. 124B (1983) 474

B

Quasielastic Neutron Transfer in the Reactions $^{208}Pb + ^{58}Ni$ and $^{208}Pb + ^{64}Ni$

K. Sapotta[x], R. Bass[+], V. Hartmann[xx], H. Noll[xx], K. Stelzer
Institut für Kernphysik der Johann Wolfgang Goethe-Universität
Frankfurt am Main

The quasielastic nucleon transfer ($Q \geq -10$ MeV) in the reactions $^{208}Pb + ^{58}Ni$ (5,9 MeV/u) and $^{208}Pb + ^{64}Ni$ (5,4 MeV/n) was investigated using data taken with the focussing time-of-flight spectrometer. The neutron transfer dominates because of the closed proton shells in Pb and Ni.

A preponderance of the neutron transfer from the heavier to the lighter nuclei as compared to the transfer in the opposite direction is observed by a factor of 4 for the $^{208}Pb + ^{64}Ni$ system and by two orders of magnitude for the $^{208}Pb + ^{58}Ni$ system. This behaviour can be explained by the ground state Q values of the different reaction channels /1/. Fig. 1 shows the transfer probabilities

$$P = \frac{d\sigma}{d\Omega} \Big/ \left[\frac{d\sigma}{d\Omega} \text{ (elastic)} + \sum \frac{d\sigma}{d\Omega} \text{ (quasielastic)} \right]$$

in their dependence on the minimal distance of approach of the centres of the nuclei D, calculated for Coulomb-like orbits. The probability for the transfer of a neutron from lead to nickel is 30% and 5% for distances of the nuclear surfaces (calculated with the half-density radii) of 3,3 and 5,3 fm respectively.

The transfer probabilities show the exponential dependence on distance expected from calculations with a semi-classical theory. Except for ^{62}Ni and ^{63}Ni, the transfer probabilities, extrapolated to smaller distances of approach, for both reacting systems intersect at $P \approx 1$ for a distance of the nuclear surfaces of about 2.5 fm.

The probability of a transfer of several neutrons (exception ^{62}Ni) can be expressed by the corresponding product of probabilities of one-neutron transfer. An enhancement of multi-nucleon transfer was not observed.

At the grazing angle ($D \approx 14{,}3$ fm) the quasielastic transfer probabilities for the transfer from the heavier nucleus (Pb) to the lighter nucleus (Ni) lie significantly lower than expected from the exponential dependence. For the transfer in the opposite direction no reduction or even a small enhancement of P is observed. The reduction of P at the grazing angle is interpreted to be due to the competition of the deep-inelastic channel. By a transfer of a nucleon to the lighter nucleus the probability for an absorption into the deep-inelastic channel is increased because the potential between the nuclei becomes more attractive, whereas after a transfer in the opposite direction the reaction partners will separate with high probability with a small loss in kinetic energy /2/.

/1/ K. Sapotta, Dissertation, Frankfurt/M., 1983
/2/ V. Hartmann, Dissertation, Frankfurt/M., 1981

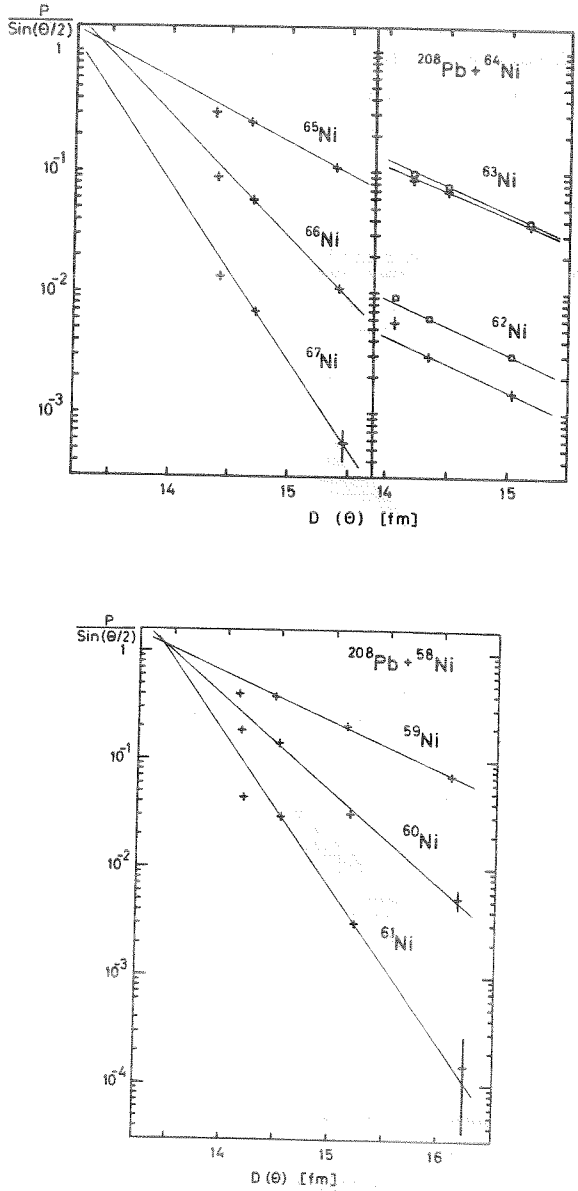


Fig. 1 Quasielastic transfer probabilities in their dependence on the nuclear distance. a) System $^{208}Pb + ^{58}Ni$, b) System $^{208}Pb + ^{64}Ni$.

+ deceased October 2nd, 1981
xx now at GSI
x now at Siemens AG, München

Strong Dominance of Closed Shells on the Diffusive Phase in ^{238}U Induced Reactions [B]

G. Beier, J. Friese, P. Kienle, H.J. Körner, Waltraud Mayer, W.A. Mayer, L. Müller, W. Wagner
Physik-Department, TU München

W. Henning
ANL, Argonne, USA

Data obtained for the $^{238}U + ^{110}Pd$ and $^{238}U + ^{112,124}Sn$ systems at incident energies near the barrier were analyzed in order to extract the influence of closed shells on the diffusive phase of inelastic transfer processes. Here we concentrate on events with a large nucleon transfer ($\Delta Z \geq 10$, $\Delta N \geq 20$) from ^{238}U to ^{110}Pd. As can be seen in Figs. 1a, b these are events with $Q < -60$ MeV, extending approximately to $Q \sim -150$ MeV. This is the region of the equilibrated diffusive nucleon exchange. The data represent the primary distribution as deduced from kinematic coincidence techniques. Figs. 2a, b indicate the most abundant Z and N values as derived from these distributions i.e. the "direction of the nucleon flux" for both partners of the reactions. The liquid drop driving potential corrected for shell effects is also shown. The dominant influence of the N = 82, 126 and Z = 82 closed shells is clearly seen. Similar behaviour is found for the ^{124}Sn target nuclei. These results demonstrate that the incident nuclei after formation of the binary complex never loose their identity completely, and their behaviour is dominated by "spherical cores" although as many as 30 nucleons and more than 60 MeV of energy are transfered.

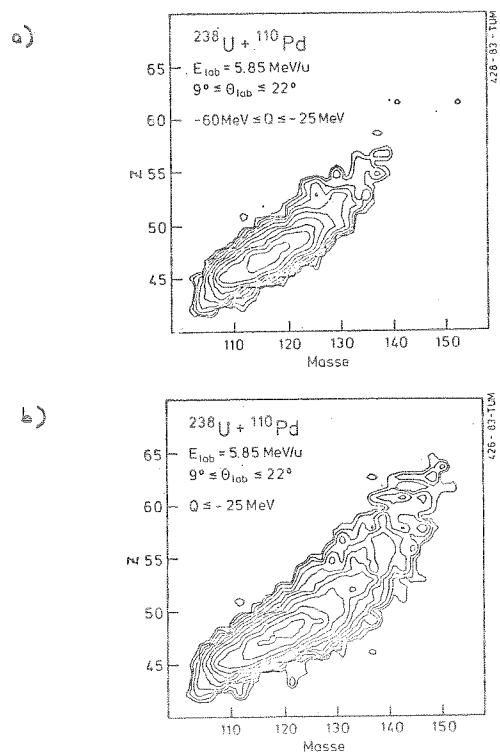


Fig. 1: Contour plot of cross sections for binary events in the $^{238}U + ^{110}Pd$ reaction.
a) All inelastic events up to Q = -60 MeV
b) All inelastic events for Q < -25 MeV.

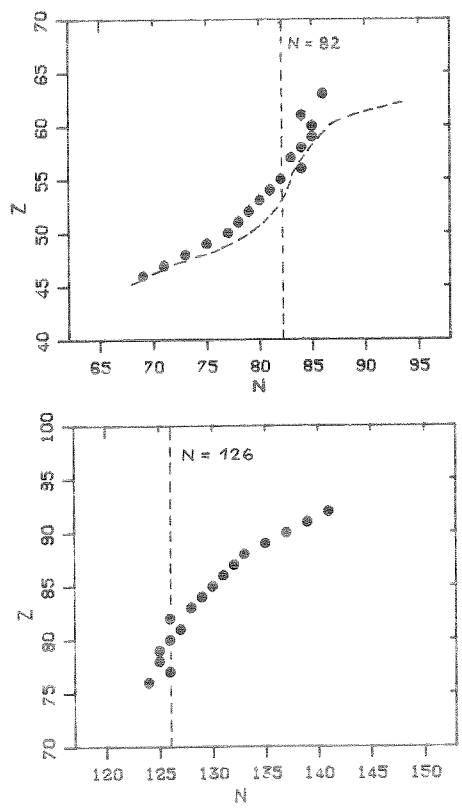


Fig. 2: Most abundant N, Z values for binary events with Q < -25 MeV in the $^{238}U + ^{110}Pd$ reaction. Uncertainties in Z and N are always ≤ one unit. The driving potential is shown in the dashed line.

Empirical Description of the Element Production in Dissipative Heavy-Ion Collisions

Hans-Jürgen Wollersheim

One of the most distinctive features of dissipative heavy-ion collisions are the element distributions of the reaction fragments. The double differential cross section $d^2\sigma/dZdE$ as a function of atomic number Z for different kinetic energy bins E are Gaussian in shape to a good approximation. The variance of the element distribution σ_z^2 increases markedly as the final total kinetic energy E decreases. In an earlier publication[1] a correlation is suggested which is remarkable due to the fact that the dependence is unique for different projectile-target combinations and bombarding energies well above the Coulomb barrier. On the basis of these experimental results the double differential cross section $d^2\sigma/dZdE$ can then be written as

$$(1) \qquad \frac{d^2\sigma}{dZdE} = N(E)\ \exp\left\{ - (Z-Z_0)^2/2\sigma_z^2(E)\right\}$$

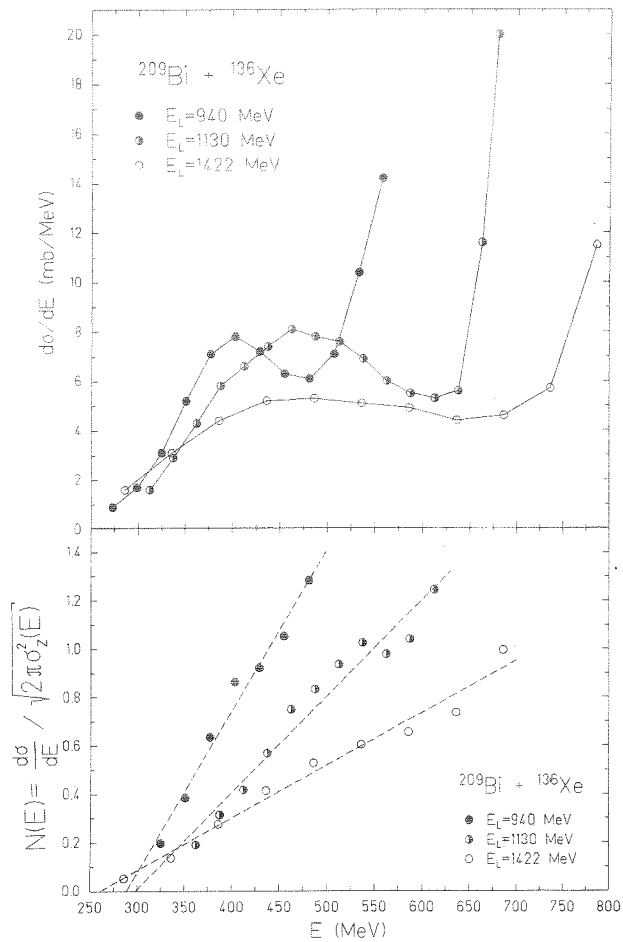
with

$$(2) \qquad \sigma_z^2(E) = \exp\left\{ - 6.07\ \frac{E-E_0}{\ell_g}\right\}$$

where ℓ_g is the grazing angular momentum, N(E) is the unknown normalization of the Gaussian distribution and E_0 is approximately the incident energy in the center-of-mass system. If one integrates Eq.1 with respect to Z, one obtains the energy distribution

$$(3) \qquad \frac{d\sigma}{dE} = N(E)\ \sqrt{2\pi\sigma_z^2(E)}$$

Since the differential cross section and the variance of the Z distribution are experimental observables, it is possible to deduce the energy dependence of the function N(E). The results of this analysis are shown in the figure for the $^{209}Bi + ^{136}Xe$ reaction measured at laboratory bombarding energies of 940, 1130 and 1422 MeV[2,3,4]. In the upper part of the figure the energy distributions $d\sigma/dE$ of the Xe-like fragments are plotted versus the final total kinetic energy E. These data are used, together with the measured variance of the Z distribution $\sigma_z^2(E)$ from the corresponding energy bin to determine the function N(E) which is displayed in the lower part for the three reactions. As can be seen, there is a nearly linear relationship between N(E) and the total kinetic energy E which develops from the common deformed Coulomb barrier V_c^{def} at approximately 284 MeV and reachs its largest value for approaching the incident energy E_0. The slope of the individual lines fitted to the data increases with decreasing bombarding energy. It is interesting to realize that there is a close similarity to the dependence of the classical



cross section $\frac{d\sigma}{d\ell} = \pi/k^2(2\ell+1)$ on the initial angular momentum ℓ if one replaces ℓ by the measured final total kinetic energy E. This replacement is plausible based on a reported [1,2,3] nearly linear relationship between $\langle\ell\rangle$ and $\langle E\rangle$. The experimental finding of a linear relation between the function N(E) and E - shown here for the $^{209}Bi + ^{136}Xe$ reaction - is typical for damped collisions. Based on the analysis of twelve heavy ion systems the function N(E) is reasonably well approximated by

$$(4) \qquad N(E) = 0.0324\left\{\frac{R_{int}^2}{E_0} - 0.190\right\}(E-V_c^{def}) \qquad \text{mb/MeV}$$

where R_{int} is the interaction radius. The good agreement of experimental element and energy distributions with the empirical expressions (Eq. 1-4) gives some confidence for predicting experimental results for different projectile-target combinations and higher incident energies.

1. H.J. Wollersheim et al., Phys.Rev. C25, 338 (1982)
2. W.U. Schröder et al., Phys.Rep. 45C, 301 (1978)
3. W.W. Wilcke et al., Phys.Rev. C22, 123 (1980)
4. H.J. Wollersheim et al., Phys.Rev. C24, 2114 (1981)

Equilibration of the Neutron to Proton Ratio for Heavy Asymmetric Systems in Heavy Ion Collisions

R. Lucas, C. Grégoire, C. Ngô, J. Poitou, E. Tomasi
DPh - N/MF, CEN Saclay, France
A. Gobbi, A. Olmi, H. Sann, G. Wirth, J.V. Kratz*
GSI Darmstadt
U. Lynen
MPI Heidelberg

The pending question whether N/Z-equilibration between complex nuclei is caused by a collective mode of high frequency analogous to the E1 giant resonance[1] or whether this equilibration results from the statistical exchange of independent nucleons[2] has attracted much theoretical interest. The models available at present differ by 1. the choice of the collective variables assuming hereby correlated motion of neutrons and protons or, conversely, independent particle propagation, 2. the transport equations, 3. the transport coefficients, and 4. the details of the collision dynamics.
We have confronted new experimental data on nuclide distributions in damped collisions of ^{208}Pb with ^{74}Ge and of ^{86}Kr with ^{197}Au measured[3] with a large area position-sensitive ionisation chamber and published radiochemical data for ^{132}Xe + ^{197}Au - collisions[2] with the predictions of three models. In the case of the ^{208}Pb + ^{74}Ge and ^{86}Kr + ^{197}Au data we have folded the theoretical distributions i) with resolution functions to take into account the finite Z- and A-resolution of the detection system and ii) with the particle evaporation pattern. The resulting theoretical (secondary) distributions are then compared to the uncorrected data. For the ^{132}Xe + ^{197}Au system the published data are representative of the primary distributions and are thus compared directly to the theoretical predictions.

Good agreement between experiment and theory is observed for the marignal and conditional variances for the quantal model[4] of Hofmann et al.. Here, however, the frequency-dependent transport coefficients were not calculated microscopically but were assumed to be constants and were fixed empirically by the asymptotic properties of the system. Also, the transfer of energy from the relative motion to the intrinsic degrees of freedom is parametrized empirically. In addition, the phonon energy of the isovector giant resonance is treated as a constant fixed by the experimental data. Some of these apparent deficiencies were removed in the model of Grégoire et al.[5] who generalized the transport equation of Hofmann to several degrees of freedom. However, the phonon energies for the N/Z-mode are still determined phenomenologically. Fig. 1 depicts for the ^{86}Kr + ^{197}Au system the agreement between the (secondary) theoretical results and the experimental data. As a second example we show in Fig. 2 a comparison of the charge widths at fixed primary mass asymmetry for ^{132}Xe + ^{197}Au with the model of Gross and Hartmann[6] which treat on a microscopic level the stochastic exchange of independent particles. Their transport equation is a Fokker-Planck equation with overdamped motion. We have used here a version where dynamical deformations of the colliding nuclei are considered. This enhances nucleon exchange in the entrance channel. All three models, even though quite different in the inherent physical assumptions, seem to reproduce the experimental variances at least qualitatively. Thus, our attempts to analyse data with existing dynamical models in their present stage of development have not succeeded to discriminate between quantal versus statistical fluctuations.

*presently at Institut für Kernchemie, Univ. Mainz

References

1. M. Berlanger et al., Z. Phys. A291, 133 (1979)
2. J.V. Kratz et al., Nucl. Phys. A357, 437 (1981)
3. R. Lucas, Thesis, Orsay (1983)
4. H. Hofmann et al., Z. Phys. A293, 229 (1979)
5. C. Grégoire et al., Phys. Lett. 99B, 17 (1981)
6. D.H.E. Gross et al., Phys. Rev. C24, 25 (1981) and Z. Phys. A299, 63 (1981)

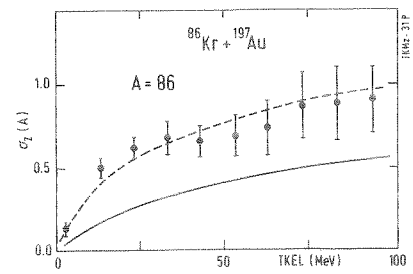


Fig.1: Comparison of the (secondary) charge widths at fixed mass for Kr + Au with the prediction of the Grégoire model[5]. The dashed line results from the primary widths (solid line) after correctiosn for particle evaporation and limited Z and A resolution.

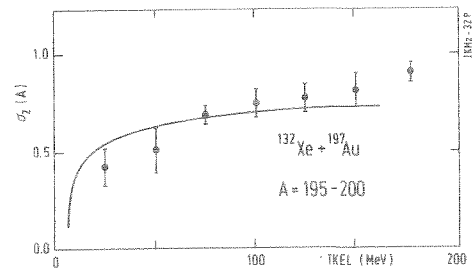


Fig.2: Charge widths at fixed primary mass for Xe + Au and the prediction of the Gross-Hartmann model[6] with dynamical deformations of the colliding nuclei.

Angular Distributions for Symmetric Fragmentation in $^{50}Ti + ^{208}Pb$ Collisions

K. Lützenkirchen and J.V. Kratz
Inst. für Kernchemie, Universität Mainz
L. Dörr and G. Wirth
GSI, Darmstadt
C. Grégoire and R. Lucas
DPh - N/MF, CEN Saclay, France

In studies of angular distributions for fragments with about half the mass of the combined system it was observed for the heaviest systems like $^{208}Pb + ^{58}Fe$ /1/ that there is a way from the entrance channel to a symmetric exit channel that bypasses the slow process of compound nucleus formation. In an attempt to search for angular momentum limits for the coexistence of complete fusion-fission, fast-fission, and deep-inelastic scattering, the angular distributions for symmetric fragmentations had been reexamined in the $^{56}Fe + ^{208}Pb$ system /2/ at E/B = 1.1, 1.2, 1.3, and 1.6 using catcher foil techniques and off-line KX-ray spectroscopy. For all values of Z (except for $(Z_1 + Z_2)/2$) angular distributions were observed that were asymmetric around $\theta_{cm} = 90^{\circ}$. The distributions were forward peaked for $Z \leq (Z_1 + Z_2)/2$ and backward peaked for the heavy complements /2/. The degree of forward-backward asymmetry and the mean anisotropies were largest at the smallest energy ($\ell_{crit} = 35\ \hbar$ in a sharp cutoff approximation) and decreased as the bombarding energy increased /2/. This might be seen as evidence for a dynamical hindrance for compound nucleus formation even below $\ell_{(B-f=0)} = 37\ \hbar$ and might help localizing the value of x_{cliff} /3/. Then, in a less critical system one might expect to see true compound nucleus fission at low ℓ values and a change to forward-backward asymmetric angular distributions at higher angular momenta.

We examined the system $^{50}Ti + ^{208}Pb$ at energies E/B = 1.06 and 1.16 using the same technique as mentioned above. Relative cross sections for $40 \leq Z \leq 83$ between 10° and 178° in the center-of-mass system were measured. The results at E/B = 1.06 for two elements (Z=47,54) near the symmetric charge split Z=52 are depicted in Figs.1,2. The solid curves are calculations in terms of the standard fission theory /4/. Within error limits, the distributions seem to be symmetric around 90°. When calculating the maximum number of partial waves contributing to the fusion cross section /1/ in a triangular sharp cutoff approximation, we arrive at a value of $K_o^2 = 25$, which is much lower than expected for a compound nucleus reaction. Larger anisotropies than expected from saddle point shapes of the rotating liquid drop model have been reported even for lighter systems /5,6/.

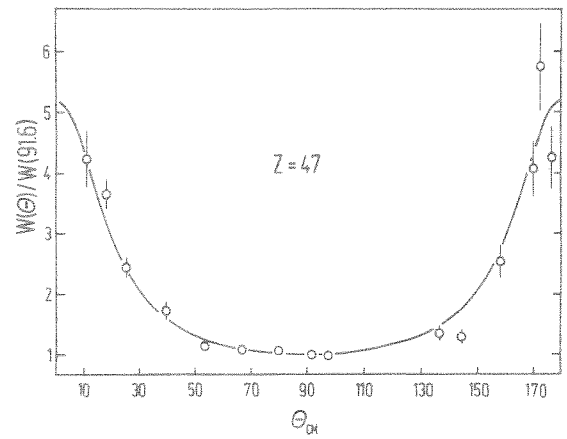


Fig 1 : Angular distribution for Z=47 in the reaction $^{50}Ti + ^{208}Pb$ at E/A = 5.0 MeV/A. The cross sections $d^2\sigma/dZd\theta$ are normalized to the one which is closest to 90°.

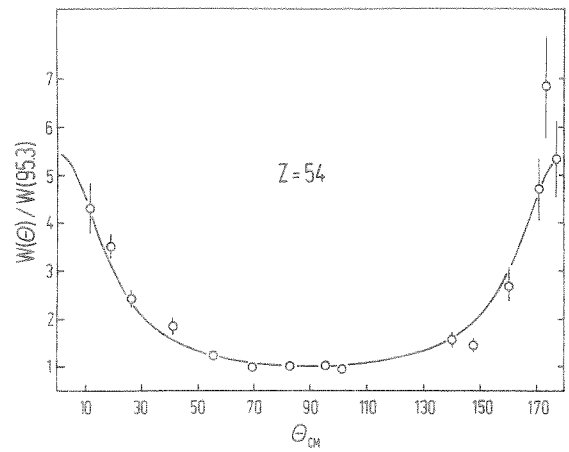


Fig 2 : Angular distribution for Z=54 in the reaction $^{50}Ti + ^{208}Pb$ at E/A = 5.0 MeV/A.

/1/ R.Bock et al., Nucl.Phys. A388, (1982) 334
/2/ G.Guarino et al., GSI Annual Report 1981
/3/ S. Bjørnholm and W. J. Swiatecki, Nucl.Phys.A391, (1982) 471
/4/ R.Vandenbosch, J.R.Huizenga, Nuclear Fission (Academic Press 1973)
/5/ H.Rossner et al., Phys.Rev. C27, (1983) 2666
/6/ M.B.Tsang et al., Phys.Rev. C28, (1983) 747

Light-particle emission in the fusion reaction $^{48}Ti+^{45}Sc$ at 16 MeV/u [B]

H.-J. Keim, B. Kohlmeyer, H. Stege, H.-A. Bösser and F. Pühlhofer
Fachbereich Physik der Philipps-Universität Marburg
W.F.W. Schneider
GSI Darmstadt

Light-particle heavy-ion coincidence measurements were performed for the reaction $^{48}Ti+^{45}Sc$ at 16 MeV/u in order to study the mechanism leading to fusion reactions in the energy range between 10 and 20 MeV/u. The experimental set-up consisted of seven solid state Si-NE104 telescopes between θ_{LAB}=-12° and -82° for the light-charged particles and two 700µm-Si-detectors at θ_{LAB}= +5° and +13° for heavy reaction products. The beam pulse was used as start signal for the time-of-flight measurements. With a time resolution of 200ps and a flight-path of 40 cm between target and Si-detectors a mass resolution of Δm/m = 4% was achieved for the evaporation residues. At +9° a TOF-ΔE-E telescope with a flight path of 170 cm was used to measure heavy products with Z- and A-separation.

The cross sections for α-particles in coincidence with fusion-like products at +13° are shown in fig. 1A in a velocity plot (v_x vs. v_z, z-axis in beam direction). When comparing to a Monte-Carlo calculation (fig. 1B) for emission from an equilibrated compound nucleus one observes distinct differences. The experimental velocity distribution is significantly broader, and there are indications in backward direction for an additional component from a slow source. The angular distribution of the α-particles is shown in fig. 2 for the same coincidence condition. In forward direction the experimental distribution is peaked much more strongly than the calculated, although a C.M.-distribution ∿ 1/sin θ was assumed in the Monte-Carlo simulation.

The interpretation of these results is complicated by two problems. First, it is not known at present to which extent additional reaction mechanisms contribute to the group of fusion-like residues. There is evidence for an interference with strongly damped binary reactions with a broad mass distribution. They might be responsible for at least part of the apparent deviations from equilibrium. Secondly, our light-particle spectra taken in coincidence with heavy ions at +5° and +9° suffer from poor statistics due to the high elastic-scattering rate at these angles. A further experiment with an improved set-up is in preparation.

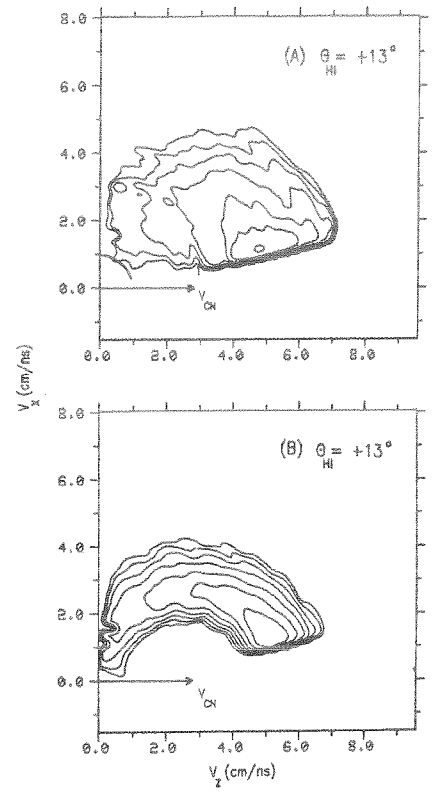


Fig. 1. Contour plots of the cross section $d^2\sigma/dv_{lab}d\Omega_{lab}$ as a function of the velocity of α-particles in coincidence with fusion-like products observed at +13 degree.
(A) Experimental results. The solid circle represents the energy threshold of the α-detectors.
(B) Results of a Monte-Carlo calculation.
The contours are expressed in arbitrary units 2^n,n=2,3,..8.

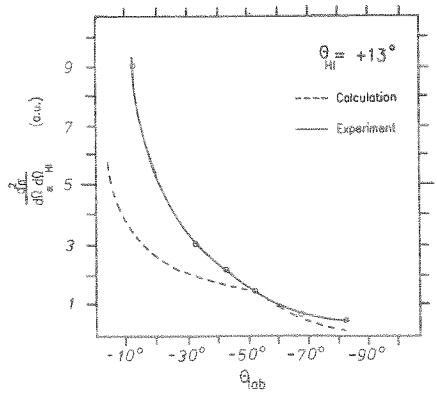


Fig. 2. Angular correlations of α-particles in coincidence with fusion-like products. The Monte-Carlo calculation (dashed curve) has been normalized to the experimental data at θ_{lab} = -52°.

B

Alpha Particle Associated Collisions of ^{208}Pb with ^{56}Fe

P.J. Brülls, H.P. Hollenbach, M. Mutterer, J. Pannicke,
J.P. Theobald and K. Weingärtner
Institut für Kernphysik, Technische Hochschule Darmstadt

Alpha particles have been recorded in coincidence with two heavy-ion fragments of the essentially binary reaction ^{208}Pb on ^{56}Fe at a projectile energy of 8.0 MeV/u. The experimental set-up, described in the proceeding annual report[1] has been extended by additional ΔE semiconductor detectors in the forward light-particle detector telescope and has been adjusted during a parasitic run with a 11.5 MeV/u ^{129}Xe beam on palladium. The following preliminary results have been obtained: The center-of-mass energy spectra of the alpha particles show a broad distribution with a maximum at 18.5 MeV. The particles are emitted by the binary heavy ion reaction products of mainly deep inelastic reactions.

Our interest was focussed on alpha and other light charged particles emitted from the neck region of the fissioning compound nucleus of the fused system[2,3]. The angular distribution of the alpha particles relative to one heavy fragment in the center-of-mass system has been evaluated, in order to find yield enhancement around 90°. Although the detector system is especially sensitive to near symmetric fusion-fission events (Fig. 1) there is no evidence for alpha emission from the neck region. From triple coincidences between alpha particles and two reaction product nuclei we conclude, that 92 ± 8 % of the alpha particles originate from deep inelastic processes close to symmetric fragmentation. Fig. 2 shows the experimental correlation between binary fragment masses and alpha particle yields. The evaluation goes on to deduce the ratio of in-to out-of-reaction-plane alpha particles.

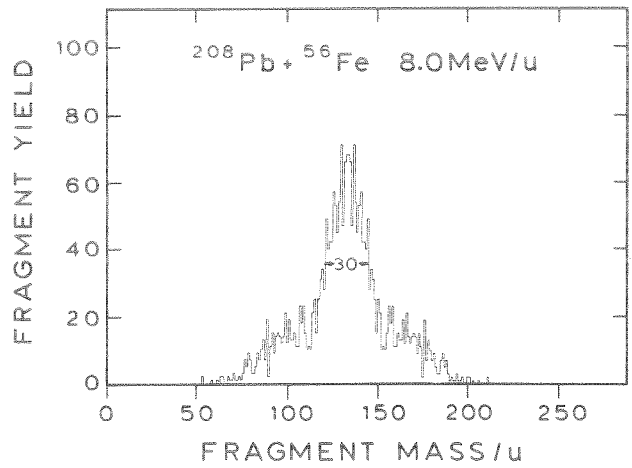


Fig. 1: Yield of heavy-ion reaction products as a function of the fragment masses

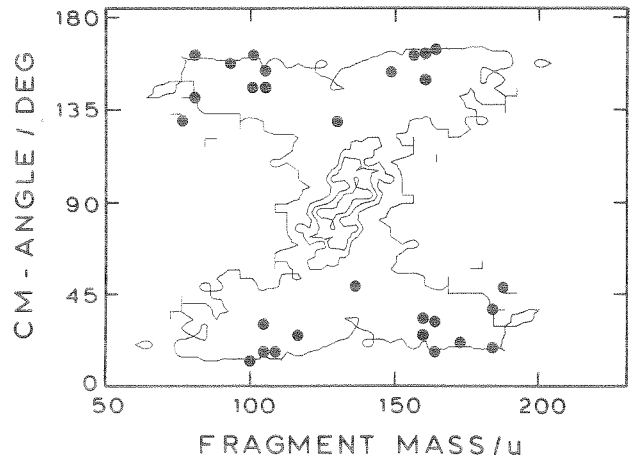


Fig. 2: Yield of heavy-ion reaction products as a function of the fragment masses and CM angles. The black dots mark fragments coincident with α-particles.

[1] P.J. Brülls, H.P. Hollenbach, M. Mutterer, J. Pannicke, J.P. Theobald, K. Weingärtner, H.W. Daues, A. Gobbi GSI-Report 83-1 (1983) 18

[2] W.W. Wilcke, J.P. Kosky, J.R. Birkelund, M.A. Butler, A.D. Dongan, J.R. Huizenga, W.U. Schröder, H.J. Wollersheim, D. Hilscher Phys. Rev. Lett. 51 (1983) 99

[3] J.P. Kosky, W.W. Wilcke, J.R. Birkelund, M.A. Butler, A.D. Butler, J.R. Huizenga, W.U. Schröder, H.J. Wollersheim, D. Hilscher Phys. Lett. 133 B (1983) 153

Evolution of Charge and Mass Transfer in the Reaction ^{92}Mo on ^{154}Sm at 14.8 MeV/u.

M. Petrovici,* R. Bock, A. Gobbi, S. Gralla, G. Guarino,** K.D. Hildenbrand, U. Lynen, W.F.J. Müller, A. Olmi,+ H. Sann, H. Stelzer, J. Tõke, and H.J. Wollersheim,
GSI Darmstadt

The study of the N/Z-equilibration is helpful in gaining insight into the processes involved in the early stage of heavy ion collisions and experimental information might discriminate among different theoretical descriptions, at least in principle[1].

We have analyzed in detail the evolution of charge and mass distributions in the ^{92}Mo + ^{154}Sm system at 14.8 MeV/u. The data are part of an extensive survey of ^{92,98}Mo-induced reactions on different targets at this energy, some general results of which have been published elsewhere[2]. The experimental set-up consisted out of a large-area ionization chamber and twelve position-sensitive avalanche detectors, which allowed to measure inclusively or exclusively binary or ternary events. For the present analysis we have used only inclusive data of the ionization chamber, since only this device measures the nuclear charge Z. In order to reconstruct primary masses and charges a multistep iterative correction on particle evaporation[3] has been applied.

Fig.1 shows contour plots of $d^2\sigma/dZ \cdot dA$ for different bins of the total kinetic energy loss (TKEL) between 20 and 180 MeV; each bin has a width of 20 MeV. The figure demonstrates how the ridge of the distributions turns and shifts off from the initial location until it finally stretches along the A/Z of the composite system. Fig.2 demonstrates, that the evolution of the mean values <Z>, <N> follows the gradient of the shell-corrected potential energy surface (PES) of the system until it reaches the bottom of the valley. Fig.3, finally, shows the charge variances as a function of TKEL for a window in mass of ±2 units around the initial projectile mass. After a fast increase during the first 80 MeV σ_Z^2 levels off for higher TKEL. The influence of the finite mass resolution is under analysis.

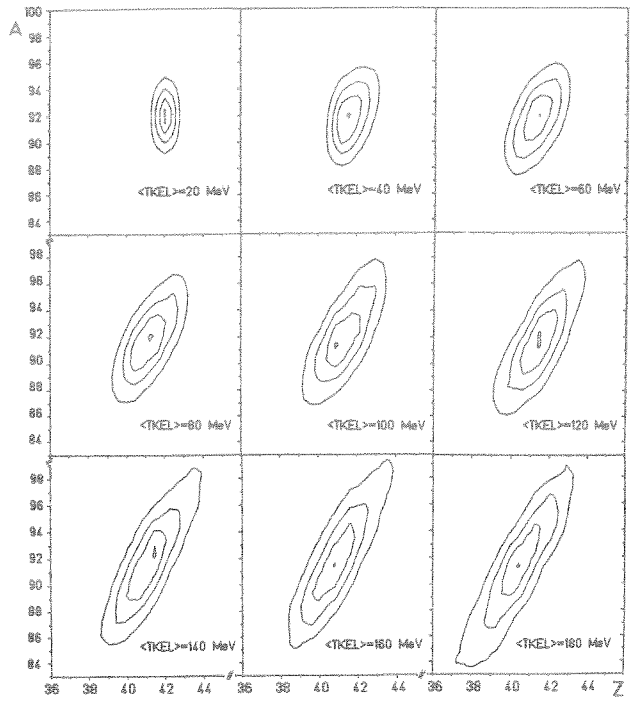


Fig.1: $d^2\sigma/dZ \cdot dA$ of the ^{92}Mo+^{154}Sm reaction at 14.8 MeV/u for consecutive bins of TKEL (20 to 180 MeV, bin width 20 MeV).

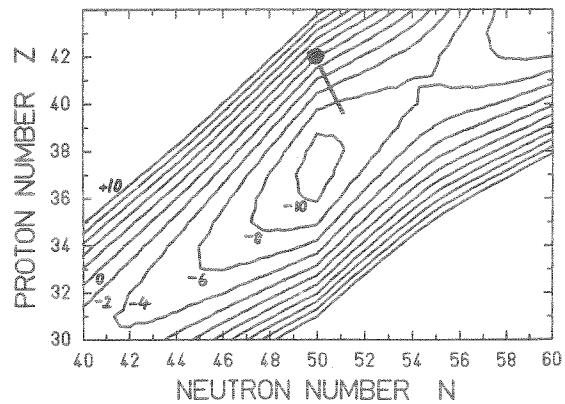


Fig.2: Shell-corrected potential energy surface of the ^{92}Mo+^{154}Sm system. The evolution of the mean values <Z>, <N> with increasing TKEL is shown by the thick solid line from injection up to <TKEL> = 200 MeV.

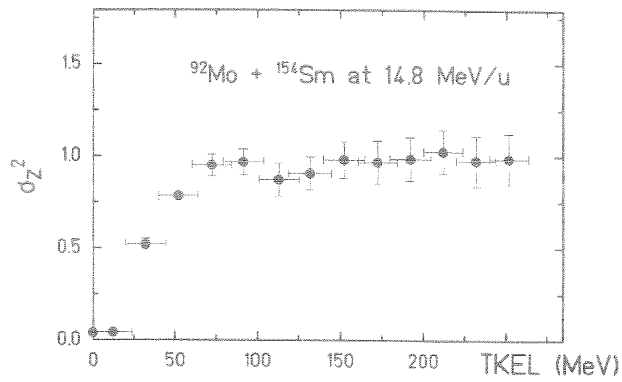


Fig.3: Charge variances as function of TKEL at fixed mass asymmetry (A=92±2 u).

* on leave from IPNE Bucharest, Romania
** University of Bari, Italy
\+ now at INFN, Florence, Italy

1 R. Lucas et al., contrib. to this Annual Report
2 M. Petrovici et al., Nucl. Phys.A387(1982)313c
3 S. Gralla et al., Z. Physik A310(1983)345

Product Distributions at High Excitation Energies in Heavy Ion Collisions at 8 to 20 MeV/u.

S. Gralla, R. Bock, Dai Guang-xi,* A. Gobbi, K.D. Hildenbrand, J. Kuźminski,**
W.F.J. Müller, U. Lynen, A. Olmi,*** M. Petrovici,+ H. Sann, H. Stelzer, J. Töke,++
and H.J. Wollersheim, GSI Darmstadt

In the $^{92}Mo + ^{92}Mo$ reaction at 14.7 MeV/u one-particle inclusive, binary and ternary exit channels were investigated with a large-area ionization chamber (IC) and a set of 12 position-sensitive avalanche detectors. From the inclusive data the charge distributions can be determined reliably only up to energy losses (TKEL) of about 200 MeV. It has been shown[1] that the 2nd moments of these distributions can be well explained within a stochastic exchange model[2] originally derived for dissipative collisions at low incident velocities.

The mass (charge) distributions at higher energy losses are better accessed by the coincidences between IC and avalanche detectors since the primary kinematical process is on the average completely determined by the measured velocity vectors. Binary processes were selected by requiring coplanarity and collinearity of two coincident fragments. Fig.1 shows the resulting diffusion plot $d^2\sigma/dTKE^*dA$; TKE^* is the total kinetic energy corrected for the difference in Coulomb energy between entrance and exit channel. At complete relaxation the mass distributions widen drastically; the tails reach masses below A=30 where they are eventually cut by experimental thresholds. This increase is shown quantitatively in fig.2 where $\ell n\sigma_Z^2$ is plotted as function of TKE/ℓ_{gr}; σ_Z^2 was calculated from $\sigma_Z = Z/A \cdot \sigma_A$. The solid line follows in its slope the systematics of Wollersheim et al.[3] (below $\sigma_Z^2 \sim 2$ it is matched to the results[2] of the stochastic exchange model), which was found in a compilation of a variety of systems at low incident energies. As it is seen in the figure it predicts well the increase of charge and mass variances with TKEL also in our case where the energy loss reaches values up to 500 MeV.

Based on this confirmation of the systematics[3] at higher energies one can therefore investigate, how, as a function of the excitation energy E^x the initial identity of target and projectile gets lost and how the nucleon exchange propagates. In fig.3 we show the calculated increase of the mass variance as a function of the temperature T ($T = \sqrt{8 \cdot E^x/A}$). The solid line connects the mass variances at different bombarding energies (8 to 20 MeV/u) at fixed TKE of 200 MeV, which is about the spherical Coulomb barrier. The variances increase like $\sigma_A^2 \propto \exp(1.52 \cdot T)$; the exponential slope is determined by the universal slope of the systematics and system-dependent quantities. For higher TKE (lower TKEL) the slope is even slightly higher. The dashed line shows the variances at 18 MeV/u for different total kinetic energies TKE. It is questionable at present whether the observed strong increase can be understood within a diffusion or a one-body dissipation picture or whether a strong contribution of two-body terms needs to be advocated.

* A.v.Humboldt-Fellow, IMP, Lanzhou, P. R. of China
** on leave from Silesian University, Katowice, Poland
*** now at INFN, Florence, Italy
\+ on leave from IPNE Bucharest, Romania
\+\+ on leave from Warsaw University, Poland

1 S. Gralla et al., Z. Physik A310(1983)345
2 M. Dakowski et. al., Nucl.Phys. A387(1982)189
3 H.J. Wollersheim et al., Phys. Rev. C25(1982)338

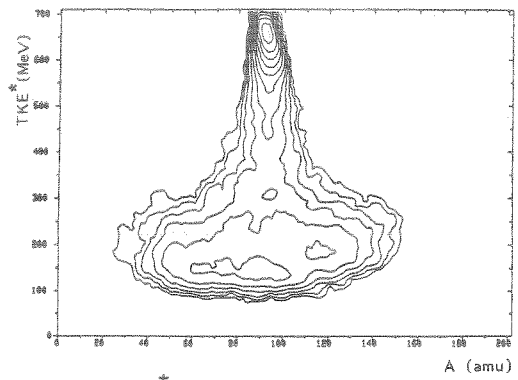


Fig1: $d^2\sigma/dTKE^*dA$ of the $^{92}Mo+^{92}Mo$ reaction at 14.7 MeV/u.

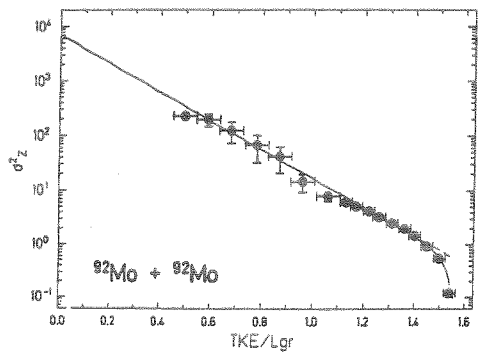


Fig.2: $\ell n\ \sigma_Z^2$ as function of TKE/ℓ_{gr}

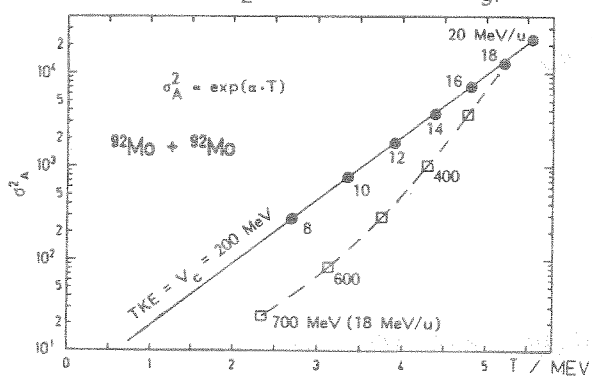


Fig.3: Calculated mass variances as function of the nuclear temperature T for different bombarding energies and fixed TKE (solid line) and for different TKE at 18 MeV/u (dashed line).

Emission of Light Charged Particles in Reactions between ^{92}Mo and ^{92}Mo at 18 MeV/u

N. Herrmann, A. Gobbi, S. Gralla, K.D. Hildenbrand, J. Kuźminski,* W.F.J. Müller, A. Olmi,** M. Petrovici,+ H. Sann, H. Stelzer, J. Tõke,++ GSI Darmstadt
P. Maurenzig, A. Stefanini, University of Florence, Italy

Protons and α-particles have been measured in coincidence with binary heavy fragments emitted in collisions of ^{92}Mo and ^{92}Mo at 18 MeV/u. The heavy products were identified by kinematical coincidences in 6 position-sensitive avalanche detectors; binary products were selected by conditions on collinearity and coplanarity. The light particles were measured in 6 scintillation detectors.[1] A picture of the whole set-up is shown elsewhere.[2]

Fig.1a and b show the Wilczynski and the diffusion plot ($d^2\sigma/dTKE.d\theta_{cm}$, $d^2\sigma/dTKE.dA$). The asymmetry at medium TKE in fig.1b is caused by the detector geometry. All distributions of p or α-particles shown in the following refer to coincidences with masses in a window from A = 82 to 102 (A_{sym}±10 u), solid lines in fig.1b.

Fig.2 shows the experimentally determined α/p ratio as a function of TKE. The dashed line is the result of a Monte-Carlo simulation using the following ingredients: (i) diffusion-, Wilczynski plot and TKE-spectrum are parametrized using known systematics in order to reproduce (after implementation of the geometry) the experimental results shown in figs.1 and 2. (ii) The binary products evaporate isotropically n, p, d and α-particles. (iii) The numbers of evaporated particles are determined by statistical model calculations[3] for the first 200 MeV of energy loss; the results are linearly extrapolated to higher excitation energies. Then the α/p ratio seen in the scintillation detectors is determined.

Obviously the simulation describes the measured solid distribution fairly well at low TKEL; it misses, however, completely the raise between TKEL ≈ 230 to 330 MeV. It is unclear in the present stage of the analysis which of the mentioned assumptions fail and lead to this discrepancy. Both the isotropic emission (since the emitting nuclei carry high angular momenta and/or strong deformations) and the extrapolation of statistical model results may be more or less wrong. Finally, emission processes might be present which are not taken into account at all. Fig.3 shows $d^2\sigma/v^\perp.dv\|.dv^\perp$ of the simulated protons in the frame of the forward going heavy product (4π-distribution) with a TKEL cut from 230 to 330 MeV. The simulation shows two circular distributions, one centered around zero, the other at negative velocities (emission from the recoils), which merge together in between the centers. This plot changes to that of fig.4, if the detector boundaries and resolution are introduced. The same representation for the measured data is shown in fig.5. The agreement between experiment and simulation is surprisingly good; on the present level of accuracy sequential evaporation from the fragments is certainly the dominating process.

* on leave from Silesian University, Katowice, Poland
** now at INFN, Florence, Italy
\+ on leave from IPNE Bucharest, Romania
++ on leave from Warsaw University, Poland

1 N. Herrmann et al., contrib. to this Annual Report
2 GSI calendar 1984, photo by A. Zschau
3 Code CASCADE, F. Pühlhofer, Nucl.Phys. A280(1977)267

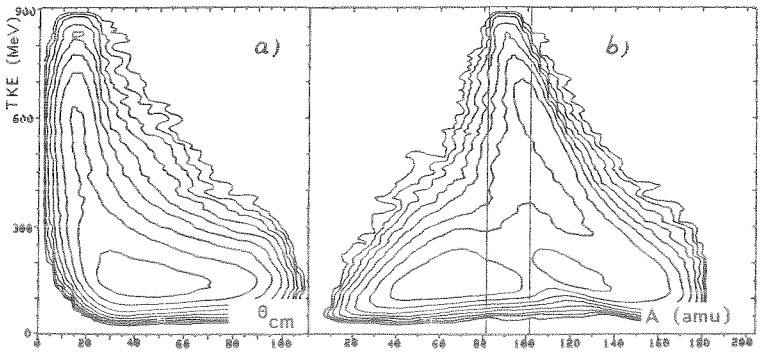


Fig.1: $d^2\sigma/dTKE.d\theta$ (a) and $d^2\sigma/dTKE.dA$ (b) of the reaction ^{92}Mo+^{92}Mo at 18 MeV/u.

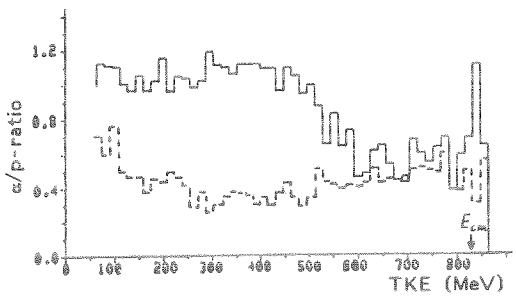


Fig.2: α/p-ratio as function of TKE; solid line: experiment dashed line: simulation (see text).

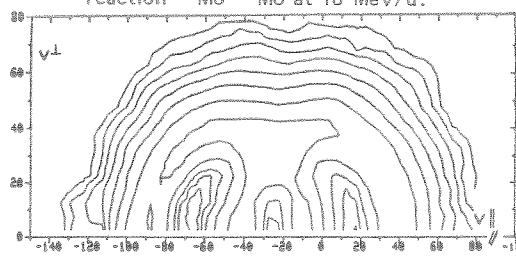


Fig.3: $d^2/v^\perp.dv\|.dv^\perp$ of protons emitted in 4π (Monte-Carlo simulation) in the frame of the forward going fragment.

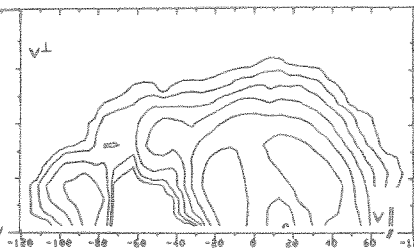


Fig.4: Same as fig.3, but with inclusion of the detector geometry.

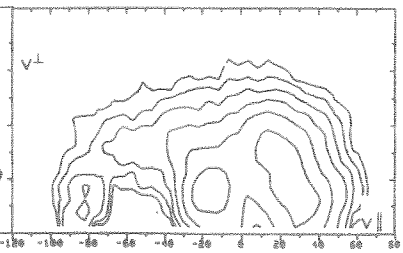


Fig.5: $d^2/v^\perp.dv\|.dv^\perp$ of measured protons.

Search for High-Energy γ-Rays in the System ^{100}Mo + ^{100}Mo at 14.7 MeV/u.

J. Kuzminski,* A. Gobbi, S. Gralla, N. Herrmann, K.D. Hildenbrand W.F.J. Müller,
A. Olmi,** M. Petrovici,+ H. Sann, R.S. Simon, H. Stelzer, J. Toke, GSI Darmstadt
P. Maurenzig and A. Stefanini, University of Florence, Italy

The emission of high energy γ-quanta (E_γ ≥10 MeV) during or shortly after a heavy ion collision is expected to be a rather rare process, which is difficult to identify because of background problems. It is, however, of considerable interest for different reasons. Energetic γ-rays may reflect the presence of collective modes built on highly excited nuclear states[1]; since the energy loss in dissipative collisions easily reaches hundreds of MeV, a large range of excitation energies can be probed in such reactions. On the other hand, since the kinetic energy is dissipated over a distance of a few fermi, energetic bremsstrahlung is expected as well[2], which could carry information on the actual slowing down of the heavy ions during their encounter.

We have carried out a first exploratory search for high energy γ-rays in coincidence with heavy products in the system ^{100}Mo+^{100}Mo at 14.7 MeV/u; the coincidence measurement allows to determine the excitation energy of the primary emitting fragment. The heavy products were detected between -30° and +30° with a large ionization chamber[3] operated in coincidence with a set-up of position-sensitive avalanche detectors.

The γ-rays were measured with a large, cylindrical NaI-detector (40 cm diameter, 30 cm depth) which was separated into 6 segments of 60°. The time resolution of each segment was about 3 ns; neutrons could be discriminated very effectively by their time of flight on the 75 cm distance between target and detector. Events were recorded on-line under the condition that at least one segment detected a γ-ray pulse height in excess of 5 MeV. The dynamic range of the detector covered pulse heights up to 50 MeV.

The singles energy spectrum of the background radiation (beam on cup and no target) shows after a steep decrease a long high energy tail; the latter is seen also without beam and is caused by the cosmic rays. The timing window on (prompt) γ-quanta and the requirement of the coincidence with a heavy fragment clear the spectrum from this background. As an example Fig.1 shows the spectrum coresponding to the highest γ-ray energy per event. In spite of the very poor statistics, a change in the spectral shape can be seen around 9 MeV; below this energy the spectrum falls exponentially, while there is an additional intensity over this exponential decrease above.

The matrix of Fig.2 displays E_γ vs. E_{lab} of the corresponding heavy fragment in the ionization chamber. On the basis of the present preliminary analysis no clear statement can be made on the energy (and hence the excitation-energy) dependence of the observed γ-yield. The results, which were obtained during a rather short exploratory beam time, have nevertheless shown that such measurements are possible with the required sensitivity.

* on leave from Silesian University, Katowice, Poland
** now at INFN, Florence, Italy
\+ on leave from IPNE Bucharest, Romania

1) J.E. Draper et al., Phys.Rev.Lett. 49 (1982) 434.
W. Hennerici et al., Nucl.Phys. A369 (1983) 329c.
2) H. Noll et al., Florence Conference 1983, p.682.
3) G. Augustinski et al., contr. to this Annual Report.

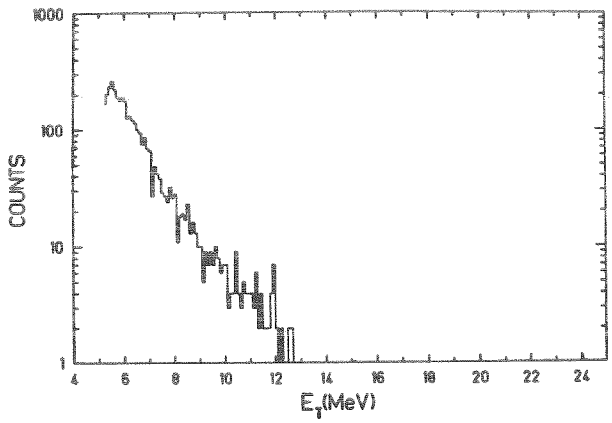


Fig. 1. Gamma-ray spectrum in coincidence with heavy products from the ^{100}Mo +^{100}Mo reaction at 14.7 MeV/u. Shown is the maximum γ-ray energy per event. The cut-off below 5 MeV is due to the experimental threshold.

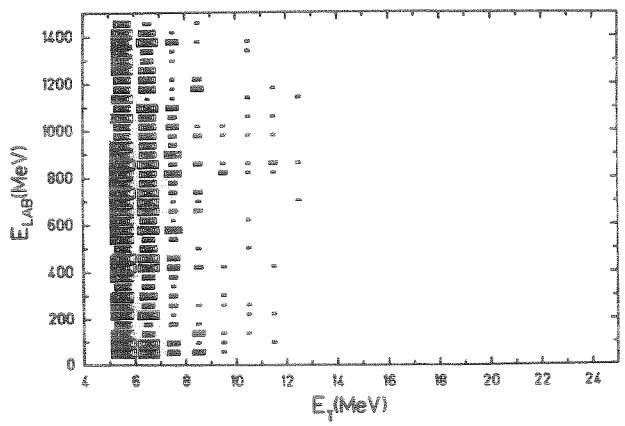


Fig. 2. Correlations of γ-ray energy and the corresponding laboratory energy of heavy products measured in the ionization chamber.

B

Evidence for reaction-channel dependent excitation-energy sharing in quasielastic reactions of ^{86}Kr with ^{208}Pb

H. Sohlbach, H. Freiesleben
Institut für Experimentalphysik, Ruhr-Universität Bochum

B. Kohlmeyer, M. Marinescu, F. Pühlhofer
FB Physik, Universität Marburg

W. F. W. Schneider, D. Schüll
GSI Darmstadt

P. Braun-Munzinger
SUNY, Stony Brook, USA

Projectile-like reaction products were measured at three incident energies (10, 13, 18.2 MeV/u) and at several angles about grazing using the magnetic spectrometer. Energy spectra for 3 Kr-isotopes of the same atomic charge state ($q = 31^+$) are displayed in Fig. 1 at 3 lab angles for the highest incident energy. The ^{86}Kr spectrum exhibits a broad structure a Q = -36 MeV. It results, as reported earlier[1], from the sequential decay of ^{87}Kr formed in the primary reaction $^{208}Pb(^{86}Kr,^{87}Kr)^{207}Pb$. At $\theta_L = 10^0$ two regions can be clearly distinguished in all spectra, one representing the primary reaction (around Q_{gg}), which reflects the shape of the spectra prior to evaporation, the other at more negative Q-values resulting from sequential decay. At $\theta_L = 12^0$ ($\theta_{gr} = 12.5^0$) the sequential bump in ^{86}Kr is nearly as strong as the primary part in ^{87}Kr, indicating, that a large fraction of primary ^{87}Kr was excited above the particle threshold, thus carrying the major part of excitation energy. The strength of the sequential bump in ^{85}Kr is rather small compared to the strength of primary ^{86}Kr. If the energy sharing is assumed to be the same for all channels, then, like in the ^{87}Kr case, ^{86}Kr should have the major part of excitation energy resulting in a strong sequential bump in ^{85}Kr, which is not observed. At $\theta_L = 9^0$ no ^{87}Kr is observed, but ^{85}Kr is still present in the primary region. There is also a small bump in ^{86}Kr, indicating again, that all of the primary produced ^{87}Kr has undergone neutron emission. This behaviour suggests that the sharing of energy differs for various reaction channels. For pick-up and stripping the major part of excitation energy is allocated to the acceptor rather than to the donator nucleus. For inelastic excitation the heavier partner is more strongly excited. In order to quantitatively check this hypothesis a Monte-Carlo simulation of the one- and two-neutron decay has been performed for Kr spectra taken at $\theta_L = 12^0$. It is found that the positions as well as the widths of the sequential decay components can only be reproduced consistently, if the excitation energy is shared in the above mentioned manner. The structures in the experimental spectra are well described up to energy losses of ≈ 100 MeV. Possibly, higher energy losses are partially due to three- and more-neutron or proton evaporation. We conclude, that in this reaction particle evaporation is the process being mainly responsible for energy losses greater than ≈ 40 MeV and as such determining the energy spectra in the measured range.

Fig. 1:

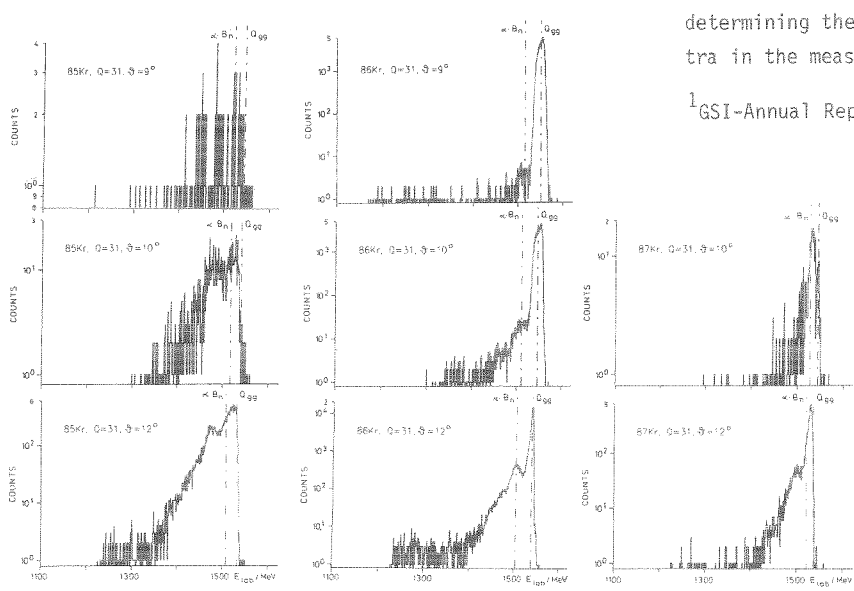
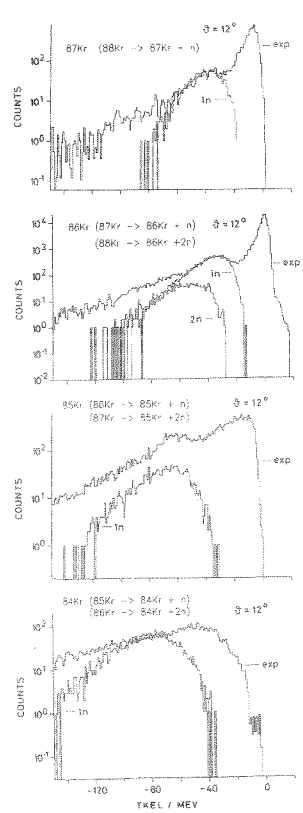


Fig. 2:



[1] GSI-Annual Report (1982)24

„Fragmentation" in the system $^{197}Au + ^{197}Au$ at energies ≤ 15 MeV/u[B]

Th. Blaich, J. V. Kratz
Institut für Kernchemie, Universität Mainz
G. Wirth, K. Sümmerer
GSI Darmstadt

Medium-heavy fragments (MHF in the mass range 10 to 40) are observed in many different reactions, e.g. in proton- or heavy-ion induced reactions at relativistic energies as well as in systems like $^{129}Xe + ^{122}Sn$ or $^{92}Mo + ^{92}Mo$ at about 10-15 MeV/u[1-4]. At present, it is not clear whether "fragmentation" is a general decay property of hot heavy nuclei which accounts for the formation of MHF in all the above mentioned reactions or whether there are several different mechanisms producing fragments in the same mass range.

We therefore started studies of the fragmentation of ^{197}Au nuclei by different projectiles. Gold was chosen as target because it is much heavier than the MHF we are interested in. At CERN, a bombardment with ^{20}Ne at 49 MeV/u is planned. At the UNILAC ^{197}Au at energies ≤ 15 MeV/u was used as a projectile. The highest excitation energy per ^{197}Au nucleus in both systems is of the same order of magnitude (~500 MeV) but the light projectile is faster than the Fermi velocity of the bound nucleons while the heavy projectile is slower. Thus in the heavy system thermalization of the excitation energy becomes conceivable. Therefore one might expect a rather dramatic change in the reaction mechanism. An indication of such a change is indicated by the behaviour of the excitation function for the formation of e.g. ^{24}Na from $^{197}Au + ^{197}Au$ which we measured at E_{lab} = 9, 11, 13 and 15 MeV/u. We calculated the ratio of the ^{24}Na cross section to the total reaction cross section, hereby using the classical formula $\sigma_r = \pi R^2(1-V_C/E_{CM})$. This ratio is shown in the figure and compared to that for formation of ^{24}Na from ^{197}Au and ^{208}Pb in proton[1] and pion[5] bombardments. With the slow projectile, the fraction of the ^{24}Na cross section is larger by two orders of magnitude.

For the $^{197}Au + ^{197}Au$ reaction, it seems unlikely that the MHF originate from the first step of binary, deeply inelastic collisions: This is demonstrated by the distribution of projected ranges of ^{24}Na which we measured at 15 MeV/u at lab angles $\theta_{lab} \leq 45^0$. It shows a maximum at the velocity of the center of mass. If one calculates the possible velocities of ^{24}Na-nuclei with the assumption that they are emitted in binary reactions with energies equal to or larger than the Viola energy one finds that in the vicinity of the velocity of the center of mass there should not appear any light fragments at all. Furthermore, the widths of the element distributions of binary HI reactions can be estimated from a universal, empirical formula found by Wollersheim et al.[6]. Application of this formula to our system shows that the widths are by far too small for such reactions to account for the large yields of ^{24}Na.

For these two reasons, production of MHF in the first, binary step of a deeply inelastic collision can be ruled out, and other mechanisms must be considered, e.g. sequential break-up of a gold-like heavy fragment or true three body-reactions.

References

1. R. Wolfgang et al., Phys. Rev. 103, 394 (1956)
2. H. H. Gutbrod et al., Nucl. Phys. A387, 177c (1982)
3. P. Glässel et al., Z. Phys. A310, 189 (1983)
4. S. Gralla et al., GSI Scientific Report 1982, p. 22
5. N. Porile et al., Phys. Rev. C18, 2231 (1978)
6. H. J. Wollersheim et al., Phys. Rev. C25, 338 (1982)

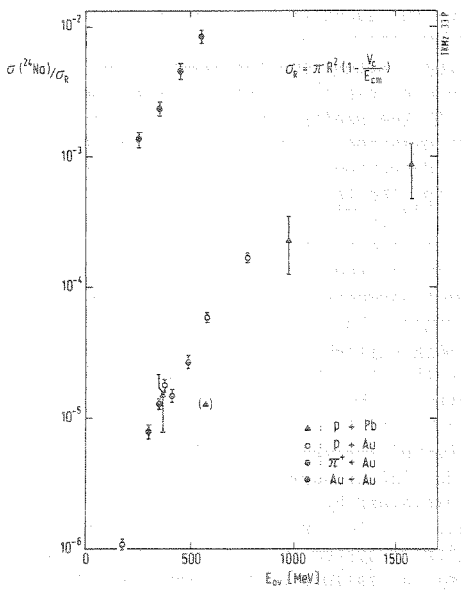


Figure: Ratios of cross sections for the formation of ^{24}Na to the total reaction cross sections $\sigma_r = \pi R^2(1-V_C/E_{CM})$ versus available energy. The $^{197}Au + ^{197}Au$ data are from this work, those for the proton and pion bombardments from refs. 1 and 5.

B

Sequential Fission in the Reaction 10 MeV/u U + U

G.Breitbach, P.Crombach, G.Fiedler, E.Koglin, E.Reichwein
II. Physikalisches Institut, JLU Giessen

Using the SSNT-detector 'ZnP' in a 2π geometry-technique [1,2,3], we analysed events with more than two heavy fragments (mass > 16u) in the exit channel of the reaction 10MeV/u ^{238}U + ^{nat}U. We found a total cross section for these multipronged events of about 2.7 barn. This value may be systematically underestimated by atmost 15% due to an angular dependent detector efficiency calculated in a Monte Carlo simulation.

We used an empirical velocity-range relation to analyse the fragment kinematics. It was taken into account that track inducing nuclei are outside the valley of stability, even after evaporation of neutrons. With a general formula [4] we estimated the number of emitted neutrons as a function of fragment mass and exitation energy.

The existence of an intermediate system can be inferred from the distribution of fragment relative velocities. As a result all analysed events can be interpreted as sequential fission processes. Regarding the fourpronged events, we could not find any correlation between the fission direction of the second reaction step, defined by the in-plane angle φ, and the relative velocity of the second step fragments (Fig.1). Such a correlation is expected, if a Coulomb final state interaction with the fragments of the other prefission nucleus occurs. Therefore we estimate the lifetime of the intermediate system to be longer than 10^{-21}s.

Fig.2 shows the quantity $m_R=m_1/(m_1+m_2)$ as a function of the in-plane angle. Here, m_1 denotes the mass of the second step fragment emitted towards the side of the contact zone of the first reaction step, and (m_1+m_2) is the mass of the prefission nucleus. There is no evidence for emission of the heavier fragments preferentially in directions opposite to the contact zone, as observed for the fast fission process in the reaction 12.5 MeV/u $^{129}Xe+^{122}Sn$.[5] However, a broadening of the mass distribution can be noticed.

This result is shown in Fig.3, where a positive definite mass asymmetry parameter is plotted versus the in-plane angle. For φ values near 0° the fission process is more asymmetric than for larger values. However, note that only the absolute value of φ has physical evidence. The sign of φ, is useful to identify effects caused by the detector properties. Events with one undetected fragment would show a positiv in-plane angle. The larger asymmetry at small in-plane angles could be explained by nonequilibrium fission, with a time scale smaller than the half rotation period of the fissioning system (10^{-20}s [6]). This effect is not induced by a failure of our analysis for specific events, as can be concluded from a numerical simulation of sequential fission and the analysis of randomly generated virtual events.

In another experiment, we irradiated ^{nat}Pb with ^{238}U ions at 16.7 MeV/u. For this reaction the CR39 detector was used to get a better detection efficiency for tracks close to the detector surface. Moreover, due to the higher velocity of the center of mass, the angular range (in the cm system) is increased where tracks can be detected. A large number of three-, four-, and fivepronged events and one event with six trajectories could be observed. This experiment is currently analysed.

1 P.A.Gottschalk et al., Phys.Rev.Letters 42, 359 (1979)
2 P.A.Gottschalk et al., Phys.Rev.C 27, 2703 (1983)
3 R.Haag et al., Z.Phys.A 316, (1984), in print
4 I.Dostrovski et al., Phys.Rev. 111, 1659 (1958)
5 P.Glaessel et al., Z.Phys.A 310, 189 (1983)
6 D.v.Harrach, Habilitation Heidelberg (1982)

Fig.1: Relative velocities of second step fragments for fourpronged events as a function of in-plane angle φ (cm system).

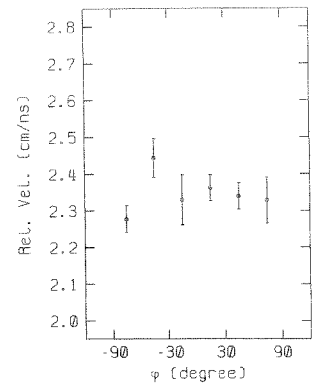


Fig.2: Distribution of events in the m_R-φ plane.

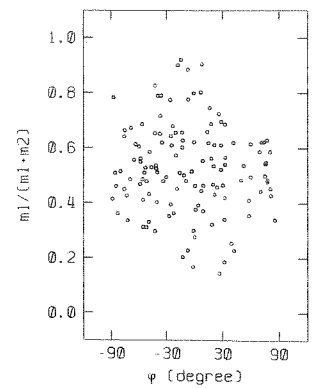
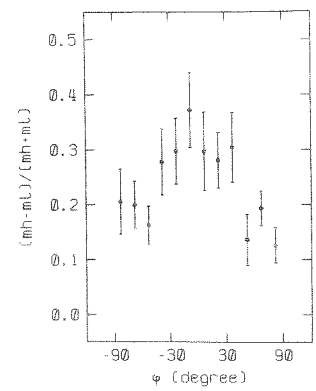


Fig.3: Asymmetry parameter as a function of the in-plane angle φ .



DETERMINATION OF REACTION PARAMETERS FROM ELASTIC SCATTERING STUDIES

H.A. KHAN, K. JAMIL, N.A. KHAN, M.A. SIAL AND R. BRANDT*

Nuclear Engineering Division
Pakistan Institute of Nuclear Science and Technology (PINSTECH)
P.O. Nilore, Rawalpindi, PAKISTAN

Kernchemie, F.B. 14, Philipps-Universitat, 3550-Marburg (Lahn), WEST GERMANY

In order to (a) determine the partial cross-sections of various types of interactions, and (b) ensure that all possible modes of interaction have been exhausted, it is of great help to make an estimation of the total reaction cross-section for the system under study. It has been shown that the use of optical and strong absorption-models along with the studies of elastic scattering of heavy projectiles can produce fairly accurate estimates of the total reaction cross-section(1). According to Frahn(2) an analytical expression for the angular distribution in elastic scattering can be obtained from Fresnel scattering model. Blair(3) has shown that the value of 'quarter-point-angle' can be usefully employed for the calculation of total reaction cross-section.

In this paper, we describe the use of mica solid state nuclear track detector for the determination of total reaction cross-section and other reaction parameters using 'quarter-point-angles' in the elastic scattering of 2380 MeV-uranium ions by ^{197}Au and ^{165}Ho target atoms.

Thin targets (thickness ~ 1 mg/cm^2) of gold and holmium were vacuum deposited on freshly cleaved mica sheets. The target-detector combinations were exposed perpendicularly to 10 MeV/u ^{238}U ions obtained from UNILAC (GSI, Darmstadt). After removing the target, and revealing the fragment tracks in 48% HF, the events were analysed using an optical microscope. The data so obtained were used to plot the variation of etched track length as a function of scattering angle. A theoretical curve for 'track length' vs. 'scattering angle' was obtained by using the following emperical range-energy relationship in mica and the elastic scattering equation:

$$V(\ell,m) = \sum_{\mu=0}^{2} \sum_{\nu=0}^{4} C_{\mu\nu} m^{\mu} \ell^{\nu} \quad \ldots\ldots (1)$$

and E_p (energy of the scattered projectile)

$$= E_{lab} \frac{M_P}{(M_P+M_T)^2} [Cos\ \zeta_p + \{(\frac{M_T}{M_P})^2 - Sin^2\zeta_p\}^{\frac{1}{2}}]^2 \quad \ldots\ldots (2)$$

where the symbols have the usual meanings.

The events lying on the theoretical curve were taken as due to elastic scattering. A curve showing variation of '$\sigma_{exp}/\sigma_{Ruth}$' vs. 'scattering angle' yielded the quarter-point-angle ($\theta_{\frac{1}{4}}$). The so determined quarter-point-angle with the following equations were used to compute the total reaction cross-sections and other reaction parameters:

$$R_{int} = \frac{1}{K} [\eta/\sin(\theta_{\frac{1}{4}}/2) + \eta] \quad \ldots\ldots (3)$$

$$R_o = R_{int}/(A_p^{1/3} + A_t^{1/3}) \quad \ldots\ldots (4)$$

$$\ell_{max} = \eta \cot(\theta_{\frac{1}{4}}/2) \quad \ldots\ldots (5)$$

$$\sigma_R = (\pi/K^2)(\ell_{max} + 0.5)^2 \quad \ldots\ldots (6)$$

values of 53.3° and 49.6° have been obtained for the quarter-point-angles for '^{197}Au + ^{238}U' and '^{165}Ho + ^{238}U' systems, respectively. The use of these values of the quarter-point-angles in equations 3 to 6 yielded values of total cross-sections and of other reaction parameters. The results have been summarized in Table 1.

Table 1

Parameter / Reaction	$\theta_{\frac{1}{4}}$ (c.m.) Degrees	R_{int} (fm)	R_o (fm)	ℓ_{max} ($\hbar$)	σ_R (mb)
10 MeV/u ^{238}U + ^{197}Au	53.3 (50.9)	15.69 (16.15)	1.306 (1.340)	721.3 (761)	2944 (3279)
10 MeV/u ^{238}U + ^{165}Ho	49.6 (47.8)	15.41 (15.79)	1.319 (1.350)	664 (761)	3055 (3326)

The values in the parenthesis are the calculated ones and have been taken from Ref.(4). The values of quarter point angles obtained by us are higher than but quite close to the theoretically predicted ones. The fair agreement between the experimental and the theoretical values shows that SSNTD-technique works well for elastic scattering studies in 'heavy ion-heavy target' system.

We are grateful to Mr. H. Folger and Dr. Reimar Spohr for kindly preparing the targets and for exposing them at GSI.

REFERENCES

1. *Birkelund, J.R.; Huizenga, J.R.; Freiesleben, H.F.; Wolf, K.L.; Unik, J.P.; and Viola, V.E: Phy. Rev. C 13 (1976) 133.*
2. *Frahn, W.E: Phys. Rev. Lett. 26 (1971) 568.*
3. *Blair, J.S: Phys. Rev. Lett. 95 (1954) 1218.*
4. *Atomic Data and Nuclear Data Tables, volume 25 number 5/6 (1980).*

The Reaction $^{238}U + ^{nat}U$ at 16.7 MeV/N (From Sequential Fission Process to light Particle Emission)

Ehsan Ullah Khan*, P. Vater and R. Brandt
Kernchemie, FB 14, Philipps-Universität, 3550 Marburg

We continued the study of 16.7 MeV/N $^{238}U + ^{nat}U$ reaction employing the 2 π -geometry technique with mica as detector [1]. We could determine experimentally the reaction cross section $\sigma_{R,exp}$ = (4750+600)mb using standard procedure. We also used 794 elastic events (binaries) to get conventional quarter point angle, $\Theta_{1/4}$ = (27.65 $\pm$ 2)°, Fig. 1. The $\Theta_{1/4}$ yields a reaction cross section $\sigma_{R,1/4}$ = (4877 $\pm$ 700)m barn. Hence σ_R obtained from the two independent methods are in good agreement. The Coulomb interaction distance R_c calculated from the independently measured $\sigma_{R,exp}$ and σ_R, $\Theta_{1/4}$ are 15.70 fm and 15.88 fm, respectively.

Fig. 2 shows the reaction cross section of three, four and five particles in the exit channels for U + U at 7.5, 9 and 16.7 MeV/N energies. Two points are worth noting; the sharp enhancement in σ_5 and even more notable decrease in σ_4 when energy increases from 9 to 16.7 MeV/N. Moreover, we have observed that $\sim$15 % of three and four prongs have one of the tracks longer than what is expected for the fission fragments in sequential fission. Since for such tracks the exact lengths could not be obtained as they are longer than the thickness of the mica plate, we can conclude from the registration properties of our mica detector that these could be possible only due to emission of energetic lighter ions with $24 \geqslant Z \geqslant 36$. Further, we noticed a large amount of "indirect" events (i.e. about 30 % of events with at least three, 50 % with four and 40 % with five fragments) having all tracks in one half azimuthal plane indicating that at least one track is missing in the other half plane as is required by the momentum conservation. Fig.3 shows an indirect event with at least five fragments in the exit channel missing the 5th track. Khan et al.[2] have already shown that σ_4 as registered by CR-39 is considerably larger than the σ_4 registered in mica for the 16.7 MeV/N U + Au reaction. It is to be noted that mica registers $m \geqslant 30$ u whereas CR-39 can register all light masses down to protons, therefore both experiments are complementing each other.

The results mentioned in preceeding paragraph exhibit a departure from a well-defined sequential fission process, as has been the case upto 10 MeV/N U energy. It seems to be onset of a new reaction mechanism where emission of energetic light fragments will play a considerable role at such a high energy. The further analysis of three, four and five prong events is underway and promises a deeper inlook into the matter.

1. Khan,E.U. et al.,GSI Scientific report 1982,83-1, 25
2. Khan,H.A. et al.,GSI Scientific report 1982,83-1, 26

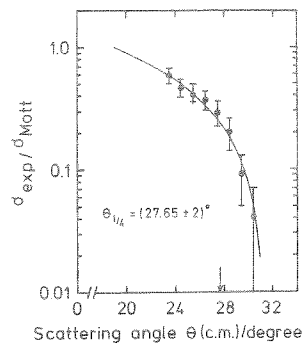


Fig. 1: $\sigma_{exp}/\sigma_{mott}$ vs. scattering angle; the bars show the statistical and experimental errors.

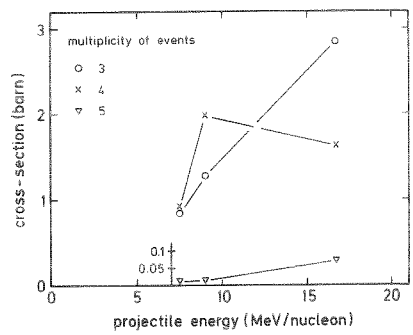


Fig. 2: Cross sections of 3, 4 and 5 particle exit channels in U+U reactions at three different energies. σ_5 increases significantly from (14±10)mb to (90+18)mb when energy increases from 9.0 to 16.7 MeV/N.

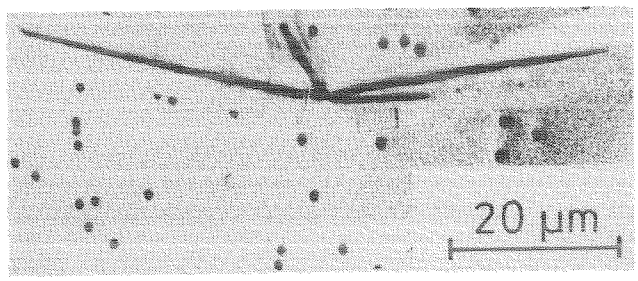


Fig. 3: An example of indirect five prong event. For details, see text.

*On leave from Physics Department, Gomal University, D.I. Khan, Pakistan.

REACTIONS OF 10 AND 16.7 MeV/NUCLEON ON ^{238}U, ^{208}Pb AND ^{197}U

M. Debeauvais, J. Ralarosy, J. Tripier and S. Jokic

Centre de Recherches Nucléaires
67037 - Strasbourg Cedex

A makrofol detector covered with targets as U, Pb or Au of 800 - 2000 $\mu g/cm^2$ were exposed to a $\sim 10^6$ U/cm^2 beam of 10 or 16.7 MeV/u perpendicularly on the detector surface. After etching we can observe, under the microscope, on the top of the detector 2 pronged events; most of them are elastic scattering. We can also find 3-, 4-, 5- and 6- pronged events corresponding to inelastic reactions.
In the following table are summarized the main results on the branching ratios of the different kind of events in U and Au.

TABLE 1

Reaction	Detector	Energy in MeV/n \ Prongs	3	4	5	6
$^{238}U + ^{238}U$	Makrofol	10	0.42	0.51	0.06	~ 0.002
	Makrofol	16.7	0.37	0.47	0.15	0.01
$^{238}U + ^{208}Pb$	Makrofol	10	0.66	0.33	0.01	
	Makrofol	16.7	0.43	0.46	0.11	
$^{238}U + ^{197}Au$	Makrofol	10	0.74	0.95	0.005	
	Makrofol	16.7	0.53	0.40	0.06	~ 0.005
	Cellulose Nitrate	16.7	0.46	0.36	0.18	

From this table it can be pointed out that :

1) when the incident energy increases the number of 3 pronged events decreases and the number of 5 pronged events increases.
2) At a given energy the number of 3 pronged events increases with decreasing target masses.
2) In Au reactions with 2 differents sensibilities of detector, the number of 5 pronged events is 3 time larger in the more sensible cellulose nitrate than in makrofol.

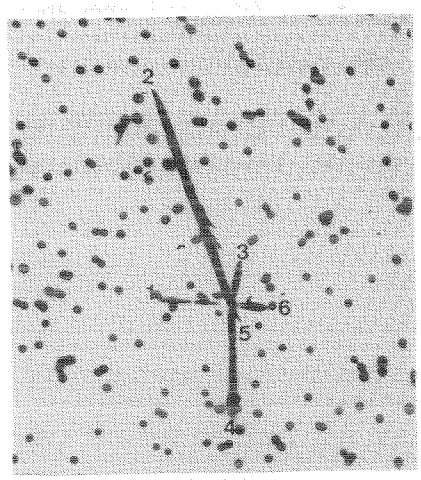


Fig. 1

In the reaction of U of 16.7 MeV/u on C we have found 3- pronged events and one 4- pronged event[1]. It is reasonable to assume that in reactions like U on U at the same energy we found 6 pronged events. In fact until now we found eleven 6-pronged events : 4 on U, 3 on Pb, 2 on Bi and 2 on Au. In Fig. 1 you can see the picture of such an event.

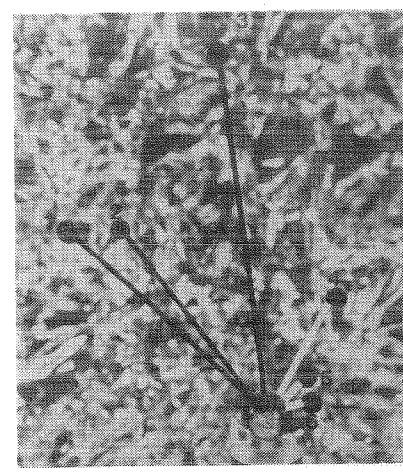


Fig. 2

In Fig. 2 is represented the same event reconstructed in space with respect to the geometrical characteristics. We think that after a deep inelastic scattering, each U partner splits in 3 fragments :
In the most cases, 2 heavy fragments and 1 lighter for each U partner, in analogy with the results found in the 3 pronged events issued from the reaction U + C at the same energy.
Because of the difficulty to mathematically resolve a system with 6 pronged events, until now we are not yet able to confirm this idea.

(1) M. Debeauvais, J. Ralarosy, J. Tripier, S. Jokic, 12th Int. Conf. on SSNTD, 4-10 Sept. Acapulco, Mexico. (1984).

Fragmentation of ^{12}C at 84 MeV/u

R. Wada, A. Gobbi, K.D. Hildenbrand, W.F.J. Müller, H. Sann, H. Stelzer
(GSI Darmstadt)
U. Lynen (Univ. Frankfurt), D. Pelte (Univ. Heidelberg), R. Trockel (Univ. Münster)

The reaction ^{12}C on ^{12}C has been measured at 84 MeV/u at the CERN-SC. The recoiling target fragments were detected in an Ionization Chamber (IC) (angular range 73° to 87°) and the projectile fragments in a 0° hodoscope (ZDH) which covered the range between 1.5° to 10° around the beam axis.

The inclusive momentum distribution of the target fragents has been compared with the simple Goldhaber formula;

$$(1)\quad \frac{d\sigma}{d\vec{P}} \propto Exp\left(-(\vec{P}-\vec{P}_0)^2/2\sigma^2\right) \;;\; \sigma^2 = \frac{m_F(m_T-m_F)}{m_T-1}\sigma_0^2$$

where m_T and m_F are the masses of the target nucleus and its fragment, respectively, and σ_0 should be a constant determined by the inclusive Fermi momenta. The analysis shows some deviations from this simple picture, in agreement with results reported by Mougey et al.[1] for projectile fragments from the same reaction.

Even stronger deviations are found for the coincident data between projectile and target fragments:

1. The momentum distribution of target fragments and the angle of projectile fragments are strongly correlated and the events show a high degree of coplanarity.
2. The charge distribution in the ZDH is nearly independent of the masses of the target like fragments.

This could be explained by a mechanism, which is found at lower energies[2], where the observed fragments result from an inelastic binary collision followed by some evaporation or break-up process. For this process the momentum distribution of the nuclei is given by

$$(2)\quad \frac{d\sigma}{d\vec{P}} \propto \int Exp\left(-(\vec{P}-\frac{m_F}{m_T}\vec{P}_3)^2/2\sigma^2\right)\phi_R(\theta_3)\,d\theta_3$$

where P_3 and $\phi_R(\theta_3)$ are the recoil momentum and the angular distribution of the target nuclei in the inelastic scattering.

For small scattering angles the angular distribution results simply from the transfer of a transverse momentum $P_\perp$ which is correlated with Q-value of the reaction[3], by

$$(3)\quad \frac{d\sigma}{dP_\perp} \propto P_\perp\, Exp\left(-P_\perp^2/2\sigma_c^2\right)$$

with

$$\sigma_c \sim \frac{1}{v}\left[1+\sqrt{1-v^2}\right]Q$$

Inserting (3) into (2), using $P_\perp \sim P_3 \cdot \theta_3$, and integrating over $P_\perp$, one obtains

$$(4)\quad \frac{d\sigma}{d\vec{P}} \propto Exp\left(-(\vec{P}-\frac{m_F}{m_T}\vec{P}_{incid})^2/2\sigma_{tot}^2\right)$$

$$(5)\quad \sigma_{tot}^2 = \sigma^2 + \left(\frac{m_F}{m_T}\right)^2\sigma_c^2$$

In eq.(5), the first term comes from the fragmentation process (break-up or evaporation) and the second term from the inelasticity of the primary reaction.

Using a Q-value of 80 MeV and σ = 120 MeV/c, which corresponds to a proton energy of about 7 MeV for the decay $^{12}C \rightarrow {}^{11}B+p$, the fit shown in fig. 1 has been obtained.

These results show that even at energies of 84 MeV/u inelastic binary collisions contribute to the fragmentation process. From the present data it is difficult to determine the cross section of this contribution. It should furthermore be noticed that the present detector arrangement (observation of the recoiling target fragment close to 90°) enhances contributions from inelastic collisions with small Q-values.

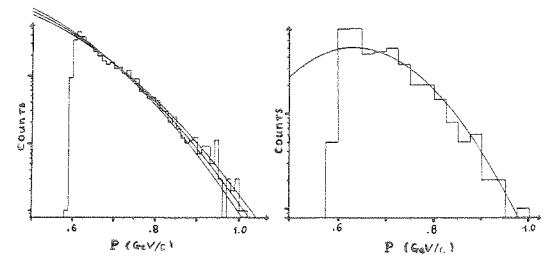


Fig.1 a) Inclusive momentum distribution of ^{11}B target fragments. b) Momentum distribution of ^{11}B target fragments in coincidence with projectile fragments observed at 8.5° in the ZDH. Solid lines are calculated from eq.(2).

References

1. J. Mougey et al., Phys.Lett.105B(1981)25
2. H. Homeyer et al., Phys.Rev.C26(1982)1335
3. N. Masuda et al., Phys.Rev.C15(1977)1598

Azimuthal Angular Correlations between Heavy Projectile Fragments and Light Particles in ^{18}O induced Reactions at 84 MeV/u

W.F.J. Müller, A.Gobbi, K.D.Hildenbrand, H. Rabe, H.Sann, H.Stelzer, R.Wada,
GSI Darmstadt
R.Glasow, K.H.Kampert, R.Santo, R. Trockel, Universität Münster
D.Pelte, U.Winkler, Universität Heidelberg
I.Bock, MPI Heidelberg
U.Lynen, Universität Frankfurt

At intermediate energies between 30-100 MeV/u the formation of a hot spot has been predicted [1], a reaction mechanism halfway between deep-inelastic scattering and participant-spectator behavior. As a localized excitation the hot spot may decay by particle evaporation as well as by heat conduction to the interior of the nuclear residues. In inclusive measurements in addition to evaporation from target and projectile a source at mid-rapidity has been observed which may result either from hot spot evaporation or from quasi-free nucleon-nucleon scattering [2].

To investigate whether the mid-rapidity source in peripheral reactions is localized at the nuclear surface a coincidence experiment has been done at the CERN-SC for the reaction ^{18}O + ^{58}Ni at 84 MeV/u. Projectile fragments have been detected in 6 scintillators covering the angular range between 1.5° and 4.5°, light particles in a 20 scintillator hodoscope covering a solid angle of 2π between 20° - 80° (forward) and 100° - 160° (backward). The set-up is almost symmetrical around the beam-axis in order to avoid systematical errors.

The azimuthal angular correlation between a projectile fragment and a light particle in the forward hemisphere of the hodoscope is shown for various projectile fragments in fig. 1. In order to select peripheral interactions only events with a total light particle multiplicity of one were used. For projectile fragments heavier than Beryllium a pronounced enhancement of light particles on the opposite side of the projectile fragment shows up which in case of Z_p=8 increases to a peak-to-valley ratio of 2:1. In order to derive an asymmetry-coefficient α the distributions were fitted with the expression:

$$R = 1 - \alpha \cos(\Delta\varphi)$$

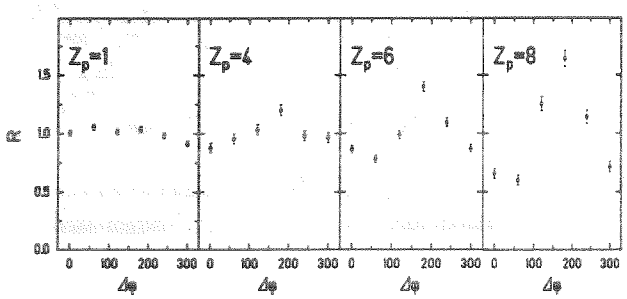


Fig. 1: Azimuthal angular correlation

The dependence of α on the projectile charge is plotted in fig. 2 for both the forward and backward hemispheres. In fig. 3 the average asymmetry for Z_p = 4..8 is shown as a function of the pulse height of the hodoscope-scintillators. Due to quenching effects and the missing particle identification this gives only a rough estimate of the particle energy. In the forward hemisphere the asymmetry increases with growing particle energy whereas at backward angles an asymmetry is observed for small energies only. For more central events where two or more light particles are observed in the hodoscope, the asymmetry is strongly reduced.

An explanation of this angular correlation due to projectile fragmentation can be ruled out since the asymmetry is also observed at backward angles and furthermore the maximum shows up for events where the full charge of the projectile is detected. With similar reasons also hydrogen impurities in the target can be excluded. In a simple hot-spot picture due to the shadowing by the target residue no pronounced peak would be expected at the opposite side of the projectile fragment. The observed asymmetry could be explained by nucleus-nucleon scattering where the projectile interacts with one or a few nucleons of the target. In this case, however, a high transparency of the target nucleus for the scattered nucleon must be assumed.

[1] R. Weiner, M. Weström, Phys.Rev.Lett. 34(1975)1523
[2] R. Glasow et al., Phys.Lett. 120B (1983) 71

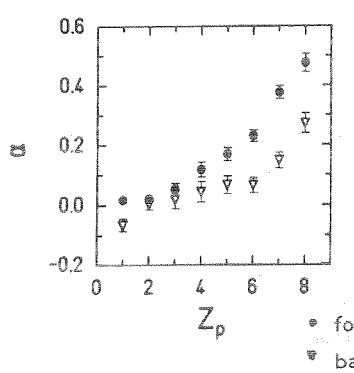


Fig. 2: Asymmetry vs. fragment charge

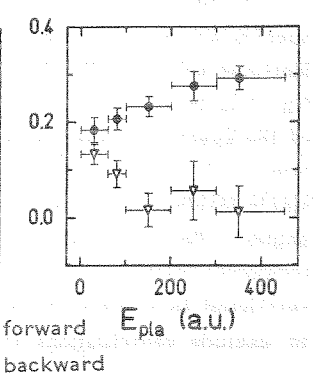


Fig. 3: Asymmetry vs. pulse height

Low Energetic Alpha Spectra in ^{12}C Induced Reactions at 84 MeV/u

R. Trockel, R. Glasow, K.H. Kampert, R. Santo (Univ. Münster)
A. Gobbi, K.D. Hildenbrand, W. Müller, H. Rabe, H. Sann, H. Stelzer, R.Wada
(GSI Darmstadt)
D. Pelte (Univ. Heidelberg)
U. Lynen (Univ. Frankfurt)

At the CERN-SC α-spectra of ^{12}C induced reactions on ^{197}Au have been investigated by use of three semiconductor telescopes consisting of 50 µm silicon surface barrier detectors(dE) and 4000µm lithium drifted silicon detectors(E). With these telescopes the energy spectra of α-particles could be measured up to 100 MeV. For higher energies separate Si-NaJ telescopes have been used[1].

The shape of the energy spectra at different angles is often interpreted in terms of "moving sources" emitting light particles isotropically in their rest frame with a Maxwell-Boltzman energy distribution. In the present analysis we will check the validity of this description for the "target like source", where because of the small values of possible source velocities ($\vartheta_s < \vartheta_{CN}$, with ϑ_{CN} = 0.025 c) ambiguities due to this source velocity are negligible. Furthermore we will distinguish peripheral from more central collisions according to the multiplicity of light charged particles measured by a "Light Ion Hodoscope(LIH)". This detector consisted of 10 plastic scintillators which covered one half of the total solid angle. If the picture of an isotropic emission from a moving source is correct, the invariant cross sections $1/\sqrt{E^{cm}} \cdot d^2\sigma/dEd\Omega$ observed at different lab angles should have identical shapes and peak intensities and only differ by a displacement in energy. These distributions are shown in fig. 1 for two different event types.

In the first part α-spectra were selected by the condition that at least three charged particles were observed in the LIH (central trigger). For the second part no charged particle except for the one in the telescope was requested (peripheral trigger).

In the central event type the maxima of the energy spectra are at nearly equal height - as expected for an isotropic emission. On the other hand it is obvious from fig. 1 is that there is a strong dependence of the slope of the spectra on the Lab angle. This trend is summarized in Table 1 were the "temperatures" extracted from single moving-source fits are compiled for different Lab angles. For these fits a source velocity of half the compound nucleus velocity was assumed. The fits were restricted to energies between 10 and 45 MeV in order to exclude contributions from the source moving with half the beam velocity which is seen in the Si-NaJ telescopes.

For peripheral collisions a large anisotropy of the yield of low energetic α-particle is observed which shows that the emission in the system of the source is non-isotropic.

Comparing peripheral and central collisions nearly identical slopes of the spectra are observed. In the framework of thermal emissions this would mean that more central collisions do not lead to higher temperatures of the target nucleus than peripheral interactions.

A handicap in the present analysis has been that the whole energy spectra could not be measured with the same telescope. This will be overcome in the next run at the CERN-SC by using telescopes consisting of several silicon detectors and a BGO scintillator.

[1] R.Glasow et al., Phys.Lett. 120B(1983)71
[2] U.Lynen et al., Nucl.Phys. A387(1982)129

Table 1: "Alpha-Temperatures" extracted under different Lab angles for central and peripheral collisions

$\theta_{Lab.}$	40°	60°	135°
central	8.1	7.1	4.2 MeV
peripheral	7.9	6.1	4.7 MeV

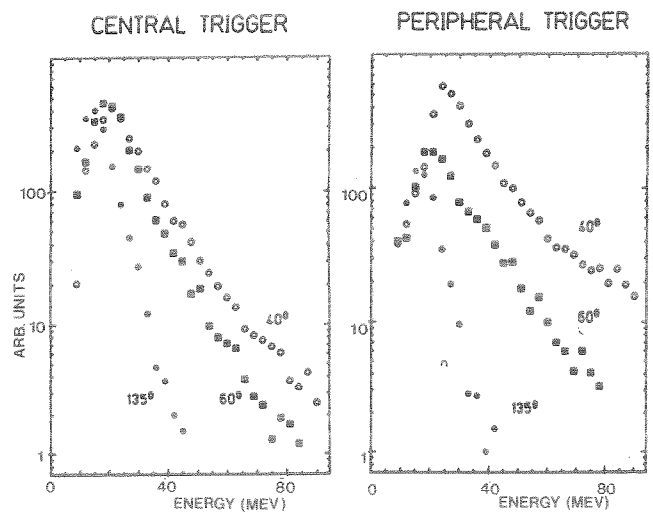


Fig 1: Invariant α-cross sections for different trigger conditions

Multiplicity Selected Light Particle Detection in Reactions with 84 MeV/u ^{12}C Projectiles

B

R. Glasow, K.H. Kampert, R. Santo, Institut für Kernphysik, Universität Münster
D. Pelte, U. Winkler, I. Phys. Institut, Universität Heidelberg
A. Gobbi, K.D. Hildenbrand, W.F.J. Müller, A. Olmi, H. Sann, H. Stelzer, GSI Darmstadt
I. Bock, U. Lynen, Max-Planck-Institut für Kernphysik, Heidelberg

At the Cern synchrocyclotron, light particle spectra of 84 MeV/u ^{12}C induced reactions have been investigated by use of 3 detector telescopes, consisting of 500 - 2000 µm Si-surface-barrier-detectors (ΔE) and 8 cm thick NaJ- and 10 cm thick plastic-scintillation counters (E_r). The analysis of the p,d,t,^{3}He and α-particle inclusive spectra in terms of a "moving source" model had indicated[1] that three sources of different origin are contributing. A further disentangling of the different contributions has been achieved by regarding the associated light particle multiplicities in a Light-Ion-Hodoscope (LIH), consisting of 20 plastic-scintillators covering about one half of the total solid angle. Following the observations at relativistic energies central collisions can be characterized by high associated multiplicities while peripheral collisions should result in a lower multiplicity in the LIH.

Fig. 1 shows, as an example, the single α-spectra (dots) from the reaction $^{12}C+^{197}Au$ at $\Theta_{Lab} = 22°$ and 30°. The dotted and solid lines represent partitions of the inclusive spectra classified according to the associated multiplicity m in the LIH. Two pecularities are clearly extracted from fig. 1: i) the bump in the m = 0 component (full line), which is obviously caused by projectile fragmentation, disappear with growing m; ii) the $m \geq 4$ component (dotted line) exposes the weakest angular dependence and a nearly pure exponential shape, suggesting a more central collision mechanism. As expected, a rapid decrease of the projectile-contribution to the α-spectra is observed between 22° and 30°. The present multiplicity trigger selection of the light particle data gives strong evidence for the existence of an "intermediate source" with high "temperatures" close to 20 MeV.

Another interesting aspect of multiplicity selection is shown in fig. 2, where particle to proton ratios in the scintillator-telescopes (full energy range) are plotted versus the associated multiplicity in the LIH for the reactions $^{12}C+^{58}Ni$ and ^{64}Ni. Especially at larger angles the ratio increases with multiplicity, indicating that the composite particles are emitted preferably in more central collisions. A comparison between ^{58}Ni and ^{64}Ni targets reveals only an effect in the normalization factor depending on the neutron to proton ratio of the ejectile. The functional dependence however, is not significantly affected.

1) R. Glasow et al., Phys.Lett.120B(1983)71 and GSI Scientific Report 1982, p. 29.

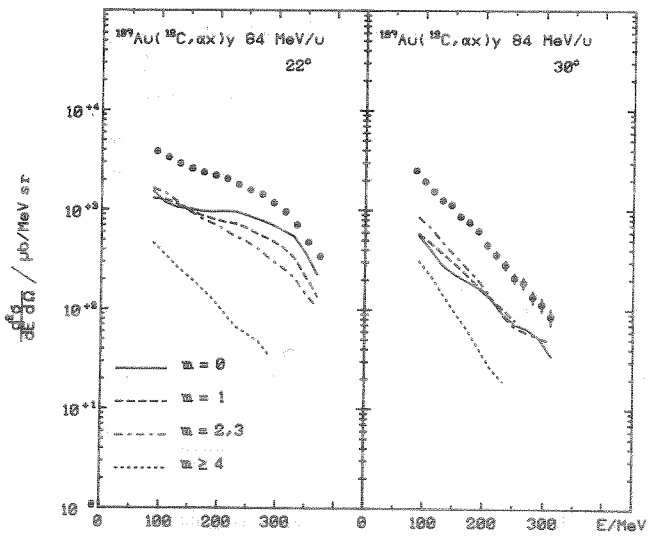


Fig. 1: α-particle spectra from $^{12}C+^{197}Au$ (dots) selected for associated multiplicities m in the LIH

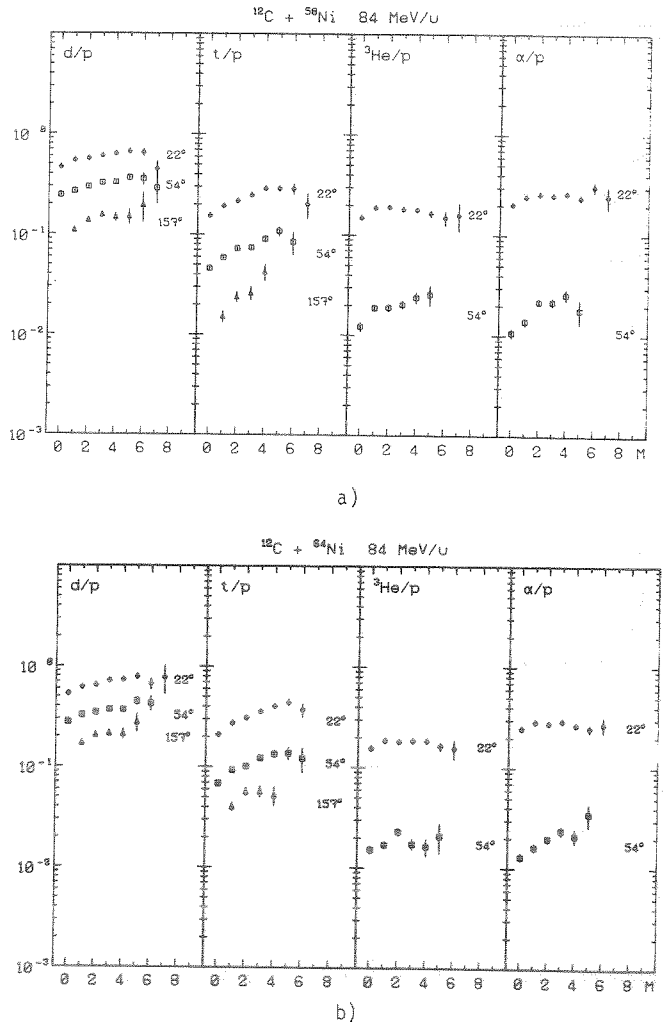


Fig. 2: Particle to proton ratios in the NaJ-telescopes versus associated multiplicity in the LIH for the reactions $^{12}C+^{58}Ni$ (a) and $^{12}C+^{64}Ni$ (b).

Emission of Fragmentation Products ($5 \leq Z_L \leq 26$) in the Interaction of 84 MeV/u ^{12}C with ^{208}Pb Targets

B. Grabez, R. Beckmann, P. Vater and R. Brandt
Kernchemie, FB 14, Philipps-Universität, 3550 Marburg

Emission of fragmentation products with $5 \leq Z_L \leq 26$ is phenomenon characteristic for high energy nuclear interactions. There exist only very limited number of experimental data concerning the emission of such fragments induced by projectiles in the intermediate energy region. The measurements were done mainly in an inclusive manner using counter techniques. In order to get informations about production mechanism of such fragments we investigated emission of target fragments with $5 \leq Z_L \leq 26$ (fragmentation) using CR-39 plastic track detector[1]. Here we can identify fragments with $\Delta Z < 1$. Our experiment has advantage to enable the exclusive measurement of all fragments with $Z \geq 3$ in correlation.

Our results show directly that fragments with $5 \leq Z_L \leq 26$ predominantly originate from binary break up. They are always observed in the correlation with heavy fragments ($36 \leq Z_L \leq 77$) except in the very limited number of the events[2]. Fig. 1 shows the distribution of the longitudinal component ($\beta_{||}$) of the velocity of the c.m. system of fragments for fragmentation and fission. Since $\beta_{||}$ can be taken to be proportional to the transfer of the linear momentum, it is evident that fragmentation originates mostly from the more central collision than the fission process.

In Table I are listed the average velocity of the c.m. system ($\beta_{||}$), source velocity for light (β_{sL}) and corresponding heavy (β_{sH}) fragments and "source" temperature for light fragments (T) calculated for fragmentation events with light fragments having atomic numbers Z_L =5, Z_L =8, $10 \leq Z_L \leq 14$ and $15 \leq Z_L \leq 26$. According to Table I the velocity of the light fragments "source" β_{sL} is practically independent of the atomic numbers of the light fragments for $Z_L \leq 14$. The same is the case for the source velocities of their corresponding heavy partners (β_{sH}). This indicates that fragments with $5 \leq Z_L \leq 14$ are produced by the same mechanism. It is questionable if this holds true also for fragments with $15 \leq Z_L \leq 26$. For the emission of that heavy "light fragments" we observe two components, which are characterised by different temperatures T_i and T_{ii} - a phenomenon not yet understood.

It can be also seen that $\beta_{||}$ and $\beta_{sL(H)}$ have different values. This means that the fragments do not originate from the excited nuclei in the thermal equilibrium as it is supposed in the process of the evaporative type.

It may be concluded that fragments observed in our experiment come from nonequilibrated emission. Theoretical models which could describe such emission of the fragments are not developed until now. Further details are given in Ref. 3.

1. B. Grabez et al., NIM, 211, 209 (1983)
2. B. Grabez et al., GSI 83-1, p. 30 (1983)
3. B. Grabez, Doktorarbeit (1984)

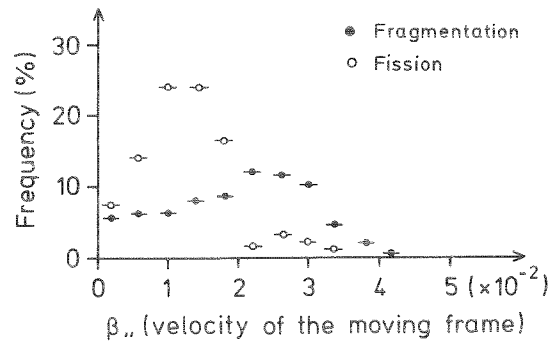


Fig. 1: Distributions of the longitudinal component of the velocity of the c.m. system for the fragmentation and fission process.

Table I: Average velocity of the c.m. system ($\beta_{||}$), "source" velocity for light (β_{sL}) and corresponding heavy (β_{sH}) fragments and "source"temperature for light fragments (T).

Z_L	$\beta_{||}$	β_{sL}	T(MeV)	β_{sH}
5	0.0238 ± 0.0020	0.0012 ± 0.0011	2.1	0.0150 ± 0.00135
8	0.0189 ± 0.0020	"	4.6	"
10 ≤ Z ≤14	0.0142 ± 0.0020	"	3.6	"
15 ≤ Z ≤ 26	0.0125 ± 0.0016	0.0084 ± 0.0020	i: 8.1 ii:16.7	0.0108 ± 0.0084
weight aver. fragmen.	0.0208 ± 0.045		3.2	

B

Cooperative Production of Pions and Photons as a Probe for the Dynamics of Nucleus-Nucleus Collisions

H. Noll[1,2], E. Grosse[1], H. Dabrowski[1], H. Heckwolf[1], O. Klepper[1], C. Michel[1], W.F.J. Müller[1], H. Stelzer[1], C. Brendel[3], W. Rösch[3], P. Braun-Munzinger[4]

[1]GSI Darmstadt, [2]Inst. f. Kernphysik Univ. Frankfurt,

[3]Inst. f. Kernphysik TH Darmstadt, [4]SUNY Stony Brook USA

It has been observed that in nucleus nucleus collisions pions - and similarly also high energy photons - are produced, whose energy is an appreciable portion of the total kinetic energy of the collision partners in their center of mass system. In such an event this energy is taken from the relative motion by slowing it down considerably. From the study of the production of high energy pions and γ-rays one hopes to get information about this deceleration process during the first stage of the collision, the simultaneous compression or heating of nuclear matter and the coupling of this excited nuclear matter to pions and photons.

The emission of neutral pions of 0 to 250 MeV kinetic energy (and γ-rays of similar energies) has been studied using the GSI lead glass detector ring. The experiments[1] were perfomed with ^{12}C and ^{18}O projectiles of 60-84 MeV/u at the CERN-SC and the 44 MeV/u ^{40}Ar beam of GANIL. The spectra are characterized by a smoothly variing part at low and an exponential fall off to high energies. Their analysis is based on the fact that radiation emitted from an accelerated source shows such an exponential fall off[2]; as is well known from classical bremsstrahlung theory, it is the Fourier transform of the acceleration function which determines this high energy part of the spectrum.

In the experiment pions (cf. Fig.1) as well as directly produced γ-rays (cf Fig.2) were observed. The slope parameters in the two "radiation" spectra are agreeing to each other surprisingly well. Noting that the pion can be considered an effective boson of the strong interaction (equivalent to the γ for the electromagnetic interaction) a scaling law for the slope parameters can be found by applying the classical bremsstrahlung formulae to the gamma as well as to the pion energy spectra. As can be seen from Fig. 1 the slope E_o and thus the slowing down time $2\tau=\hbar/E_o$ (which is in the range of 10^{-23}s) does not depend on the target mass. But it does depend on the projectile velocity β in such that E_o is observed to be nearly proportional to β. This means that the slowing down length $\lambda = \tau * c * \beta$ becomes nearly equal for all collision systems investigated; the experimental values scatter around 1.6 fm within 0.2 fm. This characteristic slowing down length, i.e. the distance over which the relative velocity of the two nuclei falls to half its value, comes out to be surprisingly short, indicating the occurence of rather violent collisions.

As has been shown in a semiclassical calculation[2], the results of such an analysis are not changed seriously when allowing for finite source dimension and non zero pion mass. The effect of the details of the elementary pion production process[3,4] and the consequences of specific collision models[4,5,6] on pion and photon production are presently under investigation.

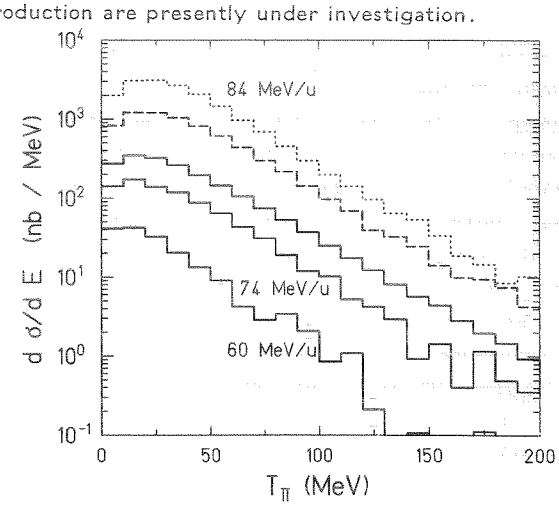


Fig. 1: Pion kinetic energy spectra for the ^{12}C + ^{12}C system as measured at 60, 74 and 84 MeV/u (drawn lines) and for ^{12}C + ^{56}Ni and ^{12}C + ^{238}U at 84 MeV/u (dashed and dotted lines, resp.). The slopes in the spectra correspond to $E_o \approx 27$ MeV, 25 MeV and 22 Mev, respectively, for the three energies.

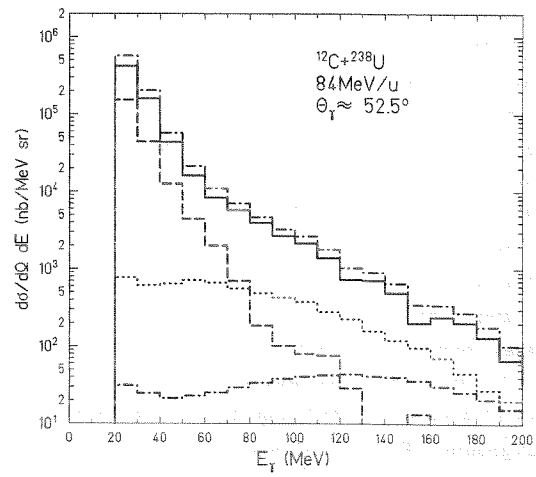


Fig. 2: Gamma ray spectra from ^{12}C + ^{238}U collisions at 84 MeV/u. From the singles spectrum (top dash-dotted line) the contributions due to π^0 decay (dotted line), cosmic rays (bottom dash-dotted line) and chance coincidences (dashed line) have to be subtracted to obtain the spectrum of the photons produced directly in the reaction (drawn line). Above 50 MeV this spectrum falls off exponentially with $E_o \approx 26$ MeV.

1. H. Heckwolf et al., this report and Z.Phys. 315 (84)243; H. Noll et al., to be published
2. D. Vasak et al., this report and subm. to Phys.Rev.
3. M. Uhlig et al., this report
4. M. Tohyama et al., to be publ. by Phys.Lett.
5. R. Shyam and J. Knoll, to be publ. by Phys.Lett.
6. W. Cassing, this report

B

Pion Production in Nucleus Nucleus collisions at Energies far below the NN-Threshold

H. Heckwolf[1], G. Bizard[6], P. Braun-Munzinger[4], C. Brendel[3], H. Dabrowski[1], E. Grosse[1], J. Julien[5], O. Klepper[1], J.L. Laville[6], C. Michel[1], A.C. Mueller[7], W.F.J. Müller[1], H. Noll[1,2], F.E. Obenshain[8], G. Pappalardo[5], P. Paul[4], J. Peter[7], L. Ricken[4], W. Rösch[3], J. Stachel[4], H. Stelzer[1], G.R. Young[8], P.H. Zhang[4]

[1]GSI Darmstadt, [2]IKF Universität Frankfurt, [3]TH Darmstadt, [4]SUNY Stony Brook (USA), [5]CEN Saclay (France). [6]Universite de Caen (France), [7]GANIL, Caen (France), [8]ORNL Oak Ridge (USA)

In N-N collisions neutral pions can be produced only above the threshold energy of 280 MeV in the laboratory. In reactions with heavy ions pion production at energies below this threshold is possible either as a consequence of the intranuclear Fermi motion[1] or alternatively through the cooperative action of several nucleons in the collision, i.e. a collective effect. First measurements[2,3] in the range from 183 down to 85 MeV/u seemed to be explainable by Fermi motion alone. However, it was demonstrated[4] recently, that with decreasing beam energy this single collision picture cannot explain the large experimental cross sections and that also the shapes of the pion spectra are not reproduced. The threshold for the Fermi-gas model lies at about 50 MeV/u and collective effects in the collision dynamics manifest themselves by a significant production of pions below this threshold. From the observed production cross section as a function of target and projectile mass, projectile energy and of the energy and angle of the outcoming pions one should get information about such collective effects.

Experiments on the production of pions in the region of the Fermi gas threshold have been performed at CERN (60-84 MeV/u ^{12}C), GANIL (44 MeV/u ^{40}Ar) and the Michigan State University superconducting cyclotron (35 MeV/u ^{14}N). The neutral pions decay into two γ-rays which are detected in an array of lead glass Cerenkov detectors[5]. To suppress the background of protons and γ-rays produced directly in the collision it was necessary to apply a 4-fold coincidence and a cut in the invariant mass. Because of the microstructure of the cyclotron beam at GANIL and MSU chance coincidences posed a severe problem, as can be seen in Fig. 1. But still the events with a proper invariant mass of around 135 MeV can be well separated from the background. Figure 2 shows the total cross sections for different projectiles and energies as a function of the target mass. The data of the π^0 production cross section follow a line proportional to A^x, where $x = 0.65$ gives the best overall fit, similar to what has been observed at higher energies[3,6].

Fig. 3 shows the total cross section as a function of the beam energy. For comparison it is useful to convert the cross sections relativ to the $^{12}C + ^{12}C$ system at the same bombarding energy per nucleon using the experimentally determined proportionality $\sigma \sim A^x \cdot A^x$. The resulting steep rise with beam energy per nucleon of the pion production cross section is well described e.g. by the bremsstrahlung model[7] which considers the pions to be emitted in a radiative process analoguous to the emission of γ's from a moving charge.

1. G. Bertsch, Phys.Rev. C15(1977)713
2. S. Nagamiya et al., Phys.Rev. C24(1981)971
3. T. Johansson et al., Phys.Rev.Lett. 48(1982)732
4. R. Shyam and J. Knoll, submitted to Phys.Lett.
5. C. Michel et al., GSI Scientific Report (1982)226
6. H. Noll et al., GSI-Scientific report (1982)32
7. D. Vasak et al., Physica Scripta 22(1980)25 and presented at Bormio 1984

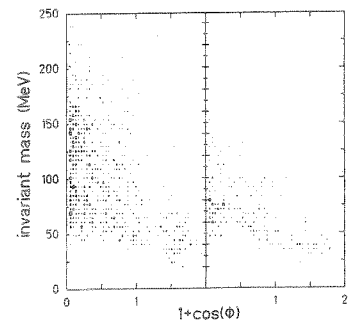


Fig. 1: Scatter plot of the events accumulated for Ar on Ca in prompt (left) and delayed (right) coincidence mode. The invariant mass of pairs of γ-rays is plotted versus the relative angle ϕ between them.

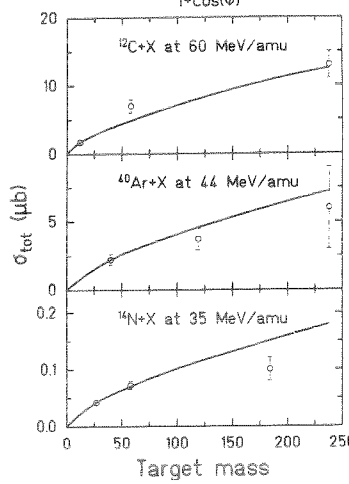


Fig. 2: Dependence of the integrated pion production cross section on the target mass for different projectiles and energies. The lines drawn show a A^x law with the normalisation on the lightest target mass.

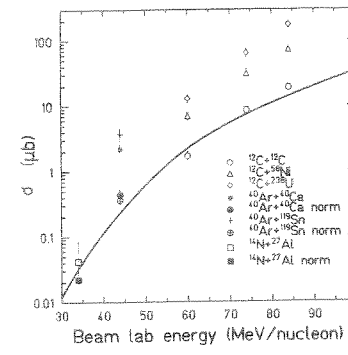


Fig. 3: Total pion production cross section measured at CERN, GANIL and MSU with ^{12}C, ^{40}Ar and ^{14}N projectiles. For comparison the GANIL and MSU data have also been renormalized to the $^{12}C + ^{12}C$ system using the $A_P^x \cdot A_T^x$ dependence. The line drawn is from ref. 7.

Pion Production as a Probe of the Nuclear Matter Equation of State

J.W. Harris, R. Stock, R. Bock, R. Brockmann, A. Sandoval, H. Ströbele (GSI Darmstadt); G. Odyniec, H.G. Pugh, L.S. Schroeder (LBL Berkeley); R.E. Renfordt, D. Schall (Univ. Heidelberg); D. Bangert, W. Rauch (Univ. Marburg); K.L. Wolf (Texas A&M University)

Equilibrium rate calculations can be used to show that thermal and chemical equilibrium should be reached during the high density stage of central nucleus-nucleus collisions and that freeze-out of the $\pi + \Delta$ chemical abundance occurs near the end of this stage, thus establishing the final pion multiplicity as a probe of the high density stage. For a mixture of π, N, and Δ gases an estimate of the extent to which chemical equilibrium is reached during the high density stage, where $\rho \sim 3\ \rho_o$ in a collision at 1 GeV/n, yields an equilibration time $\tau \approx 6 \times 10^{-24}$ s. The time necessary to reach thermal equilibrium is approximately a factor of two shorter. Using a dynamical model such as the intranuclear cascade the duration $t_{\rho max}$ of the high density stage is found to be sufficient for attaining thermal and chemical equilibrium since[1,2] $t_{\rho max} \approx 2\tau$ for Ar + KCl and $t_{\rho max} \approx 3.5\ \tau$ for La + La. However, during the expansion phase the N, π, and Δ chemical equilibration time at $\rho = 0.7\ \rho_o$ is 3×10^{-23} s $< \tau < 2 \times 10^{-22}$s assuming isoergic (lower) or isentropic (upper) expansion. This time is too long for chemical eqilibrium to be maintained through expansion since the time necessary for expansion[2] from ρ to $\rho/2$ is $\sim 10^{-23}$s. Therefore, the $\pi + \Delta$ yield will not freeze out at $\rho \sim \rho_o/2$ to ρ_o as previously assumed in fireball and hydrodynamical model studies but rather at higher densities near the onset of expansion. On the other hand thermal equilibrium, which determines the pion temperatures and source sizes, will be maintained to later times due to the large $\pi N \leftrightarrow \Delta$ cross section.

Displayed in Fig. 1 is the experimental pion multiplicity per participant after Δ decay ($\Delta \rightarrow \pi N$) extrapolated to zero impact parameter collisions of Ar + KCl as a function of beam c.m. energy. The experiment was performed at the Bevalac using the Streamer Chamber at 7 incident lab. energies from 566 to 1808 MeV/u. The techniques employed in the analysis have been described previously[3]. Predictions of the intranuclear cascade models of Cugnon[4] and Yariv-Fraenkel[5] are also shown. These models incorporate binary, quasi-free interactions of hadrons in a nucleus-nucleus collision geometry. Another approach which is strongly suggested by the above rate calculations is the use of a chemical model to predict the $\pi + \Delta$ abundance[6] along with the Rankine-Hugoniot relations for shock compression. This nuclear matter approach which has opposite mean free path assumptions from the cascade, similarly overpredicts the $\pi + \Delta$ to participant ratios.

The failure of these models to predict the observed ratios can be attributed to compressional degrees of freedom which are not incorporated in the models. The available c.m. energy can be partitioned into thermal (pion-producing) and compressional energy fractions. An estimate of the compressional energy can be made from the energy offset, represented by the arrows in Fig. 1, between the energy available in the experiment and the energy at which a given model predicts the observed pion multiplicity. The resulting compressional energies as a function of the densities predicted by the models are shown independently in Fig. 2. Both approaches yield strikingly similar results which suggest a stiff nuclear matter equation of state with the same overall structure as those recently obtained from field theory[7].

1. R. Stock et al., Phys. Rev. Lett. 49(1982)1236.
2. J.W. Harris and R. Stock, Proceedings of the Seventh Oaxtepec Symposium on Nuclear Physics, Oaxtepex, Mexico (1984) UNAM Press.
3. A. Sandoval et al., Phys. Rev. Lett. 45(1980)874 and R. Stock et al., Physica Scripta T5(1983)130.
4. J. Cugnon et al., Nucl. Phys. A352(1981)505 and Nucl. Phys. A379(1982)553.
5. Y. Yariv, priv. communication.
6. Chemical model results provided by G.D. Westfall.
7. J. Boguta and H. Stöcker, Phys. Lett. 120B(1983)289.

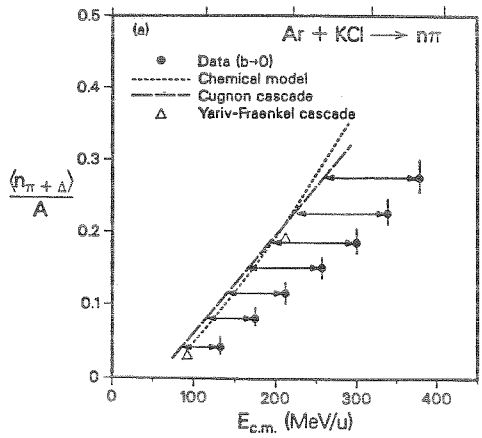


Fig. 1

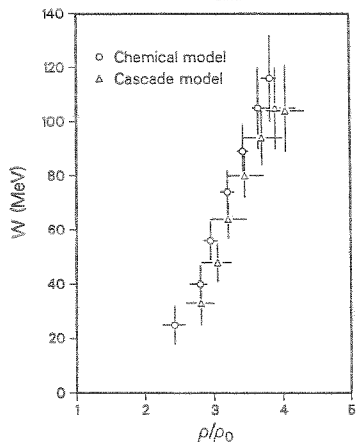


Fig. 2

Momentum flow in the 800 MeV/u Ar + Pb reaction G

R.E. Renfordt, D. Schall, K. Tittel (Univ. Heidelberg), R. Brockmann, J.W. Harris, M. Maier, A. Sandoval, R. Stock, H. Ströbele (GSI Darmstadt), H.G. Pugh, L.S. Schroeder (LBL Berkeley), K.L. Wolf (Texas A&M Univ., College Station)

Central collisions between argon and lead are analyzed in terms of global observables.

With the Berkeley Streamer Chamber all charged particles produced in collisions between 0.8 GeV/u Ar projectiles with a Pb_3O_4 target were recorded on film. A hard wave trigger selected central collisions with Pb nuclei; equivalent to an impact parameter range of 0-5 fm. Significant experimental biases are found only for particles near target rapidity due to absorption and composite particle ambiguities. Therefore, the analysis is restricted to particles in the forward hemisphere of the participant center-of-mass system. The data are compared to events generated by the intranuclear cascade code [1] appropriately modified to simulate the experimental biases. The number of participant protons is used to allow for a refined selection of impact parameters within the range given by the hardware trigger: High multiplicity defines an event sample corresponding to the most central collisions (b < 3 fm) and low multiplicity selects large impact parameters (b < 3 fm).

The momentum flux tensor [2] is used to define the global observables θ_F (direction of the main axis of the flux tensor with respect to the beam) and the event plane (defined by the main axis of the flow tensor and the beam). Fig. 1 shows the distribution $dN/d\cos\theta_F$ for low and high multiplicity selected events for both the cascade events (fig. 1a) and the data (fig. 1b). For the low multiplicity data the angular distribution peaks in the beam direction indicating that the incident momentum flux is not fully degraded in the collision. The high multiplicity events display a rather isotropic angular distribution suggesting that for these small impact parameter events the momentum distribution of the participant nucleons is randomized and the nuclei are essentially stopped. The cascade events show a similar trend but less isotropy in both samples.

The event plane as determined by the momentum flux tensor is used to study the transverse momentum projected into this plane as a function of rapidity. Fig. 2a shows in a linear contour plot the inclusive distribution P_t (projected) versus rapidity for all protons. A small but significant asymmetry with respect to the beam axis is observed. This asymmetry is not present in an analogous contour plot for the plane perpendicular to the reaction plane (fig. 2b). Cascade events do not show this asymmetry. In the high multiplicity selected subsample the shape of the contour lines for the data are consistent with isotropy (in agreement with the angular distribution of fig. 1b).

Thus central collisions of Ar with Pb at 800 MeV/u show complete stopping of the projectile in the target with subsequent thermal emission from the fireball.

[1]J. Cugnon et al., N.P. A379(1982)553
[2]M. Gyulassy et al., Phys.Lett. 110B, 185(1982)

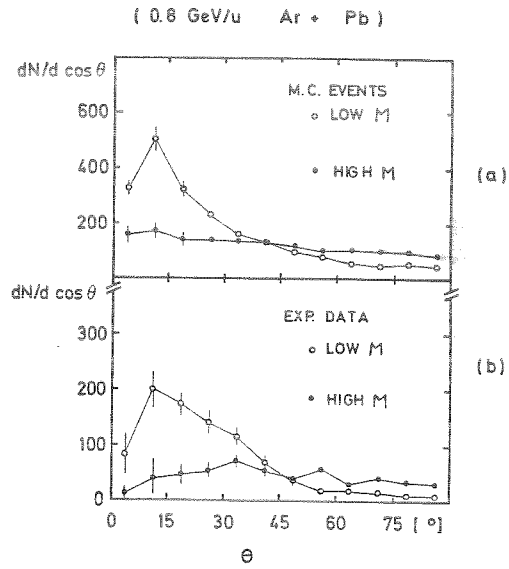


Fig. 1: Angular distribution of main axis of momentum flux tensor.

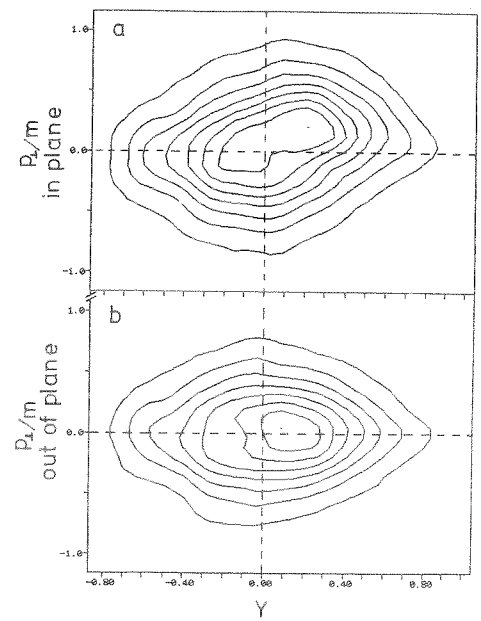


Fig. 2: Transverse momentum as a function of rapidity.

Relativisitc Nuclear Collision Studies with the Plastic Ball [G]

M. Doss, H.-A. Gustafsson, H.H. Gutbrod, K.H. Kampert, B. Kolb, H. Löhner, B. Ludewigt, A.M. Poskanzer, T. Renner, H. Riedesel, H.G. Ritter, A. Warwick, H. Wieman

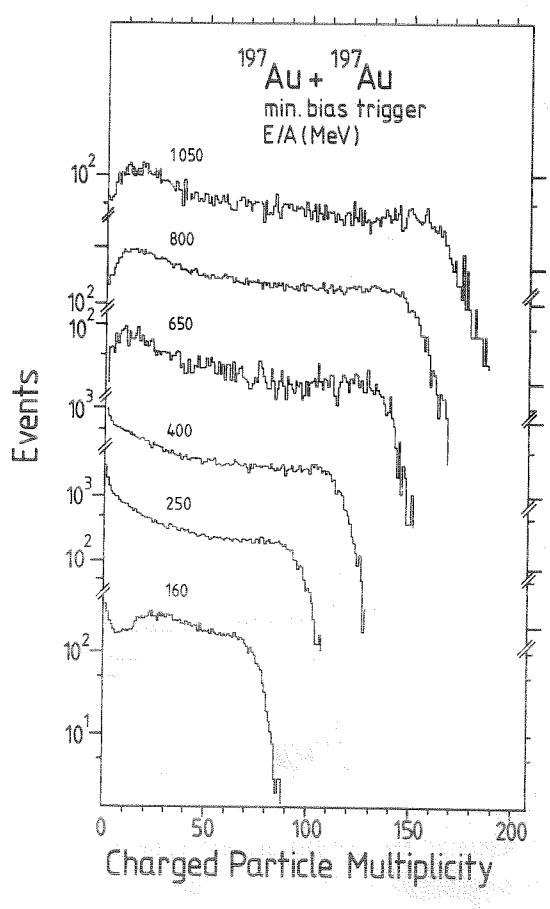
GSI Darmstadt, LBL Berkeley, Univ. Münster

The data taking program of the Plastic Ball group continued this year with the heavy beams now available at the Bevalac. As before, the goal is to study symmetric systems of round nuclei, with beam and target having the same mass for an exact determination of the center of mass. This is possible for ^{93}Nb and ^{197}Au where simple metal foils as targets can be obtained. During the early experiments with 1.05 GeV/nucleon ^{93}Nb the data taking rate was reduced to ca. 27 events/spill on tape for a central collision trigger. This was caused by the enormous increase of the particle multiplicity. To overcome the limited buffersize of the PDP-11-44 computer and prepare for the even larger eventlength expected for ^{197}Au + ^{197}Au interactions, a VAX 750 computer replaced the PDP-11-44 and thus allowed an increase in data collection of more than a factor of 3. Full excitation functions of ^{93}Nb on ^{93}Nb and ^{197}Au on ^{197}Au were measured at E/A = 160, 250, 400, 650, 800 and 1050 MeV. Fig. 1 shows the multiplicity distributions for these energies for Au + Au in the minimum bias-trigger-mode.

With heavy ion beams now available recent studies of target fragmentation with the focus on condensation or scattering phenomena can be investigated in the projectile frame. For this we designed and constructed a Zero-Degree-Detector for TOF, position and dE/dx measurement. Multiwire beamcounters (avalanche mode) have been built to allow single particle track determination especially necessary to measure very small deflection angles as expected in the projectile fragment bounce-off process. All wire chambers are equipped with newly designed high gain, low cost fast amplifiers which allow therefore a single wire readout. The full system will be employed in 1984 in an experiment of ^{197}Au + ^{197}Au and ^{197}Au on a light mass target.

A large part of the groups effort went into programming for a new energy calibration procedure which - due to the VAX 780 interactive system-allows more accuratiely to adjust and match the individual detector modules to their calibrated norm values. Another effort focussed on the global analysis (energy flow) at Berkeley and the minimum spanning tree analysis (MST) at Münster. The energy flow analysis clearly established for the first time two collective effects, the bounce-off and the side-splash. The MST analysis tries now to separate the bounce-off fragments from the participants. As an event generator to fit the data and to extract the amount of collective and purely statistical (themal) motion, the code of Fai and Randrup was modified and run on the VAX 780. A large amount of intranuclear Cascade calculations have been performed at the GSI-IBM computer system to compare any inherent collectivity with the measured one.

The final state interaction or the nuclear freeze-out at low densities was investigated via the cluster production where the temperature dependence in the cluster formation was considered besides the size of the cluster as well as that of the reaction volume. Another, totally independent study employed the two-proton correlation for determination of the freeze-out density. Both studies lead to the same system size with the same final state density of $\rho = 0.25\ \rho_o$.



Thermalization in High Energy Nuclear Collisions

H.-A. Gustafsson, H. H. Gutbrod, B. Kolb, H. Lohner, B. Ludewigt, A. M. Poskanzer,
T. Renner, H. Riedesel, H. G. Ritter, A. Warwick and H. Wieman
GSI Darmstadt, LBL Berkeley, Universitat Marburg and Universitat Munster

One of the major questions in high energy nuclear physics is to study whether thermal equilibrium is reached or whether nuclei become already transparent at Bevalac energies. The isotropy of an event can be judged by the ratio R of the average momentum components perpendicular and longitudinal to the beam axis in the center-of-mass frame shown in fig. 1 as a function of the detected fraction of all projectile and target charges. Assuming a correlation between the impact parameter and the charged particle multiplicity the increase of R with the detected fraction of all charges in the system N_z/Z can be partly understood as due to spectator or leading particle contributions. R = 1 corresponding to isotropic events is reached only for the Nb + Nb system at E/A = 400 MeV whereas at higher energies and for the smaller Ca + Ca system the projectile is not fully stopped by the target nucleus.

Since the proton spectra at $\theta_{cm} = 90^\circ$ are not disturbed by spectator contributions they were analysed with a relativistic Maxwell-Boltzmann distribution. The resulting temperature parameters (T_0) increase with the charged particle multiplicity M_c (table 1) for Ca + Ca as well as for Nb + Nb. This may indicate an approach towards equilibrium. On the other hand, the observed increase of the production of composite particles with multiplicity [1] could be responsible for the rise of the temperature by reducing the number of particles. However, a clear deviation from a Boltzmann shape that is more pronounced for higher multiplicities is seen at the very low energy part of the spectra (fig. 2). This may be caused either by the formation of composite particles, that leads to a depletion of the primordial proton yield at low energies (coalescence model), or by a spherically symmetric and expanding fireball [2] with approximately an equal amount of energy in radial expansion and in thermal motion (fig. 2).

1) H.H. Gutbrod, et al.: Phys. Lett. 127B (1983) 317 and Proceedings of the Int. Conf. on High Energy Nucl. Phys. in Balatonfured, Hungary (1983) 269
2) P.J. Siemens and J.O. Rasmussen, Phys. Rev. Lett. 42 (1979) 880

Table 1: Extracted T_0-values in MeV.

M_c	0-10	10-20	20-30	30-40	40-50	50-60
Nb + Nb	42	46	51	55	60	65
Ca + Ca	43	48	54	56		

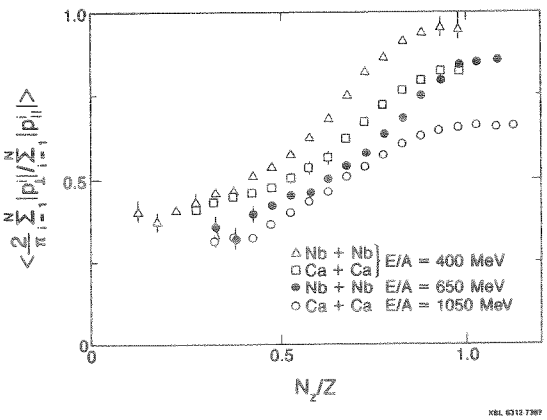


Fig. 1 : Ratio of the average perpendicular to parallel momentum as a function of N_z/Z.

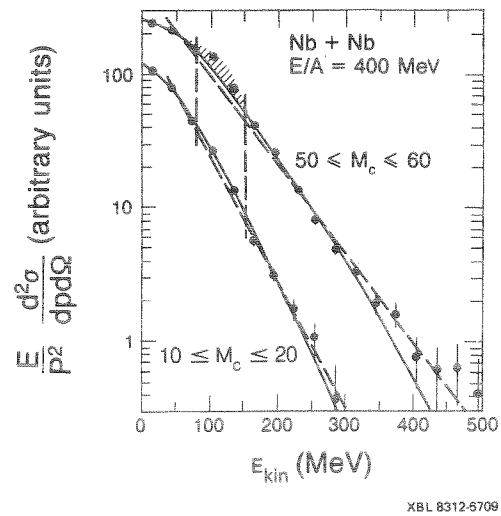


Fig. 2 : Proton spectra at $\theta_{cm} = 90^\circ$. Dots: experimental data points; dashed lines: fitted Boltzmann distributions; full lines: expanding fireball.

Radii of the Participant Region in Relativistic Nuclear Collisions Measured from Proton Proton Correlations

G

H. A. Gustafson, H. H. Gutbrod, B. Kolb, H. Lohner, B. Ludewigt, A. M. Poskanzer, T. Renner, H. Riedesel, H. G. Ritter, A. Warwick, F. Weik and H. Wieman
GSI Darmstadt, LBL Berkeley, Universitat Marburg and Universitat Munster

Relativistic heavy ion collisions produce a region of hot matter that radiates protons, pions and composite particles. The effective source size of this radiating zone, or fire ball, has been investigated by a number of groups using either proton pair correlations [1] or pion pair correlations [2,3] at small relative momenta. The application of this method in nucleus nucleus collisions is still relatively novel and an effort is being made to explore its potential and understand the significance of the measured radii. It is of particular interest to relate variations in extracted radii to different types of events.

We report here source radii as a function of event charge multiplicity for two different reactions: Ca on Ca and Nb on Nb, both at 400 MeV/nucleon. The proton proton correlations used in this study were measured at the Bevalac with the 4π plastic ball detector [4]. In these measurements the Δp resolution between pairs is limited by the finite angular size of the detector modules. A simple Monte Carlo technique that makes use of the data stream, however, overcomes this problem by adding the angular distortion to the theoretical correlation functions, thus permitting a direct comparison with our measurements. The theoretical correlation function used was taken from Koonin's paper [5] and it includes Coulomb and nuclear final state interactions between the two protons.

The extracted radii are shown as a function of charge particle multiplicity in fig. 1. For both the Ca + Ca and Nb + Nb systems the radius increases with multiplicity. The curves show the fit with the following function

$$r_g = r_o(\frac{A}{Z} N_c)^{1/3}/\sqrt{5/2}$$

where N_c is the event charge number and A/Z has been included to reflect the presence of neutrons. Our extracted radii are the radii parameter for a gaussian source distribution so by including $\sqrt{5/2}$ in the above function r_o becomes the sharp sphere radius parameter of an equivalent rms value. The value of r_o extracted from the fits is 1.9 fm, essentially the same for both the niobium and calcium systems. Comparing this directly with $r_o = 1.2$ fm, the sharp sphere r_o for normal nuclear matter, yields a participant region density of 1/4 normal nuclear density. This is the same density we extracted from our deuteron to proton ratios in conjunction with a coalescence model analysis [6]. It appears that our proton proton correlations give a measure of the freeze out radius, the radius of the last proton scattering, particularly since there is agreement with coalescence model results.

1) F. Zarbakhsh et al, Phys. Rev. Lett. 46, 1268 (1981)
2) D. Beavis et al., Phys. Rev. 27C, 910 (1983)
3) W.A. Zajc et al., Ph.D. thesis, 1982 (Report No. LBL-14864)
4) A. Baden et al., Nucl. Instr. and Meth. 203, 189 (1982)
5) S.E. Koonin, Phys. Lett. 70B, 43 (1977)
6) H.H. Gutbrod et al., Phys. Lett. 127B, 317 (1983); H.A. Gustafsson et al., to be published

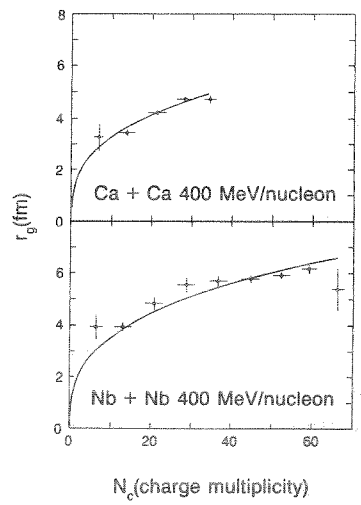


Fig. 1 : Extracted gaussian source radii as a function of total charge multiplicity (N_c) for the two systems Ca + Ca and Nb + Nb at 400 MeV/nucleon. The curves are fits to the results with the function, $r_g = r_o(\frac{A}{Z} N_c)^{1/3}/\sqrt{5/2}$.

G

Observation of strong azimuthal asymmetry between slow and fast secondaries in high energy nuclear collisions in the Plastic Ball

H.H. Gutbrod, H. Löhner, A.M. Poskanzer, T. Renner, H. Riedesel, H.G. Ritter, T. Siemiarczuk*, J. Stepaniak*, A. Warwick, F. Weik and H. Wieman (GSI Darmstadt, LBL Berkeley, Univ. Münster)

Parallel to the global analysis of the Plastic Ball[1] data (energy flow and minimum spanning tree) a very straight forward analysis for azimuthal asymmetries in the particle flow between slow and fast raction products has been performed. It is expected that energy and impact parameter dependance of the azimuthal asymmetry is a sensitive tool for reaction mechanism studies.

To study the azimuthal correlation between slow and fast secondaries, the following procedure has been developed: to each particle a vector of unit length is ascribed in the direction of the transverse component of its momentum and the resultant vectors R_S and R_F have been calculated separately for the slow (stopped in the Plastic Ball) and fast (punch through E_p > 240 MeV) secondaries. A uniform distribution of the angle α_{FS} between R_S and R_F vectors is expected if there is no azimuthal asymmetry between those groups of particles.

All the distributions, independently on the incident energy, target and projectile masses, exhibit remarkable similarity in the type of asymmetry: there is a significant excess of events with large α_{FS} angles. In order to investigate and exclude spectrometer related correlations, a Monte Carlo procedure was used to calculate the background. The Monte Carlo events were built from the real recorded particles in that way that only one particle (slow or fast) was taken from real event, ensuring that any possible two- or many-particle correlations present in real events are destroyed. The numbers of slow (n_S) and fast (n_F) particles in the Monte Carlo event were generated from the two-dimensional n_F vs. n_S experimental distribution, taking thus into account the correlation between F and S particle multiplicities. The Monte Carlo background normalized to the experimental data is shown in Fig. 1 by the dotted line. The number of Monte Carlo events was 5 to 10 times higher than the number of real ones. One can see that the background is almost uniform.

The experimental data corrected for any background asymmetry are shown in Fig. 2, where the ratio R = D-B/D+B is plotted against α_{FS}. D and B are the numbers of real and background events in the corresponding α_{FS} bin. The solid lines are drawn by hand to guide the eye. The inspection of Fig. 2 reveals that (i) the asymmetry decreases somewhat with the increase of the incident energy and that (ii) he asymmetry is stronger for the central trigger as compared to the minimum bias one. A comparison with Ca + Ca shows that for the equal mass target and projectile experiments, the asymmetry gets stronger for larger A. Furthermore the asymmetry for the NePb experiment at 0.8 GeV/n (central trigger) is less pronounced then for any other experiments with a central trigger (CaCa(1 GeV/u, 0.4 GeV/u, NbNb (0.65 GeV/u, 0.4 GeV/u)).

The observed asymmetry corroberates the findings of the energy flow analysis and sets strong constraints on the possible mechanism of nucleus nucleus collisions.

*On leave of absence from the Institute for Nuclear Studies, 00-681 Warsaw, Hoza 69, Poland

[1] A. Baden et al., Nucl. Instr. Meth. 203(1982)189

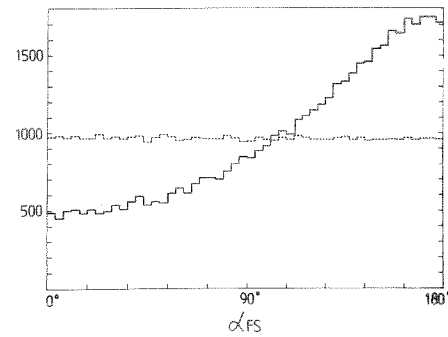


Fig. 1: α_{FS} distribution for Nb + Nb at E/A = 400 MeV minimum bias trigger.

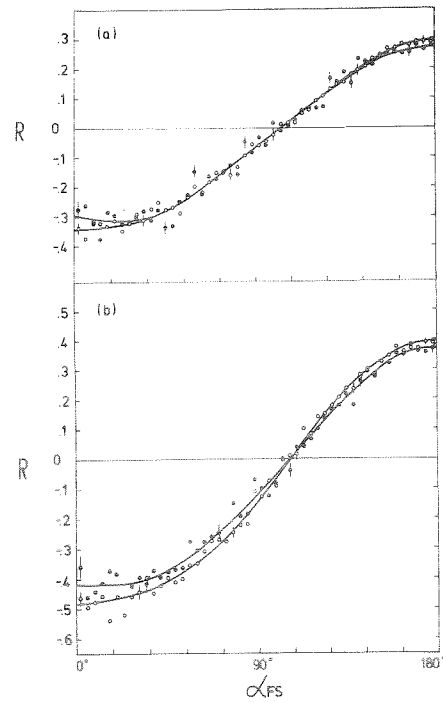


Fig. 2: R distribution as a function of α_{FS} for Nb + Nb at E/A = 400 (open circles) and E/A = 650 MeV (black dots) and a) minimum bias vs. b) central trigger.

Collective Flow Observed in Relativistic Nuclear Collisions G.

H. A. Gustafsson[b], H. H. Gutbrod[a], B. Kolb[a], H. Löhner[a], B. Ludewigt[a], A. M. Poskanzer[b], T. Renner[b], H. Riedesel[b], H. G. Ritter[a], A. Warwick[a], F. Weik[a], H. Wieman[a]

[a]GSI, Darmstadt, West Germany and [b]LBL, Berkeley, CA 94720

Data from 4π detectors like the Plastic Ball are ideally suited to study the emission patterns and event shapes of high energy nuclear collisions. The shapes predicted by hydrodynamical and intranuclear cascade calculations are quite different. The hydrodynamical model predicts prolate shapes along the beam axis for only grazing collisions. With decreasing impact parameter the flow angle increases, and reaches 90 degrees (with oblate shapes) for zero impact-parameter events[1,2]. Cascade calculations on the other hand predict zero flow angles at all impact parameters[2]. Approximately 50000 events of 400 MeV/nucleon Nb + Nb and Ca + Ca have been used for an energy flow analysis.[2] The events have been classified according to charged particle multiplicity. The distribution of the flow angle θ (angle between the major axis of the flow ellipsoid and the beam axis) is shown in Fig. 1 for different multiplicity selections. A striking difference between the Ca and Nb data can be observed. For all but the highest multiplicity bins the distribution of the flow angles for the Ca data is peaked at 0 degrees. For Nb, however, there is a finite deflection angle increasing with increasing multiplicity. The same analysis has been performed with filtered events from an cascade code calculation.[3] For both systems studied the distributions are always peaked at zero degrees. It is not so evident that the Ca + Ca collision differs from its simulation with the cascade model, whereas a new collective phenomenon definitely appears in the larger mass system which is not accounted for by the present cascade models. A more detailed study of the contour plots in the reaction plane (p_x/m versus y) reveals two collective flow effects (fig. 2): The projectile fragments are found slightly displaced from the beam axis (bounce-off), and the intermediate rapidity fragments have a preference for emission angles of 20 to 30 degrees in the center of mass system (side-splash) for the higher multiplicity events of Nb + Nb which is not evident for Ca + Ca.

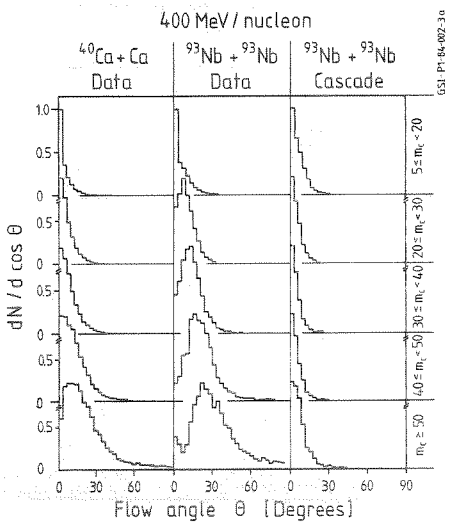


Fig. 1: Frequency distributions of the flow angle θ for two sets of data and a cascade calculation for different multiplicity bins. For the case of Ca the multiplicities are half the indicated values.

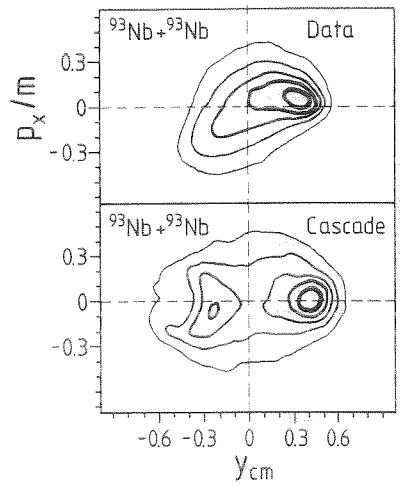


Fig. 2: Contour plots (linear contours) of p_x/m versus cm rapidity for multiplicities between 40 and 49 charged particles.

1. H. Stöcker, J. Hofmann, J. A. Maruhn and W. Greiner, Progr. in Part. and Nucl. Phys. 4, 133 (1980)
2. M. Gyulassy, K. A. Frankel, and H. Stöcker, Phys. Lett. 110B, 185 (1982).
3. Y. Yariv and Z. Fraenkel, Phys. Rev. C20, 2227 (1979).

Participant-Spectator Identification in Plastic-Ball Events

H.A. Gustafsson, H.H. Gutbrod, B. Kolb, H. Löhner, B. Ludewigt,
A.M. Poskanzer, T. Renner, H. Riedesel, H.G. Ritter, A. Warwick, F. Weik, H. Wieman
GSI Darmstadt, LBL Berkeley, Universität Marburg and Universität Münster

The analysis of Plastic Ball events with respect to identification methods for particles emitted from spectator remnants has been further continued. After first promising results from the application of the cluster algorithm "minimal spanning tree" (MST)[1] this method could be improved by optimizing the distance measure (used to define a family of particles = cluster). The efficiency was tested by analyzing events from the Yariv-Fraenkel intra nuclear cascade code[2] which had been supplemented by an additional evaporation code in order to allow the excited spectator remnants to evaporate light fragments of Z = 1 and 2 and neutrons. The final results are filtered according to the experimental Plastic Ball acceptance and then given to the MST algorithm. Using a distance between particles i and j defined by $d_{ij} = \Theta_{ij}^2 \cdot (Y_i - Y_j)^2$, where Θ_{ij} = angle between particles i and j and Y_i and Y_j are their respective rapidities, we obtain the decomposition of the total rapidity distribution (solid curve) shown in fig.1. The particles from those events showing two clearly recognized clusters are contained in the dashed (constituents of the two clusters) and dotted curve (no member of any of the two clusters). We can compare the MST results with the explicit cascade model identification (known beforehand by tagging) and find that the two clusters mostly contain particles from projectile and target remnants. However, the shaded area in fig.1 shows the fraction of particles which are misidentified as midrapidity particles, whereas the dotted curve shows particles from the midrapidity region which are misidentified as spectator particles. From this comparison we deduce that 75 % of all projectile remnants are correctly identified.

Even though this number is not yet fully satisfying, it seems justified to exploit the results of the MST analysis of experimental data on this level of accuracy, especially since from plots of triple differential cross sections a high degree of correlation is obvious between projectile and target cluster. For Nb+Nb and Ca+Ca at 400 MeV/nucleon incident energy the projectile cluster exhibits an average perpendicular momentum transfer of about 40 MeV/c per nucleon which is balanced by the same momentum transfer to the target cluster and which goes along with a slowing down in rapidity from $Y_{CM} = 0.45$ to $Y_{CM} \approx 0.38$. From these numbers we conclude an average momentum transfer (in CM) of ≈ 110 MeV/c per nucleon to the participant region and an average projectile deflection angle of 7°.

From distributions of projectile cluster angle for Nb+Nb at 400 MeV an average projectile deflection angle below 10° can be concluded for charged particle multiplicities up to 40°. The corresponding distributions of projectile cluster angle for cascade model data can be reproduced within 2° using the MST method.

Since the contribution from spectator remnants are quite prominent even at fairly large multiplicities, they are a major obstacle in extracting reliable information on flow angles from the global event analysis[3]. The selection of events with minor spectator contribution may therefore be a useful tool and will be persued in the future. First results of a combined flow and cluster analysis show a strong correlation in Ψ-angle for the direction of flow and the projectile cluster, which appear in the same reaction plane.

1) H. Löhner et al., GSI Scientific Report 83-1 (1982) p. 41
H. Löhner et al., Proceedings of the 6th Balaton Conference on Nuclear Physics 1983, p. 233
2) Y. Yariv, Z. Fraenkel, Phys. Rev. C20 (1979) 2227
3) H.G. Ritter et al., Proceedings of the 6th Balaton Conference on Nuclear Physics 1983, p. 275

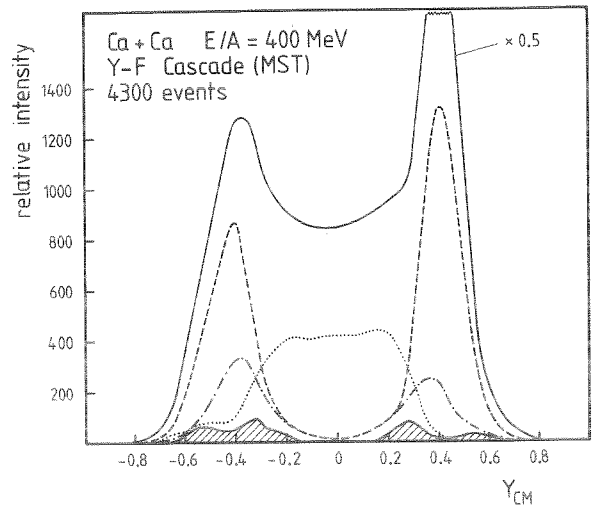


Fig. 1: Decomposition of rapidity distribution from cascade model calculation using the MST analysis (see text).

REACTIONS OF U AT 3.97 GeV/NUCLEON ON ^{12}C WITH SSNTD

M. Debeauvais, J. Ralarosy, J. Tripier and S. Jokic

CENTRE DE RECHERCHES NUCLEAIRES
67037 - Strasbourg Cedex

When a makrofol foil is exposed to a flux of 10^6 ions/cm^2 of 3.97 GeV we can see after etching events with 2, 3 and 4 tracks. These tracks represent interactions between U and the components of Makrofol (C or O). The makrofol works in this case as a 4π geometry detector. In a previous paper[1] we studied the U-C interaction at 2,38 GeV and we have found only binary events. With an U incident energy of 3.97 GeV, till now 14 ternary and 1 quaternary events have been observed in addition to binary ones.
The geometrical and kinematical study leads to the following results represented in Fig. 1 and Fig. 2.

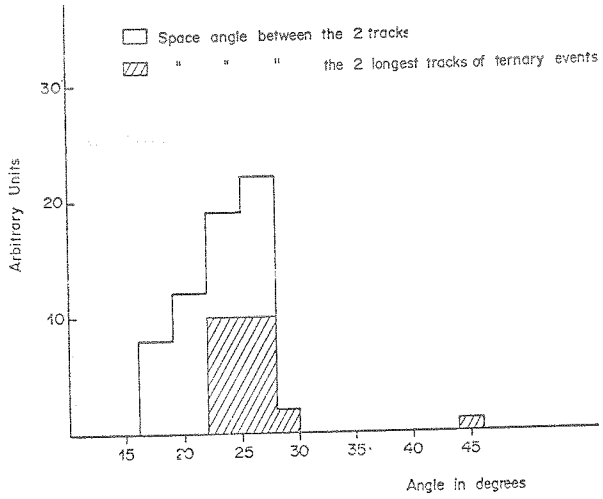


Fig. 1

The distribution of the space angle between both tracks for binary fission has the same behavior than the space angle distribution between the 2 longest tracks for the ternary events (Fig. 1). The mean value of the folding angle for binary and ternary events are 23° and 25° respectively. One of the ternary event has an angle of 44° and corresponds to a near equal mass distribution. In Fig. 2 you can also see the fragment mass distribution of binary and ternary events, we remark that the heaviest mass in both (binary and ternary) falls within the same limit and their distribution have the same shape approximately. Concerning the lightest fragment mass distribution in ternary fission we can see that the probability of ternary events increases with decreasing mass of the the lightest fragment. We have found a similar trend in a previous study of ternary fission induced by protons of 0.6 to 23 GeV on U and Pb[2].

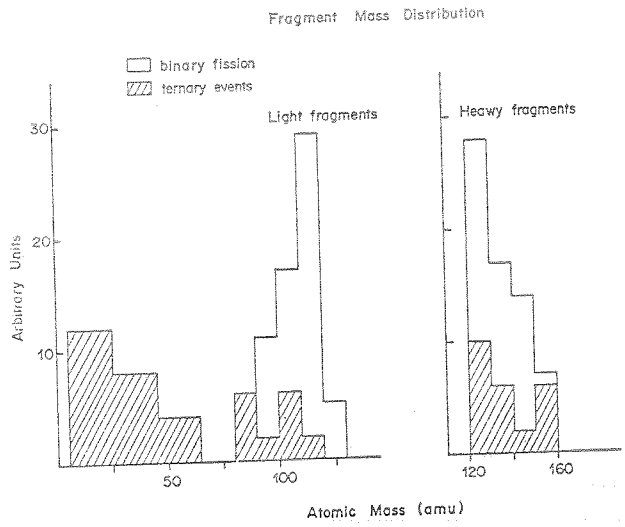


Fig. 2

We obtained with a good statistic in this reaction an exponential like curve only limited on the highest masses by the detector threshold. In the present case the statistics is very poor but nevertheless a similar tendency may occur.
In conclusion, we remark that the number of 3-pronged events increases with increasing incident energy. Most of them have two heavy masses and one light mass. This fact leads us to think that a part of binary events which have a projected angle < 180° on the detector plane are in fact ternary events. The lightest fragment escapes to the detection because of its small LET and cannot be registered in makrofol.

(1) M. Debeauvais, J. Ralarosy, J. Tripier, S. Jokic, 12th Int. Conf. on SSNTD, 4-10 Sept. 1983, Acapulco, Mexico.

(2) G. Rémy, Thesis Strasbourg 1974 (unpublished).

Radiochemical Search for Anomalons

G. Dersch, R. Beckmann, R. Brandt, T. Lund
Kernchemie, FB 14, Philipps Universität Marburg

K. Aleklett
Studsvik Science Research Laboratory, Nyköping, Sweden

E.M. Friedlander, P. Mc Gaughey, G.T. Seaborg
Lawrence Berkeley Laboratory, Berkeley, Ca, USA

W. Loveland
Oregon State University, Corvallis, Or, USA

N. Porile
Purdue University, W. Lafayette, In, USA

Last year we described a radiochemical technique to search for anomalons and study their properties[1,2]. Essentially, we bombarded two sets of two Cu-blocks (1 cm thickness) with reativistic heavy ions. We described[1], that in 24 GeV-p and 0.9 AGeV-^{40}Ar-irradiations we saw no anomalous effects, i.e. the cross-section ratio for the production of ^{24}Na as a radioactive residue of Cu target nuclei in two adjacent Cu-blocks was R_1=1.08+0.02 and the ratio of ratios for distant blocks Q=1.02+0.03, the values of R_1 and Q are defined in Ref.1. R_1 1.10 might be indicative for "fat" anomalons and Q 1.04 might be indicative for short-lived anomalons.

During 1983 we carried out three further heavy ion irradiations; a 12 AGeV ^{4}He at the CERN-PS and 2.1 AGeV ^{12}C plus 1.9 AGeV ^{40}Ar at the LBL-BEVALAC. The results are shown in Table 1 and Fig. 1. For 2.1 AGeV ^{12}C we essentially observe no anomalous effects. However, the R_1=1.36+0.03 for 1.9 AGeV ^{40}Ar is remarkably higher than R_1=1.07+0.02 for 0.9 AGeV ^{40}Ar. The reasons for this increase are being investigated at present. If it can be proven that no drastic and unexspected variations of the fragmentation pattern of ^{40}Ar take place between 0.9 and 1.9 AGeV, the increase in R_1 might be indicative for "fat" anomalons, producing copiously more activity in the downstream Cu-block than any other projektile fragments (see Fig.1). Furthermore, the Q=1.12+0.02 for 20 cm flight-path in the 12 AGeV-^{4}He irradiation might be due to either purely geometric effects ("beam blow-up") or to shortlived anomalons. This question is being studied at present.

Table 1: Preliminary results for ^{24}Na from Cu-block irradiations (R_1 and Q are defined in Ref.1)

Energy/Projektile	R_1	$Q=R_1/R_2$
24 GeV p	1.09 + 0.02	1.02 + 0.03
12 AGeV ^{4}He	1.21 + 0.02	1.06 + 0.03 1.12 + 0.02*
2.1 AGeV ^{12}C	1.12 + 0.02	1.03 + 0.02
0.9 AGeV ^{40}Ar	1.07 + 0.02	1.03 + 0.03
1.88 AGeV ^{40}Ar	1.36 + 0.02	1.07 + 0.03

*) This value was measured for 20 cm flight-path

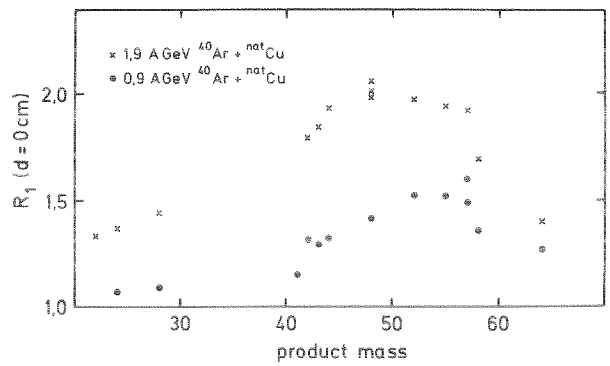


Fig. 1: The observed activity ratio in two adjacent Cu-blocks for residual radioisotopes produced by projectile fragments from ^{40}Ar at two different energies

[1] G.Dersch, et al., GSI 83-1, p. 43 (1983)
[2] E.M. Friedlander, et al., Phys. Rev. C27, 1489 (1983)

B

About the anomalous behaviour of projectile fragments of charge two

E. Ganßauge, U. Bieschke, H. Kallies, F. Killinger, N. Klein,
R. Kretschmer, A. Laschek and W. Weidner
FB Physik, Philipps-University, D-3550 Marburg, West-Germany

An anomalously short mean free path (mfp) λ^* was found some years ago for projectile fragments (PF) of charge $Z \geq 3$ by different laboratories [1].

The Marburg group claimed for this effect also for charge Z = 2 in 1981 [2]. In the meantime this was confirmed by several groups [3], although there still is not clear whether there possibly exsists some energy threshold. Therefore it was of special interest to learn about the 4.5 A GeV ^{12}C beam at Dubna that also there the Z = 2 PF's behave strange.

At this higher energy another interesting finding was published concerning the mfp dependence on the target multiplicity N_h. The distribution $\lambda^*(N_h)$, N_h being the multiplicity of heavy prongs from the target nucleus, was not at all the same for "white stars" (N_h=0) as for the N_h=1-5 group. N_h=0 preferably belongs to peripheral collisions while the other group is assigned mainly to interactions with nuclei of the CNO group in emulsion.

El-Nagi et al. [3] reported on a pronounced difference between those two groups and on an additional strange effect at N_h=1-5. At Marburg we reexamined our He-data looking for an possible N_h dependence. Our result is given in table I and fig. 1. The effect is the same as reported by the egyptian group, only the special effect at N_h=1-5 we can not confirm.

Assuming for this moment that neither the projectile nor its energy is of very much importance we lumped our data together with El-Nagi's data and show the combined results in table II and fig. 2. The F-ratios for $F_1 \equiv \lambda^*(N_h=0)/\lambda^*(N_h=1\text{-}5)$ result in a probability $P(F_1) = 1{,}3 \cdot 10^{-4}$ which corresponds to about 4 standard deviations out of normality.

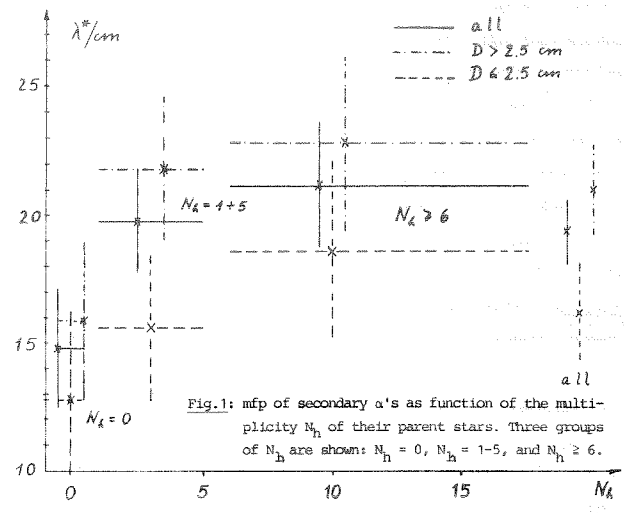


Fig.1: mfp of secondary α's as function of the multiplicity N_h of their parent stars. Three groups of N_h are shown: N_h = 0, N_h = 1-5, and $N_h \geq 6$.

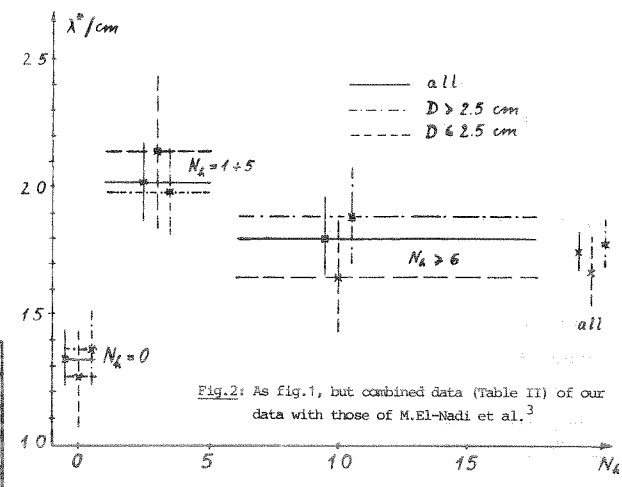


Fig.2: As fig.1, but combined data (Table II) of our data with those of M.El-Nadi et al.[3]

Table I: mfp λ^* of secondary α's (see fig.1 and legend there)

D/cm	N_h = 0			N_h = 1-5			$N_h \geq 6$		
	$\lambda^* \pm \Delta\lambda^*$	N	%	$\lambda^* \pm \Delta\lambda^*$	N	%	$\lambda^* \pm \Delta\lambda^*$	N	%
D≤2.5	12.8(3.6)	13	34	15.6(2.9)	29	32	18.6(3.6)	27	37
D>2.5	15.9(3.2)	25	66	21.8(2.8)	61	68	22.8(3.4)	46	63
all	14.8(2.4)	38	100	19.8(2.1)	90	100	21.2(2.5)	73	100

Table II: mfp λ^* of secondary α's (see fig.2 and legend there) data combined with those of M.El-Nadi et al[3].
$F_1 = \lambda^*(N_h=0)/\lambda^*(N_h=1\text{-}5)$.

D/cm	N_h = 0			N_h = 1-5			$N_h \geq 6$			$P(F_1)$
	$\lambda^* \pm \Delta\lambda^*$	N	%	$\lambda^* \pm \Delta\lambda^*$	N	%	$\lambda^* \pm \Delta\lambda^*$	N	%	
≤2.5	12.6(1.8)	49	37	21.4(3.0)	50	26	16.5(2.2)	54	35	.004₂
>2.5	13.7(1.5)	85	63	19.8(1.7)	143	74	18.9(1.9)	100	65	.004₃
all	13.3(1.1)	134	100	20.2(1.5)	193	100	18.1(1.5)	154	100	.0001₇

1. E.Friedlander et al., Phys.Rev. C 27,(1983), 1489 an references therein.
2. E.Ganssauge et al., GSI-82-ISSN 0174-081
3. Proc.of VI. High Energy Heavy Ion Study and Second Workshop on Anomalons, Berkeley, June 28-July 1,1983 LBL-16281, dec.1983, p.43 and D.Ghosh et al., Proc. of VI. High Energy Physics Symposium Mysore, India, 6.-11.Dec.1982, (Bombay, India, Dept.Atomic Energy 1982) p.140

B

Is there an energy dependence in the anomalon effect at charge two?

F.Killinger, E.Ganßauge, U.Bieschke, H.Kallies, N.Klein,
R.Kretschmer, A.Laschek and W.Weidner
FB Physik, Philipps-University, D-3550 Marburg, West-Germany

At projectile fragments of charge two the reaction mfp λ^* seems to be shorter for a few centimeters after the emission from the primary star than further downstream. This socalled anomalon effect[1] seems to increase with decreasing energy of the projectile.

Unfortunately the statistic till now does not allow to claim for a real effect, but the hint should be taken seriously, because it possibly could contain an explanation for why the anomalon effect which was established for charges $Z \geq 3$ with high statistic was for a long time not confirmed at charge two[2]. Our target was an emulsion stack irradiated with a ^{56}Fe beam of around 1.9 AGeV at the Berkeley Bevalac. By scanning along the track till the very end of the stack (potential path length 25 cm) we were able in a limited sample of λ^*-values (N=250) belonging to the first generation ("Secondaries") to make energy cuts. Fig.1 and Table I show the λ^*-distribution as a function of X_{0R}, the point where the projectile fragment originates. X_{0R} is directly connected with the energy of the fragment as E_o=1.88 AGeV corresponds to X_{0R}=0, while fragments with an energy E_o=1.4 GeV start at X_{0R}=7cm. The data have changed a bit since our first publication[3], but the effect has not changed: By inspecting Table I we see: from left to right, i.e. with the distance D from the emission point, in each energy group the mfp λ^* increases. Another tendency is seen: λ^* decreases with the distance from the starting point, i.e. with decreasing energy of the α projectile, but only in the first column! How to compare this result with the Null-results of B.Judek and P.L.Jain? B.Judek has used a long emulsion stack and followed the tracks for a rather long way. But her primary beam was oxygen which, corresponding to Bethe-Bloch, does not loos very much energy during its path trough the emulsion. Therefore she was every time above E_o~1.6 AGeV. Jain, on the other hand, was using a "short stack", irradiated with ^{40}Ar and ^{56}Fe of 2 AGeV. Again the decrease of energy is not enough for a possible threshold value of ~1.6 AGeV to be seen.

From Table II we recognize that there is also in our data no effect to be identified if we examin only the energy interval what was measured by Judek and Jain. In Table III there is shown the comparision of their data with each other and with ours. The corresponding F-test for $F=\lambda_{E>}/\lambda_{E<}$ at D≤3 cm results in a probability of P(F)=0.08%.

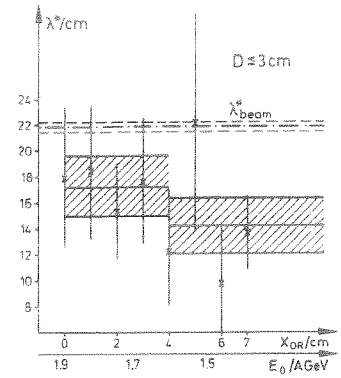


Fig.1: mfp of secondary α's as function of the energy E_o of their parent stars as it corresponds to X_{0R} (Table I, D ≤ 3 cm)
The broken line gives the value of the primary H_e-beam: λ^*_{beam} = 21.8 ± 0.5 cm
The shaded areas correspond to the differential distribution as given in Table II.

Table I: mfp of secondary α's as function of the energy E_o of their parent stars (see fig.1), integral distribution. $F_1 \equiv \lambda^*(D \leq 3cm)/\lambda^*(D>3cm)$

X_{0R}/cm	E_o/AGeV	D ≤ 3 cm		D > 3 cm		all D		P(F_1)/%
		$\lambda^* \pm \Delta\lambda^*$	N	$\lambda^* \pm \Delta\lambda^*$	N	$\lambda^* \pm \Delta\lambda^*$	N	
0	< 1.88	15.8(1.6)	100	22.7(1.9)	150	19.9(1.3)	250	0.3
1	< 1.81	15.5(1.6)	89	23.1(2.1)	125	19.9(1.4)	214	0.2
2	< 1.74	15.0(1.7)	77	21.5(2.1)	101	18.7(1.4)	178	1.1
3	< 1.68	15.0(1.9)	60	24.4(3.0)	68	20.0(1.8)	128	0.3
4	< 1.61	14.2(2.1)	47	22.6(3.3)	47	18.4(1.9)	94	1.3
5	< 1.54	14.7(2.4)	37	22.5(3.9)	33	18.4(2.2)	70	3.8
6	< 1.47	13.0(2.4)	30	36.4(9.7)	14	20.4(3.1)	44	0.04
7	< 1.41	13.7(2.7)	25	35.7(10.3)	12	20.8(3.4)	37	0.2

Table III: Comparision of our data with those of B.Judek and P.L.Jain et al.[2]

	D ≤ 3 cm		D > 3 cm	
	$\lambda^* \pm \Delta\lambda^*$	N	$\lambda^* \pm \Delta\lambda^*$	N
B.Judek	20.54(1.33)	240	20.13(0.74)	736
P.L.Jain	19.5 (1.0)	380	20.3 (1.2)	286
this work	17.2 (2.4)	53	22.7 (2.2)	103
total 1.6 E_o 2.1	19.7 (0.8)	673	20.4 (0.6)	1125
this work < 1.6AGeV	14.2 (2.1)	47	22.6 (3.3)	47

Table II: mfp of secondary α's like Table I, but differentially distributed

X_{0R}/cm	E_0/AGeV	D ≤ 3 cm		D > 3 cm	
		$\lambda^* \pm \Delta\lambda^*$	N	$\lambda^* \pm \Delta\lambda^*$	N
0-4	1.9-1.6	17.2(2.4)	53	22.7(2.2)	103
>4	<1.6	14.2(2.1)	47	22.6(3.3)	47

1. E.Friedlander et al., Phys.Rev.Lett 48(1980),1048
2. B.Judek 1977m NRC-report and P.L.Jain et al., Phys.Rev. C 25 (1982),3216
3. Sixth High Energy Heavy Ion Study And Second Workshop on Anomalons, Lawrence Berkeley Lab., June 28-July 1,1983, LBL-16281, Dec.83, p.65

Search for quasimolecular γ transitions in the $^{12}C + ^{12}C$ system at E_{CM} = 14.6 MeV

B,G

G. Koch, R.D. Fischer, W. Kühn, V. Metag, R. Mühlhans, R. Novotny, H. Ströher,
II. Physikalisches Institut, Universität Gießen
H.J. Hennrich, Max-Planck-Institut für Kernphysik, Heidelberg
D. Habs, R. Kroth, D. Schwalm, Physikalisches Institut, Universität Heidelberg
A. Lazzarini, University of Washington, Seattle, USA
R.S. Simon, GSI Darmstadt

The pronounced structures observed in $^{12}C + ^{12}C$ scattering above the Coulomb barrier are frequently interpreted in terms of a dinuclear system where two touching ^{12}C nuclei form a rather longlived molecular complex. The picture of a highly deformed intermediate system is supported by the experimental resonance energies which, as a function of spin, appear to follow the I(I + 1) pattern of rotational bands. An important test of this hypothesis is a search for the collectively enhanced γ transitions expected in these bands.

In a recent experiment[1] using the Darmstadt-Heidelberg crystal ball the γ branching ratio for the decay of the $I = 14^+$ resonance at E_{CM} = 25.7 MeV has been found to be $(6 \pm 3) \times 10^{-7}$. This value is more than an order of magnitude smaller than expected from a rigidly rotating dinuclear configuration and suggests that the particular 14^+ resonance investigated is probably a shape resonance rather than a molecular state. Experimental evidence indicates[2] that lower lying resonances exhibit a relatively larger ^{12}C width and hence probably have a simpler, quasimolecular structure. Therefore we have repeated the experiment for the 10^+ resonance at E_{CM} = 14.6 MeV.

In the experiment the scattered ^{12}C nuclei were detected in two position-sensitive ΔE-E telescopes which were mounted in the inner free space of the crystal ball, while γ rays from the excited ^{12}C nuclei as well as the possible γ decay of the molecular resonance could be observed in the individual NaI segments of the ball with close to 4π geometry. Event by event we thus establish the two-body kinematics of the collision and at the same time obtain a rather complete picture of the γ decay, since we measure the total γ-energy deposited, the energies of the individual quanta, their multiplicity and their angular distribution. By adding the pulse heights of neighbouring detector elements we have efficiencies of 70-80% for observing a high-energy γ quantum of 2-4 MeV in the upper quarter of the pulse-height distribution.

A total of 6.35×10^5 $^{12}C - ^{12}C$, γ-events have been analyzed so far. Fig. 1 shows the energy of the most energetic γ quantum per event versus the Q value of the reaction as determined from the particle kinematics. Also shown is the corresponding Q value spectrum. The spectrum is dominated by single and double inelastic ^{12}C scattering which results in one or two coincident γ rays of 4.4 MeV. Starting from the 10^+ resonance at 14.6 MeV the expected rotational γ transitions to the possible 8^+ molecular states at 12.1, 11.7, 11.4 and 11.0 MeV have transition energies between 2.5 and 3.6 MeV. The corresponding region in Fig. 1 with both ^{12}C nuclei in the ground state is indicated. No events are observed.

To give an upper limit for the γ width of the resonance we have determined the ratio of elastic to single inelastic scattering for our particle detector geometry and find that the elastic scattering is 6.3 times stronger. Using this result, one event in the quasimolecular window of Fig. 1 would correspond to a branching ratio $(\Gamma_\gamma/\Gamma_{tot})_{10^+} \approx 3 \times 10^{-7}$, which has to be compared to a theoretically expected value of $\approx 1 \times 10^{-6}$. Final conclusions have to await a more detailed analysis of the data.

1) V. Metag et al., Nucl. Phys. A409 (1983) 331c
2) W. Treu et al., Phys. Rev. C28 (1983) 237

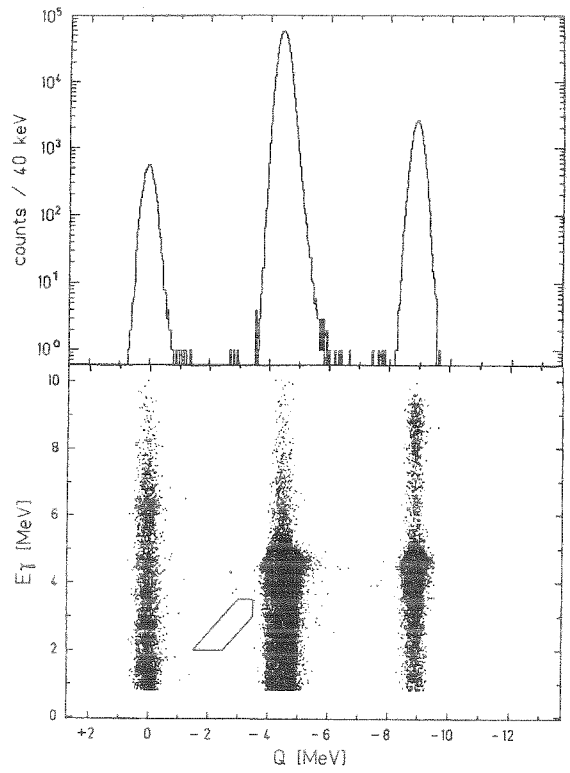


Fig. 1 Bottom: Energy of the most energetic γ quantum per event vs. the reaction Q value for $^{12}C + ^{12}C$ at E_{CM} = 14.6 MeV. The scatter plot corresponds to 6.35×10^5 events. The polygon indicates the region for possible quasimolecular γ rays deexciting the 10^+ resonance followed by elastic decay of the 8^+ structure.
Top: Q value spectrum showing single and double inelastic events as well as the random contribution of elastic scattering (Q = 0).

Double γ Decay in ^{40}Ca

R. Kroth, D. Habs, N. Kwong, J. Schirmer, D. Schwalm, M. Zirnbauer,
Max-Planck-Institut für Kernphysik und Physikalisches Institut der Universität Heidelberg
C. Broude, Weizmann Institute of Science, Rehovot, Israel

An excited nuclear level usually decays by the emission of a single γ-ray, a conversion electron or an e^+e^- pair. In a very rare second-order process the nucleus can emit simultaneously two γ-rays with variable energy, where the sum of both γ-ray energies adds up to the energy difference of the two nuclear levels. This double γ-decay was studied[1] with the Darmstadt-Heidelberg crystal ball for the first excited 0^+ level of ^{90}Zr. We report here on a recent measurement of the 2γ-decay of the 3.35 MeV 0^+ level in ^{40}Ca, which dominantly decays by e^+e^- pairs with a half-life of 2.1 ns. Earlier experiments[2] suffered from target contaminations and background from positron annihilation in flight (PAF).

We bombarded a 99.98% metallic ^{40}Ca target with a pulsed beam of 5.83 MeV protons to populate the 0^+_2 state. We measured the inelastically scattered protons with four SiLi detectors in delayed coincidence with the crystal ball; the requirement that two γ-rays occur simultaneously more than 1.6 ns after the prompt peak completely suppressed contributions from target contaminations.

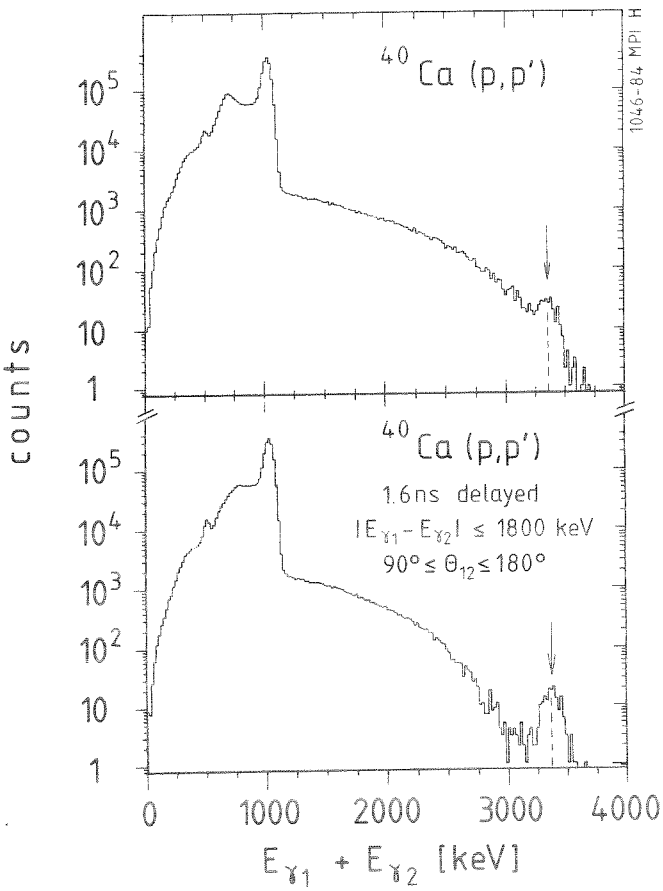


Fig. 1. a+b: 2γ sum energy spectrum of the 3.35 MeV 0^+ level of ^{40}Ca. In Fig. 1b the γ-rays from positron annihilation in flight are reduced by limiting the relative angle and the energy difference.

Fig. 1 shows the total γ-ray energy for the 0^+_2 decay. Both spectra show a strong line at 1022 keV, corresponding to positron annihilation at rest, and a broad shoulder extending up to 3.35 MeV, where the sum energy peak of the double γ-decay is expected. This shoulder is due to PAF. By special gating conditions, using the kinematic relation between the energies $E_{\gamma1}$, $E_{\gamma2}$ and the relative angle Θ_{12}, this background can be suppressed and a clean sum energy peak emerges (Fig. 1b).

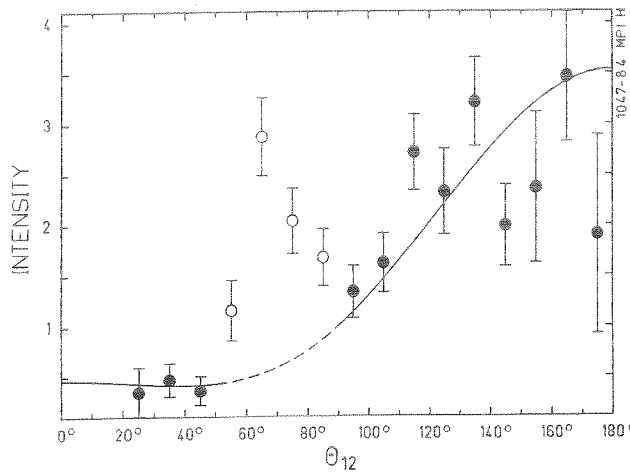


Fig. 2: 2γ angular correlation showing a strong asymmetry around 90° due to an interference between 2E1 and 2M1 transitions.

The angular correlation of the two γ-rays shown in Fig. 2 is asymmetric around 90°; thus as in ^{90}Zr[1] an interference between 2E1 and 2M1 occurs. The correlation $W_{\gamma\gamma}(E_{\gamma1},E_{\gamma2},\Theta_{12})$ is parametrized by

$$W_{\gamma\gamma}(E_{\gamma1},E_{\gamma2},\Theta_{12}) \propto E^3_{\gamma1}E^3_{\gamma2}\,|\langle 2M1\rangle^2 + \langle 2E1\rangle^2 + 4\langle 2M1\rangle\langle 2E1\rangle\cos\Theta_{12} + (\langle 2M1\rangle^2 + \langle 2E1\rangle^2)\cos^2\Theta_{12}|$$

with two real matrix elements <2M1> and <2E1>. We obtained the solid curve (Fig. 2) as a best fit to the angular correlation (excluding the region contaminated by PAF) and determined the ratio of the two matrix elements to be $\langle 2M1\rangle/\langle 2E1\rangle = -2.2\pm0.4$. From the study of the linear polarisation of the two γ-rays the other possible solution ($\langle 2E1\rangle/\langle 2M1\rangle = -2.2$) could be excluded. Besides this ratio of the two matrix elements the total branching ratio was determined to be

$$\frac{\Gamma_{2\gamma}}{\Gamma_{E_0}+\Gamma_{e^+e^-}} = (4.5\pm1.0)\cdot10^{-4}$$

The measured <2E1> and <2M1> matrix elements are discussed in ref. 3.

1) Jahresbericht MPI H (1983).
2) E. Beadsworth et al. Phys.Rev.C 8 (1973) 216.
3) GSI Annual Report (1983).

Double γ decay

D. Habs, R. Kroth, N. Kwong, J. Schirmer, D. Schwalm, M. Zirnbauer
Max-Planck-Institut für Kernphysik und Physikalisches Institut der Universität Heidelberg
C. Broude, Weizmann Institute of Science, Rehovot, Israel

With the crystal ball the two γ decay[1] of the first excited 0^+-level of ^{90}Zr and ^{40}Ca has been measured. In both cases a strong interference between a double E1 and double M1 transition is observed. A detailed theoretical treatment of this interference is given by Grechukhin[2]. We used the following definition for the reduced 2γ matrix elements:

$$<2\sigma\lambda> = (-1)^{1+\lambda(\sigma)} \cdot \sum_{\nu=1,2} \sum_{n_\nu} \frac{<0_1||\hat{n}^{\lambda-\lambda(\sigma)}\mathcal{M}(\sigma\lambda)||\lambda,n_\nu><\lambda,n_\nu||\hat{n}^{\lambda-\lambda(\sigma)}\mathcal{M}(\sigma\lambda)||0_2>}{E_{exc} - E_{n\nu} - E_{\gamma\nu}}$$

with the usual[3] matrix elements $<||\mathcal{M}(\sigma\lambda)||>$, the excitation energy E_{exc} of the initial state, and intermediate states $|\lambda,n_\nu>$ with excitation energies $E_{n\nu}$. In our measurements we determined the ratio of the two matrix elements <2E1> and <2M1> and the absolute branching ratio for the 2γ decay. They are compiled in the following table:

	^{40}Ca	^{90}Zr
$\Gamma_\gamma/(\Gamma_{E0}+\Gamma_{e^+e^-})$	$(4.5 \pm 1.0) \times 10^{-4}$	$(1.8 \pm 0.3) \times 10^{-4}$
<2E1>/<2M1>	-0.45 ± 0.09	-1.9 ± 0.2

For $0^+ \to 0^+$ decays the different contributions to the 2E1 transition almost cancel[4]. This strong hindrance of the 2E1 transition allows the 2M1 transition, which is of typical single particle strength, to compete successfully, leading to the observed interference.

For the 2M1 transitions a rather quantitative understanding can be obtained. For both nuclei (^{90}Zr; ^{40}Ca) the dominant configurations contributing to the ground and first excited 0^+ state involve two orbitals, j_1 ($1g_{9/2}$; $1f_{7/2}$) and j_2 ($2p_{1/2}$; $1d_{3/2}$), which are partially occupied. To a good approximation the corresponding spin-orbit partner j_1' ($1g_{7/2}$; $1f_{5/2}$) is totally empty and j_2' ($2p_{3/2}$; $1d_{5/2}$) is totally occupied. The double M1 decay corresponds to spin-flip transitions $j_1 \to j_1' \to j_1$ and $j_2' \to j_2 \to j_2'$. Assuming this special shell model picture the 2M1 operator can be replaced by an effective one body operator and one obtains

$$<2M1> \approx 2 \cdot (E_{exc}/2 - E_{GMD})^{-1} \cdot \sum_{\mu=p,n} \left\{ \frac{1}{2j_1+1} |<j_{1\mu}'||\mathcal{M}(M1)||j_{1\mu}>|^2 <0_1^+|\hat{n}_{1\mu}|0_2^+> - \frac{1}{2j_2+1} |<j_{2\mu}||\mathcal{M}(M1)||j_{2\mu}'>|^2 <0_1^+|\hat{n}_{2\mu}|0_2^+> \right\}$$

approximating $E_{n\nu}$ by the average M1 giant resonance energy E_{GMD} and $E_{\gamma\nu}$ by $E_{exc}/2$. The two one body transitions densities $<0_1^+|\hat{n}_{i\mu}|0_2^+>$, which depend on the structure of the two 0^+ states, have been calculated[4] using a standard shell model code. Thus we can deduce the properties of the reduced M1 matrix elements $<j||\mathcal{M}(M1)||j'>$ from the measured <2M1> values. A reduction of the M1 strength is expected to result from the renormalization of the spin and orbital g-factors. As the effective orbital g factors $g_\ell^p = 1.12$ and $g_\ell^n = -0.03$ are well known, we can determine the quenching factor γ_s, being defined as the ratio between the effective g_s-factor and g_s^{bare} of the free nucleon. The quenching factors deduced from the two γ decay are shown in fig.1 and compared to the values determined from (e,e') and (p,p') measurements[5] by summing up the M1 strengths leading to all identified 1^+ states. Obviously, good agreement is obtained between these two methods.

1) Jahresbericht GSI 1983.
2) D.P. Grechukhin, Nucl. Phys. 62 (1965) 273.
3) D. Pelte and D. Schwalm, In-Beam Gamma-ray spectroscopy with Heav Ions, in Heavy Ion Collision, Vol. 3, p. 1, North Holland Pub. Comp. 1982.
4) D. Habs et al., Double γ decay, Ein Bokek, Israel 1984, annals of the israel phys. soc. (in press).
5) A. Richter, Magnetic dipole transitions and other elementary spin excitation modes in nuclei, Florence 1983.

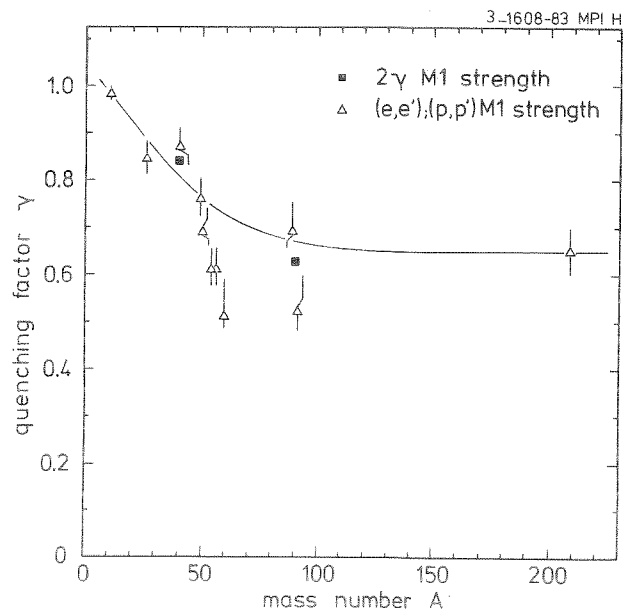


Fig. 1: Quenching factors of the spin g-factors deduced from 2γ decay and (e,e'), (p,p') measurement.

G

Gamma Decay of Giant Resonances Built on Excited Nuclear States

W. Hennerici, H.J. Hennrich, G. Himmele, R. Repnow, W. Wahl, Max-Planck-Institut für Kernphysik, Heidelberg
D. Habs, U. v. Helmolt, H.W. Heyng, R. Kroth, D. Schwalm, Physikalisches Institut, Universität Heidelberg
A. Lazzarini, University of Washington, Seattle, USA
V. Metag, II. Physikalisches Institut, Universität Gießen
R.S. Simon, GSI Darmstadt

Giant resonance transitions in the γ decay following HI-reactions offer the possibility of studying nuclear shapes and dynamics as functions of excitation energy and angular momentum. We have used the reactions $^{34}S + ^{128,130}Te$ to continue our investigation of the spin dependence of the giant dipole resonance in Er nuclei. The experiments were performed in the Darmstadt-Heidelberg NaI crystal ball as described previously[1]. However, several improvements were made to obtain data of better quality.

The first improvement is related to the energy calibration of the individual NaI segments. We used the ^{12}C (p,p'γ) reaction at 20 MeV, which gives γ lines of 4.44, 7.46, 12.71 and 15.11 MeV to establish the energy calibration well into the resonance region. Second, we obtained the response of the NaI segments to high-energy γ rays. In the ^{12}C (p,p'γ) calibration experiments we used the scattered protons to define the initial excitation of the ^{12}C nucleus. The γ ray spectra observed in coincidence with the 4.44 and 15.11 MeV state provide the corresponding γ ray lineshapes and absolute efficiencies. Computer fits then yield a general set of parameters to describe the detector response as a function of γ ray energy. Finally, we exploited the simultaneously observed neutron multiplicity in the crystal ball to separate the reactions leading to Er compound systems from background reactions with light target impurities (oxygen, carbon). The slow evaporation neutrons observed from the heavy systems are essentially absent in the latter reactions.

As an example, fig. 1 shows γ spectra observed in the reaction $^{34}S + ^{128}Te$ at 155 MeV. The spectra correspond to different γ ray multiplicities as characterized by the number N_γ of active detector elements which are prompt with respect to the beam pulse. Normalized to the average of each bin $\overline{N_\gamma}$ the spectra correspond to transitions per cascade if we neglect corrections due to double hits and efficiency loss as well as detector cross talk. Conversion of $\overline{N_\gamma}$ to spin gives the average I-values indicated in the figure.

The experimental spectra in fig. 1 are compared to results from CASCADE calculations[2]. Folded with the experimental γ response the theoretical distributions have been fitted to the experimental spectra for $E_\gamma >$ 7 MeV and yield the strengths S of the resonance transitions (relative to the energy-weighted sum rule), as well as the centroids E_R and the widths Γ.

For low spins E_R coincides with the position of the ground-state resonance observed in photo absorption. With increasing spin, however, there is a clear decrease of E_R. This spin dependence is much larger than expected from recent selfconsistent calculations[3]. A possible explanation is that the reaction mechanism might selectively populate the resonance mode perpendicular to the spin direction. This picture would agree with the observed angular distribution of the resonance transitions which shows an enhancement perpendicular to the beam ($W(0°)/W(90°) \sim 0.9$).

1) W. Hennerici et al., Nucl.Phys. A396 (1983) 329c
2) F. Pühlhofer, Nucl.Phys. A280 (1977) 267 and private communication
3) P. Ring, L.M. Robledo, J.L. Egido and M. Faber, to be published

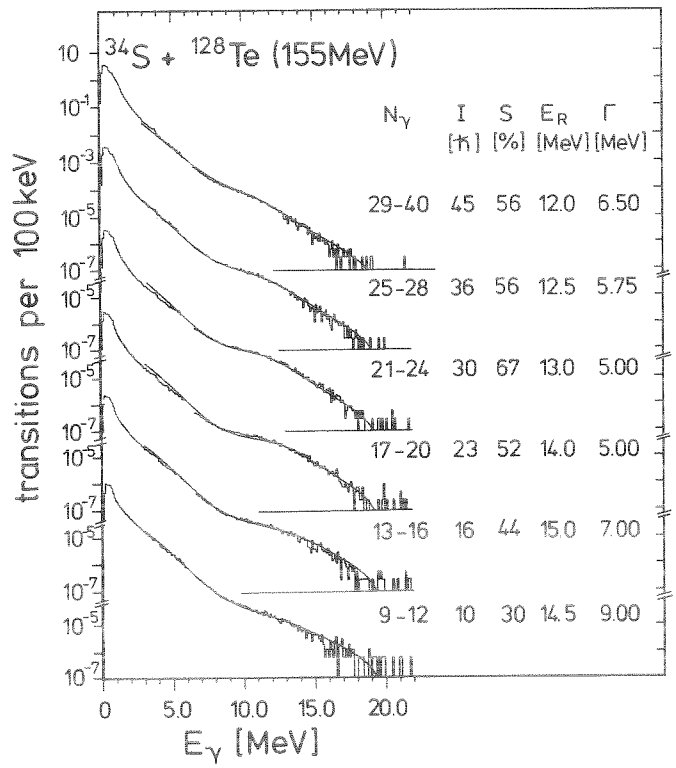


Fig. 1: γ ray spectra from the reaction 155 MeV $^{34}S + ^{128}Te$. The spectra correspond to different multiplicities N_γ of active detector modules and hence different spins; they are normalized to transitions per cascade. Indicated by the solid lines are results from CASCADE calculations where the strength S, the position E_R and the width Γ of the giant resonance have been adjusted to fit the experimental distributions for $E_\gamma \gtrsim 7$ MeV. The theoretical spectra are folded with the experimental detector response.

Measurement of Magnetic Moments in ^{156}Dy G

G. Seiler-Clark, D. Pelte, D. Schwalm, Univ. Heidelberg
H. Emling, H. Grein, E. Grosse, R. Kulessa+, C. Michel*, H.J. Wollersheim, GSI
M. Hass, Weizmann Institute, Rehovot, Israel
G.J. Kumbartzki, K.-H. Speidel, Univ. Bonn

Magnetic Moments are sensitive probes for the various alignment effects occuring in in fast rotating nuclei under the influence of the Coriolis force. As the magnetic properties of protons and neutrons are quite different a measurement of g- factors of high spin states should provide detailed information about the underlying single particle structure. In the present experiment an attempt was made to measure particularly the g- factor of the $I^{\pi} = 14^{+}_{s}$ yrare state in ^{156}Dy believed to belong to the $(\nu i_{13/2})^2$- rotation aligned s- band; from the experiment we moreover expect to obtain information about the average g- factor of higher spin states as well as individual g- factors for the low spin states in the ground state band.

As yrare states in the s- band can only be populated in (HI,xn)- reactions, the reaction ^{25}Mg(^{136}Xe,5n)^{156}Dy at 4.7 MeV/u bombarding energy was employed in the present experiment. Due to the short lifetimes of the levels of interest extremely high magnetic fields are needed to produce Larmor precession effects which are measurable via perturbed angular distributions. We therefore utilized transient magnetic fields in iron which in our case amount up to ≈ 3.6 kTesla[1]. The feeding problem inherent in (HI,xn)- reactions due to the complex deexcitation process of the nuclei produced is overcome by combining Doppler shift methods with the transient field technique in a recoil distance plunger set- up. The method is feasible if the feeding pattern as well as the decay times are known in detail;this is in fact true in the present case.[2]

The plunger set- up essentially consisted of a 0.8 mg/cm² Mg target foil and a stopper made up from a 7.4 mg/cm² annealed stretched iron foil with a thick copper backing. The target was additionally backed by a 1.8 mg/cm² Pb layer in order to slow down the Xe projectiles to below the Coulomb barrier for Xe impinging on Fe. The iron foil was polarized by an external magnetic field B= .03 T which was periodically reversed during the experiment. The compound nuclei emerged from the Pb backing at recoil velocities v ≈ .074c and traversed the recoil distances between target and iron foil appropriately chosen in order to maximise the population of particular states of interest. As the lifetime of the 14^{+}_{s}- state is 7.6ps and its effective feeding time is ≈ 2ps we chose recoil times t_r between 3.6 and 11.3 ps. After passing the iron foil within the transit time of ≈ 1 ps, during which the nuclear states precess due to the transient magnetic field, the nuclei finally come to rest in the field free environment of the copper backing.

The γ- angular distributions were detected in an array of six Ge- detectors positioned in a plane perpendicular to the field direction at angles of 180°, 110°, ±55° and ±135° and precession effects were derived from counting rates in coincidence with field directions 'up' and 'down'. The precession effects are shown in terms of the up/down counting rate double ratios R (defined in ref. 3) in fig. 1. The effect observed for transitions within the ground band (4^{+}-2^{+}, 6^{+}-4^{+}, (a)) amounts to only about half of what is expected knowing the transient field strength[1] and assuming constant collective g- factors g_c ≈ .35. This can be understood because for the longer recoil times deorientation effects decrease the anisotropy of the angular distribution patterns (for details cf. ref.3) whereas at lower distances the data are predominantly sensitive to precessions of high spin s- band states where the indicated reduction of g- factors is consistent with an aligned neutron configuration. For the 14^{+}_{s} state (b) we observe about the same precession at small recoil times as for the g- band states; in both cases the same high spin region is probed. With increasing time of flight, however, the precession effect for the 14^{+}_{s} decreases as the sensitivity to the g- factor of this level rises; for t_r =11.3ps the precession effects are close to zero with almost exclusive sensitivity to $g(14^{+}_{s})$. This suggests a strongly reduced g- factor being in accordance with a $(\nu i_{13/2})^2$ rotation aligned configuration of this level.

A quantitative analysis treating both the complex time dependence of the deexcitation and the deorientation effects consistently is currently in progress.

+ Permanent address: Institute of Physics, Jagiellonian University, Krakow, Poland

* Present address: Institute de Physique, Louvain- la-Neuve, Belgium

1. H.R. Andrews et al., Nucl. Phys. A383 (1982) 509
2. H. Emling et al., Nucl. Phys. A, in print
3. G. Seiler-Clark et al., Nucl. Phys. A399 (1983) 211

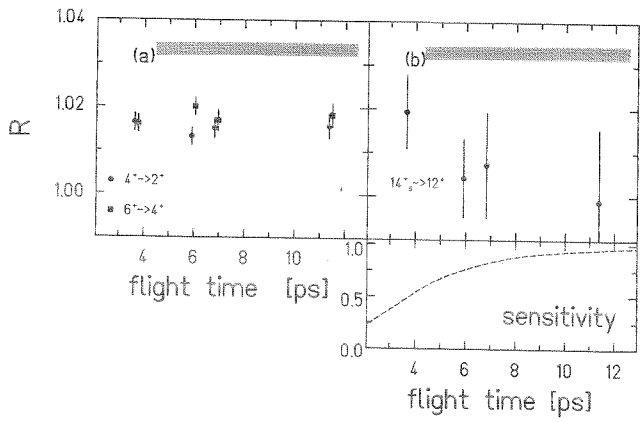


Fig.1: Precession effects for the 4^{+}-2^{+} and 6^{+}-4^{+} (a) and the 14^{+}_{s}-12^{+} transitions (b), where the sensitivity of the effects on the g- factor of the 14^{+}_{s} state is indicated. The hatched regions mark the size of the effect expected for constant collective g- factors neglecting deorientation.

Transfer and Simultaneous Coulomb Excitation in Heavy Ion Collisions

Ch. Lauterbach[2], F. Azgui[1], J. Barette[6], C.R. Bingham[3], H. Emling,[1], E. Grosse[1], M.W. Guidry[3], G. Seiler-Clark[4], W. Spreng[1], J. Stachel[5], H.J. Wollersheim[1]
[1]GSI Darmstadt, [2]LMU München, [3]UT Knoxville,
[4]Univ. Heidelberg, [5]Univ. Mainz, [6]CEN Saclay

Heavy ion induced fusion and Coulomb excitation are the standard tools used in gamma-spectroscopy studies of nuclear rotational states. However, it was recently demonstrated that yrast states of rare earth isotopes with spin up to ~ 10 h are also populated in transfer reactions at bombarding energies close to the Coulomb barrier and at particle scattering angles close to the grazing angle[1].

In principle, these findings may be understood as a transfer of nucleons associated with simultaneous Coulomb excitation in the entrance - and/or exit channels. This reaction mechanism has some intriguing aspects: (i) it allows to study high spin states in unstable neutron rich isotopes to which neither fusion nor Coulomb excitation gives access, (ii) transfer between high spin nucleon orbits might provide new nuclear structure information and (iii) the form factor of the correlated pair transfer may be used to determine the spin dependence of the pairing gap[2].

In a first attempt we studied the one-neutron transfer in the reaction of ^{161}Dy on ^{208}Pb at a bombarding energy of 5.3 MeV/u. The backscattered projectile like ions (Dy) were detected in a position sensitive avalanche ring counter at laboratory angles of $110 \leq \vartheta \leq 168°$ and $0° \leq \phi \leq 360°$. Gamma-ray spectra were recorded in coincidence with the particles in four Ge detectors positioned at angles of 0°, ± 116° and 180° with respect to the beam. The setup was essentially identical to the one used in Coulomb excitation experiments as described in ref. 3. A Doppler corrected spectrum obtained from the 0° Ge detector is shown in fig. 1.

Aside from the inelastic scattering we observed the one neutron stripping and pick up reactions. While the target ^{161}Dy is Coulomb excited up to spin $I^{\pi} = 41/2^{+}$, in the transfer channels we observe yrast states up to $I^{\pi} = 10^{+}$ and $I^{\pi} = 14^{+}$ of the ^{160}Dy and ^{162}Dy residual nuclei, respectively. The relative cross sections amount to about 4(1)% and 12(2)% of the cross section for Coulomb excitation of the state with equivalent core angular momentum, respectively; these ratios are almost independent of the spin of the excited state. It seems worth mentioning that in similar studies at other laboratories with lighter ions, i.e. in S, Ni and Xe induced one nucleon transfer reactions on rare earth isotopes, states with nearly as high spins were reached as in our study with Pb ions. This seems to indicate that at least in the one nucleon transfer, Coulomb excitation contributes only a small fraction to the spin observed in the residues.

This is in qualitative agreement to semiclassical considerations, as well as PWBA-calculations using the Code PTOLOMY[4] which indicate enhanced cross sections for the transfer of neutrons from and to orbits of high angular momentum which may couple to a rather large transferred spin.

In future experiments we plan to investigate the two-neutron-transfer reactions, which are expected[2] to proceed with transferred angular momentum zero. Therefore, in contrast to the one-neutron transfer, spin excitations are solely due to Coulomb excitation and the advantages of heavy ion beams (^{208}Pb) are obvious.

1 M.W. Guidry et al.
2 Landowne, Dasso, Broglia et al., preprint
3 S. Brüssermann et al., GSI Scient.Rep. 1982,p.46
4 S. Piper et al., private comm.

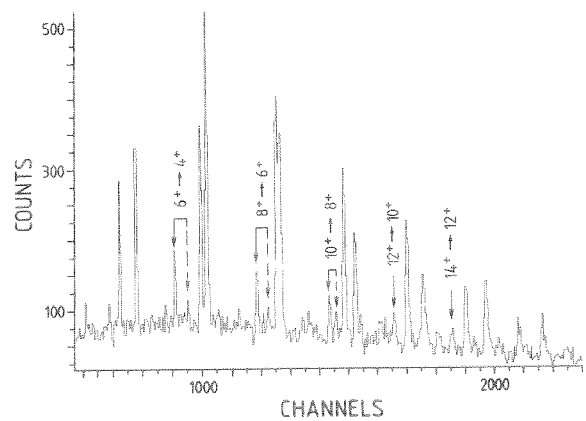


Fig. 1.
Particle-γ-coincidence spectrum obtained from the reaction ^{161}Dy on ^{208}Pb at 5.3 MeV/u bombarding energy. The bold arrows indicate transitions in ^{162}Dy, the dashed arrows transitions in ^{160}Dy. The prominent lines in the spectrum are due to inelastic scattering on the ^{161}Dy target.

Search for Shape Transitions in ^{156}Er

F. Azgui, H. Emling, W. Spreng, H.J. Wollersheim (GSI Darmstadt),
R. Kulessa (Univ. Krakow), T. Byrski, F.A. Beck, G.J. Costa, B. Haas,
C. Gehringer, J.C. Merdinger and J.P. Vivien (CRN Strasbourg)

The nuclear structure of prolate deformed isotopes in the vicinity of the yrast line is characterized by a competition of collective nuclear motion (perpendicular to the symmetry axis) and single particle alignment. As shown earlier[1], in ^{156}Er the successive alignment of $i_{13/2}$ neutron and $h_{11/2}$ proton quasiparticle pairs (q.p.) at yrast spins up to $I^{\pi}=32^{+}\hbar$ contributes about 50% of the total spin. As the aligning q.p. move in oblate orbitals with respect to the prolate core, major modifications of the nuclear shape are expected: theoretical calculations[2] based on the cranking model predict a transition from a prolate deformation ($\beta \approx 0.2$, $\gamma = 0^{o}$) towards an oblate shape ($\beta \approx 0.1$, $\gamma = 60^{o}$) at spins around 30 h. First indications for a prolate to oblate shape transition were found in the isotone $^{154}Dy_{88}$: a rather irregular behaviour of the yrast line above spin 30 and, moreover, unusually long feeding components ($\tau_F \approx 10ps$) into high spin states were observed (see ref.3).

The aim of this experiment was to verify the predicted shape transition in ^{156}Er via the measurement the of lifetimes and feeding times of high spin states. The measurement was performed at the Tandem accelerator at Strasbourg using the ^{123}Sb (^{37}Cl, 4n) reaction, while the recoil distance technique was utilized to determine the time structure of the population and deexcitation of the yrast levels. Spectra of discrete γ-rays were detected in a Ge detector at an angle of 0° relative to the beam, from which decay curves could be deduced up to the $I^{\pi}=32^{+}$ state. In order to localize the critical spin at which the expected shape transition occurs, data were taken at two bombarding energies E = 166 and 158 MeV and furthermore, the Ge-detector was operated in coincidence with a 4π NaI sum-spectrometer thus probing a wide region of entry spin states. A new recoil distance plunger device was developed that allowed to place target and plunger (10 mgr/cm^2 Au-foil) at the centre of the sum-spectrometer and to control the distance between target and plunger automatically. A high positioning accuracy (better than 1µm) was provided by three independently operated piezoelectric "Inchworm" translators, where the positioning was controlled by an optical fringe counting system and independently by a capacitance measurement. Details of the apparatus are described elsewhere in this report.

In Fig.1 we show the setup; fig.2 displays the high spin part of the spectra measured with the Ge detector at two target-plunger distances of 10µm and 5000 µm. These spectra were taken with gates on a high total γ-energy, thus suppressing contributions from reaction channels other than the 4n reaction.

The analysis showed that long lived feeding components - indicative of the shape transition - appear in the decay curves of the high spin states and that their relative intensities depend on the bombarding energy. Further analysis of these components investigating their dependence on the total γ-energy at the two bombarding energies, should allow to localize the critical spin.

1 T. Byrski et al., Phys. Lett. 102B, 235 (1981)
2 S. Aberg, Proc. Varenna Summer School, p.473, 1976
3 F. Azgui et al., GSI Scientific Report, p.50, 1982

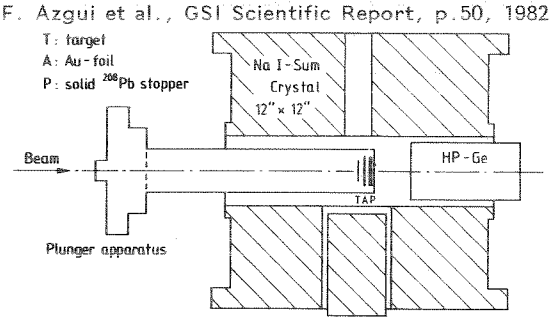


Fig.1 Experimental Set-up

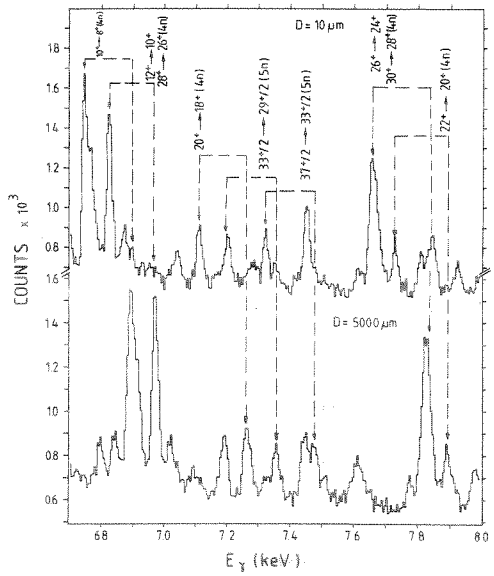


Fig.2 γ-spectra obtained for two target plunger distances of 10 and 5000 µm in coincidence with a high total γ energy

The γ-soft Triaxial Nucleus ^{196}Pt [B]

A. Mauthofer, H. Ower, K. Stelzer, Th. W. Elze, J. Idzko
Institut für Kernphysik der Universität Frankfurt am Main
H.J. Wollersheim, H. Emling, E. Grosse, P. Fuchs und D. Schwalm
GSI Darmstadt

The analysis of the Coulomb excitation experiments on the nucleus ^{196}Pt with a 4.8 MeV/u ^{208}Pb beam [1,2] has been completed. Electromagnetic transition probabilities up to the $(8^+ \rightarrow 6^+)$ transition in the ground state (gs) band and $(6^+ \rightarrow 4^+)$ transition in the γ-band as well as several interband transition moments and static moments were determined by a comparison of the experimental and calculated γ-yields over a large range of scattering angles ($64^\circ \leq \theta_{cm} \leq 150^\circ$). This rather complete set of E2-matrixelements (ME's) gives strong evidence for a γ-soft triaxial potential at moderate excitation energies in ^{196}Pt.

The analysis employed the procedure described elsewhere in this report [3]; the deorientation effect was taken into account [2]. Extensive investigations were performed in order to study the influences due to different sidebands, relative phases of ME's, M1-admixtures or E1, E2 and E4 transition moments. In the fits all ME's relevant for transitions observed in the experiment were varied individually. For the ME's of transitions not observed in the experiment, different sets obtained from theoretical models, i.e. the asymmetric rotor model (ARM) [4] with γ=28°, 30°, 32°, the generalized collective model (GCM) [5] and the interacting boson approximation (IBA-2) [6] - were used. Their influences on the deduced ME's (see above) were included in the error analysis. Representative results for ^{196}Pt are illustrated in fig. 1-3.

The deduced ME's were compared with the ARM, the GCM and the IBA-2 model. The parameters used in the GCM correspond to potential surface with mean $\langle\gamma\rangle$ of approximately 30° with a tendency towards an oblate shape, while the IBA-2 parameters are close to the γ-unstable limit. As previously stated [1] the general trend of the gs-intraband E2-moments is reproduced in all models except in the IBA-2 which fails due to its inherent spin cut-off. Clear evidence for triaxiality comes from the static moments in the gs band where the ARM favours a mean $\langle\gamma\rangle$ of 32°(fig. 1). However, the assumption of a stiff triaxial nucleus cannot reproduce the ME's associated with the γ-band (see fig. 2 and 3). The overall best agreement with all 18 determined ME's is achieved in the GCM which reveals a γ-soft nuclear potential.

1 GSI Scientific Report 1978 p.45 and 1979 p.44
2 GSI Scientific Report 1982 p.55
3 H. Grein, GSI Scientific Report 1983
4 Yadav, priv. communication
5 P.O. Hess, priv. communication
6 J. Stachel, priv. communication

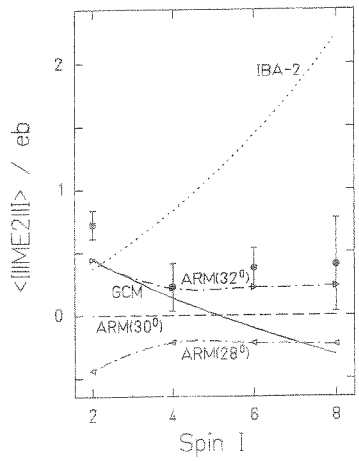


Fig.1 Diagonal Matrixelements of the ground state band

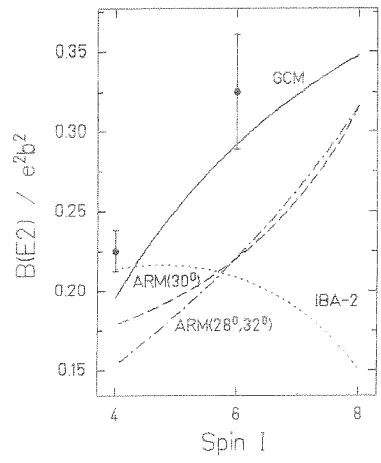


Fig.2 B(E2) for $I_\gamma \rightarrow I_g$

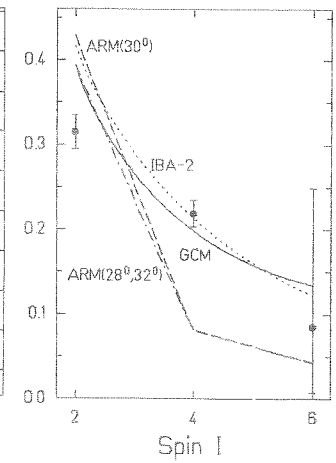


Fig.3 B(E2) for $I_\gamma \rightarrow I_\gamma$-2

Electromagnetic Properties of High Spin States in ^{242}Pu and ^{244}Pu

W. Spreng, F. Azgui, H. Emling, E. Grosse, R. Kulessa*, Ch. Michel, R.S. Simon, H.J. Wollersheim (GSI Darmstadt); M. Mutterer, J.P. Theobald (TH Darmstadt); D. Schwalm (Univ. Heidelberg); N. Trautmann (Univ. Mainz); M.S. Moore (Los Alamos SL)

Multiple Coulomb excitation by ^{208}Pb ions with 5.3 MeV/u has been used to populate high spin states in ^{242,244}Pu up to $I^{\pi}=26^{+}$ (ref. 1). From the de-excitation γ-ray yields observed with a particle-γ coincidence set-up at scattering angles $32^{0}\leq\theta_{CM}(Pb)\leq146^{0}$ the E2-transition moments within the ground state band could be determined in a nearly model independent way. Moreover, from the observation of the γ-radiation at two different angles, information about the pertubation of the γ-angular correlation due to the magnetic hyperfine field produced by the excited atoms could be obtained.

For transitions up to $I^{\pi}=14^{+}$ the time integrated de-orientation coefficients $G_2(\infty)$ have been determined from the measured attenuation of the γ-ray angular correlation (ref. 2). Using the Abragam and Pound model (ref. 3) as a phenomenological description, the attenuation coefficients were reproduced with a model parameter $\lambda_2=0.10\pm0.02$ for a velocity range of $5\%\leq v/c\leq7\%$. This value of λ_2 together with $\lambda_2/\lambda_4=0.3$ was used in the γ-decay calculations.

The E2-matrix elements between yrast states were obtained from a comparision between experimental γ-yields and a semiclassical calculation (ref. 4). For ^{244}Pu the experimental γ-yields normalized to the $10^{+}\rightarrow8^{+}$ transition are compared to the final fit in fig. 1. The B(E2)-values could be extracted with an acceptable accuracy up to $I^{\pi}=24^{+},22^{+}$ for ^{242}Pu and ^{244}Pu, respectively (fig. 2). In the case of ^{242}Pu a reasonable fit for the γ-yields of the line originally assigned to the $26^{+}\rightarrow24^{+}$ transition could only be achieved assuming this line to be a doublet of the $26^{+}\rightarrow24^{+}$ and $28^{+}\rightarrow26^{+}$ transition. This assumption could be verified in a γ-γ-coincidence measurement[5].

In both nuclei the deviations from the rigid rotor-prediction are smaller than 10%, at least below the onset of alignment around spin 22^{+}. This demonstrates that in the gsb the quadrupole deformation remains rather stable, as found also in the other well deformed actinides[6]. The observed increase of the moment of inertia below the backbend[1] can hence not be attributed to a shape change. Moreover, in the two Pu-isotopes effects of quasiparticle alignment on the level energies below spin 22^{+} are negligible, due to the sharpness of the backbending. Most likely the increasing moment of inertia reflects the reduction of the pairing force with increasing angular momentum.

*on leave from Krakow University

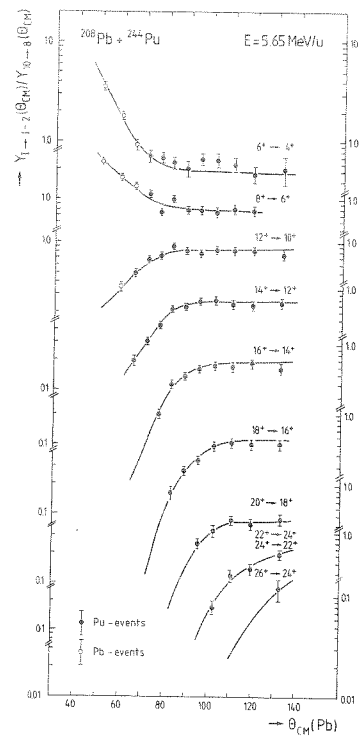


Fig. 1: Comparison of the experimental γ-yields with results from the semiclassical calculation using the B(E2)-values shown in fig. 2

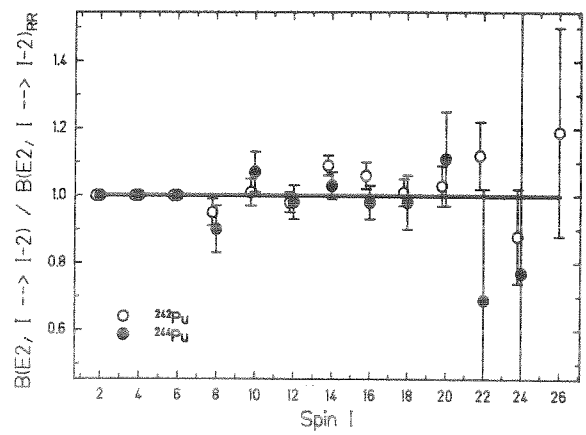


Fig. 2: Resulting B(E2)-values normalized to the rigid rotor model using $B(E2;0^{+}\rightarrow2^{+})_{RR}=13.6e^{2}b^{2}$

[1] W. Spreng et. al., Phys.Rev.Lett. 51(1983), 1522
[2] H.J. Wollersheim et. al., GSI Annual Report 1982, 53
[3] A. Abragam, R.V. Pound, Phys.Rev. 92(1953), 943
[4] H. Grein et.al., this report
[5] W. Spreng et. al., this report
[6] H. Ower et.al, Nucl. Phys. A388(1982), 421

γ-γ-Coincidence Measurement on ^{242}Pu

W. Spreng, F. Azgui, H. Emling, E. Grosse, Ch. Michel, R.S. Simon,
H.J. Wollersheim (GSI Darmstadt); M. Mutterer, J.P. Theobald (TH Darmstadt);
D. Schwalm, G. Seiler-Clark (Univ. Heidelberg); N. Trautmann (Univ. Manz);
M.S. Moore (Los Alamos SL)

Previously[1], we reported on multiple Coulomb excitation experiments of $^{242,244}Pu$ with ^{208}Pb ions. In both isotopes the ground state band (gsb) could be observed up to $I^{\pi}=26^{+}$, while in neighbouring nuclei, as ^{238}U (ref. 2) or ^{248}Cm (ref. 3) the gsb could be populated up to $I^{\pi}=30^{+}$. Because these nuclei have nearly the same B(E2)-values as the Pu isotopes, one would expect the same spin limit for all these nuclei. Obviously, in the Pu isotopes the identification of higher spins is hampered by the occurance of the backbending effect.

In order to extend the level scheme up to higher spins and to achieve unambigious level assignments in the backbending region we developed a highly efficient particle-γ-γ coincidence set-up (fig. 1). It consists of 8 Ge detectors positioned at 160° (Ge1-Ge4) and 40° (Ge5-Ge8) relative to the beam axis, subtending a solid angle of $(\Omega/4\pi)\approx 0.13$ in total. The particle detector[4] covered an angular range of $10^{\circ}\leq\theta_{Lab}\leq 20^{\circ}$, $0^{\circ}\leq\phi\leq 360^{\circ}$. The detection of the Pu ions at these low angles ensures a strong population of the high spin states. The detector was position sensitive in θ and φ, thus allowing to correct the measured γ-ray energies for the strong Doppler shifts.

A first measurement has been performed with ^{208}Pb ions of 5.3 MeV/u and a ^{242}Pu target. Preliminary γ-γ coincidence spectra with gates on different transitions are shown in fig. 2. Because the kinematical conditions did not allow to identify the particles, two peaks for each transition appear in the γ-ray spectrum (fig. 2a): one stems from the coincidence with a detected Pu ion and the other from coincidences with Pb ions. The latter event type is suppressed in the γ-γ coincidence spectra due to its low γ-multiplicity, and therefore the corresponding peaks almost dissapear in the spectra which are taken in coincidence with high spin states (fig. 2b-d).

From fig 2d it is clearly seen that the $26^{+}\rightarrow 24^{+}$ peak is coincident with another line of nearly the same energy, which is assigned to the $28^{+}\rightarrow 26^{+}$ transition. This interpretation is in agreement with the results from the B(E2)-analysis[5]. Thus backbending occurs not only in ^{244}Pu (ref. 1) but also in ^{242}Pu. From the fact, that it is present in both Pu-isotopes but not in the neighbouring elements with higher and smaller Z it seems to be evident that the $i_{(13/2)}$ proton shell is responsible for this behaviour (see also ref. 6).

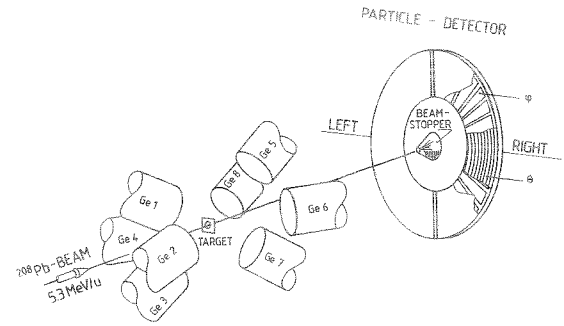


Fig 1: Schematic view of the experimental set-up

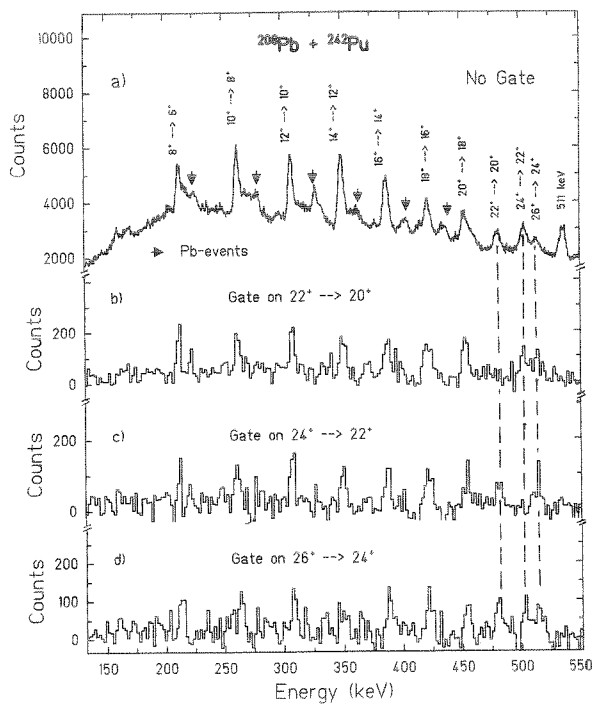


Fig 2: a) Sum of all γ-γ coincidences
b-d) Gate on one transition in each γ-detector; the coincident events in all the other detectors are summed up and the peak-background coincidences are subtracted

[1]W. Spreng et. al. , Phys. Rev. Lett. 51(1983), 1522
[2]E.Grosse et. al. , Physica scripta 24(1981), 337
[3]R.B. Piercey et. al., Phys. Rev. Lett. 46(1981),415
[4]R. Bock et. al., Nucl. Phys. A388(1982), 334
[5]W. Spreng et.al , this report
[6]J.L. Egido, P. Ring, to be published in Nucl. Phys.

Collinear Laser Spectroscopy of Fusion Produced $^{107-111}$Indium

G

G.Ulm, J.Eberz, G.Huber, H.Lochmann, R.Menges,
Institut für Physik, Universität Mainz
R.Kirchner, O.Klepper, T.U.Kühl, P.O.Larsson, D.Marx, D.Schardt,
GSI Darmstadt

The collinear fast beam laser apparatus[1], connected with the GSI on-line mass separator, has been used to measure the hyperfine structure (hfs) and isotope shift (IS) of the neutron-deficient isotopes $^{107-111}$In. High yields of 10^6 to 10^7 atoms/s of these isotopes were produced by Mo(O,pxn)In fusion reactions [2].

We studied the $5p\ ^2P_{3/2}$ - $6s\ ^2S_{1/2}$ optical transition (λ=451nm). From the hfs splittings the magnetic dipole moments and the electric spectroscopic quadrupole moments Q_S of the nuclei are evaluated by using the values of the stable isotope ^{115}In as a calibration[3] (Sternheimer correction factor of 0.87 applied). Fig.1 shows the moment values of the isotopes investigated in comparison with known moments[3-6]. For the magnetic moments excellent agreement is found. Concerning the quadrupole moments good agreement is seen for ^{109}In and ^{111}In whereas for ^{110m}In a strong discrepancy exists (the value given in ref.3 is out of scale). The constancy of the intrinsic quadrupole moments, determined from Q_S via the projection formula for a rigid axial symmetric rotor in strong coupling, indicates a nearly unchanged prolate deformation of about $\langle\beta\rangle$=0.11 for all measured isotopes.

The isotope shift values (given relative to ^{115}In) are shown in fig.1. The change of the nuclear mean square charge radius, extracted from the experimental IS data, shows a slope, which is steeper than the value given by the droplet modell. This seems to be in contradiction to the nearly constant deformation deduced from the quadrupole moments.

An interesting continuation of this work might be the investigation of still lighter indium isotopes, where surprisingly low masses have been observed recently for ^{104}In and ^{103}In[7].

We would like to thank Dr. D. Murnick for his assistance in these experiments during his stay at GSI.

1. G.Ulm et al.,in "Laser Spectroscopy VI", H.P.Weber and W.Lüthy (eds.), p.211 (1983)
2. R.Kirchner et al., contribution to this report
3. C.M.Lederer and V.S.Shirley (eds.), Table of Isotopes, 7th ed., (1978)
4. E.Hagn and E.Zech, Phys.Rev.C24, 2222 (1981)
5. E.Hagn et al., Z.Phys.A300, 339 (1981)
6. D.Vandeplassche et al., Phys.Rev.Lett.49, 1390 (1982)
7. J.M.Wouters et al., Phys.Rev.C27, 1745 (1983)

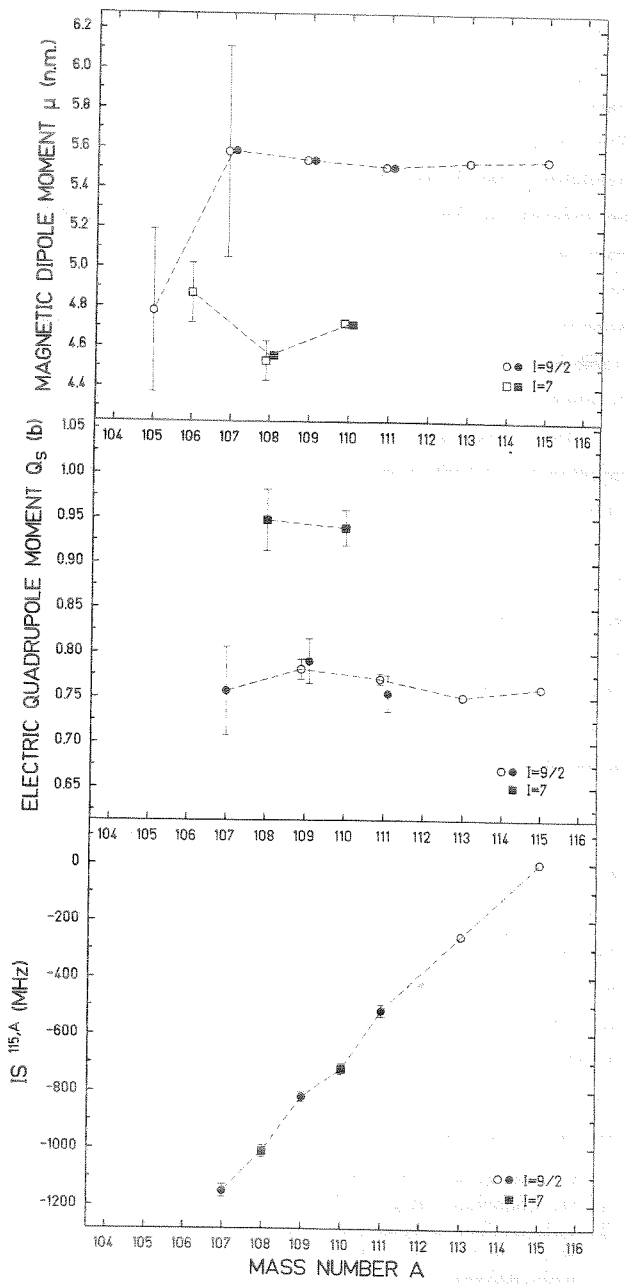


Fig.1: Nuclear moments and isotope shift values of the neutron-deficient and stable indium isotopes having the spin I=9/2 or 7. For the quadrupole moments the systematic uncertainty of the calibration value of ^{115}In (±0.13 b) has to be added to the given error bars to determine the accuracy of the absolute values. The dashed lines only serve to guide the eye. (full symbols: this work; open symbols: values given by ref. 3 - 6).

On the nuclear mean-square charge radii of tin isotopes in the mass range 104 ≤ A ≤ 124

Daniel Berdichevsky, GSI Darmstadt

and

Gerhard Ulm, Institut für Physik, Universität Mainz

In connection with the collinear laser studies underway for isotopes of indium[1] and tin[2], we studied the differences between the mean-square charge radii of the tin isotopic serie, $\delta\langle r_c^2\rangle = \langle r_c^2(Z,N)\rangle - \langle r_c^2(Z,N^*)\rangle$ with Z being proton number, and N,N* being neutron numbers of tin isotopes.

The very accurate experimental data on $\delta\langle r_c^2\rangle$ already available (ref.3) for the stable tin isotopes represent an interesting test of theoretical models which predict radii and mass properties of the nuclei. In our analysis of $\delta\langle r_c^2\rangle$ we normalize to N*=66 (^{116}Sn), which corresponds to half the distance between the magic neutron numbers 50 and 82, and compare the experimental differences $\delta\langle r_c^2\rangle$ with the predictions of the droplet model (DM) (ref.4) and the selfconsistent spherical constrained HF+BCS-method[5]. In our selfconsistent calculations we use the forces Ka (ref.6) and T1* (ref.7) plus an effective pairing interaction[5]. We find that the force Ka predict a $\delta\langle r_c^2\rangle$ in agreement with the data for the full range 112 ≤ A ≤ 124. The DM seems to deviate from experiment for the neutron-deficient nuclei and the T1* force is not in agreement for the region A ≥ 116 (see fig. 1, upper part).

Note that the HF+BCS-model with the force Ka, which yields good agreement with mass excesses values for doubly magic nuclei[5,6], shows its maximal departure from the experimental mass-excess values for ^{110,112}Sn (see fig. 1, lower part). The corresponding neutron numbers N=60,62 are close to half the distance between magic numbers N=50 and 82. This result suggests that, in the analysis of the tin isotopes using the HF+BCS-model, it should be interesting to investigate the influence of the deformation degree of freedom on the mass-excesses and the isotopic shifts $\delta\langle r_c^2\rangle$.

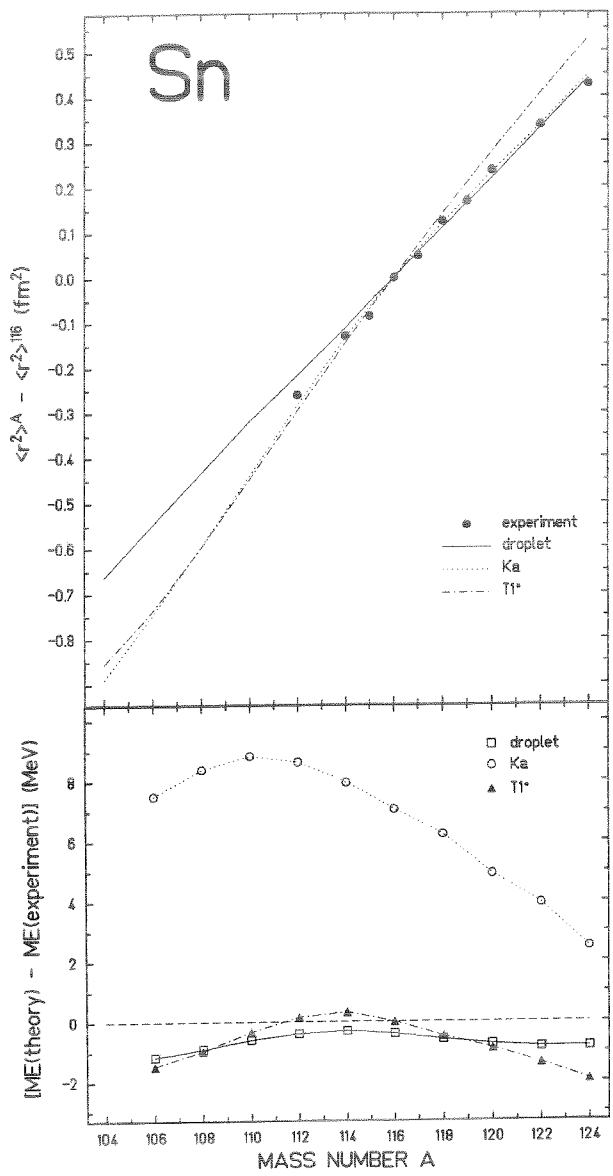


Fig. 1: Change of mean-square radii (upper part) and differences between theoretical and experimental[8,9] mass excess values (ME) (lower part) for neutron deficient and stable tin isotopes.

1) G. Ulm et al., this report
2) H. Lochmann et al., this report
3) P.E.G. Baird et al., J. Phys. B16(1983)2485
4) W.D. Myers and K.-H. Schmidt, Nucl. Phys. A 410(1983)61
5) D. Berdichevsky, thesis Giessen, 1982; U. Mosel and D. Berdichevsky Nucl. Phys. A388(1982)205
6) H.S. Köhler, Nucl. Phys. A258(1976)301
7) The T1* force has the same parameters as the T1 force according to F. Tondeur et al., Nucl. Phys. A, in press, but the HF calculations were performed as in Beiner et al., Nucl. Phys. A238(1975)296
8) W.D. Myers, 1975 Mass predictions, ed. S. Maripuu, At. Data and Nucl. Data Tables 14(1974)479
9) A. Plochocki et al., Nucl. Phys. A388(1982)93

High Yield Production of Neutron-Deficient Indium and Tin Isotopes

R. Kirchner, O. Klepper, P.-O. Larsson, D. Marx, E. Roeckl, D. Schardt
GSI Darmstadt

Collinear laser spectroscopy of radioactive isotopes has so far been restricted to neutron or proton induced reactions, and was only recently adapted to evaporation residues from heavy ion reactions[1]. To produce sufficiently intense beams of neutron-deficient indium and tin isotopes for such experiments, both maximum possible production yields and highly efficient on-line mass separation are required. The former is reached choosing strong beams of ^{16}O and isotopically enriched molybdenum targets, the latter using the original forced electron beam induced arc-discharge ion source[2] in a redesigned version (FEBIAD, type B2, fig. 1) at the GSI on-line separator. To allow for the maximum useful target thickness (about 35 mg/cm²) and due to the short recoil range of the reaction products, the target has to act simultaneously as catcher and has to be placed inside the ion source. Though molybdenum generally shows poor release properties, a release sufficiently fast (half-time about 30 s) for the isotopes of interest is obtained by using up to five thin molybdenum foils of 5 to 7 mg/cm². This target/catcher array is placed in a small target holder inserted into the anode cylinder of the ion source and sealed from the main vacuum by a tungsten window of 2 to 3 mg/cm² thickness. By inverting the anode orientation this holder can be placed either on the colder anti-cathode side of the ion source (B2-A) or on the hotter cathode side (B2-C), where the holder is additionally heated by electron bombardment from the cathode and shielded by two carbon heat-shields.

Fig. 2 shows calculated primary production rates of indium and tin for the reaction ^{16}O on $^{92,94,98}Mo$ targets for 0.5 particle-μA using the HIVAP evaporation code[3] in comparison to experimental values of mass-separated yields. Experimental errors of about 20 % do not include changes of target thickness due to evaporation of isotopically enriched target material and supplementary production in the beam stopper of natural molybdenum. The overall efficiencies measured ranged from 10 to 30 % (fig. 2). High efficiency values were generally measured at the beginning of an experiment before holes occurred in the target, which so far always happened due to overheating by either too intense ^{16}O beams and/or too hot a target position (B2-C). For future experiments efficiencies of the order of 50 % can be expected using version B2-A and adjusting the optimum temperature of the target/catchers by the ^{16}O beam intensity (0.3 to 0.5 particle-μA).

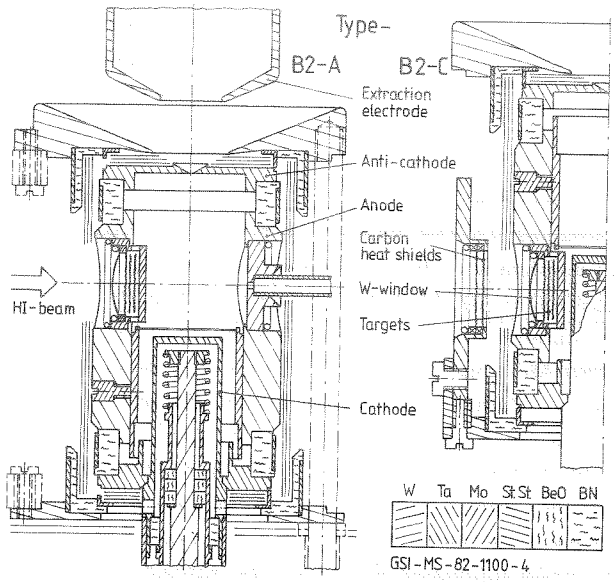


Fig. 1. FEBIAD-B2 ion source.

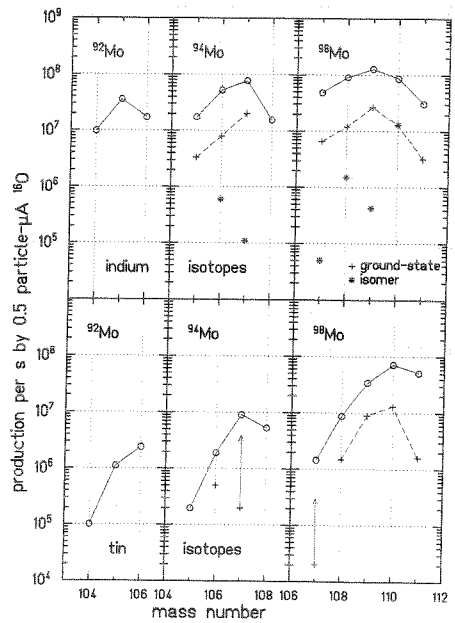


Fig. 2. Calculated primary production rates in the target (o) and measured mass separated beam intensities (+ and *) of neutron-deficient isotopes of indium and tin.

References

1. G. Ulm et al., Laser Spectroscopy VI, H. P. Weber and W. Lüthy (eds.), Springer-Verlag, Berlin 1983, p. 211, and contribution in this report.
2. R. Kirchner et al., Nucl. Instr. Meth. 133 (1976) 187.
3. W. Reisdorf, Z. Phys. A300 (1981) 227; and to be published.

B

Production of very neutron-rich isotopes in the manganese-to-nickel region at the GSI on-line mass separator

E. Runte, K.-L. Gippert, W.-D. Schmidt-Ott, P. Tidemand-Petersson
II. Physikalisches Institut der Universität Göttingen
R. Kirchner, O. Klepper, P.O. Larsson, E. Roeckl, K. Rykaczewski, D. Schardt
GSI Darmstadt
N. Kaffrell, P. Peuser
Institut für Kernchemie der Universität Mainz
M. Bernas, P. Dessagne, M. Langevin
Institut de Physique Nucléaire, Orsay

In continuation of our study[1] of neutron-rich isotopes in the manganese-to-copper region we investigated the light products from transfer reactions of 11.5 MeV/u ^{82}Se with a 46 mg/cm^2 tungsten target mounted inside the ion source (FEBIAD[2] type) of the GSI on-line mass separator. Three mass-separated beams of reaction products in the range A=52-78 were collected simultaneously at individual tape-transport systems and - after preselected accumulation times - brought into measuring positions, each of them equipped with two germanium detectors and a 0.5 mm thick plastic scintillator. We performed γX-coincidence and γ-,X-,ß-Multispectrum analyses. Beta-coincidence measurements served to suppress the γ-background.

Besides some new information on the decays of ^{60}Mn, ^{63}Fe and ^{63}Co which lead to an extension of the known decay schemes, we measured for the first time decay properties of ^{61}Mn, ^{64}Fe, ^{65}Co and ^{69}Ni (Table 1). All these nuclei have previously[3,4] been detected as being stable against particle emission. The earlier assignment[1] of a 21 s ß-activity to ^{67}Ni is now supported by the observation of accompanying γ-rays with energies fitting into the level scheme of ^{67}Cu.
As one example experimental data and results for mass 61 are given in Figs. 1,2. We observe five new γ-lines which show decay during the measuring time of 4 s, while the count rate of the known transitions from the decays of ^{61}Co and ^{61}Fe remains constant. The time analysis of those lines and of the short-lived component in the ß-time spectrum yields the half-life 0.71 s for ^{61}Mn. The decay scheme (Fig.2) was constructed on the basis of energy and intensity balances.

Table 1: Decay properties of new isotopes. The relative intensities of the strongest γ-rays are given in parentheses

Nucleus	$T_{1/2}$ (s)	Energies of γ-rays (keV)
^{61}Mn	0.71(1)	628.6(100),206.8(49)
^{64}Fe	2.0(2)	310.8
^{65}Co	1.25(5)	351.3(100),310.8(55)
^{67}Ni	21(1)	821.6(100),1115.3(105)
^{69}Ni	10(3)	679.8(100),205.6(65)

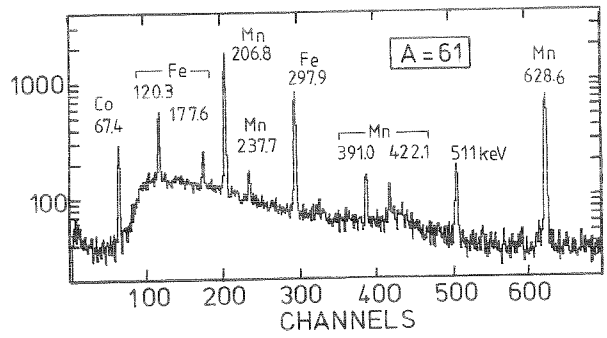


Fig. 1: Part of the γ-ray spectrum at A=61 measured with a 28% Ge(Li) detector in coincidence with ß-rays.

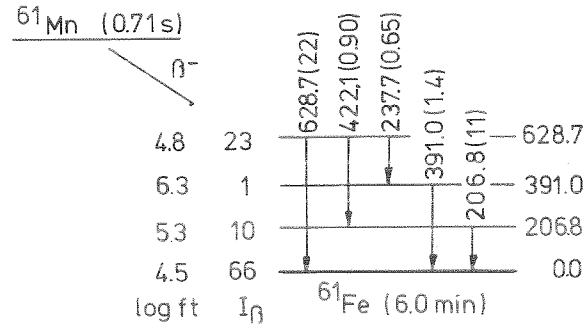


Fig. 2: The decay scheme of ^{61}Mn. The values in parentneses are absolute transition intensities per 100 ß-decays.

[1] E. Runte et al., Nucl. Phys. A399 (1983) 163
[2] R. Kirchner et al., Nucl. Instr. 186 (1981) 295
[3] D. Guerreau et al., Z. Phys. A295 (1980) 105
[4] M. Bernas et al., IPN report DRE 83-30

Coincidence measurements of β-delayed protons and γ-rays from the precursor ^{117}Ba

P. Tidemand-Petersson
II. Physikalisches Institut der Universität Göttingen
R. Kirchner, O. Klepper, W. Kurcewicz*, P.O. Larsson, E. Roeckl, D. Schardt
GSI Darmstadt
A. Płochocki, J. Żylicz
Institute of Experimental Physics, University of Warsaw
G. Nyman
Department of Physics, Chalmers University of Technology, Göteborg
I.S. Grant
Schuster Laboratory, University of Manchester

The β-delayed proton precursor ^{117}Ba, which has earlier been studied[1] at Dubna, was produced by bombardment of a 3.4 mg/cm² target of ^{63}Cu with 5.0 MeV/u ^{58}Ni ions from the UNILAC. The A=117 products were selected by the GSI on-line mass separator and implanted into the tape of a transport system, which with 4 s intervals brought the activity in front of a particle-detector telescope situated between a Ge(Li) and a Ge(i) detector, thus allowing for observation of particle-γ-ray coincidences.

A part of the γ-ray spectrum recorded with the Ge(Li) detector in coincidence with proton signals from the detector telescope is shown in fig.1. The occurence of the 394 and 622 keV lines, that have earlier been observed[2] to follow the β-decay of ^{116}Cs, indicates that parts of the proton emissions from the excited states in ^{117}Cs, which are fed by the β-decay of ^{117}Ba, are leading to the 2_1^+ and 2_2^+ states[2] at 393.5 and 1015.8 keV in ^{116}Xe. The intensities of the two transitions compared with the total proton-emission rate yield the branching ratios given in the inset of fig.1. Comparison with the corresponding ratios from statistical-model calculations indicates that ^{117}Ba most probably has I=3/2⁺.

Bogdanov et al. found[1], that agreement between calculated and experimental proton spectra could only be achieved by assuming a resonance in the β-strength function, a finding that was confirmed by a similar investigation[3] of this precursor at GSI. We have earlier shown[3], that such resonances for the precursor ^{113}Xe occured distinctly in the proton-energy dependence of the relative proton feeding of the 2^+ state in the daughter nucleus. We have, therefore, also for ^{117}Ba determined this quantity by gating on the 394 keV γ-line (fig.2). Although the statistics are prohibiting firm conclusions, there seems to be best agreement with the curve obtained with the β-strength containing a resonance structure, so that the data support earlier assumptions[1,3] of such a structure, which may origin from allowed-unhindered $7/2[413]_\pi \rightarrow 5/2[413]_\nu$ and $9/2[404]_\pi \rightarrow 7/2[404]_\nu$ β-transitions.

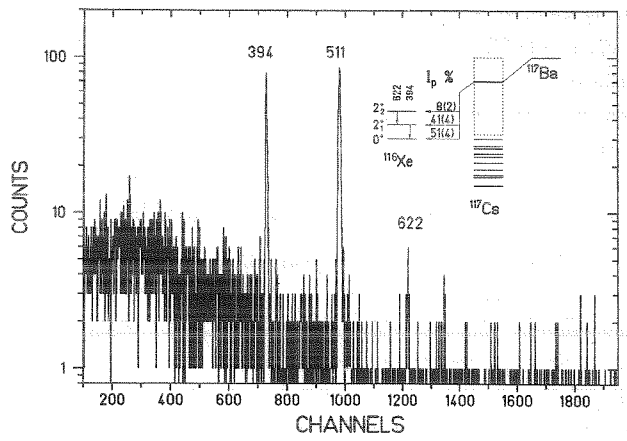


Fig.1: Part of a γ-ray spectrum recorded in coincidence with β-delayed protons from ^{117}Ba. The inset shows the decay process with the intensities of the individual proton emission transitions.

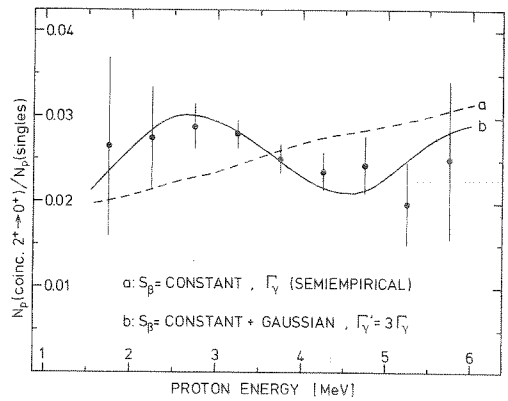


Fig.2: The fraction of β-delayed protons from ^{117}Ba observed in coincidence with the $2_1^+ \rightarrow 0^+$ γ-transition in ^{116}Xe given as a function of the proton energy. The experimental points are given together with two curves from statistical-model calculations with the assumptions given in the figure.

1. D.D. Bogdanov et al., Nucl. Phys. A303 (1978) 145
2. G. Marguier et al., Nucl. Phys. A342 (1980) 301
3. P. Tidemand-Petersson and A. Płochocki, Phys. Lett. 118B (1982) 278

*Present address: Institute of Experimental Physics, University of Warsaw

Studies on Short-Lived Praseodymium Isotopes at the HELIOS Facility

T. Karlewski, N. Hildebrand, N. Kaffrell, N. Trautmann, G. Herrmann
Institut für Kernchemie, Universität Mainz

M. Brügger
GSI, Darmstadt

The investigations for an efficient mass separation of the lanthanides[1], which serve as model elements for the heavier actinides, have been continued at the helium jet on-line mass separator facility HELIOS. With $PbCl_2$ as cluster material and an integrated skimmer-high temperature ionization source overall efficiency values of a few percent were obtained for these elements. Furthermore decay studies on neutron-rich praseodymium isotopes, produced by thermal neutron-induced fission of ^{235}U, have been performed by γ-spectroscopic measurements. A fast microprocessor controlled tape system[2,3] was used to transport the mass separated activities from the focal plane of the separator to the detector position.

The β^--decay of 2.3 min ^{148}Pr has been studied by γ-singles, γ-γ-coincidence and γ-γ-angular correlation measurements. In the latter mode $5x10^6$ coincidence events were collected per angle (at 90, 135, 180, 225, and 260 °) resulting from a total counting time of 40 h. The data analysis has not yet been completed.

With an upgraded ^{235}U-target (18 mg instead of 6.5 mg) the identification of ^{152}Pr and studies on its decay properties became possible. In a γ-multiscaling experiment, using the β-gate technique to suppress the background in the γ-ray spectra, the half-life of ^{152}Pr was determined to be 3.8±0.2 s from the decay of the strongest γ-lines at 164, 285 and 1469 keV (Fig. 1). In this experiment the mass separated activity was collected for 16 s, transported to the Ge(Li)-detectors within ∿2 s and measured for 8x2 s. Altogether 561 cycles were summed up.

In a second experiment $7.5x10^6$ γ-γ-coincidence events from the β^--decay of 3.8 s ^{152}Pr have been collected which allowed to establish a partial decay scheme for ^{152}Pr thus far not yet well known[4].

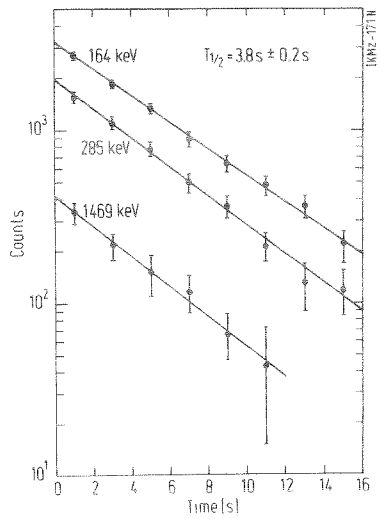


Fig. 1: Decay of the strongest γ-lines of ^{152}Pr

[1] M. Brügger et al., GSI Scientific Report 1981, GSI 82-1, p. 225 (1982)
[2] M. Brügger et al., GSI Scientific Report 1982, GSI 83-1, p. 229 (1983)
[3] M. Brügger et al., to be published
[4] J.C. Hill et al., Phys. Rev. C27, 2857 (1983)

Search for Proton Radioactivity in Fusion Reactions with ^{58}Ni Projectiles

S. Hofmann, Y.K. Agarwal, P. Armbruster, F.P. Heßberger, P.O. Larsson, G. Münzenberg
K. Poppensieker, W. Reisdorf, J.R.H. Schneider, H.-J. Schött
GSI Darmstadt

The proton activity of ^{151}Lu and ^{147}Tm [1] was assigned to the emission of a proton out of the $h_{11/2}$ orbital. The single particle shell model predicts energetically close lying levels of low spin ($\pi s_{1/2}$, $\pi d_{3/2}$) in odd-even nuclei $Z > 64$ and $N \leq 84$. These low spin states could be observed only in ^{147}Tb [2]. The relative position to the $11/2^-$ state is not known. Assuming same energy for low and high spin states we have calculated the proton decay probabilities of $1/2^+$ and $3/2^+$ states in ^{147}Tm and ^{151}Lu. The result was encouraging to search for these decays at SHIP.

The neutrons are paired in the isotones ^{151}Lu-^{150}Yb ($N = 80$) and ^{147}Tm-^{146}Er ($N = 78$). Considering the next lighter pairs of isotones (in the shell model by adding a neutron hole out of the $\nu d_{3/2}$ or $\nu s_{1/2}$ subshell) we expect a proton decay between these isotones with similar properties than in ^{147}Tm and ^{151}Lu, especially a decay with a long halflife (10-100 ms) from a high spin state ($\pi h_{11/2}\, \nu d_{3/2}^{-1}$) or ($\pi h_{11/2}\, \nu s_{1/2}^{-1}$) and a decay with a short halflife (1-10 µs) from a low spin state, e.g.($\pi s_{1/2}\, \nu d_{3/2}^{-1}$).

We have looked for these transitions in an experiment at SHIP in reactions of an ^{58}Ni beam with targets of ^{92}Mo and ^{96}Ru. The measured spectra are shown in Fig. 1. Close to the known lines from the decay of ^{147}Tm and ^{151}Lu we observed new lines in reactions to the compound nuclei ^{150}Yb at an excitation energy of $E^* = 42$ MeV and to ^{154}Hf at $E^* = 71$-78 MeV. Due to the low intensity of the new lines complete excitation functions and halflives could not yet be measured. Therefore, the assignment given in Fig. 1 is preliminary, but is consistent with all measured data and the shell model considerations given above. We want to remark the indication of a small line at 1050 keV in the uppermost spectrum. At this position we expect the proton line from the decay of ^{147}Tm produced in an αp2n evaporation channel.

Faestermann et al.[3] found the proton radioactivity of ^{113}Cs and ^{109}J in reactions to the compound nuclei ^{116}Ba and ^{112}Xe. In irradiations at SHIP these activities have been also observed.

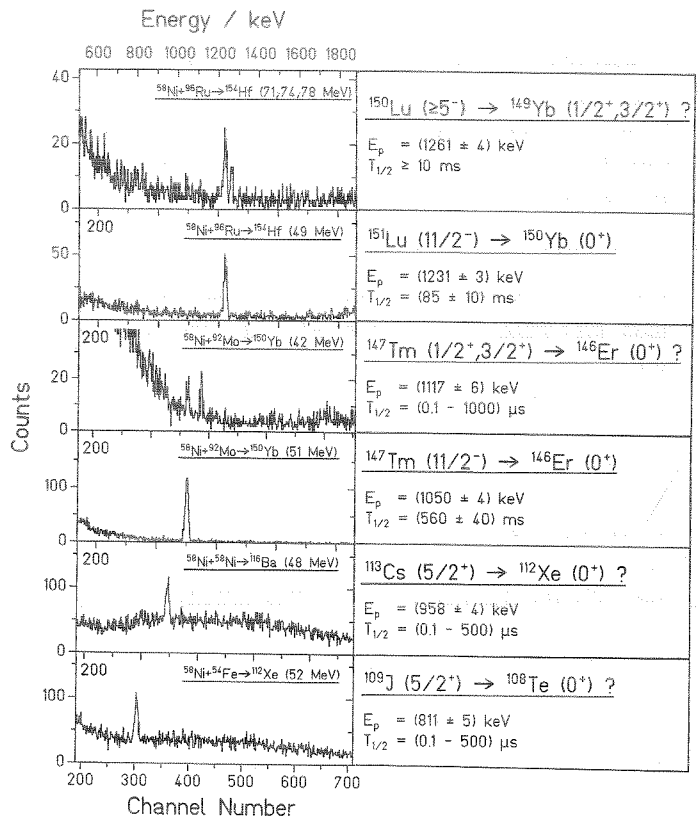


Fig. 1: Energy spectra showing the six presently known proton lines from decays of nuclei beyond the proton drip line. Spectra 1, 2, and 4 from top were measured during the 15 ms macro pauses, the other spectra during the 5 ms beam pulses. The halflife of ^{147}Tm was measured in an experiment at the GSI Online Mass Separator[1].

Table 1: Calculated (WKB method) partial proton halflives

Proton Transition	$Q_{p,nucl}$/keV	Δl	$T_{1/2,p}$
^{150}Lu(5⁻) → ^{149}Yb(1/2⁺)	1283	5	40 ms
^{151}Lu(11/2⁻) → ^{150}Yb(0⁺)	1253	5	80 ms
^{147}Tm(1/2⁺) → ^{146}Er(0⁺)	1138	0	14 µs
(3/2⁺) → (0⁺)	1138	2	140 µs
(11/2⁻) → (0⁺)	1070	5	2.8 s
^{113}Cs → ^{112}Xe	976	2	0.32 µs
	976	3	3.6 µs
	976	4	83 µs
^{109}J → ^{108}Te	828	2	5.8 µs
	828	3	70 µs
	828	4	1.7 ms

[1] GSI Annual Report 1981, GSI-82-1 (1982)
[2] Y. Nagai et al., Phys. Rev. Lett. 47, 1259 (1981)
[3] T. Faestermann et al., to be published

Identification of New Neutron Rich Isotopes of Heavy Lanthanides at the GSI On-Line Mass Separator

K. Rykaczewski, P. O. Larsson, R. Kirchner, O. Klepper, E. Roeckl, D. Schardt; (GSI Darmstadt)
K. L. Gippert, E. Runte, W.-D. Schmidt-Ott, P. Tidemand-Petersson; (Universität Göttingen)
N. Kaffrell, P. Peuser; (Universität Mainz) W. Kurcewicz, J. Żylicz; (University of Warsaw)

Extending earlier experiments[1,2] we searched for even more neutron-rich isotopes from target break-up in order to test the capabilities of this novel production path for heavy lanthanide region. Decay properties of the neutron-rich isotopes of holmium, erbium, thulium, lutetium and hafnium were studied in the mass range 171 to 184, using multinucleon transfer reactions between ~11 MeV/u ^{136}Xe and ^{238}U projectiles (typical beam intensities: 7-15 particle-nA) and ^{nat}W/Ta targets placed inside a thermal ion source[3] of the GSI on-line mass separator.

At mass number A=171 we found a short lived 45(5) s component of the electron spectrum measured by thin plastic scintillator and weak erbium K-X rays in coincidence with electrons. The new isotope ^{171}Ho or a new isomer ^{171}Er^{m} decaying by strongly converted transition, are the possible sources of this activity.

The new isotope ^{177}Tm with a half-life of 130(40) s was identified. The upper limits of the β intensities given in fig. 1, have to be considered as total feeding (including deexcitation of higher-lying levels) of the new level at 622 keV and the known 6.41 s isomeric state[4] in ^{177}Yb, respectively. For the new level at 622 keV a Nilsson configuration $5/2^-[512]_n$ is suggested on the basis of experimental systematics of these orbitals in odd ytterbium isotopes[4] and due to existence of the transitions to $7/2^-[514]_n$ and $9/2^+[624]_n$ levels.

The β and γ activity observed at mass number 184 (see fig.2) is interpreted as decay of the high spin, ground or isomeric state of the new isotope ^{184}Lu, feeding via the 8^- { $7/2^+[404]_p$, $9/2^-[514]_p$ } isomeric state the $717(6^+)$-$350(4^+)$-$107(2^+)$ keV ground state band of ^{184}Hf. An alternative explanation would be a rather strong presence of this 8^- isomer ^{184}Hf^{m} in the mass 184 beam due to the primary production in the reaction ^{136}Xe or ^{238}U + ^{nat}W/Ta. The latter assignment can be preliminarily excluded because the release of hafnium is strongly suppressed by a factor of about 10^3 compared to lutetium. The amount of primarily produced ^{184}Hf^{m} in the mass separated sample is expected to be an order of magnitude lower than the observed activity, using the measured cumulative cross section of 0.53 mb for ^{184}Hf in the reaction ^{136}Xe (8.5 MeV/u) + ^{nat}W [ref.5] and the estimated separation efficiency for hafnium of 0.1‰ [ref.6] We want to emphasize, however, that the observed beta decay half-life 20 s cannot be treated as pure ^{184}Lu half-life because of possible admixtures from beta decays of low spin state at ^{184}Lu and 8^- isomeric state at ^{184}Hf and conversion electrons from deexcitation of 8^--6^+-4^+-2^+ levels in ^{184}Hf.

It is interesting to note that due to the present interpretation ^{184}Lu was produced via three proton stripping and neutron pick-up from ^{186}W - an exotic transfer process, which has so far been observed only in very few cases in light nuclei.

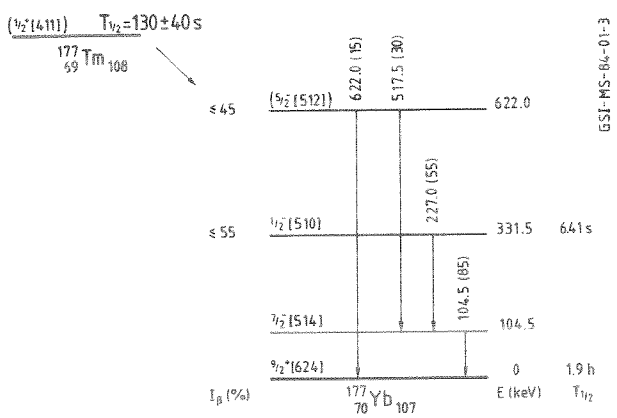


Fig.1. Partial decay scheme of ^{177}Tm. Total transition intensities are given in parentheses.

1. R. Kirchner et al., Nucl. Phys. A378 (1982) 549
2. K. Rykaczewski et al., Z. Phys. A309 (1983) 273
3. R. Kirchner et al., Nucl. Instr. and Meth. 186 (1981) 295
4. C.M. Lederer and V.S. Shirley (ed.), Table of Isotopes, 7th ed., (Wiley, New York, 1978)
5. I. Zychor et al., Nucl. Phys. A414 (1984) 301
6. G. Walter et al., KfK-Report 3417 (1982); W. Eschner et al., to be published

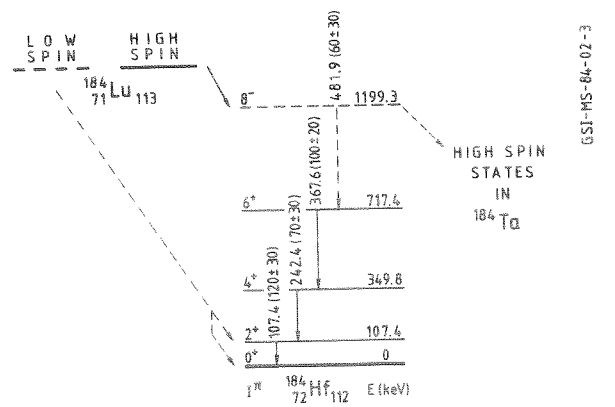


Fig.2. Part of mass 184 decay chain discussed in the text. The situation of 8^- isomeric state a 1199.3 keV suggested by weak indication for 481.9 keV transition in coincidence with electrons fits well into energy systematics of 8^- {$7/2^+[404]_p$, $9/2^-[514]_p$} isomers in even-even hafnium isotopes.

The ß-decay branching $^{180}Lu \rightarrow ^{180}Hf^{m}$ and the nucleosynthesis of $^{180}Ta^{m}$ B

W. Eschner, W.-D. Schmidt-Ott, K.-L. Gippert, E. Runte
II. Physikalisches Institut, Universität Göttingen

H. Beer, G. Walter
Kernforschungszentrum Karlsruhe

R. Kirchner, O. Klepper, E. Roeckl, D. Schardt
GSI Darmstadt

Search has been conducted for a possible β^--decay from ^{180}Lu ($T_{1/2}$ = 5.7 min) to the 8^- isomeric state in ^{180}Hf ($T_{1/2}$ = 5.5 h), to determine the post-r-process contribution to the nucleosynthesis of $^{180}Ta^{m}$ ($T_{1/2} > 10^{13}$ y, $J^{\pi} = 9^-$) via a subsequent allowed $^{180}Hf^{m} \rightarrow ^{180}Ta^{m}$ transition.

As no γ transitions feeding the 1142 keV isomer have yet been observed, an integral measurement tracing the amount of $^{180}Hf^{m}$ daughter activity was performed. We used mass-separated samples of ^{180}Lu produced in multi-nucleon transfer reactions between a 8.6 MeV/u ^{136}Xe beam from the UNILAC and a sandwiched ^{nat}W target ion source system.[1] $^{180}Hf^{m}$ was also produced in the reaction but strongly suppressed by the chemical properties of the ion source. The directly produced amount of $^{180}Hf^{m}$ is inferred from comparison with $^{177}Hf^{m}$ activity, and then substracted from the total amount, under the assumption of equal release properties for the hafnium isotopes and using the ratio of the measured cross sections for their respective production.[2]
The half-times for release from the ion source were separately determined for Lu and Hf, the former from the increase with time of the 'in-beam' collected ^{180}Lu activity which is slower than expected for immediate Lu release from the ion source, the latter from the amount of residual $^{177}Hf^{m}$ diffusing from the ion source after the end of irradiation.

Two irradiations were performed, one of 46, the other of 88 minutes duration, with a nearly constant ^{136}Xe beam of 17 particle·nA intensity. Mass 180 and 177 samples were collected in focal plane of the separator and removed immediately after the end of irradiation for subsequent γ counting with shielded Ge(Li) detectors.

The differential equations for parent-daughter decay including release from the source were set up and solved [3], assuming the rate of release to be proportional to the number of nuclei present in the source. The Lu release constant was obtained from 'in-beam' spectra to be $5^{+3}_{-2} \cdot 10^{-2}$ s^{-1} (Fig. 1), the Hf release constant was determined to be $7(2) \cdot 10^{-4}$ s^{-1}.
The value of the β^- branching in question was then calculated to be 0.46(20)%, leading to the following conclusions:

i) Assuming a theoretical branching of 0.34% for the $^{180}Hf^{m} \rightarrow ^{180}Ta^{m}$ transition as proposed by Beer [4], both slow and rapid neutron capture processes would account for only 30% of the observed solar $^{180}Ta^{m}$ abundance.

ii) An upper limit on the $^{180}Lu \rightarrow ^{180}Hf^{m}$ branching of 0.06% obtained by a chemical Lu - Hf separation approach [5] might indicate the existence of a short-lived ($T_{1/2} < 1$ min) ^{180}Lu high-spin isomer with an allowed direct transition to the 8^- ^{180}Hf isomer. However, such an isomer has not been observed in other experiments.

Thus, the problem of the nucleosynthetic origin of $^{180}Ta^{m}$ is not explicitely solved. Other possible origins have been proposed, but lacking knowledge of astrophysical parameters makes a quantitative assessment of those processes impossible up to now.

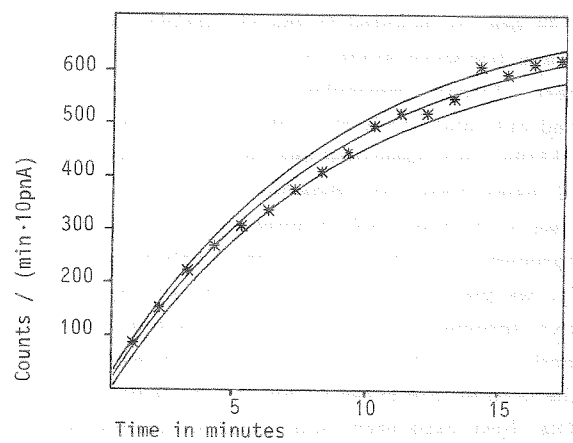


Fig. 1: 'In-beam' measurement of ^{180}Lu activity
* Registered number of 408 keV γ-rays
Center curve: best fit including release
Outer curves: error limits as stated in text

[1] R. Kirchner et al., Nucl.Phys.A 378,549 (1982)

[2] I. Zychor et al., Radiochim.Acta 33, 1 (1983)

[3] W. Eschner, Diplomarbeit, Göttingen (1984)

[4] H. Beer et al., Phys.Rev.C 26, 1404 (1982)

[5] S.E. Kellogg et al., Bull. Am. Phys. Soc. 28, 989 (1983)

Accelerator Mass Spectrometry on ^{205}Pb B

H. Ernst, G. Korschinek, P. Kubik, W. Mayer, H. Morinaga, E. Nolte, U. Ratzinger (FB Physik, Techn. Univ. MÜnchen); W. Henning, W. Kutschera (Argonne National Labratory); M. Müller, D. Schüll (GSI Darmstadt)

The radioisotope ^{205}Pb($T_{1/2}$=1.4 x 10^7y, Q_{EC} = 0.060 MeV) is a promising candidate[1] for a geophysical detection of solar neutrinos via the reaction ^{205}Tl (ν,e^-) $^{205}Pb^*$ (E*=2.3 keV). The low energy threshold makes this system most sensitive to neutrinos from the reaction $p+p \rightarrow d+e^+ + \nu$ which comprises 94 % of the total solar neutrino flux[2]. As a consequence a rather high neutrino capture rate of about 500 SNU is predicted[1,2] (1 SNU = one neutrino capture per 10^{36} target atoms and second). A determination of this rate is conceivable by measuring neutrino-produced ^{205}Pb accumulated over millions of years in a suitable Tl ore. The well known experiment of Davis[3] using the ^{37}Cl (ν, e^-) ^{37}Ar reaction yields a significantly lower neutrino flux than predicted[2] from the standard solar model. An independent measurement of this quantity is the motivation of our experiment.

The saturation concentration of ^{205}Pb in Tl due to neutrino interaction is estimated to be $^{205}Pb/Tl \sim 10^{-19}$. It seems feasible to detect such small quantities by accelerator mass spectrometry[4]. The principle of this method is as follows: A sample, e.g. prepared from Tl ore, is mounted in the ion source, accelerator and beam transport system are tuned for the isotope of interest. Isobaric molecules, isotopes and isobars are filtered out, and finally the isotopes of interest - in our case ^{205}Pb - are identified and counted by measuring A and Z using heavy ion detector techniques. The main problem is, to effectively suppress $^{204,206}Pb$ and ^{205}Tl backgrounds. For the discrimination between ^{205}Pb and ^{205}Tl, we plan to use the differential energy loss in a passive absorber[5] in connection with a high resolution magnetic spectrometer. The high energies obtainable by the UNILAC are essential for this method.

The first experiment was aimed at testing specific technical aspects of our project. A 11.4 Mev/u $^{206}Pb^{36+}$ beam was tuned into the target chamber of the GSI-magnetic spectrometer with an energy spread of <0.1 % . A mass resolution of M/ΔM~800 was obtained with source and injection magnet system, which already provided discrimination against neighbouring isotopes of the order of 10^{-5}. Background contamination arises from W metal that is used as cathode material in the iron source, because $^{205}Pb^{9+}$ and $^{182}W^{8+}$ are essentially degenerate in A/q. In the future Tantalum metal will be used instead. Of importance is also, that samples in the ion source can be changed quickly without breaking the vacuum. A new ion source with three electrodes recently developed by the UNILAC injector group will allow in future fast selection of three samples. An efficient background suppression was achieved in our experiment by the velocity focussing properties of the UNILAC, by the 180° high-dispersion (M/ΔM~1000) beam line system preceeding the spectrometer, and by the magnet spectrometer itself, positioned at 0°, in connection with the focal-plane detector. Through a time of flight measurement over the 6.5 m flight path in the spectrometer a resolution of M/ΔM~350 was obtained. The suppression of neighbouring masses near A~205 was found to be better than 10^{-8} from the ion source to the spectrometer focal plane detector.

A rather difficult part of the background suppression is the distinction of ^{205}Pb from ^{205}Tl. For this separation a passive absorber in form of a 9 cm long gas cell filled with isobutane was used. After having passed through the gas cell, ^{205}Pb and ^{205}Tl have sufficiently different energies to allow for their separation in the focal plane. A condition for that idea to work is, that the energy straggling introduced by the energy degradation is smaller than the energy loss difference between ^{205}Pb and ^{205}Tl after the gas cell. We have measured an energy straggling of δE~7MeV (FWHM) at an energy loss of 700 MeV for ^{206}Pb. The best sensitivity is obtained when the energy loss difference is about half the separation between neighbouring Tl charge states (~45 MeV).

The feasibility study of accelerator mass spectrometry with these very heavy ions is continued.

1. M.S. Freedman et al., Science 193 (1976)1117
2. J.N.Bahcall, Rev.Mod.Phys. 50 (1978)881
3. R. Davis jr., Phys.Rev.Lett. 12 (1964)302
4. Symposium on Accelerator Mass Spectrometry, Argonne (1981), ANL-PHY/81-1
5. W. Henning et al., Nucl.Instr.Meth. 184 (1981)247

Evaporation Residue Production in Fusion Reactions $^{48}Ca+^{206,208}Pb$

F.P. Heßberger, Y.K. Agarwal, P. Armbruster, A. Ghiorso*, S. Hofmann, M. Leino*, G. Münzenberg, K. Poppensieker, W. Reisdorf, K.-H. Schmidt, J.R.H. Schneider, W.F.W. Schneider, D. Vermeulen

GSI Darmstadt

*Lawrence Berkeley Laboratory, USA

The production of evaporation residues in fusion reactions $^{48}Ca + ^{206}Pb,^{208}Pb$ was investigated at SHIP at bombarding energies in the range E_{CM} = 165-183 MeV; the results are shown in fig.1. In this energy range, 2n-emission turned out to be the most probable deexcitation mode in both reactions. In $^{48}Ca + ^{206}Pb$ no α-decay of ^{253}No (1n-channel) was observed, therefore a limit σ(1n) < 10 nb is estimated; one α-decay, that can be attributed to ^{251}No (3n-channel) was observed at E_{CM} = 181 MeV, giving a cross-section of σ(3n) = 7 nb. For $^{48}Ca + ^{208}Pb$ the identification of the 1n-channel is more complicated due to similiar α-decay energies of ^{255}No and ^{254}No. As the halflives of both isotopes are rather long (3.1min and 55sec resp.), a halflife analysis was only possible for low counting rates, i.e. for the two lowest irradiation energies; here we estimated an upper limit for the 1n-channel to σ(1n) / σ(2n) ≤ 0.3; α-decays that could be attributed to ^{253}No (3n-channel) were not observed, the upper limit is therefore σ(3n) < 100 nb for E_{CM} > 181 MeV.

Literature values /1/ for decay properties of evaporation residues and their daughter products could be reproduced within the errorbars and are listed in table 1. The unexspected high production cross-sections for the system $^{48}Ca + ^{208}Pb$ published by Nitschke et al./2/ and Orlova et al./3/ could not be reproduced. These values are a factor 9-10 larger than our value (table 2); furthermore our bombarding energy for the maximum cross-section is about ΔE_{CM} ≈ 7 MeV lower than the value given in ref.2. In the case of $^{48}Ca + ^{206}Pb$ the agreement of our value to that published Flerov et al./4/ is better (table 2). We cannot explain this discrepancy in the present state, but a misfunction of SHIP is unlikely, since in the same experiment evaporation residue cross-sections for $^{48}Ca + ^{172}Yb$, ^{173}Yb, ^{176}Yb were measured. These results are in agreement to values exspected for these reactions from previous measurements $^{40}Ar + ^{176-180}Hf$ /5/.

In our experimental set-up, a carbon foil is placed ≈8 cm behind the target to equlibrate eventual high charge states, due to deexcitation of compound nuclei followed by internal conversion; in cases of excited nuclear states with lifetimes τ≈10-100 ns the change in the atomic charge predominantly will take place after passing this foil, but before entering SHIP; a drastic decrease of the transmission of SHIP will be the consequence. To exclude that such an effect has influenced our measurement, more experiments are necessary.

C.M.Lederer, V.S.Shirley Table of Isotopes, 7th edition (1978)

2.J.M.Nitschke et al. Nucl.Phys. A313 (1979) 236-250

3.O.A.Orlova et al. GSI-tr-79/10 (1979)

4.G.N.Flerov et al. Nucl.Phys. A267 (1976) 359-364

5.C.C.Sahm et. al. this report

TABLE 1: Measured decay properties of identified isotopes; for ^{252}No and ^{248}Fm, due to the low number of events (≈30), only the most intensitive α-line was identified

Isotope	E_α/keV	T_h/sec	b_{sf}
^{252}No	$8407^{+}_{-}15$	$2.5^{+0.5}_{-0.4}$	$0.24^{+}_{-}0.10$
^{248}Fm	$7873^{+}_{-}15$	$36^{+}_{-}12$	-
^{254}No	$8100^{+}_{-}15$	-	≤0.001

TABLE 2: Measured maximum evaporation residue cross-section. The values are given in μb.

Reaction	σ(ref.2)	σ(ref.3)	σ(ref.4)	σ(this work)
$^{208}Pb+^{48}Ca$	$3.4^{+}_{-}0.4$	$4.0^{+}_{-}0.6$	-	$0.39^{+}_{-}0.07$
$^{206}Pb+^{48}Ca$	-	-	0.5	$0.19^{+}_{-}0.03$

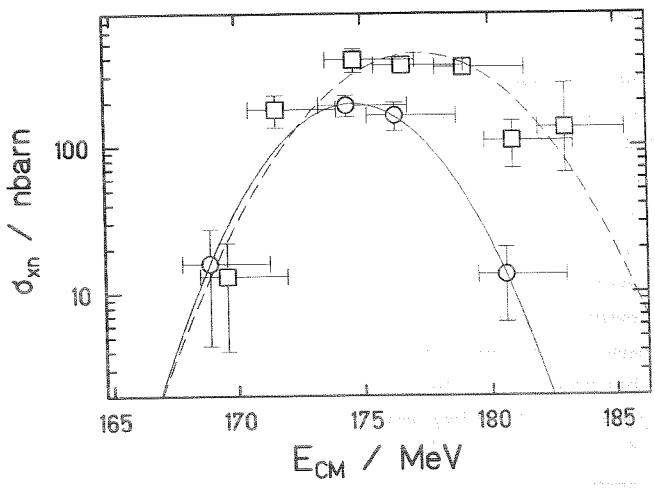


FIG.1 Measured xn-cross-sections for the systems $^{48}Ca+^{208}Pb(□)$, $^{48}Ca+^{206}Pb(○)$; the error bars in the cross-sections are statistical errors and do not include uncertanties due to transmission of SHIP. The errorbars in the energy represent the energy loss of the projectiles in the target. The curves are to guide the eye.

A Search for New Isotopes from Reactions of $^{16,18}O$ and ^{22}Ne with ^{254}Es

M. Schädel, W. Brüchle, M. Brügger, H. Gäggeler, D. Schardt, K. Sümmerer
GSI Darmstadt
R. W. Lougheed, J. H. Landrum, J. F. Wild, R. J. Dougan, A. D. Dougan, E. K. Hulet
LLNL Livermore, CA
G. D. O'Kelley
ORNL Oak Ridge, TN

From previous experiments with ^{18}O and ^{22}Ne as a projectile and ^{254}Es ($T_{1/2}$ = 276d) as a target cross sections for longer lived isotopes of elements Fm to No were obtained[1]. Based on these results, and from a comparison with isotope cross sections from similar transfer channels in reactions with ^{248}Cm[2], we estimated cross sections between 1 µb and 10 nb for yet unknown neutron-rich isotopes of elements 101 through 104. Expected half-lives for these nuclides range from one second up to a few hours.

We irradiated a 30 µg/cm² ^{254}Es target with intense beams (≤300pnA) of ^{18}O, ^{22}Ne and ^{16}O. Reaction products, recoiling from the Es target, were stopped in a KCl loaded He gas. Whereas the previous experiments[1] were performed with off-line chemistry methods, now on-line techniques were applied.

In one series of experiments products were rapidly transported (~200ms) to our rotating wheel multidetector apparatus, ROMA[3]. The activity deposited on thin plastic foils was moved stepwise to 15 sequential counting stations for α- and sf-measurements. The irradiations with 98 and 104 MeV ^{18}O (2-60 s collection times) gave a rather flat background which tended to obscure weak α-peaks. However, several not readily identifiable α-peaks were seen in addition to the one from ^{260}Lr. In 127 MeV ^{22}Ne bombardments (2-180 s collection times) the α-spectra were cleaner, and we clearly observed peaks of $^{256,257}No$ and $^{258,260}Lr$. The main α-group of ^{259}Lr was obscured by the ^{256}No peak. In this experiment ROMA was operated in a special mode[3] to enhance the observation of α-events after the possible decay of $^{265}105$. In an on-line analysis no events were observed that could be assigned as a daughter coming from the decay of $^{265}105$. There was also no indication for $^{263}105$ from a 101 MeV ^{16}O bombardment. In the α-spectrum from this experiment (Fig.1), $^{255-257}No$ and $^{258-260}Lr$ can clearly be identified. For final results we have to await the off-line analysis.

The carbon foils covering the detectors as a catcher for nuclei from α-recoils were chemically processed off-line shortly after each of the three beam runs. This was done to search for long-lived daughters such as ^{257}Fm and ^{258}Md. Long-term counting is still continuing.

A second series of experiments with the purpose of detecting those new nuclides with half-lives between several minutes and days whose α-energies would be masked in the on-line counting was carried out with the automated rapid chemistry apparatus, ARCA[4]. The measurements of chemically separated fractions of the elements No, Lr and Md began 7, 17 and 19 min after end of bombardment, respectively. Experiments were carried out with ^{18}O and ^{22}Ne as a projectile.

A careful analysis of the large amount of data accumulated is under way to search for unknown isotopes. We will be able to determine cross sections of nearly all of the known heavy isotopes up to ^{260}Lr, which will provide a large amount of new data for further and better extrapolations. For the time being, extrapolations from preliminary data indicate that the unknown isotopes $^{260,261}Md$, $^{260,261}No$ and $^{261,262}Lr$ should be produced with 1.0 to 0.1 µb cross sections. However, alpha emission from these nuclides were not readily observed.

1. M. Schädel et al., Proc. Int. Workshop on Gross Properties of Nuclei and Nuclear Excitations p. 16, XI, Hirschegg (1983), and Proc. Int. Conf. Nucl. Phys., Vol. I, p. 625, Florence (1983)
2. D. Lee et al., Phys.Rev. C 25, 286 (1982)
3. K. Sümmerer et al., contribution to this report.
4. W. Brüchle et al., contribution to this report

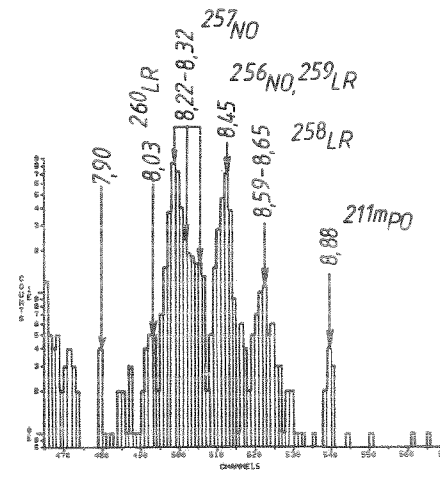


Fig.1: α-spectrum accumulated during a 12 hour irradiation of ^{254}Es with 101 MeV ^{16}O. Data are from the first detector of ROMA[3] taken with a collection time of 4 s.

Search for Superheavy Nuclei from Fusion of ^{48}Ca with ^{248}Cm at SHIP

Y.K. Agarwal, P. Armbruster, S. Hofmann, F.P. Heßberger, G. Münzenberg, K. Poppensieker, W. Reisdorf, K.-H. Schmidt, J.H.R. Schneider, W.F.W. Schneider, D. Vermeulen
GSI Darmstadt
A. Ghiorso, M. Leino, K.J. Moody
Lawrence Berkeley Laboratory, USA

Numerous unsuccessful attempts have been made to detect superheavy nuclei formed by fusion of ^{48}Ca with ^{248}Cm. From our experiments on the synthesis of the heaviest elements we had two good reasons for a new search:

(1) Even the heaviest compound systems were produced unexpectedly cold close to the Coulomb barrier, a fact not accounted for in some of the previous superheavy experiments[1].

(2) Nuclei with formation cross sections well below nanobarns were identified at SHIP, so the halflife range limited to seconds in preceeding experiments could be extended down to the microsecond range at still high sensitivity.

We irradiated ^{248}Cm targets of 400 µg/cm², electrodeposited on a 250 µg/cm² Ti backing, with ^{48}Ca at energies close to the Coulomb barrier (table). The reaction products were detected with the same setup as used in the 107 and 109 experiments[1,2]: They were separated in-flight by SHIP, passed a time-of-flight path, and were implanted into the position sensitive detector array to measure implantation energy, α-decay, and/or spontaneous fission. From time-of-flight and energy the mass of the incoming recoils could be measured with a resolution of 10 % FWHM.

The analysis was performed in two parts:

(1) Search for spontaneous fission, justified by the assumption that each superheavy nucleus on its decay path has to pass the region of fission instability around Z = 112. We could not find any spontaneous fission event to be attributed to the decay of a superheavy nucleus. One uncorrelated pulse was registered at an energy of about 90 MeV. This energy is too low for a superheavy nucleus.

(2) Search for correlated αdecays. In contrast to the heaviest elements the decay chains from possible superheavy nuclei are not expected to end in transitions of known isotopes, hence the analysis was confined to the search of evaporation residue-correlated α-decays. Fig. 1 shows this correlation plot for a lower time limit of 13 µs. Due to the long correlation time of 312 s the correlations with masses near the target mass A = 248 are random correlations between elastically scattered target-like atoms and α-decays of products around A = 220: ^{219}Ra, ^{218}Rn, ^{217}Rn, ^{215}At, ^{214}Po. The isotopes in the vicinity of the target are longlived and, hence, not visible in this plot.

Candidates for superheavy nuclei should show up in the empty region above mass 270, about 2 standard deviations from the mass of the compound nucleus and in the decay energy range between 9 and 15 MeV. In the time range from 3 µs to 13 µs also no evidence for the decay of a superheavy atom was found.

Our analysis gives no positive indication for a decay from a superheavy atom, within the time ranges and cross section limits given in the table.

E_p [MeV/u]	E* [MeV]	Dose x10^{17}	Time [h]	σ_{sf} [nb]	σ_α [nb]
4.73	18±2	0.41	21	0.36	0.72
4.88	24±2	1.0	56	0.12	0.24
5.03	30±3	1.1	81	0.12	0.24
5.17	36±2	1.1	64	0.15	0.30
5.32	42±2	0.47	28	0.38	0.76
After irradiation			160		

Table: Results of the ^{48}Ca+^{248}Cm irradiation, the cross sections refer to 95 % confidence level. The time windows for analysis are 3 µs to 6 x 10^5 s for sf and 3 µs to 312 s for evaporation residue correlated α-decays (see also Ref. 3).

[1] G. Münzenberg et al., Int. Conf. on Actinides 81, 223, Pergamon Press (1982)

[2] G. Münzenberg et al., Z. Phys. A315 (1984) 145

[3] H. Gäggeler, this Scientific Report

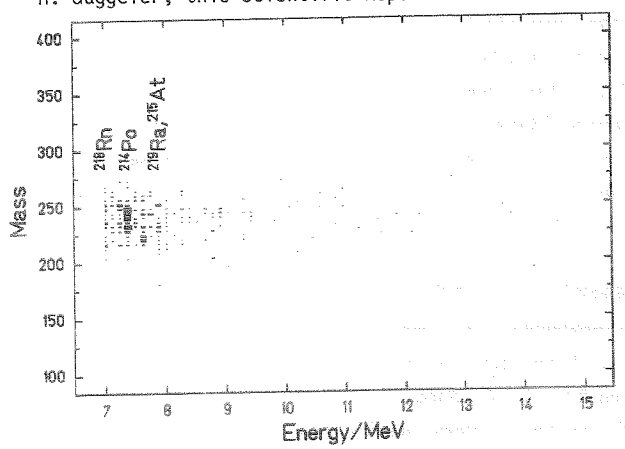


Fig. 1: Correlation plot for time and position ER correlated α-decays. Position window ± 0.8 mm, time windows: from 13 µs to 40 ms for decays during UNILAC-beam-bursts, to 312 s for decays in the beam pause.

Error Analysis in the Case of Poor Statistics [B]

K.-H. Schmidt
GSI Darmstadt

C.-C. Sahm, K. Pielenz, H.-G. Clerc
Institut für Kernphysik, TH Darmstadt

In experimental nuclear physics, often some sort of stochastic background is a possible source of errors. In the case of poor statistics, the probability that a random fluctuation of the background may simulate an event which looks like a true one must be treated exactly by use of Poisson's distribution.

Particularly, the technique of delayed coincidences is widely used for detecting time correlations between signals of different groups. Previously unknown isomeric states as well as new nuclides may be identified by linking them to the subsequent decays of their known daughter nuclei. In many cases, α decay cascades were used for this purpose.

The discovery of element 109[1] was founded on the observation of a single characteristic decay chain consisting of an evaporation residue, two consecutive α decays, and finally, a fission event. The error probability, e.g. the probability to interprete the observed event chain as a random fluctuation of the time distances between uncorrelated events, is approximately given by the following expression[2]:

$$P_{err} \approx T\,\lambda_1\,\lambda_2\,\lambda_3\,\lambda_4 \cdot \Delta t_{3,2} \cdot \Delta t_{1,3} \cdot \Delta t_{1,4} \approx 2 \cdot 10^{-18}$$

whereby the numerical values for the average counting rates λ_i of the different event groups, the total measuring time T, and the observed time differences $\Delta t_{1,i}$ as given in Ref. 1 were used.

The statistical errors of few observed events can be treated by the concept of the central confidence interval. The widely used standard deviation of a Gaussian distribution corresponds to a "standard" confidence interval with a confidence level of 68 %. In Fig. 1 fast converging expansions for the standard confidence limits of Poisson's distribution (to apply e.g. for cross sections) and of the exponential distribution (to apply e.g. for mean life times) are given.

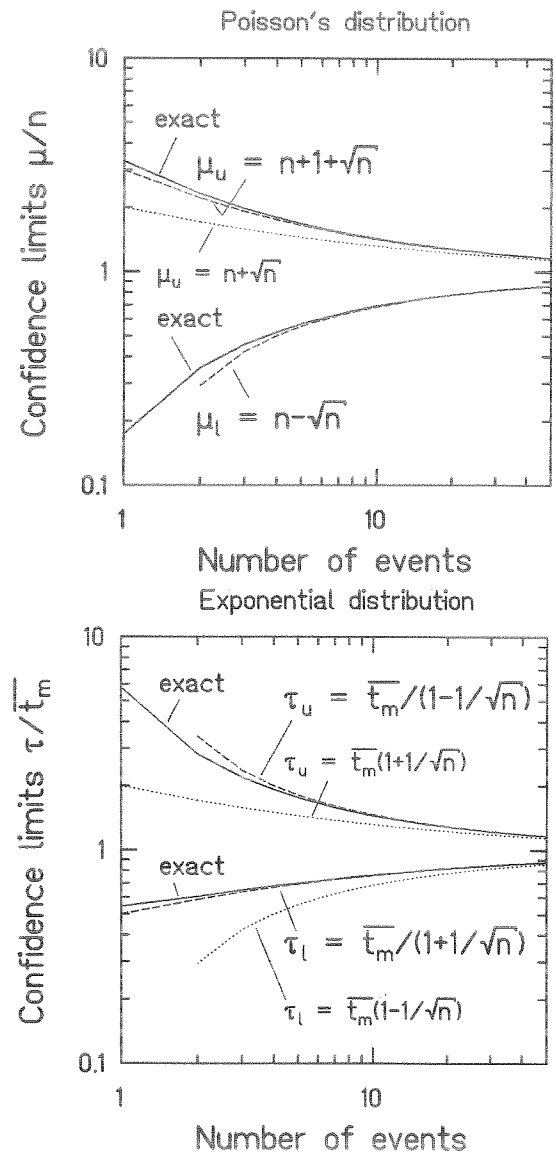


Fig. 1: Central confidence intervals for a confidence level of 68 % as a function of the number n_m of observed events.
(a): Poisson's distribution
(b): exponential distribution. In addition to the exact full curves the conventional approximations (dotted curves) and much more accurate approximations (dashed curves) are shown.

[1] G. Münzenberg, W. Reisdorf, S. Hofmann, Y.K. Agarwal, F.P. Heßberger, K. Poppensieker, J.R.H. Schneider, W.F.W. Schneider, K.-H. Schmidt, H.-J. Schött, P. Armbruster, C.-C. Sahm, D. Vermeulen, Z. Physik A309 (1982) 89 and Z. Phys. A315 (in print)

[2] K.-H. Schmidt, C.-C. Sahm, K. Pielenz, H.-G. Clerc, Z. Physik A315 (in print)

*Present address: Siemens AG, Otto Hahn Ring 6, 8000 München - 83

Fragmentation of the Intermediate Complex in the (^{48}Ca+^{248}Cm) Reaction at the Coulomb Barrier

P. Armbruster, Y.K. Agarwal, A. Ghiorso*, S. Hofmann, F.P. Heßberger, M. Leino*, K. Moody*, G. Münzenberg, K. Poppensieker, W. Reisdorf, K.-H. Schmidt, J.H.R. Schneider, W.F.W. Schneider, D. Vermeulen
GSI Darmstadt; *Lawrence Berkeley Laboratory, USA

SHIP selects reaction products emitted within a small cone of 3° in foreward direction and a preset velocity window. Besides evaporation residues we find elastically scattered target recoils and quasielastic transfer products near the target mass, together with products from more massive or fission-like reactions. The transmission of these particles is low, e.g. elastically scattered recoils have an estimated transmission of 2×10^{-4}.

In the search for SHE with ^{48}Ca on ^{248}Cm we found correlated α-decay chains. Fig. 1 shows the recoil correlated α-spectrum integrated over all irradiations performed. Fig. 2 gives two examples of decay chains found at 5.12 MeV/u. α-decays correlated to heavy nuclei are observed within the time window set for SHE all over the energy range from (6-17) MeV. In one of the chains shown, an energy of 16.79 MeV with a correlation time of 16 µs is seen. It arises from adding the unresolved decay energies of ^{216}Rn and ^{212}Po and reflects the halflife of ^{216}Rn. The independently measured mass value for all recoils entering the detector system allows to attribute the correlated events to nuclei with mass numbers in the range of (200-240). Only few uncorrelated α-decays coming from quasielastic transfer products, as ^{250}Cf and ^{246}Cm, are seen in the beam pause spectrum. 31 complete chains, as those in Fig. 2, together with about the same number of chains with missing pieces have been identified. All correlated events found in the time range (10^{-5}-10) s have been attributed to isotopes around ^{219}Fr.

The production rates of the isotopes identified are about 10^{-4} of the rates of elastically scattered target recoils. A production cross section for ^{218}Rn of about 80 µb is estimated in agreement with a radiochemical measurement[1]. The reaction sets in at 4.9 MeV/u, that is 25 MeV excitation energy in the intermediate complex. This energy equals the energy of the fusion barrier of ^{48}Ca+^{248}Cm without any 'extra-push'-energy. The yield distribution of the isotopes observed within the range (4.9-5.3) MeV/u does not change within our poor statistics. The proton to neutron ratio of the mass flow is neutron rich, $N_n/N_p \sim 2$, and the flow goes away from ^{248}Cm. Out of ^{48}Ca very neutron rich species are made, among which ^{73}Cu or ^{70}Ni will be found .. About 30 new isotopes between Ti and Cu should be accessible.

Near the barrier the intermediate complex fragments and follows after charge equilibration the drift versus symmetry. Out of the yield distribution in the elements Rn to Ra the excitation energy of the heavy fragment may be estimated. It allows for the emission of about 4 neutrons. The reaction partners stay rather cool. The total excitation energy of both fragments amounts to about 40 MeV. The positive Q-value of about 80 MeV is found in kinetic energy of the fragments and not in internal excitation energy. The exit channel configuration should be nearly as compact as the incoming (^{48}Ca+^{248}Cm) configuration at the barrier. The reaction observed resembles in this aspect the cold fragmentation in fission[2]. The rearrangement of nucleons leading to the detected isotopes seems to be much more gentle than predicted by the wall-window dissipation mechanism, which predicts an excitation energy for the main fragmentation channel of 152 MeV or about 13 nucleons emitted from the target-like fragment.[3]

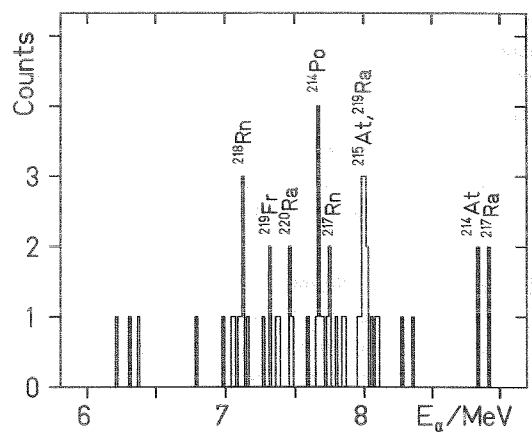


Fig. 1: α-spectrum of events correlated to isotopes in the range (200-240). Correlation time for particles 5 s.

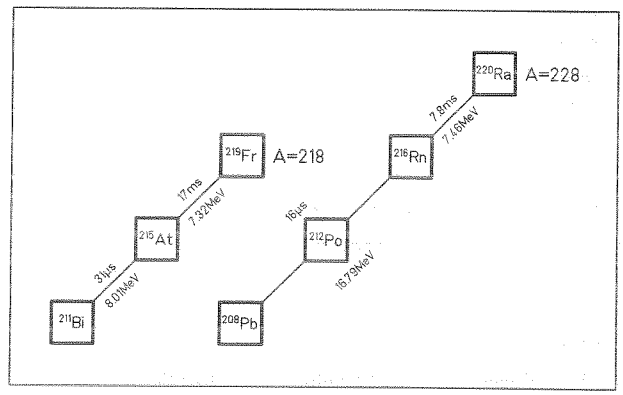


Fig. 2: α-decay chains identified, found at 5.12 MeV/u.

[1] H. Gäggeler, this report
[2] P. Armbruster, Lecture Notes in Physics 158 (1982) 1
[3] J. Blocki, private communication

Attempts to Produce Superheavy Elements in the ^{48}Ca + ^{248}Cm Reaction Applying On-Line Chemical Techniques

H. Gäggeler, W. Brüchle, M. Brügger, M. Schädel, K. Sümmerer, G. Wirth
GSI Darmstadt
C. Frink, N. Greulich, G. Herrmann*, U. Hickmann, N. Hildebrand, J. V. Kratz, N. Trautmann
Universität Mainz
K. J. Moody, G. T. Seaborg
Lawrence Berkeley Laboratory
H. Dornhöfer
Universität Göttingen

Fusion of ^{48}Ca with ^{248}Cm to form the compound nucleus $^{296}116^{188}$ is considered to be one of the most promising reactions for the synthesis of superheavy nuclei. Previous attempts to discover superheavy elements by this reaction failed, however. A possible reason is the relatively high excitation energy, some 40 MeV, introduced by choosing a projectile energy about 20 MeV above the interaction barrier[1]. More recent studies show that fusion in similar systems occurs at or even below the barrier.

These arguments led to a further attempt to search for superheavy elements by this reaction, however, at lower excitation energies of the compound nucleus $^{296}116$ of some 16 to 40 MeV. The whole program consisted of several independent experiments designed to cover

(i) the half-life region from microseconds to days in thin target experiments with the gas-filled mass separator SASSY at Berkeley and the velocity filter SHIP at GSI[2]

(ii) the half-life region from seconds to years in thick target experiments with radiochemical techniques carried out off-line to cover the long half-lives and on-line giving access to the short-lived species.

In a first series of experiments which were performed in October 1982 at LBL classical off-line chemical techniques were applied to separate spontaneously-fissioning superheavy elements from other reaction products. These attempts are described in the previous report[3]. In a second series of experiments performed in 1983 on-line chemical techniques were used to get access to much shorter-lived isotopes with half-lives down to the second range. These techniques, combinations of a gas-jet transportation system with several automated chemical separation procedures are described elsewhere[4-6]. The methods are based on the following predictions about chemical properties of superheavy elements around Z=114:

(i) Elements 112 through 117 should be volatile in their elemental state at temperatures up to about 1000 °C[4].

(ii) Some elements such as 112, 114 and 118 may even be volatile at room temperature[5].

(iii) Elements 108 through 116 should form strong anionic bromide complexes in aqueous solutions[6].

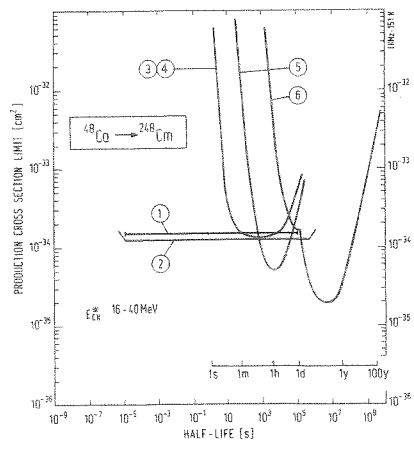
For each of these three separations a ^{248}Cm oxide target (1,72 mg/cm²) was bombarded by 233-248 MeV ^{48}Ca projectiles (measured energy range within the target) with beam integrals of (0.7-1.4)x10^{17} particles. The samples were counted on-line for alpha decay and spontaneous-fission events. The observed α-peaks can be attributed to isotopes of astatine, polonium, bismuth radon and lead. In all experiments no indication for any unknown α-line nor for any fission activity was found. In the Figure the resulting upper cross section limits on a 95 % confidence level are plotted for spontaneously-fissioning superheavy nuclei versus the half-life. In addition to the results from the chemistry experiments, the Figure also depicts the cross section limits obtained from the search experiments applying the SHIP and the SASSY systems[2].

*also GSI Darmstadt

References

1. see e.g. J.V. Kratz, Radiochim. Acta, 32, 25 (1983)
2. G. Münzenberg et al., this Scientific Report, p.
3. H. Gäggeler et al., GSI Scientific Report 1982, GSI-83-1, p. 69 (1983)
4. H. Dornhöfer et al., GSI Scientific Report 1981, GSI 82-1, p. 216 (1983)
5. N. Hildebrand et al., GSI Scientific Report 1982, GSI-83-1, p. 234 (1983)
6. W. Brüchle et al., this Scientific Report, p.

Figure:
Cross section limits for the production of spontaneously-fissioning superheavy elements, obtained with the
1: Small angle separating system SASSY (LBL)
2: Velocity filter SHIP (GSI)
3: High temperature on-line gas phase chemistry (GSI)
4: Low temperature on-line gas phase chemistry (GSI)
5: Quasi on-line solution chemistry (GSI)
6: Off-line chemistry, procedures as 3-5 (LBL, GSI)



A Search For Superheavy Elements Using the $^{48}Ca + ^{254}Es$ Reaction

R. W. Lougheed, J. H. Landrum, E. K. Hulet, J. F. Wild, R. J. Dougan, A. D. Dougan
Lawrence Livermore National Laboratory
H. Gäggeler, M. Schädel
GSI Darmstadt
K. J. Moody, G. T. Seaborg
Lawrence Berkeley Laboratory

We measured upper limits for the production of superheavy elements (SHEs), using the compound-nucleus reaction $^{48}Ca + ^{254}Es$. This combination permits the closest approach of any practical fusion reaction to the predicted island of stability at the 184-neutron shell. Theoretical calculations by Randrup et al.[1] and Fiset and Nix[2] predict that the maximum stability against spontaneous fission (SF) is at the closed 184-neutron shell for the superheavy elements. The much favored and studied $^{48}Ca + ^{248}Cm$ reaction[3,4] would produce element 116 with 178 neutrons after emission of two neutrons from the compound nucleus. The calculations of Randrup et al.[1] show, however, that the fission-barrier heights decrease very rapidly below 184 neutrons, becoming only 3 to 4 MeV at 178 neutrons, with corresponding SF half-lives of 10^{-16} y as compared with years or more at 184 neutrons. This sensitivity of SF half-life to neutron number for the SHEs dictates a very small choice of nuclear reactions that yield a product as close as possible to the 184-neutron shell. From this standpoint, the $^{48}Ca + ^{254}Es$ reaction is the most favorable compound-nucleus reaction currently available. Randrup et al.[1] predict fission barriers of greater than 6 MeV for the 2n out-product of the einsteinium reaction, with SF half-lives comparable to the alpha half-lifes.

We bombarded a 5-μg/cm² ^{254}Es target with ^{48}Ca at the SuperHILAC accelerator at the Lawrence Berkeley Laboratory (Berkeley, CA). There were four bombardments, each lasting several hours, for a total of 7.7×10^{15} ^{48}Ca particles. Two ^{48}Ca bombarding energies were used: 238 and 246 MeV. These energies are 2 MeV under and 6 MeV over the calculated Coulomb barrier, respectively. They were chosen to minimize excitation energy in the compound nucleus in order to minimize fission and the number of neutrons emitted during de-excitation.

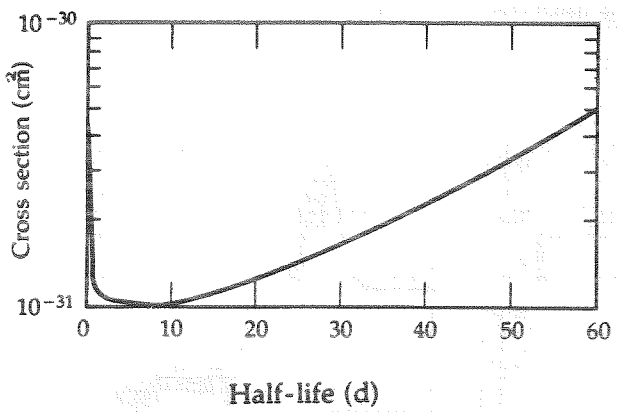
We collected recoils from the einsteinium target on metal foils, which were then chemically processed to yield SHE fractions for SF counting. Two types of chemistry were applied based on predicted properties of SHEs[5]. First, a solution chemistry procedure using sulfide precipitation and cation exchange chromatography and, second, a gas-phase chemistry was performed[5]. The time needed to run the chemical separations were about 0,5 - 2 hours and typical chemical yields for homologues of SHEs were 25 through 60%. Both types of chemistry provided excellent decontamination from the actinide elements, whose isotopes interfere by also decaying by SF. In over two months of counting, we observed no SF events in samples from either of the chemistries. By assuming the detection of two SF events in coincidence and a 50% chemical yield, we determine that the cross section for SHE production is $\leq 5 \times 10^{-32}$ cm² for half-lives of a few days for all bombardments. The Figure shows the half-life vs cross-section limits we obtained for the two solution-chemistry experiments only.

We believe that the $^{48}Ca + ^{254}Es$ reaction deserves further attention as a pathway to SHEs. The proposed production of 40 μg of ^{254}Es at Oak Ridge National Laboratory could produce a target 100 times larger than that used in our experiments. With a larger target and increased bombardment times, cross sections of about 10^{-35} cm² are achievable.

References

1. J. Randrup et al., Physica Scripta 10A, 60 (1974)
2. E. O. Fiset and J. R. Nix, Nucl. Phys. A193, 647 (1972)
3. H. Gäggeler et al., this Scientific Report, p.
4. G. Münzenberg et al., this Scientific Report, p.
5. see J. V. Kratz, Radiochim. Acta, 32, 25 (1983)

Figure: Cross-section limits for the production of SHEs as a function of half-life, from solution-chemistry experiments.



Search for Volatile Reaction Products in the Reaction $^{48}Ca + ^{248}Cm$

N. Hildebrand, C. Frink, N. Greulich, U. Hickmann, W. Kieling, N. Trautmann, G. Herrmann
Institut für Kernchemie, Universität Mainz

H. Gäggeler, K. Sümmerer, G. Wirth
GSI, Darmstadt

For the search of superheavy elements in the reaction $^{48}Ca+^{248}Cm$ on-line chemical methods, based on the predicted volatility of the elements 112-118 and on the formation of stronganionic bromide complexes of the elements 108-116 have been applied[1]. The elements 112, 114 and 118 may even be volatile at room temperature and therefore a cryogenic chamber equipped with an annular surface barrier detector and a solar cell[2] has been used for the detection of very volatile reaction products. The reaction products from the bombardment of 1.72 mg/cm^2 ^{248}Cm-oxide with 233-248 MeV ^{48}Ca projectiles were transported with an argon gas-jet using pure argon to the cryo-system. In this way the transport efficiency for non-volatile elements was decreased. The volatile products were passed through a quartz tube filled with quartz powder (64-144 mesh/cm^2) and heated to 1250 K to trap the clusters with attached non-volatile products formed during the irradiation. In a second quartz tube filled with tantalum foil (T=1000 K) traces of water were removed. After passing these traps the transport gas contains only noble-gases and very volatile products which were condensed together with the heavy noble gases in the cryo-system on a cooled solar cell (T≈50 K) operating as a fission fragment detector. With an annular surface barrier detector installed in front of the solar cell E_1/E_2 fission fragment measurements in coincidence with the photovoltaic cell and α-spectroscopy were carried out. Furthermore single fission events could be measured with the ring detector. During the irradiation time α-spectra were collected and afterwards multiscaling measurements were performed to follow the decay of the deposited activities. Fig. 1 shows an α-spectrum measured on-line for 23 h during the deposition of the gaseous products. The main activities in the α-spectra can be assigned to the radon isotopes 210-222 and their decay products. From the evaluated activities after the end of irradiation the production cross sections for the radon isotopes ^{210}Rn, ^{211}Rn, ^{212}Rn, ^{219}Rn, ^{220}Rn, ^{221}Rn, ^{222}Rn were obtained. The results are shown in fig. 2.

During the whole experimental period no spontaneous fission event was observed yielding a cross-section limit for the production of spontaneously-fissioning superheavy elements as reported in another contribution[1] to this report.

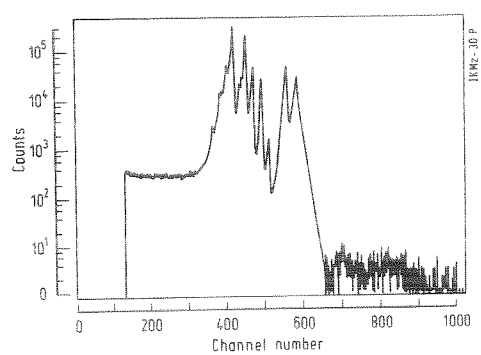


Fig. 1: On-line α-spectrum of the gaseous products in the reaction $^{48}Ca+^{248}Cm$ measured for 23 h

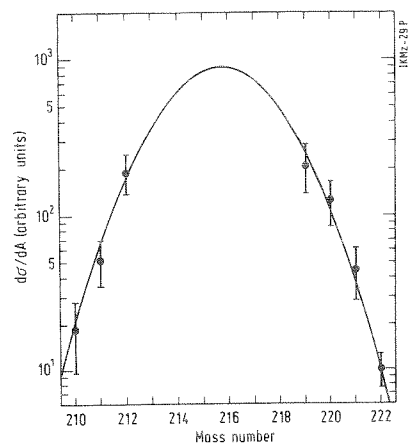


Fig. 2: Cross-sections for the production of radon isotopes in the reaction $^{48}Ca+^{248}Cm$

[1] H. Gäggeler et al., this Scientific Report 1983, p.
[2] N. Hildebrand et al., GSI Scientific Report 1982, GSI 83-1, p. 234 (1983)

B

Excitation Functions for Heavy Actinides from the Reaction of ^{48}Ca with ^{248}Cm

W. R. Daniels, M. M. Fowler, D. C. Hoffman
Los Alamos Scientific Laboratory
W. Brüchle, M. Brügger, H. Gäggeler, M. Schädel, K. Sümmerer, G. Wirth
GSI Darmstadt
Th. Blaich, G. Herrmann*, J. V. Kratz, M. Lerch, N. Trautmann
Universität Mainz
D. Lee, K. J. Moody, G. T. Seaborg
Lawrence Berkeley Laboratory
H. R. von Gunten
Universität Bern

In 1982, a collaboration was started with the goal of trying once again to produce superheavy elements from the reaction of ^{248}Cm with ^{48}Ca projectiles at energies near the Coulomb barrier[1,2]. In addition we measured the excitation functions for the production of the actinides formed during such bombardments.

The target of curium oxide was prepared by stepwise electroplating and contained 1.7 mg/cm² of Cm(96.5% ^{248}Cm, 3.5% ^{246}Cm). The target was mounted in a gas cooled target holder[2]. A gold or copper catcher foil of about 6 mg/cm² was placed behind the target to collect recoiling products. The ^{248}Cm target was irradiated with $E_{lab.}$ = 239, 263 and 288 MeV ^{48}Ca projectiles. The energy loss within the target was measured to be about 16 Mev. After each bombardment, the catcher foils were dissolved and the actinides Pu, Bk, Cf, Es and Fm were chemically isolated and final samples were prepared on discs as described elesewhere[3,4]. These samples were analysed for alpha, spontaneous fission and gamma activities. The chemical yields for the actinide separations ranged from 50 to 75%.

The evaluated cross sections for the production of isotopes of Pu, Bk, Cf, Es and Fm are listed in Table I. The peak of the excitation functions for Cf, Es and Fm appear to occur at the middle energy of 263 - 247 MeV (within the target) which is about 20 MeV above the calculated barrier of 236 MeV. This observation is in agreement with estimates[5] based on ground state Q-values and the Coulomb barriers of the initial and final systems, which show that the excitation energy, E^*, for these products at the Coulomb barrier are negative by more than 10 MeV.

The yields for the Bk isotopes which are produced most likely in quasi-elastic reactions and for the below-target transfer isotopes of Pu are highest at the highest energy.

Independent of the bombarding energy, the mass distributions for Pu, Bk, Cf, Es, and Fm peak at the most probable mass numbers A_p of 243, 249, 250, 252 and 254, respectively. These maxima correspond within one mass unit to the predicted primary most probable masses A_p calculated on the basis of potential energy considerations[6]. This tends to support the general idea of a binary transfer mechanism which results in a nucleus with low E^*, i.e. a "cold" nucleus which is not immediately destroyed by prompt fission or particle emission.

References

1. G. Münzenberg et al., this annual report
2. H. Gäggeler et al., this annual report
3. D. Lee et al., Phys. Rev. C 25, 286 (1982)
4. M. Schädel et al., Phys. Rev. Lett. 41, 469 (1978)
5. D. C. Hoffman and M. M. Hoffman, Report LA-UR-82-824, March, 1982
6. H. Freiesleben and J. V. Kratz, Physics Reports, in press

*also GSI Darmstadt

TABLE I. Cross sections for the production of heavy actinides in the bombardment of ^{248}Cm with ^{48}Ca

		223-239(MeV)[a] Cross section (μb)	s[b] (%)	247-263(MeV)[a] Cross section (μb)	s[b] (%)	272-288(MeV)[a] Cross section (μb)	s[b] (%)
Pu	243	295	17	515	17	1965	18
	245	113	19	261	17	1050	19
	246	22	50	115	18	413	31
Bk	245	11.7	22	39	15	66.5	19
	246	73	16	272	14	482	15
	248m	730	17	1690	17	2680	16
	250	690	11	2010	11	2920	11
Cf	246	0.25	5	1.4	2	1.0	18
	248	101	9	238	9	209	6
	250	413	22	2540	8	1935	2
	252	50.9	21	231	11	224	16
	253	0.81	17	8.2	21	4.0	17
	254	0.32	28	1.5	10	1.0	23
Es	252	9.46	7	28.4	4	24.3	5
	253	4.08	17	10.5	9	7.8	13
	254m	0.74	30	1.8	6	1.4	16
Fm	252	0.02	38	0.09	30	0.06	19
	254	0.28	8	0.94	6	0.71	8
	255	0.21	7	0.90	2	0.62	10
	256	0.06	30	0.25	10	0.14	17

a) Range of projectile energy within the target (laboratory system)

b) Statistical standard deviation based on the analysis of the decay data.

Gamma-Ray Catalog [G]

U. Reus and W. Westmeier
Institut für Kernchemie, Universität Marburg

The objective of this project has been the compilation and regular updating of a catalog comprising all available information on gamma-rays and X-rays from the radioactive decay of nuclides. The catalog is designed for use in the quantitative assay of radionuclides, i.e. cross-section measurements, activation analysis etc. Information about the structure and layout of the tables has been reported earlier[1,2].

To summarize, Part I of the catalog is a listing of over 32.000 gamma-rays and X-rays ordered by increasing energy. It is designed as a tool for the identification of photons from unknown origin. Part II of the catalog is ordered by mass number A and nuclear charge Z. It contains the complete data sets for 2526 nuclides and isomers, i.e. more than 47.000 gamma-ray and X-ray energies, each data set including important information on the decay of that nuclide, references, comments etc.

In view of the world-wide demand for the first edition of the catalog (published as GSI-report 79-2), which by far exceeded the limited number of copies available, we decided to publish a second, updated edition of the catalog in a journal. Works on this project were completed in 1983.

The revised edition includes published experimental results which we received before June 30, 1982. Twenty major journals have been scanned regularly and more than 500 publications have been considered for the revision. In addition, about 100 mass chains have been completely revised by means of recent evaluations published in Nuclear Data Sheets. A total of about 200 recently discovered nuclides and nuclear isomers have been introduced. The total number of photon energies listed in the catalog increased by over twenty percent. In toto, most data sets have been revised, the changes made ranging from minor in most cases to major in a few cases.

As reported earlier[1], information on X-rays emitted in radioactive decay was introduced. Since experimental results for X-ray intensities are rarely reported, most data had to be calculated from the decay schemes, using theoretical values for conversion coefficients, fluorescence yields, EC/β^+ ratios etc. As a result of these calculations, which required great effort, X-ray data are now available for the majority of those nuclides whose decay schemes are well established. Also, information on annihilation radiation is included for those nuclides where no major gamma-rays or X-rays can be measured.

The revised catalog has been published in :
Atomic Data and Nuclear Data Tables, Volume 29, (1983) 1 - 406.
Negotiations with the publisher (Academic Press, Inc.) on the commercial distribution of computer tapes containing all data sets for the catalog are in progress.

The authors wish to express their gratitude to Prof. P. Patzelt for his support of the project and to A. Merklin for his careful work in transcribing the data into the computer. Generous support from our computer center (ZRA der Philipps-Universität, Marburg) is acknowledged.

[1] U. Reus and W. Westmeier, GSI-Report 83-1, 71 (1983) and references therein.

[2] U. Reus, W. Westmeier, IAEA-Report INDC(NDS)-143/GP, 131

What do we know about the surface of nuclear charge and mass densities?

Daniel Berdichevsky, GSI Darmstadt
and
Ulrich Mosel, Institut für Theor. Physik, Universität Giessen

The surface of the mass density $\rho(r)$ and the neutron excess in the surface region play an important role in the description of dynamic processes and calculation of masses. For the charge density there exists now a large numbe of data with very high accuracy in the surface [1-3], enabling us to systemmatically study the charge densities for nuclei along the valley of β -stability[2,3]. The application of these informations to the surface width of the mass density $\rho(r)$ is, however, in no way trivial[3] and existing experimental information on mass densities is promising but limited to too few systems [4].

A detailed analisis in the framework of the spherical constrained HF+BCS-model is in so far justified. The main results of our study are: (a) the Skyrme forces Ka (ref. 5), SKM (ref. 6), and SV (ref. 7) reproduce with ≈95% accuracy the experimental pattern of the nuclear charge densities [3]. (b) The Skyrme-type forces[3] show an increase of the surface width with the ratio $\beta/K^{1.7}$, where $\beta=9t_1-5t_2$ (Skyrme-surface-parameter) and K is the nuclear matter compressibility (see fig. 1). (c) There are a small reduction of the proton width (≈2%) with increasing number of nucleons A (for A≥160) and relative large "shell" structures in the neutron width as a function of A. (d) the very non local force SV predicts an almost equal width for proton and neutron in contrast to the increase of the difference between the neutron and proton width with increasing nucleon asymmetry N > Z for the force Ka and SIII (see fig. 2). (e) The surface width of the mass densities is well given by the weighted sum of the neutron and proton surface widths.

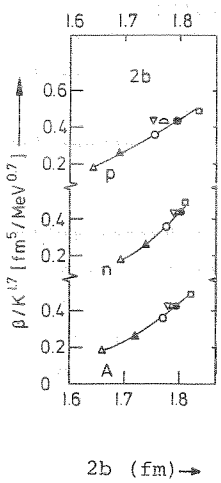


Fig. 1: For the 10 "spherical" nuclei ^{40,48}Ca, ^{54}Fe, $^{58-64}$Ni, ^{70}Zn, ^{90}Zr, and ^{208}Pb the surface parameter $\beta/K^{1.7}$ (ref. 3) is plotted as a function of twice the averaged surface width
b_q(SIII)(triangle),
b_q(SII*)(filled-triangle),
b_q(SIV)(circle)
b_q(SKM)(inverted-triangle),
b_q(Ka)(half-circle),
b_q(SV)(square). q= A, n, and p for the mass, neutron and proton surface width.

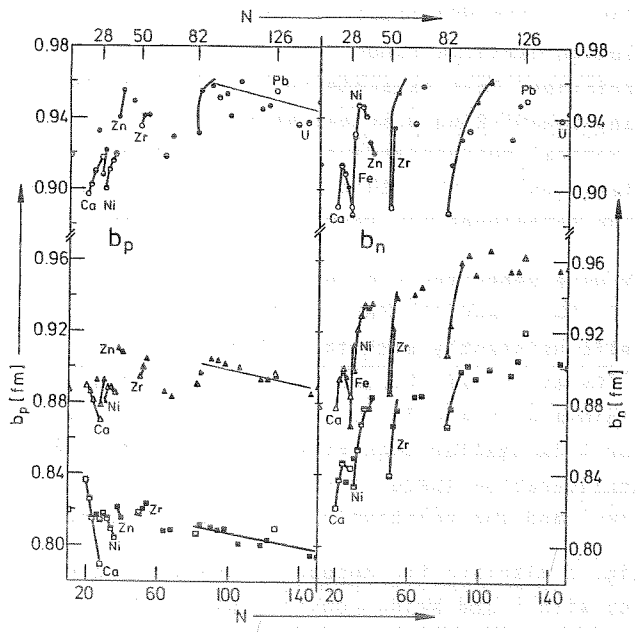


Fig. 2: Given are the proton-(left) and neutron-widths(right) b from selfconsistent HF+BCS-calculations with the forces SV (upper most part of the figure), Ka (center), and SIII (lowest part of figure) for nuclei along the valley of - stability as a function of neutron number. The b values for the isotopes Ca, Ni, Fe, Zn, and Zr are joined with solid lines. The curves emphasize the strong shell structure effects in b_n, b_p as a function of N and the decrease of the proton width for N > 82.

1) G.Fricke and J.Emmrich, private communications, 1980-1982
2) J.Friedrich and N.Voegeler, Nucl.Phys. A373(1982)192 and refs. therein
3) D.Berdichevsky,thesis Giessen,1982 and refs. therein; D. Berdichevsky and U.Mosel, Nucl. Phys. A410(1982)205, and to be published
4) G.H.Hoffmann et al., Phys. Rev. C21(1980)1488; E.Friedman, H.G.Gils, and H.Rebel, Phys. Rev. C25(1982)1551
5) H.S. Köhler, Nucl. Phys. A258(1976)301
6) H.Krivine,J.Treiner, and O.Bohigas, Nucl. Phys. A336(1980)155
7) M.Beiner et al., Nucl. Phys. A238(1975)296

Influence of Deformation on Mono- and Quadrupole Pairfields

B

K. Mühlhans and U. Mosel

Institut für Theoretische Physik, Universität Giessen

New experimental machines like the Darmstadt-Heidelberg Crystal Ball enable the experimentalists to obtain high class spectroscopical data. These data allow, at least in principle, a spectroscopical determination of pair matrix elements. It is, therefore, interesting to investigate more appropriate residual interactions than the standard monopole force.

The dependence of the strength of higher multipole pair field components on the neutron and proton number has been studied in ref. 1 where the deformation was kept fixed. The open question that, therefore, remains is the influence of the deformation on the pair fields.

For the calculations we have used a Nilsson Hamiltonian for the one body part and a Surface Delta Interaction generating the pair field which is treated selfconsistently[1,2]. The solutions of the HFB-equations were calculated including particle number projection before the variation. This is achieved by modifying the Mang-Samadi-Ring gradient method to stay in the canonical representation in each step of the iteration[2]. Within this representation projection techniques are very easily performed[2].

We have generated a grid with a step width of 0.01 for ε and 10^0 for γ calculating each point selfconsistently with the parameters fixed for ^{158}Dy as in ref. 2. The energyplane shows a minimum at $\varepsilon = 0.18$, $\gamma = 0^0$ (fig. 1). The value for ε is smaller than expected due to the small configuration space (N=5,6 neutrons, N=4,5 protons) and the relatively large pairing strength.

Fig. 2 displays the monopole strength decreasing with ε and being constant with γ in accordance with the well known fact that a monopole pair field prefers spherical configurations. The Δ_{20} component of the pair field increases with ε and decreases with γ (fig. 3). At $\varepsilon \approx 0.2$ we find some shell effects. In general the Δ_{20} component follows the Y_{20} component of the potential. This is similar for the $\sqrt{\Delta_{22}^2+\Delta_{2-2}^2}$ part of the pair field (fig. 4) which increases with ε and γ. The total quadrupole pair field $\sqrt{\Delta_{20}^2+\Delta_{22}^2+\Delta_{2-2}^2}$ is γ independent and increases with ε (fig. 5). It has, therefore, no influence on the γ value of the equilibrium deformation as long as one treats Δ_{20} and Δ_{22} with the same strength parameters as given by the SDI.

[1] K. Mühlhans, M. Diebel, K. Neergård, and U. Mosel, Phys. Lett. 120B, 44 (1983)

[2] K. Mühlhans, K. Neergård, and U. Mosel, Nucl. Phys. A, in press

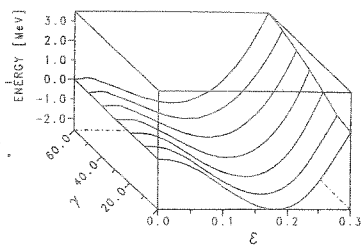


Fig. 1: Selfconsistently calculated energyplane for ^{158}Dy at I=0. Parameters as in ref. 2.

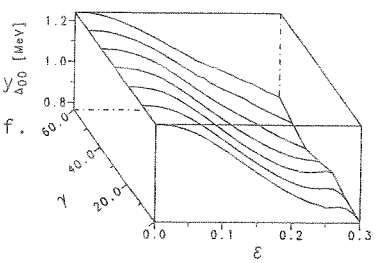


Fig. 2: Monopole pairfield (neutrons) for ^{158}Dy at I=0. Parameters as in ref. 2.

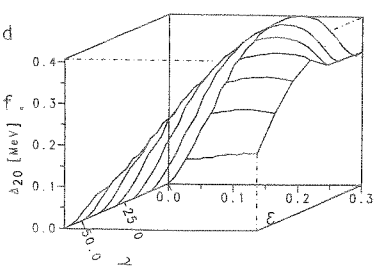


Fig. 3: Quadrupole pairfield Δ_{20} (neutrons) for ^{158}Dy at I=0. Parameters as in ref. 2.

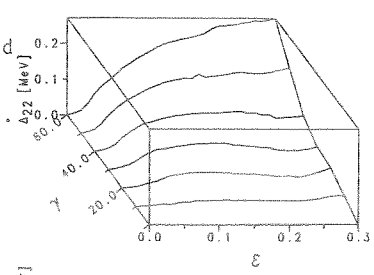


Fig. 4: Quadrupole pairfield $\sqrt{\Delta_{22}^2+\Delta_{2-2}^2}$ for ^{158}Dy at I=0. Paramters as in ref. 2.

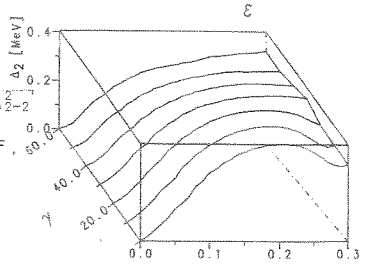


Fig. 5: Total quadrupole pairfield $\sqrt{\Delta_{20}^2+\Delta_{22}^2+\Delta_{2-2}^2}$ for ^{158}Dy at I=0. Parameters as in ref. 2.

Study of the Coriolis Attenuation for Odd-A-Nuclei

Eva M. Müller and U. Mosel

Institut für Theoretische Physik, Universität Giessen

During the last years a lot of rotational bands of even-even as well as of even-odd nuclei in the rare earth region have been studied both at GSI[1] and elsewhere. This great amount of empirical data has encouraged us to undertake a systematic study of various isotopes in this region.

We have used a modified quasiparticle-plus-rotor model, which was tested in the actinide region with good success[2]. Our model includes an interaction between the core and the quasiparticle of the form $(1-\alpha)\vec{R}\vec{j}/\Theta$, which corresponds to a spin dependence of the quasiparticle energies. It attenuates the Coriolis force and the recoil energy simultaneously[2]. The core energies are taken from the experiment by averaging the rotational band energies of the neighbouring nuclei.

The special form of our interaction leads to an increased Coriolis attenuation for increasing moments of inertia as usually present for larger spins. An explicit investigation of the spin dependence of the Coriolis force for odd-even nuclei has shown that especially the unfavoured bands need more attenuation at high angular momenta, if the core and recoil energy are treated in the way described in ref. 2 and 3.

Furthermore, the Coriolis interaction was found to depend also on the neutron number N and deformation β. At the beginning of the rare earth region the spin dependence of the quasiparticle energies increases with increasing neutron number and deformation β. This means that the Coriolis attenuation becomes weaker for the lighter isotopes. This behaviour was found for odd neutron as well as for odd proton nuclei (see fig. 1 and 2, where α represents the Coriolis attenuation factor).

[1] e.g.: H. Emling, E. Grosse, D. Schwalm, R.S. Simon, H.J. Wollersheim, D. Husar, and D. Pelte, Phys. Lett. 98B, 169 (1981)

[2] E.M. Müller and K. Neergård, Phys. Lett. Vol. 120B, 280 (1982)

[3] E.M. Müller and U. Mosel, submitted to Nucl. Phys.

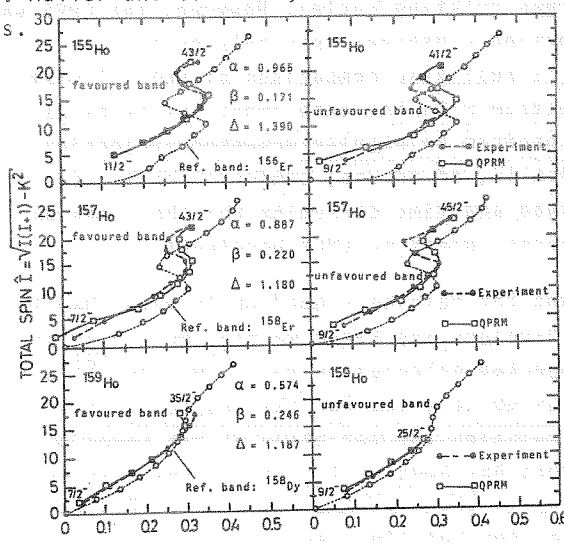


Fig. 1: Total spin $\hat{I} = \sqrt{I(I+1)-K^2}$ (K=7/2) versus the angular frequency ω for ^{155}Ho, ^{157}Ho, and ^{159}Ho. For each nucleus the experimental and theoretical $\hat{I}(\omega)$ is shown for the favoured and unfavoured band in the odd-A-nucleus in comparison to $\hat{I}(\omega)$ of the core. For the even-even nuclei $\hat{I}$ is defined by $\hat{I} = \sqrt{I(I+1)}$.

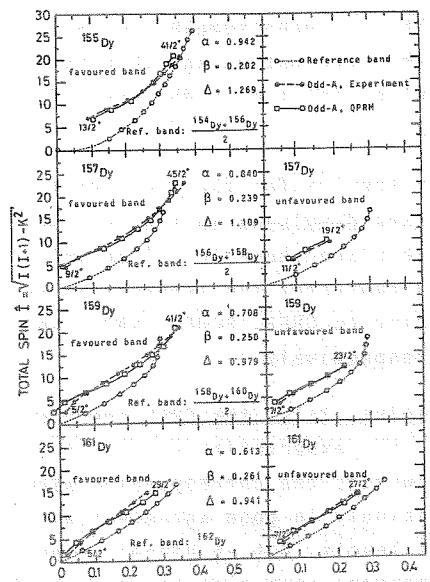


Fig. 2: Angular momentum $\hat{I}$ versus the frequency ω for ^{155}Dy, ^{157}Dy, ^{159}Dy, and ^{161}Dy. For each nucleus the same quantities as in fig. 1 are shown.

Yrast Spectra of ^{158}Dy and ^{168}Yb in the Spin Projected Cranked HFB Approach

A. Ansari*, U. Mosel, and E. Wüst

Institut für Theoretische Physik, Universität Giessen

The cranked Hartree-Fock-Bogoliubov (CHFB) theory has been very successful in providing a qualitative understanding of the structural changes with the increase of spin for the deformed rotating nuclei. However, the CHFB wavefunction conserves spin only on the average and for a realistic comparison of the calculated spectrum with the experiments it is necessary to perform an angular momentum projection[1] which is, of course, computationally very involved and time consuming for the triaxial time-reversal breaking CHFB wavefunctions.

Using the pairing + quadrupole model Hamiltonian of Baranger and Kumar we have performed spin projected calculation for ^{158}Dy and ^{168}Yb for spins up to I=16. For the projected CHFB (PCHFB) calculation the variation of the shape parameters has been restricted to the selfconsistency at the cranking level only. But for the axial non-rotating case (ω=0) the variation after projection (VAPO) is carried out with respect to the deformation parameter β and the proton and neutron pairing gaps. In another set of calculation denoted by VAPOM we have modified the quadrupole and pairing interaction strengths (all in MeV) as $\chi = 72/A^{1.4}$, G_p=26/A, G_n=21/A. This is done somewhat arbitrarily to increase the deformation and thereby the effective moment of inertia to decrease the E_2-E_0 separation.

The energy spectra for the Yrast states of ^{158}Dy and ^{168}Yb are displayed in fig. 1. The experimental levels are shown in column (c) and others (a) to (e) represent the theoretical results corresponding to CHFB, PCHFB, VAPO, and VAPOM methods, respectively.

At lower spins, I≤10, the CHFB energies which are simply the expectation values of the Hamiltonian w.r.t. the corresponding wavefunctions, are surprisingly in good agreement with the experimental levels. But at higher spins the CHFB spectrum becomes much more compressed. On the other hand the PCHFB spectrum becomes very much spread at lower spins and produces a strong backbending feature at I=12. The strong backbend should be related to the fact that usually cranking overestimates the effect of alignment. Using the above mentioned modified interaction this effect can be quite reduced.

Until I=10 the VAPO and PCHFB results are very close to each other but at higher spins the former is not favoured. The VAPOM results show a good improvement for ^{158}Dy. For the non-backbender ^{168}Yb the PCHFB results are quite reasonable but the VAPOM calculation has not shown enough improvement (VAPO has not been done).

[1] K. Hara, A. Hayasi, and P. Ring, Nucl. Phys. A385, 14 (1982).

* Permanent address: Institute of Physics, Bhubaneswar, India

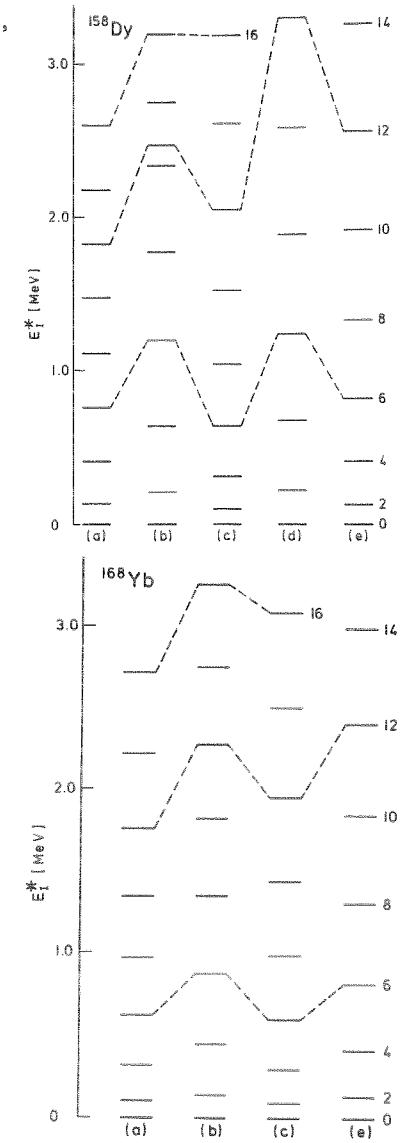


Fig. 1: Energy spectra through various approaches.

Low-Spin Structure of the S-Band [G]

A. Ansari, U. Mosel, and E. Wüst

Institut für Theoretische Physik, Universität Giessen

The backbending behaviour of the rare-earth nuclei is understood to be caused by the crossing of the ground band with the $\nu i_{13/2}$ aligned s-band. That is, the high-spin rotational states above the band crossing region are built on the aligned single particle configuration. Treating the cranked Hartree-Fock-Bogoliubov (CHFB) solutions to provide the intrinsic wavefunctions we can construct various rotational bands through the method of angular momentum projection from each cranked wavefunction. Particularly, the projected band corresponding to the aligned configuration can be identified as the s-band. We propose to investigate its properties as experimentally the low-spin states of this band are not yet established. Only for the isotones ^{164}Er and ^{166}Yb it has been extended[1] so far down to the I=8 state.

Recently we have done some number as well as spin projected CHFB calculation[2] for a few rare-earth nuclei employing the pairing+quadrupole model Hamiltonian of Baranger and Kumar[3]. The CHFB states can be designated by the value of the constrained spin $I_x=\langle\hat{J}_x\rangle=\sqrt{I(I+1)}$, where X is the cranking axis. Here we want to report our results for ^{158}Dy and ^{164}Er. For $I_x<12$ the excitation energy is parabolic in I with the minimum always at the I=0 state. Then suddenly for I_x=14-16 the energy minimum of the still parabolic curve is shifted to I=10 and 8, for ^{158}Dy and ^{164}Er, respectively, where I=10 and 8 are approximately the amount of the neutron aligned single-particle spins. This shift implies that the lower spin members of the s-band lie at higher excitation energies than the I=8-10 state.

To elucidate the microscopic structure of these states further we have calculated g-factors, whose variation with spin is displayed in fig. 1 for some CHFB states. The curves for ^{158}Dy are labelled by I_x=0,4,12, and 14 and that for ^{164}Er only for I_x=14 by Er. For I_x=0 the g-factor is a constant and for higher I_x values it becomes smaller with some weak I-dependence. But at I_x=14 i.e., corresponding to the s-band, there is a drastic decrease of g at I=2. The dashed curve shows the neutron contribution to the total g-factor for the s-band. This means that the remaining negative contribution comes from the protons that thus rotate in a sense opposite to that of the $i_{13/2}$ neutrons. The single particle $\nu i_{13/2}$ contribution and the collective spins are, therefore, antialigned against each other in the lower part of the s-band; the insert in the figure indicates their vector coupling scheme. Using the spin projected wavefunction we have calculated the proton contribution (I_p) to the total I and the former are -1.49, -1.40, -1.02, -0.52, 0.04, 0.63, 1.25, and 1.89 for I=2 to 16, respectively. In fact, the microscopically calculated proton contribution to the total g-factor for the s-band is almost entirely given by the collective value of I_p/I.

Thus, in the low spin part of the s-band the single-particle and collective angular momenta seem to be in an antialigned phase and large (negative) g-factors should help as a signature in an experimental search for the low spin members of the s-band.

[1] C.A. Fields et al., Phys. Lett. 130B, 157 (1983)

[2] E. Wüst, A. Ansari and U. Mosel, to be published

[3] M. Baranger and K. Kumar, Nucl. Phys. A110, 490, 529 (1968).

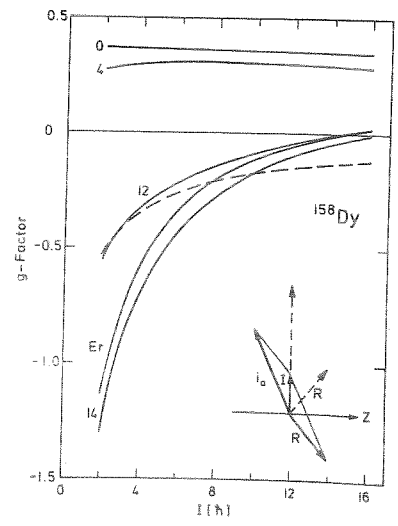


Fig. 1: g-factors for various bands as discussed in the text.

Effect of Number Projection on the Cranked HFB Results

A. Ansari, K. Mühlhans and E. Wüst

Institut für Theoretische Physik, Universität Giessen

The most well known weakness of the cranked Hartree-Fock-Bogoliubov (CHFB) theory is that the nucleon number and the angular momentum are conserved only on the average. Using the standard projection techniques, in principle, one can restore the symmetries, though, computationally these are very involved and time consuming calculations. Recently we have done such calculations[1] and we present here some results for a typical rare-earth nucleus ^{158}Dy to demonstrate the effect of number projection. Using the pairing+quadrupole model Hamiltonian of Baranger and Kumar[2] the CHFB equations are solved selfconsistently with respect to the nuclear shape parameters. The calculational details can be found in ref. 1 and other references cited therein.

It is well known that for a given pairing interaction strength, G, the gap parameter

$$\Delta = \sqrt{G}\ E_{pair}$$

becomes larger after the number projection compared to the usual cranking value. Δ can be renormalized to the latter value by reducing the value of G. We have used

$$G_p = 26/A[\text{MeV}], \quad G_n = 21/A[\text{MeV}]$$

instead of the Baranger-Kumar values of 27/A and 22/A, respectively.

In Fig. 1 we show the alignment plot where the proton and neutron contributions I_x^p and I_x^n, respectively, to the total I_x are plotted as a function of the cranking frequency ω. We can see that for the same amount of I_x^p or I_x^n the corresponding ω is slightly larger for the variation after number projection (VANP) case compared to the variation without projection case (VWNP), as in the former the amount of pairing is somewhat larger. However, the difference is small and there is no shift in the position of the critical spin where the backbend occurs in the VWNP calculation.

We have also computed the g-factors as

$$g_I = \langle \mu_x \rangle / \sqrt{I(I+1)}$$

where the μ_x denotes the X-component of the usual magnetic dipole moment operator. The variation of g-factor as a function of spin I_x is displayed in fig. 2. The full curve is the result of the VWNP calculation and the solid squares correspond to the VANP case. The triangles denote the values for the variation before number projection (VBNP) calculation and where the pairing strengths have not been modified. We see that in general all the points are following the full curve and the effect of number projection is insignificant. This result also holds if we include the quadrupole pairing[3].

Thus we may conclude that, at least within the CHFB approach, the backbending behaviour and variation of g-factors as a function of spin are not sensitive to the number projection.

[1] A. Ansari, E Wüst and K. Mühlhans, Nucl. Phys. A in press

[2] M. Baranger and K. Kumar, Nucl. Phys. A110, 490, 529 (1968)

[3] K. Mühlhans, K. Neergård and U. Mosel, Nucl. Phys. A, in press

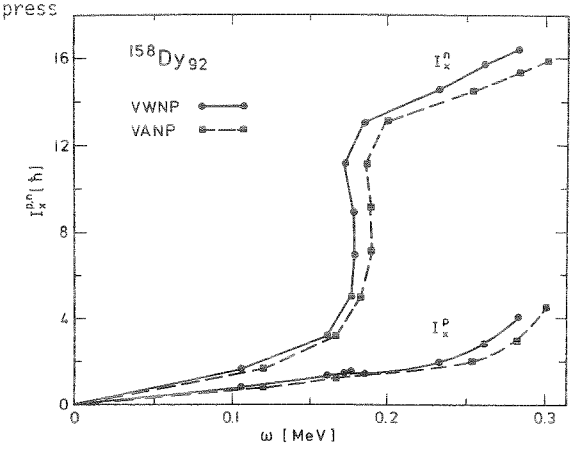


Fig. 1: Alignment plot.

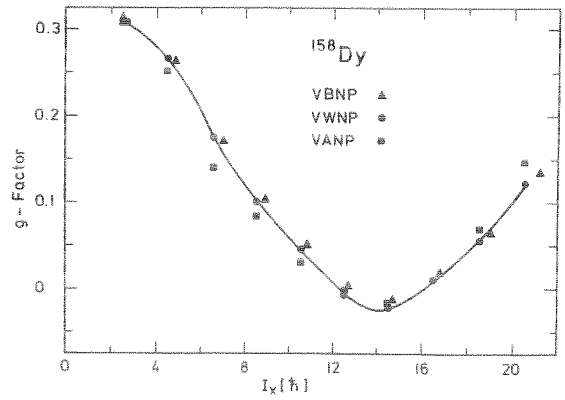


Fig. 2: Variation of g-factor with spin.

New Terms in the Nuclear Hamiltonian at High Spins B

U. Post, E. Wüst, and U. Mosel

Institut für Theoretische Physik, Universität Giessen

Although the experimental data about rotational motion of nuclei are now generally understood there are still a few theoretical problems left. We know - as well from experiment as from calculation - that the backbending of nuclei in the rare earth region is caused by an $i_{13/2}$ neutron alignment[1]. However the angular velocity where this backbending occurs is too low within all HFB-calculations up to this time (fig. 1, curves 1 and 2). In this investigation we show one possible explanation for this discrepancy, the appearance of new terms in the Hamiltonian at high spins.

The rotation of an even-even nucleus breaks the time reversal symmetry of the groundstate and leads to new terms. This fact can easily be observed for Skyrme's interaction[2]. In our calculations we substitute the well known time even part of the Skyrme Hamiltonian by the Woods-Saxon-Hamiltonian[3] and treat the time odd terms within a first order perturbation theory[4].

These calculations have shown that the time odd terms with the parameter set SK III have nearly no effect on quasi-particle energies and band-crossing in the spin region up to 30 $\hbar$. However at very high angular momentum above 50 $\hbar$ sizeable differences do appear (fig. 1, curves 2 and 3). They are due to different frequencies of the first levelcrossing of the negative parity protons (fig. 2).

The parameters of the Skyrme force are fitted to groundstate properties and, therefore, need not to be correct at higher spins. By varying the parameters we have found that the new terms include the possibility to obtain better crossing frequencies (fig. 1, curve 4). As the first reported effects at very high spins this is also predominantly due to those additional terms containing the current density. With a changed t_2-parameter these terms are equivalent to an attenuation of the cranking term. Hence they lead to a slower alignment of the first neutron pair.

[1] P. Ring, P. Schuck, The nuclear many body problem, Springer 1980

[2] Y.M. Engel et al., Nucl. Phys. A249, 215 (1975)
K.H. Passler, Nucl. Phys. A257, 253 (1976)

[3] J. Dudek, T. Werner, J. Phys., Vol.4, No.10, 1543 (1978)

[4] P.R. Surján, J. Ángyań, Phys. Rev. A28, 45 (1983)

[5] U. Post, diploma thesis, Giessen 1983

[6] H. Emling et al., Phys. Lett. 98B, 169 (1981)

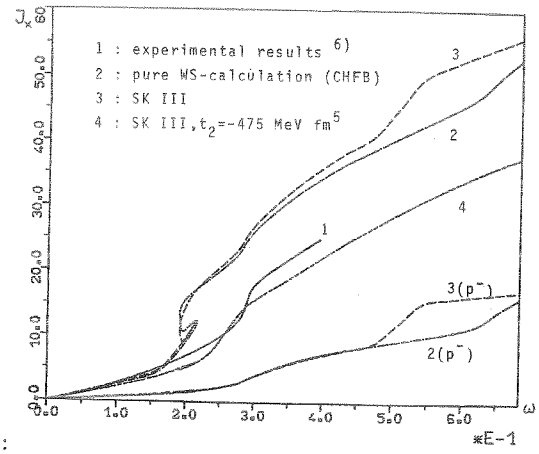
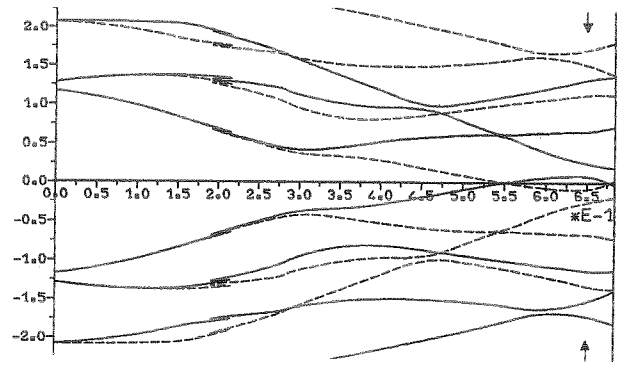
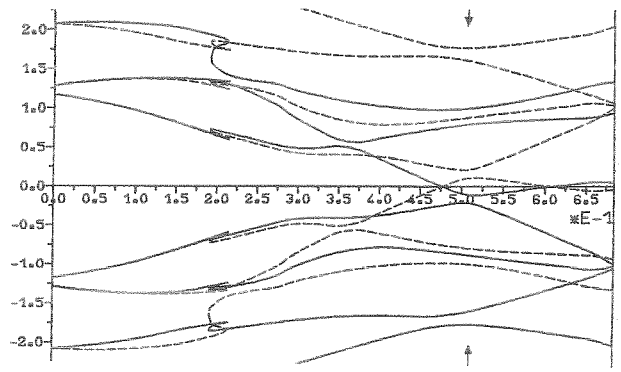


Fig. 1:
Total angular momentum J_x[$\hbar$] versus angular frequency ω[MeV/$\hbar$].



a) pure WS-calculation



b) with parameter set SK III

Fig. 2:
Quasiparticle energies [MeV] versus ω for negative parity proton states (solid: positive signature, dashed: negative signature)

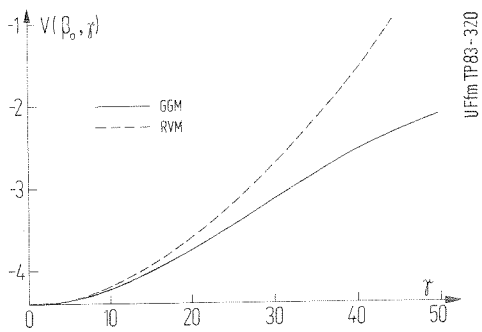
Confrontation of different collective models

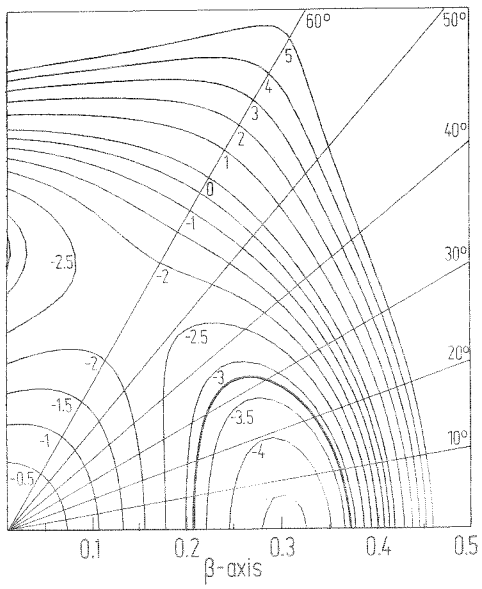
M. Seiwert, P.O. Hess, and J.A. Maruhn
Institut für Theoretische Physik, Universität Frankfurt/Main

For the nucleus $^{168}_{68}Er$, different geometrical collective models are compared to the experimental result and to calculations in the framework of the IBA[1]. It is shown, that the general collective models and IBA reproduce the experimental data with comparable fidelity, whereas the rotation-vibration model is unable to describe some special features due to its limited parametrisation of the potential. The equivalence of IBA and the general collective models is in agreement to theoretical studies concerning their mathematical relation[2]. It was shown in those calculations that IBA and the geometrical models are mathematically equivalent for large boson numbers such as N = 16 for ^{168}Er.

[1] D.D. Warner, R.F. Carsten, W.F. Davidson, Phys.Rev. C24 (1981)1713

[2] M. Moshinsky, Nucl. Phys. A338 (1980) 156:
J.N. Ginocchio, W. Kirson, Phys. Rev. Lett. 44 (1980) 1744;
J.N. Ginocchio, W. Kirson, Nucl. Phys.A350(1980) 31





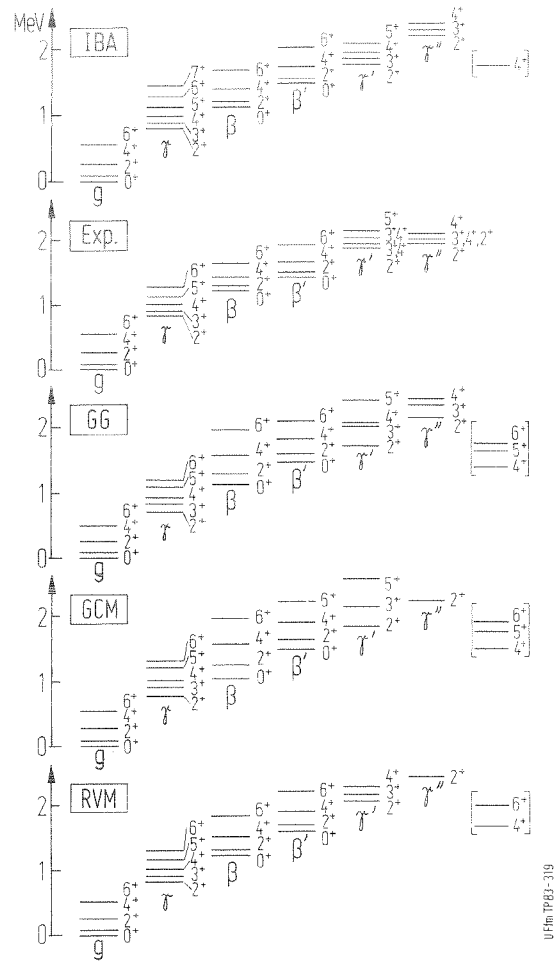


Fig. 1: Comparison of low energy spectra of ^{168}Er with experiment, calculated in terms of the Interacting-Boson Approximation (IBA), the Gneuss-Greiner Model (GG), the General Collective Model (GCM) and the Rotation-Vibration Model (RVM). In all of these models, an additional $K = 4^+$ band is predicted which is given in brackets.

Fig. 2: The Potential Energy Surface of ^{168}Er resulting from the Gneuss-Greiner Model (GGM). In the upper part the dependence on γ is shown and compared to the Rotation-Vibration Model (RVM). The lower part shows the Potential as a contour plot dependent on β and γ.

Separation of Collective and Statistical Components for Average Transition Probabilities in HFB Model

A. Baran
Institute of Physics, M. C. Sklodowska University, Lublin, Poland
K. Dietrich, P. Ring
Physik-Department TUM, Garching and GSI Darmstadt

In a gamma emission process from highly excited states of atomic nuclei it is important to recognize the main trends in the gamma trajectories /e.g. calculated within a framework of a cascade model/ on an energy - angular momentum plot.
It was proved[1,2] that the "bumped" structure of the gamma spectrum and/or statistical side feeding pattern depend strongly on the stretched transition probabilities $T(\hat{O}\lambda,\ I\to I'-\lambda)$. The fact was observed and the gamma multiplicities and average transition energies were measured in experiment as well[3].
In the HFB model presented before[4], this part of the transition probability connected to the collective or stretched transitions is hidden. It is a part of the total energy averaged transition probability.

In the following we give a short description of a possible way of extracting this part and estimating the intensity of it in the frame of the Hartree-Fock-Bogoliubov formalism.
As we have showed the energy averaged transition probability $T(\hat{O}\lambda; I\to I')$ from the initial state / I, E / to the final one / I', E' / can be written as

$$T(\hat{O}\lambda;I\to I') = C_\lambda (E-E')^{2\lambda+1}\,\bar{B}(\hat{O}\lambda;I\to I')\,\rho'(E',I'). \quad / 1 /$$

Here C_λ is a constant depending on λ, ρ' is the final level density and $\bar{B}$ is the energy averaged transition probability calculated in the 2 qp approximation[4]

$$\bar{B}(\hat{O}\lambda;I\to I') = \sum_{2'}\Big|\sum_{\mu} F(II'\lambda\mu)\,\langle 2'q_p|\hat{O}(\lambda\mu)|2q_p\rangle\Big|^2. \quad / 2 /$$

The sumation runs over all states in the energy intervals located at E and E'. Transitions between two 2 qp states are the ones we are interested in. For this case eq.2 can be rewritten as

$$\Delta^2\cdot\rho\cdot\rho'\cdot\bar{B}(\hat{O}\lambda;I\to I') = \sum_{k\ell;mn}\Big|\sum_{\mu} F(II'\lambda\mu)\,\sigma^0(\delta_{k\ell}\delta_{nm}-\delta_{\ell m}\delta_{kn}) + \sum_{\mu} F(II'\lambda\mu)(\sigma^{11}_{\ell m}\delta_{nk}-\sigma^{11}_{\ell k}\delta_{nm}-\sigma^{11}_{nm}\delta_{\ell k}+\sigma^{11}_{nk}\delta_{m\ell})\Big|^2, \quad / 3 /$$

where Δ is the energy bin in which the averaging is performed.
An expansion of the RHS of eq.3, gives the collective part in the form

$$\Delta^2 n\,\bar{B}_{coll} = \sum_{k\ell}|\sigma^0_F|^2 + 2\sum_{k>\ell}\sigma^0_F(\sigma^1_\ell+\sigma^1_k) \quad / 4 /$$

where

$$\sigma^1_\ell = \sum_\mu F(II'\lambda\mu)\,\sigma^{11}_{\ell\ell}, \quad / 5 /$$

$$\sigma^0_F = \sum_\mu F(II'\lambda\mu)\,\sigma^0_F. \quad / 6 /$$

In all formulas above σ^0 and $\sigma^{11}_{k\ell}$ are the expansion coefficients of the $\hat{O}(\lambda\mu)$ operator in a quasiparticle basis[5]

$$\hat{O} = \hat{O}^0 + \sum_{k\ell}\sigma^{11}_{k\ell}\alpha^+_k\alpha_\ell + \frac{1}{2}\sum_{k\ell}\left(\sigma^{20}_{k\ell}\alpha^+_k\alpha^+_\ell + \text{h.c.}\right). \quad / 7 /$$

It is important to note that the number "n" on the LHS of eq.4 has the meaning of the number of 2 qp states passing through the initial and the final energy bins. It may be estimated from the energy slope of the 2 qp state in the following way. Let E_i be the energy of this state. Its final position E_f is given by

$$E_f = E_i - (I_f - I_i)\frac{dE_i}{dI} = E_i - \Delta I\cdot\frac{1}{\mathcal{J}}\langle 2q_p|\hat{j}_x|2q_p\rangle \quad / 8 /$$

where we have used the definition of the moment of inertia and the form $H'=H-\omega\hat{j}_x$ for the cranked hamiltonian. If both energies E_i and E_f are in the initial and the final energy bins Δ then we add to "n" one and increase the collective probability B_{coll} on a value calculatad according to the LHS of eq.4. Doing this for all states in the initial bin and dividing B_{coll} by the final "n" we obtain the average collective part of the transition operator $\hat{O}$.
The result depends on initial and final energies and angular momenta. This is an extra dependence besides the factor $(E-E')^{2\lambda+1}$.

[1] Detailed results will be published.
M. Wakai, A. Faessler, NP A307/1978/ 349.
[2] R.J. Liotta, R.A. Sorensen, NP A297/1978/136
[3] H. Emling et al., Phys.Lett.98B/1981/169.
[4] A.Baran, K.Dietrich, GSI Report,1982,pp76-77
[5] P.Ring, P.Schuck, The Nuclear Many-Body Problem,Springer-Verlag,1980.

Renormalisation of the double folding model [B]

M.Seiwert, W. Greiner, and W. T. Pinkston

Institut für Theoretische Physik, Universität Frankfurt/Main

In the past the double folding model was successful in the description of elastic and inelastic scattering data as well as fusion cross sections. In the literature, the definitions of this model are not unique. We refer to the work of Love and Satchler[1] where realistic density profiles of Fermi-type are used. The model is constructed in analogy to electrodynamics. The nuclear force is assumed to be dependent on the length of the relative distance r alone. We write for the nuclear binding energy of a given density distribution $\rho(r)$:

$$W = \frac{1}{2} \int d^3r \int d^3r' \; \rho(\vec{r}) \; v(|\vec{r}-\vec{r}'|) \; \rho(\vec{r}') \; . \qquad (1)$$

If we consider two interacting nuclei expressing the space coordinates in their center of mass systems, we obtain:

$$\rho(r) = \rho_1(r_1) + \rho_2(r_2) \quad . \qquad (2)$$

and with eq. (1)

$$W = \int d^3\vec{r}_1 \int d^3r_2 \rho_1(\vec{r}_1) \; v(|\vec{R}-\vec{r}_1+\vec{r}_2|) \; \rho_2(\vec{r}_2) +$$

$$+ \frac{1}{2} \int d^3r_1 \int d^3r_1' \rho_1(\vec{r}_1) \; v(|\vec{r}_1-\vec{r}_1'|) \rho_1(\vec{r}_1') \quad +$$

$$+ \frac{1}{2} \int d^3r_2 \int d^3r_2' \rho_2(\vec{r}_2) \; v(|\vec{r}_2-\vec{r}_2'|) \rho_2(\vec{r}_2') \quad =$$

$$= V + W_1 + W_2 \quad . \qquad (3)$$

The binding energy is composed of an interaction part and of the binding energies of the fragments. The interaction part is usually called the nuclear potential. The results for the binding energies are unrealistic due to the assumptions about the nucleon-nucleon force. Therefore we use the Liquid Drop Model to calculate the realistic complete binding energy G:

$$G = V + W_1^{LD} + W_2^{LD} = W - W_1 - W_2 + W_1^{LD} + W_2^{LD} . \qquad (4)$$

If we change from separated nuclei to connected shapes, the separation of the density profile into ρ_1 and ρ_2 becomes arbitrary. Therefore, the usual double folding model is valid only up to the surface touching point. The observation, that the interaction part V is dominantly caused by the nuclear atmosphere, allows us to extend the model in an intuitive way. We assume, that in general the integral (1) is composed of a realistic interaction part V and an unrealistic binding energy. This unrealistic binding energy $\tilde{W}$ is obtained by integration (1) over a density profile $\tilde{\rho}(\vec{r})$, which corresponds to $\rho(\vec{r})$ but omitting the nuclear atmosphere, i.e. the square well. We write in analogy to (4):

$$G = W - \alpha\tilde{W} + W^{LD} \quad . \qquad (5)$$

The scaling factor α is necessary to obtain realistic values for spherical nuclei:

$$G = W^{LD} \iff W - \alpha\tilde{W} = 0 \iff \alpha = \frac{W}{\tilde{W}} \qquad (6)$$

α varies slightly with the mass number $A = A_1+A_2$. We find $\alpha = 0.8048$ for ^{28}Si-^{28}Si and $\alpha = 0.8677$ for ^{238}U-^{238}U.

Up to now,we are able to solve the six-dimensional integrals only for the sudden parametrisation given in eq. (2). We use a Fourier-Transformation method to decouple the integrals[2], which needs the expansion of the density distribution into spherical harmonics. Unfortunately, adiabatic shapes with atmosphere need terms up to an order of at least l = 12. Therefore, a new method to solve the integral (1) for adiabatic shapes must be evaluated.

[1] G.R. Satchler and W.G. Love, Phys. Rep. 55 (1979) 183

[2] M.J. Rhoades-Brown, V.E. Oberacker, M. Seiwert, and W. Greiner, Z. Phys. A310 (1983) 287

The Nucleus-Nucleus Potential in Molecular Resonances B

Amand Faessler, M. Ismail, M. Rashdan, L. Satpathy, W. Wadia
Institut für Theoretische Physik, Universität Tübingen

Since the discovery[1] of narrow resonances in $^{12}C + ^{12}C$ scattering, the concept of molecular resonance has been steadily gaining ground in nuclear physics[2]. The aim of this note is to adjust an internuclear potential v(R) to the resonances of the $^{12}C - ^{12}C$ system. We report here our determination of the bonding potential v(R) through such an attempt and its microscopic calculation starting from a NN-force. We start with the well-known Morse potential[3]

$$V_M(R) = B[\exp\{-2\beta(\frac{R-R_0}{R_0})\}-2\exp\{-\beta(\frac{R-R_0}{R_0})\}]+A \qquad (1)$$

This potential has four parameters namely, A, B, β and R_0. The constant A takes into account the Coulomb repulsion between the two ^{12}C inside the barrier.

We solved the Schrödinger eq. with this potential. For our analysis we took first the 28 resonances used by Erb and Bromley[2] and another 22 resonances from the work of Cindro and Greiner[4] to fit the four parameters (see fig. 1a). In Fig. 1b the results of Erb and Bromley[2] are presented for comparison. The fitted potential V_{eff} is plotted in Fig. 2 as solid line. The surprising result is the long range of the potential. This long range of the order of 20 fm can be reconciled with our present knowledge of nuclear structure if we assume that the two carbon nuclei in the molecular states have linear three α-particle structure.

A microscopic calculation of the molecular interaction potential between two ^{12}C ions within the framework of the α-particle model has been performed under the assumption that the relevant state for the molecular potential is a linear chain of three α-particles. For the NN interaction we chose the Brink-Boeker (B1) and the Volkov (V1) forces. The results agree quite well with the phenomenological fitted potential in the relevant surface region.

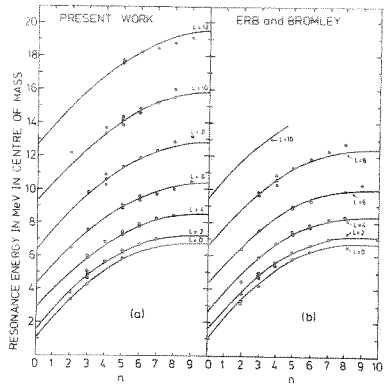


Fig. 1: Comparison of the $^{12}C + ^{12}C$ resonance spectra with two models. In (a) the solid curves were calculated using the eigenvalues of the Schrödinger equation. In (b) the solid lines are the results of Erb and Bromley [Ref. 7].

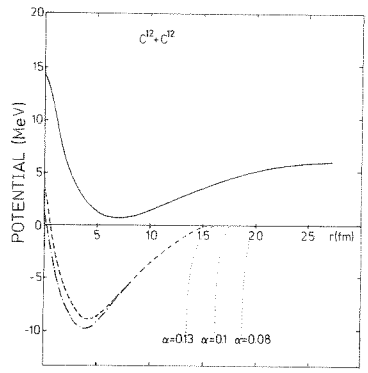


Fig. 2: The bonding potential in the $^{12}C + ^{12}C$ resonance phenomena. The solid line represents the potential V_{eff} obtained by fitting the experimental data. The region beyond 20 or 25 fm should not be taken seriously. The dashed, dot-dashed and the dotted lines are the pure nuclear part V_N of the effective potential obtained by subtracting from V_{eff} various Coulomb potentials.

[1] D.A. Bromley, J.A. Kuehrer and E. Almqvist, Phys. Rev. Lett. 4, 365 (1960)

[2] K.A. Erb and D.A. Bromley, Phys. Rev. C23, 2781 (1981)

[3] P.M. Morse, Phys. Rev. 34, 57 (1929)

[4] N. Cindro and W. Greiner, J. Phys. G (1983) in press

The Volume Contribution of the Ion-Ion Optical Potential from Realistic Complex Nucleon-Nucleon Interaction

B

Amand Faessler, M. Ismail
Institut für Theoretische Physik, Universität Tübingen

A theoretical effort to derive the heavy ion optical potential is desirable for a more systematic understanding of the energy and mass dependence. As emphasized in[1-4], a heavy ion reaction can be characterized locally as the collision of two interpenetrating nuclear matters. In momentum space such a system is associated with a Fermi sea composed of two spheres. The corresponding G-matrix is no longer hermitian since real 2p-2h excitations can now occur. As a consequence, one can achieve[1,5] a complex effective interaction from such a G-matrix. This complex interaction produces both the real and imaginary parts of the volume contribution of the optical potential.

The volume part of the optical potential $V_{opt}(R)$ at separation distance R is defined as[5] the difference between the interaction energy V(R) at distance R and the interaction energy $V(\infty)$ at infinity. It is written as:

$$V_{opt}(R) = V(R) - V(\infty) \qquad (1)$$

The interaction energy V(R) at distance R is given by the double folding integral:

$$V(R) = \frac{1}{2} \int d\underline{r}_1 d\underline{r}_2 \rho(\underline{r}_1)\rho(\underline{r}_2) V_{eff}[r_{12}, \rho(\underline{R}_{12}), \tau^{(2)}(R_{12}), K_r] \qquad (2)$$

K_r is the projectile momentum per nucleon given by:

$$K_r = \sqrt{(2m/\hbar^2)\ (E_{lab}/M_2} \qquad (3)$$

m is the nucleon mass and M_2 is the mass number of the projectile. E_{lab} is the projectile energy in the laboratory system (the target is assumed to be at rest). r_{12} and $\underline{R}_{12}$ are the relative and center of mass vectors given by:

$$\underline{r}_{12} = \underline{r}_1 - \underline{r}_2 \quad , \quad \underline{R}_{12} = \frac{1}{2}(\underline{r}_1 + \underline{r}_2)$$

$\rho(r)$ and $\tau^{(2)}(\underline{r})$ are respectively the density and the intrinsic kinetic energy density of the total heavy ion system at point $\underline{r}$.

$V_{eff}[r, \rho, \tau^{(2)}, K_r]$ is a complex effective nucleon-nucleon force defined by:

$$v(r) = \begin{cases} \frac{1}{x}(1-e^{-2x})^2\ e^{-3x} \sum_{m=0}^{6} A_m x^m = \sum_{m=0}^{6} A_m v_m^<(r) & \text{if } r<1 \text{ fm} \\ \frac{1}{x}(1-e^{-2x})^2 \sum_{m=1}^{7} Z_m e^{-mx} = \sum_{m=1}^{7} Z_m v_m^<(r) & \text{if } r<1 \text{ fm} \end{cases} \qquad (4)$$

where $x=0.7r$. The $\rho, \tau^{(2)}$ and K_r dependence are entirely contained in the A_m and Z_m coefficients.

In the present calculations we assume a Fermi type distribution for the density $\rho_i (i=1,2)$. The parameters of this distribution are taken from reference[6]. The surface region of Re V_{opt} is the only part which is important for practical purposes. For this reason we have parametrized the region of the potential beyond the last minimum by a Woods-Saxon shape:

$$V_{WS}(R) = - V_0 \ / \ [1 + \exp\ (R-R_0)/T] \qquad (5)$$

The parameter R_0 can be approximated for all systems of two heavy ions by:

$$\bar{R}_0 = (1.05\ (A_1^{1/3} + A_2^{1/3}) + 1.198)\ [fm] \qquad (6)$$

V_0/D can be described by the straight line:

$$\bar{V}_0/D = 20.73 - 0.46\ D \qquad (7)$$

with: $\quad D = A_1^{2/3} + A_2^{2/3} - (A_1 + A_2)^{2/3}$

R_I is roughly given by:

$$\bar{R}_I = 0.871\ (A_1^{1/3} + A_2^{1/3})\ [fm] \qquad (8)$$

However, we did not observe any such relation for W_0 and T_I.

[1] A. Faessler, T. Izumoto, S. Krewald, R. Sartor, Nucl. Phys. A359, 509 (1981)

[2] R. Sartor, A. Faessler, S.B. Khadkikar, Nucl. Phys., A359, 462 (1981)

[3] S.B. Khadkikar, L. Rikus, A. Faessler, R. Sartor, Nucl. Phys. A369, 495 (1981)
A. Faessler, L. Rikus, R. Sartor, Comp. Phys. Comm. 28, 275 (1983)

[4] J.E.S. Hernandez, S.A. Moszkowski, Phys. Rev. C21, 929 (1980).

[5] R. Sartor, A. Faessler, Nucl. Phys. A369, 495 (1981)

[6] F. Stancu, D.M. Brink, Nucl. Phys. A270, 236 (1976)

Studies of heavy-ion direct reactions to the continuum using the nearside-farside technique

G

D.R. Dean and U. Mosel
Institut für Theoretische Physik, Universität Giessen

H. Lenske and H.H. Wolter
Sektion Physik, Universität München

The concepts of nearside and farside (NF) scattering are extremely useful in interpreting heavy-ion reaction data, both for elastic and quasi-elastic processes. (For reviews see ref.1.) As is well known, for deep-inelastic scattering there is often a pronounced energy-angle correlation, which is usually displayed as a Wilczynski plot and interpreted as a transition from positive-angle (nearside) to negative-angle (farside) scattering with increasing energy loss. It is therefore of interest to see whether the NF technique is applicable to such continuum reactions. Due to its essentially quantum-mechanical nature, this technique is far preferable to those classical methods which also explain the form of Wilczynski plots.

The T-matrix elements necessary for this study are taken from continuum multi-step direct-reaction (MSDR) theory. In our initial studies[2] ($^{16}O+^{48}Ca$ at 103 MeV) only one-step processes were considered, but, even so, it was clear that the importance of farside scattering does increase with increasing energy loss. Encouraged by this, we have now included two-step contributions and performed more extensive calculations for the systems $^{16}O+^{48}Ti$ and $^{16}O+^{208}Pb$ at various energies[3].

Fig. 1 shows the Q dependence of the NF components of both the one- and two-step contributions to the $^{16}O+^{48}Ti$ reaction. The two main features are the changes in dominance from one- to two-step and from near- to farside scattering with increasing energy loss. The latter agrees with simple expectations and is observable in the polarization, which changes sign at Q≈-10 MeV[3]. This is the first quantum-mechanical study of such a behaviour.

The increased importance of two-step processes at higher Q values is intuitively clear and results in a broadening of the angular distribution (fig. 2). This can also be explained using a parametrized T-matrix approach which includes dynamic and statistical fluctuations, such as that developed recently[4]. In this approach statistical fluctuations are treated by allowing many "classical" trajectories, each weighted appropriately, to contribute at a given scattering angle, and it is possible to demonstrate that a realistic choice of weighting function is a Lorentzian. An NF decomposition is also inherent in this model, with which the qualitative features of deep-inelastic cross sections and polarizations are readily explained. In contrast, the MSDR-theory approach gives a quantitative quantum-mechanical description of these quantities. It is hoped to explain spin alignments using similar techniques.

It is a pleasure to acknowledge Dr. S.Y. Lee and Prof. R.L. McGrath, SUNY at Stony Brook, with whom part of this work was performed.

[1] D.R. Dean, D.Phil. thesis, University of Oxford, (1982), unpublished.
K.W. McVoy and M.S. Hussein, Prog. Part. Nucl. Phys., to appear.

[2] D.R. Dean and U. Mosel, Phys. Lett. 132B, 287 (1983).

[3] D.R. Dean, H. Lenske, U. Mosel, and H.H. Wolter, submitted to Nucl. Phys. A.

[4] S.Y. Lee, R.L. McGrath, and D.R. Dean, submitted to Phys. Rev. C.

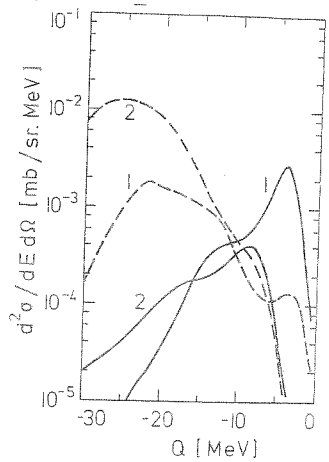


Fig. 1:
Energy-loss dependence of the nearside (solid) and farside (dashed) components of the one-step (1) and two-step (2) double-differential cross sections. $^{16}O + ^{48}Ti$, E_{lab}=125 MeV, Θ_{cm}=50°.

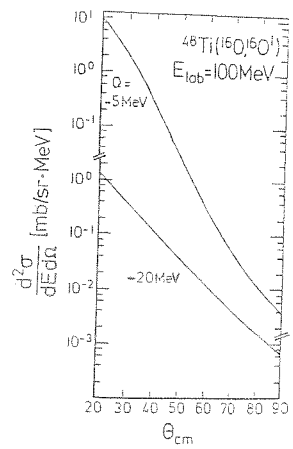


Fig. 2:
Angle dependence of the full (one- plus two-step) double-differential cross section at two Q values.

Exact First- and Second-Order Distorted Wave Methods [B]

O. Tanimura, R. Kaps, U. Mosel, and R. Wolf

Institut für Theoretische Physik, Universität Giessen

The first- and second-order distorted wave Born methods (DWBM) have been generally successful in describing the nuclear scattering even when the validity of using only the first- or second-order perturbations are not guaranteed. This is due to the fact that the distorting potentials used in the calculation are the optical potentials which contains higher-order terms in the interaction[1].

We have presented an exact and consistent formulation[2] for the first and the second-order DWBM on the basis of Feshbach's projection method.
Let us define P, Q^1, Q^2, and Q' as the operators projecting onto the initial channel, the channels excited strongly by the first- and second-order processes, and the other channels, respectively, where $Q^1+Q^2+Q'=Q$. Then the optical potential model (OPM), the T-matrices for the first- and the second order DW methods are respectively given by

$$[E-(H+\Delta V^{(Q)})_{pp}]\Psi_p^{(+)} = 0, \tag{1}$$

$$T_{Q_i p} = \langle \Phi_{Q_i}^{(-)} | Q_i [V+\Delta V^{(\bar{Q}_i)}] p | \Psi_p^{(+)} \rangle, \tag{2}$$

$$T_{Q_k^2 p} = \langle \Phi_{Q_k^2}^{(-)} | Q_k^2 \{ [V+\Delta V^{(\bar{Q}_k^2)}] + \sum_{i\in Q^1} (V+\Delta V^{(\bar{Q}_k^2)}) Q^1{}_i$$

$$\times [E^{(+)}-(H+\Delta V^{(\bar{Q}_i)})_{Q_i^1 Q_i^1}]^{-1} Q_i^1 (V+\Delta V^{(\bar{Q}_i)}) \} p | \Psi_p^{(+)} \rangle, \tag{3}$$

with

$$\Delta V^{(Q)} = VQ(E^{(+)}-H_{QQ})^{-1}QV. \tag{4}$$

Here the sufices specify the subchannels and $\bar{Q}_i=Q-Q_i$ and $\bar{Q}_k^2=Q^2+Q'-Q_k^2$.
$\Psi_p^{(+)}$ denotes the exact elastic wave function which corresponds to the OPM wave function, while $\Phi_i^{(-)}$ denotes the homogenous solution of the Hamiltonian projected onto the channel i[2]. These T-matrices are exactly equal to those of the CC method.

As a simple example we discuss the elastic and the inelastic $^{12}C+^{12}C$ scattering to the single 2^+ and the mutual 2^+ excitations at $E_{c.m.}$=30 MeV. We have assumed the Reilly potential and the derivative of its real part for the bare diagonal potential and the bare coupling interaction, respectively, where the deformation β_2=-0.45.

For the practical use it is convenient to parameterize the polarisation interaction by the derivative of the real part of the potential: The diagonal elements are parameterized by $\Delta U(r)=c\cdot\exp[(r-R)/a]/\{1+\exp[(r-R)/a]\}^2$ and the non-diagonal ones by the additional deformation $\Delta\beta_2$. The elements between the aligned coupling subchannels are listed in Table 1 for the grazing angular momentum J=18. Since these subchannels play the dominant role in the cross sections in the light heavy ion scattering, the use of the same interactions as given in Table 1 also for all J and all the other subchannels is expected to generate good approximations to the exact cross sections. In fact we found that these simple parameterizations generate nice agreement with the CC cross sections[2].

[1] R.J. Ascuitto et al., Phys. Rev. Lett. 41, 1159 (1978).

[2] O. Tanimura et al., Phys. Lett. 132B, 249 (1983)

Table 1
Parameterization factors for $\Delta U(r)$ at J=18

	ΔU_{pp} (MeV)	$\Delta U_{Q_1^1 Q_1^1}$ (MeV)	$\Delta U_{Q_1^2 Q_1^2}$ (MeV)
c	-10-5i	-7.2-4i	-1.9-0.6i
	$\Delta U_{Q_1^1 p}$ (MeV)		$\Delta U_{Q_1^2 Q_1^1}$ (MeV)
$\Delta\beta_2$	0.048+0.011i		0.048+0.015i

Polarization Effects on CC and DWBA potentials [B]

R. Wolf, O. Tanimura, and U. Mosel
Institut für Theoretische Physik, Universität Giessen

For a correct description of a scattering process all the reaction channels must be taken into account. But even in a large coupled channel calculation this is not possible. The space of states must be truncated and (in DWBA) some couplings are neglected. The excluded states and neglected couplings, however, lead to a polarization of the CC and DWBA potentials (see report by Tanimura et al.).

We have studied these truncation effects by calculating the exact polarization potential originating from the neglected couplings. The space of states is devided into four subspaces P, Q, R, and S. P contains the elastic channel and Q some inelastic channels. The influence of the R-space channels on the couplings of the (P+Q)-space is investigated. S contains all the remaining channels, whose influence is taken into account by a complex potential (background potential). In the DWBA case also the neglected couplings within the (P+Q) space have to be considered. This leads to different propagators and hence different potentials for CC and DWBA. The effective coupling potentials are:

$$(i,j\varepsilon P+Q)\quad U_{ij}^{CC}(r,r') = V_{ij}(r) + \sum_{k,l\varepsilon R} V_{ik}(r)G_{kl}^{R}(r,r')V_{lj}(r')$$

and

$$(i,j\varepsilon P+Q_i)\quad U_{ij}^{DWBA}(r,r') = V_{ij}(r) + \sum_{k,l\varepsilon R+Q\setminus\{Q_i\}} V_{ik}(r)G_{kl}^{R+Q\setminus\{Q_i\}}(r,r')V_{lj}(r')$$

Here Q_i denotes a subchannel of the Q space and V_{ij} is the bare interaction. In the usual manner, by integrating the nonlocal potentials multiplied by the corresponding channel - wavefunction and dividing by this wavefunction, a local potential can be constructed.

The calculations were carried out for the system $^{16}O+^{16}O$. The Q space is the $(0^+,3^-)$ state with its subchannels while the R-space contains the mutual 3^- and the two phonon channels. The resulting potentials are different for different channels[1]. In the CC case the elastic polarization potential is nearly zero because of the weak coupling of the two phonon states to the ground state. The inelastic potentials for the $(0^+,3^-)$ state, however, get a large polarization term, which reduces the interaction barrier (see fig. 1a). This is important for fusion reactions. The imaginary potential gets a large contribution in the surface region due to the excitation of the collective two phonon states (see fig. 1b). The coupling potential becomes stronger corresponding to an effective coupling strength $\gamma_{eff}=\gamma_{bare}+\Delta\gamma$ where $\Delta\gamma$ is about 10 % of γ_{bare}. Thus γ_{eff} is not the same as the one deduced from the B(Eγ) value.

The effective potentials for CC and DWBA also differ. This shows fig. 2a and b. The polarization contribution adds up to the bare potential in such a way that the interaction radius of the effective potential gets larger. Especially the potential for the elastic channel deviates in the DWBA case from the CC potential.

To include polarization effects in a simple way in an OM calculation we have obtained parameterizations for the polarization potential.

[1] R. Wolf, O. Tanimura, U. Mosel, Nucl. Phys. A, in press

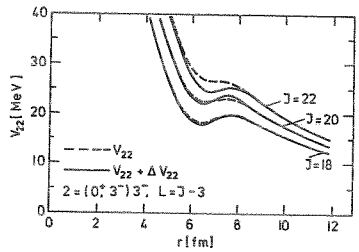


Fig. 1
Effective CC potentials for an inelastic channel.

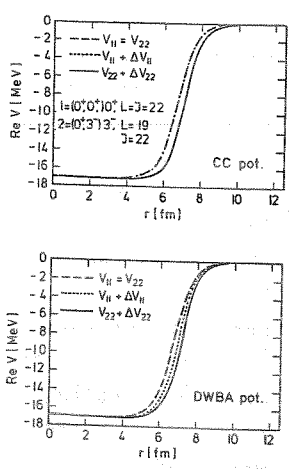


Fig. 2
Comparison of CC and DWBA potentials for two different channels.

Coupling Effects on Fusion and Reaction Cross Sections [B]

J. Makowka, U. Mosel, and R. Wolf

Institut für Theoretische Phyisk, Universität Giessen

The influence of channel couplings on fusion and reaction cross sections has been studied by means of the coupled channel formalism. First we examined the system $^{16}O+^{148}Sm$ which is experimentally known from the measurements of Stokstad et al.[1]. The coupled channel calculations were done by PTOLEMY[2]. The energy range was restricted to the region of the Coulomb barrier. Only low lying excitations of the target were taken into account.
In the threshold region the contribution from breakup channels can be neglected. Therefore, we define the fusion cross section as

$$\sigma_f = \sigma_r - \sigma_i$$

where σ_r is the reaction cross section and σ_i is the sum of the inelastic cross sections. For the calculations we used a complex Woods-Saxon type potential. Coulomb excitation was not included.
The results are shown in Fig. 1. In order to fit data, the radius parameter of the imaginary part of the potential had to be reduced from the standard value r_i=1.32 fm to r_i=0.94 fm reflecting the explicit contributions from the inelastic channels ($R_i=r_i\ A^{1/3}$).
These studies were then extended to a system where the excitation of a closed channel is possible, namely $^{12}C+^{12}C$. The effects on fusion and reaction cross sections have been studied in the energy region from 5 to 8 MeV. In this range the single 2^+ channel is open and the mutual 2^+ excitation channel is closed.
The closed channel is treated like a normal channel in the coupled channel calculation. This is possible, provided the right asymptotic behaviour of the wavefunctions is included. This can be done by extending the regular and irregular Coulomb functions to complex arguments ρ and η and choosing the proper sign for wave number and Sommerfeld parameter in the closed channel. Starting from an existing coupled channel code, a computer code was developed to handle closed and open channels simultaneously.
For the considered energy range inelastic scattering is negligeable and, therefore, according to our definition, the fusion cross section equal to the total reaction cross section.

Fig. 2 shows a comparison between different methods. Including channel couplings leads to a better reproduction of the structure in the data. The general shape of data is represented best by the full curve, which includes the mutual 2^+ as a closed channel. It should be emphasized that no fit to data was attempted so far. Instead a standard Woods-Saxon potential was used which fits scattering data at higher energies.

[1] R.G. Stokstad, Y. Eisen, S. Kaplanis, D. Pelte, U. Smilansky, and I. Torruya, Phys. Rev. Lett. 41C, 465 (1978)

[2] M.H. MacFarlane and Steven C. Pieper, ANL-76-11 ReV. 1, Argonne National Laboratory

[3] J.R. Patterson, H. Winkler, and C.S. Zaidins, Astrophys. J. 157, 367 (1969).

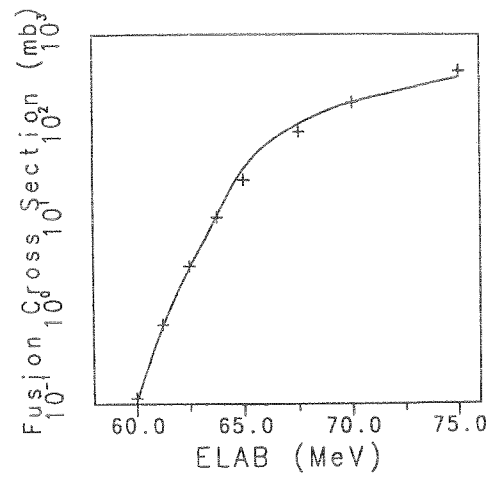


Fig. 1: Fusion cross section $^{16}O+^{148}Sm$. The curve is our calculation, the crosses are the data points from ref. 1.

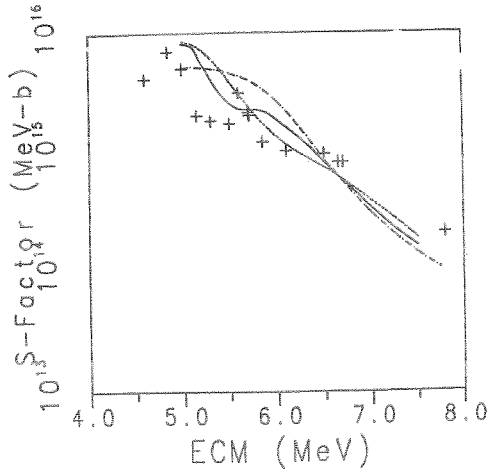


Fig. 2: $^{12}C+^{12}C$ s-factor plotted as a function of center of mass energy. The data points are taken from ref. 3. The full curve is the full calculation including the closed mutual 2^+ channel, the dashed one has only singel 2^+ included, the dashed-dotted curve is an optical model calculation with the same potential for the elastic channel.

Coupled channel calculations for the scattering of ^{28}Si on ^{28}Si

A. Thiel and W. Greiner
Institut für Theoretische Physik, Universität Frankfurt

For the scattering of ^{28}Si on ^{28}Si coupled channel calculations of the elastic scattering and inelastic single excitation of the first 2+ state of ^{28}Si are carried out.

The real coupling potentials are calculated in the framework of the adiabatic coupling model of Koennecke et al.[1]. In this model the potential energy is calculated as a function of the relative distance of the nuclei and multipole coordinates describing the deformations of the nuclear surface. If we restrict the multipoles to the quadrupoles only, described by the coordinates $\alpha_{2m}^{(1)}$ and $\alpha_{2m}^{(2)}$, the real potential energy surface can be generally expanded for equal nuclei up to quadratic terms as follows:

$$V = V^{0}(r) + V_{2}^{(1)}(r) \sum_{i=1}^{2} [\alpha_{2}^{(i)} \times Y_{2}]^{[0]} + \sum_{\Lambda=0,2,4} \{V_{\Lambda}^{(2)}(r) \sum_{i=1}^{2} [[\alpha_{2}^{(i)} \times \alpha_{2}^{(i)}]^{[\Lambda]} \times Y_{\Lambda}]^{[0]} + V_{\Lambda}^{(1,2)}(r) [[\alpha_{2}^{(1)} \times \alpha_{2}^{(2)}]^{[\Lambda]} \times Y_{\Lambda}]^{[0]} \qquad (1)$$

In the adiabatic coupling model the potentials V^{0}, $V_{2}^{(1)}$, $V^{(2)}$ and $V^{(1,2)}$ are determined by the Coulomb interaction and an effective nuclear Yukawa two-body interaction acting on the density, which is homogeneously distributed over the volume of the composite system for all relative distances.

In an optical model calculation without coupling, using the real potential $V^{0}(r)$ of Eq.(1) and an imaginary potential calculated in the framework of the statistical model[2], it could be shown that the gross structures of the calculated elastic excitation function arise from potential resonances: their energies lie slightly above the corresponding barriers of the real effective potential $V^{0}(r) + \frac{\hbar^{2} l(l+1)}{2\mu^{2}}$ and agree with those for l=34-42 $\hbar$, obtained by Betts et al.[3] from the maxima of the experimental elastic gross structure[4]. The resonating partial waves are strongly peaked in the barrier region, which means that the $^{28}Si+^{28}Si$-system forms molecular configurations at large internuclear distances ("nuclear molecular barrier resonances").

In a second step we have coupled the single excitation of the first 2+ state of ^{28}Si to the elastic channel using the coupling potential proportional to $V_{2}^{(1)}r$ of Eq.(1). Figures 1 and 2 show the resulting elastic and inelastic cross sections for $\Theta_{cm}=90^{0}$ (Fig. 1) and $\Theta_{cm}=80^{0}$ (Fig. 2) in comparison with the experimental ones of Betts et al.[5]. The coupling of the single 2+ excitation of ^{28}Si affects the elastic cross section in the energy range about 60 MeV. The finer structures in the theoretical cross sections arise due to the coupling of the barrier resonances in the considered channels.

[1] R. Könnecke, J. Guirguis, W. Greiner, and W. Scheid, J. Phys. G: Nucl. Phys. 8 (1982) 535

[2] G. Helling, W. Scheid, and W. Greiner, Phys. Lett. 36B (1971) 64

[3] R.R. Betts, S.B. DiCenzo, and J.F. Petersen, Phys.Lett. 100B (1981) 117

[4] A. Thiel, W. Greiner, and W. Scheid, to be published in Phys. Rev. C.

[5] R.R. Betts, S.B. DiCenzo, and J.F. Petersen, Phys. Rev. Lett. 43 (1979) 253

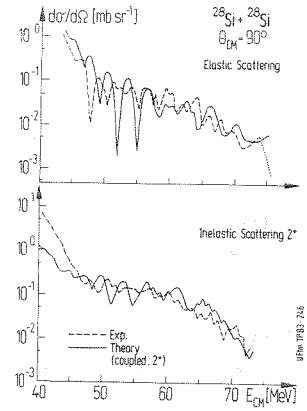


Fig. 1: The 90°-differential cross sections a) for the elastic scattering of $^{28}Si+^{28}Si$ b) for the inelastic single excitation of the first 2+ state in ^{28}Si: $^{28}Si(^{28}Si,^{28}Si^{*}(2+))^{28}Si$. The experimental data of Betts et al[5] are shown by dashed curves.

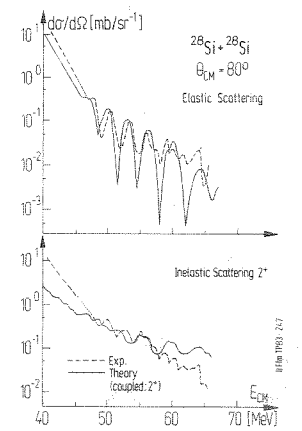


Fig. 2: The same cross sections as shown in Fig. 1, but for a scattering angle of $\Theta_{cm}=80^{0}$.

The Momentum Diffusion Tensor For The Particle Exchange Model

H. Feldmeier
Max-Planck-Institut für Kernphysik, Heidelberg
H. Spangenberger
Institut für Kernphysik, Technische Hochschule Darmstadt

Assuming a random exchange of nucleons between two colliding nuclei we worked out analytical expressions for the momentum diffusion tensor. The assumptions which enter the derivation are: The nucleons are moving with a long mean-free-path through a window in the single particle potential of the dinuclear system. The two Fermi gases left and right of the window show a mismatch in their drift velocities at the window. Once a particle has crossed the window it will loose its memory and assume the velocity distribution of the acceptor nucleus before coming back.

For small mismatch velocities ($|\vec{u}| \ll v_F$) and small temperatures ($T \ll \varepsilon_F$) the momentum diffusion tensor can be written as:

$$D_{ij} = |\vec{u}| m v_F \, D^u_{ij}(\alpha) + T \, D^T_{ij}(\alpha,\omega)$$

It consists of a "velocity part" which is proportional to the mismatch velocity $\vec{u}$ plus a "temperature part" which is proportional to the temperature T. The tensors $D^u_{ij}(\alpha)$ and $D^T_{ij}(\alpha,\omega)$ reflect the geometry of the problem which is defined by the window-normal $\hat{n}$ and the unit vector $\hat{u}$ pointing in the direction of the mismatch velocity. The two vectors define the angle α by $\cos\alpha = \hat{n}\hat{u}$. The parameter $\omega = m v_F |\vec{u}|/T$ specifies the relative contribution of the two parts. The explicit expressions are:

$$D^u_{ij} = mC\,(8/15\pi)\{(s_\alpha + c_\alpha k_\alpha)\delta_{ij} + s_\alpha \hat{n}_i\hat{n}_j + s_\alpha \hat{u}_i\hat{u}_j + k_\alpha(\hat{u}_i\hat{n}_j + \hat{n}_i\hat{u}_j)\}$$

and

$$D^T_{ij}(\alpha,\omega) = mC\,\{A_1(\alpha,\omega)\delta_{ij} + A_2(\alpha,\omega)\hat{n}_i\hat{n}_j + A_3(\alpha,\omega)\hat{u}_i\hat{u}_j + A_4(\alpha,\omega)(\hat{u}_i\hat{n}_j + \hat{n}_i\hat{u}_j)\}$$

For $0 \le \omega \le 6$ the $A_i(\alpha,\omega)$ are given by:

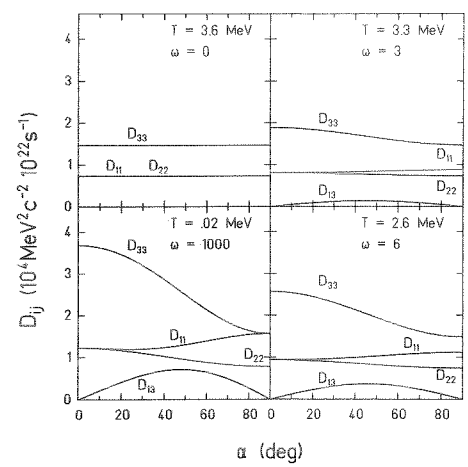
$$A_1(\alpha,\omega) = 1 - a_1(s_\alpha + c_\alpha k_\alpha) + a_2(2 - s_\alpha^2) - a_3(3s_\alpha - s_\alpha^3 + 3c_\alpha k_\alpha)$$
$$A_2(\alpha,\omega) = 1 - a_1 s_\alpha + a_2 s_\alpha^2 - a_3 2 s_\alpha^3$$
$$A_3(\alpha,\omega) = - a_1 s_\alpha + 2a_2 - a_3(6s_\alpha + 6c_\alpha k_\alpha)$$
$$A_4(\alpha,\omega) = - a_1 k_\alpha + 2a_2 c_\alpha - a_3(3s_\alpha c_\alpha + 3k_\alpha)$$

with $a_1 = 8\omega/15\pi$, $a_2 = \omega^2/72$, $a_3 = 2\omega^3/2835\pi$.

While for $\omega \ge 6$ they are approximated by:

$$A_1(\alpha,\omega) = A_1(\alpha,\omega{=}6)\,(6s_\alpha^2/\omega + 36c_\alpha^2/\omega^2)$$
$$A_i(\alpha,\omega) = A_i(\alpha,\omega{=}6)\,(6s_\alpha^2/\omega + c_\alpha^2) \quad \text{for } i = 2,3,4.$$

Here $A_i(\alpha,\omega{=}6)$ on the r.h.s. has to be taken from the above case for $\omega = 6$. The symbols c_α, s_α and k_α are short notations for $c_\alpha = \hat{u}\hat{n} = \cos\alpha$, $s_\alpha = \sin\alpha$ and $k_\alpha = (\pi/2 - \alpha)$ for $0 \le \alpha \le \pi$. The one-sided flux of particles through the window is denoted by C. It depends on the potential barrier and is proportional to the window size. Taking a typical value of $C = 2(10^{-22}s)^{-1}$ and a symmetric collision with an available kinetic energy of 1 MeV per nucleon we obtain the diffusion tensor shown in the figure. The four parts



correspond to different partitions of the conserved total energy into heat plus kinetic energy. The four non-vanishing matrixelements are displayed as a function of α and different temperatures. The coordinate system is such that $\hat{n} = (0,0,1)$ and $\hat{u} = (c_\alpha, 0, s_\alpha)$. If all kinetic energy ($\vec{u} = 0$) has been transformed to heat (T = 3.6 MeV) the tensor does not depend on α but is twice as large in the window direction than in other directions. If part of the energy is still in relative motion the α-dependence shows up. However, most important is the fact that the total strength of the fluctuations does not decrease with smaller temperature, it even increases quite in contrast to the Brownian motion picture. This is due to the increasing "velocity part".

Exchange of Particles, Momentum and Entropy Between Two Colliding Nuclei

H. Feldmeier
Max-Planck-Institut für Kernphysik, Heidelberg

A moving Fermi gas is completely specified by the following three extensive quantities:

excitation energy	$E^* = \langle \underset{\sim}{H} \rangle - E_{gs}$
number of particles	$N = \langle \underset{\sim}{N} \rangle$
center of mass momentum	$\vec{P} = \langle \underset{\sim}{\vec{P}} \rangle$

Hence the statistical operator which contains only this information is of the form

$$\underset{\sim}{R} = 1/Z \exp\{ -1/T \underset{\sim}{H} + \mu/T \underset{\sim}{N} + m\vec{u}/T \underset{\sim}{\vec{P}} \}. \qquad (1)$$

The Lagrange parameters are composed of three intensive quantities:

temperature	T
chemical potential	μ
center of mass velocity	$\vec{u}$

The mass of one nucleon is denoted by m.

The basic idea of the model is to regard each nucleus as a Fermi gas described by a statistical operator as given in eq.(1). However, there is no a priori equilibration in any of the intensive quantities between the two gases. Thus, one has two temperatures $T_{1,2}$, two chemical potentials $\mu_{1,2}$ and two c.m. velocities $\vec{u}_{1,2}$. The goal is to describe the equilibration in these quantities dynamically. In peripheral collisions the reaction time may be shorter than one or the other equilibration time so that one is able to measure the rate of equilibration in the excitation energy, the mass asymmetry and the relative motion, respectively.

The mechanism by which the two gases communicate is the exchange of particles through a window in the mean single particle potential between the two nuclei. The linearized thermodynamic equations which result from the microscopic calculation are

$$\dot{S}_{2\to1} = C\, 2\pi^2/(3\varepsilon_F)\,\{(T_2-T_1) + T/\varepsilon_F\,(\mu_2-\mu_1)\} \qquad (2)$$

$$\dot{N}_1 = C\, 2\pi^2/(3\varepsilon_F)\,\{T/\varepsilon_F(T_2-T_1) + 3/\pi^2(\mu_2-\mu_1)\} \qquad (3)$$

$$\dot{\vec{P}}_1 = C\, m\,\{(\vec{u}_2-\vec{u}_1)_\perp + 2(\vec{u}_2-\vec{u}_1)_\parallel\} \qquad (4)$$

Here, $\dot{S}_{2\to1}$ is the entropy current from nucleus 2 to nucleus 1; ε_F is the mean chemical potential and T the mean temperature. The one-sided current is indicated by C. One sees that a difference in temperature drives the entropy (heat) flux as well as the particle flux $\dot{N}_1$. The same holds for the chemical potential difference. A similar coupling is responsible for the Peltier-Seebeck effect. The coefficients in eq.(2)-(4) are for the case where there is no potential barrier in between the gases. The general case has also been worked out and has been incorporated in a trajectory calculation where all quantities are time dependent and are evolving according to the equations of motion and to the thermodynamic equations. A typical result is shown in the figure below. As in the experimental data the mass drift is strongly hindered due to the weak mobility of the nucleons. The ratio between the temperatures tends towards one but is significantly larger for peripheral collisions. For the cases shown the coupling between heat flux and particle flux does not influence the results appreciably.

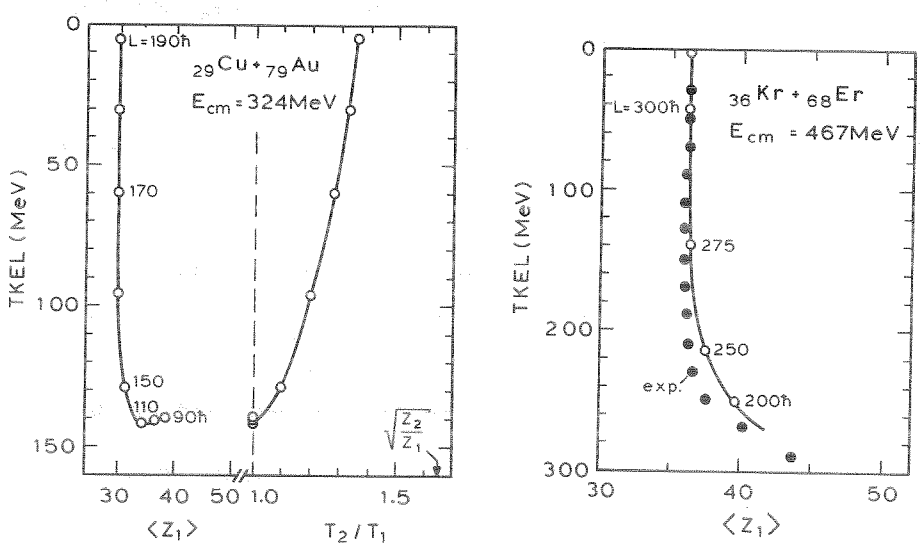


Fig.: Relation between mean energy loss and mean charge number and ratio of temperatures, respectively.

The RPA Description of Quantal Brownian Motion

C. Yannouleas
GSI, Darmstadt

The RPA model for nuclear dissipation[1-3] describes the damping of the collective motion through appropriate packets which, initialized as the collective states, evolve in time within extended subspaces larger than the restricted original subspace of the undamped collective motion.

The first step in developing the model is to describe the damping of the one-phonon RPA collective state. This one-phonon state decays in time to other more complicated many-body states degenerate with it in energy. The more complicated states form the additional subspace, which can comprise additional states of the 1p-1h structure[2] or states of the 2p-2h structure[3]. The decay of the sharp n-phonon states was also described in ref. 3). In addition, ref. 3) described the damping of coherent initial packets which are formed by shifting the ground state of the undamped oscillator specified by the frequency, ω, and the creation operator, Q_c^+, of the RPA collective phonon (this oscillator is referred to as the principal oscillator). In this last case, the expectation values of the collective coordinates obey Newton's eq. of motion for a classical damped harmonic oscillator.

The number of packets treated in refs. 1-3), however, is not large enough to allow for an adequate description of the Quantal Brownian Motion, in particular with respect to the fluctuations in the collective coordinates. This deficiency is rectified in the present work[4], where more general packets are considered. These packets are initialized as the shifted eigenstates of an undamped secondary oscillator of arbitrary frequency, $\bar{\omega}$, different in general from the frequency, ω, of the principal oscillator.

The fluctuations in the position are denoted by X_n and in the momentum by Π_n; the cross fluctuations are denoted by T_n (the index n denotes the quantum number characterizing the eigenstates of the secondary oscillator, which initialize the damped RPA packets). As shown in ref. 4) the fluctuations obey the following linear system of differential eqs. (during the early portion of the Poincaré recurrence time):

$$\dot{X}_n = 2T_n/M_c,$$

$$\dot{\Pi}_n = -2M_c\Omega^2 T_n - 2\Gamma\Pi_n + 2\Gamma\Pi_0,$$

$$\dot{T}_n = -M_c\Omega^2(X_n - X_0) + (\Pi_n - \Pi_0)/M_c - \Gamma T_n,$$

where

$$\Omega^2 = \omega^2 + \tfrac{1}{4}\Gamma^2$$

and X_0, Π_0 are the zero-point values. Γ is the decay width[1-3] of the one-phonon collective state -- either the escape width for direct particle emission or the spreading width to nuclear compound states. M_c is the the inertial parameter. This set of eqs. agrees with the system of eqs. describing the fluctuations of a classical oscillator performing a Brownian motion under the influence of a random force; however, the RPA fluctuations here are purely quantal and not statistical. In all cases, the RPA fluctuations decay to their zero-point values in the ground state of the system. This behavior contrasts sharply with both the Kostin-Kan and the Hasse-Albrecht descriptions.

From the RPA packets, one can extract the matrix elements ρ_{NM}, of the reduced density operator (which results after one traces over the reservoir indices).

The observed collective subspace is spanned by the sharp N-phonon states,

$$|N\rangle = [(Q_c^+)^N/\sqrt{N!}]\,|0\rangle,\quad N = 0,1,\ldots,\infty.$$

The reservoir is spanned by,

$$|\alpha 1\beta 1,\ldots,\alpha p\beta p\rangle = [B_{\alpha 1\beta 1}\cdots B_{\alpha p\beta p}/\sqrt{p!}]\,|0\rangle,\quad p = 0,1,\ldots,\infty,$$

where $B_{\alpha 1\beta 1} = A^+_{\alpha 1}$ when $\beta 1 = 0$ and $B_{\alpha 1\beta 1} = A_{\alpha 1}$ when $\beta 1 = 1$. The indices α's denote either the 1p-1h or the 2p-2h indices of the additional subspace, and A denotes the corresponding product of fermion operators.

The total subspace is spanned by the states:

$$|N;\alpha 1\beta 1,\ldots,\alpha p\beta p\rangle = [(Q_c^+)^N B_{\alpha 1\beta 1}\cdots B_{\alpha p\beta p}]/\sqrt{N!p!}\,|0\rangle.$$

It is found[5] that the matrix elements ρ_{NM} obey the following master eq. (during the early portion of the Poincaré reccurence time):

$$\dot{\rho}_{NM} = -i\omega(N-M)\rho_{NM} - \tfrac{1}{2}\Gamma(M+N)\rho_{NM} + \Gamma[(M+1)(N+1)]^{\frac{1}{2}}\rho_{N+1,M+1}.$$

References:

1) C. Yannouleas, Ph. D. Thesis (1982) U. of Md., College Park
2) C. Yannouleas, M. Dworzecka and J.J. Griffin, Nucl. Phys. A379 (1982) 256
3) C. Yannouleas, M. Dworzecka and J.J. Griffin, Nucl. Phys. A397 (1983) 239
4) C. Yannouleas, Preprint GSI-83-25, Physica A (in press)
5) C. Yannouleas, to be published

Closed Irreversible Equations of Motion for the One-Body Density G

P. Buck, H. Feldmeier* and F. Beck
Institut für Kernphysik, Technische Hochschule Darmstadt

Based on former work on the subject we utilized the principle of maximum entropy as the only statistical assumption to close the hierachy of coupled equations for the density matrices on the one-body level in a weak coupling limit. In our case the principle of maximum entropy consists of the following steps:[1),2)]

We assume that the relevant information on the system is the one-particle information I:

$$I=\{P,Q,a_k^+a_l;\ <P>=1,<Q>=0,<a_k^+a_l>_t=\rho_{lk}(t)\ k,l=1,2,3,\ldots\}$$

It consists of a set of selected operators and the knowledge of their expectation values. Here, P is the projection operator onto the subspace occupied by the system (e.g. the Fock space), Q=1-P is the complementary projector, and $\{a_k^+a_l\}$ denote all one-particle operators.

The next step consists in assigning to the system a statistical operator R(t) which contains the information I and nothing else[3)]. To do so, one defines the information missing in R(t) as

$$S(t) = -tr\{R(t)\ln R(t)\}$$

which is also called entropy. Supposing the expectation values $\rho_{lk}(t)$ to be known, R(t) must maximize the entropy under the constraints of the given expectation values. The solution for R(t) is

$$R(t) = P\exp\{-\lambda_o(t)-\sum_{kl}\lambda_{kl}(t)\,a_k^+a_l\}\,P\ ,$$

where the Lagrange multipliers λ_{kl} are to be determined such that $tr\{PR(t)\}=1$ and $tr\{a_k^+a_l\,R(t)\}=\rho_{lk}(t)$.

Using projection methods, Robertson[4)] derived an exact closed equation of motion for R(t). Introducing the time dependent creation operators $\{c_k^+(t)\}$ which define at each time t the eigenbasis of $\rho(t)$, the Robertson equation can be cast into the form

$$\frac{d}{dt}<c_k^+(t)c_l(t)>_t=\frac{i}{\hbar}tr\{[H-h(t),c_k^+(t)c_l(t)]R(t)\}+\int_o^t K_{kl}(t,s)ds$$

Here, H is the hamiltonion of the system (including a two-particle interaction V) and h(t) is the generator of the unitary transformation which keeps $\rho(t)$ diagonal. The integrand K(t,s) is a rather complicated object which nevertheless is a functional of the one-particle density merely. The first term in the equation is called reversible, because it does not change the information entropy S, whereas the second one gives rise to irreversibility. The one-body hamiltonian h(t) consists of a mean-field part (this turns out to be just the TDHF-hamiltonian if the assumed information includes only the mean particle number) and a fluctuating part $\delta h(t)$ which is given by

$$\delta h_{kl}(t)=-i\hbar\int_o^t K_{lk}(t,s)ds\ [<c_k^+(t)c_k(t)>_t-<c_l^+(t)c_l^+(t)>_t]^{-1}$$

Thus, the collision term does not only give rise to a change of the occupation numbers but influences also the unitary motion.

Up to now the equations are exact. In order to calculate K(t,s) explicitly, we regard H-h(t) as a weak perturbation and perform a power expansion of K(t,s). This means that the reversible motion (which is promoted by h(t)) is fully taken into account and may be rather violent.

To first order K(t,s) vanishes. In this case one ends up with the well known TDHF equations. To 2nd order, again with particle number conservation in the mean, we get:

$$K_{\lambda\mu}(t,s) = \frac{1}{\hbar^2}\{C_{\lambda\mu}(t,s) + C^*_{\mu\lambda}(t,s)\}$$

where

$$C_{\lambda\mu}(t,s) = \sum_{\alpha\beta\nu} V_{\mu\alpha\beta\nu}(t)\,V_{\beta\nu\lambda\alpha}(s)\,B_{\beta\nu\lambda\alpha}(s)\ ,$$

$$B_{\beta\nu\lambda\alpha}(t) = \hat\rho_\beta(t)\,\hat\rho_\nu(t)\,(1-\hat\rho_\lambda(t))\,(1-\hat\rho_\alpha(t)) - \hat\rho_\lambda(t)\,\hat\rho_\alpha(t)\,(1-\hat\rho_\beta(t))\,(1-\hat\rho_\nu(t))$$

$\{\hat\rho_\alpha(t)\}$: eigenvalues of $\rho(t)$

$$V_{\mu\alpha\beta\nu}(t) = <0|c_\alpha(t)c_\mu(t)\ V\ c_\beta^+(t)c_\nu^+(t)|0>$$

(two-particle interaction)

From this we arrive immediately at

$$\frac{d}{dt}(\hat\rho_\lambda(t)) = \frac{1}{\hbar^2}\sum_{\alpha\beta\nu}\{\int_o^t \mathrm{Re}[V_{\lambda\alpha\beta\nu}(t)V_{\beta\nu\lambda\alpha}(s)]B_{\beta\nu\lambda\alpha}(s)ds\}$$

Thus, the change of the occupation numbers is due to a gain term and a loss term. These are just Pauli blocking factors multiplied by transition rates.

The perturbation expansion was carried out up to third order, where the formulas are much more complicated. Also the 2nd order formula for the case of sharp particle number as a constraint is much more involved. First numerical results of a small model system and comparison to the exact solution for this case are in progress.

1) H. Feldmeier, Lecture Notes in Physics, Vol 171 (Springer, Berlin, 1982) p. 384

2) P. Buck and H. Feldmeier, Phys. Lett. 129B (1983) p.172

3) A. Katz, Principles of Statistical Mechanics - The Information Theory Approach (Freeman, San Francisco, 1967)

4) B. Robertson, in: The Maximum Entropy Formalism; R.D. Levine and M. Tribus, eds, MIT-Press) 1978.

* Max-Planck-Institut für Kernphysik, Heidelberg

Explicit Treatment of N-Body Correlations within a Density-Matrix Formalism

S.J. Wang and W. Cassing
GSI Darmstadt

Conventional density-matrix approaches[1,2] with respect to the nuclear many-body problem appear to be formally transparent but not convenient for practical purposes. This is mainly due to the fact that the formulation itself does not lead to a unique or physically obvious truncation scheme. To remedy this deficiency, many-body correlations of order n have to be separated from the density matrix of rank n defined by

$$\rho_n = \mathrm{Tr}_{(A-n)} \{\rho_A\}$$

and their time evolution has to be studied separately. Within this aim we suggest the following separation ansatz for ρ_n, i.e.

$$\rho_n = A_{(n)} \sum_{p=1}^{n-1} \rho_{n-p}\, c_p + c_n, \qquad (1)$$

with $\rho_o = 1$ and $\rho_1 = c_1$. The essential decomposition in eq.(1) is related to the action of the operators S and A. While S symmetrizes with respect to all pair indices $(x_i x_i')$ and $(x_j x_j')$ ('bosons') the operator A antisymmetrizes with respect to all exchanges between single indices x_j and x_j' ('fermions'). Both operations imply that in eq.(1) no repeated terms appear. The lower index (n) indicates that the antisymmetrization or symmetrization is carried out among n variables. The properties of eq.(1) are as follows:

i) ρ_n contains all possible correlations among n particles,

ii) ρ_n is symmetric with respect to any exchange of pairs $(x_i x_i')$ and $(x_j x_j')$ and antisymmetric with respect to any exchange of x_i' and x_j',

iii) the n-body correlations c_n have the same symmetry as ρ_n as well as all terms $\rho_{n-p}\, c_p$.

Restricting the many-body Hamiltonian to be of two-body nature, i.e.

$$H_A = \sum_{i=1}^{A} h_o(i) + \sum_{j>i=1}^{A-1} v(ij), \qquad (2)$$

the time-evolution of the quantities c_n is governed by the following set of coupled differential equations[3]

$$\begin{aligned} i\hbar\, \dot{c}_n &= [(\sum_{i=1}^{n} h_o(i) + \sum_{j>i=1}^{n-1} v(ij)), c_n] \\ &+ \mathrm{Tr}_{(n+1)} [\sum_{i=1}^{n} v(i,n+1),\, c_{n+1}] \\ &+ A_{(n)} \sum_{p=1}^{n-1} [\sum_{j>i=1}^{n-1} v(ij), \rho_{n-p}\rho_p]_L \\ &+ \sum_{p=1}^{n} \mathrm{Tr}_{(n+1)} A_{(n+1)} [\sum_{i=1}^{n} v(i,n+1),\, \rho_{n-p+1}\, \rho_p]_L \end{aligned} \qquad (3)$$

for $n \leq A$, where the lower index L denotes that only 'linked' terms have to be considered. We call a term 'linked' when a product of terms is not separable with respect to the particle indices; e.g. in $v(12)\ A_{(3)}\ (\rho_1 c_2)$ the terms

$$v(12)\ \rho_1(33')c_2(12,1'2') \quad \text{or} \quad v(12)\rho_1(32')c_2(12,1'3')$$

are separable with respect to the indices (12) (shorthand notation for $(x_1 x_2)$) while terms like $v(12)\ \rho_1(12')c_2(23,1'3')$ are not. The concept of 'linked' and 'unlinked' terms is comparable to conventional diagrammatic perturbation schemes when keeping in mind, however, that the antisymmetrization causes additional linked terms in our approach.

The reformulation of the many-body problem offers a few advantages with respect to the conventional density-matrix formalism. The number of terms contributing to the r.h.s. of eq.(3) are drastically reduced because only linked terms appear. This is of specific interest with respect to numerical applications. Furthermore eq.(3) allows for a physically transparent truncation in the rank of the correlations because it is formulated completely with respect to the correlations themselves which are expected to become less important with increasing rank n. It can be shown[3] that eq.(3) for $c_n = 0$ ($n \geq 3$) yields a generalized Bethe-Goldstone equation in the stationary limit ($\dot{c}_2 = 0$) and generalized Faddeev equations for $c_n = 0$ ($n \geq 4$) and $\dot{c}_3 = 0$. Any truncation of eqs.(3) with respect to rank n is compatible with conservation laws for one- and two-body operators. Problems, however, arise if apart from the truncation scheme ($c_n = 0$, $n > m$) additional terms are neglected in the equation for $\dot{c}_m$, i.e. especially for perturbative solutions for $c_m(t)$.

References:

1) W.C. Schieve; in "Lecture Notes in Physics 28", Springer-Verlag, 1974, p.1
2) A.Z. Akhiezer, S.V. Peletminskii; Methods of Statistical Physics, Pergamon Press, Oxford, 1981
3) S.J. Wang and W. Cassing; to be published

On Thermal Blocking Mechanism of the Mass Drift in Dissipative Heavy Ion Collisions

T. Matulewicz,* A. Gobbi and J. Tõke, GSI Darmstadt

It has been suggested recently by L. Moretto that the apparent lack of mass drift in the early stages of dissipative collisions could be due to the temperature difference between the collision partners. According to this idea, which has been subsequently chequed in schematical calculations by Moretto and Lanza [1], temperature difference resulting from the nucleon exchanges between the colliding nuclei gives rise to a nucleon flux from the smaller nucleus (which is hotter) to the bigger one. This flux, caused by the temperature difference, could eventually compensate the one due to the potential energy landscape so that the net result could be the conservation of the mass asymmetry. The idea provides at the same time an explanation of the observed internuclear thermalization of the dissipated energy.

Here we present the results of a random-walk simulation of the dissipative collision process in which, in order to explore the temperature effects, temperatures as well as the numbers of nucleons in both colliding nuclei have been followed. It has been assumed for sake of simplicity that only nucleon exchange is responsible for the kinetic energy dissipation. Like in our earlier two-dimensional random-walk simulations [2], the branching probabilities for the transfers in both directions in the mass asymmetry degree of freedom as well as the expected excitation deposits in both nuclei have been evaluated based on the theoretical formalism of the transport theory of W. Nörenberg in its form presented in [3]. Fig.1 shows the effects of the imposed temperature difference on the asymmetry in the branching probabilities, which is a measure of the driving force. These effects clearly depend on the height of the barrier between the two potential wells filled with Fermi gases (which represent the two nuclei at contact) and are noticable only when the barrier tops a few MeV below the Fermi level. The role of a relatively high barrier was pointed out in the original paper of Moretto and Lanza as well.

Fig. 2. presents results of the random walk simulations for the system A=84 + A=166. As can be seen from Fig. 2a an appropriate choice of the barrier height leads to the blocking of the drift in the initial stage of the collision. Only after most of the available kinetic energy has been dissipated and the internuclear thermal equilibrium has been reached (compare with Fig. 2b) the potential energy surface landscape begins to drive the system towards the symmetry. Such a behaviour corresponds to what was predicted by Moretto and Lanza and what is being observed in experiments.

Inclusion of the above described thermal effects in our random walk simulations reduces the mass variances, which are no longer properly approximated by the number of exchanged nucleons. The reduction is only ca. 10 % in the present A=84 + A=166 case, however, depending on the barrier height in other cases not reported here was up to 50 %.

* Warsaw University, Poland

1) L. Moretto and E. Lanza, LBL Preprint 16373,1983.
2) J. Tõke and A. Gobbi, GSI Annual Report 1981, p.91. and J. Tõke, A. Gobbi and T. Matulewicz, GSI Annual Report 1982, p.90.
3) M. Dakowski, A. Gobbi and W. Nörenberg, Nucl.Phys.A378(1982)189.

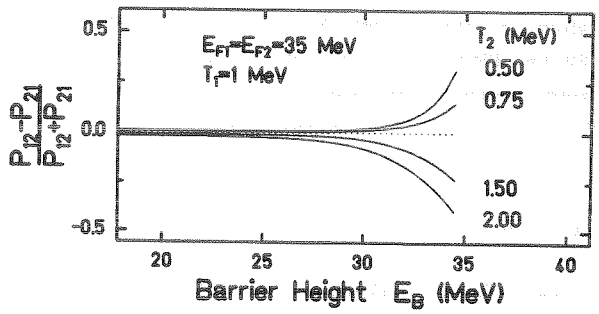


Fig. 1. Barrier height and temperature-difference dependence of the asymmetry in the nucleon transfer probabilities in the two directions between two Fermi-gas nuclei.

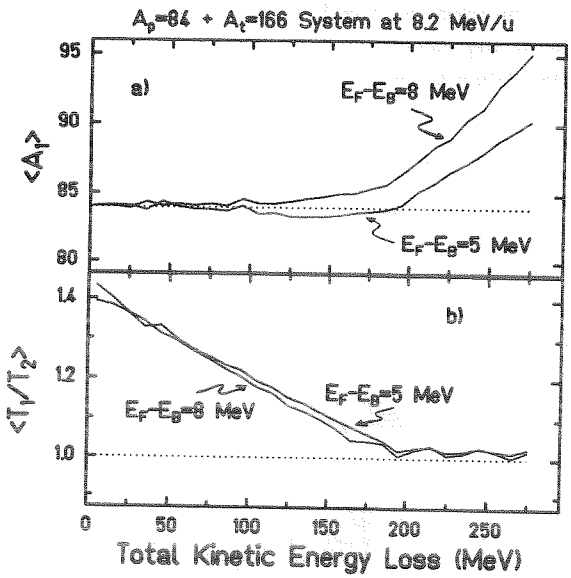


Fig. 2. Mass drift blocking and internuclar temperature equilibration seen in a random walk simulation of dissipative collisions for two values of the barrier height with respect to the Fermi level.

Time-Dependent Study of Shell Effects in Mass Transfer - The ^{136}Xe + ^{209}Bi(1130 MeV) Reaction -

B. Strack
GSI Darmstadt

We discuss the influence of shell structure effects on the mass transfer. Mass drift and -variances for the asymmetric ^{136}Xe + ^{209}Bi(1130 MeV) system are calculated.

Freiesleben and coworkers[1] considered quantitatively the consequences of shell effects on the nucleonic mass transfer by calculating the potential energy surface U for groundstate nuclei. The PES drives the particle transport by means of the following 'driving force'

$$V(A) = - D/T\ \partial_A\ U(A)$$

where D is the diffusion-coefficient and T the temperature of the system. We solve[2,3] the time-dependent Fokker-Planck-Equation for the probability f(A,t) to find a nuclear mass A at time t

$$\partial_t f(A,t) = [-\partial_A v(A) + D\partial_A]f(A,t)$$

and calculate the mean mass

$$\langle A\rangle = \int Af(A,t)dA$$

and the mass-variance

$$\sigma_A = \int (A-\langle A\rangle)^2 f(A,t)dA \quad .$$

If one compares now the experimental mass distribution[4] with the calculated mass drift and -variance one finds the following main insufficiences[5]:

a: Within the available interaction time it is not possible to reach the experimentally observed mass variances. Shell effects could be helpfull in that respect if they would be evident at high energy losses.

b: In the common FPE approach there is a strong proportionality between drift and diffusion leading to the following contradiction: Either one gets an acceptable variance with a too strong drift or one gets an acceptable drift with a far to small variance.

Figures 1,2 show this connection between drift and diffusion(variance) for different melting factors S clearly. S=1 means no shell structure and S=0 means full shell structure in the PES.

Can the use of different derived drift- and diffusion terms result in a better and systematic agreement between data and transport theories[7]?

References

1) Freiesleben, H., Hildenbrand,K.D., Pühlhofer, F. Schneider, W.F.W., Bock, R., Harrach, D.V., Specht, H.J.: Phys. A292(1979)171
2) Brosa,U.: Z. Phys. A298(1980)77
3) Strack,B.: Diploma thesis FU-Berlin 81 (unpublished)
4) Schröder, W.U., Birkelund, J.R., Huizenga, J.R., Wolf, K.L., Viola, V.E.: Phys. Rep. 45(1978)301-343
5) Brosa, U., Grossmann, S.: Talk 14. Sommer School on Nucl. Phys., Aug. 31.-Sep. 12.,1981, Mikolajki, Poland
6) Fröbrich, P., Strack, B., Durand, M.: Nucl. Phys. A406(1983)557-573
7) Feldmeier, H., Spangenberger, H.: submitted to Nucl. Phys.

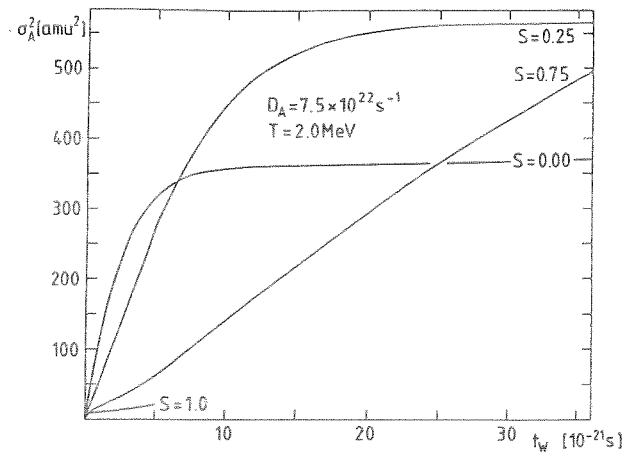


Fig. 1: Mass variance versus (interaction-)time for different melting factors S. Diffusion coefficient D and Temperature T are fixed. The short (S=1) curve shows the maximal interaction-time of a typical friction model[6]

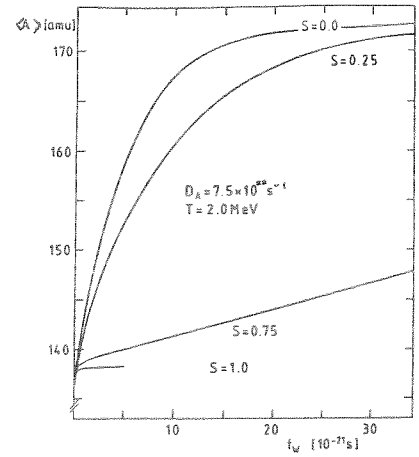


Fig. 2: Mass drift versus (interaction-)time for different melting factors S.

Non-adiabatic effects in the time dependent level crossing problem G

A. Góźdź [+], E. Werner, M. Brack
Institut für Theoretische Physik, Universität Regensburg

The main part of nonadiabatic effects of nuclear motion is often supposed to be due to intersections of energy levels[1]. To describe corrections to adiabatic collective motion, in applications, the evaluation of the jump probability at level crossings is mostly based on the known Landau-Zener asymptotic solution for an isolated two level system. However, this particular solution is obtained with somewhat unrealistic conditions: the initial and final deformations have to be very different from the deformation at the crossing point while the collective velocity is assumed to be constant. The discussion of the general solution of the LZ-model with arbitrary initial conditions[2] shows that for the jumping probabilities considered as functions of the collective velocity $\dot{\alpha}$ the following characteristic features are observed:

i) The diabatic jumping probability is an oscillating function for small $\dot{\alpha}$ with the frequency being a strongly decreasing function of the collective velocity.

ii) There exists a specific value of the collective velocity, $\dot{\alpha}_c$, which corresponds to the last minimum of the diabatic jumping probability. If $\dot{\alpha}>\dot{\alpha}_c$ the probability of a jump becomes a monotonously increasing function of $\dot{\alpha}$.

iii) The adiabatic jumping probability, J_A, is a smooth function of $\dot{\alpha}$ but it is bounded by a number $J_{Amax} \leq 1$ when $\dot{\alpha} \to \infty$. For a symmetric interval (width 2α) around the crossing one obtaines $J_{Amax}=(b\alpha)^2[(b\alpha)^2+4\delta^2]^{-1}$, where b and $2\cdot\delta$ are the difference of the diabatic level slopes and the energy gap between eigenlevels at the endpoints of the interval, respectively.

The above saturation property (iii) shows that there can be considerable contributions to J_A at large distances from the crossing point. Therefore, if the average length of intervals between successive crossings is such that J_A is appreciably smaller than one in one interval, there must be a strong dynamical influence of the "tail" of the foregoing crossings on what happens at a particular one. Consequently, the problem can not be reduced to a series of independent crossings where the situation at the end of the n-th interval serves only to define the initial conditions for the (n+1)-th interval.

[1] Nörenberg W., Phys. Lett. B104, 107 (1981), preprint GSI-82-36

[2] Góźdź A., Werner E., Brack M., to be published

[+] On leave from the University of Maria Sklodowska-Curie, Lublin, Poland.

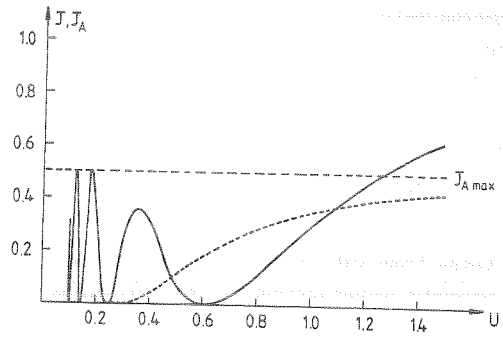


Fig. 1: Typical behaviour of the diabatic (solid line) and adiabatic (dashed line) jumping probabilities as functions of the collective velocity ($-\alpha_0=\alpha=1$ fm, b=1 MeV · fm^{-1}, δ = 0.5 MeV, u = 0.1 ÷ 1.4 MeV · fm, h = 1).

On the Dynamical Single-Particle Basis in Large-Amplitude Nuclear Motion

W. Cassing, S.J. Wang and W. Nörenberg
GSI Darmstadt

We are interested in solutions of the time-dependent single-particle (s.p.) Schrödinger equation

$$\{H(q(t)) - i\hbar\, d/dt\}|\Psi_\alpha(t)\rangle = 0 , \qquad (1)$$

depending on a time-dependent collective parameter $q(t)$, as a function of the collective velocity $\dot{q}$ or collective kinetic energy per nucleon denoted by ε^* throughout this contribution. In this respect we investigate various approximations for $\Psi_\alpha(t)$ and check the validity of the approximation as a function of time. The model we use for $H(q)$ is the Nilson-type Hamiltonian

$$H(q) = -\hbar^2/(2M)\,\Delta + M/2\,\omega_0^2\,(q(x^2+y^2) + q^{-2}z^2) - 2\hbar\omega_0\kappa\,\vec{l}\cdot\vec{s} - \hbar\omega_0\kappa\mu\,l^2 \qquad (2)$$

with κ,μ taken from the literature[1]. Expanding $\Psi_\alpha(t)$ in terms of adiabatic wavefunctions $\chi_\nu(q)$ defined by

$$\{H(q) - \varepsilon_\nu\}|\chi_\nu(q)\rangle = 0, \text{ i.e.} \qquad (3)$$
$$\Psi_\alpha(t) = \Sigma_\nu\, f_{\alpha\nu}(t)\,\chi_\nu(q(t))\exp\{-i/\hbar\int^t \varepsilon_\nu(q(t'))dt'\},$$

we find that the expansion coefficient $f_{\alpha\nu}(t)$ is a drastically changing function in time for $\dot{q} \geq 0.1\,\omega_0$ if the level $\varepsilon_\nu(q)$ exhibits a quasi-crossing type of behaviour. From this we conclude that an adiabatic approximation (3) breaks down for $\dot{q} > 0.1\,\omega_0$ or $\varepsilon^* \simeq 0.02$ MeV in case of a heavy nucleus (A = 224). In order to avoid the problem of quasi-crossings a diabatic s.p. basis $\phi_\beta(q)$ has been introduced e.g. by restoring the symmetries of the collective motion[2], i.e.

$$\{H_0(q) - \eta_\mu(q)\}|\phi_\mu^0(q)\rangle = 0$$
$$\text{with } H_0(q) = H(q) - H', \qquad (4)$$
$$H' = -2\hbar\omega_0\kappa\,(l_x s_x + l_y s_y) - \hbar\omega_0\kappa\mu(l_x^2 + l_y^2).$$

Diabatic (scaling) s.p. states $\phi_\beta(q)$ then are defined by

$$\phi_\beta(q) = \Sigma_\mu W_{\beta\mu}(q_0)\phi_\mu^0(q) \qquad (5)$$

with $W_{\beta\mu}(q_0)$ fixed by the condition that the diabatic states initially ($t=0$, $q=q_0$) are equal to the adiabatic states $\chi_\beta(q_0)$. Stationary states of the type (5) then yield a better approximation to (1) for a similar expansion as (3) if

$$\Sigma_\mu|\langle\phi_\mu|\dot{q}\frac{\partial}{\partial q}|\phi_\beta\rangle| \geq \hbar^{-1}\Sigma_\mu|\langle\phi_\mu|H'|\phi_\beta\rangle| \qquad (6)$$

i.e. if the dynamical couplings or matrix elements of $\dot{q}\,\partial/\partial q$ are larger within the basis ϕ_β than the matrix elements of H'. Numerical investigations however yield that a stationary diabatic (scaling) basis works only up to $\varepsilon^* = 0.1$ MeV[3] for the model nucleus considered (A=224). The next step in improving the basis is to account for the collective motion in first order in $\dot{q}$ by introducing a scalar function $\Phi(q,x,y,z)$,[4,5], i.e.

$$\psi_\alpha(t) \sim \phi_\alpha(q)\exp\{-i/\hbar\, M\,\dot{q}\,\Phi\}\exp\{-i/\hbar\int^t \eta_\alpha(t')dt'\}. \qquad (7)$$

This ansatz can be shown[3] to yield a good approximation to the solution of (1) up to $\varepsilon^* \sim 4$ MeV if

$$\langle\phi_\alpha|\nabla\Phi\cdot\nabla + \tfrac{1}{2}\Delta\Phi - \partial/\partial q|\phi_\beta\rangle = 0 \text{ for all } \alpha,\beta \text{ and } q \qquad (8)$$

and s.p. coupling terms due to $\ddot{q}$ can be neglected. The time-scale of the validity of (7), however, is only investigated for times smaller or comparable to the local relaxation time due to 2-body collisions given by[6]

$$\tau_{loc} \sim 2\cdot 10^{-22}\,s/\varepsilon^*. \qquad (9)$$

In case of quadrupole motion Φ turns out to be given by $\Phi = (8q)^{-1}(x^2+y^2-2z^2)$ and the s.p. states $\phi_\mu(q)$ are nothing but oscillator states which scale with the variable q. The ansatz (7) implies that the mass parameter for the collective motion is given by the irrotational flow value. On the other hand diabatic s.p. states ϕ_α for a given collective field $\nabla\Phi(q)$ may be determined from eq.(8).

We have to point out that a dynamical s.p. basis of the type (7) also holds (up to $\varepsilon^* \sim 4$ MeV) in case of nucleus-nucleus collisions[3] if the Hamiltonian (2) is given by a 2-center harmonic oscillator with spin-orbit coupling [7].

References

1) P. Ring, P. Schuck: The Nuclear Many-Body Problem (Springer, 1980)
2) W. Nörenberg: Phys. Lett. 104B (1981) 107
W. Cassing, W. Nörenberg: Nucl. Phys. A 401 (1983) 467
3) W. Cassing, S.J. Wang, W. Nörenberg: Preprint GSI-83-36
4) K.K. Kan, J.J. Griffin, Phys. Rev. C15 (1977) 1126
5) H.C. Pauli, L. Wilets, Z. Phys. A 277 (1976) 83
D. Glas, Z. Phys. A 277 (1976) 195
6) G.F. Bertsch: Z. Phys. A 289 (1978) 103
7) J. Maruhn, W. Greiner, Z. Phys. 251 (1972) 431

Traces of Landau-Zener Transitions in the Fusion Cross Section of Heavy Nuclei ?

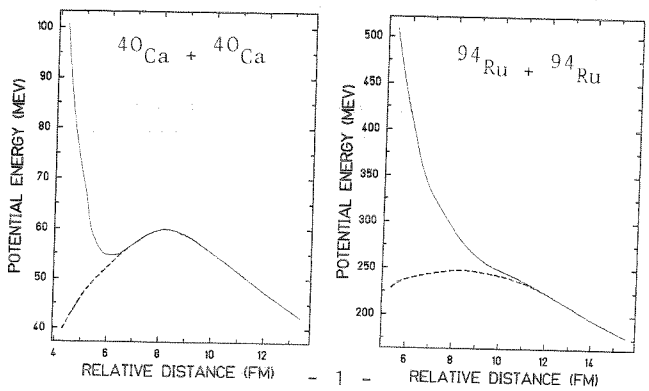
W. Cassing

GSI Darmstadt

For collective energies per nucleon within the range 0.04 MeV $\leq E_{coll}/A \ll$ 40 MeV time-dependent single-particle states can adequately be described by a travelling diabatic basis for central heavy-ion collisions[1,2]. Diabatic s.p. motion essentially implies coherent particle-hole excitations which yield an additional repulsive potential ΔV_{diab} during the initial phase of the collision. This extra potential decays in time due to two-body collisions[1,3] or due to one-body coupling matrix elements at crossings of diabatic levels if the collective energy per nucleon becomes too small[2,3]. The influence of diabatic particle-hole excitations on heavy-ion dynamics can be illustrated by plotting the nucleus-nucleus potential

$$V_{NN}(R...) = V_{ad}(R...) + \Delta V_{diab}(R...) \qquad (1)$$

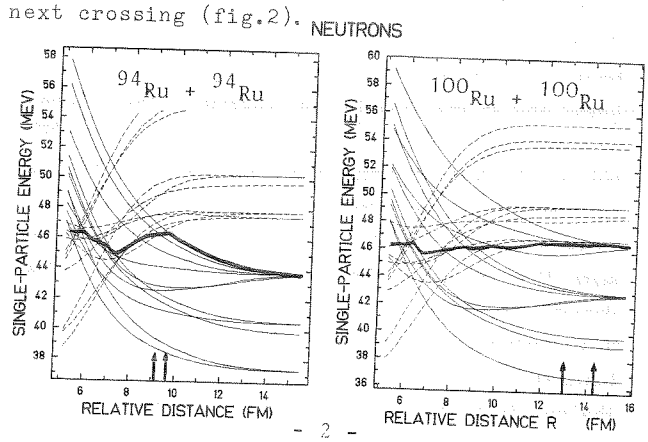
as well as the adiabatic potential V_{ad} as a function of the distance R between the center of masses of the two nuclei. The adiabatic potential V_{ad} in (1) represents the static ground state energy for fixed collective degrees of freedom[4]. In fig.1 V_{NN} (full lines) and V_{ad}



- 1 -

(dashed lines) are displayed for the systems $^{40}Ca + ^{40}Ca$ and $^{94}Ru + ^{94}Ru$ with $\Delta V_{diab}(R)$ evaluated along the line of Ref.5. The graphs indicate that at least with respect to fusion diabatic p.h. excitations play a minor role for $^{40}Ca + ^{40}Ca$ because they occur inside the interaction barrier. With increasing charge and mass, however, ($(Z^2/A)_{eff}$ = 41.2 for $^{94}Ru + ^{94}Ru$) the static (adiabatic) interaction barrier shows up for more compact shapes of the dinuclear system[6] and level crossings outside the interaction barrier become more frequent[7,8].

The influence of specific level crossings is most instructively displayed in diagrams of the type of fig.2 where all diabatic levels are shown as a function of R which cross the Fermi level (thick line) for $^{94}Ru + ^{94}Ru$ and $^{100}Ru + ^{100}Ru$ ($(Z^2/A)_{eff}$ = 38.72). While for the ^{94}Ru system the first occupied levels (full lines) are found to cross the Fermi level for R <10fm two distant crossings on the other hand are found for $^{100}Ru + ^{100}Ru$ (indicated by arrows) where the Landau-Zener transition probability should be close to 1. All other crossings for R<11fm are not important because E_{coll}/A is too small for center of mass energies close to the interaction barrier. The distant p.h. excitations, however, decay almost completely at the next crossing (fig.2).



- 2 -

Numerical calculations, in which Landau-Zener transitions as well as relaxation by two-body collisions are accounted for, show that apart from the static change of the interaction barrier for different isotopes dynamical shell effects in terms of diabatic p.h. excitations require additional energy in the relative motion in order to fuse the system[9]. In case of $^{94}Ru + ^{94}Ru$ this extra energy is close to zero while for the other (may be extreme) system $^{100}Ru + ^{100}Ru$ a maximum extra energy of 6 MeV was found.

References:

1) W. Nörenberg, Phys.Lett.104B(1981)107
2) W. Cassing et al, Preprint GSI-83-36
3) W. Cassing, W. Nörenberg, Nucl.Phys.A401 (1983)467
4) P. Möller, J.R. Nix, Nucl.Phys.A272(1976)502
5) A. Lukasiak, W. Cassing, W. Nörenberg, Preprint GSI-84-1
6) W.J. Swiatecki, Nucl.Phys.A376(1982)275
7) J.Y. Park et al, Phys.Rev.C21(1980)958
8) J. Maruhn, W. Greiner, Z.Phys.251(1972)431
9) W. Cassing, to be published

Diabatic Interaction Potential for Nucleus-Nucleus Collisions

A. Lukasiak
GSI Darmstadt

W. Nörenberg
Institut für Kernphysik der Technischen Hochschule Darmstadt and GSI Darmstadt

We have studied some characteristic properties of the diabatic potential, applicable in the description of nucleus-nucleus collisions in the energy range between a few tenths up to ca. 10 Mev/u above the interaction barrier. This diabatic interaction potential describes an intermediate physical situation between the adiabatic and the sudden approximation.

In Fig. 1 the diabatic interaction potential without Coulomb interaction is presented versus the relative distance R. It is calculated as the sum of the nuclear part of the adiabatic interaction energy (dashed line) and the energy stored in the diabatic particle-hole excitations (the difference between dash-dotted and solid lines) and in the density rearrangement (the difference between dashed and dash-dotted lines). The adiabatic part of the total diabatic interaction potential has been calculated as a double volume integral of a Yukawa-plus-exponental folding function [1]. To estimate the amount of the energy stored in the diabatic density rearrangement, we have performed a calculation of the interaction energy for the adiabatic and the diabatic density destributions. The interaction energy of the two nuclei as a function of their relative distance R is calculated in the framework of the energy-density formalism[2]. The energy stored in diabatic particle-hole excitations (calculated as a sum of all of these excitations) is much larger than the energy of the density rearrangement. The calculated total nuclear part of the diabatic potential (solid line) is attractive in the vicinity of the contact point. With decreasing R it is observed that contributions from compression start at the contact point R_c (R_c= 10.4 fm is defined by the sharp cut-off density profiles) while diabatic particle-hole excitations contribute already for smaller overlaps. The repulsive core of the potential results essentially from diabatic particle-hole excitations. In Fig. 2 the nuclear interaction potentials are plotted for the adiabatic, sudden and diabatic approach as functions of the relative distance R. Both adiabatic (dashed line) and diabatic (solid line) interaction potentials are the same as in Fig. 2. The third potential (dash-dotted line) is the proximity potential[3] in the sudden approximation. The adiabatic potential is strongly attractive, while the sudden and diabatic potentials show a strongly repulsive core. In contrast to the sudden potential, the repulsion in the diabatic potential results by 90% from the diabatic particle-hole excitations, while only 10% comes from compressional effects.

[1] P. Möller and J.R. Nix, Nucl. Phys. A361 (1981) 117.
[2] K.A. Brueckner et al., Phys. Rev. 181 (1969) 1543.
[3] J. Blocki et al., Ann. Phys. (N.Y.) 105 (1977) 427;

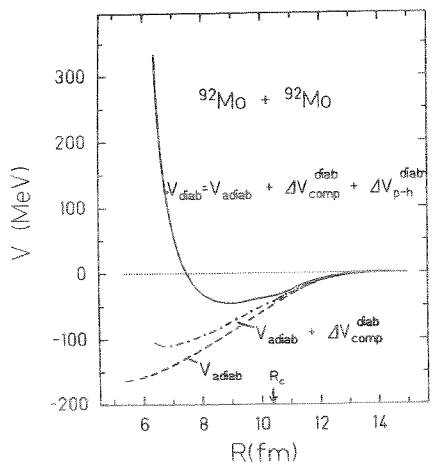


Fig. 1. The diabatic interaction potential and its components versus R.

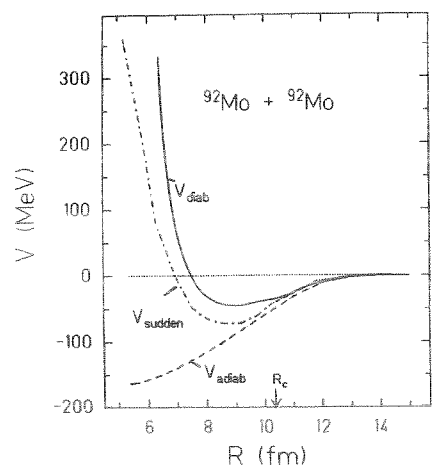


Fig. 2. The interaction potentials for ^{92}Mo + ^{92}Mo corresponding to the adiabatic, sudden and diabatic approaches versus R.

Scaling Property and Cranking Mass Tensor in the Diabatic Approach

A. Lukasiak and W. Cassing
GSI Darmstadt

W. Nörenberg
Institut für Kernphysik der Technischen Hochschule Darmstadt and GSI Darmstadt

We consider the single-particle motion in a time-dependent mean field $U(x;\vec{q}(t))$ where x denotes position, spin and isospin of the nucleon and $\vec{q} \equiv \{q_n(t)\}$ a set of time-dependent collective parameters describing the shape of the nuclear system. The solution $\Psi_\beta(t)$ of the time-dependent Schrödinger equation can be expressed as an expansion

$$|\Psi_\beta(t)\rangle = \sum_\alpha c_{\beta\alpha}(t)\, \exp[-i\{\int_0^t dt' \varepsilon_\alpha(t') - MW(x;\vec{q},\dot{\vec{q}})\}/\hbar]\, |\psi_\alpha(\vec{q})\rangle \quad (1)$$

in terms of some orthonormal stationary basis functions $|\psi_\alpha(\vec{q})\rangle$ with the initial condition $c_{\beta\alpha}(t=0)=\delta_{\beta\alpha}$. In addition to the usual energy phase factor, a collective phase factor has been introduced which is common to all states α. By applying the momentum operator $\vec{p}=-i\hbar\,\mathrm{grad}$ we see that gradW denotes an irrotational (rot gradW=0) velocity field which is imposed on the stationary wave functions. Inserting the expansion (1) into the Schrödinger equation and projecting on the state ψ_γ we find the set of coupled first-order differential equations

$$i\hbar \dot{c}_{\beta\gamma} = \sum_\alpha c_{\beta\alpha} \langle\psi_\gamma|\, H'+U_1+U_2 \,|\psi_\alpha\rangle \cdot \exp[-i\int_0^t dt'\{\varepsilon_\alpha(t') - \varepsilon_\gamma(t')\}/\hbar] \quad (2)$$

with $\varepsilon_\alpha = \langle\psi_\alpha|H|\psi_\alpha\rangle$ for the determination of the expansion coefficients $c_{\beta\alpha}$. The coupling terms are given by

$$H' = H - H_o = H - \sum_\alpha |\psi_\alpha\rangle \varepsilon_\alpha(\vec{q}) \langle\psi_\alpha| \quad (3)$$

$$U_1 = -i\hbar \{ \sum_n \dot{q}_n \partial/\partial q_n - \tfrac{1}{2}[\Delta, W] \} \quad (4)$$

$$U_2 = -\tfrac{1}{2}M(\nabla W)^2 + M\sum_n (\dot{q}_n \partial W/\partial q_n + \ddot{q}_n \partial W/\partial \dot{q}_n) \quad (5)$$

where H' is independent of the collective velocity $\dot{\vec{q}}$. The optimal choice for the stationary basis states ψ_α is defined by minimizing the couplings such that the $c_{\beta\alpha}(t)$ keep close to the initial values $\delta_{\beta\alpha}$. For larger velocities it is often more convenient to choose basis states ψ_α which have smaller dynamical couplings. We define diabatic basis states $\psi_\alpha^{diab} \equiv \phi_\alpha$ by the condition that the first-order dynamical coupling (4) vanishes[1]. Introducing the decomposition $W=\sum_n \dot{q}_n w_n(\vec{q})$ we have

$$(\partial/\partial q_n)|\phi_\alpha\rangle = \tfrac{1}{2}[\Delta, w_n]|\phi_\alpha\rangle = \{(\vec{\nabla} w_n)\cdot\vec{\nabla} + \tfrac{1}{2}(\Delta w_n)\}|\phi_\alpha\rangle \quad (6)$$

as the diabaticity criterion which is independent of $\dot{q}_n$ and hence, allows to define stationary diabatic basis states. The relation (6) ascribes the change of any diabatic state with q_n to a collective displacement field $\vec{\nabla} w_n$ which scales all wave functions in the same way.

In the diabatic limit the total energy of the system is determined by the expectation value

$$E = \sum_\alpha n_\alpha \langle\tilde{\phi}_\alpha|H|\tilde{\phi}_\alpha\rangle \quad (7)$$

where n_α denotes the occupation probability of the travelling diabatic states,

$$|\tilde{\phi}_\alpha\rangle = \exp[iMW/\hbar]\, |\phi_\alpha\rangle. \quad (8)$$

Whereas the static term (which does not depend on $\dot{q}$) is the diabatic potential, the term proportional to $\dot{q}^2$ gives the collective kinetic energy

$$T_{coll} = \sum_\alpha n_\alpha \langle\phi_\alpha|\, \tfrac{1}{2}M(\vec{\nabla}W)^2 \,|\phi_\alpha\rangle \quad (9)$$

as the sum of the collective kinetic energies for the individual nucleons in the (occupied) diabatic states. Introducing the same decomposition as in eq. (6) we find $T_{coll} = \frac{1}{2}\sum_{n,m} B_{nm}\dot{q}_n\dot{q}_m$ with the diabatic mass tensor

$$B_{nm} = M \sum_\alpha n_\alpha \langle\phi_\alpha|\, (\vec{\nabla} w_n)\cdot(\vec{\nabla} w_m)\, |\phi_\alpha\rangle . \quad (10)$$

This expression is equivalent to the cranking-model formula

$$B_{nm}^{crank} = \hbar^2 \sum_{\alpha\neq\beta} n_\alpha \langle\phi_\beta|\partial/\partial q_n|\phi_\alpha\rangle \cdot \langle\phi_\beta|\partial/\partial q_m|\phi_\alpha\rangle/(\varepsilon_\beta - \varepsilon_\alpha) + c.c \quad (11)$$

for the diabatic states ϕ_α satisfying the diabaticity condition (6), i.e. with $\vec{p}=\hbar\vec{\nabla}/i$

$$\langle\phi_\beta|\partial/\partial q_n|\phi_\alpha\rangle = -\tfrac{1}{2}\hbar^{-2}\langle\phi_\beta|\,[\vec{p}^2, w_n]\,|\phi_\alpha\rangle \quad (12)$$

$$= -\frac{M}{\hbar^2}(\varepsilon_\beta - \varepsilon_\alpha)\langle\phi_\beta|\, w_n\,|\phi_\alpha\rangle \quad (13)$$

where we have used $[T, w_n] = [H_o, w_n]$. Inserting (12) and (13) for $\langle\phi_\beta|\partial/\partial q_n|\phi_\alpha\rangle$ and $\langle\phi_\beta|\partial/\partial q_m|\phi_\alpha\rangle$, respectively, in eq. (11) and applying closure and the relation

$$[p^2, w_n]w_m + \text{h.c.} = 2[\vec{p}, w_n]\cdot[\vec{p}, w_m] \quad (14)$$

we easily varify

$$B_{nm}^{crank} = B_{nm} . \quad (15)$$

Thus we can use the cranking-mass formula (11) instead of the expression (10) and hence, we need not to calculate the velocity fields $\vec{\nabla} w_n$. Using (13) in B_{nm}^{crank} it is seen that there are no singularities at crossing of diabatic states.

[1] A. Lukasiak, W. Cassing, W. Nörenberg, GSI-84-1 Preprint, submitted to Nucl. Phys. A.

Block Diagonalization for an Improved Diabatic Basis with Full Spin-Orbit Coupling.

A. Lukasiak
GSI Darmstadt

W. Nörenberg
Institut für Kernphysik der Technischen Hochschule Darmstadt and GSI Darmstadt

The precise definition of the diabatic single-particle states $|\phi_\alpha>$ has been given in[1] where also two construction methods, namely the maximum-overlap and the maximum-symmetry method are described. The essential idea of the maximum-symmetry method is the definition of a scaling Hamiltonian H_{sc} of higher symmetry with eigenstates which have scaling properties with respect to the collective displacement field. For symmetric systems non-diagonal couplings arise mainly from the spin-orbit potential. In[1] we have neglected these non-diagonal spin-orbit terms. However, these coupling terms are not always sufficiently small. Therefore, we introduce here the following modification. Starting from the scaling Hamiltonian H_{sc} we divide the subspace of good quantum numbers, i.e. the component Ω of the angular momentum along the symmetry axis and the parity Π (for the symmetric systems considered here), into two blocks $(\Omega,\Pi)_<$ and $(\Omega,\Pi)_>$ according to wether $n_z<n_x+n_y+1$ or $n_z\geq n_x+n_y+1$ where n_x, n_y and n_z denote the numbers of nodes orthogonal to and along the symmetry axis, respectively. Diagonalizing the full spin-orbit coupling within these blocks for the separated fragments we define the linear combination of the scaling eigenstates and hence, the diabatic states like in[1]. The additional block diagonalization gives an improved diabatic representation[2] with negligible spin-orbit couplings while the dynamical couplings remain sufficiently small. Diabatic levels obtained by this refined maximum-symmetry method for ^{92}Mo + ^{92}Mo are shown in Fig. 1 and compared with the corresponding adiabatic levels. The relative distance R is defined by the distance between the mass centers calculated from the matter distributions on the left-hand and right-hand side.

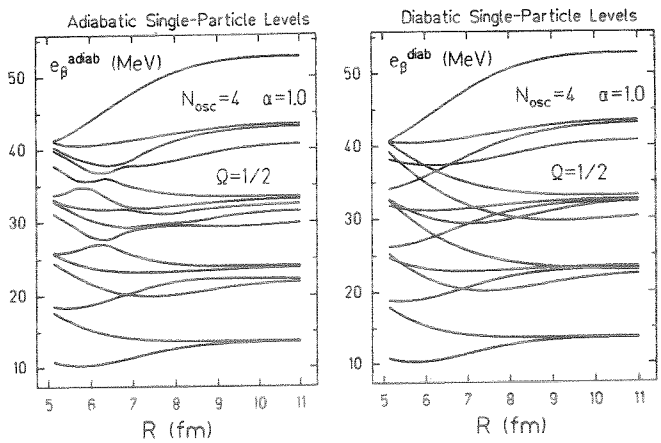


Fig. 1. Diabatic and adiabatic single-particle levels with Ω=1/2 in the symmetric two-center potential with full spin-orbit term as functions of the relative distance R.

Figure 2 shows the diabatic single-particle levels which cross the Fermi energy (heavy solid line). States which are steeply rising with decreasing R are characterized by the maximal number of nodes along the symmetry axis (z-axis), while the steeply descending states have maximal number of nodes in the direction perpendicular to the symmetry axis. On the right-hand side of Fig. 2 the initial distribution of the occupation probabilities of the diabatic states is plotted. It is not a sharp Theta-function because the diabatic states are some superposition of the adiabatic states of the separated system.

[1] A. Lukasiak, W. Cassing, W. Nörenberg, GSI-84-1 Preprint, submitted to Nucl. Phys. A.
[2] A. Lukasiak and W. Nörenberg, GSI-84-2 Preprint, submitted to Phys. Lett. B.

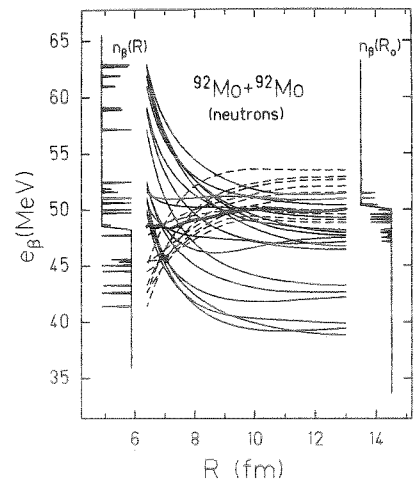


Fig. 2. Diabatic neutron levels for ^{92}Mo + ^{92}Mo around the Fermi energy (heavy solid line) versus R. The occupation probabilities resulting from the (adiabatic) ground states of the separated nuclei are indicated for the separated nuclei and for the spherical compound shape (R≈6.5fm). States which are occupied by more (less) than 50% are indicated by solid (dashed) lines.

Elastoplasticity Tensor for Nucleus-Nucleus Collisions

A. Lukasiak
GSI Darmstadt

W. Nörenberg
Institut für Kernphysik der Technischen Hochschule Darmstadt and GSI Darmstadt

We have studied incoherent aspects of large-amplitude collective nuclear motion for nucleus-nucleus collision in the energy range of a few tenths of MeV up to 10 MeV/u above the interaction barrier. The incoherent aspect is represented by residual two-body collisions which lead to statistical equilibrium within the intrinsic degrees of freedom (local equilibrium). An important consequence of the combined effects of diabatic single-particle motion and dissipative two-body collisions is a friction force with a significant retardation[1] for realistic values of the mean free path of nucleons.

For a diabatic two-center shell model, we have calculated the elastoplasticity tensor,

$$C_{ij} = - \sum_{\alpha} (\partial\varepsilon_\alpha/\partial q_i)\,(\partial\varepsilon_\alpha/\partial q_j)\,|\partial\bar{n}_\alpha/\partial\varepsilon_\alpha| \,. \qquad (1)$$

Here, ε_α denote diabatic single-particle energies, $\bar{n}_\alpha$ their local equilibrium occupations, and $q_i=\{\zeta,\delta,\varepsilon\}$ are collective variables corresponding to elongation, deformation and neck parameters. In the elastic limit the quantity (1) together with the diabatic mass parameter[2] determines harmonic oscillations. In the dissipative limit it contributes as a friction tensor to the retarded friction force[1],

$$F_i(t) = \sum_j \int dt'\, C_{ij}(t')\, \exp(-(t-t')/\tau_{loc})\,\dot{q}_j(t') \qquad (2)$$

where τ_{loc} is the local equilibration time. The retarded-friction force $F_i(t)$ describes an elastic response of the nucleus in the case of perturbations fast compared to the local equilibration time. However, for slow perturbations it describes a dissipative response.

In Fig.1, we have presented contour plots of the two diagonal components $C_{\zeta\zeta}$ and $C_{\delta\delta}$ as functions of the elongation ζ and deformation δ for two temperatures T=0.5 and T=2 MeV. For smaller temperatures both components show the same characteristic ridge arising from the strongly varying $\bar{n}_\alpha$ with q_i and corresponding to high density of the diabatic single-particle energies in the vicinity of the Fermi energy. This characteristic structure disappears at higher temperatures where the elastoplasticity tensor shows a smooth dependence on the collective variables, different, however, for the various components. The strongest dissipation of the energy occurs in the ridge. Therefore, the position of this ridge in multidimensional collective variable space, its dependence on the collective variables, as well as on temperature, might be crucial for the predictions concerning the fusion ability of the colliding systems.

[1] W. Nörenberg, Nucl. Phys. A409 (1983) 191;
S. Ayik and W. Nörenberg, Z. Phys. A309 (1982) 121.
[2] A. Lukasiak, W. Cassing, W. Nörenberg, GSI-84-1 Preprint, submitted to Nucl. Phys. A.

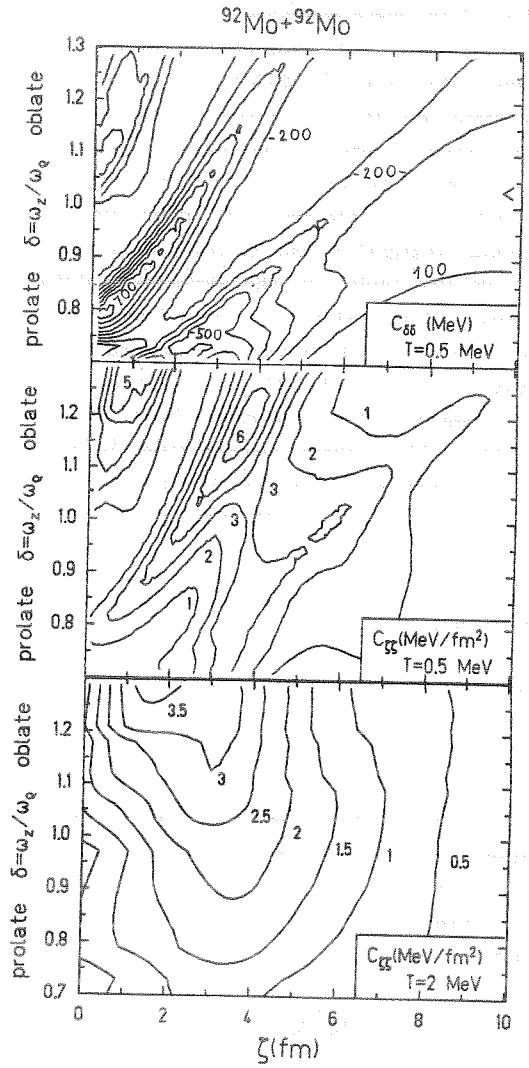


Fig. 1. (a) Contour plot of the diagonal component $C_{\delta\delta}$ of the elastoplasticity tensor for the symmetric system $^{92}Mo+^{92}Mo$ (only protons) at T=0.5 MeV. (b) The same for component $C_{\zeta\zeta}$. (c) The component $C_{\zeta\zeta}$ at T=2 MeV.

On a Fluid-Dynamical Description of Elastoplastic Fermi Systems

B. Morgenstern
GSI Darmstadt

W. Nörenberg
Institut für Kernphysik der TH Darmstadt and GSI Darmstadt

An attractive feature of fluid dynamics[1] is the possibility of describing a many-body system only by its single-particle density $n(\vec{r},t)$ and the collective velocity field $\vec{v}(\vec{r},t)$. Within this framework giant vibrations of nuclei have been approached by scaling of the wave functions with a collective displacement field. An important property of this scaling is the dynamical distortion of the local Fermi surface, giving rise to a large restoring force[2]. These considerations are restricted to small amplitudes. We have extended this fluid-dynamical description to large-amplitude deformations by including dissipation due to two-body collisions. Our starting point is the dissipative diabatic dynamics (DDD) which has been introduced[3] in order to treat simultaneously the coherence of the diabatic single-particle motion in a time-dependent mean field and the incoherence due to two-body collisions. The diabatic representation is defined by the vanishing of the coupling matrix elements proportional to $\dot{q}$ between the basis states

$$|\phi_\alpha(q,\dot{q};t)\rangle = \exp[-i\hbar^{-1}\{\int dt' \varepsilon_\alpha(t') - MW(q,\dot{q})\}]|\phi_\alpha(q)\rangle$$

which results in the scaling property

$$\partial/\partial q \; |\phi_\alpha(q)\rangle = (\vec{\nabla}w)\cdot\vec{\nabla}\,|\phi_\alpha(q)\rangle \quad .$$

For simplicity we have considered only a single collective variable q and irrotational flow, such that the velocity potential is given by $W = \dot{q}w$ with $\Delta w = 0$. Dissipation is introduced by the relaxation ansatz

$$\partial n_\alpha(t)/\partial t = -\tau^{-1}(n_\alpha - \bar{n}_\alpha)$$

for the occupation probabilities n_α. Here, τ and $\bar{n}_\alpha$ denote the intrinsic equilibration time and the equilibrium values of the n_α's.

In formulating a fluid-dynamical approach to DDD we introduce the Wigner transform $f(\vec{r},\vec{p};q,\dot{q};t)$ of the single-particle density matrix. The total energy of the system is divided into the collective kinetic energy $B\,\dot{q}^2/2$ and the collective potential energy $V(q,t)$. The mass parameter takes the irrotational flow value $B(q)$. The collective potential $V(q,t)$ contains a repulsive contribution from the deformation of the local Fermi surface and depends explicitly on time via the time dependence of the occupation probabilities $n_\alpha(t)$. The Lagrange equation determines the equation of motion

$$d/dt\{B(q)\dot{q}\} = -\partial V(q,t)/\partial q = F = \bar{F} + F'$$

for the collective variable $q(t)$. Here, $\bar{F} = -\partial\bar{V}/\partial q$ denotes the equilibrium force, while the elastoplastic force F' results from the equilibrating distorted Fermi surface and satisfies the differential equation

$$dF'/dt = (\partial F'/\partial q)\dot{q} - \tau^{-1}F'$$

with the solution $(F'(t=0) = 0)$

$$F' = -\int_0^t dt'\; C(t') \exp\,[-(t-t')/\tau]\dot{q}(t')$$

where $C(t')$ is the elastoplasticity coefficient given by

$$C(q) = (2/M)\int d^3p \int d^3r\; p_k u_{kl} u_{lj} p_j \bar{f}(\vec{r},\vec{p};q)$$

where M denotes the nucleonic mass and $u_{kl} = \partial_k\partial_l w$ is the strain tensor.

In this way we have reformulated DDD by using the Wigner transform. Introducing the local density approximation for the evaluation of the adiabatic force $\bar{F}(q)$ and the elastoplasticity coefficient $C(q)$ we arrive at a fluid-dynamical theory.

1) E. Madelung, Z. Phys. 40 (1926) 322
2) G.F. Bertsch, Nucl. Phys. A 249 (1975) 253
G. Holzwarth and G. Eckart, Nucl. Phys. A 325 (1979) 1
3) W. Nörenberg, Nucl. Phys. A 409 (1983) 191

Relaxation Times for Distorted Fermi Distributions in Intermediate Energy Nucleus - Nucleus Collisions

W. Cassing
GSI Darmstadt

M. Malvetti
Univ. Karlsruhe

H. J. Simonis
Univ. Bonn

Dynamical calculations in a time-dependent two-center oscillator-model for nucleus-nucleus collisions in the range from 15 MeV/u to 100 MeV/u show that the momentum distributions of the colliding nuclei change quite drastically[1]. Qualitatively low momentum components in k_z-(beam) direction are decreased in favour of higher momentum components in the same direction with increasing overlap in coordinate space. These high momentum components in the Wigner-distribution function ρ^W, however, change additionally in time due to two-body collisions according to a collision term of the Uehling-Uhlenbeck type in the Vlasov equation for ρ^W [2]. In order to get an idea about the relaxation or decay times of these high momentum components we assume the Wigner function to be separable in coordinate and momentum space. For overlapping densities in coordinate space we parametrize the local momentum distribution $f(\vec{k})$ by two ellipsoids with axis $a=Qk_F$ and $b=k_F$ (k_F: Fermi momentum) separated by a "relative momentum" u (fig.1) in k_z-(beam) direction. The momentum density was taken to be

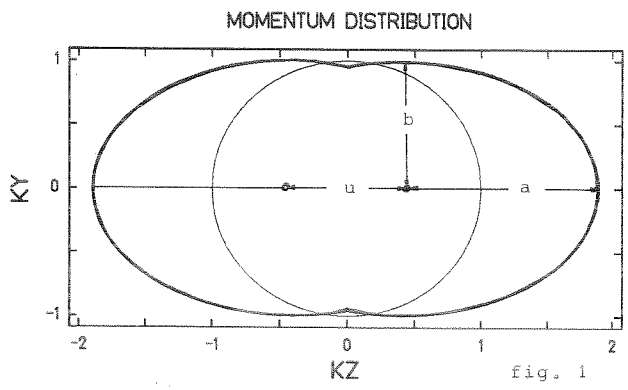


fig. 1

constant inside and zero outside as in the Fermi-gas limit, but dynamical distortions of the momentum distribution are accounted for via the parameter Q. The decay time $\tau(\vec{k})$ for a momentum component $\vec{k}$ then is given by[3,4]

$$\tau(\vec{k}) = M/(u\cdot\rho_0\cdot I(\vec{k})) \quad \text{with} \quad (1)$$

$$I(\vec{k}) = \int d^3k_2 \; \frac{|\vec{k}-\vec{k}_2|}{u} \cdot \frac{\sigma_{pp}(E)+\sigma_{np}(E)}{2} \; \frac{\Omega}{4\pi} f(\vec{k}_2) \quad (2)$$

and $f(\vec{k})$ normalized to 1. In eqs.(1),(2) M denotes the nucleon mass, $\rho_0 = 0.16\text{fm}^{-3}$, E is the energy of the nucleon-nucleon collision corresponding to the relative momentum $(\vec{k}-\vec{k}_2)/2$ and Ω is the angle of final momenta allowed by the Pauli principle. The effective nucleon-nucleon cross sections $\sigma_{pp}(E)$ and $\sigma_{np}(E)$ were adopted from Ref.5. A characteristic decay time τ_c for the change of the distribution function is finally given by the average of $\tau(\vec{k})$ over the endcaps of the distribution function in fig.1, i.e.

$$\tau_c = \int dk^3 \tau(\vec{k}) \Theta(k_F-|\vec{k}|) f(\vec{k}) / \int dk^3 \Theta(k_F-|\vec{k}|) f(\vec{k}). \quad (3)$$

The evaluation of τ_c according to (1)-(3) has been performed by Monte Carlo integration with an accuracy of 2% for τ_c. The results for τ_c $[10^{-23}\text{s}]$ are shown in fig.2 as a function of the relative velocity in units of the Fermi velocity v_F and the deformation parameter Q.

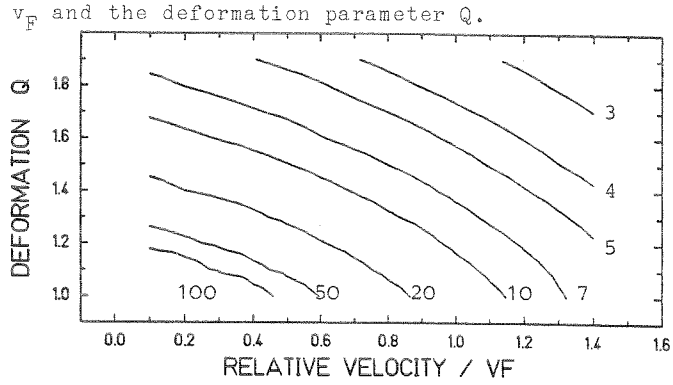


fig. 2

We find that for intermediate energy nucleus-nucleus collisions the relaxation times are roughly of the same order of magnitude than typical collision times. Coherent distortions of the momentum distributions, however, survive sufficiently long and might e.g. show up in the enhanced production of pions by nucleon-nucleon collisions.

References:

1) W.Cassing, Dynamical Correlations.... GSI Annual Report 1983
2) C.Y.Wong, H.H.Tang, Phys.Rev.Lett.40(1978)1070
3) G.F.Bertsch, Z.Phys.A289(1978)103, Phys.Rev.C15(1977)713
4) C.Toepffer, Z.Phys.A305(1982)263
5) N.Metropolis et al.Phys.Rev.110(1958)204

Nonequilibrium Light Particle Emission in Heavy-Ion Collisions: A Two Step Process !

W. Cassing

GSI Darmstadt

The emission of fast light particles in heavy-ion collisions above 10 MeV/u lab. energy[1] has been interpreted within various models involving contradictory assumptions with respect to the role of two-body collisions[2,3]. Recent numerical investigations for relaxation times show, however, that one-body 'Fermi-jets'[2] as well as contributions from two-body collisions[3] should be equally important[4].

In the present approach the direct emission of nucleons into the continuum by the time-dependent mean field is treated within a time-dependent finite axially symmetric two-center shell model which essentially reproduces TDHF dynamics. In contrast to Ref.2 distortions of the momentum distributions due to the Pauli principle are accounted for and diabatic contributions to the light particle yield[5] thus are included. The evaluation of the primary double differential light particle multiplicity is kept in close analogy to Ref.6, i.e. by recording the amplitudes of all the s.p. wavefunctions as a function of time at a fixed distance (R=18fm) from the center of the dinuclear complex for various angles Θ with respect to the beam axis and finally analysing these amplitudes with respect to their energy components by Fourier transformation. The result of such a calculation in case of $^{40}Ca + {}^{40}Ca$ at 20 MeV/u for the primary double differential neutron multiplicity $d^2N^1/dEd\Theta$ is displayed in fig.1a for various angles Θ in the CM system. The spectra are roughly exponential in energy with slightly decreasing slope parameter for increasing Θ. The neutron yield is strongly forward peaked just as in case of the Fermi-jet model[2] and the diabatic approach[6] but underestimates the fast particle yield for $\Theta \approx 90^0$[1,6]. The total multiplicity N^1 for a central collision at 20 MeV/u is 2.6.

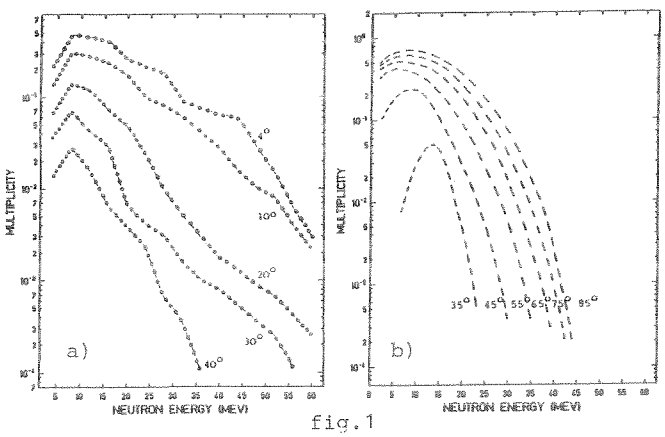


fig.1

Apart from the time-dependent mean field the one-body Wigner-distribution function changes in time due to a collision term of the Uehling-Uhlenbeck type[7], i.e. due to two-body collisions allowed by the Pauli principle. Within a preliminary approach the spectrum of scattered particles is evaluated by Monte Carlo techniques in the Thomas Fermi limit for two intersecting Fermi spheres separated by a relative momentum p which corresponds to the appropriate relative velocity above the Coulomb barrier for $^{40}Ca + {}^{40}Ca$ at 20 MeV/u. The momentum distribution of the scattered particles $\rho(\vec{k})$ turns out to be concentrated around $\Theta = 90^0$ due to the Pauli principle. Converting $\rho(\vec{k})$ into an energy-angle distribution $\tilde{\rho}(\tilde{E},\Theta)$ and assuming that all particles with $\tilde{E} \geq \varepsilon_F + 8$ MeV ≈ 45 MeV (ε_F: Fermi energy) may leave the dinuclear complex without further collisions, the secondary double differential multiplicity $d^2N^2/dEd\Theta$ is obtained (fig.1b), which shows a maximum yield for $\Theta = 90^0$ but less energetic particles as compared to fig.1a.

The total double differential neutron multiplicity finally is a superposition of the spectra in fig. 1a+b,

$$\frac{d^2N}{dEd\Theta} = f\frac{d^2N^1}{dEd\Theta} + (1-f)\frac{d^2N^2}{dEd\Theta} \qquad (1)$$

where f e.g. may be determined by the time of flight through a nucleus $t_f = 2R/v_F$ and the corresponding relaxation time τ_c[4] via $f = \exp\{-t_f/\tau_c\}$.

References:

1) E. Holub et al, Phys.Rev.C28(1983)252 and Refs. therein
2) J.P. Bondorf et al, Nucl.Phys.A333(1980)285
3) P.A. Gottschalk et al, Phys.Rev.Lett.39 (1977)1250
4) W. Cassing et al, Relaxation Times..., Annual Report GSI 1983
5) W. Cassing, W. Nörenberg, Annual Report GSI 1982,p.98, and to be published
6) U. Brosa, W. Krone, Phys.Lett.105B(1981)22
7) E.A.Uehling,G.E.Uhlenbeck,Phys.Rev.43(1933)552

BUTTERFLY- AND BELLY-DANCER-MODEL FOR NUCLEAR MOLECULES G

P.O.Hess
GSI Darmstadt
W. Greiner and W.T.Pinkston
Institut für theoretische Physik, J.W.Goethe-Universität Frankfurt, Postfach 111932,
6000 Frankfurt, W.-Germany
and
Department of Physics and Astronomy, Vanderbilt University, Nashville, Tennessee
37235, USA

In recent experiments[1], measuring the spontanous positron emission[2], the data indicated that the two nuclei stick together for a time of about 10^{-19}sec or larger. Deformation effects seem to play an important role[3]. The energically lowest configuration is the pole-pole orientation in which the distance of the two center of masses is biggest. In the pole-pole orientation the molecule can perform butterfly and belly dancer motion, besides the well known relative vibration and β and γ vibration. The first named represent entirely new collective modes of nuclear molecules.

In a nuclear molecule there are different internal systems, namely the molecular frame and the system of principal axes for each nucleus. If at least one nucleus is strongly deformed, the molecular frame is defined as such that the relative vector $\vec{r}$ lies on the z_m-axis (fig.1). Simple models can be constructed for different fixed orientations. As an example we discussed the pole-pole orientation. Furthermore no β and γ vibrations were taken into account for simplicity. As the classical hamilton function we took

$$H = \frac{1}{2}\sum_{m,i} \beta_i (-1)^m \dot{\alpha}^i_{2m}\dot{\alpha}^i_{2-m} + \frac{M}{2}\dot{\vec{r}}^2 + V_1(a^i_0, a^i_2) + V_2(r) \quad (1)$$

The first term contains the rotational and vibrational contribution of each nucleus. $V_1(a^i_0, a^i_2)$ is the potential in $a^i_0 = \beta_i \cos\gamma_i$ and $a^i_2 = (\beta_i/\sqrt{2})\sin\gamma_i$ (i=1,2). The third term represents the kinetic energy of the relative motion. $V_2(r)$ is the relative potential, which is expanded harmonically around its minimum r_0. μ is the reduced mass. H is expanded in $\varphi_1 = \varepsilon$. The zero order part has a similar structure as the Rotation-Vibration-Model (RVM)[4]. Having symmetrized the wave function, the analytic solution for the energy of the zero order part is

$$E = \frac{\hbar^2}{2\Theta_0}[I(I+1) - K^2] + \hbar^2\sqrt{\frac{C_r}{\mu}}\left(n_r + \frac{1}{2}\right) + \hbar\sqrt{\frac{C_\varepsilon}{6\beta_{20}^2}}(|K| + 2n_\varepsilon + 1) \quad (2)$$

with $\Theta_0 = 6\beta_{20}^2 + \mu r_0^2$

I is the angular momentum; K its projection on z_m; C_r and C_ε are the curvature of the potential at r_0 and ε=0. ε describes the butterfly mode. n_r and n_ε give the oscillation quanta for the relative and butterfly motion respectively. K and I take the values K=even, I=0,2,4,... if K=0 and I=K,K+1,... if K≠0. The model is applied to the system ^{238}U-^{238}U. The results are plotted in fig.2.a,b. In fig.2.a the bandheads are plotted. In fig. 2.b the distribution of angular momentum states in a 10MeV window starting at the barrier is plotted. Only those states are taken into account having a relevant energy spread (1keV<Γ<1MeV).

[1]M.Clemente et al.; Proc of the Intern. Conf on Nuclear Physics, Florence, Aug.29- Sept.3, 1983, p.693;
H.Bokemeyer et al.; ibid., p.694
[2]J.Reinhardt, U.Müller, B.Müller and W.Greiner; Z.Phys. A303, 173,(1981)
[3]M.Seiwert, W.T.Pinkston and W.Greiner; to be published
[4]J.M.Eisenberg, W.Greiner; Nuclear Theory I, North-Holland- Publishing- Company, Amsterdam (1975)

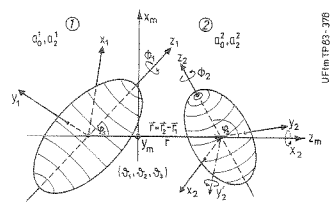


Fig.1: Definition of coordinates in the molecular frame.

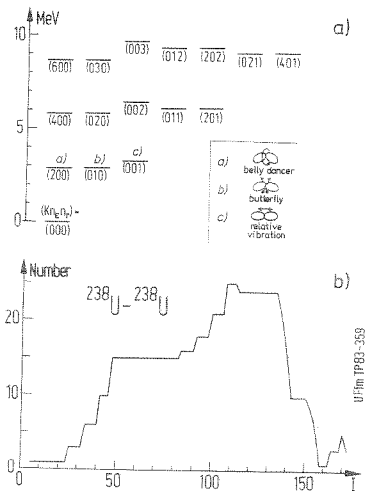


Fig.2: Typical energy spectrum for the system ^{238}U-^{238}U (a) and angular momentum distribution in a 10MeV window (b).

Study of fusion-fission potentials in superheavy systems

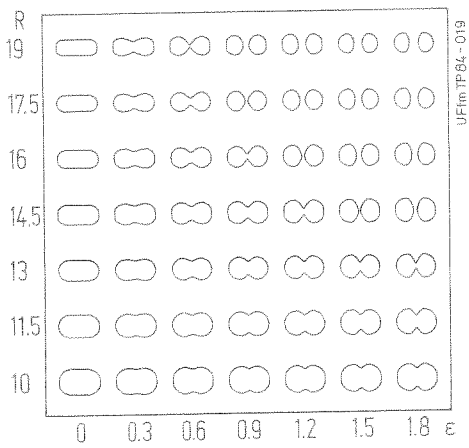
B

K. Depta, R. Herrmann, V. Schneider, Xi-zhen Wu, K.H. Ziegenhain,
J.A. Maruhn, and W. Greiner
Institut für Theoretische Physik, Universität Frankfurt/Main

We investigate the dynamics of the ^{238}U-^{238}U and $^{298}_{114}X$ system within the framework of the fragmentation theory[1]. Recent calculations concentrated on the treatment of the two-center distance R and the mass asymmetry degree of freedom $\eta=(A_1-A_2)/(A_1+A_2)$, while the influence of the neck parameter ε and the deformation of the fragments $Q_{1,2}$ has been neglected. A consistent description of the fusion-fission process should treat all degrees of freedom $(R,\eta,\varepsilon, Q_1,Q_2)$ dynamically. To reach that goal, an exact knowledge of the potential is necessary.

We consider the potential to be a sum of the liquid-drop part E_{LDM}, which is dominating, and the shell-correction δU.

In Fig. 1 b the U-U potential E_{LDM} is shown as a function of ε and R for fixed $\eta = 0$, $Q_1 = Q_2 = 1$. The variety of the corresponding shapes is illustrated in Fig. 1a. Obviously increasing ε or R leads to scission, and the influence of ε is relevant.



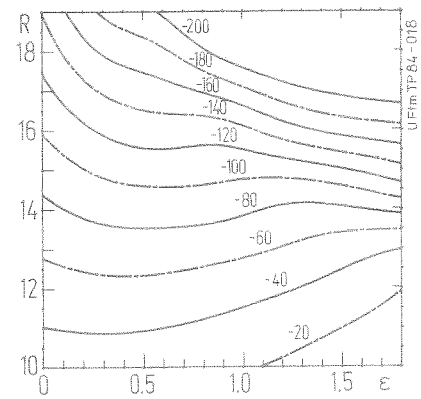
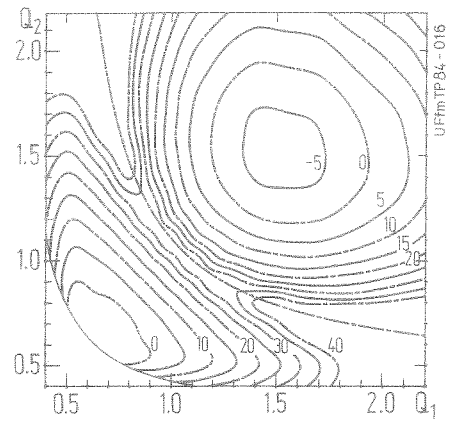
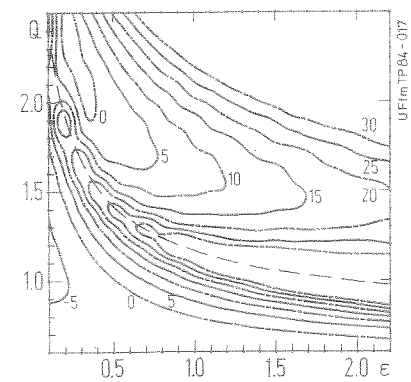


Fig. 2 gives the Q_1-Q_2 dependence of E_{LDM} for $^{258}_{114}X$ with fixed R = 12 fm, $\eta = 0$, $\varepsilon = 1.2$. The two minima are separated by a potential well. The minimum for higher Q-values (M_1) corresponds to the two separated fragments, the other (M_2) belongs to a composite system (the dashed curve gives the scissioning configuration). The depth of the minima depends on R. For small R the minimum M_2 is deeper than M_1, increasing R leads to the opposite situation, i.e. M_1 gets deeper than M_2. This general behaviour influences the dynamics of a system.



In the symmetric case $\eta = 0$ the minima are located on the $Q_1=Q_2=Q$-line. Figure 3 shows E_{LDM} of $^{298}_{114}D$ for this situation, depending on ε and Q (R=12 fm). It can be seen that the height of the potential barrier is mainly influenced by ε .



We have seen that the neck parameter ε and the deformations $Q_{1,2}$ may play an important role for the dynamics of a system via the potential. Full dynamical studies are being carried out.

[1] J.A. Maruhn, W. Greiner, and W. Scheid, Heavy Ion Collisions, Vol. II, Ed. R. Bock, North-Holland Publ. Comp., Amsterdam, 1980

Hartree-Fock and shell model calculations for the U-U compound system

L. Neise, J.A. Maruhn, and W. Greiner
Institut für Theoretische Physik, Universität Frankfurt/Main

For a better understanding of the supposed long reaction times in U-U collisions[1] it is very helpful to investigate the static properties of the corresponding compound system. Along this line spherical Hartree-Fock calculations with the Skyrme forces SK1, SK2 [2] SK3 [3], SKμ [4,5], have been carried out. Coulomb exchange has been taken into account via the Slater approximation, and corrections due to the center of mass motion have been made. The total binding energy is found to be in the order of-5.68 MeV/n (-5.5 MeV/n for Sk2). These values may be compared with a simple extrapolation of one of the usual Liquid Drop formulas[6], which gives a value of -5.73 MeV/n,i.e. a stronger binding. The proton density is strongly influenced by the Coulomb repulsion as it is shown in Fig. 1. This results in a considerable lowering of the Coulomb energy, which is of the order of 3015 MeV (3093 MeV for Sk1 which shows the smallest effect). The inhomogenity of the proton density may be an important point in future calculations of collective potential energy surfaces.

The self-consistent fields are found to be well approximated by potentials of Woods-Saxon type. So, although desirable, it is not unconditionally necessary to do deformed (constrained) Hartree-Fock calculations,which may be rather costly for systematic studies. Instead, as a first step, one can approximate the total binding energy through the expectation value of the Skyrme Hamiltonian with deformed Woods-Saxon wave functions.

This effect was also investigated by J. Fink in the framework of density functionals[7].

For this purpose a fast code has been developed, which diagonalizes potentials of the form

$$v(r,\vartheta) = \sum_k f_k(r) Y_{k,0}(\vartheta) \qquad k=0,2,4,6 \text{ (higher k can be included)}$$

with a spin-orbit force

$$V_{es} = -\lambda(\nabla v \times \vec{p}) \cdot \vec{s}$$

in the spherical oscillator basis.
(The Coulomb interaction has been taken into account via its multipole expansion).

Obviously this code is restricted to small axial and reflection symmetric deformations, a deficiency which has to be overcome in the future. As in the spherical HF calculations the neutrons show a well pronounced shell closing near N = 308 (N_{u-u} = 292).

The level density at the Fermi energy is relatively high, so that Strutinsky shell corrections are positive. No indications have been found that shell effects contribute significantly to the stabilizing of the compound system. This is also due to the fact that the variation of the shell corrections with deformation is small compared to the variation of the underlying liquid drop energy.Calculations using the expectation value method are in progress.

[1] H. Bokemeyer et al., GSI Report 1982, p. 146
[2] D. Vautherin, Phys. Rev. C5 (1972) 626
[3] M. Beiner, Nucl. Phys. A232 (1975) 29
[4] H. Krivine, Nucl. Phys. A336 (1980) 155
[5] J. Bartel, Nucl. Phys. A386 (1982) 79
[6] P.A. Seeger, Nucl. Phys A238 (1975) 491
[7] H.J. Fink,

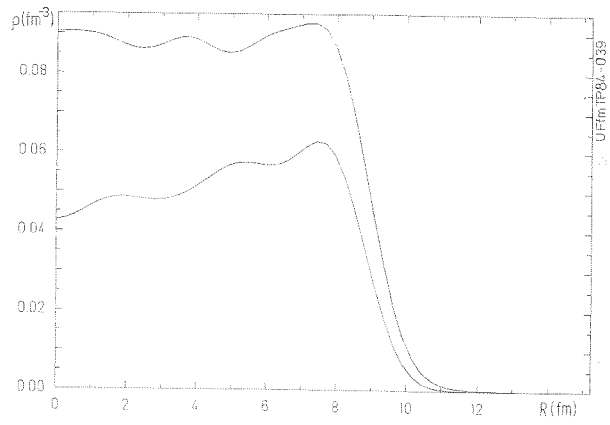


Fig. 1: Spherical proton and neutron densities of $^{476}_{184}X$, calculated with Sk1. The Sk2 shows the strongest effect in the proton density.

Investigation of ternary fission for the system ^{238}U-^{238}U

Xi-zhen Wu, J.A. Maruhn, and W. Greiner
Institut für Theoretische Physik, Universität Frankfurt/Main

With very high charges for a superheavy system it should be assumed that ternary fission becomes quite important. In order to study ternary fission we deem it appropriate to extend the TCSM[1] used for binary fission to the three center case. Within the framework of the liquid drop model (LDM) the static behaviour of ternary fission is studied. The nuclear surface used for the LDM is defined as an equipotential surface of the single-particle potential. The momentum-independent part of the potential along the Z axis and the associated nuclear shapes are illustrated in Fig. 1. Fig. 2 shows the potential energy surface of binary and ternary fission for the system ^{238}U + ^{238}U. Curve 1 is for symmetric binary fission, minimizing the energy with respect to deformations and neck parameter. Curves 2, 3, 4 are for ternary fission with fixed mass asymmetries of A_1/A_2 = 1.0, 6.0, 0.6, respectively.

For small deformations the potentials for the binary and ternary fission are not much different. However, the potentials of binary fission are much lower than that of ternary fission for large deformations. Along the ternary fission path the scission configurations are more stretched and more constricted than those of the corresponding binary shapes. Fig. 3 shows the neck parameter of the system ^{238}U + ^{238}U as a function of length for various mass asymmetries by minimizing the energy with respect to the deformations and neck parameters. In symmetric binary fission (curve 1) the neck is formed very easily between 24 and 25 fm, where scission occurs. In ternary fission (curves 2, 3, 4, 5 are for ternary fission with mass asymmetries of A_1/A_2 = 1.0, 4.0, 6.0, 8.0, respectively) the rapid rising of the necks occurs at rather larger length. This means that the occurrence of ternary fission will be much less than that of binary fission, because before undergoing these large deformations binary fission occurs.

[1] J. Hahn, H.-J. Lustig, and W. Greiner, Z. Naturf. 32a (1977) 215

[2] A.R. Degheidy and J.A. Maruhn, Z. Physik A290 (1979) 205

Acknowledgement: We like to thank K. Depta, R. Herrmann, K.H. Ziegenhain for many useful discussions as well as Dr. H.J. Lustig for using his programme.

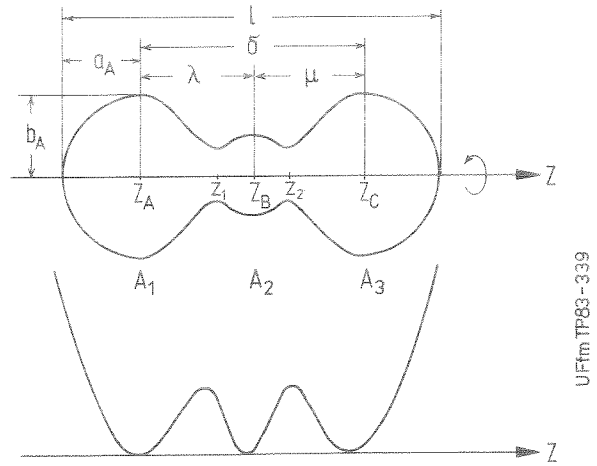


Fig. 1: The three-center potential along the Z-axis and associated nuclear shapes.

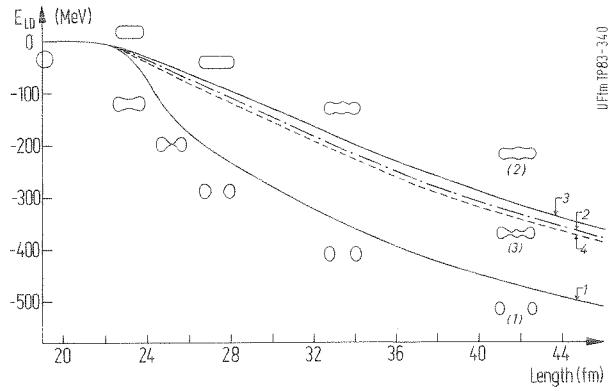


Fig. 2: Dependence of E_{LD} on the length for binary and ternary fission for the system ^{238}U + ^{238}U.

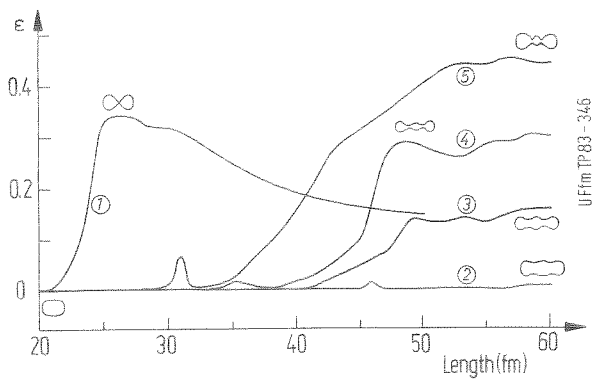


Fig. 3: The neck parameter of the system $^{184}_{476}$ as a function of the length along the minimum energy path of binary and ternary fission.

The Heavy-Ion Potential at Intermediate Energy G

M. Trefz, A. Faessler, W.H. Dickhoff
Institut für Theoretische Physik, Universität Tübingen

L. Rikus
I. Institut für Experimentalphysik, Universität Hamburg

S.B. Khadkikar
Physical Research Institute, Ahmedabad, Indien

One of the interesting quantities in nucleus-nucleus scattering is the total reaction cross section as a function of energy. It has recently been suggested[1] that this reaction cross section is dominated by nucleon-nucleon collisions. The authors of ref. 1 claim that the use of experimental cross sections for NN-scattering in Glauber-like calculations provides sufficient physical information to describe the reaction cross sections as a function of energy. In a recent publication[2] this problem is attacked from a more microscopic point of view. Representing nucleus-nucleus collisions by two colliding nuclear matters in momentum space one can construct the real and imaginary part of the optical potential (OP) following the methods developed in ref. 3. From the complex binding energy obtained in the reaction (G-) matrix approximation and a local density approximation it is possible to obtain the socalled volume contribution to the optical potential which allows to calculate apart from the reaction cross section also angular distributions. Clearly no surface contribution can directly be obtained from a nuclear matter calculation. Therefore it has been attempted to calculate the contribution of the surface by including the influence of collective surface excitations directly in finite nuclei[4]. A comparison of the differential cross sections obtained with and without surface contributions with experimental data of ^{12}C on ^{12}C at 1016 MeV is given in Fig. 1. Clearly there is no improvement when 1p1h excitations are taken into account. Also the reaction cross section as a function of energy for ^{12}C on ^{12}C has not really the right trend[2]. Since the underlying concepts in the calculation of ref. 2) should be flexible enough to describe the physics underlying the calculation of ref. 1, it is attempted to trace back the differences between these calculations by using as a reference the nuclear T-matrix to compare results obtained with the nuclear G-matrix which takes into account Pauli blocking and Fermimotion. In addition some technical improvements in the program which calculates the energy density are made which allows a correct treatment of the dependence of the imaginary part on the intrinsic kinetic energy. We show in Fig. 2 new results for the real part of the OP obtained with the T-and G-matrix interaction for ^{12}C + ^{12}C at 1016 MeV showing a rather different shape and depth for both approaches. These new results may therefore shed light on the discrepancy between the calculation of ref. 1 and 3 and may lead to a better understanding of the dominant contribution to the HI optical potential.

[1] R.M. DeVries and J.C. Peng, Phys. Rev. C22, 1055 (1980)

[2] A. Faessler, L Rikus and S.B. Khadkikar, Nucl. Phys. A401, 471 (1981)

[3] T. Izumoto, S. Krewald and A. Faessler, Nucl. Phys. A357, 471 (1981)

[4] R.A. Broglia and A. Winther, Heavy Ion Reactions, (Benjamin, Reading, Massachusetts 1981)

[5] M. Buenerd et al., Phys. Lett. 102B, 242 (1981)

[6] M. Trefz, A. Faessler and W.H. Dickhoff, to be publ.

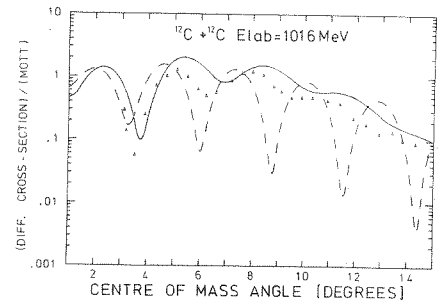


Fig. 1: The differential cross section divided by the Mott cross section for ^{12}C + ^{12}C at E_{lab}= 1016 MeV calculated with the volume optical potential (full line) and the full optical potential (dashed line) and compared with experiment[5].

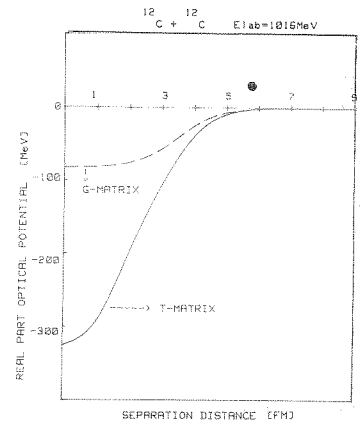


Fig. 2: Real part of the optical potential for ^{12}C + ^{12}C at E_{lab}=1016 MeV. The full curve gives the T-matrix result while the full curve is obtained from the reaction matrix.

Cold break-up of spectator nuclei in nucleus-nucleus collisions at high energy B,G

J. Aichelin, J. Hüfner and R. Ibarra
Institut für Theoretische Physik der Universität Heidelberg
und Max-Planck-Institut für Kernphysik, Heidelberg

Inclusive data from fragmentation reactions of the type $A_P + A_T \rightarrow Z + X$ are analysed and a reaction mechanism is proposed. A projectile A_P(p, He, O or Ne) collides with a target A_T (Au) and one fragment with charge Z and energy E is observed at a solid angle Ω. Projectile energies vary between 84 AMeV and several AGeV. We[2] propose a parametrization for the triple differential cross section $d^3\sigma/d\Omega dE dZ$ with six free parameters. This is our picture: the fragments originate from an isotropic decay of an intermediate nucleus (spectator matter) which moves with velocity v_{CM}. In this system the momentum distribution is a Gaussian with a shift and a width. The width can be interpreted as a temperature (of order 12 MeV) but we think that the width originates from Fermi motion. The Coulomb barrier is quantitatively reproduced if one assumes that the fragments are not evaporated from the surface but originate from any location in the intermediate system. Fig. 1 shows several examples for the experimental and fitted double differential cross sections $d^2\sigma/d\Omega dE$.

The Z-dependence $d\sigma/dZ$ is found to follow a law

$$\frac{d\sigma}{dZ} = \sigma_F \cdot (\exp(1.8Z/\sqrt{Z_0}) - 1)^{-1}$$

where Z_0 is the charge of the target minus the fireball nucleons. The value of Z_0 determines completely the shape of $d\sigma/dZ$. Our fit is as good as with a power law $Z^{-\tau}$ where the power τ is adjusted (Fig. 2). We need no free parameter.

When one analyses the energy and projectile dependence of the adjusted parameters, the following picture arises: the projectile drills a hole into the target, the remaining spectator matter does not come to thermal equilibrium but rather breaks, maybe like the shattering of glass.

[1] A.I. Warwick et al., Phys. Rev. C27 (1983) 1083
[2] J. Aichelin, J. Hüfner and R. Ibarra, to be published in Phys. Lett. B and Phys. Rev. C

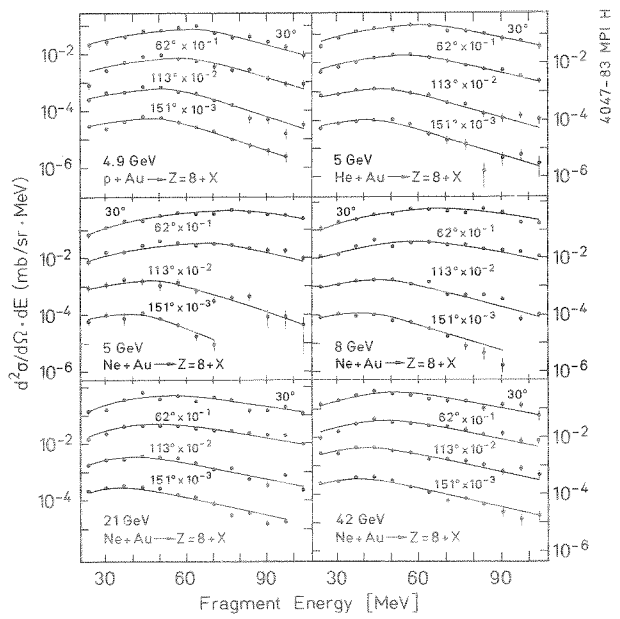


Fig. 1: The experimental data[1] and fitted curves to the double differential cross sections $d^2\sigma/d\Omega dE$ for several angles (30^0,60^0,90^0 and 120^0) and various combinations of projectiles and energies.

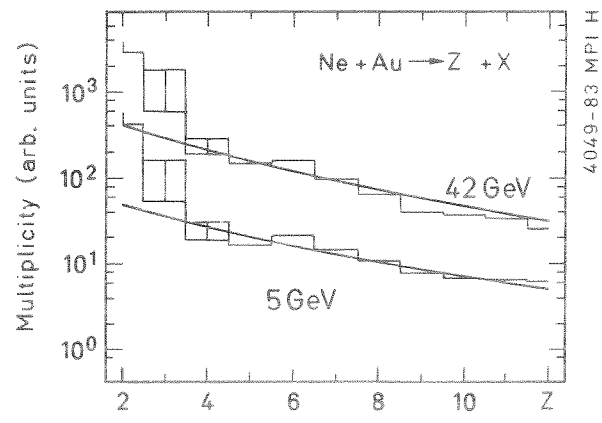


Fig. 2: Experimental and theoretical charge yield curves $d\sigma/dZ$. Only the absolute values have been adjusted.

EXPANSION AND DISASSEMBLY PHASE OF ENERGETIC NUCLEAR REACTIONS:

- A PROBLEM OF DYNAMICAL INSTABILITIES ? -

B. Strack and J. Knoll
GSI Darmstadt

The expansion phase of a hot nuclear system as created in an energetic heavy-ion collision is calculated and discussed by a selfconsistent field-theoretical model which considers dynamical growth of instabilities arising from strong fluctuations of the one-body density. First multiplicity distributions and mass spectra resulting from a series of numerical runs in a 2 + 1 dimensional model world are presented and discussed.

Consider an energetic reaction of two nuclei with its initial entropy generating phase forming a highly excited and compressed nuclear system. How does such a system finally disassemble after its expansion to the limits of dynamical stability? While earlier disregarded, the interest in this question has grown recently[1] [2]. How small or big are the stable nuclear fragments? Up to now this problem has been discussed by quasi-static concepts, envoking a freeze-out at the 'end' of the expansion[3] [4]. Even chemical dynamics in terms of rate equations[5] may not make too much sense as the range of nuclear 'bonds' still exceed the spacing among nucleons before break-up.

Thus, there is a need for an entirely dynamical description of the expansion phase, as suggested by us last year[6]. As nuclear binding is of genuine wave mechanical nature, the Pauli-pressure determines the nuclear sizes, not the range of the forces, we consider the following field theory model. It comprises three ingredients: a) the definition of the initial configuration of the expansion phase, b) the dynamics that cranks this configuration through the instability region, and c) a definition of the final stable fragments.
a: We assume a macrodynamical model which provides the information upon the one-body density matrix $f^0(r,p)$ at time t=0 the starting time of the expansion phase. At this time we represent the system by an ensemble of pure states (Slater determinants), such that the ensemble average reproduces f^0.
b: Each of these pure states is the propagated selfconsistently in its proper one-body field (like in TDHF) until stable fragments are built up.
c: A fragment is defined as the connected area in space where the density exceeds a certain threshold value (0.1 of the saturation value in our case).

As compared to ordinary mean field theories at finite temperature which treat the whole statistical ensemble in a single common mean field, here each individual state evolves in its proper one-body field. Thus we account for fluctuations in the one-body field, which in turn generates the various forms the system can granulate. In fact, the high entropy (S≈2 to 4) of the ensemble of pure states cause strong fluctuations in the one-body field[6].

As an example the density distribution of fragments is illustrated for one pure state pertaining to the ensemble of 50 MeV at time 72 fm/c (see fig. 1).

The number of final fragments and hence the multiplicity distribution are a sensitive function of the excitation energy (see fig. 2). The binding effect included in the calculation are not only seen in the dynamics displayed in fig. 1 but also in the characteristic differences in the resulting mass spectra.

Note in particular the quite flat mass distribution in the T= 20 MeV case relative to the strong fall off at T= 50 MeV. Is this a signature of a critical behaviour[7] of the system?

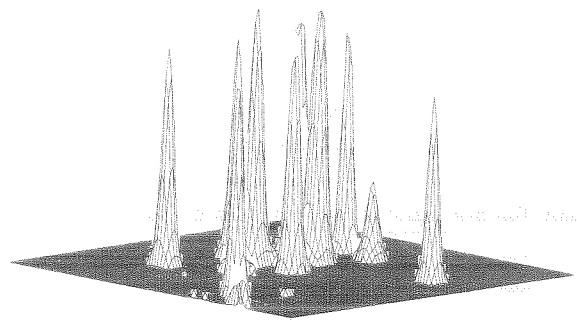


Fig. 1: Density plot over the two dim. configuration space for T= 50 MeV and time 72 fm/c for one event. The number of stable fragments is here 10 .

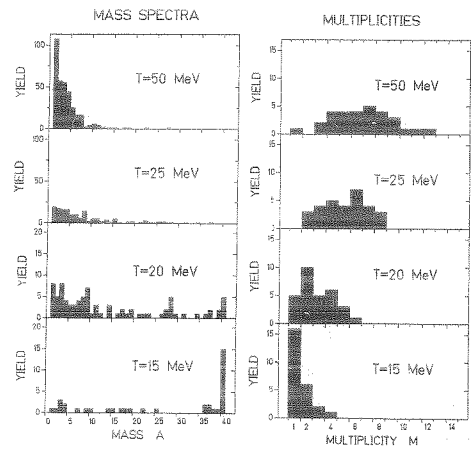


Fig. 2: Mass spectra and multiplicities at four values of T and initial compression of $3\rho^0$ resulting from the ensemble average of thirty runs for each T.

References

1) G.Bertsch, P.J. Siemens, Phys. Lett. 126B(1983)9
2) D.K. Scott, MSUCL peprint-434, September 1983
3) A.Z. Mekjian, Phys. Rev. Lett. 38(1977)640, Phys. Rev. C17(1978) 1051
4) H. Gutbrod et al., Phys. Rev. Lett. 37(1976)667 H. Sato, K. Yazaki, Phys. Lett. 98B(1981)153
5) I. Montvay, J. Zimanyi, Nucl.Phys.A316(1979)490
6) B. Strack,J. Knoll, GSI Scientific Report 1982,119 B. Strack,J. Knoll, Z. Phys. A315(1984)249
7) M.E. Fisher, Physics 3(1967),255

Equilibration of a three component nuclear system in heavy-ion collisions

B,G

A. Rosenhauer, L.P. Csernai, J.A. Maruhn, and W. Greiner
Institut für Theoretische Physik, Universität Frankfurt am Main

Among semiclassical macroscopic models the application of kinetic theory and hydrodynamic concepts in nuclear physics provides us with a tool to study high energy heavy-ion collisions.

In the three component kinetic model[1] we investigate the process of thermal equilibration by calculating the total momentum distribution function of a three component system. The first and second component is attributed to the nucleons of target and projectile, while a third component is taken into account to study the formation of thermalized matter in the course of the reaction. It is assumed that the distributions of the incoming nuclei are equilibrated ones and that collisions of nucleons belonging to different distribution components populate the thermalized matter component. Then, by means of Boltzmann transport theory the time evolution of such a three-component system for infinite uniform nuclear matter is calculated taking into account the pre-equilibrium emission of nucleons.

In contrast to the former three-fluid hydrodynamic model[2], the kinetic approach imitates the conditions of the reaction only at relatively early times in the central region of the collision, when the change of the distribution due to spatial convection should be of minor importance. This restriction, however, allows us to follow the process of equilibration of the three component system in detail, as we are able to determine the time evolution of the velocity distribution of all particles involved in the reaction at an intermediate energy range of 0.1 - 0.4 GeV/n where elastic binary scattering will be the dominant process driving the system towards equilibrium.

In Fig. 1 the total velocity distribution F(v,t) in direction of the beam axis ($F_{\parallel}$) and perpendicular to it ($F_{\perp}$) is shown. The peak $F_{\parallel}$ around the beam velocity is reduced as soon as the nucleons of target and projetile start colliding on each other and the underpopulated region around the center of velocity space is filled up, while in perpendicular direction $F_{\perp}$ exhibits the shape of a Maxwellian distribution.

At late stages of the reaction a broad distribution $F_{\parallel}$ with a slowly decreasing shape for $v < v_{beam}$ is left, whereas for large velocities an exponential decrease is observed. The distribution perpendicular to the beam axis maintains the shape of a thermal distribution, which becomes considerably broader in time indicating increasing transverse temperatures. In the case of a symmetric collision of 0.1 GeV/n $F_{\parallel}$ and $F_{\perp}$ almost coincide in the final stage so that a complete equlibration of the system can be assumed, while at 0.2 and 0.4 GeV/n a slight anisotrophy is observable especially if nucleons carrying larger momenta are selected.

The distribution of singly collided particles Z(v) at different reaction times demonstrates how the system is driven towards the final stage. Those particles support a population of the hole around the center of velocity space and the development of the shoulder in the shape of the total velocity distribution, especially at higher beam energies. Note that at the beginning of the reaction $F_{\perp}$ and $F_{\parallel}$ coincide, but as soon as the third component develops, a slight anisotropy is observable. In the course of the collision the distribution Z(v) becomes essentially broader and finally disappears due to the depletion of non-thermalized nucleons.

[1] A. Rosenhauer, L.P. Csernai, J.A. Maruhn, W. Greiner, UFTP Preprint 71/1983;
A. Rosenhauer, Nuovo Cim. A71 (1982) 215

[2] L.P. Csernai, I. Lovas, J.A. Maruhn, A. Rosenhauer, J. Zimányi, W. Greiner, Phys. Rev. C26 (1982) 149

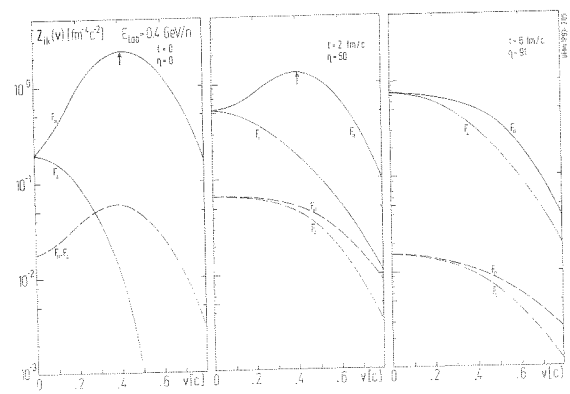


Fig. 1: Velocity distribution of all emitted particles (full lines) and that of singly collided nucleons (dashed lines) in the direction of the beam axis ($F_{\parallel}$) and orthogonal to it ($F_{\perp}$) at different reaction times. The parameter $\eta = n_3/n_{tot}$ specifies the percentage of nucleons converted to the thermalized component. The initial flow velocity v_{beam} is indicated by arrows.

FLOW ANALYSIS OF RELATIVISTIC NUCLEAR COLLISSIONS

B.G

-Influence of Self-consistent Interaction-

J. Theis
GSI, Darmstadt

H. Stöcker, G. Graebner, G. Buchwald, J. Maruhn
and W. Greiner
Institut für theoretische Physik, Universität Frankfurt

We have extended the conventional fluiddynamics including interactions via a relativistic mean field theory[1]. The equations of motion can be formulated in terms of the total momentum and energy density:

$$\partial_t(\gamma\rho) + \vec{\nabla}(\vec{u}\gamma\rho) = 0$$

$$\partial_t\vec{M}+\vec{\nabla}\cdot(\vec{u}\vec{M})=-\vec{\nabla}[P_n-\tfrac{1}{2}m_s^2\bar{\Phi}^2-(B/3)\bar{\Phi}^3-(C/4)\bar{\Phi}^4+\tfrac{1}{2}m_v^2\bar{V}_o^2]$$

$$\partial_t h + \vec{\nabla}\vec{M}=-\vec{\nabla}[\vec{u}P_n-\tfrac{1}{2}m_s^2\vec{u}\bar{\Phi}^2-(B/3)\bar{\Phi}^3-(C/4)\bar{\Phi}^4+\tfrac{1}{2}m_v^2\vec{u}\bar{V}_o^2]$$

$$\bar{\Phi} = (g_s\rho_s-B\bar{\Phi}-C\bar{\Phi})/m_s^2 = (M/g_s)(1-M^*/M)$$

$$\bar{V}_o = (g_v/m_v^2)\rho$$

The laboratory momentum $\vec{M}$ and energy density h are related to the total energy density and the pressure in the local rest frame via $\vec{M}=\gamma^2\vec{u}(E+P)$ and $h=\gamma^2(E+P)-P$. The fluid-dynamic equations obtained are similar to the conventional ones[2] used in the analysis of relativistic heavy ion collisions, if we identify the total pressure P with a sum of partial pressures arising from the nucleons and the meson fields. Although the equations of motion look similar to the conventional conservation equations, there is an essential difference arising from the effective mass $x=M^*/M$. M^*c^2 is a function of baryon density and excitation energy (temperature), given by the selfconsistency relation:

$$x=1-C_s^2\left[\frac{\gamma}{(2\pi)^3}\int d^3k(n(T)+\bar{n}(T))x/\sqrt{k^2+x^2} + b(1-x)^2-c(1-x)^3\right]$$

This leads to a relativistic self-consistent description for the pressure and the energy density, which finally yields a thermal behaviour different from the conventional fluid dynamic one. We studied the effects of different equations of state resulting from linear and nonlinear mean field models in the event-by-event kinetic flow analysis[3] and found a variation of the flow angle and flow ratios. For U-U at bombarding energy of 0.8 GeV/N we find a difference of about 10°-15° in the deflection angle.

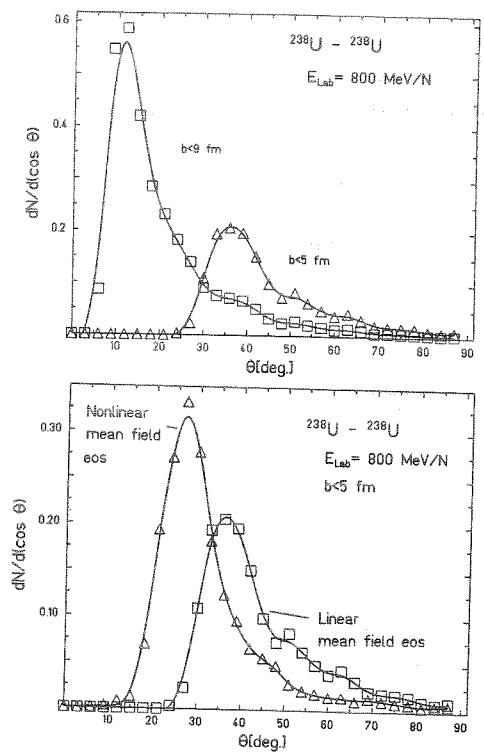


Fig.1: Distribution dN/dcosΘ of flow angles for U+U at E_{Lab}=800 MeV/N for different selfconsistent mean field equations of state (eos). a) For the linear mean field eos two selections of impact parameter ranges are shown. A strong sidewards peak can be seen. b) For the nonelinear mean field eos the sidewards maxima is shifted to smaller flow angles.

References:

1. J. Theis, G. Graebner, J. Maruhn and W. Greiner, Int. Top. Meet. on High Energy Nucl. Phys., Balatonfüred, Hungary, 1983
2. G. Graebner, Phd. Thesis, Uni. Frankfurt, 1984
3. M. Gyulassy, K. Frankel and H. Stöcker, Phys. Lett.44, 725, 1980

Nuclear compression in high multiplicity selected collisions of $^{93}Nb(E_{lab}=0,4$ GeV/n) + ^{93}Nb in view of recent data [B,G]

G. Buchwald, G. Graebner, D. Barthel, J.A. Maruhn,
W. Greiner, and H. Stöcker
Institut für Theoretische Physik, Universität Frankfurt/Main

On the basis of the nuclear fluid dynamical model a kinetic flow analysis of high multiplicity selected collisions of ^{93}Nb (E_{lab}=0,4 GeV(n) + ^{93}Nb is performed[1]. The results are compared with experimental data from the Plastic Ball group[2] and with intranuclear cascade calculations[2].

Fig. 1 shows the distribution of flow angles, dN/d cosΘ. The general behaviour of the flow pattern in the fluid dynamical model is as follows: The flow angle rises smoothly from 0° at large impact parameters to 90° at b=o. Since the contribution of zero impact parameter to the actual experiment is negligible, the theory has to sample over a range of impact parameters

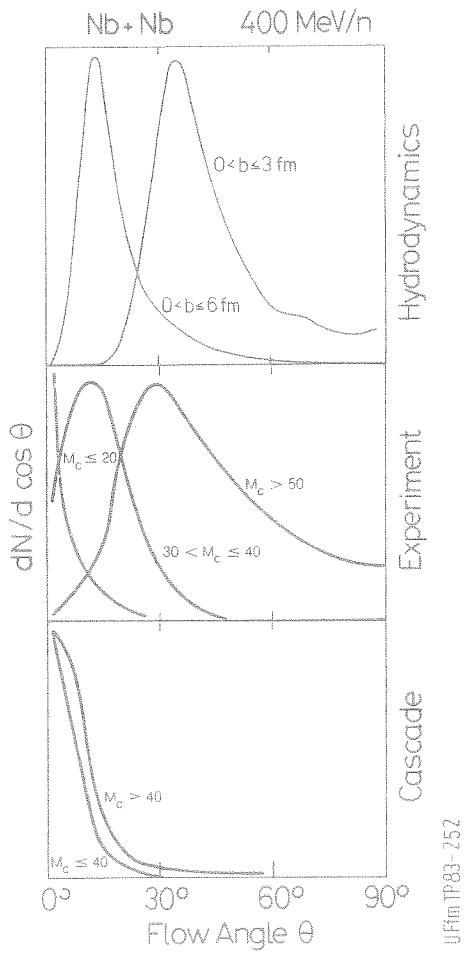


Fig. 1: Distribution dN/d cosΘ of flow angles for Nb+Nb at E_{lab}=400 MeV/n.
a) Fluid dynamical result. Collisions with 0<b≤3fm correspond to high multiplicity selected events, b≤6fm corresponds to intermediate multiplicities
b) Experimental results for different multiplicities
c) Results of a cascade calculation

We show two selections of impact parameter ranges, namely from b=o to 3 fm and from b=o to 6 fm, corresponding to average charged particle multiplicities of M=46 and M=35 respectively.

The results can be compared with data quantitatively. For high multiplicities (M>50) the data show a strong sidewards peak at Θ ~30°. This peak is rather broad and for large angles there seems to be an isotropic contribution. The hydro calculations for Θ < b ≤ 3 fm yield comparable multiplicities together with a very similar dN/d cosΘ distribution, whereas the cascade calculations do not exhibit the observed features.

The data for intermediate multiplicities 30 < M <40 show peaking at more forward angles. The peak is at about 10° and there is no contribution to very high Θ. Hydrodynamical calculations give these multiplicities for reaction with b ≤ 6 fm. Again the comparison of hydrodynamics and data leads to a good agreement, whereas the cascade calculation fails to reproduce the data.

More detailed comparisons between calculations and data, being presently under way, are expected to yield clues on the behaviour of nuclear matter in high energy heavy ion collisions.

[1] G. Buchwald, G. Graebner, J. Theis, J.A. Maruhn, and W. Greiner, Universität Frankfurt, preprint UFTP 122/1983 and
H. Stöcker, G. Buchwald, L.P. Csernai, G. Graebner, J.A. Maruhn, and W. Greiner, Nucl. Phys. A387(1982)205c

[2] H.G. Ritter, H.A. Gustafson, H.H. Gutbrod, B. Kolb, H. Löhner, B. Ludewigt, A.M. Poskanzer, T. Renner, H. Riedesel, A. Warwick, F. Weik, H. Wiemann, "Global Analysis of Relativistic Nuclear Collisions Detected by the Plastic Ball", presented at the Int. Top. Meeting on High Energy Nuclear Physics, Balantonföred, Hungary, June 6-11, 1983, LBL preprint 16110

Deformed nuclei in the 3D-nuclear fluid dynamical model [B,G]

D. Barthel, G. Buchwald, G. Graebner, M. Seiwert, J.A. Maruhn, W. Greiner
Institut für Theoretische Physik, Universität Frankfurt/Main

The influence of the deformation of nuclei on several observables was studied for $^{238}U + ^{238}U$ at bombarding energies between 80 and 250 MeV/u. It was investigated how the observables vary in dependence of bombarding energy, equation of state and initial orientation of the nuclei.

Up to now it was argued, that exotic phenomena in the equation of state, such as density isomers, should be observed as jumps in the excitation functions of characteristic quantities. We will discuss in the following how these jumps are smeared out if deformations are taken into account. If no second minimum in the equation of state is included, the maximum density in the collision for example lies in a relatively small interval of $\rho/\rho_0 = 2 \pm .05$ for all orientations at 115 MeV/u bombarding energy (Fig. 1).

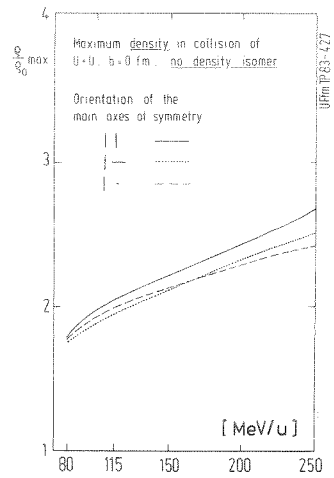


Fig. 1: Excitation function for the maximum density. Different initial orientations for collisions, which were investigated without density isomer.

If a second minimum is included in the equation of state, the maximum density varies over $\rho/\rho_0 = 2.3 \pm .4$ in the region of 115 MeV/u, where the phase transition should occur (Fig. 2). However, the statistical weight of the end-on-end collision (upper curve) is zero and therefore the isomeric jump in the excitation function should nevertheless be manifest through the increased width.
Furthermore, the initial orientation of the colliding nuclei is responsible for different energy flow patterns (Fig. 3). The aspect ratio diminishes towards higher bombarding energies for all initial orientations, but it is higher for orientations with a big overlap in nuclear matter. Calculations with and without inclusion of a density isomer however show very similar aspect ratios. The same holds true for the excitation function of the maximum thermal energy in the collision.

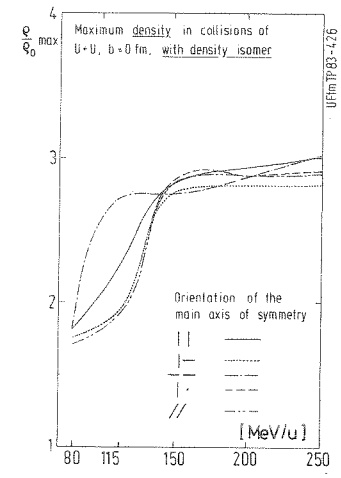


Fig. 2: Excitation function for the maximum density. Different initial orientations for collisions, which were investigated with a density isomer in the equation of state.

Analyzing the triple differential cross section $\partial^3\sigma/\partial v \partial\varphi\partial E$ we hope to learn more about the nuclear equation of state by detailed comparison with future data. These studies are now in progress.

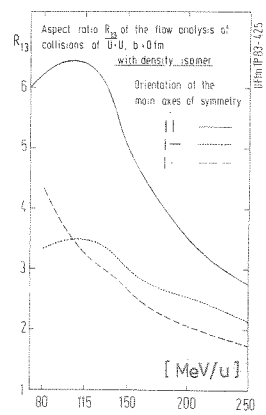


Fig. 3: Excitation function for the aspect rato R_{13}. Three representative initial orientations for collisions, investigated with density isomer

Comparison of intermediate energy fluid dynamical calculations with recent MSU $^{40}Ar(137\ MeV/n)+^{197}Au$ data

B,G

G. Buchwald, G. Graebner, T. Rentzsch, J.A. Maruhn,
W. Greiner, and H.Stöcker
Institut für Theoretische Physik, Universität Frankfurt/Main

Three dimensional viscous fluid dynamical calculations have been performed for the reaction $^{40}Ar+^{197}Au$ at 137 MeV/n. The calculated ^{3}He and triton cross sections are compared to recent data. One of the motivations for these experiments is the possibility of creating nuclear matter at higher than groundstate densities but at moderate temperatures. Another important subject of investigation is to find the dominant reaction mechanism in this transitional regime from the mean field dominated lower energies where the TDHF-methods are applicable to the many body collision dominated higher energies[1,2]. Since the question of the reaction mechanism and of the nucleonic mean free path seems to be completely open at present, we have taken the following point of view: We will attempt to answer these questions by a detailed comparison of the results of the hydrodynamical model, which assumes $\lambda<<R$, with the experimental data[3].

The important transport properties of nuclear matter, i.e. in our description the dissipative terms in the Navier-Stokes equations, are included in full geometry which allows for the study of intermediate impact parameter reactions. Furthermore, we include a realistic treatment of the nuclear binding and the final thermal emission of free nucleons from the hot system[2]. The final fragmentation was described in a statistical model[2].

The particle cross sections are then calculated by transforming the internal thermal momentum distribution for each partial density in every fluid element to the lab system with the corresponding flow velocity. The inclusive cross sections are obtained by a weighted averaging over the impact parameters.
Fig. 1 compares recent 137 MeV/n Ar+Au-data of B. Jacak, G.D. Wertfall et al.[3] to the results of our calculations.
The upper frame shows the inclusive double differential ^{3}He cross section, the lower frame compares the results for tritons. In both cases the overall shape as well as the angular dependence of the spectra agree reasonably well.

Especially the tendency of the ^{3}He spectrum to decrease with decreasing energy and the opposite behaviour of the triton spectrum are reproduced fairly well by our calculations. This systematic behaviour is caused by the fact that the Au target is neutron rich. Therefore, at low energies, neutron-rich reaction products such as triton are produced preferentially whereas proton-rich ^{3}He production is suppressed.
The agreement between data and calculation seems to indicate that a fluid dynamical description might be reasonable already in the energy regime $E_{lab}\sim 100$ MeV/n.

[1] B. Jakobsson et al., Phys. Lett. 102B (1981) 121 and B. Jakobsson,Univ. of Lund preprint LUIP 8208,June 1983; R. Glasow, G. Gaul, B. Ludewigt, R. Santo, H. Ho, W. Kuhn, U. Lynen,and W.F. Müller, Phys.Lett.120B(1983) 71

[2] G. Buchwald, G. Graebner, J. Theis, J.A. Maruhn, W. Greiner, H. Stöcker, Phys.Rev.C28(3) (1983) 1119

[3] B.V. Jacak, G.D. Westfall, C.K. Gelbke, L.H. Harwood, W.G. Lynch, D.K. Scott, H. Stöcker, M.B. Tsang, T.J.M. Symons, Phys. Rev. Lett 51(20) (1983) 1846 and B.V. Jacak and G.D. Westfall, private communication

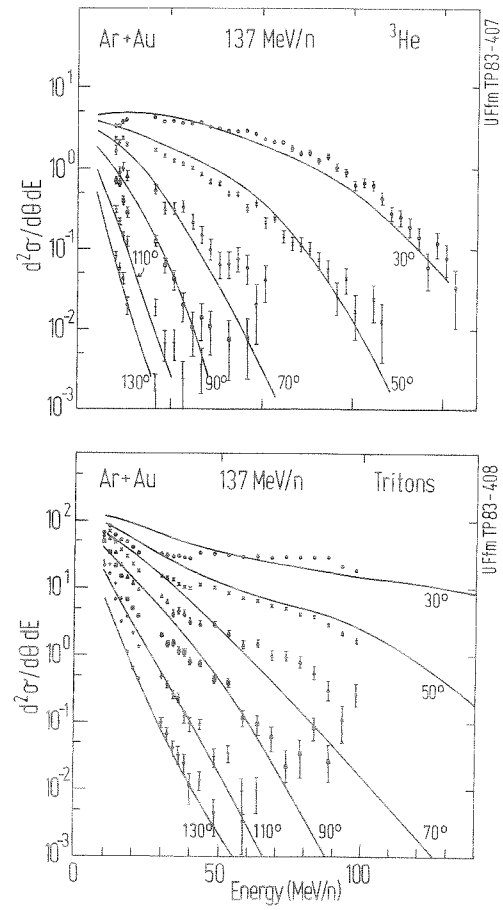


Fig. 1: Comparison between experimental and theoretical data for $^{40}Ar(137\ MeV/n) + ^{197}Au$. Full lines correspond to the calculations, dots represent the experimental data.
The upper frame shows a comparison for ^{3}He production; the lower frame compares triton data.

Dynamical Correlations in Intermediate Energy Nucleus - Nucleus Collisions

W. Cassing

GSI Darmstadt

Nucleus-nucleus collisions in the energy range from roughly 15 MeV/u to 150 MeV/u may serve as an experimental probe for the competition between one-body and two-body effects in nuclear matter far from equilibrium. A sufficiently sophisticated description of the dynamics is given by the Vlasov equation[1] with an additional collision term of the Uehling-Uhlenbeck type[2], a nonlinear partial integro-differential equation for the Wigner-distribution function. Neglecting the collision term, the Vlasov equation may essentially be considered as equivalent to a time-dependent one-body Schrödinger-equation[3] describing coherent excitations of the system, while the collision term drives the nuclear system to equilibrium by means of two-body collisions which are allowed according to the Pauli principle. Early studies within one-dimensional TDHF calculations[4] indicate that high momentum components of the Wigner function may be generated for colliding pieces of nuclear matter which might be important for the production of pions[5].

In order to study the connection between the momentum distributions and a time-dependent mean field for three-dimensional finite size nuclei model calculations have been performed with the two-center shell-model Hamiltonian $H(z_0)=-\hbar^2/(2M)\Delta+\frac{M}{2}\omega^2(z_0)(x^2+y^2+z^2-2|z|z_0+z_0^2)$. The parameter z_0 is a function of time and describes half the distance between the centers of the mean fields. The time-dependence of $z_0(t)$ was determined by the laboratory bombarding energy and the constraint that the sum over all s.p. levels was constant in time. The initial conditions for the solution of the time-dependent Schrödinger equation were assumed to be symmetric and antisymmetric eigenstates of $H(z_0(t=0)=5.5fm)$ for the system $^{40}Ca + ^{40}Ca$ boosted in $\pm z$ direction with half of the appropriate relative velocity above the corresponding Coulomb barrier. A Fourier-Bessel transformation has been applied to the time-dependent s.p. states (in cylindrical coordinates) and the momentum distributions $f(k_\rho,k_z;t)$ have been evaluated by summing over all states. The function $f(k_\rho,k_z)$ is displayed in fig.1 for $^{40}Ca + ^{40}Ca$ at 30 MeV/u and various times in units of 10^{-23}s. The contour plots of $f(k_\rho,k_z;t)$ show that the total momentum distribution changes

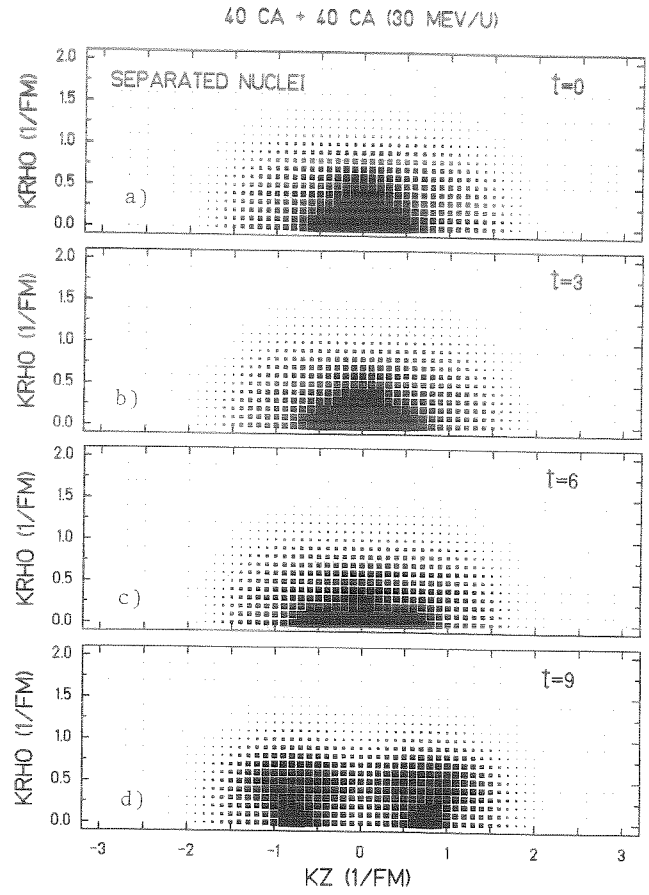


fig. 1

quite drastically in time essentially decreasing low momentum components in favour of higher momentum components in k_z-(beam) direction. The elongation of the momentum distribution in k_z-direction divided by the extension in k_ρ-direction for strongly overlapping nuclei may be considered as a measure of the nonequilibrium state of nuclear matter which will be driven to equilibrium by two-body collisions on time scales as given by fig.2 of Ref.6. Due to the lack of selfconsistency in the present calculations TDHF investigations in more than one dimension should be performed and analyzed in the sense described above.

References:

1) G.F.Bertsch,in "Nuclear Physics with Heavy Ions and Mesons",ed.by R.Balian et al, North-Holland 1978,p.175
2) C.Y.Wong,H.H.Tang,Phys.Rev.Lett.40(1978)1070
3) H.H.K.Tang et al,Phys.Lett.101B(1981)10
4) H.S.Köhler,H.Flocard,Nucl.Phys.A323(1979)189
5) M.Tohyama,R.Kaps,D.Masak,U.Mosel, Preprint Univ. Gießen 1983
6) W.Cassing,M.Malvetti,H.J.Simonis, Relaxation Times...,Annual Report GSI 1983

On the Influence of a Time - Dependent Mean Field on Subthreshold Pion Production in Nucleus - Nucleus Collisions

W. Cassing

GSI Darmstadt

Subthreshold pion production in intermediate energy nucleus-nucleus collisions has gained vivid interest on experimental and theoretical side because cooperative nuclear motion should be responsible for the production mechanism at least for energies below 50 MeV/u[1-3]. Apart from contributions of multi-nucleon scattering[1] dynamical distortions of the momentum-energy distributions might be equally well important for the production mechanism as suggested in Ref.4. Recent studies within a time-dependent two-center oscillator-model show that the distortions of the momentum distributions are quite significant and a drastic enhancement of momentum components in the direction of the collision axis appears during the collision[5]. Such types of many-body correlations have been completely neglected in the nucleon-nucleon scattering models so far[2,6].

In order to test the sensitivity of the pion yield to such distortions the local momentum distributions $f(\vec{k},t)$ for overlapping densities in coordinate space are parametrized by two ellipsoids with axis $a = Q \cdot k_F$ in k_z-direction and $b = k_F$ in $k_{x,y}$-direction (k_F: Fermi momentum) separated by a relative momentum u as in Ref.7. The number of pions produced per unit time and volume by nucleon-nucleon collisions then is given by[2]

$$\frac{dN_\pi}{dtdV} = \frac{4}{M}\,\rho_0^2 \int d^3k_1 \int d^3k_2\, \sigma_\pi(E)\,|\vec{k}_1-\vec{k}_2|\, f(\vec{k}_1) f(\vec{k}_2) \times \left\{\frac{\text{n+n phase space in medium}}{\text{n+n free phase space}}\right\} \qquad (1)$$

with $\rho_0 = 0.16\text{fm}^{-3}$ and $f(\vec{k})$ normalized to 1. The integral (1) was evaluated by Monte Carlo techniques with roughly 5% accuracy and an average cross section for pion production $\sigma_\pi(E)$ from Ref.8, where E is the energy of the corresponding nucleon-nucleon collision with relative momentum $(\vec{k}_1-\vec{k}_2)/2$.

The numerical results for the pion production rate are displayed in fig.1 as a function of the relative velocity in units of the Fermi velocity v_F and the deformation parameter Q. The lines represent constant pion yields which increase by a factor 10 from line to line. In order to see

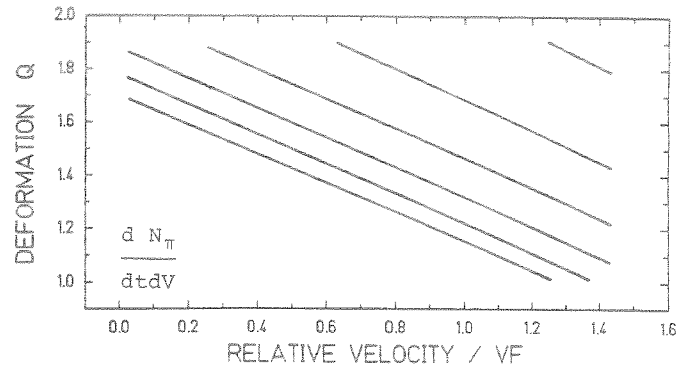


fig. 1

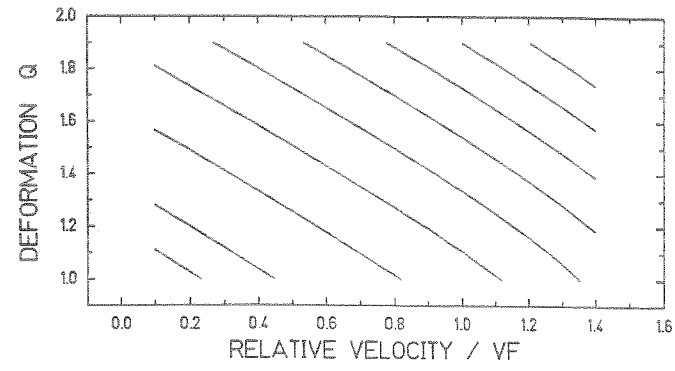


fig. 2

an effect we need the lines of constant energy per volume in the parameter space for $f(\vec{k})$ which are depicted in fig.2. Combining figs.1 and 2 it becomes obvious that along a line of constant energy the pion yield increases drastically with increasing distortion Q of the momentum distribution. Thermalization due to two-body collisions changes the lines of constant energy because the thermal energy per unit volume has to be subtracted. Numerical calculations with respect to relaxation times of the momentum distribution $f(\vec{k})$ investigated show however that at least for energies below 50 MeV/u coherent distortions should survive up to 10^{-22} s[7].

References:

1) R.Shyam,J.Knoll,Preprint GSI-83-22
2) G.F.Bertsch,Phys.Rev.C15(1977)713
3) D.Vasak et al,Phys.Lett.93B(1980)243
4) M.Tohyama,R.Kaps,D.Masak,U.Mosel, Preprint Univ. Gießen 1983
5) W.Cassing, Dynamical Correlations..., GSI Annual Report 1883
6) T.Johansson et al,Phys.Rev.Lett.48(1982)732
7) W.Cassing,M.Malvetti,H.J.Simonis, Relaxation Times...,GSI Annual Report 1983
8) Prakash et al,Stonybrook,NBI,to be published

Pion Production at Subthreshold Energies
Nucleon-Nucleon Single Collision Vs. Co-operative Mechanisms

R. Shyam and J. Knoll
GSI Darmstadt

Significant production cross-sections of charged[1] as well as of neutral[2] pions have recently been observed in the collision of two nuclei at the beam energies below the threshold (290 MeV/A) of the production process NN → NNΠ. The earliest suggestion to understand this process dates back to Fermi. This exploits the fact that initial intrinsic nucleonic motion offers the necessary extra boost for the elementary nucleon-nucleon (N-N) pion production process. This idea has recently been reconsiderd in a N-N single collision (NNSC) mechanism to explain the subthreshold pion production. However, with decreasing beam energy this mechanism may become insufficient, and other mechanisms involving the participation of more than two nucleons in the pion production process may become increasingly important. In this report our aim is to re-examine the NNSC mechanism carefully and to study the kinematical implications of the co-operative production mechanisms on the pion spectra.

In the calculations performed so far with NNSC model, the Fermi-gas prescription has been used to describe the initial nucleonic configurations. We improved on this aspect by means of a shell model prescription which distributes the nucleons in descrete bound orbits irrespective of the size of the momenta. This makes the NNSC model void of 'spurious energy sources'. With this improvement the NNSC model calculations with harmonic oscillator wave functions which fit (P,γ) data upto intrinsic momenta of 500 MeV/C, underestimate the yields of the pion data by almost two orders of magnitude and predict much steeper slopes for the spectra (Fig. 1)[3]. Thus there is a need of a mechanism other than the NNSC model.

In this context we have considered a mechanism which involves the co-operative action of several of the target and projectile nucleons in pooling their energies in producing a pion. As a further co-operation among the nucleons we consider also the formation of fragments of various mass compositions in the final channel along with the produced pion. Our calculations (which is based on an extension of the phase-space model of Knoll) involve one density parameter. With a value for this parameter equal to the normal nuclear matter density (which is held fixed throughout) our model provides a reasonable description of the experimental data (both absolute yields and slopes) for the beam energies ranging between 35 MeV/A - 200 MeV/A , and for a number of combinations of colliding nuclei. One typical result is shown in fig. 2[4]. Note the importance of fragment formation in the final channel.

References

1) T. Johansson et al., Phys. Rev. Lett. 48 (1982) 732
2) H. Noll et al., GSI Scientific Report 1982 and to be published
3) R. Shyam and J. Knoll, Phys. Lett. B (In press); GSI-preprint 22-83
4) R. Shyam and J. Knoll, Nucl. Phys. A (To be published)

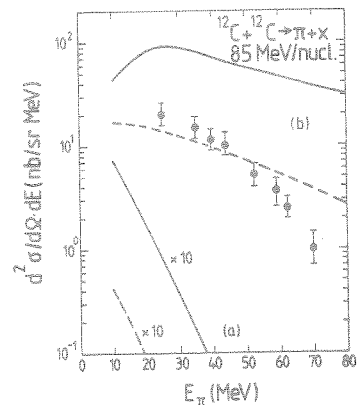


Fig.1. Pion production cross-section at 90° laboratory angle, calculated with NNSC model. The group of curves (a) with a standard harmonic oscillator shell model prescription for the intrinsic nucleonic motion, and group (b) with a Fermi-gas prescription for this; solid and dashed curves correspond to NN-dπ and NN→NNπ channels respectively.

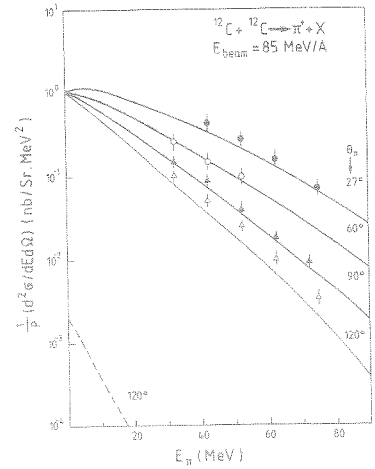


Fig.2. Pion production cross-section calculated with our model. The dashed curve corresponds to the calculations performed assuming only nucleons alongwith the pion in the final channel, for $\theta_\pi = 120^\circ$.

Mean Field Approach to Pion Production in Intermediate Energy Heavy Ion Collisions [B]

M. Tohyama, R. Kaps, D. Masak, and U. Mosel

Institut für Theoretische Physik, Universität Giessen

Since cooperative effects may play an essential role in heavy-ion subthreshold pion production, it is necessary to incorporate the dynamics of the collision into the theory. We do this here by using the time-dependent Hartree-Fock (TDHF) theory for the description of the dynamical evolution of the nucleus-nucleus collision. The Fermi motion, Pauli blocking, as well as dynamical distortions of the energy-momentum distributions are all inherent in this theory.

The inclusive number N of produced pions with momentum p and energy $\omega = \sqrt{p^2+m_\pi^2}$ is given in terms of the pion source function $j(x)$[1,2],

$$2\omega\frac{dN}{d^3p} = \frac{1}{(2\pi)^3}\int d^4x_1 d^4x_2 e^{ip(x_2-x_1)}\langle\Psi_{in}|j^+(x_1)j(x_2)|\Psi_{in}\rangle \quad (1)$$

Here $|\Psi_{in}\rangle$ is the Heisenberg "in" state of the colliding system. We calculate the pion source function both in the one nucleon model (ONM) and in the two nucleon model (TNM)[3].

The number of produced pions are calculated for collisions of slabs with thickness of 4.6 fm. The spectra of produced pions obtained in the ONM are shown in the upper part of the figure for various incident energies. The right hand scale denotes the cross section estimated by $\frac{d^3\sigma}{d^3p} = \frac{dN}{d^3p}\int S(b)2\pi b\,db$. Here S(b) is the area of the overlapping section of the two colliding nuclei at impact parameter b. The absolute value is by an order of magnitude smaller than experimental data[4]. The dependence of the number of produced pions on the incident energies is also too small.

The pion spectra obtained from the pion source function in the TNM are shown in the lower part of the figure. Here we use the simplified transition operator given by Grossmann et al.[3] for (p,π) reactions. Compared to the spectra obtained in the ONM, the TNM spectra have by about an order of magnitude larger cross sections. The larger cross section is due to the fact that nucleons with lower momenta can contribute to the pion production in the TNM.

Again, as in the ONM calculations, the cross section does not increase fast enough with bombarding energy, possibly as a consequence of the one-dimensional geometry.

[1] P. Carruthers and F. Zachariasen, Rev. Mod. Phys. 55, 245 (1983).

[2] M. Tohyama et al., to be published in Phys. Lett. B.

[3] Z. Grossmann et al., Ann. Phys. (N.Y.) 84, 348 (1974).

[4] W. Benenson et al., Phys. Rev. Lett. 43, 683, (1979); 44, 55 (1980).

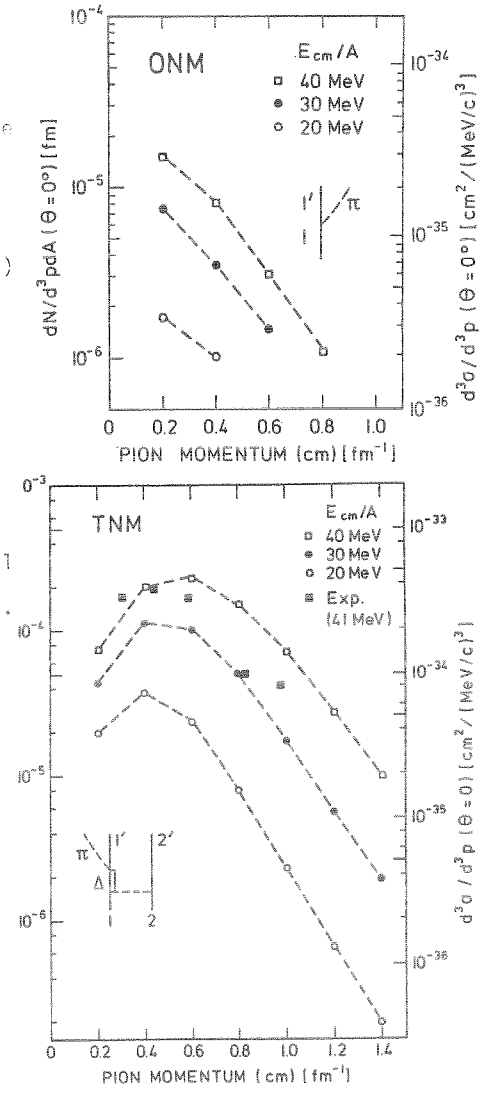


Fig. 1: Momentum spectra of pions produced in the forward direction per unit area as obtained in the ONM (upper part) and in the TNM (lower part). The right hand scale denotes the cross section calculated for the $^{20}Ne + ^{20}Ne$ collision. The experimental data are from ref. 4.

Antisymmetrization and π-Production [B]

D. Masak, R. Kaps, U. Mosel, and M. Tohyama

Institut für Theoretische Physik, Universität Giessen

Since the discovery of subthreshold π-production[1] there have been several attempts to explain this effect in so called first collision models. Particularly crucial for this explanation are the momentum distributions of the nuclei involved in the collision. We have, therefore, studied the effects of antisymmetrization on these distribution and more generally on the Wigner function.

In our calculations we used boosted harmonic oscillator wave functions[2,3]:

$$\Psi(x) = e^{\pm ikx}\Psi_{HO}(x)$$

and the total wave function:

$$\phi(x) = A[\Psi_1 \cdots \Psi_{N1}\ \Psi_{N+1} \cdots \Psi_{2N}]$$

where the states 1,...N and N+1,...2N are centered around -R and +R, respectively.
The Wigner transformation for two wavefunctions K_1 and K_2 is given by:

$$(*)\ f_{K_1K_2}(x,p) = \frac{1}{2\pi}\int_{-\infty}^{+\infty} ds e^{ips}\Psi^*_{K_1}(x+\tfrac{s}{2})\Psi_{K_2}(x-\tfrac{s}{2})$$

$$= \frac{(-1)^{K2}}{\pi}\left(\frac{K_2!}{K_1!}\right)^{1/2} 2^{\frac{K_1-K_2}{2}} e^{-(x^2+p^2)}$$

$$(x+ip)^{K_1-K_2} L^{K_1-K_2}_{K_2}(2x^2+2p^2)$$

in the harmonic oscillator case[4]. L is the associated Laguerre polynomical.

The two pictures show the Wignerfunction of the total system (static refers to the calculation without antisymmetrization). In the shown case these are two ^{16}O nuclei at 40 MeV/A-lab-energy and a distance of 1 nuclear radius. The dotted lines represent the negative part of the Wignerfunction. Note that the static solution does not have a negative part, which is obvious from (*). It is clearly seen that the antisymmetrization depletes the momentum distribution at small p's thus opening phase space for the final state after the collision. At the same time it enhances the high momentum components thus increasing the π-production yield.

[1] W. Benenson et al., Phys. Rev. Lett. 43, 683 (1979)

[2] J. Fleckner, U. Mosel, Nucl. Phys. A211, 170 (1977)

[3] T. Fliessbach, Z. Phys. 238, 329 (1970)

[4] S. Shlomo, J. Phys. A16, 3463 (1983)

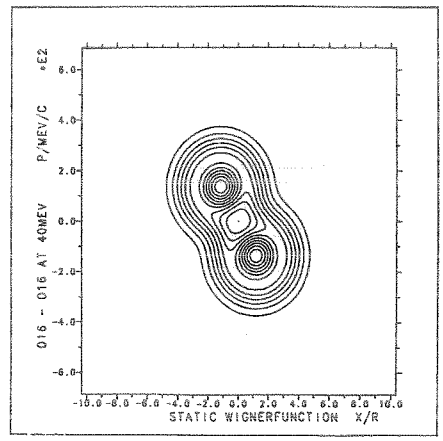


Fig. 1:
Wigner function without antisymmetrization of ^{16}O-^{16}O system at 40 MeV/lab and distance R (R radius of ^{16}O, R=2.34 fm) in arbitrary units.

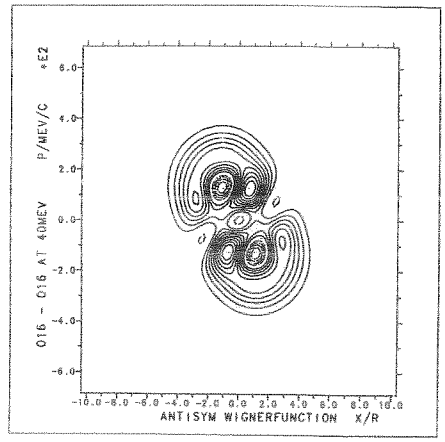


Fig. 2:
Wignerfunction with antisymmetrization of ^{16}O-^{16}O system at 40 MeV/lab and distance R in arbitrary units.
Full line: positive part.
Dashed-dotted: negative part.

Pion Bremsstrahlung far below the single N-N threshold G

D. Vasak, B. Müller, and W. Greiner
Institut für Theoretische Physik, Universität Frankfurt/Main

We apply the bremsstrahlung model for pion production[1] to heavy-ion collisions far below the single N-N threshold. In this energy regime the production of pions must be a collective effect[2] and cannot be explained by models known from high-energy heavy-ion physics (e.g., thermal, Fermi-motion). Our model reproduces the C+C π^0+X data by Noll et al.[3], when the deceleration parameter of the theory is once adjusted (at E_{LAB} =74 MeV/n)[4]. The experimental angular distribution (Fig. 1a) can be explained(by assuming strong correlations between the target and projectile spin-distributions in the reaction zone)as well as the angle-integrated spectra (Fig. 1b). Together with thermally produced pions calculated in a simple shock-wave calculation (dashed line) the pion bremsstrahlung gives a satisfactory qualitative description (Fig. 1c) of the available data[5-8].

Other processes which are also sensitive to the dynamics of the collision could be used equally well to test independently the assumptions underlying our model. The γ-ray bremsstrahlung spectra calculated with the same trajectories are depicted in Fig. 2. Note that for $E_\gamma \gtrsim 30$ MeV where they are not contaminated by photons from nuclear transitions, we still predict μb-cross-sections for $E_{LAB}/n \gtrsim 60$ MeV!

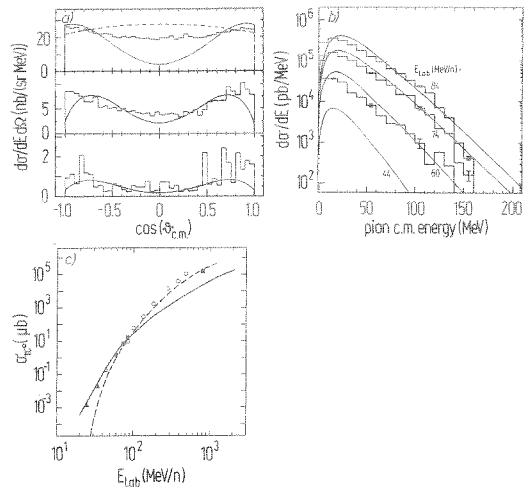


Fig. 1: Pion bremsstrahlung from $^{12}C+^{12}C \rightarrow \pi^0$+X reactions. The deceleration parameter is ν=0.38: (a) The angular distribution for pions produced at 84 MeV/n in the energy region 0-50 MeV (top), 50-100 MeV and 100-150 MeV, respectively. The data are from ref. 4. (b) The angle-integrated spectra at ion energies between 44 and 84 MeV/n. (c) The excitation function. The data are taken from ref. 4 (solid dots), 7 (open circles), 5 (open triangles), 6 (solid triangles), and 8 (solid squares). The dashed line exhibits the thermal pions.

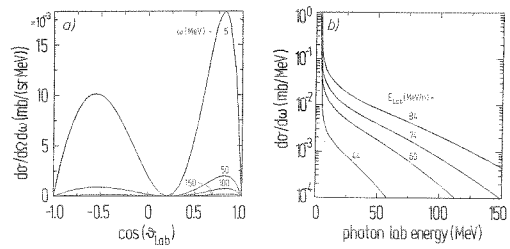


Fig. 2: The γ-ray bremsstrahlung from $^{12}C+^{12}C \rightarrow \gamma$+X reactions: (a) The double-differential cross section at 85 MeV/n in the lab system. (b) The angle-integrated γ-ray spectra in the lab-system.

[1] D. Vasak, B. Müller, and W. Greiner, Phys.Scr.22 (1980) 25;
D. Vasak, H. Stöcker, B. Müller, and W. Greiner, Phys. Lett. 93B (1980) 243

[2] D. Vasak, B. Müller, and W. Greiner, preprint UFTP 116 (1983), to be published

[3] R. Shyam and J.Knoll, Subthreshold Pion Production, GSI preprint (1983), to be published

[4] E. Grosse, Proc. Int. Workshop on Gross Properties of Nuclei and Nuclear Excitations,XI. Hirschegg,Austria, 1983, p.65

[5] H. Noll et al., Proc. Int.Conf. on Nuclear Physics, Florence, 1983, p.682

[6] P. Braun-Munzinger et al., Pion Production in Heavy Ion Collisions at E_{lab}/A=35 MeV, to be published

[7] W. Benenson et al., Phys. Rev.Lett.43 (1979), 683, and 44 (1980) 54E;
B. Jakobsson, Proc. Nordic Meeting in Nucl. Physics, Fuglso, Denmark, 1982
T. Johansson et al, Phys. Rev.Lett. 48 (1982) 732
J.P. Sullivan et al., Phys. Rev. 25C (1982) 1499

[8] S. Nagamiya et al., Phys. Rev. 24C (1981) 971

Isospin statistics [B]

M. Uhlig, D. Vasak, C.S. Warke, J.A. Maruhn, and W. Greiner
Institut für Theoretische Physik, Universität Frankfurt/Main

One subtle point in the pion-bremsstrahlung model[1] is the classical expression that is used for the pion-nucleon coupling current $j(x)$. Independent of the (pseudo-scalar or pseudo-vector) way of coupling (PS or PV) the expression that has to be replaced is

$$j_k \sim \partial_\mu Q_k^\mu = \partial_\mu(\bar{\psi}\gamma^5\gamma^\mu\tau_k\psi) \quad .$$

Without isospin content the current has been reduced by Takabayasi[2]. If one accounts for the isospin by a statistical factor $w(A_p)$ the classical expression reads:

$$Q_k^\mu = w(A_p) \cdot \rho_s \sigma^\mu \cdot I_k$$

with ρ_s the scalar density, the spin vector σ^μ and a unit vector in isospin space I_k, and A_p the number of projectile nucleons.

To approximate the factor w, D. Vasak[1] used a simple statistical model which is based on the following assumptions:

1. Every target-nucleon collides once with the target nucleus.
2. The isospin is built up by the individual nucleon-nucleon collisions by the following prescription: $t_f = t_i + \Delta t$ where Δt has the values -1, 0, +1. The main simplification is to assume that all allowed values Δt are equally probable.

The result of this model is $w(A_p) \cong \sqrt{A_p}$.

To check the validity of these assumptions and to present a perhaps more reliable approximation is the aim of this work.

The first improvement consists in extracting the probability of the collisions with a certain Δt out of the experimental cross sections of nucleon-nucleon reactions rather than taking them all equal.
The needed information can be deduced only from nucleon-nucleon reactions with definite isospin-change, namely NN→NNπ (as the lowest in energy). Lock[3] has decomposed the available cross sections into their isospin content.
Based upon this analysis one can deduce the following ratios at low energies:

$$\frac{\sigma_{-1}}{\sigma_0} \cong 10 \qquad \frac{\sigma_{+1}}{\sigma_0} \approx 0.25$$

where the index refers to the relative isospin change of the nucleons.

The exact way how these ratios are included in the statistical weights that are attributed to each isospin value[4] cannot be summarized in a few words but one can argue that due to the extreme deviation from 1 taking this effect into consideration yields a quite different mean isospin value. The build-up of large isospin values t is hindered by the dominance of isospin reducing reactions σ_{-1}. Because t cannot fall below the starting value t_0 (which is zero for light nuclei) nevertheless after several collisions a small isospin $t > t_0$ is built up.

The major uncertainty of that description is whether one can use the measured NN→NNπ cross section also for virtual pions. To circumvent this problem we made an independent approach by considering a cascade of A_p nucleon target collisions. In that model the isospin is built up only due to the repeated coupling of a single nucleon to the target. The only parameters of this model are the abundance of neutrons and protons in the projectile and the initial isospin state of the target $|T_0, T_0>$. All the development of isospin as a function of the number of collisions m is governed by the Clebsch-Gordan coefficients. The resulting isospin is much larger than in the preceding model but still smaller than the $\sqrt{m}$. For higher values of m the T-curve is described by $\sqrt{m/2}$.

[1] D. Vasak, Diploma thesis (1978)
D. Vasak, B.Müller, W. Greiner, Phys.Scr.22 (1980)25
D. Vasak, H. Stöcker, B. Müller, W. Greiner, Phys. Lett. 93B(3) (1980)243
D. Vasak, B. Müller, W. Greiner, UFTP Preprint 116/1983

[2] T. Takabayasi, Progr.Theor.Phys. (Suppl.) 4 (1957) 1

[3] W.O. Lock et al., Intermediate Energy Physics, London 1970; G. Jones: AIP Conf Prof. 79 (1982) 15

[4] M. Uhlig et al., to be published

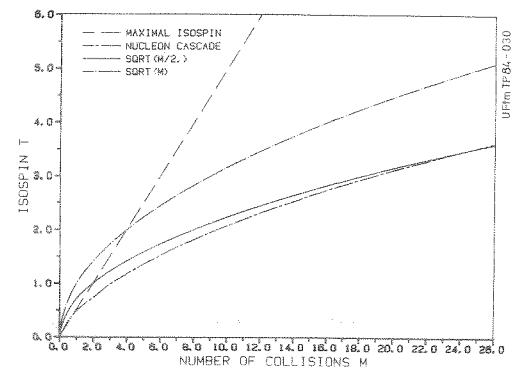


Fig. 1: Isospin T as a function of the number of collisions m .

Pion bremsstrahlung coupled to hydrodynamics B

M. Uhlig, D. Vasak, G. Buchwald, J.A. Maruhn, and W. Greiner
Institut für Theoretische Physik, Universität Frankfurt/Main

The pion bremsstrahlung model[1] describes the low energy pion production in heavy ion collisions as due to the collective deceleration of the projectile which produces a partial shake-off of the surrounding pion cloud - in close analogy to the classical photon bremsstrahlung. D. Vasak's model[1] needs as input the trajectory of the heavy ions and the space and time variation of the densities.

The existing - very successful - model depends quite sensitively on the deceleration parameter of the simple schematic trajectory.

To replace the schematic trajectory and to remove the uncertainties is the aim in introducing a hydrodynamical description of the underlying heavy ion dynamics of the process. To use hydrodynamics one has to introduce hydrodynamical quantities in the pion production formalism:

The double differential cross section can be written as[1]

$$\frac{d^2E}{dp_0 d\Omega} = \frac{1}{16\pi^3} p_0 p \sum_k |\tilde{J}_k(p)|^2$$

where $\tilde{J}_k(p)$ is the Fourier transform of the pion current density

$$J_k(x) = \frac{g_\pi}{2M} \partial_\mu Q_k^\mu$$

with the pion nucleon coupling current

$$Q_k^\mu = \bar{\psi} \gamma_5 \gamma^\mu \tau_k \psi \quad .$$

If one introduces the material derivative $\frac{D}{Dt}$ one can follow the photon bremsstrahlung-scheme[2] and obtains:

$$\tilde{J}_k(p) = \int d^4x \; e^{-ipx} \frac{D}{Dt} \left[\frac{Q^k \cdot p}{p_0 - \vec{p}\vec{v}} \right] \quad .$$

The coupling current Q_k^μ is treated as in the existing model[1,3] and is reduced to a product of spin vector, scalar density ρ_s and a statistical factor. The spin vector is obtained by assuming a Lorentz transformation with the negative local (transport) velocity of the fluid of a spin $(0,\vec{s})$ in the rest system. Because the scalar density is related to the hydrodynamical density all the factors of the coupling current Q_k^μ can be expressed in terms of hydrodynamical quantities, that is density, velocity and acceleration of the fluid cells (as a function of time and space).

Calculations which use the well tested three-dimensional hydrodynamical programs[4] are in preparation.

[1] D. Vasak, Diploma thesis (1978)
D. Vasak, B. Müller, W. Greiner, Phys. Scr. 22 (1980) 25
D. Vasak, H. Stöcker, B. Müller, and W. Greiner, Phys. Lett. 93B(3) (1980) 243
D. Vasak, B. Müller, and W. Greiner, UFTP Preprint 116/1983

[2] J.D. Jackson, Classical electrodynamics, New York, 1975

[3] M. Uhlig et al., this report and to be published

[4] G. Buchwald, G. Graebner, J. Theis, J.A. Maruhn, W. Greiner, H. Stöcker, Phys. Rev. C24(1) (1981) 135
H. Stöcker, G. Buchwald, G.Graebner, P. Subramanian, J.A. Maruhn, W. Greiner, B. Jacak, G. Westfall, Nucl. Phys. A400 (1983) 63
G. Buchwald, G. Graebner, J. Theis, J.A. Maruhn, W. Greiner, H. Stöcker, Phys. Rev. C28(3) (1983) 1119

PHASE TRANSITION OF THE BARYON-ANTIBARYON PLASMA IN A NONLINEAR RELATIVISTIC MEAN FIELD THEORY

G

J. Theis
GSI, Darmstadt
H. Stöcker, J.A Maruhn and W. Greiner
Institut für theoretische Physik, Universität Frankfurt

We recently investigated[1] the phase structure of the n-$\bar{n}$ plasma in a linear selfconsistent relativistic field theoretical model of nuclear matter[2] and found that a phase transition occurs at T=200 MeV for vanishing chemical potential. This transition give rise to a temperature dependence of the total energy density and pressure similar to recent QCD calculations[3] (Fig.1). However the linear mean field theory has the disadvantage that it is not capable of describing correctly the compressibility and effective mass of ground state nuclear matter. The inclusion[4] of a phenomenological nonlinear scalar meson interaction into this model allows for a correct description of the bulk properties of nuclear matter. Fixing the 4 dimensionless coupling constants C_s^2, C_v^2, $B=b/g_s^3$, $C=c/g_s^4$, we found similar phase transitions in the nonlinear model, indicating that the couplings can be chosen not to destroy the phase structure of the mean field model (Fig.2). The phase structure of the model is described by the effective Lagrangian

$$\mathcal{L} = -\frac{1}{2}\bar{\Psi}[\gamma^\mu\partial_\mu + M]\Psi - \frac{1}{2}(\partial_\mu\phi)(\partial^\mu\phi) - U(\phi) - \frac{1}{4}F_{\mu\nu}F^{\mu\nu} - \frac{m_v}{2}\omega_\mu\omega^\mu + g_s\bar{\Psi}\phi\Psi + ig_v\bar{\Psi}\gamma_\mu\omega^\mu\Psi$$

where the potential function $U(\Phi)$ is given by

$$U(\phi) = \frac{m_s}{2}\phi^2 + \frac{B}{3}\phi^3 + \frac{C}{4}\phi^4$$

The thermodynamical quantities can be calculated in the mean field approximation for $\rho=\mu=0$, yielding for the dimensionless energy density:

$$\varepsilon = \frac{1}{2C_s^2}(1-x)^2 - \frac{b}{3}(1-x)^3 + \frac{c}{4}(1-x)^4 + \frac{\gamma\Theta x^3}{\pi^2}\sum_n \frac{(-1)^{n-1}}{n}\left[K_1\left(\frac{nx}{\Theta}\right) + \frac{3\Theta}{nx}K_2\left(\frac{nx}{\Theta}\right)\right]$$

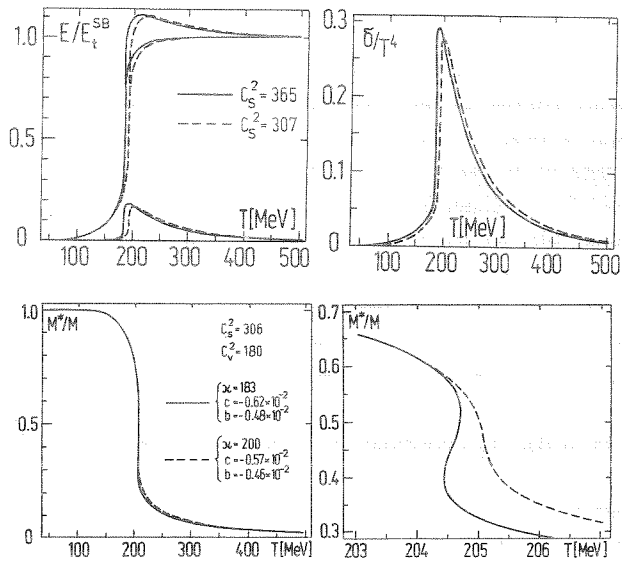
and the total pressure

$$p = -\frac{1}{2C_s^2}(1-x)^2 - \frac{b}{3}(1-x)^3 + \frac{c}{4}(1-x)^4 + \frac{\gamma\Theta x}{\pi^2}\sum_n \frac{(-1)^{n-1}}{n}K_1\left(\frac{nx}{\Theta}\right)$$

where the effective mass $M^* = xM$ is defined by

$$x = 1 - C_s^2\frac{\gamma\Theta x}{\pi^2}\sum_n \frac{(-1)^{n-1}}{n}K_1\left(\frac{nx}{\Theta}\right) - C_s^2\left[b(1-x)^2 - c(1-x)^3\right]$$

Here K_1 and K_2 stand for the modified Bessel-functions of first and second order, respectively. Fig.2 contains the solution x of the self consistency equation as a function of the temperature T. The most striking feature is the sudden decoupling of the baryonic system to almost free zero-mass nucleons.



Figures :

1. In the upper right picture for $\rho=\mu=0$ the temperature dependence of the energy densities (divided by the Stefan Boltzmann limit) is shown. In the left figure the function $\delta=E/3 - P$ is shown. Both figures can be compared with a recent QCD calculation[3]
2. for $\rho_v=\mu=0$ the solutions $x=M^*/M$ of the self consistency equation in the nonlinear mean field model is plotted for different values of b and c, but fixed values of C_s^2 and C_v^2. Part b) contains the same results but with a stretched temperature axis near the transition point.

References

1. Theis J., Graebner G., Buchwald G., Maruhn J., Stöcker H., Polonyi J. and Greiner W., Phys. Rev. D28, 2286, (1983)
2. Walecka J., Phys. Lett.59b, 109, (1975)
3. Montvay I. and Pietarinen E., Prepr. No.:HU82-8, Helsinki
4. Boguta J. and Bodmer A., Nucl. Phys.A292, 413, (1977)

INSTABILITY OF HIGH TEMPERATURE BARYONIC MATTER IN A RELATIVISTIC MEAN FIELD THEORY

G

J. Theis, T. Biro
GSI, Darmstadt
and W. Greiner
Institut für theoretische Physik, Universität Frankfurt

In a recent investigation[1] the stability of the homogenous solution of the linear relativistic mean field model[2] was studied. It was found that in the density regime $.005 \leq \rho \leq 0.15$ fm^{-3} and for temperatures T<35 MeV it becomes unstable against density- (or field-) perturbations with wavelength larger than a critical size[1] In this approach we apply the formalism for the low density ($\rho < 0.2$ fm^{-3}), high temperature (T≈200 MeV) regime, where in a recent publication[3] a phase transition of the nuclear system to a nucleon- antinucleon plasma was found.

In order to investigate the stability of that solution one has to add small perturbative components to the attractive scalar and the repulsive vector meson fields, which are space and time dependent. Then the eigenfrequencies of the Fourier expansion of these components are determined. These eigenfrequencies ω are in general complex; yielding for $\mathrm{Im}(\omega) \geq 0$ stable mean field solutions, but results for $\mathrm{Im}(\omega) < 0$ in exponentielly growing perturbations. In the last case the mean field solutions are unstable against such perturbations.

In Fig. 1 the quantity $\omega^2 - k^2$ is plotted as a function of the temperature at different densities for the coupled scalar and vector density fluctuations. The region of weak instability where $\omega^2 - k^2 < 0$ can be seen.

In the schematic plot (Fig.2) both unstable regions in the linear mean field model are depicted. In the low temperature regime (T<35 MeV, $\rho \leq 0.15$ fm^{-3}) the baryon fluid to gas phase transition is obvious, while for high temperatures (T≈200 MeV, $\rho \leq 0.02$ fm^{-3}) the phase transition of the baryonic system to the asymptotically massless state can be seen.

The latter posibility may have interasting astrophysical consequences for the early universe resulting larger fluctuations in the masses of galaxy-clusters than an equilibrium thermodynamical primordial stage.

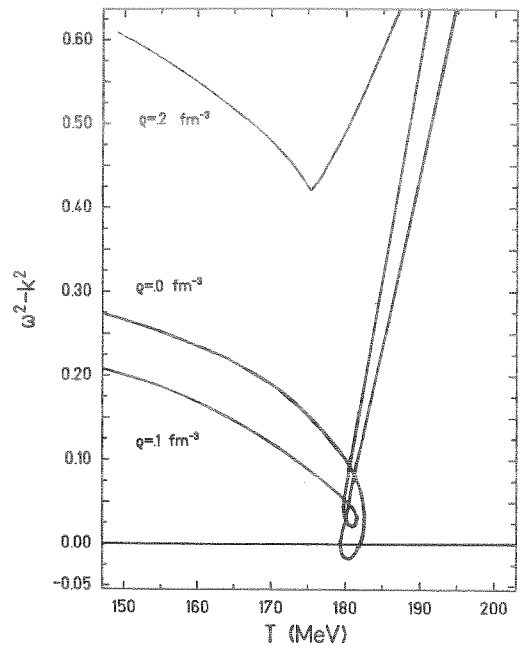


Fig.1: For different densities ρ the function $\omega^2 - k^2$ is plotted versus the temperature T for coupled scalar and baryon density fluctuations, showing the instabilitiy region where $\omega^2 - k^2 < 0$.

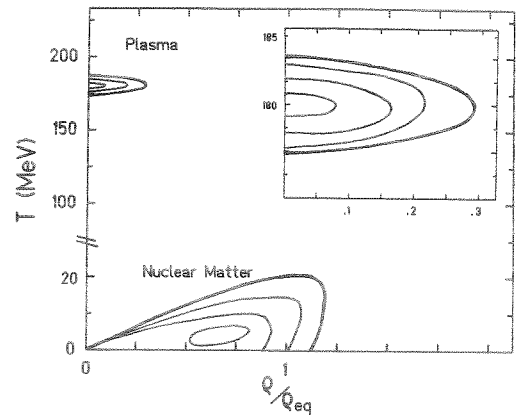


Fig.2: Schematic plot of the instability regime in the T/ρ-plane. The charakteristic curves corresponds to different critical sizes. The outer curves always corresponds to $R_{crit}^{=\infty}$.

References

1) Biro T., Bondorf J. and Zimanyi J., NBI-preprint-83, 38
2) Theis J., Graebner G., Buchwald G., Maruhn J., Stöcker H., Polonyi J. and Greiner W., Phys. Rev. D28, 2286, (1983)
3) Walecka J., Phys. Lett.59b, 109, (1975)

SIMULATION OF DYNAMICAL INSTABILITIES IN THE DECONFINEMENT PHASE TRANSITION

G

J. Theis
GSI, Darmstadt

H. Stöcker, G. Graebner, J. Maruhn and W. Greiner
Institut für theoretische Physik, Universität Frankfurt

The deconfinement phase transition in the central rapidity region of high energy heavy ion collisions is studied via a relativistic selfconsistent mean field equation of state which shows the same characteristics as lattice QCD Monte-Carlo data[1,2] embedded in a relativistic fluid dynamic model. The equations of motion formulated in terms of mass, momentum and energy conservation are:

$$\partial_t(\gamma\rho) + \vec{\nabla}(\vec{u}\gamma\rho) = 0 \qquad (1)$$

$$\partial_t M + \vec{\nabla}\cdot(\vec{u}\vec{M}) = -\vec{\nabla}[P_n - \tfrac{1}{2}m_s^2\bar{\Phi}^2 - (B/3)\bar{\Phi}^3 - (C/4)\bar{\Phi}^4 + \tfrac{1}{2}m_V^2\bar{V}_o^2] \qquad (2)$$

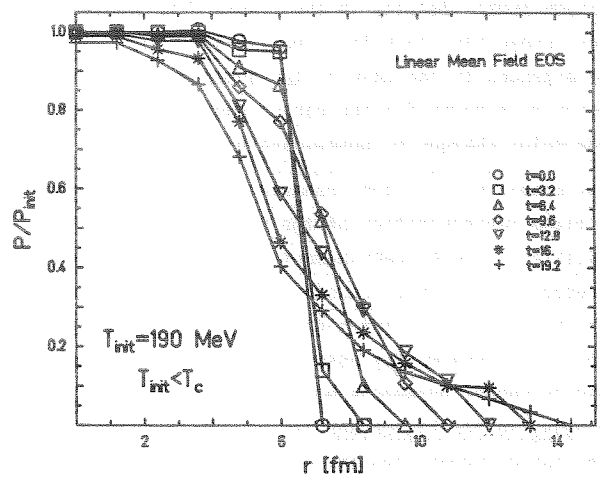
$$\partial_t h + \vec{\nabla}\vec{M} = -\vec{\nabla}[\vec{u}P_n - \tfrac{1}{2}m_s^2\vec{u}\bar{\Phi}^2 - (B/3)\bar{\Phi}^3 - (C/4)\bar{\Phi}^4 + \tfrac{1}{2}m_V^2\vec{u}\bar{V}_o^2] \qquad (3)$$

$$\bar{\Phi} = (g_s\rho_s - B\bar{\Phi} - C\bar{\Phi})/m_s^2 = (M/g_s)(1 - M^*/M) \qquad (4)$$

$$\bar{V}_o = (g_V/m_V^2)\rho \qquad (5)$$

The laboratory momentum $\vec{M}$ and energy density h are related to the total energy density and the pressure in the local rest frame via $\vec{M} = \gamma^2\vec{u}(E+P)$ and $h = \gamma^2(E+P) - P$.

In this approach we simulate the effect of the phase transition from the asymptotically zero mass state to the hadronic matter in a 3+1 dimensional numerical integration of the fluid dynamic equations of motion. Initializing the hot radial symmetric blob of highly excited matter with constant energy densities above and below the critical energy density defined by the the phase transition, we find a drastic difference in the expansion of the hot fireball. In Fig. 1 the pressure normalized by the initial maximum pressure is shown as function of the radius for different expansion times. For initial temperatures T_{init} just below T_c, we observe ordinare rarefaction waves. For $T_{init} > T_c$, a dynamical instability occurs due to the thermodynamic properties of the system. This instability leads to a sharp discontiniuity in the pressure profiles. The transverse momentum distributions of these two different scenaries show an increase in $p_\perp$ if the deconfinement transition occurs.



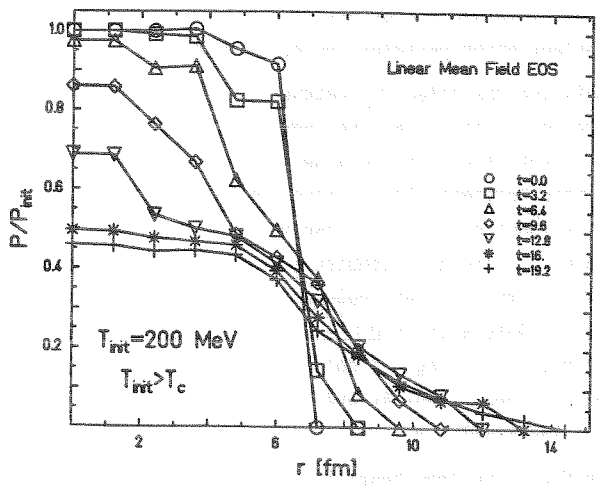


Fig.1: The normalized pressure is shown as a function of the radial coordinate for different expansion times. In Figur a) the expansion is shown for an initial temperature $T_{init} < T_c$, while for b) $T_{init} > T_c$.

References

1) Theis J., Graebner G., Buchwald G., Maruhn J., Stöcker H., Polonyi J. and Greiner W., Phys. Rev. D28, 2286, (1983)

2) Montvay I. and Pietarinen E., Prepr. No.:HU82-8, Helsinki

Color-singlet droplets at finite baryon number density [B]

H.Th. Elze and W. Greiner
Institut für Theoretische Physik, Universität Frankfurt/Main

J. Rafelski
Department of Physics, University of Cape Town, South Africa

Extending previously reported results on the thermodynamical properties of the color-singlet quark-gluon-plasma[1], we continue to study confinement effects semi-phenomenologically also in the case of non-vanishing baryon number density in the plasma. The group-theoretical projection technique described earlier[2] can easily be extended to the case of the inner $U_A(1)xSU_c(3)$ symmetry to account for the baryon number as well as for the color charges of quarks and gluons.

The actual calculations reported below are performed in a mixed representation of the partition function[3] : dictated by color confinement the $SU_c(3)$ degrees of freedom are treated canonically in order to restrict the many-particle states exactly to the colorless sector; but since we may assume a considerable exchange of baryon number between a plasma droplet formed e.g. in a heavy ion collision and its surrounding, we describe the baryon number density by a chemical potential μ. Beyond the colorless character of physical states we include the confining property of QCD by a phenomenological volume energy $B \cdot V$ like in other bag models and neglect other perturbative corrections.

Defining the effective degeneracy D_{eff} of single-particle energy levels as the energy of a colorless plasma of quarks and gluons divided by the corresponding Stefan-Boltzmann-limit value, we show in Fig. 1 D_{eff} as a function $TV^{1/3}$ for two values of the chemical potential and also compare it with the constant reduction of the internal degrees of freedom due to perturbative interactions $O(\alpha_s)$ alone. We observe that the gradual "freezing" of color is reduced by a finite baryon number density and is suppressed completely in the limit $\mu/T \to \infty$.

In Fig. 2 we show resulting stability limit curves $\mu(T)$ for small quark-glue-plasma droplets obtained from their ultrarelativistic equation of state by the condition that the total pressure on a droplet vanishes, $0 \stackrel{!}{=} P_{internal} - B$. One observes how drastically colorlessness can influence the properties of small droplets as compared to the Stefan-Boltzmann-limit and lowest order perturbative results respectively: the smaller the droplet the more reduction of the internal pressure.

These are important effects for any consideration of nucleation of plasma droplets in hot and compressed hadronic matter as well as for the study of experimental decay properties of the quark-glue-phase[3].

[1] H.-Th. Elze et al., GSI Scientific Report 1982, 132

[2] H.-Th. Elze et al., Phys. Lett. 124B (1983) 515

[3] H.-Th. Elze, W. Greiner, and J. Rafelski, to be published

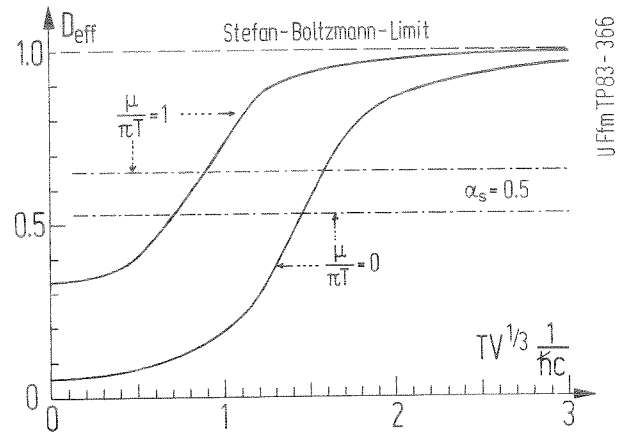


Fig. 1: The effective degeneracy D_{eff} as function of $TV^{1/3}$.

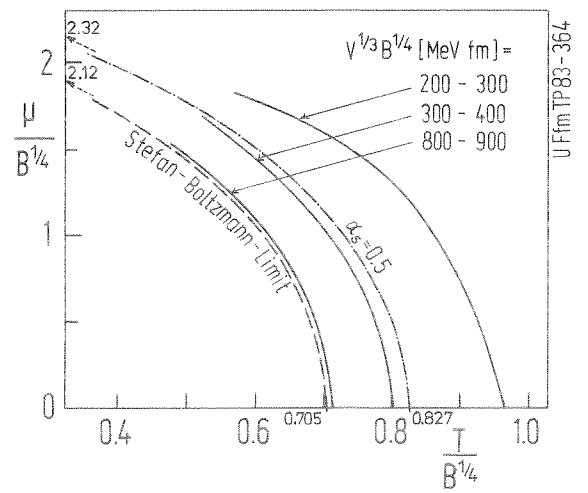


Fig. 2: The quark chemical potential at vanishing total droplet pressure as a function of temperature

Fission of bags in spontaneous quark-antiquark pair-production in supercrtical colour fields

B

D. Vasak, K.-H. Wietschorke, B. Müller, and W. Greiner
Institut für Theoretische Physik, Universität Frankfurt/Main

We describe the fission of heavy quarkonia as the decay of the bag vacuum state by spontaneous creation of a light quark-antiquark pair due to supercritical colour-electric fields. In the adiabatic approximation the heavy quarks are reduced to two point charges Q and $\bar{Q}$ fixed at the foci of a prolate ellipsoidal M.I.T. bag. We solve the Dirac equation with corresponding quasi-abelian potential (Fig. 1) numerically and estimate the critical bag deformation x_{cr} (x is the ratio of the long and short half-axes) where the lowest single particle energy is minimal. For the value $\frac{4}{3}\alpha_s$=0.385 of the strong coupling constant we find x_{cr}=1.88 (cf. Fig. 2). At this deformation the wave function changes its location. This may be interpreted as spontaneous decay of the subcritical vacuum[1]. Accounting for the fact that at the bag walls the kinetic energy of the quarks and the field pressure is balanced by the vacuum pressure $B^{1/4}$, the corresponding critical $Q\bar{Q}$-distance is R_{cr}=2.2 fm (we take $B^{1/4}$=235 MeV from Ref. 2). We show that this "critical distance" lies just above the classical turning points of those $b\bar{b}$- and $c\bar{c}$-resonances which are presently known (Fig. 3).

[1] D. Vasak, K.-H. Wietschorke, B. Müller, and W.Greiner, Z.Phys. C21 (1983) 119

[2] P. Hasenfratz et al., Phys. Scr. 23 (1981) 914

[3] M. Roos et al., Phys. Lett. 111B (1983) 1

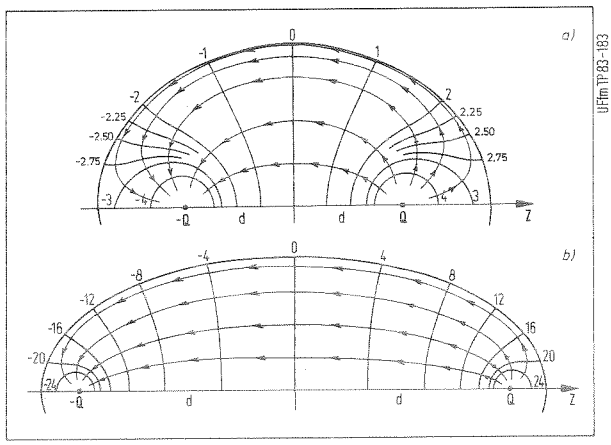


Fig. 1: The equipotential lines of the $Q\bar{Q}$-potential in units $Q/4\pi d$, and the lines of force given by $-\vec{\nabla}\Phi$ (lines with arrows). The potential produced by two charges Q and -Q and modified by the confining boundary, is plotted here for different deformations: a) x=1.2, b) x=1.9.

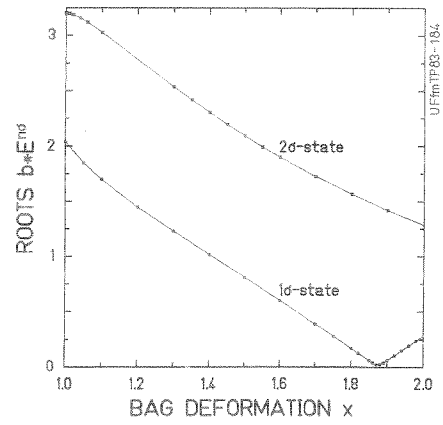


Fig. 2: The scale independent energy eigenvalue $(bE)^{n\sigma}$ for the value $J_z=\frac{1}{2}$ (indicated by σ) of the z-component of the total angular momentum.

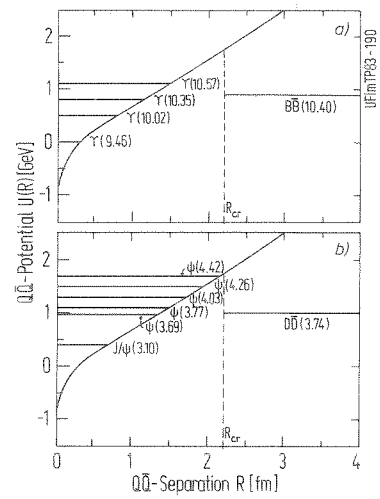


Fig.3 : If the potential energy U(R) (solid line) with α=0.385 and $B^{1/4}$=235 MeV is used in a Schrödinger equation[2] to describe the radial motion of two heavy quarks Q and $\bar{Q}$, (a) the bottomonium and (b) the charmonium masses can be calculated. In order to obtain the actual mass of the meson, the masses of the constituent quarks (m_c=1.35 GeV for the charmed and m_b=4.75 GeV for the bottom quark) have to be added to the eigenvalue of the Schrödinger equation. The results agree well with experimental data[3] which are indicated in the figure by thick horizontal lines. The potential is modified at R_{cr}, since beyond this point the QQ-system will prefer to exist in the form of two atom-like mesons $Q\bar{q}$ + $\bar{Q}q$. The masses of the $b\bar{u}$, $\bar{b}u$ (B-mesons) and $c\bar{u}$, $\bar{c}u$ (D-mesons) pairs with the current masses of the constituent quarks subtracted, too, fix the asymptotic value U(R) for $R > R_{cr}$. Indeed, resonances with binding energies above the barrier $U(R_{cr}) \approx 1.8$ GeV have not yet been discovered.

2. Atomic Physics

		PAGE
2.1	Superheavy Quasi-Atoms and Inner Shell Excitation Mechanism	148
2.2	Few Electron Systems, Recoil Ions and Capture Processes	156
2.3	Theory	168

Studies of the Positron Structure in (U+U)-Collisions via Determination of the Source Velocity

E. Berdermann, J. Kemmer, P. Kienle, H. Tsertos, W. Wagner (TU München)
F. Bosch, C. Kozhuharov (GSI Darmstadt); W. Koenig (MPI Heidelberg)

Utilizing a new experimental set-up, described into detail in this Annual Report, we addressed the question of the origin of the observed narrow positron line in U+U collisions at 1.4 GeV [1].

The observed positron line at 300 keV (c.m.) positron kinetic energy and with a width of 80 keV[1] can be focussed onto the total length of the PAGODA-counter at fixed magnetic field. For this run the energy range from 245 keV to 335 keV has been chosen, subdivided by the PAGODA "roofs" into 11 subintervals.

Both the particle and the positron counters are azimuth angle sensitive and are mounted symmetrically around the beam axis which is also the symmetry axis of the toroidal magnetic field for the e^+-momentum analysis.

If the positron line is emitted from the transiently formed quasi-atom, moving toward the beam/symmetry axis with the c.m. velocity ($\beta_{cm} = 0.056$), the measured yield in the laboratory should be independent on the positron emission angle relative to the particle scattering plane which, at fixed polar detection angles for the particles and for the positrons, is defined by the corresponding azimuth detection angles. Furthermore, if the observed width of 80 keV[1] is defined only by the life time of the positron emitting source, the yield distribution along the focal plane should remain also unchanged and independent on the azimuth angle.

A different picture is expected to occur, if the line is of nuclear origin with the corresponding long life time and much narrower intrinsic width. Since in this case the positron source, i.e. the scattered particle, moves with a velocity defined by the polar and azimuthal angles, the positron line could be focussed within the narrow momentum range, defined by **one single** pagoda "roof", only if the e^+-azimuth angle matches the kinematic conditions given by the Lorentz transformation from the c.m. to the Lab. system (n.b. ß-rays are "always" relativistic). This leads to a pronounced anisotropy as a function of the e^+-azimuth angle and to a strong difference in the yield of one pagoda sub-unit ("roof") to the yields of the other sub-units.

It can be easily seen in this context that the yields from the dynamically induced pair creation remain also independent on the azimuth angle, whereas the continuous background from the pair creation due to nuclear excitations is transformed from the c.m. to the Lab. system according to :

$$(d^2\sigma/dE_e d\Omega_e)/(d^2\sigma'/dE'_e d\Omega'_e) = p'_e/p_e$$

with p_e - the positron momentum.

In the first run the experimental arrangement was tested with δ-rays. Fig. 1 displays the relative δ-ray yields as a function of the δ-ray azimuth angle for a selected (polar) particle scattering angle between 35° and 55° in the laboratory. No significant deviation from an isotropic distribution (thick horizontal line) can be observed, corroborating thus the assumption for the δ-emission from the quasi atom.

The rather modest statistics for the positron measurement does not allow far reaching conclusions yet. Fig. 2 shows some preliminary results for 267 keV e^+-kinetic energy. Further experiments are in progress.

[1] GSI-preprint 84-8, January 1984

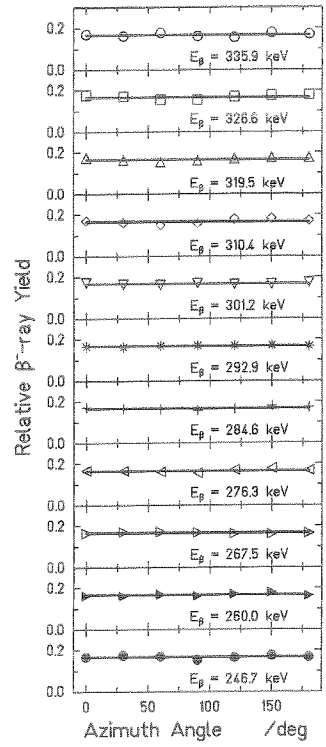


Fig. 1: Relative δ-ray yields normalized to the total yield as a function of the relative angle to the scattering plane for eleven kinetic energies as shown. The thick horizontal line indicated gives the average of 1/6 expected for isotropic emission.

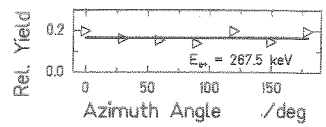


Fig. 2: The relative positron yields at 267 keV (Lab.) as a function of the relative angle to the scattering plane.

On the Origin of the Structure in Positron Spectra from U + Cm Collisions[B]

H. Bokemeyer, H. Folger, H. Grein, Y. Kido (GSI Darmstadt)
T. Cowan, J.S. Greenberg, J. Schweppe (Yale Univ.)
K. Bethge, A. Gruppe, K.E. Stiebing (Univ. Frankfurt)
D. Schwalm (Univ. Heidelberg), P. Vincent (Rutgers Univ.), R. Fonte (Univ. Catania)
H. Backe, M. Begemann, M. Klüver, N. Trautmann (Univ. Mainz)

Following the first observation of a well defined narrow peak structure at 316±10 keV (FWHM ≈ 75 keV) in e^+ spectra from U+Cm collisions[1], additional measurements are being pursued to elucidate the kinematic conditions associated with the emergence of the structure above the dynamic atomic and nuclear backgrounds, and to explore atomic and nuclear alternative sources. Significant improvements in the capabilities of the apparatus particularly include doubling the broad-band e^+-detection efficiency and extending the low energy cut-off to <100 keV, as well as improving the ion angular resolution to <0.8°. Target composition and deterioration in the beam remain important considerations in these measurements.

The question of peak origin is being addressed with two experimental approaches: In one of these, a search is being conducted for γ-rays and internal conversion electrons which should accompany nuclear transitions producing positrons. The second approach exploits the measured width and shape of the e^+ peak together with the influence of the Doppler effect on the peak shape to provide information on its source and eventually on the intrinsic (natural) line width. Figure 1 demonstrates that translating the e^+ peak intensity to γ-ray and e^-emission through well known branching ratios leads to γ-ray (for E1 and higher multipoles) and e^- spectra (for EO transitions) which greatly exceed the intensity of the simultaneously measured spectra. The nuclear sources are, thereby, ruled out for reasonable K-shell occupation. Only for the very improbable conditions that there be nearly two K-shell vacancies which live for $>10^5$ times the neutral atom K-vacancy lifetime is there a possibility of reproducing the structureless measured γ-ray and e^- spectra. The line-shape analysis of the peak observed in the narrow band of projectile energies between 6.0 and 6.2 MeV/u (equivalent to the target thickness) at ~ 45° scattering, combined with previous observations at laboratory angles of 28°<θ<40° and 50°<θ<62°, indicates (Fig. 2) that the line width appears to be independent of scattering angle and compatible with center of mass emission. All these observations seem to contradict assigning the peak to nuclear decays in the separate nuclei.

1. J. Schweppe et al., Phys.Rev.Lett,51(1983)2261

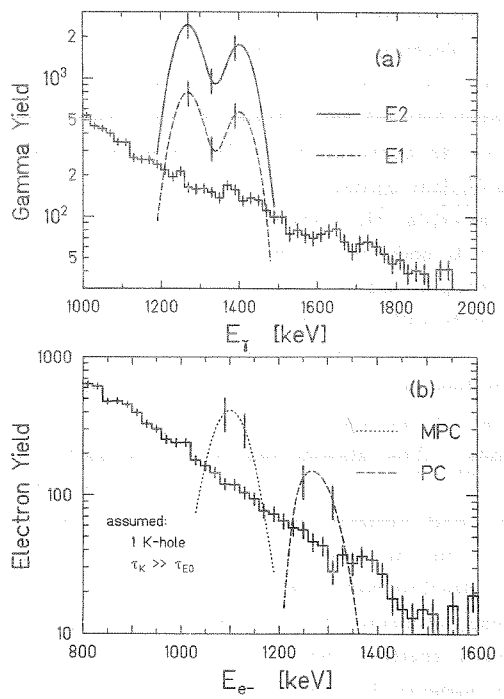


Fig. 1: Measured γ- and e^--spectra compared (a) with γ-ray lines expected from the e^+-intensity assuming E1 or E2 transitions in the U or Cm nucleus and (b) with internal conversion lines expected from normal (PC) or monoenergetic (MPC) internal pair conversion.

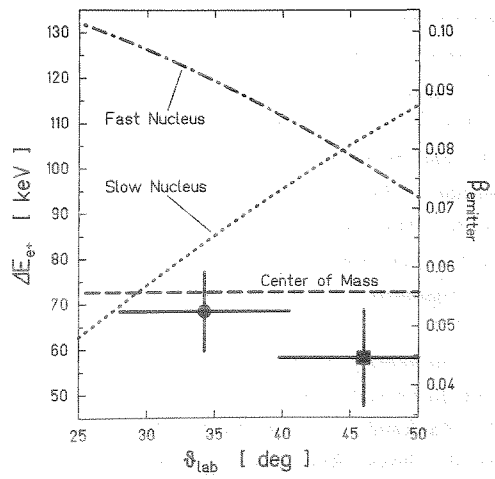


Fig. 2: Observed line-widths as function of ion scattering angle. The experimental width depends linearly on emitter velocity (right scale). The curves show the dependence of the velocity or width on scattering angle for different assumptions of emission as indicated. The measured widths favor CM-emission.

Positron Production in Elastic and Dissipative Heavy Ion Reactions

E. Bozek*, U. Gollerthan, E. Kankeleit, G. Klotz, M. Krämer
R. Krieg, U. Meyer, H. Oeschler, P. Senger
Institut für Kernphysik der TH Darmstadt

In recent positron experiments with the TORI Spectrometer[1] at X8 we extended the study of nuclear contact times in dissipative U + U reactions from 5.9 up to 10.0 MeV/u beam energy. The spectral distributions of the δ-electrons and positrons emitted in very heavy ion encounters reflect the Fourier frequencies of the time evolution of the collision process and hence are sensitive to perturbations of the Coulomb trajectories due to nuclear contact[2].

As an example, fig.1 shows atomic positron spectra for the U + U collision system at 8.4 MeV/u, measured in coincidence to elastic scattering and to sequential fission events indicating dissipative reactions. The spectra are corrected for positrons of nuclear origin, a contribution which is estimated by investigating positron- and γ-ray spectra emitted in U + Tm and U + Pd collisions. The steeper high-energetic decline in the latter spectrum results from phase-shift effects between ingoing and outgoing positron production amplitudes. This is due to a contact time which varies between T = 0 (grazing collisions) and T = $1.5*10^{-21}$s (central collisions) according to a quantitative analysis[3].

Elastically scattered heavy ions are separated from fission fragments by their angular correlation measured by a pair of position sensitive gas counters. This is demonstrated in fig.2a, showing a 2-dimensional plot of the polar angles of the reaction products for the U + U reaction at 8.4 MeV/u.

Fluctuations in the δ-electron and positron spectra are predicted for narrow time-delay distributions[4]. Related to this question subgroups in impact parameter or Q value can be selected by separating the fission reactions into 3- and 4-body events. This is achieved by reading out both ends of the delay-line chain of the particle counters in combination with the energy-loss information. Fig.2b shows the subclass of 4-body events for the reaction U + U at 8.4 MeV/u, plotted versus the averaged measured scattering angles of two fission fragments.

1. E. Kankeleit et al., GSI Scientific Report 1981; and to be published in Nucl. Instr. and Meth.
2. E. Kankeleit, Nukleonika 25,253(1980); H. Backe et al., Phys. Rev. Lett. 50,1830 (1983).
3. U. Müller et al.,Z. Phys. A313,263(1983) and private communication.
4. G. Soff et al.,Phys. Rev. Lett. 43,181(1979).

*) Inst. of Nucl. Phys., Cracow/Poland

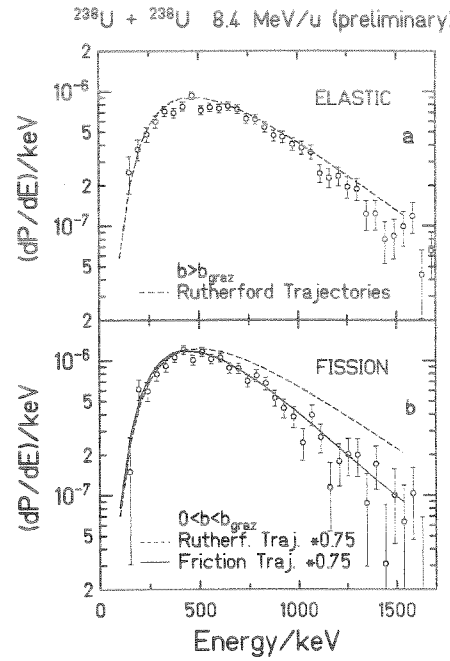


Fig.1: Positron spectra from U + U collisions at 8.4 MeV/u in coincicence to elastic and quasielastic scattering (a) and to fission reactions (b).

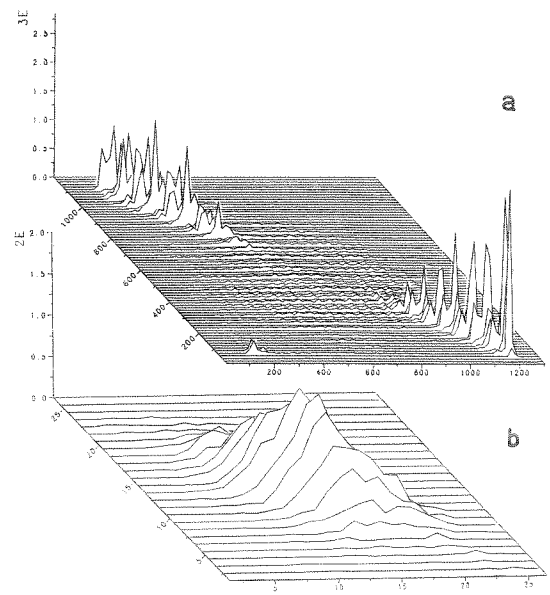


Fig.2: U + U 8.4 MeV/u:
a) Angular correlation between the emitted fragments exhibiting the two classes: elastic scattering and deep-inelastic collisions observed by their fission decay.
b) Subclass of 4-body events shown as a function of the two averaged measured scattering angles of the two pairs of fission fragments.

High Energy δ-Rays from Pb-Pb and Pb-Cm Collisions [G]

P. Armbruster, F. Bosch, C. Kozhuharov,
GSI Darmstadt
E. Berdermann, P. Kienle, H. Tsertos, W. Wagner
TU München
J.B. Wilhelmy
Los Alamos, USA

The (^{208}Pb+^{208}Pb)-collision system gives for bombarding energies below the Coulomb barrier the unique opportunity to study high energy δ-ray spectra from very heavy quasi-atoms without any distortions due to nuclear de-excitation processes.

For this reason it was chosen in our first attempt to establish a new experimental method for determination of the emitting source. The experimental arrangement, consisting of the "orange"-β-spectrometer, an annular parallel plate avalanche counter for particle - and plastic scintillator counters for electron-detection is symmetrical around the beam axis.

The particle detector is both polar (θ) and azimuth (φ) angle sensitive, whereas the electron counter is azimuth angle sensitive only, with a polar angle definition given by the entrance slits. Thus, if the δ-electrons are emitted from the quasi-atom which moves toward the beam/symmetry axis with the c.m. velocity, the δ-ray spectra are expected to be isotropic with respect to the azimuth angle.

Figure 1 shows as illustrative example δ-ray spectra for two different electron and particle azimuth angles (curves a and b) in the kinetic energy region between 500 keV and 1 MeV. Since both spectra overlap completely within the statistical errors, curve b has been shifted along the ordinate. These results clearly demonstrate that δ-rays are indeed emitted from the combined system and not from the separated nuclei. For the latter case a pronounced dependence of the yields on the azimuthal angle should occur. Curve c in Fig. 1 shows the same spectrum for the (^{208}Pb+^{207}Pb)-collision system which is also shifted along the y-axis and also overlaps with the curves for the ^{208}Pb-target. Since no significant contributions from internal conversion lines are expected in this kinetic energy region, this experimental finding corroborates the expectations for δ-ray production from the quasi-atom with $Z_u = Z_p+Z_t$ due to the time-changing Coulomb-field.

In our next measurement we studied δ-rays from the heaviest available asymmetric collision system Pb+Cm, where δ-rays associated with the characteristic X-rays of the heavier collision partner allow to separate to some extent the contributions from the 1sσ-quasi-atomic shell. The definition of the particle- and X-ray angles was sufficiently good in order to resolve the Pb and Cm K-X rays using NaI scintillation counters. Figure 2 shows as first preliminary results two spectra for a selected range of particle scattering angles as indicated both for δ-ray-projectile-recoil-coincidences as well as for an additional coincidence with the Cm-K-X rays. Further analysis of the data is in progress.

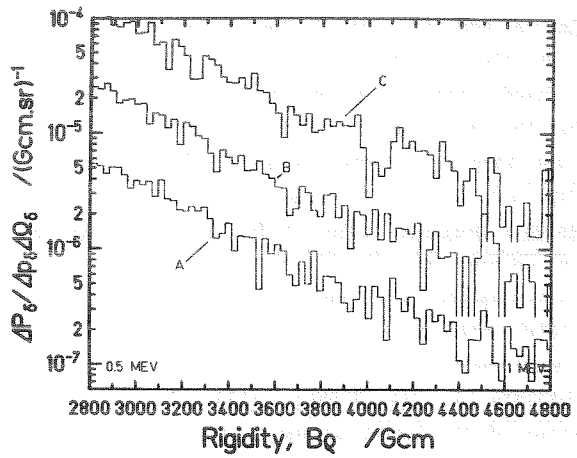


Fig. 1: δ-ray emission probabilities for the collision systems ^{208}Pb+^{208}Pb (curves A+B) and for ^{208}Pb+^{207}Pb (curve c). The emission angle relative to the scattering plane is 60° for the spectra A and C, and 0° for curve B. The spectra B and C are shifted toward the ordinate.

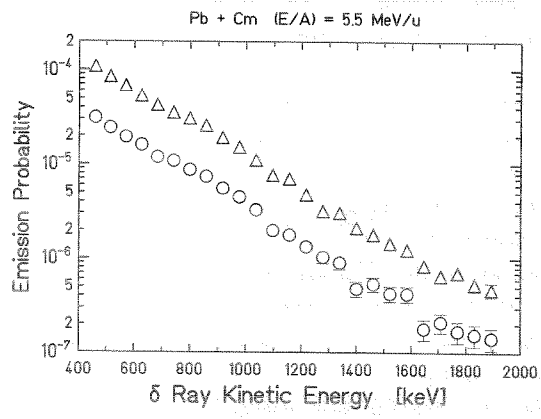


Fig. 2: δ-ray emission probability (in the kinetic energy range from 450 keV and 2 MeV for (Pb+Cm)-collisions. The upper spectrum is associated with particles scattering between 20° and 50°. An additional Cm-K-X-ray coincidence is required for the lower spectrum.

Strong Differences between K-Shell Excitation Probabilities in Solid and Gas Targets for Very Heavy Collision Systems

B. Liu*, D. Liesen, and A. Warczak**
GSI Darmstadt
*Permanent Address: Institute of Modern Physics, Lanzhou, CHINA
**Permanent Address: Jagellonian University, Cracow, POLAND

Strong experimental evidence is available that in very heavy ion-atom collisions the K-shell excitation probability of the lighter collision partner (mostly the $2p_{1/2\sigma}$ excitation) depends non-monotonously on the projectile velocity and that it drops much more slowly with impact parameter than expected[1]. In order to study the second point in more detial, the influence of the state of the target on the K- and L-shell excitation was investigated. For this purpose, a gas target has been installed in the Stripperhalle to look for possible differences between solid and gas targets at a fixed projectile energy in collision systems with almost the same value of the total charge Z_1+Z_2.

The gas target is formed by gas-flow through a thin needle and a big turbopump in order to get a reasonable pressure ratio ($\sim$100) between target and target chamber. With the aid of a fourfold slit-system the slit-scattering was kept to be smaller than 7 % of the total intensity for all scattering angles.

The experimental results for the K shell excitation probability of the lighter collision partner as function of the impact parameter are shown in Fig. 1 for Pb+Xe and U+Sn collisions which is in both cases the $2p_{1/2\sigma}$ excitation. Three remarkable differences between the two sets of data are to be noticed: 1) The absolute value of the excitation probability is in the solid target (40 $\mu g/cm^2$) more than a factor of 10 larger than in the gaseous target. 2) For $b < 200$ fm the excitation probability flattens out in the gas target data, whereas in the solid target data P(b) steadily increases with decreasing b. 3) For $b \geq 200$ fm the excitation probability falls off in the gas target much steeper than in the solid target.

Especially the last point gives a hint to a rough understanding of some of the above mentioned peculiar features of the $2p_{1/2\sigma}$ excitation probability. The solid target data are rather well described by an exponential of the form exp(-b/a) with a = 128 fm for all b, while such an expression fits the gas target data only for $b \geq 200$ fm with the much smaller fall-off constant a = 50 fm. Using the well known Bang-Hansteen Scaling Rule energy transfers of 42 keV and 95 keV, respectively, are calculated from these fall-off constants. These values suggest that the excitation of the $2p_{1/2\sigma}$ orbital in solid targets is dominated by a transition of the $2p_{1/2}$ electron into united atom states with n = 3 which have vacancies with probabilities of 10^{-1} in solid targets. In contrast, in gaseous targets those empty states are not available and the $2p_{1/2\sigma}$ electron has to experience a much higher energy transfer ($\sim$ 95 keV) for an excitation which results in a steeper fall-off constant a. Consequently, for spectroscopic studies of the $2p_{1/2\sigma}$ excitation even in very heavy systems it is indispensable to perform gas target experiments.

[1] D. Liesen, GSI-Report, GSI-83-5

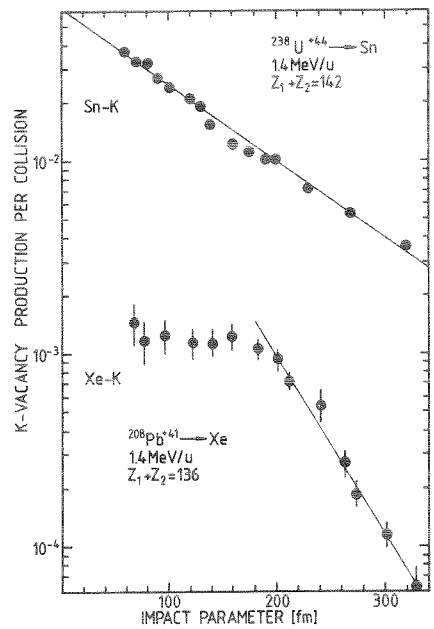


Fig. 1: K-shell excitation probability in the lighter of both collision partners for a solid and a gas target vs. impact parameter.

Structures in the Sn-K and Ag-K Vacancy Production at 1.4 MeV/u Projectile Energy

A. Warczak*, D. Liesen, B. Liu**
GSI Darmstadt
*Permanent Address: Jagollonian University, Crakow, POLAND
**Permanent Address: Institute of Modern Physics, Lanzhou, CHINA

In the previous Scientific Report[1] we showed the first experimental observations of structures in the inner-shell vacancy production probability P(b) as a function of the impact parameter b. As those structures turned out to depend on the target thickness, we studied in a series of experiments in the Stripperhalle the dependence in more detail using 50 and 7 $\mu g/cm^2$ Sn targets and a 60 $\mu g/m^2$ Ag target. These targets were bombarded with U^{+44} and with Pb^{+q} ions, where q had the values 30, 36, 38, and 41. Because the first data showed that the oscillations in P(b) appear predominantly at small impact parameters ($b \lesssim 150$ fm), kinematic coincidences between scattered projectiles and recoil target atoms have been registered in order to establish an unambiguous relation with scattering angle and impact parameter also at small b.

The results for the target K vacancy production probability are plotted in Figs. 1 and 2: Fig. 1 gives the influence of the target thickness, while Fig. 2 shows the dependence on the projectile charge state. In the present impact parameter region the Sn-K vacancy production is hardly dependent on the target thickness whereas at larger b(> 200 fm) the Sn-K excitation in the thick exceeds that in the thin target about a factor of 1.5. Superimposed on the general trend of P(b) which can be reproduced by a superposition of a direct excitation and a rotational coupling (solid line in Fig. 1) are weak oscillations which show up much clearer in the Ag-K vacancy production (Fig. 2).

While the positions of the maxima depend only very weakly on q, their relative intensities vary strongly but not monotonously with the charge state: The Ag-K vacancy production is largest for q = 36, while for q = 41 it almost equals that of q = 30. We note that in this case no satisfactory agreement between experiment and direct excitation plus rotational coupling model can be achieved, because this model does not reproduce the regular structures in the data and that the origin of the oscillations is not obvious.

[1] GSI Scientific Report 1982, GSI 83-1, pp. 149 and 150

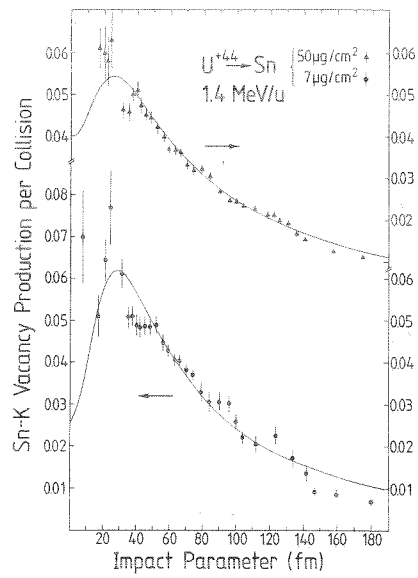


Fig. 1: Sn-K vacancy production vs. impact parameter b; solid lines give the shape of P(b) acc. to a direct excitation plus a rotational coupling model.

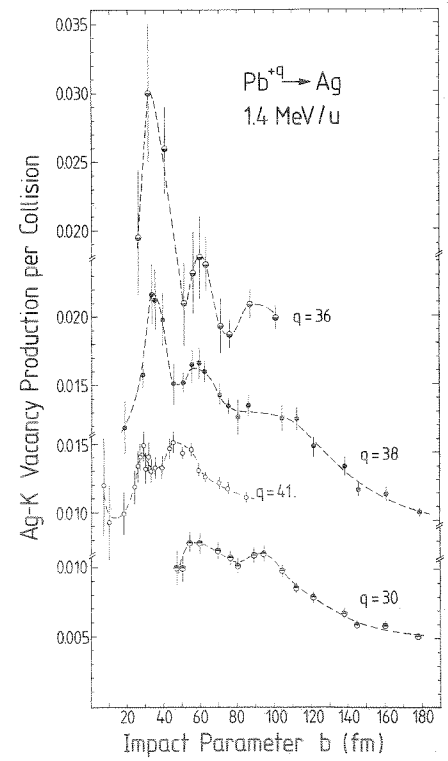


Fig. 2: Ag-K vacancy production vs. impact parameter for different charge states q.

Quasimolecular L → K and M → K Vacancy Transfer in 3.6 MeV/u Sm^{q+} — Xe Collisions

P.H. Mokler, D.H.H. Hoffmann, W.A. Schönfeldt, and A. Warczak*

GSI Darmstadt

*Permanent Address: Instytut Fizyki, Universytet Jagiellónski, Kraków, Poland

Using the acceleration - stripping - deceleration method (A-S-D) highly-charged heavy ions can be produced and the quasimolecular vacancy transfer in inner shells can be studied effectively even in extremely heavy collision systems. First investigations showed that in the symmetric Xe^{q+}-Xe collision system (Z_1+Z_2 = 108) - for which in the u.a.-L shell the spin-orbit splitting amounts to 1/3 of the u.a.-L shell binding energy - the rotational L → K vacancy transfer seems to be dominant for high incoming charges[1,2]. The goal of this investigation was to study the quasimolecular inner shell vacancy transfer in even heavier but slightly asymmetric collisions.

Using the A-S-D method 3.6 MeV/u (and 4.7 MeV/u) Sm^{+q} ions with charge states q ranging from 38 up to 54 - i.e. O-like Sm-ions - have been produced and the K excitation of Xe target atoms has been investigated under single collision conditions. In Fig. 1 the Xe-K excitation cross sections are given as a function of the incoming charge state. Two inflection points are seen, one at Ne-like projectiles and another one at Ar-like projectiles.

The strong cross section increase beyond Ne-like ions is attributed to the rotational L → K vacancy transfer - in classical notation $2p_\pi$-$2p_\sigma$ coupling. The cross section increase $\Delta\sigma_{L \to K}/\Delta q$ = 2.3±0.3 kb (at 3.6 MeV/u) can be compared to the scaled non-relativistic TBV-value[3] of 5.7 kb using a pure statistical factor of 1/6. Relativistic calculations will decrease this value only slightly[4] - despite the large u.a.-L shell spin-orbit splitting, see the Sm - Xe correlation diagram in Fig. 2.

The slight cross section increase between Ar- and Ne-like projectiles is caused by M → K vacancy transfer; more precisely by incoming 3s, 3p1/2, and 3p3/2 vacancies. The cross section increase $\Delta\sigma_{M \to K}/\Delta q$ = 0.12 ± 0.03 kb (3.6 MeV/u) may be explained by a two step process including a radial and a rotational coupling; a one step rotational coupling may also be possible. Impact parameter measurements for Xe^{+q}-Xe collisions[2] indicate that a rotational coupling for this charge state region may also be active. Surprisingly, below Ar-like projectiles the excitation is independent on charge state. In how far the spatial distribution of the incoming 3d electron leads always to an ionization at larger internuclear distances or whether the vacancy transfer mechanism selects between incoming 3p and 3d electrons is unclear.

Fig. 1

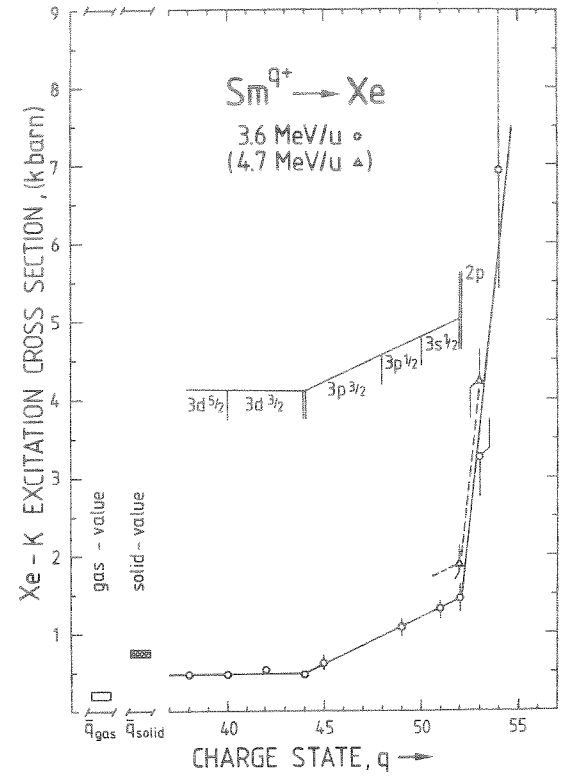
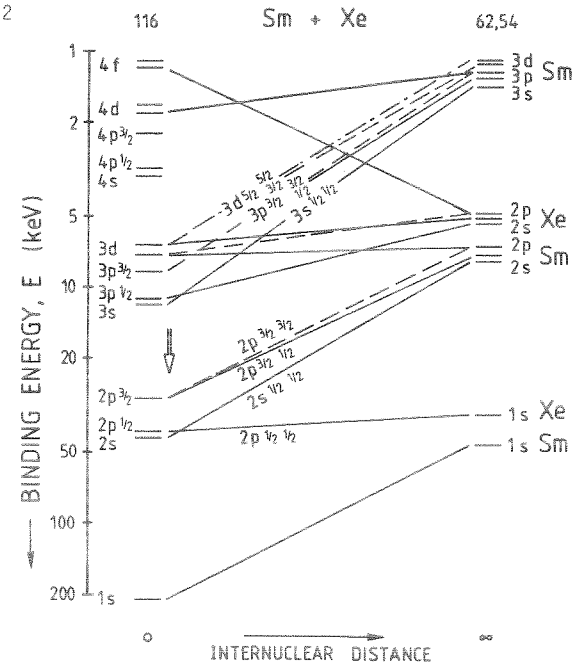


Fig. 2



[1] P.H. Mokler et al., NIM (1984) accepted

[2] R. Schuch et al., J. Phys. B16 (1983) 2029

[3] K. Taulbjerg et al., J. Phys. B19 (1976) 1351

[4] D. Jakubassa et al., J. Phys. B13 (1980) 757

Interferences in Quasimolecular X-Rays from 2,7 MeV/u Ge^{31+} - Kr Collisions

B

R. Schuch, A. Oppenländer, J. Konrad, M. Schulz
Physikalisches Institut der Universität, 6900 Heidelberg
P.H. Mokler
GSI Darmstadt
W. Schadt, H. Schmidt-Böcking
Institut für Kernphysik der Universität, 6000 Frankfurt

In near symmetric collisions of hydrogenlike projectiles an interference structure in the spectra of quasimolecular x-rays (MO) has been found already in light collision systems (Cl-Ar)[1,2]. In order to observe such an interference structure the following conditions have to be fulfilled. The hydrogenlike projectile ions should have low velocities compared to the relevant mean electron orbiting velocities. The target has to be a well localized gas target to ensure single collisions even for K-electron capture and to define the trajectory by a coincidence with scattered particles. It could be shown[2], that spectroscopic information about the 1sσ-2pπ transition-energy as function of the internuclear distance could be obtained from the structure in the MO x-ray spectra. These investigations were therefore extended to heavier collision systems, where the Ge^{31+}-Kr system was selected.

A Ge-beam was proststripped at 8.6 MeV/u after Alvarez III of the Unilac and then decelerated to 2.7 MeV/u with the single resonators. The charge state 31+ of the beam could be selected with the beam transport magnets. Fig.1 shows a schematic view of the set-up with the multiple differential pumped Kr-gas target (P_1,P_2,P_3,P_4 are pumping stages). The pressure in the gas cell was selected by a pressure dependence of the radiative electron capture yield. With two Ge(I) detectors covered by Al and Cu-absorbers the quasimolecular x-rays at 90° relativ to the beam direction were detected in coincidence with particle signals from a parallel-plate avalanche detector.

In Fig.2 a true coincident x-ray spectrum for the impact parameter region of 490-600 fm is shown. The spectrum is also corrected for the atten uation of the Al and Cu absorber. This correction factor is 2 at 20 keV and decreases rapidly to one with increasing energy. At about 22 keV a minimum in the x-ray spectrum is observed. The full line represents a calculation of the spectral shape by solving the Fourier-integral according to ref.3. The quasimolecular binding energies used in this calculation were adjusted at asymptotic neutral atom values. The agreement in the region of the maximum is reasonable, the minimum in the experimental spectrum is filled up. By fitting the solutions of the Fourier integrals to the spectra at different impact parameters quasimolecular transition energies can be obtained.

References
1. I. Tserruya et al., P.R.L. 50, 30, 1983
2. R. Schuch et al., to be published
3. B. Müller, Phys. of El. and At. Collisions, 481, Seattle 1975

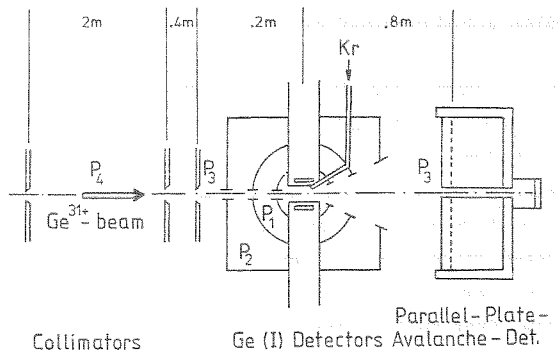


Fig.1 Schematic view of the experimental set-up

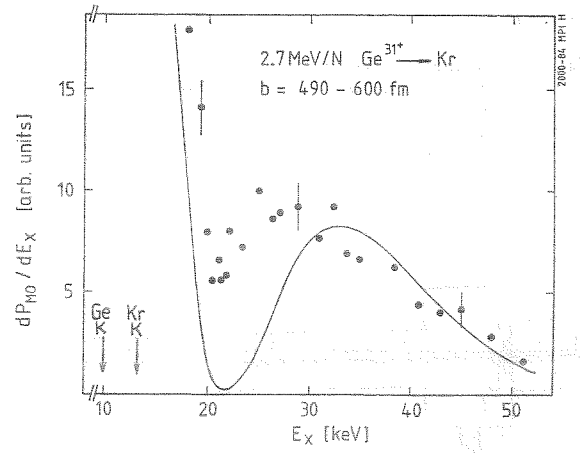


Fig.2 Quasimolecular x ray spectrum for impact parameters 490 - 600 fm

Heavy Ion Beam Pumped Gas Lasers [B]

A. Ulrich, P. Kienle
Technische Universität München
D.E. Murnick*, D.H.H. Hoffmann, H.F. Beyer
GSI Darmstadt

First experiments to pump gas lasers from infrared to x-ray wavelengths with a 1.9 GeV ^{132}Xe beam from the UNILAC accelerator were carried out. Laser action at 1.73, 2.06, and 2.63 µm from Xe and some promising spectroscopic results at the shorter wavelengths were found.

Like multiphoton excitation with a short, high power pump-laser pulse, pumping with ion beams is one of the techniques proposed to achieve the high power densities necessary for UV, VUV, and x-ray lasers[1]. Pumping of (IR-) lasers with beams of atomic numbers Z > 1 (3.5 MeV ^{4}He, 80 MeV ^{16}O, 100 MeV ^{32}S) has recently been demonstrated at the Munich tandem- and Stuttgart Dynamitron accelerators and the same setup shown in Fig. 1 was used here. In addition, optical spectra were taken from the light emitted along the beam axis using a grating monochromator.

Since pulsed lasers need a high pumping power but only for a short time (e.g. nsec) the beam current was maximized but the duty cycle reduced to (1 % - 3 %) to avoid damage to the entrance foil.

Laser action was found in a 240 mbar Ar (99 %) - Xe (1 %) mixture using an optical resonator with two gold coated mirrors of 4m radius of curvature. First, the laser operated at the 2.63 µm line in Xe which is known from nuclear reactor pumped laser[3] and switched to the strong 1.73 µm line after a realignment of the resonator. Due to the µsec lifetime of the IR laser levels the output power shown in Fig. 2 followed the macrostructure of the UNILAC. With a power meter measuring the non-optimized output reflected off the Brewster angle window an average value of 0.35 mW was measured.

Fig. 1: Schematic sketch of the setup with the beam excited volume B, the 1 mg/cm² Ti-entrance foil F, the laser mirrors L, the Brewster window of the cell W, a monochromator M, the detectors D, and a mechanical shutter S to proof laser action.

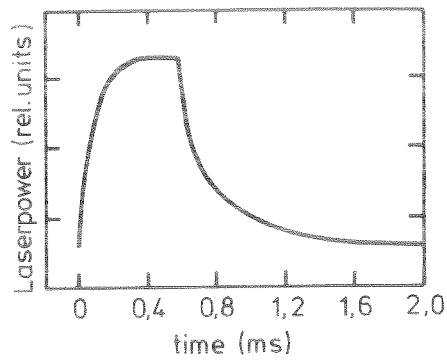


Fig. 2: Output power of the beam pumped laser.

An attempt was made to obtain lasing in the argon ion system using pure argon gas. No visible laser was obtained, the discharge observed on the color TV appeared quite weak and a monochromator scan of the visible fluorescence showed only weak lines. A monochromator scan of the near UV, however, showed several intense lines of the region of laser transitions reported for Ar^{2+} and Ar^{3+}. The intensity of some of the lines were non-linear in pressure indicating good candidates for laser systems. Similarly a UV spectrum of nitrogen gas indicated several potential laser transitions.

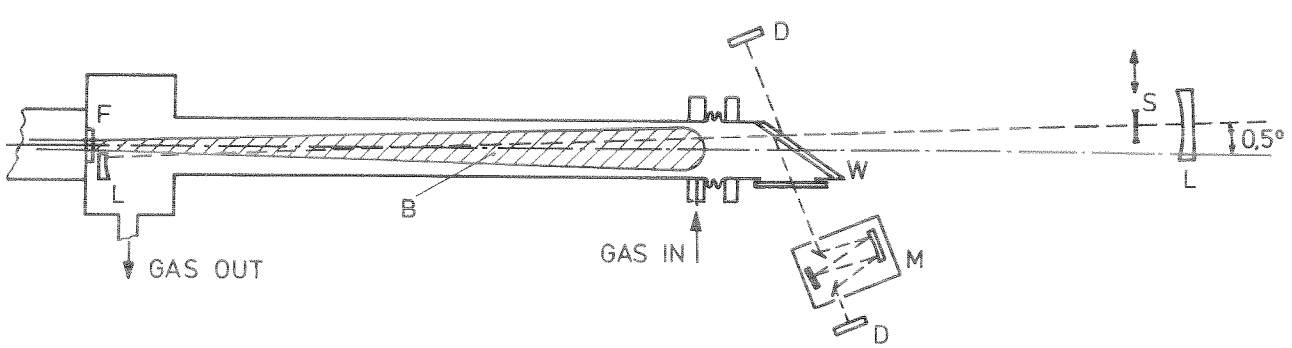
Finally, an attempt was made to survey the soft x-ray spectrum in the forward direction using a shielded Si(Li) x-ray spectrometer 1 m from the target. The count rates during the beam pulse, however, exceeded the capabilities of the detector system.

[1] "Review of Short Wavelength Lasers", R. Wayant and R. Elton, IEEE Proc. 64, 1059 (1976)

[2] A. Ulrich, H. Bohn, P. Kienle, and G.J. Perlow, Appl. Phys. Lett. 42, 782 (1983)

[3] R.J. De Young, Appl. Phys. Lett. 38 297 (1981)

*Humboldt Awardee; Permanent Address: AT&T Bell Laboratories, Holmdale, N.J.



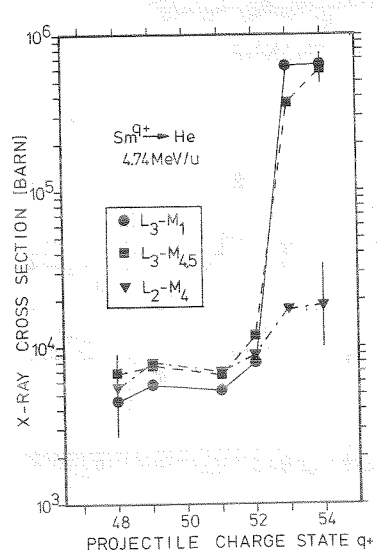
Anomalous L X-Ray Transitions of Highly Ionized, Fast Projectiles

W.A. Schönfeldt, D.H.H. Hoffmann, P.H. Mokler, A. Warczak*
GSI Darmstadt
*Permanent Address: Jagellonian University, Cracow, POLAND

A surprising result in Xe^{q+} + Xe collisions at 3.6 MeV/u[1] was the measured Xe-L_ℓ/L_α x-ray emission ratio which changed dramatically as function of the initial charge state q^+ = 44, 45, 46, 47 of the projectile. To understand this effect, we investigated between 3.6 and 4.7 MeV/u the projectile L x-ray emission in asymmetric Sm^{q+} + Xe, Ar, He collisions at closed (q^+ = 48-52) and open (q^+ = 53,54) projectile L-shell (Fig. 1). In asymmetric collisions the projectile- and target-x-rays as well as the projectile L_ℓ and L_α-transitions are separated. The agreement in L_ℓ/L_α ratios of all the measured systems (Fig. 2) show a clear q_L^i-dependent trend (q_L^i is the number of incoming L-vacancies) and point to a common process. We found that the measured ratios L_ℓ/L_α (q_L) $\tilde{=}$ 0.7 - 2.0 can be explained by a partial metastability of the M-subshells in such highly ionized projectiles. For instance a projectile with one L_3 vacancy and a captured electron in the M_5-shell can have total angular momenta of J_i = 1, 2, 3, 4; however the x ray decay (M_5-L_3) has to result in an angular momentum J_f = 0 (closed L-shell), see Fig. 3.

The selection rules of electric dipole transitions (ΔJ = 0, 1) force inner M-shell transitions (Δn = 0) for M_5 -electrons with J_i = 2, 3, 4, which ends up in an increased M_1-subshell population, and therefore in an increased M_1-L_3/M_5-L_3 x-ray ratio. Using calculated transition rates for the (Δn = 0)-decay[2] and if we assume for instance a statistical J_i-population of all the possible 3d levels, we yield ratios of L_ℓ/L_α = 2.1/0.81/0.3 for q_L^i = 1/2/3, see dash-dotted line in Fig. 2.

Fig. 1



To get a better agreement with the experiment the electron population in the projectile M-shell after capture and cascading processes has to be investigated.

[1] P.H. Mokler et al., GSI Annual Report 1982

[2] B.P. Das, priv. comm. and I.P. Grant et al., to be published

Fig. 2

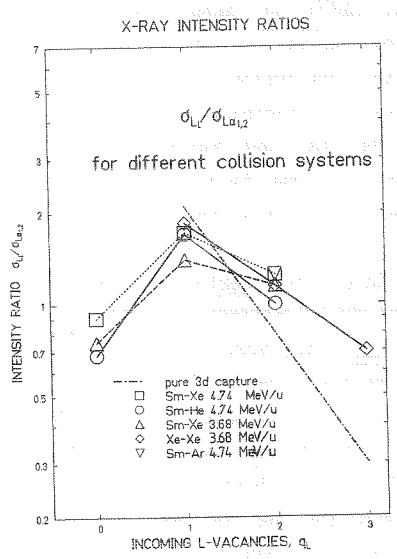
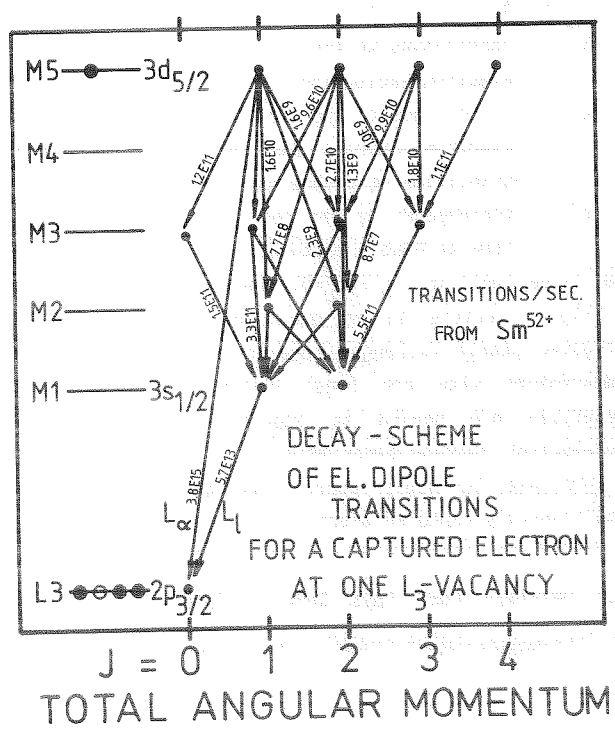


Fig. 3



X-Ray Emission after Multielectron Capture into Highly Charged Sm^{q+}-Projectiles

W.A. Schönfeldt, D.H.H. Hoffmann, P.H. Mokler, A. Warczak*
GSI Darmstadt
*Permanent Address: Jagellonian University, Cracow, POLAND

The cross sections and energy positions of x-rays from highly charged projectiles may strongly depend on the incoming charge state as well as on the number of captured electrons in a single collision. Fig. 1 shows calculated charge state dependent energy positions of $L_\ell(M_1\text{-}L_3)$ and $L_{\alpha 1}(M_5\text{-}L_3)$ x-ray transitions assuming the ground state configuration of Sm^{q+} (q^+ = 48-54). The calculations were performed with the relativistic Dirac-Fock-Program of Desclaux[1] and demonstrate a x-ray energy shift of about 138 eV per L-shell vacancy. This shift is about the same as the Si(Li)-detector resolution (190 eV at 5.9 keV x-ray energy). Hence, for instance it should be possible to distinguish the one- and two-electron capture of a single collision at two incoming L-vacancies (q = 54) by x-ray emission. This case we consider in the following.

The measured Sm-L x-ray spectra were Gauss-fitted with the calculated energy positions and the detector FWHM; the $L_{\alpha 1}$ and $L_{\alpha 2}$-lines were arbitrarily set to be of the same intensity (Fig. 2). The lower end of the energy position bars in Fig. 2 give the resultant amplitudes of the fit for the various charge states. The fluctuations at the bottom indicate the difference between fit-function and the measured spectrum. The resultant x-ray cross sections $\sigma_X(q_L^f)$ depend on the remaining Sm L spectator vacancies q_L^f and are shown in Fig. 3 for Sm^{54+} → Xe, Ar.

- σ_X (q_L^f=2) corresponds to the x-ray emission at single electron excitation
- σ_X (q_L^f=1) corresponds to the x-ray emission at single electron capture and the first electron transition at double capture
- σ_X (q_L^f=0) corresponds to the second electron transition at double capture.

The large part of σ_X (q_L^f=0) indicate that double (multiple) capture is of great importance in high energetic charge exchange processes, but coincidence measurements with the final charge state of the projectile are needed to separate the one- and two-electron capture parts at q_L^f = 1. Then it should be possible to study correlation effects of two simultaneously captured electrons.

[1] J.P. Desclaux, Comp. Phys. Comm. 9 (1975) 31

Fig. 1

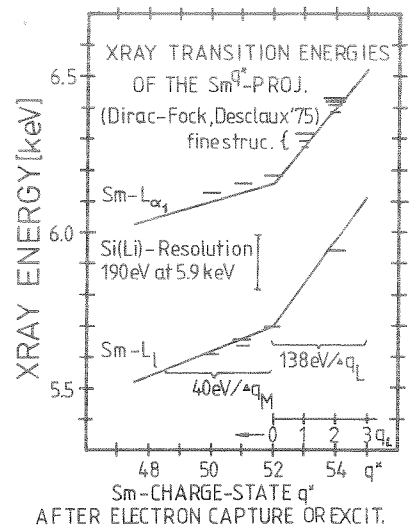


Fig. 2

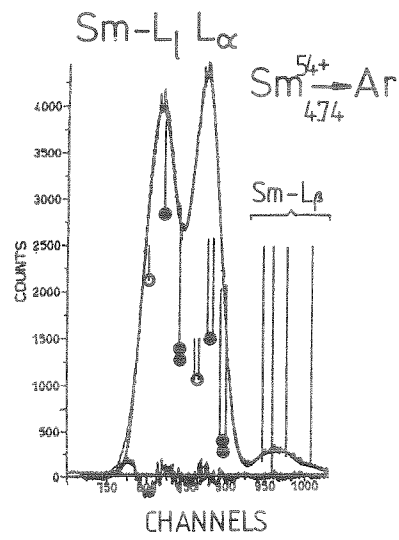
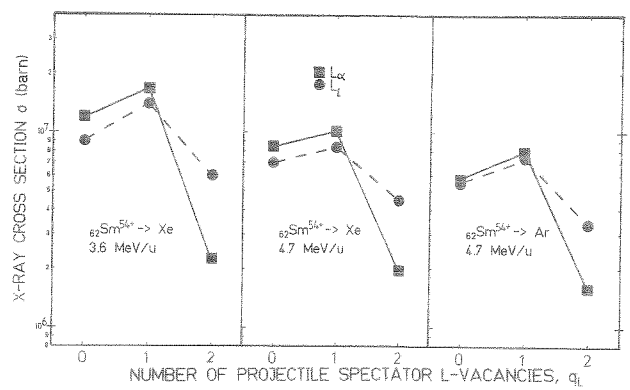


Fig. 3



A New Method for a Precision Measurement of the 1s-Binding Energy in Few Electron High Z-Atoms

W. Koenig, B. Martin, J. Soltani
MPI Heidelberg
F. Bosch, C. Kozhuharov, R. Mann
GSI Darmstadt

With 18 MeV/u $^{155}_{64}$Gd-ions provided by the UNILAC a new method for a precise determination of the K-shell binding energy in He- and H-like high Z-ions was tested experimentally.

This method is based on a measurement of K-conversion electrons emitted from a fast moving Coulomb-excited heavy nucleus ($\beta_N \gtrsim 0.2$) of a few electron ion, where the kinetic energy T_e of the conversion electrons is very small in the rest frame of the nucleus (a few hundred eV or even smaller), i.e. where the γ-transition energy ΔE_γ nearly matches with the K-shell binding energy E_K. Due to the relativistic transformation of the reference frame, however, those low energy electrons have an energy of several keV in the lab.-system, depending on their emission angle. Hence - supposed ΔE_γ and β_N are known precisely - the relative accuracy $\Delta E_K/E_K$ of K-binding energy determination is improved by a factor ε with respect to the kinetic energy determination $\Delta T_e/T_e$ of the electron, where ε is the ratio $\tilde{T}_e/E_K$ in the **rest frame** of the nucleus. For ε in the order of 10^{-2}, a relative accuracy for the electron energy in the lab.-system in the order of 10^{-3} (obtainable by standard techniques) corresponds therefore to an accuracy $\Delta E_K/E_K \gtrsim 10^{-5}$. Therewith, it should become possible to determine the QED-effects (selfenergy, vacuum polarization) for the 1s binding energy in high Z-atoms with few electrons on a level far below 1 eV.

In a first experiment a 100 µm thick gold target (for maximizing Coulomb-excitation) was bombarded with 17.9 MeV/u $^{155}_{64}$Gd-ions at a charge state q = 56 (Fig. 1). The projectiles scattered to $\pm$ 5° (lab.) were detected in two position sensitive parallel-plate avalanche counters. The associated electrons emitted at lab.-angles of 0° $\pm$ 1° and 180° $\pm$ 1° with respect to the 5° scattered ^{155}Gd-ions were energy-analyzed in an electrostatic analysator (McPherson) and focussed onto a position sensitive channelplate. For H-like ^{155}Gd-ions one expects for K-conversion electrons of the first excited state (ΔE_γ = 60010 eV, M1-transition) an electron energy in the rest frame of $\gtrsim$ 950 eV corresponding to (4726$\pm$5) eV and (17017$\pm$17) eV in the lab.- system for emission at 180° $\pm$ 1° and 0° $\pm$ 1°, respectively. Due to the relativistic solid angle transformation (forward focussing) the detection efficiency is considerably enlarged in the lab.-system ($d\Omega/d\Omega^* \gtrsim 18$).

In order to reduce the large background of directly ionized electrons (δ-electrons), a target-collimator-system was used by which all prompt electrons were accelerated by a negative high voltage at the target onto energies beyond 20 keV.

On the other hand, it became guaranteed that the **delayed** emission of the conversion electrons from the isomeric first excited state (τ_γ = 0.2 ns $\hat{=}$ 1.2 cm time of flight for $\beta_N \gtrsim 0.2$) happened from an essentially field-free position.

From measured electron cross sections with and without target high voltage applied, the reduction of the background as a function of electron energy was obtained. Although a large suppression could be achieved - at the expected position of 180°-electrons of the H-like ^{155}Gd (4.5 keV) in the order of 200 - no evidence of a conversion line from He-or H-like atoms could be found during the beam time of 1 1/3 days, in contrast to expectations based on calculated charge state fractions behind a carbon target for 18 MeV/u Gd-ions at q = 56 (Nikolajev, $\langle q \rangle$ = 59.5, σ_q = 4). For the isomeric first excited state of ^{155}Gd this mean charge state should be even enhanced considerably due to multiple internal conversion followed by Auger-cascades. If, on the other hand, these calculations are not overestimating the real high q-fractions by more than an order of magnitude, than a further background reduction by a factor 2 (which seems to be possible) should allow a clear detection of these lines within a beam time of 2 - 3 days.

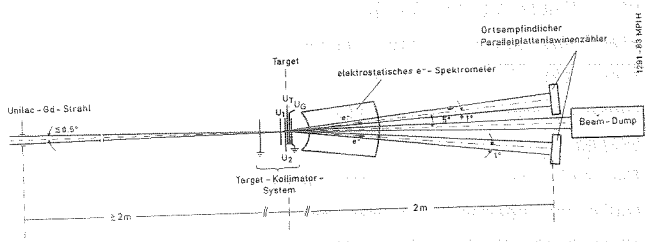


Fig. 1: Experimental set-up for the detection of conversion electrons emitted at 0° and 180° (lab.) from 5° scattered, highly ionized ^{155}Gd-atoms.

High Precision Spectroscopic Studies in H- and He-like Kr Ions

J.P. Briand, P. Indelicato, and M. Tavernier
Université Paris VI
H.F. Beyer, D. Liesen, B. Liu*, and A. Warczak**
GSI Darmstadt
*Permanent Address: Institute of Modern Physics, Lanzhou, CHINA
**Permanent Address: Jagellonian University, Cracow, POLAND

H- and He-like ions provide in atomic physics the most elementary systems for studies of relativistic corrections and quantum electrodynamic effects in the electron-nucleus and in the electron-electron interaction, because the experimental results can be directly compared with the corresponding theoretical calculations. The aim of the present experiment was threefold: To observe the $2s_{1/2}$-$1s_{1/2}$ M1 transition in H-like Kr, to determine the $2p_{1/2}$- $2p_{3/2}$ fine structure splitting in H-like Kr, and to measure the wavelengths of the lines in the decay of the $n = 2$ levels in He-like Kr. For all the three cases theoretical predictions are available[1-4].

The experiment performed used the beam-foil technique. Beams of 18 MeV/u Kr^{34+} and Kr^{35+} ions passed through a thin (~ 20 µg/cm²) C foil; the lines emitted in the decay of the excited states were observed just behind the foil with a flat crystal spectrometer mounted at 90° to the beam direction. The extension of the target was determined by a moveable, 80 µ wide slit. The spectrometer itself was located about 3 m away from the target and consisted of a flat Si(220) crystal which reflected x rays into a position sensitive detector of the backgammon type with a resolution of 100 µ. All the rotations and translations of the system were remotely directed and controlled. For reference purposes, different materials (Cu, Mo, Rb) were placed at the target position and bombarded with electrons several times during the Kr run. From the accurately known wavelengths of the K_α transitions in these elements the crystal spectrometer was calibrated.

The last two of the three marks for this experiment could be reached. It was not possible, however, to observe the M1 transition the energy of which is about 1.8 eV larger than that of the $2p_{1/2}$ - $1s_{1/2}$ $Ly_{\alpha 1}$ transition (E_x ~ 13.5 keV). Probably the reasons are a still somewhat too low energy resolution of the spectrometer and - due to the small intensity of the Kr^{35+} beam combined with the small spectrometer efficiency - too bad statistics for the H-like Kr. The results for the fine structure splitting in Kr^{35+} and for the wavelengths of the decay of the $^1P_1$, $^3P_2$, and $^3P_1$ states in Kr^{34+} are given in the Tab. together with the corresponding theoretical results. The experimental errors mainly stem from the uncertainty of the beam energy, the error of the angle between beam axis and spectrometer, and the uncertainty of the calibration lines. The experimental value for the fine-structure splitting is slightly larger than calculated and thus shows the same tendency as already found in lighter systems. In order to solve these problems, measurements over a wider Z-range using a spectrometer with very high dispersion are planned. For the He-like system the experiemtnal results for the $^1P_1$ and the $^3P_2$ states agree quite well with the calculations which for the $^3P_1$, however, give systematically higher transition energies than the experiment.

H-like Kr

Fine-structure splitting: Exp.: (80.8±1) eV
Theo.: 79.6 eV[1]

He-like Kr

	Exp. (eV)	Theo. (eV)		
$^1P_1$-$^1S_0$	13113.8±1.2	13112.9[2]	13114.6[3]	13114.9[4]
$^3P_2$-$^1S_0$	13091.2±1.5	13091.1		13091.2
$^3P_1$-$^1S_0$	13023.8±1.4	13028.3	13026.4	13026.5

[1] P. Mohr, Ann. Phys. 88, 26 (1974); W.R. Johnson and G. Soff, private communication

[2] U.J. Safronova, Phys. Scripta 23, 241 (1981)

[3] G.W.F. Drake, Phys. Rev. A14, 565 (1976)

[4] J.P. Desclaux, private communication

Lamb Shift Measuremens in High Z Hydrogenic Ions

J.S. Brown, B.P. Duval, H.A. Klein, J. Laursen, A.F. McClelland, P.H. Mokler* and J.D. Silver

University of Oxford, Clarendon Laboratory, Parks Road, Oxford OXI 3PU

*GSI Darmstadt

The $1s^2S_{1/2}$-$2p\ ^2P_{1/2,3/2}$ transition energies in hydrogen and hydrogenic ions may be calculated analytically using the Dirac equation, with small corrections for finite nuclear mass and size, and for hyperfine structure if the ion has nuclear spin. Further corrections are predicted by quantum electrodynamics (qed) including the electron anomalous magnetic moment and radiative level shifts. Ground state Lamb shift measurements in high Z hydrogenic ions can be made by accurately determining the $1s^2S_{1/2}$-$2p\ ^2P_{1/2,3/2}$ transition energies and subtracting a calculated nonradiative value for these intervals. This is not a new idea; it is embodied in the doctoral work of B. Edlen[1] who noticed a discrepancy between his measured value for the $1s\ ^2S_{1/2}$-$2p^2P_{1/2,3/2}$ transitions in Li^{++} and calculated (non qed) values, and the same principle has been used by G. Herzberg[2] for a measurement in He^+. The use of this technique was proposed in connection with fast beam sources of high Z hydrogenic ions some years ago[3]. More recently another possible technique was proposed: inter-comparison of Lyα and Balmer β transitions in the hydrogenic ion under study. This latter proposal has some similarities with experiments of Hänsch et al. in neutral hydrogen[4], and takes advantage of the fact that in the absence of relativistic effects, the energies of the n=1-2 Lyα and the n=2-4 Balmer β transitions are in the ratio 4:1. Since the Lyα and Balmer β transitions in the ions we wish to study are in the X-ray region, we may therefore make a "differential" measurement of the $1s\ ^2S_{1/2}$ ground state Lamb shift, via simultaneous observation of the Lyα and Balmer β decays in fourth and first order of diffraction respectively, with a crystal spectrometer. The feasibility of these difficult experiments depends crucially on the yield of X-rays which can be obtained from the source of hydrogenic ions studied. Indications from work carried out in Oxford[5] are that the beam foil source should be of sufficient strength to justify an initial investigation of the feasibility of experiments to measure Lamb shifts via measurements in hydrogenic ions such as Kr^{35+}.

In November 1983 a Si(Li) detector was used at GSI to observe X-rays from a 19.3 MeV/A Kr^{3+} ion beam incident on a carbon foil. Figure 1 shows a typical spectrum. The data obtained are useful in that they give us a quantitative measure of the X-ray yield of transitions in Kr^{34+} and Kr^{35+}, and enable us to predict with some accuracy the signal strength to be expected in the next stage of our experiment. This will involve observing spectra in the same wavelength region using a curved crystal spectrometer to obtain higher spectral resolution.

Acknowledgements

We should like to thank the atomic physics group at GSI for their kind hospitality and acknowledge excellent help and support of laboratory staff at GSI and in Oxford.

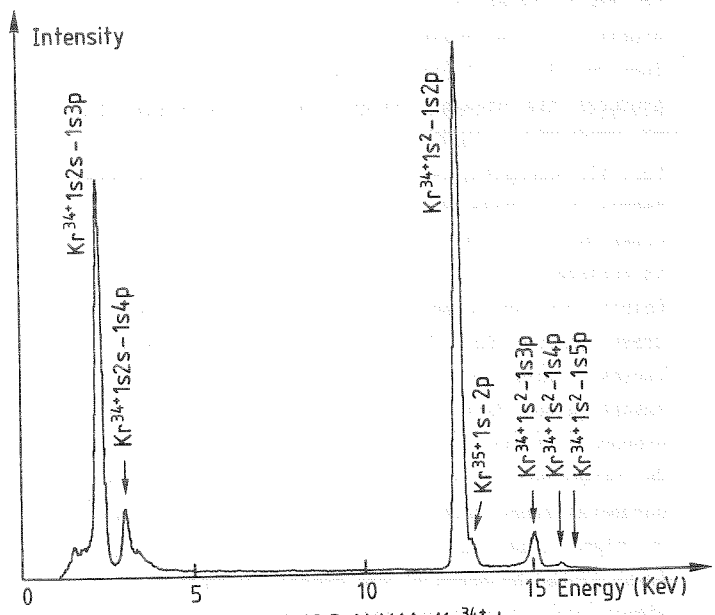


Fig.1, Si(Li) spectrum of 19.3 MeV/A Kr^{34+} beam on 200 μg/cm² carbon foil.

References

1) B. Edlen, Nova Acta Regiae Societatis Scientiarum Upsaliensis Ser. IV Vol. 9, 1934, p. 29.

2) G. Herzberg, Proc. Roy. Soc. A234, 516, 1956.

3) J.D. Silver, Invited Review at SAS 79, Tuscon, Arizona; Review at Workshop on Foundations of Relativistic Theory of Atomic Structure, ANL 1980, and private communication to R. Marrus, 1978.

4) T.W. Hänsch, in Atomic Physics 8, Plenum Press, New York 1983. Editors I. Lindgren, A. Rosen and S. Svanberg, p. 55.

5) I.A. Armour et al., J. de Phys. C1, 40, 211 1979; J. Phys. B13, 2701, 1980; J. Phys. B14, 3563, 1981.

Recoil Ion Production Cross Sections for 3.6 - 15.5 MeV/amu Uranium Bombardment of Rare Gas Targets

B

S. Kelbch*, R. Mann, P. Richard**, H. Schmidt-Böcking*, T. Ullrich*
GSI Darmstadt
*Institut für Kernphysik, Universität Frankfurt/M.
**Kansas State University, Manhattan, USA

Cross sections for the production of recoil ions were measured for U^{n+} on Ar and Xe collisions with projectile energies ranging from 3.6 to 15.5 MeV/amu and projectile charge states between 60 and 75, using a recoil ion - projectile ion coincidence method.

The aim of these experiments was to determine the most effective way to produce high charge state ions with low recoil energies as function of projectile velocity and different reaction mechanisms. A charge state analysis of both collision partners enabled the separation of these different reaction channels like direct ionization or ionization accompanied by capture into the projectile (CI).

For the Ar target direct ionization is the dominant process for the production of highly charged recoil ions as Fig. 1 illustrates, whereas for Xe mainly CI produces the highest charge states q observed (Fig. 2). From total capture cross sections also measured for all energies, as well as from the coincidence recoil ion production a strong decrease of the CI cross sections with increasing projectile velocity v_p is noticed.

Despite the enhancement of q in CI collisions, the cross section for the highest q number reaches its largest value at the highest projectile energies investigated. This can be seen in Fig. 3, indicating pronounced shifts to lower q values for decreasing v_p. We interprete this to be due to a smaller impact parameter range selected by the CI collisions because of higher momentum components of the captured electrons probed by means of the projectile velocity. This simply means that electrons capable of being captured by the fast projectile are found more closely to the nucleus. In this range the simultaneous outer shell ionization peaks at higher recoil ion charge states than for the lower velocity.

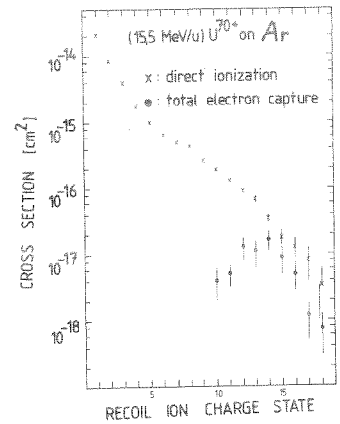


Fig. 1: Total recoil ion charge state (q) production of Ar for collisions without and with electron capture into U^{n+} projectiles.

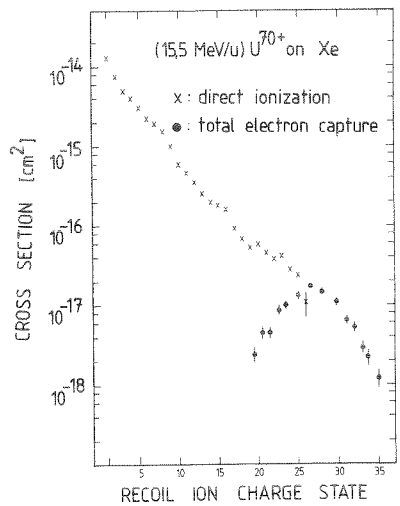


Fig. 2: As Fig. 1 but for Xe target. The highest charge states result from capture collisions.

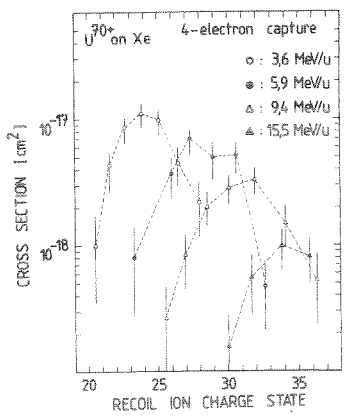


Fig. 3: Recoil ion production from capture collisions independence of projectile energy.

Observation of Highly Charged-Recoil Ions for High Resolution Spectroscopy*

S. Chen, H.A. Schüssler, U. Trebus, and J. Zhang
Dept. of Physics, Texas A&M University
W. Becker and R. Mann
GSI Darmstadt

It is well known that a high energy heavy ion beam can remove in a single collision all or a large number of electrons from a target atom without transferring much energy to the nucleus. In this way copious amounts of near thermal energy (a few eV) highly charged ions are produced. The production of these recoils ions makes high resolution microwave-[1] or laser-spectroscopy of slow highly charged few- or one-electron ions possible, thereby allowing exacting tests of the various relativistical and quantum electrodynamical contributions to the hyperfine structure splitting of these simple and fundamentally important few-electron atomic systems.

A prerequisite of such high resolution spectroscopy is that the recoil ions are efficiently extracted from the production region and transported without increasing their energy spread to an observation region located in ultra high vacuum ($< 10^{-10}$ torr). It is planned to inject slow recoil ions into a radio-frequency ion trap and store them for extended periods of time (many minutes or hours). So far the first stage of the experiment namely the production of intense almost monoenergetic beams of highly charged ions was optimized for the noble gases helium, neon, argon, krypton, and xenon as targets, when colliding with 1.4 MeV/u Ne^{7+} and U^{44+} beams. Two ways of ion extraction and ion manipulation were used. One uses a 180° double-focussing analysing magnet[2], the other a double-quadrupole Wienfilter double-quadrupole combination (Fig. 1). Typical charge state spectra obtained with the magnetic spectrometer (Fig. 2) and the Wienfilter arrangement (Fig. 3) are displayed. In obtaining the charge state spectra emphasis was placed on obtaining large numbers of extracted ions rather than achieving high charge state and mass resolution. Therefore, in both spectrometers a large aperture of 4 mm diameter was placed at the entrance and no aperture at the exit of the apparatus. In the experiments the intensity of the primary ion beam and the density of the gas target were varied, to obtain information on the production mechanism of highly charged recoil ions.

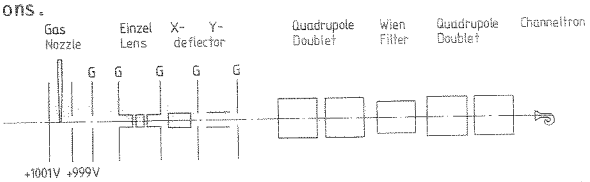


Fig. 1: Experimental arrangement for observing highly charged recoil ions.

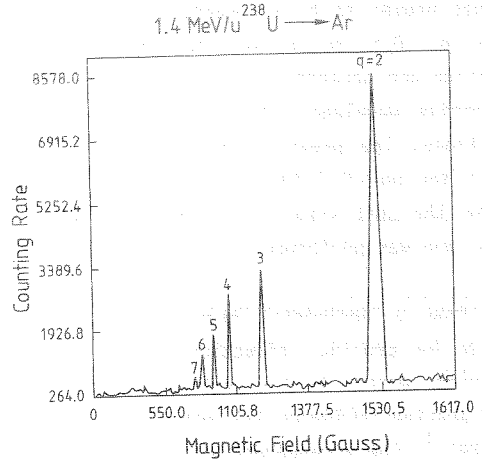


Fig. 2: Charge state spectrum of Ar using the 180° analysing magnet and an extraction voltage of 400 V.

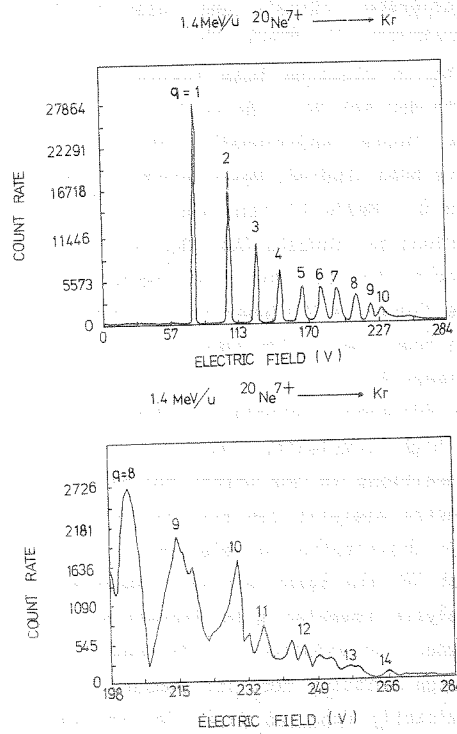


Fig. 3: Charge-state spectrum of Kr using the Wienfilter and an extraction voltage of 1000 V.

*This research was supported in part by the U.S. National Science Foundation.

[1] H.A. Schüssler, E.N. Fortson, and G.H. Dehmelt, Phys. Rev. 187 (1969) 5

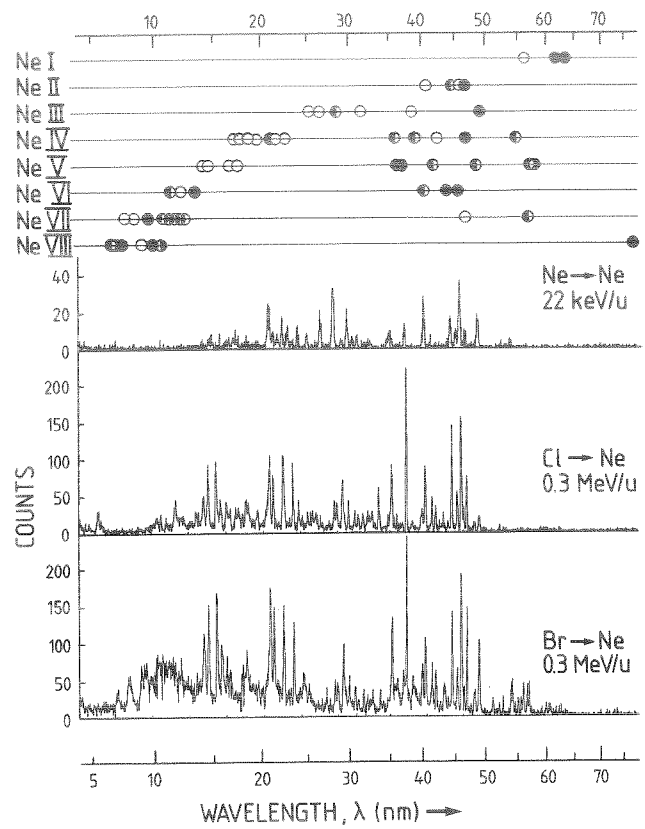
[2] R. Mann, GSI Annual Report 1982, p. 158 and GSI Ann. Rep. 1983

Soft X-Ray Spectroscopy of Ion-Induced Ne Recoils

F. Folkmann, N. Eisum, and P.H. Mokler*
Institute of Physics, University of Århus, DENMARK
*GSI Darmstadt

Recoil ion spectroscopy after heavy-ion atom bombardment has proven to be a powerful method in the x-ray region of 0.5 to 5 keV for investigating both excitation and secondary capture mechanisms as well as for precise wavelength determination of few electron transitions. The present investigation has been done to test the possibilities of the recoil ion spectroscopy in the soft x-ray region 300 eV - 10 eV (∿ 4 - 100 nm) and was performed at the Institute of Physics, Århus.

Light from a horizontal beam-excited gas cell was focussed by grazing reflection from a gold coated, ellipsoidal mirror to the vertical entrance slit of a 2.2 m grazing-incidence VUV monochromator (McPherson Model-247)[1]. The arrangement was optically aligned and set up with a grazing angle of 86° and a 600 l/mm grating for test purposes first at a 600 keV accelerator (Giraf) and later at the 6 MV Tandem Accelerator in Århus. The system has been calibrated with an electron beam excited Ne target and tested with 450 keV Ne^+ - Ne collisions, see top spectrum in the Figure. Additionally, other gases (CH_4, He, Ar) have been studied. Measurements at the Tandem with 0.3 and 0.7 MeV/u Cl ions and 0.3 MeV/u Br ions, using various gas targets (Ne, CH_4, Ar) have been performed. Spectra for 0.3 MeV/u ion impact on Ne are shown in the figure. A stripper foil in front of the gas cell has been used in the shown cases to get highly charged primary ions.



The VUV-spectra display in contrast to K x-ray spectra a high complexity including, for instance, many transitions to and within the Ne-L shell. A detailed spectra analysis can give information on the population distribution of electrons in the recoils, where most of the terms are well separated. A first data analysis revealed with increasing projectile atomic number - as expected - an increasing ionization of the photon emitting recoils; compare the position of the dominantly expected lines for the various ionization states according to Ref. 2; see top of the figure.

In Ne-Ne collisions radiation from single and double ionized Ne are dominant, whereas for Cl and Br impact higher ionization states contribute increasingly. Additionally, a strong population variation was observed as a function of the projectile charge (with/without stripper foil). Parts of the spectra are blended by projectile radiation which may produce broad structures in the region 6 - 14 nm. Using small spectrometer slits the projectile radiation can strongly be suppressed against recoil lines. The results show that for well selected collision partners the soft x-radiation intensity is strong enough to study the population of states in recoils with a grazing incidence VUV spectrometer. The relative efficiency measured for the spectrometer in comparison to a crystal spectrometer (ARL; Pb-stearad) dropped from 10^{-2} around 10 nm to $3x10^{-4}$ at around 6 nm.

[1] G. Sørensen, Journal de Physique C1, 40 (1979) 157

[2] R.L. Kelly, ORNL-5922 (1982)

Q-Value Spectroscopy of Recoil Ions Colliding with Rare Gas Atoms

R. Mann, S. Bayerbach, S. Hagmann*, B. Warczak
GSI Darmstadt
*Kansas State University

The study of kinetic energy distributions of highly charged ions after electron capture collisions with neutrals requires high resolving spectrometers as well as quasi monoenergetic incident ion beams.

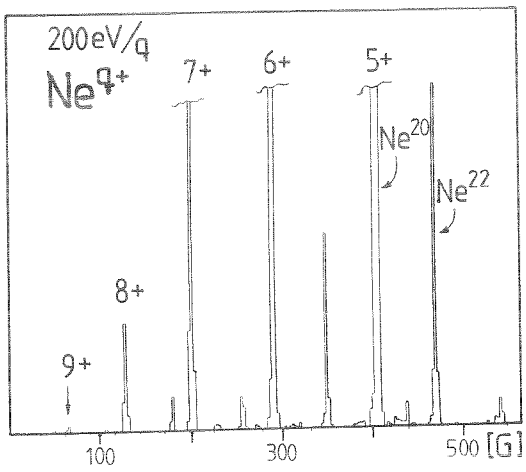


Fig. 1: Ne-charge state spectrum.

Figure 1 shows a fraction of charge state distribution of Ne^{q+} recoil ions pumped by 1.4 MeV/u Ar^{12+} projectiles and extracted at 200 V. A distinct separation of isotopes 20 from 22 is obtained by a 180° analyzing magnet (resolution $\Delta p/p \sim 5 \times 10^{-3}$). A subsequent electrostatic analyzer fixed the energy of the throughpassing ions at a width of 0.2 eV q before they penetrated a gas target and a second electrostatic spectrometer used for energy analysis.

Figure 2 displays examples of energy spectra of 195.6 eV/q Ar^{10+} and Ar^{9+} ions after collisions with Xe and He targets. For Xe the population of n = 6 and n = 7 Rydberg states in Ar is clearly resolved and pronounced peaks of transferionization channels (T) where a second electron is transferred to the continuum are detected. For He target the capture is more exoergic and smaller crossing radii (R_x) are involved. The kinetic energy released to the He is noticeable and broad peaks shifted towards lower energies than expected[2] from a classical crossing at n_c are observed. The importance of the collision kinematics seen by the analyzer system has been recently demonstrated[1] for Ne^{q+}+He.

A general behaviour of the exoergicities of charge exchange collisions between highly charged ions and neutrals is displayed in Fig. 3. ΔE increases with q in accordance with a strictly classical model calculation[2] (CB-model), however, an oscillatory behaviour $\Delta E(q)$ is noticed for the single capture channel, rendering the energy resonance when n_c reaches an integer value (main shell n). The smaller ΔE in He collisions compared to the CB-model is presumably due to the translational energy carried away by He. The transferionization channel shows a smooth dependence $\Delta E(q)$ for the many electron collision system J^{q+}+Xe. This might be explained by a large number of exit channels open for a two electron transfer which cannot be separated as in the one electron case.

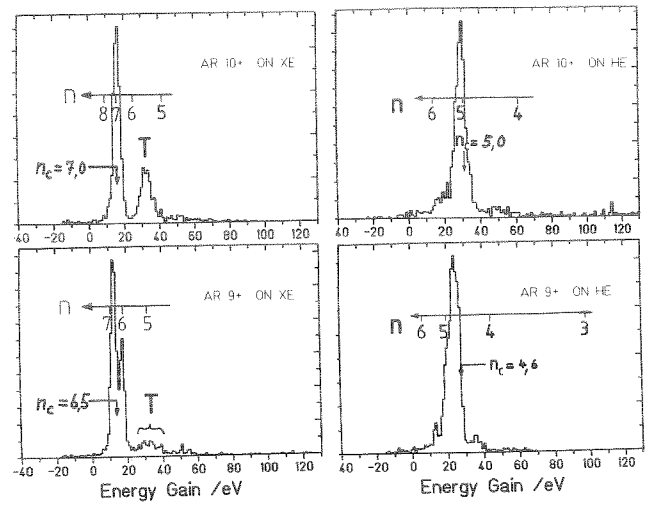


Fig. 2: Energy gain-spectra from single capture.

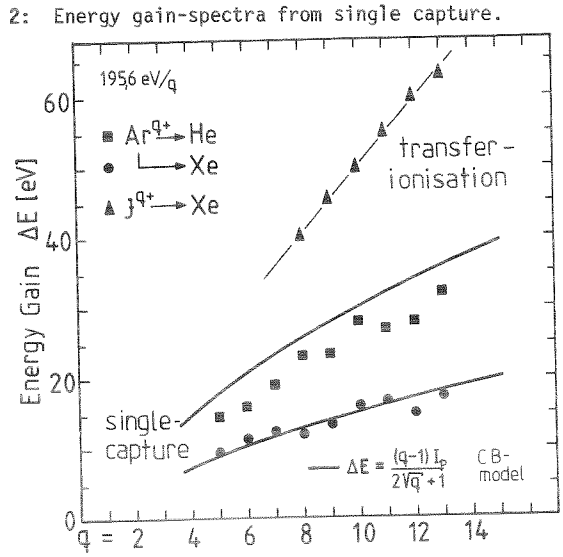


Fig. 3: Charge state dependence of energy defect ΔE. I_p is the ionization potential of the target.

[1] C. Schmeissner, C.L. Cocke, and R. Mann, to be published
[2] R. Mann, F. Folkmann, and H.F. Beyer, J. Phys. B14 1161 (1981)

Charge Transfer Involving Multiply Charged Ions [G]

A. Müller, B. Schuch, W. Groh, P.C. Kester, I. Wirkner-Bott, E. Salzborn
Institut für Kernphysik, Strahlenzentrum, Universität Giessen

When electrons are transferred from an atom to a highly charged ion incident with low kinetic energy the target is likely to loose additional electrons:

$$A^{q+} + B \rightarrow A^{(q-k)+} + B^{i+} + (i-k)e \qquad (1)$$

This process is termed transfer ionization (TI)[1]. Comprehensive measurements have been performed to obtain the charge state distributions of target ions produced in TI collisions of slow ($v << v_o = 2.2 \times 10^8$ cm/s) multiply charged ions and rare gas target atoms[2]. Correlations of the target-ion charge-state spectra with the number of electrons captured by the projectile were observed by using a time-of-flight-coincidence method.

The data for multiple electron capture can be understood on the basis of a statistical interpretation of TI[3]. The key parameter is given by the maximum potential energy ΔE available in the collision system rather than the kinetic energy.

TI can proceed via many individual reaction channels in all of which potential energy is given to electrons initially belonging to the target. Because of the large number of reaction paths (which were not specified in the experiments) a statistical description of TI seemed a reasonable approach. The assumption is that ΔE is distributed among the remaining outer shell electrons not captured by the projectile and that an electron can be ejected when it gains enough energy to overcome an averaged ionization potential $<I_B>$ which is characteristic for the target. From this picture the probability for the emission of a number of target electrons can be calculated without using any fit parameters.

An important implication of the statistical model is the prediction of a scaling behaviour of low energy TI collisions involving multiply charged ions: the charge-state fractions F_i of target ions B^{i+} with a given number k of electrons captured (see eq. 1) should fall on common curves for all projectile-target combinations $A^{q+} + B$ when plotted as a function of $\Delta E/<I_B>$. Fig. 1 shows the result for k=2 and includes all experimentally investigated collision systems, i.e. more than 80 different combinations of A^{q+} and B.

The type of experiments described above was extended to higher collision energies. At $v \geq v_o$ also endoergic processes begin to play a role. Presently, the experimental results are evaluated and interpreted.

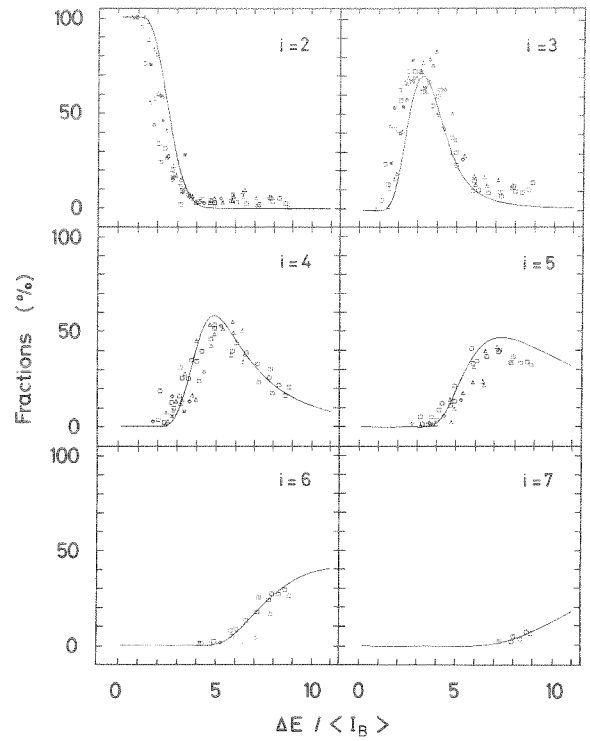


Fig. 1: Charge state fractions of target ions B^{i+} produced in reactions (1) with k=2. The figure contains data for more than 80 different collision systems investigated. Target symbols: Ne (*), Ar (Δ), Kr (◇), and Xe (□). The solid lines represent the results of the statistical model.

[1] A.Müller, W.Groh, E.Salzborn
Electronic and Atomic Collisions,
XIII ICPEAC, Invited papers and progress reports, in press

[2] W.Groh, A.Müller, A.S.Schlachter and E.Salzborn
J.Phys.B: Atom.Molec.Phys. 16, 1997 (1983)

[3] A.Müller, W.Groh and E.Salzborn
Phys.Rev.Lett. 51, 107 (1983)

Collinear Laser Spectroscopy on Fast Atomic Beams of Tin and Germanium

H.Lochmann, J.Eberz, G.Huber, R.Menges, G.Ulm
Institut für Physik, Universität Mainz
T.U.Kühl, GSI Darmstadt

According to the experiments of collinear laser spectroscopy with the aim to get information about the change of mean square nuclear charge radii, magnetic dipole and electric quadrupole moments in chains of isotopes in the region of Z = 50 (1) from the measurements of hyperfine structure and isotope shifts we performed test measurements on the stable isotopes of tin and its chemical homologeous germanium at the GSI off - line mass separator.

The properties of tin are of principal interest, once because of its closed proton shell at Z = 50 and on the other because the neutron number approaches on the neutron - deficient wing the shell closure at N = 50 and on the neutron - rich wing it extends over the shell closure at N = 82.

Optical excitation is easily achieved from the metastable $^1S_0$ - level to the $^1P_1$ - level with cw - dye lasers. Figure 1) gives the corresponding atomic level scheme of tin and germanium. The $^1S_0$ - level is populated by a charge exchange process between a sodium vapour target and a mass separated 30 - keV ion beam from a FEBIAD - plasma ion source. The signal detection assembly is described in detail in reference (2).

The figures 2a,b) present as an example the detected fluorescence signals for ^{119}Sn (I = 1/2) and ^{73}Ge (I = 9/2) from the $^1P_1$ - level, which show a resolved hyperfine structure splitting due to the deviation from pure LS - coupling in the $^1P_1$ - configuration.

The optical detection sensitivity and the production yield for fusion produced radioactive tin isotopes on the neutron - deficient wing of the tin isotope chain (3) are already sufficient for measurements on - line.

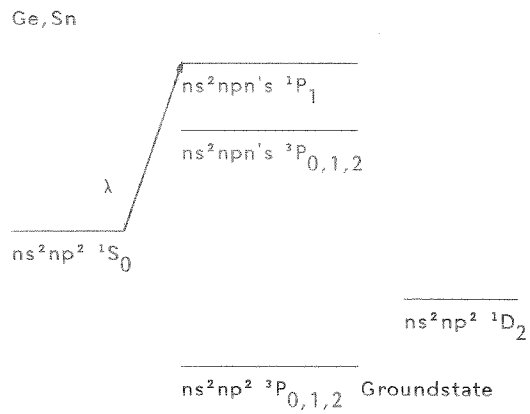


Fig.1: Atomic level scheme of Sn(n = 5, n' = 6, λ = 452,6 nm) and Ge(n = 4, n' = 5, λ = 422,8 nm).

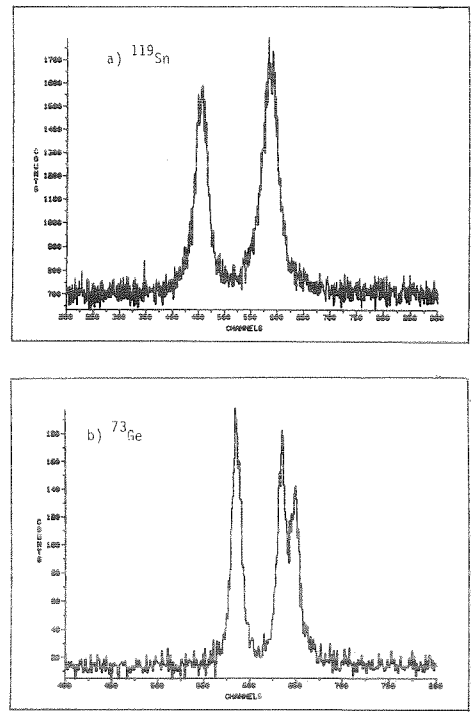


Fig.2: Fluorescence signals from the npn's $^1P_1$ - levels from Sn(a) and Ge(b) showing the hyperfine structure splitting.

References:
1. G.Ulm et al. contribution to this report
2. G.Ulm et al.,in "Laser Spectroscopy 6", H.P.Weber and W.Lüthy (eds.), p.211 (1983)
3. R.Kirchner et al., contribution to this report

Lamb-Shift Corrections in Hydrogen-like Atoms [B]

W. R. Johnson and G. Soff
Institut für Theoretische Physik der Universität Frankfurt and
GSI Darmstadt

We tabulated[1] the theoretical energy levels of hydrogen-like atoms in the range $1 \le Z \le 110$. Quantum electrodynamical corrections to the binding energies of K- and L-shell electrons are listed. The Lamb-shift corrections are presented in terms of the function $F(Z\alpha)$ which is defined via[2]

$$\Delta E = \frac{\alpha}{\pi} \frac{(Z\alpha)^4}{n^3} F(Z\alpha)\, mc^2.$$

ΔE denotes the level shift, n the principal quantum number, Z the nuclear charge number, $\alpha \approx 1/137$ the fine structure constant and m the electron rest mass. As example we list the various contributions to the Lamb-shift of K-shell electrons for the elements Sr (Z=38) and U(Z=92) and the corresponding error estimates

	F(Zα) Z=38		Z=92	
S	2.2042	7	1.4914	7
S-FS	-0.0006	6	-0.0266	15
U	-0.2410		-0.4064	
U-FS	0.0003		0.0179	
WK	0.0030	1	0.0194	37
HO	0.0013	13	0.0013	13
FS	0.0563	9	0.8038	104
RR	0.0007	7	0.0005	5
LS	2.0243	19	1.9012	112

The abbreviations in this table have the following meaning. S: self-energy[2-4], S-FS: finite nuclear size correction[5-7] to the self energy, U: level shift due to the Uehling potential, U-FS: finite nuclear size correction to the Uehling potential[10], WK: Wichmann Kroll terms to the vacuum polarization of the order $(Z\alpha)^3$, $(Z\alpha)^5$ and $(Z\alpha)^7$ (see refs. 11 and 12), HO: higher order vacuum polarization corrections, FS: finite nuclear size correction to the Dirac binding energy, RR: relativistic recoil corrections, LS: total Lamb shift. The dominant contribution to the Lamb-shift is provided by the self-energy. The nuclear radii for the evaluation of the finite nuclear size corrections are taken from the tables 8 and 9. For elements where no accurate radius is known we computed the nuclear rms-radius $\langle r^2 \rangle^{\frac{1}{2}}$ according to the formula given in the figure. For the most stable isotopes this formula has an accuracy of 0.05 fm. For the total binding energy of a K-shell electron we obtained in units of cm^{-1}: E(Z=38) = -161514400 ±100 and E(Z=92) = -1063210000 ±22000. The uncertainty of the nuclear radius of uranium dominates the latter error.

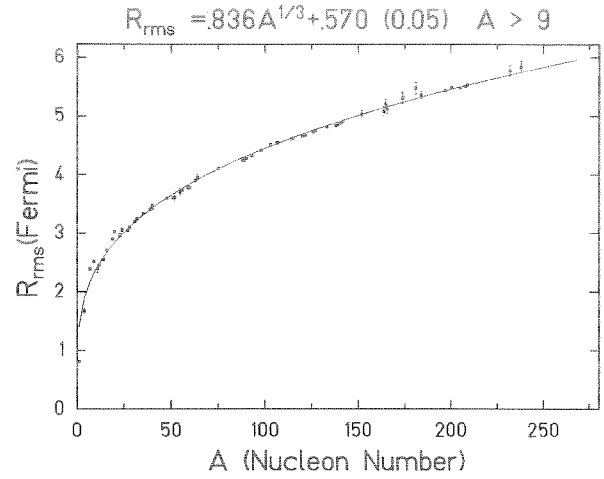


Fig. 1: Rms-radii $\langle r^2 \rangle^{\frac{1}{2}}$ of the most stable isotopes in the periodic table. For A > 9 the interpolation formula has an accuracy of 0.05 fm.

References

1. W.R. Johnson, G. Soff, preprint.
2. P.J. Mohr, Theoretical Energy Levels of Hydrogen-like Atoms, $10 \le Z \le 40$, preprint (1983)
3. P.J. Mohr. Ann. Phys. (NY) 88, 26 (1974)
4. P.J. Mohr. Ann. Phys. (NY) 88, 52 (1974)
5. A.M. Desiderio, W.R. Johnson, Phys. Rev. A3, 1267 (1971)
6. K.T. Cheng, W.R. Johnson, Phys. Rev. A14, 1943 (1976)
7. G. Soff, P. Schlüter, B. Müller, W. Greiner, Phys. Rev. Lett. 48, 1465 (1982)
8. C.W. de Jager, H. de Vries, C. de Vries, At. Data and Nuc. Data Tables 14, 479 (1974)
9. R. Engfer, H. Schneuwly, J.L. Vuilleumier, H.K. Walter, A. Zehnder, At. Data and Nuc. Data Tables 14, 509 (1974)
10. S. Klarsfeld, Phys. Lett. 66B, 86 (1977)
11. J. Blomqvist, Nucl. Phys. B48, 95 (1972)
12. E. Borie, G.A. Rinker, Rev. Mod. Phys. 54, 67 (1982)

Electron Excitations in Asymmetric Heavy Ion Collisions [B]

G. Mehler, T. de Reus, J. Reinhardt, B. Müller, W. Greiner
Institut für Theoretische Physik der Universität Frankfurt

G. Soff and U. Müller
GSI Darmstadt

A successful method calculating δ-electron, positron and K-hole production in heavy-ion collisions is the expansion of the time dependent Dirac wave function in a basis $\phi_k(r,t)$

$$\psi_q(r,t) = \Sigma_k a_{qk}(t)\, \phi_k(r,t)\, e^{-i\chi_k(t)}$$

ψ_q is the one-electron wave function, referring to the q-th electron. The summation on the right hand side of the equation runs over discrete and continuum states. Projection leads to a set of coupled differential equations for the occupation amplitudes $a_{qk}(t)$ ($\hbar$=c=1)

$$\Sigma_k \dot{a}_{qk}(t) \langle\phi_j|\phi_k\rangle e^{-i(\chi_k(t)-\chi_j(t))}$$

$$-i \Sigma_k a_{qk}(t) \langle\phi_j|\phi_k\rangle \dot{\chi}_k(t)\, e^{-i(\chi_k(t)-\chi_j(t))}$$

$$= -\Sigma_k a_{qk}(t) \langle\phi_j|\partial/\partial t + i\, H(t)|\phi_k\rangle\, e^{-i(\chi_k(t)-\chi_j(t))}$$

This is a general formulation, where no specific assumption is made about the basis $\phi_k(r,t)$, the phases $\chi_k(t)$ or the Hamiltonian H(t). Using the semiclassical approximation and the orthonormal basis of eigenfunctions of the stationary two-centre Dirac Hamiltonian leads to the well known coupled equations for the molecular occupation amplitudes[1]. This method has been successfull to describe heavy, nearly symmetric systems. In an approach to describe light, and non-adiabatic collision systems, we use as basis the eigenfunctions of the atomic Dirac Hamiltonian

$$H^o_D\, \phi_i(r) = E_i\, \phi_i$$

$$H^o_D = \vec{\alpha}\,\vec{p} + \beta\, m + V_T(r)$$

The potential $V_T(r)$ takes the finite size of the target nucleus into account, assuming it to be a homogeneously charged sphere. In this basis the phases $\chi_k(t)$ are given by $\chi_k(t) = E_k t$. The total Hamiltonian reads

$$H = H^o_D + V_P = \vec{\alpha}\,\vec{p} + \beta\, m + V_T(r) - Z_P e^2/|\vec{r}_c - \vec{R}_{TC}|$$

The last term is the Coulomb potential of the projectile. Z_P and $\vec{R}_{TC}(t)$ are the charge of the projectile nucleus and the two-centre distance of the colliding nuclei, respectively. $\vec{r}_e$ is the electron coordinate. In this orthonormal basis and with this Hamiltonian the system of coupled equations simplifies to

$$\dot{a}_{qj}(t) = -\Sigma_k a_{qk}(t) \langle\phi_j|V_P|\phi_k\rangle\, e^{-i(E_k-E_j)t}$$

Note that the summation includes also the indices k=j. The diagonal matrix elements represent the change of energy in first order for each eigenstate due to the additional potential V_P. The correction for the binding energy is therefore automatically included in the present formalism. V_P can be expressed in terms of a multipole expansion. As V_P does not mix the spinor components of the Dirac state, the calculation of the matrix element can be split off in an integration over the solid angle Ω times an integration over r. This leads to

$$M_{jk} \equiv \langle \phi_j|V_P|\phi_k\rangle = \Sigma_l\, Y_{l,\Delta m}\, W_{j,k}\, R_{j,k}(R_{TC}(t))$$

$Y_{l,\Delta m}$ is a spherical harmonic. Its argument θ(t) refers to the angle between the z-axis of the coordinate system and the location of the projectile. The argument φ, which fixes the scattering plane, can be set to zero. Δm denotes the difference between the magnetic quantum numbers of the final and the initial state $\Delta m = m(\phi_j) - m(\phi_k)$. $W_{j,k}$ is the term resulting from the integration over the solide angle. It can be expressed as a sum of products of 3j-symbols and Clebsch-Gordon coefficients. $R_{j,k}(R_{TC}(t))$ results from the integration over the radial coordinate. It depends parametrically on $R_{TC}(t)$.

The recoil effect of the target can be taken into account in a first order approximation by a correction of the dipole matrix element[2]. Our approach has very promising aspects. It can be extended to include electron-electron interactions. It may also be applied to heavier systems if in the basis additonal states of the projectile and/or states of the united system are included.

Numerical calculations are in progress.

References

1. G. Soff, J. Reinhard, B. Müller and W. Greiner, Z Physik A294, 137 (1980)
2. P.A. Amundsen, J. Phys. B18, 3197 (1978)

Charge Transfer in the Presence of a Nuclear Resonance

D.H. Jakubaßa-Amundsen
Physik-Department, Technische Universität München
P.A. Amundsen
NORDITA, Kopenhagen

The study of atomic ionisation or charge transfer processes during resonant nuclear scattering provides a unique tool to get information on the nuclear reaction parameters as well as on atomic transition amplitudes. The time-delay of the projectile causes a change in the relative phases of the atomic transition amplitudes before and after the nuclear interaction, leading to a resonance structure in the transition probability. In case of ionisation, this effect was found both experimentally and theoretically[1].

Charge transfer is more sensitive to such interference phenomena because it is a higher-order theory. For electron capture by a light projectile ($Z_P \ll Z_T$) the strong potential Born approximation[2] can be applied such that the transition amplitude

$$a_{fi} = \int d\vec{K}\, d\vec{q}\, \langle \phi_f \varphi_f^P \,|\, \phi_{\vec{K}} \hat{q} \rangle$$
$$\{ \langle \phi_{\vec{K}} \varphi^T_{\vec{q},\omega} \,|\, V_N \,|\, \varphi_i^T \vec{K}_i \rangle + \langle \phi_{\vec{K}} \varphi^T_{\vec{q},\omega} \,|\, V_P \,|\, \varphi_i^T \phi_i \rangle \} \qquad (1)$$

consists of an excitation matrix element and an overlap term which describes the capture after excitation. ϕ_i, ϕ_f and $\phi_{\vec{K}}$ are nuclear scattering states and $\varphi_i^T(\varphi_f^P)$ describes the bound target (projectile) electron while $\varphi^T_{\vec{q},\omega}$ is a target off-shell continuum state. $|\vec{q}\rangle$ and $|\vec{K}_i\rangle$ is an electronic and nuclear plane wave, respectively. The first term denotes the recoil capture by means of the internuclear potential V_N, while the second term is the capture due to the projectile field V_P.

Eq.(1) can be decomposed into three parts

$$a_{fi} = a_{in} f(E_f) + a_m f(E_m) + a_{out} f(E_i) \qquad (2)$$

according to both excitation and capture on the incoming (a_{in}) or outgoing (a_{out}) part of the collision and a third term describing excitation in the incoming and capture in the outgoing channel, being multiplied with the nuclear scattering amplitude f. E is the internuclear energy in the initial (i), final (f) and intermediate (m) state.

In order to observe resonance effects, the energy transferred to the electron in a collision with velocity v must be of the order of the resonance width Γ

$$\Delta E = E_f - E_i = \varepsilon_f^P + v^2/2 - \varepsilon_i^T \simeq \Gamma \qquad (3)$$

(ε_f^P and ε_i^T are the electronic bound-state energies), however, contrary to ionisation, a structure in the transition probability P is also seen when (3) is not strictly valid (cf.Fig.1).

Fig.1 shows the capture probability for p on Ni as a function of projectile energy for 90° scattering angle in the case of an isolated s-wave resonance at E_R = 3.151 MeV. Its width Γ_R = 5.6 keV compares well with $\Delta E \approx 10$ keV. The change in $P(\vartheta)$ at $E_P \approx E_R$ is nearly a factor of 10 bigger than in case of ionisation[1].

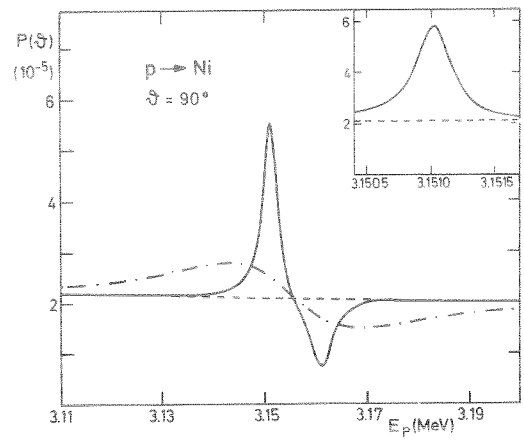


Fig.1: Capture probability across the 3.151 MeV resonance with $\Gamma = \Gamma_R$ (full curve), $\Gamma = 10\,\Gamma_R$ (dash-dot curve) and $\Gamma = 0.1\,\Gamma_R$ (insert). The dashed curve is a semiclassical calculation (without resonance)[3].

[1] J.S.Blair et al, Phys.Rev.Lett. 41, 1712 (1978)

[2] J.Macek and R.Shakeshaft, Phys.Rev. A22, 1441 (1980)

[3] P.A.Amundsen and D.H.Jakubaßa-Amundsen, to be published in J.Phys.B

Inner Shell Vacancy Formation in Deep-Inelastic Heavy-Ion Collisions [B]

U. Müller and G. Soff
GSI Darmstadt
J. Reinhardt, T. de Reus, B. Müller, and W. Greiner
Institut für Theoretische Physik, Universität Frankfurt

In this Report we will discuss the formation of inner-shell vacancies in deep-inelastic heavy-ion reactions. Within our semiclassical description of electronic excitations in atomic collisions we have adapted trajectories calculated from two nuclear macroscopic friction models. J.R. Birkelund et al.[1] based their model (furtheron denoted as Model I) on the proximity nuclear potential of Błocki et al., the Coulomb potential of Bondorf et al. (which was restricted to the normal Coulomb potential in our calculations), and the one-body nuclear friction in the proximity formalism of Randrup. They incorporated the intrinsic rotation of the ions. On the other hand, R. Schmidt et al.[2] proposed a model (Model II), which, additionally, accounts for neck formation in the separating system. Thereby one is able to explain the experimentally observed energy loss, where up to ~ 30% energy dissipation (for b ~ 0) can be achieved.

Strong deviations from a Coulomb trajectory and increased reaction times are found in both models (Fig. 1). E.g., for U + U at a bombarding energy of E_{Lab} = 7.5 MeV/u, Model II predicts delay times up to $\Delta T \sim 1.1 \cdot 10^{-21}$s defined with respect to the point of nuclear separation. We note that it is impossible to give an unambiguous definition of the time delay in the presence of energy dissipation. Thus we have introduced an atomic interaction sphere R_{at} defining the delay time ΔT with reference to this distance.

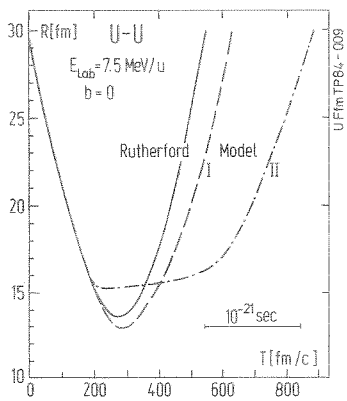
Recently experiments have been performed by Ch. Stoller et al.[3] to study the dependence of vacancy formation on the Q-value and thus on the nuclear reaction time in 7.5 MeV/u U + U collisions. We thus can compare the theoretical yield for $P_K(Q)$ with the experimental data. The theoretical probabilities are reduced by a factor ~ .9 to fit the experimental value at Q = 0. The dashed-dotted line in Fig. 2 refers to Model I, whereas the dashed curve denotes Model II.

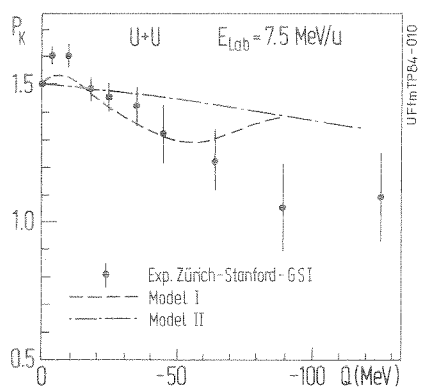
For low Q-values, the model of Birkelund et al.[1] seems to be more appropriate, but for higher energy losses both models fail to explain the experimentally measured K-hole probabilities.

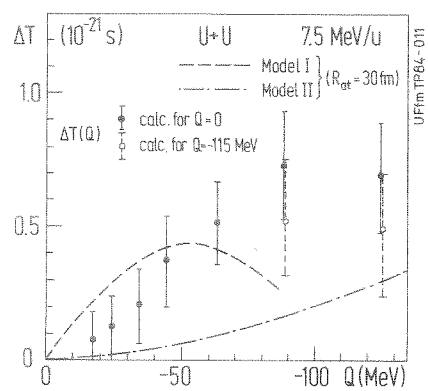
In a less sophisticated analysis using a schematic model for the nuclear time delay[4], one can calculate the probability for K-hole production as a function of delay time T which is used as a free parameter. Taking the experimental data at face value one can relate the measured Q-value to a delay time T by comparing the experimental probabilities with the theoretical $P_K(T)$. The full bars in Fig. 3 represent the result of such an analysis neglecting energy dissipation in the schematic trajectory model. The inclusion of energy dissipation leads to somewhat smaller delay times, c.f. the dashed bars at high Q-values. One can see that within this schematic comparison even for small Q-values Model I would not follow the experimental data, in contrast to our conclusions from Fig. 2. We thus conclude that measurements of atomic excitations do not simply gauge nuclear time scales, but are sensitive to the nuclear motion during a reaction as well.

References

1. J.R. Birkelund et al., Phys. Rep. 56 (1979) 107
2. R. Schmidt et al., Nucl. Phys. A311 (1978) 247
3. Ch. Stoller et al., GSI Sc. Rep. 1982 (1983) 19
   W.E. Meyerhof and J.F. Chemin, to be published
4. U. Müller et al., Z. Phys. A297 (1980) 357







Atomic Excitations and the Time Structure of Nuclear Reactions [B]

J. Reinhardt, B. Müller, and W. Greiner
Institut für Theoretische Physik, Universität Frankfurt
U. Müller, GSI Darmstadt
U. Heinz, Dept. of Physics and Astronomy, Vanderbilt University, Nashville, Tenn.

Atomic excitations may be used to study the dynamics of nuclear reactions ('atomic clock') through, e.g., structures in the spectra of emitted electrons and positrons and variations of the K-hole production. The description of processes of this kind is facilitated if the atomic and nuclear excitations take place in different spatial regions. Starting from quantum scattering theory the cross section can be expressed in terms of the semiclassical atomic excitation amplitudes[1]. The latter can be factorized in terms of incoming and outgoing amplitudes connected through the nuclear S-matrix [2,1]. Averaging the cross section over the spread in beam energy, ΔE, introduces the nuclear autocorrelation function $A_{\ell'\ell}(E',E) = \langle S_{\ell'}(E')\, S^{*}_{\ell}(E)\rangle$.

Introducing a Fourier transformation it is found[3] that the cross section for an atomic excitation $i \to f$ can be written as an integral over delay times

$$\left\langle \frac{d\sigma_{if}}{d\Omega} \right\rangle = \int_0^\infty dT \; |a_{if,T}|^2 \; \frac{d\sigma_{nuc}}{d\Omega}(T,\theta) \quad ,$$

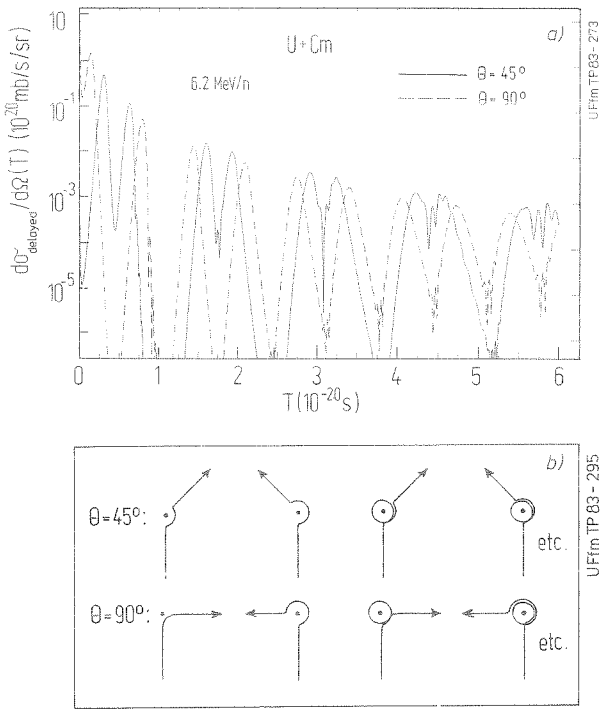
where $|a_{if,T}|^2$ is the atomic excitation probability calculated for a fixed delay time T. The time dependent nuclear cross section

$$\frac{d\sigma_{nuc}}{d\Omega}(T,\theta) = 1/4K^2 \sum_{\ell\ell'} (2\ell+1)\,(2\ell'+1)\, e^{2i(\sigma_{\ell'}-\sigma_{\ell})} \cdot P_\ell P_{\ell'}\, f^{E}_{\ell\ell'}(T)$$

is expressed in terms of the Fourier transform $f^{E}_{\ell\ell'}(T)$ of the nuclear autocorrelation function.

We have applied this formalism to a model for the nuclear elastic scattering amplitude consisting of Breit-Wigner resonances $S_\ell(E) = (E-E_\ell - i\Gamma_\ell/2)/(E-E_\ell+i\Gamma_\ell/2)$. Specifically, E_ℓ and Γ_ℓ were taken as the energy and width of a rotational band of resonances produced by a pocket in the internuclear potential. Then the time distribution function can be determined analytically. The cross section is split into direct and delayed components

$$\frac{d\sigma_{nuc}}{d\Omega}(T,\theta) = \frac{d\sigma_{Ruth}}{d\Omega}(\theta)\,\delta(T) + \text{interf. term} + \frac{2\Delta E}{4K^2}\left|\sum_\ell (2\ell+1)\, e^{2i\sigma_\ell} P_\ell \; \frac{\Gamma_\ell}{E-E_\ell+i\Delta E}\; e^{[-i(E_\ell - i\Gamma_\ell/2)T]}\right|^2 .$$



For the example of U+Cm collisions at 6.2 MeV/u, assuming a single band of resonances, the Figure shows the delayed nuclear cross section. Regular sharp peaks are observed which demonstrates that the nuclear system behaves like a classical rotor with a well defined orbital period. This 'lighthouse effect' is replaced by a more complicated pattern if several bands with different band head energies are present. The application of the model to spontaneous positron production is discussed separately[4].

References

1. U. Heinz et al., Ann. Phys. 151 (1983) 227
2. T. Tomoda and H.A. Weidenmüller, Phys. Rev. C28 (1983) 739
3. J. Reinhardt et al., Phys. Rev. A28 (1983) 2558
4. U. Heinz et al., 'Beam energy dependence of ...', this volume

Beam Energy Dependence of Spontaneous Positron Production in Delayed Nuclear Collisions [B]

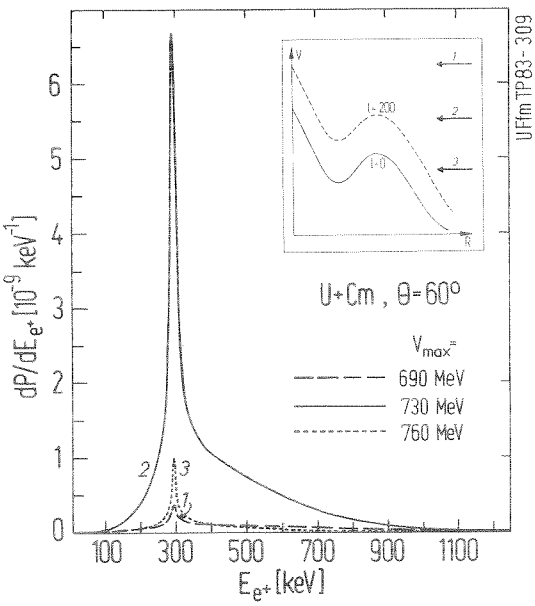
U. Heinz, Dept. of Physics and Astronomy, Vanderbilt University, Nashville, Tenn.
U. Müller, GSI Darmstadt
J. Reinhardt, B. Müller, and W. Greiner
Institut für Theoretische Physik, Universität Frankfurt

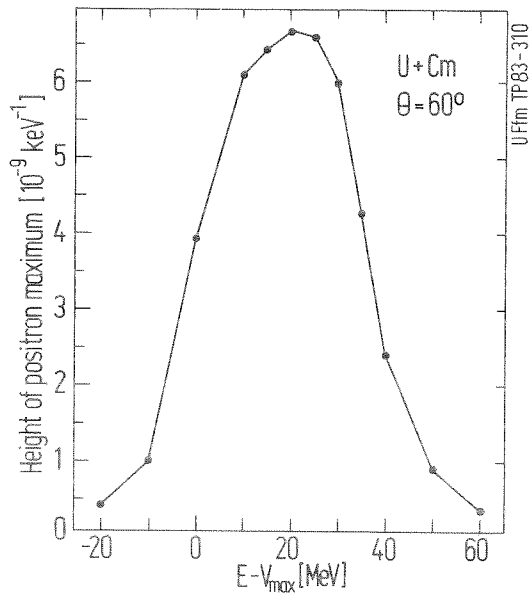
Recent measurements of positron emission spectra from U+U, U+Th and U+Cm collisions close to the Coulomb barrier[1,2] have exhibited sharp line structures, which have been interpreted[3] as spontaneous positron emission from giant nuclear systems with lifetimes $T>10^{-20}$s. As a first step towards a quantitative understanding of this process we consider a quantum mechanical model for elastic nuclear scattering involving an internuclear potential with a pocket.

Atomic excitations in collisions with nuclear contact can be described using the semiclassical electronic excitation amplitudes while the nuclear dynamics enters through the nuclear S-matrix[4,5]. Assuming the existence of a nuclear potential pocket[6] deep enough to support a number of N≥1 rotational bands based on separate vibrational states we parametrize the nuclear scattering amplitude as $S_\ell(E) = \Pi\,(E-E_{n\ell}-i\Gamma_{n\ell}/2)/(E-E_{n\ell}+i\Gamma_{n\ell}/2)$. We assume a set of very closely spaced resonances at energies $E_{n\ell}=E_n+\gamma\ell(\ell+1)$, γ=.7 keV, with widths $\Gamma_{n\ell}$ following from the semiclassical tunneling probability through a parabolic barrier. Positron spectra are obtained by integrating over the reaction time distribution which is given by the Fourier transform of the nuclear autocorrelation function.

The existence of high-reaching rotational bands of nuclear resonances results in a considerable probability for long delay times which is reflected by the occurence of sharp lines in the positron spectra. This is demonstrated in Fig. 1 which shows the potential pocket and the positron spectra (from delayed collisions only!) for three impact energies. Ten rotational bands with equally spaced band head energies below the top of the barrier have been assumed. The excitation function of the positron peak (Fig. 2) has a narrow maximum near the energy of the potential barrier V_{max}, which is easily understood: At energies far below the barrier, resonances are too narrow to be excited; far above the barrier, the beam can only hit high-lying short-lived resonances leading to a low chance for spontaneous positron production.

Although the model explains the important features of the experimental results, the predicted intensities are too small by several orders of magnitude, since the required narrow nuclear resonances can be reached only by tunneling through the barrier. We expect that the inclusion of inelastic processes ('double resonance mechanism') will increase the entrance width, eventually leading to a quantitative understanding of the observed positron line.





1. M. Clemente et al., 'Narrow positron lines from U-U and U-Th collisions', preprint, 1983
2. J. Schweppe et al., Phys. Rev. Lett. 51 (1983) 2261
3. J. Reinhardt et al., Z. Physik A303 (1981) 173
4. T. Tomoda and H.A. Weidenmüller, Phys. Rev. C28 (1983) 739
5. U. Heinz et al., Ann. Phys. 151 (1983) 227
6. M. Seiwert et al., to be published

On the evidence for spontaneous positron production in heavy ion collisions

B

T. de Reus, J. Reinhardt, B. Müller, and W. Greiner
Institut für Theoretische Physik, Universität Frankfurt/Main

U. Müller and G. Soff
GSI Darmstadt

In the newest generation of experiments dealing with the detection of line structures in positron spectra two groups successfully detected peaks in U+U and U+Cm collisions having width and intensities which depend sensitively on the beam energy. Ch. Kozhuharov, P. Kienle et al.[1-3] measured at three different beam energies (E_{Lab}=5.7 MeV/u , 5.9 MeV/u and 6.2 MeV/u) positron spectra for U+U.

In an independent experiment H. Bokemeyer, J.S. Greenberg, D. Schwalm et al.[4-6] measured positron spectra in U+Pb, U+U and U+Cm collisions at 5.9 MeV/u laboratory energy (and 5.8 MeV/u for U+Cm resp.).

As pointed out earlier[7], we expect a line structure to develop in positron spectra if nuclear time delays occur in the order of 10^{-20}sec. In Fig. 1 recent experimental data of Schweppe et al.[8] are displayed, who have measured positron emission probabilities in U+Cm collisions at 5.8 MeV/u, where a peak shows up at $E_{e^+}\approx 316\pm5$ keV having a width of $\Delta E \lesssim 80$ keV in the upper part of the picture, where $100^o \lesssim \Theta_{CM} \lesssim 130^o$. In this coupled channel calculation[9] we included electron screening effects[10] and let the nuclei approach to R=16 fm in a schematic model. The minimum delay time required is $T \gtrsim 6.5\ 10^{-20}$sec for spontaneously emitted positrons being created in a fraction of $q = P_{e^+}(exp)/P_{e^+}(theor.) \approx 1.75\ 10^{-3}$ delayed collisions per elastically scattered ion. Assuming fully isotropic break-up of the giant nuclear system, the nuclear reaction cross section becomes $\sigma^N \cong 30$ mb.

The lower part of Fig. 1 displays the distant collisions ($50^o \lesssim \Theta_{CM} \lesssim 80^o$) where no structures occur.

Alternatively, it was argued that internal pair conversion following nuclear Coulomb excitation might be the origin of the peak. To discuss this point, we turn to the system U+U at E_{Lab}=5.73 MeV/u, where a peak structure has been measured[1-3] around $E_{e^+} \cong 320$ keV having a width of about 70 keV.

In the case of electric monopole transitions, the following two processes could lead to sharp structures in the positron spectrum: (a) pair conversion (b) monoenergetic pair conversion, where an electron from the lower continuum is transferred to a hole in a bound state. In the first case a positron spectrum of triangular shape is expected, having a sharp cut-off energy[11]. Superimposing this upon the dynamical spectrum, the positron peak should display a full width at half maximum of about 130 keV, which is nearly a factor two larger than the observed width. In contrast to this, in case of monoenergetic pair conversion, the width of the main peak (at E_{e^+}=320 keV) is solely determined by the experimental broadening, but a second structure around $E_{e^+} \approx 190$ keV from the concurring pair conversion should also show up. However, since conversion positrons are always accompanied by K-conversion electrons, the δ-electron spectrum forms a crucial test for the conversion hypothesis. In Fig. 2 we display the δ-electron spectrum for U+U (solid line) including bumps of different heights due to EO-conversion of K-shell electrons for different K-hole numbers x (x=.25: dotted, x=1: dashed, x=1.75: dashed-dotted) for the transition energy $\omega = 2.37\ m_0c^2$. Up to now such a structure was not observed in the corresponding δ-electron spectra[12]. Thus there seems to be evidence, that the decay of the neutral vacuum has been observed experimentally through the existence of long living nuclear molecules.

1 E. Berdermann et al., GSI-Scientific Rep. 81-2 (1980) 128
2 P. Kienle and coworkers, NATO-ASI-B80, Plenum N.Y., (1981) 293
3 E. Berdermann et al., GSI-Scientific Rep. 83-1 (1983) 147
4 H. Bokemeyer et al., NATO-ASI-B80, Plenum N.Y. (1981) 273
5 H. Bokemeyer et al., GSI-Scientific Rep. 83-1 (1982) 146
6 J.S. Greenberg, W. Greiner, Phys. Today, Aug 1982, 24
7 J. Reinhardt et al., Z. Physik A303 (1981) 173
8 J. Schweppe et al., Phys. Rev. Lett. 51 (1983) 2261
9 U. Müller et al., Z. Physik A313 (1983) 263
10 T. de Reus et al., GSI-Preprint 83-18 (1983) and J. Phys. B, in press
11 P. Schlüter et al., Z. Phys. A314 (1983) 297
12 M. Clemente et al., XIII ICPEAC, Berlin (1983) 435

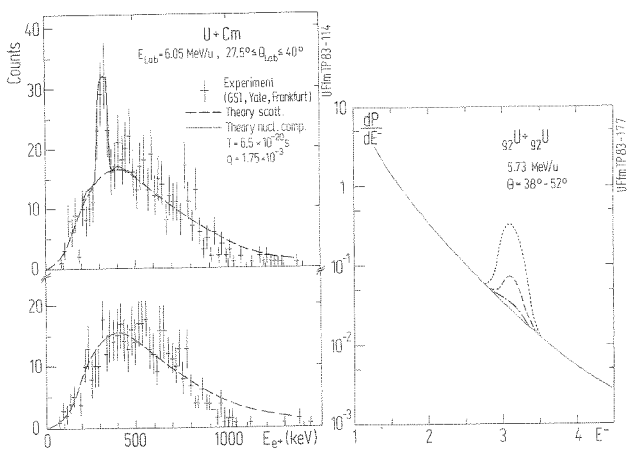


Fig. 1: Positron emission versus kinetic energy in U+Cm collisions. Fig. 2: δ-electron spectrum including bumps due to hypothetical EO-conversion.

Spectra of δ-Electrons and Positrons Emitted in Deep-Inelastic Heavy-Ion Reactions [B]

U. Müller and G. Soff
GSI Darmstadt
J. Reinhardt, T. de Reus, B. Müller, and W. Greiner
Institut für Theoretische Physik, Universität Frankfurt

Information on the development of deep-inelastic heavy-ion reactions can be gained by studying their influence on electron emission and positron creation. We have calculated excitation spectra within a semiclassical model using two macroscopic friction models for the nuclear reaction[1,2]. Both models lead to a rather gentle modification of the nuclear motion with only short delay times $T \sim 1 \cdot 10^{-21}$s. Thus it is obvious[3] that the spectra are modified only slightly. Positron spectra show a gradual enhancement at their maxima as well as a drift towards lower kinetic positron energies when going to more inelastic collisions. The spectra of emitted δ-electrons decrease considerably and fall off more steeply. However, united atom effects like spontaneous creation of positrons for supercritical heavy-ion collisions will not be visible.

Recently experimental energy spectra of δ-electrons and positrons emitted in U+U and U+Cm collisions above the Coulomb barrier have been published by H. Backe et al.[4]. To get a signature for close contact the atomic excitations have been measured in coincidence with fission fragments, which are detected in a laboratory angular window of $\theta_{Lab} = 45^0 \pm 10^0$.

For a quantitative comparison with the experiment one has to integrate the theoretical impact parameter dependent spectra over all values of b which lead to a nuclear reaction, weighted by the probability $w_f(b)$ to induce nuclear fission and by the probability $w_D(b)$ of detection within the given lab angle.

Values for the fission probability can be derived from measurements of H. Freiesleben et al.[5] who investigated the elastic (and quasielastic) angular distribution for 7.42 MeV/u U + U collisions. Although a procedure to determine $w_f(b)$ from these data is not unique, the final results depend only slightly on the estimates used. The calculated[6] detection probabilities as well have no large effect on the δ-electron and positron spectra, thus we approximate $w_D = 1$.

Figs. 1 and 2 show the experimental data[4] for δ-electron and positron emission in 7.5 MeV/u U + U collisions in comparison with theoretical results including electron shielding. Dashed lines display spectra calculated with the trajectories of the model of R. Schmidt et al.[2], dotted lines represent the calculations for model trajectories of J.R. Birkelund et al.[1]. For comparison δ-electron and positron spectra are shown where pure Rutherford scattering is assumed, thus simulating 'transparent' nuclear matter (solid lines). In all calculations the trajectories of a binary system have been used, assuming that the fission process (which is delayed[7] by $\sim 10^{-20}$s) does not severely modify excitation processes.

All theoretical δ-electron probabilities have been scaled up by a common factor 1.4 to obtain agreement with the experimental δ-electron data for 7.5 MeV/u U + U elastic scattering. The absolute values then might seem to favour the nuclear model of Birkelund et al.[1], however, the slope is reproduced better by calculations depending on trajectories of the second model[2], which leads to larger reaction times (e.g. $\sim 1.1 \cdot 10^{-21}$s instead of $\sim .3 \cdot 10^{-21}$s for head-on collisions).

For the spectra of positrons, measured under the same experimental conditions, the situation is less satisfactory. In Fig. 2, a common scaling factor .85 has been used to reduce the theoretical probabilities which now was adapted to get agreement with experimental data[4] at 5.9 MeV/u elastic U + U collisions. Due to the large error bars no final conclusions can be drawn from these data but the fall-off with energy seems to be too steep to find an explanation consistent with the electron spectra.

References

1. J.R. Birkelund et al., Phys. Rep. 56 (1979) 107
2. R. Schmidt et al., Nucl. Phys. A311 (1978) 247
3. J. Reinhardt et al., Z. Phys. A303 (1981) 173
4. H. Backe et al., Phys. Rev. Lett. 50 (1983) 1838
5. H. Freiesleben et al., Z. Phys. A292 (1979) 171
6. U. Gollerthan, private communication
7. P. Glässel et al., Phys. Rev. Lett. 43 (1979) 1483

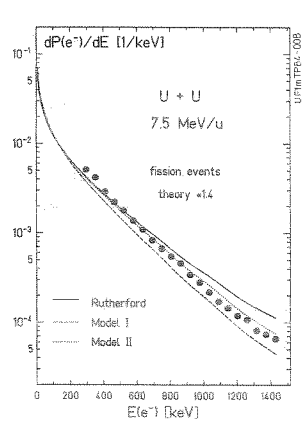


Fig. 1.

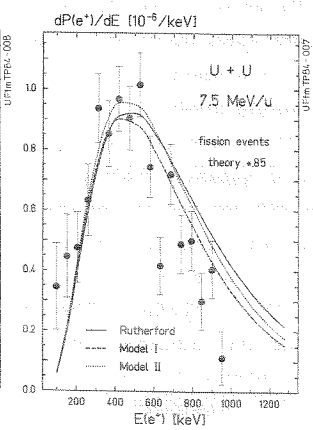


Fig. 2.

Delta Electron Spectra in J-U and Au-U collisions [B]

G. Mehler, T. de Reus, J. Reinhardt, B. Müller, and W. Greiner
Institut für Theoretische Physik der Universität Frankfurt

G. Soff and U. Müller
GSI Darmstadt

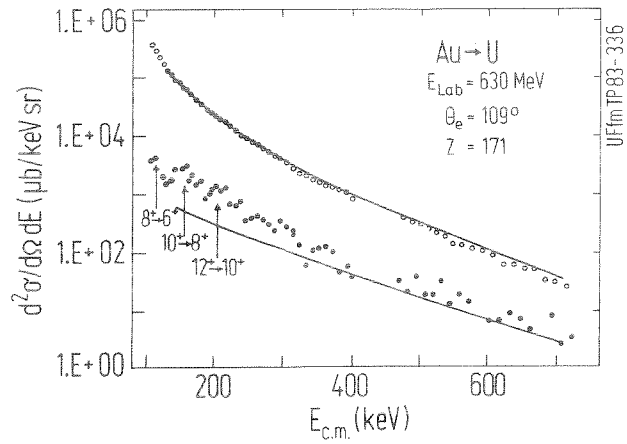
Delta electrons in coincidence with the K-x rays of both collision partners as well as the total emission of δ-electrons have been measured by Koenig, Herath-Banda, Ramayya and collaborators[1]. The superheavy systems Au-U and J-U are considered for bombarding energies well below the Coulomb barrier. We calculated the total number of δ-electrons and the coincident rate with K-x rays of the heavier collision partner by solving a set of coupled differential equations, derived from the time dependent Dirac equation. The monopole approximation for the two-centre potential is applied. We took account of the electron-electron interaction in the framework of the relativistic selfconsistent field method[2].
For the number of δ-electrons in coincidence with a 1s atomic hole the following formula is applied

$$N_{E,1s} = N_{E,1s\sigma} + W\, N_{E,2p\frac{1}{2}\sigma}$$

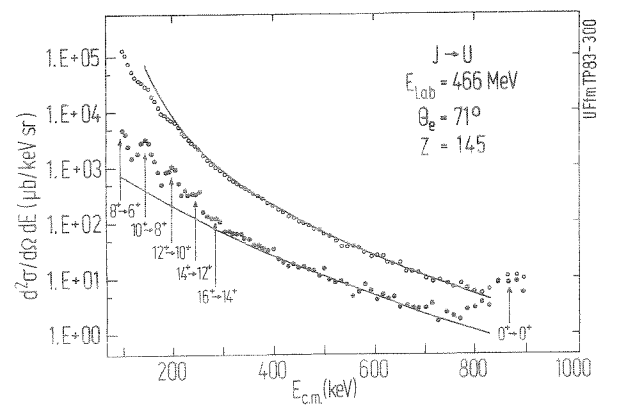
$N_{E,1s\sigma}$ is the number of coincidences of δ-electrons with the energy E with holes in the 1sσ molecular level. $N_{E,2p\frac{1}{2}\sigma}$ is the corresponding term for the $2p\frac{1}{2}\sigma$ level. These expressions are extensively discussed in ref. 3. Due to the effect of vacancy sharing, holes created in the 2pσ molecular state can also lead to a 1s atomic hole in the collision partner with the higher nuclear charge. The second term of the above equation takes account of this by weighing the number of δ-electron coincidences with a $2p\frac{1}{2}\sigma$ molecular level with the vacancy sharing factor[4] W.
In the figures we compare our results for the double differential cross section with the experimental data. Remarkable agreement is achieved for the total and the 1sσ coincident spectra for the slope as well as for the absolute numbers. There is almost no vacancy sharing in the J-U system due to its asymmetry. In the system Au-U vacancy sharing effects raise the coincident rate by 50% for the low energy part (≈150 keV) and 20% for the high energy part of the spectrum. The bumps in the coincidence spectra arise from internal conversions in the U-nucleus. The corresponding nuclear transitions are indicated. We are grateful to W. Koenig and his collaborators for making their data available for us prior to publication.

References

1. W. Koenig, Herath-Banda, Ramayya et al., private communication and to be published
2. T. de Reus, J. Reinhardt, B. Müller, W. Greiner, G. Soff and U. Müller, GSI-83-18, Preprint
3. G. Soff, J. Reinhardt, B. Müller and W. Greiner, Z. Phys. A294, 137 (1980)
4. W. Meyerhof, R. Anholt and T. Saylor, Phys. Rev. A16, 169 (1977)



1. Experimental double differential cross sections for the total δ-electron yield (open circles) and the 1s atomic coincident yield (full circles) versus kinetic electron energy in the system Au+U at E_{Lab} = 630 MeV bombarding energy compared to coupled channel results (full lines).



2. The same as in Fig. 1 for the system J-U at a bombarding energy E_{Lab} = 466 MeV.

Relativistic Wave Packets and Delta-Electron Emission

H.-J. Bär and G. Soff
GSI Darmstadt

Traditionally electron excitation processes involving the continuum are treated in perturbation theory. In many occasions, however, rather sophisticated considerations of intermediate transitions between the free-particle states are necessary. For example, it was demonstrated[1,2] that the continuum-continuum coupling yield a non- negligible contribution to the energy spectrum of δ-electrons emitted in superheavy quasimolecular systems. One elementary approach is to include explicitly the continuum states in a chosen basis set, suitable for a coupled channel description of the investigated problem. As a consequence the resulting coupled channel equations are entangled with an integration over continuum states which technically may be performed only in a discretisized manner. Here one specific free-particle state is assumed to be representative for a given interval Δ of the integration variable. As an alternative we employed wave packets for a proper description of free electron states in superheavy quasimolecules.

Taking the large component G(r) and the small component F(r) of the radial Dirac wavefunction for continuum states we construct the corresponding wave packet components according to

$$u_1(r) = \frac{1}{\sqrt{\Delta E}} \int_{E_0-\Delta E/2}^{E_0+\Delta E/2} G(r)\, dE$$

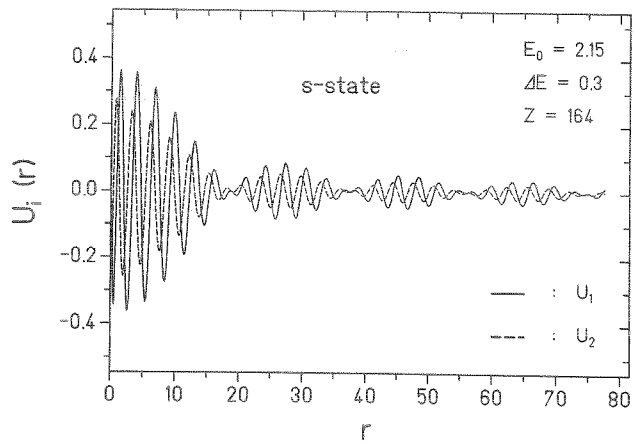
$$u_2(r) = \frac{1}{\sqrt{\Delta E}} \int_{E_0-\Delta E/2}^{E_0+\Delta E/2} F(r)\, dE$$

This implies the normalization

$$\int_0^\infty u_1^2(r) + u_2^2(r)\, dr = 1$$

which formally agrees with the norm of the bound state wavefunctions. E_0 is the total energy of the electron state which is described by $u_1(r)$ and $u_2(r)$. The descrete character of the wave packets allow an easy implementation as part of the basis set in coupled state calculations. Fig. 1 shows the radial components $u_1(r)$ and $u_2(r)$ of relativistic wave packets in natural units versus the radial coordinate r. The s-state (κ=-1) with the total energy E_0 = 2.15 in the atom Z = 164 is considered. The chosen superposition of monochromatic waves leads to a 1/r-envelope[3] of the radial wave packet components $u_1(r)$ and $u_2(r)$. Similar to the bound states the wave packets are normalized to unity. Furthermore we could demonstrate that despite of violating the completeness relation they may be well employed in calculations of electron excitations to the continuum. In the evaluation of ∂/∂R-matrix elements we replaced the final continuum states by a relativistic wave packet. The computed matrix elements differ at most by a fraction 10^{-3} from the coupling strength employed in ref. 1 and 2.

In a second application of relativistic wave packets we could show that radiative transitions from electron states in the negative energy continuum to a bound state imbedded as a resonance in this continuum are completely negligible in connection with the spontaneous positron emission.



References

1. J. Reinhardt, B. Müller, W. Greiner, G. Soff, Phys. Rev. Lett. 43 (1979) 1307
2. G. Soff, J. Reinhardt, B. Müller, W. Greiner, Z. Physik A294 (1980) 137
3. U. Heinz, B. Müller, W. Greiner, Phys. Rev. A23 (1981) 562

δ- Electron Emission in Strong Projectile Fields

G

2.3

D.H.Jakubaßa-Amundsen

Physik-Department, Technische Universität München

Electrons which are emitted from light target atoms (T) in fast collisions with heavy, highly stripped projectiles (P) may be used to investigate the influence of strong perturbing fields. Thereby one may profit by the fact that the spectrum of the ejected electrons at fixed emission angle ϑ_f shows two distinct structures: the classical binary encounter peak at an energy $E_f=2v^2\cdot\cos^2\vartheta_f$, where v is the projectile velocity, and the forward peak at $v^2/2$ if ϑ_f is near zero.

For heavy projectiles ($Z_P \gg Z_T$) we suggest a description of the δ-electrons by means of charge transfer to the projectile continuum states, a theory which is well suited to explain the forward peak[1]. Thereby, in contrast to the first order Born approximation, multiple interactions with the strong projectile field are taken into account. In the framework of the semiclassical impulse approximation[2], the transition amplitude results from the ejection of the target electron into a continuum projectile state $\psi^P_{\vec{q}-\vec{v}}$ with momentum $\vec{q}-\vec{v}$ and a subsequent inelastic scattering on the target field V_T:[3]

$$a_{fi} = -i\int_{-\infty}^{\infty} dt \int d\vec{q}\; \varphi_i^T(\vec{q}) \langle \psi^P_{\vec{k}_f-\vec{v}} | V_T | \psi^P_{\vec{q}-\vec{v}} \rangle \cdot e^{i\vec{q}\vec{b}}\, e^{i(\varepsilon_f - E_i - \frac{v^2}{2} + \vec{q}\vec{v})t}$$

Here, a straight-line path with impact parameter b is used, $\varphi_i^T(\vec{q})$ is the initial electronic state in momentum space, E_i the initial and $\varepsilon_f=(\vec{k}_f-\vec{v})^2/2$ the final electronic energy in the projectile frame.

Fig.1 shows the forward peak for electrons from Ar^{18+}-He collisions where the cross section has been averaged over the experimental angular resolution ($\Delta\vartheta_f=1.7^\circ$) and energy resolution ($\Delta E_f=3.4\%$). Its strong asymmetry results from a discontinuity at $\vec{k}_f=\vec{v}$ which reflects the influence of the target field on the projectile scattering states, dependent on the direction of their momentum.

The forward peak in Ne^{10+}-He collisions is shown in Fig. 2 ($\Delta\vartheta_f=1.4^\circ$, $\Delta E_f=0.7\%$). Although in both cases the data [4,5] are normalised to theory, the experimental shape is well reproduced.

The validity of the above theory extends down to $k_f \gtrsim vZ_T/Z_P$, independent of the emission angle ϑ_f. It fails for $k_f=0$ as the influence of the target field on the ejected electron can then no longer be treated in first order.

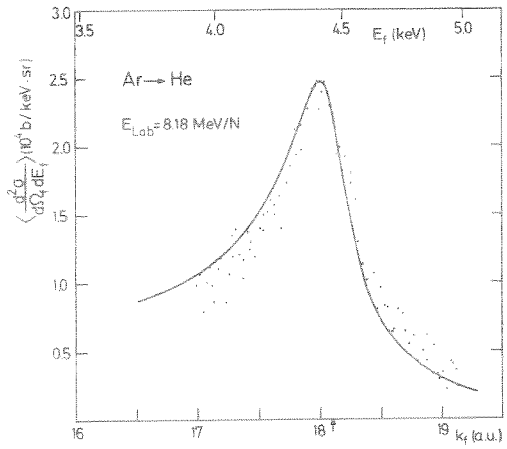


Fig.1: Differential cross section at $\vartheta_f=0^\circ$; full line, present theory; data points from Ref.4.

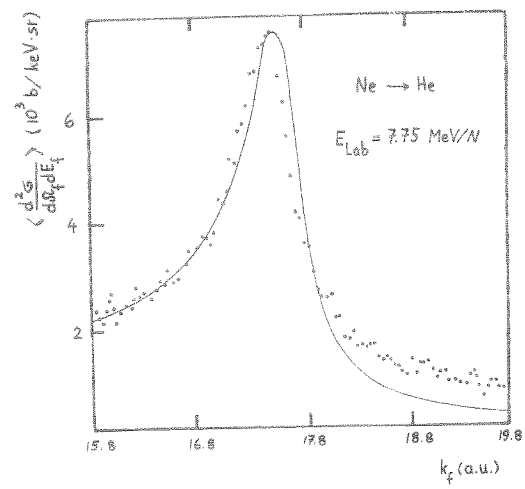


Fig.2: Differential cross section at $\vartheta_f=0^\circ$; full line, present theory; data points from Ref.5.

[1] J.Macek, Phys.Rev.A1, 235 (1970)

[2] J.S.Briggs, J.Phys.B10, 3075 (1977)

[3] D.H.Jakubaßa-Amundsen, J.Phys.B16, 1767 (1983)

[4] M.Breinig et al, Phys.Rev.A25, 3015 (1982)

[5] S.D.Berry et al, Proc.X-ray Conference, Eugene, USA (1982)

Atomic Excitation Processes in Nuclear Reactions with Three-Body Break-Up [B]

U. Müller
GSI Darmstadt
J. Reinhardt, T. de Reus, B. Müller, and W. Greiner
Institut für Theoretische Physik, Universität Frankfurt

In another Report[1] we investigated the influence of modified nuclear trajectories in deep-inelastic heavy-ion reactions leading to fission on atomic excitation processes. We assumed the fission process to happen at internuclear distances large enough[2] that it does not severely disturb processes like δ-electron emission or positron creation. Here we want to investigate the consequences of an immediate ternary break-up of the compound nucleus Z = 184 formed in a U + U collision at 7.5 MeV/u. Reactions of this kind have been observed[3] in lighter collision systems like Kr + Er or Xe + Sn at 12.5 MeV/u.

We restrict our discussion to a particularly simple case: The incoming path of the two nuclei is a Rutherford trajectory of zero angular momentum up to the distance of closest approach. After a time interval T three fragments of equal mass ($1/3\ A_{tot}$) separate from each other in fully symmetric break-up (relative angles $\vartheta = 120^0$ in the centre of mass system). Due to the chosen special geometry this motion is equivalent to the separation of two nuclei with modified kinematical conditions if one restricts attention to the monopole part of the Coulomb potential seen by the electrons. To conserve energy the starting point for the outgoing trajectory, $2\tilde{a}$, has to be larger than 2a. The outgoing motion is described by a Rutherford trajectory with the replacements

$$2a \rightarrow 2\tilde{a} = 16/9\ \sqrt{3}\ a \quad ; \quad Z \rightarrow \tilde{Z} = 2/3\ \sqrt{2\sqrt{3}}\ Z.$$

The nuclear reaction time T is used as a free parameter to match both parts of the trajectory (Fig. 1).

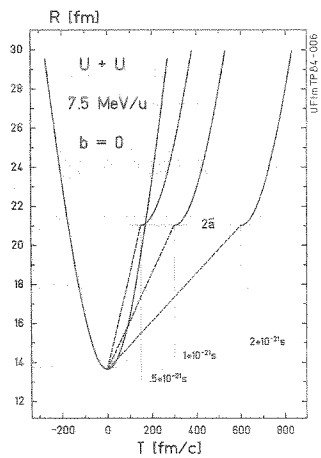


Fig. 1.

in Fig. 2a we compare positron spectra from the two-body break-up (2B) (full lines) and from the ternary break-up (3B) (dashed lines) for three different reaction times T = .5, 1, and 2 • 10^{-21}s. As expected case 2B yields higher positron production probabilities for larger reaction times due to the larger (on the average) spontaneous decay width. For smaller times T, however, case 3B exceeds 2B in the high-energy region due to the high radial velocity $\dot{\tilde{R}} = (2\tilde{a}-2a)/T$.

Fig. 2b shows δ-electron spectra for the same kinematical conditions. Obviously for the reaction times shown spectra from the 2B-case always exceed those from the ternary break-up. However, for even smaller times T we expect more induced excitations for case 3B due to the higher radial velocity.

We have presented a study of atomic excitations in a ternary break-up of Z = 184. We conclude that the change of kinematics has an influence on the excitation processes. However, the model used is very schematic (especially in treating the motion during the break-up process) so that quantitative conclusions should not be drawn.

References

1. U. Müller et al., 'Spectra of δ-Electrons and Positrons ...', Contribution to this Sc. Rep.
2. P. Glässel et al., Phys. Rev. Lett. 43 (1979) 1483
3. P. Glässel et al., Z. Phys. A310 (1983) 189

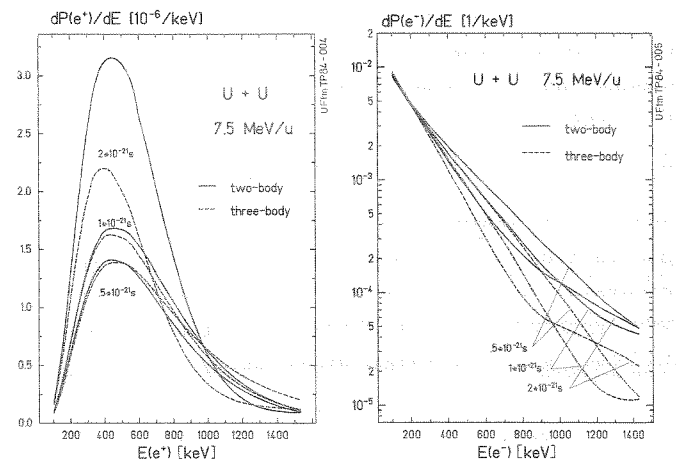


Fig. 2.

K-shell ionization in relativistic heavy-ion collisions [BG]

U. Becker, S.R. Valluri, N. Grün, W. Scheid
Institut für Theoretische Physik der Justus-Liebig-Universität Giessen

In order to study the effect of electromagnetic fields of relativistic projectiles on the ionization of relativistic bound electrons, we calculate ionization probabilities using the semiclassical approximation (SCA). We start with the analytical expression for the ionization probability, derived by Amundsen and Aashamar[1] in the framework of the first order time dependent perturbation theory, and use relativistic Dirac-wave functions for the electrons. In the independent electron approximation one obtains the following probability of ionization of a $1s_{1/2}$-electron by a projectile with charge $Z_p e$ moving on a straight line trajectory with velocity v and impact parameter b (E_f is the final energy of the ionized electron):

$$\frac{dP}{dE_f} = \frac{1}{2j_i+1} \sum_{\mu_i,\mu_f} |a_{fi}|^2 \qquad (1)$$

$$a_{fi} = \frac{i\Gamma Z_p e^2}{\hbar} \int_{-\infty}^{\infty} dt \exp\left(\frac{i}{\hbar}(E_f-E_i)t\right) \langle\psi_f| \frac{1-\beta\alpha_3}{r'} |\psi_i\rangle , \qquad (2)$$

where

$$r' = \left((x-b)^2+y^2+\Gamma^2(z-vt)^2\right)^{1/2}, \quad \beta=\frac{v}{c}, \quad \Gamma=(1-\beta^2)^{-1/2}$$

$$\alpha_3 = \begin{pmatrix} 0 & \sigma_3 \\ \sigma_3 & 0 \end{pmatrix} \quad , \quad \sigma_3 = \begin{pmatrix} 1 & 0 \\ 0 & -1 \end{pmatrix}$$

With a Fourier transformation and a subsequent multipole expansion of the transition operator one gets the following expression for the amplitudes[1]:

$$a_{fi} = \frac{i}{\hbar} \frac{8\pi Z_p e^2}{v} \sum_{\ell,m} i^{\ell-m} \int_0^{\infty} ds \, \frac{s}{s^2-q^2\beta^2} \cdot$$

$$\langle\psi_f| (1-\beta\alpha_3) j_\ell(sr) Y_\ell^m(\hat{r}) |\psi_i\rangle \, B_{\ell m}(b,q,s)$$

$$B_{\ell m} = \Theta(s-q) Y_\ell^m(\cos^{-1} q/s, 0) J_m(b\sqrt{s^2-q^2}) \qquad (3)$$

$$q = (E_f-E_i)/\hbar v$$

In order to calculate the matrix element in Equ.(3) we use the results given by Jakubaßa-Amundsen and Amundsen[2]. The matrix element can be written as

$$\langle\psi_f| (1-\beta\alpha_3) j_\ell(sr) Y_\ell^m(\hat{r}) |\psi_i\rangle = \sum_{i=1}^{3} A_i R_i(s) \quad , \qquad (4)$$

where the A_i depend on the angular momenta and spin quantum numbers and the R_i are the radial integrals, which can be written as a finite sum over hypergeometric functions. The final integral over s is performed numerically.

We have carried out calculations for Ca^{20+} incident on U at a velocity of 0.8 c and an impact parameter b=0. This system we have recently investigated by solving the time-dependent Dirac equation by a finite difference method[3]. Figs.1 and 2 show the probability for the ionization of a $1s_{1/2}$-electron into the $s_{1/2}$- and $p_{3/2}$-continua, respectively, as a function of E_f. The remaining differences between the results of the SCA (full curves) and the direct numerical integration (dotted curves) may have various causes. The SCA is a first order calculation, whereas the finite difference method has numerical errors due to the finiteness of the grid. In the studied example the $\beta\alpha_3/r'$-term of Eq.(2) contributes significantly only to the transition to the $p_{3/2}$-continuum (Fig.2), where it lowers the probability by a factor of 0.7.

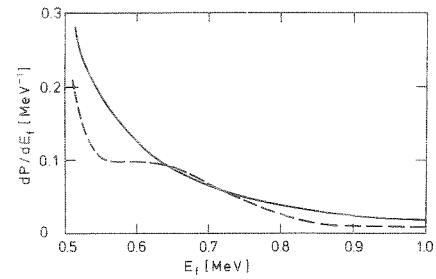


Fig.1: dP/dE_f for the excitation of the $s_{1/2}$-continuum

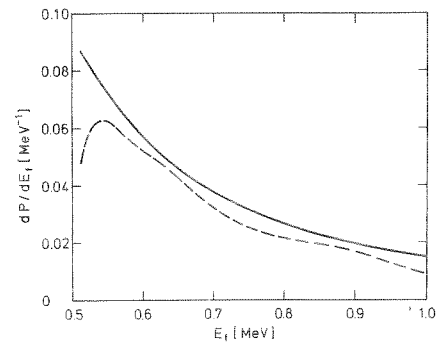


Fig.2: dP/dE_f for the excitation of the $p_{3/2}$-continuum

[1] P.A. Amundsen, K. Aashamar, J.Phys.B 14, 4047 (1981)

[2] D.H. Jakubaßa-Amundsen, P.A. Amundsen, Z.Phys. A 298, 13 (1980)

[3] U. Becker et al., J.Phys.B 16, 1967 (1983)

Relativistic Bound State Wavefunctions in Momentum Space [B]

G. Soff and U. Müller
GSI Darmstadt

P. Schlüter, K.-H. Wietschorke, T. de Reus, G. Mehler, J. Reinhardt, B. Müller and W. Greiner
Institut für Theoretische Physik der Universität Frankfurt

We start from the spatial representation of the relativistic bound state wavefunctions

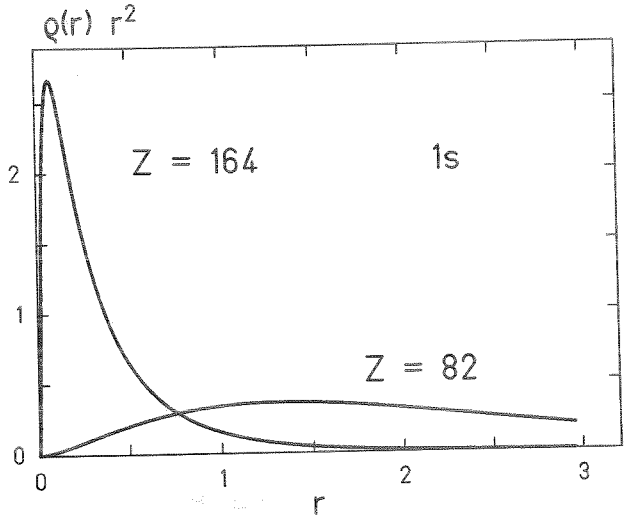
$$\Psi(\vec{r}) = \begin{pmatrix} g(r)\ \Omega^{\mu}_{\kappa}(\theta,\phi) \\ if(r)\ \Omega^{\mu}_{-\kappa}(\theta,\phi) \end{pmatrix}$$

with

$$\Omega^{\mu}_{\kappa} = \sum_{m=\pm\frac{1}{2}} (l,\tfrac{1}{2},j;\mu-m,m)\ Y_l^{\mu-m}(\theta,\phi)\ \chi^m ;$$

$$\chi^{1/2} = \begin{pmatrix}1\\0\end{pmatrix}; \qquad \chi^{-1/2} = \begin{pmatrix}0\\1\end{pmatrix}$$

$\Psi(\vec{r})$ is normalized to unity in the usual manner.



In fig. 1 we plot the radial density ρr^2 of a K-shell electron in the Coulomb field of a lead nucleus (Z = 82). The familiar broad distribution is depicted. The doubling of the nuclear charge causes a striking localization of the K-shell wavefunction within one Compton wavelength of the electron. The maximum of ρr^2 is situated close to the nucleus. The corresponding energy eigenvalues are $E_{1s}(Z=82) = 0.801342$ and $E_{1s}(Z=164) = -0.678260$.

The Fourier transformed wavefunction is defined by

$$\Psi(\vec{p}) = (2\pi)^{-3/2} \int \Psi(\vec{r})\ e^{-ipr}\ d^3r$$

We employ the representation

$$e^{i\vec{p}\vec{r}} = 4\pi \sum_{L=0}^{\infty} i^L\ j_L(pr) \sum_{M=-L}^{L} Y^*_{LM}(\theta,\phi)\ Y_{LM}(\theta',\phi')$$

where the vector $\vec{p}$ has the spherical coordinates p, θ', ϕ'. It follows

$$\Psi(p) = (2/\pi)^{\frac{1}{2}} \int_0^{\infty} r^2 \begin{pmatrix} i^{-l}\, g(r)\, j_l(pr)\, \Omega^{\mu}_{\kappa}(\theta',\phi') \\ i^{-\bar{l}+1}\, f(r)\, j_{\bar{l}}(pr)\, \Omega^{\mu}_{-\kappa}(\theta',\phi') \end{pmatrix} dr$$

We define

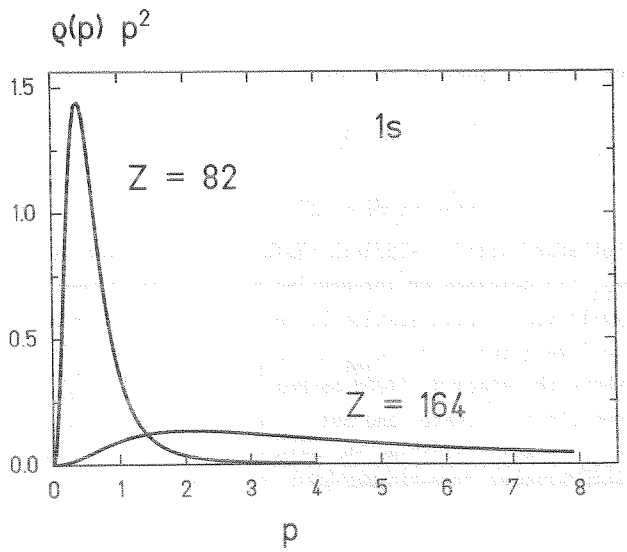
$$g(p) = (2/\pi)^{1/2} \int_0^{\infty} g(r)\, j_l(pr)\, r^2\, dr$$

$$f(p) = (2/\pi)^{1/2} \int_0^{\infty} f(r)\, j_{\bar{l}}(pr)\, r^2\, dr$$

$\bar{l}$ is orbital angular momentum quantum number related to $-\kappa$. The Dirac wavefunctions in momentum space are normalized according to

$$\int_0^{\infty} [g^2(p) + f^2(p)]\, p^2\, dp = 1$$

In fig. 2 the momentum distribution $\rho(p)\, p^2 = (f^2(p) + g^2(p))*p^2$ of 1s-electrons is plotted in natural units. As in fig. 1 the nuclear charges Z = 82 and Z = 164 are considered. The momentum distribution of the K-shell wavefunction in lead is obviously sharply localized within the domain $p < 1$, whereas for the superheavy system Z = 164 rather high momenta components are contained in the considered bound state wavefunction. Even at $p \approx 8$ the momentum density is still considerably large.



The zero-point energy in quantum electrodynamics

G. Plunien, B. Müller, and W. Greiner
Institut für Theoretische Physik, Universität Frankfurt/Main

In quantum field theory the occurrence of divergent zero-point energies is a well-known ambiguity, which one usually removes by a formal subtraction (normal ordering). However, this elimination is not fully satisfying because questions about its physical meaning remain. As an attempt, in order to demonstrate further physical implications of the zero-point energy of quantum fields, we consider the QED vacuum.

The vacuum energy of the electron-positron field in the presence of electromagnetic fields created by arbitrary configurations of external sources, has to be defined as a difference of zero-point energies[1]. If $E_o[A=o]$ and $E_o[A]$ denote the formally divergent vacuum expectation values of the free Dirac-Hamiltonian and of that which includes external fields, respectively, the vacuum energy reads in analogy to the definition of Casimir-energies:

$$E_{vac}[A] = E_o[A] - E_o[A=o] \quad . \tag{1}$$

The vacuum energy is treated as a function of a set of parameters λ, which characterize the configuration of external sources (e.g., λ can determine the geometry or just can measure the field strength). A general expression for the infinitesimal change E_{vac} caused by infinitesimal variation $\delta\lambda$ can be derived from the equivalent local formulation. Using the relation between the symmetric energy-momentum-tensor and the electron propagator

$$\langle o|\delta\Theta^{\mu\nu}(x,\lambda)|o\rangle = \frac{1}{4}\{Tr[\gamma^{\mu}(\partial^{\nu}-\partial'^{\nu})\delta S(x,x',\lambda)] + (\mu\leftrightarrow\nu)\}_{|x'=x} \tag{2}$$

One finally gets in the case of static external fields:

$$\delta E_{vac}(\lambda) = \int d^3x(-i)\, Tr[\gamma^o H_D(\vec{x},\lambda)\, \delta S(\vec{x},\vec{x},\lambda)] - \int d^3x\, \delta A_{\mu}(\vec{x},\lambda)\, J^{\mu}_{vp}(\vec{x},\lambda) \tag{3}$$

For weak, static, electric fields the vacuum energy $E_{vac}(\lambda)$ obtained by integrating eq. (3) describes (virtual) vacuum polarisation-corrections $E_{vp}(\lambda)$ to the Coulomb-interaction: $E_{vac}(\lambda) = E_{vp}(\lambda)$. For values λ_{cr} where the electric field becomes overcritical (e.g.,for one electron-state) one gets a further contribution $E_{res}(\lambda)$ which contains the effect of spontaneous positron emission (first term of eq. (3))and real vacuum polarisation:

$$E_{vac}(\lambda) = E_{res}(\lambda) + E_{vp}(\lambda) \tag{4}$$

The dependence of the vacuum energy on the strength of an external field is illustrated in Fig. 1. It shows E_{vac} as a function of Z for a homogeneously charged sphere. For $Z \lesssim Z_{cr}$ the first order vacuum polarisation dominates the behaviour. But for Z greater than critical values, the contributions from the vacuum decay lead to a sudden lowering by the resonance energies of the corresponding overcritical states.

The role of E_{vac} as an additional interaction potential can be demonstrated if one considers two nuclei as external sources and taking the two-center-distance R as the parameter λ. At large distances the vacuum energy is identical with the Uehling correction to the Coulomb interaction. For superheavy systems like U+U the field becomes overcritical if $R \leq R_{cr}$, thus $E_{vac}(R)$ is reduced by the corresponding energy $E_{res}(R)$. A calculation of E_{vac} for the system U+U considering extended nuclei is shown in Fig. 2.

[1] J. Schwinger, Phys. Rev. 94 (1954) 1362

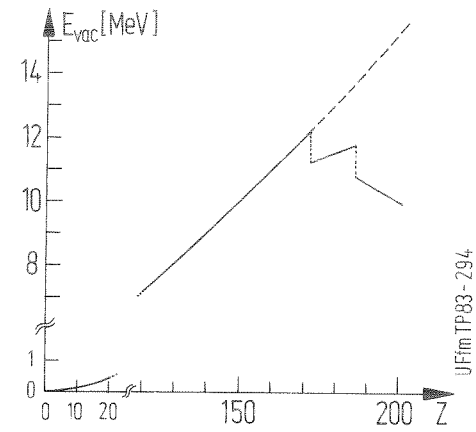


Fig. 1

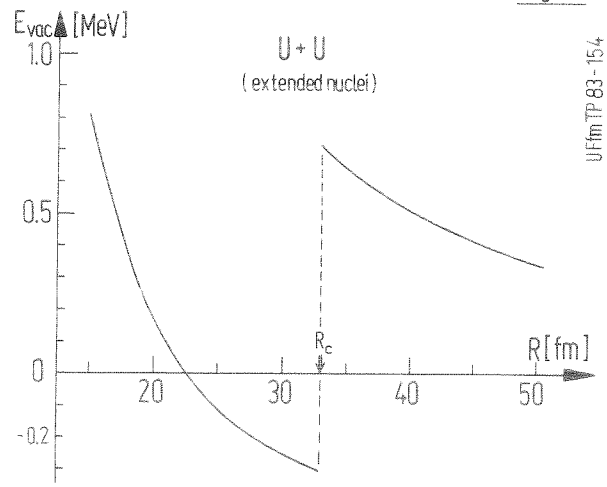


Fig. 2

Bound Electron States in Critical Magnetic Fields B

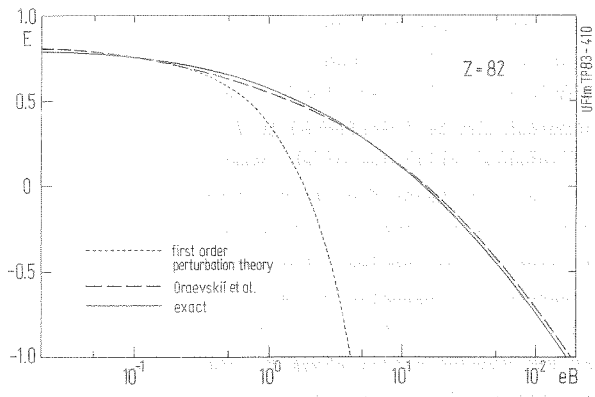
K.-H. Wietschorke, P. Schlüter and W. Greiner
Institut für Theoretische Physik der Universität Frankfurt
and
G. Soff
GSI Darmstadt

We solved the Dirac equation for bound electron states in an electromagnetic potential. Especially we investigated the behaviour of the ground state electron in the combined field generated by the atomic nucleus ($-Z\alpha/r$) and an external homogeneous magnetic field ($B\vec{e}_z$). Our special interest is concerned with the region of strong magnetic fields where first order perturbation theory[2] (anomalous Zeeman effect) may not be applied to obtain correct energy eigenvalues. The principle effect of the magnetic field is to localize the electron density more and more to the axis of rotational symmetry (z-axis). In consequence the charge density slides deeper into the Coulomb potential, which may be partly balanced by an increase of kinetic energy. Together with the interaction energy between the spin and the magnetic field the binding energy will be enhanced to the order of twice the electron rest mass for sufficiently strong fields. In terms of Dirac's electron theory this means that the ground state reaches the negative energy continuum ($E = -1$).

The lack of an analytical solution of the Dirac equation for this type of a non-spherical symmetric potential requires a numerical treatment. Making use of the rotational symmetry and the parity invariance it is possible to reduce the Dirac equation to a coupled set of partial differential equations in two variables. In spherical coordinates the Hamiltonian becomes[1]

$$H = -i\{\alpha_1 \frac{1}{r}\,\partial_\vartheta + \alpha_3 \partial_r\} + \alpha_2\,(\mu/(r\sin\vartheta) + eB/2\,r\sin\vartheta) + \beta - Z\alpha/r.$$

Here μ denotes the z-component of the total angular momentum. To solve the eigenvalue problem we approximated the wave functions in the angle coordinate by a linear combination of B-Splines[3] of variable order. Employing the Galerkin variational procedure we can reduce the problem to a system of ordinary differential equations in the radial coordinate. The application of a multishooting procedure and of a sophisticated matching method leads to a rapidly converging algorithm.



The energy eigenvalue of the ground state in lead (Z=82) is shown in the figure versus the magnetic field strength in natural units. There our results are compared with the energy of first order perturbation theory[2] and the approximation of Oraevskii et al.[4] which is valid for strong magnetic fields. For weak magnetic fields the computed energy eigenvalues agree well with analytical results derived in the framework of first order perturbation theory. For strong magnetic fields good agreement with the data of Oraevskii et al. is achieved. The critical magnetic field strength for spontaneous electron- positron pair production was found to be $B \approx 10^{16}$ G.

References:

1. P. Schlüter, K.-H. Wietschorke and W. Greiner, J. Phys. A16 (1983), 1999-2016
2. M.E. Rose, Relativistische Elektronentheorie, BI, Mannheim, 1971
3. C. de Boor, A Practical Guide to Splines, Springer, New York, 1978
4. V.N. Oraevskii, A.I. Rex and V.B. Semikoz, JETP 45 (1977), 428-435

Molecular Ring Currents from Magnetic Monopoles

M. Kleber

Physik-Department, Technische Universität München

The peculiar properties of magnetic monopoles passing through matter are of general interest. Apart from Cabrera's report[1] of a possible monopole event, the hunting of this interesting particle was, so far, without success. In order to stalk the basic particle of magnetism, Cabrera made use of the fact that magnetically charged particles passing across a wire induce an electric current in that wire. It was our purpose to show[2] how this effect persists in organic ring molecules.

It is well known that the π- electrons on benzene rings are similar in many ways to electrons on simple spatially fixed loops except that angular momentum can be transferred to the benzene ring in integral multiples of $6\hbar$. However, the π-electrons are far from being free to run around the benzene ring. These electrons, instead, will hop from atom to atom. It was unclear[3] how hopping will be influenced by a magnetic monopole.

Our calculation[2] showed that the absolute values of the hopping matrix elements remain unchanged, but their relative phases will be modified. We applied Hückel's MO theory to neutral ring molecules with N = 4r + 2 carbon atoms. It was found that a π-electron with initial energy

$$\varepsilon_s(t=-\infty) = \text{const} + 2\beta \cos\left[\frac{2\pi}{N} s\right] \qquad |s| = 0,1,\ldots N$$

(see Fig. 1) will change its energy to

$$\varepsilon_s(t=\infty) = \text{const} + 2\beta \cos\left[\frac{2\pi}{N}\left(s + \frac{2eg}{\hbar c}\right)\right]$$

whenever a slow magnetic monopole has passed through the ring molecule. Using the minimum Dirac value, $2eg/\hbar c = 1$ it is clear that a slow magnetic monopole will transfer N units of angular momentum $\hbar$ to the ring every time it passes through the ring and, no angular momentum if it misses. Our result is independent from the strength of the hopping matrix elements. The phrase "ring current" is a subject of discussion among chemists but in this context it stands for transfer of angular momentum.

A point magnetic charge is slow with respect to the π-electrons if its velocity satisfies

$$v < b|\beta|/\hbar.$$

Here b is the bond length and -β the energy which binds each carbon atom to its neighbours on either side. For benzene we have b = 1.4 Å and β = -0.8 eV. Adiabatic collisions hence take place at velocities $v < 5.7 \cdot 10^{-4} c$.

If a monopole passes through the center of the ring it will create a ring current of angular momentum $6\hbar$ at all impact velocities. Therefore one expects the cross section for producing this current always to be close to the geometric cross section of the ring. In that respect the situation is similar to (macroscopic) superconducting ring detectors where a knowledge of the monopole's velocity is not needed.

In this context two methods for detecting magnetic monopoles should be considered:

i) detection of ring currents by nuclear magnetic resonance.

ii) detection of ring currents via their optical decay. Here wave functions beyond the MO theory are required.

We note that within the large family of cyclic polyenes, benzene, naphtaline and kekuline ("superbenzene")[4] are candidates for ring currents.

1 B. Cabrera, Phys.Rev.Lett. 48, 1378 (1982)

2 M. Kleber, Z.Physik A314, 251 (1983)

3 S.D. Drell et al. Phys.Rev.Lett. 50, 644 (1983)

4 F. Diederich et al. Angew.Chem.Int.Ed. 17, 372 (1978)

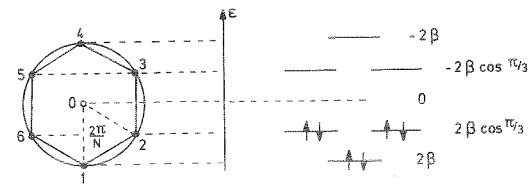


Fig. 1 Orbital energy levels in benzene (N=6)

Relativistic Many-Body Approach to the Photoionization of Cesium

W. R. Johnson and G. Soff
Institut für Theoretische Physik der Universität Frankfurt and
GSI Darmstadt

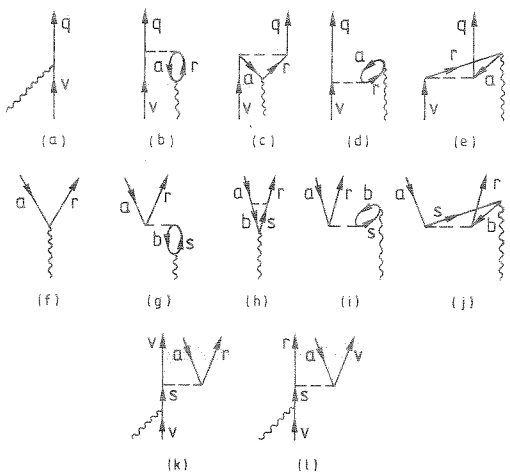
A relativistic many-body technique which includes particle-hole excitations of the atomic core was developed to describe the photoexcitation of alkali atoms. The technique is used to study the photoionization of cesium near threshold. The photoionization of cesium has been of considerable interest. One expects a high degree of spin polarization for photoelectrons produced by circularly polarized light due to the large spin-orbit interaction.

The objective of the present work[1] is to develop a relativistic many-body method to treat both strong spin-orbit effects and correlation effects in open-shell systems. For closed-shell systems the relativistic random-phase approximation (RRPA) has been already successfully applied to understand the interplay of relativistic and correlation effects.

We employ techniques based on many-body perturbation theory. We take our vacuum state to be the N-1 electron ionic core, which is described by self-consistent DF orbitals. Ignoring the effects of core excitation, the photoionization amplitude is described by the diagram in Fig. 1a, where the solid lines represent DF orbitals in the self-consistent field of the core. The first order core polarization corrections are due to the particle-hole excitations described in the diagrams of Fig. 1 b-e. The core excitation diagrams shown in Fig. 1f are in turn subject to the correlation corrections illustrated in Fig. 1 g-l. By iterating the diagrams of Fig. 1 at the photon vertex we arrive at coupled equations, similar to those of the closed-shell RRPA.

In the upper panel of Fig. 2 we compare the predicted energy dependence of the cross section σ given by the present calculation with results of DF calculations, and with the atomic beam measurements of ref. 4. The two DF curves labled DF(L) and DF(V) are the results of calculations ignoring core excitations. The corresponding length and velocity results including core excitation, labled L and V, are found to be in substantially better agreement with each other and with the measured cross section than are the DF results.

The calculated transverse spin polarization P_γ is of particular interest since P_γ is non-zero for unpolarized incident radiation. In summary we have developed a method for incorporating the dominant effects of correlations within a relativistic framework for simple open-shell systems.



References

1. W.R. Johnson and G. Soff, Phys. Rev. Lett. 50, 1361 (1983)
2. U. Heinzmann, J. Kessler, and J. Lorenz, Z. Phys. 240, 42 (1970)
3. G. Baum, M.S. Lubell, and W. Raith, Phys. Rev. A5, 1073 (1973)
4. T.B. Cook, F.B. Dunning, G.W. Foltz, and R.F. Stebbings, Phys. Rev. A15, 1526 (1977)

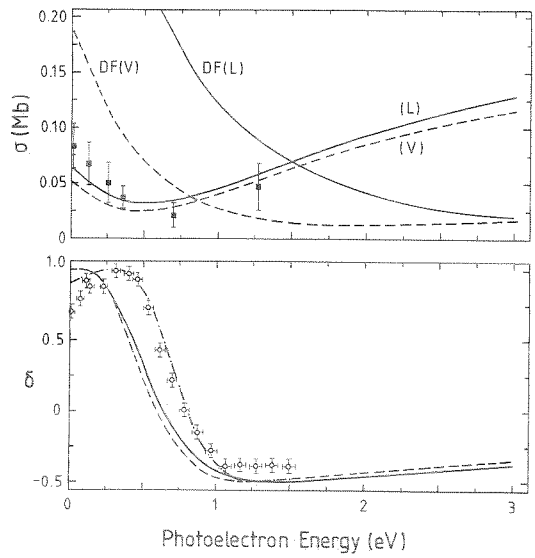


Fig 2. Upper panel: Photoionization cross section for cesium. ⊕: Measurements of Ref. 4. (L), (V): Present calculations including core excitations using length ——, and velocity --- gauges. Lower panel: Spin polarization δ of the total photoionization flux for cesium. ·-·-·: Values inferred from measurements of Ref. 3. ⊕: Measurements of Ref. 2. ——: Present calculations in length gauge and ---: in velocity gauge.

G

Screening Effects in Relativistic Many Body Systems

R.M. Dreizler, E. Engel, E.K.U. Groß and P. Malzacher

Institut für Theoretische Physik

Universität Frankfurt/Main

As a first step towards a consistent inclusion of screening effects in the discussion of heavy atomic scattering systems, we attempt to formulate and solve relativistic density functional models. In view of the complexity of the problem a twopronged approach has been followed.

1.) Derivation of a relativistic extended Thomas-Fermi model on the basis of the Dirac equation including the lowest order electron-electron interaction terms. Using a suitable ansatz for the density operator a density representation of the kinetic energy had been obtained[1] with the aid of the gradient expansion technique. This has been augmented by a discussion of the exchange contribution[2]. First attempts to solve the corresponding variational equations in a relativistic TFDW-model yields a reasonable, but not quite satisfactory description of the groundstates of relativistic atomic systems[3]. Further numerical investigation of these nonlinear differential equations is necessary before a solution with two centre boundary conditions (appropriate to scattering situations) can be attempted.

2.) Derivation of density functional models on the basis of field theory. Following the work of Baker and Pirner[4], who consider a nonrelativistic system of fermions, which move in an external potential and interact via the exchange of scalar mesons, we undertook a reformulation of the functional approach to this field theoretical system, which emphasises the use of gradient expansion techniques in connection with saddle point methods. First steps to derive a density functional model of QED (electrons, positrons in an external potential interacting via the exchange of photons) along the same lines are in progress.

[1] R.M. Dreizler, E.K.U. Groß, Proc. Nato ASI on QED of Strong Fields, ed. W. Greiner, Plenum Publishing Co (1983), p.383

[2] E. Engel, R.M. Dreizler (to be published)

[3] E.K.U. Groß, R.M. Dreizler, Proc. Nato Summer School on Density Functional Methods, Alcabideche, Portugal (to be published Sept. 1984, Plenum Publishing Co)

[4] G.A. Baker, H.J. Pirner, Ann. Phys. 148, 168(1983).

Volume Isotope Shift Calculations for IIa- and IIb-Elements

G. Torbohm, B. Fricke
Fachbereich Physik, Gesamthochschule Kassel

A. Rosén
Chalmers University of Technology, Göteborg

The physics of highly ionized heavy atomic systems is one of the main research projects in atomic physics at GSI. Electronic binding energies in many-electron as well as in one-electron systems are very interesting, both, from the experimental and the theroretical point of view. This can be seen by the large number of research activities at GSI, e.g. concerning the Lamb-shift problem. Another area leading to interesting information on the atom are transition probabilities. From the experimental point of view a large variety of atomic physics experiments can now be performed due to a large number of high accuracy spectrometers available at GSI.

Therefore, we started calculations of the isotope shift of many-electron atomic systems. This is very interesting as it allows to deduce nuclear information, provided electronic information (the wave function) is available. The simplest quantity in this connection is the volume isotope shift ΔE_{VIS} which is proportional to the electron charge density at the nucleus.

In general the volume isotope shift ΔE_{VIS} can be written as a sum of the four integrals:

$$E_{VIS} = \iint d\vec{r}\, d\vec{r}\,' \frac{1}{|\vec{r}-\vec{r}\,'|} \{\rho_{N_1}(\vec{r})\rho_{C_1}(\vec{r}\,') - \rho_{N_1}(\vec{r})\rho_{C_2}(\vec{r}\,') - \rho_{N_2}(\vec{r}\,')\rho_{C_1}(\vec{r}\,') + \rho_{N_2}(\vec{r})\rho_{C_2}(\vec{r}\,')\}$$

where ρ_N is the nuclear charge distribution of the two isotopes N_1 and N_2 and ρ_C the electronic charge distribution of the two electronic configurations C_1 and C_2. Usually a spherical nucleus is assumed which changes the denominator from $|\vec{r}-\vec{r}\,'|$ to $r_>$, this means the larger of the two values $|\vec{r}|$ and $|\vec{r}\,'|$ during the integration. If the electron density at the nucleus is expressed as a polynominal

$$\rho_C = a_0 + a_2 r^2 + a_4 r^4 + \ldots$$

each of the above integrals can be expressed as

$$-\frac{2\pi}{3} Ze^2 a_0 \langle r^2\rangle_N - \frac{\pi}{5} Ze^2 a_2 \langle r^4\rangle_N - \frac{2\pi}{21} Ze^2 a_4 \langle r^6\rangle_N - \ldots$$

If we take the difference of the four integrals we get

$$\Delta E_{IVS} = -\frac{2\pi}{3} Ze^2 \left(\Delta a_0 \Delta\langle r^2\rangle_N + \frac{3}{10} \Delta a_2 \Delta\langle r^4\rangle_N + \frac{1}{7} \Delta a_4 \Delta\langle r^6\rangle_N + \ldots\right)$$

with Δa_0 the difference of the electronic densities in the two configurations at r=0, usually written as $\Delta|\Psi(o)|^2$, and $\Delta\langle r^n\rangle$ the difference of the expectation values of r^n over the nuclear charge distribution of the nuclei. The last expression can be written in several ways. Its simplest form, however, is

$$\Delta E_{VIS} = F \cdot \Delta\langle r^2\rangle_N \cdot K$$

with F the electronic factor

$$F = \frac{2\pi}{3} Ze^2 \Delta|\Psi(o)|^2$$

and K corrects for the higher moments of the nuclear charge distribution.

Being interested in heavy systems we use the multi-configuration relativistic Dirac-Fock method[1] to calculate the electron wave functions of the atoms in specific states.

The alkali-earth elements are characterized by two additional electrons above a closed nobel gas configuration. Therefore, core excitation contributions in the multi-configuration procedure can be disregarded initially. Nevertheless, a large number of low-lying configurations have to be taken into account[2]. For the ground state $ns^2\ ^1S_o$ configuration all J=0 configurations were taken into account which can be constructed from the $ns_{1/2}$, $np_{1/2}$, $np_{3/2}$, $(n-1)d_{3/2}$, and $(n-1)d_{5/2}$ one-electron levels. For the upper $^3P_1$ level of the resonance transition in these elements we introduce all $J=1^-$ configurations which can be constructed from the same one-electron states.

Table 1 shows the results of the F values for the resonance transition of the IIa-elements Mg, Ca, Sr, Ba, and Ra, and the IIb-elements Zn, Cd, and Hg.

[1] J.P. Desclaux, Comp.Phys.Comm. 9, 31 (1975)

[2] This is discussed in some detail for Ba in: B. Fricke, P. Grundevik, I. Lindgreen, G. Olsson, T. Olsson, A. Rosén, and G. Torbohm, Phys.Lett. 97A, 182 (1983)

Table 1
Values of F for the transitions (a) $ns^2\ ^1S_o$-$nsnp\ ^3P_1$, and (b) $ns^2\ ^1S_o$-$nsnp\ ^1P_1$

Z	element	F [GHz/fm^{-2}] (a)	(b)
12	Mg	o,o66	o,o52
2o	Ca	o,155	o,159
38	Sr	0,752	o,771
56	Ba	2,55	2,99
88	Ra	27,7	28,1
3o	Zn	o,987	o,724
48	Cd	4,16	3,15
8o	Hg	5,54	4,6o

Search for an Optimal Basis-Set for Relativistic Molecular Calculations. I.: The H_2^+-Problem

G

H. Hartung, B. Fricke, W.-D. Sepp, D. Kolb

Fachbereich Physik, Gesamthochschule Kassel

The main quantity of a molecular or quasi-molecular many-electron system is the total energy. In general, it cannot be calculated exactly, therefore, an approximative numerical procedure, accurate enough to be comparable to experimental data, must be selected. On the other hand, the most famous theoretical test for any molecular method is the comparison with the analytically solvable H_2^+-problem. As we are interested in scattering systems, with internuclear distances smaller than molecular bond lengths, the methods of quantum chemistry[1] are not quite adequate. Further, the full numerical[2] solution of heavy ion systems is not feasible up to now due to the limited computer capacity. To tackle the molecular problem we use the well known MO-LCAO-DFS model[3] in prolate spheroidal space coordinates. As basis functions we use numerical atomic DFS wave functions centered around the nuclei. In addition, basis functions are used which result from a potential representing the many-electron monopole part of the molecular two-center potential.

As the total energy in this approximation is very sensitive to the choice of basis functions we use the system H_2^+ as a test of quality for different basis sets. To get a feeling for a good representation of the quasi-molecular wave functions in the range of intermediate internuclear distances R we selected the molecular bond length R = 1.o a.u.

In Table 1 eigenvalues for the $1_{\sigma g}$-state are listed. These correspond to the total energy E_T of the H_2^+ ground state

$$E_T = \varepsilon_{1\sigma g} + \frac{1}{R}.$$

In the two-center case only hydrogen wave functions were selected. The three-center case contains additional monopole wave functions. In both cases the convergence to the value of the analytical solution[4] $\varepsilon_{1\sigma g} = 1.45179$ is very slow. This behaviour is due to the weakly bound wave functions having their radial maximum outside the region of relevant electron density, and so their contribution to the inner part of the molecular orbital is very small. Additionally, their oscillatory behaviour gives rise to numerical problems for very large basis sets.

This difficulty can be avoided by using wave functions with a radial maximum in the molecular dimension, however, of varying asymptotic behaviour. The 4-, 6-, and 11-center cases in Table 1 show the progress in convergence. Higher Z wave functions, with a compatible radial maximum to H_2^+ dimensions (2.o a.u.), are used in addition to the minimal basis set. Due to this treatment the accuracy increases rapidly. Thus, the relative accuracy is better than $5 \cdot 1o^{-4}$ for the largest basis set.

In Table 2 the total energies as function of R are given for the 11-center basis set. The accuracy is better than o.o2 eV for all values. Therefore, is should prove to be quite promising to use the strategy described above for obtaining an optimal basis set in an analogous calculation of heavy relativistic systems for which total energy calculations are still scarce.

[1] B.I. Dunlap, J.W.D. Conolly, and J.R. Sabin, J.Chem. Phys. 71 (1979) 3396

[2] L. Laaksonen, P. Pyykkö, and D. Sundholm, Chem.Phys. Lett. 96 (1983) 1

[3] W.-D. Sepp. D. Kolb. H. Hartung, W. Sengler, and B. Fricke, Abstr.XIII ICPEAC, Berlin 1983, p.356

[4] H. Wind, J.Chem.Phys. 42 (1965) 2371

Table 1

H_2^+ ground state eigenvalues

Basis States	no.of centers atomic	monopole	Eigenvalue $-\varepsilon_{1\sigma g}$(a.u.)
2-center basis	2	0	
$2(H_{1s})$			1.28838
$2(H_{1s,2s,2p})$			1.31563
3-center basis	2	1	
$2(H_{1s,2s,2p})+He^{Mon}_{3s}$			1.32181
$2(H_{1s-3d})+He^{Mon}_{3s,3p,3d}$			1.34921
4-center basis	4	0	
$2(H_{1s}+He_{1s})$			1.421o4
$2(H_{1s}+He_{2s})$			1.42677
$2(H_{1s}+He_{1s,2s})$			1.43893
6-center basis	6	0	
$2(H_{1s}+He_{1s,2s,2p}+Li_{2s,2p,3p})$			1.45o45
11-center basis	1o	1	
$2(H_{1s}+He_{1s,2s,2p}+Li_{2s,2p,3p}+Be_{3p}+B_{3d})+He^{Mon}_{2s,2p,3s,3p}$			1.45113
Exact value from the analytic non-relativistic solution[4]			1.45179

Table 2

H_2^+ ground state eigenvalues and total energies E_T for an 11-center basis

R	$-\varepsilon_{1\sigma g}$ (a.u.)	$-\varepsilon_{1\sigma g}$(a.u.) exact	$\Delta(^o/oo)$	$-E_T$(ev)	$-E_T$(eV) exact
1.o	1.45113	1.45179	< o.46	12.276	12.294
1.5	1.24863	1.24899	< o.29	15.836	15.846
2.o	1.1o235	1.1o263	< o.26	16.391	16.399
2.5	o.99368	o.99382	< o.15	16.155	16.159
3.o	o.91o79	o.91o9o	< o.12	15.714	15.717
4.o	o.79588	o.796o9	< o.26	14.854	14.86o
6.o	o.67848	o.67864	< o.24	13.928	13.932
8.o	o.62752	o.62757	< o.1	13.675	13.676

Advantages and Problems of Higher Order Finite-Element-Methods

W. Schulze, D. Kolb, B. Fricke
Fachbereich Physik, Gesamthochschule Kassel

The time-dependent Schrödinger- or Dirac-equation, which describes an ion-atom collision, can be re-written into coupled-channel equations. The channels can be taken to be the adiabatic states of the quasi-molecule and the matrix elements between the channels describe the time dependence. The stationary solutions of the adiabatic quasi-molecular problem, which are very good physically, can be achieved by solving a molecular Dirac-(Hartree)-Fock procedure. Our aim is to get good solutions of this problem by solving the two-dimensional Schrödinger- or Dirac-equation by a Finite-Element-Method.

To get an idea of convergence, accuracy, and possible limitations of Finite-Element-Methods we tested model potentials in rotational symmetric coordinates. Test cases were a cylindrical cavity potential (V=0 inside, V=∞ outside), the Harmonic Oscillator (H.O.), and the Point Coulomb-Potential, where the solutions are known analytically. The potentials were approximated by polynominals which, however, in the Coulomb-case show poor convergence. Then an analytical calculation of the element integrals is needed. The following figure displays the dependence of the relative error on the number of equidistantly spaced nodal points, and the order of elements used.

The asymptotic convergence of the Finite-Element-Method ranges from n^{-1} (n: number of nodal points) for first order elements to n^{-5} for quintic elements (fift order, see ref.2). Through extrapolation one expects a relative error of the eigenvalues of $1o^{-6}$ for quintic elements, and 5oo nodal points in the cylindrical-resonator-case, whereas for the H.O. they will have an error of $5\cdot1o^{-6}$. As expected, the equidistant mesh point distribution is the better one for the constant potential. Modifying the mesh point distribution (e.g., square root grid for the H.O.) results in better eigenvalues for the H.O. by a factor 5. However, another problem arises: A rapid increase in non-orthogonality manifests itself in the wide ranges of eigenvalues of the norm matrix. By using equidistant mesh points the highest and lowest values of the norm matrix differed by 3 decades, only, and for the non-equidistant grid the difference ranged up to 14 decades. At present this limits the flexibility in choice of point distributions. We hope to remove these non-orthogonal characteristics by using suitable coordinates (e.g., prolate spheroidal ones in the two-center Coulomb-case)[1] together with orthogonal polynominals as shape functions, according to Galerkin's Idea[2] that shape functions should be as similar as possible to the expected solutions. Accordingly appropriate element integrals for the Coulomb problem are:

$$I = \sum_{n,m,i,j} C_{nmij} \iint W(u,v) \Big\{ \sum_{k=0}^{i} \mathcal{L}_k(u)\mathcal{L}_{i-k}(v) - \sum_{k'=0}^{i-1} \mathcal{L}_{k'}(u)\mathcal{L}_{i-h-1}(v) \Big\} \cdot \Big\{ \sum_{\ell=0}^{j} \mathcal{L}_\ell(u)\mathcal{L}_{j-\ell}(-v) - \sum_{\ell'=0}^{j-1} \mathcal{L}_{\ell'}(u)\mathcal{L}_{j-\ell'-1}(-v) \Big\} e^{-(u+v)}\, du\,dv$$

where

$u = \frac{1}{2}(\cosh\eta + \cos\theta)$

$v = \frac{1}{2}(\cosh\eta - \cos\theta)$ (η,θ: Prolate Spheroidal Coordinates)

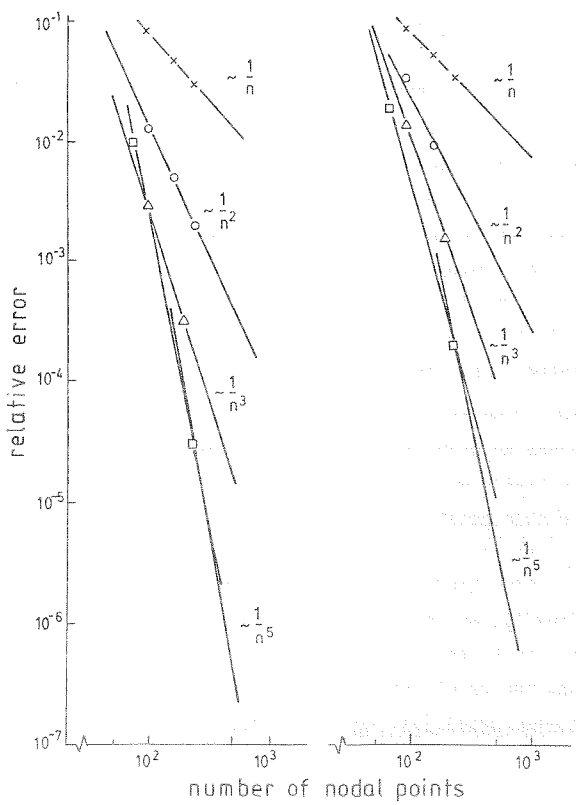
$$W(u,v) = \frac{1}{\sqrt{r_k^2 + 4v^2}} + \frac{1}{\sqrt{r_k^2 + 4u^2}} \qquad \text{(Coulomb-Term)}$$

$\mathcal{L}_i(x)$: Laguerre-polynominals

This treatment is expected to be superior to the commonly used powers of x,y. Extensions to two-center elements, and relativistic applications, after proper coordinate transformations, are in progress.

[1] W. Schulze and D. Kolb, GSI-Scientific Report 1981

[2] G. Strang, G.J. Fix, An Analysis of the Finite-Element-Method 1973, by Prehtice Hall Inc., Englewood Cliffs, N.Y.



A Fast Solution of the Two-Dimensional Poisson-Equation for Di-Atomic Molecules

W. Sengler, D. Kolb, B. Fricke
Fachbereich Physik, Gesamthochschule Kassel

In every numerical procedure, to calculate atomic or molecular systems in a self-consistent way, the problem of calculating the potential V of a given charge density ρ arises. The numerical solution of the Poisson-equation

$$\Delta V = 4\pi\rho$$

is trivial in one dimension (atomic case). However, already for the two-dimensional case (di-atomic molecule) the solution is non-trivial. The very simple treatment - the Mulliken population analysis - reducing the two-dimensional problem to a one-dimensional one, is usable only up to an accuracy of $1o^{-2}$ in the potential. Therefore, we developed a fast numerical procedure to solve the problem with an accuracy of $\lesssim 1o^{-5}$ in the potential and $\lesssim 1o^{-6}$ in the total energy.

The Poisson-equation in elliptic hyperbolic coordinates reads:

$$\frac{\partial^2\phi}{\partial\eta^2} + \cosh\eta\,\frac{\partial\phi}{\partial\eta} + \frac{\partial^2\phi}{\partial\theta^2} + \cos\theta\,\frac{\partial\phi}{\partial\theta} = -a^2(\sinh^2\eta+\sin^2\theta)\cdot 4\pi\rho$$

By discretisation we reduce this equation to an algebraic problem. This can be solved efficiently by matrix algorithms[1]. In order to optimize the distribution of the η,θ-surfaces in each space we introduce new coordinates x_a, y_a. The transformations are

$$x_a = \cosh\eta \qquad 1 \lesssim x_a \lesssim \infty$$

$$y_a = \cos\theta \qquad -1 \lesssim y_a \lesssim 1$$

$$x_a = D\cdot x_n - E x_n e^{-F x_n} + 1 \qquad x_n = 0,\infty$$

$$y_a = B\left(1/5 - \frac{1}{1+e^{\,y_n/R}}\right) \qquad y_n = -1,1$$

when B, R, D, E, and F are free parameters.

This transformation results in a large number of grid points in the vincinity of the nuclei and only a few grid points in the outer domain which in an actual calculation is cut off at about 3o a.u. As out there the potential changes slowly into a $\frac{1}{r}$ potential, it can be treated analytically. The contour diagrams of the potential in the coordinates x_n, y_n, and in cylindrical coordinates are shown in Figs. 1 and 2.

However, the most important increase in accuracy was obtained by using the following iteration procedure:

1. Initially we calculate the potential by solving the Poisson-equation described above: $\rho_0 \rightarrow V_1$.
2. We then calculate the charge density of the potential by using higher order differentiation: $V_1 \rightarrow \rho_1$.
3. Finally, we define a difference charge density: $(\rho_0-\rho_1)$ and solve the P.E. again: $(\rho_0-\rho_1) \rightarrow \delta V_1$.
4. Now the resulting potential δV_1 is added to the former potential: $V_2 = V_1 + \delta V_1$.

The iteration procedure is completed when no further increase in accuracy occurs. Usually two iterations seem to be sufficient. Due to this iterative procedure we gain two orders of magnitude in the accuracy of the potential. This program was tested with numerical charge density of well known potentials, e.g. Mulliken charge densities. The results of our tests for Ni^{2+}-Ni^{2+} are shown in Fig.3 for 1.4 a.u. distance. We obtained similar results for systems like Xe^{2+}-Xe^{2+}, Pb^{2+}-Pb^{2+} at distances between o.16 and 2.4 a.u.

[1] P.N. Swarztrauber, and R.A. Sweet, ACM Trans.Math. Software 5, 352 (1979)

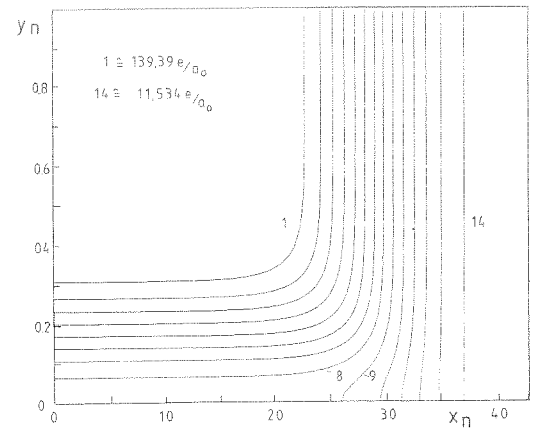


Fig.1: Linear contour diagram of the potential in coordinates x_n, y_n.

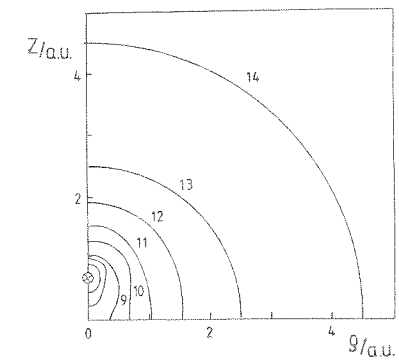


Fig.2: Linear contour diagram of the potential in cylindrical coordinates ρ, Z.

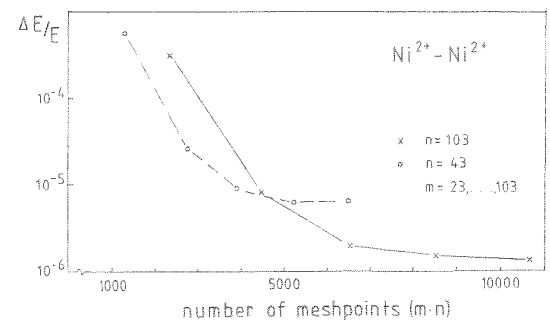


Fig.3: error-dependence of total energy on number of mesh points.

Exact HF-calculations of symmetry violation in heavy atoms

A. Schäfer, B. Müller, and W. Greiner
Institut für Theoretische Physik, Universität Frankfurt/Main

In the last years several predictions of symmetry-violating effects have been made by field-theoretical models. The most famous is the P-violation described by the Glashow-Salam-Weinberg model[1]. It is a general feature of these effects to be enhanced in high Z systems. We developed a general scheme to calculate them by solving the exact, symmetry-breaking Dirac-equation. In what follows we will demonstrate our method for the case of parity violation in Cs due to the neutral-currents.

From the Glashow-Salam-Weinberg model we derive the Hamiltonian:

$$\hat{H}\,\psi = \{\vec{\alpha}\cdot\vec{p}+\beta m+V_{cb}(r)+\rho(r)\gamma_5\}\psi \quad . \tag{1}$$

Here $\rho(r)$ is a linear combination of the density distribution of the protons, $\rho_p(r)$ and neutrons, $\rho_n(r)$ inside the nucleus.

$$\rho_p(r) = -\frac{G}{\sqrt{2}}(c_{1o}\,\rho_p(r) + C_{1n}\rho_n(r)) \tag{2}$$

with the constants G, $C_{1p} = \frac{1}{2} - 2\sin^2\vartheta_w$, $C_{1n} = -\frac{1}{2}$.

$V_{cb}(r)$ is calculated from the charge distribution. The angular momentum operator still commutes with $\hat{H}$ which allows for the ansatz [$(g_\kappa, g_{-\kappa}, f_\kappa, f_{-\kappa})$ =:F is real]

$$\psi(x) = \frac{1}{r}\begin{pmatrix} ig_\kappa(r)\,\chi^M_\kappa(\vartheta,\varphi) - g_{-\kappa}(r)\,\chi^M_{-\kappa}(\vartheta,\varphi) \\ f_\kappa(r)\,\chi^M_{-\kappa}(\vartheta,\varphi) - if_{-\kappa}(r)\,\chi^M_\kappa(\vartheta,\varphi) \end{pmatrix} \tag{3}$$

We take into account the electro-magnetic electron-electron-interaction as well as the parity violating electron-electron-interaction due to neutral currents.

The preliminary results agree quite well with the experiment[2]. The advantages of our scheme as compared to other calculations are:

1. We solve the exact equations instead of doing perturbation theory;
2. Given a linear Hamiltonian we are able to calculate any kind of symmetry-breaking effect, even if the additional interaction is not restricted to a small domain (e.g. the parity violating electron-electron-interaction);
3. Higher order calculations are highly facilitated because our approach contains an implicit summation of an infinite series of perturbative diagrams.

[1] Reviewed in Atomic Physics 7, Plenum Press (1981) by C. Bouchiat and E.P. Commins

[2] C. Bouchiat and C.A. Piketty, Phys. Lett. 128B (1983) 73

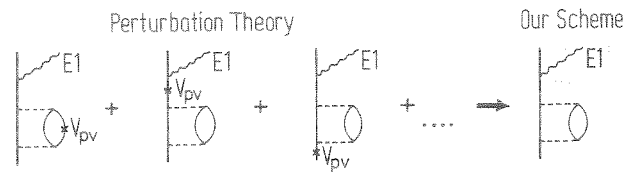


Fig. 1: The reduction of the number of graphs appearing in higher order calculations.

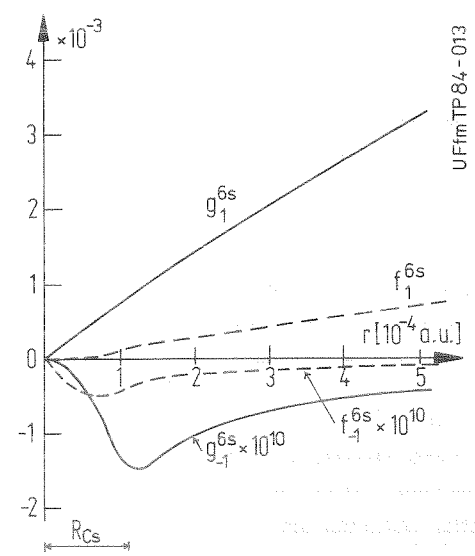


Fig. 2: The g_1 and g_{-1} components of the 6_s-state near to the origin.
(R_{cs} = radius of the cesium nucleus)

Bound State Solutions of the Klein-Gordon Equation for Strong Potentials

W. Fleischer and G. Soff
GSI Darmstadt

We explicitly construct normalized solutions of the Klein-Gordon equation for various types of attractive potentials. Special emphasis was laid on the determination of critical potential strengths, i.e. the onset of spontaneous pair creation of spin-0 particles. In the vicinity of these critical values the single-particle interpretation breaks down.
As example we consider here the solution of the radial Klein-Gordon equation

$$\left[\frac{d^2}{dr^2} - \frac{l(l+1)}{r^2} + k^2 \right] u(r) = 0$$

with $k^2 = (E - V(r))^2 - 1$ for a spherical symmetric exponential potential[2]

$$V(r) = -Z\alpha \exp(-r/a)$$

The separation ansatz $u(r) = \exp\{r/(2a)\}\, w(t)$ and the substitution $t = 2iZ\alpha a \exp(-r/a)$ leads to the solution

$$u(r) = N \exp\{r/(2a)\}\, M_{\lambda,\mu}(2iZ\alpha a \exp(-r/a))$$

with

$$M_{\lambda,\mu}(t) = e^{-t/2}\, t^{\frac{1}{2}+\mu}\, {}_1F_1(\tfrac{1}{2}+\mu-\lambda, 1+2\mu; t)\ ,$$
$$\lambda = -iEa \text{ and } \mu = (1-E^2)^{\frac{1}{2}}\, a.$$

The bound-state spectrum follows from the requirement that $u(r)$ vanishes at $r = 0$, which yields

$${}_1F_1(\tfrac{1}{2}+\mu-\lambda, 1+2\mu; 2iZ\alpha a) = 0$$

This implicit equation determines the energy eigenvalues for s-states. The normalization factor N is computed numerically according to the condition

$$\int_0^\infty \rho(r)\, r^2\, dr = \pm 1$$

with the radial density $\rho(r)\, r^2 = (E - V(r))\, u^2(r)$.
The calculated energy eigenvalues E of a pion in an exponential potential are plotted in fig. 1 versus the coupling strength parameter Z. Only the strongest bound s-state is considered. The fall-off constant was fixed to a = 0.2 in natural units. We obtained $Z_{cr} \approx 2158$. The occurence of the antiparticle bound state thus is directly correlated with the range of the interaction[1]. In fig. 2 we show the radial density ρr^2 for the critical value Z = 2158. ρr^2 for the antiparticle bound state is displayed by the dashed line[3]. The corresponding energy eigenvalues are given explicitly.

References

1) L.I. Schiff, H. Snyder, J. Weinberg, Phys. Rev. 57 (1940) 315
2) M. Bawin, J.P. Lavine, Nuovo Cim. 23A (1974) 311
3) W. Fleischer, G. Soff, GSI-Preprint

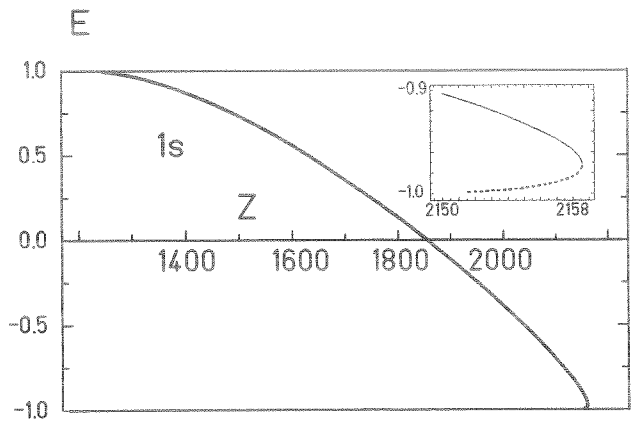


Fig. 1: The energy eigenvalue of a pion in an exponential potential versus the coupling strength parameter Z. Also energy eigenvalues E for antiparticle bound states were computed. The insert displays E for $2150 \le Z \le 2158$. The dashed line indicates E for the antiparticle state.

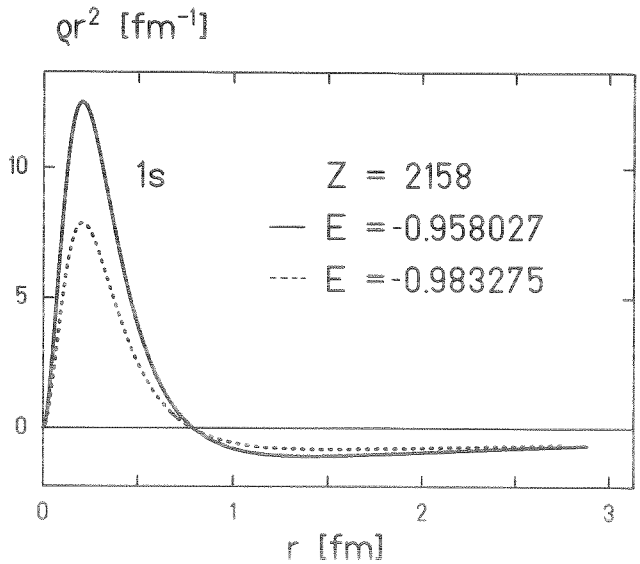


Fig. 2: The radial density ρr^2 of a π-meson, which occupies the 1s-state in an exponential potential. The dashed line denotes ρr^2 for the antiparticle bound state.

3. Radiation Effects

		PAGE
3.1	Radiation Effects in Biological Systems	194
3.2	Radiation Effects in Solids	210

THE EFFECTS OF HEAVY IONS ON PM2 PHAGES [G]

A.M.Kellerer, M.Laßmann, H.Roos, W.-H.Thomas, A.Wenning, F.Zilker · Inst.f.Med.Strahlenkunde, Universität Würzburg

The experimental studies of the effects of heavy ions on the activity of PM2-phages and the production of single and double strand breaks in the phage DNA have been continued. During the past year there has been little beam time with sufficiently energetic heavy ions (E/amu>7MeV) for these experiments. Therefore, and also in view of the importance of the problem, efforts where focussed on the improvement of the strand-break analysis, with special attention to the assessment of small DNA fragments that can be formed in the track cores of heavy ions.

The strand-break analysis is performed by electrophoresis in horizontal agarose slab gels. Three peaks can be separated that contain the native, i.e. undamaged, DNA molecules, the DNA molecules with at least one single strand break but with no double strand breaks, and the DNA molecules with exactly one double strand break. DNA from molecules with several double strand breaks does not appear in a discrete peak; we have, accordingly, sought a technique to collect this fraction of the DNA.

In the earlier approach we used a pure agarose gel matrix followed by a mixed agarose ion exchange cellulose matrix that acts as a barrier for the fast migrating small fragments. However, differences of charge-carrier mobility between the gel and the barrier often caused rupture of the matrix. The ion-exchange barrier was therefore replaced by a membrane that has little influence on charge-carrier mobility but can collect all DNA fragments with at least 20 base pairs. Although the modified technique has proved functional, further work will be required before dose-effect relations for different heavy ions are obtained.

Even without correction for the small fragments that were not accessible by the former technique essential differences in the action of heavy ions and of sparsely ionizing radiations have been identified.

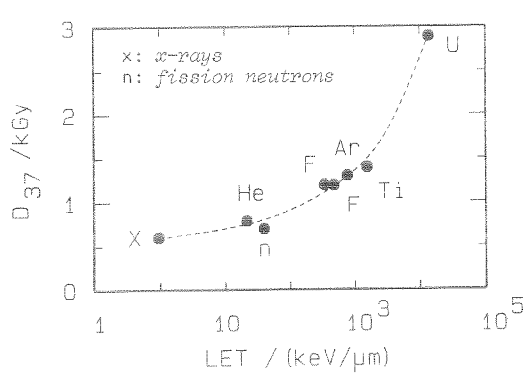
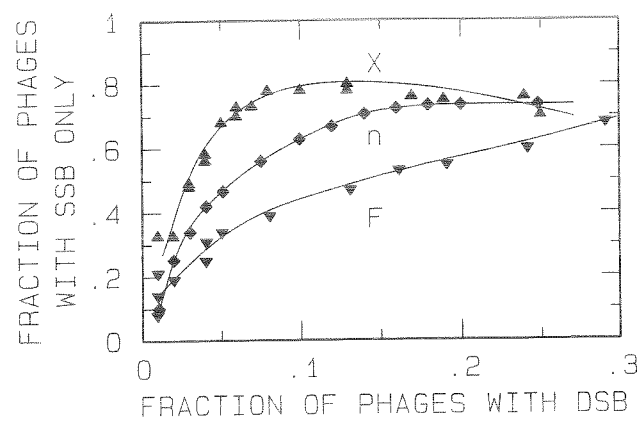


Fig.1 gives the mean inactivation doses for the different types of radiation, i.e. the doses where 37% of the DNA molecules remain in their native form. The increased inactivation doses for the densely ionizing radiations do not imply a reduced effectiveness of these radiations for DNA damage. They are merely due to a saturation effect in those molecules that happen to be close to the core of a heavy ion track. The experimental evidence for an increased effectiveness in the production of double strand breaks by densely ionizing radiation is given in Fig.2. The data in this figure demonstrate a higher rate of double strand breaks at comparable rates of single strand breaks. It is evident that this effect is central to the enhanced biological effectiveness of densely ionizing radiations in mammalian cells, where repair processes can compensate most of the single strand damage but probably only a minor fraction of the double strand damage. Further studies that include the analysis of the small fragments are therefore of particular interest.



To permit computations of microdosimetric parameters and distributions that are relevant to the interpretation of the phage-irradiation experiments a Monte-Carlo program for simulations of the heavy ion tracks has been implemented. The original version of the program was generated by Brenner and Zaider, Columbia University, and Wilson, Battelle North-West. The program, in its present form, permits the simulation of short track segments of heavy ions up to several MeV/amu in water. We are now extrapolating the energy dependence of the ionization-cross sections of the heavy ions to higher energies on the basis of the binary encounter model, averaging over a hydrogen-like velocity distribution of the target electrons according to Rudd, Gregoire and Crooks. As proposed by Paretzke, the cross sections are those of protons, appropriately scaled. With these and some further modifications we expect to simulate the energies that can presently be attained at the Unilac.

Induction of DNA strand breaks by high LET irradiations

M. Larsson, L. Hieber

GSI Darmstadt

Desoxyribonucleic acid, or DNA is known to be the major radiosensitive target in the cell nucleus, in all biological systems. Investigations of radiation damage on isolated DNA in solution have therefore been of great interest in radiobiology.

In order to see whether the ratio of DNA single strand breaks (SSBs) and double strand breaks (DSBs) is proportional to the energy deposition of heavy charged particles, we examined the induction of SSBs and DSBs by heavy ions, accelerated in the UNILAC, with a very high linear energy transfer (LET).

The simian virus 40 (SV40) supercoiled DNA was delivered from Betheseda Laboratories. Samples of 20 µl with a DNA content of 20 µg/ml were irradiated as already described[1]. The yields of undamaged DNA molecules and of molecules with SSBs and DSBs were separated by agarose gel electrophoresis[2] and determined by densitometric measurements using a Zeiss MQ3 spectrophotometer.

SV40 DNA has been irradiated with particles differing in atomic number ($26<Z<92$) whereby the LET alters from 1800 to 16000 keV/µm. The heavier projectiles like ^{238}U showed a higher efficiency in induction of strand breaks than the lighter ones (^{56}Fe, ^{84}Kr). This is shown in table 1, where we have listed the inactivation cross sections, a parameter for the probability of DNA damage. The difference in DNA breakage efficiency between lighter and heavier particles is shown more clearly in Figures 1 and 2, where the yield of undamaged DNA molecules is plotted as a function of absorbed dose at various energies.

Hitherto, most investigations by others have covered only a LET range up to about 1000 keV/µm. From these experiments an increase of the inactivation cross section up to an LET of 100-200 keV/µm and after that a plateau was propagated. In contrast, our experiments showed a variation in the inactivation cross sections even at higher LET values.

Similar observations are known from other biological endpoints either inactivation of mammalian[1] and yeast[3] cells or chromosomal[4] aberrations. To support the trend presented here, further experiments are under way.

Table 1

Inactivation cross sections and LET values for DNA SV40 after exposure to heavy charged particles. For all energies except for ^{238}U 1.2 MeV/u [5] LET values have been calculated using ref. [6].

Ion	E_{target} (MeV/u)	LET (keV/µm)	Inactivation cross section (μm^2) SSB	DSB
^{238}U	12.6	14.600	19.46	1.43
^{238}U	7.3	16.000	17.43	0.93
^{238}U	1.2	12.800	0.41	-
^{56}Fe	16.4	1.820	0.67	0.057
^{56}Fe	12.7	2.130	0.68	0.057
^{56}Fe	6.5	2.900	0.66	0.054
^{84}Kr	15.0	3.400	1.60	0.043
^{84}Kr	13.0	3.850	1.38	0.041
^{84}Kr	4.9	5.200	0.33	0.004

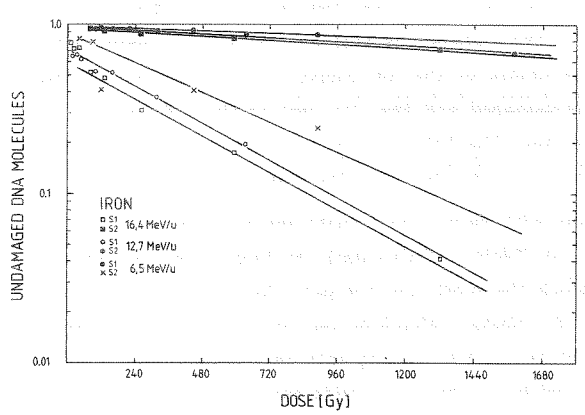


Fig. 1: Undamaged DNA SV40 versus absorbed dose.
S1=DNA without any breaks,
S2=DNA without DSBs

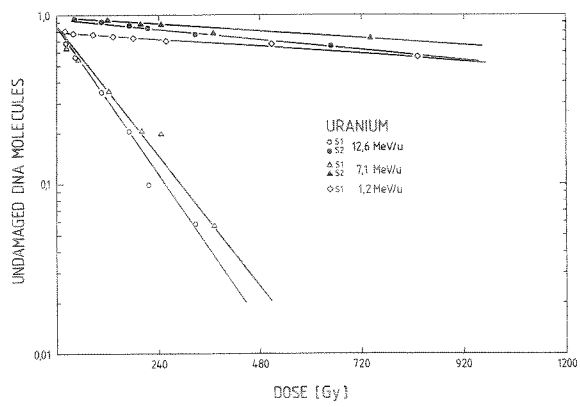


Fig. 2: Undamaged DNA SV40 versus absorbed dose,
S1=DNA without any breaks,
S2=DNA without DSBs.

[1] G. Kraft et al., Proceeding of the 8th Conference on Microdosimetry, Jülich, 1982

[2] R. Roots et al., Biochem. Bioph. Res. Comm. 1981

[3] F. Schöpfer et al., Rad. Res. 82, 235-243, 1980

[4] W. Müller, this report

[5] H. Geissel GSI-Report, 1982-12.

[6] F. Hubert et al., Range and stopping tables, 1980

DNA Strand Breaks in Mammalian Cells Exposed to Low-energetic Heavy Ions

B. Rydberg, GWI Uppsala

The DNA unwinding method[1] was used to estimate DNA strand breakage in V79 cells. The method is based on measurements of the rate of unwinding of the DNA double helix in weak alkaline solutions, where breaks in DNA serve as starting points for the unwinding process. Experiments were carried out to see if the breaks were clustered on the DNA molecule. This was done by comparison of the unwinding rates in two different alkaline solutions (A and B)[2] which for widely separated breaks, in a standard treatment time of 30 min, give rise to MW = 10^8 and MW = 10^9 daltons respectively of single-stranded DNA per break. The results presented in Fig. 1 show that the unwinding of DNA for cells exposed to 0,2 MeV/u Pb-ions were not much different in solution A and B (in contrast to X-ray-exposed cells). This probably means that the breaks are clustered, with a distance between breaks within the clusters of less than MW = 10^8 daltons. A simple interpretation is that only the DNA present within the penumbra of the ion tracks (r = 0,04 μm for 0.2 MeV/u Pb) is damaged and that the rest of the DNA is unaffected. The total number of breaks in the clusters cannot be estimated from this data.

Results with various ions (with the alkali B solution) are shown in Table 1. Particularly striking is the low efficiency by which the most low-energetic ions produce increased DNA unwinding. Calculated per unit dose (in Gy) these ions produce an unwinding rate that is only 1/2000 of that produced by X-rays. The difference in unwinding induction between the various ions in Table 1 is larger than the difference in cell-killing. However, if the repair taking place in 4 hr at 37°C is taken into account, the remaining unwinding rate in alkali B correlates well with cell-killing (shown by the relatively constant value in the last column in Table 1). Such a correlation has previously been shown[3] for ionizing radiation in the LET-range of 1-270 keV/μm, and is here extended to higher LET and various penumbra radii. In view of the clustering effect, the relevance of this observation remains uncertain.

[1] B. Rydberg, Radiat. Res. 61, 274-287 (1975)
[2] B. Rydberg, FEBS Lett. 54, 196-200 (1975)
[3] R. Roots et al., Radiat. Res. 78, 38-49 (1979)

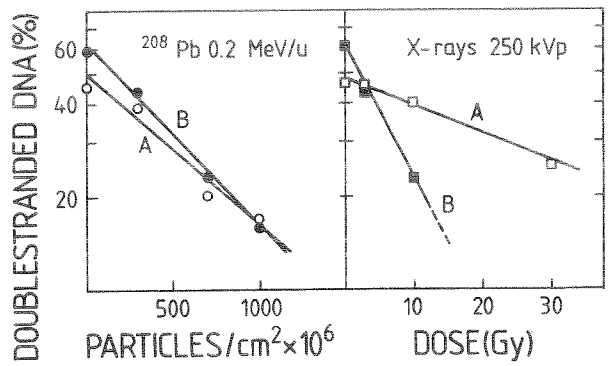


Fig. 1: The amount of DNA remaining doublestranded after 30 min treatment in alkali solution A and B (see text) versus dose of Pb-ions or X-rays.

Inactivation cross sections for spores of Bacillus subtilis.

M. Schäfer, R. Facius, H. Bücker

DFVLR, Institut für Flugmedizin, Köln

In our experiments we use spores of Bacillus subtilis to investigate the radiobiological effects of heavy ions as a function of their energy and atomic number. Monolayers of spores on glass supports are irradiated a in dry state and the surviving fraction is measured as a function of the particle fluence. Within the experimental errors these survival curves are exponential and their slope, which characterizes the effectiveness of the particles, is interpreted as a formal inactivation cross section. These cross sections are to be compared with experimental results, where the inactivation probability of single ions is measured as a function of the radial distance from the particle's path[1].

In an intermediate energy range, where the effective charge of the heavy ions is still well below its maximum, the atomic number, we found a single linear dependence of the inactivation cross sections on only the square of the effectice charge for all ions in this energy range[2]. Further experiments in this energy range did confirm this finding.

For a given ion the cross sections rise to a particle specific maximum with increasing energy and decrease gradually above that most efficient energy, which again is particle dependent. Only for the highest atomic numbers this decrease appears to be much more abrupt.

Two experiments with Xenon and Lead ions at 1.4 Mev/u primary energy were performed to investigate the radiobiological effectiveness in the lower energy range. Different hostaphan absorbers were used to achieve these lower energies. The preliminary results are shown in Fig. 1. It clearly demonstrates that the cross sections reach a minimum with decreasing energy. For energies below that minimal effective energy the cross sections surprisingly increase again, although the energy loss of the ions continues to decrease rapidly. Also in terms of radial dose or the penumbra radius[3] of the secondary electrons this increase is opposite to their energy beheaviour and can therefore not be explained by them. Again it appears that also in this energy range another reaction mechanism becomes effective.

[1] M. Schäfer, R. Facius, H. Bücker, in: Radiation Protection, Proc. 8th Symp. on Microdosimetry, J. Booz, H.G. Ebert, eds., p. 755-764, 1982

[2] M. Schäfer, R. Facius, H. Bücker, GSI Report 1981, GSI 82-1, p. 183

[3] J. Kiefer et al., Adv. Space Res. 3(No. 8/I), 1983, p. 115-125

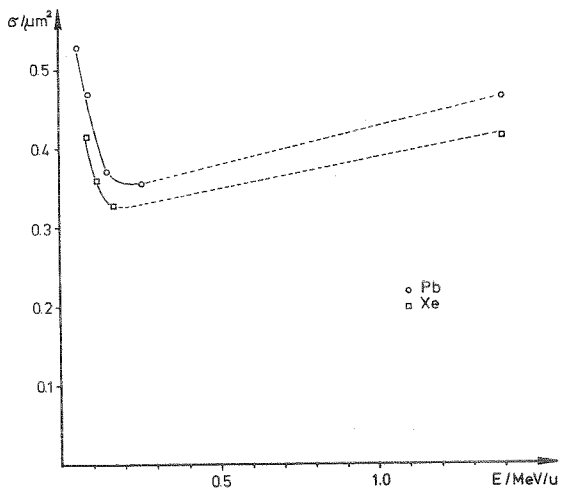


Fig. 1 Inactivation cross sections as the function of the specific energy

Heavy ion effects on B. subtilis spores: Inactivation, repair and mutation induction [G]

K. Baltschukat[+], H. Bücker[*], R. Facius[*], G. Horneck[*], M. Schäfer[*]
[+] Universität Frankfurt/Main, [*] DFVLR - Flugmedizin, Köln 90

The heavy ion irradiation experiments with bacterial spores are extended to various repair deficient and auxotrophic B. subtilis strains. The aim of this study is to test the importance of genetically determined repair processes and the induction of mutations, which might primarily be related to the missrepair of radiation induced DNA-damages.

After irradiation, survival was determined as colony forming ability. Differences in the inactivation of the five bacterial strains give a measure of the reparability of lethal damages. Mutation induction after heavy ion irradiation was investigated by a forward mutation (resistance to 150 µg/ml sodium azide) and the reversion of an auxotrophic marker (hisB101). Designation of the B. subtilis strains, together with their repair deficienies and auxotrophic markers, are listed in table 1.

We are now able to present some first results of heavy ion irradiation experiments: Survival curves from an experiment with Xe-ions of 3.4 MeV/u are shown in fig. 1. The repair deficient strains were considerably more sensitive than the wild type strain. In addition the mutation frequency of the irradiated spores was increased. However, three experiments with very low particle energies (Fe-, Xe- and Pb-ions of about 0.3 MeV/u) show neither a difference in inactivation of the five bacterial strains nor any induction of mutations.

These preliminary results indicate the role of low LET δ-rays in the biological action of heavy ions, as mentioned by other authors[1]. An extension of the experiments to other ions and particle energies is in preparation.

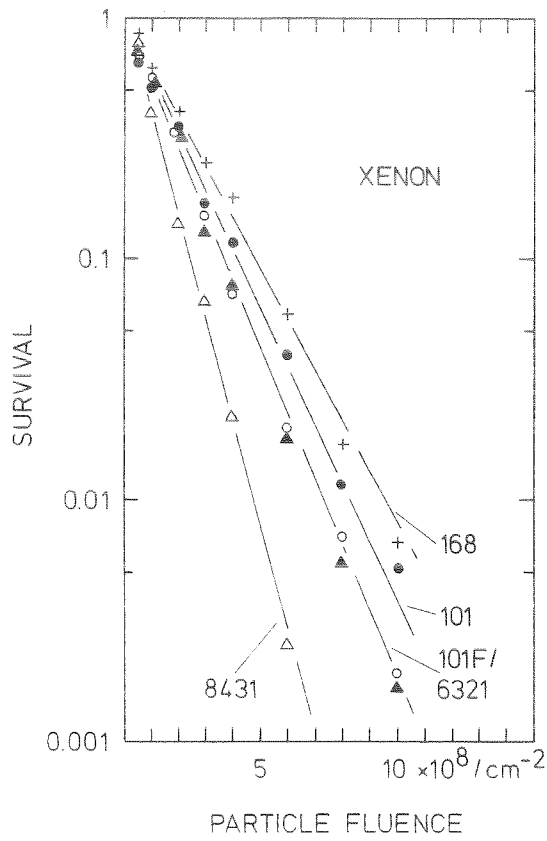


Fig. 1: Survival of various repair deficient B. subtilis strains after irradiation with Xe-ions of 3.4 MeV/u

genetic marker	strain				
	168	HA 101	HA 101F	TKJ 6321	TKJ 8431
uvr	+	+	+	–	–
ssp-1	+	+	+	–	–
rec A1	+	+	+	+	–
pol A1	+	+	–	–	+
his	+	–	–	–	–
met	+	–	–	–	–
leu	+	–	–	+	+
lys	+	+	+	+	–
thy	+	+	+	+	–

Tab. 1: Genetic markers of the B. subtilis strains used

[1] F.Schöpfer et al., Radiat.Res. 92, 30, 1982

The inactivation of dry yeast cells by protons in the energy range below 2 MeV

G

M. Kost, E. Schneider, J. Kiefer, J. Günzl, E. Huttel, P. Keiner
Strahlenzentrum, Universität Gießen

The analysis of the results of heavy ion experiments with different cellular systems lead to the conclusion that the δ-electron - penumbra around the track core of the heavy ion plays an important role in the inactivation of the cells. Low energy ions produce only short range electrons. Schöpfer et al[1] reported inactivation cross sections from survival experiments with dry yeast cells after exposure to different ions of 1.4 MeV/u in dependence of linear energy transfer (LET). To extend the LET range to lower values and to obtain more information about the interaction of lighter particles with short ranges experiments with protons were started. Their properties are advantageous in this respect: they are low Z particles with comparatively low LET; the δ-electron penumbra is neglegible and they have a short range with a sharp Bragg peak.

Diploid wild type yeast cells were deposited on membrane filters on a circular area of 1 cm diameter and carefully dried[1]. After exposure the cells were resuspended in water, diluted and plated on YEPD agar. From the survival curves obtained inactivation cross sections were calculated.

The protons were produced in a 2 MeV-Tandem accelerator (Giessen Polarization Facility); the energy was stepwise reduced by aluminum foils upstream of an analysing bending magnet. The particle fluence was determined by means of a faraday cup close to the target position and of a plastic particle detector (CR 39). The beam current was controlled between the exposures and was found to be constant within 5 - 10%.

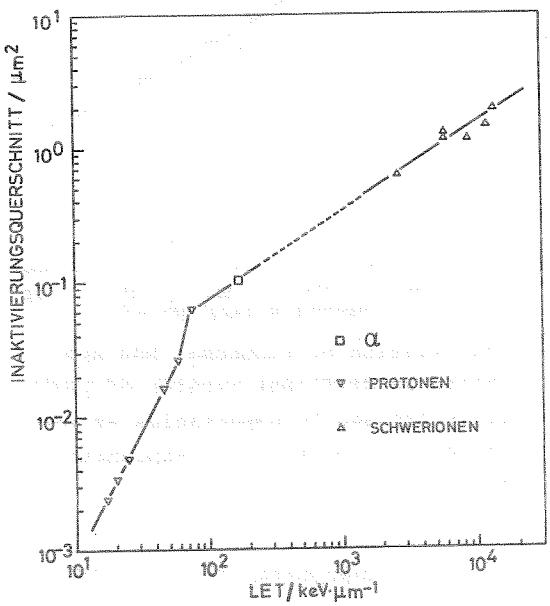


Fig.1: Inactivation cross sections of dry yeast cells from proton and heavy ion experiments versus LET

The following table shows the results of one set of experiments:

Energy/MeV	σ/µm²	Energy/MeV	σ/µm²
2	0.0024	0.46	0.026
1.3	0.0048	0.25	0.064
0.65	0.017	0.14	0.0036

The inactivation cross section (σ) increases when the proton energy is reduced (increasing LET). With the lowest energy the cross section drops again; this is due to the short range of the 140 keV protons so that the sensitive site of the cell is not completely reached. Due to technical reasons the energy could not be reduced further. Using the most recent range data of Janni[2] it is estimated that the sensitive site has a distance of about 1.2 - 1.5µm from the cell surface which agrees reasonable with the position of the nucleus. In Fig. 1 the inactivation cross sections are plotted versus LET for the proton used (LET below 100 keV/µm), α-particles (LET = 170 keV/µm) and the heavy ion experiments by Schöpfer et al[1]. The graph shows that after a quadratic increase the slope of the curve changes in the LET range between 100 and 1000 keV/µm to a value below 1. If one compares the proton results with results of high energy particles with wet cells in the same LET range, one finds that the slope in the proton experiment is considerably steeper than in the heavy ions experiment. It is not clear, however, whether this is due to the different cell systems or the particles used.

[1] F. Schöpfer et al., Radiat.Res. 82,235-243(1980)
2J.F. Janni, Atomic Data and Nuclear Data Tables, 27, 147 - 529 (1982)
[3] E.Schneider, J. Howard, Proc. VIIth Symp. Microdos., Harwood, London, 1341-1351 (1980)

Recovery from transcription inhibition in yeast cells exposed to charged particles [G]

K.J. Weber, E. Schneider and J. Kiefer

Strahlenzentrum, Universität Giessen

Recovery from potentially lethal damage ("liquid holding recovery", "delayed plating-recovery") was reported to occur in yeast even after exposure to high-LET radiation, such as α-particles[1] or even very heavy ions[2]. The molecular mechanism underlying this process is unknown. It is not restricted to colony forming ability but acts also on X-ray-induced inhibition of transcription[3]. The present study shows that it can also be demonstrated with α-particles. The experimental probe was the synthesis of ribosomal RNA (r - RNA).

If diploid wild-type cells of Saccharomyces cerevisiae (strain 211) are exposed to ^{241}Am-α-particles (0.65 MeV/u) at room temperature the inhibition of r - RNA synthesis shows a dose-response curve with a pronounced resistant tail.

Since shading effects could be excluded, it should be tested whether metabolic activities in cells during the extended exposure periods (up to 1 hr) might influence the shape of the inactivation curve. Consequently, wild type cells were irradiated under identical conditions with the exception, that the temperature during exposure was lowered to 4°C. This treatment resultet in a drastic decrease of synthetic capacity at higher particle fluences; the same inactivation data were measured for a radiation sensitive strain (rad 51) which is defective in recovery ability for survival exposed both at room temperature and 4 °C (figure 1).

These findings support the assumption that recovery processes occur even after high-LET irradiations. The unusual shape of the dose-response curves may be explained with the known kinetics of recovery after exposure to X-rays: during a given time-interval always a fraction of the induced transcription inhibiting lesions are removed. In consequence, from the initial slope the number of lesions induced can be derived, a final decrease in the terminal part of the inactivation curve represents the fraction of remaining ("non-repaired") damage. Using more data, discrimination between relative amounts of repaired and non-repaired damage will be possible with special emphasize on track-structure dependencies .

[1] Schneider, E. and Kiefer, J., Int. J. Radiat. Biol. 29, 77 (1976

[2] Kiefer, J., Rase, S., Schöpfer, F., Schneider, E., Weber, K.J. and Kraft, G., Adv. Spaces Res., Vol. 3, No. 8, pp. 115 - 125 (1983

[3] Weber, K.J. and Kiefer, J., Brit. J. Cancer, in press

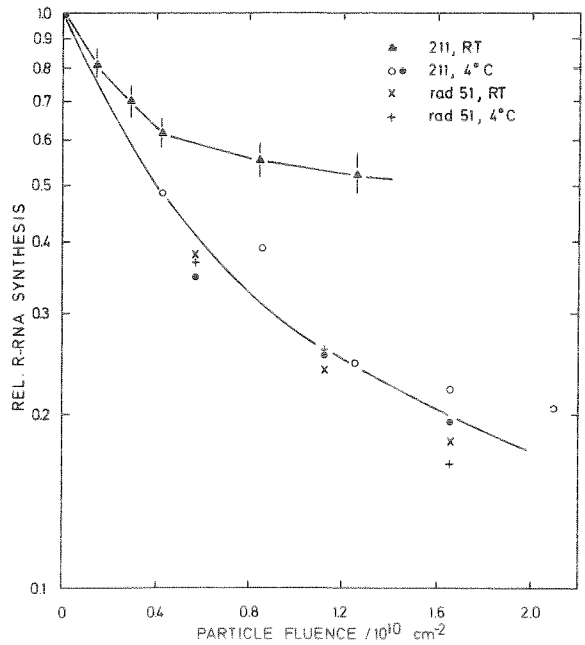


Fig. 1: Inactivation of ribosomal RNA synthesis in different strains of yeast cells exposed to α-particles at room-temperature or 4°C (for explanation see text).

Interpretation of heavy ion survival data: Influence of energy density.

Jürgen Kiefer
Strahlenzentrum der Justus-Liebig-Universität
Giessen, Germany

The principal formalism for the quantitative interpretation of heavy ion action on cells was previously outlined[1,2]. In the case of exponential survival curves the surviving fraction y is given by

$$y = \exp\left[-\sigma_o \phi (1 - \int f_1(z) e^{-k \cdot z} dz)\right] \qquad (1)$$

where σ_o is the cross section of the sensitive site, ϕ the ion fluence, z the specific energy in the sensitive site, $f_1(z)$ its distribution for single traversals and k the inactivation coefficient. As a first approximation k was taken from X-ray survival curves but the agreement between theory and experiment was poor[1]. This is due to the fact that biologically significant lesions are more effectively induced by densely ionizing radiations. Dose and hence also its microdosimetric counterpart specific energy z do therefore not uniquely determine the survival probability of a cell. z in equation (1) has to be replaced by an effective specific energy z' whose value depends also on the spatial pattern of energy deposition.

There is no obvious way to derive z' from first principles, a semi-empirical approach is therefore suggested. It is based on the known dependence of inactivation cross sections on LET with lighter ions. If the inactivation cross sections are normalized with respect to their saturation values and plotted versus energy density in the track core data from yeast[3,4], bacterial spores[5] and human diploid fibroblasts[6] fall on the same line (fig. 1). For this kind of analysis a certain size of the infinitesimal mass element has to be assumed. Following an analysis of experiments with ultrasoft X-rays[7] a cylinder with a diameter of 4 nm was chosen. The track core energy density in such sites was calculated according to the beam model of Chatterjee and Schaefer[8]. The points in figure 1 can be reasonable fitted to the expression

$$\sigma/\sigma_o = 1 - \exp(-a\rho - b\rho^2) \qquad (2)$$

where ρ is energy density and a and b parameters. Non-linear regression analysis yielded

$$a = 3.92 \times 10^{-11}\ \mu m^3\ (ev)^{-1}$$
$$b = 1.92 \times 10^{-20}\ \mu m^6\ (ev)^{-2}$$

(The density of the mass elements was taken as unity)

The parameter a provides an estimate for the probability to induce a biologically significant lesion if the spatial pattern of energy deposition does not contribute and may be compared to X-ray data as obtained by Goodhead and Brenner[7]. From their calculations with 250 KV-X-rays the probability to have an energy absorbtion of 100 eV in a sphere with 4 nm diameter is about 3×10^{-7}/Gy while the present analysis yields 2.45×10^{-7}/Gy. It suggests, that the deposition of about 100 eV in a 4 nm site constitutes a critical event.

Non-linear effects as indicated by the parameter b become important for energy densities > $a/b \cong 2 \times 10^9$ eV μm^{-3}. This figure may be used to estimate how far from the track core of heavy ions they may be important. On the basis of the beam model used[8] this distance amounts to about 40 nm for Uranium ions and is progressively smaller for lighter ones. This somewhat surprising result shows that non-linear effects may play only a minor - but not insignificant - role in the penumbra region.

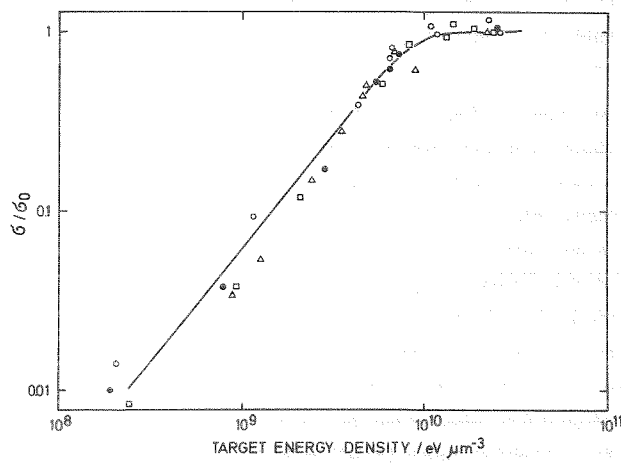


Fig.1: Normalized inactivation cross sections versus energy density in 4 nm sites. o: yeast[3], ●: yeast[4], □: bacterial spores[5], Δ: human fibroblasts[6]

References:
1. J. Kiefer, Proc. 8th Symp. Microdosimetry, 1983, p.729
2. GSI Sci. Rep. 1982, p. 196
3. J.A. Sayeg et al.-Radiat. Res. 10, 449 (1959)
4. T.A. Manney et al.-Radiat.Res. 18, 374 (1963)
5. E.L. Powers et al.- Int.J.Radiat.Biol. 14, 313 (1968)
6. R. Cox, W.K. Masson - Int.J.Radiat. Biol. 36, 149 (1979)
7. D.T. Goodhead, D.J. Brenner - Phys.Med.Biol. 28, 485 (1983)
8. A.Chatterjee, H.J.Schaefer-Rad.Env.Biophys. 13, 215 (1976)

G

Chromosome aberrations in V 79 Chinese hamster cells produced by heavy charged particles

W. Müller, H.G. Miltenburger
TH Darmstadt

G. Kraft
GSI Darmstadt

Measurements of cell inactivation induced by high LET (Linear Energy Transfer) radiation give only informations about radiation action in general[1,2,3]. For a better knowledge of radiation effects in the cellular target (cell nucleus) we investigated the induction of chromosome aberrations in Chinese hamster cells after exposure to heavy ions with different Z (^{18}Ar, ^{26}Fe, ^{92}U) and LET (1200-15000) keV/µm with regard to characterisation and quantitative analysis.

V79 Chinese hamster cells were grown in MEM with Hanks salts supplemented with 10 % FCS, 0.12 mg/ml Bycomycin and 2 mmol Glutamin at 37° C.

2×10^5 cells were seeded into 35 mm petri dishes 24 hours before the experiments and incubated at 37° C. Mitotic cell cultures were prepared by adding of 0.05 µg/ml Colcemide to the culture medium 3 hours before radiation treatment and harvested directly after irradiation. Exponentially growing cells were incubated again for 4 or 12 hours after exposure. The last 3 hours of the incubation time, Colcemide was present in the medium, too. Chromosome preparation was done by standard procedures. For each experimental point 150 metaphases were scored and types of aberrations were specified as breaks, deletions, fragments, exchanges, dicentrics and disintigrations.

As shown in Fig. 1 and 3 the percentage of cells having aberrations increases with increasing particle fluence with a saturation effect at higher fluences. Particles with a higher atomic number (Z) like Uranium are more effective in aberration induction. For each atomic number, the yield of aberrations increases with increasing energy. This is more pronounced in Fig. 2, where we have plotted the rate of cells with aberrations for iron particles with 4 different energies. Additionally the percentage of cells with chromosome aberrations per particle fluence after exposure to an uranium beam (Z=92) is higher (up to 82 %) in cells irradiated in mitosis than in exponentially growing cells (30 %) as can be seen in Fig. 3. This effect is mainly due to a very high number of disintegrations of chromosomes in mitotic cells in contrast to low Z particle beams [4].

In conclusion, the induction of chromosome aberrations in mammalian cells by heavy charged particles is dependent on the particle energy as well as on atomic number. At low to middle Z (^{18}Ar, ^{26}Fe) there is a steeper increase in effectiveness with increasing energy. In contrast, the effectivity at high Z (^{92}U) differs only slightly, probably due to cellular processes like cell cycle arrest which inhibit cell progression into mitosis [5,6].

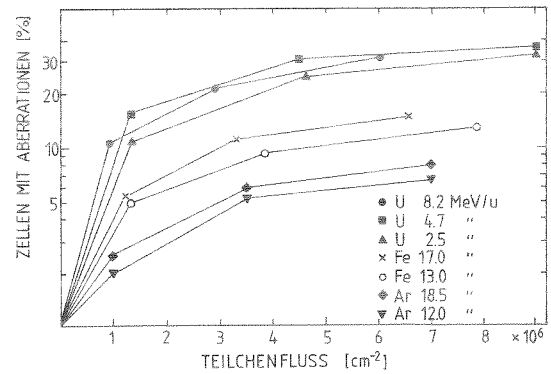


Fig. 1: Number of cells showing aberrations 4 hours after irradiation with different ions and energies

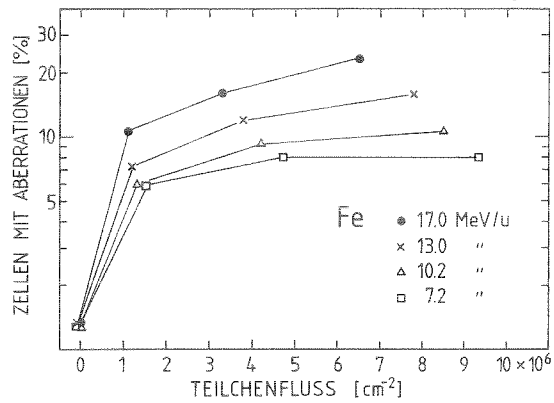


Fig. 2: Number of cells having aberrations 12 hours after irradiation with Fe-ions.

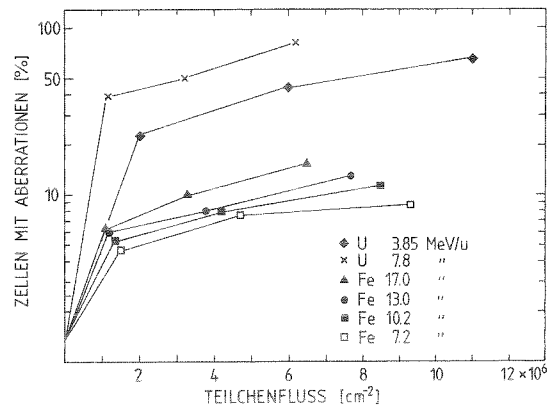


Fig. 3: Number of mitotic cells with aberrations in percent.

[1] G. Kraft, W. Kraft-Weyrather, H. Meister, H.G. Miltenburger, H.Wulf
in Microdosimetry; Proceedings of the eighth Symposium Jülich 1982, p. 743-753

[2] H. Wulf, H.G. Miltenburger, G. Kraft; GSI Report 1981, p. 189

[3] G. Kraft et al., GSI Report 1982, p. 199

[4] W. Müller, H.G. Miltenburger, G. Kraft; GSI Report 1982, p. 197

[5] L. Hieber, this Report

[6] C. Lücke-Huhle, L. Hieber, R.D. Wegner, Int. J. Radiat. Biol. 1983, Vol. 43, No. 2, 123-132

Heavy ion induced alterations in proliferation kinetics of mammalian cells

L. Hieber, M. Larsson, D. Pollet and G. Kraft
GSI Darmstadt

Exposure of mammalian cells to ionizing radiation with a LET (linear energy transfer) higher than X- or γ -rays results in remarkable differences of the cell reaction[1,2]. This is not restricted to cell inactivation, but concerns also other biological effects like DNA strand breakage[3], chromosomal aberrations[4,5] and last not least changes in cell cycle progression. The latter is an important radiobiological parameter for testing radiation action in mammalian cells.

Wheras low LET X- or γ-rays (LET 2-10 keV/µm) induce a division delay mainly by lengthening of the DNA synthetic phase (S-phase) of the cell cycle, radiation with a LET of 100 to 200 keV/µm like alpha particles leads to a severe arrest in G2-phase[6]. Now we have measured the proliferation kinetics of V79 chinese hamster cells after exposure to different heavy ion beams accelerated at the UNILAC with LETs up to $\sim$16.000 keV/u[7].

For irradiation 10^5 cells were seeded into petri dishes 24 hours prior to the experiments and incubated at 37°. Treatment was performed under exponential growing conditions at a cell density of 3-4 x $10^4/cm^2$. After irradiation the cells were incubated again for time intervals from 2 to 24 hours. Then the cells were trypsinized, fixed with ethanol and the DNA of the cells was stained with 33258 Hoechst dye. Cell cycle changes were analysed in a flow cytometer (Phywe ICP 22) equipped with a multichannel analyser. The distribution of the fluorescence intensity of the DNA was displayed as analog printouts from the multichannel memory content. The percentage of the cells in the cycle phases G1, S and G2+M were estimated from the area under the DNA histogram using a computer program.

Figure 1 shows a series of DNA histograms of V 79 cells treated with 4.5 x $10^6/cm^2$ nickel particles with an energy of 5 MeV/u corresponding to a survival rate of 0.1. In the first time interval (0-4 hours) the number of cells in S-phase increase with a contemporary decrease of G1 cells. After an almost normal time in S-phase the cells reach G2+M and accumulate there for a longer time than the usual G2 duration of about 2 hours. The maximum of the G2+M compartment is obtained at 12 to 14 hours after exposure. The treatment with nickel ions (LET $\sim$3.600 keV/µm) is more efficient with respect to G2 arrest than a 5.9 MeV/u uranium beam (LET $\sim$16.000 keV/µ) as shown in Figure 2. For comparison the data of Lücke-Huhle and Hieber with ^{241}Am alpha particles (120 keV/µ)are included in the plot.

From the present data the effectiveness of particle radiation in respect to G2 arrest seems to decrease with increasing LET in the range from 200 to 16.000 keV/µ. But this is correct only if one compares the data at the same survival level and not at identical particle fluences and energies deposited in the cellular target.

1 Raju, M.R., Rad. Res. 84, 16 (1980)
2 Lücke-Huhle, C. et al., Rad. Res. 79, 97 (1979)
3 Rydberg, B., this report
4 Müller, W., this report
5 Lücke-Huhle, C. et al., Int. J.Rad.Biol., 43, 123 (1983)
6 Lücke-Huhle, C. et al., Rad.Environ.Biophys., 20, 172 (1982)
7 Hubert, Nuclear data (calculation of LET data) (1980)

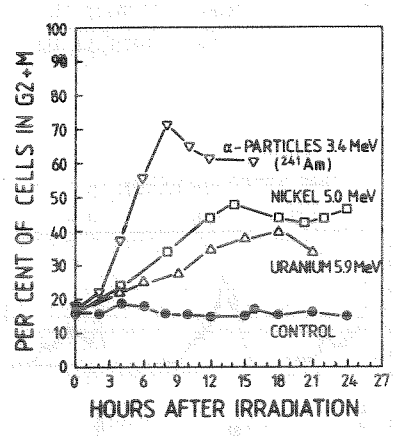


Fig. 2: Time course of G2+M accumulation induced by different radiation quality.

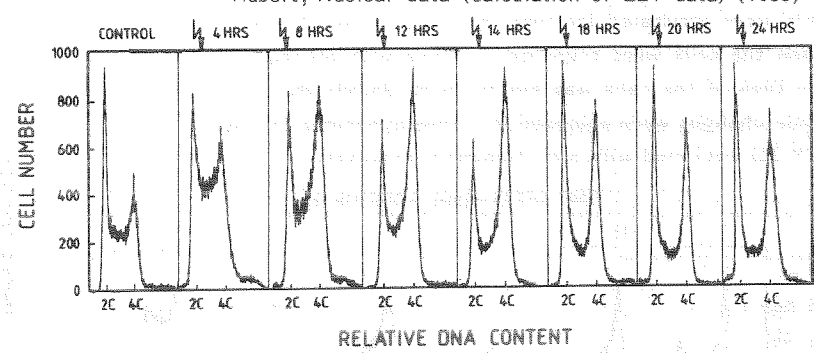


Fig. 1: DNA histograms of V 79 cells after exposure to 5.0 MeV/u nickel particles. The applied fluence of 4.5 x $10^6/cm^2$ corresponds to a survival rate of 0.1. Samples were taken at the indicated time intervals after irradiation. G1 and G2 cells possess a relative DNA content of 2C and 4C, respectively. S cells have an intermediate amount of DNA.

Proliferation Kinetics of Irradiated Cell Populations Determined by the Bromodeoxyuridine-33258H Technique

E.Kuchinka, L.Hieber, G.Kraft
GSI Darmstadt

Irradiation of mammalian cells with ionizing radiation of different qualities leads to different cell reactions as described by Hieber[1]. The proliferation kinetics of V79 Chinese hamster cells after exposure to different heavy ion beams accelerated at the UNILAC with various LETs up to 16.000keV/µm have been measured by flow cytometry[1]. These measurements give no information about differences in radiosensitivity depending on the cell age.

By the bromodeoxyuridine-33258H technique it is possible to determine the duration of the G_2 phase of various cell cohorts and therefore can give us such data without synchronizing exponentially growing cells[2,3].

This method has been adapted to V79 Chinese hamster cells in our laboratories.

Cultures of V79 cells were grown in medium containing 1,0 mg/l bromodeoxyuridine (BUdR) and were stained with the fluorescent dye 33258H (a bisbenzimidazole derivative) for flow cytometric analysis. During exposure to BUdR the cells replace thymidine by BUdR in their newly synthesized DNA. The new DNA strand is not stainable with 33258H, which is highly specific for thymidine[4]. Therefore the amount of DNA stainable with 33258H remains constant for each cell after addition of BUdR until cell division. By addition of BUdR at different times before and after irradiation the mean transit times through G_2 phase of the cell cycle of various cell cohorts can be measured.

Cells were cultured as described by Hieber[1]. Exponentially growing cells were irradiated at a density of $3\text{-}4\times10^4$ cells/cm^2. Before or after irradiation the medium was replaced by conditioned medium containing 1 µg/ml BUdR and 0,8 µg/ml deoxycytidine. Again the cells were incubated for time intervals up to 12 hours. Then the cells were trypsinized, fixed with ethanol and the DNA of the cells was stained with 33258H dye. Cell cycle changes were analysed in a flow cytometer (Phywe ICP 22) equipped with a multichannel analyser.

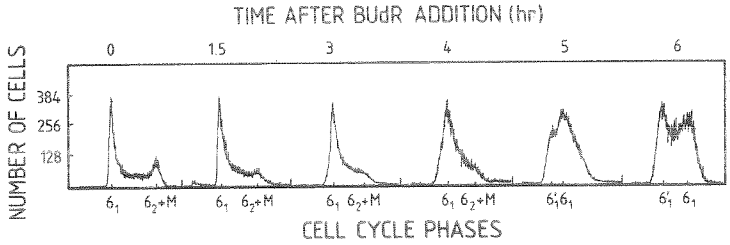


Figure 1: control, BUdR conc.1,0 mg/l, expl. see text

Figure 1 shows a series of flow cytometric histograms of exponentially proliferating V79 cells recorded at different time intervals after addition of BUdR to the culture medium. The histogram recorded 1.5 hr after BUdR addition has a much smaller G_2 + M Peak as compared to the control, indicating that some of the original G_2 + M cells have divided. The 4 hr histogram shows that late S cells have divided and now appear on the ascending part of the G_1 Peak, and the last two histograms, 5 and 6 hr, show an increasing number of the original G_1 cells after mitosis, appearing at G_1'.

Our first heavy ion experiment is shown in figure 2 where we treated the cells with $2{,}5\times10^6/cm^2$ nickel particles with an energy of 5 MeV/u corresponding to a survival rate of 0,3 and a LET of 3.600 keV/µm. BUdR was added immediately after irradiation.

12 hr after BUdR addition all original G_2 + M cells of the control series are found behind mitosis. In contrast the irradiated cells show still a visible G_2 + M peak.

From the present data it seems that most cells being in G_2 + M phase during irradiation were blocked in G_2 for a longer time than 12 hours. In further experiments we will determine the duration of the G_2 block in cells irradiated in G_1 and S phase.

References

1. Hieber,L.,this report
2. Beck,H.-P., Cell Tissue Kinet.(1978)11,139
3. Böhmer,R.-M., Cell Tissue Kinet.(1979)12,101
4. Müller,W. et al., Eur. J. Biochem.(1975)54,385

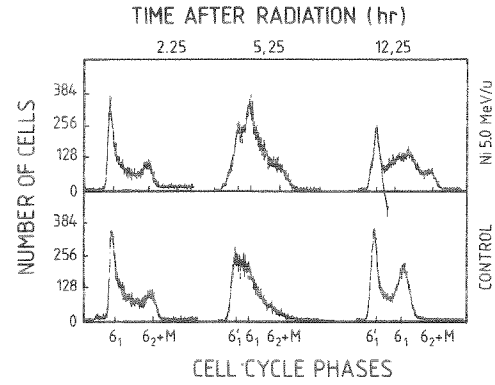


Figure 2: irradiated cells, Ni 5MeV/u,+ control

Inactivation of mammalian multicell spheroids by heavy charged particles

M. Schuber and G. Kraft, GSI Darmstadt

The inactivation of mammalian monolayer cells by heavy ions has been studied intensively in the preceding reports.[1,2] In order to study the influence of a tumor-like cell morphology on the inactivation after heavy ion irradiation we used multicellular spheroids of the V 79 Chinese hamster line. For several reasons, spheroids are considered to mimic the microenvironment of cells in a growing tumor: small spheroids with rapidly growing cells are similar to normal proliferative tissues, in larger spheroids limitations in the supply with oxygen and nutrients produce a stress situation like in tumor nodules. Therefore the spheroid system is often characterized as an *in vitro* tumor model.[3,4]
The methods for culturing V 79 spheroids in suspension have been derived elsewhere.[5,6] For irradiation, the spheroids were attached to the petri dishes several hours prior to the experiment. After irradiation, they were dissociated with 0.25 % trypsin into single cells and plated out like the monolayer cells for colony formation.

X-ray experiments were carried out with spheroids of different sizes up to a mean diameter of 1100 µm. Cell survival as a function of the x-ray dose is given in figure 1. Compared to the monolayer, small spheroids of 80 and 200 µm show an increasing radioresistance. This kind of response can be interpreted by the three-dimensional contact of the cells in a spheroid. This so-called contact effect is supposed to be mediated by gap junctions which enable a intercellular communication of ions and small molecules.[7,8,9] As the spheroids enlarge to 800 µm, the survival curve becomes a shape of radioresistance caused by a proportion of hypoxic and necrotic cells in the core of the spheroid.[3] This effect becomes more expressed with spheroids of 1100 µm.
For heavy ion irradiation, figure 2 shows a comparison between V 79 monolayers and spheroids after irradiation with Uranium of 5.9 and 8.6 MeV/u. Due to the limited range of the heavy ion beam, only small spheroids of 80 and 120 µm could be measured. A significant enhancement in cell survival occurs for the spheroid form at both energies. The cross section of inactivation σ is reduced from 56 to 25 μm^2 at an energy of 5.9 MeV/u and from 71 to 35 μm^2 at an energy of 8.6 MeV/u. Whether similar effects of an enhanced spheroid survival can be observed with other heavy ions and higher energies remains to be demonstrated in further experiments with the UNILAC.

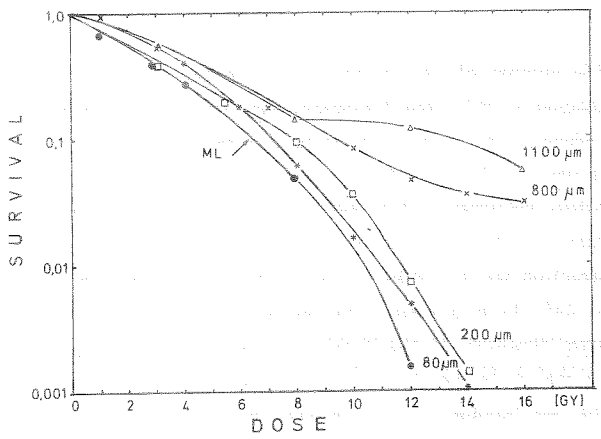


Fig. 1: Survival of V 79 cells as a function of the x-ray dose is plotted for monolayers (ML) and for spheroids of different sizes. Monolayers and spheroids were irradiated with 250 kV x-rays at room temperature.

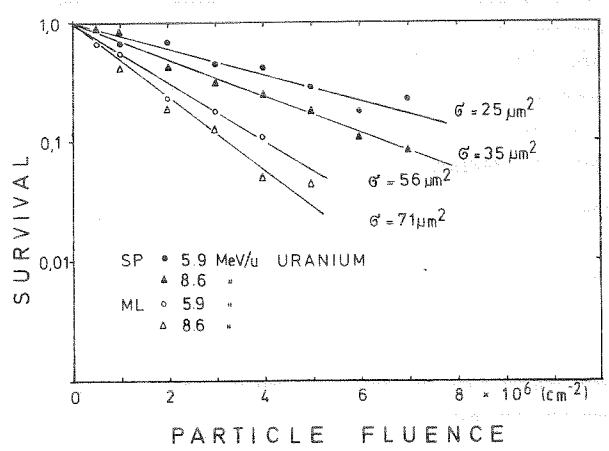


Fig. 2: Survival of V 79 cells as a function of particle fluence for Uranium ions of 5.9 and 8.6 MeV/u: Comparison between monolayers (open symbols) and spheroids (closed symbols).

References:

[1] GSI - Scientific Report 1981, p. 189
[2] GSI - Scientific Report 1982, p. 199
[3] Sutherland and Durand, Current Topics Rad. Res. 11, 87 (1976)
[4] Durand and Sutherland, Exp. Cell Res. 71, 75 (1972)
[5] Sutherland, Mc Credie and Inch, J. Nat. Cancer Inst. 46, 113 (1971)
[6] Sutherland and Durand, Int. J. Rad. Biol. 23, 235 (1973)
[7] Dertinger, Hinz und Jakobs, Biophys. Struct. Mech. 9, 89 (1982)
[8] Dertinger and Hülser, Radiat. Environ. Biophys. 19, 101 (1981)
[9] Azarnia and Larsen, Intercellular Communic., Planum Press, p. 145 (1977)

APPLICATION OF THE TEXTURE ANALYSE SYSTEM (T.A.S.) FOR COLONY COUNTING

B. Warczak*, W. Kraft-Weyrather, G. Kraft

GSI Darmstadt

The number of cell colonies must be counted for many samples in different biological experiments. Such a procedure is very time consuming and therefore, we attempt to use the Texture Analyse System (T.A.S.) for the colony counting. T.A.S. permits the separation of the details of the analysed picture. Using only the T.A.S. instruction we are able to count the objects characterized by definite brightness (gray value) and to measure their area. However, if the details overlap, the number of them counted by a simple "count" instruction is smaller than the real number of colonies and must be corrected. A similar problem has been already discussed in /1/ and /2/ for a counting of nuclear tracks. The probabilities to find single, double and multiple clumps calculated in /1/ have been applied for our problems.

The statistical expressions obtained in /1/ have been tested carefully in our laboratory in respect to biological problems. The number of clumps was counted by T.A.S. using a simple "count" instruction and then the real numbers of colonies were calculated by T.A.S. by means of special programs taking into account the statistical correction factors.

The number of single, double and multiple colonies has been counted for 40 samples on the T.A.S. monitor (manual method) as a function of the coverage estimated by T.A.S. and thus the experimental probabilities for finding such groups of colonies have been found. It has been shown that the analytical expressions from /1/ describe the experimental values /3/ very well.

Moreover, the numbers of colonies have been counted by the T.A.S. system and by the manual method for a few hundred samples. The "hand" to T.A.S. ratio is presented in Fig. 1.

It is very impressive that the "hand" to T.A.S. ratio as a function of the colony number is very good approximated by the straight line (Fig. 1). For colony numbers higher than about 400 the "hand" to T.A.S. ratio is systematically higher than 1, but in all cases not more than 10 %.

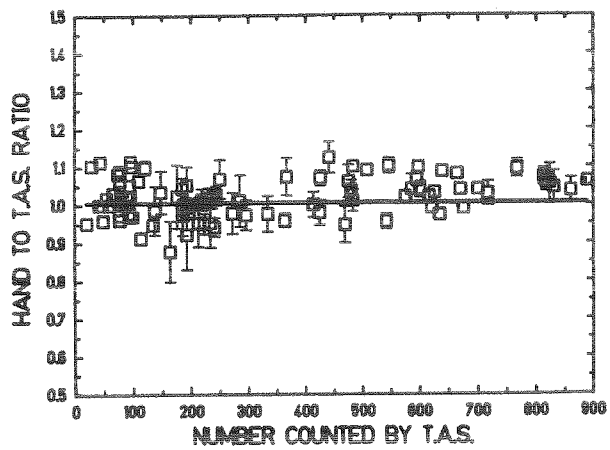


Fig. 1: Comparison of the "hand-made" data to the T.A.S. data as a function of the colonies number.

/1/ C. Riedel and R. Spohr, Radiation Effects, 1979, Vol. 42, 69

/2/ B.S. Barashenkov, JINR P14-10532, Dubna, 1977

/3/ B. Warczak, W. Kraft-Weyrather, G. Kraft, to be published.

* Permanent address: Jagellonian University, Institute of Physics, 30-059 Krakow, Poland.

G

SEARCH FOR CRITICAL TARGET SITES OF THE CELL NUCLEUS EXPERIMENTS WITH HEAVY IONS IN THE KEV REGIME

G. Kraft, W. Kraft-Weyrather, H. G. Miltenburger, W. Müller, M. Schuber

GSI Darmstadt T H Darmstadt

It is evident from the so-called suicide experiments (Burki et al.), that the most sensitive target for cell killing consists of the DNA, which is nearly homogeneous distributed in the nucleus of a cell except in mitosis. But previous experiments at the Unilac have shown that even for the highest LET values the inactivation cross section can be much smaller than the geometrical cross section of the cell nucleus. Several traversals of heavy ions through the cell nucleus are necessary to kill the cell, and the cells have a high chance to survive a single hit by a heavy ion even if the energy deposition of the ion is much higher than the comparable X-ray dose for cell killing. Therefore, we may conclude that either the radiosensitivity of the cell is much lower for heavy ion action or that there may be only some small areas within the cell of higher radiosensitivity than the bulk DNA material.

In our experiments we have examined the hypothesis that higher radiosensitivity is associated with a finite area just below the nuclear membrane (Cole et al., 1980). Fully hydrated and exponentially growing V79 Chinese hamster cells have been exposed to a low energetic heavy particle beam (E ≈ 300 keV) having a residual range of 10µm in water. The range of the particle beam was decreased in steps of ~ 1µm by inserting thin mylar foils in front of the cells.

The survival and the induction of chromosome aberrations are measured as a function of the penetration depth of the particle beam. The raw data given in Figure 1, 2 are not corrected for the range straggling of the primary beam, which is in the order of Δ R ~ 2µm (Laichter et al., 1982). For both biological end points, cell killing and chromosome aberration, a steep increase of the measured effect is observed between the 2 and 4 µm penetration depth.

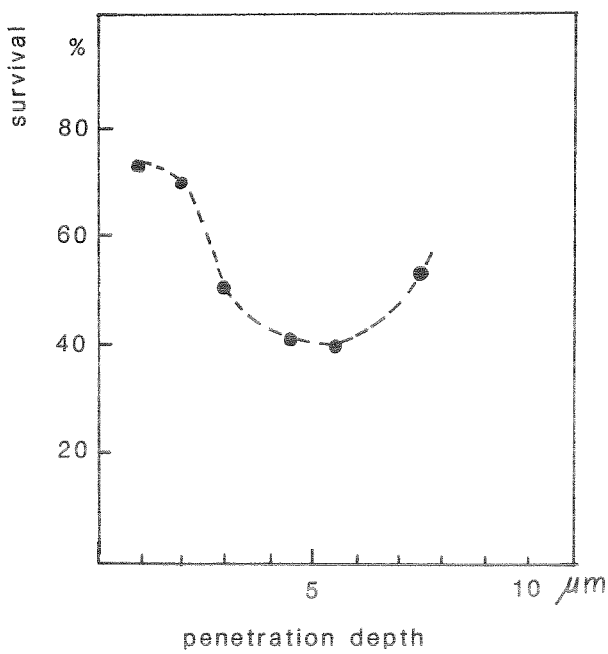


Figure 1. Surviving fraction of V79 mammalian cells as a function of penetration depth of a low energetic heavy ion beam.

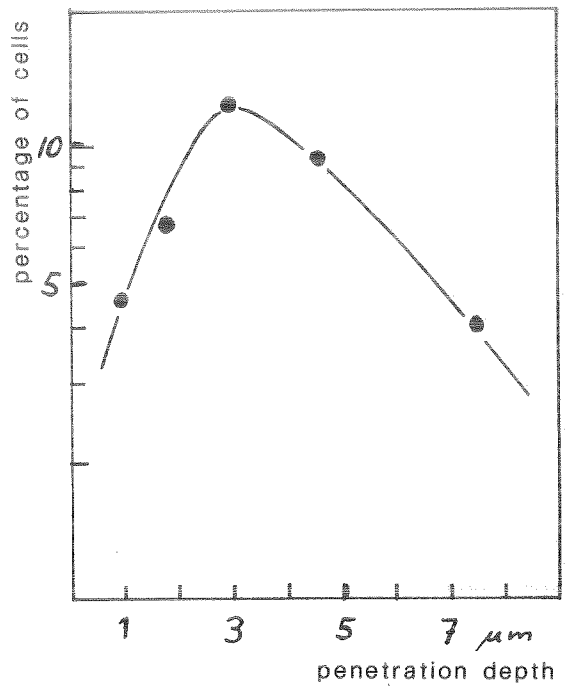


Figure 2. Percentage of cells having chromosomal aberrations after heavy ion bombardment as a function of penetration depth.

This finding is in excellent agreement with the previous experiment of Cole et al., 1980, in which the four biological measurements of inactivation, division delay, DNA breaks and mutation have been measured using α-particles and electron beams with various residual ranges between 1 and 50 µm. In their experiment the same increase of the particle efficiency was observed, when the energy deposition is maximized near the nuclear membrane. They concluded that a significant fraction of the DNA (~10%) associated with the nuclear membrane is more radiosensitive than the bulk DNA.

In contrast to the α-particle experiment, we found a significant decrease of the particle efficiency for the deeper particle penetration, which is more pronounced at low doses and disappears at higher doses. This difference from the experiment with lighter ions may be related to an increasing recombination probability of the primary physical and chemical reaction products with increasing local ionization density, which must be explored in future experiments using particle beams of different LETs.

REFERENCES

Burki, H. G. Critical DNA damage and mammalian cell reproduction. J. Mol. Biol. 103, 559-610 (1976).

Cole, A., et al. Mechanisms of cell injury. Radiation Biology in Cancer Research p.33-55, ed. R. Meyn, H. R. Withers, NY (1980).

Laichter, Y., et al. Range profiles for uranium ions in solids. Phys. Rev. A 26, 1915-23 (1982).

BIOLOGICAL EFFECTS OF URANIUM IONS- EXPERIMENTS WITH HEAVY IONS AT RELATIVISTIC ENERGIES

G. Kraft, E. A. Blakely, W. Kraft-Weyrather, W. Müller, H. G. Miltenburger
R. Roots, W. Schimmerling, C. A. Tobias, M. Wong, T. C. Yang

Lawrence Berkeley Laboratory, Berkeley, CA

GSI Darmstadt T H Darmstadt

Very heavy ions such as uranium are now accelerated to relativisitc energies (E > 900 MeV/u) at the Bevalac. Although these ions will probably never be used for medical applications, the high velocity ($\beta > 0.8$) combined with high LET values offer the possibility to study the biological response to ionizing radiation under extreme conditions.

In track segment experiments the biological effectiveness of an uranium beam was measured at various cellular and molecular levels, such as the inactivation of mammalian cells, induction chromosome aberration and transformation, and the induction of strand breaks of DNA in solution.

There are two major difficulties in completing these experiments: the low production rate of the uranium ions at the Bevalac (< 10^7 particles per minute), and, secondly, the high fragmentation rate of the uranium ions (σ = 3-10 barn) which breaks the uranium ions mostly into two "medium " heavy fragments. The large number of nuclear fragments is clearly visible in the Bragg curve (Figure 1) as a long tail of ionization extending far beyond the range of the primary uranium ions. In order to obtain a uranium beam free of fragments, it is necessary to minimize the absorber material in front of the biological target. The dosimetry was, therefore, performed with a scintillation counter downstream of the bio-samples. Simultaneously, with each sample glass plates were exposed to the beam, and the number of particle tracks was counted as an independent check on the particle dose.

In Figure 2 the survival of Chinese hamster cells is compared with the survival of T1 human cells as a function of particle dose of a 400 MeV/u uranium beam which has an LET of 2600 keV/µm. The slope of the two survival curves is nearly exponential and corresponds to a ratio of the inactivation cross section of $\frac{\sigma_{V79}}{\sigma_{T1}} = 0.80$. A similar ratio of the inactivation cross section was obtained at low energy experiments, but the absolute inactivation efficiency (σ (V79) ~ 120µm^2) is lower than what would be predicted from a straightforward extrapolation of the low energy data. Other predictions of the inactivation efficiency, which are based on track structure models, yield a cross section of about 60µm^2 which is much lower than the experimental values.

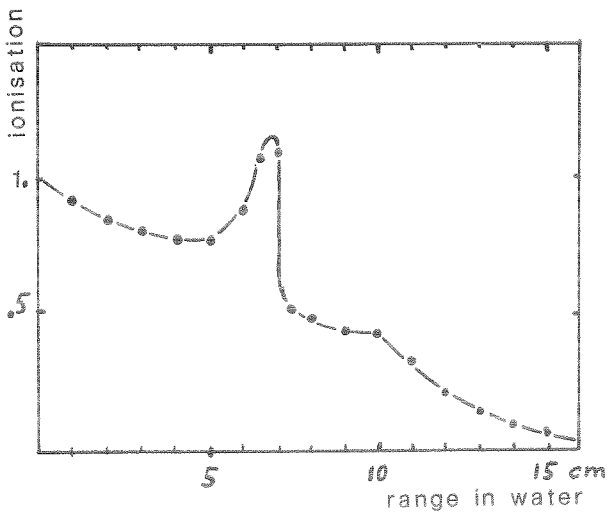


Figure 1. Bragg curve of a 960 MeV/u uranium beam in water.

In the chromosome aberration experiment and in the transformation and strand break experiment a similar trend is found in a preliminary analysis: the efficiency per uranium particle is not drastically different from the low energy data, and the relative biological effectiveness (RBE) compared to X rays is still smaller than one.

However, the results from these first measurements using relativistic uranium ions together with previous measurements using low energetic uranium ions (G. Kraft et al., 1981) show, that the current theories of the biological effectiveness of energy deposition of particle radiation (Katz et al., 1971, Gunther et al., 1983) have to be revised.

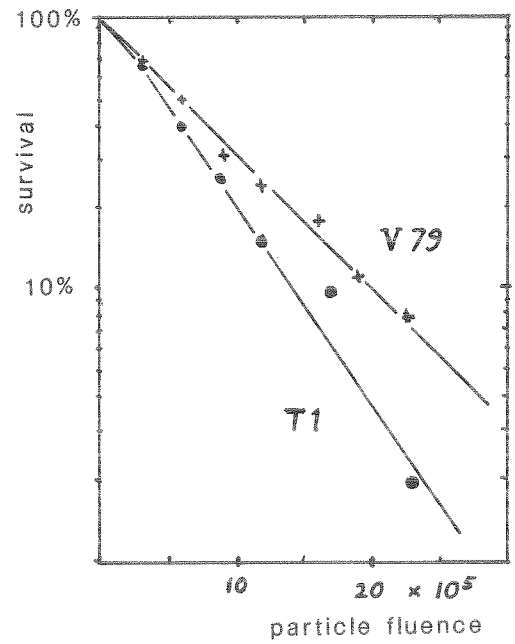


Figure 2. Survival of V7G Chinese hamster and T1 human cells as a function of particle fluence of a 400 MeV/u uranium beam.

REFERENCES

Katz, R., et al. Inactivation of cells by heavy ion bombardment. Rad. Research 47, 402-425 (1971).

Gunther, K. and W. Schulz. Biophysical theory of radiation action. Akademie Verlag, Berlin (1983).

Kraft, G., et al. The influence of radiation quality on the biological effectiveness of heavy charged particles. Proceedings of the 8th Symposium of Microdosimetry, Julich, 27 September-1 October (1982).

Heavy ion experiments with plant seeds and spores [B]

U. Bork, K. Koller-Lampert, M.E. Starke, A.R. Kranz
Botanisches Institut, J.W. Goethe-Universität, Frankfurt am Main

The BIOSTACK-conception of nuclear track detectors sandwiched with biological objects offers the advantage to localize more precisely individual radiation effects inside the tissue or cell. For BIOSTACK experiments on the biological effect of cosmic radiation during space flight[1] qualification tests were further improved by use of heavy ions of high atomic number and energetic velocity (HZE) produced by the UNILAC of GSI, Darmstadt.

Presently, energies available are limited up to 20 MeV/n but the linear particle fluency has been varied from 10^5 to $5x10^8$ p/cm². For irradiation the gilded sample holder adapted to UNILAC machine[2] was used where Plastic petri dishes containing the dry detector or wet filter paper with seeds or spores fixed on the detector surface were exposed to the beam.

After irradiation and dosimetric control of the detector culturing of irradiated M_1 plants started with aseptic germination and seedling's development. Growth continued after transfer of vital plantlets to standard soil in a greenhouse. In the radicle test the root length of 7 to 11 days old seedlings was measured.

With dry seeds of Arabidopsis decrease of survival in M_1 was exponential with variant linear reduction in the fluency range of 10^7 to 10^8 p/cm² depending on the kind of velocity of the HZE-particle (Tab.1). For high energetic U, linear decrease is steeper at lower fluency rates than for Kr ions which, evidently shows that the hit range inside the embryonic seed cells is probably larger with element of higher Z. The particle beam of lower energy (5.9 MeV/n) doesn't yield significant decrease of surviving plants because of insufficient particle penetration; in water penetration is: 5.9 MeV/n=87µm for Kr, 104µm for U; 16.2 MeV/n=270µm for Kr and for U, respectively. Therefore with U ions at lower fluencies survival of more sensitive wet seeds is not reduced.

The radicle test in M_1, however, shows that with increasing particle densities the mean length of seedling's root is reduced at high energetic expositions of U particles as well as lower ones of Kr. This result shows that there must be a stronger effect on the root growth which is in agreement with earlier findings[3], since the apical meristem of the radicle is not so deeply located inside the seed; thus, the particle penetration may be sufficient in this case. The last interpretation is supported by significant stronger root length reduction per dose of higher energetic U particles (t-test for $5x10^6$ p/cm², $\alpha \leq .01$).

Further morphological and physiological characters of M_1 and M_2 plants (i.e. multicaulus and dwarf plants) were also affected significantly by doses above 10^6 p/cm². Seedlings evidently hit by HZE-particles (U 16MeV/n and Ar728 MeV/n, Fig.2a) showed drastic defects of tissue and tumours, an effect which was firstly reported for carbon ions in this plant[4].

Estimation of the number of particles per object hit under variant HZE-fluences yield the critical range above 10^6p/cm² which is equal to one or more hits per meristem cell of the embryo. This estimation indicates that the cross section of the primary HZE-effect is of the range of ~ 200µm². Preliminary results of HZE-experiments with ascospores of Sordaria fimicola (Fig.2b) confirm this range of cross section[5]. However, in dry diploid yeast cells there was no unequivocal dependence of mutation induction cross section on linear energy transfer (LET) but also a prominent influence of specific ion energy[6]. This was explained by the action of long-ranging δ-electrons[7].

[1] H. Bücker, Publ. Langley Research Center, Hampton, Virg. pp. 128-132 (1981)
[2] G. Kraft et al., Nucl. Instrum. Meth. 168, 175 (1980)
[3] K. Koller-Lampert, A.R. Kranz, Arabid. Inf. Serv. 19, 73 (1982)
[4] Y. Hirono et al., Radiat. Bot. 8, 449-456 (1968)
[5] A.R. Kranz, Int. J. Radiat. Biol. 43, in press (1983)
[6] J. Kiefer et al., Int. J. Radiat. Biol. 42, 591-600 (1982)
[7] F. Schöpfer et al., Radiat. Res. 82, 235-243 (1980)

Table 1

Survival of Arabidopsis seedlings (En-2) after HZE-irradiation with variant heavy ions and fluencies.

heavy ion MeV/n	control	10^5	10^6	$5x10^6$	10^7	$3x10^7$	$5x10^7$	10^8	$5x10^8$
U 16.2	97.5	95.0	59.4	61.4	-	5.1	0.0	-	-
U 5.9	88.0	84.4	88.0	-	76.7	-	-	-	-
Kr 18.0	91.2	-	-	30.0	26.1	-	-	8.0	0.0
Kr 5.9	91.2	-	-	75.8	84.0	-	91.2	93.0	80.0

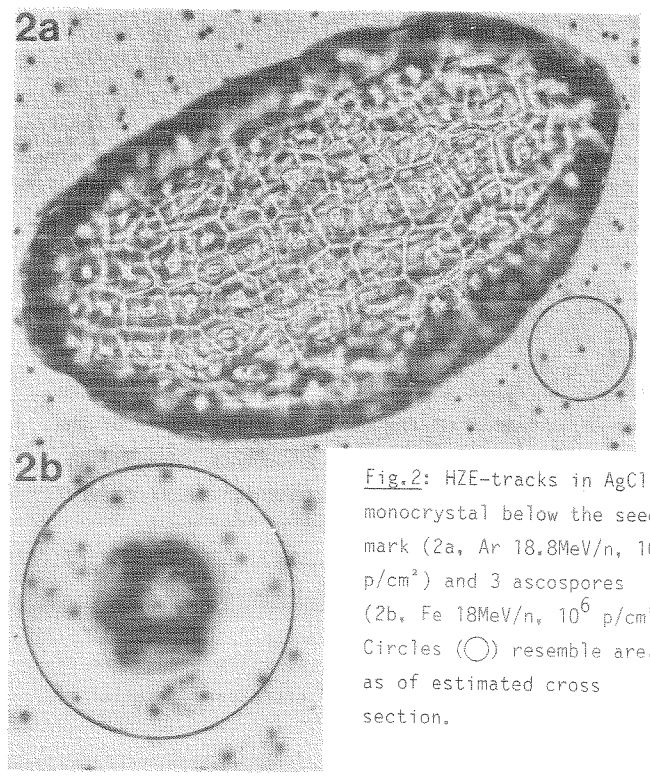


Fig.2: HZE-tracks in AgCl monocrystal below the seed mark (2a, Ar 18.8MeV/n, 10^6 p/cm²) and 3 ascospores (2b, Fe 18MeV/n, 10^6 p/cm²). Circles (◯) resemble areas of estimated cross section.

Investigation of Ion Induced Defects in Insulators by Small Angle Scattering G

D. Albrecht, P. Armbruster, R. Spohr
GSI Darmstadt
M. Roth
ILL Grenoble
K. Schaupert
II. Physikalisches Institut, Universität Gießen
H. Stuhrmann
Institut für Physikalische Chemie, Universität Mainz

Neutron- and X-ray small angle scattering were used to investigate the ion induced tracks in mica and two plastics (Hostaphan, Polystyrol). Because of the short duration of the track creation process it is only possible to observe the quasi equilibrium state which settles short time after irradiation.

The measurements show that an average track can be described as a continuous cylinder with a Gaussian density reduction in radial direction. In one kind of samples, Hostaphan, the cylindrical tracks show additionally nearly periodical waists. But it can be assumed that this is a consequence of the partly crystalline structure of the material. More investigations are needed to prove this and to show whether a new method for the analysis of this kind of materials eventually is found.

The measurements have verified our working hypothesis that the number of atoms displaced of the track region is proportional to the energy loss of the heavy ion. Moreover, a higher energy loss of the ion produces not only a larger track diameter **a** but also a correspondingly larger density difference between the track and the undisturbed sample material. Including data on the time dependent growing of the track and the contemporary decrease of the density-difference the following description of an average track is given.

$$a = P_{Ka} \cdot \sqrt[3]{\frac{dE}{dx}} \cdot e^{\xi t} \quad (1) \qquad \frac{\Delta\rho_{max}}{\rho_{sample}} = P_{K\rho} \cdot \sqrt[3]{\frac{dE}{dx}}\, e^{-2\xi t} \quad (2)$$

and

$$\frac{\Delta\rho_{track}}{\rho_{sample}} = \frac{\Delta\rho_{max}}{\rho_{sample}} \cdot \chi \cdot e^{-r^2/a^2} \quad (3)$$

Where ξ is a time constant, P_{ka} and $P_{k\rho}$ are constant factors, dE/dx is the specific energy loss, $\Delta\rho_{max}$ the maximum variation of the density in the middle of the track, $\Delta\rho_{track}$ the density difference between the track and unirradiated sample material. x is equal 1 for mica and Polystyrol (PS) and

$$\chi = C_2 \cdot \cos\frac{2\pi}{\bar{z}} z \quad \text{for Hostaphan}$$

C_2 gives the depth of the waist, $\bar{z}$ the mean value of their distance, and z is the coordinate parallel to the track axis. The determined values of the constants are shown in the following table:

Material	P_{Ka} $\sqrt[3]{\frac{mg\cdot cm}{MeV}}$	$P_{K\rho}$ $\sqrt[-3]{\frac{MeV\cdot cm^2}{mg}}$	ξ [d^{-1}]	$\bar{z}$ [nm]	C_2
Mica	$7\cdot10^{-8}$	$1.7\cdot10^{-2}$	$86\cdot10^{-6}$	-	-
Hostaphan	$10\cdot10^{-8}$	$1.6\cdot10^{-2}$	$328\cdot10^{-6}$	55-68**	0.6-10**
PS*	$8\cdot10^{-8}$	-	-	-	-

*only results for uranium tracks are available
**only measurable for uranium tracks

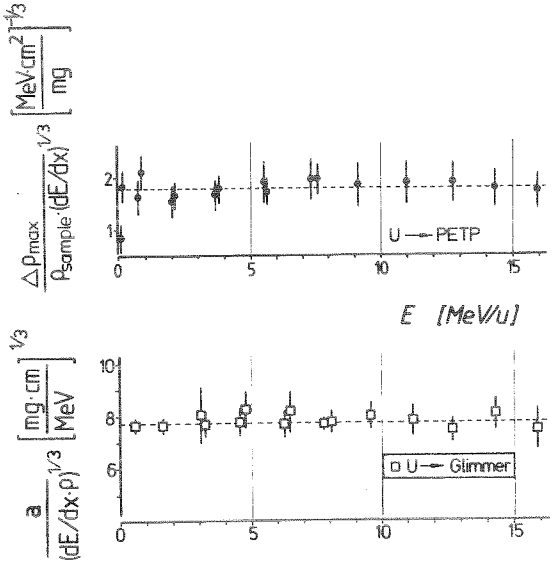


Fig. 1: Proof of equations (1) and (2).

Here no separation for different ions is made. The measurements show that the constants $P_{k\rho}$ and P_{ka}, in good approximation, are independent of the mass of the ion. Whether this holds also for different kinds of sample materials needs additional investigations.

With Eq. (3) we are not only able to predict the track size, but the integration of Eq. (3) delivers the number of missing atoms in the track which is proportional to the energy loss of the ion. The energy loss divided by the number of atoms therefore is a constant with an approximate value of 110 eV for mica and 25 eV for Hostaphan.

For more detailed information see /1/.

[1] D. Albrecht, GSI-Report 83-13

Structure Determination of Nuclear Tracks Using H_2O/D_2O Contrast Variation

K. Schaupert, G. Fiedler
II. Physikalisches Institut, Universität Gießen

D. Albrecht, P. Armbruster, R. Spohr
GSI Darmstadt

M. Roth
ILL Grenoble

H. Stuhrmann
Institut für Physikalische Chemie, Universität Mainz

As observed in previous measurements[1], water can diffuse into defects created by fast heavy ions in a polymer foil. By choosing appropriate mixtures of D_2O and H_2O one can alter the contrast between certain parts of the defect and the matrix material in neutron small angle scattering experiments. This method is known as 'Contrast Variation' [2].

In 1983 two neutron small angle scattering experiments at ILL-Grenoble were carried out, examining samples of Hostaphan (Kalle, West Germany) and mica, in order to explore the applicability of Contrast Variation to the structure determination of latent nuclear tracks. The samples were irradiated at the UNILAC of GSI with uranium ions with 8.6 MeV/u and areal doses of 2×10^{10} and 4×10^{10} ions/cm^2. Subsequently, the samples were soaked in various mixtures of D_2O and H_2O.

The experiments with Hostaphan showed a decrease of the scattering amplitude of tracks filled with D_2O of up to 46 %. This is attributed to the reduced density difference between track and matrix material in filled tracks. Using a set of mixtures of D_2O and H_2O we were able to show that the tracks cannot be filled completely. In Hostaphan only 25 % of the track volume is reached by the fluid.

The radial density distribution in the defects can be fitted by a Gaussian function[1]. A characteristic value is the radius a at which the density difference falls to 1/e of its maximum value. Filled tracks show an increase in the radius a up to 14 %; the reason could be that the fluid only reaches a central part of the defect, thus diminishing the maximum density difference. This leads to a larger distance a at which the density difference falls of to 1/e (Fig. 1).

In Hostaphan we observed a time dependence of the contrast of filled tracks. After approximately 3 h of soaking, the maximum contrast difference between soaked and dry samples was obtained. 95 % of the maximum value was already reached after 40 minutes. A soaking time of 27 days reduced the contrast difference to 40 % of the maximum value. We assume that the fluid penetrates the matrix material with a much smaller diffusion constant. Therefore, the contrast difference is reduced in the long range.

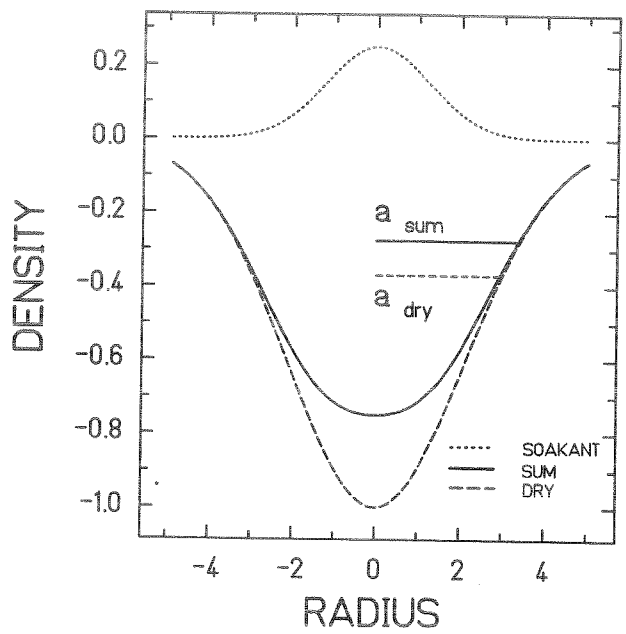


Fig. 1: Density variation in empty and filled tracks.

The diffusion seems to be reversible to a certain extent. Foils stored for 2 days in vacuum showed a scattering amplitude as if 60 % of the fluid had been removed. The track radius a decreased to nearly the value of unsoaked foils.

Measurements on mica showed that diffusion, originally observed in Hostaphan, does not occur to the same extent in this material. Considering the statistical uncertainty of the data one cane rule out the diffusion to be more than 10 % of the amount observed in Hostaphan. This may be due to the smaller track radius of 3.5 nm in mica vs. 5.9 nm in Hostaphan, while the maximum density difference is comparable. However, as indicated by an increased track radius in soaked mica, diffusion also occurs in this material.

[1] D. Albrecht, GSI Report 83-13

[2] H. Stuhrmann, Chemie in unserer Zeit, 13 (1979) pp. 11-22

AN APPROACH TO SIMULATE SOLAR WIND EROSION OF EXTRATERRESTRIAL SURFACES

K.Thiel, U.Saßmannshausen
Institut für Kernchemie der Universität zu Köln

Solar wind H- and He-sputtering is known to be the main shaping factor in the erosion of the fine-grained lunar regolith and strongly influences SCR-ion implantation profiles and ion saturation values of single dust grains on the moon.

In order to reduce irradiation times of the solar wind simulation experiments, carried out at GSI, ions heavier than He were included ($^4He^+$, $^{14}N^+$, $^{20}Ne^+$, $^{40}Ar^+$, $^{56}Fe^+$, $^{84}Kr^+$, and $^{nat}Xe^+$) and ion energies extended to 50...100 keV (~ solar flare energies).

As being representative for rockforming lunar mineral phases plagioclase, augite, olivine, ilmenite, silicate and Ni-Fe-phases of the meteorite "Brenham" and 4 types of glasses were chosen as targets. For most of the targets sputtering yields were determined for selected crystal planes and normal ion incidence. In cases where crystallographic effects were expected, the angle of ion incidence was varied in 15° steps from 0° to 60°.

Typical irradiation conditions for a 1 mm diameter ion beam are 0.8...3 μA ion current and 1...5 x 10^{18} cm^{-2} total ion dose at a working pressure of 1.3 x 10^{-7} to 2.7 x 10^{-5} Pa. Electrical charge build-up on the target was carefully compensated by electron flooding[1]. "On-line" ion flux monitoring was achieved by a specially designed Faraday ring-cup with remote-controlled shutter device.

The amount of sputtered target material was measured using the Tolansky interference method in the case of crystalline minerals and the particle track technique in the case of U- and Th-doped glasses[2]. The sputtering yields typically varied from 0.013 atoms/ion for bytownite irradiated with 50 keV $^4He^+$-ions to 9.1 atoms/ion for U-doped phosphate glass irradiated with 70 keV $^{nat}Xe^+$-ions[3].

Theoretical conversion of the experimental ion masses, energies and sputter yield results to lunar conditions (~ 1 keV H^+- and He^+-ions) should give consistent data for the lunar sputter erosion if the theory is applicable to the parameter range in question. Such a theoretical conversion of experimental sputtering data to lunar conditions was done by other groups using especially the theory of Smith[4]. Applying this theory to our measurements one gets a calculated solar wind H-He erosion rate, which depends on the ion mass used in the accelerator experiment (cf.Fig.1). This is a clear indication that the Smith theory cannot be used to convert sputter rates obtained with ions heavier than e.g. nitrogen to lunar parameters.

By extrapolating the values measured for the lighter ions to He and H and accounting for selenographic latitude and earth magnetospheric shielding of the moon[2], one obtains a solar wind sputtering rate for the Apollo 16 landing site between 0.021 Å/y (plagioclase) and 0.054 Å/y (olivine).

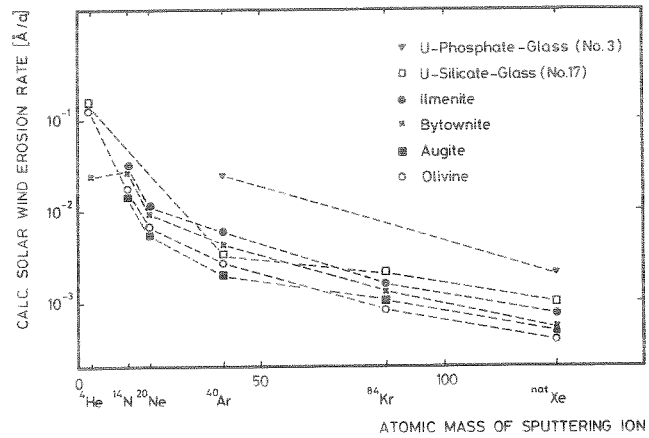


Fig.1: Solar wind erosion rate of glasses and rock-forming minerals calculated from experimental sputtering yield data using the theory of Smith.

[1] K.Thiel, H.Külzer, W.Herr, Nucl.Tracks 4, 19-26 (1980)

[2] K.Thiel, U.Saßmannshausen, H.Külzer, W.Herr, Radiation Effects 64, 83-88 (1982)

[3] U.Saßmannshausen, Thesis, Univ. Köln (1983)

[4] D.L.Smith, J.Nucl.Mat. 75, 20 (1978)

ION-INDUCED SPUTTERING OF SELECTED SELENIDES AND TELLURIDES

G.Freisem-Broda and K.Thiel
Institut für Kernchemie der Universität zu Köln

B.Wolf
GSI Darmstadt

The sputtering behaviour of the two-component semiconductors ZnSe, CdSe, ZnTe, CdTe was systematically investigated at the 300 kV-UNILAC-Test-Injector.

Single crystals of high purity material (4N for the Zn-compounds, 5N for the Cd-compounds) were prepared as 5 x 5 x 0.5 mm polished platelets with their large surface parallel to the [001] -crystal plane.

Yield and angular distribution of the sputtered particles under $^{84}Kr^{+}$-bombardment (working pressure $\leq 5 \times 10^{-5}$ Pa) were measured as a function of ion dose ($0.6...6 \times 10^{18} cm^{-2}$), ion energy (50...400 keV) and angle of incidence ($0^{o}...75^{o}$). To record the angular distribution of the emitted target atoms a special catcher technique was applied[1]. Total and differential sputtering yields were determined by INAA and ß-γ-autoradiography, respectively.

The preliminary results for the targets indicate that

- the sputtering yield increases with increasing ion dose,
- at oblique angles of ion incidence the relative sputtering yield $Y(\vartheta)/Y(0^{o})$ initially increases faster than $\cos^{-5/3}\vartheta$, which is predicted by the Sigmund theory for a target-mass/ion-mass ratio $\lesssim 3$ (Fig.1),
- the sputter yield reaches a maximum at ~ 100...200 keV and rapidly decreases at higher energies,
- sputtering in the linear collision cascade regime is indicated by the observation of focussing collision sequences (cf.Fig.2),
- in the dose interval $0.6...6 \times 10^{18} cm^{-2}$ no preferential sputtering was observed.

To verify unbiassed deviations from ordinary collision cascade theory the target surface relief possibly inducing geometric effects is presently being investigated by SEM-techniques.

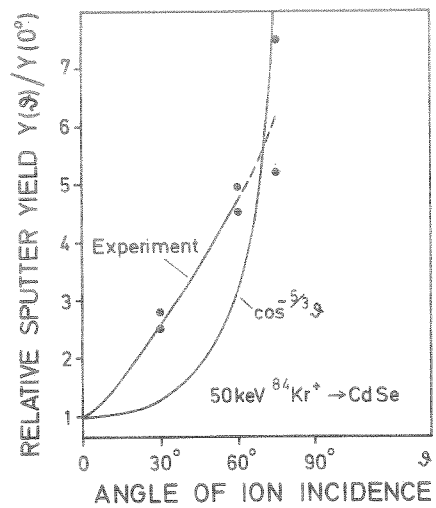


Fig.1: Relative sputtering yield of CdSe for 50 keV $^{84}Kr^{+}$-ions vs. angle of ion incidence. For comparison the $\cos^{-5/3}\vartheta$ curve is also given. At angles $\gtrsim 60^{o}$ re-sputtering of deposited target material from the catcher foil is no longer negligible (dashed part of the experimental curve).

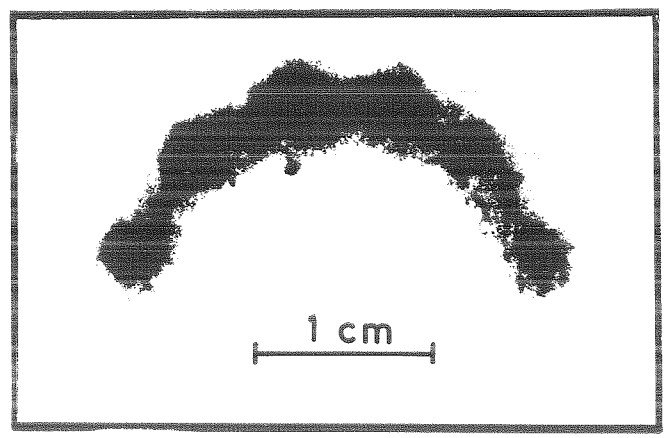


Fig.2: $ß^{-}$-autoradiograph of ^{115m}Cd-activity on the catcher foil for ^{84}Kr-induced sputtering of CdSe (structure: wurtzite, space group $P6_3mc$) after n-activation. The dark spots show enhanced sputter deposition due to focussed collision sequences along the <111>-axis.

[1] K.Thiel, H.Külzer, W.Herr, Nucl.Tracks 4, 19-26 (1980)

SPUTTERING AND IMPLANT BEHAVIOUR OF LiF:U-SINGLE CRYSTALS UNDER HEAVY ION BOMBARDMENT

K.Thiel, U.Saßmannshausen, U.Bangert*
Institut für Kernchemie der Universität zu Köln

D.E.Arafah
M.A.P.S., University of Sussex, Brighton, UK.

K.Recker
Mineralogisch-Petrologisches Institut der Universität Bonn

B.Wolf
GSI Darmstadt

It is known that collision cascade sputtering of alkali halides may suffer strong interference by high sputtering yields due to electronic excitation and thermal effects[1]. In a series of experiments at the 300 kV-Test-Injector at GSI it was shown that in the case of U-doped LiF-single crystals U-concentrations in the sub-percent range may cause even more complex deviation from the ordinary collision cascade mechanism of sputtering[2].

To study this effect five LiF:U-systems were chosen containing 0.325, 0.133, 0.115, 0.060 and 0.029 wt-% of uranium. Ion irradiation was performed with 200 keV $^{40}Ar^{+}$- and $^{84}Kr^{+}$-ions at a flux density of 100-150 $\mu A/cm^2$ on a 2 mm diameter beam spot. The fluence range covered by the experiments was $3x10^{15}$ to $4x10^{18}$ ions/cm^2.

To determine the amount of material and the species of the sputtered target atoms the particle track technique (making use of the reactions $^{6}Li(n,\alpha)$ and $^{235}U(n,f)$) and the Tolansky interference method were employed. Ion-induced changes in the chemical composition of the radiation affected surface layer of the targets were investigated by Rutherford backscattering (RBS)- and nuclear reaction analysis (NRA)-techniques, using the apparatus at the University of Sussex in Brighton. The NRA-data for Li and F were derived from measuring the reactions $^{7}Li(p,\alpha)$ and $^{19}F(p,\alpha)$ induced by 1.5 MeV protons.

Compared with pure LiF the total sputtering yield of LiF:U is enhanced by U-concentrations of less than ~0.06%. At higher U-concentrations the sputter yield again decreases and reaches the value of pure LiF at ~0.3% U. This effect is attributed to at least two processes affecting sputter yield contrarily:

- "evaporation" of volatile U fluorides and
- "blocking" of F- and H-center diffusion by uranium.

Besides effects that depend on the concentration of uranium several ion dose effects became apparent[2] especially in the dose range where stoichiometric sputtering is not yet reached. In this disequilibrium phase of target erosion, according to collision cascade theory, Li being the lightest target component should be preferentially sputtered. This was,however, not observed (cf.Fig.1).

For 200 keV ^{40}Ar-ions doses of less than ~10^{18} ions/cm^2 are still in the non-stoichiometric range of sputtering. As Fig.1 shows, in this range the erosion rate of U (closed circles) exceeds the emission of Li (crosses) up to a factor of 4.

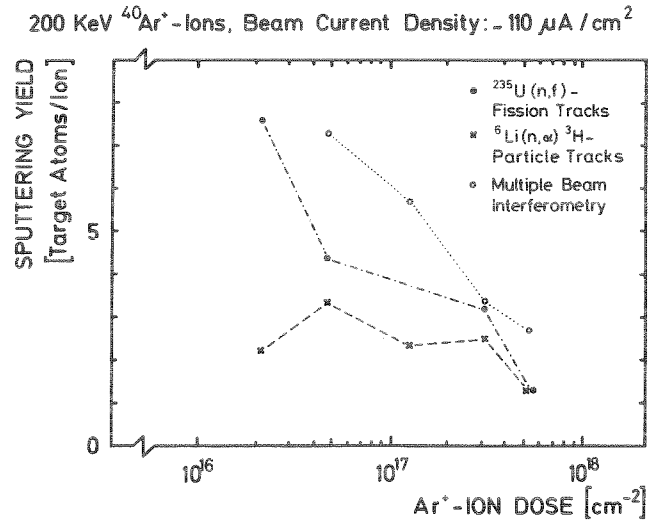


Fig.1: Sputtering yield of U-doped LiF crystals irradiated with 200 keV $^{40}Ar^{+}$-ions at normal incidence (Li and U sputtering yields were normalized to 100 % element content in the target).

[1] J.P.Biersack and E.Santner, Nucl.Instr.and Meth. 198, 29 (1982)

[2] K.Thiel, U.Saßmannshausen, D.E.Arafah and K.Recker, Nucl.Instr.and Meth.(1984)(in press)

*Present address: Dept.Electronic and Electrical Engng.,University of Surrey,Guildford, UK.

Influence of Heavy Ion Induced Radiation Damage on the Piezoelectric Properties of PVDF

B. Hahn*, B.E. Fischer
GSI Darmstadt
*Deutsches-Kunststoff-Institut, Darmstadt

PVDF = Polyvinylidenfluoride $(CF_2 - CH_2)_n$ is a partly crystalline polymer, the monomer of which possesses a strong electric dipole moment due to the CF_2 group. It forms at least 5 different crystal-modifications (α, β, γ, δ, ε) of which 3 (β, γ, δ) are polar. Prepared from the melt PVDF contains mainly α-type unpolar crystals which can be almost completely transformed into the polar β-type crystals by uniaxial stretching. These crystals can be permanently aligned by a strong external field. Thus an uniaxially stretched foil of PVDF exhibits a permanent macroscopic electric dipole moment and a strong piezoelectric effect after polarization in an electrical field of about 1 MV/cm. Remarkably the polar crystals themselves show a much smaller piezoelectric effect than the compound material containing crystalline and amorphous phases together. (Here amorphous means anything less ordered than the crystalline phase.) Therefore the amorphous phase must play a decisive role for the piezoelectric response of the compound material. To elucidate this role, several different methods have been tried to introduce structural defects in a controlled manner.[1] One of these was irradiation by heavy ions in a preliminary experiment.

Fig. 1 shows how the piezoelectric coefficients d_{31} and d_{32} (explained in fig. 2) have been affected by irradiation with argon ions: At the highest dose both coefficients become smaller, as one would expect for increasing amounts of disorder introduced into a polar structure. But surprisingly at a dose of $5 \cdot 10^{11}$ ions/cm² d_{32} rises to twice its original value whereas d_{31} stays almost constant, indicating that the amorphous phase is preferentially (and advantageously) affected. Therefore it seems worthwhile to extend these measurements to lower doses.

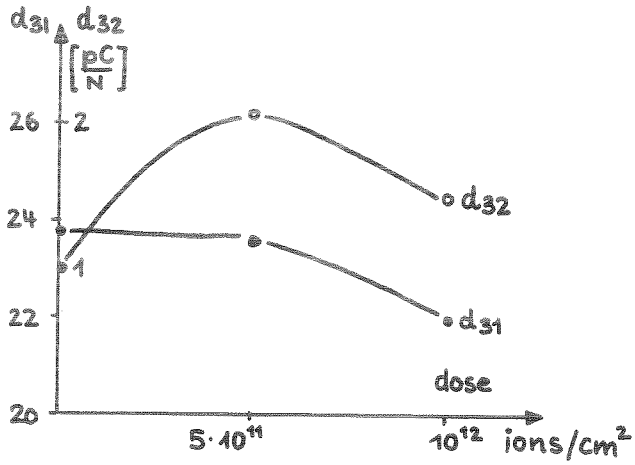


Fig. 1 Influence of heavy ion irradiation on the piezoelectric coefficients of PVDF.

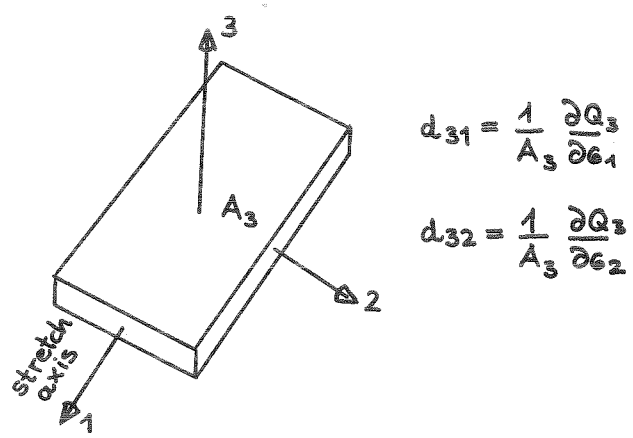


Fig. 2 Definition of the piezoelectric coefficients. d_{31} and d_{32} give the magnitude of the piezoeffect measured over the electrode area A_3 if the foil is stretched in the 1- and 2-direction respectively.

Reference

1) B. Hahn, Piezo- und pyroelektrische Eigenschaften von Polyvinylidenfluorid / Polymethylmethacrylat-Mischungen, Ph.D. Thesis, 1983

* present address: IBM, 5600 Cottle Road, San Jose, Calif. 95193, USA

B.E. Fischer, GSI Darmstadt
K.-D. Hummel, participant of GSI's student program 1983

The method of producing graded index antireflecting surfaces by the nuclear track technique, described in GSI annual report 1982, p. 207, has now been applied to metaphosphate glass[1] (Leitz ZNP) using 1.4 MeV/u nickel ions and compared to the socalled neutral-solution-processing-method[2]. The results are shown in fig. 1a and b.

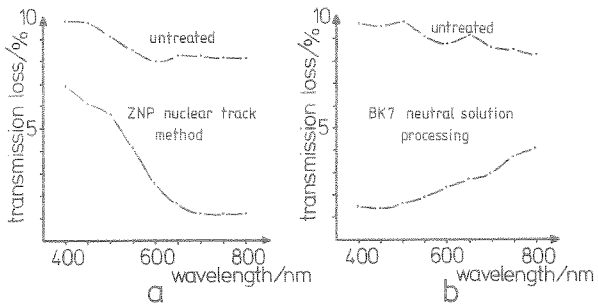


Fig. 1

a) Transmission loss through a PK50 glass plate of 2 mm thickness. Upper curve untreated surfaces. Lower curve ZNP glass irradiated by 7 x 10^{11} 1.4 MeV/u nickel ions per cm^2 on both sides and etched in 0.06 n NaOH for 4 min. at 20° C.

b) Transmission loss through Schott borosilicate glass BK7. Upper curve untreated surfaces. Lower curve both surfaces treated by neutral-solution processing[1]. (26h in solution of 0.034-M Na_2HAsO_4 and 1.3 x $1o^{-3}$-M Al^{3+} in distilled water at 87°C.)

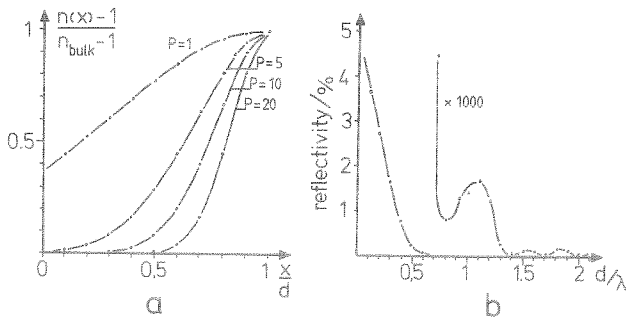


Fig. 2

a) Theoretical curves for refractive index n(x) as a function of depth, calculated for various values of porosity P (P = track density x cross-section of an individual etched track).

b) Reflectivity of one surface, calculated for P=5 and bulk refractive index n=1.5 as function of d/λ = thickness of graded-index layer divided by wavelength.

At the same time a more accurate theory of graded-index surfaces produced by the nuclear track technique has been worked out (by K.-D. Hummel). The theoretical results in fig. 2 clearly show the big advantage of the method, namely that it is inherently a broad band antireflection treatment. For this reason it is also effective for a wide range of angles of incidence as long as the depth d of the etched track cones is sufficiently large. In fact reflectivity is negligible against bulk absorption for most angles of incidence.

Unfortunately a comparison of theory (fig. 2b) and experiment (fig. 1a) shows that still a lot is to be done to reduce light scattering at small wavelengths far enough to realize the promises of the method.

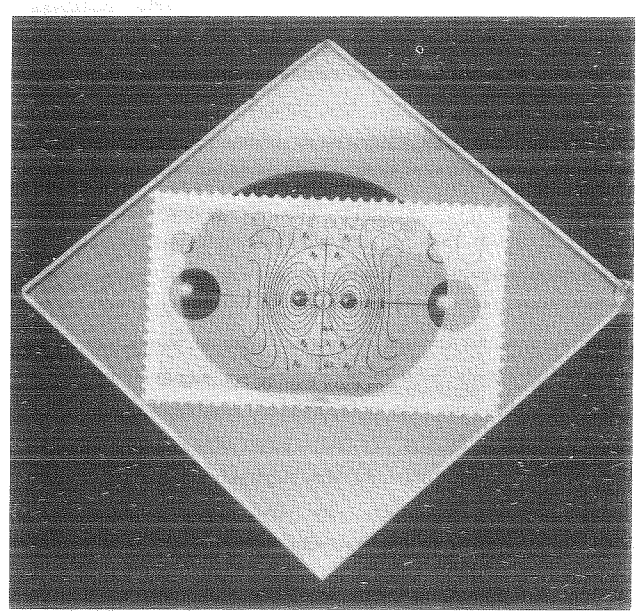


Fig. 3: Looking through a graded index antireflecting surface. The central round area has been treated as described in fig. 1a.

References

1. J. Aschenbach, G. Fiedler, H. Schreck-Köllner, and G. Siegert; Special Glasses as Energy Detectors for Fission Fragments; Nucl. Instr. Meth. 116, 389 (1974)

2. L.M. Cook, W.H. Lowdermilk, D. Milam and J.E. Swain
Antireflective surfaces for high-energy laser optics formed by neutral-solution procesing
Applied Optics, Vol. 21, No. 8, April 15, 1982

Manufacture of Single-Pore Membranes

H. Gaiser, H.-R. Kiesewetter, K. Poppensieker, R. Spohr
Gesellschaft fuer Schwerionenforschung, Darmstadt

K. Schaupert
Universitaet Giessen

The nuclear track technique is capable of generating very precise channels in many insulators and enables the manufacture of single-pore membranes for medical diagnostics.[1] . Recently, Hoechst AG has ordered 10,000 single pore membranes for performing clinical tests which will be manufactured by the following system (Figure 1):

Rapid Irradiation System

- The heart of the system is a commercial cine-camera of the 35-mm norm, normally applied in x ray diagnostics[2] .
- As membrane material a 30 µm thick film strip of polycarbonate[3] is used.
- The ion irradiation is performed outside the vacuum chamber using a titanium window of 5 µm thickness and 2 mm diameter. Behind the window, the beam is restricted to a diameter of 0.2 mm by a diaphragm connected to the camera.
- Particles that penetrate the film strip are detected by a surface barrier detector. The detected events activate simultaneously the UNILAC beam shutter ($\tau \approx 100$ µs) and the transport to the next frame of the film strip ($\tau \approx 0.3$ s) at a distance of 19 mm.
- For easier location of the single pores, the film strip is marked in regular intervals by multiple irradiations, creating visible markers after etching. In the same way, unwanted double irradiations are marked.

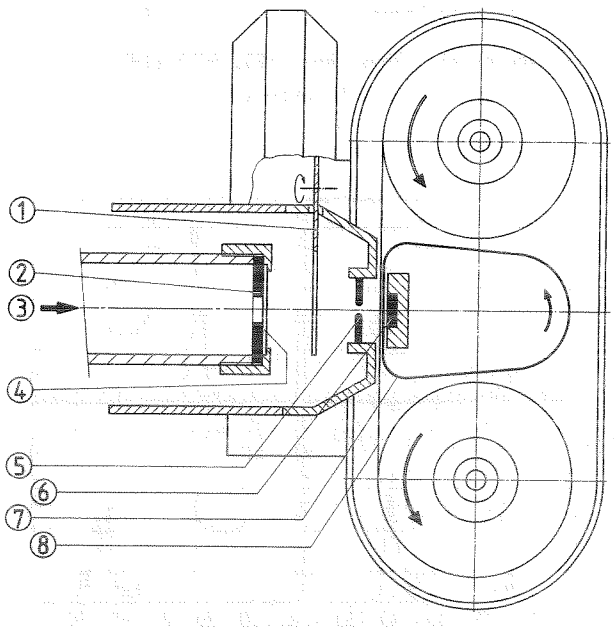


Figure 1. Principle of rapid irradiation system. (1) mechanical beam shutter, (2) window aperture, (3) beam direction, (4) window foil, (5) beam defining aperture, (6) surface barrier detector, (7) film transport loop, (8) irradiated film strip.

A first test run of the system was carried out on December 19, 1983. During 15 min of beam time about 1,000 irradiations were performed.

Etching

As the passage time of red blood cells through a single-pore membrane depends critically on the diameter of the pore, it is important to generate pores with a small pore size variation. In order to obtain identical etching conditions over the length of the film strip, a cyclic etching bath was used.

Control of the Pore Sizes

The present task requires pores of 4.5 µm diameter with a maximum deviation of ± 0.2 µm (4 %). In order to obtain the pore size distributions for different etching conditions, large-area irradiations were performed on a film strip of 50 m length on August 19, 1983. During 90 s of beam time, roughly 1,000 beam spots of one cm^2 area were generated with an areal dose of about 10^6 ions per cm^2. After etching, holes of approximately 6.4 µm nominal diameter were obtained. The holes were controlled by image analysis using an optical microscope and yielded the following results:

- The reproducibility has a maximum deviation of ± 0.1 µm on one specific hole, measured repeatedly from different starting positions.
- Although the half-width of the diameter distribution is relatively small (< ± 0.2 µm), the measured maximum deviation of about ± 0.5 µm is too large. Therefore, at present, each individual hole must be controlled optically.

---

[1] H.G. Roggenkamp, F. Jung, H. Kiesewetter: **Ein Geraet zur elektrischen Messung der Verformbarkeit von Erythrozyten.** Biomedizinische Technik, vol.28, pp. 100-104 (1983)

[2] Fa. ARRI, Tuerkenstr. 89, D-8000 Munich 40

[3] Makrofol N, Bayer AG, Dormagen, FRG

Heavy ion track etching in olivine

C. Perron, M. Maury, P. Pellas
CNRS and Museum d'Histoire Naturelle, Paris, France
V.P. Perelygin, S.G. Stetsenko
Joint Institute for Nuclear Research, Dubna, USSR

In the course of a study of track lengths and track etch rates of energetic heavy ions, in olivine crystals ($(Mg,Fe)_2SiO_4$) it has been realized how important a role the etching process itself can play, about as important, in many cases, as that of the radiation damage structure of the latent tracks. This is specially true for the very long tracks (> 2.5 mm!) of relativistic U ions (to be published), whose proper revelation requires a perfect command of track etching. We thus made a systematic study of this process in olivine, using 16 MeV/u U ion tracks. Some results are presented here.

16 MeV/u U ions are well suited for such a study, since we have shown that, for these ions at this energy, the track etch rate is constant along the ion path, down to about 10 µm from the end of the range. This is because the linear density of extended defects in the latent track is so high that all defects overlap[1], so that all portions of all tracks should have the same etch rate, equal to that of an extended defect. Any difference in behaviour from track to track can thus, in principle, be attributed to the etching process.

After irradiation, natural olivine crystals of both terrestrial and meteoritic origin were etched in WN etchant - a mixture specially designed for olivine[2]- of slightly varying composition and for varying times, but, in any case, of duration too short to reveal the tracks to the end of the range (at 16 MeV/u, a U ion track is ∿100µm long in olivine). Fig. 1 shows measured track length distributions after (a) and (b) a 20 mn and 60 mn etch in WN etchant at pH=8.0; (c) and (d) a 20 mn and 60 mn etch in WN etchant at pH=7.8. These 4 runs were performed on fragments of the same crystal, so that the orientation of the tracks with respect to the crystallographic axes, and the chemical composition of the crystal were the same in all 4 cases. The circles schematize the increase of the track "diameter" in 1 hour.

We note that the etch rate decreases while the etching proceeds: from (a) and (c) to (b) and (d) respectively, the etching time has been increased by a factor of 3, but the mean track length by only a factor of ∿2. In the case of very long tracks, the track etch rate reaches a value close to zero, long before the whole etchable length has been revealed, which is particularly disturbing when length measurements are made for particle identification purposes. Then it is clear that a slight decrease of the pH of the etchant gives more narrow track length distributions, but significantly increases the bulk etch rate of the crystal (the track etch rate is not much changed). The broad distributions in (a) and (b) are probably due to heterogeneities of some kind (chemical impurities ?) which block the etching of some tracks. In this respect, an etchant with a lower pH is more efficient, but is nevertheless not well suited for the revelation of very long tracks, because of the lower value of the ratio of track etch rate to bulk etch rate. Similar experiments have been made with a modified WN etchant (the proportion of oxalic acid was increased) such as is used by the Dubna group. At pH=7.8, the track etch rate is slightly larger (> 50 µm in 1 hour), but the bulk etch rate remains low ("diameter" increase of ∿ 0.4 µm/h), which makes it a better etchant for long tracks. The length distributions are, however, broader than in Fig. 1 (c) and (d).

It seems clear to us that extreme attention should be given to the etching conditions when revealing very long tracks, wether artificial (accelerator-produced), or natural (Cosmic Ray tracks in meteorites). In particular, on the basis of these results, we are now trying to develop techniques to etch tracks from several points along the ion path, in order to reliably reveal the full etchable length.

[1] E. Dartyge et al., Phys. Rev. B23, 5213 (1981)
[2] S. Krishnaswami et al., Science 174, 287 (1971)

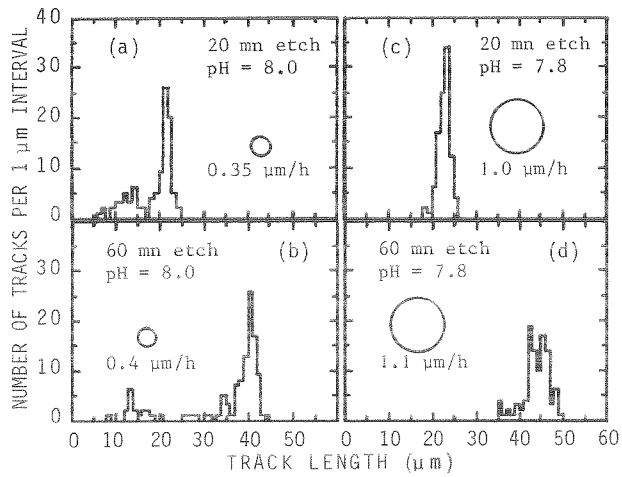


Fig. 1: 16 MeV/u U ion track length distributions after etching fragments of the same olivine crystal in WN etchant at pH, and for times as indicated. The circles schematically represent the increase of the track "diameters" in 1 hour.

Modification of the CR-39 microfilter pores

M. Berndt and J. Krause, G. Siegmon, R. Beaujean and W. Enge

Institut für Reine und Angewandte Kernphysik
Universität Kiel, D-2300 Kiel (FRG)

In previous works (BERNDT et al. 1982, 1983) the CR-39 microfilter was already presented. TRESS et al. (1982) have shown that the air throughput through a mica microfilter can be increased by nearly one order of magnitude by rounding off the entrances of the filter pores. The reason might be that the rounded off entrances may allow a smoother air flow through the capillaries than the sharp etched filter pores. The rounded off pore entrances can be obtained by a two-step etching process using H_2F_2 and boiling NaOH as etchants for mica (KHAN, H.A. and KHAN, N.A., 1981). In a similar way the entrances of the CR-39 microfilter pores can be modified.

In 1979 SOMOGYI and HUNYADI have described a multistage etching procedure with NaOH and the so-called PEW_x solution (PEW_x = 15g KOH + xg C_2H_5OH + (85-x)g H_2O) that can be used e.g. for distinguishing the short- and long-range tracks in a CR-39 detector. These etchants have different ratios between the track etching rate along the track and the bulk etching rate resulting in different etch-pits. This effect can be used for producing CR-39 microfilters with rounded off pore entrances.

A laboratory specimen was obtained by irradiating a 90 µm thick CR-39 sheet (manufactured by Pershore Moulding Ltd.; Pershore, Worcestershire, England) containing about 1% dioctyl phthalat. The irradiations were carried out by the GSI, Darmstadt (FRG), with ^{56}Fe-ions (10^6 ions/cm^2) having a specific energy of 16.3 MeV/nucl.. When only using 6n NaOH (120 min., 70°C) as an etchant the ratio between the track etching rate and the bulk etching rate is so high that we get a microfilter with cylindric pores:

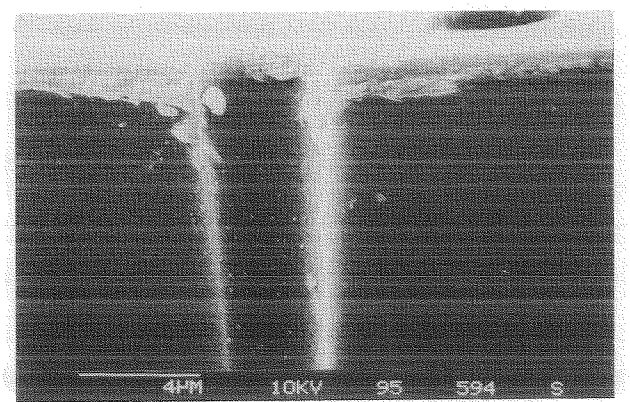


Fig. 1 A cut through a pore of a CR-39 microfilter by using only 6n NaOH as etchant (BERNDT et al., 1982)

To get a microfilter with rounded off pore entrances we used a three-step etching procedure: first PEW_{65} (78°C, 30 sec.), then PEW_{40} (78°C, 10 sec.) and finally 6n NaOH (70°C, 120 min.). The following micrograph is showing a cross-cut through a pore of this filter.

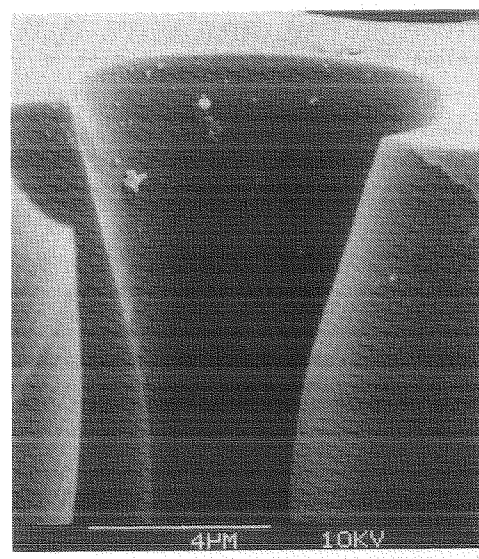


Fig. 2 A filter pore of a CR-39 microfilter after a three-step etching procedure

This micrograph is showing very clearly the rounded off entrance of a CR-39 microfilter pore after the etching procedure described above.

Using a multistage etching procedure with 6n NaOH and PEW_x it is possible to round off the entrances of the CR-39 microfilter. This modification of the filter pores should increase considerably the air throughput through this microfilter as it does in mica microfilters.

Acknowledgement-The authors like to thank Dr. C. Samtleben, Mr. W. Reimann and Mrs. U. Schuldt (Kiel University) for the SEM photos with the SEM Cambridge S 150 and Dr. R. Spohr for the performance of the exposure at the GSI.

BERNDT, M., SIEGMON, G., BEAUJEAN, R. and ENGE, W.: GSI Scientific Report 1982, p. 208

BERNDT, M., SIEGMON, G., BEAUJEAN, R. and ENGE, W.: Proceedings of the 12th International Conference on Solid State Nuclear Track Detectors, Acapulco, Mexico, 1983, Pergamon Press

KHAN, H.A., KHAN, N.A. and SPOHR, R.: Nuclear Instruments and Methods 189 (1981) 577-581

TRESS, G., ELLINGER, M., KHAN, E.U., KHAN, H.A., VATER, P., BRANDT, R., KADNER, M.:Nuclear Tracks, Vol. 6, No. 2/3, p. 87-97, 1982

SOMOGYI, G. and HUNYADI, I.: Proceedings of the 10th SSNTD Conference, Lyon, France 1979, Pergamon Press, p.443-452

Nuclear Track Filters Made of Quartz Crystals, to be used in Environmental Protection

M. Plachky, G. Tress, E.U. Khan, P. Vater, R. Brandt
Kernchemie, Philipps-Universität Marburg

W. Holländer
Fraunhofer-Institut für Toxikologie und Aerosolforschung, Münster

The purpose of these investigations is to develop a technique for the on-line measurement of aerosols. " AT " - cutted quartz oscillators are irradiated with heavy ions at GSI and then etched to get filters. Density, shape and size of the holes can be chosen according to need similar to those of mica filters. Such a quartz filter provides a very sensitive balance to determine the mass of tiny aerosol particles; the characteristic frequency of the oscillator depends on its mass; loaded with particles, the mass and therefore the frequency change. It is known that practically a change of mass $\Delta m \simeq 10^{-9}$ g/cm² gives a change in frequency Δf = 1 Hz, keeping other conditions constant.

As mentioned above to get the desired hole size and useful hole shape, which depends on crystallographic orientation of the cut and on the etchant, we started systematic studies of etching characteristics of "AT"-cutted quartz. After irradiating quartz of 80 and 100 µm thickness and 8 mm diameter with heavy ions from the UNILAC we proceeded as follows:

1. Etching with 48% HF at room temperature for several hours results in holes with triangular shape. The surface becomes rough with a saw tooth like structure.
2. Etching with 15 N KOH for several hours at 130 °C (keeping the normality constant) results in prolate shaped entrances.
3. The above procedure but with 15 N NaOH leads to hole entrances as shown in Fig. 1.
4. Etching in two steps with KOH and then with NaOH (both 15 N, 130 °C, several hours) results in holes with polygonal entrances, Fig. 2.

The filters produced with procedure 3 & 4 suit better for filtration than the others.

SEM investigations, Fig. 3, show the parallel channels of the pores. Preliminary experiments indicate that the quartz filters also oscillate. Further studies are in progress in order to check the resonating properties of these new filters. Continued investigations are needed to get hole densities, shapes and sizes best suited to obtain quartz filters with optimum properties.

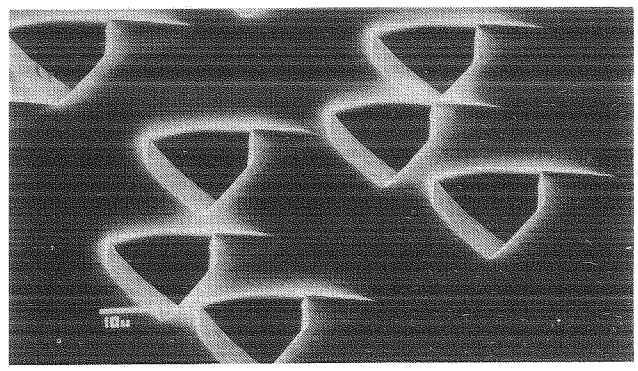


Fig. 1. Nuclear track filter, produced by irradiation of quartz crystal with heavy ions and subsequent etching in NaOH.

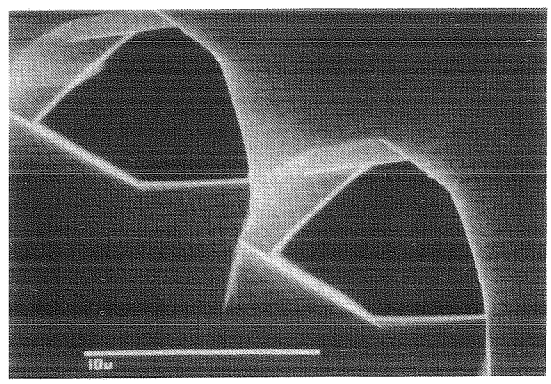


Fig. 2. A filter as in Fig. 2, but etched in KOH and additionally in NaOH.

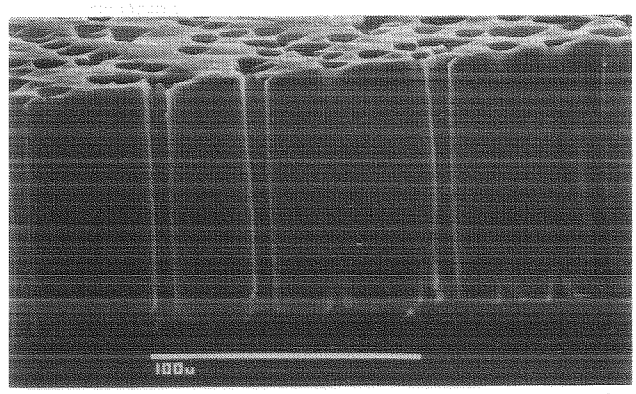


Fig. 3. Cross-section of the filter in Fig. 2, showing parallel channels.

The Gas Flow through Mica Nuclear Track Microfilters: Experiments and Calculations Using a Capillary Model

G. Tress, P. Vater, R. Brandt
Kernchemie, FB 14, Philipps-Universität, 3550 Marburg

In order to understand the properties of our Mica Nuclear Track Microfilters MNM better, we carried out some studies. The air flow through MNM has been measured experimentally at 300°C gas temperature and pressure drops up to 0.2 bar. The through put can be calculated using a semiempirical capillary model[1,2,3].

The experimental results of the gas flow $\dot{V}$ through mica filters (thickness $l \leq 102$ µm, pore size 0.3 µm$\leq k \leq$16 µm, porosity$\varepsilon \leq$10 %) are shown in Fig.1 for $\dot{V} = f(\Delta p)$ and Fig. 2 for $\dot{V} = f(\bar{k})$.

The measurements using filters with sharp-edged and rounded-off entrance and exit channels indicate that $\dot{V}$ is the same at given ε and k. The gas flow through the capillaries is always laminar and can be characterized according to the pore size[1,3]:

a) $k > 8$ µm: the flow is viscose (Hagen-Poiseulle-region);

b) 0.5 µm $< k <$ 8 µm: the region of gas slippage;

c) $k <$ 0.5 µm: the transient region.

$\dot{V}$ shows a linear dependence on $\sqrt{1/T}$, but not on Δp with T = const. For the pore size $k > 8$ µm $\dot{V}$ depends on ε.

It is not possible to describe the gas flow through a single micafilter capillary with the classical hydrodynamic equations[3]. However, a modified capillary model, originally developed by J. Machãcova, K. Spurny et al. for Nuclepore-filters[2], allows the calculation of the gas flow through mica filters. The experimental data for all the flow regions (classic region, region of slippage, transient region) are fitted by the following equation (p_1 = 1 bar)[3]:

$$\Delta p_{calc} = (p_1 + \frac{C}{k/2}) - \left[(p_1 + \frac{C}{k/2})^2 - \frac{1.14 \cdot 10^{-2} \cdot p_1 \cdot l \cdot u \cdot \eta}{(k/2)^2} \exp. \frac{k^2}{l}\right]^{0.5}$$

(C = 0.0305, u = air flow velocity, η = dynamic gas viscosity)

Fig. 3 shows a good agreement between Δp_{exp} and Δp_{calc}.

1. G. Tress et al., Journ. of Aerosol Science 1983, in print
2. J. Machãcova et al., Coll. Czech. Chem. Commun 35 (1970) 2087
3. G. Tress, Dissertation, Kernchemie, Uni Marburg 1983, unpublished

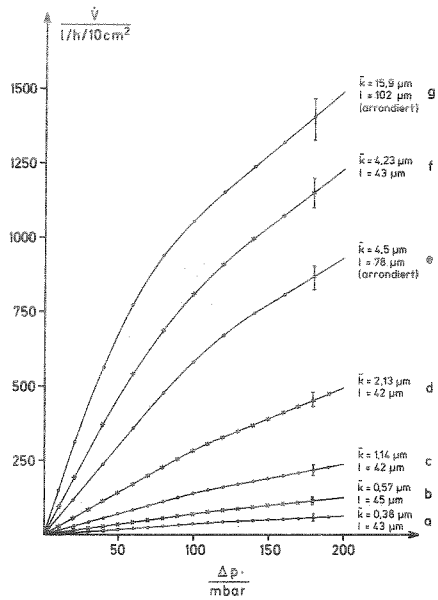


Fig. 1: Air flow $\dot{V}_{exp}$ (porosity ε = 5%) through mica filters as a function of pressure drop Δp at different pore sizes k (T=20°C, 42µm $\leq l \leq$102µm).

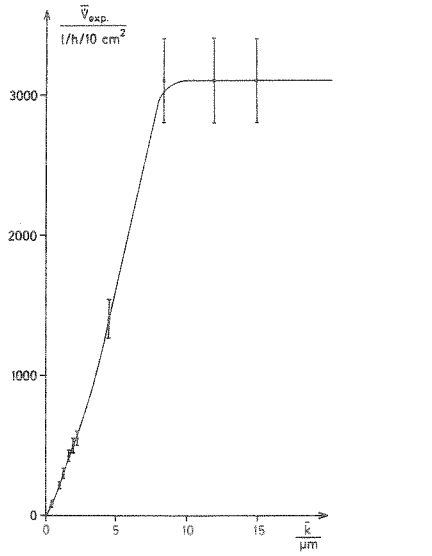


Fig. 2: Air flow $\dot{V}_{exp}$ (porosity ε = 5%) through mica filters as a function of the pore size k (1:40 to 45µm) measured at gas temperature of 20°C and Δp = 200 mbar.

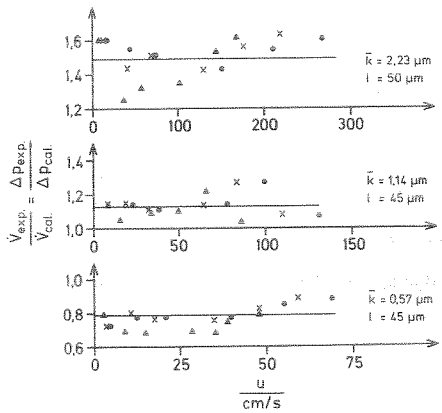


Fig. 3: $\Delta p_{exp}/\Delta p_{calc}$ as a function of the air flow velocity u up to 300°C gas temperature (● 20°C, x 100°C, ▲300°C)

Secondary Ion Emission from Amino-Acids as Function of Projectile Velocity

O. Becker, W. Knippelberg and K. Wien
Institut für Kernphysik, TH-Darmstadt

Using the beam facilities of the Stripper Hall the amino-acids Valine and Phenylalanine were bombarded by Gd ions having energies from 0.047 to 1.40 MeV/N, in order to initiate the emission of secondary ions from the target surface. The targets were produced by evaporating a 2000 Å layer of the organic material onto Al-foils. The original beam energy was varied by means of degrader foils. The methods of secondary ion spectroscopy have been described elsewhere[1].

The aim of these experiments was to investigate, how the formation of ions depends on the projectile velocity and effective charge or specific energy loss and also on the chemical and physical properties of the target. So far our earlier results concerning the charge state dependence[2] or emission of ions due to impurities on metallic surfaces[1] are hardly to explain in terms of available desorption models. Only in the case of metal ions ejected from metal surfaces, where the electronic stopping power is less important, a combination of the conventional sputter theory and a special ionisation mechanism gives a satisfying description[3].

Fig. 1 shows yield curves of undestroyed protonated or deprotonated molecular ions. For projectile velocities $v_{Gd} < 0.9$cm/ns the curves of the positive ions follow approximately $(dE/dx)^2_{el}$, in case of the negative ions the

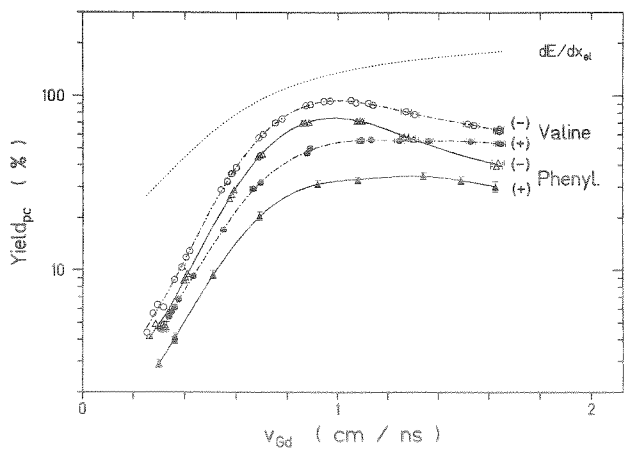


Fig. 1: Yields of the $(M+1)^+$ and $(M-1)^-$ Ions of Valine and Phenylalanine (including yields of several weak satellite lines) per incident Gd ion as function of projectile velocity. The index pc (= partially corrected) indicates that the yields are corrected for dead-time losses but not for ion-detection efficiency and transmission (74 %). $(dE/dx)_{el}$ is given in arbitrary units.

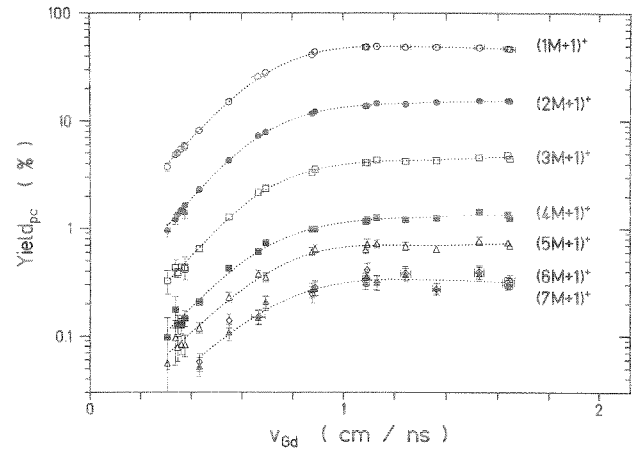


Fig. 2: Yields of Valine cluster ions (M = molecular mass number) presented in a similiar way as in Fig. 1.

slopes are steeper. A remarkable observation is the distinct decrease of the $(M-1)^-$ yields above $v_{Gd} = 1$cm/ns despite the fact that the energy deposited around the projectile path is still increasing with v_{Gd}. This result ist probably due to the distribution of electronic excitation carried by δ-electrons into the solid[4]. The additional Phenyl group of Phenylalanine has only little influence, - the decrease in the high velocity part of the curves is slightly more expressed for Phenylalanine.

With respect to a multi-hit theory of Sundqvist et al.[5] one would expect that the increase of yields with v_{Gd} should be more pronounced for molecules of large extension such as cluster ions of Valine. The first 7 Valine-cluster ions could be detected, i.e. the cluster diameter changed by at least a factor of 1.9. Their yield curves presented in fig. 2, however, follow more or less the same slope.

[1] O. Becker, W. Knippelberg and K. Wien, Physica Scripta, Vol. T6, 117 (1983)

[2] W. Guthier, O. Becker, W. Knippelberg, U. Weikert, K. Wien, S. Della Negra, Y. LeBeyec, P. Wieser and R. Wurster, Int. J. Mass Spectrom. Ion Phys., 53, 185 (1983)

[3] W. Knippelberg, Thesis, Institut für Kernphysik der TH-Darmstadt, 1984

[4] C.C. Watson and T.A. Tombrello, preprint BAP-33, to be published in Rad. Effects.

[5] B. Sundqvist, A. Hedin, P. Håkansson, I. Kamensky, J. Kjellberg, M. Salephour, G. Säwe and S. Widdigasekera, Int. J. Mass Spectrom. Ion Phys., 53, 167 (1983)

A RESEARCH PROGRAM FOR STUDYING THE USE OF ION BEAM TECHNIQUES FOR CORROSION PROTECTION

H.Ferber, W.Ensinger, A.Meger, Ph.Munn, G.K.Wolf; Physikalisch-Chemisches Institut der Universität Heidelberg. H.Folger; GSI Darmstadt

Since 1981 we run a test program for exploring potential applications of ion beam techniques in the field of corrosion. It is coordinated by DECHEMA and funded by BMFT. We collaborate with the corrosion laboratories of the company BAYER and Institut für Werkstoff-Forschung der DFVLR, Köln. A major part of the necessary ion irradiations is done with the 300 keV test accelerator at GSI. A short progress report is given below:

1. Corrosion of titanium in strong acids

The corrosion of titanium in strong acids is a problem in many chemical plants. Commercially available alloys with 0,2 Pd help to overcome these problems, but are rather expensive. In our earlier work[1] we could show that implantation of Pd ions in titanium substrates lead to a very corrosion resistant surface layer protecting the substrate. Much less palladium is needed for this treatment in comparison with the bulk alloy. During 1983 we tested different types of palladium layers on titanium:

Ti+ 50nm Pd evaporated on the substrate
Ti+ 50nm Pd electrodeposited on the subst.
The above layers with subsequent bombardment with rare gas ions of different energy, in order to intermix layer and substrate.

All these treatments resulted in a good corrosion resistance. But, the bombarded ones were mechanically more stable and showed much less flaking of Pd during the corrosion tests. The order of performance was:

Ti+ $Pd_{electr.}$ $\gg$ Ti+ $Pd_{evap.}$ $\gg$ Ti+ $Pd_{electr.}$ + 2-400 keV Kr^+ $\gg$ Ti+ Pd_{evap} + 2-400 keV Kr^+.

The best layers protect titanium for at least one year and have excellent adhesion and mechanical stability. Experiments under practical industrial conditions are in preparation.

2. Corrosion of stainless steel in strong acids

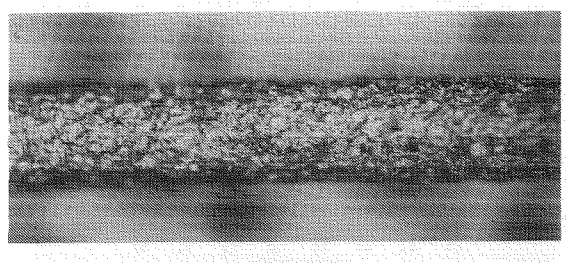
Stainless steel corrodes as titanium actively in strong acids. In presence of oxygen and small amounts of noble metals the passivity can be maintained. We attempted therefore to get the same effect by implantation of small quantities of noble metal ions. We could demonstrate that a steel sample with 5×10^{16} Pd^+/cm^2 stayed passive for more than 80 days in 20% H_2SO_4 while an untreated sample became active in less than 1 day. The difference in corrosion rate determined by neutron activation analysis was nearly 3 orders of magnitude. The dissolution of the Pd-implanted sample proceeded only with $\approx$1nm/day. Fig.1 and 2 show microscope pictures of an untreated and Pd-implanted, resp., steel needle after 20 days in 20% H_2SO_4. They illustrate the long term protection achieved with a 50 nm thick implanted layer containing only 10-15 µg Pd/cm^2.

3. Stress Corrosion Cracking of Aluminium Alloys

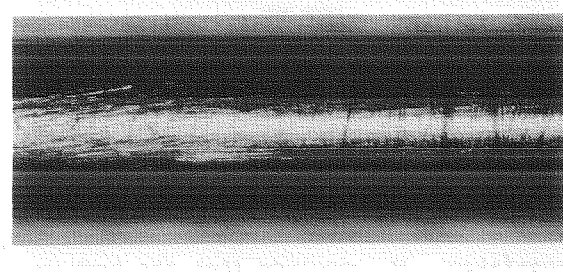
Many aluminium alloys of the type used in the aircraft industry suffer from a tendency for stress corrosion cracking. We were able to show that the implantation of silver ions in a thin surface layer of the alloy resulted in a substantial improvement of the performance. The samples were tested under constant load and constant strain rate in 3,5% NaCl solution at 80°C. With a load of $\sigma \approx 400$MPa we measured for non-irradiated samples an average time to failure of 1,8 h for implanted ones of 20 h. The experiments under constant strain rate, on the other hand, showed no difference. From this behaviour we conclude that the implanted silver segregates at the grain boundaries of the alloy, and impedes the initiation of cracks. The crack growth, however, is not affected by implantation.

[1] J. Dressler et al., GSI- 83-1(1983)213

a)



b)



Figs.1 and 2: Untreated (a) and Pd-implanted (b) steel needles (X60) after corroding 20 days in 20% H_2SO_4.

HYDROGEN TRAPPING IN ION-BOMBARDED IRON STUDIED BY THE $^{1}H(^{15}N,\alpha\gamma)^{12}C$ - REACTION

G.Frech, G.Reiss, G.K.Wolf; Physikalisch-Chemisches Institut der Universität Heidelberg+

The solubility of hydrogen in defect-free α-iron is very low ($\leq$0,1 atom ppm). In iron, however, containing defects (dislocations, grain boundaries, phase boundaries) or impurities one finds enrichments of many orders of magnitude. It is very important to study and understand this phenomena because hydrogen causes one of the most dangerous types of corrosion, namely stress corrosion cracking. Ion implantation is a very good and controllable way of introducing known quantities of all types of impurities in host metals. The concentration profiles are known and therefore trapping of hydrogen in this region can be easily distinguished from other uniformely distributed traps.

We performed such studies using the 300 keV test accelerator of GSI for implantation and the hydrogen equipment at the MPI für Kernphysik, Heidelberg. The hydrogen is analysed quantitatively by means of the $^{1}H(^{15}N,\alpha\gamma)^{12}C$-reaction.

In the earlier work the detection limit of the technique could be lowered by 2-3 orders of magnitude down to $\geq$ 10 atom ppm. Only after this development the method was applicable to the iron system.

In figures 1-4 the resulting hydrogen profiles below the surface of a pure annealed iron sample, and samples in which high doses of helium, gold and cerium have been implanted are presented. After the implantation the metals were electrolytically charged with hydrogen.

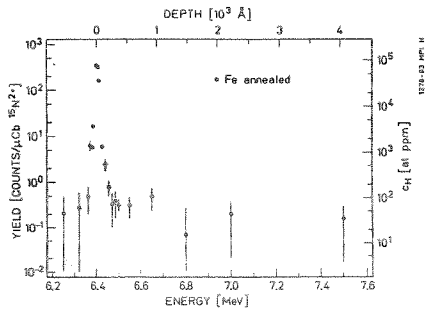


Fig.1: Hydrogen profile of pure uncharged annealed iron below the surface

The pure uncharged iron (fig.1) shows only a surface peak of absorbed hydrogen. Inside the material the peak decreases fast to the limit of detection. In the He-implanted sample (fig.2) one observes in the He-region a hydrogen content >1atom%. We conclude that the hydrogen is trapped at the inner surface of helium bubbles. Implanted cerium (fig.3) also traps hydrogen

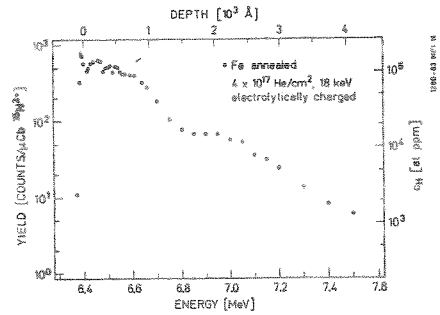


Fig.2: He-implanted iron, electrolytically charged. Hydrogen concentration $\gtrsim$1atom%

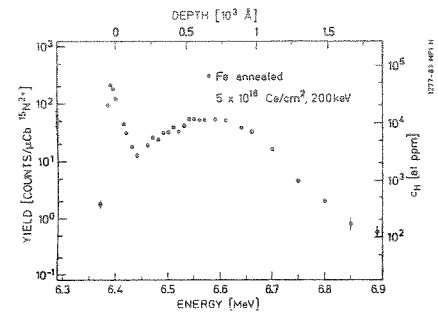


Fig.3: H-profile of cerium implanted iron

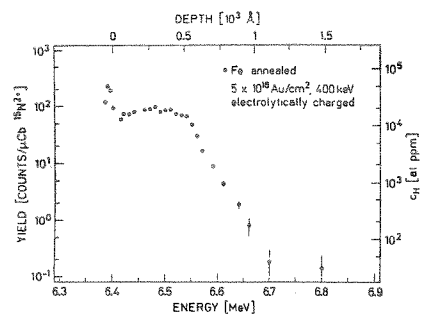


Fig.4: H-profile of gold-implanted iron

near its own position in the iron lattice. This is easily understandable becaus of its high affinity to hydrogen.

In the gold implanted sample, however, the maximum hydrogen content is found between the surface and the gold position in the region of maximum defect density, corresponding to the non-ability of gold to bond hydrogen.

+ Partly in collaboration with S.Kalbitzer and coworkers, MPI für Kernphysik, Heidelberg

IMPROVED MECHANICAL PROPERTIES OF ION BOMBARDED PRESS TOOLS

G.K.Wolf, B.Traving. Physikalisch-Chemisches Institut der Universität Heidelberg+

Ion Implantation is a potential method for improving mechanical properties as hardness, friction and wear of materials. Specially the bombardment with nitrogen ions resulted in increased hardness and reduced wear of steels and tungsten carbide. In England and USA the industrial application of nitrogen implantation in tools is already in its first stage.
We attempted to apply ion implantation to the field of metal forming and to demonstrate its use for wear reduction. As model system we have chosen the pressing of small bowls. This process is application oriented and allows the choice of well defined experimental parameters.

1.Experimental:

Irradiations: The press tools consisting of very hard steel (S-6-5-2 with 4%Cr, 5%Mo, 2%V, 6,5%W) were irradiated with nitrogen ions of 100-200 keV energy at the 300 keV test accelerator of GSI using a newly designed target chamber for manipulations of complicated shaped work pieces.
Press process: The differently treated press tool were tested over a period of 10^4 test pressings in a test mashine at Stuttgart.
Wear analysis: During the test the change of diameter of the tool or the formed bowl is determined and recorded. In addition we developed a method for analysing the amount of tungsten transfered from the tool to the bowl by means of neutron activation analysis. Because of the very low limit of detection of only 1ng W we were able to analyse the material transfer for every single forming process. Unfortunately this method is only applicable for forming materials containing no traces of tungsten, a condition which is mostly not fulfilled.

2. Results

We could demonstrate the benificial action of the implanted nitrogen. One has to define a criterium for the maximum tolerable wear. A possibility is to choose a reduction of the diameter of the press tool of 0.02 mm. The situation for this case is illustrated in figure 1. For the untrated tools we reach our criterium after 3000 pressings. A non-uniformly irradiated tool shows already improved performance. Uniformly irradiated tools ($4x10^{17}N^+/cm^2$ and $6x10^{17}N^+/cm^2$) enable much more forming operations- in the best case more than twice as much- until they are subject to the same amount of wear as the untreated ones.
These results are a good basis for future studies on the behaviour of tools consisting of steels with different compositions.

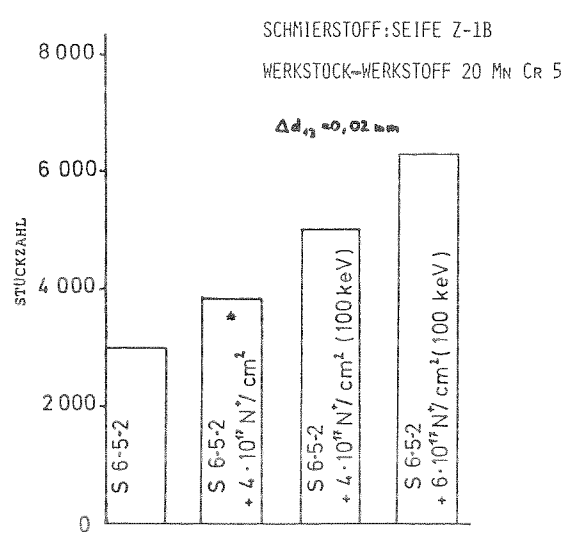


Fig.1: Number of forming operations resulting in 0,02 mm diameter reduction of differently treated press tools (* non-uniform implantation).

+In collaboration with K.Pöhlandt, E.Nehl und M.Weiergräber, Institut für Umformtechnik der Universität Stuttgart

4. Developments		PAGE
4.1	Target and Stripper Technology, Chemical Procedures	228
4.2	Experimental Set-Ups	236
4.3	Detectors	253
4.4	Electronics, Computing Center and Workshops	267

Preparations of Heavy-Ion Targets

H. Folger, W. Hartmann, J. Klemm and W. Thalheimer

The life time of most of the targets being bombarded with high intensity at the UNILAC is very short. This means that large numbers of targets have to be prepared each year as can be seen from the following comparison for 1981 through 1983 (Numbers normalized to 20x20 mm areas):

Target preparation procedure	Number of targets in: 1981	1982	1983
Cold rollings	1 220	3 101	1 655
Carbon sublimation-condensations	2 190	4 292	4 451
Focused ion-beam sputterings	110	90	178
Vacuum evaporation-condensations	1 810	3 517	2 592
Total number of targets	5 290	11 000	8 876

Some aspects and examples for target preparation procedures are mentioned.

Cold rolling of metals between stainless steel plates is important to prepare self-supported target foils thicker than about 0.5 mg/cm^2. In the case of stable isotopes, the materials mostly have to be pretreated by an electron beam in a high-vacuum apparatus in order to convert the metallic powders into metal beads. Intermediate annealing is necessary to roll Mo isotopes. The oxides of isotopes of Ca, Dy, Er, and Yb have to be converted into the metals in a high-vacuum reductive-distillation procedure; the obtained metals are oxygen-sensitive and have to be rolled in a glove-box system. All the different target materials being rolled in 1983 are listed below:
Ag, ^{109}Ag, Al, Au, Ca, ^{40,42,44}Ca, Cd, ^{116}Cd, Co, Cu, ^{63}Cu, ^{160}Dy, Er, ^{164,170}Er, Fe, ^{56}Fe, Gd, Ho, In, ^{24,25,26}Mg, Mo, ^{92,94,95,96,97,98,100}Mo, Ni, ^{58,60,61}Ni, ^{62,64}Ni, Nb, Pb, ^{207,208}Pb, Pd, ^{108,110}Pd, Pt, Rh, Sn, ^{116}Sn, Ta, Th, Ti, Tm, U, W, Y, ^{172,173,176}Yb, ^{66}Zn, Zr, ^{92,94,96}Zr/Pb.

Two different procedures are in use for high-vacuum sublimation-condensation of carbon: Foils of 0.003 to 0.1 mg/cm^2 area density are obtained from resistance-heating of spectrographite rods; the foils, 3915 in 1983, have a wide variety of applications as targets, target backings, degraders, monitor foils, stripper foils at the UNILAC at 1.4 MeV/u, etc. Thick foils of 0.1 to 0.76 mg/cm^2 can be prepared in a new set-up by subliming carbon by means of an electron-beam and depositing the layers on glass plates mounted to a rotating target-substrate fixture; the thick layers, 536 in 1983, are needed as targets, catcher foils, backings, post-strippers at the UNILAC at energies of 8 to 11 MeV/u, charge-transfer foils in the production of highly charged ions, etc.

In heavy-ion sputter depositions with a focused beam of 1 mA of Ar^+ at 10 kV it is possible to prepare targets even of high melting-point elements with a high yield; thus only 2.3 mg of ^{96}Zr were necessary to obtain 5 targets of 0.1 mg/cm^2 on 15 mm diameter carbon backings. Investigations are continued to gain more and more self-supported sputter targets rather than targets on backings, mostly 0.03 mg/cm^2 of carbon. The sputtered targets are: Ag/C, Nb/C, Ni, ^{60,62}Ni, Pt/C, Pt/Ta, ^{185,187}Re, ^{102}Ru/C, ^{96}Ru/Ta, Si/C, Ta/Al, Ta/C, Ti/C, ^{182,184,186}W, and Zr/C.

High-vacuum evaporation-condensation is the most generally used technique in the preparation of very thin (0.002 to 20 mg/cm^2) and extremely pure accelerator targets. With various types of evaporators the vaporization of target materials is achieved at temperatures ranging from 520 K for Se to 3500 K for W. In one case only 2.5 mg of $^{130}BaF_2$ were available to prepare 2 targets of 0.6 mg/cm^2 on spots of 9 mm in diameter. In other cases poisonous substances like Tl or radioactive materials like ThF_4 or U had to be evaporated under special precautions. New experience was gained in numerous computer-controlled vapor depositions. About 70 different types of targets were prepared in 1983: Ag, Ag/C, Ag/CR39, Al, Al/C, Au, Au/C, Au/CR39, BaF_2/C, $^{130,132,134}BaF_2$/C, Bi/Pb, Cr/steel, Cu, CsJ/Al, CsJ/C, Co, Er/Mo, Er/Be, Ge/C, C/$GdCl_3$/C, C/GdF_3/C, Ir/Ni-Cr/glass, KBr/C, KJ/C, ^{100}Mo/Bi, NaCl/C, Ni, Ni/C, Pb, ^{206,208}Pb, ^{206,207,208}Pb/C, C/^{206,207,208}Pb/C, Pb/CR39, Pb/^{92,94,96}Zr, Pd/glass, Pd/Fe, Pd/Ni, Pd/Ti, Pt/C, RbBr/C, Sb, Sc, ^{144,154}Sm, Sn, ^{124}Sn, SrF_2/C, Tb/Be, ThF_4/C, Ti, Ti/C, Tl/Cu, Tl/Mo, Tl/Nb, Tl/Ti, U/C, C/U/C, Ti/U/C, Be/U/Au, and W.

Of great importance for experiments at the UNILAC with pulsed high-intensity heavy-ion beams was the development and preparation of large 'banana-like' targets for the use on fast rotating target wheels (see fig.1).

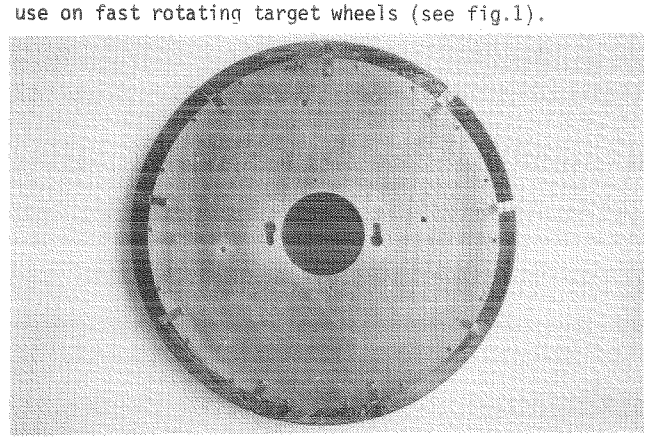


Fig. 1: 310-mm-diameter target wheel equipped with 9 Au targets of a total length of nearly 1 meter.

The Medium-Current Mass Separator

K. H. Behr, A. Brünle, C. Bruske, K. Burkard, M. Chen*, W. Hüller, R. Kirchner, F. Nickel, E. Roeckl
GSI Darmstadt

At the beginning of 1983 the construction of the medium-current mass separator[1,2,3] was completed. The pumping system with the control units was tested, and a vacuum of about $5 \cdot 10^{-7}$ torr was measured in all chambers along the beam line. With an operating ion source, in which e.g. a krypton plasma is confined, the vacuum in the ion source region is about 10^{-5} torr. During the initial tests of the high-voltage power supply, certain electronic parts of the supply were regularly destroyed by sparking. With newly designed driver electronics these failures are now eliminated. Various other electronic units of the separator were protected against high-voltage sparks by stepwise improving the shieldings of sensitive electronics. The only remaining trouble was caused by rf-electromagnetic waves emitted during high-voltage breakdowns, which disturbed neighbouring computers. A solution of this problem was the construction of a large Faraday cave around the high-voltage regions.

Tests of the whole separator were performed with krypton beams. Ion currents up to 2 mA of $^{84}Kr^{1+}$ were measured in the focal plane, and the beam shape was improved by α- and β- coils[2]. In a krypton spectrum the impurity in a mass line resulting from the tails of neighbouring masses were determined to approximately $5 \cdot 10^{-3}$. Asymmetric currents in the α-coils were used to compensate a small vertical deflection of the beam due to the large and asymmetric fringing field of the main magnet. This was very important for a sufficient transmission of the beam through the retardation chamber behind the focal plane. The transmission was measured to be 69%, and together with the transmission of approximately 90% from ion source to focal plane an overall transmission of approximately 60% can be reached. The ionization efficiency of the Bernas-Nier source was measured with ^{129}Xe to be approximately 30%, so that in this case the overall efficiency of the separation amounts to approximately 20%.

First metal beams with currents of 100 µA of $^{64}Zn^{1+}$ and of 25 µA of $^{120}Sn^{1+}$ were produced with the source by heating up the natural metals to temperatures with sufficient vapour pressures. Fig.1 shows a spectrum of tin isotopes in the focal plane chamber. With the help of chemical reactions between the hot tin metal and CCl_4 vapour a beam current of 350 µA of ^{120}Sn (natural abundance: 32%) could easily be reached. With a simple device placed in the focal plane chamber, isotopically pure tin targets were produced. As can be seen in Fig.2, the mechanism of self-sputtering served as a tool for target preparations. For test purposes ^{120}Sn targets with thicknesses of about 45 and 220 µg/cm² were made from natural tin material. Then ^{112}Sn targets with thicknesses of about 40 µg/cm² were prepared from natural material by using a beam current of 10 µA. From isotopically enriched material (36 mg of tin with 68% of ^{112}Sn), targets with 80 and 150 µg/cm² were produced with a ^{112}Sn beam current of 600 µA. These ^{112}Sn targets were used successfully in an experiment at the magnetic spectrometer at GSI.

1. K. H.Behr et al., GSI Scientific Report 1981, p. 212
2. K. H. Behr et al., GSI Scientific Report 1982, p. 218
3. F. Nickel, GSI Nachrichten 1-84, Jan. 1984

*Nucl. Res. Inst. of Shanghai,
Shanghai, People's Republic of China

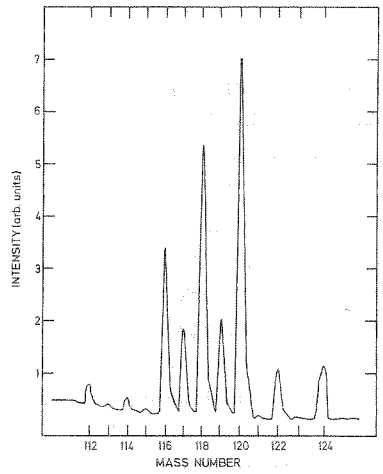


Fig.1 : Tin isotopes measured in the focal plane chamber. The small peak at mass 113 is due to an impurity. The beam current of the ^{120}Sn line is about 1 µA.

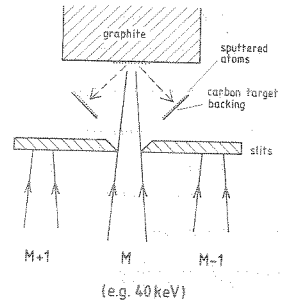


Fig.2 : A simple sputtering device for target preparation.

Continuous Gaschemical Separations of Nuclear Reaction Products with Fluorinating Agents

U. Hickmann, N. Trautmann, G. Herrmann
Institut für Kernchemie, Universität Mainz

The connection of a gas-jet recoil-transport system with a thermochromatographic column offers a fast method for the separation of complex reaction product mixtures[1]. In most applications of such technique reported so far, KCl-clusters loaded with reaction products were collected and destroyed in a quartz-wool catcher, kept at 1000 °C and the released products were volatilized by adding a reactive gas with subsequent separation in a thermochromatographic column. Another possibility consists in direct chemical reactions with the jet gas itself by mixing a reactive component to the carrier-gas and operating the gas-jet without any cluster material. Here volatile compounds of fission products are formed by recoil reactions within the target-area and can be transported to a separation or detection system[2]. Following these approaches we have investigated the application of fluorinating agents for efficient volatilization of fission products as model elements for a broad region of the periodic table.

In a first series of experiments the thermochromatographic system was coupled to a cluster jet and hydrogen fluoride (37 vol.-% in the carrier-gas) was used as the reactive gas. Although the fluorides are normally the most volatile compounds among the halides, the measured deposition temperatures of tellurium, molybdenum and technetium were found to be about 400 °C higher than with other hydrogen halides. Therefore, another reagent, bromine trifluoride, was used for a more efficient fluorination. Bromine trifluoride dissociates at 800 °C into bromine monofluoride and atomic fluorine. It was used in a 1 % mixture with argon (0.1 l/min). The experiments were carried out with an empty column and a charcoal trap placed at the cold end of the column for the adsorption of very volatile fluorides. The temperature of the quartz-wool plug was varied between room temperature and 995 °C. Under these conditions, fluorination and volatilization occurred at about 800 °C, the temperature needed for destroying the KCl-clusters. The fluorides of antimony, technetium, iodine, tellurium and molybdenum were found in the charcoal trap.

Separation of these elements was achieved in a column filled with quartz powder (64 mesh/cm^2). As fig. 1 shows, tellurium, molybdenum and part of the technetium are now distributed along the column. The rest of technetium, antimony and iodine are found in the charcoal trap. The less volatile fluorides of the alkaline earths, yttrium and the lanthanides are deposited close to the starting position. Zirconium is deposited separately from these elements at 800 °C.

In another series of experiments, hydrogen fluoride was fed directly into a target-chamber made of teflon. Under these conditions short-lived arsenic isotopes could be separated continuously from the other fission-products, which were either retained in the target-chamber or trapped by means of selective adsorbing materials: Volatile compounds of Te, Sb and Mo were caught in a quartz-wool plug at room temperature. A second trap kept at 350 °C was filled with silver-coated quartz powder to retain the halides and the decay products of the noble gases. Finally arsenic was absorbed on di-(2-ethylhexyl)orthophosphoric acid (HDEHP). A γ-ray spectrum of the HDEHP-trap, measured on-line for 1 min shows the isotopes $^{80-84}$As (fig. 2). ^{85}As ($t_{1/2}$=2 s) was also identified by summing up 50 spectra measured for 2 s each. Contaminations occurred only by noble gases passing the HDEHP-trap and by ^{20}F (an activation product of HF), which could not be absorbed entirely in the Ag/SiO_2-trap.

[1] U. Hickmann et al., Nucl. Instr. Meth. 174, 507 (1980)
[2] M. Zendel et al., Radiochim. Acta 29, 17 (1981)

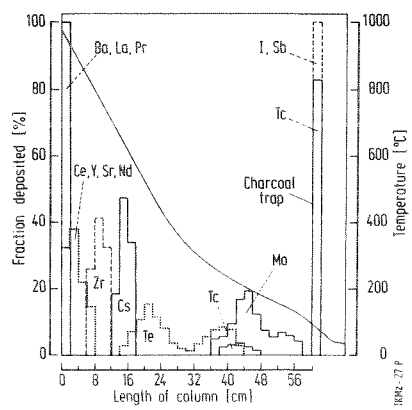


Fig. 1: Distribution of the fluorides in the thermochromatographic column with 1 vol.-% of bromine trifluoride

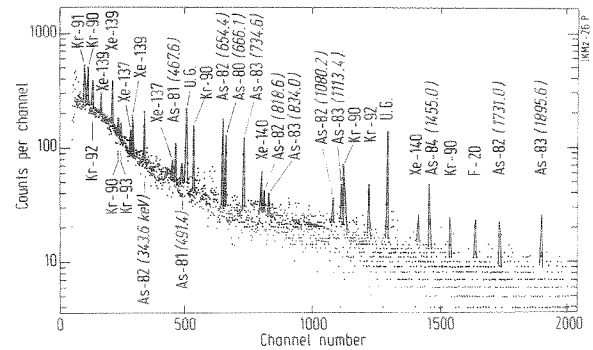


Fig. 2: γ-ray spectrum of the As-fraction measured on-line for 1 min

Preparation and Gaschromatographic Separation of Actinide Hexafluoracetylacetonates

G

N. Greulich, N. Trautmann, G. Herrmann
Institut für Kernchemie, Universität Mainz

Gaschromatography is a potential, fastmethod for unravelling actinide mixtures, if suitable actinide compounds with high volatility and sufficient thermal stability can be synthesized. Homologous lanthanide elements have already been gaschromatographically separated as mixed ligand complexes of hexafluoracetylacetone (HHFA) and tri-n-butylphosphate (TBP)[1]. In this report, first experiments are described to extend this method to the separation of ^{232}Th, ^{233}Pa, ^{238}U, ^{239}Np, ^{239}Pu and ^{241}Am in their most stable oxidation states, as well as to trivalent ^{239}Pu.

For preparing the mixed ligand complexes, the actinides were extracted within 30 s from 1.0 ml of 0.1 N nitric acid (Pu^{3+} was stabilized with hydroxylamine) with 1.0 ml of 0.05 M HHFA and 0.035 M TBP, DPSO (dipropylsulfone) or TOPO (trioctylphosphineoxide) as synergistic reagents in cyclohexane[2]. The distribution coefficients (see table 1) were calculated either from γ-measurements for ^{232}Th, ^{233}Pa, ^{238}U and ^{239}Np or from integral α-measurements for ^{239}Pu and ^{241}Am after evaporation of the solvents.

Table 1

Distribution coefficients for the extraction of some actinide ions from 0.1 N HNO_3 with a mixture of 0.05 M HHFA and synergistic reagents (0.035 M) in cyclohexane

Actinide ion	Synergistic reagent		
	TOPO	DPSO	TBP
Th^{4+}	58±16	-	1.3±0.2
PaO_2^+	4.0±0.8	1.5±0.4	0.25±0.04
UO_2^{2+}	31±8	-	14±3
NpO_2^+	0.22±0.03	0.18±0.03	0.083±0.01
Pu^{3+}	22±6	12±3	14±1.3
Pu^{4+}	34±1.3	26±4	32±3
Am^{3+}	75±16	68±9	56±5

The variation of the distribution coefficients within one column of table 1 can be explained by differences in the ionic radii and the chemical properties of the central ions. The distribution coefficients increase with increasing nucleophilic power of the applied synergistic reagent.

The volatilization of the synthesized mixed ligand complexes was investigated with a gaschromatographic system described elsewhere[1]. The outlet of the separation column was connected to an apparatus for gaschemical preparation of samples for α- and sf-measurements[3]. The investigated actinides with a valence state higher than 3+ could not be volatilized and remained entirely in the injector of the gaschromatograph. Significant volatilization was observed with the trivalent complexes of Am and Pu. Fig. 1 shows the yields of Pu^{3+}- and Am^{3+}-HHFA/TBP-complexes collected on a nickel-foil as a function of the column temperature. The experimental conditions were: Carrier-gas flow 56 ml/min N_2 loaded with 27 mol-% HHFA, empty glass column 2 m long by 2.4 mm inner diameter, injection temperature 30 °C above column temperature, retention time ≤ 5 min. The resolution of the α-peaks was 43 keV FWHM, if TBP was used as synergistic reagent, with TOPO- and DPSO-adducts a much worser resolution was obtained. The described method should enable the separation of trivalent actinides from higher valence states within a few minutes.

[1] N. Greulich et al., GSI Scientific Report 82-1, 219 (1981) and GSI Scientific Report 83-1, 221 (1982)
[2] W.C. Butts and C.V. Banks, Anal. Chem. 42, 133 (1970)
[3] U. Hickmann et al., GSI Scientific Report 82-1, 217 (1981)

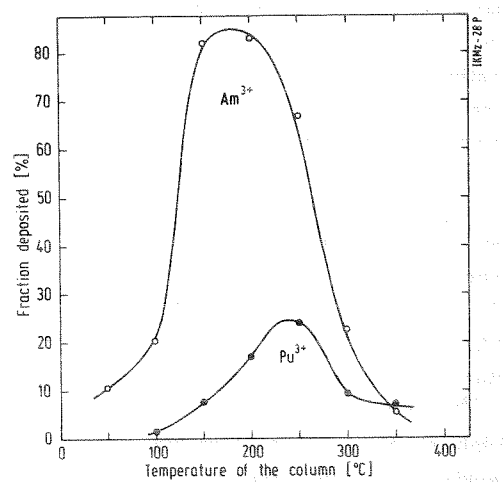


Fig. 1: Yield of americium- and plutonium-hexafluoracetylacetonate (TBP as synergistic reagent) collected at the outlet of a gaschromatographic system and plotted as a function of the column temperature. For further explanations see text.

Determination of Adsorption Enthalpies for Polonium on Metal Surfaces by On-Line Isothermal Gaschromatography

H. Gäggeler
GSI Darmstadt
B. Eichler
Joint Institute for Nuclear Research, Dubna, USSR
N. Greulich
Universität Mainz
H. Dornhöfer
Universität Göttingen

In the course of recent attempts to produce superheavy elements by heavy ion reactions, the element polonium received a lot of attention because its chemical behaviour should be quite similar to that of some of the expected superheavy elements around Z=114[1]. In addition, since no stable isotope of polonium exists, its chemical properties can be studied with a few atoms only, a prerequisite for extrapolations into the region of superheavy elements, because expectations of production rates for such elements in heavy ion reactions are on a one-atom-per-day scale only! Therefore, in recent years investigations of the gaschromatographic behaviour of polonium have been performed[2-5] with the same technique frequently used in chemical attempts to separate superheavy elements[6]. The most recent attempts to search for superheavy elements applying chemical techniques have been performed using on-line separations such as isothermal gaschromatography[7]. In this contribution we study the adsorption behaviour of polonium, in the form of its short-lived isotope $^{211m}Po(T_{1/2}=25.5\ s)$, with different surface materials such as quartz or several metals. This nuclide was produced at the Göttingen cyclotron and was continously transported into a chromatographic column using a gas-jet transportation system. We then measured the retention time within the chromatographic column as a function of the temperature using the radioactive decay of ^{211m}Po as a clock. This method was first outlined by Rudolph et al.[8]. All experimental details are given elsewhere[9]. In Table I the measured retention data are listed for Po on SiO_2, Pt, Au, Ag, Cu, and Pd. In order to deduce adsorption enthalpies from these on-line measurements, we derived a thermodynamical equation which is based on the same model assumptions used already in gas-adsorption studies with gas-thermochromatography[10], finally resulting in

$$(1)\quad \Delta H_a^o = -RT \ln\left[\left(\frac{t_r v_o^T}{z T_o \phi} - 1\right) v / \left(a \exp\{\Delta S_a^o/R\}\right)\right]$$

with t_r=retention time, v_o=gas flow rate, z=column length, v=free column volume, a=free column surface per unit of length, ϕ=cross section of the tube, and ΔS_a^o=adsorption entropy, calculated according to Ref.10. The ΔH_a^o(exp.) values from Table I were thus calculated from the experimental retention data. Also given are ΔH_a^o-values from the literature which were obtained from thermochromatographic or desorption studies[11]. The last column of Table I summarizes calculated ΔH_a^o-values as they result from a semiempirical model of metal-metal interactions[12]. Clearly there is good agreement between our data and the literature values and also with the calculated enthalpies. This result gives us confidence to apply the same technique in investigations of the thermodynamical properties of exotic species such as very heavy elements which can be produced on a scale of only a few atoms.

References

1. B. Eichler, Kernenergie, 19, 302 (1976)
2. B. Eichler et al., Preprint JINR P12, Dubna (1976)
3. B. Eichler et al. Radiochim. Acta 26, 193 (1979)
4. H. Gäggeler et al., Report GSI-79-11, p. 155 (1979)
5. S. Hübener et al., Radiochim. Acta, 27, 157 (1980)
6. see e.g. J.V. Kratz, Radiochim. Acta, 32, 25 (1983)
7. H. Gäggeler et al., this Scientific Report, p.
8. J. Rudolph and K. Bächmann, Radiochim. Acta, 27, 105 (1980)
9. N. Greulich et al., GSI Scientific Report 1981, GSI-82-1, p. 218 (1982)
10. B. Eichler and I. Zvara, Radiochim. Acta, 30, 233 (1982)
11. B. Eichler et al., to be published
12. B. Eichler Report ZfK-396, Rossendorf (1979)

Table I:

Adsorption behaviour of polonium on different surfaces

Surface	Column length (cm)	Temperature[a] (K)	$-H_a^o$ (exp.)[b] (kJ/Mol)	$-H_a^o$(exp.)[c] (kJ/Mol)	$-H_a^o$(calc.)[d] (kJ/Mol)
SiO_2	15	633	123.4	---	---
Ag	1o	833	165.4	---	232
Au	1o	1133	223.7	196/2oo	2oo
Cu	1o	893	18o.8	157/193	178
Pd	1o	>1373	>277.9	3o2	3o1
Pd	o.8	1298	289.7		
Pt	7	923	186.9	196/211/ 279/28o	238

a) for a retention time $t_r=T_{1/2}(^{211m}Po)=25.5$ s
b) calculated with eq.(1)
c) values from Ref. 11
d) calculated according to Ref. 12

Chemical Separation of Astatine from Bi/Pb-Targets[B]

S. Zauner, J. V. Kratz, E. Kuchinka
Institut für Kernchemie, Universität Mainz
W. Brüchle, H. Gäggeler,
GSI Darmstadt

For the radiochemical detection of the presumably very rare reaction channel $^{207}_{82}Pb$ ($^{4}_{2}He$, π^-) $^{211}_{85}At$ (pionic fusion[1]) a selective chemical separation of astatine from polonium, bismuth, lead and from spallation and fission products with high decontamination factors is necessary. At the same time it is desirable to prepare the astatine sample as a weightless source for α-particle spectroscopy. To this end, the volatilization of elementary astatine and its re-condensation on a cooled metal surface[2] seemed to be most attractive.

We have produced $^{210,211}At$ tracer activities at the Karlsruhe cyclotron by bombarding ^{209}Bi-targets with 30 MeV α-particles. These, together with 20 mg of lead, were heated to 1000° C in a gas flow of 100 ml/min Ar and 10 ml/min H_2 for 15 min in a quartz tube, see Fig. 1. Under these conditions both astatine and polonium are volatilized. Inside oven 2 (600°C) the quartz tube was lined with Pd foil of 4 cm length which absorbs polonium while astatine passes through. Fig.2 shows the yield of astatine as a function of the temperature of oven 2. It is evident that temperatures ≥ 500° C are necessary in order to avoid losses of astatine to the Pd surface. Astatine is then condensed on a cooled Ni-foil (1 mg/cm^2) covered with ~40 µg/cm^2 of vapour-deposited Pd. Decontamination factors from polonium were of the order of 10^5 in this one-step chemistry and the chemical yield of astatine was 91±7%. The Pd-Ni-substrate foils for the astatine sources are sufficiently thin to allow for α-particle spectroscopy on both sides of the source by large area silicon detectors with a total efficiency of 65%.

First bombardments of 20 mg/cm^2 $^{nat.}$Pb-targets with 2.5 µA α-particles of 130 MeV at the Jülich cyclotron showed that the decontamination from polonium of this one-step chemistry was not sufficient to detect subnanobarn cross sections of astatine in the presence of tens of millibarns of polonium. Also, an extremely high level of beta radiation caused by fission products, in particular by iodine, jeopardized the function of the silicon detectors for α-particle spectroscopy. This called for additional chemical purification: The bombarded lead-targets are now dissolved in 500 µl of 3.5M HNO_3. Astatine is then deposited in the presence of hydroxyl-ammonium chloride and ammonium acetate buffer on a 2 cm^2 Au-foil. The latter is rinsed with acetone, dried, and heated in the quartz tube (Fig.1) for 15 min to 900°C (oven 2 at 600°C) under otherwise identical conditions as given above for the one-step gas-phase chemistry. Chemical yields for the combined procedure are close to 80%. The separation now produces sources wich are well-suited for a highly sensitive search for ^{211}At from the $^{207}_{82}Pb(^{4}_{2}He, \pi^-)$ reaction by α-particle spectroscopy.

References

1. K. Klingenbeck et al., Phys. Rev. Lett. 47, 1654 (1981)
2. U. Hickmann et al., GSI Scientific Report 1981, p. 217

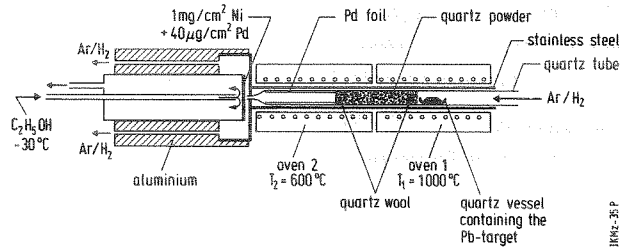


Fig.1: Apparatus for the volatilization and re-condensation of astatine

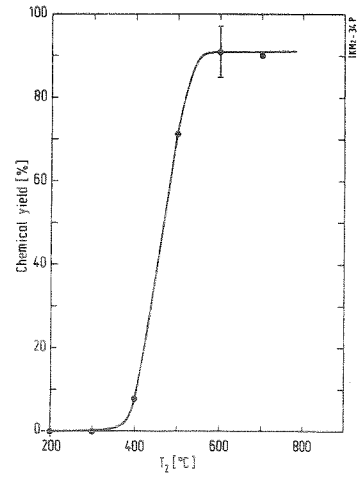


Fig.2: Chemical yield of astatine measured on the Pd-Ni foil as a function of the temperature of oven 2. The temperature of oven 1 is 1000° C. The error bar on the data point at 600° C corresponds to the standard deviation of ten experiments.

Solubility of Calcium Acetylacetonate in Methyl-tert.-butyl Ether (MTB) G

A. Knöchel, H. Röhl
Institut für Anorganische und Angewandte Chemie, Universität Hamburg

Calcium salts generally display a very low solubility in aprotic organic solvents. It appears, therefore, that the extractability of Ca-ions from aqueous solutions can be accomplished only in the presence of anions capable of forming ion-pairs.

The association behaviour of calcium acetylacetonate in methyl-tert.-butyl ether (MTB) was investigated. In this solvent (which is suitable for extraction) the position of equilibrium of the ion-pair as well as the solubility are within a region accessible to UV-measurements. The saturation concentration at roomtemperature was

$$c_s\,(Ca(acac)_2) = (6.2 \pm 0.1)\cdot 10^{-5}\ M$$

In this region the concentrations employed display in all cases proportionality to the extinctions of the various absorbtion maxima ($\varepsilon = 11600$)
($n \rightarrow \pi^*$, Acetylacetonate, MTB : 270 nm $< \lambda_{max} <$ 285 nm).

The dependence of the absorbtion maximum on the applied concentration is illustrated in Fig. 1.

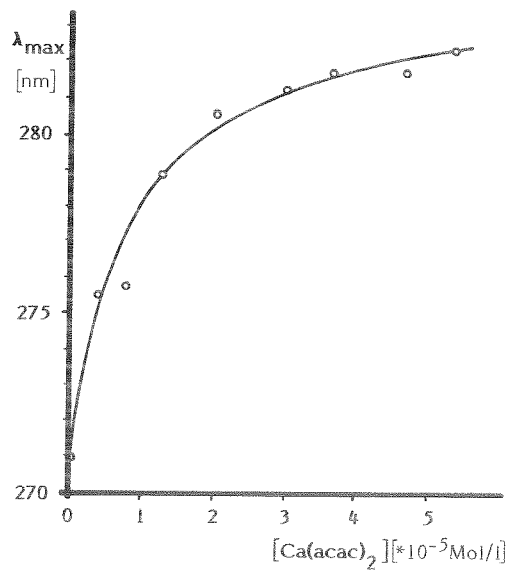


Fig. 1 Dependence of the absorbtion maxima λ_{max} on the calcium acetylacetonate concentration
(smooth line: Resulting from optimization of the characteristic values, see below)

If the limiting value λ_{max} for $[Ca(acac)_2] \rightarrow 0$ is represented by the absorbtion maximum of the free (i.e. not bound to Ca^{2+}) acetylacetonate (λ_{free}) and that for $[Ca(acac)_2] \rightarrow \infty$ (i.e. bound to Ca^{2+}) by λ_{com}, then the position of the absorbtion maximum observed in each case (λ_{exp}) can be described by (1):

$$\lambda_{exp} = \lambda_{free} + \frac{[acac]_{com}}{([acac]_{free} + [acac]_{com})} \cdot (\lambda_{com} - \lambda_{free}) \quad (1)$$

The prevailing concentrations of the free acetylacetonate at the applied calcium acetylacetonate concentrations c_o can be calculated in a corresponding manner (2):

$$[acac^-] = \frac{\lambda_{com} - \lambda_{exp}}{\lambda_{com} - \lambda_{free}} \cdot 2\,c_o \quad (2)$$

From the electron neutrality (3), mass balance (4), and the equilibrium conditions (5) and (6)

$$[acac^-] = 2[Ca^{2+}] + [Ca(acac)^+] \quad (3)$$

$$c_o = [Ca(acac)_2] + [Ca(acac)^+] + [Ca^{2+}] \quad (4)$$

$$K_1 = \frac{[Ca(acac)^+]}{[Ca^{2+}][acac^-]} \quad (5)$$

$$K_2 = \frac{[Ca(acac)_2]}{[Ca(acac)^+][acac^-]} \quad (6)$$

an expression (7) can be derived, which, together with (2) describe the relations between λ_{free}, λ_{com}, K_1 and K_2.

$$K_2 = \frac{2c_o - K_1\cdot[acac^-]^2 + (K_1\cdot c_o - 1)\cdot[acac^-]}{K_1\cdot[acac^-]^3} \quad (7)$$

Optimization of these values (with respect to minimum scattering of K_2-constants ($K_2 \neq f(c_o)$) obtainable for the various pairs of values with the help of (7)) yielded:

$\lambda_{com} = 285.7$ nm $K_1 = 6.5\cdot 10^4$ l/Mol
$\lambda_{free} = 270.4$ nm $K_2 = 1.7\cdot 10^5$ l/Mol.

The solubility of the calcium acetylacetonate in MTB could be slightly improved through the application of the bicyclic aminopolyether 2.2.2. .

The dependence of the saturation concentration of the calcium acetylacetonate on the concentration of the ligand is described in (8):

$$[Ca(acac)_2]_{sat} = 1.254\cdot 10^{-2} * [2.2.2.]_{appl} + 2.73\cdot 10^{-5} \quad (8)$$
$$(r=0.972;\ n=6).$$

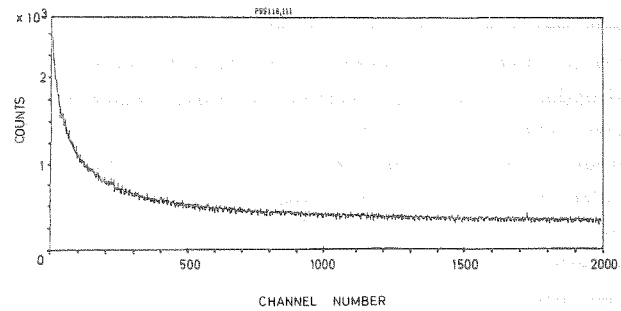
G

FURTHER INVESTIGATIONS ON HYDROGENATED CARBON FOILS

H. Baumann, K. Bethge, F. Rauch, W. Reeh
Institut für Kernphysik, Universität Frankfurt

H. Wirth
MPI für Kernphysik, Heidelberg

Hydrogenated thin carbon foils prepared by plasma-deposition from hydrocarbon gases and by ion beam sputtering of graphite /1,2/ were investigated with respect to hydrogen effusion under ion bombardment. In dc glow discharge-carbon foils the hydrogen content (H/C ratio) amounts to 0.38 corresponding to 27 at%. Under same discharge parameters this ratio is independent of the kind of hydrocarbon gases used (CH_4, C_2H_6, C_2H_4, C_2H_2). In sputtered carbon foils the H-concentration varies between 0.2 to 0.3 depending on the partial pressure of hydrogen and hydrocarbon gases inside the vacuum system. The measurements have been performed by the nuclear resonance reaction $^1H(^{15}N, \alpha\gamma)^{12}C$. For both kinds of foils an in-depth mobility of hydrogen was observed under ion beam impact. The H-content decreases inside the irradiated region throughout the whole thickness of the foils. The amount of hydrogen release depends on the ion fluence only. Some hydrogen (~ 0.04), however, remains even if high fluences are applied. The curve of the hydrogen loss can be described by three different exponential decays (fig. 1), corresponding to three decay constants with the dimension cm^2. Though an explanation of this experimental result is still missing, it may indicate that several hydrogen carbon bonds with different strength are present. To get more information about the behaviour of the hydrogenated carbon foils under ion bombardment, irradiation experiments have been started for foils with varying temperatures between 77 K and 800 K .



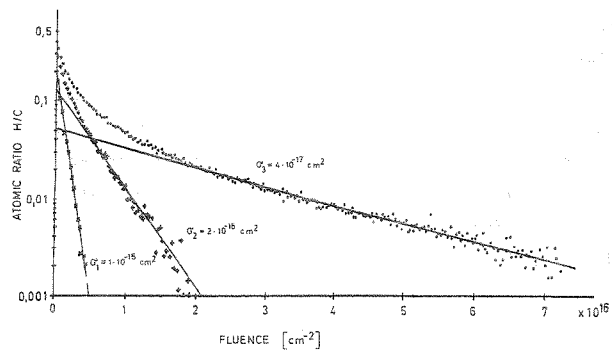


Fig. 1 Variation of the hydrogen concentration of a glow discharge foil (~ 15 µg/cm^2) as a function of the beam fluence (^{15}N-ions/cm^2)

/1/ H. Baumann, K. Bethge, W. Reeh, H. Stiehl, H. Wirth, Jahresbericht GSI (1981) Annual report

/2/ H. Baumann, K. Bethge, F. Rauch, W. Reeh, H. Wirth, Jahresbericht GSI (1982) Annual report

A Position-Sensitive Twin Ionization Chamber For Experiments at High Incident Energies.

G. Augustinski, H.J. Beeskow, H. Daues, A. Gobbi, S. Gralla, K.D. Hildenbrand, J. Kuźminski,* M. Ludwig, W.F.J. Müller, A. Olmi,** W. Quick, H. Sann, H. Stelzer, J. Töke,*** GSI Darmstadt

Our experimental set-up[1] has been improved by a new large-area, position sensitive ionization chamber (IC) of wide angular acceptance (fig.1). Its main feature is the complete vacuum-tight separation of the upper and lower half by a solid metal plate. This allows not only coincidences between these halves (that has been possible also with the previously used chambers) but also to adjust the gas pressure or even the gas type to the dynamical situation of heavy ion reactions at higher incident energies, where the products to be detected normally cover a large dynamical range. Both halves are further subdivided into a left and right section, respectively. They have cathode and Frisch grid in common, but are split in all other devices; hence one can read out 4 completely separated quadrants.

The two anode sections are tilted so that the distance from the middle plate which bears the cathodes is shortest near the entrance window. In order to maintain an approximately constant field strength along the particles' path the cathodes are divided in stripes of increasing lengths connected via a resistor chain which makes the effective cathode voltage decrease from the rear end towards the window region. The layout of the anode sections is sketched in fig.2. Two of the anode stripes are cut into triangular saw-teeth[2]; signals from both sides can be used to obtain the in-plane incident angle; this information is alternative to the position from the θ-grid placed between Frisch grid and anodes. It is less precise but can be used over a larger dynamical range.

Both halves of the entrance window cover 10x80 cm² with a dead zone of only 4 cm in between. (Ω_{tot} = 280 msr at 70 cm distance from the target). Placed with its center at 0° the IC covers a range from -30° to +30° which is enough to include the grazing angle of practically all systems at incident energies above 12 MeV/u. Nevertheless it can be moved together with the scattering chamber as a whole around the target.

In a first experiment the IC was used to study dissipative collisions of Mo + Mo at 12, 14.7 and 18 MeV/u incident energy. It was operated with CH_4 at 150 torr and CF_4 at 110 torr, respectively. Fig.3 demonstrates the resolution of different elements over the total range of observed fragments. Fig.4 shows the X-Y plot of the two right quadrants (the circular shadow is due to the cup which cuts at 3°); the vertical shadowed stripes are due to the support bars of the entrance window (1.5 mm thick, 8 cm apart) which demonstrates the excellent position resolution.

* on leave from Silesian University, Katowice, Poland
** now at INFN, Florence, Italy
***on leave from Warsaw University, Poland

1 G. Augustinski et al., Annual Report 1981, p.221
2 G. Rosner et al., NIM 188(1981)561

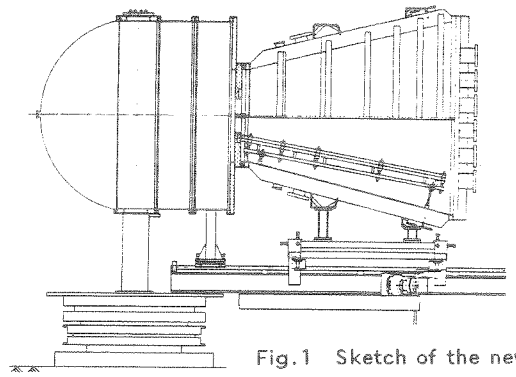


Fig.1 Sketch of the new set-up

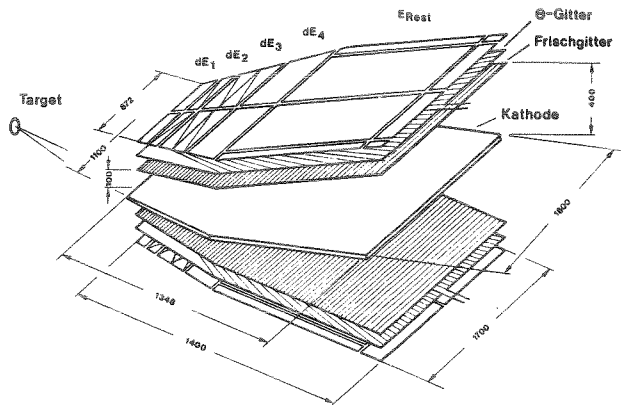


Fig.2 Sketch of the upper and lower anode section

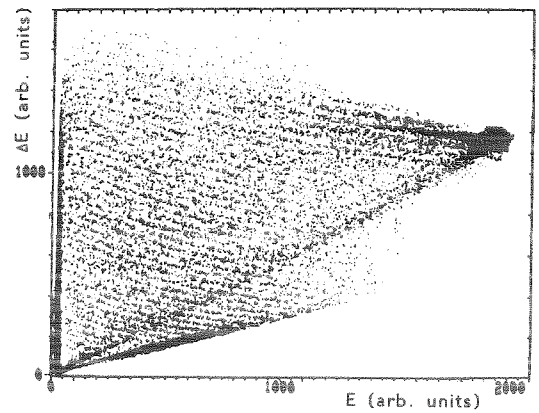


Fig.3 ΔE-E plot of products $^{92}Mo+^{92}Mo$ at 14.7 MeV/u

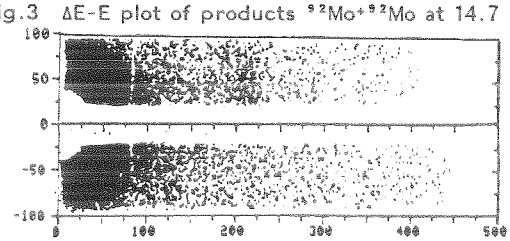


Fig.4 X-Y plot of the two right quadrants

Position-Sensitive Scintillation Detectors for Light Charged Particles.

N. Herrmann, A. Gobbi, S. Gralla, K.D. Hildenbrand, J. Kuźminski,* M. Ludwig, W.F.J. Müller, A. Olmi,** W. Quick, H. Stelzer, J. Tōke,*** GSI Darmstadt

Charged light particles emitted during or after a dissipative collision may, like neutrons, serve as a probe of the deexcitation mechanism. Semiconductor telescopes are for economical reasons no longer appropriate for such experiments; both the active area and the thickness of available types is not sufficient.

Scintillators offer a cheap and convenient solution of this problem. Our experimental set-up[1] has therefore been extended by 6 scintillation detectors each covering a solid angle of 220 msr. They are made from 1 cm thick stripes of an organic scintillator (NE 102A) of 110x5 cm² area; 2 of them are straight, 4 are bent with a radius of 50 cm in order to fit into the scattering chamber. The complete set-up was used[2] to study the Mo+Mo reaction at 12, 14.7 and 18 MeV/u.

The scintillators were light-tightly packed in Al-foils of 10μ thickness and mounted back to back onto stripes of Al of same size and shape as the scintillators to increase the mechanical stability. Cylindrical holders were attached to both ends of these stripes, inside which phototubes (Valvo XP2230B) were pressed against the polished scintillator end surfaces; the tube bases were filled with epoxy. The signals from both ends were split and used for amplitude information (E_1,E_2) and as stop signals for the time of flight (t_1,t_2) with respect to the beam pulse. The particle's time of flight is proportional to the sum of the two times, its energy proportional to the geometrical mean value of the amplitudes E_1 and E_2:

$$TOF \propto t_1 + t_1 \qquad E \propto \sqrt{E_1 \cdot E_2}$$

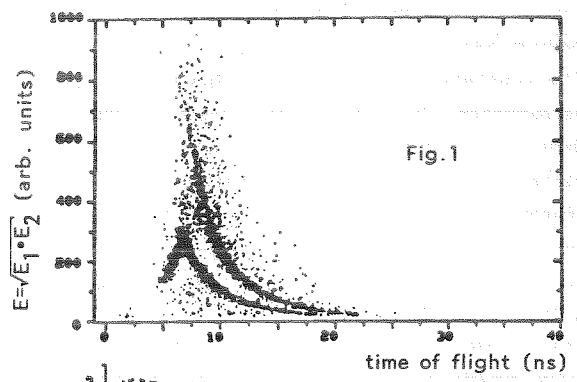
Time of flight and kinetic energy allow to determine the mass of the particle. Fig.1 shows an E-TOF-matrix of fragments detected in $^{92}Mo + ^{92}Mo$ at 18 MeV/u in one of the bent scintillators: The two branches which correspond to H and He are well separated (an isotope separation is not possible); the H branch stops and bends back at about 35 MeV, the energy from which on the protons penetrate the scintillator. Because of this fact and because of the quenching which makes the light output a complicated function of the primary energy, the energy is derived from the time of flight once the mass is known. Fig. 2 shows the lab energy spectra for the events shown in fig. 1. The incidence position X and hence the angle can be derived in two ways, either from the time difference or via the energy ratio:

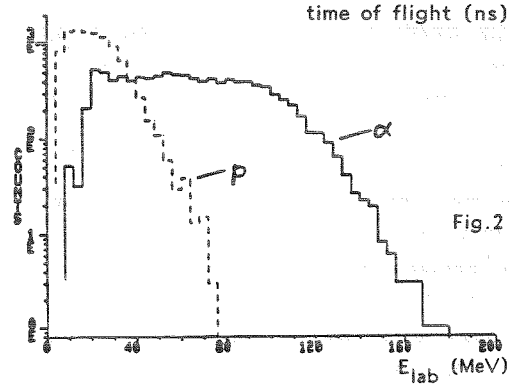
$$X_1 \propto t_1 - t_2 \qquad X_1 \propto \ln(E_1/E_2)$$

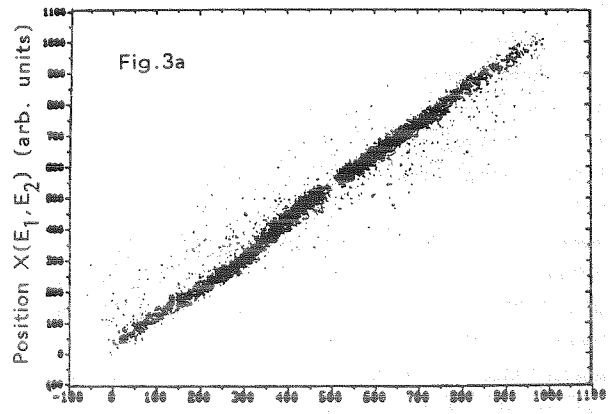
Fig. 3a shows these two quantities plotted against each other; the dip in the center is caused by a 2 cm broad piece of Al positioned in the middle between the two ends. From the projection on the X(t)-axis (fig. 3b) the resolution can be estimated to about 1.5 cm, which points to a time resolution of about 150 ps. The resolution in energy from time of flight varies from 3 to 9%.

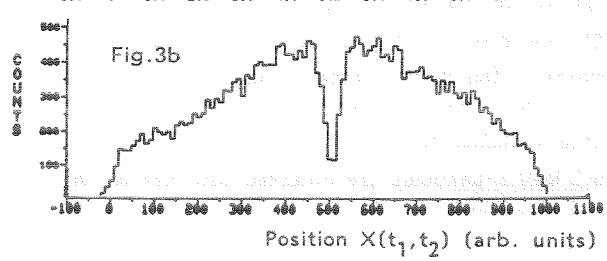
* on leave from Silesian University, Katowice, Poland
** now at INFN, Florence, Italy
*** on leave from Warsaw University, Poland

1 G. Augustinski et al., previous contribution
2 N. Herrmann, contrib. to this Annual Report









A New Heavy Ion Lanterne

G. Augustinski, H.J. Beeskow, H.W. Daues, U. Lynen, H. Stelzer and R. Wada (GSI Darmstadt)

Since several years low pressure gaseous detectors have been successfully used in experiments with a 84MeV/amu ^{12}C beam at the SC/CERN[1]. In this set-up up to twelve of these counters with a trapezoidal shape are arranged around the target, covering a solid angle of nearly 2π. They record the time-of-arrival, the emission angles θ and ϕ and an energy-loss signal, which yields a rough Z-estimate of the light and medium-heavy fragments.

The counters used up to now showed an overall good performance, but, to correct some of the observed defiencies, a new type of avalanche counter has been designed. Emphasis has been put to i) a high detection efficiency for low Z-particles ($Z \leq 6$), ii) a good ΔE resolution (20 - 25 %), with keeping a low low-energy cut-off (~100 KeV/amu) and an overall good time-resolution ($\Delta t \sim 200$ ps FWHM). Fig. 1 shows a schematic view of the new type of counter. It consists of three grids labelled ΔE, Y and X and a metallized thin foil T. The grids are made of 20 µ gold-plated tungsten wire with 1 mm spacing. The potentials are such (cf. fig. 1) that there are two independent high-electric field gaps with gas amplification. The two windows, which keep the counting gas heptane at 3.5 mb are on -600 V and -510 V resp. Primary electrons produced in the 5 mm gap between the entrance window and the ΔE grid drift into the 3 mm wide ΔE-Y gap, where they are moderately amplified by gas-multiplication. A slow, ($t_R \sim 50$ ns) and 100 ns wide signal appears on ΔE and Y, well suited for a pulse height and position measurement. Fig. 2 shows the pulse-height spectrum of a ^{252}Cf-source. Two factors ensure such a good ΔE-resolution: i) the electron collection gap between window and ΔE grid, and ii) the moderate gas gain in the amplification zone.

A fast timing signal is derived from the 3 mm wide high field gap between T and X. The pulse-height and time-measurement are thus completely decoupled and do not influence each other. Fig. 3 shows a timing spectrum of a ^{252}Cf source. The time-resolution of the counter itself is < 200 ps FWHM, when taking into account the energy-loss straggling in the start-counter and the velocity-distribution of the fission fragments.

The position is obtained by the two grids X and Y by means of the delay-line technique, using tapped delay-line chips. The binning is 4 mm and the positon resolution is limited by this.

6.2 MeV α-particles are detected with nearly 100 % efficiency on the T-foil, the X-coordinate shows a somewhat less efficiency. The Y coordinate does not see the α's, whereas the ΔE-signal is again full efficient for α's. The pulse-height ratio between α's and fission fragments is in the order of 1:90.

The elements for a new heavy ion lanterne are currently being assembled and tested in our lab.

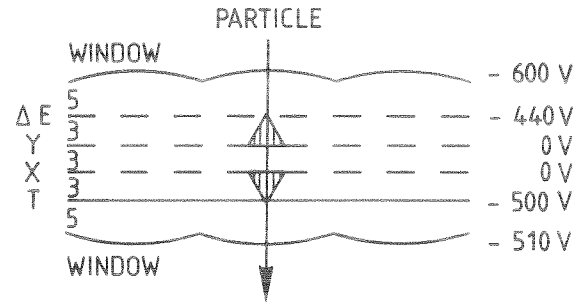


Fig. 1: Schematic view of the counter

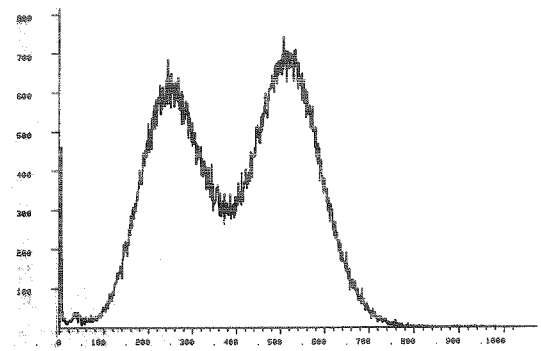


Fig. 2: Pulse-height distribution of ^{252}Cf-fission fragments.

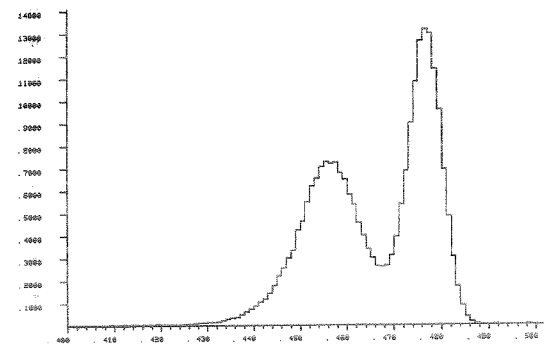


Fig. 3: Timing spectrum of fission fragments (1ch=100 ps).

Reference

1) U. Lynen, R. Bock, Y.T. Chu, P. Doll, R. Glasgow, A. Gobbi, K.D. Hildenbrand, H. Ho, W. Kühn, H. Löhner, W.F.J. Müller, A. Olmi, D. Pelte, H. Sann, R. Santo, H. Stelzer, U. Winkler, invited talk at the Int. Conf. on Selected Aspects of Heavy Ion Reactions, Saclay, May 3-7, 1982, Nucl. Phys. A387(1982)129.

G

A setup for coincidence measurements between π^0's and forward going charged particles from intermediate energy nuclear collisions

A. Oskarsson[1], P. Grimm[1], E. Grosse[1], H. Heckwolf[1], C. Michel[*], H. Noll[1,2]
[1]GSI Darmstadt, [2]IKF Frankfurt

Single particle inclusive measurements of π^0's and high energy γ-rays produced from nucleus nucleus collisions below 100 MeV/A beam energy have indicated the presence of cooperative or collective processes to be important[1]. Nuclear collisions at these energies are characterized by the fragmentation into many nuclear fragments. We have designed a hodoscope for the measurement of all charged particles in the forward cone to be operated together with a modified version of the lead glass ring[2], which we use for the detection of π^0's and high energy γ-rays.

The geometrical acceptance of the π^0 spectrometer has been increased by making the converter ring cover a larger solid angle and doubling the number of lead glass absorbers. The 40 absorbers are now arranged in two rings, one above the other, providing the same angular resolution between the two γ's from the π^0 decay as before. According to Monte Carlo calculations (EGS-code) the new absorber arrangement offers better containment of the shower and thus a better energy resolution. The overall geometrical efficiency (fig. 2) has increased by a factor of 2. Plexiglas Cerenkov detectors (low γ sensitivity), inserted in front of the converters, reduce the charged particle background in the measurement of directly produced high energy γ-rays from the nuclear collision.

The hodoscope, fig. 1, uses 64 plastic scintillators arranged in the following way: 4 rings of 16 detectors cover from 3° to 18.5°, so that the angular range of each gives similar counting rates in all detectors. Each ring has one layer of 8 ΔE detectors (3 mm) and a second layer of 8 E detectors. The E detectors are shifted 22.5° as compared to the ΔE detectors thus providing an improved azimuthal angle resolution. Finally, the ΔE detector for the next inner ring also serves to detect the particles which pass through the E detector.

The thicknesses of the E detectors have been chosen to optimize the resolution for particles in the mid rapidity region, allowing fragmentation-like particles pass through and stopping the fragments which have lost kinetic energy in the reaction and thus possibly contributed to the pion production. The two inner rings (3-9°) are suitable for fragments with $2 \leq Z \leq Z_{proj}$ (neighbouring Z resolved for $Z_{proj} \leq 10$) while the outer rings detect mainly light fragments (and resolve their Z and A reasonably well). The energy calibration can be done with the known detector response for particles just passing through the E detector.

The hodoscope detectors are placed inside the vacuum scattering chamber with the light-guides going through the chamber wall to the PM tubes outside. Thus the whole forward cone (3-18.5°) is covered without any dead areas than those arising from the detector segmentation.

The hodoscope is mainly aimed for use with lighter heavy ions at energies 50-100 MeV/A. With change of scintillator thicknesses it can be optimized for other beams. The first use of the coincidence setup will be with 86 MeV/A ^{12}C and 48 MeV/A ^{20}Ne projectiles at the CERN SC and 20 MeV/A Kr at GSI, both runs scheduled for the spring of 1984.

[1] H. Heckwolf et al., this report
[2] H. Noll et al., this report
[*] now at Universite de Louvain, Belgium

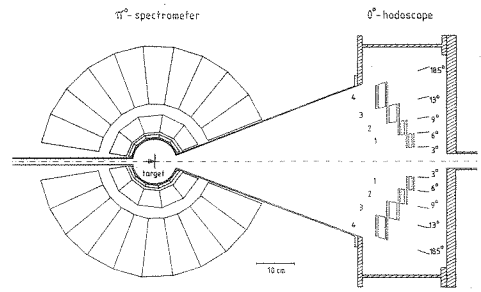


Fig. 1: Scheme of the experimental setup

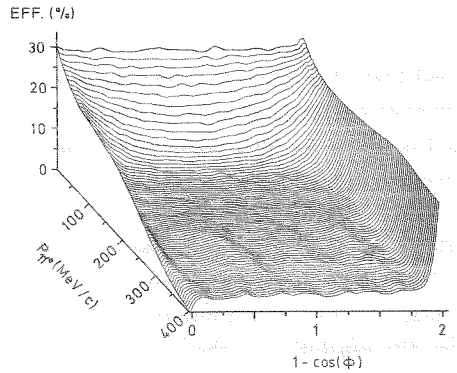


Fig. 2: Geometrical efficiency plotted versus the pion angle and momentum

G

Calibration Measurements and Monte Carlo Calculations for a Lead Glass Cerenkov Detector

H. Noll[1,2] C. Michel[1*], C. Brendel[3], E. Grosse[1], O. Klepper[1],
W.F.J. Müller[1], W. Rösch[3], H. Stelzer[1]
[1] GSI Darmstadt; [2] IKF Universität Frankfurt; [3] TH Darmstadt

The GSI lead glass spectrometer[1] for high energy γ-rays was calibrated with γ-rays from the decay of low energy π^0's. The π^- (p,n) π^0 charge exchange reaction was performed at a stopped π^- beam from the CERN SC to produce the π^0's. The results of this experiment were compared to Monte Carlo calculations to obtain proper calibration parameters for these.

The experimental set-up is shown in Fig. 1. Scintillators S_1 and S_2 defined the incoming beam which not only contained pions but also muons and electrons. To suppress the electrons we have used a gas Čerenkov counter C. The beam was slowed down in a beryllium degrader (26 cm thick), defined in scintillator S_3 and stopped in the active target S_4 (2.5x2.5x2.5 cm³) made from organic scintillator material. The scintillator S_5 was used as a veto counter for unstopped pions and muons. A stopped π^- is defined by signals of proper pulse height in scintillators S_2, S_3, S_4 and no signal in the gas Čerenkov counter and the veto counter S_5. The capture occurs most probably when the π^- is at rest; it produces an isotropic distribution of π^0's of 2.9 MeV kinetic energy (or 28 MeV/c momentum). The π^0 decays into two γ's with a characteristic continuous γ-ray distribution ranging from 55 to 83 MeV.

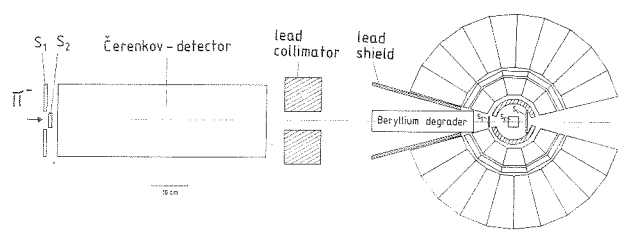


Fig. 1: Experimental set-up for calibrating the π^0 spectrometer via the charge exchange reaction of stopped π^- with protons.

This distribution was used to test the Monte Carlo simulation of the spectrometer with the code EGS (cf.ref.1) and to calculate the Čerenkov light collection efficiency in the converters and absorbers. The measured Čerenkov light spectra for this particular γ-ray distribution are shown in Fig. 2. By comparing the spectra measured in the converters and absorbers to the respective Monte Carlo calculation a simultaneous calibration of the light collection efficiency of converters and absorbers is possible. To test this calibration we verified that it minimizes the resolution in the invariant mass spectrum.

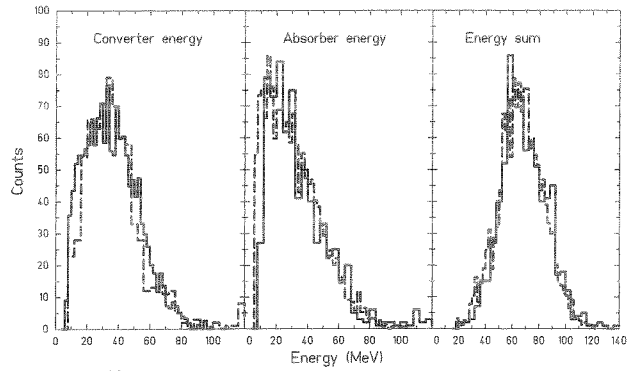


Fig. 2: Čerenkov light output spectra for the converters, absorbers and their correlated sum as measured in the π^- (p,n) π^0 reaction. The dashed lines represent the result of the Monte Carlo simulation.

The results of the measurement with the charge exchange reaction allow the determination of the characteristics of the spectrometer for low π^0 momentum. The measured invariant mass is shown in Fig. 3. In Table 1 we compare the experimental and calculated resolution obtained for these π^0's of about 28 MeV/c momentum. As can be seen the agreement between calculated and measured width of the invariant mass and momentum distributions is satisfactory. The small deviation in the centroids is due to the loss of parts of the shower through the boundaries of the lead glass. The good agreement indicates that the widths are governed by the statistics of the Čerenkov light production and its collection (the thresholds in the spectra correspond to only five photoelectrons equivalent to E_γ = 8 MeV).

[1] C. Michel et al., GSI Scient. Report 1982, 83-1 p. 226 and to be published

* now at Université de Louvain, Belgium

Fig. 3: Invariant mass of the two γ-rays produced from the decay of 28 MeV/c π^0's. The dashed line represents the result of the simulation of the π^0 detection.

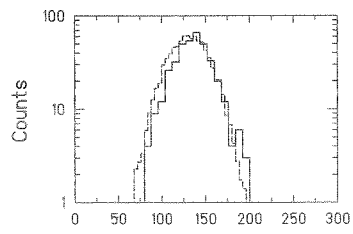


Table 1:

	Source	Centroid calc.	Centroid meas.	rms dev. calc.	rms dev. meas.
Invariant Mass [MeV]	135	130.7	135	22.6	22.0
π^0 Momentum [MeV/c]	28.1	38.4	43.2	15.6	16.5

A forward Scintillator Hodoscope for the Streamer Chamber Facility

G

R. Brockmann, J.W. Harris, M. Maier, A. Sandoval, R. Stock, H. Ströbele (GSI Darmstadt), R.E. Renfordt, D. Schall (Univ.Heidelberg), D. Bangert, W. Rauch (FB Physik, Univ. Marburg), P. Eitner, G. Odyniec, H.G. Pugh (LBL Berkeley), A. Dacal, M. Ortiz (UNAM, Mexico)

At the present time the main effort of our collaboration is to study in detail the interaction of heavy nuclear systems (e.g. La + La) and isolate collective effects that cannot be explained by binary nucleon-nucleon collisions. Of special interest is also the degree of thermalization and chemical equilibrium between nucleons and deltas and total pion production in these reactions.

Crucial for the analysis of the data is the determination of the impact parameter of the interaction. For heavy nuclei this can be done by measuring the projectile fragments that survive the interaction with essentially the beam velocity (projectile spectators).

To enhance the ability of the Streamer Chamber to detect forward-going fragments emitted in a cone between 0 and 9 degrees, a highly segmented hodoscope has been constructed. The segmentation of the hodoscope was determined by an extensive Monte Carlo calculation in which the known cross-sections for nuclear fragmentation have been incorporated. The criterium for the segmentation was to maintain a double hit probability below 5 %. The hodoscope measures the energy loss (dE/dx) in the 1" thick scintillators and determines the time of flight between the trigger counter in the Streamer Chamber and the hodoscope.

A prototype hodoscope was tested in the beam. These measurements showed that the required charge and time-of-flight resolution could be met, to do charge identification up to Z=20. Together with the rigidity measured in the Streamer Chamber this allows for mass identification of the hydrogen and helium isotopes. These measurements also showed that to cover the dynamical range of the pulse height spectrum from protons to heavy fragments near Fe a dynode read out is necessary.

A schematic view of the hodoscope is shown in Fig. 1. It consists of 384 scintillator counters, which are divided into 9 subgroups, with an unequal number of channels in each subcroup. Fig. 2 shows 3 of the subunits. The hodoscope can be moved up and down to match the deflection of the charged fragments at different energies for a given magnetic field of the streamer chamber. It can also be rotated by 90 degrees into a horizontal position to accept cosmic ray particles for calibration. During the run the calibration will be controlled by a laser driven optical system. The hodoscope is assembled and set up behind the Streamer Chamber Magnet and the first data will be taken in the Spring of 1984.

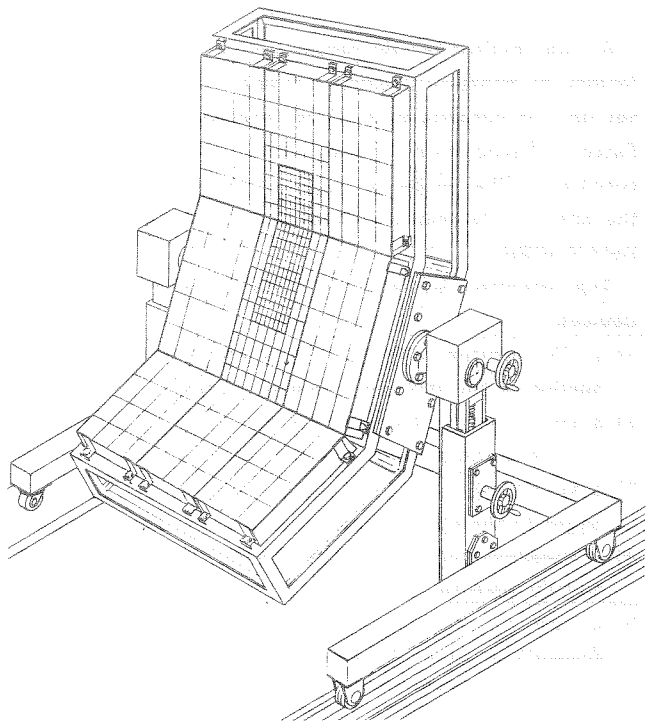


Fig. 1: Schematic view of the forward angle hodoscope.

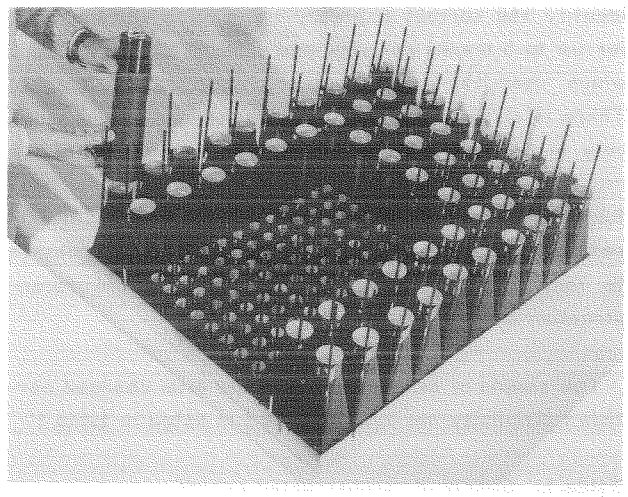


Fig. 2: A subunit of the hodoscope. The phototubes are air-coupled with an Al cone to the square 1" thick scintillators mounted on a grid.

G

Automatic track measurement on streamer chamber pictures with high multiplicity events

D. Schall, K. Tittel (Institut für Hochenergiephysik, Universität Heidelberg);
H. Ströbele (GSI Darmstadt)

At the Institut für Hochenergiephysik in Heidelberg a facility to measure streamer chamber pictures has been set up. It consists of a PEPR (Precision Encoding and Pattern Recognition) device controlled by a PDP-10 computer. The system is highly interactive and allows the operator to take complete control over the measurement process.

The operator environment consists of the following devices:

1) 2 TV monitors showing the whole and an enlarged section of the streamer chamber picture.
2) a computer display for visualization of track measurements and program control indicators
3) a keybord/printer for program flow control and messages to the operator
4) a speedball for manual positioning fo a cross hair on the TV-picture.
5) a fast film transport (allowing speeds of up to 50 frames/s ≈ 5m/s) for efficient positioning of pictures with rare events.

Each track is measured in at least 2 views and subsequently reconstructed in space. Details of the measuring process are given in fig. 1. The correct selection of track images in the 3 views for the reconstruction of a single space curve is the most problematic part of the measurement procedure. It is done under complete control of the operator. However, the computer helps to identify the correct triple by means of a storage bank for up to 5 tracks per view and a permutation algorithm which uses the newly measured and stored tracks. There is also the possibility to reconstruct with 2 views only and to predict the 3 new. By positioning of the cross hair the prediction is presented to the operator for inspection and measurement. These improvements reduced the measuring time per track from 3.5 minutes to less than 1 minute without affecting the reconstruction efficiency (fig. 2).

The sample of events for which the total charged particle multiplicity has been analyzed is listed in table 1.

Table 1: Sample of reconstructed events

Reaction	events	<tracks> /event	<meas.time> /event
0.8 GeV/A Ar + Pb	957	49.6	60 min.
0.8 GeV/A Ar + KCl	392	29.5	30 min.
1.8 GeV/A Ar + KCl	497	39.6	45 min.

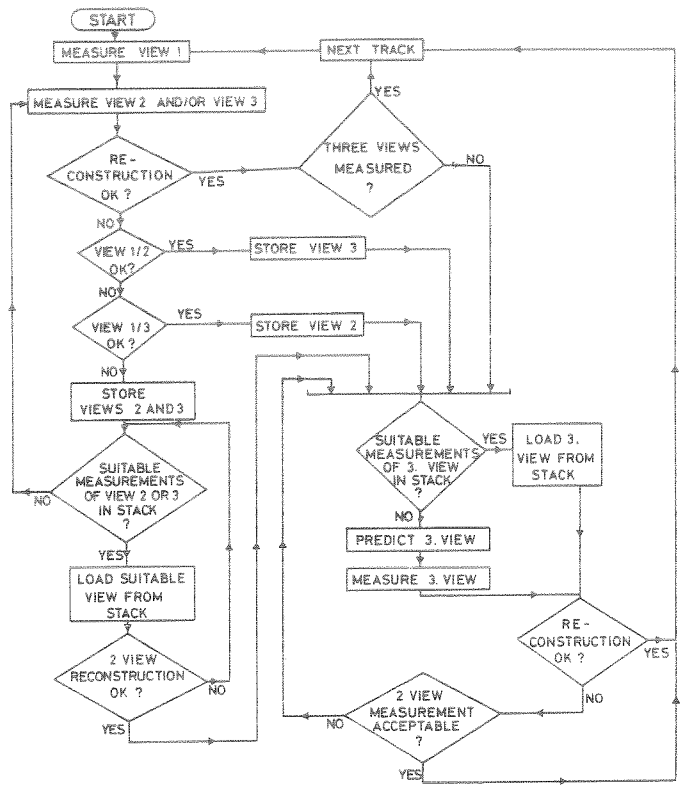


Fig.1: Logic of track measurement

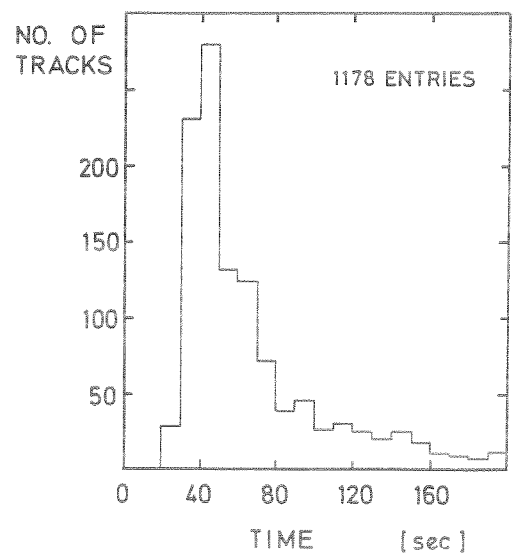


Fig. 2: Measuring time per track

A New High Precision Recoil Distance Plunger Apparatus [G]

H. Emling, F. Azgui, H. Grein, G. Seiler-Clark, H.Sitta (GSI Darmstadt)

The determination of the mean lifetimes of excited nuclear states is an important aspect in nuclear structure studies. During the past decade, particular interest evolved to explore the properties of nuclei at high angular momentum where lifetimes typically are in the order of 10^{-12} seconds. Recent studies[1] proved that lifetimes of $\geq 10^{-13}$ seconds can be measured using the Recoil Distance Method (RDM) in conjunction with heavy ion beams. Moreover, the RDM now seems to become a suitable technique for the determination of nuclear magnetic moments of short lived levels[2]. Presently, experimental studies very often utilize 4π γ-detection systems thus allowing an almost complete tracing of the complex decay of high spin states.

In this report we describe a newly constructed plunger apparatus which in particular was designed to fit into 4π γ-detectors, i.e. our sum crystal and the crystal ball. The principles of the RDM may be found in ref. 1; a plunger device essentially consists of a target and a stopper foil which have to be aligned parallel to each other. The nuclear lifetimes are obtained from counting the decays in flight relative to the decays in the stopper. Therefore, the measurement of short lifetimes requires the accurate positioning of the target relative to the stopper at distances of a few micrometers.

A photograph of our new system is shown in fig. 1 and constructional details may be taken from fig. 2. The entire mechanism is contained in a cylindrical vacuum chamber with the beam direction as the symmetry axis. Both target and plunger foil are mounted on 1 mm thin aluminium frames; very flat foil surfaces are attainable by a stretching technique as described in ref. 3. A transmission of > 93% for γ-ray energies > 300 keV is obtained for all angles outside a cone of 14° in the backward hemisphere. The frames holding the target and the stopper foils are supported on three invar rods; the three rods of the plunger are attached firmly to the housing, while the supporting rods of the target are coupled to three piezoelectric "Inchworm" translators. The translators and control systems were purchased from Burleigh Instruments, however, we incorporated a microcomputer which allows a very convenient operation of the system.

A high positioning accuracy was ensured since three independent control methods were utilized:

- to each of the three translators a interferometer is attached which determines the position to ± 0.5 µm. Within that accuracy the translator motion is free of backlash and the absolute position is reproducible over the full range of the motion (25 mm).
- the target and the stopper are electrically insulated; therefore, a capacitance measurement can be applied which, at low distances, is sensitive to variations of ~ 0.1 µm.
- within one operational interval of 1.2 µm, given by the maximum extension of the piezo crystals, a continuous relative positioning is possible, controlled by the voltage applied to the piezo crystals. Preliminary measurements resulted in an accuracy of ~0.1 µm.

Since the three Inchworm translators move independently the target can be tilted about any axis in the plane parallel to the stopper. To first order, the capacitance varies as the square of the tilt angle between target and stopper; thus, the measurement of the capacitance in dependence of the tilt angle provides a very convenient technique to align the mechanism parallel. In contrast to optical methods proposed earlier, this procedure is quantitative and can be carried out at under real experimental conditions, i.e. in vacuum and with beam.

The good performance of this new system could be demonstrated in first experiments[4].

1. H. Emling et al., Nucl.Phys. in print
2. G. Seiler-Clark et al., this report
3. J.L. Gallant, N.I.M. 81(1980)27
4. F. Azgui et al., this report

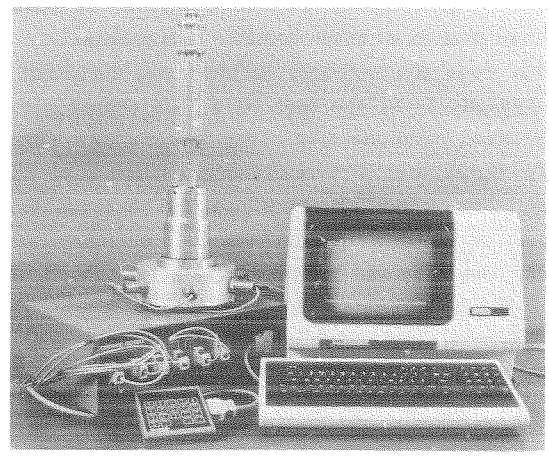


Fig. 1: Photograph of the plunger apparatus and the control systems.

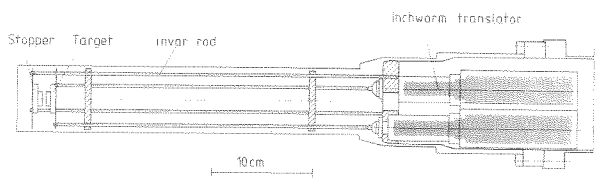


Fig. 2: Layout of the plunger mechanism.

Design of a High Performance Compton Suppression Spectrometer

Ch. Michel[+], F. Azgui, H. Emling, H. Grein, E. Grosse and
H.J. Wollersheim (GSI Darmstadt)

The interest in γ-ray Compton Suppression Spectrometers (CSS) has renewed since the recent development of Bismut Germanate (BGO) scintillators allows the design of rather efficient and compact Anti Compton shields. Depending on the particular configuration of the CSS, Compton suppression factors (CSF) in the order of 5-10 are expected, i.e. up to 70% of the detected γ-ray intensity is contained in the full energy peak. In the following we report the result of extensive design studies of CSS aiming at high performance and at low costs.

In the energy range that is of interest for nuclear γ-ray spectroscopy, realistic estimates of the performance of CSS are obtained from Monte Carlo methods which are described in refs.1,2. Excellent properties were found for a new type of CSS configuration: The system consists of three independent high purity Germanium detectors (a planar crystal followed by two identical coreless crystals) surrounded by a BGO annulus to which a NaI backscatter crystal is coupled. A schematic layout of the spectrometer which has the favourable cylindrical symmetry is shown in Fig.1. This spectrometer can be used in various modes being adapted to specific experimental requirements (see ref.2). Here, we only present the results from the Monte Carlo simulations of the "standard" Compton suppression mode where the central Ge detector is operated in coincidence to all other detector components.

In this mode the response function was simulated for two "typical" γ-ray sources: (i) a ^{60}Co source and (ii) an idealized rotational-like γ-ray cascade with a multiplicity M_γ=25 and a γ-ray energy spacing of ΔE_γ = 60keV. The latter source allows the investigation of various multiplicity effects[2] whose tendency is to reduce the Compton suppression factor. Fig.2 illustrates the behaviour of the central detector for these two sources: part (a) shows the suppressed and unsuppressed spectra for the ^{60}Co source; part (b) displays the corresponding CSF, and, superimposed, the isolated contributions from the front and rear detectors and from the symmetric shield; part (c) displays the suppressed and unsuppressed spectra for the rotational cascade, part (d) shows the corresponding CSF. As can be seen, a reduction of the Compton background by a factor ~8 is obtained on the average. Comparison with simulation calculations for various CSS configurations proposed at other laboratories, clearly demonstrates the high performance of the system considered here.

A prototype of this new Compton Suppression Spectrometer is presently under construction. The individual detector components have already been tested and the complete system should be available early in 1984.

+ Present address: Institut de Physique, Chemin du Cyclotron, Louvain-la-neuve

1) Ch. Michel et al., GSI Scientific Report 1983, p.224
2) Ch. Michel et al., to be published

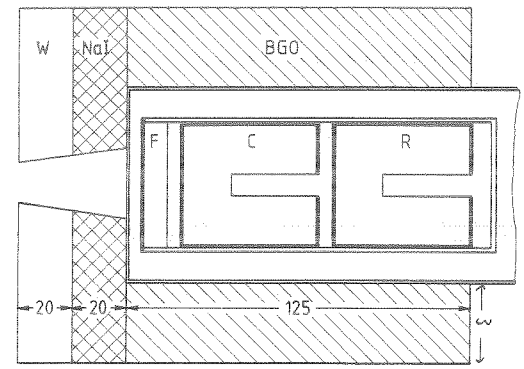


Fig.1: Proposed CSS configuration. F,C,R,W, denote the three Ge detectors and a tungsten collimator, respectively.

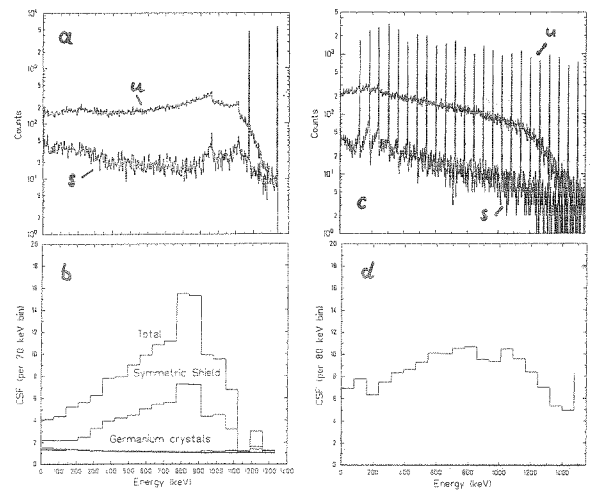


Fig.2: a,c: Monte Carlo simulations of suppressed (s) and unsuppressed (u) spectra for two investigated γ-ray sources;
b,d: corresponding Compton suppression factors for γ-energy intervalls of 70 keV.

An Electrostatic Separator Designed for the NaI Crystal Ball Spectrometer B

W. Bonin and M. Dahlinger
Institut für Kernphysik, Technische Hochschule Darmstadt

D. Habs and B. Schwartz
Physikalisches Institut der Universität Heidelberg

H. Grösch and R.S. Simon
GSI Darmstadt

The intense background radiation from fission and deep inelastic reactions represents a basic difficulty for the γ ray spectroscopy following fusion reactions at high angular momentum. To reduce this background it is necessary to isolate the recoiling evaporation residues from possible fission fragments and deep inelastic reaction products as well as from the main stream of noninteracting beam particles. For recoils having low velocity and sufficiently high charge an effective separation already is possible in a simple electrostatic field. Such a separator[1] has been used for the investigation of the shortlived actinides[2] where internal conversion in the deexcitation process leads to high atomic charge of the recoiling ions. To investigate higher angular momenta and to extend the studies to more unstable compound systems we suggest to combine the selectivity of the separator with the selectivity of the NaI crystal ball which is provided by the additional information on the γ ray multiplicity and the total γ decay energy.

Fig. 1 shows the separator and the target chamber together with a cut through the central plane of the crystal ball. The recoiling ions leave the thin target ($\cong$ 150 $\mu g/cm^2$) and enter the separator through a narrow collimating slit. Separation occurs in the transverse electric field between a solid electrode of polished aluminium (+HV) and a grid structure at ground potential. As indicated by the dashed trajectory, the positively charged recoils are deflected, pass through the grid and register in a surface barrier detector. Computer calculations applied to the reaction ^{208}Pb (^{18}O, 4n) ^{222}Th at 93 MeV beam energy for instance show an overall detection efficiency of 30%.

The design of the separator essentially preserves the 4π geometry of the crystal ball. For the conical shape chosen one has to remove only 1 segment at the beam exit while the 6 neighbouring segments can be displaced radially. Together with 1 segment at the beam entrance and another segment at 90° to the beam for the target rod this leads to a loss in γ ray solid angle of less than 6%. Target chamber and separator are built out of 1.5 mm stainless steel to keep the γ ray absorption small.

The separator has been voltage tested at 65 kV and will be available for first experiments in spring 1984.

1) M. Dahlinger, W. Bonin, E. Kankeleit and H. Backe, to be published in Nucl. Instr. and Meth.
2) W. Bonin, M. Dahlinger, S. Glienke, E. Kankeleit, M. Krämer, D. Habs, B. Schwartz and H. Backe, Z. Physik A310 (1983) 249

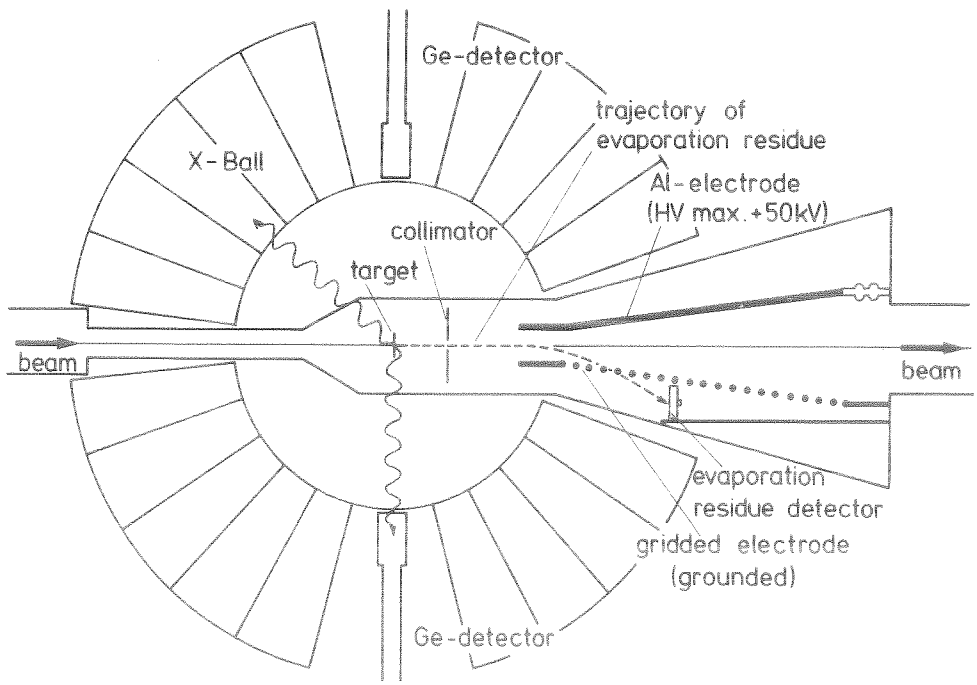


Fig. 1: Schematic view of the separator inside the NaI crystal ball (not to scale). For high resolution γ-ray spectroscopy of the separated residues crystal ball segments may be replaced by Ge detectors.

ROMA - A Rotating Wheel Multidetector Apparatus used in Experiments with ^{254}Es as a Target

K. Sümmerer, M. Brügger, W. Brüchle, H. Gäggeler, E. Jäger, M. Schädel,
D. Schardt, E. Schimpf
GSI Darmstadt

Rotating wheel systems connected to gas jet transport capillaries have proven to be useful devices for studying short-lived activities with half-lives in the order of seconds. We have set up such a system at GSI to detect α-particles and correlated fission fragments from the decay of neutron-rich actinide and trans-actinide isotopes formed in the reactions ^{16,18}O, ^{22}Ne + ^{254}Es[1]. An earlier version of this device, in conjunction with on-line gas phase chemistry (OLGA), has been used in a search for superheavy elements with the ^{48}Ca + ^{248}Cm reactions [2]. We utilize a He/KCl-cluster jet to transport recoiling reaction products into the ROMA system, where they are deposited on thin polypropylene foils (about 70 µg/cm²) mounted on a 64-position wheel. After a preset collection time (typically 2-30 seconds), the activity is moved between pairs of surface barrier detectors to measure α- and spontaneous fission decays. The wheel is rotated by a stepping motor controlled by a GSI 8085 microprocessor which is in turn coupled via CAMAC to the PDP11 computer of the GSI data acquisition system.

The inner part of th ROMA system is shown in the photograph (fig.1). Detector pairs are mounted at 15 out of 64 available positions. Three sets of 16 polypropylene foils are located in 48 out of the 64 positions around the perimeter of the rotating catcher wheel. To reduce the build-up of longer lived activities, a fresh foil set is brought into position every two hours. After the three sets available have been used, the wheel chamber is opened and the entire collector wheel exchanged.

The remaining 16 positions of the wheel are left blank to allow for observation of daughter decays: when, during the on-line analysis, an α-event is found to fall within a preset energy window (mother decay), the weel is moved in such a way that the blank positions are located in front of the detectors. In this way the observation of subsequent decays of the daughter activity implanted by nuclear recoil into thin carbon foils covering the detectors is enhanced. After a preset time during which possible daughter decays are recorded, normal wheel indexing is resumed.

The data acquisition includes standard α- and sf-spectroscopy recorded event-by-event to measure energies, half-lives, and time correlations. To facilitate data taking with 30 surface barrier detectors, the analog signals of sets of eight detectors each were multiplexed by an ORTEC 476-8 multiplexer. Each detector was identified by routing bits stored in a bit pattern unit. A test pulse distributor[3] was specifically designed for this set-up to facilitate the time-consuming calibration of the detectors.

1. M. Schädel et al., contribution to this report, p.
2. H. Gäggeler et al., contribution to this report, p.
3. W. Brüchle, contribution to this report, p.

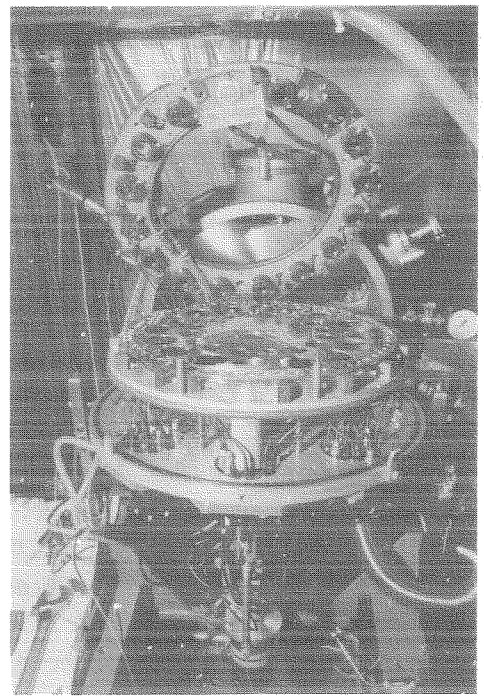


Fig.1: The rotating wheel multidetector apparatus, ROMA, as used in experiments with ^{254}Es as a target. The photograph shows the lid of the vacuum chamber slid outwards and turned by 90°. The catcher wheel and one set of 15 surface barrier detectors are in a horizontal position now. The second set of detectors is moved upwards to replace the wheel and ease access to the detectors.

The Status of ARCA - Automated Rapid Chemistry Apparatus

W. Brüchle, M. Brügger, B. Haefner, M. Schädel, E. Schimpf
GSI Darmstadt

We adapted our microprocessor-controlled automated rapid chemistry apparatus, ARCA[1], to the needs of two different types of experiments.

The first one, a search for superheavy elements (SHE) in the $^{48}Ca + ^{248}Cm$ reaction[2], required a fast and effective separation of elements Os through Po and their homologues Z=108 through 116 from actinide elements so that the expected spontaneous fission (sf) decay of the SHE's would not be obscured by interfering spontaneously fissioning actinides. We used a very simple cation exchange column separation with a separation factor of about 10^4. This method is based on the predicted tendency that elements 108 through 116 should form strong anionic complexes in aqueous solution thus being not bound to a cation exchange resin while the cationic species of actinides are strongly retarded. Reaction products recoiling out of the ^{248}Cm target are stopped and transported in a KCl loaded cluster jet with He as a carrier gas from the irradiation position at Y3 over ca. 80 m into our chemistry laboratory. No significant losses were observed, and the transport time of approximately 10 s is negligible compared to the 30 min time interval while the activity from the jet was collected on a quartz frit (D4) in ARCA. Every 30 min the activity was dissolved in 0.1 m HBr/Br_2 and pumped through the (100x1.75) mm cation exchange column (AG 50 W x 8, - 400 mesh) at a flow rate of 3. ml/min for 10 s. Eluting a SHE fraction was completed after another 60 s of pumping 0.8m HBr/Br_2. The solution at the outlet of the column was continuously evaporated. This made it possible to use just the last few drops to rinse the glass and to have a sample ready for counting on a Au-coated 33 µg/cm² C-foil within 2.3 min after end of bombardment (EOB). Counting each sample between two Si(Au) surface barrier detectors for sf and α-activity started 3 min after EOB. ARCA went successfully through 88 irradiations and automated chemistry cycles accumulating 1.3×10^{17} ^{48}Ca particles on the ^{248}Cm target[2].

In a second experimental series we wanted to measure cross sections for transfer products from an ^{254}Es target and searched for new isotopes of elements 101 (Md) through 103 (Lr) with minute half-lives[3]. This required a very delicate and precise separation between individual transcurium elements which was difficult to achieve in an automated chemistry apparatus. The flow scheme is shown in Fig.1. The activity was washed from the quartz frit in 0.03 m HCl and loaded onto a HDEHP column, a Sr^{2+} fraction was discarded and a No^{2+} fraction eluted with 0.03 m HNO_3 and loaded onto a cation exchange column. With two pumps in operation we simultaneously eluted a No^{2+} fraction with 4m HCl from the cation exchange column and, after washing with 1.0m HNO_3, a Md,Lr fraction with 4m HCl from the HDEHP column. Using a T connector, a stream of 2.0 m NH_4OH was added to the 4m HCl from the HDEHP column to bring down the H^+ concentration to about 1.0 m. The Md, Lr from this solution was loaded on a second cation exchange column. After washing with H_2O and NH_4Cl the elements Lr and Md were eluted with α-hydroxyisobutyric acid as individual fractions. The cycle time (collection time) was 30 min, and the final separation of the No, Lr and Md fractions was completed after 4.7, 12.5 and 14.2 min, respectively. We ran a total number of 29 automated separation cycles while the ^{254}Es target was bombarded with ^{18}O and ^{22}Ne[3].

As a major change from the early version of ARCA we decided to control the system now with a GSI 8085 microprocessor system[4] with two floppy disc drives. BASIC is now the command language, which makes programming simple and flexible. To operate more than one valve at a time all four 16 channel driver units for the 24V magnetic valves were modified.

1. W. Schorstein et al., GSI Scientific Report 1981, GSI-82-1, p. 220 (1982)
2. H. Gäggeler et al., this Scientific Report, p.
3. M. Schädel et al., this Scientific Report, p.
4. G. Englert et al., GSI Scientific Report 79, GSI-80-3, p. 196 (1980)

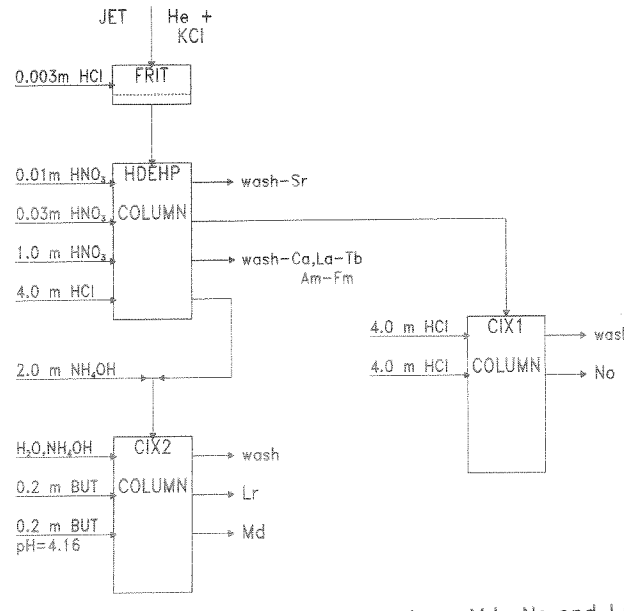


Fig.1: Flow scheme for a three column Md, No and Lr separation used in experiments with ^{254}Es as a target[3].

High Resolution Detection System for Positron Studies with the "Orange"-β-Spectrometer

G

E. Berdermann, J. Kemmer, P. Kienle, H. Tsertos, W. Wagner
TU München
F. Bosch, C. Kozhuharov
GSI Darmstadt
W. Koenig
MPI Heidelberg

A new set-up for positron spectroscopy has been developed and tested successfully.

The new PAGODA-β-detector is divided into 12 identical sub-units placed along the spectrometer axis (Fig. 1). Each unit consisting of 6 trapezoidal detectors forms a hexagonal truncated pyramide arranged around the spectrometer/beam axis. Therewith converting the spectrometer into a spectrograph we achieved good momentum resolution ($\Delta p/p \approx$ 2-3 % for every sub-unit) within the large total momentum interval accepted ($\Delta p/p$ = 24 %) for every constant value of the magnetic field.

The 72 silicon-semiconductor-chips are fabricated by the detector laboratory of the TU München (division E12 of the Physics Department) using the ion implantation technique. By cooling down the detectors to $\approx$ -10° C the leakage current per unit (6x300 mm^2, 500 µm thickness, 380 pF total capacitance) is reduced to $\approx$ 30 nA and the energy resolution at 320 keV (^{133}Ba K-conversion electrons) is improved to better than 10 keV. The cathodes of each detector sub-unit are connected to a charge sensitive preamplifier and the anodes of a "row" are connected to another one. This matrix-arrangement reduces the number of amplifiers (18 instead of 72) and allows the measurement of a large energy range with good resolution and high background suppression.

From U-U collisions at 1400 MeV we obtained for positrons at 320 keV an intrinsic energy resolution of the detector of about 11 keV (Fig. 2). In order to maintain the good optical properties of the β-spectrometer, the "diameter" of the counter was chosen to 40 mm. The accepted positrons (110° to 150° relative to the beam axis) impinge nearly perpendicularly on the detector minimizing, thus, the backscattering.

The scattered heavy ions are recorded by a θ- and ϕ-position sensitive parallel-plate avalanche counter covering an angular range from 15° to 55°. The overall time resolution for positrons associated with scattered particles is about 9 ns.

By this new detection system the emission angle of positrons relative to the particle scattering plane can be measured. Therewith velocity and direction of the positron emitting source can be determined experimentally which would give the decisive information about the origin of the observed narrow positron line in U-U collisions. In one of the runs we used high beam currents (approx. 4 particle nA) with a target-wheel which carries nine 50x8 mm large targets and which is synchronised with the duty cycle of the accelerator, in order to gain better statistics.

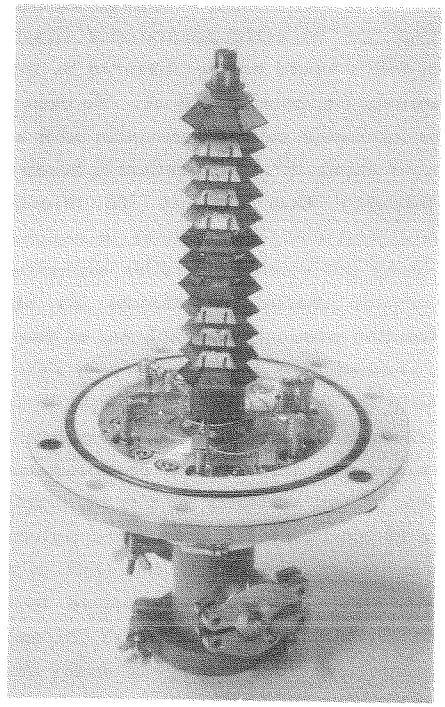


Fig. 1: The PAGODA-counter consisting of 12x6 trapezoidal silicon detectors of 500 µm thickness.

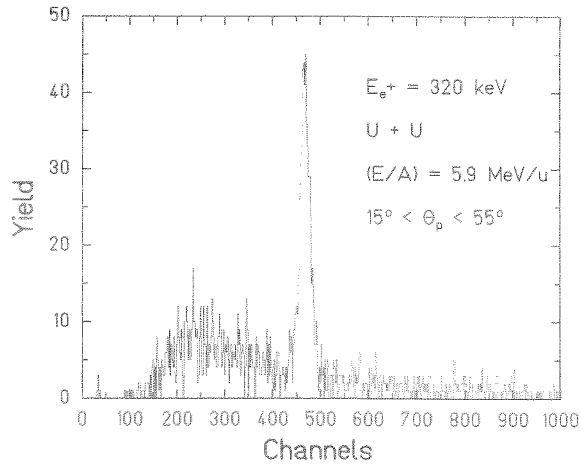


Fig. 2: In beam positron spectrum of one sub-unit of the PAGODA-detector, analyzed on-line, for a focussed momentum bin ($\Delta p/p$) $\approx$ 2.5 %. The intrinsic energy resolution is about 11 keV.

An Alkali Atomic Beam for Charge Exchange in Collinear Laser Spectroscopy

G.Berthes, G.Huber, R.Menges, H.Lochmann, G.Ulm
Institut für Physik, Universität Mainz

Collinear spectroscopy often makes use of the charge exchange of an ion beam with an alkali vapour for the preparation of fast neutral atoms (Ref.1 and Ref.2).
In order to investigate also short lived atomic states, it is necessary to observe fluorescence signals at the region of charge exchange. We have developed a set up with a supersonic dense sodium atomic beam, which allows an efficient charge exchange with an ion beam at the focal point of an elliptic mirror, which focusses the fluorescence light on a photomultiplier (Fig.1).
With this configuration we also avoid problems with optical pumping accuring between separated charge exchange and fluorescence detection regions (Ref.3).
In the light of an expanded single mode dye laser beam at the sodium D1 resonance the absorbing atom beam is shown in the photograph (Fig.2). The divergence $\vartheta_{1/2} = 2.5°$ agrees with the line width at low densities (95 MHz) (Fig.3a). At the maximum density these absorption profiles yield the pattern shown in figure 3b. From this pattern, which is the saturation of the lorentzian wing of the absorption, the sodium beam density can be evaluated to 3×10^{14}atoms/cm². From the flux measured by surface ionisation and the target thickness from the absorption profiles, we determined the value of the beam velocity <v>=1200 m/s.

In order to use this system for long measurement times, the beam forming system will be modified for a recycling of the condensed sodium vapour.

Ref.1: G.Ulm et al., contribution to this report
Ref.2: H.Lochmann et al., contribution to this report
Ref.3: G.Ulm et al., in "Laser Spectroscopy VI", H.P.Weber and W.Lüthy (eds.), p.211 (1983)

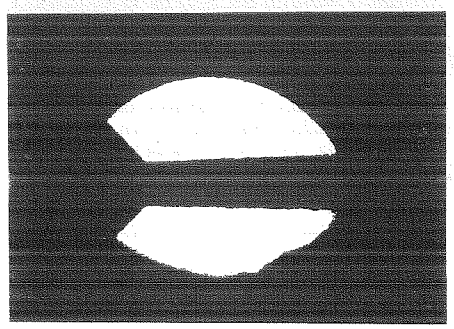


Fig.2: Photograph of the absorbing beam and the skimmer (laser beam expanded)

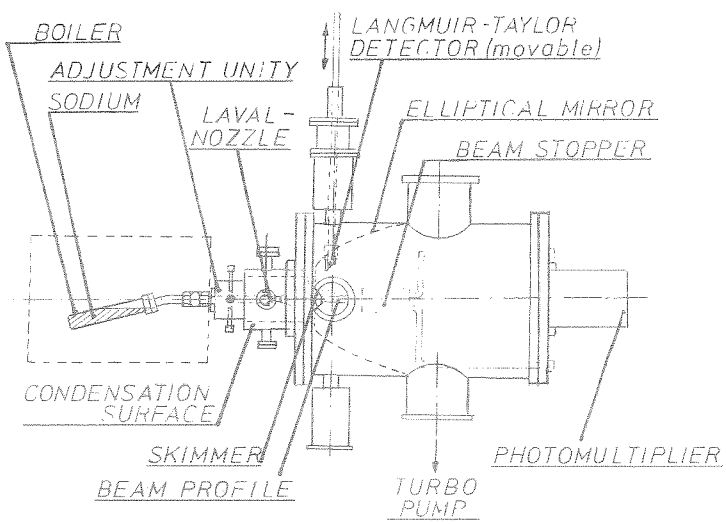


Fig.1: Set up of the supersonic jet

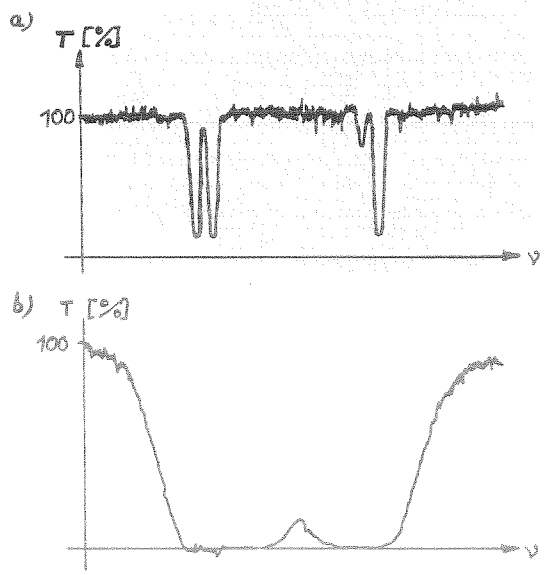


Fig.3a: Transmission at low beam densities (line width: 95 MHz)
Fig.3b: Transmission at maximum beam density (Lorentzian broadening)

The Scanning Ion Microscope - A Progress Report

B.E. Fischer, GSI Darmstadt
H. Bräuer, Techn. Büro, Frankfurt

The last year has brought a tremendous improvement in image quality and resolution. By improved scan control it became possible to suppress the macropulse structure of the accelerator that has spoiled the images of the microscope so far. Improved processing of the detector signals and a new high resolution display have led to sharper images with better grey scale representation, as fig. 1 shows.

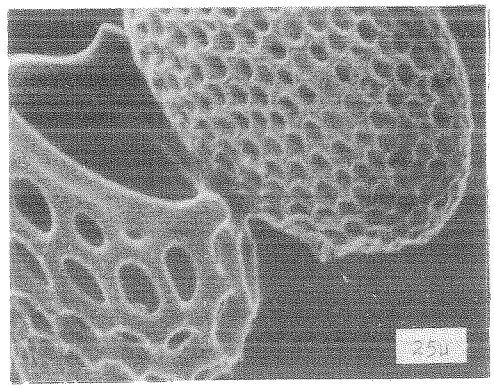


Fig. 1 Scanning ion micrograph of an uncoated radiolaria specimen. The image brightness is determined by the intensity of secondary electron emission after ion impact. (^{16}O ions .4 MeV/u.

Higher beam currents from the accelerator (egs. 500 nA ^{16}O on the object slits; still low compared to proton microprobes) allowed the use of 100 µm ∅ lens apertures, which, together with an improved focussing strategy, led to a resolution of 0.7 µm as demonstrated in fig. 2.

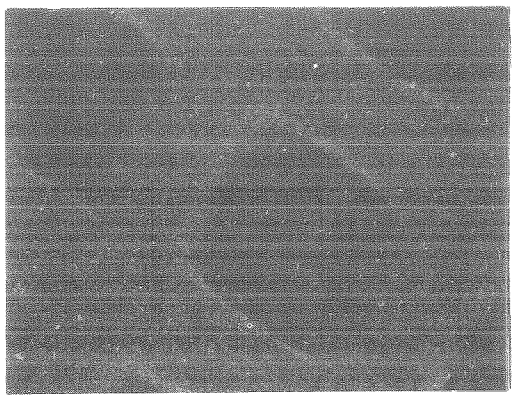


Fig. 2 Scanning ion micrograph of a grid with 25 µm period. Secondary electron imaging. Resolution 0.7 µm. (^{50}Ti ions 1.4 MeV/u).

Focusing strategy

As even under the most favourable conditions the current in the focus is not larger than 1 fA, it is difficult, (and in most cases, when the current is 100 times lower it is nearly impossible) to find the exact focus in a reasonable time. Therefore we developed a strategy that gives a statistically significant information about the optimum focus in the shortest possible time:

1. A coarse focus is found by producing a secondary electron image of a grid with a 200 µm period, while the object slits are wide open. The image of the grid is observed on a storage display, where it is easier to see, whether a particular setting of the lens currents leads to a sharper image, especially when it takes many seconds to accumulate enough points for a recognizable image.
2. Then the object slits are closed down to 20 x 20 µm² and a grid with a 25 µm period is imaged also by secondary electrons. To use the weak ion beam most effectively the scan is restricted to the smallest area that still shows a significant structure in the x- and y-direction.
3. Then only the largest secondary electron signals are selected for imaging. These signals are produced by ions which just touch the grid edges in passing and thereby release electrons over a longer part of their track. So the width of the imaged edges gives a direct indication of the beam spot size and the scatter of a few image points is sufficient to determine if the lens currents have been set for the sharpest possible focus (fig. 3).

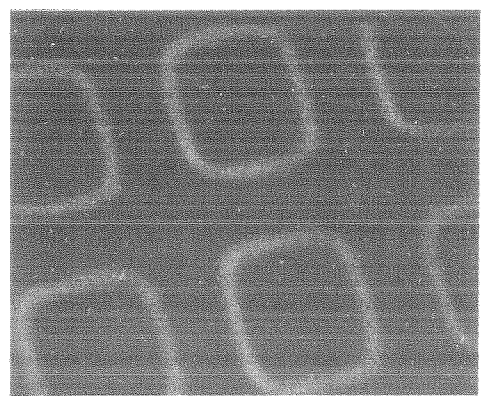


Fig. 3 Secondary electron image of a grid with a 25 µm period. By selecting only the largest secondary electron signals only the grid-edges become visible. Here the beam spot is about 2.5 x 2.5 µm. Note that no halo is visible at all (projectile ions ^{16}O 1.4 MeV/u).

Material contrast in secondary electron imaging

Like the Heidelerg proton-microprobe-group[1], we tried to find out if different chemical elements can be discriminated in secondary electron imaging and if heavy ions might eventually give better results. As examples fig. 4 shows the result for a multielement target embedded in epoxy resin, and fig. 5 part of an integrated circuit.

There appears to be no distinctive material contrast except for the very high-Z-materials. Much stronger is the edge contrast and the contrast between conducting and insulating parts of the target. (By the way, a careful look on the Heidelberg data might equally well

lead to the same conclusion). Interestingly insulating parts of a specimen appear dark in ion microscopy whereas they look bright in electron microscoy because a positively charged surface tends to keep its electrons. Though high Z projectile ions release much more secondary electrons than protons[2], so that one might expect a clearer signal for heavier ions, we were so far not able to find significant differences to the Heidelberg data concerning material contrast using Oxygen, Titanium and Xenon ions.



Fig. 4 Secondary electron imaging of a multielement target (from above: 24 µm Ta (Z=73), 45 µm Mo (Z=42), 40 µm Cu (Z=29), 50 µm Ti (Z=22) and 50 µm Al (Z=13)) embedded in epoxy-resin. Projectile ions ^{16}O, 1.4 MeV/u
a) Brightness of the image determined by the amplitude of the secondary electron signal.
b) Like a) but small amplitudes rejected.



Fig. 5 Secondary electron image of a part of an integrated circuit. (^{16}O ions, 1.4 MeV/u) There is a weak material contrast between the gold contact pad and the aluminium conductors. But the contrast between differently oriented parts of the gold wire, between aluminium and the insulating SiO_2 layer is dominating.

Ion Transmission Imaging

Because of the low beam current it is necessary to use imaging processes that make the most efficient use of every projectile ion. Certainly the most efficient process is ion transmission imaging, as every single ion is capable to probe the thickness of a specimen to an accuracy of better than 1 %, and it can be detected in a semiconductor detector with 100 % efficiency. The only problem is the almost immediate destruction of the detector, if the microbeam is allowed to hit the same position of the detector for a few seconds. As this leads only to a pointwise destruction of the detector, the problem has been solved by keeping the detector constantly in motion by a small detector-"wiggler". Fig. 6 shows some micrographs which have been taken by this technique.

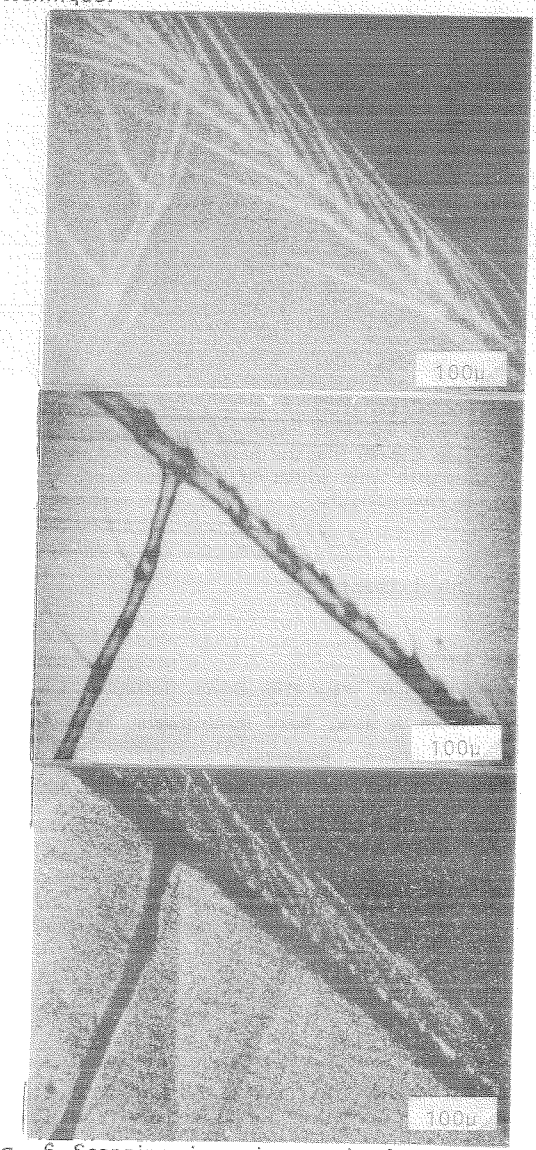


Fig. 6 Scanning ion micrograph of a part of a fly's wing. ^{16}O ions 1.4 MeV/u.
a) imaged by secondary electrons → mainly edge contrast.
b) imaged by transmitted ions. The brightness of the image is proportional to the energy of the transmitted ions → areal density contrast.
c) imaged by transmitted ions but with a window set on small energy losses: small thickness variations which are ivisible in a) and b) are enhanced.

Production of Microstructures

A definite advantage of heavy ions compared to protons is their usefulness for the production of microstructures in a wide variety of different materials[3]. To produce a desired microstructure, the microbeam is used to "write" a latent damage pattern into a solid under computer control. A subsequent etching step then develops the desired microstructure. Fully developed this technique might offer the possibilty to produce microstructures up to 200 µm deep with micrometer accuracy. As a first step in this direction we have "written" an artifical pattern in a resin called CR-39. The result is shown in fig. 7.

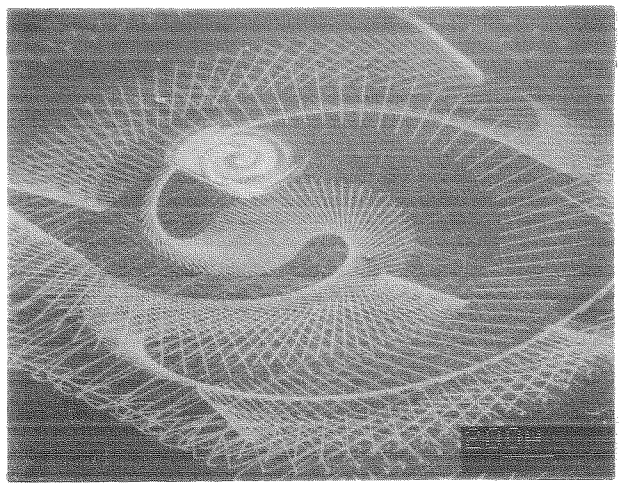


Fig. 7 Scanning electron micrograph of a micropattern "written" into CR-39 plastic material by 1.4 MeV/u ^{16}O ions. The depth and width of the microgrooves is 10 µm and 4 µm respectively.

Technical Developments

1. Beam switch
   A walnut size magnetic beam deflector has been built from a new, easy machinable, iron-powder-epoxy compound material[4], which offers high magnetic fields and low losses at moderate high frequencies. Mounted in the plane of the object slits, where it does not affect the position of the focal spot, it is used for beam switching ($t_{on,off}$ < 100 µs), fine tuning, and for compensating small fixed frequency beam wiggles.

2. Scan control unit
   The existing scan patterns (sawtooth, triangle; line-scan frame-scan; single or repetitive; various fixed speeds or speed controlled by ion current or any other external voltage; scan synchronization by AC line or any other signal to avoid image blurring by external stray fields) have been extended by the addition of a module which allows arbitrary scan frame shrinking and shift operations and to rotate scan lines to any desired orientation. The scan pattern of fig. 7 for example has been produced by this module and experiments to use it for microscopic computer tomography are under way.

3. Beam diagnostic
   As the beam scanner described in GSI annual report 1981, p. 238, could not be synchronized to the pulsed beam of the UNILAC, a new system using a rotating sense wire was devised. A DC-micromotor, the rotation frequency of which is locked to the UNILAC-macropulse-frequency, is moving the sense wire through the beam in two perpendicular directions. A special feature of the system is its extreme sensitivity range: It can detect single ions hitting the wire as well as the largest currents the UNILAC can deliver. The whole system (including the motor) easily fits into a 100 mm diameter beam tube and up to 4 units can be controlled by a standard single width NIM module.

References

1. Ch. Enders et al., Jahresbericht 1982, p. 55, 56 Max-Planck-Inst. f. Kernphysik, Heidelberg.
2. H.J. Frischkorn et al., Total Yield and Escape Depth of Electrons from Heavy Ion Solid Interactions;
   IEEE Transactions on Nuclear Science, Vol. NS-30, No. 2, April 1983, pp 931-933.
3. B.E. Fischer and R. Spohr
   Heavy Ion Microlithography - A New Tool to Generate and Investigate Submicroscopic Structures
   Nucl. Instr. and Meth. 168(1980)241-246
4. Corovac EF 9625, produced by Vakuumschmelze GmbH, D-6450 Hanau 1, Grüner Weg 37.

Further Developments on Gas-filled Heavy Ion Detectors

N. Shenhav and H. Stelzer, GSI Darmstadt

Three important conclusions, drawn from the accumulated experience with gas-filled heavy ion detectors, served as the major guide-lines for the new design of this type of detector. These conclusions are: 1) at least one metal foil electrode is necessary to generate a signal with good timing properties, 2) the detector windows should not be involved directly in signal generation, to avoid a position dependence of the detector characteristic, 3) the energy-loss signal should be taken from a region with a high gas amplification. This last conclusion is based on the observation of quenching effects in gaps with high gas amplification, which show up in a ratio of only 1:30 of the pulse-height of α's and fission fragments of a ^{252}Cf-source. In wide-gap structures (6 mm or wider) with a much lower gas gain this ratio is about 1:90, as expected from dE/dx tables. Quenching effects destroy the linear relation between pulse-height and energy-loss of the particle in the counter gas, but the efficient detection of particles with widely varying dE/dx in the detector and the subsequent electronics is now much easier. The dynamic range of the Z-values of the heavy ions which can be efficiently detected is now greatly increased.

A schematic view of the counter is shown in fig. 1. The central electrode T is a 1.5 μ Hostafan foil evaporated on both sides with silver and gives the time- and ΔE-information. Two orthogonal wire grids (20 μ diameter spacing 1 mm) are mounted on both sides of the foil electrode and determine the position in X and Y. The width of the gap is 3 mm. The read-out is performed by means of the delay-line technique in bins of 4 mm. Typical applied potentials at an operating gas pressure of 3.5 mb heptane are indicated in fig. 1. The detector shows a better timing performance when the primary electrons drift and multiply from the foil towards the grids and not vice versa. Both avalanches produced at the grids induce a positive signal on T.

Up to now the detector has been tested with a ^{252}Cf-source and showed good performance. Fig. 2 shows the timing spectrum of the light and heavy fragments. The light group shows 600 ps FWHM which means an intrinsic time-resolution of the counter of <200 ps FWHM, taking into account the intrinsic velocity distribution and energy-loss fluctuations of the fragments. The position resolution is in this case limited by the binning of 4 mm, the bins are clearly resolved. Fig. 3 shows a ΔE- spectrum of ^{252}Cf-fission fragments. The peak-to-valley ratio is slightly worse than measured in a wide-gap with a low gain (cf. preceeding contribution).

The efficiency of the timing signal for 6.2 MeV α-particles is nearly 100 %. For the position determination in the two coordinates this value goes down to about 50 % at a threshold high enough that the huge signals of the fission fragments still yield a good position information.

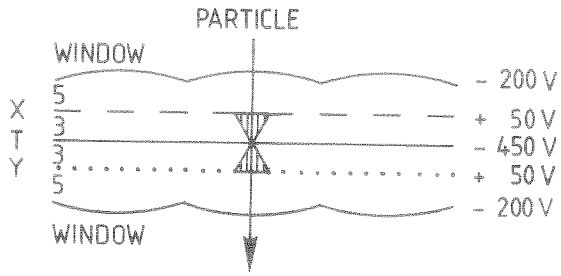


Fig. 1 Schematic view of the counter.

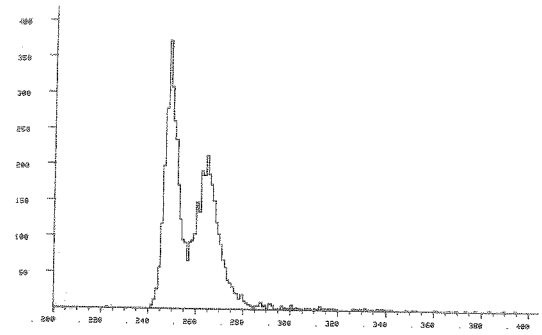


Fig. 2 Timing spectrum of ^{252}Cf fission fragments (1 ch = 100 ps).

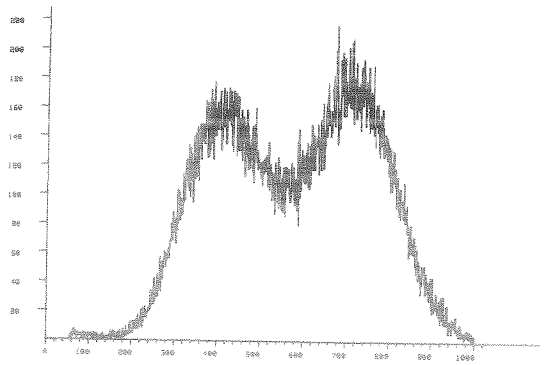


Fig. 3 Pulse-height distribution of fission-fragments.

Tests of an ionization chamber designed for Bragg-curve spectroscopy [B]

U. Helm, C. Schmitt, C.-C. Sahm, H.-G. Clerc
Institut für Kernphysik, Technische Hochschule Darmstadt

The Bragg-curve spectroscopy (BCS) proposed by Gruhn has been applied mainly to the identification of high-energy heavy ions with typical energies of 4 MeV/u[1-3]. It is the aim of the present investigation to exploit the method for the identification of low energy heavy ions near 1 MeV/u. So far, BCS was applied to low energy heavy ions only for the nuclear charge determination in the special case of mass- and velocity separated fission products[4].

A 1.4 MeV/u Au-beam in the stripper hall was scattered from a stainless steel wire target, and the recoiling ions were detected by an ionization chamber with its electric field parallel to the incoming particles. Signals proportional to the total energy E and to the maximum energy loss $(dE/dx)_{max}$ were derived. In addition, the rise time of the integrated anode pulse was determined, which is connected to the particle range. In Fig. 1b Au-ions in the energy range 60 to 80 MeV cannot be separated from the light recoil ions. However, the Bragg curves (see. Fig. 2) are quite different, which leads to different rise times, see Fig. 1 a. A window on the rise time can therefore be used to eliminate the Au-ions, see Fig. 1 c.

For energies above 100 MeV, a resolution of $Z/\Delta Z \approx 70$ was obtained for Z = 26. The resolution of the total energy was measured with a Ge-beam of 1.4 MeV/u to be 400 keV FWHM (not corrected for the energy width of the beam in the stripper hall).

In addition to the derivation of analogous signals, the Bragg curves were digitized by using a transient recorder[5], see Fig. 2. A detailed analysis of these Bragg curves is planned.

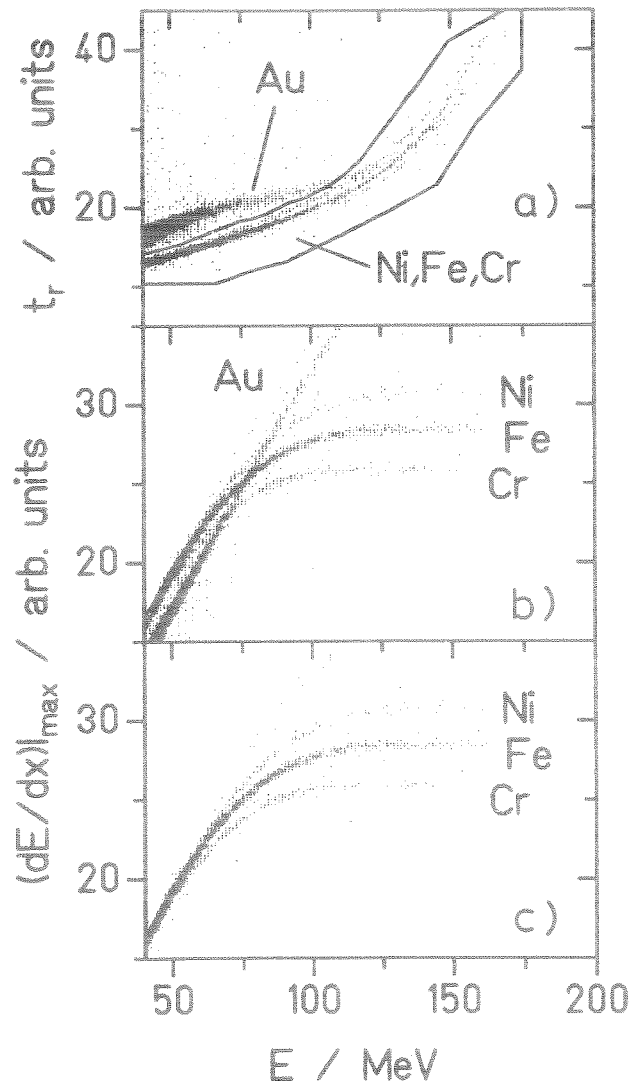


Fig. 1 : a) rise time of the integrated anode signal as a function of the energy
b) maximum specific energy loss as a function of the energy for Cr, Ni, Fe and Au
c) same as b), but with a window on the rise time as indicated in a)

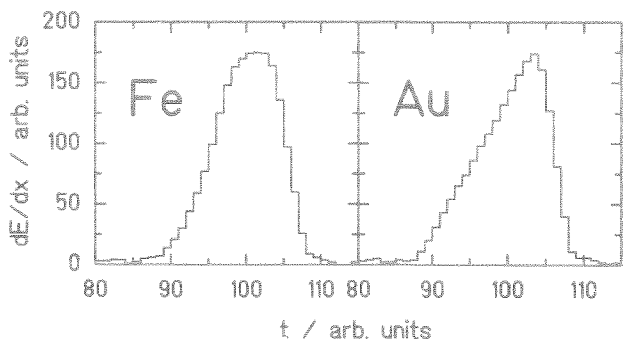


Fig. 2: Digitized Bragg curves for Fe and Au of 60 MeV

References

[1] C.R. Gruhn, INS Int. Conf. on Radiation detectors, Tokyo, Japan (1981), and C.R. Gruhn et al., Nucl. Instr. and Meth. 196 (1982) 33

[2] Ch. Schiessl et al., Nucl. Instr. and Meth. 192 (1982) 291

[3] J.M. Asselineau et al., Nucl. Instr. and Meth. 204 (1982) 109

[4] A. Oed et al., Nucl. Instr. and Meth. 205 (1983) 451

[5] R. Albrecht and H.P. Liebold, private communication

Luminescence Processes in Heavy-Ion Excited Scintillation Gases and Bragg-Curve Spectrometry with a Scintillation Drift Chamber

F.-J. Hambsch, P. Grimm, M. Mutterer, J. Pannicke and J.P. Theobald

Institut für Kernphysik, Technische Hochschule Darmstadt

Scintillation decay in Xe and He-Xe: Decay-time studies on rare-gas luminescence following excitation by charged particle impact[1] have been continued using heavy ions of 1.4 MeV/amu and applying single-photon techniques. In pure Xe, the decay structure measured at various pressures below 1 bar (see eg. Fig. 1a) can be well explained by the second VUV continuum emission, i.e. the decay of Σ_1^+ and Σ_3^+ molecular states (τ_1 = 3.6 ± 0.3 ns, τ_3 = 109 ± 7 ns) created by excited atomic states through three-body collisions. The collisional reaction constants k_1 and k_3 were determined to be (6.0 ± 0.4). 10^{-32}cm ^{6}s^{-1} and (3.6 ± 0.2)·10^{-32}cm ^{6}s^{-1}, respectively. In He doped with Xe, the scintillation time structure measured at various Xe concentrations and gas pressures (e.g. Fig. 1b) reveals an efficient energy transfer from the host gas to the dopant and a strong enhancement in the formation of the Xenon Σ_1^+ molecular state by three-body collisions with a He atom being the third collisional partner. Both pure Xe and He-Xe were found to be highly luminous and fast scintillators useful for detector applications.

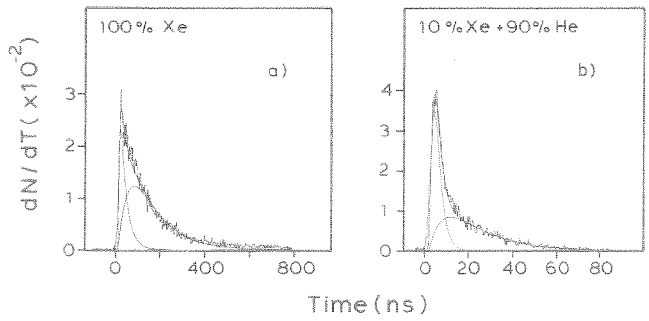


Fig. 1: Scintillation decay of (a) Xe at 760 torr, and (6) He + 10 % Xe at 200 torr, fitted to theoretical models.

Scintillation Bragg Chamber: The chamber (Fig.2) is constructed similar to an ionization chamber[2,3], but the Bragg curves, i.e. the ionization density distribution along an individual heavy-particle track, is not deduced from the electron current between Frisch grid and anode but from the signal of secondary scintillations which is induced by the electrons in the high-field region between Frisch and anode grid and measured by a photomultiplier. The high intensity of this light source enables to trace Bragg curves without influence of electronic noise; the prompt scintillation pulse emitted from the heavy-particle track serves as time-zero trigger.
We have studied Bragg curves of 1.4 MeV/amu ^{129}Xe and ^{205}Tl ions stopped in various binary gas mixtures of He-Xe (with 10 to 50 % Xe) and Ar-N_2 (1 to 10 % N_2) using the transient recorder TR 1000 developed at GSI. If the heavy components Xe and Ar dominate in the gas mixtures, the measured Bragg curves (Fig. 3 b) are observed to vary only at the end of the heavy-particle trace where nuclear collisions are frequent. If the energy loss comes dominantly from the low-Z gas components He and N_2, this effect is reduced but strong fluctuations are observed throughout the total length of the curves (Fig. 3 a).

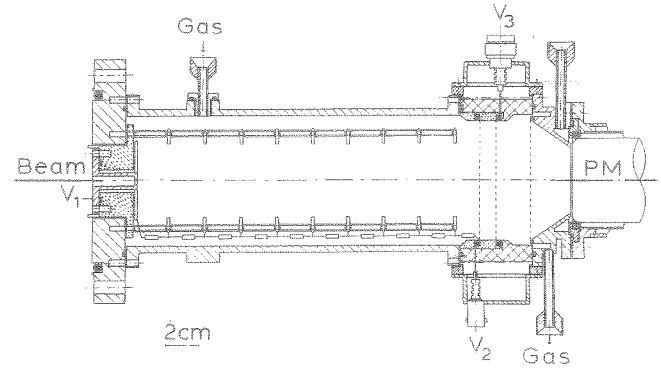


Fig. 2: Scintillation Bragg Chamber

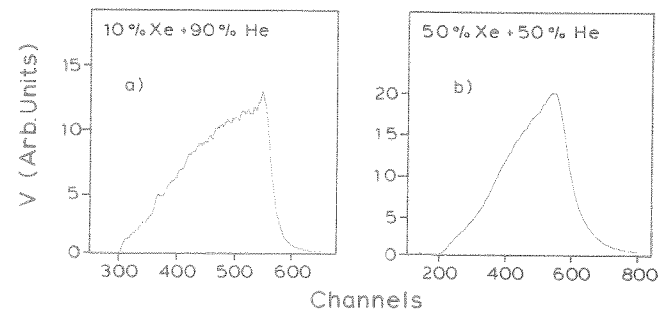


Fig. 3: Bragg curves for 1.4 MeV/amu ^{129}Xe ions stopped in (a) 90 % He + 10 % Xe (200 ns per channel) and in (b) 50 % He + 50 % Xe (50 ns per channel).

It is assumed that here single nuclear collisions with a momentum transfer out of the heavy particle direction modulate the ionization density distribution along the track. The observed fluctuations seem to limit the accuracy with which atomic numbers of fission fragments can be resolved by the method of Bragg spectroscopy.

References

[1] M. Mutterer et al., Lecture Notes in Physics 178 (1983) 63

[2] C.R. Gruhn et al., Nucl. Instr. Methods 196 (1982) 33

[3] U. Helm et al., this report

Light Particle Detection by BGO-Scintillators with Photodiode Readout

B,G

R. Glasow, K.H. Kampert, H. Löhner and G. Gaul
Institut für Kernphysik, Universität Münster

The applicability of a BGO crystal coupled to a photodiode for detection of light charged particles from medium energy nuclear reactions in the particle energy range of some ten to some hundred MeV, was investigated in an experiment using the 172 MeV α-particle beam from the Julic isochronous cyclotron.

Due to the high density ($\rho = 7.13$ g/cm^3) of BGO, the 1 x 1 x 1 cm^3 crystals are able to totally stop protons of about 70 MeV and α-particles of about 275 MeV*. The particle identification was achieved by the usual ΔE-E-technique with a 1000 μm Silicon surface barrier detector.

The ΔE-E_{rest}-scatterplot of such an arrangement demonstrates the particle resolution between p,d,t,^{3}He- and α-particles (fig. 2). A pecularity of this device is that the punch through particles which directly hit the depletion layer of the photodiode, give a very high E_{rest}-signal which therefore does not disturb the lower mass particle spectra but can potentially be used as an anticoincidence signal. To determine the energy resolution of the BGO-detector, the kinematical coincidence between protons and the recoil α-particles was used.

Fig. 3 shows the inclusive (upper part) and the coincident (lower part) proton spectrum, which were measured at $\Theta_{lab} = 45°$ with a Mylar target. The derived energy resolution of this elastic proton peak at $E_p = 52$ MeV is about 1.5 MeV (fwhm) and therefore comparable to the values observed with NaI(Tl) scintillators coupled to photomultipliers.

The great advantages of this detector which make it attractive as a replacement for classical scintillation counters, is the very compact construction due to the high stopping power of BGO and the small size of the photodiode, the insensitivity to magnetic fields and the absence of a voltage divider and a high voltage supply. Further investigations concerning the differential light output and the quenching factors of BGO are in progress.

*(In our experiment the BGO crystal (HARSHAW) was glued to a S1723-04 Silicon photodiode (HAMAMATSU).

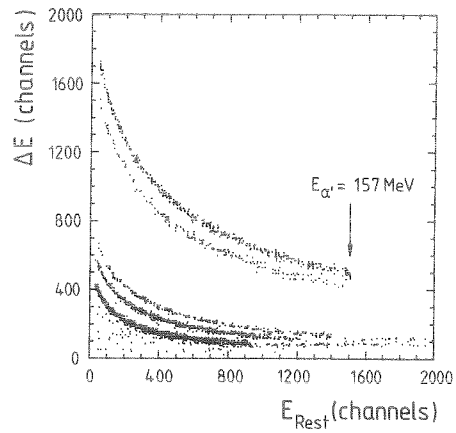


Fig. 2: ΔE-E_{rest}-scatterplot for the reaction α(172 MeV) + ^{58}Ni at $\Theta_{lab} = 35°$.

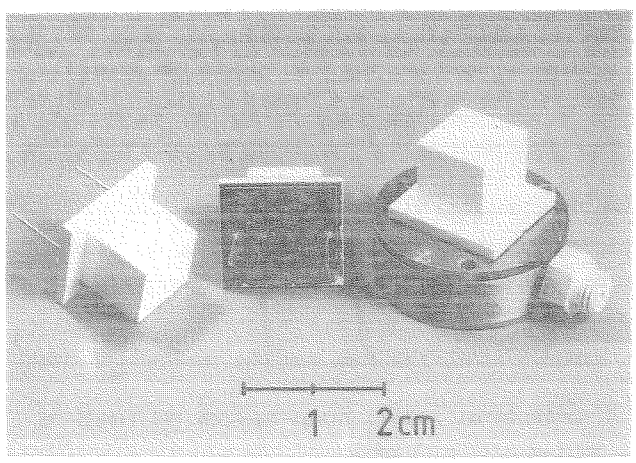


Fig. 1: BGO crystals (1 cm^3) mounted to a 1 cm^2 sensitive area photodiode and painted with TiO_2 as a light reflector.

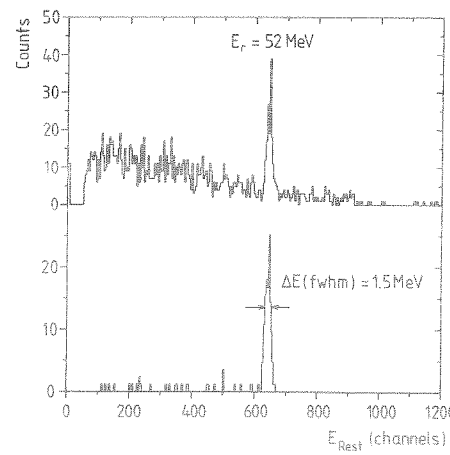


Fig. 3: Inclusive (upper part) and coincident (lower part) spectra of the reaction p(α,α)p for E_α = 172 MeV and $\Theta_{lab} = 45°$.

A low mass multistep Zero Degree Detector for studies of the Multifragmentation of relativistic nuclei

R. Albrecht, H.W. Daues, M. Doss, H.A. Gustafsson, H.H. Gutbrod, K.H. Kampert, B. Kolb, H. Löhner, B. Ludewigt, A.M. Poskanzer, H.G. Ritter, H. Stelzer, H. Wieman

GSI Darmstadt, LBL Berkeley, Universität Münster

The multifragmentation of heavy nuclei in high energy collisions has been established[1] by bombarding light projectiles on heavy targets like Au or U. Due to the extreme low velocities of the target fragments only parts of this fragmentation process could be studied. Recently a bounce-off process for projectile fragments could be measured with the Plastic Ball. With Au and U beams now available at the Bevalav one can study both the bounce-off process and the multifragmentation simultaneously in the projectile frame. At low energies of ~100 MeV/nucleon also deep inelastic processes have to be considered to be of interest.

To prepare for these studies a zero degree low-mass detector was designed and built and incorporated into the Plastic Ball system[2]. In Fig. 1 the configuration of the wire-planes is shown. Each plane consists of 20 µ thick wires spaced 1 mm apart. 3 wires are combined to one pad in the x,y, z plane and 6 wires are combined in thew-plane. Each pad is read out individually via an amplifier and a charge sensing ADC (LRS 2282A) (see Annual Report of R. Albrecht and K. Schultze).

The first part of the detector (part A) is an avalanche counter with premultiplication on one side, i.e. electrons produced between the planes labeled HV2 and HV3 are multiplied at HV2 and then at X for a second time (voltage HV1 = HV2). This detector measures TOF from the start detector (ca. 9 meter upstream) and the position of the fragments. The second part of the detector (part B) is operated in the proportional mode but also in a two-step-amplification in order to reduce spacecharge effects at the wire. Besides the position w, y, z this detector part B is expected to yield some resolution in dE/dx for very heavy systems. The dynamic range is expected to go from Au projectiles to Ne fragments. The operation pressure is approximately 3 Torr of Heptane.

In the first tests it could be shown that such a ultra low mass detector works indeed with relativistic beams of Ne and Au. The operation voltage was found to be quite different for the two beams. Since the beam is passing through the detector at a high rate (~5 x 10^4 s) interactions with wires cause large discharges which require modifications on the HV-system. Due to FM-noise large RF-shields had to be built. The first test results show that the detector has a position resolution of better than 3 mm and a time resolution between 500 ~1000 ps. The dE/dx resolution is probably due to unstable voltage condition - not better than 50 %.

The detector improved already the understanding of the bias imposed on Plastic Ball data in the central trigger mode.

[1] A.I. Warwick et al., Phys.Rev. C 27 (1983) 1083
[2] A. Baden et al., NIM 203 (1982) 189

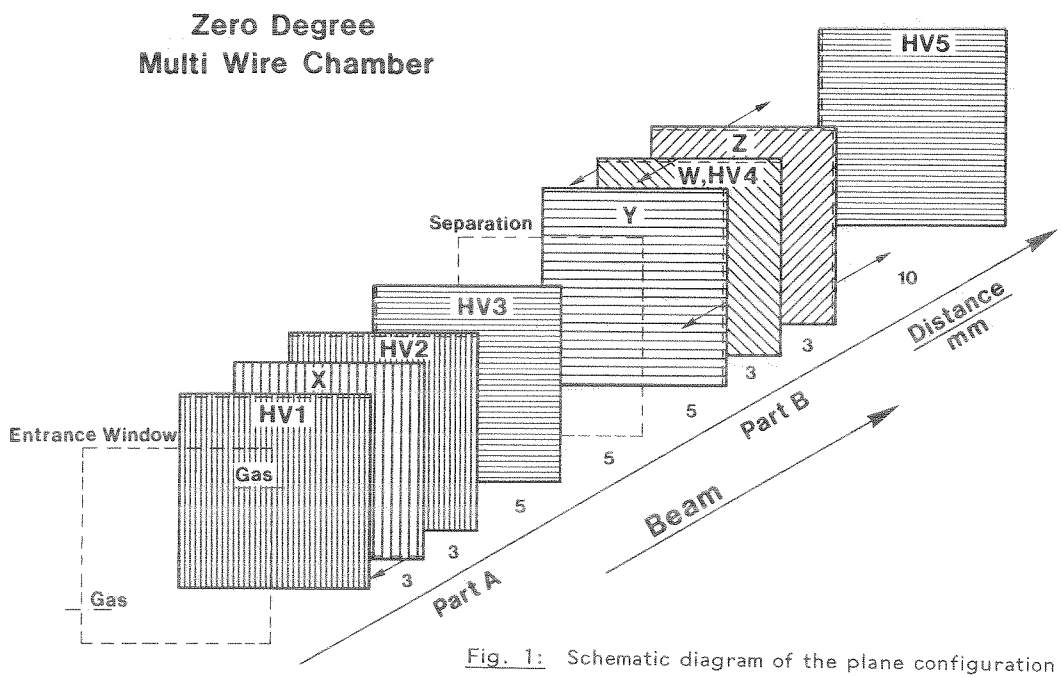


Fig. 1: Schematic diagram of the plane configuration of the Zero-degree detector.

Time-of-Flight Measurements with Plastic-Ball Modules [G]

H.A. Gustafsson, H.H. Gutbrod, B. Kolb, B. Ludewigt, A. M. Poskanzer,
H.G. Ritter, H. Wieman, GSI Darmstadt, LBL Berkeley, Universität Marburg
R. Glasow, K.H. Kampert, H. Löhner, Institut für Kernphysik, Universität Münster

The timing properties of some individual standard plastic-ball modules[1] have been investigated in an experiment using the 172 MeV α-particle beam from the Julic isochronous cyclotron.

In this experiment we measured kinematical coincidences between protons from a mylar target, detected by a single module at $\Theta_{lab} = 30°$, and the recoil α-particles, which were measured with a smaller plastic-scintillator (Ø 38 x 100 mm NE 102A coupled to a RCA 4517 photomultiplier) placed at $\Theta_{lab} = 14°$. In this arrangement with particle energies of 81 MeV protons and 90 MeV α-particles we obtained a time resolution of 500 ps (fwhm). Since from earlier tests with cosmic ray muons both of these detectors are known to have similar time response when used in a coincidence with a third thin reference plastic scintillator, the intrinsic time resolution of the plastic ball module can be estimated to be smaller than 350 ps.

Based on these results a further test was performed under realistic conditions during the last plastic ball experiment with 160 MeV/nucleon Au on Au. Since the "mall"modules in the angular range of 9° to 30° are positioned at a distance of 80 cm from the target, the time of flight (TOF) for 8 of these modules was additionally recorded on tape using the GSI-CF8001 octal CFD and the Le Croy 2229 TDC. A time resolution of 350 ps (fwhm) was obtained with the upstream beam counter[1] as time reference. The detailed analysis of the test results is still in progress but the usefullness of the additional time information may already be deduced from fig. 1, where the linearized time signal T_{line} is plotted versus the ΔE-ADC channel. T_{lin} was calculated from the plot TOF versus E_{total} and is proportional to A while ΔE is proportional to Z . From the good A and Z resolution in fig. 1 it can be estimated that a considerable improvement in particle identification can be achieved especially in the ΔE-E-region around the punch-through point for protons ($E_p = 240$ MeV).

The time resolution for particles stopped in the CaF_2 layer of the module has not yet been evaluated but would be of great interest in order to yield additional A-resolution for heavy fragments.

[1] A. Baden et al., Nuclear Instrum. and Methods, 203 (1982) 189

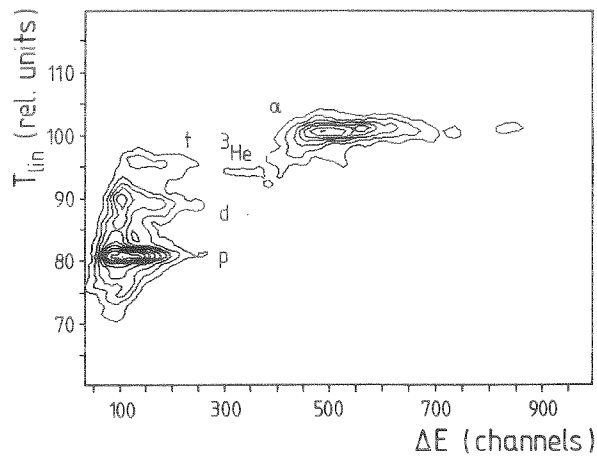


Fig. 1: Linearized Time-of-Flight versus ΔE for the reaction Au+Au (160 MeV/nucleon).

Investigation of the ^{238}U Ion Tracks Registered in ChaoYang No.1 Polycarbonate

Kang Tie-sheng , Zhai Peng-ji
Institute of High Energy Physics, Academia Sinica

ChaoYang No.1 polycarbonate is a SSNTD with excellent etching behaviour. The film were irradiated by ^{238}U (14.2Mev/Nucl.)ions accelerated by UNILAC of the GSI Darmstadt. The dip were 45° and 60° respectivly. The irradiated film were etched in 6.25N N_aOH at 40°C. The average track length L for various etching times have been measured using OLYMPUS optical microscope. Fig.1 shows a function curve of L vs t.

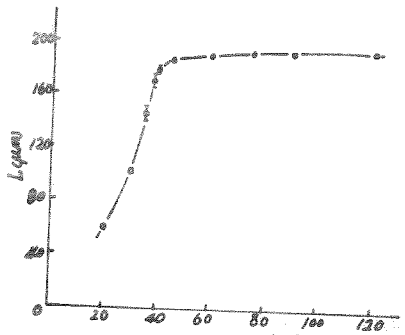


Fig.1: A function curve of L vs t

The range-energy relation and restricted energy loos rate REL of ^{238}U ions in ChaoYang No.1 polycarbonate has been calculated theoretically according to the formula dE/dX[1] and Benton's method[2] respectively(see fig.2). The bulk etching velocity V_B of the film used in this work was 0.24μm/hr. It can be seen from fig.1 that at the early stage L increased sharply with t suggesting $V_T >> V_B$, then L no longer increased showing the arrival of the etching solution at the end of the range of the particle. So the range of ^{238}U (14.2Mev/Nucl.) of (195.0±2.0μm) was detemined. This value is agree with the theoretical one (202.7 μm). The microphotograph of ^{238}U track was shown in fig.3.

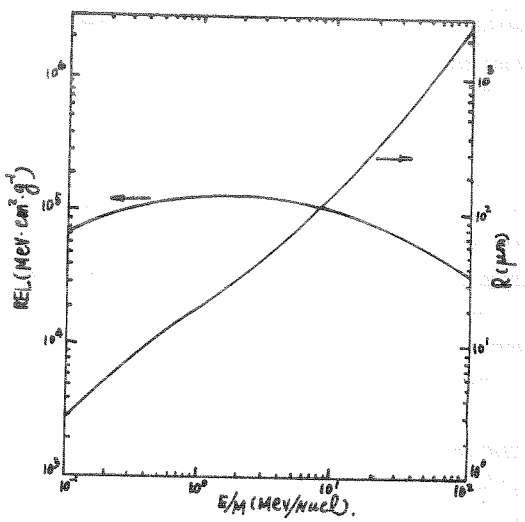


Fig.2: Relation of range and REL with energy of ^{238}U ion in ChaoYang No.1 polycarbonate

Range R can be expressed approximately by a equation $R=M/Z^2 f(\beta)$. So the charge resolution rate and the mass resolution estimated from precision of the range detemined by this work will be of 0.5% and 1% respectively. In fig.4, the $V_T \sim$REL curve obtained from fig.1 and 2 is shown. It can be known from fig.4 that the response range to $V_T \sim$ REL relation of this material is very wide. So it will be an useful detector for the investigation of heavy charged particles.

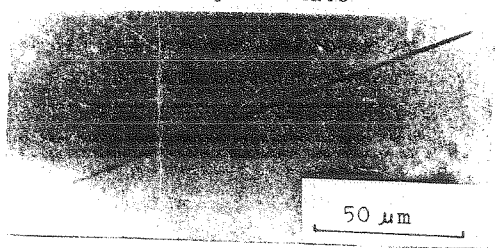


Fig.3: The microphotograph of ^{238}U track in ChaoYang No.1 polycarbonate

We wish to thank Dr.R.Spohr of the GSI,Darmstadt, for making theUNILAC irradiation possible.

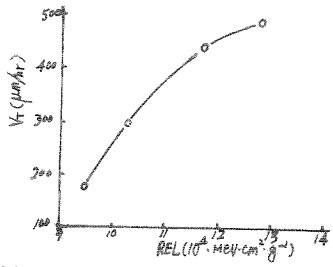


Fig.4: Relation of V_T and REL

[1] Kuninori Endo and Tadayoshi Doke, Japan, J. Appl. Phys. Vol. 12(1973)No.9.1403.

[2] E.V. Benton, USNRDL--TR--68--14.

ETCHING RATES ALONG HEAVY ION LATENT DAMAGE TRAILS

HAMEED AHMED KHAN & NAEEM AHMAD KHAN

Nuclear Engineering Division
Pakistan Institute of Nuclear Science and Technology (PINSTECH)
P.O. Nilore, Rawalpindi, PAKISTAN

It is important to determine the response of a track detector to different types of charged particles. Normally, variation of Track Etching Rate is studied as a function of the ionization rate, so as to obtain the Response Curve of the track detector under investigation (1-3). A comparison of the response curves of different types of SSNTDs enables us to select an appropriate detector suitable for a particular experiment. We employed charged particles such as ^{238}U, ^{208}Pb, ^{136}Xe, ^{84}Kr, ^{18}O, ^{16}O, ^{12}C, ^{4}He, protons, etc. for obtaining the response curves of different track detectors.

Strips of Muscovite mica, Hostaphan, CR-39, phosphate glass, vitreous quartz glass, and soda lime glass, dielectric track detectors were exposed to a variety of charged particles. The exposed detectors were etched along enough to enlarge whole of the latent damage trails However, differential etching (etching in steps) was also employed by interrupting the etching process at various stages before the etchant could reach the end of the latent damage trail. The differential etching step was taken with a view to measure the track etching velocity (V_t) at various points along the length of a damage trail.

The values of V_t/V_g were also obtained directly from the SEM-analysis. Cone angles were measured by using Scanning Electron Microscopy (SEM). Cone angle (σ), the critical angle of etching (θ_c), and the Etch Rate Ratio (V_t/V_g) are related as follows:

$$V_t/V_g = \text{Cosec}\ \theta_c = \text{Cosec}\ \sigma/2 \qquad \ldots\ldots(1)$$

Equation (1) can be used to determine 'V_t/V_g' from the cone angles determined by SEM-analysis.

Variation of V_t/V_g of Muscovite Mica, Hostaphan plastic, CR-39 plastic, phosphate glass , vitreous quartz glass, and soda lime glass, as a function of Z^2_{eff}/β^2 of charged particles is shown in Figure 1. The following features of the set of curves given in Figure 1 are noteworthy:

1. *Among the detectors investigated, soda lime and CR-39 have the minimum and the maximum sensitivities, respectively;*
2. *The values of Etch-Rate-Ratios (ERR=V_t/V_g) of phosphate glass are almost one order of magnitude higher than that of a soda lime glass;*
3. *For low Z^2_{eff}/β^2 values, Hostaphan has higher sensitivity than Muscovite mica. The curves for these two detectors cross-over for Z^2_{eff}/β^2 value of $\sim 10^5$ after which mica track detector shows higher sensitivity than Hostaphan;*
4. *The cross-over point of the curves for (a) Muscovite mica, and (b) phosphate glass is at Z^2_{eff}/β^2 value of $\sim 5\times10^4$;*
5. *$(ERR)_{mica} \sim 2(ERR)_{phosphate\ glass}$, for $Z^2_{eff}/\beta^2 > 10^5$.*

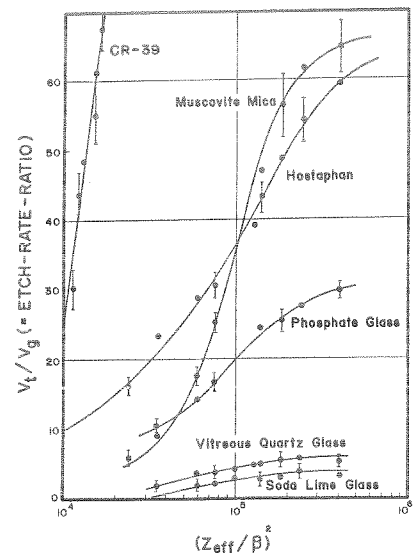


Figure 1

Variation of Etch-Rate-Ratio as a function of Z^2_{eff}/β^2 for some of the commonly used SSNTD

The authors would like to thank our colleagues at (a) CERN, (b) GSI, (C) MPI (Heidelberg), (d) Birmingham University (UK), and (C) PINSTECH, for their invaluable help during the exposure of the detectors, and for useful discussions. The research grant of International Atomic Energy (IAEA) under contract # RB/3455 is also gratefully acknowledged.

REFERENCES

1. *R.L. Fleischer, P.B.Price, and R.M. Walker: Nuclear Tracks in Solids: Principles and Applications, University of California Press, Berkeley (1975)*
2. *D.L. Henshaw, S. Amin, V.M. Clapham, P.H. Fowler, D.J. Webster, A. Thompson, and D.O.Sullivan:Preceedings of 11th ICSSNTD, Bristol, September, 7-12 (1981) PP.115-118.*
3. *H.A. Khan, R.Brandt, N.A. Khan, and K. Jamil: Nuclear Tracks (in press).*

STUDIES OF ETCHED CHANNELS IN HOSTAPHAN AND CR-39 PLASTIC TRACK DETECTORS

HAMEED AHMED KHAN & NAEEM AHMAD KHAN
Nuclear Engineering Division
Pakistan Institute of Nuclear Science & Technology
P.O. Nilore, Rawalpindi, PAKISTAN

REINHARD BRANDT
Kernchemie, F.B. 14, Philipps Universitat, 3550 - Marburg, WEST GERMANY

Recently, two new plastics namely Hostaphan and CR-39 were introduced as charged particle track detectors(1,2) The detectors have been found to possess some unique characteristics. They have extended the sensitivity limits far beyond the one experienced with the previously existing SSNTDs. In this paper we summarize results obtained from studies carried out to (a) improve the quality of the etched channels, and (b) maximize the track registration efficiencies (3 - 5).

Hostaphan and CR-39 plastic sheets having different thicknesses were exposed to a variety of charged particles. The etching of Hostaphan detectors was carried out at (40 ± 1)°C in five different solutions consisting of (a) 6N NaOH, (b) distilled water, and (c) Methanol in the following proportions:

Solution A : 50% 6N NaOH + 50% H_2O
Solution B : 45% 6N NaOH + 45% H_2O + 10% CH_3OH
Solution C : 33% 6N NaOH + 33% H_2O + 33% CH_3OH
Solution D : 25% 6N NaOH + 25% H_2O + 50% CH_3OH
Solution E : 5% 6N NaOH + 45% H_2O + 50% CH_3OH

The CR-39 detectors were etched in 6N NaOH and 6N KOH, kept at 70 ± 1°C. A comparison of the results obtained by etching Hostaphan in solutions A to D showed that the reponse of Solution C is the best. The exposed Hostaphan detectors were etched in Solution C, and SEM analysis of the etched channels was carried out. The values of cone angles and the critical angles of etching alongwith the detection efficiencies (calculated in 2 π -geometry exposures) have been summarized in Table 1. An increase in cone angle and θ_c with decreasing charge of the incoming ions is quite evident. The values of the critical angles of etching obtained from SEM studies of CR-39 detectors exposed to a variety of charged particles have been summarised in Table. 2

A systematic increase in the efficiency with decreasing energy of ^{12}C and ^{16}O ions was observed. One interesting feature of these results was found to be that ^{16}O- and ^{12}C- ions having energies as high as 1 GeV manage to produce etchable damage trails. The track registration and development efficiency (in 2 π -exposures) of CR-39 detectors for such intermediate energy ions is of the order of 55% for ^{16}O-and about 30% for ^{12}C-ions.

TABLE 1

CHARGED PARTICLE	CRITICAL ANGLE OF ETCHING (θ_c)	TRACK REGISTRATION EFFICIENCY (η)
2380 MeV ^{238}U	1° 15'	97.8 %
1768 MeV ^{208}Pb	1° 40'	97.1 %
1050 MeV ^{84}Kr	2° 10'	96.2 %
Fission Fragments	2° 45'	95.2 %
1548 MeV ^{18}O	65° 00'	9.4 %
1712 MeV ^{16}O	76° 15'	2.9 %
1032 MeV ^{12}C	82° 30'	0.9 %

TABLE 2

CHARGED PARTICLE	ENERGY (MeV)	CRITICAL ANGLE OF ETCHING
^{238}U-IONS [1]	2380.0	0.9°
^{208}Pb-IONS [1]	1768.0	1.2°
^{84}Kr-IONS [1]	1050.0	1.3°
FISSION FRAGMENTS [1]	Spontaneous Fission of ^{252}Cf	1.5°
^{16}O-IONS [2]	1070.0 586.0 106.0 73.0	27.9° 26.4° 12.5° 9.0°
^{12}C-IONS [2]	1032.0 386.0 102.0	53.5° 26.5° 19.5°

ETCHING CONDITIONS: 6N NaOH, (70±1)°C:[1] 1h;[2] 8h.

In order to construct a common curve for different types of charged particles, the parameter of Restricted Energy Loss (REL) was computed for both light and heavy charged particles. The variations of critical angle of etching and the track registration efficiency of CR-39 seem to be smoothly varying curves. The etching of CR-39 was also carried out by using 6N aqueous solution of KOH (kept at 70 ± 1°C).

The authors wish to thank various colleagues at the UNILAC (GSI) for their invaluable help in target exposures. Financial support by the International Atomic Energy Agency (IAEA) under Research contract # RB/3455 is gratefully acknowledged.

REFERENCES

1. *Hameed A. Khan and R. Spohr: GSI (Darmstadt) Internal Report (unpublished).*
2. *E.V. Bention and N.M. Ceglio: Proceedings of 10th International Conference on Solid State Nuclear Track Detectors, Lyon (1979), pp.747 - 754.*
3. *R.L. Fleischer, P.B. Price, and R.M. Walker: Nuclear Tracks in Solids: Principles and Applications, University of California Press, Berkeley (1975).*
4. *Hameed A. Khan: Nuclear Instruments & Methods 173 (1980) 43.*
5. *Hameed A. Khan and S.A. Durrani: Nuclear Instruments and Methods 98 (1972) 229.*

LIMITATION OF CONVENTIONAL GEOMETRY FACTOR FORMULAE WHEN USED FOR 'SOURCE - SOLID STATE TRACK DETECTOR' SYSTEMS

HAMEED A. KHAN AND NAEEM A. KHAN

Nuclear Engineering Division
Pakistan Institute of Nuclear Science and Technology (PINSTECH)
P.O. Nilore, Rawalpindi, PAKISTAN

The critical angles of etching (1-3) not only control the track registration and development efficiencies of SSNTDs, but also impose some severe restrictions on the conventional geometry factor formulae. Here, we give a brief account of the above mentioned geometrical limitations. Also, Critical Distances (D_c) have been calculated for (a) point sources, and (b) extended sources, in combination with circular solid state track detectors.*

The geometry Factor+ (G_p) of a circular disc for a point source is given as follows:

$$G_p = \Omega_p/4$$

According to Jaffey (4), the Geometry Factor in the case of a point source lying at a distance 'D' from, and on the axis of, a circular detector of radius 'R' is given by:

$$G_p = \tfrac{1}{2}\left[1-D/(R^2+D^2)^{\frac{1}{2}}\right] \quad \ldots\ldots\ldots\ldots\ldots\ldots(1)$$

However, the 'Maximum Geometry Factor' of a 'Point Source-SSNTD' system is given by:

$$(G_p)_{maximum} = \tfrac{1}{2}\left[1-D_c/(R^2+D_c)^{\frac{1}{2}}\right] \ldots\ldots\ldots\ldots(2)$$

where 'R' is the radius of a circular SSNTD, 'θ_c' is the critical angle of etching, and D_c (= R tan θ_c for a system consisting of a point source and a circular SSNTD) is the 'critical Distance'. Inserting the values of D_c in Equation 2, we get:

$$(G_p)_{maximum} = \tfrac{1}{2}\left[1-R\tan_c/(R^2+R^2\tan^2\theta_c)^{\frac{1}{2}}\right] \ldots\ldots(3)$$

$$(G_p)_{maximum} = \tfrac{1}{2}(1-\sin\theta_c) = \tfrac{1}{2}\eta \quad \ldots\ldots\ldots\ldots\ldots(4)$$

where 'η' is the track registration efficiency in 2π-geometry (2,3).

The geometrical restrictions become even more stringent when a track detector is employed in combination with an extended source. For such a an arrangement, the 'source-detector' distance would be safe only if no angle of incidence (from any point on the extended source and on any point on the track detector) is less than the critical angle of etching.

Let us consider a system consisting of an extended source (radius 'r') and a track detector (radius 'R') at a distance 'D' from each other. G_e, the conventional Geometry Factor for the circular detector is given by (4):

$$G_e = G_p - \frac{3}{16}r^2\left[R^2D/(R^2+D^2)^{5/2}\right] + \frac{5}{32}r^4\left[R^2D/(R^2+D^2)^{9/2}\right]x\left[D^2-\frac{3}{4}R^2\right] + \ldots\ldots\ldots\ldots(5)$$

and $D_c = (R+r)\tan\theta_c \ldots\ldots\ldots\ldots\ldots\ldots\ldots\ldots(6)$

inserting this value of 'D' in Equation (5), we get

$$G_e = G_p - \frac{3}{16}r^2\left\{\left[R^2\tan_c(R+r)\right]/\left[R^2+(R+r)^2\tan^2\theta_c\right]^{5/2}\right\} + \frac{5}{32}r^4\left\{\left[R^2\tan_c(R+r)\right]/\left[R^2+(R+r)^2\tan^2\theta_c\right]^{9/2}\right\} x\left\{(R+r)^2\tan^2\theta_c - \frac{3}{4}R^2\right\} + \ldots\ldots\ldots\ldots\ldots\ldots(7)$$

Thus, the conventional geometry factor fromulae have limitations when applied to source detector systems employing track detectors.

The critical angle of etching of the commonly available track detectors for ^{84}Kr *ions (obtained from GSI, Darmstadt) were determined by us and were used to obtain the critical distances for the systems employing track detectors along with point sources, respectively (Fig:1)*

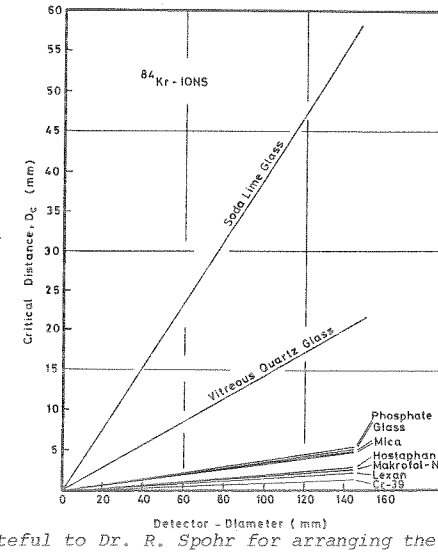


Figure :1 Variation of critical Distances as a Function of the detector size for different types of SSNTD

We are grateful to Dr. R. Spohr for arranging the heavy ion exposures at GSI and to Professor Dr. R.Brandt for many fruitful discussions.

REFERENCES.

1. *R.L. Fleischer, P.B. Price, and R.M.Walker: Nuclear Tracks in Solids (University of California Press, Berkeley, (1975).*
2. *Hameed Ahmed Khan and S.A. Durrani. Nuclear Instruments & Methods 98 (1972) 229*
3. *Hameed Ahmed Khan. Nuclear Instruments & Methods 173 (1980) 43.*
4. *A.H. Jaffey. Review of Scientific Instruments 25 (1954) 349.*

* *It is defined as the minimum distance between the charged particle source and the track detector at which the conventional geometry factor formulae are applicable.*

\+ *Defined as the ratio of the solid angle subtended at a point source by a circular disc (Ω_p) to the total solid angle (4π).*

A RESULT OF STOCHASTIC GEOMETRY FOR TRACK-ETCHING DOSIMETRY G

A. M. Kellerer and H. Roos · Institut für Med.Strahlenkunde der Universität Würzburg

Dosimetry for the biology experiments at the Unilac is performed by track etching. We evaluate the etched glass samples automatically on a simple image analyzer (Leitz-Classimat) coupled to a microcomputer and a step motor for automatic focussing. Seeking an analysis with rigorous edge and overlap corrections we have obtained a result of geometric probability that is applicable also to other systems, e.g. to the automatic counting of bacterial colonies or of cell clones in mammalian cell cultures. The result will here be exemplified in its relation to track-etching studies.

The etched pits cover a certain area within the field of reference (*rectangular area on the diagram*). The covered configuration is called C (*blank area in the diagram*). At low fluences the pits are separated. At higher fluences, for example in accidentally over-exposed or over-etched samples, a considerable degree of random overlap occurs. Available algorithms (1,2) provide corrections that are suitable under common conditions; but they require regular shapes of the random objects and are limited to moderate degrees of overlap. The new method utilizes only the fundamental geometric measures. It remains valid regardless of the shapes of the objects and their variations. Unlike earlier approaches, it accounts also for the edge effects.

There are three fundamental *measures* of a geometric object in the plane: *area*, *perimeter*, and *Euler-Poincaré characteristic*. The characteristic has the value 1 for a simply connected object, 0 for a connected object with one hole, and (n-m) for a figure that consists of n separate pieces with m enclosed holes.

The new result (3) links the three measures of the observed configuration C with the average measures of the individual figures, i.e. of the etched pits. Let A and B be area and perimeter of the field of reference, and let a and b be the mean area and perimeter of the etched pits. The characteristic is 1 for the field of reference and for the pits. The fluence, i.e. the average number of pits per unit area, is λ. It is also called *Poisson intensity*, and $\Psi=a\lambda$ is termed the *nominal coverage*. The quantities determined by the image analysis equipment are the area, α, the perimeter, β, and the characteristic, χ, of C. From these observed quantities one can estimate λ, a, and b:

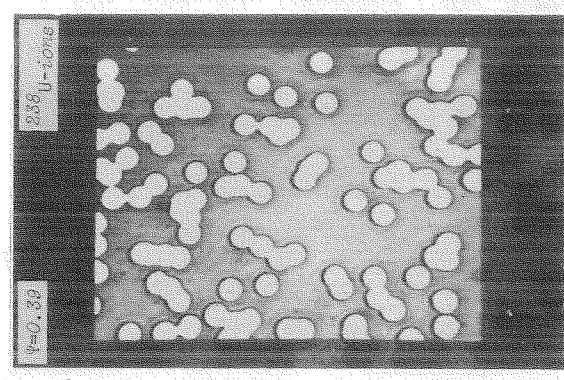
$$\lambda = \frac{\chi-1}{A-\alpha} + \frac{1}{A}\cdot\frac{\beta B}{2\pi A(A-\alpha)} + \frac{\beta^2}{4\pi(A-\alpha)^2}$$

$$a = -\ln(1-\alpha/A)/\lambda$$

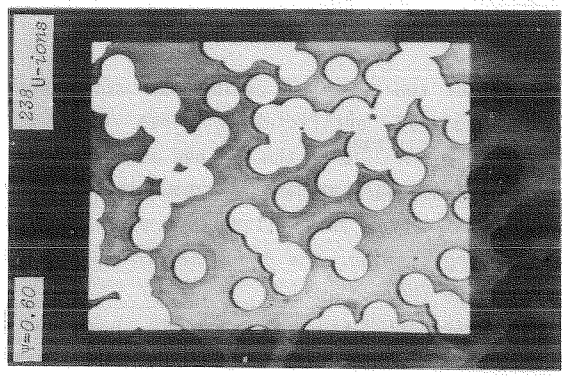
$$b = \beta/\lambda(A-\alpha)$$

For convenience β excludes any parts on the boundary of the field of reference. If the shape of the random objects is known, it suffices to determine χ and α (4).

Computer simulations with a variety of shapes (4) have demonstrated the applicability of the method even at high nominal coverage. The diagram gives, as example, segments of over-etched glass samples and the observed and estimated parameters.



Observed parameters: χ = 41 α = 0.32 β = 15.6
Machine estimates: λ = 87.4 a = 0.0045 b = 0.26
Visual count: λ = 96



Observed parameters: χ = 18 α = 0.45 β = 15.5
Machine estimates: λ = 77.2 a = 0.008 b = 0.35
Visual count: λ = 81

Fig.1 Segments (A=1, B=4.05) from over-etched glass samples with the observed quantities α, β, and χ and the estimates of the number of pits, λ, and their mean area, a, and mean perimeter, b.

References:

1 C.Riedel and R.Spohr, Statistical Properties of Etched Nuclear Tracks, Rad.Effects 42, 69-75 (1979)

2 B.S.Barashenkov, Über die Porendispersion bei Kernfiltern, GSI-tr-19/77 (1977)

3 A.M.Kellerer, On the Number of Clumps Resulting from the Overlap of Randomly Placed Figures in the Plane, J.Appl.Prob.20, 126-135 (1983)

4 A.M.Kellerer, Counting Figures in Planar Random Configurations, subm.for publication.

Are Long Tracks in Meteoric Olivines Possibly Due to SHE in Cosmic Rays?

R. Dersch, E.U. Khan, P. Vater, E. Friedlander*, V. Perelygin**, R. Brandt
Kernchemie, FB 14, Philipps-Universität, 3550 Marburg

Recently, very long tracks in meteoric olivines have been observed by Perelygin et al.[1]. A microphotograph of a typical "very long track" is shown in Fig. 1. It was obtained after annealing meteoric olivines for 32 hours at 430°C and subsequent etching. It is conceivable, however it has not been proved that these "very long tracks" could be due to SHE in Cosmic Rays. Altogether, six such "very long tracks" have been observed[1].

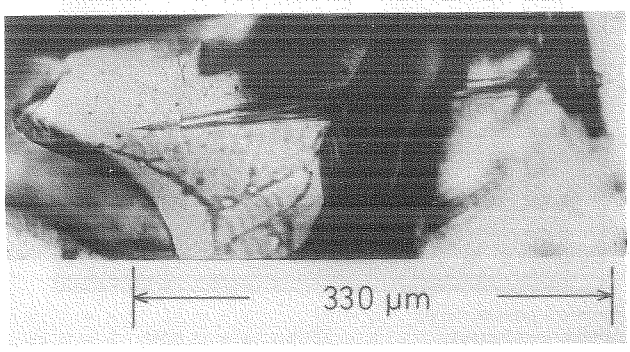


Fig. 1: A "very long track" in meteoric olivine obtained after annealing (430°C, 32 h). (From the group, responsible for Ref. 1.)

We carried out two types of calibration experiments:
1. We irradiated artificial olivines with 8.7, 14.0 and 16.7 MeV/N ^{238}U at the GSI and etched thereafter with the standard etchant. As shown in Fig. 2, we observe rather narrow and well-defined distributions. For this energy region, the track length is linearly proportional to the energy.
2. We irradiated artificial olivines with 1 GeV/N-^{238}U from the BEVALAC. As U-ions give etchable tracks only at rather low energies (≲150 MeV/N, the exact value has to be determined experimentally), we have to reduce the U-ion energy with an Al-block. In this way, we also simulate the conditions in outer space: the olivines to be etched on earth have been exposed to Cosmic Rays behind several cm "shielding". The olivines were etched for 260 h and the observed correlation between track-length and thickness of Al-block, which is also a measure of the U-energy, is shown in Fig. 3. Each "cross" represents a fully etched track, each "open circle" represents a track not fully etched. The energy of the U-ion increases with the X-axis, due to the tilt in the Al-block. The quantitative analysis of this picture is in progress. It is however clear that we do not observe sharp and well-defined track length distributions anymore. Until now, it was assumed that the maximum etchable track length of U-ions in olivines is approx. 800 µm whereas we observe tracks as long as 1422 µm.

It is therefore concluded to continue the calibration experiments of olivine crystals irradiated with U-ions at GSI and Berkeley. As a next step we want to study the behaviour of the irradiated olivines to the annealing (430°C for 32 h). Additionally, it is also to be studied whether the track lengths are influenced by their directions relative to various crystallographic axes of the olivines.

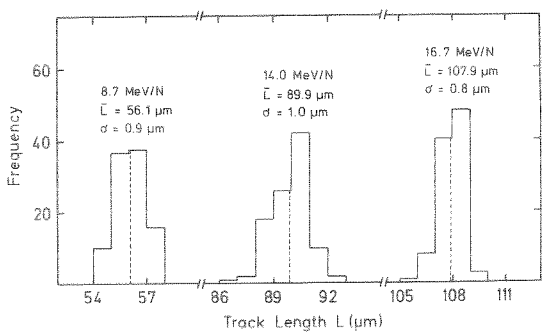


Fig. 2: Track length distributions of U-projectiles of 8.7, 14.0 and 16.7 MeV/N in artificial olivines.

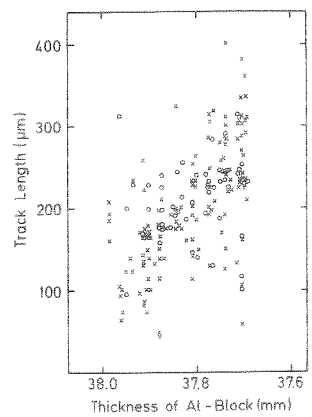


Fig. 3: Track length in artificial olivine vs. thickness of Al-block.

1. Perelygin et al. (Dubna-Marburg-GSI-Belgrad-Paris-Wien-Kurukschetra-Collaboration), Proc. Int. School on Heavy Ion Physics, Aluschta (USSR), in print.

*Visiting scientist from Lawrence Berkeley Laboratory, Berkeley, Calif.
**Visiting scientist from Joint Institute of Nuclear Research, Dubna.

Tracks of Heavy Ions in Evaporated Selenium-Films

B. Pischel, F. Granzer
Abteilung für Wissenschaftliche Photographie
Institut für Angewandte Physik
Universität Frankfurt am Main

Introduction

If materials which, like e.g. selenium, transform very easily from its amorphous into its crystalline phase, are exposed to heavy ions, then it should be possible to study:

a) the influence of the specific state of the target - amorphous or crystalline - on the formation and structure of the latent track
b) the possibility of the penetrating heavy ion to initiate or to stimulate the corresponding phase transformation along its track.

In a preliminary study of the interaction of high energetic heavy ions with selenium, thin selenium-films, exposed to a beam of ^{238}U-ions, have been examined with the transmission electron microscope (TEM).

Experimental

Selenium-films with thicknesses ranging between 300 and 400 Å were deposited onto a clean glass substrate (microscope slide) by evaporating high purity granulated selenium out of a molybdenium crucible at 230° C in a vacuum of 10^{-6} Torr. With the temperature of the glass substrate held at 20° C the structure of the deposited selenium-films were completely amorphous, in full agreement with previous work [1,2].

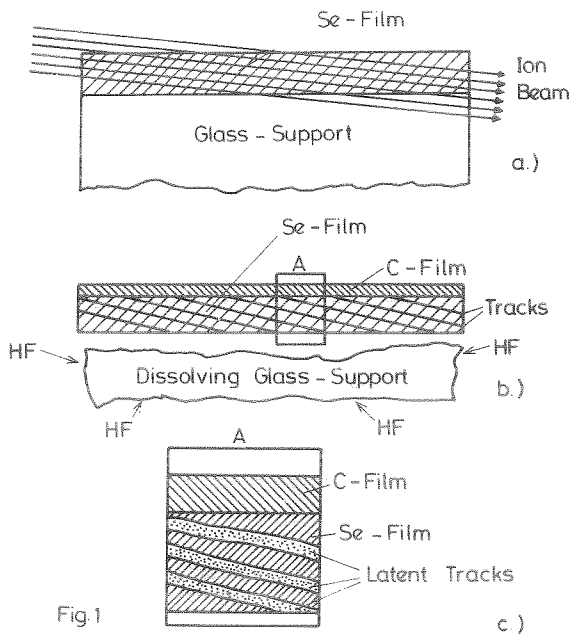
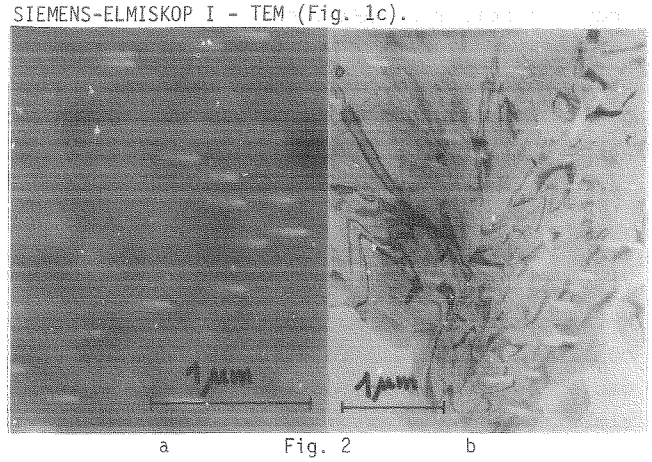


Fig. 1

These films - still on the backing glass substrate - have been exposed to a beam of ^{238}U-ions with 8 MeV per nucleon for a few minutes in the UNILAC (GSI-Darmstadt). The irradiation dose was about 10^{10} ions/cm^2, the maximum angle of incidence 4° (see Fig. 1a).
In order to stabilize the selenium-film for its subsequent preparation and its examination in the TEM, a thin carbon-film was evaporated onto the selenium-film. Then the C-Se-double-film was detached from the glass-substrate by bathing the glass-slide in diluted hydrofluoric acid (Fig. 1b) and some of the small film pieces were picked up on a grid for examination in the SIEMENS-ELMISKOP I - TEM (Fig. 1c).



a Fig. 2 b

Results

In the electron micrograph of Fig. 2a the comet-like tracks, with diameters of about 300 Å released by the ^{238}U-ions in the amorphous Se-film, are clearly visible. Without going into the details of the damaging mechanism the observed contrast profiles of the tracks suggest to assume that the penetrating ion has displaced some material from the core of the track into the adjacent region, thus creating an inner bright region of reduced density, surrounded by a dark region of enhanced density (see e.g. Fig. 5 of [3]). As shown in Fig. 2b, the bright core regions of the tracks remain stable (do not recover) if the Se-film transforms from its amorphous into its crystalline phase upon heating in the TEM.

[1] H. Richter, W. Kulcke, H. Specht, Z. Naturforschg. 7a, 511 (1952)

[2] H. Richter, F. Herre, Z. Naturforschg. 13a, 874 (1958)

[3] B.E. Fischer, R. Spohr, Rev. Mod. Phys. 55, 907 (1983)

Radiochromic detectors as a tool to monitor heavy ion particle fluence.

E. Schneider, G. Döll, M. Kost
Strahlenzentrum, Universität Giessen

G. Lenz
GSI Darmstadt

Various aminotriphenyl methane dye derivates with certain organic activators are sensitive to ionizing radiation and ultraviolet light. The change from colorless to a colored state occurs gradually as a direct function of the radiation exposure received . A detector film basing on this effect was developed to measure high doses and dose distributions in intense radiation fields (Far West Technology, Goleta, Ca., USA). The detector is a 50 µm thin Nylon film containing 10 - 15 % of a cyanide as colourless dye precursor. The change of optical density at the wavelength of maximal absorption (600 nm) is the measure for the received dose.

First experiments with this radiochromic dye film dose meter to analyse particle radiations were performed by J.W. Hansen et al[1] . They concluded from their results that the dye film can serve as a useful detector to test particle track theories.

In radiobiological experiments with particle radiation from accelerators the exact determination of the particle fluence at target position is very important. Usually glass or certain plastics are irradiated, etched and the tracks are microscopically counted. This method, however, is limited to relatively low particle fluences (3-4 x 10^6 particles/cm²). The radiochromic detectors are, because of their low sensitivity, very suitable for high particle fluences. Depending on the effective charge and on the velocity of the particles a wide range from about 10^7 to 10^{12} particles/cm² can be coverend. The homogeneity over the target area of several cm² also can be examined.

Fig. 1 shows as an example the dependency of the optical absorption at 600 nm from the particle fluence for 7.1 MeV/u uranium ions. Generally the extinction at 600 nm depends linearly on the particle fluence over a range of at least 2 decades. Fig. 2 demonstrates qualitatively how the sensitivity of the systems depends on the kind of ions used. In this graph the U-, Kr- and Ar-ions have approximately the same specific energy (5-7 MeV/u), the energy of the α-particles and the protons is 2.6 MeV and 2 MeV respectively. With uranium ions a number of particles almost by a factor of 1000 lower is sufficient to produce the same colouring as with protons. This indicates a dependency of the effect of the track structure as Hansen et al assumed. A correlation between the colouring effect and the specific energy of the ions, i.e. the range of recondary electrons, could not yet be significantly demonstrated. There are indications that it correlates similar to Z_{eff}^2/β^2 as the cellular inactivation cross section of yeast cells does.

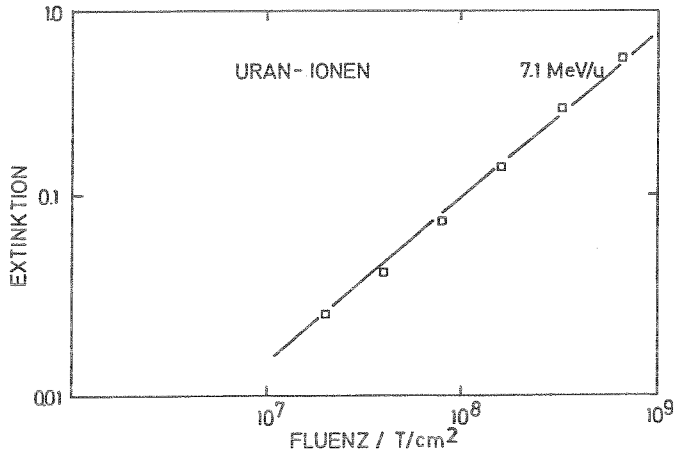


Fig. 1: Optical absorption at 600 nm versus particle fluence for 7.1 MeV/u U-ions

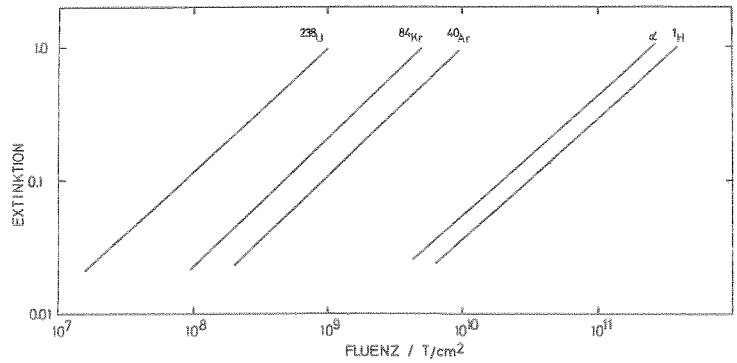


Fig. 2: Comparison of the Radiochromic effect for 5 ions

[1] Hansen J.W. et al, Proc.VIIth Symp.Microdos, Londen, 821(1981)

Experimental Electronics Department (Elektronik/Experimente)

R. Albrecht, J. Dengler, G. Eidmann, H.-G. Essel, A. Fehres, H. Hammal, H. Hardel, J. Hoffmann, H. P. Liebold, H.-G. Martens, W. Meufels, K. Mömerzheim, K. Poppensieker, A. Przybyla, D. Quis, M. Richter, H.-G. Schmidt, G. Schneider, R. Schulze, K. Senft, E. Sturm

GSI Darmstadt

The Experimental Electronics Department is involved in development and maintenance of electronic systems and equipment. They are used for data processing and control in experiments at the UNILAC as well as at outsite experiments of GSI groups (e. g. LBL, Berkeley or CERN). The activities of the department include analog and digital signal processing, the digital online computer systems (hardware and software), control systems, and the assistance of experimentalists.

Detectors and Signal Processing

In 1983, about 250 NIM modules and over 500 photomultiplier bases were built. These modules were added either to the GSI NIM-pool or had completed the equipment of large experiments. Nearly 2000 different coaxial cables with a total length of about 30 km were assembled. These cables are used for signal transmission as well as for delay purposes.

The following list of new modules were added to the GSI NIM-pool in 1983:

- The octal Constant Fraction Discriminator, CF8000. It has internal hybrid delays and gated baseline restorers. The outputs for energy (AC-coupled), time (ECL-line), common sum energy, multiplicity, and logical-OR as well as an inhibit input make the new module a more universal discriminator than the older quad module CF4000.

- The 8x8 Coincidence logic unit, CO8000. This module handles eight input and eight output channels and allows coincidences or anticoincidences between any combination of input signals. It is intended to be used as a central event coincidence box procuding different types of event signals like singles, 2-fold coincidences, 3-fold coincidences etc. out of the detector signals.

- The eight channel Trigger Box, TB8000. The module will be used together with the CO8000. It contains eight channels of rate reduction prescalers to allow selection of the event rate for different types of events. One may think e.g. of high reduction for singles, lower reduction for 2-fold coincidences, and no reduction for 3-fold coincidences.

- The octal Variable nanosecond Delay unit, DV8000. The DV8000 is intended to be a compact alternative to the usual 1/12 NIM switchable single cable delays used for Fast NIM signals. The module has eight independent channels for delays between 15 and 55 ns, adjustable continuously from the frontpanel. Time shifts by temperature are less than 4 ps/°C, which is less than that of cable delays.

- The octal Logic Delay unit, DL8000. It delays Fast NIM signals by up to 380 ns. This 1/12 NIM module replaces 600 m of RG58 cable. The use of the expensive hybrid delays pays off, since the cheaper delay cables need a signal refreshment by an additional module. The temperature stability of the delay is about 6 ps/°C, which is much better than that of cable delays.

- The ADC Multiplexer, AM8000. According to our inhouse specifications about the digital I/O of ADCs (differential lines), this module multiplexes up to eight ADCs to one standard ADC-like output. The range of the ADCs, the range of the memory to store the data, and the section in which an ADC will be stored are switch-selectable on the front panel. The input is buffered by an First-In-First-Out (FIFO) buffer with 64 16-bit words. The output can be connected to an ADC-CAMAC adapter AD1000, to the CAMAC memory increment unit MR1000, or directly to a CANBERRA multichannel analyzer input.

Since we extensively use ECL integrated circuits in our modules, it is obvious to use the ECL standards also for the interconnection between modules. In addition we want to cut the costs for the interconnections of NIM and CAMAC modules. Because of that, we introduced a new standard of interconnection, using the definitions of LeCroy ECL-line and adding an eight channel connector to the 16 channel LeCroy standard.
Using differential ECL-line drivers and transmitters, all signals are transmitted via simple twisted pair flat cables with multiple pin connectors on each side. So we abandon the expensive coaxial cables and connectors. In addition, the noise insensibility is better and ground loops are avoided, as they occur with single ended pulses. The input impedance of ECL circuits is intrinsically high, which allows to feed many circuits in different modules by the single driver. The last input will then be terminated.

The following modules have already ECL-line connectors:

- The octal constant fraction discriminator CF8000 has an octal ECL-line output on the rear panel.
- The trigger box TB8000 has octal outputs to be connected to ECL-line CAMAC scalers.
- An ECL-line version of the octal logic delay DL8010.
- The ECL-NIM-ECL converter EC1600 with 16-fold connectors and the EC1601 with two octal connectors for input and output.
- A 16 channel 3-input coincidence unit CO1600 using 16-fold ECL-line inputs is under test.

During the last years, about 30 different NIM modules have been developed for the GSI NIM-pool and larger experiments. To get free capacity for new developments, we gave licence for the production of modules to external producers. As one result, other institutes may buy these modules in an easy way.

Within the last years, the design and layout of printed circuit boards took an increasing amount of money and time. In 1983, GSI bought a computerized layout system to reduce these effects. This system (CADE) runs on our VAX-11/780. As expected we had severe problems during the initial phase, but finally we got a first printed circuit board at the end of 1983. This system will give us a better and changeable documentation for our developments than we have had before.

Online Computer and Control Systems

In 1983, again over 80% of all experiments at GSI used a computer for the online data acquisition of their experimental data. More than 90% of them used the standard GSI online data acquisition system GOLDA, which had been developed by the department and which is under its support.

In 1983, the main hardware activities were concentrated on the development of the new sorting and readout CAMAC module TADEX. It is a general purpose nuclear data acquisition system based on an auxiliary crate controller. For data acquisition, CAMAC dataway control is transferred to the TADEX module. It then transmits data directly from the CAMAC dataway through direct memory access (DMA) to the DEC VAX, PDP-11, or LSI-11 host computer. The DMA interface to the UNIBUS or Q-BUS TADMA-U and TADMA-Q was also developed. The TADEX modules were produced and tested, multi-layer versions for the DMA-modules will be produced and tested in 1984. These devices will become the 'second generation' standard readout system at GSI within 1984.

The development of a new CAMAC 8-fold ADC with 4096 channels was started in 1983 in cooperation with SILENA, Milan. These ADC modules will be available in 1984.

In the future FASTBUS and CAMAC will be the two data acquisition hardware standards for nuclear and particle physics. GSI has to get experiences in the FASTBUS hardware and therefore a FASTBUS crate together with some test modules were bought for test purposes.

The GOLDA software running on PDP-11 computers is used for accumulating experimental data, raw analysis, and monitoring. The system is part of the general EDAS system which also includes the IBM system SATAN. In 1983, the GOLDA subsystem was expanded to the following features:

- several new commands which are connected with the GOLDA-SATAN coupled mode,
- a new GOLDA test version MH supporting the new TADEX-TADMA hardware.

In the last years there was an increasing number of demands to the data acquisition system from the UNILAC experiments. There are also new demands connected with experiments at CERN and the planned upgrade of the GSI accelerator facilities to new synchrotrons. In addition it is almost impossible to expand the hardware and the software of the present online system GOLDA. Therefore the PDP-11 online-computers have to be replaced by VAX-11 computers. The design of a new data acquisition system GOOSY (GSI Online Offline SYstem) started in 1983 in collaboration with the GSI computer center. It will be a PL/I based system running on VAX-11 (VMS) as well as on IBM computers. The implementation of GOOSY on the VAX-11 computers will have the highest priority in 1984. For more details see also "GOOSY, A New Acquisition and Analysis System for Experiment Data".

In 1983, a VAX-11/750 computer system (6 MBytes memory, 3 RA81 Winchester disk drives with 400 MBytes each, a TU80 magtape, an Ethernet/DECnet connection to the existing VAX-11/780) was bought together with a MDB CAMAC branch driver. It will be used for dedicated experiments at the UNILAC and at CERN. Within the next years, all online computers at GSI will be replaced by VAX-11s.

A small PDP-11/23 system is used for controlling the magnetic and electrostatic elements of the velocity filter SHIP. In 1983, this system was improved in hardware and software.

A control system for the experimental setup of the applied heavy ion research group will also be based on a PDP-11/23 with a single CAMAC crate and RSX-11M operating system. In 1983, the experimental setup was improved including an INTEL 8085 controlled sample changer, beam stopper, and diagnostic elements. The computer control for all devices of this setup has already been designed and will be realized in 1984.

For small applications in experiment control (vacuum control, target position control etc.) a single board computer SBC-11 (DEC Falcon) was used instead of fixed hardware solutions. Working with the SBC-11, the change of the needs may be adapted easily without changing the hardware. The use of a PDP-11 family computer allows us to use any PDP-11 or VAX system at GSI for development and test of the software.

Development of an Hybrid Current Sensitive Preamplifier VT130 for the 0°-Multiwire Detector of the Plastic Ball

R. Albrecht and R. Schulze
GSI Darmstadt

Collective read out was not sufficient to get the multi-hit resolution necessary for the 0°-Detector[1], of the Plastic Ball. Groups of three wires have been connected to one separate preamplifier. To resolve multi-hit ambiguities in position and to measure time and energy, four planes of wires had to be read out. This results in a total amount of 662 preamplifier channels. Fig. 1 shows a part of the printed circuit board, which contains in total four channels of the preamplifier VT130. Surface mounted chips as well as conventional DIL integrated circuits were used. This made the preamplifier as small as 2x5 cm². The pure production costs are about 70 DM/channel including the output connector of 10 DM/channel. This four channel board is shielded by a tin plate and is inserted in a motherboard. The distance between preamplifier and the wires are less than 10 cm.

The risetime of the output of 3.5 ns and a differentiation time constant of 50 ns at the input allow high count rates occuring in a detector traversed by the beam.

The low input impedance of 33 Ω fits best to high input capacities. Fig. 2 shows the electron noise charge (ENC) as a function of the capacity parallel to the input for different preamplifier circuits and transistors taken from W.D. Farr[2]. The data for our inverting version VT130-I, an emitter-base circuit with shunt feedback of an emitter current of i_e =2.7 mA are added to Fig. 2. With an ENC of 1900 e^- running at c_p = 0 pf and a slope of only 82 e^-/pf it is even better suited for high capacity applications than the common-base preamplifier from the Univ. of Heidelberg, used in the JADE collaboration at DESY. The source or emitter followers using bipolar transistors (BFT24), J-Fet, and GaAs-Fet are superior for low input capacities. But it is possible to build a high input impedance version of the VT130 corresponding to the BFT24-line.

Inverting as well as non-inverting versions of the VT130 have been built. The older non-inverting version has an ENC of 3000 e^-. This value can be improved to the values of the inverting VT130-I by using two stages of inverting amplifiers instead of two non-inverting stages.

Output pulses of up to -3 V and 3.5 ns risetime are fed into a 50 Ω line. The amplification of these devices is variable within a wide range. A gain of 240, 480, and 920 have been used in this experiment.

References:

[1] R. Albrecht et. al., GSI Scientific Report 1983
[2] W.D. Farr, Nucl. Instr. and Meth. 206(1983)159

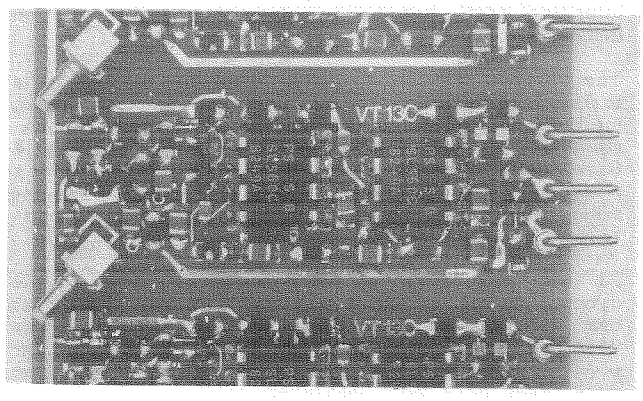


Fig. 1: Printed circuit board of the preamplifier VT130. The shielding is removed.

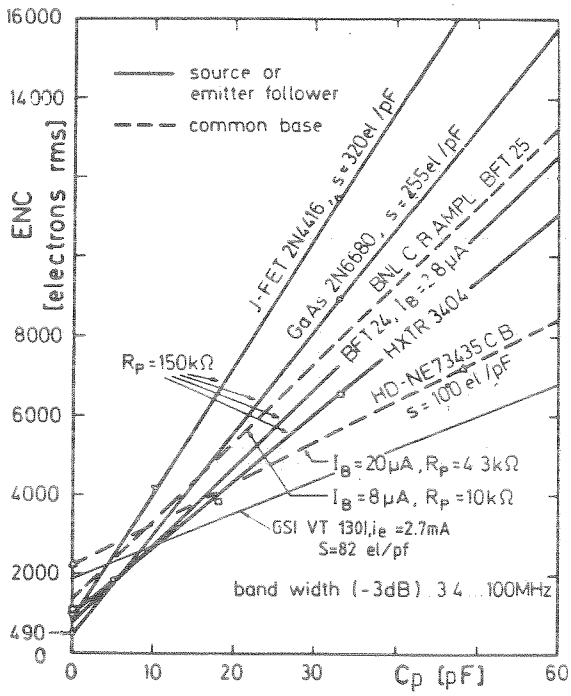


Fig. 2: Electron noise charge (ENC) as a function of the capacity parallel to the input.

Performance of the GSI Constant Fraction Discriminators CF4000 and CF8000

R. Albrecht, O. Althoff*, A. Höhler**, R. Schulze

GSI Darmstadt

*Universität Mainz, Participant of the GSI student program

**Universität Gießen, Participant of the GSI student program

Since 1980 constant fraction discriminators (CFD) have been built at GSI, following the design of M.M. Maier, Marburg/LBL-Berkeley. The number of channels built has been doubled every year resulting in more than 1000 channles in 1983. In 1982, the new 8-channel version with internal delay hybrids, gated baseline restores, inhibit input, and outputs for energy, time (ECL), common multiplicity, sum-energy, and logical OR was produced first for the GSI/LBL Plastic-Ball collaboration. This CF8000 has become available for experiments at the UNILAC in 1983 and has been added to the GSI NIM-pool. During the GSI student program, intensive tests had been made with constant fraction discriminators.

The purpose of a discriminator in nuclear electronics is to produce a standard output signal from an analog input signal to define the time of an event. The constant fraction discriminator gives an output signal at a fixed delay after a constant fraction of the pulse's rise-time. This guarantees good time informations for pulses of constant shapes within a wide range of amplitudes.

For the measurement of the delay as a function of the dynamic range of input signals, a pulser signal has been fed into the CFD via a variable attenuator. The CFD time output stopped a time-to-amplitude converter (TAC) that was started by a reference signal. The time differences have been measured using a multi-channel analyzer (MCA). The delay of the attenuator has been taken into account. The correction factors have been determined by measuring the phase differences at different attenuation factors at 200 MHz with a vector voltmeter. The systematic errors of this correction have been ±8.5 ps. Fig. 1 shows the delay as a function of the amplitude of the input signal (log-scale) for different constant fraction discriminators. The test pulses have had a rise-time of 5 ns and a decay-time of 15 ns. The walk adjustments for the CF4000, TC 454, and ORTEC 934 have been done by optimizing the performance curves. The resulting walk has been about 2 mV more positive than the well known 'equal brightness' recipe for CF4000 and TC 454. The bigger shift of the CF8000 is due to the symmetric walk adjust, done by the automatic baseline restorer instead of the better asymmetric adjust.

Fig. 2 shows the performance of the CFDs at a faster rise-time of the test pulses. The large time shift at high pulse amplitudes for CF4000, CF8000, and TC 454 are a property of the fast discriminator-IC SP9687, used in these modules. The ORTEC 934 using the older AM687 IC does not show that behavior. An improvement of the rise at large amplitudes might be possible, using the already announced new IC AM9687.

For longer decay time pulses the delay of the CFD is rather insensitive as soon as it is long enough (0.8 - 1.0 times the rise-time). The coarse setting of the delay possible in the CF8000 is thus sufficient. The threshold setting has no influence on the performance above the threshold.

The temperature stability of the CF4000 has been measured to be less than 3 ps/°C. Due to reduce the power consumption by the circuit design, the count rate capability is not higher than 15 MHz for the CF4000 and 40 MHz for the CF8000 depending on the dead time setting. There is no decline of the performance with increasing count rate.

For a 5 V input signal there is no triggering of other channels as long as the threshold is higher than 3-4 mV for both the CF4000 and the CF8000.

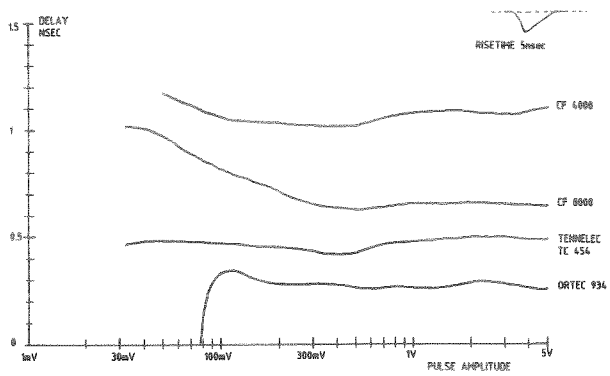


Fig. 1: Delay as a function of the amplitude of the input signal for differnet constant fraction discriminators. CF4000: fraction f=0.25, delay τ=5 ns (1 m), threshold u=10 mV; CF8000: f=0.4, τ=6 ns, u=10 mV; TC 454: f=0.2, τ=5 ns (1 m), u=30 mV, 1:2 internal attenuation; ORTEC 934: f=0.2, τ=5 ns (1 m), u=30 mV.

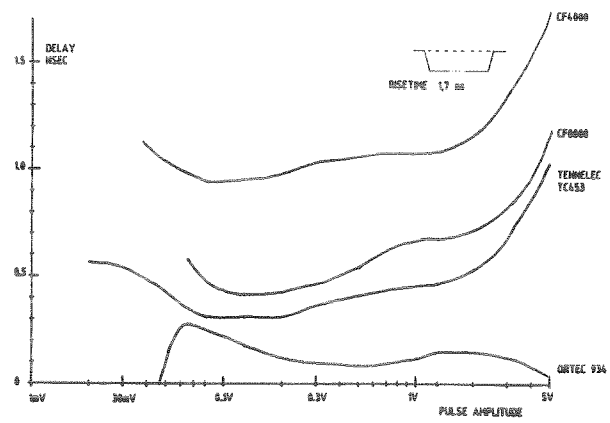


Fig. 2: Same as Fig. 1 besides rise-time of input signal is now 1.7 ns.

A PROGRAMMABLE PULSE DISTRIBUTOR FOR 32 DETECTORS

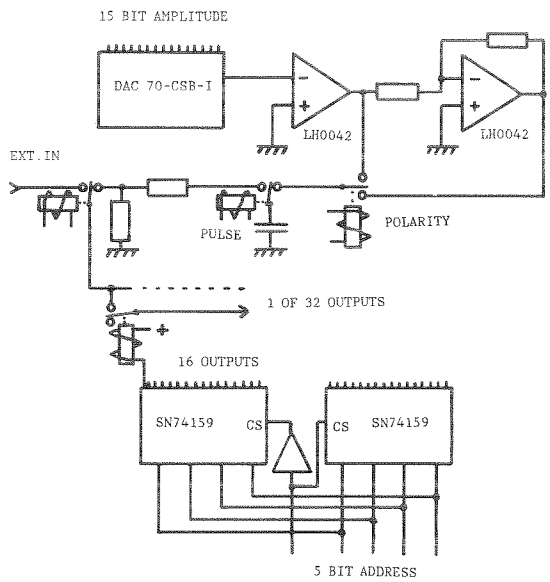
W.Brüchle, GSI Darmstadt

To check the stability of several surface-barrier detectors we formerly used a GSI- designed pulse distributor (FX086) which could direct calibration pulses from an Ortec pulser to 32 preamplifiers. A disadvantage was that all detectors were supplied with the same pulse amplitude and polarity.

With the increasing use of multidetector counting systems like "ROMA" [1] a new and more flexible design of a test pulse distributor suggested itself. This new pulse distributor contains a computer controlled precision pulser. Amplitude, polarity, and frequency can be defined by a low-cost homecomputer VC20. 32 outputs can be active in any order. For these purposes the 8 bit userport of the VC20 was extended to 24 bit with two 8 bit D-registers (74LS374). By use of drivers (SN49701) and optical coupling (ILD74) a trouble-free operation can be achieved at more than 100m distance between the control system and the pulser.

The reference voltage (max. ±10V) is produced by a 16 bit DAC (DAC70-CSB-I) and two operational amplifiers (LH0042). The maximum nonlinearity is ±0.003% of full scale range with ±14ppm/°C maximum gain drift. With this reference voltage (polarity switched by a computer controlled relais) a capacitor is charged. This capacitor is discharged when a special mercury relay is energized. The discharge path is determined by the setting of one out of 32 relays. Which output is active can be defined by computer via two decoders (SN74159). There is an option to use only external pulses and distribute them. In this case the computer can count the external pulses by an external trigger input.

The use of the machine is simplified by a Basic- controlled menu which is displayed on screen. After calibration with a standard source the computer calculates calibration coefficients (comparable with normalize- and attenuation- values in a normal pulser) , which also can be stored on tape. Now the desired energies can be typed in, instead of choosing relative amplitudes. In a continuous mode used for calibration control a high-energy pulse alternates with a low-energy pulse, every two seconds the next output is switched on. Maximum frequency is 20Hz.



Schematic drawing of the Pulse Distributor

1) K.Sümmerer et al., this report

Determination of Matrix Elements from Multiple Coulomb Excitation Experiments

H. Grein, H. Emling (GSI, Darmstadt)
J. Stachel (Univ. Mainz)[1]

From Multiple Coulomb excitation(MCE) experiments in principle, all electromagnetic matrix elements involved in the excitation and deexcitation process can be calculated. The MCE cross-sections are calculated with sufficient accuracy in the semiclassical approximation, while a fully quantum mechanical treatment of the γ-decay exists. However, there is a complex correlation between the many parameters, i.e. matrix elements, and therefore, a special fitting procedure is needed to avoid time consuming computations.

Our approach was to describe the correlation between the parameters by a so called sensitivity matrix, using a linear expansion of the calculated γ-yields y_i with respect to the parameters $\{M_j\}=\{M_1,\ldots,M_m\}$:

$$y_i(\{M_j+\Delta M_j\}) = y_i(\{M_j\}) + \sum_j C_i(M_j)\cdot\Delta M_j .$$

The elements of the sensitivity matrix are determined as:

$$C_i(M_j) = \frac{y_i(M_1,\ldots M_j+\Delta M_j,\ldots,M_m) - y_i(\{M_j\})}{\Delta M_j}$$

Starting from an arbitrary set of parameters $\{M_j\}$, an improved set of parameters $\{M_j+\Delta M_j\}$ is obtained by an appropriate minimization of the differences between experimental and calculated yields. In principle, a standard χ^2 procedure could be used; this minimization will, however, raise problems if some parameters have a very small sensitivity on all calculated values. In this case, small inaccuracies of experimental and/or calculated values due to systematic errors will result in large unphysical changes of the parameters with a low sensitivity to the values. Therefore we introduced non-statistical weights:

$$S_i(P_j) = \sqrt{|C_i(M_j)|}^{\,n} \Big/ \sum_{j=1}^{m} \sqrt{|C_i(M_j)|}^{\,n}$$

and minimize the expression

$$F^2 = \sum_i \frac{\sum_j [y_i^{exp} - y_i(\{M_j\})]\cdot S_i(M_j)\cdot C_i(M_j)\cdot\Delta M_j]^2}{\sigma_i^2} ,$$

where σ_i denotes the statistical errors. The influence of the different weighting orders governed by the exponent n, on the convergence of the minimization is discussed in detail in ref. 1.

The total fitting procedure consists of an iteration of alternating F^2 minimizations and Coulex calculations; at several steps during the minimization it may be neccesary to recalculate the sensitivity matrix.

To run this procedure in a transparent way, we built a program package(see Fig. 1):

- In the program WALKYRE the semiclassical Coulomb excitation calculations are carried out and in TRISTAN we determine the γ-yields from the nuclear decay[2],
- GOLIAT normalizes the experimental and calculated values, generates the sensitivity matrix and prepares the data for the fit
- ALADIN performs the χ^2 minimization using the approach descibed above utilizig the minimisation package MINUIT[3].
- at several points of the fitting procedure, the results may be viewed using the graphic package HPLOT[4].

The program package as described here, was used in the analysis of MCE data of strongly deformed as well as transitional nuclei, where up to 50 parameters had to be handled.

In particular, using this procedure it was possible to deduce static quadrupole moments of high spin states (up to spin 8^+) for the first time; illustrative examples may be found in ref. 1 and 5.

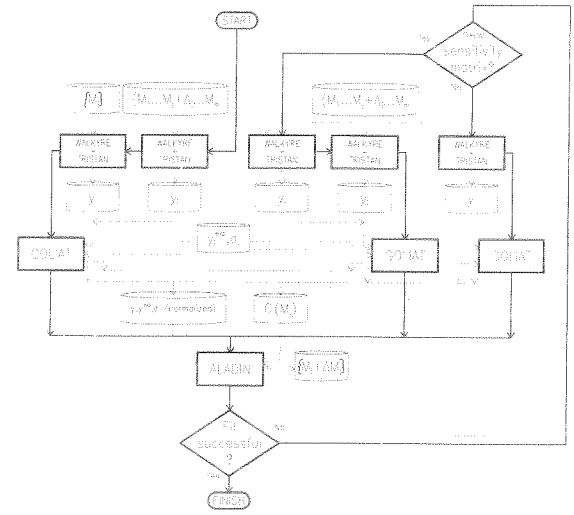


Fig. 1: Flow diagram of the fitting procedure.

[1] present address: SUNY, Stony Brook, New York, USA

1) J. Stachel et al., GSI Preprint 83 - 20
2) H. Ower, Ph. D. thesis, 1980
3) F. James, M. Roos, CPC, 10(1975) 343-367
4) R. Brun, H. Watkins, CERN DD/US/17
5) A. Mauthofer et al., this report

MONA, A Data Acquisition System for VAX Computers

Burkhard W. Kolb
GSI Darmstadt

The PDP11/44 on-line computer limited the data rate that could be accumulated in the Plastic Ball experiment. The bus activity in the PDP11/44 and the very limited amount of buffer space introduced a large dead time in the system. The higher multiplicities expected from heavier target-projectile systems, possible with the upgraded Bevalac, and additional experimental equipment aggravated this problem. A VAX 11/750 promised to overcome those difficulties as it provides large physical memory, can accommodate four bus systems and is in addition compatible with the existing VAX 11/780. The interface to CAMAC the MBD (micro programmed branch driver) resides on the UNIBUS, while the tape drives and the system disk are connected to MASSBUS adaptors. One disk drive is shared between the VAX11/750, the VAX11/780 and the streamer chamber PDP11/44 and is used for on-line analysis[1] of the running experiment.

After a survey of existing software a new driver for the MBD was written, designed specially for the transfer of large amounts of data with minimal overhead. The existing micro-code for the MBD was modified only in the parts which take care of the communication with the UNIBUS. The experiment specific code remained essentially unchanged, except for some improvements related to the larger buffer sizes.

The new data acquisition program in the VAX was written and tested with a simulated input before the VAX11/750 was delivered. It consists basically out of one process handling the buffers and several command processes which communicate with event flags and data in a global section. There are six buffers of 32kwords each which are used in a circular manner. MONA queues two buffers to the MBD-driver which in fact starts the MBD program with the first of the two buffers. The MBD waits for LAMs from CAMAC and then reads out the event into the buffer. As soon as the buffer is almost filled the MBD interrupts the VAX, the VAX sends a new buffer to the MBD, then the just returned buffer is scanned and checked for consistency. The buffer is then marked for logging to tape and disk. The actual transfer to tape and or shared disk is started only when the scanning of the buffer revealed a spill-off-event, in order not to slow down CAMAC transfers during the spill. In this case or when there is no more free buffer all waiting buffers are queued to the logging devices. When the output is finished the buffers are marked as free. Every time a change in the status of a buffer is detected MONA checks if there are still two buffers queued to the MBD. If there are less than two and there are still free buffers another buffer is queued to the MBD. This ensures that the time required for a buffer change is minimized because the driver immediately starts a new transfer when the previous one has finished. In addition the buffer change takes place when there is no event pending in the MBD because the MBD code checks after each event if there is enough space left for the next event. This is possible now because the maximum event size of about 4kwords is small compared to the buffer size of 32kwords.

The scanning of each buffer event by event does not slow down the data acquisition because the MBD is already transferring data to the next buffer. Collisions of memory fetches by the VAX and transfers by the MBD are avoided because the bandwidth of the CMI (the internal bus in the VAX 11/750) is much higher than the bandwidth of the UNIBUS. The overhead for QIOs, interrupt handling and buffer housekeeping is reduced through the use of large buffers. Speed measurements during the first beam time in November showed the new system to be at least a factor of three faster than the old one. The achieved data rate was 200000 bytes per spill of 1 second. There was no visible dead time due to buffer changes. Further improvements have now to focus on the MBD and the CAMAC system.

The new system proved to be very reliable, there was not a single restart necessary during the whole beam time period of two weeks. The very limited amount of simple commands made the system easy to use.

[1] B. Kolb, GSI Scientific Report 1982, GSI 83-1, (1983) 247

GOOSY, A New Acquisition and Analysis System for Experiment Data

F. Busch, H.-G. Essel, H. Göringer, H. Grein, V. Hartmann, J. Hoffmann,
J. Lowsky, D. Marinescu, W. F. J. Müller, M. Richter, G. Schneider, K. Winkelmann

GSI Darmstadt

The growing requirements of experiments performed at the UNILAC, as well as the high energy experiments at Berkeley, CERN, and GANIL, and the proposed experiments at the planned GSI synchrotron accelerator ask for much more functions in computerized data acquisition than presently available at GSI. A new data acquisition and analysis system is required for the following reasons:

- The new experiments will produce data with more complexity and structure.
- The present GOLDA system using the PDP-11 hardware is no longer expandable neither in functionality nor in memory and throughput.
- In the SATAN system now running on IBM computers, required new features are difficult to implement using the present structures.

The design of the new data acquisition and processing system GOOSY (GSI Online Offline SYstem) has been started in the middle of 1983. The concepts are based on the experiences with the present systems and the needs of future experiments. GOOSY will run on computers of the DEC VAX-family under the operating system VMS, and on IBM mainframes under MVS-XA. A VAX data acquisition station will provide 4-32 MBytes of memory and 1-5 GBytes of mass storage. The programming language will be PL/I on both types of computers. Whereas the data acquisition will run on VAX computers only, the final analysis of experimental data can be performed on VAX or IBM computers. All systems used for data acquisition or data analysis will be connected by high speed data transmission lines.

The main features of the new system GOOSY will be:

- High Flexibility

  The system kernel will be split into independent programs. A system may be tailored individually for different applications. Programs specific for experiments are simply added to the system programs during session time.

- Data Security

  Data taking and storing on mass storage media is independent of the user's programs and other system programs. Any error in these programs will not effect the data acquisition in the online mode. Furthermore all data generated by the analysis programs are saved even in case of an abnormal termination.

- Multiple Analysis

  It will be possible to control several analysis programs working on the same raw data flow from one or several terminals. This will allow the experimentalists to implement a graded system for parallel monitoring, analyzing, controlling, and setting up. All programs may be modified separately while the experiment is running.

- Data Management

  A data management will be implemented to provide access to data common to several programs. On the VAX side, it uses the Global Section feature of VMS. On the IBM computers, the Cross Memory Service (CMS) of MVS may be used.
  All elements of this data management (spectra, conditions, global parameters, pictures, parameters of the experimental set-up, etc.) are located in data bases. They can be referenced in programs or commands by their names. Because the data bases are self describing they can be exchanged easily among different computer types.

- Enhanced Analysis Tools

  A new condition concept will provide various methods to control the program flow of the analysis. Several types of conditions like single window tests, fast multiple window tests, pattern matches, and boolean expressions of conditions are supported. Statistics on the execution frequency for different branches of analysis programs are available.
  In addition to the analysis programs, spectra and conditions can be created and deleted interactively at run-time of the analysis. Dynamic conditions may be used as filters for the accumulation of dynamic spectra as well as for scatter plots on graphic terminals. Any scalar data element known to the data management can be specified interactively as a parameter for the accumulation, the condition tests or the scatter plots.

- Frontend Processing

  CAMAC will be interfaced to the VAX computers by a microprogrammable CAMAC branch driver (MBD) and by the new GSI data acquisition hardware TADEX-TADMA. Within the next years a FASTBUS system will be available, too. The control and calibration of the experimental set-ups and electronics is supported by special system features. The new system will be expanded to use µ-processors in CAMAC or FASTBUS for distributed data processing.

COMPUTING CENTER

(H.Egger, S.Glückert, H.Hultzsch, J.Lowsky, O.Siart)
GSI Darmstadt

Installation Activities

Besides a series of additions and modifications of peripheral equipment, three major exchanges of central processing units were necessary during May, August and December 1983, in order to allow for the required computing capacity within budget limits. The result of these activities again is a nearly fully symmetric computer array with two general purpose processors, two attached processors for high speed numeric processing, three teleprocessing computers, two communication computers for high speed data capture, and other peripherals shown in the general overview configuration plan of figure 1. The major installation activities throughout the year are indicated in the following list:

- replacement of the Teleprocessing Controller Memorex 1270 by a second Teleprocessing Computer Memorex 1380
- installation of an IBM 3705 Teleprocessing Computer
- upgrade of one 3274-D01 Local Terminal Controller to a capacity of 32 lines
- upgrade of IBM 3081-D16 (no.1) from 16 to 24 channels
- replacement of IBM 3033-U12/12 by 3081-D24/24 (no.2)
- installation of a third laser printer IBM 6670
- upgrade of IBM 3081-D16/24 (no.1) to 3081-K16/24
- removal of the FPS AP190-L Array Processor
- installation of a fourth IBM 3274 Local Terminal Controller with 32 lines
- upgrade of the Attached Processor FPS-164-#1 from 256 to 512 kwords including two magnetic disk drives
- replacement of IBM 3081-K16/24 (no.1) by IBM 3081-D24/24 (no.3)
- installation of the Attached Processor FPS-164-#2
- installation of three additional colour raster display units (IBM 3279 and Memorex 2079)
- replacement of IBM 3081-D24/24 (no.2) by 3081-D32/24 (no.4) with increased storage capacity
- delivery of thin film technology magnetic disk drives IBM 3380/3880 allowing for additional 10.2 Gigabyte direct access storage capacity

The detailed description of the machinery, including data paths and addresses, with status of end December 1983 is given in figure 2 on the following page.

The overall aims of these installation activities were both increased availability of computing services, achieved by higher hardware and software reliability using up-to-date technology, as well as by the higher throughput by increases of data paths, processing power, main and direct access storage capacity, and end user devices. As a result, end user service interruptions for experiment data analysis, nuclear model simulation, and other activities have been reduced significantly. Following these goals, within a few years, a replacement of equipment together with enhanced software techniques will allow for nearly uninterrupted computing services throughout the year.

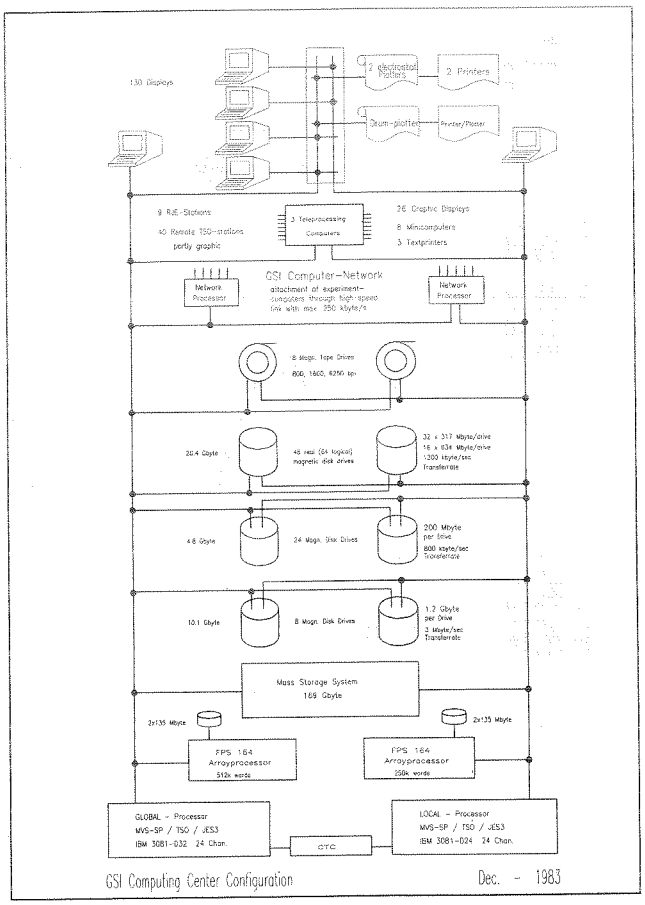


Figure 1: General overview configuration plan.

Operations and Services

The two general purpose computers were operated under MVS/SP 1.3.2 (Multiple Virtual Storage/System Product) with TSO/ISPF (Time Sharing Option/Interactive Systems Programming Facility) and the Job Entry System JES3 for input/output spooling and access coordination activities, allowing for minimum manpower requirements both for operations and system support as well as achieving the desired uniform users' access characteristics independent of its current DP-activities.

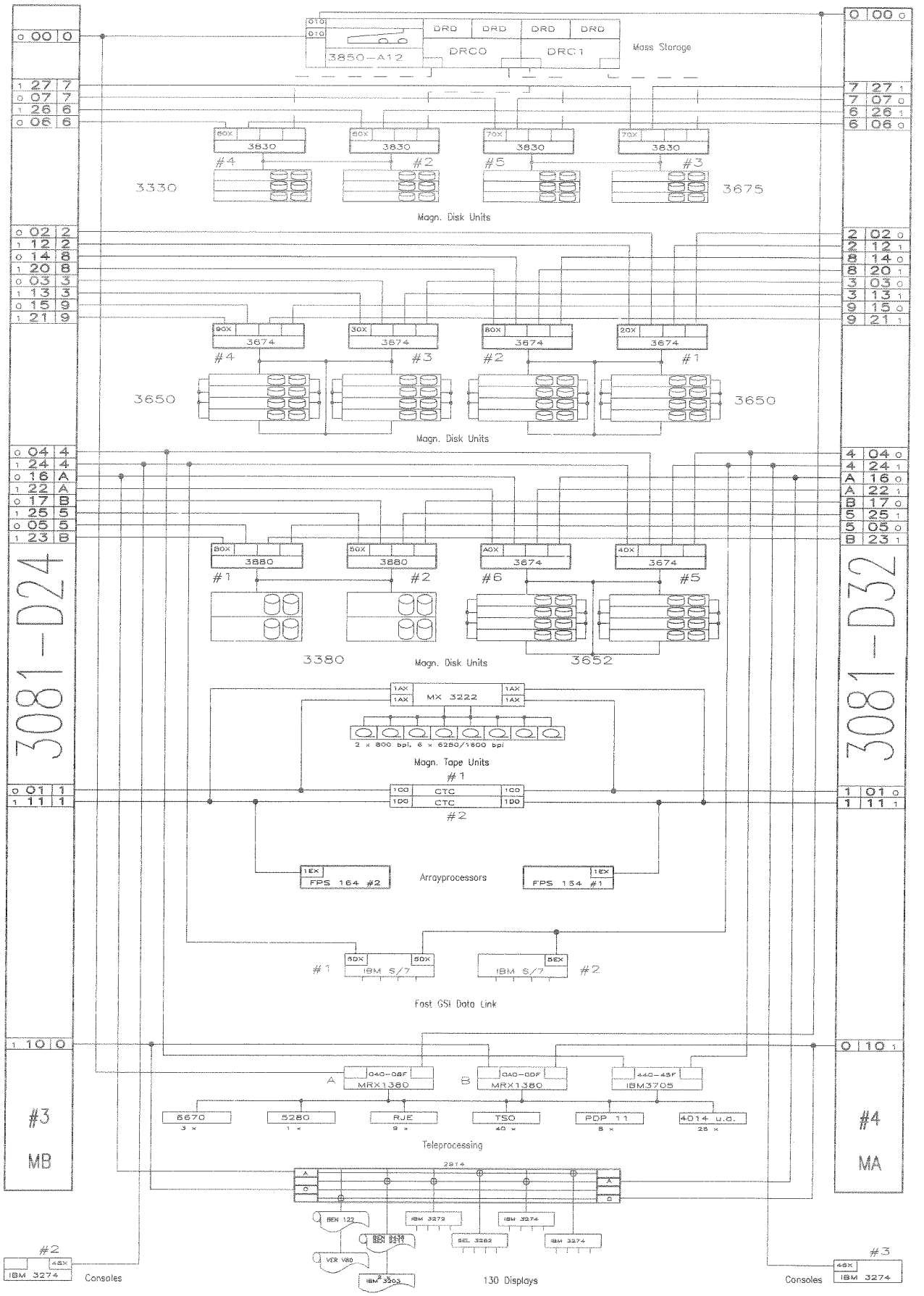


Figure 2: Detailed configuration description with data paths and addressing scheme.

Computer services are normally scheduled 24 hours a day with an interruption of interactive services of about one hour on working days for early morning's dataset savings, needed for back up in case of device failure. But services for experiments and batch processing are not interrupted regularly. Maintenance activities are usually performed without interruption of user services, except occasional check-out or switching of electric power supply or air- and water conditioning.

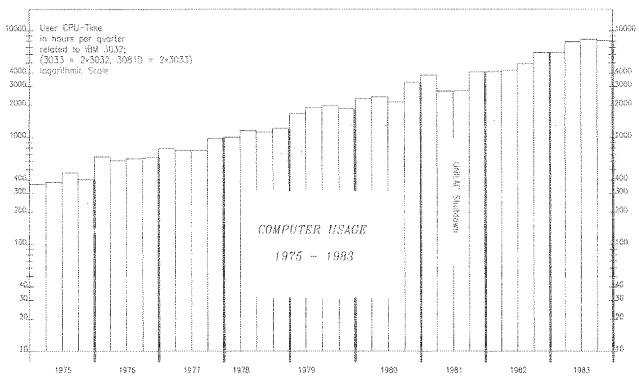


Figure 3: User-CPU-time from 1975 to 1983 per quarter of a year.

Consumption of computing resources mainly arises both from experiment related processing and numerical simulation to about equal shares, while other areas like document preparation and administration are of minor effect on capacity needs. Computer usage is displayed in six diagrams. The overall user CPU-time produced by all general purpose processors throughout the year is displayed in figure 3; for ease of comparison all machinery is normalized to the processor IBM 3032 which has been used until August 1982. The user CPU-time consumed within the GSI developed Experiment Data Acquisition and Analysis System EDAS is displayed in figure 4, while figure 5 shows the scheduled versus the achieved production time added for both computers respectively. Figure 6 represents the CPU-efficiency averaged for all processors in the computer array. In total 286.377 jobs were run in 1983 while the users worked in 168.065 interactive sessions under TSO/ISPF as shown in figure 7. By the end of the year, about 64.000 individual datasets, experiment analysis related VSAM datasets and members in partitioned datasets not counted, have been kept on direct access storage devices including the mass storage system.

The two array processors FPS-164 are operated both under APEX (Attached Processor Executive) and SJE (Single Job Executive). Since FPS-164-#2 went into operations late in 1983, only the usage of FPS-164-#1 is displayed in figure 8. Major instabilities had occured after

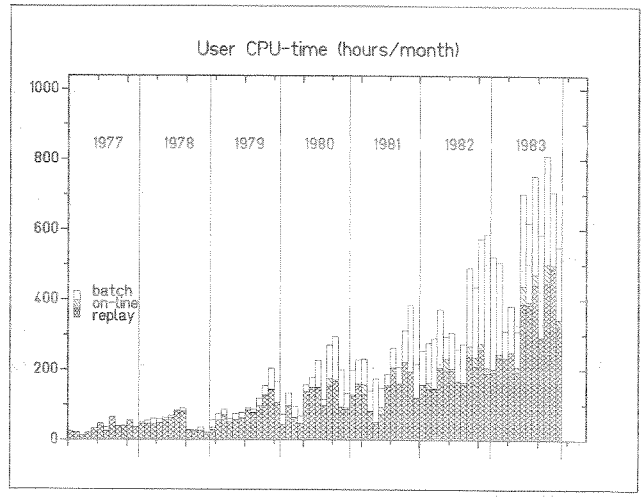


Figure 4: User-CPU-time for experiment data acquisition and analysis tasks running under EDAS from 1977 to 1983 per month in batch, life, and replay mode.

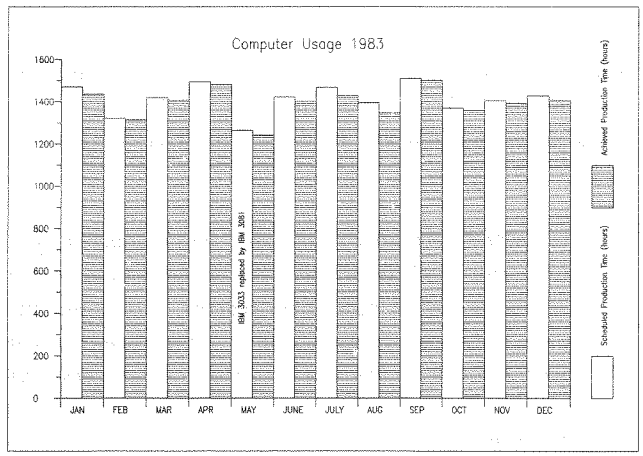


Figure 5: Schedules and achieved production time in 1983.

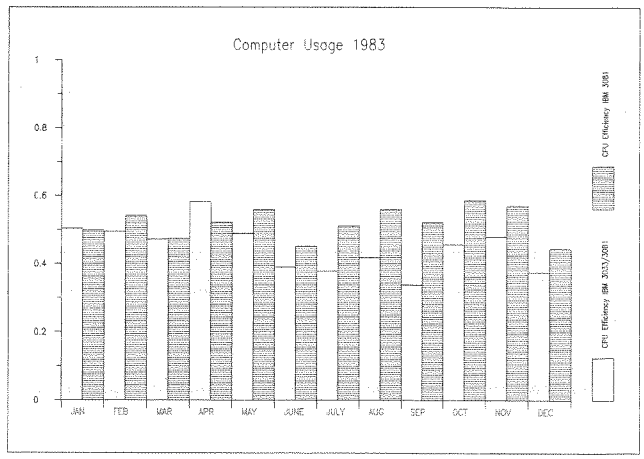


Figure 6: CPU-efficiency of the processors 3033 and 3081 in 1983. CPU-efficiency is CPU-time in problem status divided by the achieved production time.

the reorganisation activities which were scheduled together with the installation of FPS-164-#2. While both APEX and SJE currently allow only for one user at a time, three different JES3-job classes have been introduced in order to operate short running jobs always before long simulation runs. SJE-II soon will allow for multiple job execution at one time by roll-in/roll-out techniques locally handled by SJE.

In order to allow for a better response time when accessing user datasets, three major steps were initiated throughout the year:

- upgrade to ten disk drives for user datasets
- restructuring the catalogues carrying the entries for user datasets
- replacement of the GSI developed migration and back-up system MAKUP by the software-product HSM (Hierarchical Storage Management).

These steps reduced the load of the Mass Storage System which had operated with its maximum cartridge mount capacity of well over 5.000 per day over longer periods, thus being the major reason for poor user's response time when accessing datasets stored on the Mass Storage System.

Due to limited personnel resources, user's support, user education and assistance cannot be covered to an extension similar to other computing centres. But interactive facilities including communications have been largely enhanced throughout the year, so that in many cases the user actually faces a better service. Besides the standard help facilities, which are available for all software systems including the GSI-developed experiment analysis and graphic systems, the Interactive Instructional Presentation System, IIPS has been added to the software services. As a first step, classes on DP-related English for German users, introduction to Assembler Language, and introduction to Document Processing have been offered. All classes are well accepted by users from all functional levels including scientists, technicians, as well as secretaries.

An electronic mail system has been introduced as a trial to allow for easier communication between all user groups. Besides communication facilities itself, this system includes a handling system for all types of messages, organized in folders, which can be accessed individually.

The language FORTRAN77 has been introduced with the compiler VS-FORTRAN (IBM), allowing for 31 bit address space under MVS/XA, but FORTRAN-H, optimization enhancement, still remains the fastest compiler for the

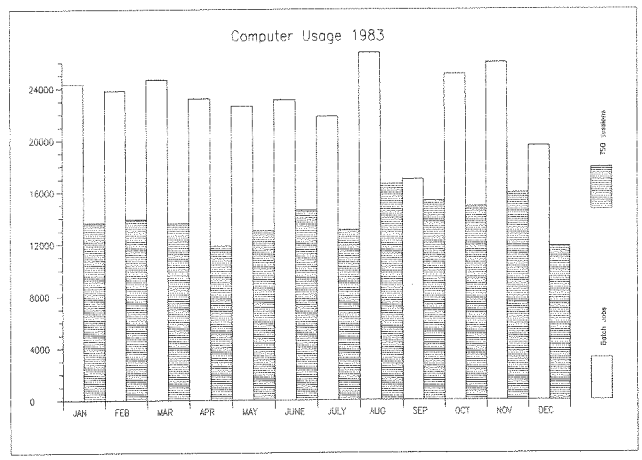


Figure 7: The number of batch jobs and interactive sessions on a monthly basis in 1983.

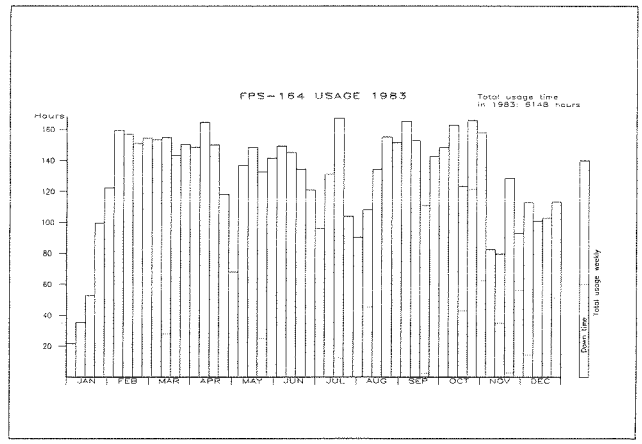


Figure 8: Allocation time of the array processor FPS-164-#1 in 1983.

execution of large code. Within the basic software, NJE (Network Job Entry) allows now for the exchange of batch jobs as well as messages between the computing centers at DESY, Hamburg and KFA, Jülich, preparing for the access to EARN (European Academic and Research Network) as well.

The current telecommunication network, allowing access to the GSI computing facilities from local and remote terminals as well as from other local or remote computers, is displayed in figure 9.

Besides the two GSI-developed software systems EDAS (Experimental Data Acquisition System) and GNOM (Graphics and Numeric Operation Method), the following program packages are supplied to the users of the GSI computing facilities:

FORTRAN-G Compiler	PL/I Optimizing Compiler
FORTRAN-H Compiler	PL/I Checkout Compiler

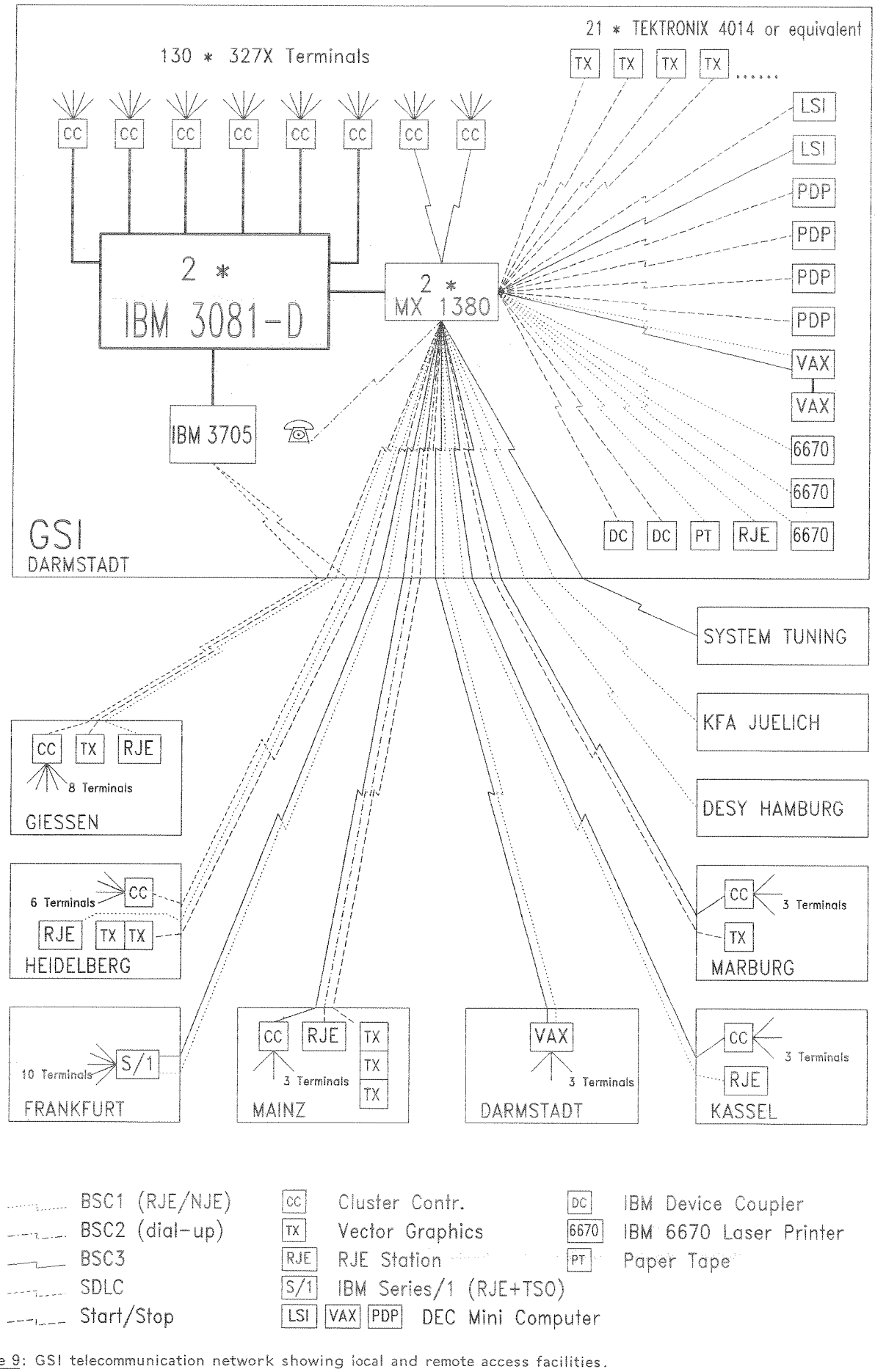


Figure 9: GSI telecommunication network showing local and remote access facilities.

FORTRAN H Opt. Enhanc.	PL/I FORMAC Translator
FORTRAN Interactive Debug	PASCAL Compiler (THD)
FORTRAN-PL/I Translator	PL-11 Compiler
VS-FORTRAN	Interactive Instr.Progr.Sys
WATFIV FORTRAN Compiler	SPEAKEASY Interpreter
SFORTRAN Makroprocessor	VS-COBOL
FORTRAN Mult.Prec.Arithm.	VS-ASSEMBLER
SPITBOL Compiler	SYNPLOT Syntaxgraphs
RUNOFF Textformatting	SOAP Parsergenerator
SCRIPT/DCF Textformatting	SLDGL Differ. Equ. Sol.
SCRIPT-6670 Textformatting	SSP Scient. Subr. Pack.
FORMAC Alg. Man. Lang.	PLMATH Scientific Subr.
REDUCE Alg. Man. Lang.	CPC Program Library
SCHOONSCHIP Alg.Man.Lang.	CERN Program Library
TSO Command Package	DESY Program Library
SPF Struct. Progr. Facility	EISPACK Eigenvalue Subr.
PCF Access Control	LDTS Local Display Simul.
RACF Data Security	GDDM Graph. Data Display
Westinghouse Fast Dump/Rest.	CALCOMP Graphics Softw.
MSI Multiple Syst. Int. Fac.	AGF Plotfile Interpreter
CA-Sort Computer Ass. Sort	ACF-TCAM Telec. Access.
OMEGAMON Monitor	SAM/E Sequ. Access Meth.
Information/System Info/Libr.	MVS Module Packer
Mass Storage System Aids	SPICE for FPS-164
FPS-164 Compiler & Libraries	NJE,Network Job Execut.
DF/DSS Data Services	6670 Font Editing

The TSO utilities will be no longer provided at GSI computers, but major commands such as COPY or LIST will be available as GSI-developed facilities.

In 1983, computer operations had to overcome the challenge of running on-line sessions for experiments at the UNILAC on 142 days with up to three of these sessions in parallel. Requirements for continuous avalability were not achieved completely but the results demonstrate the major advantage of powerful computing resources for data capture and on-line analysis in complex experiments. Compared to earlier years, the efficiency of supporting on-line experiments has increased significantly thus reaching an acceptable quality level. The experience in using central computing facilities for real-time processing was summarized in a paper to appear shortly in IEEE Transactions of Nuclear Science describing the general advantages of implying central computing services into high speed data capture and immediate analysis tasks.

As a result of the growing data oriented activities, tape mounts increased to well over 300 per work day in average. These demands require additional automation of standard procedures such as HSM-supervised data saving procedures, thus allowing computer operations to enhance the service functions due to an offload from other jobs. The amount of magnetic tapes needed for storing data captured from on-line experiments also has increased much faster than anticipated. The areas available for the magnetic tape inventory soon will be loaded completely. Solutions for alternative storage capacity will be required soon.

System Software

The Operating System MVS-SP (Multiple Virtual Storage - System Product) has been upgraded to Version 1.3.2, PUT-level 8301, while JES3 (Job Entry Subsystem 3) was generated as level 1.3.1. With these software components system software was operated highly stable, especially since repetitively occurring problems with ACF-TCAM have been analysed and solved after a long lasting search process. With the installation of NCP (Network Control Program) together with the teleprocessing controller IBM 3705, SNA (Systems Network Architecture) was introduced in order to service remote coloured graphics display units, used for experiment data analysis operations. Later on, communications mechanisms, using the PTT-supplied DATEX-P and DATEX-L services will be introduced for remote access to GSI computing services. In the later part of 1983, the preparations for the installation of MVS/XA (MVS/Extended Architecture) were initiated allowing both for 31 bit address space (2 Gigabytes) as well as enhanced channel performances. MVS/XA is intended to go into floor operations within the first quarter of 1984.

Tuning, since many years is regarded as a major issue claiming for both users satisfaction in interactive operations as well as usage of computer components, thus guaranteeing for high efficiency with respect to throughput and costs. GSI-specific performance characteristics service highly demanding interactive experiment data analysis tasks with similar response times as standard interactive operations such as editing, formatting or compiling, while the data analysis tasks require much higher computing resources. Thus, the available computing facilities are adequately shared between high priority data analysis tasks and other activities. Interactive data analysis may consume up to about 60 % of all resources, if other activities are waiting for service, but each service group - interactive users, data analysis tasks, or batch processing - may achieve additional resources if other service groups do not request their shares.

Experiment Data Processing

F. Busch, D. Croome, H. Göringer, V. Hartmann, J. Lowsky, D. Marinescu,
K. Winkelmann, G. Zaidman

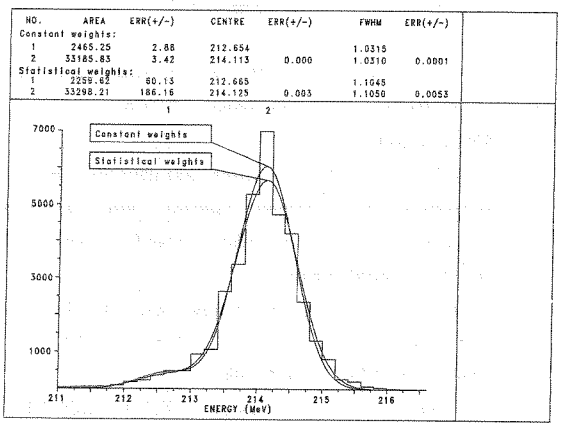
GSI Darmstadt

The System to Analyze Tremendous Amounts of Nuclear Data (SATAN), the mainframe part of the Experimental Data Acquisition and Analysis System (EDAS) of GSI, was developed further to match the growing requirements of on-line and off-line operations.

The interactive data evaluation was improved by a variety of new or modified commands supporting the following functions:

- Two-dimensional free form conditions, defined by closed polygon lines, can be created or changed interactively to be used in analysis programs or to manipulate parts of two-dimensional spectra (see special report).

- Interactive graphics, which enable the modification of the current display by adding text or simple graphic objects, have become more flexible. The figure below shows a fitted SATAN spectrum with the results transferred from the terminal and with a new description of axes.



- The management of global parameters as part of a common data structure was extended essentially (see special report). The integration into the command decoder allows for the substitution of text strings containing parts of SATAN commands by these parameters; display and fit data can be accessed by the global parameter interface program.

- The interactive use of arithmetics was improved. Desc calculator functions as add, subtract, multiply, divide, power and exponentials, working on numerical constants or global parameters are implemented; frequently used mathematical and physical constants are available as global parameters.

- Several commands allow input values to be specified in the short loop notation (a [TO z [BY s]]).

- The help facility was extended by tutorials which demonstrate an exemplary use of some SATAN commands.

With the increasing complexity of analysis programs the compilation time as well as the execution time were growing, too. For this reason, several analysis programs of SATAN users were studied for compilation and execution time optimization. The execution time of these programs was decreased by up to 15 % through optimizing the loop, which processes the event data.

A graphics interface to SATAN was made available to user written programs. Several procedures are provided to choose line, marker, and text attributes; to plot a cluster or polygon; to write a line of text; to locate a point by the cursor. Coordinates can be entered alternatively in units of centimeters, of the picture size, or according to the actual display axes.

A new data structure for the description of the analyzer was implemented providing data elements for calibration, error bars, and extended comments for spectra.

The description of the EDAS system was completely revised and published in three volumes. The introduction into the concepts and usage of the system was entirely rewritten. It contains detailed instructions and examples of how to write analysis programs, and a description of the available commands; the user interfaces are summarized and described; a functional description of the EDAS fit package and the package for spectrum deconvolution is given. This new description of the EDAS system represents the status of SATAN version 5, which is running as the normal version since September, 1983.

Temporary data sets as well as the analyzer library now reside on real disks. The user can define a variety of analyzer libraries, which therefore may be kept small. As a result, the access time to the temporary storage and to SATAN analyzers is reduced significantly.

The integration of front end computers for experiment control and the central computers for data analysis and large scale data processing was developed further. Two disks with a capacity of six high density magnetic tapes are now dedicated to the data acquisition during a running experiment. New data sets are created automatically after a specified number of bytes has been written. These consecutive numbered data sets can be moved to any output device using one command.

AN INTER-ADDRESS SPACE COMMUNICATION SUB-SYSTEM FOR MVS

D. C. Marinescu, H. Hultzsch, J. Lowsky
GSI, Darmstadt

The existing standard software support for MVS (Multiple Virtual Storage) Operating System does not provide for a user controlled inter-address space communication.

To fill-up this gap, a sub-system of MVS was designed and is currently implemented. It uses the CMS (Cross Memory Services) supported by the 308x hardware and available in MVS starting with release 1.3.1. ECF (Enhanced Communication Facility) allows two active address spaces to communicate with each other via messages. Any address space, A, which wishes to communicate, issues an OFFER, making itself available; any other address space, say B, may establish a communication path to it by issuing a CONNECT request for A. After a successful CONNECT the requester obtains a TOKEN which uniquely identifies its partner; a TOKEN is a logical name of a communication partner which may be either a TSO user (in this case the user identification -userid- must be specified in the CONNECT request), a batch job (the job name must be given) or a started task. Subsequently, each partner may SEND or RECEIVE messages from any other address space connected to it, until one of the partners performs a DISCONNECT.

In the current implementation, up to 120 address spaces may use ECF simultaneously and any of them may be connected up to 50 others, at any time. These 'ECF generation parameters' are thought for an MVS/XA environment and they can be easily adapted to another environment. ECF provides an asynchronous communication and allows up to 10 messages to be queued for any given address space. A message may have a length of 1 Byte to 32 Kbyte and it may contain data (graphic data, numeric data, text), control information or code; ECF provides a fully transparent communication mode. Each ECF function returns a completion code and additional information (e.g. a SEND returns the number of messages in the INBOX of the communication partner).

Any user sub-system which reaches a certain level of complexity must perform a number of actions in parallel. In MVS this can be done by using multi-tasking. In this case, communication among different tasks is done via shared-memory; in addition, each environment must use the synchronization primitives of MVS (POST, EVENTS) either directly or via a high language environment (PL/I for example). The obvious risk of dead-lock situations, overwriting shared memory, performing its own scheduling, make this solution not particularly attractive.

ECF provides an elegant way of designing a complex user sub-system in which different parallel activities take place in different address spaces and communicate via messages. In such a design one can take advantage of the scheduling mechanisms already built into MVS, there is no danger of overwriting, the dead-locks cannot occur since every partner has the ability to receive a message when it is appropriate for him and to take any action in case a message did not arrive in time. In addition, some functions of the sub-system may be executed in dedicated 'service address spaces', in behalf of all sub-system's users. This reduces the virtual storage requirements by avoiding code duplication.

ECF brings within the user reach a facility already exploited by the MVS itself which uses a number of address spaces (PCAUTH, GRS, CONSOLE, MASTER, etc.) to perform its functions.

ECF consists of the following components:

- A monitor program, ECFMON, which runs as a started task in its own address space, ECFAS.
  ECFMON consists of:
  - a nucleus, ECFNUC, which establishes the communication environment (using CMS), provides an operator communication interface and error handling capabilities,
  - a set of functional routines, ECFPC1-ECFPC5, which perform the services offered by ECF and
  - a set of auxiliary routines.
- A set of user interface routines (OFFER, CONNECT, SEND, RECEIVE, DISCONN), available in PL/I or FORTAN from a run-time library. Each user interface routine performs a PC (Program Call) to the corresponding functional routine in ECFMON.

Any application using ECF must design its own 'application layer' which interprets the messages sent via ECF and ensures proper use of the 'transmission layer'.

Preliminary measurements indicate that ECF provides an efficient communication mechanism. With a 3081 model D, a SEND and RECEIVE, from PL/I environment, needs about 6.3 msec CPU time for a 32 Kbyte message, with all overheads included. For a 4 Kbyte message this time interval is 2.5 msec. In the case of 32 Kbyte message the data is moved at a rate of about 10 Mbyte/sec from the sender's address space to ECFAS, while for a 4 Kbyte message this rate is of about 3.2 Mbyte/sec.

The Free Form Conditions in SATAN

H. Göringer
GSI Darmstadt

A key function of EDAS, the Experiment Data acquisition and Analysis system, is the evaluation of experiment data using analysis conditions and the storage and further handling of results with the help of analyzers. For many purposes, however, the simple 'rectangular' condition, defined by lower and upper limits for all analyzer (spectrum) dimensions, is not sufficient. This is the case, for example, if two-dimensional distributions containing curved structures, such as nuclear charge versus neutron number, energy versus energy loss, or many calibration curves, must be analyzed in detail.

Therefore the concept of the condition has been generalized in SATAN. In the two-dimensional case, the condition is now defined by a closed polygon line of any shape. The extension of the free form conditions to n dimensions is provided.

The free form conditions are given by the coordinates and the order of the points defining the corresponding polygon. The analysis of data under a free form condition, that means the check if a data point, specified by channel numbers, is located inside or outside a polygon, follows the strategy:

1. It is checked, if the data point is located inside the smallest rectangle surrounding the polygon.

2. If true, the number of intersections of all polygon edges with a straight line connecting the data point and an arbitrary point outside the polygon is determined. If this number is odd, the data point is located inside the polygon, otherwise it is located outside.

The algorithms for the analysis of the second step were already available in several programs written by SATAN users (*) for their own purposes. Therefore appropriate parts of these programs have been integrated into the SATAN software.

For the implementation, two conflicting aspects had to be considered. The more numerical informations are kept from a polygon, the faster the analysis runs; however, more storage space is required. The following compromise has been realized:

- In the analyzer library, of course, only the point coordinates defining the condition are stored (in correct order).

- Additionally the coordinate ranges, offsets and slopes of all polygon edges for each free form condition once created are kept during the whole SATAN session to avoid slowing down the analysis.

These parameters must be calculated again for each condition retrieved from the libraray.

Beyond data analysis including the live display, the free form conditions can be handled interactively by several SATAN commands:

- The polygons can be drawn and graphically created and modified.

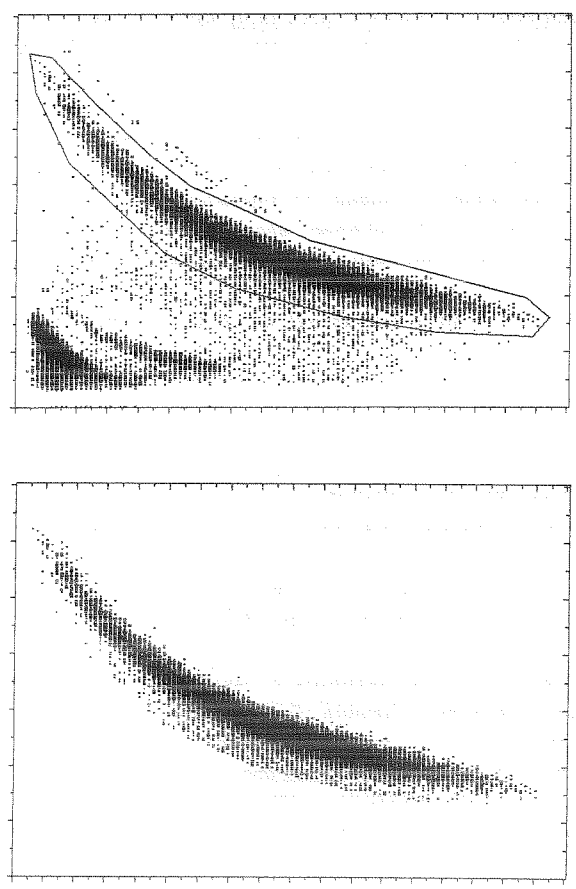
- The point coordinates defining free form conditions can be read into SATAN from partitioned data sets using global parameters.

- They can be copied from existing conditions.

- They can be stored to (and retrieved from) the analyzer library.

- The analyzer contents inside or outside a free form condition can be modified interactively.

As an example, the following figure shows ΔE/E distributions of light nuclei produced in a fission experiment. The upper part contains the whole spectrum and a polygon enclosing the distribution for one mass. In the lower part, the spectrum is set to zero outside the polygon.



(*) H. Grein, K. H. Schmidt, GSI
M. Krämer, TH Darmstadt

The Concept of Common Data Structures in SATAN

V. Hartmann, G. Zaidman
GSI Darmstadt

Within the data analysis system EDAS, the requirement to change numerical constants or to control the data flow in analysis routines interactively was met by means of 'global parameters'. A small number of integer variables could be defined to be accessed both by analysis programs and EDAS commands. Thus calibrations or other calculations could be performed with variables, the exact values of which were unknown when writing the program; or flags could be set for the conditional execution of parts of a procedure.

To fulfill the growing demands of the data analysis, however, type and scope of these parameters proved to be insufficient. Hence, a program package has been integrated in SATAN providing for an extended and more flexible application of global parameters. The main features are:

- An arbitrary number of parameters may be used, limited by storage capacity only.
- An essential subset of types of PL/I variables is available: bit aligned, short and long integer, single and double precision floating point, and character varying of any length.
- Both scalars and arrays of up to 15 dimensions are supported.
- With each parameter an explanatory text may be stored.

Beyond the usage in analysis programs, the global parameters are intended to establish a connection between different SATAN components. An easy transfer of data between commands is rendered possible performing both input and output via these parameters. This is actually realized in two fields.

Entering SATAN commands or executing command lists has become more flexible. Generally, any substring of a command may be replaced by a global parameter name preceded by a special symbol. In addition, single numerical arguments of a command (and in some commands even lists of numbers) may be directly specified by the name of a numeric global parameter.

The handling of the fit routines is facilitated by means of global parameters. The actual values of fit parameters as well as results (function values, errors, correlation coefficients, gross and net moments) may be stored into global parameters and thus e.g. saved on a data set. Vice versa, starting values and limits for fit parameters may be specified using these parameters.

A basic requirement for an easy application of these features is the possibility to declare (and delete) parameters interactively, independent of an analysis routine.

Global parameters are accessible both in resident and dynamically loaded programs. A unique identification via the name is guaranteed, even if several procedures contain declarations of different subsets of parameters in arbitrary order.
While it is obvious that a global parameter can be used in procedure statements like any PL/I variable, a SATAN command allows for interactive basic operations (addition, subtraction, multiplication, division, power, minimum, maximum) combining parameters (scalars as well as arrays) or numerical constants. To facilitate these desk calculator functions, a few frequently used mathematical and physical constants (e, π, c, $\hbar$, etc.) may be created by another command.

In order to make different values of global parameters available at any time, they may be written to and read from a user defined partitioned data set of any format. A member can easily be edited for an optional number of parameters which are represented by the name, (in case of an array followed by the extents per dimension in parentheses,) and the data in any legal PL/I format. Strings covering several records may be flagged to be concatenated. Comments may be placed anywhere.

Special attention was payed to an easy interactive usage of global parameters by a simple command syntax and reasonable defaults (e.g. for data set names). Accessing (change, save, list etc.) many parameters by a single command is facilitated by the following rules:

- Specifying whole arrays, arguments may be omitted.
- Cross sections or even non-connected parts of an array may be addressed by index loops.
- A name followed by a special symbol stands for all parameter names beginning with the respective characters.
- If no parameter name is given, all parameters declared so far are affected.

The entire program package which comprises a program code size of about 150 kbyte is loaded and released dynamically at run time.

Enhancements to the SIMPLE Preprocessor

Doris Croome and Klaus Winkelmann
GSI Darmstadt

To allow a greater flexibility when evaluating experiment data at GSI with the system EDAS ('Experiment Data Acquisition and Analysis System', [1]), the user has to write his specific analysis program. To assist him, a problem oriented language extension is offered: SIMPLE, the 'System Independent Macro Programming Language of EDAS' allows a unified way of writing the analysis on both computers currently used for data acquisition and analysis at GSI, the mini-computer (PDP-11 with the software system GOLDA) and the mainframe (IBM 3081 with SATAN).

New language elements for EDAS specific functions are implemented by means of macros. A valid macro always starts with a '$' sign and has the syntax as indicated in the figure below. The text processing language SPITBOL [2] was used to write the compiler which does the text replacement. It runs on the mainframe and expands the macros in PL-11 or PL/I code respectively. Compared to the familiar PL/I preprocessor language it has following advantages:

- higher functionality: Arrays, tables and user-defined data structures as well as recursive functions are supported and extensive debugging facilities are provided. Thus more complex argumentlists can be processed and concise text manipulation by few instructions becomes possible.
- much higher speed (up to a factor of 30).

This concept of a text replacing macro language with a compiler written in SPITBOL has proven to be well suited for EDAS. Furthermore SPITBOL is now available on DEC VAX-11 computers. So this concept will be kept for the new experiment data analysis system which is currently being developed.

The SIMPLE Compiler can be divided into two parts:

1. The scanner, which is SATAN/GOLDA independent. It reads the input text, ignores comments and examines the remainder for PL/I or PL-11 type statements (text followed by a semi-colon). If a macro is found, the scanner checks if it is valid, builds up the data structure and passes it to a subroutine of the macro compiler.
2. The macro compiler, which exists in two versions (for SATAN and GOLDA). It has following functions:
   - syntactical checking
   - limited logical checking
   - generation of the PL/I or PL-11 code
   - informatory and error output
   - compile stop upon discovering of severe errors.

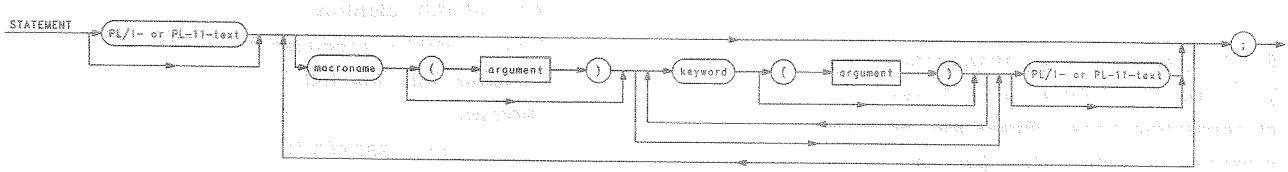
The following extensions to SIMPLE have been implemented during the last year:

- A new macro to insert PL/I debugging prefixes and/or to specify the initial storage size.
- Assignments and dyadic arithmetic operations in the well known PL/I notation can be written in a macro. This avoids having to write arithmetic in clumsy PL-11 notation.
- All macros related to operations with floating point numbers on the PDP-11 have been rewritten to use the built-in floating point hardware.
- Macros to declare single precision floating point and integer numbers can now be used to declare arrays; furthermore initialization is possible.
- In some macros, generated inline code was replaced by calls to assembler routines to decrease execution time.
- The arguments of some SATAN macros can now consist of PL/I variables instead of mere constants.
- Global parameters can now be declared and initialized. Optionally, a comment may be stored with the parameter.

Furthermore various tools have been developed, which are prerequisites to forthcoming extensions:

- The DECLARE statement of PL/I can now be analyzed. This allows a table of variables and its attributes to be built up.
- The SIMPLE precompiler scans the text twice. During the first pass he remembers certain items in a table, which will be read during the second pass to produce code conditionally.
  These two extensions will take care of a complete declaration of all system variables (used by a macro or by the user) and will avoid double declarations.
- Some macros had to be modified to run also in dynamically loaded programs. This is mandatory to allow an analysis program, which can be dynamically modified during the EDAS session.
- Optionally the macro which does the accumulation will generate a call to an assembler subroutine. In this way many local variables can be dropped, which leads to considerable shorter compile times and for most programs also to shorter execution time.

[1] K.Winkelmann: 'Notes on a large Analysis System for Heavy Ion Physics Experiments', Angewandte Informatik 10, 440 (1983)
[2] R.B.K.Dewar, SPITBOL Manual Version 2.0, Illinois Institute of Technology, 1971.



Syntax of a SIMPLE-statement

Foil Generator

W. Kynast
GSI Darmstadt

In a scientific environment the display of results for publications and presentations is a major task, requiring a utility for the generation of charts and foils. This system must be easy to learn and easy to handle, but, on the other hand, it must support the presentation of complex graphics. The interactive graphics system GNOM (Graphics and Numeric Operating Method) is an excellent base to fulfill these requirements. For all elements needed such as text, lists, tables, boxes, graphics, macros similar to the command structure of SCRIPT/DCF were implemented as GNOM procedures. Five predefined fonts are part of this system. Their attributes are collected in the standard type table and presented in figure 1. They were choosen to meet the special requirements of overhead projection.

	Var.name	H1	H2	H3	H4	H5
letter height (mm)	@TH	9	7.5	6	4.5	3
letter width (mm)	@TB	11	8.5	7	5.5	3.8
font number	@FONT	3	3	6	6	6
line width	@WIDTH	8	6	4	3	2
color	@COLOR	2	3	4	1	1
centered?	@CENTER	'Y'	'Y'	'N'	'N'	'N'
underline?	@US	1	2	1	0	0
capital letters?	@CAPS	'Y'	'N'	'N'	'N'	'N'
space (mm)	@SPACE	13	11	9	7	5

The user may establish his own specific global type tables thus overwriting the standard type table of FOLIE. Additionally it is possible to change all layout parameters locally within a foil. Especially simple words or phrases can be highlighted in many different ways.

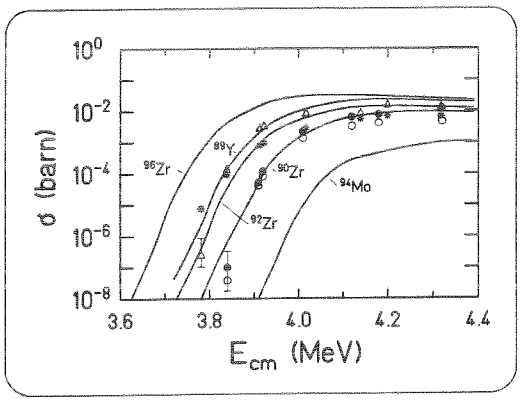
There are easy to handle commands to build up complex tables of text or data elements. The alignment may be defined for each column to be left flush, right flush or centered. Each line may have different width, linestyle and color attributes. The whole table - as any other part of the foil - may be surrounded by a box.

Simple diagrams, e.g. flowcharts or hierarchical diagrams may be composed using boxes and different kinds of connecting lines. Boxes may be nested and may be contained in tables. Any part of a foil may be rotated. Pictures created by other graphics programs may be included via the AGF-plotfile. If the features of FOLIE are not sufficient to create more complicated pictures, one may use the full scope of the GNOM language.

The FOLIE Users Manual was written with the goal to allow the usage of the system without any experience in GNOM or even in programming.
It should be noticed that the development of FOLIE including all documentation took one man about 4 weeks. This was possible because of the powerful GNOM system, which we used as both implementation language and host system.
As example the foil shown below contains a picture produced with the help of SATAN and included into FOLIE via the AGF-plotfile.

AGF-plotfile pictures

Now a picture produced by SATAN will be included into the foil:



All features of FOLIE such as boxes are available to produce a good-looking foil.

The sequence of commands generating the example above is given in the next diagram.

```
:FRAME
.H2
AGF-plotfile pictures
Now a picture produced by SATAN will be
included into the foil:
:BOXANF
:PIC picture; 180#(3/4*180); 'center'
:BOXEND 0.05
All features of FOLIE such as boxes are
available to produce a good-looking foil.
```

GRAPHICS AND NUMERIC OPERATING METHOD (GNOM)

I. Giese; W. Kynast, M. Feyerabend, H. Chytrek
GSI Darmstadt

In 1983, the improved version 2.1 of the interactive programming language GNOM was completed. Additionaly, a large number of GNOM application procedures were developed. GNOM is used now in about 500 sessions per month in average.

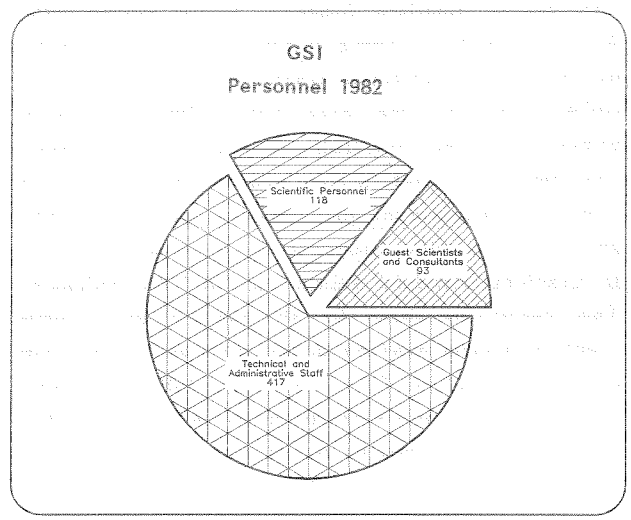
The system GNOM runs at GSI, at KFA/Jülich, and at GMD/Bonn, while DKFZ/Heidelberg is preparing for the installation early 1984.

In addition to other extensions, the new version has the following features:

- the DOBY/ENDBY commands allow graphics attributes to be valid for a sequence of graphics statements, especially used with graphics procedures;
- run time improvement: storing the parser tables decreases the run time by 20 to 30 percent;
- binding of user generated PL/1- and FORTRAN-procedures: by dynamic fetch mechanisms, user's own procedures with input and update parameters are callable from all GNOM levels in the same manner as system commands (GNOMCMD, GNOMPLI)
- improvement of the procedure facilities, e.g. local procedures existing only inside a given procedure;
- new control structure additions, e.g. ANDFOR for synchronous loop variables, or SKIPFOR for following the current loop statements in the current loop;
- new concepts for error and interrupt handling using the GNOM keyword facility (user actions in ERRORCOMMAND and INTERRUPTCOMMAND keywords);
- improved graphics primitives, e.g. rotated or centered text;
- new commands and functions, e.g. SORT, CPUTIME, DOMAIN, FIXSCALE;
- many additional values for linestyles, widths and markers;
- improved graphics input command, and the new input device TABLET;
- echo and repetition of the last command, with and without the menu of the parser program;
- extended timesharing interface for SPF, particularly allowing for direct TSO commands;
- enlarged and improved documentations (reference manual and tutorial) with many pictures and examples.

Furthermore the new library concept with a large number of application procedures from a common GNOM library is available. This library consists of about 40 procedures, among others:

- foil generation system (described in a special report);
- general hatching procedure for complex polygons;
- "affin" function for pseudo three dimensional graphics;
- axis drawing procedure with several options specific for a scientific environment;
- general graphics dialog system with user or system defined "graphics basic objects" for documentation, pictures like circuit diagrams, flow charts, and floor plans;
- "pie chart" procedure system;

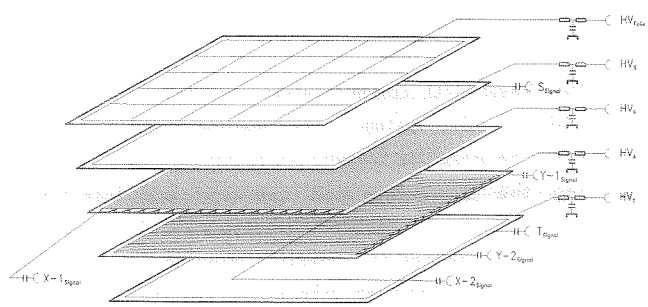


GNOM statements to create the picture above:

```
torte -> @gsi_personnel_82
torten_titel 'GSI Personnel 1982'
torten_segment 93; 'Guest Scientists and Consultants 93' +
                   //schraffur (45, -45;  3, 7); abstand(10)
torten_segment 118; 'Scientific Personnel 118' +
                   //schraffur (30, 0;  7, 4); abstand(10)
torten_segment 417; 'Technical and Administrative Staff 417' +
                   //schraffur (90, 30, -30;  10)
torten_ende
```

- simple interface for drawing rational mathematical functions;
- graphics utility procedures for arcs, line sets, and others;
- general commands for parameter tests, reference trees, or short directory listings.

The GNOM applications in GSI were concentrated on documentation, but with the availability of graphics procedures the usage of GNOM functions will be most efficient in many other areas such as data display, simulation analysis, algorithms development etc. The examples given show a particle detector (parallel plate counter) and a pie chart diagram.



AGF PLOTFILE INTERPRETER

I. Giese, K. Schwinn
GSI Darmstadt

The AGF Plotfile is a device independent graphics standard for the storage and transportation of graphics information, defined by AGF research centers in Germany. It is the predecessor of the metafile of the international standard Graphical Kernel System GKS. At GSI, the AGF Plotfile Interpreter was first implemented for the interactive graphics programming system GNOM in 1981 and then generalized in 1982 to a general graphics device interface for all GSI graphics programs. This interpreter now is also used in the interactive experiment data analysis system SATAN, and in most graphics programs using the earlier de facto graphics standard known as CALCOMP software. This mechanism allows for the usage of all available graphics devices available at GSI such as Benson drum and raster plotters, Tektronix storage tubes, IBM color raster terminals and Versatec raster plotters. In addition graphics data may be stored in the virtual graphics devices 'AGF Plotfile' and 'GNOM'.

The interpreter program was improved in 1983 in several areas:

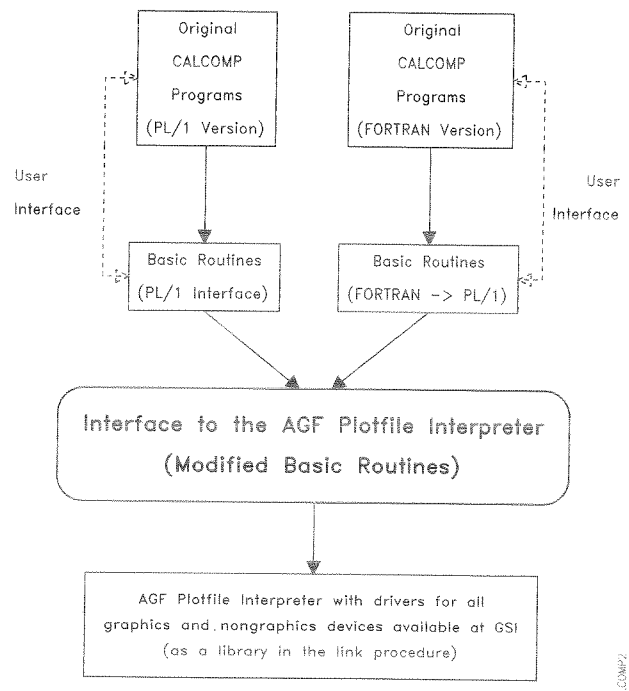
- in order to achieve application program independency, the interface was generalized for easy binding with other programs, e. g. SATAN or GNOM;
- the stand alone version of the AGF Plotfile "read and interpret" program (PLOT) was accomplished;
- a graphics tablet was implemented for graphics input in connection with the Tektronix storage tube device;
- the hardware text facility of the Tektronix storage tubes were implemented as a special font;
- new enlarged and unified number definitions for linestyle, width and marker were implemented;
- correction and completion of the connection between the CALCOMP software and the AGF Plotfile Interpreter, i.e. all facilities of the earlier used CALCOMP implementation are available now in the new Plotfile environment;
- the basic I/O communication interface to TCAM, which is the system access method for the dialog with the graphics terminal, was improved by reducing the subroutine call overhead and inserting enhanced error recovery mechanisms. This allows for the detection of defective graphics devices in order to continue an interactive session after the occurance of an error. Earlier in such a situation, without this recovery, the session had to be discontinued, usually combined with a loss of results already achieved;
- the program size was reduced by a factor of two after the reorganization of the interface to the CALCOMP basic software (see figure).

Graphics in the AGF Plotfile format can be generated at any computer type and interpreted at any location where a Plotfile interpreter is available. Especially their facility allows for the conversion of output from the layout development system for electric circuits CADE which operates on the DEC VAX computers. CADE output is converted to AGF Plotfile format and sent to the IBM mainframe, where several plot devices are available for printing. Using the TSO command PLOT the real graphics output is drawn on a selected device by transferring AGF Plotfile data to actually required control information.

An other example is the use of CALCOMP or SATAN generated pictures within GNOM, for example combined with the new foil creation system described in a special report.

The new configuration of the interface CALCOMP and AGF Plotfile Interpreter is described below.

Organization of the new CALCOMP software



DATA MANAGEMENT

Christoph Besthorn, Gerhard Schuette, Otto Siart
GSI Darmstadt

In the area of user data handling at GSI, some fundamental innovations were introduced in 1983. The GSI developed system for data backup and migration between real disk volumes and the Mass Storage System (MSS) turned out to become inadequate to manage the permanently increasing amount of user data. To overcome the difficulties, several improvements were implemented, but in the long run the transition to a more powerful data handling system was inevitable, thus requiring the installation of the IBM program product HSM (Hierarchical Storage Manager).

While the earlier system was based on several analysis and transfer jobs executing at night, HSM is a permanently running task on both computers moving data sets on users' requests at any time. The migration part of HSM provides data transfer between three access levels of data. Currently or recently used data are held on 'Primary Volumes'. Data sets not accessed for some time are compacted and migrated to 'ML1 Volumes' (migration level 1) and later on to 'ML2 Volumes' (migration level 2). At GSI, the Primary Volumes are ten 200 MBytes disks (USER01 - USER10), the ML1 Volumes are three 317 MBytes disks, while ML2 is a pool of MSS volumes. The main migration activity is done during night hours, providing sufficient free space on the Primary Volumes for the next working day, currently about 20%. HSM satisfies requests to access migrated data sets immediately by recalling them to Primary Volumes. That means, users' actual data accesses are exclusively addressed to real disk volumes and never to the MSS. This frequently needed access to the MSS in the past has been the major reason for poor interactive performance. The backup part of HSM provides data backup on data set basis, while the earlier system created volume backups. Per default, for every user data set two backup versions are maintained on MSS volumes. As the introduction of HSM means to move all MSS data sets to new MSS volumes dedicated to HSM, the impact of HSM to an installation with preexisting rules of data management is very strong. Planning of new data management strategies with HSM initially required a preliminary test installation, succeeded by gradually moving into full operation. In order to guarantee HSM compatibility and manageability, a set of GSI specific utilities for system maintenance and user information had to be implemented or modified.

In the old data handling system the capacity of one MSS volume owned by one user was a kind of natural limit of data space consumption per user. With HSM, no such limitation is inherent. In order to monitor the total space allocated to any one user and to prevent waste of data space, an installation specific modification of data set allocation is necessary. Based on a standard MVS allocation exit, the mechanism disables users' new allocations, when predefined limitations have been reached.

Catalog management in 1983 was improved with the complete replacement of the VSAM catalog concept by the Integrated Catalog Facility (ICF), providing significantly faster data set access and reduced catalog space.

VSAM is used for the storage of experimental data and spectra collected by the EDAS package (Experimental Data Acquisition System) as well as graphic data of GNOM (Graphics and Numeric Operating Method) in order to allow for fast information retrieval out of large data sets. Currently, the data stored requires 1200 MBytes on disks and 1000 MBytes on MSS. Due to the increasing number of VSAM data sets the change to the ICF catalog structure was very profitable, allowing for shorter serving times and simplified handling. Management of VSAM data sets is organised by GSI developed programs performing both backup of recently modified data sets and compression of full volumes. Four user commands are available for the handling of VSAM data sets:

- VCOMP to compress a data set, reduce the number of extents, and increase its size if required
- VDEF to define new VSAM data sets which comply with GSI specific name and internal structure conventions
- VBACKUP to store immediate backup or retrieve backup of specified VSAM generations;
- VTAPE to transfer VSAM data sets between magnetic tape and disk.

Together with these utility commands, VSAM has proven as an efficient tool for the storage and retrieval of large amounts of data in a dynamically changing environment.

ENHANCEMENTS IN TELECOMMUNICATIONS

F. Busch
GSI Darmstadt

High quality communication services play a key role in pertaining availability of central resources. At GSI, presently this range is mainly covered by a steadily growing number of terminals, RJE stations and minicomputers connected in "star topologie" to the central resources. It has proven to become a major task to maintain the large variety of communication hard- and software adopting and integrating new concepts. The major aim is, to maintain a service quality that corresponds to the technological state of the art and to make it available to as many users as possible.

Fig.9 of the contribution "Computing Center" shows the present configuration of communication facilities. About 130 terminals of the 3270 family, some with color graphics, are locally connected to the hosts by means of cluster controllers, e.g. IBM 3272/3274. The two communication controllers Memorex 1380 and the newly installed communication processor IBM 3705 provide "remote" attachement of RJE stations, 3270 terminals, TEKTRONIX 4014 (TX) or equivalent graphics displays, typewriter terminals and minicomputers.

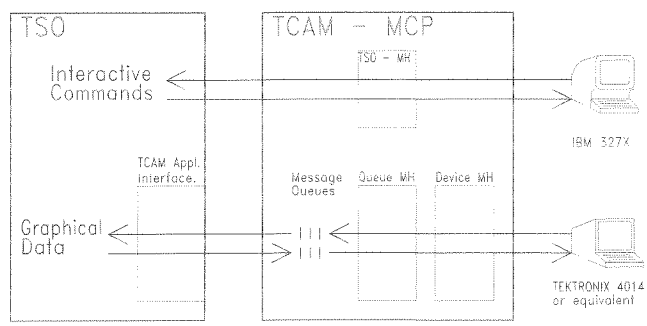
The Telecommunication Access Method Message Control Program, TCAM-MCP, residing in the host, provides the basic interface between applications, e.g. TSO, and terminals. It supervises all communication equipment, with exception of RJE/NJE lines handled by JES3, and organizes the flow of information by means of message handlers (MHs). Some basic functions like adaption to modems, line speeds (300 to 9.600 Baud) and protocols (BSC1, BSC2, BSC3, S/S and SNA/SDLC), polling of stations and recovery of transmission errors, however, are partly covered by software running in the communication controllers.

A speciality at GSI is the two-station concept, being largely used for Experimant Data Analysis and other interactive graphics activities. It combines the benefits of a fullscreen device for interactive session control with the high quality graphics capabilities of a vector graphics station. The graphical data are passed to TCAM via an application interface routine, built on special TCAM macros, allowing for access to a TCAM message queue. Two additional message handlers, a queue side and a device side one, are required to forward messages to their destinations. A "TCAMON" command, entered on the TX at the beginning of a session, enables operation of these alternate MHs. The simplified environment of the two-station mode, is shown below.

In the past, however, the two-station mode was found to be a source of TCAM break-downs and instabilities: TX stations occasionally stopped operation and TCAM was paralyzed because its message buffer pool was flooded with unsent information. The latter problem could be solved by a modification of the Queue Message Handler in the TCAM-MCP. In addition, another mechanism was implemented in the TCAM application interface routines in order to detect and recover from service interruptions. Thus, in the second half of 1983, highly stable operations could be achieved.

The Network Control Program (NCP) in the IBM 3705 was created and integrated together with TCAM into an SNA (System Network Architecture) environment allowing for color graphics applications on remote IBM 3279 terminals. The bit-oriented line protocol SDLC revealed improved throughput and error recovery in comparison to BSC.

For the future, there is a strong need for innovation, e.g. for fast color graphics displays, color printers and intelligent work stations (CAD/CAM stations and Personal Computers) integrated into a local area network. One project on this way is to migrate from TCAM to VTAM (Virtual Telecommunication Access Method). A fast connection must be established to the new VAX-type experiment computers. On the other hand, wide area communication facilities are demanded. Pathes into the public DATEX-P network are required, while interfaces to the European Academic Research Network (EARN) and the american BITNET will become reality during the second quarter of 1984.



The two-Station mode for graphical applications

USER AND SYSTEM INTERFACES FOR COMMUNICATION

Ursula Ernst, GSI Darmstadt

A new electronic mail system for use under TSO (Time Sharing Option - interactive communication system of MVS) and SPF (System Productivity Facility - fullscreen facility of TSO) was intrduced in July 1983. This system is a complete replacement of a less powerful version installed a year before. With the new version three different user interfaces providing the same functions are offered: TSO command interface, SPF interface and a TSO prompter interface. In addition to sending and reading mail messages various administrating functions enable the user to answer, archive, copy, forward, store, delete a mail message. Addressing by natural names and distribution lists eases sending, and file folders give an additional means for administration. Mail messages are kept in VSAM datasets, one mailbox dataset and one mail envelope dataset per user. Two VSAM datasets are provided to store the names, addresses and userids of all MAIL users: the Node Directory dataset and the Phone Directory dataset. An additional VSAM dataset for each user contains user defined distribution lists. All user datasets for mail communication are located on a single volume (type 3350) and are cataloged separately from other user datasets in a special usercatalog. On both systems the TSOMAIL System Communications Driver is running permanently as a system task to distribute mail messages to the users. Mail messages are stored by the user into his mailbox, and a request is submitted to the SCD to store it into the mailbox dataset of the recipient. Another function of the SCD is updating the Node Directory Dataset according to requests of an authorized administrator.

The MVS/TSO Mail Facility was installed under a joint study aggreement of GSI and IBM Thomas J. Watson Research Center at Yorktown Heights in order to gain and exchange experiences, to give suggestions for further development and to keep track of the development of the planned steps at IBM.

Since the introduction of the MVS/TSO Mail Facility different kinds of users take part in the mail communication. A major part of TSO users is located at the remote stations of the universities and laboratories connected to GSI computer complex, another group are the sectretaries using the mail facility for keeping track of communication within GSI. With the SPF interface, the MVS/TSO Mail Facility is easy to use for well trained computer personnel as well as for secretaries or managers.

There are still some malfunctions, and performance improvement is required in some cases. The next step of development at IBM Research will be the interface to a new function of TSO, TRANSMIT/RECEIVE (or IDTF - Interactive Data Transmission Facility), to realize mail communication among different systems. This new function of TSO will be available with the new version of the operating system MVS/Extended Architecture.

Prerequisite for the new function of TSO is a feature provided by the job entry subsystem JES3 of the operating system MVS/SP: Networking. This feature allows the transfer of jobs, job output, datasets, messages, and commands among nodes in a network of systems. Nodes can be JES3 complexes or other systems with compatible networking capabilities such as VM/SP RSCS (Remote Spooling Communication System) or MVS/SP JES2 NJE. Nodes can be connected directly (adjacent nodes) or via one or more other nodes (non-adjacent nodes). Connections between nodes must be BSC (binary synchronous communication) communication lines or channel-to-channel adapters (CTC). Operator control is provided by JES3 console service in order to establish line connections, to keep track of jobs coming in or going out to other nodes, to trace lines and to submit operator commands and messages to other nodes. Data provided for a remote node is written to JES3 Spool Dataset and compacted for transmission.

JES3 Networking is the prerequisite interface for communication between the node of EARN (European Academic and Research Network) and the JES3 processor complex of GSI. The node of EARN will be running under VM/SP with the compatible networking interface of RSCS. Prerequisite tests for communication between the processor complex of GSI and systems with different networking interfaces are running satisfactorily since the beginning of December 1983 with KFA, Jülich, connecting to the MVS JES2 system as well as to the VM RSCS node. Another connection will become active in January 1984 to DESY, Hamburg, running an MVS/SP JES3 complex. When EARN will be working transfer of data to KFA and other locations will then be realized via the central node of EARN.

JES3 Networking and other networking interfaces mentioned before provide the transmission of datasets, but under the current MVS/SP running on GSI processors, this function of TSO is not yet available. Only job input and job output is transmitted. The new facility for transferring datasets and basic mail communication called IDTF will be part of TSO/E of MVS/SP 2.1.1 (MVS/XA - Extended Architecture), a fundamentally updated version of MVS, which will be implemented during the first quarter of 1984.

Both, MVS/TSO Mail Facility as an efficient tool for communication and JES3 Networking as an interface between computer systems are a fundamental prerequisite for communication among laboratories and universities improving coordination and integration of scientific work.

Engineering and Technology

E. Malwitz, K. Blasche, W. Bleuel, H. Gaiser, C. Hoffmann, K. Illert
H.-R. Kiesewetter, U. Kopf, W. Schmidt
GSI Darmstadt

Engineering Department

Fig. 1 shows the distribution of engineering effort in 1983. It is nearly the same as in 1982. Miscellaneous includes time spent on the manufacture of single-pore membranes. Altogether about 37 % of the total effort was again used for experiment facilities. Activities for SIS, which include the transfer line from the Unilac to SIS, have increased a small amount at the expense of work for the Unilac.

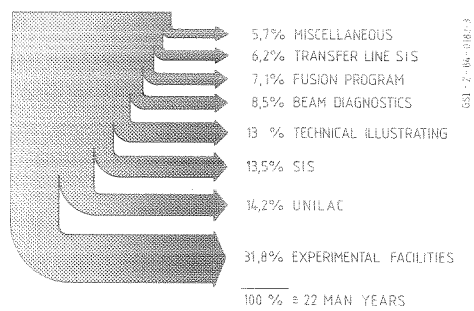


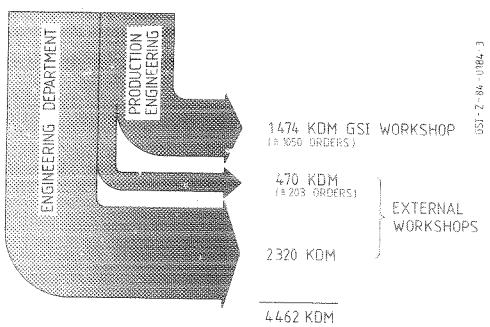
Fig. 1: Distribution of engineering effort in 1983.

Production Engineering

As shown in Fig. 2, altogether 1050 orders were prepared for the GSI workshops and 203 orders were sent to external companies. In addition the production engineers have written most of the 82 programs for the NC milling machine. The simpler programs were prepared by the machine operators. At the end of 1983 a second NC milling machine was installed. With a rotary table at this new machine, programming of axially symmetrical parts will now be easier. Nevertheless, programming of the NC machines needs to be improved. For instance, a system is required to be able to check the geometrical paths of the working tools at a graphic display instead of testing the programs directly on the NC machines. For the control unit Sinumerik 3 M of the new machine a special graphic display will be available for delivery in the near future. In addition, installation of a CAE-system is planned. This will also be used for NC programming.

Workshops

The mechanical workshop handled 550 jobs, the heavy workshop 418 and the technological laboratory 82. About 15 % of the workshop capacity was again required for small tasks that had to be handled immediately. At the end of the year a strong trend to overload the mechanical workshop was seen. This was due to orders for several complicated devices each requiring 200 or more working hours. In general, such orders should be



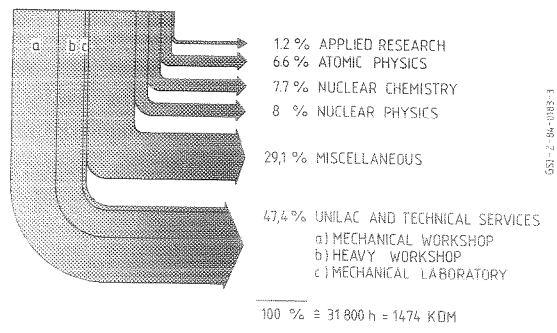


Fig. 2: Distribution of internal and external orders handled by the technical department in 1983 (left) and distribution of workload for the central workshop in 1983 (right).

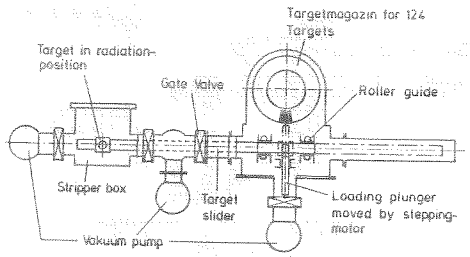


Fig. 3: New stripper foil magazine for the UNILAC stripper section.

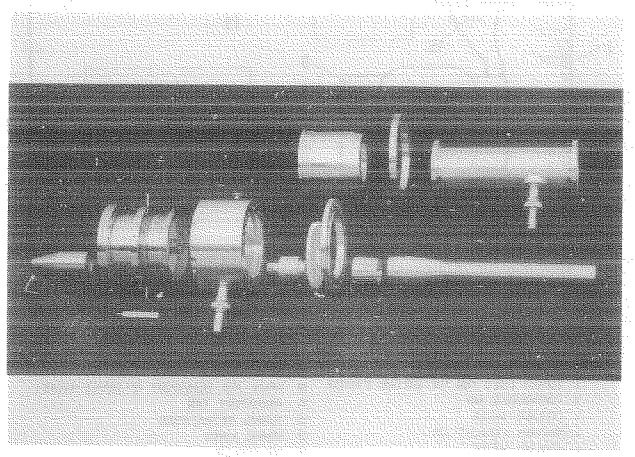


Fig. 4: New coupling loop for the single gap cavities of the UNILAC.

filled, at least in part, in external companies as only 13 man-years are available for production in the GSI workshop. However, external production is often made impossible, because the quoted delivery times are too long or because the technical documentation is inadequate for submission.

UNILAC

In the stripper section of the Unilac, stripper foils have been mounted on a target drum that could be used to place up to 200 different foils into the beam. These stripper foils with a diameter of 10 mm have been rather small for the beam cross-section at this position. In addition replacement of foils has been rather complicated. Therefore a new device as shown in Fig. 3 was developed. Up to 124 foils with a diameter of 25 mm can now be mounted on a magazine drum. From this magazine any stripper foil can be brought to a horizontal target holder rod by means of a loading plunger. The target holder is used to shift the target into the beam position. With two gate valves between the stripper box and the magazine chamber it is possible to keep the latter under vacuum when the device is mounted in the stripper section.

In the single gap cavity section all coupling loops will be replaced since the ceramic domes, which now separate the loops from the linac vacuum, were often destroyed by electron multipactoring. Therefore a new coupling loop was developed with a ceramic disk as vacuum window in the coaxial line (Fig. 4). The manufacture of these new loops required an elaborate brazing process to join the ceramic disk to the RF line.

Beam transfer line from UNILAC to SIS

For the beam transfer line from UNILAC to SIS various laminated dipole and quadrupole magnets must be built. In addition, many different laminated magnets for the SIS facilities will be manufactured later. Therefore, a set of stacking and bonding devices was designed that can be used for all these different magnet cores. The sheet material for all transfer magnets was ordered so that construction of all transfer magnets can take place in 1984. All coils for the transfer magnets were ordered in December 1983.

SIS

The design of the SIS 18 ring with all components was completed. Installation of all components and the arrangement of the supply lines in the 3 m × 4 m tunnel as well as transportation of the large ring components were checked (Fig. 5). For the alignment of the ring magnets a concept was prepared and the alignment marks around the tunnel were planned.

Ordering of the SIS magnets had to be postponed. However, the auxiliary equipment for manufacturing of the magnet cores was designed and ordered. All vacuum chambers which are needed in each of the 12 SIS periods were designed, i.e. the dipole chamber, the long

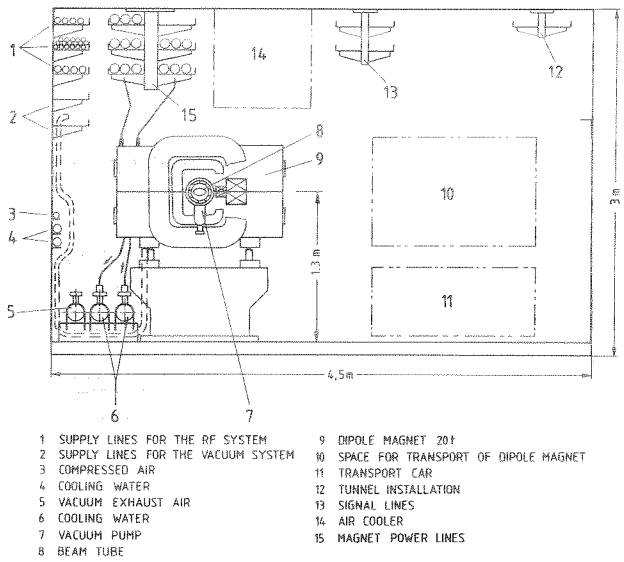


Fig. 5: Design study for the installation of magnets and of feed lines in the SIS 18 tunnel.

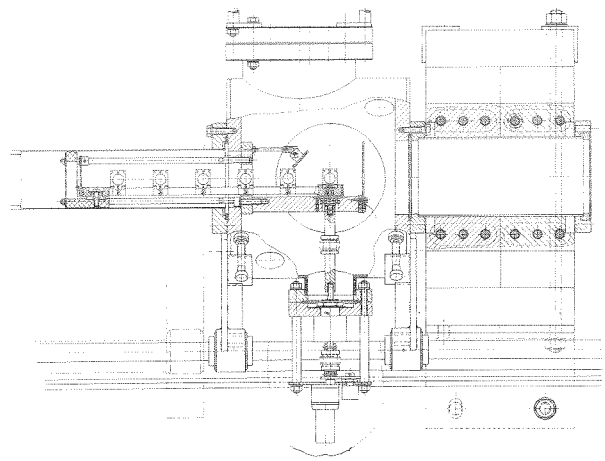


Fig. 6: Target transportion on a tooth belt into a position inside the velocity filter SHIP.

straight quadrupole chamber, and a special chamber between two neighbouring dipole magnets which is used for the installation of beam diagnostic equipment and of titanium sublimation pumps. A prototype of the latter chamber is under construction. For the magnet chambers, which must be manufactured from 0.2-0.3 mm sheet material, either corrugation of the sheet material or stiffening ribs are being studied.

RFQ Linear Accelerator

In 1983 the first RFQ section was assembled and tested. After successful test runs four more sections were ordered. The design of the new sections was improved in several points:

a) modification of cooling channels with a reduction of about 40 % for the milling time
b) installation of manholes in the tanks and relocation of the welding seams on the tanks in order to reduce thermal deformation
c) improvement of RF contacts between the vanes and the pole holders.

The four new sections are now under construction.

Experiment facilities

For experiments in the velocity filter SHIP, targets need to be moved into a barely accessible internal position. Fig. 6 shows the device which is used to transport the targets on a tooth belt through the beam tube into a position inside SHIP.

For the manufacture of large quantities of single-pore membranes a rapid irradiation system was designed. The heart of the system is a commercial 35 mm cine-camera. A 30 µm thin film of polycarbonate is used as membrane material. With the addition of an endless film loop of high tensile strength as support, a high traverse speed of 50 pictures per second should be achieved (Fig. 7).

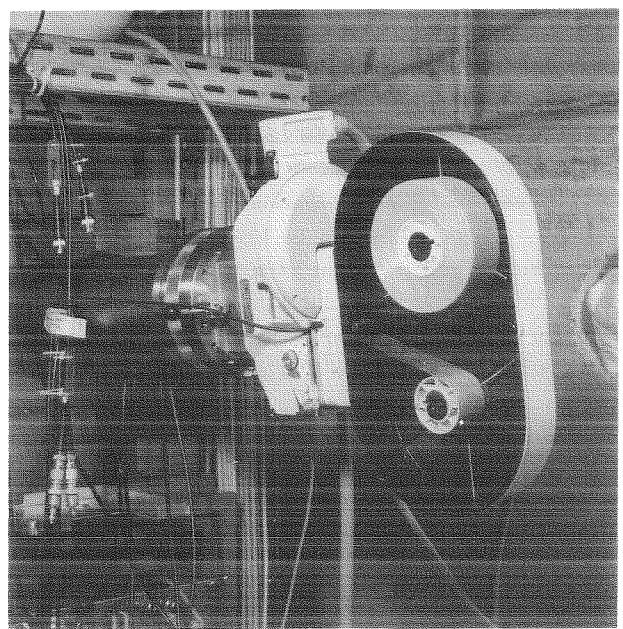


Fig. 7: Rapid irradiation system for the manufacture of single-pore membranes using a commercial cine-camera.

Electroplating Workshop

H. Gaiser, H. Eckhardt, K. Blasche
GSI Darmstadt

During the recent years surface refinement by chemical and electrochemical procedures has played an important role in the construction of accelerator and experiment facilities. The broad spectrum of refinement procedures, which were applied in the electroplating workshop, reaches from copper plating of large Alvarez cavity sections to the etching of heavy ion tracks in 30 µm thin foil material for the production of single-pore membranes with a pore diameter of 4.5 microns.

Last year copper plating of Unilac components like the Alvarez end plates and silver plating of coaxial RF power lines was one of the major activities. In addition various accelerator components were copper plated for several laboratories, e.g.

TU München:	REBEKA, a 1:2 RF cavity model for SUSE
CEA Saclay:	The complete RFQ injector linac for Saturne
BNL Brookhaven:	Four RFQ vanes
KFA Jülich:	Prototyp RFQ vanes

Copper plating of RFQ vanes requires an extreme uniform thickness of the copper layer since the vane tips are machined to a tolerance of ± 0.02 mm. By field computation and a series of trials the cathode geometry was optimized (Fig. 1). Table 1 shows that the required precision of ± 20 µm could be achieved.

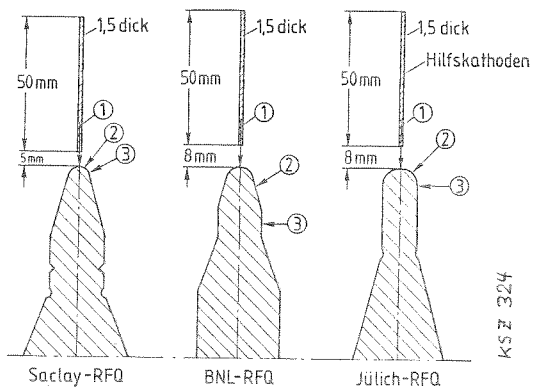


Fig. 1: Cathode geometry for the copper plating of RFQ vanes. Figures 1 to 3 mark the position of check-points for the thickness measurement.

Table 1: Uniformity of copper thickness in µm as measured at 3 check-points for RFQ vanes.

check-point	1	2	3	design value
Saclay RFQ	65	68	78	70
BNL RFQ	110	125	110	120
Jülich RFQ	66	84	92	80

Other interesting activities were:

a) The production of extremely precise spherical shells for a spectrometer set up from galvanoplastic copper.

b) Chemical and electro polishing of laminated magnets. In laminated magnets the pole surface quality was improved by grinding. Grinding leads to short circuits between neighbouring sheets. However, the chemical and electro polishing was an efficient etching procedure to remove the short circuits.

c) Electro polishing of 150 µm perfectly round holes for beam collimators.

As mentioned before the production of tens of thousands of single-pore membranes for measuring deformability of individual red blood cells requires an elaborate etching procedure of heavy ion particle tracks in a 30 µm thin polycarbonate film. Fig. 2 shows the device which is used to transport the film continuously through the etching bath.

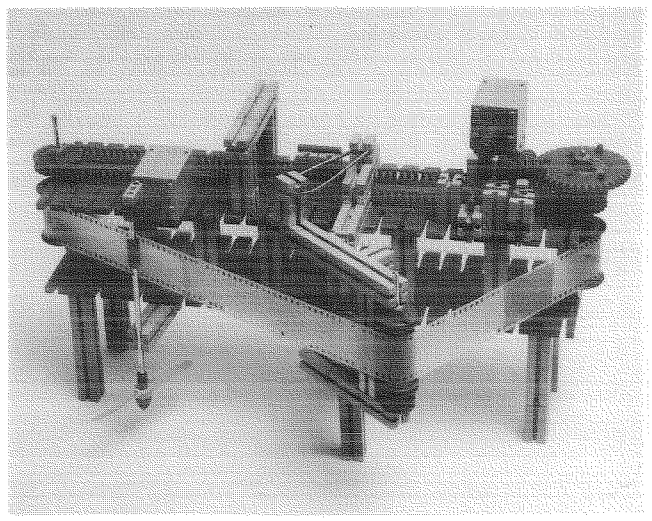


Fig. 2: Transport device which was used to lead 30 µm polycarbonate film through the etching bath.

5. Accelerator	PAGE
5.1 UNILAC Performance and Ameliorations	298
5.2 Accelerator Projects	311

Unilac Operation

N. Angert, G. Hutter, J. Klabunde, M. Müller, P. Strehl, D. Wilms
GSI Darmstadt

The Unilac was operated in the same sequence as in the previous years, usually 3 weeks of operation followed by one week of maintenance. However, in the spring and in the fall there were two maintenance periods of two weeks each. This resulted in 38 operation weeks with 5855 operation hours. Table 1 shows the distribution of operation time in 1983. The 3709 hours beam on target for the main beam is the highest value during 8 years of Unilac operation. Fig. 1 displays the Unilac operation statistics since 1976. It indicates also that this improvement results from decreasing down time, source replacement time, and tune-up time. The steadily improving performance of the Unilac was only interrupted in 1982, the year after the upgrading, when the Unilac had to be recommissioned with many new components and some new features.

Target Time, Main Beam	3709 h	
Target Time, Parasitic Beam		796 h
Acc. Experim. and Developm.	368 h	
Beam Tune-Up	820 h	
Unscheduled Down Time	767 h	
Maintenance	191 h	
Total Operation Time	5855 h	

Table 1: Unilac operation times in 1983.

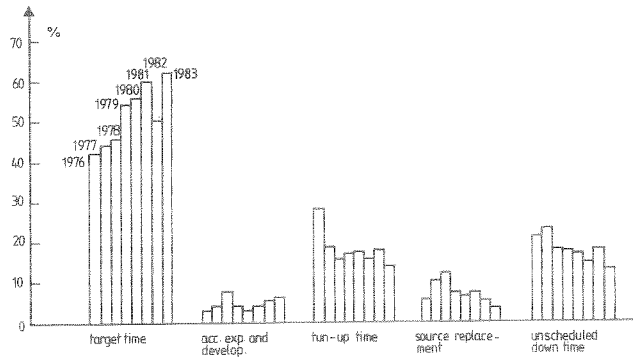


Fig. 1: Statistics of eight years Unilac operation.

Table 2 shows the list of the 33 different isotopes which were accelerated in 1983. 48 experiments were provided with main beam; 15 of them were supplied in addition with parasitic beam, mainly for experiment tune-up. This list reflects the wide range of beams, but also the dominant role of very heavy elements like uranium, at the Unilac. The high fraction of ^{48}Ca beam was due to two long runs in a search for superheavy elements. The distribution of energies during the past year is shown in Fig. 2. It indicates the further shift of beam energies toward higher energies with clear peaks at the output energies of Alvarez tank 3 (8.6 MeV/u) and Alvarez tank 4 (11.4 MeV/u), as well as at the maximum energies for medium and heavy mass ions at 18 to 19 MeV/u. The high energies caused some problems since the shielding in the experimental areas had to be extended considerably. This resulted in displacements of the beam lines of up to several millimeters due to the heavy weight of the concrete shielding. This displacement was most disturbing at the transition between the accelerator tunnel and the experimental area in the beam switchyard and the shortened beam splitting system. The latter had to undergo some modification to allow easier tuning and more parasitic beam time in the future. The experimental possibilities at the Unilac were extended by the installation of a fast rf chopper, which is described in another contribution in this annual report. For the future variation of the Unilac output energy from pulse to pulse, computer calculations of particle dynamics have been completed and the procurement of pulsed magnets, quadrupoles, steerers and power supplies has been started.

^{14}N	48 h	^{92}Mo	34 h
^{16}O	128 h	^{100}Mo	98 h
^{18}O	80 h	^{120}Sn	72 h
^{22}Ne	28 h	^{129}Xe	147 h
^{40}Ar	54 h	^{132}Xe	111 h
^{40}Ca	170 h	^{134}Xe	19 h
^{48}Ca	570 h	^{136}Xe	87 h
^{48}Ti	100 h	^{144}Sm	17 h
^{50}Ti	27 h	^{152}Sm	67 h
^{56}Fe	50 h	^{154}Sm	20 h
^{58}Ni	162 h	^{155}Gd	73 h
^{70}Ge	127 h	^{161}Dy	48 h
^{74}Ge	53 h	^{197}Au	73 h
^{82}Se	36 h	^{205}Tl	10 h
^{84}Kr	140 h	^{206}Pb	20 h
^{90}Zr	47 h	^{208}Pb	210 h
	^{238}U 775 h		

Table 2: List of accelerated isotopes and corresponding target hours in 1983.

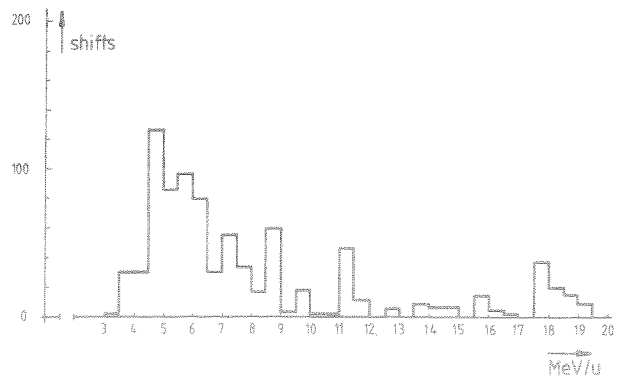


Fig. 2: Statistics of Unilac ion energies.

M.Müller, W.Jacoby, M.M. Khaouli, J.Bossler, H.Emig, N.Hofmann
K.-D.Leible, M.Stork, H.Krichbaum, H.-P.Kurz, R.Rulfs, K.Schneider
GSI Darmstadt

Technical Improvements

All the 25 PIG sources (for north and south injector) have been equipped with new designed watercooled puller electrodes now providing better electrode adjustment during ion source operation when high total currents are extracted (> = 80 mA pulse).

In the ion source discharge geometry the short circuitry problem between sputter electrode and anode was practically solved by the development of a new "sputtershort" burn off power supply (see: The "Sputtershort" Circuit, this report).

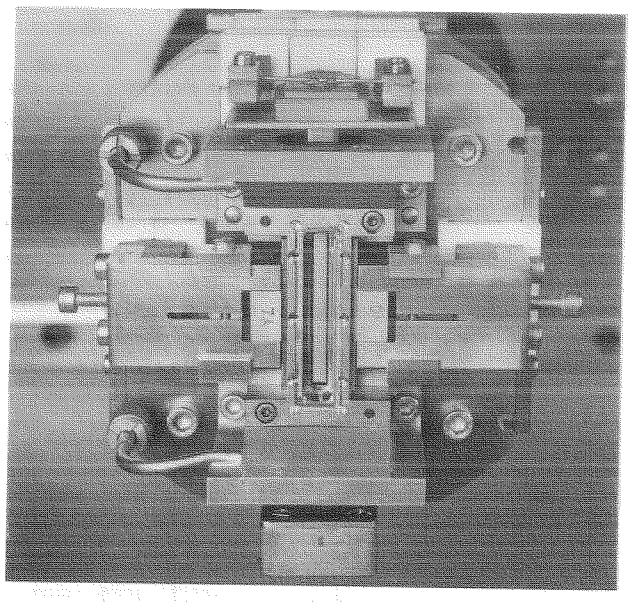


Fig. 1: Three sputter electrode PIG source (anode slit removed)

An ion source prototype (Fig. 1) allowing the alternative use of three, even assorted sputter electrodes was developed and tested. By pushing a button the ion source can be switched from one metal ion beam to another one without changing the source. Also when the ion source is made up for three equal sputter electrodes a longer lifetime can be expected.

A four gap low gradient geometry for the acceleration column was carefully tested at the northern injector. The double benefit, lower X-ray level and very short conditioning time (a few minutes up to 260 kV) was transferred to the southern injector.

Ion Beam Preparations and General Studies

For some elements special ion source operation methods are necessary to provide stable, long time intensive ion beams. So, particularly for tungsten, it was found that cathode-sputtering in an oxygen discharge, supported by normal sputtering of a tungsten electrode delivered best results. The chaotic ion source behaviour when sputtering a pure selenium electrode got under control using a lead-selenium alloy.

In the two long time ^{48}Ca runs (600 hours together) again the gold alloy technics was successfully used. The atom percentage of the isotopic pure ^{48}Ca in the sputter electrode metal mixture was reduced to 3 % (resp. 6 %) instead of 4 % (resp. 8 %), as formerly done, and delivered easily the required ion current on the high energy target (see Fig. 2).

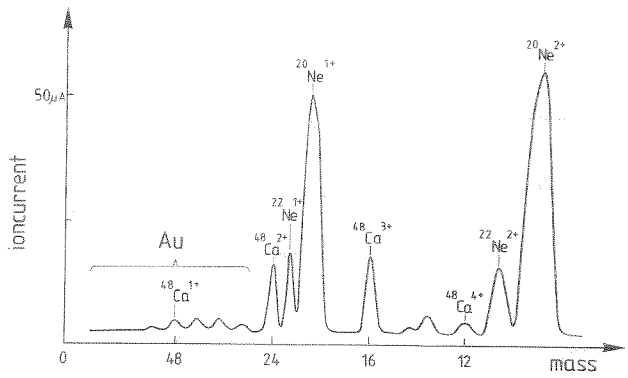


Fig. 2: Charge state spectrum of Au-^{48}Ca (3 %) alloy sputtered in a neon discharge, recorded at the PIG source of Unilac injector-south

The ^{48}Ca consumption in the source was below 1 mg/h for the "physical" run (120 pnA beam on target) and 1.4 mg/h for the "chemical" run (up to 200 pnA beam on target). The influence of the sputter electrode width on the sputter material consumption rate was examined in detail. With 4,3 and 2 mm wide sputter electrodes the ion source was operated to produce always a .2 mA cw. Cu 4^+ beam for 6 hours. The 2 mm electrode showed a 30 % lower consumption rate in terms of (mg/mA • h) compared to the 4 mm electrode. This result might be of some interest for expensive or rare isotopes.

Side Activities

In the course of a student's diploma work in technical engineering an ion beam detector (TEDI) for simultaneous measurements of the ion beam's thermal power and electrical current was developed and thoroughly tested. The detector is a combination of a well shielded faradaycup with a calorimeter and gives results with an accuracy of about 5 % in the range from 10 watts beam power up to 300 watts. Precisely calibrated, the TEDI can be used also as an energy detector for ion beams either energetic or intensive.

The work with the compact-PIG-source at present is directed on the production of high charge state ions around Ar 6^+ preferably in low magnetic fields. Parameter studies also on the ion extraction are going on.

The PIG Source "Sputtershort" Circuit

M. Müller, M.M. Khaouli and R. Rulfs
GSI Darmstadt

Introduction

Metal ion beams for the Unilac are produced using the sputtering effect in the PIG discharge. Short circuitry between the sputter electrode and the discharge chamber takes place frequently depending on the rather different discharge and operating conditions. Most of the sputtered material is condensing at the anode chamber walls forming more or less compact layers, thin films or whiskers. Low melting point materials even reevaporate, the anode presumed to be hot enough, and contribute to the ion source's metal ion efficiency. The gap between the sputter electrode and the anode is .5 mm (according to the average Debye-length of the PIG plasma), narrow enough to become bridged especially during the deadtime between two pulses when the source electrodes are cooling down at its surfaces. The massive stainless steel anode remains at high temperature for longer time than the small, well cooled sputter electrode which is collecting quickly evaporated material thereby favouring the whisker growth. In every case a "sputtershort" causes total loss of beam for some time - the worst case is a one hour ion source service.

Short Circuitry Burn Off Devices

Before 1981, when the ion source was equipped with small sputter electrodes (surface: 15 x 7 mm²) a "sputtershort" was burned off by aid of a simple device as shown in Fig. 1.

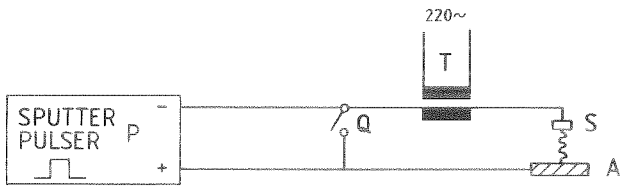


Fig. 1: Early "sputtershort" burn off device. Q: air pressure driven switcher. T: transformer 50 V/2 A. S: sputter electrode. A: anode. P: sputter pulser.

The transformer T in the short circuit was switched on manually to heat up the thin metal conductors between sputter electrode and anode until evaporation cuts the short. This device worked partly successful but it proved to be too weak when in 1981 long sputter electrodes (surface: 45 x 4 (7) mm²) were introduced. An improved version of the "sputtershort" burner is shown in Fig. 2.

The transformer was replaced by a powerful capacitor (stored energy: 100 Ws) switched also manually by the operator. Now the beam loss time depends only on the reaction velocity of man - still much too long.

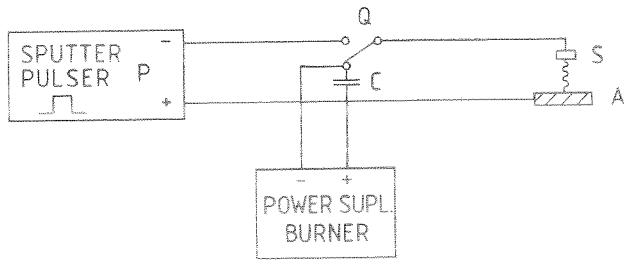


Fig. 2: Improved version of "sputtershort" burn off device.

Like the PIG discharge the sputter electrode potential is pulsed as well. The available time of at least 10 ms between two pulses (max. pulse length: 10 ms) is used for a watch-dog electronics to look for an eventually existing sputter electrode short circuit. This watch-dog electronics completes the sputter electrode circuitry as shown in Fig. 3.

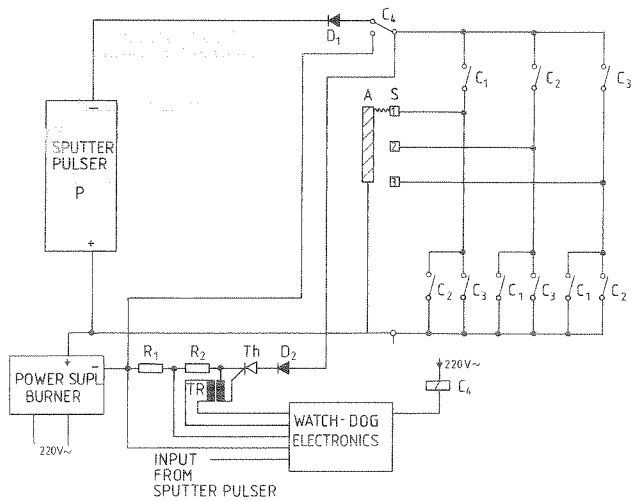


Fig. 3: "Sputtershort" burn off circuit diagram, accomplished by the three sputter electrode switching system (see "Unilac Injector", this report).

The circuit, built up by the elements R1, R2, Th, D2, the bridge A-S and the burner power supply, serves as searcher for the "sputtershort". From the sputter voltage signal a 10.5 ms delayed ignitor pulse for the thyristor Th is derived. In case of a short, there is an electrical current Ii = Ubr/R1 + R2 causing a voltage drop along R1 and triggering a time delay element to activate the switcher C4 which finally switches the burner directly to the "sputtershort". During this time the searcher circuit is shortened and the thyristor expires. A certain time later the switcher C4 is opened and sputtering for ion production goes on without significant loss of beam.

Improvements to the Unilac RF System

G. Hutter, W. Gutowski, W. Hartmann, G. Kube,
A. Morhardt, H. Valter, W. Vinzenz
GSI Darmstadt

The amplitude regulation loops of all rf amplifiers of the Unilac have been operated in a closed loop mode with the accelerator voltages. This operating mode has the disadvantage that a breakdown of the cavity voltage by an arc or by multipactoring leads to maximum rf output power (demanded by the regulator) into a mismatched load. Frequently, sparking of the amplifier cavities or the rf lines followed under these conditions, together with crowbar firing of the power supplies. Amplifiers with common power supplies were particularly effected by this problem. A protection system to avoid this had to be introduced for all rf amplifiers.

An analogue feedback circuit has existed in the 650 kW/27 MHz amplifiers. Making it faster and in addition monitoring the amplifier cavity voltage solved the problem there. At the 1.6 MW/108 MHz amplifiers, a digital interlock was built that disconnects the rf drive within 50 µs under fault conditions for the rest of the actual Unilac pulse. This does not influence the next normal 50 Hz synchronous pulse until a fault condition occurs again. Since the old measurement apparatus of the 100 kW/108 MHz amplifiers only processed averaged signals for most of the interesting values, a prototype of a completely new analogue measurement device[1] was built. It rapidly detects and monitors anode-and g2 current, output and reflected power, amplifier cavity voltage and anode loss of the final amplifiers and the drivers and has a feedback for all signals via an "analogue comparator".

For further development work of rf circuits, electronic devices, rf shielding measures and for tube tests, three new test stands were installed. The amplifier of the fourth Alvarez cavity, which is not always used in Unilac operation, had a large coaxial switch installed in its output line together with a 600 kW soda load. Two test stands for the 180 kW amplifiers were built with new 100 kVA and 20 kVA power supplies. The rf lines of these test stands are connected via a 2-way coaxial switch either to the above mentioned 600 kW load or to an x-ray shielded single-gap test cavity. A high percentage of the available test time during the past year was used to reduce rf radiation emitted outside the enclosure. Tests by the regulatory body (Deutsche Bundespost) of the upgraded Unilac rf system for acceptable emission were passed in October 1983.

The four common anode power supplies for each ten 180 kW amplifiers and their drivers had high failure rates because of mechanical aging of the motor driven isolating switches. All forty switches were replaced by a GSI-developed magnetic switch.

To achieve higher reliability and more output power at a better power-to-price ratio, a replacement of the Siemens tube RS1082CW in the final stage of the 180 kW amplifiers of the Unilac was studied. Since an improved input circuitry had been ordered in 1982 for all 29 amplifiers of this type, our investigations had to be reduced to tubes mechanically similar to the old one. The BBC tube CQ25-2 and the Siemens tube RS1084CJ fulfilled this requirement and, with integrated cooling jackets and higher maximum anode dissipation, promised higher output power.

The CQ25-2 was easily adapted by a change of the water connections and the anode flange. All circuits remained tunable in the range of the normal plungers. Dc tests showed a strong tendency of this tube to produce parasitic self oscillations in the region of 1.2 GHz, starting with anode currents of about 1 A. In rf operation, parasitic oscillations were also present in a medium range of output power. A pulsed output power of 192 kW could be reached, but with a low power amplification of < 13 dB.

The main difference between the RS1084CJ and the RS1082CW is the length of the active system, which is about 25 % larger for the RS1084CJ. The filament transformer, the support of the anode cooling jacket and the water connection had to be changed for adapting this tube.

Static current up to the maximum anode dissipation did not lead to parasitic oscillations, although this tube has a mutual conductance of 84 mA/V instead of 65 mA/V of the CQ25-2 and the RS2082CW. The tuning range of all circuits was large enough to compensate for the differences of the interelectrode capacitances.

In rf operation, 260 kW peak output power could be easily achieved with 25 % duty cycle. With the high power amplification factor of 30 (!), the driver amplifier was required to deliver even less power than for 180 kW output with the old tube. The efficiency of the anode rf conversion (without feed through drive power, filament-, g1- and g2 dissipation) was 77 %. The harmonic spectrum was acceptably low. After the test tube was in routine Unilac operation for three months without problems, it was decided to convert gradually all the 29 amplifiers to the RS1084CJ until the existing spare tubes are used up.

Reference

[1] G. Kube, GSI internal report, to be published.

Tests of a new 1.6 MW/108 MHz Amplifier-Powertube Combination

G. Hutter
GSI Darmstadt
K.H. Knobbe, Herfurth GmbH, Hamburg
I. Beling, J. Denteler, Siemens AG, Berlin, München

The Siemens tube RS2074SK, installed in a coaxial "GSI-type" amplifier cavity as well as a prototype amplifier with circular discs as resonant structures around an Eimac tube 8973 have shown their ability to deliver 1.6 MW pulsed rf power at 108 MHz with a duty cycle of 25 %[1].

The conversion from the 8973 to the RS2074SK inside the circular disc cavity was the object of an agreement between GSI, Siemens AG und Herfurth GmbH. The necessary adapting set, consisting of new input circuitry, some rings for the contacts of the tube socket and anode, a changed water connection, a larger rf filter for the filament feed lines and a new filament transformer was finished at the end of 1982.

First tests in 1983 showed that the new circuit between cathode and g1 was easily tunable to 108 MHz. The tuning range of the mainly unchanged g1-g2 circuit was large enough to compensate the tube change. The frequency shift of the anode -g2 circuit, however, was unexpectedly high. Instead of the wanted 108 MHz only 89 MHz were achieved, far out of the range of the normal tuner. The earlier measured short circuit resonances of the two tube types[1] explain about 10 MHz shift in the 3/4 λ anode resonator. Most of the remaining 9 MHz shift is produced by the changed anode support, as the circular discs remained the same.

To reach 108 MHz again, the final short circuit plane of the anode resonator (Fig. 1(1)) was provisionally shifted by the use of many additional spring contacted copper sheets (Fig.1(2)).

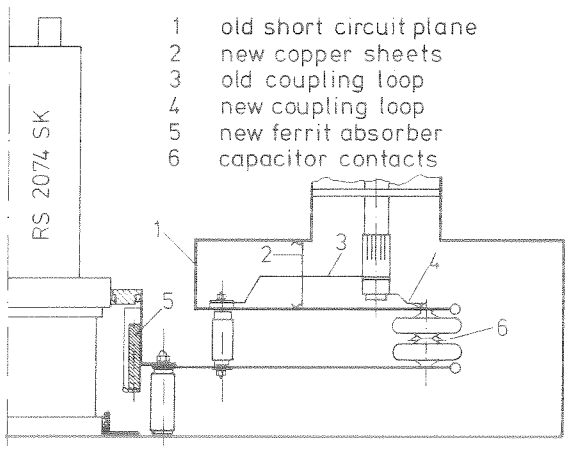


Fig. 1: Anode resonator

With applied dc voltages and a pulsed dc anode current, the tube produced two parasitic mode combinations at 565/1267 MHz and 705/1409 MHz.

The 705/1409 MHz modes started with pulse currents of 1.5 A, while the 565/1267 MHz modes led to supply trips at 30 A. Several absorbers tested, like resistors around the anode-ceramic or ferrites in the tube socket, showed no damping influence.

With rf drive, 1 MW pulsed power could be achieved. At this level, oscillations at 1267 MHz, arcs in the output cavity and high g2-current were the limiting factors. The high g2-current was a negative result of the added short circuit sheets, as those reduced the active space of the two inductive output coupling loops (Fig. 1(3)). This could be improved by a direct spring contact of the inner conductor of the output line to the circular disc (Fig. 1(4)), but loses the variation of load transformation.

Since additional resistors in the anode circuit were unable to damp the 1267 MHz oscillation, an absorber device was installed using the same principle[2] that is used with great success in the GSI type cavities (Fig. 1(5)).

Tests with dc current showed that the 705/1409 MHz modes were no longer present, while a 1250 MHz oscillation occured in a current range of 10-20 A.

In rf operation, starting with 5 % duty cycle, 1.6 MW could be achieved immediately without any parasitic oscillation. One could increase the duty cycle to the nominal 25 %, but no stable operation was possible. Sparks in the rf line to the waterload (burnt insulators), in the anode circuit (burnt spring contacts) and between cathode and g2 (too short distances by lack of symmetry) led to frequent breakdowns. After an improvement of these weak parts, the amplifier ran 7 hours uninterrupted at full power in December 1983. This test was ended by arcs in the anode circuit, caused by destroyed contacts of several dc block capacitors (Fig. 1(6)). In the old Eimac version, these capacitors had been placed in the current minimum. Since this field distribution was shifted by the additional short circuits, the capacitors had to withstand not only the current of the travelling wave, but also more than 1/3 of the resonant current.

Conclusion: It has been shown that the Siemens tube RS2074SK together with a sufficient damping is also able to deliver 1.6 MW with 25 % duty cycle when fitted into the Herfurth type amplifier. For reliable operation, the provisional test set up needs further improvements.

[1] G. Hutter, IEEE Trans.Nucl.Sci., Vol. NS-30, 1983
[2] G. Hutter, "Absorber", Application for a Patent 1981

1.5 MHz / 4.5 MHz RF-Chopper for the Unilac

W. Gutowski, G. Hutter
GSI Darmstadt

For an extension of the experimental possibilities at the Unilac, a resonant rf-chopper for the experimental hall was built that is able to kick 2 of 3 or 8 of 9 μ bunches out of the beam. The normal 27 MHz bunch separation of 37 ns can be increased to 110 ns or 330 ns by this device. Used together with a 9 MHz prebuncher developed parallel, the intensity loss of the chopper can be reduced by a factor of 2.5.

The main capacitance of a balanced series circuit, which is made resonant for 1.5 MHz or 4.5 MHz by two tunable and two disconnectable inductances (Fig. 1) is made of two 1 m long deflector plates. The Unilac beam passes the deflector plates only at the zero-axis crossing of the choosen frequency.

The newly developed rf system for delivering the necessary rf voltage consists further of a programmable frequency divider, an electronic phase-shifter, phase-, amplitude- and eigenfrequency-regulation, a 200 W solid state broad-band amplifier with push-pull output, control and monitoring system and power supplies (Fig. 2).

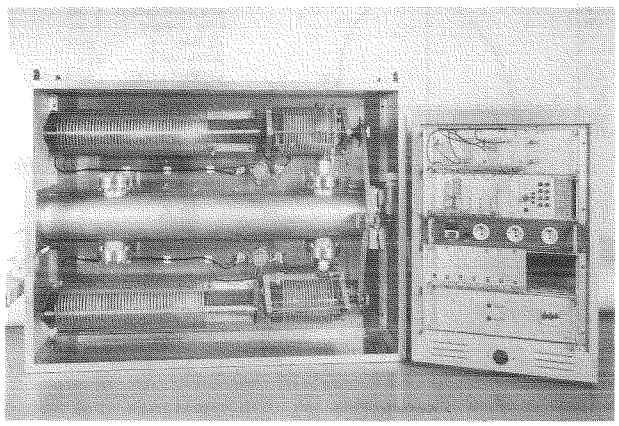


Fig. 2: Chopper with control unit

The block diagram of the signal conditioning circuit is shown in Fig. 1. First, the Unilac frequency of 27.12 MHz is digitized by a temperature-compensated Schmitt-trigger, which switches at zero input voltage.

By this a phase-jitter due to changed input amplitudes and temperature differences is minimized. The following programmable divider ($f_{out} = f_{in}/2(n+1)$, n = 1,2,3...) produces the wanted 4.5 MHz or 1.5 MHz (n = 2 or 8). This rectangular wave, phase-stable to the 27 MHz, is connected to one of the two inputs of a phase-frequency-detector. The output signal of this detector controls a VCO, which delivers a sinusoidal output signal near the wanted frequency. The feedback of this signal to the second input of the phase-frequency-detector closes the "phase-lock loop" circuit and synchronizes the output of the VCO with the digital input frequency.

By adding a dc voltage to the input of the VCO, the phase of its output can be shifted by ± 200 degrees. The same circuit, with some modifications, is also used for the phase-regulation. As the phase of the deflecting voltage should be regulated directly, an additional problem appears. For thermal reasons, the chopper is not driven cw, but with the normal Unilac macropulses. During the long (~ 15 ms) pauses between macropulses, the feedback of the phase lock receives no signal from the cavity. This would lead to a large frequency shift of the VCO. Once out of its limited bandwidth, the resonator could never be filled again and the VCO would never be able to lock. Therefore this input of the frequency-phase-detector is switched during the pauses from the resonator voltage to the output of the VCO, which locks this again to the input frequency.

In the next stage the phase-regulated rf is pulsed and amplitude-regulated by a PIN modulator and a PID controller. Finally a multistage amplifier drives the resonant circuit in series.

In the feedlines to the resonator, a phase-discriminator measures the phase between voltage and current. If the phase-relation becomes intolerably high, a motor adjusts the variable coils until the phase angle is zero and the resonator is retuned again.

In November 1983 the chopper was successfully used in 4.5 MHz operation in an experiment for the search of high spin-isomeres.

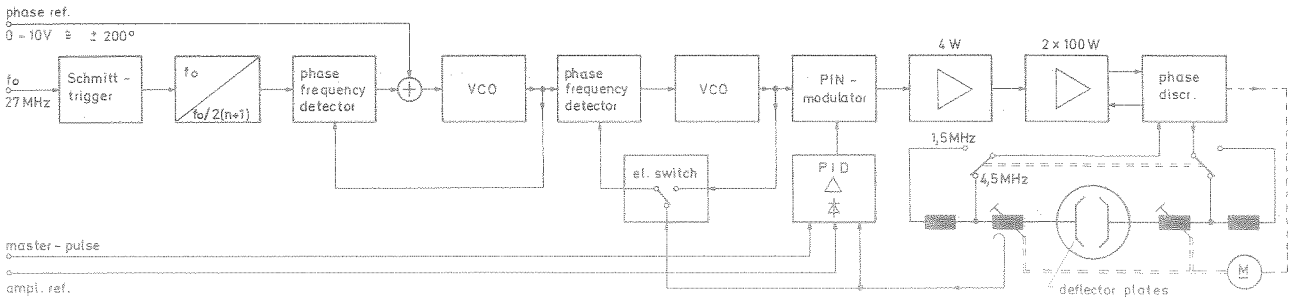


Fig. 1: Signal conditioning block diagram

Longitudinal Emittance Measurements

P. Strehl
GSI Darmstadt

For many experiments at the Unilac a knowledge and optimization of the beam parameters in the longitudinal phase space is essential. A measurement of those parameters is needed even for the operateurs, who have to set up all the rf-structures correctly. Therefore a procedure for determinating emittance ellipses in the ΔW-, Δφ-plane was developed and tested at the Unilac. The method described below may be applied at all rf-accelerators if bunch lengths can be measured.

Approximating the particle distribution in the ΔW-, Δφ-plane by ellipses two different algorithms can be used for the evaluation of the relevant ellipse parameters α, β, γ, ε.[1] The simpler method is based on a measurement of the bunch lengths at different positions along the accelerators as a function of the drift lengths and may be performed very easily by taking advantage of the capacitive pick-up system installed along the Unilac. The other one uses an rf-cavity operated +90 or -90 degrees stable phase to change the energy spread as a function of the rf-amplitude and, therefore, the bunch length at a single pick-up. This method is illustrated schematically in Fig. 1.

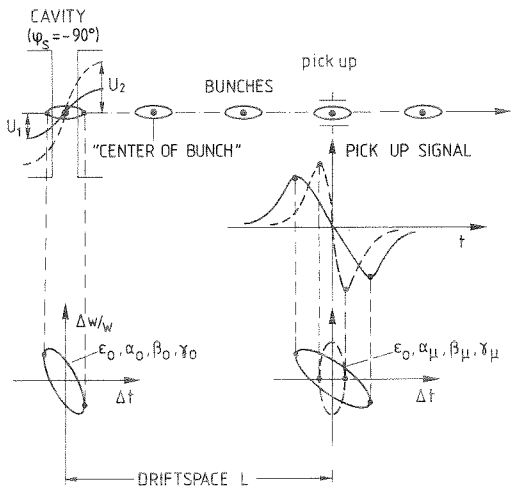


Fig. 1: Phase space measurement by using an rf-cavity with ϕs = -90° and variable rf-amplitude.

Both methods mentioned above use the relation between the ellipse parameter β and the measurable bunch width Δt to solve the algebraic equations derived from the transformation laws of emittance ellipse parameters for a drift space and/or the action of an rf-cavity. The mathematical procedure for the determination of α, β, γ, ε is straight forward as can be seen in the table of formulas. Although only three measured bunch lengths are needed to solve the equations, the measurement of more than 3 points is recommended to apply a least square fit algorithm implemented in the program.

FORMULAS

SINGLE PARTICLE TRANSFORMATION:

$$\begin{bmatrix} \Delta\varphi_1 \\ \Delta W_1/W_0 \end{bmatrix} = \begin{bmatrix} \alpha_{11} & \alpha_{12} \\ \alpha_{21} & \alpha_{22} \end{bmatrix} \begin{bmatrix} \Delta\varphi_0 \\ \Delta W_0/W_0 \end{bmatrix}$$

DRIFT SPACE: $\alpha_{11}=1$; $\alpha_{12}=K$; $\alpha_{21}=0$; $\alpha_{22}=1$; $K=-F_1 \cdot L\,(m)/\beta c$; $F_1=\pi \cdot f/1000c$

Rf-RESONATOR(±90°): $\alpha_{11}=1$, $\alpha_{12}=0$; $\alpha_{21}=D$; $\alpha_{22}=1$

$D=\zeta \cdot U \cdot T/W$; ζ = CHARGE STATE; U = MAXIMUM Rf-VOLTAGE; T = TRANSIT TIME FACTOR

Rf-RESONATOR + DRIFT SPACE: $\alpha_{11}=1+KD$; $\alpha_{12}=K$; $\alpha_{21}=D$; $\alpha_{22}=1$

TRANSFORMATION OF ELLIPSE PARAMETER β:

$$\beta_1 = \alpha_{11}^2 \beta_0 - 2\alpha_{11}\alpha_{12}\alpha_0 + \alpha_{12}^2 \gamma_0$$

EQUATION FOR LEAST SQUARES FIT: $A_\mu = B_\mu x + C_\mu y + E_\mu z$

$x = \varepsilon\beta_0$; $y = \varepsilon\alpha_0$; $z = \varepsilon\gamma_0$; $\varepsilon = \sqrt{xz - y^2}$

$A_\mu = (F_2 \cdot \Delta t_\mu)^2$; F_2=const. ; $B_\mu = (1+K_\mu D_\mu)^2$; $C_\mu = -2K_\mu(1+K_\mu D_\mu)$; $E_\mu = K_\mu^2$

Fig. 2 shows a computer plot of the calculated emittance ellipse at the output of the Wideröe prestripper accelerator using 4 capacitive pick-ups behind Wideröe tank 4 for the measurement of bunch length. For practical reasons the parameters ΔW/W, the relative energy spread, and Δt, the bunch length have been chosen for the ordinate and abscissa, respectively.

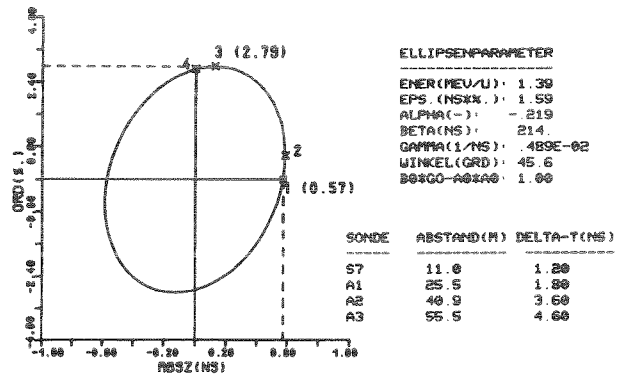


Fig. 2: Example for a computer plot.

Two of the coordinates in the emittance plot are of interest:

$\sqrt{\varepsilon\gamma}$ = Ordinate of point 3, which gives the maximum energy spread, and

$\sqrt{\varepsilon/\gamma}$ = Abscissa of point 1, related to the smallest bunch lengths, that may be achieved for a drifting beam. Many measurements under various accelerator conditions have been made. The accelerator experiments showed that the interesting parameters are very strongly influenced by accelerator conditions such as multiple charge state acceleration, use of rebunchers and the adjusted final energy. There is also a strong dependence on the proper setting of rf-parameters. Alvarez tank 1 in particular shows a strong variation of beam quality with the rf-amplitude.

Reference
[1] K.G. Steffen, "High Energy Beam Optics", Wiley, N.Y. 1965.

Unilac Beam Diagnostics with Particle Detectors

A. Ziem, P. Borisch
GSI Darmstadt

A system of six semiconductor detectors and one channel plate was installed at selected positions along the Unilac to provide effective optimization of beam parameters in the longitudinal phase space. Taking advantage of modern nuclear electronics as shown in Fig. 1 the following measurements can be performed:

- Determination of the beam energy spread ΔW
- Observation of time structure of the bunches
- Measurement of longitudinal emittance.

The semiconductors are of "surface barrier"-type with an active area of 50 mm and a 500 µm depletion depth, which ensures a complete stopping of all kind of ions up to the maximum Unilac energy. The semiconductors are mounted on standard compressed air actuators. Protection of the detectors against destruction by the beam and adjustment of counting rates is provided by a set of three beam attenuators installed at selected positions along the Unilac. The evaluation of the raw data is performed by an 8 k multichannel analyzer which will be linked to a computer in the future.

There are in principle two different methods to observe the beam quality (see Fig. 1). The pulse height distribution from the detector represents the energy distribution of the particles and, therefore, the energy spread can be determined directly by analyzing these signals. Unfortunately the energy resolution is only in the order of 1 % which has to be compared to typical Unilac values of some 1/10 %. Therefore only a strong mismatch of the machine can be observed in this case.

Taking advantage of the very stable Unilac rf-reference signal a time-of-flight technique is applied which results in an excellent time resolution better than 50 ps (see Fig. 2). This method has proven to be very useful for the optimization of time structure of the bunches. Combining both methods by using the channel plate in front of a semiconductor detector as a start detector the intensity distribution as a function of ΔW and Δt (i.e. the longitudinal emittance) can be displayed immediately.

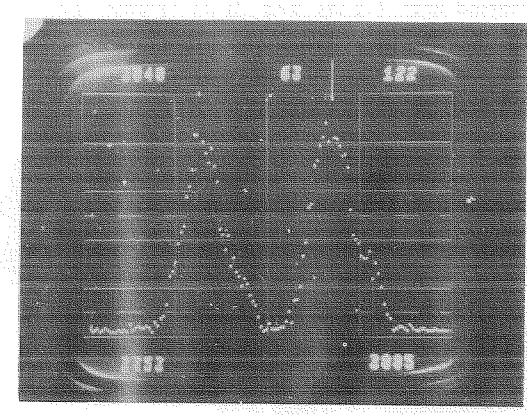


Fig. 2: Example of bunch length measurement ($^{48}Ti^{12+}$, 16 MeV/u resolution 10.5 ps per channel, FWHM 160 ps.

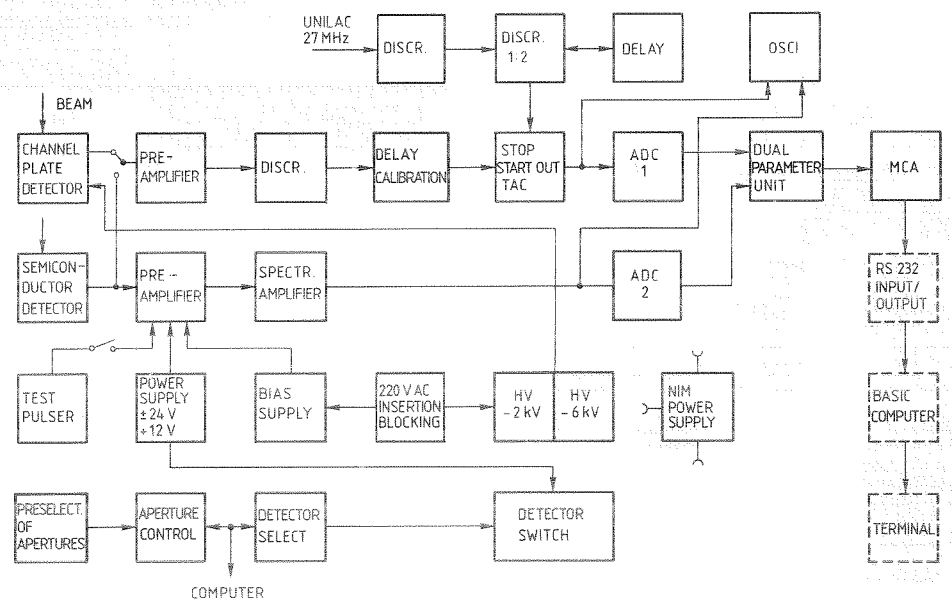


Fig. 1: Block-Diagram of the Unilac detection system for energy spread and time structure.

Capacitive Pick-Up versus Inductive Loop Monitor

H. Vilhjalmsson - GSI Darmstadt
M. Witzky - Fachhochschule Wiesbaden, Abt. Rüsselsheim

The aim of the study was to confirm the existing theory[1] with respect to signal amplitudes and shapes from beam monitors. Of further interest was the detection of beam displacement with two oppositedly mounted loop monitors which cannot be observed with circular capacitive pick-ups[2]. Therefore a 50 Ω loop monitor with 4 single loops in parallel was developed[3]. Its bandwidth is > 3 GHz with $\rho \leq 2\ \%$ @ t_r = 30 ps (time domain reflectometer). For bench tests two monitors of 5 cm and 40 cm length were built and tested with 1.2 ns and .3 ns (FWHM) unipolar(+) pulses. The reproduction of the 1.2 ns pulse was excellent, while the .3 ns pulse showed ringing at 3.14 GHz (Fig. 1 and 2).

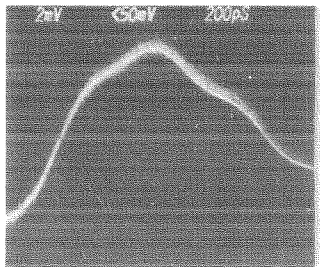


Fig. 1: 1.2 ns pulses (signals identical)

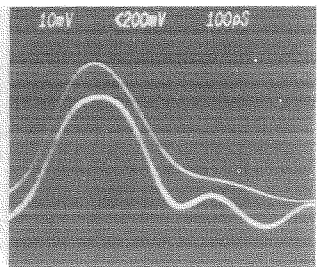


Fig. 2: .3 ns pulses (coupled signal with ringing)

Tests under beam were done with a set-up of two 5 cm monitors opposite each other in the horizontal plane as shown in Fig. 3. No attempts were made to match the inductive and capacitive pick-ups in lenght or aperture (5 : 1 cm and 8 : 3.5 cm).

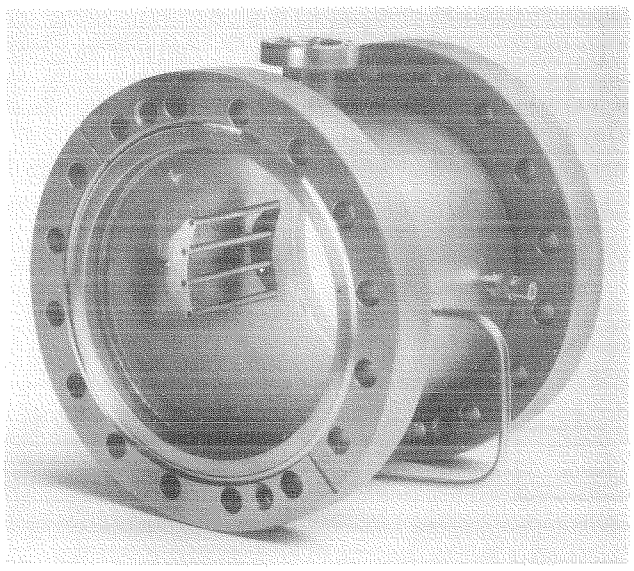


Fig. 3: Test set-up (length = 130 mm, inner diameter = 100 mm)

Results:

a) Signal shapes are in very good agreement with the theory.
b) The ratio of signal amplitudes (capacitive/inductive Σ-signal) was calculated to be 4.8. Measured was a ratio of 3. Considering bandwidth limitations (oscilloscope) and approximation with triangular bunch shape, the results are consistent (Fig. 4).
c) Beam displacement was observed with an oscilloscope and a spectrum analyzer (Fig. 5 to 7). The latter has the inherent advantage of higher sensitivity. The resolution with spectrum analyzer was ~ .5 dB/mm in the region of ± 5 mm around beam centre line. Nonlinearities were not observed within this limited range.

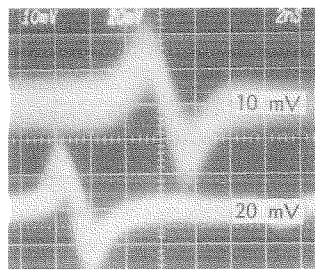


Fig. 4: Σ-signal (upper trace) and signal from cap. pick-up

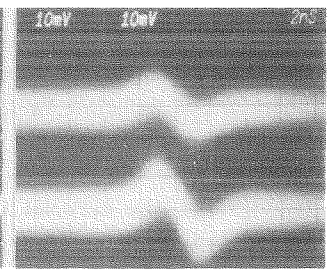


Fig. 5: Monitor signals (upper trace = left monitor)

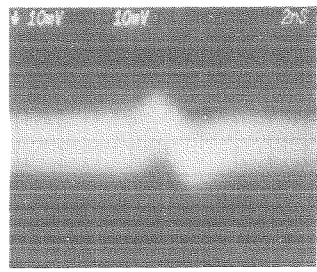


Fig. 6: Δ-signal (right minus left)

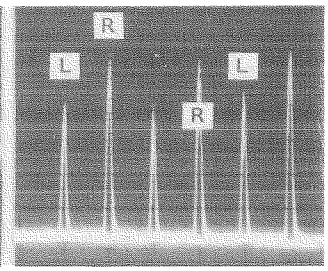


Fig. 7: Displacement observed with spectrum analyzer at 2 dB/div. (left monitor = lower spectrum)

References

[1] J. Glatz et al., Phasen- und Bunchformmessung am Unilac mit kapazitiven Sonden, GSI 73-1, Febr. 1973.
[2] P. Strehl et al., Das Phasensondensystem am Unilac, GSI 79-13, Dez. 1979.
[3] M. Witzky, Vergleich von induktiven und kapazitiven Pick-up- Systemen, Diplomarbeit, Jan. 1984.

The Beam Structure Demodulator
- A Nondestructive Current Monitoring System -

N. Schneider
GSI Darmstadt

At the Unilac different beam diagnostic systems are available: Faraday-cups, profile-grids and also current-transformers which are nondestructive, but not sufficiently sensitive. Therefore it was decided to develop a nondestructive and highly sensitive current monitoring system.
The solution resulted in an electronic signal processing system, well known in high frequency receiving stages.

As shown in Fig. 1 a newly designed capacitive pick-up is coupled with a coil to form a circuit, resonant at 81.3 MHz and is front-ended with an impedance converter ①. The 3rd harmonic of the 27.1 MHz Unilac rf-acceleration frequency proved to be convenient because of the good signal-to-noise ratio and low interference with the accelerator rf-generators.

The rf-signal (Fig. 2) is amplified, using an automatic gain stage ② and a second narrowband amplifier. The following demodulator ③ gives the demodulated Unilac macropulse (Fig. 3) at the output ④. In addition this signal shows the ion source modulation with a bandwidth of about 1 MHz.
After integration ⑤ in a regulator amplifier ⑥ a regulator current is generated. Owing to the nearly logarithmic characteristic of the PIN-diodes in the automatic gain stage the logarithmic signal at the output ⑦ is proportional to the beam current over about four decades above 10 nA. This current is indicated on analogue instruments and, converted by ADC's, is delivered to computers for further processing.
In this way a nondestructive, sensitive beam current monitoring system, which is easily controlled by computers, is obtained.

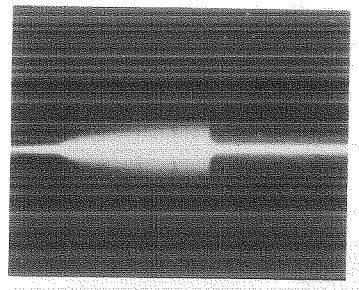


Fig. 2: Amplified rf-signal of the capacitive pick-up (1 ms/Div, 50 mV/Div, $^{232}Th^{10+}$, 200 nA beam current).

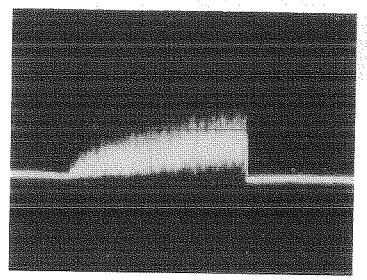


Fig. 3: Demodulated rf-signal (1 ms/Div, .5 V/Div).

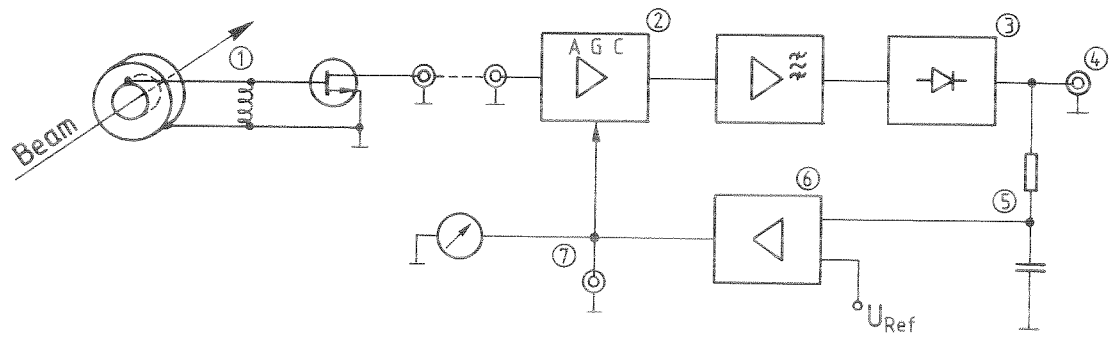


Fig. 1: Block-Diagram of the electronic processing equipment.

A Control System for the Unilac Injector

W. Jacoby, M.M. Khaouli, M. Müller
GSI Darmstadt

A computer control system for the Unilac injector was developed. A prototype is running an ion source test facility built up to study the injector control tasks as were source operation, ion beam extraction and diagnosis as well as production and optimization of charge state and mass spectra. A console was built up with respect to injector operating.

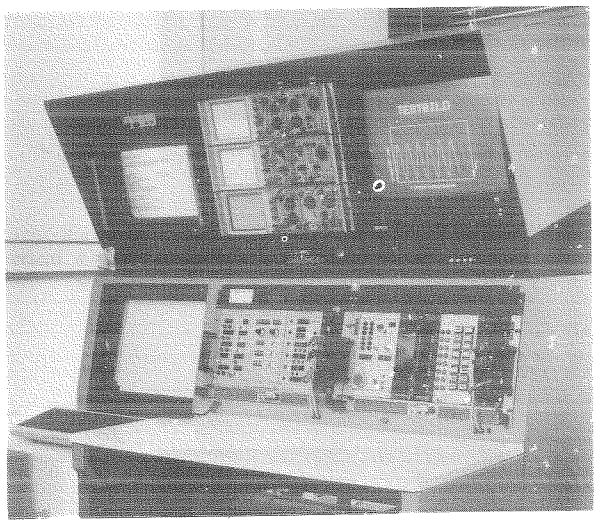


Fig. 1: The console.

Experimental Setup

The main parts of the facility are the test stand (ion source, extraction, beam line, and diagnosis), the CAMAC interface, and the console.

The practices of ion beam preparation - first recording a charge state spectrum and then running a mass spectrum of the desired charge state - are the same as the injector's.

All data are collected in machine-crates and then transferred via light link on a serial CAMAC branch highway to the console-crates. The CAMAC highway is controlled by a microcomputer.

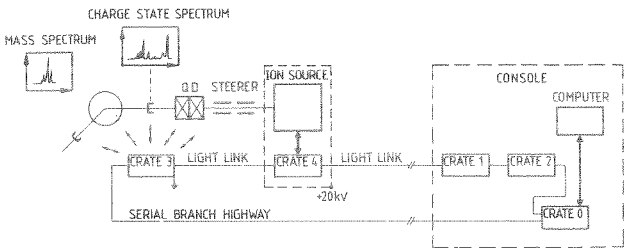


Fig. 2: Schematics of the test facility.

Rules of Development

The control system was built up with respect to the following topics:

- the number of light links had to be minimal → serial data transfer system
- the development time had to be short → system electronics - CAMAC
- the data polling had to be avoided → interrupt driven data transfer
- the user programs should be written and debugged easily → CATY5 CAMAC interpreter[1]
- non integrated interfacing should be avoided → the console control modules are CAMAC modules, control modules are test modules as well
- adjustment and service should be done by a single person → TTY connections are situated close to every part of the test facility
- all parameters of the test stand should be observed and adjusted in parallel → dedicated control modules.

Experimental Results



The control system is in permanent operation for more than eight months. Most failures are due to voltage drops of the line. Inspite of working under high voltage conditions the data transfer modules - serial branch driver, controllers and U-ports have not been destroyed. The setup can be controlled manually or computer aided. In manual mode there is no limitation for the operator's actions.

Fig. 3: The Kr isotopes of charge state 4^+ recorded by the control system.

The high speed of data transfer allows direct undelayed operating.

The computer aided mode will provide a guide line for the operator through the steps to produce and optimize an ion beam. Spectra will be recorded by scan programs and data will be obtained from other computers to set parameters. These programs are presently under development.

Spectra of Argon, Krypton and Xenon have been recorded, the quality of which matches those of the Unilac injector, there recorded without computer system. The profound operating principles of the injector have found to be valid for the new control system, too.

Yet the possibility of storing and recalling data offers a method to increase the reproducibility of injector operation.

Reference:

[1] Published by U.K. CAMAC Association

Development of a Pulsed Power-Supply

G. Breitenberger, R. Steiner
GSI Darmstadt

The UNILAC will be upgraded for pulse-to-pulse modulation to gain more flexibility in supplying the experiments with beams of different particles and energies and in serving as an injector into a synchrotron. As many as 50 dc-power-supplies for magnets must be replaced by pulsed ones. The dc-power-supplies do not provide the voltage U = LI for switching, which in some cases exceeds the dc-voltage by a factor of ten. The regulation loops are too slow for 25 Hz-operation and the efficiency of series regulators is too low in case of pulsing. On the other hand, 25 Hz-modulation cannot be achieved by conventional thyristor-switching from the electrical mains.

A prototype power-supply has been built to meet the requirements in switching speed, high efficiency, current precision and ripple better than 10^{-3} of nominal current I_N , and low cost. The magnet current, as shown in fig. 1, must ramp in 15 msec from one level to another. The difference of two subsequent levels might in worst case be the full nominal current.

The technique adopted for the prototype is a controlled bridge of switching transistors, as shown in Fig. 2, which has some advantages over a combination of switches and a series regulator.

For the bridge, Darlington transistor modules with nominal current of 300 A, nominal voltage of 450 V, with integrated diodes capable for the full reverse current, have been used. With optimal cooling, one module can dissipate 1,3 kW.

A major advantage of the transistor modules over conventional transistor banks is the potential-free cooling plate. With this feature, all modules (as many as ten for high current, high voltage) can be mounted in a very compact block onto one cooling plate with low inductances of the cabling between the elements. This evidently is important for current switching. The driver circuitry for the modules is mounted very close to the transistors and is optically decoupled from the regulator potential.

The operation principle for a unipolar power-supply is as follows: For ramping up, T1 and T4 are switched on. When the magnet current exceeds the correct value I_M (represented by a reference voltage) by $\Delta I = 5 \cdot 10^{-4} I_N$, T4 turns off with T1 still on. The current freewheels via T1 and D3. For $I_M - \Delta I$, T4 switches on again and takes over the current of D3, ramping the current up to $I_M + \Delta I$, and so on. The maximum switching rate is 25 kHz.

For ramping down, T1 and T4 are turned off (T2 and T3 remaining in off-state all the time), and the magnet discharges via D2, D3 into the capacitor-bank C1.

For high inductances, high voltages for ramping are needed. To limit the power dissipation of the switches and to reduce the switching rate, a second capacitor bank C2, an additional switch T5 and the diode D6 are implemented. The current ramps up via T5, T1 and T4, and down via D5, D3, and D2. The flattop current is supplied via D6, T1 on and T4 switching, while T5 is turned off. With the second capacitor bank C2 at (roughly) $U = L \cdot I_{max}$, U_d can be as low as $U = R \cdot I_{max}$ plus some volts for the voltage drop in D6, T1, and T4, thus again reducing power losses and switching rate of T4.

The same bridge is used for unipolar and bipolar power-supplies. For the unipolar ones, only T1, T4 (and, eventually, T5) are controlled, with D2, D3 serving as freewheeling diodes for the ramping down period. For bipolar types, all transistors are controlled. So, by just adding two more control-units, a normal power-supply can be transformed into a bipolar one.

Tests have shown that magnet currents up to 250 A can be achieved with one single bridge. Some care must be taken to keep T4 in its safe operating area. Short-time energy shocks at switching time must be absorbed in a ciruitry parallel to T4.

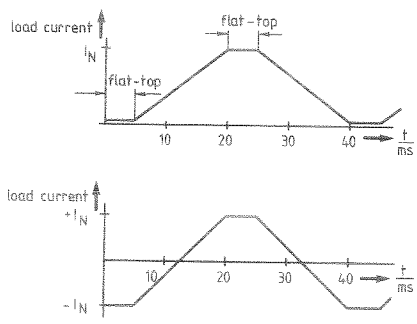


Fig. 1: Timing of unipolar and bipolar current

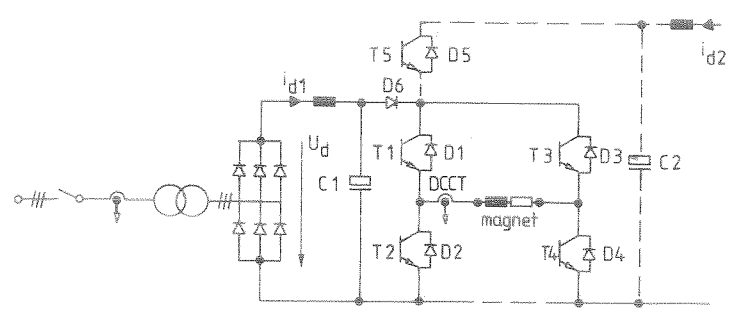


Fig. 2: Power part of the pulsed power supply

An ECR Source for Highly Stripped Ions

H. Schulte
GSI Darmstadt

Following the work on our first test source a larger, more versatile ECR source was finished by the end of the last year. The main design features of the new device were listed in the last report. First test runs showed immediately that the changes to the test source design had been successful. ECR heating of the plasma electrons is most obviously indicated by strong x-ray emission and the production of high charge state ions.

The new source (Fig. 1) consists of a 40 cm long, 5 cm diam. tubular copper microwave cavity surrounded by a set of seven coils which create a magnetic mirror field. The end coils 1,2,6,7 and the centre triplet (3,4,5) are separately powered for trimming of the field shape. A permanent magnet hexapole is inserted between the coils and the discharge tube. The composition of the two fields makes a minimum B structure with a closed resonance surface at 5 kG (indicated by the broken line), which should be well away from all cavity walls.

At the back end of the tube there is a pumping port and a waveguide feedthrough for RF power (14 GHz). Gas is fed in through a small bore in the centre of the end plate. The ion beam is extracted through an 8 mm diam. aperture at the opposite end of the tube near the front field maximum. The extractor bore is also 8 mm diam.. Normally an extraction voltage of 20 kV is used with a 30 mm gap width.

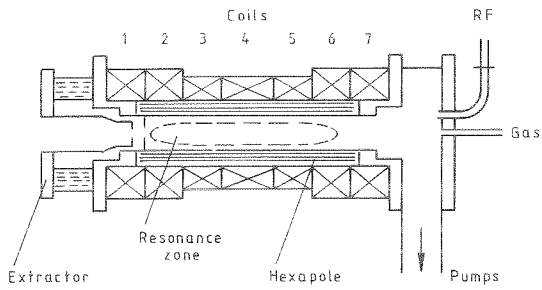


Fig. 1: Schematic of the GSI ECR source

The beam transport and analyzing system consists of an electrostatic quadrupole doublet at 0.6 m from the source and a circular dipole magnet at 2.4 m that serves as a 45° spectrometer. Ion currents are recorded in a shielded Faraday cup with 5 mm slit width. There is a second variable entrance slit 0.7 m in front of the dipole. The vacuum in the beam line is 10^{-7} Torr with the source operating.

A discharge is easily ignited in the source cavity at an RF power of 100 W. The optimum working pressure is estimated to be around 5×10^{-6} Torr. Pressure readings in the pumping port are normally a factor of 5 lower.

Test runs have been done so far only with oxygen and neon. The discharge parameters were optimized for the production of high charge states. This reflects some change in source behaviour and the strategy of development work. The new source seems more adapted (like other ECR sources) for the production of higher charge states at relatively low current (current density around 1 mA/cm²) and the ECR source is therefore no longer thought of as a possible replacement for the Unilac PIGs. Instead we decided to explore the capabilities of this source for the production of highly or totally stripped ions.

Optimizing the discharge parameters for high charge state generation requires careful control of the gas flow into the source (approx. 2 cm³/h STP). It is also sensitive to the coil currents (i.e. shape of the mirror field), though there is more than one "good" set of coil currents. This phenomenon is not yet understood but seems to reflect some plasma-wall interaction.

With a focused beam, charge spectra of oxygen and neon can be obtained easily up to $^{16}O^{7+}$ and $^{20}Ne^{8+}$ with intensities listed below. The search for the highest charge states, however, was badly hampered by impurity lines and the limited resolution of the analyzing system. Hydrogen, carbon, nitrogen and oxygen seem always to be present in the discharge due to outgassing of the cavity walls. Because of this $^{16}O^{8+}$ and $^{20}Ne^{10+}$ are obscured by H_2^+ and $^{18}O^{8+}$ (from a 98 % enriched sample) and $^{20}Ne^{9+}$ were not resolved from $^{16}O^{7+}$ impurity.

Z	1	2	3	4	5	6	7	8	9	10	
O	45	30	20	15	6	2	0.1	(30 pA)*			μA el
Ne	40	25	15	10	5	2	0.6	0.15	(50 pA)*		μA el

* unfocused beam ($^{18}O^{8+}$)

To obtain a better resolution we used an unfocused beam through an 8 mm entrance for the spectrometer and a 1 mm slit width at the Faraday cup. This drastically reduced the beam intensity and only 30 pA of $^{18}O^{8+}$ and 50 pA of $^{20}Ne^{9+}$ were measured. However, from H_2 intensity and scaling with other focused beam data we estimate that a factor of 100 could be gained with better beam optics and an appropriate spectrometer.

Further improvements of the source are expected with the installation of a 1st-stage plasma source and a variable gap extractor, but already it can deliver useful beams of highly stripped light ions for atomic physics experiments.

SIS - The Synchrotron Facility for Heavy Ions

K. Blasche, D. Böhne, B. Franzke, H. Prange, R. Steiner
GSI Darmstadt

In Spring of '83 the construction of the two-stage SIS synchrotron facility SIS 18 and SIS 100 was revised. It was proposed to replace the second-stage SIS 100 either by a smaller synchrotron SIS 65 ($B\rho$ = 65 Tm) or by a high-energy heavy ion collider with super conducting magnets[1]. A fast cycling synchrotron SIS 65 would provide high particle currents. Especially high proton currents could be used for the production of various secondary beams[2].

In a heavy ion collider facility very high centre-of-mass energies could be achieved. At present different groups in the USA study the construction of a heavy ion collider for top beam energies between 30 GeV/u and 100 GeV/u.

In addition, construction of a small experiment and storage ring (ESR) was studied. As mentioned in the '82 Annual Report the distance between SIS 18 and the experiment area provides adequate space for an optional ring, which could be used for beam cooling, in-ring experiments, beam storing or beam stacking. Meanwhile interest in such a small ring has grown. It was proposed to use it for accelerator studies in the heavy ion fusion program, and for a high temperature experiment that was designed to study the interaction of heavy ion beams with a fusion target[3].

It was recognized that a synchrotron storage ring facility, i.e. SIS 18 and the experiment and storage ring ESR would be highly desirable for the GSI research program in the near future. Later on the construction of a high energy collider facility could extend the range of energies for heavy ion collisions to CM-energies of several 10 GeV/u. Fig. 1 shows the arrangement of SIS 18 and ESR on the GSI site. The Unilac beam is transferred from the left side via the basement of the existing experiment hall to the underground tunnel of the SIS 18 ring. The beam from the SIS is either slowly extracted and sent into the new high energy experiment hall, or fast extracted and transferred to the ESR. In order to maintain the RF bunch structure the latter should have an integer fraction of the SIS 18 circumference. Since the small storage ring shall be used for the accumulation of completely stripped uranium ions, it is designed for a magnetic rigidity of at least $B\rho$ = 7 Tm. Hence, a circumference $C_{ESR} = 1/2\ C_{SIS} \approx 98$ m was chosen. At present a lattice design with six long straight sections of about 7 m length is being studied.

Project status: The SIS 18 ring design is completed. Prototypes for the RF-, vacuum and control system and injection components are well advanced. Procurement could start early in 1985. Only the building concept has to be revised in order to include the small storage ring and its linkage to the SIS 18 and to the experiment area. For the ESR a preliminary layout of the lattice was made. Yet the implications of the large variety of nuclear and atomic physics experiments, and especially the design of two merging beams are still under discussion. A final ring design is expected for the end of 1984. Another year will be required for the design of the components.

A completion of both rings near the end of 1988 is the present project aim, assuming appropriate funding rates and increase in engineering support.

References:

[1] Zwischenbericht zur SIS Zwei-Ring-Anlage
GSI-SIS-INT/83-1
[2] Modifikation des SIS-Vorschlags vom November 1981
GSI-SIS/83-1
[3] Vorschlag eines Speicherring-Experiments SITAR für gekühlte Schwerionen im Hochstrombetrieb
GSI-SIT-INT/83

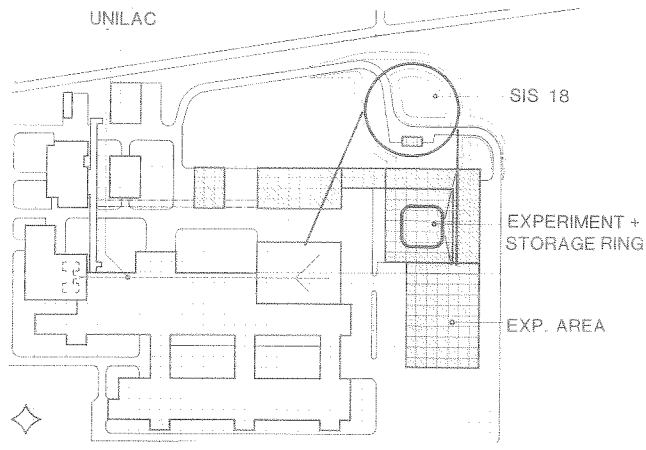


Fig. 1: Site layout for the synchrotron facility with SIS 18 and an experiment and storage ring.

Multiturn-injection for high currents

H. Eickhoff
GSI Darmstadt

A) Introduction

In most existing synchrotrons, in which 'multiturn-injection' is used, the injected current is relatively small, and the 'Laslett-tune shift' due to space charge is less than 0.25. For high currents, however, ($\Delta Q \gtrsim 0.25$) a lot of space charge effects have to be considered for the multiturn-injection (influence of resonances, emittance- growth, etc.) These effects are not only important for heavy ion fusion drivers, where the injection of very intense beams over a few turns is intended; they are as important for the SIS-project, where the injection of up to 100 turns is considered.

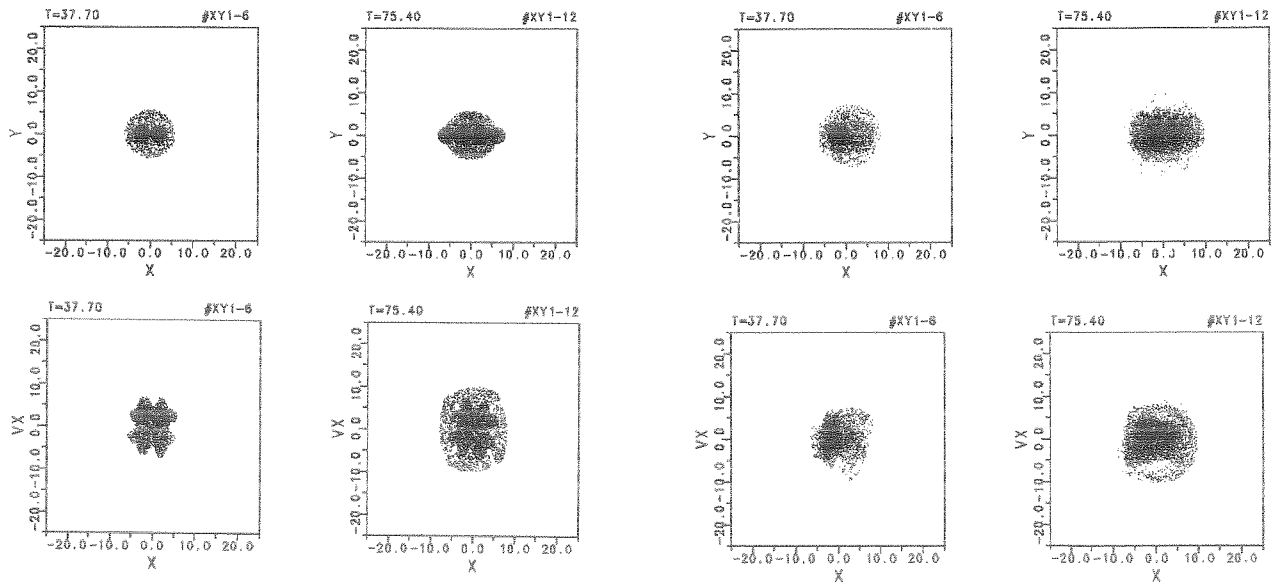
B) Calculations

The calculations have been performed with a modified version of the computer code SCOP2, a two dimensional particle-simulation code, which solves the envelope-equation for a sample of particles, taking space charge effects into account (1).
It is possible to perform calculations for different initial particle distributions (K-V-distr., waterbag-distr. and gaussian distr.) and for constant or periodic focusing structures.
For the calculation of multiturn injection the program had to be modified in order to take the time dependent displacement of the closed orbit during the injection process and the variing particle number into account.

In order to limit statistical errors the program has to work with a sufficient number of particles inside the emittance area. The time steps between two sequential calculations has to be relatively small in order to take the betatron motion of the particles properly into account.
Due to these requirements the calculations of the real injection process are very time consuming. The first test runs are based on simple assumptions (initial K-V-distibution, constant gradient focusing, ideal machine) and the results are therefore very preliminary.
In Fig. 1 a comparison is shown for a 12-turn injection with and without space charge ($Q = 1.25$), the tune shift due to space charge is assumed to be 0.1. The times correspond to the situation when 6 (T=37.7) and 12 (T=75.4) turns are injected.

The first results show, that the space charge effects even at a relatively low tune shift have a strong impact on the shape and orientation of the injected emittances, so that this influence on the injection procedure has to be considered very carefully.

1) I. Bozsik, I. Hofmann, Nuc. Instr. and Meth., 187(1981)



a) current = 0

b) current ≠ 0

Fig. 1: Phase space diagrams for multiturn injection

A Novel Method of Bunching Slowly Extracted Synchrotron Beams.

B. Franzke, GSI - Darmstadt

Extreme longitudinal bunching of ion beams is practiced at rf-linacs, cyclotrons and even direct voltage machines. At synchrotrons there is, up to the present, no practical experience with the production of short bunches suitable for time of flight analysis of collision products. A very promising idea has been described in the SIS-proposal. Its characteristic feature is the conservation of the good injector linac (UNILAC) beam bunches during multiturn injection, acceleration, and slow extraction in SIS 18. For this reason, high harmonic (h=38) instead of the standard (h=4) accelerating cavities are required. The most important disadvantage of this mode of operation is the drastic reduction of the mean ion current out of SIS, due to longitudinal space charge forces which tend to destroy the good bunch structure. Compared to the values given by the vertical Laslett tune spread of $\Delta Q_v \leq 0.25$ the number of ions per acceleration cycle is reduced by roughly a factor 100. The following procedure being investigated by numerical simulation may be considered as an attempt to overcome this strong reduction of beam current out of SIS 18:

→ Multiturn injection, rf-capture, and acceleration are performed in the standard operation mode, i.e. by using the h=4 cavities. On the flat top, the mean ion momentum is slightly above the extraction level p_{ext}, and the momentum spread is decreased to $\Delta p/p \approx 0.1\%$ by slow debunching. Due to the natural chromaticity of the ring $\xi_h \approx -1.3$ the horizontal betatron tune Q_h is a sufficient strong function of the ion momentum to enable a 'momentum discriminating' extraction method.

→ Q_h is set to the value where ions with momenta p_{ext} would be on a sextupole resonance line ($Q_{res}=13/3$ for SIS 18). The exciting sextupoles are switched on. At this time the beam is circulating nearly unperturbated because Q_h of all ions is far enough from the resonance value.

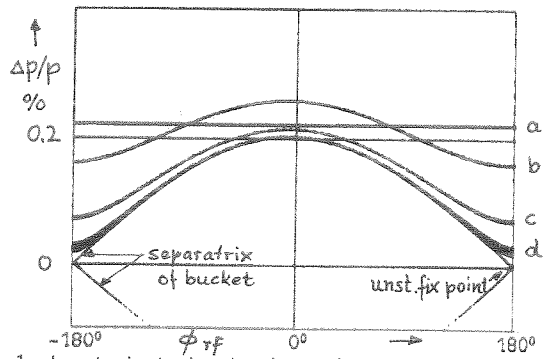


Fig. 1: Ion trajectories in the $\Delta p/p$ vs. rf-phase plane of SIS 18 at different stages of the extraction procedure: (a) without rf, (b) full rf-amplitude, (c,d) decelerated vs. p_{ext}.

→ A high harmonic, fixed frequency cavity is switched on forming empty rf-buckets which are stationary with respect to p_{ext}. The rf-voltage is increased slowly to an amplitude depending on the electrical rigidity of the beam. The beam momenta stably oscillate outside the stationary rf-buckets. Near the unstable fix points at ($\phi_{rf}=\pm 180°, p=p_{ext}$) the ion momenta come close to but do not cross the resonance line p_{ext} or Q_{res}, respectively (Fig. 1).

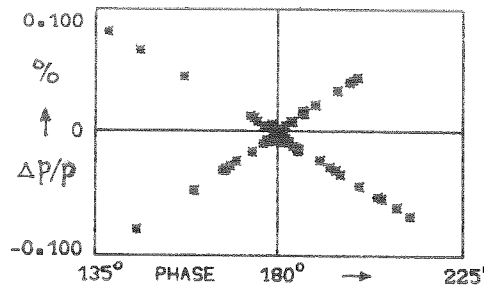


Fig. 2: Distribution in longitudinal phase plane of ions extracted out of SIS 18 by the described method (simulation!). Approximately 90 out of 100 coasting particles were extracted, 50% inside the small core of the bunch.
Bunch core: $\tau \approx \pm 0.3$ ns, $\Delta p/p \approx \pm 1 \times 10^{-4}$
Beam: 453 MeV/u-U^{92+}, $Q_h = 4.33$, $Q_v = 3.4$
Rf: h=38 (42 MHz), $U_{rf} = 300$ kV
Axial DC-Voltage: $U_{ax} = -25$ V

→ The beam is pushed slowly towards resonance: either by increasing the rf-amplitude or better by an axial DC-voltage from an induction module as installed in Saturne II at Saclay. The rf-phase precession of ions that pass the fix points close to p_{ext} is very small. Their horizontal betatron amplitudes are increased from turn to turn. They reach the gap of the electrostatic septum and are deflected into the extraction channel. The extracted beam is bunched around the fix point with respect to both rf-phase and momentum (Fig. 2).

→ The bunch structure may be improved by a rf-deflector working on a higher harmonic of the bunch frequency. The beam current in the extraction channel may be measured and controlled by a feed back system acting on the rf-amplitude or the current change rate of the induction module.

On the Ion Optical Transfer Matrix of Dipole Magnets as Given by the Shape of Their End Fields

B. Langenbeck
GSI Darmstadt

The contribution of the stray fields of the magnet ends to the ion optical behavior of a beam transport system is the more important the larger the apertures of the system are. A procedure was developed to determine the ion optical transformation matrix of homogeneous dipole magnets with parallel end contours taking fully into account the effect of the stray fields upon them without any approximations. The special design of bending magnets with parallel end faces which is in many cases induced by their construction from iron laminae is frequently chosen for the use in particle accelerators and is also foreseen for the proposed large aperture heavy ion synchrotron SIS.

Field measurements in those magnets may be easily represented in a single Carthesian coordinate system with the axis ξ and σ as is indicated in figure 1. In the magnet midplane normally only a z-component (perpendicular to the midplane) of the flux density will be present which does not depend on the ξ-coordinate because we assume homogeneity of the field in the center of the dipole. Figure 2 shows a typical graph of a measured field distribution along the σ-axis. If the poles are not rectangular but curved in adaptation to the central ion trajectory to save weight we still assume that the measurements were done perpendicular to the magnet ends. In the magnet center which in many cases is then not easy to reach by the measurement equipment we put the distribution function $b(\sigma) = B(\sigma)/B_o$ equal to unity.

The ion optical matrix elements C, S, D and T as given in the curved coordinate system x-s-z, also indicated in figure 1, are defined by the equations[1,2]

$$x_1 = C_x\, x_o + S_x\, x_o' + D\, \Delta p/p_o$$

$$x_1' = C_x'\, x_o + S_x'\, x_o' + D'\, \Delta p/p_o$$

$$z_1 = C_z\, z_o + S_z\, z_o'$$

$$z_1' = C_z'\, z_o + S_z'\, z_o'$$

$$\Delta \ell = T_C\, x_o + T_S\, x_o' + T_D\, \Delta p/p_o$$

where one calls

- C cosine like trajectories
- S sine like trajectories
- D dispersion trajectory and
- T path length coefficients

x_o, x_o', z_o, z_o' and x_1, x_1', z_1, z_1' are the phase space coordinates of the particle when reaching and leaving the field distribution respectively. $\Delta p/p_o$ and $\Delta \ell$ mean the deviations of momentum and path length from the values of a particle on the central trajectory.

In the dispersive plane the matrix elements are given by

$$C_x = \cos\beta_2 / \cos\beta_1 \quad , \quad C_x' = 0$$

$$S_x = I \cos\beta_2 \cos\beta_1 \quad , \quad S_x' = 1/C_x$$

$$D = -J/\rho_o \cos\beta_2 \quad , \quad D' = -\ell_m/\rho_o/\cos\beta_2$$

$$T_C = -\ell_m/\rho_o/\cos\beta_1 \quad , \quad T_S = (J - \ell_m\, I) \cos\beta_1/\rho_o$$

$$T_D = (\ell_m\, J - K)/(\rho_o)^2$$

β_1 and β_2 mean the angles of the central trajectory with the normale onto the entrance and exit pole contour (fig.1), ℓ_m the magnetic length and ρ_o the effective bending radius:

$$\ell_m = \int b(\sigma)\, d\sigma$$

$$\rho_o = \ell_m/[\sin\beta_2 + \sin\beta_1]$$

For the type of magnet discussed here $\beta_1 + \beta_2 = \alpha$ with α being the deflection angle. For a symmetrical use of the magnet in an accelerator we have $\beta_1 = \beta_2 = \alpha/2$.

I, J and K represent the integrals

$$I = \int [1-f^2(\sigma)]^{-3/2}\, d\sigma$$

$$J = \int g(\sigma)\, [1-f^2(\sigma)]^{-3/2}\, d\sigma$$

$$K = \int g^2(\sigma)\, [1-f^2(\sigma)]^{-3/2}\, d\sigma$$

The two functions $g(\sigma)$ and $f(\sigma)$ of the integrands are given by the distribution function $b(\sigma)$

$$g(\sigma) = \int_0^\sigma b(\eta)\, d\eta$$

$$f(\sigma) = g(\sigma)/\rho_o - \sin\beta_1$$

If the x-axis of the curved coordinate system is oriented into the opposite direction compared with the definition in figure 1, the matrix elements D, D', T_C and T_S change their sign.

To determine the matrix elements of the non-dispersive plane we must solve the differential equations

$$(1-f^2)\, d^2C/d\sigma^2 - f\, df/d\sigma\, dC/d\sigma - f\, d^2f/d\sigma^2\, C = 0$$

$$(1-f^2)\, d^2S/d\sigma^2 - f\, df/d\sigma\, dS/d\sigma - f\, d^2f/d\sigma^2\, S = 0$$

with the initial conditions

$$C(0) = 1\ ,\ dC/d\sigma(0) = 0$$

$$S(0) = 0\ ,\ dS/d\sigma(0) = 1/\cos\beta_1$$

The matrix elements are

$$C_z = C(\sigma_e)\ ,\ C_z' = dC/d\sigma(\sigma_e)\cos\beta_2$$

$$S_z = S(\sigma_e)\ ,\ S_z' = dS/d\sigma(\sigma_e)\cos\beta_2$$

The solutions of the differential equations can not be given in elementary terms. But this is not a big handicap. Programming of the equations does not mean more work than evaluation of the integrals I, J and K in the dispersive plane if one takes advantage of the routine RKGS in the scientific subroutine package[3] (Runge-Kutta method).

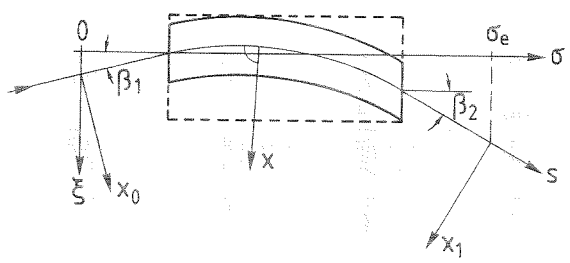


Fig. 1: Coordinate systems for field measurements (ξ-σ) and for ion optic (x-s) in a bending magnet with parallel end faces.

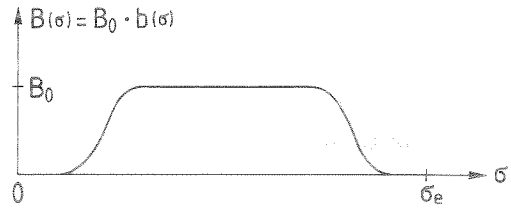


Fig. 2: Typical graph of field measurements in a bending magnet with parallel end faces.

References:

[1] Klaus G. Steffen, High Energy Beam Optics, Interscience Publishers (1965)

[2] Karl L. Brown, SLAC 75, Stanford University (1967)

[3] Scientific Subroutine Package (SSP), International Business Machines (IBM)

MIRKO - An Interactive Program for Beam Lines and Synchrotrons

B. Franczak
GSI Darmstadt

Introduction and Summary

The interactive computer program MIRKO is operated from a terminal and has a command structure, which enables the user to edit data, perform calculations, and to obtain alpha or graphics output on the terminal in any desired sequence. With graphics one can recognize the properties of an optical system much faster than with numbers only. Thus modifications of input data depending on the results of calculations can be made easily without stopping and restarting the program.
Higher order effects can sometimes influence the first order design. Therefore, particle tracking capability was included in MIRKO as well as the calculation of stop band widths for synchrotrons. Consequently a large variety of phenomena can be studied with one program in one session based upon exactly the same data for the optical system and the possibility of fast switching between the different features.

At present about 110 commands are available and the following list gives an impression of what can be done with MIRKO:

- Editing of optical systems - input of new elements, copy, move, delete groups of elements, change parameters, define variables, list elements on the terminal

- Optimization and fitting - define constraints, list on terminal, perform fitting calculations, restore previous status if iteration failed

- Graphics - plot of ellipses, envelopes on a graphics display, fit envelopes using the cursor, define mode of envelopes

- Alpha output on terminal - envelopes, ellipses at the end, kind of particle, beam current, behavior of reference particle, momentum resolution in phase space, transfer matrix, elapsed CPU-time

- Synchrotron design - define normal period, number of periods, evaluate tune, chromaticity, transition energy, closed orbit, tune the machine to given values, for multipoles: calculate stopband widths, perform particle tracking, find fixed points and separatrices

- Documentation - list all data describing the system on the line printer, plot envelopes and ellipses on the plotter, prepare data for auxiliary programs: plot of tune and chromaticity vs. momentum, transition energy vs. tune

- Data storage - save system and beam on direct access dataset, save quadrupole settings only, save procedures, read system, rename, delete in dataset, skip to another system, list all stored systems.

2. Linear Optics

Optical elements as well as the beam are represented by 6×6 matrices. The theory has been described elsewhere[1]. The following elements can be treated: drift space, quadrupole, dipole, pole face rotation, misalignment, and arbitary matrices. For nondispersive systems the matrix dimensions can be set to 4, thus reducing the required CPU-time considerably.
As an alternative to the ellipse notation single particles can also be transformed through the system. This allows the investigation of the behavior of particles with different momenta in dispersive systems.
Up to 6 parameters of the optical elements can be defined as variables to meet some fitting constraints. These can be elements of the beam matrix at the end of the system, elements of the transfer matrix, or their sum or difference, and several others.

Beam envelopes are calculated along the system and can be displayed on a graphics terminal. Fig. 1 shows the horizontal envelope through a focussing channel with triplets, one of them being misaligned.

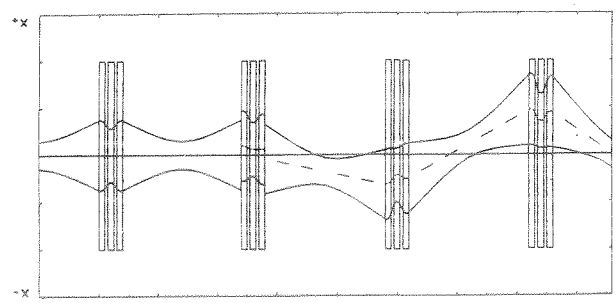


Fig. 1: Horizontal envelope in a triplet channel, the second triplet is misaligned, and the dashed line shows the center of the beam.

Cyclic Accelerators consist basically of beam lines with a periodic structure. Therefore, an optical system calculated with MIRKO can be considered as a superperiod of

a synchrotron. Now the frequency of betatron oscillations (Q-value), the transition energy, and the stationary ellipsoid (alpha and beta functions) can be evaluated and set as the input beam. It is possible to tune the maschine to given Q-values using the strengths of the quadrupoles, or anything else, as variables.
At high currents the eletrostatic forces between the particles cannot be neglected. In the case of constant current density over the cross section, the defocussing forces become linear, and under this assumption MIRKO can calculate the effects of space charge using thin lenses.

3. Aberrations and Chromaticity

The chromaticity is defined as the derivative of the tune (Q-value) with respect to the momentum deviation. It is determined by aberrations of second order in the system, while higher order contributions cause the chromaticity itself to be dependent on momentum.
In MIRKO a reference particle is defined, which is tracked through the system and takes into account all aberrations according to its actual coordinates in six dimensional phase space.

For chromaticity evaluation a particle with small momentum deviation is put on its closed orbit.

A. Dragt describes a method for exact numerical calculation of chromaticity[2]. He also gives detailed lattice data for the proposed protron storage ring at Los Alamos. Using these data chromaticity calculations with MIRKO differ less than 10^{-4} from his results. Also with sextupoles for chromaticity correction the difference is about 10^{-3}.

4. Tracking through Nonlinear Elements

In MIRKO normal elements are represented by first order matrices only and all multipoles are introduced by thin nonlinear lenses. This approximation seems to be tolerable, since multipoles are usually weak compared to the normal elements. Such a thin lens leaves the transverse spatial coordinates of a particle unchanged, while a contribution depending on these is added to the slopes (kick). Thus phase space is conserved when passing a thin multipole.

MIRKO provides interactive graphics for investigation of problems concerning fixed points, separatrices, slow extraction, nonlinear motion etc. The starting coordinates in transverse phase space can be set with the cursor and a key stroke represents a command i.e. to transform and display several times, to look for fixed points, generate pattern of input points, etc. Fig. 2 shows as an example the particle behavior close to a third integer resonance used for extraction and inside a half integer stopband stabilized with octupoles.

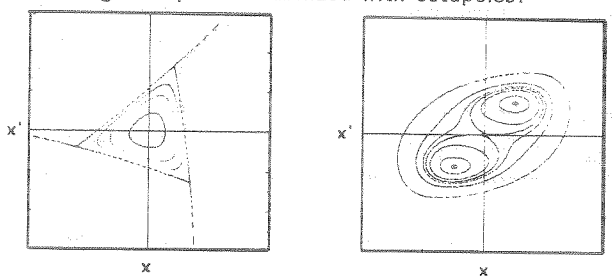


Fig. 2: Particle tracking in horizontal phase space. Left: close to a third integer resonance, three unstable fixed points with separatrices and several closed and open lines for invariants of motion, dots represent particle coordinates after 3 revolutions. Right: inside a half integer resonance exited by a perturbing quadrupole, stabilized for higher amplitudes by octupoled.

Reference:

[1] K.L. Brown, SLAC-Report 75(1969)

[2] A.J. Dragt, Exact Numerical Calculation of Chromaticity in Small Rings, Particle Accelerators Vol.12(1982), pp. 205-218

Energy, Luminosity, and Current Limits for a Heavy Ion Collider

K. Blasche
GSI Darmstadt

1. ENERGY

In a colliding beam device the total energy E_{CM} which is available in the centre-of-mass system (CM) of the two colliding nuclei is simply the sum of the total energies E_i of each collision partner, i.e. $E_{CM} = 2E_i$. For a conventional accelerator where a particle with total energy E_i impinges upon one of the same mass at rest in the target, the energy in the CM-system is given by $E_{CM} = mc^2\sqrt{(2\ E_1/mc^2)+2}$ where mc^2 is the rest energy of the particles. In this case the CM-system is moving and absorbs a large fraction of the available energy. In Fig. 1 the kinetic CM-energy $T_{CM} = E_{CM} - 2mc^2$ is plotted for both a heavy ion synchrotron and a collider. With a collider of moderate size which is designed for a magnetic rigidity of $B\rho$ = 65 Tm (ISR: $B\rho$ = 105 Tm) the same CM-energies of about 15 GeV/u could be provided as with a very large synchrotron like the SPS ($B\rho$ = 1250 Tm).

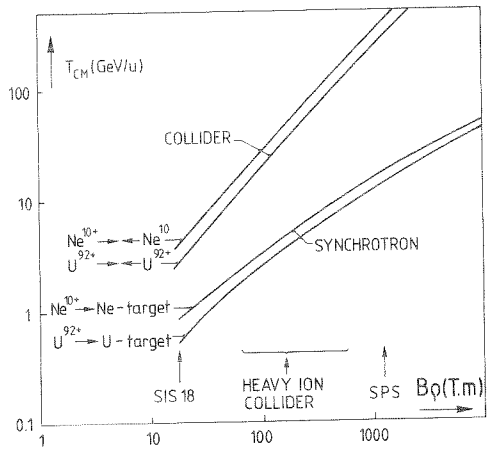


Fig. 1: Kinetic CM-energies for collider experiments (a) and for projectile-target experiments (b).

2. LUMINOSITY

Another significant parameter in a collider is the luminosity L which determines the reaction rate N_R for any specific reaction with a cross-section σ i.e. $N_R = L \cdot \sigma$. To a first approximation the total cross-section for two colliding heavy ion beams is given by the size of the nuclei, i.e. for neon about $\sigma_{Ne} = 10\ \pi \cdot 10^{-26}$cm² and for uranium about $\sigma_U = 50\ \pi \cdot 10^{-26}$cm². Therefore about 1000 reactions/s (about 1 % or 10 of those may be central collisions) could be expected at luminosities $L_{Ne} = 3 \cdot 10^{27}$cm^{-2}s^{-1} for neon and $L_U = 6 \cdot 10^{26}$cm^{-2}s^{-1} for uranium (Fig. 2).

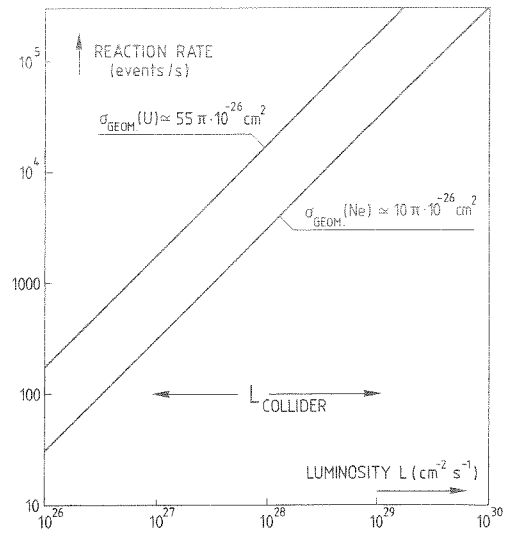


Fig. 2: Luminosities for a heavy ion collider

The luminosity in a collider is [1]

$$L = \frac{1}{ce^2} \frac{I_1 \cdot I_2}{h\ tg\ \alpha/2}$$

where

I_1, I_2 are the circulating particle currents,
h is the beam height, and
α is the crossing angle in the horizontal plane.

In the ISR α was fixed at 14.77°. However, for a new intersection design α = 1° may be feasible. Beam height at the intersection is given by $h \approx 2\sqrt{(E/\pi) \cdot \beta_{vi}}$ i.e. for $E = 4\pi \cdot 10^{-6}$m and for β_{vi} = 1 m we get h = 0.4 cm. The limits for the particle current will be discussed in the following paragraph. The maximum particle currents are about 1 A for neon and 0.1 A for uranium.

With $1/(ce^2) = 1.3 \cdot 10^{-27} A^{-2} s^{-1} cm^{-1}$ the following luminosities result: $L_{Ne} = 4 \cdot 10^{29}$cm^{-2}s^{-1} for neon and $L_U = 4 \cdot 10^{-27}$cm^{-2}s^{-1} for uranium; the total reaction rates which could be expected with these luminosities are 100000 s^{-1} for neon and 7000 s^{-1} for uranium beams. Furthermore, it should be discussed thoroughly, if beam cooling and bunching could give even greater luminosities.

3. PARTICLE CURRENTS

The number of heavy ions one can accumulate in a collider ring is restricted by the available aperture and the density of the injected beams. In principle the six-dimensional hyper-volume in x,x'; y,y'; $\Delta p/p$, z is available for accumulation. The ISR way to fill part of it is RF-stacking. Consider the particle distribution in the $(\Delta E/E,t)$ phase plane shown in Fig. 3 after injection of two synchrotron pulses which fill the circumference. The area available for stacking is shaded in the diagram. Now, the maximum number n_p of pulses which can be stacked is equal to the ratio of the total area to the area occupied by the four bunches of one synchrotron pulse. Both areas may be expressed in terms of $\Delta p/mc$ and Φ_{RF} since these are canonically conjugated coordinates:

$$n_p = \frac{(\Delta p/p)_c \, (p/mc) 2\pi}{4 \, A_B}$$

The bunch area A_B is determined by the adiabatic RF trapping process at injection into the synchrotron that serves as an injector machine for the collider facility. RF-trapping of the Unilac beam in a heavy ion synchrotron leads to $A_B \approx 0.001$.

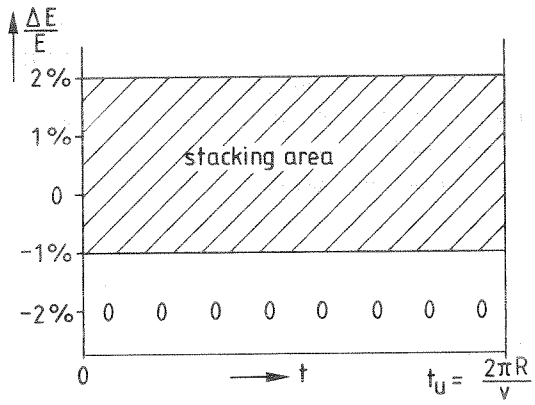


Fig. 3: RF stacking in the phase plane

If the collider is designed to accept a momentum spread of $(\Delta p/p)_c = 0.02$ the maximum number of synchrotron pulses will be $n_p = 35\ \beta\gamma$. By multiplication with the number of ions N_{SIS} per synchrotron pulse and with the efficiency η of the RF-stacking process we get the maximum number of ions per collider ring $N_c = n_p \cdot N_{SIS} \cdot \eta = 35\ \beta\gamma \cdot N_{SIS} \cdot \eta$. The term $\beta\gamma = p/mc$ indicates that the particle current in the collider facility is proportional to the momentum at injection. For $\eta = 0.66$ and injection energies of 1 GeV/u for uranium and 2 GeV/u for neon the particle currents I_{pc} and the electrical currents I_{ec} listed in Table 1 result.

Table 1:

	n_p	N_{SIS}	N_c	I_{pc}	I_{ec}
Neon	90	$1 \cdot 10^{11}$	$6 \cdot 10^{12}$	0.7 A	7 A
Uranium	60	$2 \cdot 10^{10}$	$9 \cdot 10^{11}$	0.1 A	9 A

In Fig. 4 the number of ions N_c which can be stacked in a collider ring is plotted versus injection energy. In addition the current limit for a Laslett Q-shift $\Delta Q = 0.05$ and the limit due to longitudinal microwave instabilities are shown. For energies below 0.5 GeV/u it is the Q-shift that limits the current, above 8 GeV/u microwave instabilities set a limit, and between these energies the collider current is restricted by the stacking process.

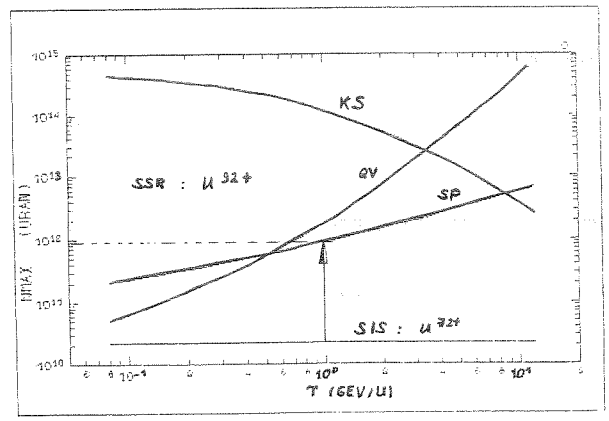


Fig. 4: Maximum number of ions which can be stacked in a collider with regard to the RF stacking process (SP), incoherent Laslett tune shift (QV), and longitudinal microwave instabilities (KS).

Reference:

[1] G. Guignard, Selection of Formulae Concerning Proton Storage Rings, CERN 77-10

Status of the SIS 18 injection system

W. Bourgeois, H. Eickhoff, B. Franzke
GSI Darmstadt

Based on the final layout of the injection channel to SIS 18[1] in 1983 design and partially manufacturing of the most important components was started:

1. Closed Orbit Bumper Magnets

Because of the rapid change of the magnetic flux density of about 1000 T/s in the bumper magnets a yoke material of high electric resistivity is required. We intend to use COROVAC, which is much less expensive than any ferrite, and, in addition, seems to have better magnetic and mechanical properties.[2]
During the student-program at the GSI some calculations have been performed concerning the impact of the coil eddy currents. Due to the rapid change of the magnetic flux the coil has to be as thin as possible in order to avoid perturbing field inhomogenities. The final design of the full set of four bumper magnets, which will be installed in the ring, and a vertical deflector for the injection beam line are depending on test operation of a prototype magnet.
Parallel to the magnet design the development of a suitable pulsed power supply has been started. A low power model for 1 kA and the design values for the current drop 1.4×10^3 kA/s $\leq dI/dt \leq 1.4 \times 10^4$ kA/s is now under construction and will serve to supply the prototype magnet. The maximum current of the magnet for SIS 18 will be about 7000 A. To minimize the power consumption a relatively small pulse of about 3 msec length will be applied to the magnet. It is intended to form the required shape of this pulse with a function generator, which will be amplified by the power supply.

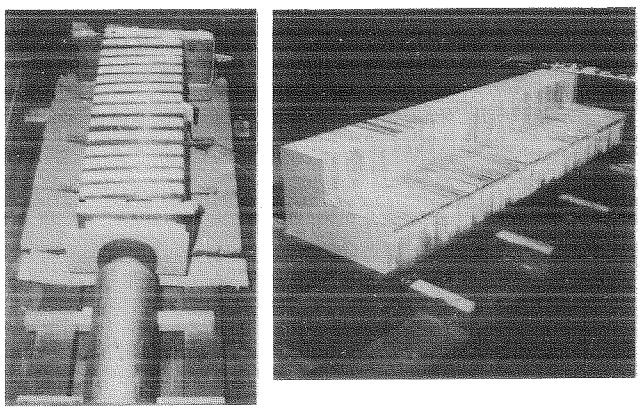


Fig. 1
half yoke during pasting — complete half-yoke

2. Electrostatic Septum

The features of the septum unit are described in a special paper in this report.[3] At the present, the following parts are being manufactured:

a) 300 kV power supply (by external firm)
b) UHV-housing box for the septum and clearing electrodes (by external firm)
c) electrodes with suspensions and feedthroughs (mostly by GSI workshops)

Completion of all mechanical parts and UHV-components as well as the installation of the high voltage supply is scheduled for the second quarter of 1984, the test operation for the rest of the year.

3. Inflector Magnets

The 9° beam inflection into the gap of the electrostatic septum is made by a pair of 4.5°-magnets. As the inflectors are very close to the beam circulating in SIS 18, we had to choose a septum magnet design. The yokes are sheeted to allow pulsed operation, and can be removed to enable baking out of the magnet vacuum chambers. Realignment of the magnets after reassembling the magnets is performed by a special suspension of the yoke parts. Fig. 1 shows the pasting of a magnet yoke.
The coils consist of 10 windings with a cross section of 20 mm^2. The required current for the maximal magnetic ridgidity of 4.5 Tm is 3000 A, which means a power consumption at DC-operation of about 42 kW. The maximal power for pulsed operation is 53 kW for a current rise of 30 kA/s; for this operation the mean value of the power losses are about 14 kW at 3 Hz repetition rate.
With the exception of the coil insulation (epoxy), the inflection unit is ready to be installed. For test operation, we intend to use the main dipole prototype supply.

References

[1] H.Eickhoff, B. Franzke, Beam Injection Line to SIS 12, GSI 83-1, 280 (1983)
[2] COROVAC is a trade mark of Vakuumschmelze Hanau
[3] see this report

Design of the Electrostatic Injection Septum for SIS 18

W. Bourgeois, H. Eickhoff, B. Franzke
GSI - Darmstadt

The electrostatic septum unit gives the final bend of 40 mrad to the beam being injected into SIS 18. The number of ions per acceleration cycle is planned to be raised by injecting many turns in series, which must be arranged efficiently on the horizontal acceptance of the machine. Hence, the separation between the circulating beam traversing the hollow anode and the one being injected through the gap between the bending electrodes has to be held as narrow as possible. Furtherly, the electric field of max. 200 kV must be sufficiently shielded to avoid perturbing influence on the circulating beam. Therefore, the most critical part of the anode, the septum, is built up out of numerous thin wires (wire septum) which seem to be more reliable than a metallic foil.

The shape of the 1.5 m long deflecting electrodes is approximated to the radius of 30 m of the inflection orbit by division into three straight sections. The deflection electrodes are installed in an UHV-housing, fixed by four linearly movable feed-throughs and supplied over a 300 kV-feed-through. Inside the anode, space is left for the circulating beam. Clearing electrodes prevent secondary ions from diffusion into the high electric field, where they could be accelerated to the cathode and initialize field break downs. With the exception of the cathode, all parts inside the vacuum are bakable up to 300°C, which is necessary to reach the design vacuum of 1 nPa.

Anode: The vertical frame work of this electrode is similar to the construction of a hull. Along the first 2/3 of the bend, where the separation between the beams is more than 5 mm, the septum is made out of a stainless steel sheet. Along remaining 560 mm 280 equidistantly spaced 0.1 mm thick tungsten-rhenium wires are tightened by 560 springs, which also have to pull, in the case of damage, the wire halfs out of the electric field.

Cathode: The smooth surface of the AlMg3-cathode has a 10 µm thick oxide layer by which the field electron emission of the surface is reduced. Due to this layer the baking temperature of the cathode is limited to 150°C.

Clearing electrodes: A pair of metallic sheets is mounted on insulators inside the anode hole and will be supplied by ±5 kV max..

300 kV-Feed-Through: The requirements for this part are fortunately matched by a design for the recently completed LEAR at CERN.

Linear Feed-Throughs: Mainly due to the baking out requirements, the design used at the UNILAC had to be changed. The stroke of ±15 mm is necessary for alignment and HT-conditionning, which requires larger distance between electrodes (normally 20 mm).

UHV-housing: The cylindric chamber of 2000 mm length and 450 mm diameter is made out of stainless steel 1.4435. The material is glowed at 950°C for 3 hours under vacuum of 5 mPa. The completely cleaned and assembled septum unit will be baked out for 24 hours at 300°C and pumped down to the design pressure by two Ti-sublimation pumps and an ion sputter triode with total pumping speed of nearly 2500 ℓ/s.

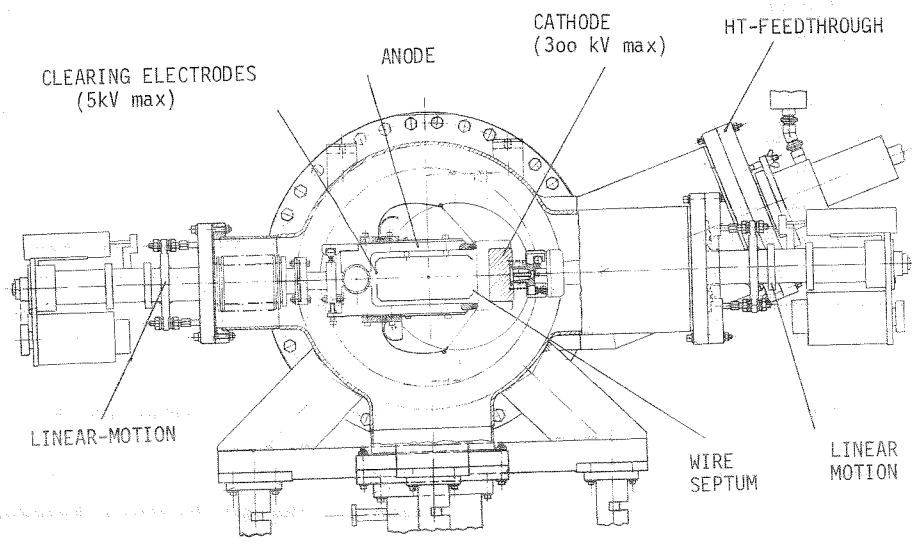


Fig. 1: Cross section of the electrostatic septum unit for the SIS 18-injection.

Activities on the SIS Prototyp Accelerating Station

M. Emmerling, K. Kaspar, A. Gasper
GSI Darmstadt

Most of the central problems connected with the prototype cavity seemed to be solved already one year ago, as shown in (1). However, it turned out that a lot of details had and has to be worked out yet.

Much time was spent on efforts to understand spurious resonances occuring in the cavity. Besides the original configuration of the dc bias windings a second configuration with higher electrical symmetry was investigated intensively. Details are given in (2).

It seems that many of the resonances above about 10 MHz cannot be suppressed below a certain level by simple means like blocking capacitors or similar. After looking more closely into the interaction between the ion beem and the cavity it seems clear that the remaining resonances will not affect the operation of the SIS 12. Part of these considerations are described in (3).

Tests with the control system revealed that the bandwidth of the cavity tuning system was much lower than expected. On one side, this was caused by too large blocking capacitors used on the bias windings, and their values had to be decreased again. On the other side, it became clear that the response time of the dc bias supply was not fast enough. To increase the response time, the output stage of the bias power supply has been completely redesigned. More details are given in (4).

Much time had to be spent for relatively simple but time-consuming technical questions. The ceramic insulators which support the bias windings heat up to above 100°C under full power. A few of them was broken and caused serious rf discharges. It was expected that this problem could easily be solved by replacing the material called "Frequenta" by 99.7 % alumina. After receiving some sample insulators developed for this purpose, it was found that, under the same conditions, the new insulators become even hotter than the old ones. So, the question of insulators is still open. However, another "Frequenta" insulator type available from stock gives very good results. As the diameter of this type is slightly larger, it can only be used in the cavity after some simple but elaborate mechanical changes. These will be made if no other solution is found.

The six bias windings consist of about 72 copper elements which are screwed together. The contacts of some of the connections had become worse after being opened several times. These connections heated up considerably under full dc current and also increased the overheating of the ceramic insulators. The dc windings were disassembled, and all the contact surfaces were silverplated. The connections remain nearly cold now.

In the final cavities, all parts under vacuum will have to be baked out to about 300°C. This possibility has not yet been realized in the prototype. It is planned to use coaxial heating elements welded along the inner conductors and to the vacuum flanges of the gap insulator. A thermal insulation between the heated parts and the rest of the cavity would be very useful, but it would probably be necessary to remove this insulation during normal operation of the cavity. Calculations (5) showed that the thermal insulation can be omitted without any risk for the ferrite rings, as long as these are cooled by the existing ferrite cooling disks.

The rf power stage of the prototype cavity has been improved in several respects. Among others, the anode water cooling circuit has been changed from normal to deionized water. The several meters of water hoses insulating the anode from ground have been replaced by glass tubes of about 0.5 m in length. As soon as available, the glass tubes will be replaced by alumina tubes.

In parallel with the studies and improvements on the prototype, the technical design of the whole accelerating station has been revised and updated as far as possible. A complete redesign of the rf power stage is underway.

(1) M. Emmerling, K. Kaspar, K. Sato, A. Gasper, Measurements on the SIS Prototype Accelerating Station, GSI Annual Report 1982

(2) K. Kaspar, M. Emmerling, New Configuration of the Bias Windings in the SIS Prototype Cavity, GSI Annual Report 1983

(3) K. Kaspar, Beam Loading and Beam-Cavity Interactions in the SIS Cavities, GSI Annual Report 83

(4) M. Emmerling, K. Kaspar, Tests of the Control Loops of the SIS Prototype Accelerating Station, GSI Annual Report 1983

(5) C. Riedel, GSI, private communication

Beam Loading and Beam-Cavity Interactions in the SIS Cavities

K. Kaspar
GSI Darmstadt

The interaction between the ion beam and the cavity can be described with the equivalent circuit in Fig.1 (1): an LCR resonant circuit driven by two current sources, the amplifier current $\vec{Ja}$ and the beam current $\vec{Jb}$. These currents generate the voltages $\vec{Ua}$ and $\vec{Ub}$ in the cavity and the total gap voltage $\vec{Ug}$ is equal to the superposition of both. Using the Fourier series of $\vec{Ja}$ and $\vec{Jb}$ and complex representation one obtains

$$\vec{Ua} = \sum_n Rp(n\cdot fo)\cdot\vec{Ja}(n\cdot fo) = Rp(fo)\cdot\vec{Ja}(fo), \quad n=1,2,\ldots$$

$$\vec{Ub} = \sum_n Rp(n\cdot fo)\cdot\vec{Jb}(n\cdot fo) = Rp(fo)\cdot\vec{Jb}(fo)$$

$$\vec{Ug} = \vec{Ua} + \vec{Ub}$$

Fig.2 gives an example of the impedance $Rp(n\cdot fo)$ of a cavity and of possible Fourier spectra of $\vec{Ja}$ and $\vec{Jb}$. As long as Rp follows the "clean" solid resonance curve and the amplitudes of the higher harmonics are low enough, it is sufficient to consider the fundamental components $\vec{Ja}(fo)$ and $\vec{Jb}(fo)$ only. For an ion beam with arbitrarily shaped short bunches one finds the simple relation

$$\left|\vec{Jb}(fo)\right| = 2\cdot Jbav\ , \quad Jbav = \text{mean beam current.}$$

With 2·10E12 protons/sec in the SIS and fo=6 MHz one has about $\left|\vec{Jb}(fo)\right|$=1 A peak. The amplifier current for the nominal gap voltage is about $\left|\vec{Ja}(fo)\right|$=5 A peak.

For illustration: if the amplifier current is turned off, amplitude and phase of the gap voltage generated by the beam will be such that the beam is decelerated by about 20% of the normal accelerating voltage.

For phase stable acceleration a certain phase shift between $\vec{Ua}$ and $\vec{Ub}$ is required. As a consequence, the gap voltage $\vec{Ug}=\vec{Ua}+\vec{Ub}$ with beam can differ seriously in phase and amplitude from the gap voltage $\vec{Ug}=\vec{Ua}$ without beam - if no additional measures are taken. If only the fundamental Fourier components are considered these errors can be fully compensated by an adequate detuning of the cavity. As a very welcome result, one finds that the needed detuning is automatically performed by the usual systems for cavity resonance and amplitude control.

In a complex system like a ferrite-tuned cavity the main resonance is usually accompanied by spurious resonances at higher frequencies, as indicated by the dotted curves in Fig.2. First, such spurious resonances have to be eliminated as far as possible. Second, the harmonic contents of $\vec{Ja}$ and $\vec{Jb}$ have to be kept as low as possible. For $\vec{Ja}$ this can be controlled well enough by means of the amplifier working point. For $\vec{Jb}$ the harmonic contents are strongly dependent of the bunch length. For very short bunches even very high harmonics of $\vec{Jb}$ can give important contributions to the total gap voltage when they coincide with spurious resonances. The detuning of the cavity does not compensate the effect of higher harmonics.

Measurements in the prototype cavity show that the impedance of the cavity for spurious resonances in the range up to 20 MHz is by at least a factor of 10 lower than for the cavity resonant frequency. With the maximum current ratio of $|Jb/Ja|$=0.2 given above, the contribution of higher beam harmonics will be less than 2 % of the accelerating voltage, in the worst case.

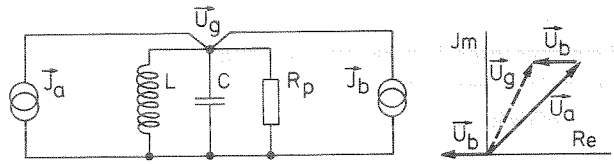


Fig. 1: Equivalent circuit of a beam-loaded cavity

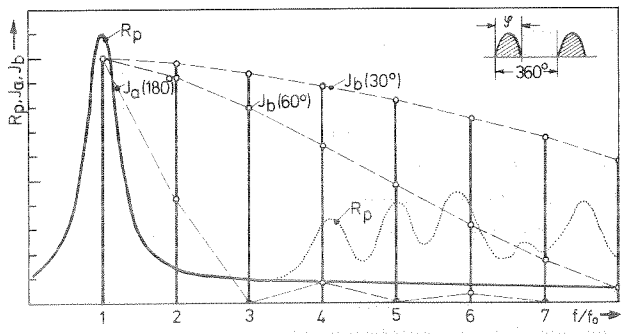


Fig. 2: Examples for the cavity impedance Rp and possible Fourier spectra of the amplifier current $\vec{Ja}$ and the beam current $\vec{Jb}$

(1) Physics of High Energy Particle Accelerators (Fermilab Summer School 1981), AIP Conf. Proc. Nr.87

New Configuration of the Bias Windings in the SIS Prototype Cavity

K. Kaspar, M. Emmerling
GSI Darmstadt

The SIS prototype cavity is designed for six figure-of-eight dc bias windings. Fig.1 shows schematically the longitudinal sections of the six windings and their mutual electric connections, as used in the original design. The arrows on the lines mean the direction of the dc current, the +, -, and 0 signs indicate the rf voltages at a given moment. The windings around the left ferrite stack are for the most part on the same rf potential as the near-by parts of the cavity. This is not the case for the windings around the right ferrite stack, and means a relatively high electric asymmetry of the whole cavity. It was assumed that spurious resonances in the cavity might be caused by this asymmetry.

It was found that the given bias windings can be assembled to an entirely symmetric configuration, just by changing part of the interconnections. The result is shown in Fig.2. As an additional advantage, the number of cross-overs in the gap region is reduced from six to three. Problems of access to the gap and of space for the connections between the gap and the amplifier are considerably faciliated in this way. The maximum electric field strengths between the windings and the surrounding parts remain the same as in the first configuration. Only between the cross-overs in the gap region the electric field is increased by the factor two. However, no problems were expected nor observed here.

Both configurations have been tested intensively, with full power in the whole frequency range, and with various types of blocking capacitors installed in different places. It turned out that the second configuration does not bring a substantial change or improvement of the spurious resonances. Both configurations seem to be nearly identical for most of the electrical properties. However, for mechanical reasons, the new configuration is so advantageous that it will be kept in the future.

The purpose of the blocking condensors shown in Fig.1 and Fig.2 is to subdevide the bias windings into electrically shorter sections with higher self-resonant frequencies. With no blocking elements at all, the six bias windings resonate at about 3.4 and 6 MHz, independently of the cavity tuning. With seven blocking elements, as shown in the figures, several resonances on the windings start above 10 MHz. More blocking elements bring no further improvements. For the new configuration, the situation remains the same with only the four elements on the left side. The rf currents passing over the blocking elements are relatively high. This means considerable voltage drops and power losses on the elements. Maximum capacities would be desireable for this reason. Too large capacities reduce the bandwidth of the tuning system, however. A total capacity of 100 nF per blocking element was found as a good compromise for both requirements. The remaining rf voltage on the dc input lines is less than 3*10E-3 of the gap voltage then. Two high current LC filters reduce this voltage to less than 100 mV at the output of the dc bias supply.

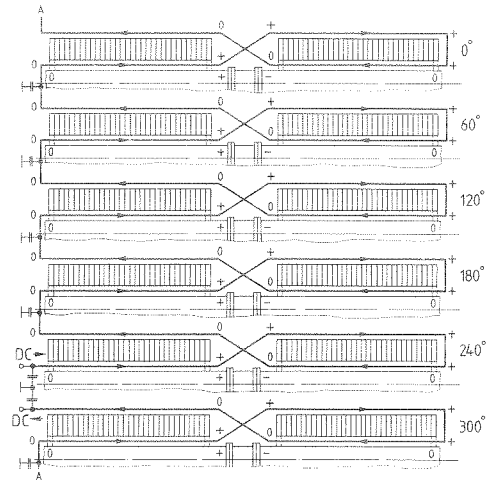


Fig. 1: Schematic of the old configuration of the dc bias windings. Disadvantages: electrical asymmetry and six cross-overs in the gap region

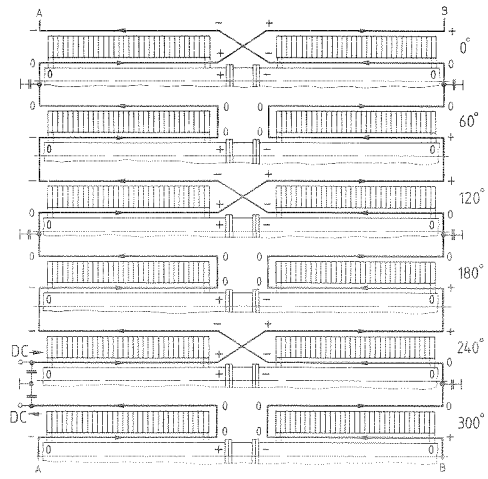


Fig. 2: New configuration of the dc bias windings with full electrical symmetry and only three cross-overs in the gap region

Tests of the Control Loops of the SIS Prototype Accelerating Station

M. Emmerling, K. Kaspar
GSI Darmstadt

The closed-loop control systems for rf cavity tuning and rf amplitude were studied at the SIS prototype accelerating station. The amplitude loop caused no great problems. But it was impossible to reach the same performance of the cavity tuning loop as formerly obtained with the test cavity.

By these tests the power supply for the dc bias-windings was simply used as an emitter follower, the internal regulation loop was not used. The most limiting factor in reaching the possible bandwidth were the collector base capacities of the power transistors (approx. 108 • 500 pF). Combined with the self induction of the cavity tuning loop (up to 2.5 mH), the system had (by considering the transistor current gain of 150) a 3 dB bandwidth of 1 kHz.

To overcome this effect, the emitter stages were replaced by cascade stages (see circuit diagram). At first it was tried to rebuild the existing cooling plates for the transistors. Arranging the transistors, which belong to a common driver transistor on different plates, caused difficulties with self-oscillations at 3 MHz. So the double number of transistors as original were placed at one cooling plate. This could easily be done. It was possible to connect 5 transistor pairs to one driver transistor without self-oscillation. However, the power transistors (2N 5685) with 300 W dissipation could only be loaded with 100 W, because in the new arrangement the distance between transistors and cooling water channel was too long. So it was decided to build a completely new cooling plate. Now this plate is mechanically finished, but not tested electrically.

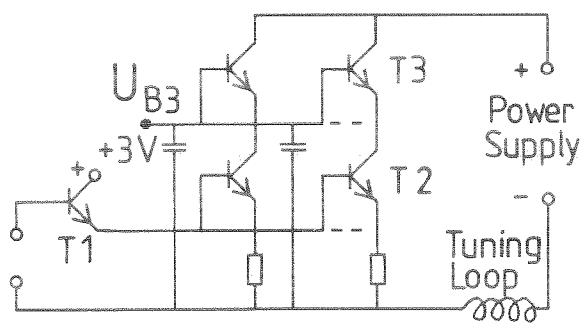
In the meantime, tests with the rebuilt transistor plate showed, that now the current through the transistors is in phase with the driving voltage up to a modulation frequency of 10 kHz. However, this current is divided between the tuning loops and the blocking capacitors to ground. For this reason the blocking capacitors should be lower than 100 nF. Difficulties, which resulted from reducing the values of the blocking capacitors are described in this report elsewhere.

Having raised the bandwidth of the power transistors they became more sensitive to interference from the power supply. Especially the abrupt change in current, each time when a rectifier diode was cut-off, induced a voltage peak. Therefore the transistor plate had to be brought out of the rack of the power supply and installed in some distance.

Furthermore, the cavity tuning loop tends to self-oscillation due to improper shielding of the cavity. But even in case of a good rf shielding of the cavity, the stray magnetic field of the bias windings (which is not reduced by the ferrite rings) remains. Each modulation of the bias current induces a voltage in the cables around the cavity and can reach the input of the phase loop amplifier. When the cavity is installed in the synchrotron tunnel, the distance to the amplifier of ≈ 100 m will prevent any self-oscilllation. But now in the prototype phase this is a serious problem. All sensitive components were rearranged as far as possible from the cavity, which solved the problem for the moment.

As another problem, it was found, that the ferrite rings have a very sharp mechanical resonance at 4.4 kHz. Tests with a single ring showed, that the resonance is the same whether the ferrite rings are pressed together in the cavity or not. The resonance is excited by the modulated tuning current due to magnetostriction, which is very high for this special sort of ferrites. One ferrite ring was broken by this measurement. Before having finished the new transistor plate, it cannot be estimated if this resonance will limit the bandwidth of the cavity tuning loop.

Up to now the gap voltage was measured by means of a rectifier directly connected to a high-impedance capacitive voltage divider. In future the rectifier will be placed outside the synchrotron tunnel in order to protect it from radiation. The connection is made with a terminated coaxial cable. To keep the voltage divider frequency independent (from 0.9 to 6.5 MHz), the base capacitor must have less than 1 Ω, therefore a capacity of 150 nF. It was realized with 70 closely packed small ceramic capacitors. After proper shielding of the output signal from the capacitive divider current, the measuring device worked well.



Report of the Ultra High Vacuum Activities

P. Finke, A. Kritzer, H. Prange
GSI Darmstadt

In the first quarter of 1983 the investigations of the UHV prototyp test section have been finished. The main results have been summarized in a final report. Practical experience obtained from these studies was used in the preparation of the technical specifications of the main components of the SIS vacuum system as well as in the construction of dipole and quadrupole chambers. These magnet vacuum chambers are connected by multi-functional intermediate pumping chambers. They are integrated units providing facilities for the compensation of thermal expansion, for mechanical adjustment, for beam diagnostics, for vacuum pumping and measurements.

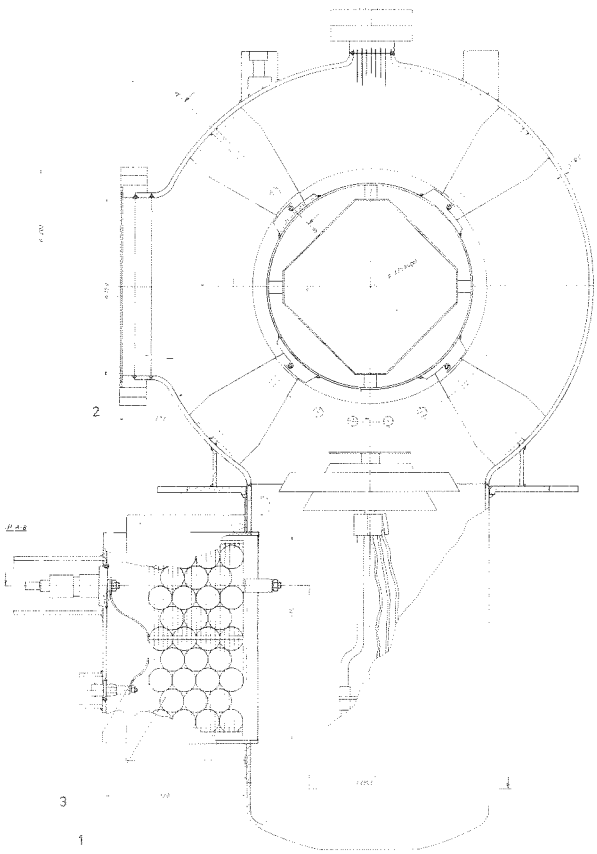


Fig. 1: Intermediate pumping chamber
1-Ion getter pumping cell
2-housing of the ion getter pump
3-electrical feed through

As shown in Fig. 1, the pumping chamber has a spherical shape with two compensating elements on two sides in beam direction. In the center of the sphere the beam diagnostic elements are located. Perpendicular to the beam direction a cylindrical housing for booster type vacuum pumps is attached. After finishing the construction mechanical parts of the chamber have been ordered and will be finally assembled and tested at GSI site. Analyzing various laboratory tests, data were specified for the expected gas desorption rate and gas composition as well as for the gas flow conductance and the corresponding pressure profile. These data were used in the design of the geometry of the titanium evaporation pumps and for the selection of the integrated ion getter pumping cells to provide the necessary pumping speed for the nobel gases and methane. In the context different pumping cells both of the diode and triode type were tested by means of a Fischer-Momsen dome. For the prototype a 40 ℓ/s diode cell with 20 % pumping speed for nobel gases was chosen.

The leak current of this cell is of the order of nA which gives a proportionality of ion current to pressure down to the low 10^{-10}mbar level. Thus ion getter pumps can be used to indicate the pressure profile of the SIS Ring. For this purpose in 1983 a new cold cathode measuring device working to the low 10^{-10}mbar range was tested. Discussions with the manufactorer of the measuring device have shown the possibility to apply a modified version of the read out unit as a combined power supply plus precise pressure measuring device for the scheduled ion getter pumping cells.

In our previous laboratory test we observed unexpected damages of the titanium helixes. In order to avoid such failures in the future SIS a current stabilized power supply with the capability of external helix temperature control was built up at GSI. Tests of this device are in progress. Special effort will be made to determine optimal and reproducible conditions for the lifetime and for evaporation rates of the titanium helixes.

In order to study the thermal insulation of dipole chambers for in situ bake out up to 150°C theoretical evaluations were carried out for the heat flux in the dipole magnet core. In the calculations a computer program package based on the finite element method was applied. Taking into account heat conduction in iron as well as thermal convection and radiation it was concluded that expected temperatures remain well below the critical temperature at which the epoxy resin used in the laminated iron core starts to melt.

SIS-CONTROLSYSTEM

H. Brandis, R. Kühn, E. Schaffner
GSI Darmstadt

System-Layout

For the design of the SIS control system some conditions had been of major importance:

- The system must be able to easily "grow" with future requirements. This leads to modularity and expandability of all components.
- New technical developments should be employed to ensure sufficient lifetime. As a consequence, the control system is based on modern 16 (32) bit microprocessor systems.
- Manpower and budget are limited for the installation of the system as well as for maintenance. So standards and products of the market are used with minimum of in-house development in hard- and software.
- The control system should also be applicable to other machines and experimental setups.

To meet these requirements the following structure has been choosen:

- A communication network, which grants equal access rights to all participant node-computers without restriction on the number of nodes actually connected.
- Node-computers for process control
  timing
  man-machine-communication
  general services

  For general services and part of man-machine-communication one node-computer will be a VAX, the node-computers for the other tasks will be multiprocessor-crates (MPC) consisting of several 16(32) bit microprocessors (Multibus with 8086, future: e.g. Multibus II with iAPX 286, iAPX 386).

  Despite its disadvantages (connectors) Multibus had been chosen because a lot of different CPU-, memory- and interface-boards made by several producers are available on the market. Software developed for Multibus will be usable without major changes on Multibus II which will avoid the disadvantages of Multibus and will be supported as a future industrial standard by even more producers. Production of Multibus II-boards starts in '84.

  A MPC for process control will consist of

  a network-communication-processor to establish communication to the other node-computers
  a general data processor
  private and global memory
  an equipment-communication-processor to establish communication to the subsystems connected via the I/O-channel.
- MIL 1553 Bus as I/O-channel to several microcomputers to which the process-devices are connected.
- Microcomputer to serve the process-devices.

  Operations on devices are initiated by requests transmitted from the controlling MPC and are executed one time, periodically or after device-interrupt according to the request by device-dependent user-service-routines. The results of these operations are transmitted back to the controlling MPC and via the communication network to the node-computer which issued the request. Each microcomputer serves only one class of devices (e.g. magnets).

  A database stored in EPROM describes all devices connected to the specific microcomputer. On request the contents of this database is transmitted via MIL-Bus and communication network to the requesting node-computer. This allows any node-computer to build up its own database describing all devices of the accelerator.

Communication in the SIS Control System

The concept of a modular computer system allows to increase the number of the participant computers without changing the layout and the basic software of the system. These computers, marked as network nodes, provide the processing power for the user's implementation of task-specific algorithms in a well-defined software environment. The idea of modular extensibility can also be used for the device layer and its connections to the control system. New devices, represented by their microprocessor systems, can be connected to the network nodes without changing the software on that node.

For the communication between network nodes Ethernet will be used. This medium provides concurrent, non priority controlled access from and to each computer in the network. The physical transfer rate is 10 Mbit/sec, which will be derated by the speed of the computer interfaces and the communication software which controls the access to Ethernet.

It is intended to keep the transfer load lower than 25 % of the maximum. At higher transfer rates collisions

might cause problems on Ethernet.

For the device-micros, strict master-slave communication with controllable timing conditions is used. Slaves are all device-micros, while master is the Equipment Communication Processor (ECP) of the network node. As communication medium the serial 1Mbit/sec MIL 1553-B-standard has been chosen because of its proven reliability, industrial support with VLSI-interface-chips, and its low protocol overhead at still relatively high speed.

A communication protocol for the Ethernet network down to the microprocessor systems via the MIL-busses has been developed, which bases on the "ISO reference model for open systems interconnection" and considers the partitioning of the communication tasks into different layers. The definition of the communication layers are defined as follows:

- Physical layer (1)
  The physical layer is realised with the media Ethernet and its computer interfaces
- Data link layer (2)
  The data link layer is realised with the driver-modules of the operating system on the network nodes
- Network layer (3)
  The network layer is not realised in every network node. There is one special network node, the "Internet Gateway", which has the task to connect multiple Ethernet-subnets and rout the communication packets between these subnets.
- Transport layer (4)
  The transport layer implements a connectionless data-packet transfer (Datagram-transfer technique). Each network node has the same access rights to communicate with each other without the restrictions of connection and reservation of virtuell point-to-point connections.
  The reservation of computer systems by establishing a temporary point-to-point connection would increase the overhead without an advantage of data integrity and communication security in the SIS control system.

For the communication protocol on the Ethernet a maximum packet length for each data transfer was defined to optimize the memory-management on each network-node. The goal is to handle memory areas with a fixed length for the reception and transmission of data packets which is easier than handling data packets with variable lengths. Moreover the data communication on the UNILAC network has shown, that there are no or only a few applications which need to transmit long data packets.

Another feature of the SIS communication protocol is the possibility for the transmitter of a message to demand an acknowledge packet from the receiver. This increase of data security has the disadvantage of an increased communication overhead on the network. It is expected that there is no necessity to use this feature because of the very high data integrity of Ethernet.

The communication protocol on the Ethernet influences the protocol on the MIL-Busses, because in most cases data packets which are transmitted on the Ethernet must be routed to the microprocessor systems via MIL-bus. To decrease the amount of data on the MIL-bus, non-important data for the destination-microprocessor system, such as the destination-process name in the network-node, the message number and acknowledge indicator, are eliminated from the communication header, because they are of no use for the addressing for retransmission. This compression of the communication header is sensible because the physical transfer rate on the MIL-bus is lower (1 Megabit/sec) than that on the Ethernet. Therefore it is important to avoid unnecessary data as much as possible.

The addressing capabilities in the Ethernet/MIL communication protocol

To each network node in the Ethernet network a network number is assigned which is independent of the physical Ethernet address. The attachment of network-node number and physical Ethernet address is done in the startup phase of the total network system. Each network node transmits its network-node number and physical Ethernet address via broadcast message to all other network nodes which retransmit on reception of the "connect" request their own network-node number and their physical Ethernet address to the requestor.

This auto-configuration makes it possible to add new network nodes or change Ethernet controller on existing network nodes without manual alteration of the table "network-node number ↔ physical Ethernet address" in all the other network nodes.

The communication protocol header contains the source as well as the destination node number to enable a retransmission.

The microprocessor systems on the MIL-busses are addressed with a microprocessor number (µP number).

This µP number will be used to address each micro-processor system on the MIL-bus with assistance of the table."µP number ↔ physical MIL-bus address" established during the startup sequence with an equal auto-configuration algorithm as described above.

The Databases for SIS-Control

The need for collecting and maintaining all the SIS-

control-data in a structured manner is evident and need not to be discuessed further. The organisation and handling of data in that way shall be called a "database".

According to the different structures and tasks of control-computers there will be 3 types of databases: the device-database located in equipment controlling 8-bit micro-systems, the database in the multi-processor-crates (MPC'S), and the central database in the VAX. The contents and the structure of all databases is determined by the following considerations:

- by the question, which data are needed or supplied on the appropriate level
- by the request, that the databases within the MPC's and in the VAX must be generated by auto-configuration from the device-databases
- and by the request, that all databases on all - computers must have compatible structures (because of the auto-configuration and for effective access).

The device-database contains static data only and will be generated by the developpers of the devices (supported by easy-to-handle programs). A database with dynamic data does not exist on this level. Rather may the new intelligent interfaces to the devices, the so-called "Steuer-Einheiten", with their dual-port-ram be interpreted as decentralized dynamic databases.

The main task of the databases within the MPC's is translation and mapping. That means, "high-level"-requests for device-control (name, status, current etc.) must be converted to communication parameters like the numbers of MPC and device-micro, to the MIL-bus-address and device-function.

The central database on the VAX contains all device-databases and dynamic data and some other data more (see "auto-configuration").

The auto-configuration of the databases in MPCs and VAX is the way to avoid inconsistency between the contents of the databases and the "real world". Using the "Broadcast-Message"-feature of ETHERNET these databases are loaded from the device-databases at system-initialisation and updated in case of (hardware-) modifications. But there is some data, which should not be included in the device-databases (e.g. large theoretical data) and there is some other data, which cannot be there, because it is overlapping several device-micros. For that data a second (off-line) source for the loading of the central database is provided.
Compatibility of the databases on the different levels of control is achieved by the same structure and the same mechanism of access. Access to data is performed via index-tables with a key. Primary key is the name of the devices. Secondary keys like type or location of a device or combinations of these keys are optional.

For fast access with primary (and optional secondary keys) the loading of the index-tables and the access via these tables is performed by use of a hash-algorithm.

All databases are core-resident. This is evident for the device-micros and the MPC's, because they do not have mass-storage-devices (discs). The reason for core-residency on the VAX is a powerful system-service of VMS, which takes an automatic, actual backup of the core-database to disc, while the accesses are fast core-operations and not slow disc-operations.

For loading of and access to all databases a structured high-level-language (PASCAL or MODULA-2) is used. Database-handling becomes very simple through the "record"-structures which are features of these languages. All elements of the database are called by their names, faulty address- and offset-calculations are not necessary. The other reason is the compatibility. With minor modifications the database-handling-routines run on all types of computers.

Status

To build up the system described above the following steps were completed:

- Installation of an Ethernet-Network connecting (beside others) a VAX 11/780 and a MPC consisting of two 8086 boards.
- Definition of the protokoll (ISO layer 4) for Ethernet and MIL-Bus. The format of messages on the MIL-Bus is similar to that used on Ethernet to avoid complicated translations.
- Design and implementation of a monitor for the microcomputers. This monitor receives the request-packages from the controlling MPC, calls the user-service-routines specified in the package furnishing them with input-data and collects the return-data from the called routines into a return-package to send it back to the origin of the requests.
- Definition of a database-structure which can be implemented in any of the computers in the system, tests on the VAX and on the micro-computers whether this structure is usable.
- Survey of an interpreter language to ease access to all devices for the operator:
  The NODAL-interpreter, which is under construction at CERN using MODULA2, will be used. For this reason GSI personell will participate in the development.

Finite-Element Calculations in Accelerator Design

C. Riedel
GSI Darmstadt

In various accelerator design tasks, problems arise which are related to the evaluation of stresses and strains in loaded mechanical structures as well as of heat transfer and temperature profiles. Due to complex geometrical shapes and loading conditions ordinary engineering methods provide only rough estimations of the interesting physical quantities. In the last years computer program packets became available which can be used for finite-element calculations of rather complex structures. In such calculations, reasonable accuracy and moderate computer CPU-time were achieved.

In general, the structures are described by a number of nodal points (in some cases up to a few thousands). These nodes are used to form finite elements of different types. Typical element types are: three-dimensional truss and beam elements, plane stress membrane elements, two- and three-dimensional finite elements, plate and shell elements.

In mechanical structures, up to six degrees of freedom can be associated with each node. For each degree of freedom boundary conditions can be assigned. In the static analysis combined load conditions of surface pressure, hydrostatic loads, inertia loads (e.g. earth quakes) and thermal loads can be applied. Several types of dynamic analysis can be carried out:

- eigenvalue/vector solution with determination of system mode shape and frequencies;
- dynamic response analysis for orbitrary time dependent loads using mode superposition or numerical integration;
- response spectrum analysis for the calculation of r.m.s. stresses and deflections due to input displacement (or acceleration spectrum);
- frequency response analysis to calculate the response of a structure to steady sinusoidal-base motion of various frequencies.

As a result of the program structure plotting with plots of undeformed and/or deformed structures is possible. Lines of equal stress values can be plotted for desired cross sections in the structure.

In the case of heat conduction, structures are treated in an analog manner. The heat transfer equations are derived from the statement of heat flow equilibrium at the nodes at any time. These heat balance equations must be modified by boundary conditions, such as exposition by a know heat flux or given temperature values at certain nodes. Convection and radiation surface elements as well as cooling pipe elements can be used.

For the IBM at GSI various finite-element programs for the described problems have been adapted. Problems can be solved in batch mode or in an interactive manner supported by graphical display of the resulting stress or temperature fields. Various auxiliary programs were developed for the generation of modal meshs and for the graphical documentation of results.

The following topics were treated using finite-element calculations:

- stress conditions in thin-walled vacuum elements;
- temperature profiles in magnets under conditions of baking of vacuum elements;
- design of cooling conditions and heat/stress load of ferrite rings used in tuning of rf-cavities;
- temperature profiles and heat-induced deflections of elements for the ion source CHORDIS[1].

Further applications are in progress.

References

[1] R. Keller, P. Spädtke, F. Nöhmayer, Int. Ion Engineering Congr., Kyoto, p. 25 (1983)

6. Inertial Confinement Fusion

A Revision of the HIBALL Driver Accelerator

I. Hofmann, R.W. Müller
GSI Darmstadt

The accelerator scenario for the HIBALL reactor study[1] defined in 1981/82 has been revised since in the following steps:

1. Bi^{2+} has been replaced by Bi^{+} in order to reduce space charge problems in the storage rings, at the expense of a doubled linac length. As a benefit, the final beam emittances can be reduced by a factor of two in both planes, to $3 \cdot 10^{-5}$ m. In spite of the higher particle stiffness, the smaller emittance greatly favors the design of the final lenses, which now may have a much smaller cross section, and can be made with unsaturated iron cores.
2. As an intermediate step, a scenario was studied which promises a very short filling time of the storage rings (1 ms) so that less than three e-foldings of the microwave instability, following the linearized theory, should occur[2]. The linac current had to be raised to the large value of 660 mA which is still in accordance with space-charge transport theory, but demands excessive cost for RF installation, because it has to generate more than 7.5 GW of r.f. power in short pulses. The cost for the r.f. generators would amount to about half of the total driver cost.
3. Recent progress in simulation of the microwave instability suggests that, due to favorable nonlinear effects, the acceptable storage time can be made much longer than anticipated from the linearized theory[3,4]. On this basis we have proposed a revised scenario with 4 ms storage ring filling time, and a linac current reduced to the comfortable value of 165 mA. This promises a better balance between the load on the linac and storage rings from the design and cost point of view.

The revised scenario is shown in fig. 1. It is based on a "funneled" RF linac with 8 sources. The 80 MHz micro-pulse trains are interrupted every 2 µs by 0.4 µs long gaps which allow periodic switching by a square-wave r.f. deflector into two transfer rings. Into each of these transfer rings trains of 100 macro-pulses are sent, each macro-pulse being 1.6 µs long followed by a gap of 2.4 µs. They are folded by 10-turn injection into 10 circulating pulses. Immediately after completing the stack, the pulses are extracted, both ring contents are combined transversely, and folded by 5-turn injection into two bunches in one of the storage rings. These storage rings are equipped with r.f. systems providing r.f. buckets to conserve the bunches. The process of filling the ten storage rings is finished after generation of 2000 macropulses by the linac, i.e. after 4 ms. The first storage ring has to keep its charge for at least 3.6 ms. After that, and when the pellet count-down signal is given by the pellet position-and-velocity sensor, all the storage ring contents are transferred into the buncher rings, undergo fast bunching within about 400 µs, and are shot to the pellet through 20 beam lines and final lenses.

Acknowledgements

A. Jahnke, then at IPP Garching, contributed very much to the first two steps described in this paper. The authors are indebted to their colleagues D. Böhne, K. Beckert and B. Franzke for helpful discussions.

References

1. B. Badger et al., "HIBALL - A Conceptual Heavy Ion Beam Driven Fusion Reactor Study", Reports KfK 3202 and UWFDM-450 (1981)
2. I. Hofmann, A. Jahnke, K. Beckert, D. Böhne and R.W. Müller, IEEE Trans. Nucl. Sci. NS-30, 3070 (1983)
3. I. Hofmann, I. Boszik and A. Jahnke, IEEE Trans. Nucl. Sci. NS-30, 2546 (1983)
4. I. Hofmann and I. Boszik, Nonlinear Phenomena in Computer Simulation of the Microwave Instability, GSI annual report 1983.

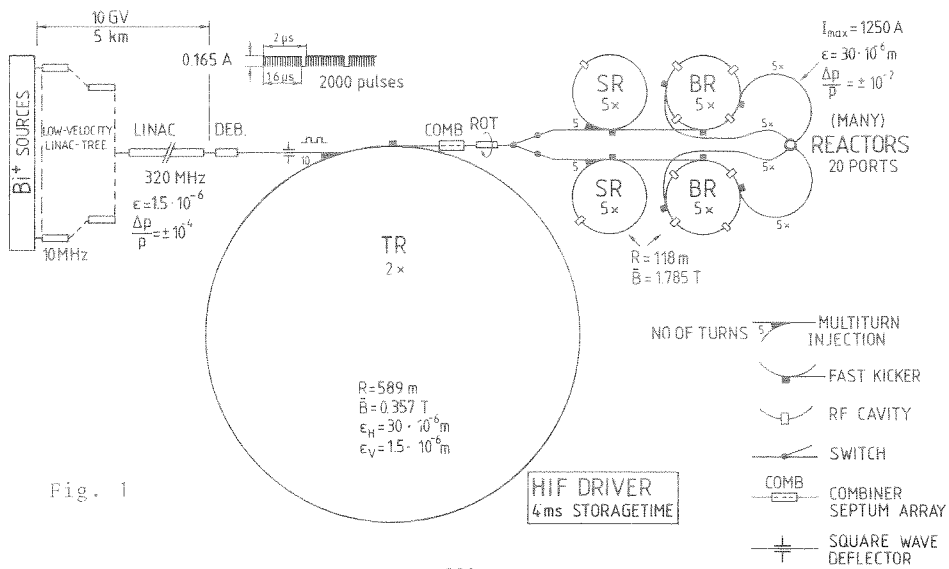


Fig. 1

Study on the SITAR-Storage Ring Experiment [B]

I. Hofmann, K. Beckert, D. Böhne, B. Franzke, R.W. Müller
GSI Darmstadt

The preliminary concept of a heavy ion storage ring SITAR (Schwer-Ionen-Test-Akkumulator-Ring) has been studied as a possible main experiment for the second phase of the German Heavy Ion Fusion Program covering the period of 1985-90. The scientific goal of SITAR is to develop storage ring physics and technology for high currents of heavy ions and to explore the effectiveness of electron cooling of heavy ions. Electron cooling is promising for a future high-temperature target experiment. The high-current experiments are expected to answer the key questions that have been identified for a heavy ion fusion accelerator, both at the level of a next-step target experiment[1] and a reactor-size driver accelerator. The interest in electron cooling of the stored heavy ions is two-fold: it promises a substantially improved performance for a high-temperature target experiment and it opens new areas of research at GSI in the fields of atomic and nuclear physics.

Design Constraints

A preliminary lattice design for SITAR has been based on the requirements of high-current and electron cooling. Plans for using this ring for atomic and nuclear physics applications are expected to result in additional requirements, presumably higher magnetic stiffness with a larger radius and higher number of superperiods. Requirements have been[2]:

1. A maximum magnetic stiffness of 5 Teslameter.
2. At least four long straight sections for injection, extraction, RF cavities and the cooling device.
3. The option of zero dispersion on the straight sections.
4. The working region should be free of systematic resonances up to 5th order.
5. Transverse chromaticities should be small in order to have the working region dominated by space charge.
6. Small beam divergence ("temperature") on the straight sections to reduce the cooling time.
7. Transverse acceptance of 100 × 25 π mm mrad.

Experimental Program

1. High-Current Operation

The high-current limits of the storage ring can be reached for light ions (p, He^{+}, Ne^{2+}) with the Unilac as injector, by observing the space charge limit of the first Wideröe tank (0.375 × A/q mA). The full list of questions to be addressed is:

(a) De-Bunching of Linac beam (final $\Delta p/p$?)
(b) Control of dilution in multi-turn injection
(c) Transverse space charge limit
(d) Transverse resistive wall instability
(e) Microwave Instability for coasting and bunched beam
(f) Holding of high-current bunch
(g) Fast compression with resonance crossing
(h) Bunch merging to attain single bunch on target

2. Electron Cooling

The first series of experiments is to test the capabilities of electron cooling of protons when approaching the high-current limits of the storage ring (instabilities, resonances, etc.). The demands herefore are comparable to the electron cooling experiments of protons already successfully performed in other laboratories, with the exception that we require maximum proton intensity.

The second series would address the question of life-time of partially stripped heavy ions with regard to:

(a) rest gas ionisation (expected to be negligible during cooling if 10^{-11}mbar pressure is achieved)
(b) intra-beam exchange (acceptable if $\sigma < 10^{-15}cm^2$)
(c) recombination with cooling electrons

Cross sections for (b) and (c) are not well-known and should thus be measured as part of the proposed experiments. A simple model for (c) promises that the recombination time is $10^2 \ldots 10^3$ times longer than the cooling time[3].

During performance of this study it was also recognized that a seccessful demonstration of the high-current operation and the electron cooling would lead to a phase space density of the beam sufficiently high to warrant a first-step target experiment. Obviously, a storage ring with higher magnetic rigidity and thus higher maximum kinetic energy would promise higher target temperatures. In particular we found that re-injection into the SIS-18 synchrotron could raise the temperature for volume heating to the interesting regime of 20-30 eV.

References

[1] Möglichkeiten zur Untersuchung dichter, heißer Materie mit einem Schwerionen-Synchrotron, K. Beckert et al., GSI-83-10, Internal Report, 1983.
[2] B. Franzke, SIS-INT/83-5, GSI Internal Report, 1983
[3] Möhl, D., and Kilian, K., CERN Report CERN-EP/82-214 (1982)

B

An improved criterion for stability of coherent motion in circular accelerators

K. Beckert, H. Eickhoff, V.G. Vaccaro*
GSI Darmstadt
* Instituto di Elettrotecnica, Universita di Napoli

In HIBALL[1] and in comparable scenarios for heavy-ion-fusion drivers the performance of the storage rings plays a vital role. Conflicting demands (high intensity, low energy, small momentum spread) have the consequence that traditional stability criteria cannot be fulfilled for these rings. Because of the strong space charge forces involved, the beam is both transversely and longitudinally unstable[2] if no suitable measures are taken to stabilize the beam. The space charge effect leads to an imaginary part of the coupling impedance in the order of $k\Omega$ (in comparison to several 10Ω for relativistic energies). This value is far outside of the normal stability region, and therefore every resistive component of the coupling impedance makes the beam unstable. It has been shown[3] that the onset of these instabilities can be suppressed or at least delayed by Landau damping, if some fraction of the total beam intensity is used to form a stabilizing tail of the distribution function. The goal of the present work was to give a systematic study of the influence of the tails on the stability diagrams, and to derive new and more detailed criteria. As a stability diagram we denote the traditional mapping of the complex, normalized ω-plane onto the V',U'-plane[4]. The normalized coupling constants V' and U' are directly related to the coupling impedance and describe the interaction of the disturbed particle beam with its surrounding (beam pipe). The position of the actual working point in the V',U'-plane, which is devided into stable and unstable areas, then gives the wanted information. Stability is reached if the working point belongs to a stable region.

To derive the required stability criteria we had to solve analytically the corresponding dispersion integrals for standard distributions plus suitable tails. Finally, we used a distribution function with a central part gently smoothing on the right to zero and on the left to a plateau of length T and height B. The plateau is followed by a slope of length ξ, smoothing to zero as well. The total amount of particles in the tail is N = T*B = 1-A, with A being the normalized number of particles in the standard distribution.

The expectation was that it should be possible to obtain a closed island of stability above the normal stability area, and that the size of the island should depend strongly on the tail parameters. These points could be fully confirmed by numerical calculations. One can see that additional large stable regions with boundary values $(V',U')_{max}$ appear in the upper plane in the vicinity of the imaginary axis. As a matter of fact, the results show that the stable region due to the main part of the distribution is unaffected by the tail. On the other hand, the shape of the additional stability region is practically unaffected by the shape of the main part of the distribution function; its position and area is mainly governed by the percentage of particles in the tail.

To be able to draw relevant conclusions on beam stability problems, relations between the coordinates (V',U') of a point in the complex impedance plane and the tail parameters (T,B,ξ,N) had to be found. They are given by the following equations:

Transversal : $2(T+\xi)^{1.5} * N / \xi * V'_{max} \cong 4.75$

$$U'_{max} / (T+\xi) \cong 0.55 \quad .$$

Longitudinal: $T^2 * N / V'_{max} \cong 0.06$

$$(T+\xi) / U'_{max} \cong 0.10 \quad .$$

To use these equations one has to determine first the position of the working point and to derive therefrom the required values $(V',U')_{max}$. Then, appropriate tail parameters are chosen and the calculated particle distribution has to be generated. However, the practical application of these results is an open problem, because no experimental experience exists so far. It might even be that appropriate tails are formed automatically under the influence of strong space charge forces.

References

/1/ HIBALL - A Conceptional Heavy-Ion-Beam-Driven Fusion Reactor Study; KfK and UWFDM (1981).
/2/ J.L.Laclare, GSI-82-8, p.278.
/3/ I.Hoffmann et al., IEEE Vol. NS-30, No.4, August 1983, p.2546.
/4/ K.Huebner et al., CERN-ISR-TH-RF/69-23,1969.

B

Nonlinear Phenomena in Computer Simulation of the Microwave Instability

I. Hofmann and I. Bozsik
GSI Darmstadt

In storage rings with high currents of nonrelativistic heavy ions, as considered for drivers in inertial fusion, control of the resistive microwave instability has been recognized as a key issue during the last HIF workshop[1] held at GSI in 1982. By means of computer simulation with the particle-in-cell code SCOP-RZ[2] we have shown that the predictions from the linearized theory of instability are over-pessimistic. This is due to an early nonlinear saturation of the instability, which prevents a harmful broadening of the momentum distribution. The main effect of the initially unstable behavior is the development of a thin stabilizing tail in the momentum distribution towards lower momenta, which produces enough Landau damping to suppress any further microwave activity.

The main concern has been the effect of a broad band (Q = 1) resonator centered at about the lowest magnetic cut-off frequency $\omega_c = \gamma\Omega_o$ R/h; this resonator is supposed to describe the effect of many cross section variations. The impedance of this resonator (~ 10 Ω) is supplimented by the large (purely capacitative) impedance due to space charge (Im Z ≥ 1 kΩ). The large ratio ImZ/ReZ of about 100 is the reason, why nonlinear coupling effects dominate over the growth of a single mode for HIF parameters. In Fig. 1 a,b we show the momentum distributions for two distinct cases. Case (a) refers to a nearly relativistic beam with ImZ/ReZ = 2 and a momentum width, wich is a factor 2.2 below the Keil-Schnell stability limit. The distribution becomes rapidly unstable and shows the expected overall broadening. In case (b) we have assumed ImZ/ReZ = 16 and a momentum width that is even a factor 4 below the Keil-Schnell limit. The instability is substantially weaker and stops after having developped a stabilizing tail. The main part of the distribution remains narrow, hence the initially high phase space density is not diluted. The fraction of total intensity within the stabilizing tail decreases with increasing ratio ImZ/ReZ. For the heavy ion fusion case, where this ratio is about 100, we thus expect only a few per cent of tail population. This result of simulation is consistent with the prediction of stability obtained from solving the dispersion integral for a narrow Gaussian momentum distribution with a broad stabilizing tail[3] (of Gaussian shape, but containing only a few per cent of total intensity), as an approximation to the saturated distribution obtained from simulation.

In the future experimental verification of this stabilizing mechanism is highly desirable. Such experiments will have to check whether the predicted rapid coupling to higher harmonics above the cut-off frequency takes place in a real machine to the same degree as in the simulation, where the deviations (in impedance) from a circular conducting pipe have been incorporated in the simplified model of a Q = 1-resonator near cut-off.

References:

[1] Proc. of the Symposium on Accelerator Aspects of Heavy Ion Fusion, GSI Darmstadt, 1982, p. 356.

[2] I. Hofmann, Proc. Conf. on Computing in Accelerator Design and Operation, Berlin, paper A 203, 1983.

[3] I. Hofmann, I. Bozsik and A. Jahnke, IEEE Trans.Nucl.Sci. NS-30, 2546 (1983)

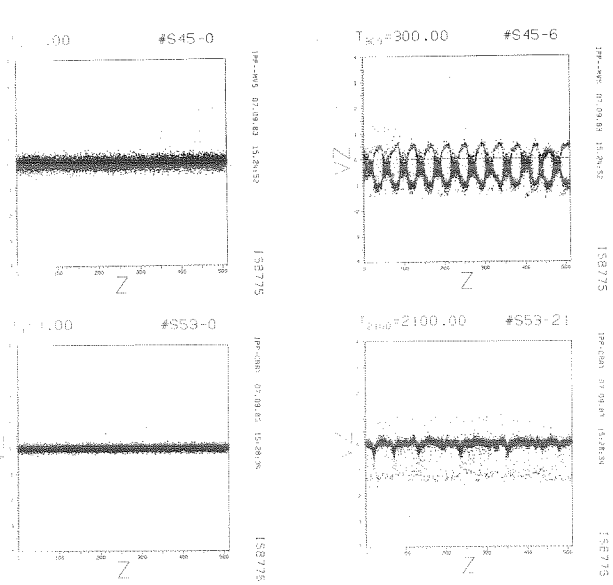


Fig.1: Projections into longitudinal phase plane.

a) nearly relativistic case

b) non-relativistic case

HIGH-CURRENT ION SOURCES DEVELOPMENT

R. Keller and P. Spädtke
GSI Darmstadt

The work with high-current ion sources concentrated on two main lines: beam production for various experiments and improvement of individual source components. This already indicates that the basic development of the source system CHORDIS [1] (Cold/HOt Reflex Discharge Ion Source) has been satisfactorily concluded; consequently, GSI had two more sources manufactured. For optimum performance in different applications, however, there still remain many items to be revised, according to the operating experiences.

A new standard accel/decel extraction system was constructed for the cold source version CORDIS, with much more reliability regarding HV sparking and mechanical stability. An analogous system for the hot version HORDIS, see fig. 1, is in preparation. Some computer calculations [2] of temperature distributions, expansion motions, and mechanical stresses to be expected gave valuable hints for its design.

The influence of various potentials, applied to the two reflector electrodes of the gas source CORDIS, on discharge and beam characteristics was investigated, but only small effects were found. The best performance was obtained connecting the reflector on cathode side to the nagative cathode leg and biasing the other one still more negative.

In a series of computer simulations using the code AXCEL-GSI [3], the optimum aperture profile for an accel/decel extraction system was looked for under the constraints of easy manufacturing, high current share within the given acceptance, and conservative operation conditions. Excellent coincidence was found between code prediction, 8.5 mA argon ions, and really measured current, 8.2 mA, for the finally chosen configuration. The beam served to produce metallic ion clusters for laser spectroscopy experiments [4]. During the test run, HV sparks occured only two times in three hours, and the filament life-time exceeded 80 hours at 1.5 kW d.c. discharge power.

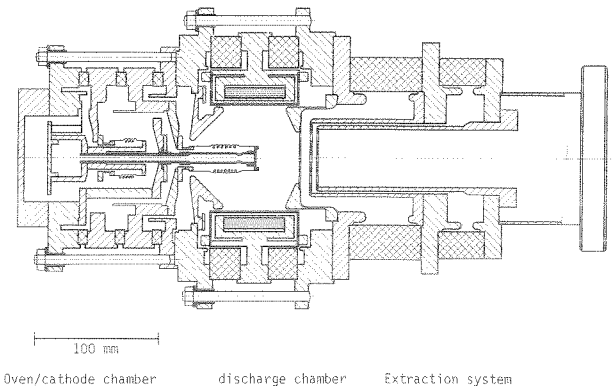
For the metal source HORDIS, two main problems arose when working with calcium and lithium. First, much vapour condensates on the screen electrode of the extraction system, especially with a pulsed discharge. Thus, for a given voltage, a wider gap must be chosen than usual with CORDIS, leading to less beam brightness. Secondly, liquid feeding material leaked out of the oven back side; alternative designs for the back cover are actually being tested. As a top result, 58.5 mA d.c. of Li^+ were measured [5] at 30 kV.

As part of GSI projects, high-current beams were produced [6] on the 300 kV accelerator for the beam transport experiment [7] and the RFQ accelerator [8], using the prototype source ELSIRE [9]. Some runs on the UNILAC demonstrated that with CORDIS the beam microstructure can be much cleaner than with the normally used PIG sources [10].

In the experiments dedicated to the hollow-beam transport system [11], of 30 mA injected argon ion current only 3 mA could be measured at the end of the system; this low transmission may be due to a wrong emittance orientation at the entrance plane.

References

1 R.Keller, P.Spädtke, F.Nöhmayer: Int.Ion Engineering Congr., Kyoto, p. 25 (1983)
2 Calculations done by C.Riedel and E. Labinsky, GSI Darmstadt
3 P.Spädtke: GSI-83-9, GSI Darmstadt (1983)
4 P.Fayet, R.Keller, L.Wöste: Int. Laser Conf., Guangzhou, P. R. China (1983)
5 Collaboration with H.Bay, IPP Jülich
6 P.Spädtke, R.Keller: This Scientific Report
7 J.Klabunde, M.Reiser, A.Schönlein, P.Spädtke, J. Struckmeier: Particle Acc. Conf., Santa Fe (1983)
8 R.W.Müller et al.: Int. Symp. Heavy Ion Acc. and Appl. to Inertial Fusion, Tokyo (1984)
9 R.Keller: Nucl. Instr. Meth. 189, 97 (1981)
10 J.Klabunde et al.: to be published, GSI Darmstadt
11 P.Krejcik, R.Keller: Int. Ion Engineering Congr., Kyoto, p. 549 (1983)



High-Current Ion Source HORDIS for Non-Volatile Elements

COMPUTER SIMULATION OF HIGH-CURRENT DC BEAM TRANSPORT

Peter Spädtke, GSI Darmstadt

Computer codes have been increasingly used in the field of high-current ion-optics during the last years. With the help of several programs the solution of different problems can be optimized, for example extraction systems for high-current ion sources. Additionally these programs help to study beam optics phenomena. The status of a special kind of these codes will be reported.

In the case of a high-current dc-beam (no time dependence), space-charge plays an important role if there is no compensation. Analytical solutions of the resulting beam potentials are known only for very special ion distribution functions. One possibility to find a self-consistent particle-distribution function with numerical methods is the following:

First the electrostatic potential for a given geometry without space-charge is calculated. After this, particle trajectories and simultaneously the ion space-charge distribution function are calculated. Then the nonlinear Poisson equation is solved again and so on until this procedure converges. In this case the self consistent ion distribution function is found for the given starting conditions of the ion beam. These conditions are described by the beam emittance.

In the case of cylindrical symmetry the problem is two-dimensional and can be solved by the program AXCEL-GSI[2] which has the following advantages:

-The code is interactive. By implementing Carre's[1] method, the subroutine solving Poisson's equation is very fast.

-The graphic output includes three different options (see fig.1), compatible with the new graphic system. This output ensures a fast feedback to the user.

-Program dimensions have been increased to reduce the discretisation error of the mesh. It is possible to define up to 130.000 node points, and up to 1000 rays can be traced through the potential.

-The treatment of partial space-charge compensation is optional.

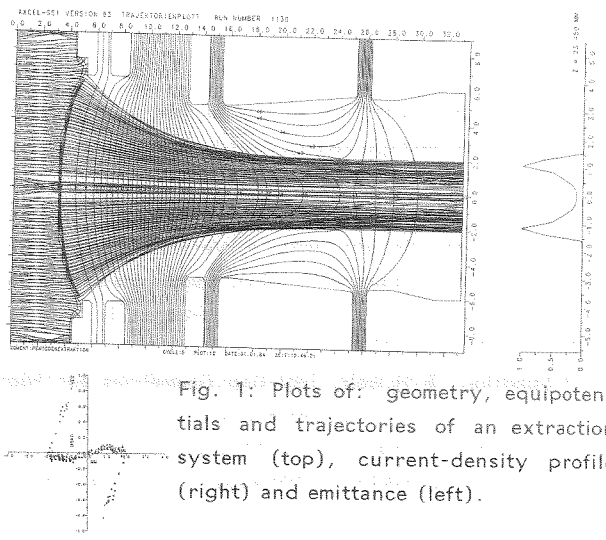


Fig. 1: Plots of: geometry, equipotentials and trajectories of an extraction system (top), current-density profile (right) and emittance (left).

If there is no symmetry, then the three-dimensional program KOBRA3 which calculates the nonlinear Poisson equation has to be used. Magnetic fields can be introduced analytically or by the help of other programs. After this, trajectories can be calculated with three dimensions. To improve the flexibility of the program, the code has been broken up into its logical parts:

-Creation of the node information
-Poisson solver
-Calculation of magnetic flux-density
-Raytracing and calculation of space-charge distribution
-plot
-edit.

The program works with a nonuniform node mesh, in which the distances between nearest node point and geometry are calculated exactly. This method reduces the discretisation error.

As an example for the flexibility of the program fig.2 shows an ion beam (O^{6+}, 72keV, emittance ε = 200mm mrad, start diameter ∅ 4mm) passing through a magnetic solenoid with a tilt of 50mrad with respect to the geometrical axis.

The magnetic flux density distribution has been calculated with the two-dimensional code POISSON, transformed into three dimensions and then transferred to KOBRA3.

[1] B.A.Carre, 'The Determination of the Optimum Accelerating Factor for Successive Overrelaxation', Computer Journal, Vol.4, No.1 (1961)

[2] P.Spädtke, 'AXCEL-GSI Interaktives Simulationsprogramm zur Berechnung von zweidimensionalen Potentialverteilungen elektrostatischer Anordnungen sowie von Ionenbahnen in elektrostatischen Feldern unter Berücksichtigung der Raumladung', GSI-Report 83-9

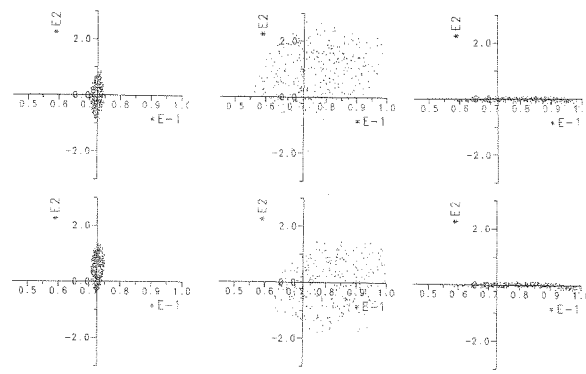


Fig.2: Emittance of the beam in the beginning (left), in the midplane (middle) and at the end (right) of the solenoid.
First row : x,x'-emittance, second row y,y'-emittance

PRE-ACCELERATION OF HIGH-CURRENT DC ION BEAMS

P.Spädtke, H.Emig , R.Keller, J.Klabunde,
K.D.Leible, D.Vogt, B.H.Wolf
GSI Darmstadt

For the heavy-ion fusion project a high-quality ion beam with a very high current-density on the pellet is essential. To generate such a high-brightness high-current ion beam an optimized ion beam extraction system from the ion source and an optimized accelerating column are required. Such a column is needed since no direct extraction system (up to 300kV for J^+ for injection into the MAXILAC[1]) exists. In the range of ion currents we are working with, it has been shown that single-gap acceleration is better suited than low-gradient, multi-gap acceleration[2]. Beyond the acceleration-gap the space-charge compensation of the beam will be achieved by collisions with residual gas atoms. It should be preserved by inserting negative screen electrodes at those places, where electrons are expected to leak out of the beam (see fig.1).

For two different HF-accelerators high-current beams have been delivered in the last year at GSI. In both cases we looked for the best possible beam quality at the highest current which could still be transported.

-High current injection into the Wideröe-tank of the UNILAC with 11.7keV/amu injection energy. In all cases the ion source CORDIS[3] has been used. Injected ions were H^+, N^+, Ne^+, Ar^{++}. The results are listed in tab.1.

Extr.	Gap/mm	U_{ac}/kV	Ion	I_{FC}/mA
EX4	180	45+160*	H^+	5.5
EX1	100	26+134	N^+	5.0
EX2	100	32+117	Ne^+	8.0
EX3	180	25+200	Ne^+	10.0
EX3	180	37+210	Ne^+	20.0
EX3	180	30+210	Ne^{++}	1.2
EX4	180	43+190	Ne^+	12.0
EX3	180	25+190	Ar^+	16.0
EX3	180	25+190	Ar^{++}	3.0

Tab.1: Measured currents I_{FC} in a Faraday-cup with ∅ 30mm aperture, after 8m beam-transport, behind the 77.5° inflector magnet.

* For H^+, the Wideröe-tank 1 is used as a focusing channel without acceleration. EX1-3 are triode extraction systems with single- (1,2) or multi-aperture bores (3), whereas EX4 is a single-aperture pentode extraction system. U_{ac} are the extraction- and the acceleration-voltages. The apertures in the acceleration electrodes were ∅40mm (high potential) and ∅50mm (ground).

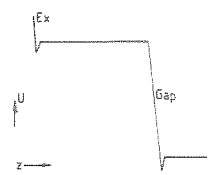


Fig.1: Potential on the beam axis. The negative screen electrodes reflect the beam electrons.

-High current injection into the RFQ-tank MAXILAC at the 300kV-accelerator of GSI, with 2.2keV/amu. Injected ions were Ar^+ and Kr^+. In this experiment we still work with the prototype ion source ELSIRE[4].

Extr.	Gap/mm	U_{ac}/kV	Ion	I_{FC}/mA
EX1	30	30+80	Ar^+	8.0
EX3	30	15+65	Ar^+	6.0
EX3	30	20+90	Ar^+	12.0
EX3	30	25+110	Ar^+	16.0
EX3	30	30+120	Kr^+	14.0
EX3	60	30+160	Kr^+	20.0

Tab.2: Measured optimized currents in a Faraday-cup with an aperture of ∅ 30mm directly behind the gap.

The acceleration of the lower mass is difficult because of the low injection energy of 90keV, required by the acceptance of the RFQ. With an extraction voltage of 30kV there remained only 60kV to accelerate (and to match) the high-current beam. While for the single-aperture the resulting electric field is high enough, a higher gradient is necessary for the multi-aperture due to the higher current. Because the gap-length must be long enough to ensure normal operating up to 300kV at a parallel beam-line, we did not reach optimized operation.

For Kr^+ an injection energy of 180keV is required. Therefore, we had to increase the gap-width to match the beam into the RFQ-acceptance.

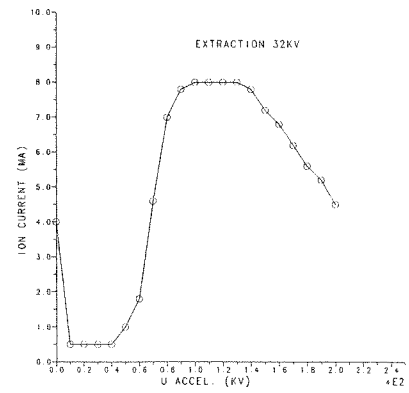


Fig. 2: Typical behaviour of ion current as a function of acceleration voltage (tab.1, third row).

[1] R.W.Müller, U.Kopf, J.Bolle, S.Arai, P.Spädtke, 'Experimental Results with a Very-Heavy-Ion RFQ Accelerating Structure at GSI', Symp. on Heavy Ion Accelerators and Their Applications to Inertial Fusion, Tokyo (1984)

[2] P.Spädtke, B.H.Wolf, 'HV-Gap Geometries for High Current Heavy Ion Acceleration and Beam Transport', Low Energy Ion Beams, Loughborough (1983)

[3] R.Keller, P.Spädtke, F.Nöhmayer, The International Ion Engineering Congress, Kyoto (1983)

[4] R.Keller, Nucl. Instr. Meth. 189, 97 (1981)

DEVELOPMENTS IN THE HIGH-CURRENT HOLLOW BEAM TEST EXPERIMENT

B

P. Krejcik, KFA Jülich
R. Keller and P. Spädtke, GSI Darmstadt

A test stand for transporting high-current hollow beams has been described in previous reports[1,2]. The facility is designed to study the properties of such beams under strong space charge conditions when strong focusing lenses are employed. The lenses used are of the radial field focusing electrostatic coaxial cylinder type. This precludes any neutralisation of the beam occuring and thus closely resembles the situation in an RF accelerating structure. Results from this test experiment are therefore applicable to the design of high-current injector accelerators based on this focusing principle[3].

The activities at the hollow beam test stand over the last year can be summarized as follows: transporting the beam through the full quota of 12 focusing cells; a study of diagnostic techniques for measuring the transmission efficiency of the system; measurement of beam emittance at the entrance to the focusing channel; characterizing the effects of beam pulse length on the active optical elements; and further studying the properties of the system via particle simulations using the code AXCEL-GSI[4].

The commissioning of the test stand was described in last year's report[2] along with a survey of the inevitable teething problems associated with such a new device. However, we could bring the stand to the state where about 30 mA could be injected into the periodic focusing section of the transport line. The beam current at the end of the transport line was measured as a function of the voltage applied to the lenses. This test indicated the presence of two main problems: namely that the beam loading of the high voltage supplies for the lenses and extraction could wildly alter the focusing tune during the beam pulse; and secondly that a severe mismatch still existed between the ion source emittance and the focusing channel acceptance.

The first problem could be neatly solved by firstly operating the ion source with much shorter pulses (100 μs) and secondly connecting large capacitors parallel to the lenses.

The response of the transport section with these stabilized operating conditions was then as predicted, with the transmitted current increasing steadily as the lens voltages were increased. In the periodic focusing section all the negative lenses are excited at the same potential and all the positive lenses are also at a common potential.

As the tune in the periodic channel is raised the lenses in the matching section must also be changed and it was found that better optimization was achieved if the first lens in the periodic section could also be independently adjusted. However, the transmitted current ceased to increase over 3 mA once the tune in the transport section reached about 20° indicating that a serious mismatch still existed between the ion source and the transport section.

To quantify a mismatch condition one should ideally diagnose simultaneously the beam at the entrance and exit of the transport section. Since space is always a limiting factor in low energy beam transport systems, the only possibility here was a beam transformer (Rogowski coil) that could be located outside of the vacuum. Unfortunately the large diameter of the coil necessitated by the large hollow beam diameter made the coil an excellent antenna for RF noise making this type of measurements impossible.

Emittance measurements after the ion source showed a much greater beam divergence than was expected. In fact, in the short drift space between the ion source and the matching doublet the hollow beam made an axial crossover. Such a mismatch cannot be corrected by the lenses, so a large fraction of the beam is lost on the central rod of the matching section. This effect is now being studied to see if the ion source characteristics can be changed to give a less divergent beam. If not, the lenses must be repositioned nearer to the ion source in order to accept the beam before the crossover occurs.

References

1 P.Krejcik: GSI 83-1, GSI Darmstadt, p.295 (1983)
2 P.Krejcik, R.Keller: GSI 83-1, p. 296 (1983)
3 P.Krejcik: IEEE Trans. Nucl. Sci. NS-30, p. 3168 (1983)
4 P.Spädtke: GSI-83-9, GSI Darmstadt (1983)

Heavy Ion RFQ Accelerator "MAXILAC"

R.W. Müller, U. Kopf, J. Bolle, S. Arai*, P. Spädtke

GSI Darmstadt

*INS Tokyo, Japan

The 1.55 m long first module of the heavy ion RFQ accelerator MAXILAC[1,2], which is the first high-intensity linac for ions heavier than Li^+, has been taken into operation.

In May the theoretical resonance resistance of the cavity, of 262 kOhms, was reached. After a few days of conditioning, r.f. voltages of 130 kV could be held. Higher voltages (155 kV for $^{127}I^+$) require some more X-ray screening.

In October a $^{40}Ar^+$ beam from an ELSIRE source, accelerated to 92 keV, was injected. A strong beam current, of the order of several milliamperes, was accepted immediately. The maximum ion current at the end of the structure has been 6 mA, for which a relative betatron tune depression in the gentle-buncher region of 30 % is calculated.

Improvements made in the meantime have been:

a) Installation of a matching-out section similar to the matching-in section, but only 1 $\beta\lambda$ long. This device, which can be installed and removed very quickly, improves the beam quality at the output remarkably.

b) Rearranged beam optics at the input end (better matching), and defining beam entrance apertures, improved the purity of the beam, they especially removed some spill beam in the space between bunches.

c) Calorimetric measurements have been done to determine the average particle energy, and to get insight into the capture rate. At the design voltage, the capture rate is between 60 and 80 % depending on injection parameters (this was the situation before improvement (b) had been made, new data have not yet been taken). The r.f. voltage has been recalibrated by looking at the emitted X-ray spectrum.

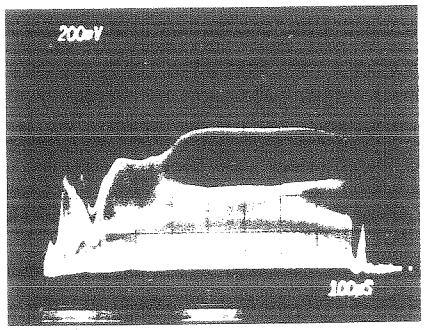


Fig. 1

8mA

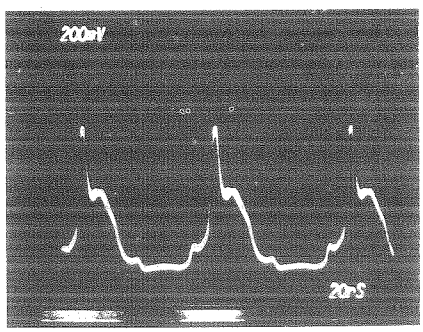


Fig. 2

8mA

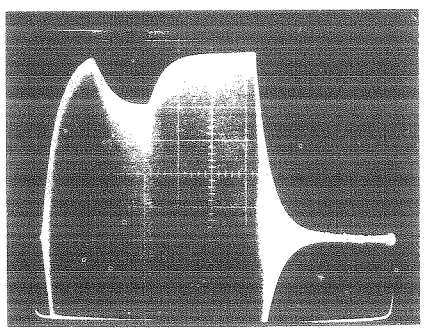


Fig. 3

10 kV

Fig. 1 shows the current from a fast 50 Ohms cup. This current is 3 times higher than the true ion current because of secondary electrons (the true ion current is measured by a second, long but slow cup). Fig. 2 shows the same current over a different time scale; these micro-bunch shapes look as expected from theory, and have the proper length of 30 nanoseconds (see fig. 4).

The first 400 microseconds of the pulse of fig. 1 are not very clean. Fig. 3 shows why this happens. It shows an r.f. signal coupled out of the cavity. The 27 %-voltage drop which occurs some time after the onset of the beam, is the well-known beam load effect.

Tasks for the near future will be: Measuring and improving the beam properties, accelerating heavier ions, and proceeding in completing the accelerator by four more modules.

References:

[1] R.W. Müller, L.W. Funk, U. Kopf. GSI 82-1, 312

[2] R.W. Müller, U. Kopf, L.W. Funk. GSI 83-1, 289

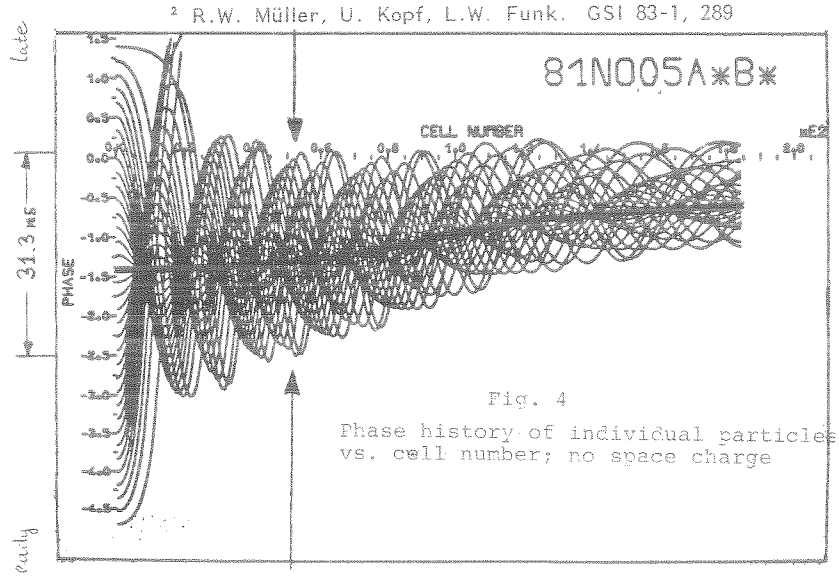


Fig. 4
Phase history of individual particles vs. cell number; no space charge

DEVELOPMENT OF SPLIT COAXIAL RFQ-RESONATORS B

H. Klein, W. Neumann, H. Deitinghoff, P. Junior, K. Langbein,
P. Leipe, G. Riehl, A. Schempp
Institut für Angewandte Physik der Universität Frankfurt am Main

R. W. Müller
GSI Darmstadt

Based on a proposal for a heavy ion RFQ using split coaxial resonators[1] a proton model scaled 1:4 was built up at the Institut für Angewandte Physik in collaboration with GSI. Results of extensive experiments have been reported in [2,3]. While the energy distribution of the accelerated beam agreed well with predicted values[4], problems appeared mainly with the transverse matching of the beam. Fig. 1 shows the transmitted current behind each section as a function of rf-voltage. The raise in current up to voltages of 4 kV is mainly caused by higher σ_{0t}. The drop of transmitted current behind tank 3 led to the detection of a radial 2 mm misalignment of drift tubes in tank 3.
Simulation of particle dynamics using the PARMTEQ-code[5], which was modified to treat electric fields with higher spatial harmonics, showed the reason of the matching problems. For the design value of 1.9 kV rf-voltage and σ_{0t} = 20° the higher spatial harmonics of the focussing gradient cause a drop in acceptance from the expected value of 225 mm mrad (unnorm.) to values between 50 and 100 mm mrad. Fig. 2 shows the calculated acceptances for different input phases. With an emittance measuring device, developed at GSI, a source emittance of 320 mm mrad was determined, which has to be compared with calculated acceptance. Transmission simulation with this emittance (fig. 4) agreed well with the measured transmission shown in fig. 1. PARMTEQ-simulation reveals also that the current limit is lower than predicted by smooth-approximation-theory. Tab. 1 presents theoretical current limits and results of actual experiments. The influence of higher spatial harmonics reduces current limits.
According to the experience with the proton model the RFQ design has been modified[7]. A higher σ_{0t} was chosen and influence of spatial harmonics has been reduced. The acceptances (fig. 5) show the improvement. PARMTEQ-simulation[6] yields a current limit of 9.6 mA compared to the estimate by smooth approximation of 10 mA for Ar^+-ions. Fig. 6 shows the particle oscillations in phase/energy phase-space for this case. For the first installed section, the simulation gives a current limit of 11 mA. In a first experiment at GSI, which is reported in[7], a beam current of 6 mA was obtained.
Computations have been done at GSI and the Hochschulrechenzentrum of the University of Frankfurt.

Tab. 1: Current limits in the proton model

rf-voltage	theor. value	PARMTEQ simulation	reached in experiment
1900 V	400 µA	60 µA	20 µA
4000 V	3500 µA	700 µA	100 µA

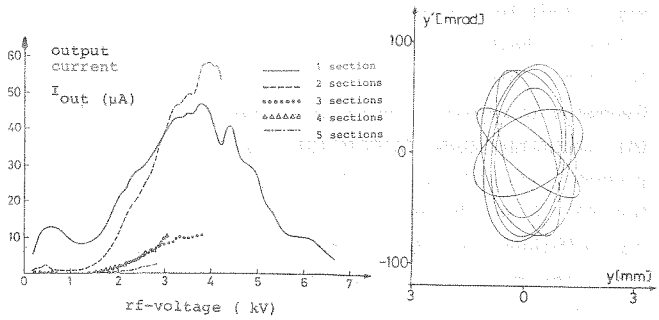


Fig. 1 Output current as function of rf voltage
Fig. 2 Transverse acceptance of the proton model

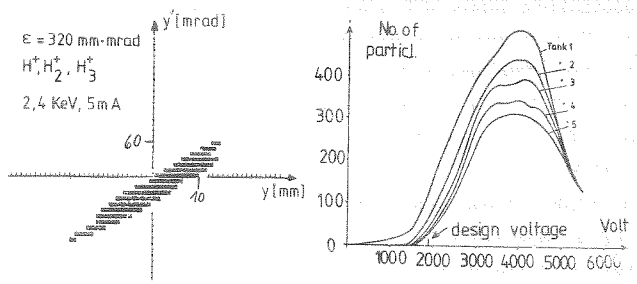


Fig. 3 Ion source emittance
Fig. 4 PARMTEQ-simulation of transmission ε_{in} = 300 mm mrad

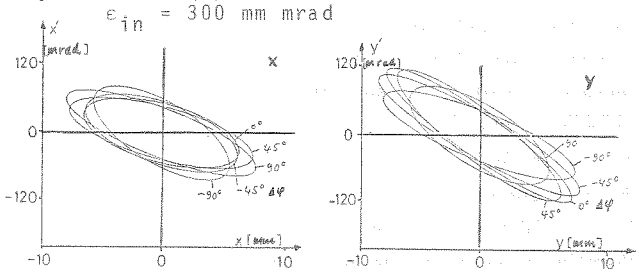


Fig. 5 Transverse acceptances of the MAXILAC-RFQ. Ar^+, 90 kV, α = 360 mm mrad

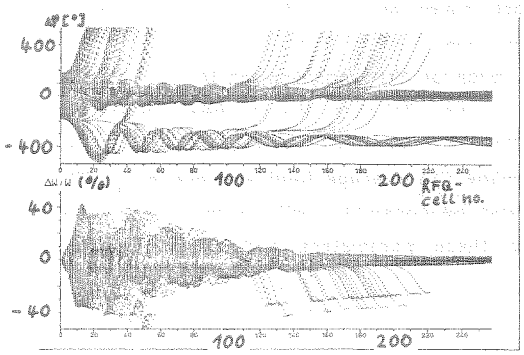


Fig. 6 Particle oscillation in MAXILAC, 9.6 mA

References

1) R.W. Müller, GSI-Rep. 79-7 (1979)
2) GSI annual reports of heavy ion fusion, GSI Reps. 81-3, p. 12; 82-6, p. 24; 83-2, p. 9
3) H. Klein, IEEE Trans. Nucl. Sci., Vol.NS-30 4 (1983), part II, p. 3313
4) J. Müller, Dr. thesis, Univ. of Frankfurt, Institut für Angewandte Physik, 1983
5) W. Neumann, Univ. of Frankfurt, Inst. für Angew. Physik, Int. Rep. 83-25 (unpubl.)
6) W. Neumann, Univ. of Frankfurt, Inst. f. Angew. Physik, Int. Rep. 83-30 (unpubl.)
7) R.W. Müller et al., GSI-84-5 preprint

B

Drift-Tube Geometry Optimization

J. Ungrin+
GSI Darmstadt

The high current linac injector for the storage rings for heavy ion fusion will require a large investment in installed rf power[1]. This investment can be reduced if the accelerator structure efficiency can be increased. A study of the effective shunt impedance, ZT^2, as a function of cell geometry has been made for the low-energy drift-tube section of such a linac. The HIBALL reference design frequency of 108 MHz[2] for the Alvarez section has been used.

Geometry optimization calculations have been made with the computer code SUPERFISH starting with the cell geometry of UNILAC. At the start of the Alvarez section ($\beta \sim 0.06$) the main difficulty occurs with maintaining sufficient room to package the quadrupole magnet within the drift-tube. The drift-tube bore hole size and the ratio of the accelerating gap length, G, to the cell length, L, are the two parameters available to optimize ZT^2. The bore hole size must be kept as small as beam acceptance limits will allow. At $\beta = 0.06$ ZT^2 increases by 25 % as the bore radius is decreased from 2.0 cm to 1.0 cm. The maximum ZT^2 is obtained at $\beta = 0.06$ with $G/L \sim 0.15$ - a value somewhat smaller than the value of 0.25 used on UNILAC. The improvement in ZT^2 is ~ 11 %.

At higher beam energy the drift-tube length increases and a face angle can be introduced on the drift-tube face to increase ZT^2. Fig. 1 shows ZT^2 as a function of G/L for face angles from 0° to 30° at $\beta = 0.112$ (6 MeV/u). Also shown on the figure is the maximum field on the drift-tube surface, E_s, (normalized to an average axial field of 1.0 MV/m). As the face angle increases both ZT^2 and the maximum surface field increase. The G/L value at which the maximum ZT^2 occurs decreases from 0.18 at 0° face angle to 0.08 at a 30° face angle.

For a given G/L as the face angle increases the cell diameter must be increased to maintain the correct resonant frequency. Fig. 2 shows the cell diameter and surface fields as a function of G/L for the four face angles shown in Fig. 1.

How much of the improvement in ZT^2 with face angle can be used depends also on beam dynamics and cost (capital vs operating) optimization. These parameters determine the average field and hence E_s. This E_s value must be consistent with acceptable sparking rates. Using these parameters and a series of curves like Fig. 1 and 2 an optimized geometry along the linac can be chosen.

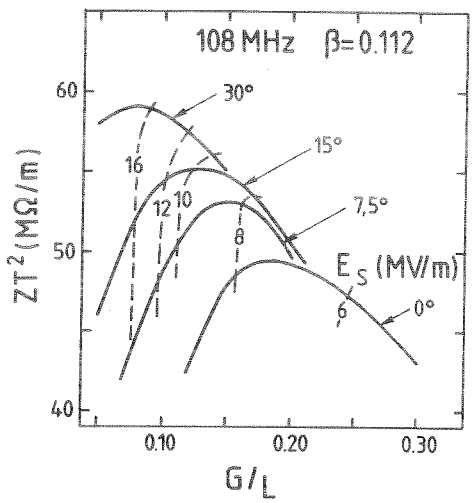


Fig. 1: ZT^2 vs G/L for various drift-tube face angles. E_s is surface field normalized to $E_0 = 1.0$ MV/m. Drift-tube bore radius 1.0 cm, diamter 20 cm, nose radius 0.3 cm, outer radius 2.0 cm and stem radius 2.5 cm.

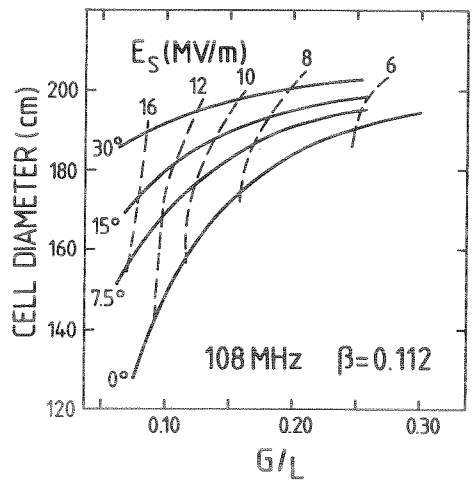


Fig. 2: Cell diameter vs G/L for various face angles.

References

(1) R.W. Müller and K. Beckert in GSI 83-1, 286.
(2) Proc. of the Symposium of Accelerator Aspects of Heavy Ion Fusion GSI-82-8.

+ Visiting scientist from AECL, Chalk River

K-V AND GAUSS DISTRIBUTIONS AT INCREASING INTENSITIES

J. Struckmeier , J. Klabunde , M. Reiser*

GSI - Darmstadt

In view of the fact that a Gauss distribution comes perhaps closest to a real beam, we investigated its behavior over a wide parameter range of decreasing σ values (i.e. increasing intensity) and compared it with a K-V distribution. We made a large number of simulation runs for the two distributions at fixed values of $\sigma_0 = 90°$ and $\sigma_0 = 60°$ using the geometry of the GSI channel[1].

a) $\sigma_0 = 90°$

Fig. 1 shows the r.m.s. emittance growth after 100 cells for a K-V and a Gauss distribution at $\sigma_0=90°$ and various values of σ. As can be seen, the two types of distribution functions behave quite differently:

- The K-V distribution shows the expected emittance growth due to a third-order instability[2] in the region $60° \geq \sigma \geq 38°$. The sharp decrease of the emittance growth at $\sigma \approx 38°$ indicates that the third-order instability is no longer present. As σ decreases, i.e. at higher intensities, the fourth- and higher-order modes take effect in the region $\sigma < 37°$.
- The Gauss distribution shows a monotonic increase in the emittance growth factors as σ decreases. One part of that emittance growth can be attributed to the "homogenization" effect discussed in Ref. 3 and Ref. 4 since a sharp rise in the r.m.s. emittance occurs within the first cell. The emittance growth as calculated from our formulae are indicated by the dashed line for the lower boundary value and by the dotted line for the upper one. It is seen that the actual emittance growth is considerably larger than the formulae predict. This difference suggests that the action of the resonances in the region $\sigma < 60°$ is still present.

b) $\sigma_0 = 60°$

Fig. 2 shows the r.m.s. emittance growth after 50 cells for a K-V and a Gauss distribution at $\sigma_0=60°$. For the K-V distribution, no emittance growth occurs above $\sigma=10°$. Below that value, a small growth is obtained, which is due to a fourth-order instability mode.
The emittance growth factors for the Gauss distribution obtained from particle simulations lie exactly between those calculated from the emittance growth formulae mentioned above, as the comparison of the dashed and the dotted analytical curves with the simulation results indicates. This suggests that the Gauss distribution, like the K-V distribution is also stable with respect to fourth and higher-order modes under these conditions, and that the emittance growth can be explained in terms of the "homogenization" effect. This explanation is confirmed by the fact, that in all simulation runs at values of σ greater than 10° no further emittance growth is observed after the initial change of the charge distribution in the first period of the channel.

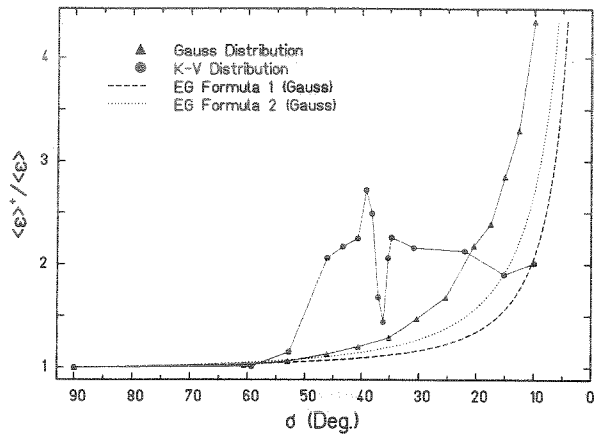


Fig. 1 : Emittance growth factors versus σ after 100 cells of the GSI quadrupole channel for initial K-V and Gauss distributions at $\sigma_0=90°$

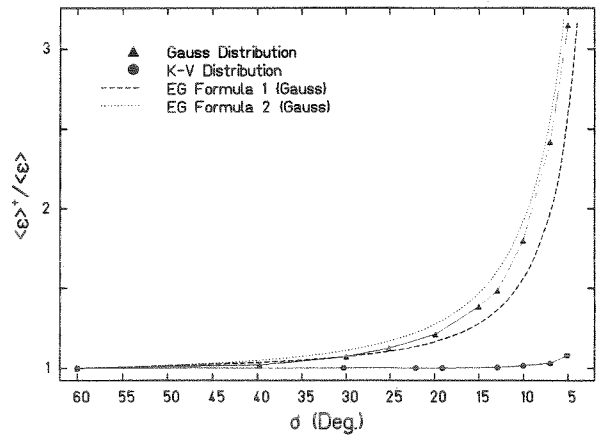


Fig. 2 : Emittance growth factors versus σ after 50 cells of the GSI quadrupole channel for initial K-V and Gauss distributions at $\sigma_0=60°$

References

[1] J.Klabunde, M.Reiser, A.Schönlein, P.Spädtke, and J.Struckmeier, IEEE Trans.Nucl.Sci. 30, 2543 (1983)

[2] I.Hofmann, L.J.Laslett, L.Smith, and I.Haber Particle Accelerators, 13, 145 (1983)

[3] J.Struckmeier, J.Klabunde, M.Reiser, GSI Preprint 83-33, to be published in "Particle Accelerators"

[4] J.Struckmeier, J.Klabunde, M.Reiser, this annual report

* University of Maryland

EMITTANCE GROWTH DUE TO A CHANGE OF THE PARTICLE DISTRIBUTION

J. Struckmeier , J. Klabunde , M. Reiser*

GSI - Darmstadt

The K-V distribution is the only one for which a self-consistent beam matching is possible in a linear periodic quadrupole channel. Since non-K-V distributions are not stationary if the space charge forces are not negligible, they undergo a complete change during the transformation through a beam transport line, leading to a more homogeneous charge distribution in real space. The left column of Fig. 1 shows the real space projections of a K-V, waterbag, parabolic, conical and Gauss particle phase space distribution, defined in Ref. 1, whereas the right column shows the location of the particles in real space as they occur having been tracked through one period of the GSI quadrupole channel[2] at $\sigma_0=60°$, $\sigma=15°$. This process of a reorganization of the particle phase space distribution towards a more self-consistent, i.e. stationary one yields an increase of the quantities $\langle r^2 \rangle$ and $\langle r'^2 \rangle$, hence an increase of the r.m.s. emittance of the beam, resulting from the transformation of internal field energy associated with the initial charge distribution to additional transverse kinetic and potential energy of the beam in the focusing channel.

In order to obtain an analytical estimation of that emittance growth, an r.m.s.-matched non-K-V distribution that changes its charge density in real space towards a homogeneous one is treated as an equivalent K-V distribution that becomes "heated up".

The amount of the "initial" emittance growth depends on the type of the initial distribution and increases from the waterbag over the parabolic and conical towards the Gauss distribution. For each distribution we calculated a dimensionless geometry factor "f", which describes the difference between the field energy ΔW of the appropriate distribution and that of a K-V beam. For example, this factor amounts to ≈0.03861 for a Gauss distribution.

Assuming first that this difference is transformed into kinetic and potential energy and secondly into kinetic energy only via homogenization of the charge density in real space, one obtains the following estimations for the "initial" emittance growth:

$$\sqrt{1 + f\cdot\left(\frac{\sigma_0^2}{\sigma^2} - 1\right)} < \frac{\langle\varepsilon\rangle^+}{\langle\varepsilon\rangle} < \sqrt{1 + 2f\cdot\left(\frac{\sigma_0^2}{\sigma^2} - 1\right)}$$

The results obtained with these formulae have been found in good agreement with those obtained by the simulation studies for $\sigma_0 = 60°$ where no K-V instabilities[3,4] are observed and where the "homogenization" is the only source of emittance growth. This specific "initial" emittance growth of the not self-consistent particle distributions is due to the internal matching of the charges to the linear external forces and holds even for perfectly r.m.s.-matched beams. Therefore it is only a result of the type of particle distribution used at the start of the simulations.

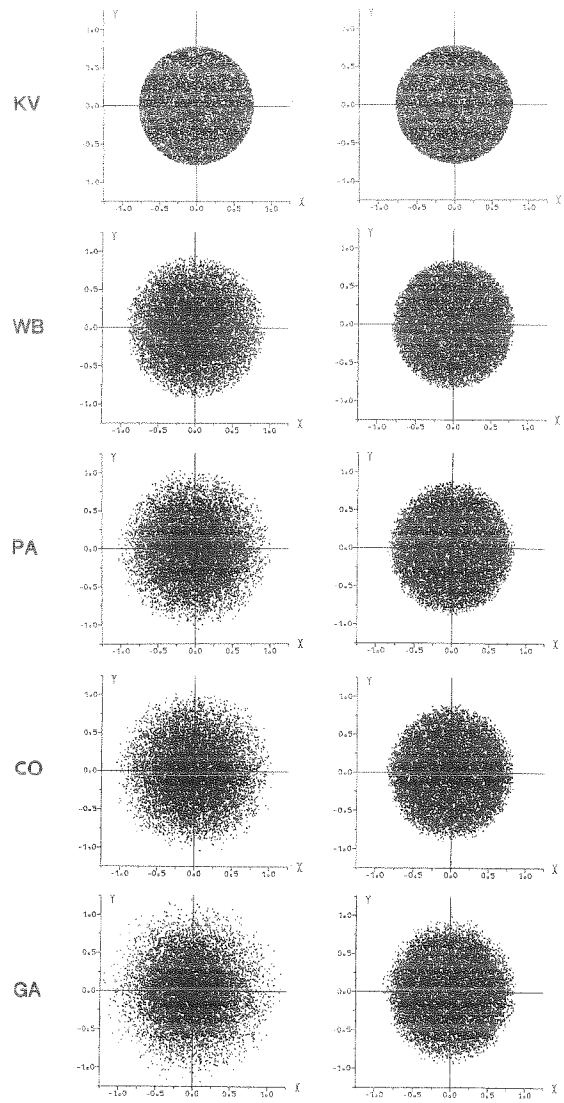


Fig.1 : Real space projections of K-V, waterbag, parabolic, conical and Gauss distributions before and after the first cell of the GSI quadrupole channel at $\sigma_0=60°$, $\sigma=15°$

References

[1] J.Struckmeier, J.Klabunde, M.Reiser, GSI Preprint 83-33, to be published in "Particle Accelerators"

[2] J.Klabunde, M.Reiser, A.Schönlein, P.Spädtke, and J.Struckmeier, IEEE Trans.Nucl.Sci. 30, 2543 (1983)

[3] I.Hofmann, L.J.Laslett, L.Smith, and I.Haber Particle Accelerators, 13, 145 (1983)

[4] J.Struckmeier, J.Klabunde, M.Reiser, this annual report

* University of Maryland

TRANSPORT OF INTENSE ION BEAMS IN A QUADRUPOLE DOUBLET

B

A.Schönlein, J. Klabunde
GSI - Darmstadt

Measurements of the space charge potential of an ion beam at the GSI periodic transport channel show , that the space charge compensation varies along the beam pulse. Electrons created by ionisation of the residual gas atoms are 'trapped' by the ion space charge potential and cause partial space charge neutralisation. At the front end of the beam pulse the space charge is not compensated[1].

In order to investigate the influence of the space charge compensation on the emittance growth and on the transport of an intense ion beam in a quadrupole doublet the emittance was measured with a 200µs time window along the beam pulse at the entrance and at the exit of the quadrupole doublet. The gradients of both quadrupoles were the same. The measurements were carried out with 190keV Ar^{1+} ions.

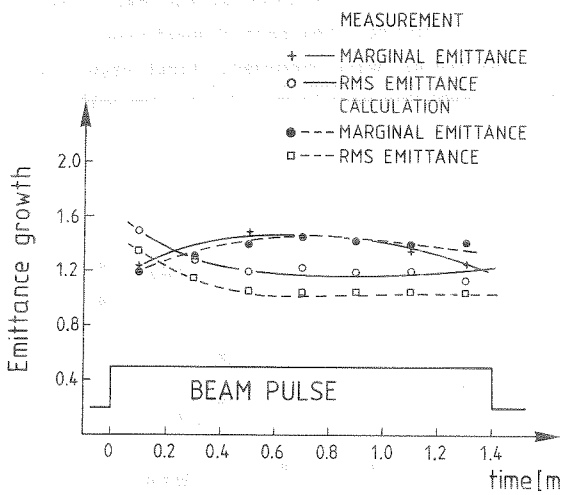


Fig.1: Emittance growth in a quadrupole doublet along the beam pulse.
Field strength 466.8G/cm, I = 1.3mA.

Fig.1 shows the emittance growth along the beam pulse for the marginal and the r.m.s. emittance. The dotted lines are obtained by multi-particle simulations. The input emittance for these simulatons is generated from the measured entrance emittance. The simulation agrees with the experiment, if partial compensation of a certain region of the beam pulse is assumed.

The emittance growth of the r.m.s. and the marginal emittance shows a different behaviour. It seems that the center of the beam pulse is compressed in the middle in comparison with the front end of the pulse. The brightness in the region at the end of the pulse is 7 times higher than at the front end. The average beam radius is reduced by a factor of two in the compensated part of the pulse. Therefore the effective space charge forces in the compensated region of the pulse could be higher than in the uncompensated part.

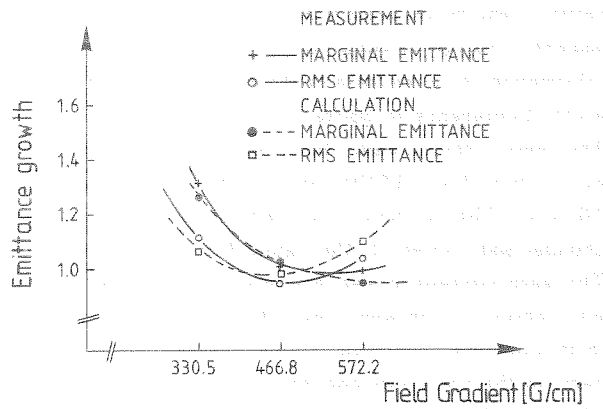


Fig.2: Emittance growth in a quadrupole doublet at different field strengths, measured in the compensated part of the beam pulse (I = 1.6mA).

Fig.2 shows the emittance growth for the compensated part of the beam pulse at different quadrupole settings corresponding to the phase advance $\sigma_o = 60^o, 90^o, 120^o$. The measured ion beam current was 1.6mA. Again, a good agreement with the computer simulations was achieved, if the current used in the calculation was reduced to about 60%.

In the uncompensated region of the beam pulse, a quantitative agreement between measurements and computations was abtained including the full ion current.

As an example, Fig.3 shows the calculated and measured emittance of the x,x'-plane. The measured wings are very well reproduced by the computer simulation.

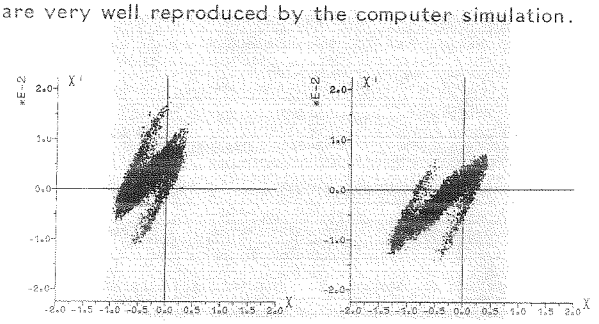


Fig.3: Calculated und measured output emittance of the x,x'-plane.

REFERENCES

[1] J. Klabunde, M. Reiser, A. Schönlein, P. Spädtke, J. Struckmeier, IEEE Trans., NS-30, No.4, 1983

Experimental Results of the Beam Transport Experiment at GSI

J. Klabunde, A. Schönlein, J. Struckmeier, P. Spädtke
GSI Darmstadt

The objectives and the description of the apparatus of the GSI high current beam transport experiment were given in previous reports[1,2]. Here the first experimental results of beam transport in six periods of the magnetic FODO channel are reported. More detailed information is given in a contribution to the 1983 Accelerator Conference in Santa Fe, USA.[3]

The experiments have been carried out with an Ar^+ beam from the ELSIRE ion source at the energy of 190 keV. The current at the entrance of the transport channel was varied in the range from 0.1 mA to 3 mA. The zero-current phase advance of the FODO-channel was adjusted between $\sigma_0 = 60°$ and $\sigma_0 = 120°$. A large-aperture magnetic triplet serves to match the beam to the transport channel.

Along the beam line clearing electrodes are installed to eliminate the electrons from the beam. The beam potential has been measured by a special device developed at the University of Frankfurt[4]. It measures the energy of the residual gas ions diffusing out of the beam. The measurements demonstrate that the ion beam space charge and thus the amount of space charge neutralization varies within the beam pulse. Measurements with a 50 µs-window indicate that after about 300 µs from the beginning of the beam pulse the space charge potential reaches a minimum value. The beam is partially charge neutralized in this part of the pulse, even if the vacuum pressure was increased up to 1×10^{-5} Torr. The change of the beam potential along the beam pulse was qualitatively confirmed by measurements with a simple potential probe as shown in Fig. 1.

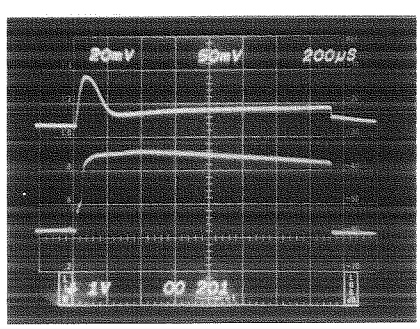


Fig. 1: Space charge potential (upper trace) along the beam pulse (lower trace)

The computer-controlled emittance measuring device, a conventional slit-collector system, can be started at different times within the beam pulse except for the first 300 µs interval, which is used for electronic adjustment of the current amplifiers. For that reason, emittance growth could be measured at this stage of experiments only in the partially compensated part of the beam pulse.

Fig. 2 shows the emittance growth as a function of the beam current and the quadrupole field. The strong dependence on the beam current is evident. The growth rate is relatively independent of the focusing strength in the region below $\sigma_0 = 90°$, and increases rapidly with σ_0 above $\sigma_0 = 90°$. It may be indicative of the presence of envelope instabilities even though the beam is partially neutralized. In another series of experiments the behaviour of the beam at the beginning of the pulse were studied. The control electronics of the emittance apparatus were modified. First results are reported in a separate contribution to this report[5].

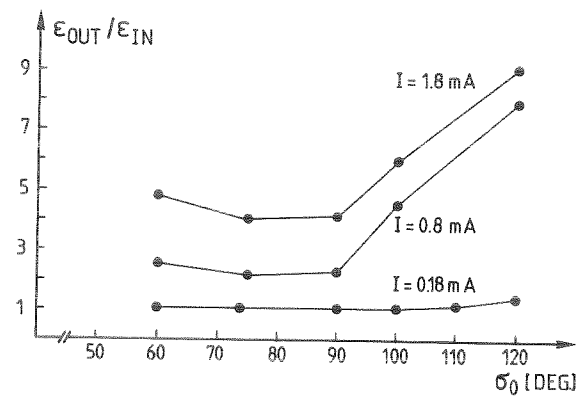


Fig. 2: Emittance growth versus σ_0 for different currents

References

[1] J. Klabunde, GSI-Report 82-1.
[2] J. Klabunde, M. Reiser, A. Schönlein, P. Spädtke, GSI-Report 83-1.
[3] J. Klabunde, M. Reiser, A. Schönlein, P. Spädtke, J. Struckmeier, IEEE Trans. Nucl. Sci. 30, 2543 (1983).
[4] P. Kreisler, H. Baumann, K. Bethge, GSI-Report 83-2.
[5] A. Schönlein, J. Klabunde, this report.

X-Ray Production in Collisions of Relativistic Heavy Ions and Atoms [B]

R. Anholt, W.E. Meyerhof, J.D. Molitoris, C. Stoller
Stanford University
H. Bowman, J. Rasmussen, J.S. Xu
LBL Berkeley
D.H.H. Hoffmann
GSI Darmstadt

Inner shell excitation and vacancy production at relativistic heavy ion impact velocities has been explored very little until recently[1,2]. Detailed knowledge of all cross sections for processes leading to x-ray emission from target atoms and the projectile is of great importance for heavy ion driven inertial confinement fusion, to calculate the amount of energy transferred from translational into radiation energy during the deceleration process of the heavy ion in the fusion target.

At the Berkeley Bevalac target and projectile K-shell vacancy production cross sections have been measured for three projectiles $_{92}U$ (418 MeV/u), $_{54}Xe$ (200 MeV/u, 100 MeV/u), and $_{57}La$ (175 meV/u) incident on solid targets with atomic numbers Z ranging from $4 \leq Z \leq 92$.

Vacancy production in the target K-shell is induced by two processes: (i) ionization and (ii) capture of a K-shell electron (radiative or non-radiative) into the projectile. Figure 1 shows the target K-shell vacancy production for $_{57}La$ (E = 175 MeV/u) incident on solid targets. In this double logarithmic presentation the data are well described by a straight line indicating a power law dependence of the cross section ($\sigma_t \sim Z_t^{-\alpha}$ α = 2.80).

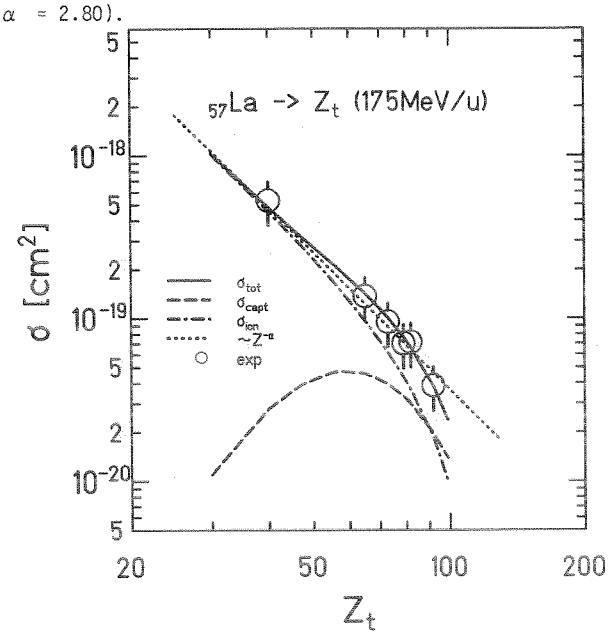


Fig. 1: Target K-shell vacancy production.

Projectile K-shell vacancy production proceeds mainly through ionization and excitation (1s - 2p) of a K-shell electron. Though radiative and non-radiative capture to projectile inner-shell vacancies will change the electron population of the inner shells but with an only small effect on x-ray production. In Fig. 2 the experimental results for U K_α x-ray emission are shown. The cross section also displays a power law dependence with $\sigma_p \sim Z_t^{\alpha}$ and $\alpha \approx 2$.

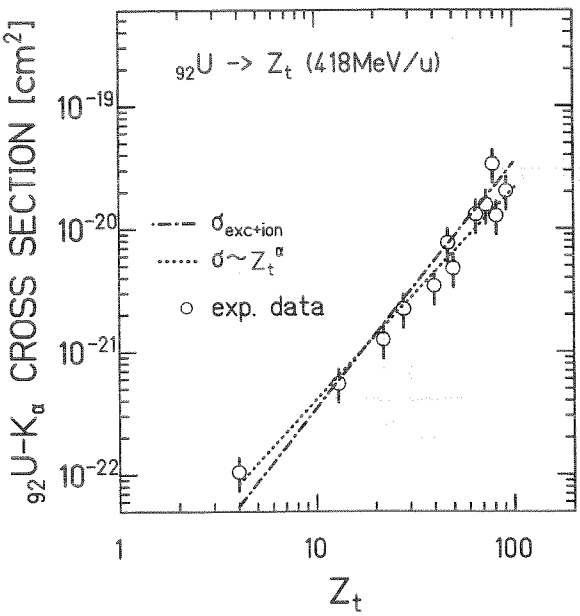


Fig. 2: Projectile K-shell vacancy production.

A first attempt to explain the gross behaviour of the observed cross sections within the framework of simple models has been carried out. At GSI a model was applied, where the interaction between the projectile and the target electrons or the target nucleus and the projectile electrons is mediated via an equivalent spectrum of virtual photons. Thus, the ionization or excitation cross section are obtained by folding the virtual photon spectrum with the ionization cross section and the (1s-2p) excitation cross section. Results of this model calculations are shown in Figs. 1 and 2.

[1] R. Anholt et al., Phys. Lett 5917 (1977) 429

[2] R. Anholt, Phys. Rev. A19 (1979) 1004

Radiative Electron Capture by Relativistic Heavy Ions

B

R. Anholt, W.E. Meyerhof, C. Stoller, J.D. Molitoris
Stanford University
H. Bowman, J. Rasmussen, J.-S. Xu
LBL Berkeley
D.H.H. Hoffmann
GSI Darmstadt

An important source of x-ray emission from fast moving, highly stripped heavy ions passing through matter is the radiative electron capture process (REC), where the ion captures a target electron into an inner shell vacancy directly. The simultaneously emitted x-ray photon can be observed with an energy well above the highest characteristic x-ray lines of the projectile.

In order to study the REC process for heavy ions at relativistic velocities ($\beta \gtrsim 0.5$) we have measured cross sections and angular distributions for a number of projectiles incident on solid state targets. The experiment was carried out at the Berkeley Bevalac. Projectiles used were $_{92}U$, $_{57}La$, and $_{54}Xe$ with energies between 100 and 400 MeV/u.

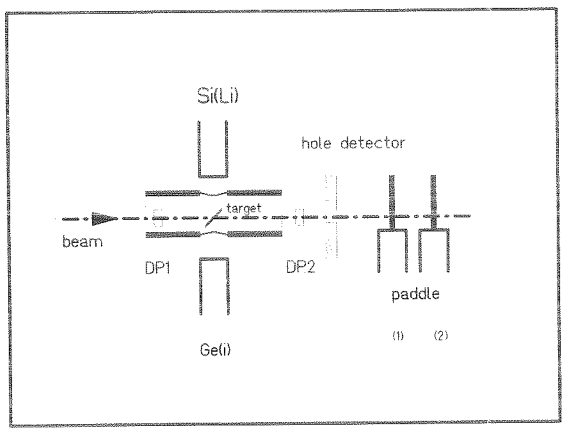


Fig. 1: Set-up of the experiment.

In Fig. 1 the experimental set-up is shown. Projectiles traversing the target were counted by requiring a coincidence between two surface barrier detectors (DP1,DP2) placed in front and behind the target. X-rays were detected with a Si(Li) and a Ge(i) detector and the events were required to be in coincidence with the beam defining pulses from the surface barrier detectors. A large background reduction was achieved by this experimental procedure.

Figure 2 shows a typical x-ray spectrum for Xe ions (190 MeV/u) incident on Be. At the low energy end of the spectrum the Doppler shifted characteristic K and K transitions of Xe appear and near 200 keV the broad REC peak for capture into the projectile K-shell is clearly visible.

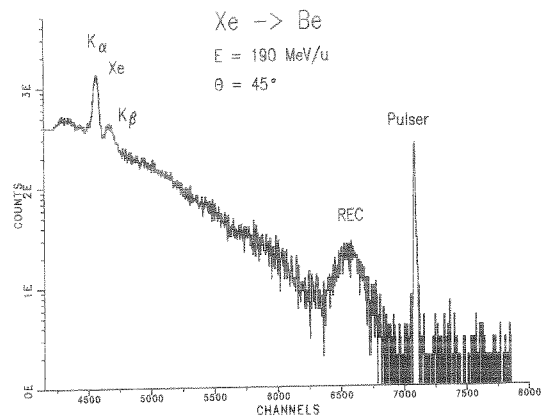


Fig. 2: X-ray spectrum for Xe-Be collisions at 190 MeV/u.

A first result of an angular distribution measurement is presented in Fig. 3 showing the differential cross section of K-shell REC for La on Be. The experimental data are well described by a $\sin^2\theta$ distribution indicating that the expected forward peaking of the angular distribution due to Doppler transformation is nearly cancelled by retardation effects as proposed by Spindler et al.[1].

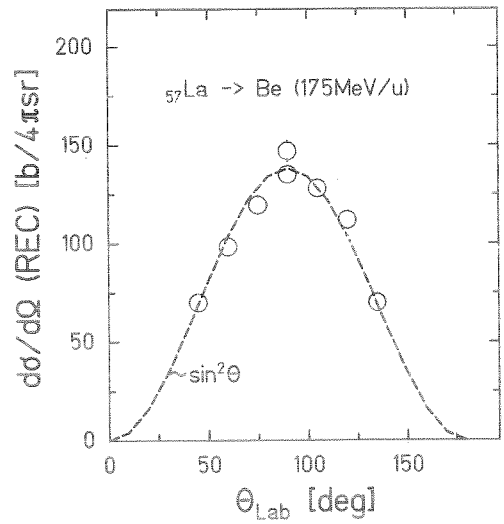


Fig. 3: REC-angular distribution.

[1] E. Spindler, H.-D. Betz, and F. Bell, Phys. Rev. Lett. 42 (1979) 832

Precision X-Ray Wavelength Measurements in Few-Electron Argon Recoil Ions

H.F. Beyer, R.D. Deslattes*, R.E. LaVilla*, P.H. Mokler
GSI Darmstadt
F. Folkmann
University of Aarhus, DENMARK
K.-H. Schartner
I. Phys. Institut, Universität Gießen
*National Bureau of Standards, Washington, D.C.

Heavy ion fusion compression experiments will have to use diagnostic techniques based on spectroscopic analyses of the x-ray and XUV emission. X-ray line shift and broadening in one and two-electron spectra have already been shown to be useful diagnostic indicators for compression density and confinement especially when a high Z diagnostic seed is used in a low Z target material[1]. The x-ray line shifts are expected due to shielding by free electrons and the change of the dielectric function.

The present experimental program has been started in order

(1) to relate a hot target experiment with a source where the same atomic states prevail but under well controlled experimental conditions
(2) to provide experimental reference data in vacuum
(3) to measure the ls QED contribution in a high Z one-electron atom
(4) to develop apparatus which will be useful in future hot target experiments.

In the experiment the wavelengths of the hydrogen and helium-like argon resonance lines are determined in an argon gas target bombarded by 5.9 MeV/amu U ions. A survey measurement was reported previously [2]. Here we report on the measurement of the $2p_{1/2}$, $2p_{3/2} \rightarrow 1s$ transitions with improved accuracy. The method is based on a direct comparison with the wavelengths of the closelying potassium K_α lines induced by fluorescence of a KCl probe. For this purpose the potassium K_α lines have been remeasured at the National Bureau of Standards (NBS) in Washington. There a very similar mode of excitation was used as in the online calibration procedure at GSI and the x rays were dispersed by a double flat crystal spectrometer.

The apparatus used at the UNILAC is schematically shown in Fig. 1. A uranium beam of 5.9 MeV/amu traverses one of four closed gas cells containing 100 mbar argon. On one side of the ion beam the calibration source is located consisting of an electron gun, a titanium anode and a KCl fluorescence target. A chopper anti-synchronizes the calibration x rays. On the other side a Johann-type crystal spectrometer built and tested at NBS is capable of viewing both the calibration and the argon x rays. The spectrometer is equipped with a cylindrically bent

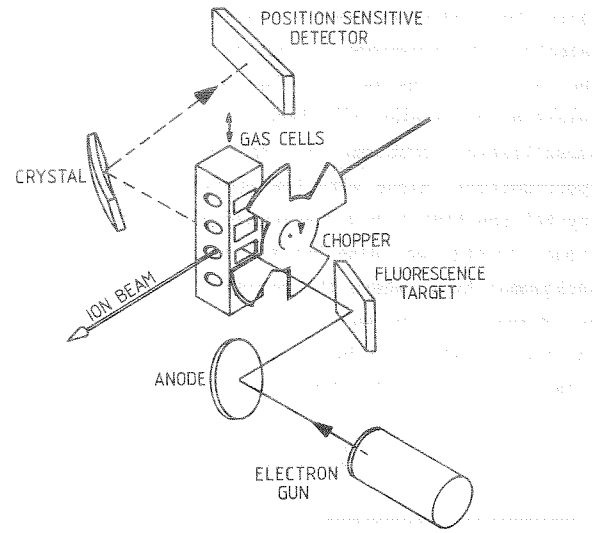


Fig. 1: Schematic view of the apparatus.

Silll crystal and with a position-sensitive proportional counter of the backgammon type located on the Rowland circle. A description of a new backgammon detector built at GSI is given in this annual report. The calibration spectra as well as the argon spectra were fitted with approximate Voigt profiles. The accuracy of the position for the Lyman-α lines was merely determined by the nonlinearity of the detector. Therefore, special attention was payed to this point in the development of the next generation experiment. Table 1 gives the experimental wavelengths together with the theoretical results by Johnson and Soff[3].

	λ_{exp}/Å	λ_{th}/Å
$2p_{1/2}$	3.73636(16)	3.73652
$2p_{3/2}$	3.73109(24)	3.73110

[1] J.D. Kilkenny, R.W. Lee, M.H. Key, and J.G. Lunney, Phys. Rev. A22 (1980) 2746
B. Yaakobi, S. Skupsky, R.L. McCrory, C.F. Hooper, H. Deckman, P. Bourke, and J.M. Soures, Phys. Rev. Lett. 44 (1980) 1072
S. Skupsky, Phys. Rev. A21 (1980) 1316

[2] H.F. Beyer, R. Mann, F. Folkmann, and P.H. Mokler, J. Phys. B15 (1982) 3853

[3] G. Soff and W. Johnson, to be published

Position-Sensitive Proportional Counter for X-Ray Spectroscopy [B]

H.F. Beyer
GSI Darmstadt
R.D. Deslattes
National Bureau of Standards, Washington, D.C.

Crystal spectrometers are presently in use for precision wavelength measurements in one- and two-electron ions[1]. Those instruments employ a cylindrically bent crystal and a position-sensitive x-ray detector. The advantage of such an arrangement is that the spectral region of interest is multiplexed resulting in a high efficiency and avoidance of beam normalization problems as observed with scanning spectrometers. Along with the construction of two new crystal spectrometers a new position-sensitive proportional counter was also built. The detector is of the backgammon type[2] where the position signal is derived by charge division on a split cathode. This type of position encoding has been previously applied for both x-ray[2,3] and particle[4] detection.

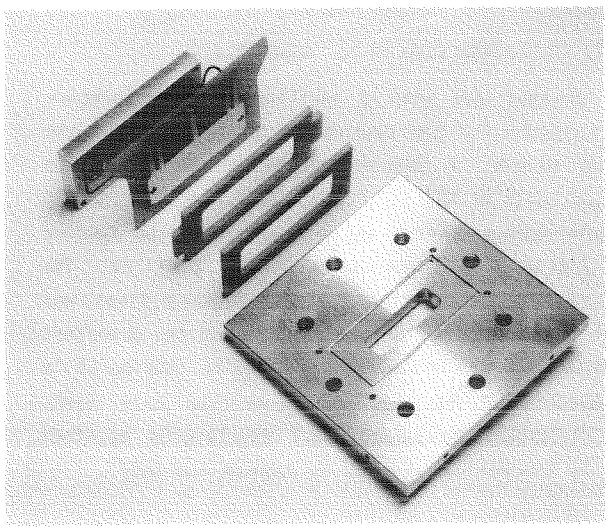


Fig. 1: Exploded view of the detector.

Our detector is characterized by a very simple construction design. An exploded view is given in Fig. 1. The detector window plate with an opening of 12 mm x 40 mm carries a thin beryllium foil (not yet mounted in the figure). On top of the plate is mounted the anode frame with one gold-plated tungsten wire, the anode-cathode spacer and the backgammon cathode fabricated by standard electronic circuit board techniques. An additional rear plate bears the gas connections. The detector was operated at one atmosphere Xe/CH_4 mixture and at a high voltage of 1600 V. Two Canberra model 970D charge- sensitive preamplifiers were used for the two cathod signals (R and L) and a GSI preamplifier, which has a lower gain, was used to derive the anode-wire signal W. The signals were, after main amplification, sent into three ADCs at the PDP-11 computer and the position was calculated as R/(L+R). For calibrating the detector a ^{55}Fe radioactive source collimated down to $\lesssim$ 100 µm could be translated before the detector window with a mechanical precision of better than 1 µm. In order to achieve a good linearity it is essential to have equal electronic gain in the left and right channel. Therefore, a careful gain-setting algorithm was carried out under operational conditions. After that there was not any noticeable change in peak position when changing gas gain by an order of magnitude or gating with various pulse-height windows. After that the detector was mapped by scaning the source in steps of 1 mm. Figure 2 shows the result revealing an excellent linearity over the entire range. Because of the rather large width of the collimator the FWHM position resolution can only be estimated to be less than 100 µm. A remarkable result is that the small residuals still present (magnified by a factor of 100 in Fig. 2) are not due to statistical scatter but follow a reproduceable systematic trend which can be corrected for when ultimate precision is needed.

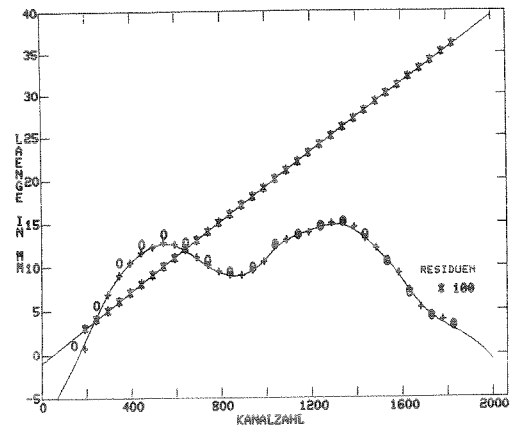


Fig. 2: Calibration curve with linear fit and residuals. Data points + and 0 are taken at two different days.

[1] This annual report
[2] R. Allemand et G. Thomas, Nucl. Inst. Meth. 137 (1976) 141
[3] R.D. Deslattes, R.E. LaVilla, P.L. Cowan, and A. Henins, Phys. Rev. A27 (1983) 923
[4] G. Rosner, B. Heck, J. Pochodzalla, G. Hlawatsch, B. Kolb, and A. Miczaika, Nucl. Inst. Meth. 188 (1981) 561

B

Growth of foil distortions in Rayleigh-Taylor instable configurations

G. Buchwald, D. Barthel, J. Cieza, and J.A. Maruhn
Institut für Theoretische Physik, Universität Frankfurt/Main

In heavy ion driven inertial confinement fusion it is important to achieve a uniform and spherical symmetric compression of the pellet. Deviations from this ideal compression pattern may be caused by geometrical asymmetries in the beam deposition and by Rayleigh-Taylor instabilities.

Basic investigations on the sensivity of a pellet shell to Rayleigh-Taylor instabilities(RTI) can be done considering a foil of dense material above lower density material exposed to a gravitational field. In the very early stage of a RTI its development can be described analytically in a linear approach[1], where the amplitude of the distortion is A~sinh(nt) with the growth rate $n^2 = gkAt$. Here g is the acceleration, k stands for the wave number and At is the Atwood number $At = \frac{\rho_1-\rho_2}{\rho_1+\rho_2}$. As time proceeds the strong nonlinearity of the Navier-Stokes equations requires a numerical treatment of the problem.

One point of major interest are the growth rates of RTI's. In Fig. 1 we compare the numerical growth of a RTI-spike (full line) with the behaviour expected from the linear approach (dotted line). For this example an Atwood-number of At = 0.33 and an acceleration of $g = 10^{17}$ cm/s² was chosen.

In the first 1,8 ns the two models yield the same growth. But then a strong deviation of the two methods can be seen. This is because in the numerical simulation the resulting RTI-spike starts to fall freely through the lighter material. After 3ns the spike length is about 60% smaller than predicted by the linear approach.

In Fig. 1 only the functional form of the growth was discussed. The absolute value of n extracted by a fit to A~sinh(nt) from the early stage of the simulation is about 30% lower than the value expected from the linear approach. This may be due to Kelvin-Helmholtz-instabilities developing at the spike and due to the shape of the spike, both having an influence on the flow properties.

This is not considered in the linear approach. From this stage of our numerical studies, RTI's seem to grow by far slower than expected by analytical estimates. The inset of nonlinear behaviour, however, depends on the Atwood number. This is shown in Fig. 2.

[1] S. Chandrasekhar, "Hydrodynamic and Hydromagnetic Stability", Clarendon Press, Oxford, 1961.

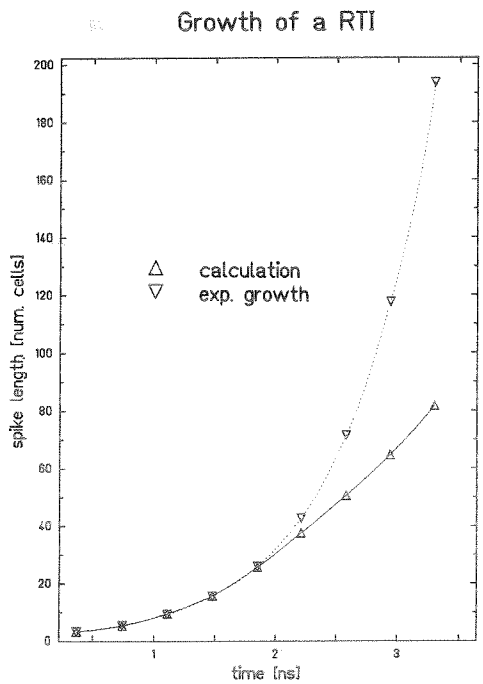


Fig. 1: Spike length of a growing RTI versus time. The full line corresponds to the numerical simulation, the dotted line belongs to the behaviour expected from a linear approach.

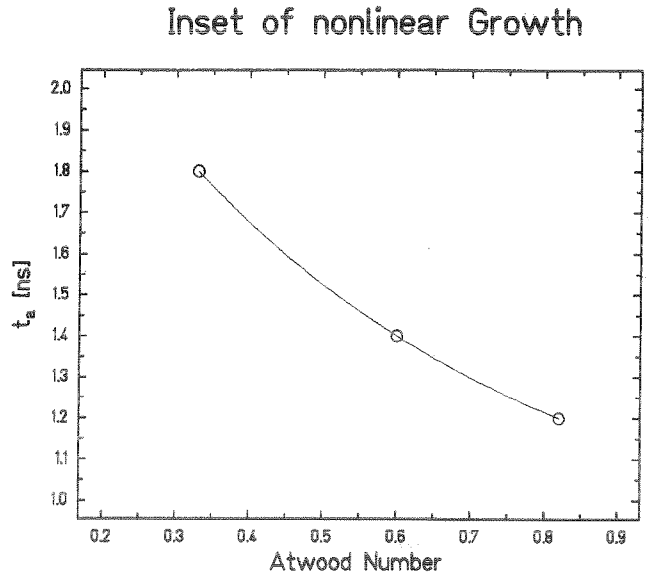


Fig. 2: The typical time when the numerically determined growth deviates from the analytically expected behaviour depends on the Atwood-number.

Critical thickness of foils in Raleigh-Taylor instable configurations B

G. Buchwald, D. Barthel, J. Cieza, and J.A. Maruhn
Institut für Theoretische Physik, Universität Frankfurt/Main

Distorted foils in Raleigh-Taylor (RTI) instable configurations provide a good tool to investigate the corresponding problems in ICF-pellet compression. As only the very early stage of RT-development can be described analytically by linear approaches, detailed studies have to be done numerically.

The very early stage of the numerical simulation should be comparable with these linear approaches. In the following we will compare the results of such an analytic approach[1] with our simultations. In Ref. 1 the critical wave length for a foil distortion is estimated analytically for a non-viscous incompressible fluid. Here the growth rate of an initial distortion is supposed to have a maximum. The fluid-foil is exposed to gravitation.

The equation to determine the critical wave length of an initial foil perturbation is found to be[1]:

$$(1/\chi_M)^2 = 1 + \log(\Delta/\xi)\,\log(\chi_M)^2 \qquad (1)$$

with

$$\chi_M = \sqrt{\lambda_M/(2\pi\Delta)} \quad . \qquad (2)$$

Δ is the foil thickness and ξ is the initial amplitude of the distortion.

Distortions with an initial amplitude being much lower than the foil thickness ($\Delta/\xi \sim 10^3$) have a critical wavelength $\lambda_M \sim \Delta$. In our studies $4 < \Delta/\xi < 40$.

As we will vary the foil thickness in our numerical simulations, whereas λ and ξ are kept constant, eq.(1) is transformed to

$$\Delta_M = \lambda/2\pi\,(1-\log(\lambda/2\pi\xi)) \qquad (3)$$

in order to determine a critical foil thickness. For λ=.8 mm and ξ=.025 mm eq.(3) yields $\Delta_M \approx 0{,}3$ mm.

Fig. 1 shows the early stage growth rates of the numerical simulations.

Independent of the Atwood number there is a maximum at $\Delta \sim 0{,}26$ mm. This is in good agreement with the analytic estimate. However, the maxima at each Atwood-number are not exceeding the average growth rates by 10%. For larger foil thickness there seems to be a saturation in growth rates, whereas for smaller foil thickness the growth rate is decreased.

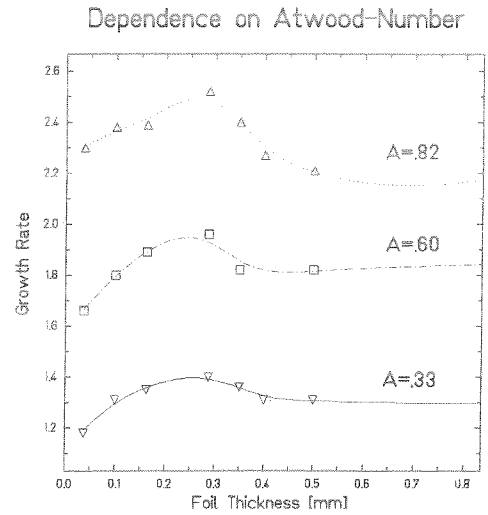


Fig. 1: Growth rates of the early RTI development versus thickness of the distorted foil. The calculation is performed for Atwood-numbers A=0.82; 0.60; and 0.33.

This means, that in spite of the existence of a critical wave length (resp. a critical foil thickness) there is no dramatical influence of these extrema on the pellet stability.

Additionally, the growth of the instability is damped, when the system leaves the region, where the linear analytic approach is valid. In our case this happens after the first few ns.

[1] B.R. Suydam, "Break-up of an Accelerated Shell Owing to Rayleigh-Taylor Instability", Los Alamos Nat. Lab., Informal Report LA-7291-Ms, 1978

7. Annex

		PAGE
7.1	Scientific Activities outside GSI	
7.1.1	Publications	354
7.1.2	Conference Contributions	366
7.1.3	Seminars at other Institutes	382
7.1.4	Lectures and Courses	391
7.2	Scientific Activities within GSI	
7.2.1	Conferences and Seminars on Research Proposals	392
7.2.2	Seminars at GSI	393
7.2.3	GSI-Preprints	396
7.2.4	GSI-Reports	398
7.2.5	Visiting Groups at GSI	399
7.3	Scientific Committees, Directorate and Personal	400
7.4	Scientific Cooperation	403
7.5	Author Index	408

Albinska, M., Belery, P., Delbar, Th., El Masri, Y., Gregare, Gh., Michel, C., Vervier, J., Albinski, J., Grotwoski, K., Kopta, S., Kozik, T., Planeta, R., Paic, G.
Fusion in the $^{20}Ne + ^{24}Mg$ system
Phys. Rev. C27, 501 (1983)

Anholt, R., Jakubaßa-Amundsen, D.H., Amundsen, P.A., Aashamar, K.
Direct Pair Production in Heavy-Ion-Atom Collisions
Phys. Rev. A27, 680 (1983)

Arafah, D.E., Bangert, U., Thiel, K., Townsend, P.D.
Ion Range Studies of Cerium Implanted CaF_2
Nucl. Instr. Meth. 209/210, 1105 (1983)

Armbruster, P.
On the Limitations of Production of Exotic Nuclei by Fusion
Universita and Istituto Nazionale di Fisica, Milano, p.347 (1983)

Armbruster, P.
Synthesis of Nuclei at the Limits of Nuclear Stability
Europhysics News, Vol. 14, No. 819, p. 4 (1983)

Backe, H., Senger, P., Bonin, W., Kankeleit, E., Krämer, M., Krieg, R., Metag, V., Trautmann, N., Wilhelmy, J.B.
Estimates of the Nuclear Time Delay in Dissipative U+U and U+Cm Collisions Derived from the Shape of Positron and δ-Ray Spectra
Phys. Rev. Lett. 50, 1838 (1983)

Bangert, D., Freiesleben, H.
Further Evidence for Nuclear Rolling Friction Acting in Heavy-Ion Induced Reactions
Z. Phys. A310, 229 (1983)

Bangert, U., Arafah, D.E., Saßmannshausen, U., Thiel, K., Townsend, P.D.
Radiation Enhanced Diffusion of Krypton and Uranium Impurities in LIF
Nucl. Instr. Meth. 209/210, 1111 (1983)

Batsch, T., Richter, M., Spieler, H., Zhou Y.-Y.
A General Purpose Nuclear Data Acquisition System Based on am Auxiliary Crate Controller
IEEE Trans. Nucl. Science, NS-30, No. 5, 3864 (1983)

Baur, G., Shyam, R., Rösel, F., Trautmann, D.
Calculations of Proton-Neutron Coincidence Cross-Sections in 56 MeV Deuteron-Induced Break-Up Reactions by Post Form Distorted Wave Born Approximation
Phys. Rev. C28, 946 (1983)

Becker, U., Grün, N., Scheid, W.
Solution of the Time-Dependent Dirac-Equation by the Finite Difference Method and Application for $Ca^{20+} + U^{91+}$
J. Phys. B16, 1967 (1983)

Bertsche, U., Illiakis, G., Kraft, G.
Inactivation of Ehrlich Ascites Tumor Cells by Heavy Ions
Rad. Res. 95, 57 (1983)

Bock, R.
Heavy Ion Beams for Inertial Confinement Fusion
Lectures of the 1982 Intern. Summer School of Nuclear Physics, Poiana Brasov, Romania, World Scientific Publ. Co., p. 497 (1983)

Bock, R.
Heavy Ion Fusion
IEEE Transactions on Nuclear Science, NS-30, No. 4, pp. 3049 (1983)

Bock, R.
Intermediate Energy Heavy Ion Collisions
Nucl. Phys. A409, 321c (1983)

Bock, R., Böhne, D., Hoffmann, I., Kessler, G., Kulcinski, G.L., Meyer-ter-Vehn, J., v. Möllendorff, U., Moses, G.A., Müller, R.W., Sviatoslavsky, I., Vogelsang, W.
HIBALL - A Conceptual Design Study on a Commercial Size Heavy Ion Beam Fusion Electrical Power Plant
Fusion Reactor Design and Technology, Vol. I, IAEA-TC-392/29, p. 497 (1983)

Böhne, D.
Beschleunigeraspekte der schwerioneninduzierten Trägheitsfusion
Atomwirtschaft und Atomtechnik 1, 41 (1983)

Bohne, W., Freiesleben, H., Grabisch, K., Hildenbrand, K.D., Kollatz, M., Lehr, H., Öschler, H.
Complete Fusion in Peripherial Collisions observed in the Reaction ^{16}O on ^{146}Nd at 10 MeV/u
Phys. Lett. 127B, 177 (1983)

Bokemeyer, H., Folger, H., Grein, H., Kido, Y., Cowan, T., Greenberg, J.S., Schweppe, J., Bethge, K., Gruppe, A., Merten, R., Odenweller, Th., Stiebing, K.E., Schwalm, D., Vincent, P., Trautmann, N.
Positronenemission in überkritischen Schwerionen-Stoßsystemen
EAS-4, 4. Arbeitsbericht 'Energiereiche atomare Stöße', April 83, p. 15 (1983)

Bork, U., Kranz, A.R.
A Computerized System for Microdosimetric Measurements of HZE-Particle with Seeds and Ascospores
Arabid. Inf. Serv. 20, 19 (1983)

Bosch, F.
Experiments on the Excitation of the Innermost Electrons in Extremely Strong Fields
Quantum Electrodynamics of Strong Fields, (W. Greiner ed.), Plenum Publishing Corporation, p. 155 (1983)

Bosch, F.
Inner Shell Electrons in Superheavy Quasiatoms
Atomic Physics of Highly Ionized Atoms, (E. Marrus ed.), Plenum Press New York, p. 291 (1983)

Boszik, I., Hoffmann, I., Jahnke, A., Müller, R.W.
Numerical Investigation of Bunch-Merging in a Heavy-Ion-Synchrotron
Proceedings, Conference on Computing in Accelerator Design and Operation, Berlin, Paper A202 (1983)

Boszik, I., Hoffmann, I., Jahnke, A., Müller, R.W.
Nonlinear Aspects of Landau Damping in Computer Simulation of the Microwave Instability
Proceedings, Conference on Computing in Accelerator Design and Operation, Berlin, Paper A203 (1983)

Brendel, C., Carter, J., Beck, F., Richter, A., Schrieder, G., Schüll, D., Delic, G., Lemmer, R.H.
Single Nucleon Transfer Reactions in a Core Excitation Model for ^{48}Ti Incident on ^{42}Ca at 8 MeV/amu
Phys. Lett. 124B, 474 (1983)

Brown, B., Ströbele, H. et al.
Production of High-Transverse-Energy Events in p-Nucleus Collision at 40 GeV/c
Phys.Rev. Lett. 50, 1 (1983)

Buchwald, G., Graebner, G., Theis, J., Maruhn, J.A., Greiner, W. Stöcker, H.
Viscous Fluid Dynamical Calculations of the Reaction ^{12}C (85 MeV/nucl.) + ^{197}Au
Phys. Rev. C28, 1119 (1983)

Carter, J., Brendel, C., Richter, A., Schrieder, G., Feldmeier, H., Bohne, W., Grabisch, K., Lehr, H., Morgenstern, H.
On the Fusion Dynamics of ^{40}Ar + ^{40}Ca - Fusion-Fission and Fusion-Evaporation
Z. Phys. A313, 57 (1983)

Cassing, W., Nörenberg, W.
On the Role of Memory Effects for Dissipation and Diffusion in Slow Collective Nuclear Motion
Nucl. Phys. A401, 467 (1983)

Cassing, W., Stingl, M., Weiguny, A.
Scattering with Absorptive Interaction; Energy Dependent Potentials
Phys. Rev. C27, 1901 (1983)

Cassing, W., Lukasiak, A., Nörenberg, W.
Dissipative Diabatic Dynamics (DDD): A Theory for Heavy-Ion Collisions between TDHF and Transport Theories
Proceedings, XIth International Workshop on Gross Properties of Nuclei and Nuclear Excitations, Hirschegg, Austria, Jan. 1983, (H. Feldmeier ed.), p. 107 (1983)

Cassing, W., Dhar, A.K., Lukasiak, A., Nörenberg, W.
Diabatic Aspects of Single-Particle Collective Nuclear Motion within the Time-Dependent Hartree-Fock Theory
Z. Phys. A314, 309 (1983)

Cindro, N., Greiner, W.
Anharmonic Vibration-Rotation Approach to Quasi-Molecular Spectra
J. Phys. G9, L175 (1983)

Clemente, M., Berdermann, E., Kienle, P., Tsertos, H., Wagner, W., Bosch, F., Kozhuharov, C., Koenig, W.
Pair Creation in "Overcritical" Coulomb Fields
Abstracts of Contributed Papers, XIIIth International Conference on the Physics of Electronic and Atomic Collisions, Berlin, Germany, 26.07. - 02.08. 1983, (J. Eichler, W. Fritsch, I.V. Hertel, N. Stlterfoht, U. Wille eds.), p. 435 (1983)

Csernai, L.P., Stöcker, H., Subramanian, P.R., Buchwald, G., Graebner, G., Rosenhauer, A., Maruhn, J.A., Greiner, W.
Fragment Emission in Relativistic Heavy Ion Reactions
Phys. Rev. C28, 2001 (1983)

Dean, D.R., Mosel, U.
A Nearside-Farside Analysis of Deep Inelastic Reactions
Phys. Lett. 132B, 287 (1983)

Elberfeld, W., Kleber, M.
Use of Ehrenfest's Principle for Inelastic Collisions
J. Phys. B16, 3557 (1983)

Elze, H.-Th., Greiner, W., Rafelski, J.
On the Color-Singlet Quark-Glue Plasma
Phys. Lett. 124B, 515 (1983)

Ewald, H., Münzenberg, G., Armbruster, P.
Das Geschwindigkeitsfilter SHIP - Ein Instrument zur Erforschung neuer Kerne weitab der Stabilität
Phys. Blätter 12, 398 (1983)

Faessler, A., Rikus, L., Sartor, L.
Real and Imaginary Part of the Heavy Ion Optical Potential from a Realistic Nucleon-Nucleon Interaction
Comp. Phys. Comm. 28, 275 (1983)

Faessler, A., Rikus, L., Khadkikar, S.B.
The Heavy Ion Potential and Its Increasing Transparency at Intermediate Energies
Nucl. Phys. A401, 157 (1983)

Faessler, A.
Perspectives in Heavy Ion Physics
Nucl. Phys. A400, 565c (1983)

Faessler, A.
Does Pion Condensation Prevent Pion Condensation?
Quantum Electrodynamics of Strong Fields 701 (1983), W. Greiner ed., NATO Advanced Study Institute Series

Fischer, B.E.
A New Antireflection Treatment for Optical Surfaces by the Nuclear Track Method
Nucl. Instr. Meth. 216, 265 (1983)

Fischer, B.E., Spohr, R.
Production and Use of Nuclear Tracks: Imprinting Structure on Solids
Reviews of Modern Physics, 55, 907 (1983)

Folger, H., Klemm, J., Thalheimer, W.
Rotating Target-Substrate Fixtures in the Vapor Deposition of Bismuth
Proceedings, XIth World Conference of the International Nuclear Target Development Society, Seattle, Washington, USA, Oct. 1982, p. 67 (1983)

Folger, H., Hartmann, W., Klemm, J., Thalheimer, W.
Targets Prepared at GSI in 1980 and 1981 by Evaporation, Rolling, and Sputtering
Proceedings, Xth World Conference of the International Nuclear Target Development Society, Rehovot, Israel, Oct. 1981, p. 224 (1983)

Folger, H., Klemm, J., Müller, M.
Preparation of Nuclear Accelerator Targets by Focused Ion Beam Sputter Deposition
IEEE Trans. Nucl. Science NS-30, No. 2, 1568 (1983)

Fricke, B., Hartung, H.
Interatomic Potential Structure in Highly Ionized Scattering Systems
Physica Scripta, T3, 244 (1983)

Fricke, B., Sepp, W.-D.
Relativistic Calculations of Superheavy Quasi-Molecules
Relativistic Effects in Atoms, Molecules and Solids (G.L. Malli ed.), Plenum Press New York, London, p. 519 (1983)

Fricke, B., Rashid, K.
Relativistic Atomic Level Calculations with Nuclei Carrying Additional Fractional Charges
Z. Phys. A311, 283 (1983)

Fricke, B., Grundevik, P., Lindgreen, I., Olsson, G., Olsson, T., Rosen, A., Torbohm, G.
State Dependent Volume Isotops Shift Analysis of the Low Lying States of Ba I and Ba II
Phys. Lett. 97A, 183 (1983)

Gäggeler, H., von Gunten, H.R., Rössler, E., Oeschler, H., Schotterer, U.,
^{210}Pb-Dating of Cold Alpine Firn/Ice Cores from Colle Gnifetti, Switzerland
Journal of Glaciology, 29, 101 (1983)

Gäggeler, H., Brüchle, W., Brügger, M., Schädel, M., Sümmerer, K., Wirth, G., Ghiorso, A., Gregorich, K.E., Lee, D., Moody,K.J., Seaborg, G.T., Welch, R.B., Wilmarth, P., Herrmann, G., Kratz, J.V., Trautmann, N., Hidelbrand, N., Hickmann, U., Frink, C., Greulich, N., Hoffman, D.C., Fowler, M., von Gunten, H.R.,
Recent Attempts to Produce Superheavy Elements by the ^{48}Ca + ^{248}Cm Reaction
Proceedings, XXI Winter Meeting on Nuclear Physcis, 24-28 January, Bormio, Italy, p. 366 (1983)

Gottschalk, P.A., Grawert, G., Vater, P., Brandt, R.
The Two-, Three- and Four-Particle Exit Channels in the Reactions 806 MeV Kr + U
Phys. Rev. 2, 2703 (1983)

Gralla, S., Dai, G.X., Gobbi, A., Hildenbrand, K.D., Müller, W.F.J., Olmi. A., Petrovici, M., Stelzer, H., Toke, J., Lynen, U., Wollersheim, H.J., and Bock, R.
Moments of Charge Distributions in the Reactions ^{92}Mo ^{92}Mo at 14.7 MeV/u
Z. Phys. A310, 345 (1983)

Greiner, W.
Highlights of the Conference
Proceedings, International Conference on Heavy Ion Physics and Nuclear Physics, 21.03. - 26.03. 1983, Catania, Italy
Nucl. Phys. A409, 395 (1983)

Groh, W., Müller, A., Schlachter, A.S., Salzborn, E.
Transfer Ionization in Slow Collisions of Multiply Charged Ions with Atoms
J. Phys. B16, 1997 (1983)

Grün, N., Scheid, W.
Absorption of Waves by Complex Surface Layers in the Solution of the Schrödinger Equation by Finite Difference Methods
Computer Physics Communications 30, 243 (1983)

Grün, N., Scheid, W.
Calculation of the Impact Parameter Dependence of the Charge Exchange for Li^{3+} + H at 10.5 keV by the Finite Difference Method
J. Phys. B16, L425 (1983)

Güttner, F., Koenig, W., Lutz, N., Martin, B., Skapa, H., Soltani, J., Banda, H., Ramayya, A.V., Bosch, F., Kozhuharov, C.
Study of Inner Quasiatomic Shells (Z_u = 132-171) by Means of δ-Ray Spectroscopy in Asymmetric Collisions
Abstracts of Contributed Papers, XIIIth International Conference on the Physics of Electronic and Atomic Collisions, Berlin, Germany, 26.07. - 02.08. 1983, (J. Eichler, W. Fritsch, I.V. Hertel, N. Stolterfoht, U. Wille eds.), p. 364 (1983)

Güttner, F., Koenig, W., Lutz, N., Martin, B., Skapa, H., Soltani, J., Banda, H., Ramayya, A.V., Bosch, F., Kozhuharov, C.
Influence of the Nuclear Reaction Time onto the δ-Electron Emission Studied by the Reaction I → Au, Bi at 795 and 840 MeV
Abstracts of Contributed Papers, XIIIth International Conference on the Physics of Electronic and Atomic Collisions, Berlin, Germany, 26.07. - 02.08. 1983, (J. Eichler, W. Fritsch, I.V. Hertel, N. Stolterfoht, U. Wille eds.), p. 439 (1983)

Gustafsson, H.A., Gutbrod, H.H., Kolb, B., Ludewigt, B., Poskanzer, A.M., Renner, T., Riedesel, H., Ritter, H.G., Warwick, A.I., Wieman, H.H.
Search for Short-Lived Anomalons in Projectile Fragmentation
Phys. Rev. Lett. 51, 363 (1983)

Gutbrod, H.H., Löhner, H., Poskanzer, A.M., Renner, T., Riedesel, H., Ritter, H.G., Warwick, A., Weik, F., Wieman, H.
4 π Physics with the Plastic Ball
Nucl. Phys. A400, 343 (1983)

Gutbrod, H.H., Löhner, H., Poskanzer, A.M., Renner, T., Riedesel, H., Ritter, H.G., Warwick, A., Weik, F., Wieman, H.
Cluster Formation Observed with a 4 π Detector and the Question of Entropy Production in High Energy Nuclear Collisions
Phys. Lett. 127B, 317 (1983)

Habs, D., Helmolt, v. U., Heyng, H.W., Kroth, R., Kolb, B., Pelte, D., Schwalm, D., Hennerici, W., Hennrich, H.J., Himmel, G., Repnow, R., Wahl, W., Adelberger, E., Lazzarini, A., Simon, R.S., Albrecht, R., Metag, V.
First Results from the Darmstadt-Heidelberg Cyrstal Ball
High Angular Momentum Properties of Nuclei, (N.R. Johnson ed.), Nuclear Science Research Conference Series (Harwood Academic Publications, New York), Vol. 4, p. 451 (1983)

Habs, D., Helmolt, v. U., Heyng, H.W., Kroth, R., Kolb, B., Pelte, D., Schwalm, D., Specht, H.J., Hennerici, W., Hennrich, H.J., Himmel, G., Repnow, R., Wahl, W., Simon, R.S., Albrecht,, R., Metag, V.
First Results on γ-ray Spectroscopy in the Second Minimum of ^{238}U and ^{240}Pu
Phys.Scripta T5, 185 (1983)

Hamilton, J.H., Greiner, W.
Frontiers in Nuclear Science
Portugaliae Physica 14, 1 (1983)

Hansen, P., Heitmann, H., Strocka, B., Spohr, R.
Der Einfluß von Ionenstrahlen auf die magnetischen Eigenschaften von ferrimagnetischen Schichten
Fachinformationszentrum Karlsruhe, Report BMFT-FB T83-048, p.1 (1983)

Heinz, U.
Kinetic Theory for Plasma with Non-Abelian Interactions
Phys. Rev. Lett. 51, 351 (1983)

Heinz, U., Müller, B., Greiner, W.
Quantum Mechanical Treatment of Electron-Positron Excitations in Heavy Ion Collisions with Nuclear Contact
Ann. Phys. 151, 227 (1983)

Heinz, U., Reinhardt, J., Müller, B., Greiner, W., Müller, U.
Beam Energy Dependence of Spontaneous Positron Creation in Delayed Nuclear Collisions
Z. Phys. A314, 125 (1983)

Hennerici, W., Metag, V., Hennrich, H.J., Repnow, R., Wahl, W., Habs, D., Helmer, K., Helmolt, v. U., Heyng, H.W., Kolb, B., Pelte, D., Schwalm, D., Simon, R.S., Albrecht, R.
Spin Dependence and Angular Correlation of Giant Resonances Studied in (HI,xn) Reactions
Nucl. Phys. A396, 329c (1983)

Hess, P.O., Seiwert, M., Maruhn, J.A., Greiner, W., Ramayya, A.V.
Application of the General Collective Model
Proceedings, XXIst International Winter Meeting on Nuclear Physics, Bormio, Italy, 1983, p. 105 (1983)

Hildenbrand, K.D., Freiesleben, H., Gobbi, A., Lynen, U., Olmi, A., Sann, H., Wu, E.C.
On the Influence of Shell Structure in Dissipative Collisions
Nucl. Phys. A405, 179 (1983)

Hingmann, R., Clerc, H.-G., Sahm, C.-C., Vermeulen, D., Schmidt, K.-H., Keller, J.G.
Evidence for an Isomeric State in ^{216}Th
Nucl. Phys. A404, 51 (1983)

Hingmann, R., Clerc, H.-G., Sahm, C.-C., Vermeulen, D., Schmidt, K.-H., Keller, J.G.
Identification of ^{222}U and ^{221}Pa by α-Correlation Chains
Z. Phys. A313, 141 (1983)

Hoffmann, D.H.H., Richter, A., Schrieder, G., Seegebarth, K.
Cross Section for the Reaction $^{12}C(e,p)^{11}Be$ and its Relevance to the Formation of ^{11}B in Active Galaxies
Astrophys. J. 271, 398 (1983)

Hoffmann, I., Boszik, I., Jahnke, A.
Theoretical Study of High-Current Beams in Storage Rings
IEEE Trans. Nucl. Science NS-30, 2546 (1983)

Hoffmann, I., Jahnke, A., Beckert, K., Böhne, D., Müller, R.W.
Improvements on the HIBALL Heavy Ion Fusion Driver
IEEE Trans. Nucl. Science NS-30, 3070 (1983)

Hofmann, S.
Experimente zur Grundzustands-Protonenradioaktivität
Atomenergie-Kerntechnik 42, 157 (1983)

Holzmann, R., Kuzminski, J., Loiselet, M., Van Hove, M.A., and Vervier, J.
Proton Nature of the Second Backbending near N=90
Phys. Rev. Lett. 50, 1834 (1983)

Hutter, G.
Comparison of Three 108 MHz Systems for 1.6 MW
IEEE Trans. Nucl. Science NS-30, 3417 (1983)

Jakubaßa-Amundsen, D.H.
Electron Emission in Asymmetric Collisions with Fast, Heavy Projectiles via Continuum Charge Transfer
J. Phys. B16, 1767 (1983)

Jakubaßa-Amundsen, D.H., Amundsen, P.A., Aashamar, K.
Impact-Parameter Dependence of K-Shell Ionization in Slow Collisions of Near-Symmetric Relativistic Atoms
J. Phys. B16, 1047 (1983)

Janssens, R.V.F., Chowdhury, P., Emling, H., Frekers, D., Khoo, T.L., Kühn, W., Chung, Y.H., Daly, P.J., Grabowski, Z.W., Kortelahti, M., Frauendorf, S. and Zhang, J.Y.
Aligned $\upsilon_{13/2}$ Band Coupled to Different Shapes in ^{186}Hg
Phys. Lett. 131B, 35 (1983)

Jiang, C., Christensen, P.R., Hansen, O., Pontoppidan, S., Videbaek, F., Bond, P.D., Schüll, D., Shen, W., Freiesleben, H., Busch, F., Flynn, E.R.
Obtaining of the High Energy-Resolution Spectra of Heavy-Ion on a QQDQ Magnetic Spectrometer
Chin. Journ. Nucl. Phys. 5, 35 (1983)

Jiang, C., Christensen, P.R., Hansen, O., Pontoppidan, S., Videbaek, F., Bond, P.D., Schüll, D., Shen, W., Freiesleben, H., Busch, F., Flynn, E.R.
A Semiclassical Model used for Elastic and Inelastic Scattering of Heavy Ion
Chin. Journ. Nucl. Phys. 5, 156 (1983)

Johnson, W.R., Soff, G.
Relativistic Many-Body Approach to the Photoionization of Cesium
Phys. Rev. Lett. 50, 1361 (1983)

Kaps, R., Mosel, U., Wolf, R.
Polarization Effects for Elastic and Inelastic Scattering with an Adiabatic-Propagator Approximation
Z. Phys. A314, 317 (1983)

Keller, J.G., Clerc, H.-G., Schmidt, K.-H., Agarwal, Y.K., Heßberger, F.P., Hingmann, R., Münzenberg, G., Reisdorf, W., Sahm, C.-C.
Observation of Radiative Capture in the Reaction $^{90}Zr + ^{90}Zr$
Z. Phys. A311, 243 (1983)

Khoo, T.L., Chowdhury, P., Emling, H., Frekers, D., Janssens, R.V.F., Kuhn, W., Kortelahti, M., Pakkanen, A., Broda, R., Chung, Y.H., Daly, P.J., Grabowski, Z.W., Helppi, H., Haas, F., Kasagi, J., Ronningen, R.M. and Azgui, F.
Shape Transitions at High Spin
High Angular Momentum Properties of Nuclei, (N.R. Johnson ed.), Nuclear Science Research Conference Series, Vol. 4, p. 179 (1983)

Khoo, T.L., Chowdhury, P., Admad, I., Borggreen, J., Emling, H., Frekers, D., Janssens, R.V.F., Pakkanen, A., Chung, Y.H., Daly, P.J., Faber, S.R., Grabowski, Z., Helppi, H., Kortelahti, M. and Wilson, J.
Shell Structure at High Spin and the Influence on Nuclear Shapes
Proceedings, INS International Symposium on Dynamics of Nuclear Collective Motion, Mt. Fuji, July 6-10, 1982, p. 256 (1983)

Khoo, T.L., Chowdhury, P., Emling, H., Frekers, D., Janssens, R.V.F., Kühn, W., Pakkanen, A., Chung, Y.H., Daly, P.J., Grabowski, Z.W., Helppi, H., Kortelahti, M., Bjornholm, S., Borggreen, J., Pedersen, J., Sletten, G.
Nuclear Shape Transitions and Some Properties of Aligned-Particle Configurations at High Spin
Physica Scripta, T5, 16 (1983)

Kiefer, J., Rase, S., Schöpfer, F., Schneider, E., Weber, K.J., Kraft, G.
Heavy Ion Action on Yeast Cells: Inhibition of Ribosomal RNA Synthesis, Loss of Colony Forming Ability and Induction of Mutants
Adv. Space Res. 3, 115 (1983)

Kiefer, J.
On the Interpretation of Heavy Ion Survival Data
Proceedings, VIIIth Symposium Microdosimetry, Luxemburg, EUR 8395 en, p. 729 (1983)

Kienle, P.
Pair Creation in Heavy Ion-Atom Collisions
Quantum Electrodynamics of Strong Fields, Plenum Publishing Corporation, p. 293 (1983)

Kirsch, J., Müller, B., Greiner, W.
Interference Effects in MO X-Ray Spectra Caused by Nuclear Sticking
Phys. Lett. 94A, 151 (1983)

Klabunde, J., Reiser, M., Schönlein, A., Spädtke, P., Struckmeier, J.
Studies of Heavy Ion Beam Transport in a Magnetic Quadrupole Channel
IEEE Trans. Nucl. Science, NS-30, 2543 (1983)

Kleber, M.
Molecular Ring Currents Induced by Magnetic Monopoles
Z. Phys. A314, 251 (1983)

Klepper, O., Roeckl, E.,
Fast On-Line Spectroscopy of Exotic Nuclei
Lecture Notes in Physics 178, 244 (1983)

Knoll, J.
The Dynamics of Heavy-Ion Reactions at Relativistic Energies
Physica Scripta T5, 118 (1983)

Knoll, J., Strack, B.
Expansion and Disassembly Phase of Energetic Nuclear Reactions - A Problem of Dynamical Instabilities?
Z. Phys. A315, 249 (1983)

Koch, P., Rafelski, J., Greiner, W.
Strange Hadrons in Hot Nuclear Matter
Phys. Lett. 123B, 151 (1983)

Könnecke, R., Greiner, W., Scheid, W.
Molecular Interpretation of the Neutron Transfer in the Reaction $^{13}C(^{13}C, ^{12}C)^{14}C$ within the Two-Center Shell Model
Phys. Rev. Lett. 51, 366 (1983)

Koller-Lampert, K., Kranz, A.R.
Heavy Ion Experiments with Arabidopsis Seeds
Arabid. Inf. Serv. 20, 27 (1983)

Kosky, J.P., Wilcke, W.W., Birkelund, J.R., Butler, M.A., Dougan, A.D., Huizenga, J.R., Schröder, W.U., Wollersheim, H.J., Hilscher, D.
Alpha-Particle Emission in the Strongly Damped Reaction of $^{165}Ho + ^{56}Fe$ at 8.3 MeV/Nucleon
Phys. Lett. 133B, 153 (1983)

Kozhuharov, C.
δ-Ray Spectroscopy of Quasi-Atoms
Quantum Electrodynamics of Strong Fields (W. Greiner ed.), Plenum Press New York, London, p. 317 (1983)

Kraft, G., Kraft-Weyrather, W., Meister, H., Miltenburger, H.G., Roots, R., Wulf, H.
The Influence of Radiation Quality on the Effectiveness of Heavy Charged Particles
Radiation Protection, Proceedings, VIIIth Symposium on Microdosimetry, Brussels, p. 743 (1983)

Kraft, G., Kraft-Weyrather, W., Meister, H., Miltenburger, H.G., Schuber, M., Wulf, H.
Inactivation of Mammalian Cells Exposed to Heavy Charged Particle Beams
Proceedings, VIIth International Congres of Radiation Research, Amsterdam, D4-16 (1983)

Kratz, J.V.,
The Search for Superheavy Elements
Radiochim. Acta 32, 25 (1983)

Krause, J., Kleber, M.
Variational Method for the Time-Dependent Dirac Equation
Quantum Electrodynamics of Strong Fields (W. Greiner ed.), Plenum Press, p. 489 (1983)

Kulessa, R., DeVito, R.P., Emling, H., Grosse, E., Schwalm, D., Simon, R.S., Lefebvre, A., Briancon, Ch., Walen, R.J., Sletten, G., Elze, Th.W.
High-j Proton and Neutron Alignment in the Odd Actinides ^{235}U and ^{237}Np
Z. Phys. A 312, 135 (1983)

Kunz, J., Mosel, U.
Rotational Motion at Finite Temperature
Nucl. Phys. A406, 269 (1983)

Kuzminski, J., Holzmann, R., Loiselet, M., Van Hove, M.A., and Vervier, J.
A versatile noble-gas scintillator detector for Coulomb Excitation experiments
Nucl. Instr. Meth. 217, 449 (1983)

Larsson, P.O., Batsch, T., Kirchner, T., Klepper, O., Kurcewicz, W., Roeckl, E., Schardt, D. Feix, W.F., Nyman, G., Tidemand-Petersson, P.,
Direct Proton Decay of 0.56-s ^{147}Tm and Search for this Decay Mode Among Very Neutron-Deficient Isotopes with $53 \leq Z \leq 67$
Z. Phys. A314, 9 (1983)

Löhner, H., Gutbrod, H.H., Poskanzer, A.M., Renner, T., Riedesel, H., Ritter, H.G., Warwick, A., Weik, F., Wieman, H.,
Charged Particle Exclusive Measurement with the Plastic Ball Spectrometer
Nucl. Phys. A409, 365c (1983)

Lukasiak, A., Cassing, W., Nörenberg, W.
Coherent and Incoherent Aspects of Heavy-Ion Collisons
Proceedings, XXI International Winter Meeting on Nuclear Physics, Bormio, Italy, Jan. 1983, (I. Iori ed.), p. 231 (1983)

Lynen, U., Bock, I., Müller, W.F.J., Gobbi, A., Hildenbrand, K.D., Olmi, A., Sann, H., Stelzer, H., Pelte, D., Winkler, U., Glasow, R., Kampert, K.H., Santo, R.
The Use of Large Area-Detectors in Heavy Ion Collisions at Intermediate Energies
Nucl. Phys. A409, 385c (1983)

Maor, D., Liesen, D., Mokler, P.H., Rosner, B., Schmidt-Böcking, H., Schuch, R.
Inner Shell Excitation Probabilities in Intermediate Heavy, Asymmetric Ion-Atom Collisions
Phys. Rev. A27, 2881 (1983)

Maor, D., Stachura, Z., Mokler, P.H., Liu, B., Liesen, D.
Rotational Coupling in Asymmetric Ion-Atom Collisions
J. Phys. B16, L733 (1983)

Mehler, G., de Reus, T., Müller, U., Reinhardt, J., Soff, G., Wietschorke, K.-H., Müller, B., Greiner, W.
δ-Elektronenemission und K-Loch-Erzeugung im Schwerionenstoß unter Verwendung eines Dirac-Fock-Slater Potentials
Proceedings, EAS-4, Energiereiche atomare Stöße 1983, (B. Fricke ed.), p. 129 (1983)

Metag, V., Fischer, R.D., Kühn, W., Mühlhans, R., Novotny, R., Habs, D., Helmolt, v. U., Heyng, H.W., Kroth, R., Pelte, D., Schwalm, D., Hennerici, W., Hennrich, H.J., Himmele, G., Jaeschke, E., Repnow, R., Wahl, W., Adelburger, E., Lazzarini, A., Simon, R.S., Albrecht, R., Kolb, B.
Physics with 4π-γ-Detectors
Nucl. Phys. A409, 331c (1983)

Metag, V., Habs, D., Helmer, K., Helmolt, v. U., Heyng, H.W., Kolb, B., Pelte, D., Schwalm, D., Hennerici, W., Hennrich, H.J., Himmele, G., Jaeschke, E., Repnow, R., Wahl, W., Simon R.S., Albrecht, R.
The Darmstadt-Heidelberg-Crystal-Ball
Lecture Notes in Physics 178, 163 (1983)

Michel, C.,
Subtreshold π^0 Production in Heavy Ion Collisions
Proceedings, XXIth International Winter Meeting on Nuclear Physics, Bormio, Italy 1983, p. 539 (1983)

Mokler, P.H., Liesen, D.
X-Rays from Superheavy Collision Systems
Plenum Press, Progress in Atomic Spectroscopy, Part C, p. 321 (1983)

Molzahn, D., Lund, T., Brandt, R., Hagebo, E., Haldorsen, I.R., Richard-Serre, C., ISOLDE Collaboration
Yields of Transtarget Products on the Interaction of 86 MeV/A ^{12}C-Ions with Pb and Bi Targets
J. Radioanalyt. Chemistry 80, 109 (1983)

Mühlhans, K., Diebel, M., Neergard, K., Mosel, U.
Influence of Shell Structure on Multipole Pairing
Phys. Lett. 120B, 44 (1983)

Mühlhans, K., Müller, E.M., Mosel, U., Goodman, A.L.
Multipole Pair Fields at Finite Temperature
Z. Phys. A313, 133 (1983)

Müller, A., Groh, W., Kneißl, U., Heil, R., Ströher, H., Salzborn, E.
Production of Multiply Charged Rare-Gas Ions by Relativistic Electrons
J. Phys. B16, 2039 (1983)

Müller, A., Groh, W., Salzborn, E.
A Statistical Interpretation of Transfer-Ionization in Slow Collisions of Multiply Charged Ions with Atoms
Phys. Rev. Lett. 51, 107 (1983)

Müller, B., Reinhardt, J., Greiner, W., Soff, G.
Critical Remarks on a Scaling Law for Inner-Shell Ionization
Z. Phys. A311, 151 (1983)

Müller, E.M., Neergard, K.
On the Interpretation of Rotational Bands in Odd Actinide Nuclei
Phys. Lett. 120B, 280 (1983)

Müller, U., de Reus, T., Reinhardt, J., Soff, G., Wietschorke, K.-H., Schlüter, P., Müller, B., Greiner, W.
Der Einfluß elektronischer Abschirmung und nuklearer Haftzeiten auf atomare Positronenspektren in Schwerionenstößen
Proceedings, EAS-4, Energiereiche atomare Stöße 1983, (B. Fricke ed.), p. 131 (1983)

Müller, U., Soff, G., de Reus, T., Reinhardt, J., Müller, B., Greiner, W.
Positrons from Supercritical Fields of Giant Nuclear Systems
Z. Phys. A313, 263 (1983)

Müller, U., Soff, G., Reinhardt, J., de Reus, T., Müller, B., Greiner, W.
Extreme Superheavy Nuclear Systems with Z=184 and their Investigations by Positrons from Supercritical Fields
Nuclear Collective Dynamics (D. Bucurescu, V. Ceausescu, N.V. Zamfir eds.) p. 477 (1983)

Müller, U., Reinhardt, J., de Reus, T., Schlüter, P., Soff, G., Wietschorke, K.-H., Müller, B., Greiner, W.
Theory of Positron Creation in Supercritical Quasi-Molecules
Proceedings, NATO Advanced Study Institute on Quantum Electrodynamics of Strong Fields, 15.06. -26.06. 1981, Lahnstein/Rhein, Germany, (W. Greiner ed.) Series B80, Plenum New York, p. 195 (1983)

Müller, W., Miltenburger, H.G., Kraft, G.
Chromosome Aberrations in Chinese Hamster Cell Cultures Induced by Heavy Ion Irradiation
Proceedings, VIIth International Congres of Radiation Research, Amsterdam, B4-28 (1983)

Mutterer, M., Grimm, P., Heckwolf, H., Pannicke, J., Spreng, W., Theobald, J.P.
Response of Gas Scintillators to Heavy Charged Particles
Lecture Notes in Physics 178, 63 (1983)

Neergard, K., Wüst, E.
On the Calculation of Matrixelements of Operators between Symmetry Projected Bogolyubov States
Nucl. Phys. A402, 311 (1983)

Nickel, F.,
The Influence of Temperature on Stripper Foil Lifetimes
Atomnaya Technika Za Rubezom, 10, p. 39 (1983)

Nörenberg, W.
Dissipative Diabatic Dynamics
Nucl. Phys. A400, 275 (1983)

Nörenberg, W.
Dissipative Diabatic Dynamics: A Shell Model Approach to Large-Amplitude Collective Nuclear Motion
Nucl. Phys. A409, 191 (1983)

v. Oertzen, W., Gebauer, B., Gamp, A., Bohlen, H.G., Busch, F., Schüll, D.
Pairing Effects in Quasi-Elastic Neutron Transfer Between Tin Isotopes
Z. Phys. A313, 189 (1983)

Oeschler, H., Kollatz, M., Bohne, W., Grabisch, K., Lehr, H., Freiesleben, H., Hildenbrand, K.D.
Compelete Fusion in Peripheral Collisions Observed in the Reaction ^{16}O on ^{146}Nd at 10 MeV/u
Phys. Lett. 127B, 177 (1983)

Pellas, P., Perron, C., Crozaz, G., Perelygin, V.P., Stetsenko, S.G.
Fission Track Age and Cooling Rate of the Marjalahti Pallasite Earth Planet
Sci. Lett. 64, 319 (1983)

zu Putlitz, G., Siegert, G.
Neue Elemente an der Grenze der Stabilität von Kernmaterie
Naturwissenschaften 70, 383 (1983)

Reinhardt, J., Müller, B., Greiner, W., Müller, U.
Description of Atomic Excitations in Heavy-Ion Reactions
Phys. Rev. A28, 2558 (1983)

de Reus, U., Westmeier, W.
Catalog of Gamma Rays from Radioactive Decay - Part I
Atomic Data and Nuclear Data Tables 29, 1 (1983)

de Reus, U., Westmeier, W.
Catalog of Gamma Rays from Radioactive Decay - Part II
Atomic Data and Nuclear Data Tables 29, 193 (1983)

Rhoades-Brown, M.J., Oberacker, V.E., Seiwert, M., Greiner, W.
Potential Pockets in the ^{238}U-^{238}U System and their Possible Consequences
Z. Phys. A310, 287 (1983)

Roeckl, E.
Exotic Nuclei in Deep-Inelastic and Fusion Reactions
Nucl. Phys. A400, 131c (1983)

Roeckl, E.,
Heavy Ion Reactions and Nuclear Structure Far From the Beta Stability Line
Nukleonika 26, 971 (1983)

Röschenthaler, D., Betz, H.D., Rothermel, J., Jakubaßa-Amundsen, D.H.
Ionization of Fast Rydberg Ions in Collisions with Target Atoms
J. Phys. B16, L233 (1983)

Runte, E., Schmidt-Ott, W.-D., Tidemand-Petersson, P., Kirchner, R., Klepper, O., Kurcewicz, W., Roeckl, E., Kaffrell, N., Peuser, P., Rykaczewski, K., Bernas, M., Dessagne, P., Langevin, M.,
Decay Studies of Neutron-Rich Products From ^{76}Ge Induced Multinucleon Transfer Reactions Including the New Isotopes ^{62}Mn, ^{63}Fe and $^{71/72/73}Cu$
Nucl. Phys. A399, 163 (1983)

Rykaczewski, K., Kirchner, R., Kurcewicz, W., Schardt, D., Kaffrell, N., Peuser, P., Runte, E., Schmidt-Ott, W.-D., Tidemand-Petersson, P., Gippert, K.-L.,
The New Neutron-Rich Isotope ^{183}Lu
Z. Phys. A309, 273 (1983)

Salzborn, E., Groh, W., Müller, A., Schlachter, A.S.
Transfer Ionozation in Collisions between Multiply Charged Ions and Atoms at keV Energies
Physica Scripta T3, 148 (1983)

Sandorfi, A.M., Barrette, J., Collins, M.T., Hoffmann, D.H.H., Kreiner, A.J., Branford, D., Steadman, S.G., Wigging, J.
The Characteristics of Electric Dipole Strength Built on Highly-Excited Continuum States
Phys. Lett. 130B, 19 (1983)

Sandoval, A., Bock, R., Brockmann, R., Dacal, A., Harris, J.W., Maier, M., Ortiz, M.E., Pugh, H.G., Rauch, W., Renfordt, R.E., Riess, F., Schroeder, L.S., Stock, R., Ströbele, H., and Wolf, K.L.
Streamer Chamber Experiments
Nucl. Phys. A400, 365c (1983)

Sandulescu, A., Cusson, R.Y., Greiner, W.
Time-Dependent Hartree-Fock Study of Alpha-Decay
Lett. Nuovo Cim. 36, 321 (1983)

Schäfer, A., Müller, B., Greiner, W.
New Scheme for Spontaneous Symmetry Breaking of Color SU(3)
Phys. Rev. Lett. 50, 2047 (1983)

Schlachter, A.S., Berkner, K.H., Beyer, H.F., Graham, .W.G., Groh, W., Mann, R., Müller, A., Olson, R.E., Pyle, R.V., Stearns, J.W., Tanis, I.A.
Collisions of Fast Highly Charged Ions in Gas Targets: Ionization, Recoil-Ion Production, and Charge Transfer
Physica Scripta T3, 153 (1983)

Schlachter, A.S., Groh, W., Müller, A., Salzborn, E.
Transfer Ionization in Slow Multiply Charged Ion-Atom Collisions
IEEE Trans. Nucl. Science, NS-30, 1008 (1983)

Schlüter, P., de Reus, T., Reinhardt, J., Müller, B., Soff, G.
Can the Observed Structures in Positron Spectra be Caused by Internal Conversion?
Z. Phys. A314, 297 (1983)

Schneider, J.R.H., Hofmann, S., Heßberger, F.P., Münzenberg, G., Reisdorf, W., Armbruster, P.
Alpha-Decay of New Neutron Deficient Gold, Mercury, and Thallium Isotopes
Z. Phys. A312, 21 (1983)

Schuch, R., Justiniano, E., Hoffmann, R., Schadt, W., Schmidt-Böcking, H., Mokler, P.H., Bosch, F., Schönfeldt, W.A., Stachura, Z.
K-Shell Excitation by K- to L-Shell Charge Transfer in Slow Kr^{q+}-K and Xe^{q+}-Xe Collisions
J. Phys. B16, 2029 (1983)

Schüll, D., Shen, W., Freiesleben, H., Busch, F., Bangert, D., Pühlhofer, F.
The Correlation and Uncorrelation Neutron Exchange and Neutron Rich Flow in Damped Collision
Phys. Ener. Fort. et Phys. Nucl. 7, 229 (1983)

Schüll, D.
"The GSI Magnetic Spectrometer" in "Detectors in Heavy Ion Reactions"
Lecture Notes in Physics, Springer, (W. v. Oertzen ed.), p. 80 (1983)

Schwalm D.
Positron Emission from Superheavy Quasiatoms
Proceedings, XIIIth International Conference on the Physics of Electronic and Atomic Collisions, ICPEAC, Berlin 1983, p. 295 (1983)

Schwalm, D.
Collective Properties of Nuclei at High Spin from B(E2) Values
High Angular Momentum Properties of Nuclei, Nuclear Science Research Conference Series (N.R. Johnson ed.), Harwood Academic Publications, New York, Vol. 4, p. 451 (1983)

Schwalm, D.
Electromagnetic Properties of High Spin States
Nucl. Phys. A396, 339 (1983)

Schweppe, J., Gruppe, A., Bethge, K., Bokemeyer, H., Cowan, T., Folger, H., Greenberg, J.S., Grein, H., Ito, S., Schule, R., Schwalm, D., Stiebing, K.E., Trautmann, N., Vincent, P., and Waldschmidt, M.
Observation of a Peak Structure in Positron Spectra from U+Cm Collisions
Phys.Rev.Lett. 51, 2261 (1983)

Seiler-Clark, G., Pelte, D., Emling, H., Balanda, A., Grein, H., Grosse, E., Kulessa, R., Schwalm, D., Wollersheim, H.J., Hass, M., Kumbartzki, G.J. and Speidel, K.H.
Magnetic Moments in the Backbending Region of ^{158}Dy
Nucl. Phys. A399, 211 (1983)

Shanker, R., Vasak, D., Warke, C.S., Greiner, W., Müller, B.
String-Like Solutions and Regge Trajectories in a Cylindrically Deformed Quark Bag Model
Z. Phys. C18, 327 (1983)

Shen, Wen-qing, Schüll, D., Freiesleben, Busch, F., Bangert, D., Pühlhofer, F.
Neutron Rich Isotopes ^{54}Ti, ^{56}V, ^{57}V, ^{58}Cr produced in Bombardment of ^{56}Fe Target with 790 MeV ^{136}Xe ions
Phys. Ener. Fort. et Phys. Nucl. Vol. 6, No. 4, 465 (1983)

Shyam, R., Baur, G., Budzanowski, A., Bojowald, J., Dabrowski, H., Mayer-Böricke, C., Oelert, W., Riepe, G., Rogge, M., Türek, P., Rösel, F., Trautmann, D.
Explanation of ^{3}He and Triton Rates in the Alpha Break-Up Inclusive Cross Sections
Phys. Rev. C27, 2393 (1983)

Siegert, G.
Die Gesellschaft für Schwerionenforschung, GSI Darmstadt
Physik und Didaktik 3, 221 (1983)

Siegert, G.
Schwerionen in der Anwendung
Enzyklopädie Naturwissenschaft und Technik, Jahresband 1983, Verlag Moderne Industrie, p. 503

Siegert, G., Simen, R.H.
Ein winziges Stück Neutronenstern
Geschichten, die die Forschung schreibt, Vol. 2, Deutscher Forschungsdienst, p. 140 (1983)

Siegert, G.
Die 0,005 Sekunden des Elements 109
Geschichten, die die Forschung schreibt, Vol. 2, Deutscher Forschungsdienst, p. 143 (1983)

Siegert, G.
Der erste Fingerabdruck eines neuen Elementes
Technik heute 10, 16 (1983)

Skarnemark, G., Broden, K., Mao Yun, Kaffrell, N., Trautmann, N.
Rapid Continuous Separation Procedures for Arsenic and Ruthenium from Complex Reaction Product Mixtures
Radiochim. Acta 33, 97 (1983)

Soff, G., Schlüter, P., Wietschorke, K.-H., de Reus, T., Reinhardt, J., Müller, U., Mehler, G., Müller, B., Greiner, W.
Elektronische Übergangszeiten in überkritischen Compound Systemen
Proceedings, EAS-4, Energiereiche atomare Stöße 1983, (B. Fricke ed.), p. 134 (1983)

Soff, G., de Reus, T., Müller, U., Reinhardt, J., Schlüter, P., Wietschorke, K.-H., Müller, B., Greiner, W.
Spectroscopy of Superheavy Quasimolecules
Proceedings, NATO Advanced Study Institute on Quantum Electrodynamics of Strong Fields, 15.06. -26.06. 1981, Lahnstein/Rhein, Germany, (W. Greiner ed.), Series B80, Plenum New York, p. 233, Appendix 266 (1983)

Soff, G., Müller, U., de Reus, T., Schlüter, P., Schäfer, A., Reinhardt, J., Müller, B., Greiner, W.
Electron Excitation Processes and Quantum Electrodynamics in High Z-Systems
Proceedings, NATO Advanced Study Institute on Atomic Physics of Highly Ionized Atoms, June 1982, Cargese, France (R. Marrus ed.), Series B96, Plenum New York, p. 177 (1983)

Soff, G., Müller, U., de Reus, T., Schlüter, P., Reinhardt, J., Müller, B., Greiner, W.
Electron Excitation and Positron Emission in Quasi-Molecular Collisions of Very Heavy Ions
Proceedings, NATO Advanced Study Institute on Fundamental Processes in Energetic Atomic Collisions, Sept. 1982, Maratea, Italy, (H.O. Lutz, J.S. Briggs, H. Kleinpoppen eds.), Series B103, Plenum New York, p. 649 (1983)

Spreng, W., Azgui, F., Emling, H., Grosse, E., Kulessa, R., Michel, Ch., Schwalm, D., Simon, R.S., Wollersheim, H.J., Mutterer, M., Theobald, J.P., Moore, M.S., Trautmann, N., Egido, J.L., and Ring, P.
First Observation of Backbending in an Actinide Nucleus
Phys. Rev. Lett. 51, 1522 (1983)

Spreng, W., Azgui, F., Emling, H., Grosse, E., Kulessa, R., Michel, Ch., Simon, R.S., Wollersheim, H.J., Schwalm, D., Trautmann, N., Mutterer, M., Theobald, J.P., Moore, M.S., Egido, J.L., and Ring, P.
Sudden Alignment of $i_{13/2}$ Protons in ^{242}Pu and ^{244}Pu
Phys. Rev. Lett. 51, 1522 (1983)

Stock, R., Bock, R., Brockmann, R., Dacal, A., Harris, J.W., Maier, M., Ortiz, M.E., Pugh, H.G., Renfordt, R.E., Sandoval, A., Schroeder, L.S., Ströbele, H., and Wolf, K.L.
Compression Effects in Relativistic Nucleus-Nucleus Collisions
Physica Scripta T5, 30 (1983)

Stöcker, H., Buchwald, G., Csernai, L.P., Subramanian, P.R., Theis, J., Maruhn, J.A., Greiner, W.
Dynamics of Medium Energy Nuclear Collisions
Phys. Scripta T5, 108 (1983)

Stöcker, H., Buchwald, G., Graebner, G., Subramanian, P.R., Maruhn, J.A., Greiner, W., Jacac, B.V., Westfall, G.D.
Prospects of Intermediate Energy Nuclear Collisions
Nucl. Phys. A400, 63c (1983)

Strayer, M.R., Cusson, R.Y., Stöcker, H., Maruhn, J.A., Greiner, W.
Time-Dependent Hartree-Fock Studies of Superheavy Molecules
Phys. Rev. C28, 228 (1983)

Ströbele, H., Brockmann, R., Harris, J.W., Maier, M., Pugh, H.G., Renfordt, R.E., Riess, F., Sandoval, A., Schroeder, L.S., Stock, R., Tittel, K., Wolf, K.L.
Charged-Particle Exclusive Analysis of Central Ar + KCl and Ar + Pb Reactions at 1.8 and 0.8 GeV/Nucleon
Phys. Rev. C27, 1349 (1983)

Tanimura, O., Wolf, R., Mosel, U.
Dominant Angular Momentum of Gross Structure in Inelastic $^{12}C + ^{12}C(2^+)$ Scattering
Phys. Lett. 120B, 275 (1983)

Tanimura, O., Wolf, R., Mosel, U.
Gross Structure Resonance at 24.3 MeV in $^{12}C + ^{12}C(2^+)$
Phys. Lett. 128B, 375 (1983)

Tanimura, O., Wolf, R., Kaps, R., Mosel, U.
Exact First- and Second-Order Distorted-Wave Born Methods
Phys. Lett. 132B, 249 (1983)

Theobald, J.P.
Nuclear Fission: From Saddle to Scission
Nuclear Data for Science and Technology (K.H. Böckhoff ed.), D. Reidel Publ. Co., Dortrecht, Boston, London, p. 719 (1983)

Theis, J., Graebner, G., Buchwald, G., Maruhn, J.A., Stöcker, H., Greiner, W., Polonyi, J.
Phase Transition of the Nucleon Antinucleon Plasma in a Relativistic Mean-Field Theory
Phys. Rev. D28, 2286 (1983)

Trautmann, N., Weber, M., Gembalies-Datz, D., Heimann, R., Folger, H., Hartmann, W.
Preparation of Actinide Targets by Molecular Plating for Experiments with Heavy Ions
Proceedings, XIth World Conference of the International Nuclear Target Development Society, Seattle, Washington, USA, Oct. 1982, p. 120 (1983)

Tripathi, R.K., Faessler, A.
Effects of Isobars at Finite Temperature in Pion Condensation in ^{16}O
Phys. Lett. 120B, 54 (1983)

Ulm, G., Eberz, J., Huber, G., Kaplan, D., Lochmann, H., Kirchner, R., Klepper, O., Kühl, T. U., Marx, D., Larsson, P. O., Roeckl, E., Schardt, D.,
Collinear Laser Spectroscopy of Fusion Produced Indium Isotopes
Laser Spectroscopy II, Springer, Berlin, p. 211 (1983)

Vasak, D., Shanker, R., Müller, B., Greiner, W.
Deformed Solutions of the MIT Quark Bag Model
J. Phys. G9, 511 (1983)

Vasak, D., Wietschorke, K.-H., Müller, B., Greiner, W.
Fission of Bags by Spontaneous Quark-Antiquark Pair-Production in Supercritical Fields
Z. Phys. C21, 119 (1983)

Wang, S.J., Cassing, W., Nörenberg, W.
Comparison of Collective Mass Parameters from the Generator Coordinate Method and the Cranking Model
Phys. Lett. 131B, 265 (1983)

Warczak, A., Liesen, D., Maor, D., Mokler, P.H., Schönfeldt, W.A.
K and L X-Ray Excitation in Very Heavy Ion-Atom Collisions Near K-L Level Matching
J. Phys. B16, 1575 (1983)

Warwick, W.I., Wieman, H.H., Gutbrod, H.H., Maier, M.R., Peter, J., Ritter, H.G., Stelzer, H., Weik, F., Freedman, M., Henderson, D.J., Kaufman, S.B., Steinberg, E.P., Wilkins, B.D.
Breakup of Spectator Residues in Relativistic Nuclear Collisions
Phys. Rev. C27, 1083 (1983)

Weber, K.J., Kiefer, J.
Radiation Sensitivity of Transcription in Yeast Cells - Influence of Target Size
Proceedings, VIIIth Symposium Microdosimetry, Luxemburg, EUR 8395 en, p. 507 (1983)

Westmeier, W., Brosa, U.
Quasi-Elastic Reaction Cross Sections
Z. Phys. A312, 261 (1983)

Wilcke, W.W., Kosky, J.P., Birkelund, J.R., Butler, M.A., Dougan, A.D., Huizenga, J.R., Schröder, W.U., Wollersheim, H.J., Hilscher, D.
New Mechanism of α-Particle Production in Heavy-Ion-Induced Fission
Phys. Rev. Lett. 51, 99 (1983)

Wolf, G.K.
Verschleiß- und Korrisionsschutz durch Ionenstrahltechniken
THD Schriftenreihe Wissenschaft und Technik 20, 85 (1983)

Wolf, G.K., Zucholl, K., O'Grady, W.E., Folger, H.
Ion Implanted Catalysts for Fuel Cell Reactions
Nucl. Instr. Meth. 209/210, 835 (1983)

Wolf, G.K., Ferber, H.
Corrosion of Metastable Iron Alloys in Aqueous Solutions
Nucl. Instr. Meth. 209/210, 197 (1983)

Wu E., Hildenbrand, K.D., Gobbi, A., Olmi, A., Sann, H., Freiesleben, H., Lynen, U.
Influence of Shell Structure on Deep Inelastic Collisions
Phys. Ener. Fort. et Phys. Nucl. 7, 379 (1983)

Wüst, E., Mosel, U., Kunz, J., Andresen, H.G., Müller, M.
Test of Nuclear Currents in Transverse Electron Scattering
Nucl. Phys. A402, 235 (1983)

Wüst, E., Mosel, U., Kunz, J., Schuh, A.
Test of Vibrational Current Distributions in Transverse Electron Scattering
Nucl. Phys. A406, 285 (1983)

Yannouleas, C., Dworzecka, M., Griffin, J.J.
Microscopic Nuclear Dissipation II: Damping of Collective States in Subspaces which Include 2p-2h States
Nucl. Phys. A397, 239 (1983)

Yannouleas, C.
The RPA Description of Nonlinear Quantum Friction
Proceedings, XXI International Winter Meeting on Nuclear Physics, Bormio, Italy 1983, p. 245 (1983)

Zychor, I., Rykaczewski, K., Ahrens, H., Folger, H., Kurcewicz, W., Sümmerer, K., Kaffrell, N., Trautmann, N.
Hafnium and Lutetium Isomers Produced in Heavy-Ion Collisions of 7.6 MeV/u ^{40}Ar, 8.5 MeV/u ^{84}Kr and 8.5 MeV/u ^{136}Xe on ^{nat}W Targets
Radiochim. Acta 33, 1 (1983)

Aachen, Germany: Plasma Physics and Controlled Fusion, 05.09. - 09.09. 1983

R. Bock
Status and Perspectives of Heavy Ion Fusion

Acapulco, Mexico: XIIth International Conference on Solid State Nuclear Track Detectors, 04.09. - 10.09. 1983

M. Debeauvais, J. Ralarosy, J. Tripier, S. Jokic
Reactions of 10 and 16.7 MeV Per Nucleon ^{238}U on ^{238}U, ^{208}Pb, ^{197}Au and ^{12}C Recorded within "SSNTD"

L.L. Kashkarov, G.V. Kalinina, V.I. Vernadesky, V.P. Perelygin, S.G. Stetsenko, P. Vater, R. Brandt
Thermal Stability of Tracks in Pyroxenes

H.A. Khan, N.A. Khan, K. Jamil, R. Brandt
Annealing of Heavy Ion Latent Damage Trails in Muscovite Mica and CR-39 Plastic Track Detectors

H.A. Khan, K. Jamil, N.A. Khan, M. Aslam Sial, R. Brandt
Elastic Scattering of 10 MeV/n-^{238}U-Ions by ^{197}Au and ^{165}Ho

H.A. Khan, M. Aslam Sial, N.A. Khan, G. Hussain, R. Brandt, J.W.N. Tuyn
Multifragment Emission in the Interaction of 86 MeV/n ^{18}O-Ions with ^{197}Au, ^{184}W and ^{107}Ag

P. Vater, E.U. Khan, R. Beckmann, R. Brandt
Five-Pronged Fission Events, Quite Abundantly Observed in the Interactions of 16.7 MeV/u $^{238}U + ^{nat}U$ Using Mica SSNTD

P. Vater, E.U. Khan, G. Tress, R. Dersch, R. Brandt, H. Wild, H. Albrecht
A Mica Microfilter Cascade Fractionator to Measure the Size Distribution of Aerosols Produced in a Core Melting Experiment

Albuquerque, USA: IInd International Conference on Radiation Effects in Insulators, 30.05. - 03.06. 1983

P. Pellas, C. Perron
Track Formation Models: A Short Review

K. Thiel, U. Saßmannshausen, D.E. Arafah
Preferential Sputtering and Ion Induced Changes in the Composition of Pure and U-Doped LiF-Single Crystals

G.K. Wolf, K. Zucholl
Katalytic Properties of Ion Bombarded Non-Metals

Alcabideche, Portugal: Nato ASI On Density Functional Methods in Physics, 05.09. - 16.09. 1983

E.K.U. Groß, R.M. Dreizler
Density Functional Approach to Time-Dependent and to Relativistic Systems

Alushta, Crimea, USSR: International School Seminar on Heavy Ion Physics, 14.04. - 21.04. 1983

P. Armbruster
Recent Findings on the Road to the Limits of Fusion

H. Gäggeler
Recent Attempts to Produce Superheavy Elements by the $^{48}Ca + ^{248}Cm$ Reaction Applying Chemical Techniques

H. Gäggeler, W. Brüchle, M. Brügger, M. Schädel, K. Sümmerer, G. Wirth, A. Ghiorso, K.E. Gregorich, D. Lee, K.J. Moody, G.T. Seaborg, R.B. Welch, P. Wilmarth, G. Herrmann, J.V. Kratz, N. Trautmann, N. Hildebrand, U. Hickmann, C. Frink, N. Greulich, D.C. Hoffman, M.M. Fowler, H. R. von Gunten
Recent Attempts to Produce Superheavy Elements by the $^{48}Ca + ^{248}Cm$ Reaction

S. Hofmann
Decay Studies of Nuclei Near the Proton Drip Line

P. Kienle
Deep Inelastic Collisions of Heavy Ions and Positron Production at Bombarding Energies Close to the Coulomb Barrier

O. Klepper
Properties of Nuclei Far From Stability Studied Recently at the GSI On-Line Mass Separator

W. Nörenberg
Dissipative Diabatic Dynamics: A Shell-Model Approach to Large-Amplitude Collective Nuclear Motion

V.P. Perelygin, S.G. Stetsenko, O. Otgonsuren, R. Ignatova, G.J. Starodub, T. Tanevo, M. Chaiduk, P. Vater, R. Brandt, R. Spohr, M. Bütüchi, B. Jakupi, R. Antanasijevic, S. Todorovic, D.S. Jadav, A.P. Sharma, P. Pellas, K. Perron, G. Kural
Über die Suche und Indentifizierung der Spuren überschwerer kosmischer Kerne in Olivinen extraterrestrischer Herkunft

Amsterdam, The Netherlands: Spore Radiation Biology Meeting, 09.07. 1983

K. Baltschukat, H. Bücker, R. Facius, M. Schäfer
Inactivation of Bacillus Subtilis Spores by Very Heavy Ions: Dependence of Cross Sections on E, Z^2_{eff} and Z^2_{eff}/β^2

A.R. Kranz
Qualification Tests for Sordaria Ascospores in HZE-Radiation Experiments

M. Schäfer, R, Facius, H. Bücker
Some Aspects of Heavy Ion Effects in Irradiation Experiments with Spores of Bacillus Subtilis

Amsterdam, The Netherlands: VIIth International Conference on Radiation Research, 18.07. - 22.07. 1983

E. Schneider, F. Schöpfer, J. Kiefer
The Oxygen Effects in Yeast Cells Exposed to High LET Particle Radiation

Argonne, Illinois, USA: Workshop 1983 of the International Nuclear Target Development Society, 07.09. - 09.09. 1983

H. Folger, W. Hartmann, J. Klemm, W. Thalheimer
Special Aspects of Targets for High-Intensity Heavy-Ion Accelerator Beams

Autrans, France: XIth European Conference on Physics and Chemistry of Complex Nuclear Reactions, 05.09. - 09.09. 1983

R. Brandt
Test of Radiochemical Techniques in the Study of Anomalons

A. Rox, B Jäckel, R.A. Esterlund, W. Westmeier, U. Reus, H. Schulte, P. Patzelt
Extra Push in the System $^{238}U + ^{nat}Fe$

K. Sümmerer, W. Brüchle, M. Brügger, H. Gäggeler, M. Schädel, G. Wirth, A. Ghiorso, K.E. Gregorich, D. Lee, K.J. Moody, G.T. Seaborg, R.B. Welch, P. Wilmarth, G. Herrmann, J.V. Kratz, N. Trautmann, N. Hildebrand, U. Hickmann, C. Frink, N. Greulich, D. C. Hoffman, M.M. Fowler, H.R. von Gunten
Recent Attempts to Produce Superheavy Elements in the $^{48}Ca + ^{248}Cm$ Reaction

W. Westmeier
Particle-to-Fission Competition at High Excitation Energies

Baden-Baden, Gemany: VII. Inernational Symposium on Column Liquid Chromatography, 03.05. - 06.05. 1983

M. Schädel, W. Brüchle, B. Haefner, W. Schorstein
Pressurized Liquid Chromatography in Radiochemical Searches for Superheavy Elements.

Bad Honnef, Germany: SNQ-Workshop, 01.02. - 02.02. 1983

P. Kienle
Kernphysikalische Nutzung der Spallations-Neutronenquelle

Bad Iburg, Germany: Xth International Conference on Atomic Collisions in Solids, 18.07. - 22.07. 1983

D. Albrecht, P. Armbruster, M. Roth, K. Schaupert, R. Spohr, H. Stuhrmann
Small-Angle Scattering from Oriented Latent Nuclear Tracks

Balatonfured, Hungary: VIth International Conference on High Energy Nuclear Physics, 06.06. - 11.06. 1983

H.A. Gutbrod, H.A. Gustafsson, B. Kolb, H. Löhner, B. Ludewigt, A.M. Poskanzer, T. Renner, H. Riedesel, H.G. Ritter, A. Warwick, F. Weik, H. Wieman
4 π Data of Relativistic Nuclear Collisions

H.H. Gutbrod, A.I.Warwick
Aspects of Data on the Breakup of Highly Excited Nuclei

J. Knoll
Subthreshold Pion Production - A Cooperative Process?

H. Löhner, B. Ludewigt, H.A. Gustafsson, H.H. Gutbrod, B. Kolb, A.M. Poskanzer, T. Renner, H. Riedesel, H.G. Ritter, A. Warwick, F. Weik, H. Wieman
Participant Spectator Identification in Plastic Ball Events Using a Cluster Algorithm

U. Müller
Relativistic Nuclear Fluid Dynamics Coupled to Classical Meson Fields

H.G. Ritter, H.A. Gustafsson, H.H.Gutbrod, B. Kolb, H. Löhner, B. Ludewigt, A.M. Poskanzer,T. Renner, H. Riedesel, A. Warwick, F. Weik, H. Wieman
Global Analysis of Relativistic Nuclear Collisions Detected by the Plastic Ball

H.Wieman, H.A. Gustaffson, H.H. Gutbrod, B. Kolb, H. Löhner, B. Ludewigt, A.M. Poskanzer, T. Renner, H.Riedesel, H.G. Ritter, A. Warwick, F. Weik
Two Particle Correlations Observed with the Plastic Ball

Baltimore, USA: Spring Meeting of the American Physical Society, 18.04. - 21.04. 1983

D. Frekers, P. Chowdhury, H. Emling, R.V.F. Janssens, T.L. Khoo, R. Broda, Y.H. Chung, P.J. Daly, Z.W. Grabowski, H. Helppi, M. Kortelahti, S. Frauendorf, Z.Y. Zhang
Properties of Nuclear Shapes in Light Hg-Isotopes at High Spin

H.A. Gustafsson
A Search for Short-Lived Anomalons in Projectile Fragmentation

J.W. Harris, R. Brockmann, K.L. Wolf, E.K. Jackson, H.G. Pugh, G. Laroche, L.S. Schroeder, R.N. Treuhaft, G. Krebs and P. Kirk
Midrapidity Pion Production in 1.05 GeV/n ^{40}Ca + ^{40}Ca Collisions

B. Ludewigt
Nuclear Stopping and Thermalization in Relativistic Heavy Ion Collisions

A.M. Poskanzer
Global Analysis in Relativistic Heavy Ion Collisions

T. Renner
Cluster Production in Relativistic Heavy Ion Reactions

A. Sandoval, R. Brockmann, A. Dacal, J.W. Harris, M. Maier, G.Odyniec, M.E. Ortiz, H.G. Pugh, W. Rauch, R.E.Renfordt, L.S. Schroeder, R.Stock, H. Ströbele
The Streamer Chamber as a Tool of Heavy Ion Research

R. Stock
Compression Effects in Relativistic Nucleus-Nucleus Collisions

H. Ströbele, R. Brockmann, J.W. Harris, M. Maier, R.E. Renfordt, F. Riess, A. Sandoval, R. Stock, K.L. Wolf, H.G. Pugh, L.S. Schroeder
Momentum Flux Analysis of Central 800 MeV/n Ar + Pb and 1.8 GeV/n Ar + KCl Reactions

C. Yannouleas, M. Dworzecka, J.J. Griffin
Wall Formula as Special Case of RPA Dissipation

Bangalore, India: XVIIIth International Cosmic Ray Conference, 22.08. - 03.09. 1983

C. Perron, P. Pellas
Can We Get the Cosmic Ray Actinide Abundance from the Study of Tracks in Meteorites?

Bayreuth, Germany: Jahrestagung der Gesellschaft fuer Genetik, 02.06. - 03. 06. 1983

K. Koller-Lampert, A.R. Kranz, M. Starke
Relative biologische und strahlengenetische Wirksamkeit unterschiedlich beschleunigter Schwerionen bei Arabidopsis thaliana

Bergerac, France: Inner Shell Ionisation and Nuclear Physics, 01.05. - 06.05. 1983

C. Kozhuharov
Spectra of Positrons Emitted in (U+U)-Collisions

U. Müller
Positron Production in Heavy Ion Collisions with Nuclear Contact

P. Senger, H. Backe, W. Bonin, E. Kankeleit, M. Krämer, R. Krieg, V. Metag, J.B. Wilhelmy
Estimates of the Nuclear Time Delay in Dissipative U + U Collisions Derived from the Shape of Positron and δ-Ray Spectra

Berkeley, USA: Conference in Real Time Computer Application in Nuclear and Particle Physics, 15.05. - 19.05. 1983

B. Kolb
LISA, an On- and Off-line Data Analyzing Program

Berkeley, USA: VIth High Energy Heavy Ion Summer Study and Second Workshop on Anomalons, 28.06. - 01.07. 1983

R. Brockmann, J.W. Harris, M. Maier, A. Sandoval, R. Stock, H. Ströbele, K.L. Wolf, H.G. Pugh, L.S. Schroeder, R.E. Renfordt
Pion Spectra in the Reaction Ar + KCl at 1.8 GeV/Nucleon

E. Grosse
Cooperative Effects in Subthreshold Pion Production

H.A. Gustafsson, H.H. Gutbrod, B. Kolb, B. Ludewigt, A.M. Poskanzer, T. Renner, H. Riedesel, H.G. Ritter, A. Warwick, F. Weik, H. Wieman
A Search for Short-Lived Anomalons in Projectile Fragmentation

J.W. Harris, D. Bangert, R. Bock, R. Brockmann, A. Dacal, M. Maier, G. Odyniec, M.E. Ortiz, H.G. Pugh, W. Rauch, R.E. Renfordt, A. Sandoval, L.S. Schroeder, R. Stock, H. Ströbele, K.L. Wolf
Evidence on the Equation of State of Nuclear Matter at High Densities

R.E. Renfordt, R. Brockmann, J.W. Harris, M. Maier, F. Riess, A. Sandoval, R. Stock, H. Ströbele, K.L. Wolf, H.G. Pugh, L.S. Schroeder, D. Schall, K. Tittel
Search for Flow in the Reaction Ar + Pb

H.G. Ritter, H.A. Gustafsson, H.H. Gutbrod, B. Kolb, H. Löhner, B. Ludewigt, A.M. Poskanzer, T. Renner, H. Riedesel, A. Warwick, F. Weik, H. Wieman
Results Obtained Using the Plastic Ball

R. Shyam, J. Knoll
Subthreshold Pion Production in Nucleus-Nucleus Collisions - A Co-Operative Process

A. Warwick, H. Wieman, H.H. Gutbrod, H.G. Ritter, H. Stelzer, F. Weik, S.B. Kaufman, E.P. Steinberg, B.D. Wilkins
Aspects of Data on the Breakup of Highly Excited Nuclei

H. Wieman, H.A. Gustafsson, H.H. Gutbrod, B. Kolb, H. Löhner, B. Ludewigt, A.M. Poskanzer, T. Renner, H. Riedesel, H.G. Ritter, A. Warwick, F. Weik
Two Particle Correlations Observed with the Plastic Ball Detector

Berlin, Germany: XIIIth International Conference on the Physics of Electronic and Atomic Collisions, 27.07. - 02.08. 1983

M. Clemente, E. Berdermann, P. Kienle, H. Tsertos, W. Wagner, F. Bosch, C. Kozhuharov, W. Koenig
Pair Creation in Overcritical Coulomb Fields

H.D. Dohmann, D. Liesen, E. Pfeng
Wavelengths of Transitions in Few Electron Spectra of Titanium

W. Elberfeld, M. Kleber
Use of Ehrenfest's Principle for Inelastic Collisions

W. Groh, A. Müller, B. Schuch, A.S. Schlachter, E. Salzborn
Transfer Ionization and Coulomb Ionization in Collisions of Multiply Charged Ions with Atoms

J.E. Hansen, W.R. Johnson, G. Soff
Realstivistic Many-Body Approach to the Photoionization of Alkali Atoms

H. Hartung, B. Fricke, W.-D. Sepp
Potential Energy Surfaces for Di-Atomic Molecules

D.H.H. Hoffmann, P.H. Mokler, W.A. Schönfeldt, A. Warczak, Z. Stachura
Electron Capture into N-, O-, and F-like Xe and Sm Ions at 3.6 MeV/u

R. Hoffmann, R. Schuch, E. Justiniano, W. Schadt, H. Schmidt-Böcking, P.H. Mokler, F. Bosch, W.A. Schönfeldt, Z. Stachura
K-Shell Excitation by K- to L-Shell Charge Transfer in Slow Kr^{q+} -Xe Collisions

J. Krause, M. Kleber
The Electrons Path Through Phase Space During Heavy Ion Impact

B. Liu, W. Enders, D. Liesen, R. Schulze
Construction and Performance of a Position-Sensitive Particle Detector with Delay Line Readout

D. Maor, Z. Stachura, P.H. Mokler, B. Liu, D. Liesen
Rotational Coupling in Asymmetric Ion-Atom Collisions

P.H. Mokler, D.H.H. Hoffmann, W.A. Schönfeldt, Z. Stachura, A. Warczak
Inner Shell Vacancy Transfer Studied with Highly Ionized, Decelerated Heavy Ions

A. Müller
Transfer Ionization by Multiply Charged Ions

W.A. Schönfeldt, D.H.H. Hoffmann, P.H. Mokler, A. Warczak
M-Subshell Effects in Electron-Capture to Sm^{q+} Ions

R. Schuch, W. Groh, A. Müller, E. Salzborn, H.F. Beyer, W.A. Schönfeldt, P.H. Mokler
Coincidence Measurements of Recoil-Ion Charge-State Spectra Produced by Ionization and Charge Transfer in Collisions of 1.4 MeV/u Highly Charged Ions and Rare-Gas Atoms

W. Schulze, D. Kolb
Atomic and Molecular Properties from Finite Element Method Calculations

D. Schwalm
Positron Emission from Superheavy Quasiatoms

W.-D. Sepp, D. Kolb, H. Hartung, W. Sengler, B. Fricke
Development of an Accurate Numerical Dirac-Fock-Slater Program for Di-Atomic Molecules

W.-D. Sepp
Calculations of Coupling Matrix Elements for Di-Atomic Systems in an Atomic Basis

S.R. Valluri, U. Becker, N. Grün, W. Scheid
Semiclassical Approximation of the Time-Dependent Dirac Equation with First Order Perturbation Theory and Finite Difference Method

A. Warczak, H.D. Dohmann, D. Liesen, B. Liu
Inner Shell Vacancy Production in Asymmetric Heavy Ion-Atom Collisions

Bormio, Italy: XXI International Winter Meeting on Nuclear Physics, 24.01. - 29.01. 1983

P. Armbruster
On the Limits of Fusion - And the Making of Elements 107 and 109

E. Badralexe, R.K. Gupta, M. Münchow, W. Scheid
On the Proton and Neutron Distributions in Dissipative Heavy Ion Collisions

H. Gäggeler, W. Brüchle, M. Brügger, M. Schädel, K. Sümmerer, G. Wirth, A. Ghiorso, K.E. Gregorich, D. Lee, J.J. Moody, G.T. Seaborg, R.B. Welch, P. Wilmarth, G. Herrmann, J.V. Kratz, N. Trautmann, N. Hildebrand, U. Hickman C. Frink, N. Greulich, D.C. Hoffman, M.M. Fowler, H.R. von Gunten
Recent Attempts to Produce Superheavy Elements by the $^{48}Ca + ^{248}Cm$ Reaction

P.O. Hess, M. Seiwert, J.A. Maruhn, W. Greiner, A.V. Ramayya
Application of the General Collective Model

A. Lukasiak, W. Cassing, W. Nörenberg
Coherent and Incoherent Aspects of Heavy-Ion Collisions

Ch. Michel
Subthreshold π^0 Production in Heavy Ion Collisions

U. Mosel
How Do Nuclei Really Rotate or Vibrate?

K. Mühlhans, U. Mosel, K. Neergard, M. Diebel, E.M. Müller
Multipole Pair-Fields at High-Temperature and Spin

G. Sletten, S. Bjornholm, J. Borggreen, J. Pedersen, P. Chowdhury, H. Emling, D. Frekers, R.V.F. Janssens, T.L. Khoo, Y.H. Chung, M. Kortelahti
High Spin Configurations in ^{147}Gd from Alignment of Seven, Nine and Eleven Particles

Brookhaven, USA: Quark Matter 83, 26.09. - 29.09. 1983

R. Bock
Accelerator Concept at GSI

H.H. Gutbrod, C. Rubbia
Workshop on 4 π Detectors in Ultrarelativistic Heavy Ion Collisions

R. Stock
Future Experiments in Ultra-Relativistic Ion Collisions

Catania, Italy: International Conference on Heavy-Ion Physics and Nuclear Physics, 21.03. - 26.03. 1983

R. Bock
Intermediate Energy Heavy-Ion Collisions

H. Löhner
Charged Particle Exclusive Measurements with the Plastic Ball Spectrometer

A. Lukasiak, W. Nörenberg
On Diabatic Shell-Structure Effects in Heavy-Ion Collisions

W. Nörenberg
Dissipative Diabatic Dynamics: A Shell-Model Approach to Large-Amplitude Collective Nuclear Motion

W. Spreng, H. Emling, E. Grosse, R.S. Simon, H.J. Wollersheim, M. Mutterer, J.P. Theobald, D. Schwalm, M.S. Moore, R. Kulessa
Backbending in Actinides

H.J. Wollersheim, W.W. Wilcke, J.R. Birkelund, J.R. Huizenga
Influence of the Impact Parameter on Element Distribution in Dissipative Heavy-Ion Collisions

Crete, Greece: Europhysics Study Conference on Frontiers of γ- and x-Ray Spectroscopy, 27.06 - 01.07. 1983

Ch. Michel
Design of Compton Suppression Spectrometer by Monte Carlo Methods: The Segmentation of the Germanium Allows to Define a New Configuration

Florence, Italy: International Conference on Nuclear Physics, 29.08. - 03.09. 1983

Y.K. Agarwal, P. Armbruster, W. Brüchle, M. Brügger, J.P. Dufour, H. Gäggeler, S. Hoffmann, F.P. Hessberger, P. Lemmertz, G. Münzenberg, K. Poppensieker, W. Reisdorf, M. Schädel, K.-H. Schmidt, J.H.R. Schneider, W.F.W. Schneider, K. Sümmerer, D. Vermeulen, G. Wirth, A. Ghiorso, K.E. Gregorich, D. Lee, M. Leino, K.J. Moody, G.T. Seaborg, R.B. Welch, P. Wilmarth, S. Yashita, C. Frink, N. Greulich, G. Herrmann, U. Hickmann, N. Hildebrand, J.V. Kratz, N. Trautmann, M.M. Fowler, D.C. Hoffman, H.R. von Gunten, H. Dornhöfer
Recent Attempts to Produce Superheavy Elements in the $^{48}Ca + ^{248}Cm$ Reaction

A. Ansari, S.C.K. Nair
Discontinuities in $^{170,174}Yb$ Isotopes at Very High Spins

A. Ansari, E. Wüst, U. Mosel
Magnetic Moment and Nuclear Structure at High Spins

P. Armbruster
Cold Fusion - A New Road to Heavy Elements

G. Beier, J. Friese, W. Henning, P. Kienle, H.J. Körner, Waltraud Mayer, W.A. Mayer, L. Müller, W. Wagner
Shell Effects in the Reaction Mechanism of ^{238}U - Induced Deep Inelastic Scattering Near the Coulomb Barrier

D. Berdichevsky, U. Mosel
What Do We Know about the Surface of Nuclear Charge and Mass Densities?

H. Bokemeyer, H. Folger, H. Grein, T. Cowan, J.S. Greenberg, J. Schweppe, K. Bethge. A. Gruppe, K.E. Stiebing, D. Schalm, P. Vincent, N. Trautmann
Observation of Peak Structure in Positron Spectra from Superheavy Collision Systems

C. Brendel, J. Carter, F. Beck, G. Delic, R.H. Lemmer, A. Richter, G. Schrieder, D. Schüll,
One and Two Neutron Transfer Reactions in a Core Excitation Model for the $^{48}Ti + ^{42}Ca$ System

W. Brüchle, M. Brügger, H. Gäggeler, M. Schädel, K. Sümmerer, G. Wirth, C. Frink, N. Greulich, G. Herrmann, U. Hickmann, N. Hildebrand, J.V. Kratz, N. Trautmann, A. Ghiorso, K.E. Gregorich, D. Lee, K.J. Moody, G.T. Seaborg, R.B. Welch, P. Wilmarth, W.R. Daniels, J.M. Fowler, D.C. Hoffman H.R. von Gunten, H. Dornhöfer,
Recent Attemtps to Produce Superheavy Elements in the $^{48}Ca + ^{248}Cm$ Reaction

S. Brüssermann, K.P. Lieb, P. Sona, H. Emling, E. Grosse, J. Stachel
Multiple Coulomb Excitation of ^{82}Kr

W. Cassing, W. Nörenberg
Nonequilibrium Light Particle Emission in Nucleus-Nucleus Collisions

M. Clemente, E. Berdermann, P. Kienle, H. Tsertos, W. Wagner, F. Bosch, C. Kozhuharov, W. Koenig
Observation of Positron Lines in Heavy Ion Collisions

M. Nessi, Ch. Stoller, E. Morenzoni, W. Wölfli, W.E. Meyerhof, J.D. Molitoris, E. Grosse, Ch. Michel
Reaction Times in the Deep Inelastic Nuclear Reaction U+U and U+Pb

H. Noll, H. Dabrowski, E. Grosse, H. Heckwolf, O. Klepper, Ch. Michel, W.F.J. Müller, H. Stelzer, C. Brendel, W. Rösch, P. Braun-Munzinger, J. Julien, G. Papalardo, G. Bizard, J.L. Laville, A. Müller, J. Peter
Cooperative Effects Observed in the Neutral Pion and High Energy Gamma Emission from Nuclear Collisions

M. Schädel, R.W. Lougheed, J.H. Landrum, J.F. Wild, R.J. Dougan, A.D. Hoover, E.K. Hulet, G.R. Bethune, A. Ghiorso, M.J. Nurmia, L.P. Somerville, K.J. Moody, and G.T. Seaborg
Heavy Actinide Products from Reactions with ^{254}Es

W. Spreng, F. Azgui, H. Emling, E. Grosse, R. Kulessa, Ch. Michel, R.S. Simon, H.J. Wollersheim, M. Mutterer, D. Schwalm
Backbending in the Yrast Sequence of ^{244}Pu

J. Stachel, N. Kaffrell, H. Emling, H. Grein, E. Grosse, Ch. Michel, D. Schwalm, F.R. May
Collectivity and Aligment Phenomena at Triaxial Deformation

O. Tanimura, R. Wolf, R. Kaps, U. Mosel
Formulations for Exact One- and Two-Step DWBA Methods

O. Tanimura, R. Kaps, R. Wolf, U. Mosel
Optical Potentials in One- and Two Step DWBA

O. Tanimura, R. Wolf, U. Mosel
Gross Structure Resonance at 24.3 MeV in ^{12}C + $^{12}C(2^+)$

O. Tanimura, R. Wolf, U. Mosel
Molecular Resonance in Inelastic ^{16}O + ^{16}O Scattering

M. Tohyama, S. Yamaji
Effects of Two Particle-Two Hole Excitations on the Mass Distributions in Ion-Ion Collisions

M. Tohyama, R. Kaps, D. Masak, U. Mosel
Mean Field Approximation to Pion Production in Intermediate Energy Heavy Ion Collisions

C. Yannouleas
Extension of RPA Dissipation to Large Amplitude Collective Motion

Frankfurt am Main, Germany: IVth EARDHE-Congress on Higher Education by the Year 2000, 05.09. - 10.09. 1983

A.R. Kranz, U. Bork, B. Kirchheim, K. Koller-Lampert, M.E. Starke
Biological Effects of Single HZE-Particles in Cosmic Radiation

Glasgow, Great Britain: XIth Gray Meeting, 03.07. - 08.07. 1983

J. Kiefer
Recovery after Exposure to High LET Radiation

K.J. Weber, J. Kiefer
Recovery from Transcription Inhibition in Irradiated Yeast Cells

Guangzhou, People's Republic of China: International Conference on Lasers, 05.09. - 08.09. 1983

P. Fayet, R. Keller, L. Wöste
Laser Spectroscopy of Sputtered Cluster Ions

Harwell, Great Britain: Alpha Particle Spectrometry and Low Level Measurement, 10.05. - 13.05. 1983

S. Hofmann
Detector System for Investigation of Proton Radioactivity and New Elements at SHIP

Heidelberg, Germany: IIIrd International Conference on Particle Induced X-Ray Emission (PIXE) and its Analytical Applications, 18.07. - 22.07. 1983

D.H.H. Hoffmann, C. Brendel, H. Genz, W. Löw, A. Richter
Application of Relativistic Electrons for the Quantitative Analysis of Trace Elements

Hirschegg, Austria: XIth International Workshop on Gross Properties of Nuclei and Nuclear Excitations, 17.01. - 22.01. 1983

W. Cassing, A. Lukasiak, W. Nörenberg
Dissipative Diabatic Dynamics (DDD): A Theory for Heavy Ion Collisions between TDHF and Transport Theories

E. Grosse
Possible Cooperative Effects Observed in the Neutral Pion Production from Nucleus-Nucleus Collisions

K.D. Hildenbrand
Reactions Induced by Heavy Ions at Incident Energies above 12 MeV/u

S. Hofmann
Experiments for Investigation of Proton Radioactivity at SHIP

R. Kirchner, O. Klepper, W. Kurcewicz, P. O. Larsson, E. Roeckl, D. Schardt, G. Nyman, P. Tidemand-Petersson
Studies of Very Neutron-Deficient Nuclei at and Beyond the Proton Drip Line

G. Münzenberg, Y.K. Agrarwal, F.P. Heßberger, S. Hofmann, K. Poppensieker, W. Reisdorf, J.R.H. Schneider, W.F.W. Schneider, K.-H. Schmidt, H.-J. Schött, P. Armbruster, C.C. Sahm, D. Vermeulen
New Elements

R.E. Renfordt
Exclusive Analysis of Ar + KCl and Ar + Pb Reactions

M. Schädel, R.W. Lougheed, J.H. Landrum, J.F. Wild, R.J. Dougan, A.D. Hoover, E.K. Hulet, G.R. Bethune, A. Ghiorso, M.J. Nurmia, L.P. Somerville, K.J. Moody, and G.T. Seaborg
Heavy Actinide Products from Reactions with ^{254}Es: Results and Prospects

P. Tidemand-Petersson, E. Runte, W.-D. Schmidt-Ott, K.-L. Gippert, R. Kirchner, O. Klepper, W. Kurcewicz, E. Roeckl, D. Schardt, N. Kaffrell, P. Peuser, K. Rykaczewski, M. Bernas, P. Dessagne, M. Langevin
Decay Studies of Very Neutron-Rich Isotopes Produced in Multinucleon Transfer Reactions

Hirschegg, Austria: Fusion Target Meeting 07.02. - 11. 02. 1983

R.W. Müller
High-Temperature Target Experiments with Heavy Ion Synchrotrons

Interlaken, Switzerland: Sixth International Conference on Laser Spectroscopy, 27.06. - 01.07 1983

G. Ulm, J. Eberz, G. Huber, D. Kaplan, H. Lochmann, R. Kirchner, O. Klepper, T.U. Kühl, D. Marx, P.O. Larsson, E. Roeckl, D. Schardt
Collinear Laser Spectroscopy of Fusion Produced Indium Isotopes

Koeln/Porz, Germany: BIOSTACK-Experimenter Meeting, 26.01. - 27.01. 1983

A.R. Kranz
Proposal and Experiences for Using Euraryotic Plant Cells in Advanced Biostack-Experiments

Konstanz, Germany: Tagung der Astronomischen Gesellschaft, 21.03. - 25.03. 1983

A. Faessler
Kernmaterie unter extremen Bedingungen

Kyoto, Japan: International Ion Engineerig Congress, 12.09. - 16.09. 1983

N. Angert
Upgrading of Unilac

N. Angert, R. Keller, M. Müller
Duoplasmatron and PIG Ion Sources for Highly Charged Heavy Ions

R. Keller, P. Spädtke, F. Nöhmayer
A High-Current Ion Source System for Non-Volatile Elements and Gases

P. Krejcik, R. Keller
Hollow Beam Technology for High-Current Ion Beams

Lahore, Pakistan: PAEC - KfK Joint Seminar on Application of Radioisotopes in Industry, 20.03. - 22.03. 1983

R. Brandt, G. Tress, M. Ellinger, P. Vater, M. Kadner, H.A. Khan, N.A. Khan
Mica Track Microfilters in a Cascade Particle Fractionator at an Industrial Plant

Liverpool, Great Britain: Nuclear Structure and Particle Physics, 23.03. - 25.03. 1983

U. Mosel
Inelastic Scattering of "Light" Heavy Ions

Los Angeles, USA: Meeting of the American Physical Society, 23.03. 1983

P. Armbruster
Cold Fusion, A New Road to Heavy Elements

Loughborough, Great Britain: IIIrd International Conference On Low Energy Ion Beams, 28.03. - 31.03. 1983

R. Keller, F. Nöhmayer, P. Spädtke, M.-H. Schönenberg
CORDIS - an Improved High-Current Ion Source for Gases

P. Krejcik, R. Keller
A High-Current Beam Transport Facility for Hollow Beams

P. Spädtke, B.H. Wolf
HV-Gap Geometries for High-Current Heavy Ion Acceleration and Beam Transport

Louvain-la-Neuve, Belgium: Nuclear Physics Workshop, 01.06. 1983

P. Armbruster
On the Synthesis of Nuclei at the Limits of Nuclear Stability

Madrid, Spain: XVth EGAS Conference, 05.07. - 08.07. 1983

G. Ulm, J. Eberz, G. Huber, H. Lochmann, R. Kirchner, O. Klepper, T. U.Kühl, D. Marx, P. O. Larsson, D. Schardt
On-Line Collinear Fast-Beam Laser Spectroscopy of Fusion-Produced Indium Isotopes

Mainz, Germany: Seminar ueber Fragen der Nuklearen Astrophysik, 13.10. - 15.10. 1983

E. Roeckl
Produktion neutronenreicher Kerne in Schwerionenreaktionen

Manchester, England: Manchester University, 01.12. 1983

O. Klepper
Spectroscopy of Very Neutron-Deficient Nuclei Close to ^{100}Sn

Mikolajki, Poland: XVth Masurian Summer School on Nuclear Physics, 5.09. - 17.09. 1983

U. Brosa, W. Westmeier
Merging: What Discriminates Quasielastic from Deep-Inelastic Processes

J. Reinhardt, W. Greiner, U. Heinz, P.O. Hess, B. Müller, U. Müller, T. de Reus, P. Schlüter, M. Seiwert, G. Soff, D. Vasak
The Decay of the Vacuum in Supercritical Fields of Giant Nuclear Systems

D. Schardt
Direct and Beta-Delayed Proton Decay of Very Neutron-Deficient Rare-Earth Isotopes

Muenchen, Germany: XIth Annual Conference of the Association for Aerosol Research, 14.09. - 16.09. 1983

G. Tress, E.U. Khan, H.A. Vater, R. Brandt, M. Kadner
Fractionation of Aerosols Using a Mica Microfilter Cascade Fractionator at the NUKEM-Sinteroven

Muenchen, Germany: Jahrestagung Deutsche Gesellschaft fuer Biophysik, 10.10. - 12.10. 1983

J. Kiefer, F. Schöpfer, E. Schneider
Erholung in Hefezellen nach Schwerionenbestrahlung

M. Kost, E. Schneider, J. Kiefer
Inaktivierung getrockneter Hefezellen durch Protonen verschiedener Energien

E. Schneider, M. Kost, G. Döll
Strahlensensible Farbdetektoren (Radiochromic Detectors) als Dosimeter für Teilchenstrahlung

Muenster, Germany: Fruehjahrstagung Kernphysik, 21.03. - 25.03. 1983

Y.K. Agarwal, H. Emling, E. Grosse, C. Günther, K.Hardt, R. Kulessa, P. Schüler, W. Spreng, J. Stachel, H.J. Wollersheim
Multiple Coulomb Excitation of ^{202}Hg and ^{204}Hg

H. Ahrens, J.P. Bocquet, N. Kaffrell, B.D. Kern, H. Lawin, K. Shizuma, K. Sistemich, G. Tittel, N. Trautmann
Rotational Structure in ^{101}Zr, ^{103}Mo, ^{105}Mo

P. Armbruster, E. Berdermann, F. Bosch, M. Clemente, P. Kienle, W. Koenig, C. Kozhuharov, H. Tsertos, W. Wagner
δ-Rays Emitted in Heavy Ion Collisions

F. Azgui, H. Emling, E. Grosse, C. Michel, D. Schwalm, H.J. Wollersheim
Lifetimes of High Spin States in ^{154}Dy

E. Badralexe, R.K. Gupta, M. Münchow, W. Scheid
Non-Perturbative Quantum Treatment of Mass and Charge Degrees of Freedom Interacting with an Environment for Deep Inelastic Collisions

D. Bangert, B. Kohlmeyer, F. Pühlhofer, F. Busch, D. Schüll, H. Freiesleben
Energy Dissipation, Drift and Diffusion by Stochastical Nucleon Exchange

G. Beier, J. Friese, P. Kienle, H.J. Körner, Waltraud Mayer, W.A. Mayer, L. Müller, W. Wagner
Indications of Coherent Nucleon Flow in ^{238}U Induced Deep Inelastic Scattering Near the Coulomb Barrier

D. Berdichevsky, U. Mosel
Analysis of the Influence of Nuclear Asymmetry and Coulomb Force on the Nuclear Densities

S. Bjornholm, R. Bock, Guang-xi Dai, A. Gobi, S. Gralla, G. Guarino, K.D. Hildenbrand, J. Kuzminski, U. Lynen, W.F.J. Müller, A. Olmi, H. Stelzer, J. Toke
Remembrance of the Ingoing Channel Configuration During the Formation and the Decay of a Fused Nucleus

R. Bock, U. Lynen, D. Pelte, U. Winkler, A. Gobbi, K.D. Hildenbrand, W.F.J. Müller, A. Olmi, H. Sann, H. Stelzer
Origin of Medium-Heavy Elements Produced in Heavy Ion Reactions at 84 MeV/u

H. Bokemeyer, H. Folger, H. Grein, Y. Kido, T. Cowan, J.S. Greenberg, J. Schweppe, K. Bethge, A. Gruppe, R. Merten, Th. Odenweller, K.E. Stiebing, D. Schwalm, P. Vincent, N. Trautmann
Search for Spontaneous Positron Emission in Superheavy Quasimolecules

E. Bozek, U. Gollerthan, E. Kankeleit, G. Klotz, M. Krämer, R. Krieg, U. Meyer, H. Oeschler, P. Senger
Positron Production in Peripheral and Close Collisions Measured with the New Tori-Spectrometer

C. Brendel, J. Carter, F. Beck, A. Richter, G. Schrieder, D. Schüll, G. Delic, R.H. Lemmer
Core Excitation in Single Nucleon Transfer Reactions for the $^{48}Ti + ^{42}Ca$ System

M. Brügger, N. Trautmann, G. Herrmann, A.K. Mazumdar, H. Wagner, W. Walcher
A High Efficient High Temperature Ionization Source for the Heliumjet On-Line Isotope Separator HELIOS

S. Brüssermann, H. Emling, E. Grosse, K.P. Lieb, P. Sona, J. Stachel
Multiple Coulomb Excitation of ^{82}Kr

J. Carter, H. Feldmeier, C. Brendel, A. Richter, G. Schrieder, W. Bohne, K. Grabisch, H. Lehr, H. Morgenstern
Fusion of ^{40}Ar and ^{40}Ca at High Incident Energies

W. Cassing, A. Lukasiak, W. Nörenberg
Perspectives of Diabatic Single-Particle Motion in Heavy-Ion Collisions

M. Clemente, E. Berdermann, P. Kienle, H. Tsertos, W. Wagner, F. Bosch, C. Kozhuharov, W. Koenig
Investigation of Positrons Emitted in Heavy Ion-Atom Collisions from the Systems U + U and U + Th

H.-G. Clerc, R. Hingmann, C.-C. Sahm, D. Vermeulen, J.G. Keller, K.-H. Schmidt
Discovery of New Isotopes and Isomeres of the Elements Rn, Th, Pa and U

H.-G. Clerc, M. Mutterer, C. Schmitt, J.P. Theobald, J.P. Bocquet, A. Guessous, R. Brissot, F. Gönnenwein, P. Armbruster, D. Engelhardt, U. Quade, K. Rudolph
Nuclear Mass- and Charge Distribution of the Thermal Neutron Induced Fission of ^{239}Pu

M. Diebel, U. Mosel, K. Mühlhans, E.M. Müller, K. Neergard
Multipole Pair Fields at Various Conditions

G. Domogala, H. Freiesleben
Ionenoptische Eigenschaften eines Niederenergie-Choppers

H. Emling, F. Azgui, P. Chowdhury, Y.H Chung, P. Daly, D. Frekers, C. Grabowski, R.V. Janssens, T.L. Khoo, M. Korthelati, W. Kühn, A. Pakkanen
Time Structure of the Feeding into Spin States in $^{152,154}Dy$

G. Feige, R. Brandt, T. Lund, D. Molzahn, D.C. Hoffman, S.J. de Villiers, A.G. Gancarz, G. W. Knobeloch, F.O. Lawrence
Upper Limits for the Concentration of the Superheavy Elementary Particle ($^{247}CmX^-$) and Other Transuranium Nuclides in Salt Brines

H. Fuchs, D. Hilscher, H. Homeyer, G. Ingold, U. Jahnke, R. Brand, G. Feige, E. Koop
Heavy Ion Experiments with a 4π Neutron Multiplicity Detector

H. Gäggeler, W. Brüchle, M. Brügger, C. Frink, M.M. Fowler, K. Gregorich, N. Greulich, H.R. von Gunten, G. Herrmann, U. Hickmann, N. Hildebrand, D.C. Hoffman, J.V. Kratz, J. Lerch, D. Lee, K.J. Moody, M. Schädel, G.T. Seaborg, K. Sümmerer, N. Trautmann, G. Wirth
Recent Attempts to Produce Superheavy Elements by the $^{48}Ca + ^{248}Cm$ Reaction

J. Gerl, Th.W. Elze, H. Ower, K. Keppler, H. Bohn, T. Faestermann, N. Kaffrell, N. Trautmann
Spectroscopy of Excited Collective Bands in Actinide Nuclei

B. Grabez, R. Beckmann, P. Vater, R. Brandt
Target Products in the Interaction of 84 MeV/u ^{12}C with ^{208}Pb, as Studied with CR-39

S. Gralla, R. Bock, A. Gobbi, K.D. Hildenbrand, U. Lynen, W.F.J. Müller, A. Olmi, M. Petrovici, H. Stelzer, J. Toke, H.J. Wollersheim
Reactions Induced by Heavy Projectiles at Incident Energies at 15 MeV/u

F. Güttner, W. Koenig, N. Lutz, B. Martin, H. Skapa, J. Soltani, H. Banda, A.V. Ramayya, F. Bosch, C. Kozhuharov
Influence of the Nuclear Reaction Time onto the δ-Electron Emission Studied by the Reaction I→Au, Bi at 795 and 840 MeV

F. Güttner, W. Koenig, N. Lutz, B. Martin, H. Skapa, J. Soltani, H. Banda, A.V. Ramayya, F. Bosch, C. Kozhuharov
Study of Inner Quasiatomic Shells (Z_u= 132-171) by Means of δ-Electron Spectroscopy in asymmetric Collisions

H.A. Gustafsson, H.H. Gutbrod, B. Kolb, B. Ludewigt, A.M. Poskanzer, T. Renner, H. Riedesel, H.G. Ritter, A. Warwick, H. Wieman
Search for Anomalons

H.H. Gutbrod, H. Löhner, A.M. Poskanzer, T. Renner, H. Riedesel, H.G. Ritter, A. Warwick, F. Weik, H. Wieman
4 π Physics with the Plastic Ball

H.J. Hennrich, W. Hennerici, G. Himmele, R. Repnow, W. Wahl, D. Habs, K. Helmer, U. v. Helmholt, H.W. Heyng, B. Kolb, D. Pelte, D. Schwalm, R.S. Simon, R. Albrecht, R.D. Fischer, W. Kühn, V. Metag, R. Mühlhans
Suche nach kollektiven γ-Übergängen im quasimolekularen ^{12}C + ^{12}C System

F.P. Hessberger, K.D. Hildenbrand, S. Hofmann, G. Münzenberg, W. Reisdorf, K.-H. Schmidt, J.R.H. Schneider, K. Sümmerer, G. Wirth, J.V. Kratz, K. Schlitt
Further Investigations of Fusion Mechanisms at the Barrier

P. Hill, N. Kaffrell, J. Stachel, D. Schwalm, F. Azgui, H. Emling, E. Grosse, Ch. Michel, W. Spreng, H.-J. Wollersheim
Spin Dependence of Deformation in ^{152}Gd

R. Holzmann, J. Kuzminski, M. Loiselet, M.A. van Hove, and J. Vervier
High Spin States in the Odd-Nuclei ^{159}Tm and ^{157}Er

N. Kaffrell, H. Tetzlaff, N. Trautmann, P. Hill, S. Höglund, G. Skarnemark, J. Alstad, K. Wolfsberg, P. de Gelder, E. Jacobs
Neutron-Rich Nuclei in the Mass Region A=110

R. Kaps, U. Mosel, O. Tanimura, R. Wolf
Polarization Effects in the Scattering of Vibrating Nuclei

J.G. Keller, K.-H. Schmidt, H.-G. Clerc, D. Vermeulen
The Influence of Shell Effects on the Cross Section for Heavy Evaporation Residues from Fusion Reactions

J. Kuzminski, R. Holzmann, M. Loiselet, M.A. van Hove, and J. Vervier
Gas Scintillator Detector for Coulomb Excitation Experiments

P. O. Larsson, T. Batsch, R. Kirchner, O. Klepper, W. Kurcewicz, E. Roeckl, D. Schardt, G. Nyman, P. Tidemand-Petersson
Direct Proton Decay of 0.56-s ^{147}Tm and Search for This Decay Mode Among Very Neutron-Deficient Isotopes with 61 ≤ Z ≤ 67

M.Loiselet, R. Holzmann, J. Kuzminski, M.A. van Hove, and J. Vervier
Lifetime measurement in ^{197}Au

K. Lützenkirchen, J.V. Kratz, W. Brüchle, H. Gäggeler, K. Sümmerer, G. Wirth
Dynamical Hindrance for Fusion of $^{76}_{32}Ge$ with $^{170}_{68}Er$

Ch. Michel, F. Azgui, H. Emling, E. Grosse, H.J. Wollersheim
Monte-Carlo Simulation of a HPGe-BGO Compton Suppression Spectrometer

Ch. Michel, H. Noll, H. Heckwolf, E. Grosse, H. Dabrowski, W.F.J. Müller, H. Stelzer, O. Klepper, P. Braun-Munzinger, C. Brendel, W. Rösch
Pion Production at Intermediate Energy Nucleus-Nucleus Collisions

U. Mosel
Electromagnetic Moments as a Probe for Alignment

U. Mosel, O. Tanimura, R. Wolf
Polarization Potentials for Elastic and Inelastic Scattering

U. Mosel, O. Tanimura, R. Wolf
Spin Assignments of Gross Structure in ^{12}C + $^{12}C(2^+)$ Scattering

U. Mosel, E.M. Müller, K. Neergard
Interpretation of Rotational Bands in Odd-A-Nuclei

U. Mosel, U. Post, E. Wüst
Single Particle Levels of Rotating Nuclei

U. Mosel, E. Wüst
Can One See Current Distributions of Rotating Nuclei?

U. Müller, G. Soff, J. Reinhardt, T. de Reus, P. Schlüter, K.-H. Wietschorke, B. Müller, W. Greiner
Positron Emission in Heavy-Ion Collisions with Nuclear Reactions

W.F.J. Müller, A. Gobbi, K.D. Hildenbrand, A. Olmi, H. Sann, H. Stelzer, I. Bock, U. Lynen, D. Pelte, U. Winkler, R. Glasow, K.-H. Kampert, R. Santo
Reaction-Mechanisms in Medium-Energy Heavy Ion Collisions

M. Münchow, R.K. Gupta, W. Scheid
Dependence of the Frictional Force on Deformation and Orientation in Heavy Ion Collisions and Application to $^{238}U + ^{238}U$

M. Mutterer, P. Grimm, F.-J. Hambusch, H. Heckwolf, J. Pannicke, W. Spreng, J.P. Theobald
Response of Gas Scintillators to Heavy Charged Particles

W. von Oertzen, B. Gebauer, A. Gamp, H.G. Bohlen, D. Schüll, F. Busch
Pairing Effects in Sub-Coulomb Neutron Transfer Between Tin Isotopes

A. Rox, W. Westmeier, R.A. Esterlund, B. Jäckel, P. Patzelt
Symmetric Fragmentation in the System $^{238}U + ^{nat}Fe$

E. Runte, P. Tidemand-Petersson, W.-D. Schmidt-Ott, K. L. Gippert, R. Kirchner, O. Klepper, W. Kurcewicz, E. Roeckl, N. Kaffrell, P. Peuser, K. Rykaczewski
Decay Studies of Very Neutron-Rich Isotopes Produced in Multinucleon Transfer Reactions

M. Schädel, R.W. Lougheed, J.H. Landrum, J.F. Wild, R.J. Douga A.D. Hoover, E.K. Hulet, A. Ghiorso, M.J. Nurmia, L.P. Somervill K.J. Moody, and G.T. Seaborg
Heavy Neutronrich Actinide Products from Reactions of ^{18}O and ^{22}Ne with ^{254}Es

K. Schlitt, F. Hessberger, K. Hildenbrand, S. Hofmann, G. Münzenberg, W. Reisdorf, K.-H. Schmidt, J.R.H. Schneider, W.F.W. Schneider, K. Sümmerer, G. Wirth, J.V. Kratz
Further Investigations of Fusion Mechanisms at the Barrier

G. Schütz, W. Mayer, S. Schuhbeck, K. Hartel, F. Bosch, P. Kienle
Physik in Grenzbereichen

P. Senger, H. Backe, W. Bonin, E. Kankeleit, M. Krämer, R. Krieg, V. Metag, J.B. Wilhelmy
Effects of Nuclear Reaction Times on the Shape of δ-Ray and Positron Spectra

W. Spreng, H. Emling, E. Grosse, R. Kulessa, R.S. Simon, H.J. Wollersheim, M. Mutterer, J.P. Theobald, D. Schwalm, M.S. Moore, P. Ring, J.L. Egido
Backbending in $^{242,244}Pu$

J. Stachel, P. Hill, N. Kaffrell, H. Emling, H. Grein, E. Grosse, R. Kulessa, Ch. Michel, H.-J. Wollersheim, D. Schwalm, S. Brüssermann
Evidence for Non-Axial Nuclear Shape from Electromagnetic Moments

R. Stock
Kernmaterie bei hoher Dichte

U. Tharun, H.J. Keim, U. Knitz, P. Peuser, N. Trautmann, G. Herrmann, G. Wirth
A Low Background Detection System for Fragments and Neutrons from Spontaneous Fission Sources

J. Toke, A. Gobbi, R. Matulewicz
Random-Walk Simulation of Exchange of Nucleons between Nuclei with Specific Shell Structure

A.I. Warwick, H. Wieman, H.H. Gutbrod, M.R. Maier, J. Peter, H.G. Ritter, H. Stelzer, F. Weik, M. Freedman, D.J. Henderson, S.B. Kaufman, E.P. Steinberg, B.D. Wilkins
The Breakup of Spectator Residues in Relativistic Nuclear Collisions

W. Westmeier, R.A. Esterlund, A. Rox, P. Patzelt
Further Evidence for "Extra Push"

W. Westmeier, R.A. Esterlund, P. Patzelt
First Order Dynamic Correction to Competitive Fission Probabilities

G. Wirth, W. Brüchle, Fan Wo, H. Gäggeler, K. Sümmerer, J.V. Kratz, J. Lerch, N. Trautmann
Sub-Coulomb Transfer in Collisions of ^{238}U with ^{238}U

Nagoya, Japan: Meeting on Atomic Collision Data for Diagnostics of Magnetic Fusion Plasmas, 29.08. - 02.09. 1983

E. Salzborn
Electron Capture and Electron Impact Ionization of Multiply Charged Ions

New Delhi, India: XVth International Congress of Genetics, 12.12. - 21.12. 1983

K. Koller-Lampert, A.R. Kranz, M. Starke
Effects of Heavy Ionizing Particles (HZE) in Arabidopsis

New London, USA: Gordon Research Conference on Nuclear Chemistry, 20.06. - 24.06. 1983

E. Grosse
Pion Production in Nucleus-Nucleus Collisions at Energies Far Below the Nucleon-Nucleon Threshold

Notre Dame, Indiana, USA: Nuclear Physics Division APS Meeting, 13.10. - 15.10. 1983

H.G. Ritter
New Physics with the Plastic Ball

Oaxtepec, Mexico: VIth Oaxtepec Meeting on Nuclear Physics, 03.01. - 06.01. 1983

A. Sandoval
The Nuclear Matter Equation of State

Oberstdorf, Germany: 4. Arbeitstagung "Energiereiche Atomare Stoesse", 30.01. - 05.02. 1983

U. Becker, N. Grün, W. Scheid
Lösung der zeitabhängigen Dirac-Gleichung mit der Methode der Finiten Elemente und Anwendung auf das System $Ca^{20+} + U^{91+}$

H. Bokemeyer, H. Folger, H. Grein, Y. Kido, T. Cowan, J.S. Greenberg, J. Schweppe, K. Bethge, A. Gruppe, R. Merten, Th. Odenweller, K.E. Stiebing, D. Schwalm, P. Vincent, N. Trautmann
Positronenemission in überkritischen Schwerionen-Stoßsystemen

H.D. Dohmann, D. Liesen, E. Pfeng
Wellenlängenmessung in Wenigelektronensystemen des Titans

D.H.H. Hoffmann, P.H. Mokler, W.A. Schönfeldt, A. Warczak, Z. Stachura
Elektroneneinfang in N-, O- und F-ähnliche Xe und Sm Projektile bei 3.6 MeV/u

E. Justiniano, H. Schmidt-Böcking, R. Schuch, R. Hoffmann, W. Schadt, P.H. Mokler, F. Bosch, W.A. Schönfeldt, Z. Stachura
K-Schalenanregung durch K-L Ladungstransfer in langsamen Kr-Kr und Xe-Xe Stößen

M. Kleber, W. Elberfeld
Das Ehrenfest-Theorem für inelastische Streuprozesse

J. Krause, M. Kleber
Der Weg eines Elektrons durch den Phasenraum beim Schwerionenstoß

G. Mehler, T. de Reus, U. Müller, J. Reinhardt, G. Soff, K.-H. Wietschorke, P. Schlüter, B. Müller, W. Greiner
δ-Elektronen-Emission und K-Loch-Erzeugung im Schwerionenstoß unter Verwendung eines Dirac-Fock-Slater-Potentials

P.H. Mokler, D.H.H. Hoffmann, W.A. Schönfeldt, Z. Stachura, A. Waczak
Kopplung in inneren Schalen schwerer Stoßmoleküle untersucht mit hochgeladenen, abgebremsten Ionen

A. Müller
Eine statistische Theorie der Transferionisation

U. Müller, T. de Reus J. Reinhardt, G. Soff, K.-H. Wietschorke, P. Schlüter, B. Müller, W. Greiner
Der Einfluß elektronischer Abschirmung und nuklearer Haftzeiten auf atomare Positronenspektren in Schwerionenstößen

E. Salzborn
Erzeugung mehrfach geladener Edelgasionen mit relativistischen Elektronen

W.A. Schönfeldt, D.H.H. Hoffmann, P.H. Mokler, A. Warczak
Einfluß der Projektil-M-Unterschalen beim Elektroneneinfang in Sm^{9+} Ionen

G. Soff, P. Schlüter, K.-H. Wietschorke, T. de Reus, J. Reinhardt, U. Müller, G. Mehler, B. Müller, W. Greiner
Elektronische Übergangszeiten in überkritischen Compound-Systemen

Ch. Stoller, M. Nessi, W. Wölfli, W.E. Meyerhof, J.D. Molitoris, E. Morenzoni, E. Grosse, Ch. Michel
Die K-Ionisationswahrscheinlichkeit als Uhr für die Reaktionszeit in tiefinelastischen Reaktionen

Osaka, Japan: RCNF International Symposium on Light Ion Reaction Mechanism, 16.05. - 20.05. 1983

R. Shyam, G. Baur, F. Rösel, D. Trautmann
Post Form DWBA Description of Coincidence Spectra in Light Ion Induced Break-Up Reactions

Padua, Italy: Nuclear Physics at Large Tandem Accelerators, 16.03. - 18.03. 1983

J. de Boer, Ch. Lauterbach, Ch. Mittag, F. Riess, Ch. Schandera, Ch. Briancon, A. Lefebvre, C.F. Liang, J.P. Thibaud, R.T. Walen, H. Emling, R.S. Simon, A. Celler, R. Kulessa
Coulomb Excitation of ^{230}Th

Regensburg, Germany: Fruejahrstagung der Deutschen Physikalischen Gesellschaft, 14.03. - 18.03. 1983

H.D. Dohmann, E. Pfeng
Wellenlängenmessung an wasserstoffähnlichem Titan

J. Eberz, G. Huber, G. Ulm, T. Kühl
Druckverbreitung und -verschiebung der (λ=410nm) Indium Linie

W. Groh, A. Müller, A.S. Schlachter, H.F. Beyer, R. Mann, R.E. Olson
Erzeugung hochgeladener Edelgasionen durch Schwerionenstoß

F. Güttner, W. Koenig, N. Lutz, B. Martin, H. Skapa, J. Soltani, H. Banda, A.V. Ramayya, F. Bosch, C. Kozhuharov
Untersuchung innerer Schalen quasiatomarer Systeme (Z_u= 132-171) mittels δ-Electronen Spektroskopie an asymmetrischen Stoßsystemen

F. Güttner, W. Koenig, N. Lutz, B. Martin, H. Skapa, J. Soltani, H. Banda, A.V. Ramayya, F. Bosch, C. Kozhuharov
Einfluß der nuclearen Reaktionszeit auf die δ-Elektronen Spektroskopie, untersucht anhand der Reaktion I→Au, Bi bei 795 and 840 MeV

H. Hartung, W.-D. Sepp, B. Fricke, D. Kolb
Interatomare Potentiale bei mittleren Kernabständen

H. Heinemann, W.-D. Sepp, D. Kolb, B. Fricke
Versuch einer relativistischen Cluster-Rechnung zur Adsorbtion an Metalloberflächen

B. Liu, W. Enders, D. Liesen, R. Schulze
Eigenschaften eines ortsempfindlichen Parallelplattenzählers mit Verzögerungsleitung für energetische, geladene Teilchen

B. Liu, H.D. Dohmann, D. Liesen, A. Warczak
Anregungswahrscheinlichkeit von L- und K-Schalen in Stoßsystemen mit einer Gesamtladung $80 \leq Z \leq 180$

G. Mehler, G. Soff, T. de Reus, U. Müller, J. Reinhardt, P. Schlüter, K.-H. Wietschorke, B. Müller, W. Greiner
δ-Electron-Spectra and K-Hole Production Rates in Heavy Ion Collisions

R. Menges, G. Huber, G. Ulm, T. Kühl
2-Photonenspektroskopie an Rydbergzuständen im Indium I

P.H. Mokler, W.A. Schömfeldt, D. H.H. Hoffmann, Z. Stachura, A. Warczack
Schalendifferentieller Elektroneneinfang in hochgeladenen schweren Ionen bei niedrigen Stoßgeschwindigkeiten

A. Müller, W. Groh, E. Salzborn
Eine statistische Theorie zur Transfer-Ionisation

A. Müller, W. Groh, U. Kneissl, R. Heil, H. Ströher, E. Salzborn
Mehrfachionisation von Edelgasatomen durch relativistische Elektronen

E. Salzborn
Elektroneneinfang in Stößen zwischen hochgeladenen Ionen und Atomen

W. Schulze, D. Kolb
Behandlung zweidimensionaler quantenmechanischer Probleme mit Hilfe Finiter-Elemente-Methode

W. Sengler, D. Kolb, B. Fricke
Lösung der Poissongleichung für zweiatomige molekulare Ladungsverteilungen in elliptisch hyperbolischen Koordinaten

W.-D. Sepp, D. Kolb, H. Hartung, B. Fricke
Gekoppelte Kanäle-Rechnungen mit relativistischen SCF-Matrixelementen

G. Torbohm, B. Fricke, A. Rosen
Rechnungen zum Volumenbeitrag in der Hyperfeinstruktur von Ba I

A. Ulrich, H. Bohn, P. Kienle, G.J. Perlow
Ein mit einem Schwerionenstrahl gepumpter He-Ar-Laser

W. Wahl, D. Habs, R. Kroth, D. Schwalm, H.J. Specht, V. Metag, R.S. Simon
Obere Grenze für den Axionszerfall von Orthopositronium

Riso, Denmark: Workshop on Nuclear Structure at High Spin, 24.05. - 27.05. 1983

R.S. Simon
Limits for the Decay of Positronium in Photon and a Light Neutral Boson

Santa Fe, New Mexico, USA: 1983 Particle Accelerator Conference, 21.03. - 23.03. 1983

N. Angert
Status Report on the Upgraded Unilac

R. Bock
Heavy Ion Fusion

G. Hutter
Comparison of Three 108 MHz Systems for 1.6 MW

J. Klabunde, M. Reiser, A. Schönlein, P. Spädtke, J. Struckmeier
Studies of Heavy Ion Beam Transport in a Magnetic Quadrupole Channel

Savitaipale, Finland: Finish Summer School on Nuclear Spectroscopy, 06.06. -10.06. 1983

H. Emling
Nuclear Moments of High Spin States

Schleching, Germany: Expertentreffen fuer Kernphysik, 02.03. - 11.03. 1983

F. Bosch
Kernphysikalische Aspekte der Schwerionenatomphysik

C. Kozhuharov
Energieverteilung von Positronen, emittiert in (U+U)-Stößen

G. Soff
Einfluß der Elektron-Elektron Wechselwirkung auf Elektronenanregungsprozesse im Stoß schwerer Ionen

Seattle, USA: 185th Annual Meeting of the American Chemical Society, 21.03. - 25.03. 1983

G. Herrmann
Further Attempts to Produce Superheavy Elements by Heavy Ion Reactions

T. Lund, B. Grabez, D. Molzahn, R. Beckmann, R. Brandt, E. Hagebo, I. Haldorsen
The Interaction of Pb with 84 MeV/u ^{12}C-Ions

H. Riedesel
The Plastic Ball, a 4 π Detector for the Investigation of Relativistic Heavy Ion Collisions

H. Wieman
Target Fragmentation with Heavy Ions

Seeheim/Darmstadt, Germany: Workshop on Heavy Particles in Biology and Medicine, 27.06. - 29.06. 1983

E. Blakely
Cellular and Molecular Effects, ^{4}He to ^{40}Ar

L. Hieber, C. Lücke-Huhle
DNA Repair and Genome Amplification in Mammalian Cells During Alpha-Radiation Induced G2 Arrest

K. Koller-Lampert, A. R. Kranz
Heavy Ion Effects on the Survival of Eukaryotic Cells

G. Kraft
Cellular and Molecular Effects A > ^{40}Ar

M. Schäfer
The Action of Heavy Ions on Spores of Bacillus Subtilis

F. Schöpfer, E. Schneider, J. Kiefer, S. Rase
Inactivation of Yeast Cells by Accelerated Heavy Ions

Stony Brook, USA: Conference on Nuclear Physics with Heavy Ions, 14.04. - 16.04. 1983

P. Braun-Munzinger, H. Sohlbach, H. Freiesleben, B. Kohlmeyer, M. Marinescu, F. Pühlhofer, W.F.W. Schneider, D. Schüll
Dynamics of Quasielastic Excitations in the System $^{86}Kr + ^{208}Pb$ at $E_{lab} > 8$ MeV/u

G. Münzenberg, Y.K. Agrarwal, F.P. Heßberger, S. Hofmann, K. Poppensieker, W. Reisdorf, J.R.H. Schneider, W.F.W. Schneider, K.-H. Schmidt, H.-J. Schött, P. Armbruster, C.C. Sahm, D. Vermeulen
New Elements

D. Schwalm
The Role of g-Factors in High Spin State Studies

Tempe, Arizona, USA: VIth International Conference on Ion Beam Analysis, 23.05. - 27.05. 1983

G. Frech, G.K. Wolf, H. Damjantschitsch, M. Weiser, S. Kalbitzer
Defect Trapping of Hydrogen in Iron Studied by the $^{1}H(^{15}N,\alpha\,\gamma)^{12}C$ Reaction

Tilton, New Hampshire, USA: Gordon Conference on Nuclear Physics, 15.08. - 19.08. 1983

R.S. Simon
4π-γ-Ray Spectroscopy - New Perspectives for Nuclear Structure Studies

R. Stock
An Approach toward the Nuclear Matter Equation of State

Uppsala, Schweden: CELSIUS-Workshop, 08.11. 1983

J. Knoll
Subthreshold Pion Production - A Perspective for Celsius

Utrecht, The Netherlands: VIIIth International Seminar on Ion-Atom Collisions, 04.08. - 05.08. 1983

H. Bokemeyer
Positron Production in High Energy Collisions between Heavy Ions

E. Salzborn
Collisions of Highly Charged Ions: Multiple Electron Capture and Ionization: An Introduction

Vilnius, UdSSR: V. Deutsch-sowjetisches Laserseminar, 20.9. - 24.9. 1983

T. Kühl
Laser Spectroscopy of Fusion Products

Washington, USA: 164th Meeting of the Electrochemical Society, 09.10. - 14.10. 1983

G.K. Wolf, J. Dressler, W. Ensinger, A. Meger, Ph. Munn
Effects of Ion Bombardment on the Aqueous Corrosion of Iron Metals and Titanium

Washington, USA: Department of Energy DOE Meeting, 24.01. - 25.01. 1983

R.W. Müller
High-Temperature Target Experiments with Heavy Ion Synchrotons

Angert, N.
Heavy Ion Sources for Accelerators
Institute for Nuclear Study, Tokyo, Japan, 20.09. 1983

Angert, N.
Heavy Ion Source Development at GSI
Peking University, Beijing, People's Rep. China, 23.09. 1983

Angert, N.
The UNILAC, from the Study Group to 20 MeV/u
Peking University, Beijing, People's Rep. China, 23.09. 1983

Armbruster, P.
Über die Herstellung der Elemente 107 und 109
Universität Tübingen, Germany, 02.02. 1983

Armbruster, P.
Reise an die Grenzen nuklearer Stabilität
Universität Saarbrücken, Germany, 19.05. 1983

Armbruster, P.
Les Limitations de Fusion - Production des Elements 107 et 109
Centre de Recherche Nucleaire, Strasbourg, France, 02.06. 1983

Azgui, F.
Etude de Transition de Forme a Haut Moment Angulaire Dans le Noyau ^{154}Dy
University of Nice, France, 05.07. 1983

Azgui, F.
Etude de Transition de Forme a Haut Moment Angulaire
Centre de Recherche Nucleaire, Strasbourg, France, 25.01. 1983

Berdichevsky, D.
Systematische Untersuchung der Ladungs- und Massendichte von Atomkernen
Universität Regensburg, Germany, Feb. 1983

Berdichevsky, D.
Systematic Analysis of Nuclear Charge and Mass Densities
University of Catania, Italy, March 1983

Berdichevsky, D.
Analysis of the Influence of Nuclear Asymmetry and Coulomb Force on the Nuclear Densities
Universita de Barcelona, Spain, March 1983

Berdichevsky, D.
Estudio Systematico de las Densidades Nucleares de Carga y de Mass Atomkernen
Universita de Sevilla, Spain, April 1983

Berdichevsky, D.
Analisis del Efecto Sobre las Densidades Nucleares Producido por la Asimetria Nuclear (Exceso de Neutrones) y la Fuerza de Coulomb
Universita de Sevilla, Spain, April 1983

Berdichevsky, D.
Analysis of the Influence of Nuclear Asymmetry and Coulomb Force on the Nuclear Densities
University of Gent, Belgium, June 1983

Berdichevsky, D.
Nuclear Density: From Finite Nuclei to Infinite Nuclear Matter
University of Bruxelles, Belgium, June 1983

Bock, R.
Inertial Confinement Fusion with Heavy Ion Beams
Universite de Bordeaux, France, 14.10. 1983

Böhne, D.
Supraleitung in Ringbeschleunigern
Universität Frankfurt, Germany, 01.07. 1983

Bosch, F.
Überschwere Quasiatome
Universität Kaiserslautern, Germany, 07.02. 1983

Bosch, F.
Elektronen in überkritischen Feldern
Universität Münster, Germany, 26.05. 1983

Bosch, F.
Innerschalenionisation in überkritischen Feldern
Universität Erlangen, Germany, 04.07. 1983

Brandt, R.
Recent Results from Heavy Ion Research Using Solid State Track Detectors
Peshawar University, Pakistan, 03.03. 1983

Brandt, R.
Recent Results from Heavy Ion Research Using Solid State Track Detectors
Lahore University, Pakistan, 09.03. 1983

Brandt, R.
Recent Results from Heavy Ion Research Using Solid State Track Detectors
Islamabad University, Pakistan, 15.03. 1983

Brandt, R.
Recent Results from Heavy Ion Research Using Solid State Track Detectors
Gomal University, Pakistan, 16.03. 1983

Brandt, R.
Recent Results from Heavy Ion Research Using Solid State Track Detectors
Multan University, Pakistan, 19.03. 1983

Brandt, R.
Recent Results from Heavy Ion Research Using Solid State Track Detectors
PINSTECH, Rawalpindi, Pakistan, 26.03. 1983

Brandt, R.
Search for Superheavy Elements
Universität Marburg, Germany, 22.11. 1983

Cassing, W.
Dissipative Diabatic Dynamics: A Theory for Heavy Ion Collisions between TDHF and Transport Theories
Institut de Physique Nucleaire, Orsay, France, 28.02. 1983

Cassing, W.
Aspects of Diabatic Single-Particle Motion in Nucleus-Nucleus Collisions
Michigan State University, USA, 25.05. 1983

Cassing, W.
Aspects of Diabatic Single-Particle Motion in Nucleus-Nucleus Collisions
University of Rochester, USA, 02.06. 1983

Cassing, W.
Nonequilibrium Light Particle Emission in Nucleus-Nucleus Collisions
Oak Ridge National Laboratory, USA, 09.06. 1983

Cassing, W.
Light Particles and Pions from Heavy-Ion Reactions
University of Maryland, USA, 14.06. 1983

Cassing, W.
Nichtgleichgewichtsprozesse in niederenergetischen Schwerionen
Universität Marburg, Germany, 28.06. 1983

Cassing, W.
Nonequilibrium Aspects of Low Energy Nucleus-Nucleus Collisions
University of Catania, Italy, 14.12. 1983

Dean, D.
Decompositions in Heavy-Ion Scattering
Universität München, Germany, Oct. 1983

Dreizler, R.M.
Relativistic Density Functional Methods
University of Coimbra, Portugal, 10.03. 1983

Emling, H.
Prolate to Oblate Shape Transition in ^{154}Dy
Niels Bohr Institute, Kopenhagen, Denmark, 15.02. 1983

Emling, H.
Rotationsinduzierte Deformationsänderungen in Lanthanidkernen
Universität Gießen, Germany, 09.06. 1983

Freiesleben, H.
N/Z-Equilibration in Heavy-Ion Reactions
Institut Laue-Langevin, Grenoble, France, 02.03. 1983

Fricke, B.
Über den Stand relativistischer Atom- und Molekülstrukturrechnungen
Universität Duisburg, Germany, 24.01. 1983

Fricke, B.
Berechnungen zum elektronischen Faktor in der Isotopieverschiebung
Universität Mainz, Germany, 01.06. 1983

Fricke, B.
Relativistic Calculations of Atomic Structure
University of Lund, Sweden, 19.08. 1983

Gäggeler, H.
Suche nach superschweren Elementen - ein Kapitel moderner Alchemie
Universität Bern, Switzerland, 03.02. 1983

Gäggeler, H.
Neueste Experimente zur Suche nach superschweren Elementen aus der Reaktion von $^{48}Ca + ^{248}Cm$
Hahn-Meitner Institut, Berlin, Germany, 13.06. 1983

Gäggeler, H.
Recent Attemtps to Produce Superheavy Elements by the $^{48}Ca + ^{248}Cm$ Reaction
Centre d'Etude Nucleaire, Saclay, France, 17.06. 1983

Gozdz, A.
Exact Solution for the Landau-Zener Problem
Centre d'Etude Nucleaire Grenoble, France, 28.06. 1983

Gozdz, A.
Non-Adiabatic Effects in Large Amplitude Nuclear Motion
Technische Universität München, Germany, 06.12. 1983

Grosse, E.
Pionenproduktion unter der Schwelle
Universität Mainz, Germany, 01.06. 1983

Grosse, E.
Subthreshold Pion Production in Heavy Ion Collisions
National Laboratory, Brookhaven USA, 14.06. 1983

Grosse, E.
Production of Neutral Pions and High Energy Gamma Rays with Heavy Ions
State University of New York, Stony Brook, USA, 17.06. 1983

Grosse, E.
Emission of Photons and Neutral Pions from Nucleus-Nucleus Collisions
Michigan State University, East Lansing, Cyclotron Laboratory, USA, 27.06. 1983

Grosse, E.
Kollektive Pionenproduktion in Kern-Kern Stößen
Universität Heidelberg, Germany, 28.10.1983

Grosse, E.
Collective Effects in the Emission of Pions from Heavy Ion Collisions
Grand Accelerateur National des Ions Lourds, Caen, France, 09.11. 1983

Grosse, E.
Kollektive Pionenproduktion in Kern-Kern-Stößen
Universität Erlangen, Germany, 21.11. 1983

Grosse, E.
Kollektive Effekte in der Pionenproduktion mit schweren Ionen
Technische Universität und Universität München, Germany, 02.12. 1983

Grosse, E.
Kollektive Effekte in der Pionenproduktion aus Kern-Kern-Stößen
Technische Hochschule Darmstadt, Germany, 07.12.1983

Gustafsson, H.A.
A Search for Short-Lived Anomalons in Projectile Fragmentation
Lawrence Berkeley Laboratory, USA, 15.03. 1983

Herrmann, G.
Versuche zur Synthese superschwerer Elemente
Technische Hochschule Darmstadt, Germany, 20.05. 1983

Herrmann, G.
Versuche zur Synthese superschwerer Elemente
Universität Frankfurt, Germany, 20.10. 1983

Heßberger, F.P.
Fusion schwerer Ionen
Technische Hochschule Darmstadt, Germany, 07.07. 1983

Hildenbrand, K.D.
Reaktionen mit 84 MeV/u ^{12}C am Synchrocyclotron des CERN
Technische Hochschule Darmstadt, Germany, 06.01. 1983

Hildenbrand, K.D.
2- und 3-Körperzerfälle im Schwerionenstoß bei 12-15 MeV/u
Universität Mainz, Germany, 13.07. 1983

Hildenbrand, K.D.
Recent Developments of Heavy Ion Detectors at GSI
Institute of Modern Physics, Lanzhou, Peoples Rep. China, 07.09. 1983

Hildenbrand, K.D.
Dissipative Collisions at High Incident Energies
Institute of Modern Physics, Lanzhou, Peoples Rep. China, 09.09. 1983

Hildenbrand, K.D.
Reactions Induced with ^{12}C at 83 MeV/u
Institute of Modern Physics, Lanzhou, Peoples Rep. China, 09.09. 1983

Hoffmann, D.H.H.
Experiments with Highly Charged Decelerated Heavy Ions
Stanford University, USA, Nov. 1983

Keller, R.
Brillanz von Hochstrom-Ionenquellen
Universität Frankfurt, Germany, 14.01. 1983

Keller, R.
Fasci Ionici e Cannoni d'Ioni
Universita della Calabria, Cosenza, Italy, 27.06. 1983

Keller, R.
Ion Source Development at GSI
University of Nagoya, Japan, 16.09. 1983

Keller, R.
GSI Development of HIF Sources and Low Energy Beam Transport
University of Tokyo, Japan, 20.09. 1983

Kienle, P.
Positronenerzeugung in Schwerionenstößen
Universität Heidelberg, Germany, 21.01. 1983

Kienle, P.
Strukturen in Positronenspektren in Stößen überkritischer Systeme
Universität Regensburg, Germany, 14.03. 1983

Kleber, M.
Zur Wechselwirkung von Dirac Monopolen mit Materie
Universität Erlangen, Germany, 14.07. 1983

Kleber, M.
Dynamische Optimierung von Stoßproblemen
Max-Planck Institut für Quantenoptik, München, Germany, 25.07. 1983

Klepper, O.
Spectroscopy of Very Neutron-Deficient Nuclei Close to ^{100}Sn
University of Manchester, Great Britain, 01.12. 1983

Knoll, J.
Cooperative Mechanisms in Energetic Nuclear Reactions
Centre National de la Recherche Scientifique Straßburg, France, 03.02. 1983

Knoll, J.
Subthreshold in Pion Production - A Cooperative Process?
Niels Bohr Institute Kopenhagen, Denmark, 09.05. 1983

Knoll, J.
Strings in Ultra-Relativistic Nucleus-Nucleus Collisions
Central Institute for Nuclear Research Budapest, Hungary, 15.06. 1983

Knoll, J.
Subthreshold in Pion Production - A Cooperative Mechanism?
Grand Accelerateur National des Ions Lourds, Caen, France, 20.10. 1983

Knoll, J.
Expansions- und Aufbruchphase energetischer Schwerionenreaktionen
Technische Hochschule Darmstadt, Germany, 08.12. 1983

Knoll, J.
Die Expansionsphase energetischer Schwerionenreaktionen - ein Problem dynamischer Instabilitäten
Universität und Technische Universität München, Germany, 13.12. 1983

Knoll, J.
Die Pionenproduktion unterhalb der Schwelle
Technische Universität München, Germany, 13.12. 1983

Körner, H.-J.
Kernreaktionen mit sehr schweren Ionen
Universität Gießen, Germany, 09.05. 1983

Körner, H.-J.
Experimente zum Studium der Physik hoch beschleunigter schwerer Ionen am UNILAC Beschleuniger der Gesellschaft für Schwerionenforschung (GSI) in Darmstadt
Akademie für Lehrerfortbildung, Dillingen, Germany, 22.10. 1983

Körner, H.-J.
Der UNILAC-Beschleuniger in Darmstadt als Werkzeug für physikalische Spitzenforschung in Deutschland
Hochschule der Bundeswehr, Neubiberg, Germany, 01.12. 1983

Kraft, G.
Anwendung schwerer Ionen in der Strahlentherapie
Deutsches Krebsforschungszentrum, Heidelberg, Germany, 16.02. 1983

Kraft, G.
Strahlenqualität und biologische Wirksamkeit
Deutsche Forschungs- und Versuchsanstalt für Luft- und Raumfahrt, Köln, Germany, 24.02. 1983

Kraft, G.
Anwendung von schweren Ionen in Biologie und Medizin
Universität des Saarlandes, Homburg, Germany, 09.04. 1983

Kraft, G.
What Do We Learn from Radiobiology Experiments with Very Heavy Ions?
Lawrence Berkeley Laboratory, USA, 14.11. 1983

Kraft, G.
Radiation Effects with Very Heavy Ions
British Columbia Cancer Foundation, Vancouver, Canada, 02.12. 1983

Kroth, R.
Untersuchung von doppelten Gamma-Zerfällen mit der Kristallkugel
Universität Bonn, Germany, 10.11. 1983

Kroth, R.
La Double Emission Gamma et d'autres Experiences a la Boule de Cristal de Darmstadt-Heidelberg
Universität Bordeaux, France, 25.11. 1983

Kühl, T.
Laserspektroskopie an Fusionsprodukten
Technische Hochschule Darmstadt, Germany, 24.11. 1983

Liesen, D.
Atomare Stöße bei Energien von meV bis MeV -Ähnlichkeiten und Unterschiede
Universität Heidelberg, Germany, 30.05. 1983

Loehner, H.
Analysis of Plastic Ball 4 π Events for Relativistic Heavy Ion Reactions
Accelerator Laboratory for Nuclear Physics, Groningen, The Netherlands, 12.07. 1983

Ludewigt, B.
Nuclear Stopping and Thermalization
Lawrence Berkeley Laboratory, USA, 17.05. 1983

Mann, R.
Spektroskopie mit und an langsamen hochgeladenen Rückstoßionen
Universität Mainz, Germany, 13.07. 1983

Michel, Ch.
Production de π^0 en-dessous du Seuil Lors de Collisions d'Ions Lourds
Institute de Physique Corpusculaire, Louvain-la-Neuve, Belgium, 17.05. 1983

Michel, Ch.
Nouveau Concept en Spectrometrie Anti-Compton
Institute de Physique Corpusculaire, Louvain-la-Neuve, Belgium, 18.05. 1983

Michel, Ch.
Design of Compton Suppression Spectrometers by Monte Carlo Methods
Max-Planck-Institut, Heidelberg, Germany, 12.07. 1983

Michel, Ch.
Design of Compton Suppression Spectrometers by Monte Carlo Methods
Vrye Universiteit, Amsterdam, The Netherlands, 07.09. 1983

Michel, Ch.
Design of Compton Suppression Spectrometers by Monte Carlo Methods
Centre de Spectrometrie Nucleaire et de Spectroscopie de Masse, Orsay, France, 03.10. 1983

Mokler, P.H.
Superheavy Quasiatoms
University of Oxford, Great Britain, 07.03. 1983

Mokler, P.H.
Ladungszustandsabhängigkeit der Röntgenemission bei Schwerion-Atom- Stößen
Universität Mainz, Germany, 01.06. 1983

Mokler, P.H.
Heavy and Superheavy Atomic Collision Systems
Ioffe Institute, Leningrad, USSR, 10.06. 1983

Mokler, P.H.
Heavy and Superheavy Atomic Collision Systems
University of Leningrad, USSR, 13.06. 1983

Mokler, P.H.
Heavy and Superheavy Atomic Collision Systems
Arifov Institute, Tashkent, USSR, 16.06. 1983

Mokler, P.H.
Charge State Dependence of X-Ray Emission in Heavy Atomic Collision Systems
Joint Institute of Nuclear Research, Dubna, USSR, 21.06. 1983

Molzahn, D.
Experiments with 86 MeV/u ^{12}C-Ions at CERN
Brookhaven National Laboratory, Long Island, USA, 11. 03. 1983

Mosel, U.
Test of Collective Current Distributions in Transverse ELectron Scattering
Argonne National Laboratory, USA, March 1983

Mosel, U.
How do Nuclei Really Rotate or Vibrate?
National Institute for Nuclear and Accelerator Physics, Amsterdam, The Netherlands, May 1983

Mosel, U.
How do Nuclei Really Rotate or Vibrate?
Accelerator Laboratory for Nuclear Physics, Groningen, The Netherlands, May 1983

Mosel, U.
Wie rotieren und vibrieren die Atomkerne wirklich?
Universität Göttingen, Germany, June 1983

Mosel, U.
Pion Production in Heavy Ion Collisions
State University of New York, Stony Brook, USA, Aug. 1983

Mosel, U.
Wie rotieren und vibrieren die Atomkerne? Test von Stromverteilungen in transversaler Elektronenstreuung
Universität Tübingen, Germany, Nov. 1983

Mühlhans, K.
State-Dependent Pairing in Cranked HFB Calculations
Daresbury Laboratory, Oct. 1983

Müller, A.
Electron Impact Ionization of Multiply Charged Ions
Institute for Atomic and Molecular Physics, Amsterdam, The Netherlands, 07.11. 1983

Müller, A.
Transfer Ionization in Collisions of Multiply Charged Ions with Atoms
Rijksuniversiteit Utrecht, The Netherlands, 08.11. 1983

Müller, A.
Multiple Ionization Processes in Collisions Involving Multiply Charged Ions
Universite Louvain le Neuve, Belgium, 08.12. 1983

Müller, R.W.
Schwerionen-Trägheitseinschluß: Schnelle Ionen zur Zündung des Fusionsreaktors
Physikalischer Verein Frankfurt, Germany, 19.10. 1983

Münzenberg, G.
Heaviest Elements at SHIP
Institut Nationale de Physique Nucleaire et de Physique des Particules, Orsay, France, 31.01. 1983

Münzenberg, G.
Investigation of the Heaviest Elements at SHIP
Grand Accelerateur National des Ions Lourds, Caen, France, 01.02. 1983

Münzenberg, G.
Nachweis der schwersten Elemente am SHIP
Technische Universität München, Germany, 10.06. 1983

Münzenberg, G.
Nachweis der schwersten Elemente am SHIP
Universität Hamburg, Germany, 16.06. 1983

Münzenberg, G.
Das Geschwindigkeitsfilter SHIP, ein Instrument zum Nachweis der schwersten Kerne
Universität Gießen, Germany, 01.11. 1983

Münzenberg, G.
SHIP and the Investigation of Exotic Nuclei from Heavy Ion Fusion
Instituto Nationale de Fisica Nucleare, Padua, Italy, 12.12. 1983

Nörenberg, W.
Zusammenwirken kohärenter und inkohärenter Prozesse in Schwerionenreaktionen
Hahn-Meitner Institut Berlin, Germany, 31.01. 1983

Nörenberg, W.
Gibt es Riesenresonanzschwingungen großer Amplitude in Kern-Kern-Stößen?
Technische Hochschule Darmstadt, Germany, 28.03. 1983

Nörenberg, W.
Gibt es Riesenresonanzschwingungen großer Amplitude in Kern-Kern-Stößen?
Universität Marburg, Germany, 26.05. 1983

Nörenberg, W.
Dissipative Diabatic Dynamics
University of Milano, Italy, 03.10. 1983

Nörenberg, W.
Elasto-Plastic Behaviour of Nuclear Matter in Nucleus-Nucleus Collisions
University of Florence, Italy, 11.10. 1983

Nörenberg, W.
Large-Amplitude Giant Motion in Nucleus-Nucleus Collisions
Laboratori Nazionali Legnaro, Padua, Italy, 14.10. 1983

Nörenberg, W.
Elastoplastisches Verhalten von Atomkernen
Technische Hochschule Darmstadt, Germany, 24.10. 1983

Nörenberg, W.
Elastoplastic Behaviour of Nuclei
Universität Heidelberg, Germany, 19.12. 1983

zu Putlitz, G.
Atomic Physics
Krakow, Poland, 23.02. 1983

zu Putlitz, G.
Experiments with Heavy Ions at GSI, Darmstadt
Krakow, Poland, 24.02. 1983

zu Putlitz, G.
Experiments with Heavy Ions at GSI, Darmstadt
Warzawa, Poland, 25.02. 1983

zu Putlitz, G.
Accelerators for Nuclear Physics
Kopenhagen, Denmark, 21.03. 1983

zu Putlitz, G.
New Insights in the Physics of Nuclear Matter
San Remo, Italy, 05.05. 1983

zu Putlitz, G.
Großforschung und Hochschulen
Darmstadt, Germany, 09.05. 1983

zu Putlitz, G.
Experimente mit schweren Ionen bei der GSI in Darmstadt
Berlin, Germany, 19.05. 1983

Richter, M.
Future Plans for Data Acquisition at GSI
National Laboratory Argonne, Illinois, USA, 06.05. 1983

Richter, M.
A General Purpose Nuclear Data Acquisition System Based on an Auxiliary Crate Controller
Lawrence Berkeley Laboratory, USA, 17.05. 1983

Ritter, H.G.
New Results from the Plastic Ball
Lawrence Berkeley Laboratory, USA, 23.05. 1983

Ritter, H.G.
Nuclear Matter at High Temperature and High Density
Lawrence Berkeley Laboratory, USA, 16.11. 1983

Roeckl, E.
Untersuchung exotischer Kerne am GSI On-Line-Massenseparator
Universität Bonn, Germany, 10.02. 1983

Salzborn, E.
Experimente mit niederenergetischen, mehrfach geladenen Ionen
Kernforschungszentrum Karlsruhe, Germany, 22.02. 1983

Salzborn, E.
Elektroneneinfang in Stößen zwischen hochgeladenen Ionen und Atomen
Universität Kaiserslautern, Germany, 19.05. 1983

Salzborn, E.
Transfer-Ionisation in Stößen zwischen hochgeladenen Ionen und Atomen
Universität Bielefeld, Germany, 24.06. 1983

Salzborn, E.
Ladungsaustausch bei Stößen zwischen hochgeladenen Ionen und Atomen
Universität Münster, Germany, 27.06. 1983

Salzborn, E.
Neuere Ergebnisse zur Ionisation von Ionen durch Elektronenstoß
Max-Planck Institut für Plasmaphysik,
Garching/München, Germany, 21.09. 1983

Salzborn, E.
Experiments with Multiply Charged Ions: Transfer-Ionization and Electron Impact Ionization
Oak Ridge National Laboratory, USA, 17.11. 1983

Salzborn, E.
Transfer-Ionization in Multicharged Ion-Atom Collisions
University of Missouri, Rolla, USA, 22.11. 1983

Salzborn, E.
Transfer-Ionization in Multicharged Ion-Atom Collisions
Kansas State University, Manhattan, USA, 25.11. 1983

Salzborn, E.
Single and Multiple Ionization of Multiply Charged Ions by Electron Impact
Joint Institute for Laboratory Astrophysics, University of Colorado, Boulder, USA, 29.11. 1983

Salzborn, E.
Transfer-Ionization in Multicharged Ion-Atom Collisions
Lawrence Berkeley Laboratory, USA, 01.12. 1983

Salzborn, E.
Experimente mit niederenergetischen hochgeladenen Ionen
Universität Bonn, Germany, 13.12. 1983

Schädel, M.
Kernreaktionen mit ^{254}Es als Target: Ergebnisse und Zukunftsaussichten
Universität Mainz, Germany, 26.01. 1983

Schardt, D.
Kerne nahe und jenseits der Proton-Drip-Line im Gebiet der Seltenen Erden
Technische Universität München, Germany, 06.07. 1983

Schwalm. D.
Zur Struktur schnell rotierender Atomkerne
Universität Basel, Switzerland, 11.02. 1983

Schwalm, D.
On the Measurement of Rare γ-decay Modes With the Heidelberg-Darmstadt Crystal Ball Spectrometer
National Laboratory, Brookhaven, USA, 06.04. 1983

Schwalm, D.
The Structure of Fast Rotating Nuclei
National Laboratory, Brookhaven, USA, 12.04. 1983

Schwalm, D.
Neue Möglichkeiten der γ-Spektroskopie mit dem Kristallkugelspektrometer
Kernforschungsanlage Jülich, Germany, 11.07. 1983

Shyam, R.
Subthreshold Pion Production in Nuclear Collisions
University of Tokyo, Japan, 23.05. 1983

Shyam, R.
Subthreshold Pion Production in Nucleus-Nucleus Collisions
Kernforschungsanlage Jülich, Germany, 17.11. 1983

Shyam, R.
Subthreshold Pion Production in Heavy-Ion Collision - A Collective Phenomenon?
University of Lund, Sweden, 29.11. 1983

Shyam, R.
Projectile Break-Up Reactions in Nucleus-Nucleus Collisions
University of Connecticut, USA, 06.07. 1983

Siegert, G.
Utilisation des Ions Lourds dans la Recherche Appliquee
Grand Accelerateur National des Ions Lourds, Caen, France, 17. 05. 1983

Siegert, G.
Applications des Ions Lourds
Centre d'Etude Nucleaire, Saclay, France, 19. 05. 1983

Simon, R.S.
Untersuchung der hochenergetischen γ Komponente im Riesenresonanzbereich nach Fusionsreaktionen
Hahn-Meitner-Institut, Berlin, Germany, 07.03. 1983

Simon, R.S.
The High Energy Component in the γ Decay Following Compound Nucleus Reactions
Niels-Bohr-Institut, Kopenhagen, Denmark, 14.03. 1983

Simon, R.S.
Double γ Decay of ^{90}Zr
University of Pittsburgh, USA, 24.08. 1983

Soff, G.
Neue Phänomene der Atomphysik in superschweren Systemen
Universität Basel, Switzerland, 10.02. 1983

Soff, G.
Atomgewicht 500 - Nachweis durch spontane Positronen
Universität Münster, Germany, 25.04. 1983

Soff, G.
Fourieranalyse
Fachhochschule Würzburg, Germany, 22.07. 1983

Soff, G.
Atomgewicht 500 - Science Fiction oder Realität?
Fachhochschule Würzburg, Germany, 22.07. 1983

Spreng, W.
Backbending in ^{242}Pu and ^{244}Pu
Technische Hochschule Darmstadt, Germany, 17.02.1983

Stock, R.
Kompression von Kernmaterie
Universität Bonn, Germany, April 1983

Stock, R.
Kernmaterie bei hoher Dichte und Temperatur
Technische Universität München, Germany, June 1983

Stock, R.
Die Zustandsgleichung von Kernmaterie
Universität Erlangen, Germany, June 1983

Stock, R.
Kernmaterie bei hoher Dichte
Hahn-Meitner Institut, Berlin, Germany, Nov. 1983

Stock, R.
Verdichtung von Kernmaterie
Max-Planck Institut Heidelberg, Germany, Dec. 1983

Tanimura, O.
Exact One- and Two-Step Distorted-Wave Born Methods
Hahn-Meitner Institut Berlin, Germany, May 1983

Trautmann, N.
Suche nach superschweren Elementen in Schwerionenreaktionen
Universität Bonn, Germany, 30.06. 1983

Westmeier, W.
Hochauflösende Alpha-Spektrometrie
Physikalisch-Technische Bundesanstalt Braunschweig, Germany, 12.12. 1983

Wieman, H.
Two Particle Correlations
Lawrence Berkeley Laboratory, USA, 17.05. 1983

Wüst, E.
Neue Aspekte kollektiver Ströme
Universität Mainz, Germany, Jan. 1983

Wüst, E.
Transverse Formfactors for Inelastic e-Scattering in the Cranking Collective Model
University St. Andrews, Sept. 1983

Yannouleas, C.
Nuclear Dissipation as Damping of Collective Motion in the Time-Dependent RPA and Extensions of It
Institut Laue-Langevin, Grenoble, France, 12.01. 1983

Yannouleas, C.
The RPA Description of Nuclear Friction
Nuclear Research Center "Democritos", Athens, Greece, 24.05. 1983

Yannouleas, C.
The RPA Description of the Quantum Damped Harmonic Oscillator
University of Crete, Greece, 19.10. 1983

Yannouleas, C.
On Nuclear Dissipation
University of Thessaloniki, Greece, 27.10. 1983

Yannouleas, C.
On Nuclear Dissipation
Institut des Sciences Nucleaires, Grenoble, France, 15.11. 1983

7.1.4 Lectures and Courses

F. Beck, W. Nörenberg, H. Feldmeier, J. Knoll	Theoretical Heavy Ion Workshop (GSI Darmstadt)
H. Bokemeyer	Methoden und Ergebnisse der Schwerionenforschung III und IV (Universität Frankfurt)
S. Glückert	Programmierung mathematisch-technischer Probleme (FH Darmstadt)
S. Glückert	Rechnerarchitektur (FH Darmstadt)
G. Herrmann	Chemie der schwersten Elemente (Universität Mainz)
G. Herrmann	Chemische Aspekte der Kerntechnik (Universität Mainz)
G. Herrmann	Kernchemisches Praktikum I und II (Universität Mainz)
P.O. Hess	Nuclear Collective Models (Universite de Neuchatel)
E. Kankeleit E. Roeckl	Seminar über Nuklearwaffen (TH Darmstadt)
J. Klabunde	Grundlegende Kapitel der Physik (FH Darmstadt)
H.-J. Kluge E. Roeckl	Seminar über Meßmethoden und Modelle für Kernmassen (Universität Mainz)
H.-J. Kluge E. Roeckl	Kerneigenschaften aus Hyperfeinwechselwirkung (Universität Mainz)
H.-J. Kluge E. Roeckl	Seminar über Kerneigenschaften aus Hyperfeinwechselwirkung (Universität Mainz)
D. Liesen	Physikalisches Praktikum für Informatiker (FH Darmstadt)
P.H. Mokler	Übungen zur Physik I und II (TH Darmstadt)
W. Nörenberg	Einführung in die Theorie der Kernreaktionen I und II (TH Darmstadt)
E. Roeckl	Entwicklungsstand und Probleme der Wiederaufarbeitung von Kernbrennstoffen (Universität Mainz)
G. Soff	Allgemeine Relativitätstheorie (Universität Frankfurt)
G. Soff	Kosmologische Modelle (Universität Frankfurt)
R. Stock, J. Knoll	Seminar über Hochenergie Kernreaktionen (GSI Darmstadt)
K. Winkelmann	FORTRAN für Fortgeschrittene (FH Darmstadt)
K. Winkelmann	Rechnerarchitektur (FH Darmstadt)

7.2.1 Conferences and Seminars on Research Proposals

12.01. 1983	Research Seminar Positron Creation, Superheavy Elements
10.03. 1983	Research Seminar Atomic and Nuclear Physics, Data Processing
18.05. 1983	Research Seminar Nuclear Physics, Biology, Nuclear Track Technology, Detectors and Targets
30.05.-03.06. 1983	Workshop on Developments of the Cascade Model
13.06.-16.06. 1983	Introduction to Heavy Ion Research for High School Students and Teachers
27.06.-29.06. 1983	Heavy Particles In Biology and Medicine
05.07.-06.07. 1983	Workshop on Spallation Neutron Sources
15.08.-07.10. 1983	Introduction to Heavy Ion Research for Students
24.08. 1983	Research Seminar Nuclear and Atomic Physics, Computing Center
12.10. 1983	Research Seminar Nuclear Physics, Nuclear Track Technology
14.12. 1983	Research Seminar Nuclear Physics, Ion-Sources, off-line Mass-Separator

11.01.	J.Hüfner Heidelberg	Cleavage: Schnelle Fragmentierung von Kernen in Hochenergiereaktionen
11.01.	E.L. Alpen Berkeley	The Berkeley Heavy Ion Radiotherapy Program and a Dedicated Medical Accelerator
12.01.	N. Frascaria Orsay	Are Giant Resonances Excited in Heavy Ion Collisions?
18.01.	H.Gerischer Berlin	Photoelektrochemische Energieumwandlung
19.01.	R. Mann Darmstadt	Experiment mit langsamen Rückstoßionen
25.01.	J. Rafelski Frankfurt	Schmelzen des Vakuums in der Schwerionenreaktion
25.01.	C. Hardy Chalk River	Superallowed Beta Decay: Weak Interaction Studies at High Precision
26.01.	H.Spangenberg Darmstadt	Quantenmechanische Beugungsphänomene in dissipativen Schwerionenreaktionen
31.01.	H. Schulz Rossendorf	Properties of Hot Nuclear Matter
01.02.	Dr. Heinrich Siegen	Status der Anomalonen
02.02.	F.May Rossendorf	Einführung in die Theorie der Kernrotationen
02.02.	H. Noll Darmstadt	Produktion von neutralen Pionen in Schwerionenstößen unter 100 MeV/u
04.02.	F. May Rossendorf	Einführung in die Theorie der Kernrotationen
08.02.	D. Vasak Frankfurt/M	Pionenerzeugung als Bremsstrahlung in Hochenergiereaktionen schwerer Ionen
08.02.	H.v.d. Schmidt Bonn	Leistungsfähige Experimentrechner für universelle Anwendungen auf der Basis von MC68K'
08.02.	G. Bertsch East Lansing	Motion in Fermi Systems
09.02.	F. May Rossendorf	Einführung in die Theorie Kernrotation
09.02.	J. Toke Darmstadt	On the Random-Walk Description of the Evolution of the Dinuclear Complex in the N-Z Plane
11.02.	F. May Rossendorf	Einführung in die Theorie der Kernrotation
16.02.	F. May Rossendorf	Einführung in die Theorie der Kernrotation
16.02.	J. Friedrich Mainz	Bestimmung der Skyrme-Parameter aus einer systematischen Analyse von Kernladungsverteilungen und Bindungsenergien
16.02.	W. Reisdorf Darmstadt	Fusion an der Barriere
18.02.	F. May Rossendorf	Einführung in die Theorie der Kernrotation
23.02.	F. May Rossendorf	Einführung in die Theorie der Kernrotation
23.02.	F. May Rossendorf	Rotierende Quasiteilchen - eine Sonde für Formfreiheitsgrade des Atomkerns
25.02.	F. May Rossendorf	Einführung in die Theorie der Kernrotation
02.03.	J. Gerl Frankfurt	Neuere Untersuchungen zur Struktur von Aktinidenkernen mit Hilfe der Coulombanregung
09.03.	G. Huber Mainz	On-line Laserspektroskopie bei GSI
16.03.	P. Fröbrich Berlin	Deep-Inelastic Collisions and Fusion of Heavy Ions Within a Surface-Friction Model
16.03.	Ch. Schandera München	Messung der γ-Zirkularpolaristion in Kr-induzierten Reaktionen
12.04.	D. Drechsel Mainz	Mittelenergiephysik mit elektromagnetischer Wechselwirkung.
13.04.	S. Gralla Darmstadt	Reaktionsmechanismen im System ^{92}Mo + ^{92}Mo bei 15 MeV/u Einschußenergie
19.04.	D. Dubbers Heidelberg	Der β-Zerfall freier Neutronen
20.04.	J.P. Theobald Darmstdt	Teilchenemission bei Spaltung und bei Schwerionenstößen
21.04.	K. Kajantie Helsinki	Hydrodynamics of Ultrarelativistic Nucleus-Nucleus Collisions
26.04.	I.I. Rabi New York	Physics at Mid Century
26.04.	T. Biro Budapest	Analytical Hadrochemistry
27.04.	Ch. Töpffer Erlangen	Relaxation in der Fermi-Flüssigkeit
27.04.	J. Blomquist Stockholm	Collective Gamov Teller Decays of ^{56}Ni, ^{100}Sn and ^{164}Pb
03.05.	H. Feshbach East Lansing	Statistical Theory of Multi-Step Nuclear Reactions
03.05.	W. Reisdorf Darmstadt	Fusion: Ueberschüsse und Defizite
04.05.	T. Biro Budapest	A Continuous Neutral Net Model of Dynamical Structure Formation in the Brain
04.05.	B. Fischer Darmstadt	Schwerionen-Mikroskopie: Wie und Warum?
10.05.	W.D. Schmidt-Ott Göttingen	Spektroskopie aus neutronenreichen Kernen aus Transferreaktionen
11.05.	R.W.Müller Darmstadt	Hochstrombetrieb im Schwerionen-Synchrotron und ein Hochtemperatur-Target Experiment
16.05.	J.M. Nitschke Berkeley	Bericht über den Berkeley On-Line Isotopentrenner OASIS
17.05.	D. Möhl Geneva	Der CERN Niederenergie-Antiprotonenring LEAR
17.05.	C. Detraz Caen	Recent Research on the Properties of Some Light Neutron Rich Nuclei
18.05.	J.Keller Darmstadt	Experimenteller Nachweis der Strahleneinfangsreaktionen ^{90}Zr + ^{90}Zr → ^{180}Hg+xγ

18.05.	H.Feldmeier Heidelberg	The Maximum-Entropy Concept for not Equilibrized Systems
24.05.	R. Lucas Caen	Neutron-Proton Equilibration in Damped Heavy-Ions-Collisions
25.05.	E. Blakeley Darmstadt	Recent Radiobiological Experiments at the Bevalac/LBL
25.05.	S.J. Wang Darmstadt	Equations for the Time-Dependent Many-Body Correlation in the Density Matrix Hierarchy
31.05.	M. Gyulassy Berkeley	Formation of the Quark-Gluon Plasma above 5 Gev/u
01.06.	D.S. Aberg Lund	Deformation Changes in Rotating Nuclei
07.06.	S.M. Polikanov Darmstadt	Muon-Induced Fission
14.06.	Glendening Berkeley	Evaporation from a Quark-Gluon Plasma by Fission of Chromelectric Flux Tubes
14.06.	J. Rafelski Geneva	Das Quark-Gluon Plasma und seine Beobachtung
15.06.	Y. Penionzhkevich K.D. Schilling Dubna	Experimentelle Untersuchungen zur niederenergetischen Spaltung sowie zur Emission hochenergetischer leichter Teilchen in Schwerionenreaktionen im JINR Dubna
15.06.	K. Blasche Darmstadt	Hochenergiebeschleuniger für schwere Ionen
21.06.	E.Recknagel Konstanz	Physik isolierter Mikrocluster
28.06.	K.-P. Streit Geneva	Baryonen mit Charm
29.06.	D. Berdichevsky Giessen	Analysis of the Influence of Nuclear Asymmetry and Coulomb Force on the Nuclear Densities
12.07.	R.Gyufko Heidelberg	Bestimmung des Masseexzesses und der Protonenseparation in 147 Tb
03.08.	J. Wood Atlanta/USA	Shape Coexistence and Nuclei in the Region of Closed Shells
10.08.	G. Kraft Darmstadt	Biologie-Experimente am Unilac
17.08.	D. Sperber Troy	Fast Particle Emission or Pre-Equilibrium Processes in Heavy-Ion Reactions
24.08.	C. Yannouleas Darmstadt	The RPA Description of the Quantum Damped Harmonic Oscillator
31.08.	R. Stock Darmstadt	Die geplanten Schwerionenexperimente am SPS/CERN
06.09.	S. Nagamiya Tokyo	Probing Short-Range Properties in Proton-Nucleus and Nucleus-Nucleus Collisions
07.09.	S. Polikanov Darmstadt	Search for Superheavy Relics
13.09.	H.J. Lustig Darmstadt	Erfahrungen m. dem FPS 164
14.09.	S. Kubono INS Tokyo	High Spin States in ^{28}Si and ^{32}S via (HI, $\alpha\alpha$) Reactions
14.09.	M. Jezabek Crakow	Estimate of Energy-Density in Central Heavy-Ion Collisions at Ultra Relativistic Energies
15.09.	V.D. Glogor Maryland	Real Time Programming Languages
21.09.	Chr. Toeppfer Erlangen	Viskoelastizität von Fermi-Flüssigkeiten
21.09.	R.Wada Darmstadt	Alpha Emission from Nucleus-Nucleus Collisions
23.09.	L.P. Presnyakov Moskau	Charge Exchange and Ionisation in Ion-Atomic Collisions
28.09.	W. Cassing C. Yannouleas Darmstadt	Report on Florence Meeting
28.09.	T.L.Khoo Argonne	Suppression of Neutron Emission After Heavy Fusion; is Shape Relaxation Affected by a Superdeformed Minimum?
05.10.	K. Rykaczewski Warsaw	Investigation of Very Neutron-Rich Isotopes Produced in Multi-Nucleon Tranfer Reactions
11.10.	I.Giese Darmstadt	Graphische Normung (GKS, GSPC)
13.10.	U. Lynen Frankfurt	Ultra-Relativistic Nucleus-Nucleus-Collisions
18.10.	J. Sager Frankfurt	Installationserfahrungen mit XA
18.10.	I. Hofmann Darmstadt	Erzeugung von Hochintensitätspulsen f. d. Schwerionen-Trägheitsfusion mit Elektronenkühlung
19.10.	Dr. Blümel Munich	Pion Condensates in Finite Nuclei
19.10.	M. Kreck Mainz	Über ein mathematisches Modell zur Berechnung des Vernichtungspotentionals von Atomraketen
25.10.	F. Goldhammer	IGL Interactive Graphic Library
25.10.	K.H. Schindl Geneva	Der CERN-PS-Komplex, eine Vielteichenquelle
26.10.	H. Reinhardt Dresden	Geometrical Approach to Dissipation in the Time Evolution of Many Body System
26.10.	Ch. Michel Darmstadt	Simulation of γ-Detectors in the 50 keV-GeV Energy Range and their Use in Low and Intermediate Energy Heavy-Ion Physics
27.10.	B. Franzke Darmstadt	SITAR-Experimentierring
01.11.	J. Ellis Geneva	Cosmological Relics from Unified Theories
02.11.	R. Shyam Darmstadt	Subthreshold Pion Production in Nucleus-Nucleus Collisions
02.11.	A.G. Demin Dubna	Last Results of Experiments on Synthesis of Transfermium Nuclei in Dubna
03.11.	H. Eickhoff Darmstadt	T A R N

08.11.	W. Kynast Darmstadt	Neues vom GNOM
08.11.	B. Fischer Darmstadt	Das Schwerionenraster-mikroskop der GSI Ergebnisse u. Perspektiven
09.11.	Z. Sujkowski Groningen	K-Ionization of (HI, xn) Reaction Residues
10.11.	R. Arnold Garching	Charge Changing Ionic Collisions as a Method for Increasing Specific Deposition Energy in HIF Drivers
15.11.	R. Broglia Copenhagn	Subbarier Fusion Reactions
17.11.	R.W. Müller Darmstadt	Status RFQ
22.11.	J. Cugon Liege	K^+ Production and the Hot Phase of High Energy Heavy-Ion Reactions
22.11.	Th. Walcher Geneva	Hyperkerne und Kernkräfte
23.11.	B. Giraud Geneva	Time-Independent Wave Packet Theory of Collisions
23.11.	K.J. Moody Berkeley	Actinide Production in the Reaction of Heavy-Ions with ^{248}Cm
24.11.	J. Meyer-ter-Vehn Garching	Zylindrische Target-implosion mit Schwerionen-strahlen
29.11.	I. Derado Garching	Investigation of Proton- and Antiproton Interactions with nuclei at 200 Gev/c
30.11.	J. Knoll Darmstadt	Bericht von der Brookhaven Konferenz (Teil II).
01.12.	K. Blasche Darmstadt	Synchrotron Resonanzen
06.12.	E. Nolte Munich	Schwerionenexperimente am Münchener Nachbeschleuniger
07.12.	H. Feldmeier Heidelberg	Drift und Fluktuationen der Masse und des Relativ-impulses bei Kern-Kern Stößen
07.12.	J. Knoll Darmstadt	The Expansion and Disassembly Phase of Energetic Heavy-Ion Reactions: A Problem of Dynamical Instabilities
14.12.	W. Nazarewicz Lund	Stable Octupole Nuclear Deformation and Possible Rotational Consequences
14.12.	H. Wollnik Gießen	Ionenoptische Rechnungen zur Endfokussierung
20.12.	V. Metag Gießen	Physik mit der Darmstadt-Heidelberger Kristallkugel
21.12.	R. Stock Darmstadt	10 Jahre relativistische Schwerionenphysik am Bevalac/Berkeley

7.2.3 GSI-Preprints

83 - 1 U. Müller, G. Soff, J. Reinhardt, T. de Reus, B. Müller, and W. Greiner
Extreme Superheavy Nuclear Systems with Z=184 and their Investigation by Positrons from Supercritical Fields

83 - 2 D. Schüll
Das GSI Magnetic Spectrometer

83 - 3 W.R. Johnson, and G. Soff
Relativistic Many-Body Approach to the Photoionization of Cesium

83 - 4 R. Kulessa, R.P. DeVito, H. Emling, E. Grosse, D. Schwalm, R.S. Simon, A. Lefebvre, Ch. Briancon, R.J. Walen, G. Sletten, Th.W. Elze
High-j Proton and Neutron Alignment in the Odd Actinides ^{235}U and ^{237}Np

83 - 5 S. Gralla, Dai Guang-xi, A. Gobbi, K.D. Hildenbrand, W.F.J. Müller, A. Olmi, M. Petrovici, H. Stelzer, J. Toke, H.J. Wollersheim, R. Bock, and U. Lynen
Moments of Charge Distributions in the Reaction $^{92}Mo+^{92}Mo$ at 14.7 MeV/u

83 - 6 D. Schwalm
Collective Properties of Nuclei at High Spin from B(E2)-Values

83 - 7 J. Theis, G. Graebner, G. Buchwald, J. Maruhn, W. Greiner, H. Stöcker, J. Polonyi
Phase Transition of the Nucleon-Antinucleon Plasma in a Relativistic Mean Field Theory

83 - 8 W. Cassing, A. Lukasiak, W. Nörenberg
Dissipative Diabatic Dynamics (DDD): A Theory for Heavy-Ion Collisions Between TDHF and Transport Theories

83 - 9 H. Gäggeler, W. Brüchle, M. Brügger, K. Sümmerer, G. Wirth, A. Ghiorso, K.E. Gregorich, D. Lee, K.J. Moody, G.T. Seaborg, R.B. Welch, P. Wilmarth, G. Herrmann, J.V. Kratz, N. Trautmann, N. Hildebrand, U. Hickmann, C. Frink, N. Greulich, D.C. Hoffman, M. Fowler, H.R. von Gunten
Recent Attempts to Produce Superheavy Elements by the $^{48}Ca + ^{248}Cm$ Reaction

83 - 10 U. Müller, G. Soff , T. de Reus, J. Reinhardt, B. Müller, W. Greiner
Positrons from Supercritical Fields of Giant Nuclear Systems

83 - 11 J. Struckmeier, M. Reiser
Theoretical Studies of Envelope Oscillations and Instabilities of Mismatched Charged Particle Beams in Periodic Focusing Channels

83 - 12 W. Nörenberg
Dissipative Diabatic Dynamics: A Shell Approach to Large-Amplitude Collective Nuclear Motion

83 - 13 R. Shyam, G. Baur, F. Rösel, D. Trautmann
Post-Form DWBA Description of Coincidence Spectra in Light Ion Induced Break-Up Reactions

83 - 14 P. Schlüter, T. de Reus, J. Reinhardt, B. Müller, G. Soff
Are the Observed Structures in Positron Spectra Caused by Internal Conversion?

83 - 15 P.O. Larsson, T. Batsch, R. Kirchner, O. Klepper, W. Kurcewicz, E. Roeckl, D. Schardt, W.F. Feix, G. Nyman, P. Tidemand-Petersson
Direct Proton Decay of 0.56-s ^{147}Tm and Search for this decay Mode Among Very Neutron-Deficient Isotopes with $53 \leq Z \leq 67$

83 - 16 S.J. Wang, W. Cassing, W. Nörenberg
Comparison of Collective Mass Parameter from the Generator Coordinate Methode and the Cranking Model

83 - 17 S.J. Wang
Extension of the Time-Dependent Mean Field Theory Within the Liouville Space of the One-Body Density Matrix

83 - 18 T.H.J. de Reus, J. Reinhardt, B. Müller, W. Greiner, G. Soff, U. Müller
The Influence of Electron-Electron Interaction on Inner-Shell Excitation Processes in Heavy Ion Collisions

83 - 19 T. Siemiarczuk, J. Stepaniak, P. Zielinski
Structures in the Neutron-Proton Mass Spectrum in the Deuteron Break-Up Reaction

83 - 20 J. Stachel, P. Hill, N. Kaffrell, H. Emling, E. Grosse, Ch. Michel, H.-J. Wollersheim, D. Schwalm, S. Brüssermann, F.R. May
Collective and Single Particle Degrees of Freedom in ^{104}Ru

83 - 21 J. Theis, G. Graebner, J. Maruhn, W. Greiner
Relativistic Nuclear Fluid Dynamics Coupled to Classical Meson Fields

83 - 22 R. Shyam and J. Knoll
Subthreshold Pion Production in Nucleus-Nucleus Collisions. A Co-Operative Process!

83 - 23 H. Emling, E. Grosse, R. Kulessa, D. Schwalm, H.-J. Wollersheim
Rotation Induced Shape Transitions in Dy-Nuclei

83 - 24 W. Cassing, A.K. Dhar, A. Lukasiak, W. Nörenberg
Diabatic Aspects of Single-Particle Motion within the Time-Dependent Hartree-Fock Theory

83 - 25 C. Yannouleas
The RPA Description of the Quantum Damped Harmonic Oscillator

83 - 26 W. Spreng, F. Azgui, H. Emling, E. Grosse, R. Kulessa, Ch. Michel, D. Schwalm, R.S. Simon, H.-J. Wollersheim, M. Mutterer, J.P. Theobald, M.S. Moore, N. Trautmann, J.L. Egido, P. Ring
First Observation of Backbending in an Actinide Nucleus

83 - 27 E. Grosse
Collective Effects in Subthreshold Pion Production

83 - 28 G. Soff, U. Müller
Physik in superschweren Atomen

83 - 29 G. Münzenberg, W. Reisdorf, S. Hofmann, Y.K. Agarwal, F.P. Heßberger, K. Poppensieker, J.R.H. Schneider, W.F.W. Schneider, K.-H. Schmidt, H.-J. Schött, P. Armbruster, C.-C. Sahm, D. Vermeulen
Evidence for Element 109 from the Correlated Decay Sequence Following the Fusion of ^{58}Fe with ^{209}Bi

83 - 30 P. Armbruster
Cold Fusion - A New Road to Heavy Elements

83 - 31 D. Schwalm
Positron Emission from Superheavy Quasiatoms

83 - 32 G. Baur, F. Rösel, D. Trautmann, R. Shyam
Fragmentation Processes in Nuclear Reactions

83 - 33 J. Struckmeier, J. Klabunde, M. Reiser
On the Stability and Emittance Growth of Different Particle Phase-Space Distributions in a Long Magnetic Quadrupole Channel

83 - 34 K.-H. Schmidt, J.G. Keller, D. Vermeulen
Temperature-Induced Deformation - A Possible Mechanism for Washing out Spherical Shell Effects in the Nuclear Level Density

83 - 35 K.-H. Schmidt, C.-C. Sahm, K. Pielenz, H.-G. Clerc
Some Remarks on the Error Analysis in the Case of Poor Statistics

83 - 36 W. Cassing, S.J. Wang, W. Nörenberg
On the Dynamical Single-Particle Basis in Large-Amplitude Nuclear Motion

83 - 37 J. Schweppe, A. Gruppe, K. Bethge, H. Bokemeyer, T. Cowan, H. Folger, J.S. Greenberg, H. Grein, S. Ito, R. Schule, D. Schwalm, K.E. Stiebing, N. Trautmann, P. Vincent, M. Waldschmidt
Observation of a Peak Structure in Positron Spectra of U+Cm Collisions

83 - 38 B. Strack, J. Knoll
Expansion and Disassemply Phase of Energetic Nuclear Reactions:
- A Problem of Dynamical Instabilities ? -

83 - 38a H. Gäggeler, T. Sikkeland, G. Wirth, W. Brüchle, W. Bögl, G. Franz, G. Herrmann, J.V. Kratz, M. Schädel, K. Sümmerer, W. Weber
Probing Sub-Barrier Fusion and Extra-Push by Measuring Fermium Evaporation Residues in Different Heavy Ion Reactions

7.2.4 GSI-Reports

83 - 1 Scientific Report 1982

83 - 2 Fusions Jahresbericht

83 - 3 H. Wulf
Der Einfluß von Schwerionenstrahlen auf das Überleben und Wachstum von Säugetierzellen in vitro

83 - 4 Experimental-Data Acquisition and Analysis System
Volume I: Introduction and Concepts
Volume II: Commands
Volume III: Procedures

83 - 5 D. Liesen
Experimente zur Anregung von inneren Elektronen in überschweren Stoßsystemen

83 - 6 J. Rafelski, M. Danos
Perspectives in High Energy Nuclear Collisions

83 - 7 G. Seiler-Clark
Magnetische Momente von Hochspin-Rotationszuständen in ^{158}Dy und ^{164}Dy

83 - 8 F- und E-Programm 1983-1985

83 - 9 P. Spätdke
Axcel - GSI interaktives Simulationsprogramm zur Berechnung von zweidimensionalen Potentialverteilungen elektrostatischer Anordnungen sowie von Ionenbahnen in elektrostatischen Feldern unter Berücksichtigung der Raumladung

83 - 10 K. Beckert, R. Bock, D. Böhne, I. Hofmann, R.W. Müller, I. Brezina, H. Wollnik, R. Arnold, J. Meyer-ter-Vehn
Möglichkeiten zur Untersuchung dichter, heißer Materie mit einem Schwerionen-Synchrotron

83 - 11 S. Arai
Split Coaxial RFQ Structure

83 - 12 J.G. Schukraft
Dynamische Eigenschaften der Coulombspaltung

83 - 13 D.J. Albrecht
Untersuchung der von schweren Ionen in Dielektrika erzeugten Defektstrukturen mittels Kleinwinkelstreuung

83 - 14 Bericht des Gutachterausschusses Kernphysik und Schwerionenforschung 1980-1982(mit Anlage)

83 - 15 H.G. Grunder
An Isochronous Ring Approach to Heavy Ion Fusion

7.2.5 Visiting Groups at GSI

13.01.	Bettina Schule, Frankfurt	28
14.01.	Hohe Landesschule, Hanau	19
17.01.	Bert Brecht Schule, Darmstadt	11
19.01.	Heinrich v. Gagern Gymn., Frankfurt	14
24.01.	Goethegymnasium, Bensheim	32
24.01.	Gymnasium, Darmstadt	15
24.01.	Hilda Gymnasium, Koblenz	27
25.01.	Drei-Eich-Schule, Langen	39
25.01.	Ricarda-Huch Gymn., Sprendlingen	13
25.01.	Fa. Elima, Dieburg	8
26.01.	Univ. Louvain, Belgien	19
26.01.	Fachhochschule Darmstadt	19
27.01.	Main-Taunus Gymn., Hofheim	59
27.01.	Justus-Liebig Schule, Darmstadt	38
31.01.	Ludwig Geisler Schule, Hanau	12
31.01.	Büchner Gymn., Frankfurt	15
01.02.	Chemielabor, Fa. Merck, Darmstadt	9
03.02.	Gruppe von Jugendlichen	10
10.02.	Finanzamt Darmstadt	15
11.02.	Studenten, TH Darmstadt	30
15.02.	Kant-Schule, Rüsselsheim	21
22.02.	Georg Büchner Schule, Darmstadt	17
24.02.	Fachoberschule, Bensheim	8
26.02.	Techn.-Verb. Rhein-Main, Heidelberg	37
28.02.	American High School, Frankfurt	27
03.03.	Dahlberg Gymnasium, Aschaffenburg	22
07.03.	Schule, Mannheim	21
11.03.	Mech. Werkstatt, TH Darmstadt	19
11.03.	Bürgerverein, Eberstadt	7
17.03.	Polizei, Wiesbaden	19
17.03.	Engl. Inst., Gymnasium, Heidelberg	15
18.03.	Staatl. Gymnasium, Kaiserslautern	30
22.03.	Gymnasium, Großkrotzenburg	13
11.04.	Studentenprogramm	19
11.04.	Kommunale Jugendwoche	29
14.04.	Flugsicherung, Frankfurt	17
15.04.	Personalleiter der AGF Einricht.	18
18.04.	Deutschorden Gymn., Bad Mergentheim	29
19.04.	American High School, Frankfurt	12
19.04.	Rhein Main Air Base, Frankfurt	25
20.04.	Martin Luther Gymn., Rimbach	16
21.04.	Gymnasium, Beverungen	20
22.04.	Studenten, TH Darmstadt	25
25.04.	Erasmus-Kittler Schule, Darmstadt	25
25.04.	Nassovia, Studentenverb., Darmstadt	11
25.04.	Monania, Studentenverb., Darmstadt	19
26.04.	Ludwig Georg Gymn., Darmstadt	10
26.04.	Deutschorden Gymn. Bad. Mergentheim	26
29.04.	Fernmaldeamt, Darmstadt	24
29.04.	Auszubildende, Fa. Schenck Darmstadt	20
29.04.	Studenverbindung, Darmstadt	6
05.05.	Technnisches Gymnasium,Mainz	34
05.05.	Gymnasium, Groß-Gerau	20
06.05.	Friedr.-Ebert, Gymnasium,Müllheim	12
09.05.	Abendgymnasium II, Frankfurt/M	13
10.05.	Gymnasium, Walldorf, Baden	31
10.05.	Westdeutsche Rektorenkonferenz,	19
11.05.	Gustav-Heinemann Schule, Rüsselsheim,	13
16.05.	Physikstudenten, Gießen,	15
17.05.	CDU Frauenkreis, Darmstadt	17
19.05.	Robert-Mayer Gymnasium, Heilbronn	30
20.05.	Boxberg Gymnasium, Heidelberg	12
25.05.	Bischof Neuenheim Gymn., Königstein	35
25.05.	FH-Würzburg/Schweinfurt, Studenten	20
26.05.	Berufliches Gymnasium, Mainz	19
30.05.	Seminar Marienhöhe, Darmstadt	18
30.05.	IHK-Darmstadt, Ausbilder, Darmstadt	53
04.06.	Sportverein Wixhausen	27
08.06.	Gymnasium, Stutensee	10
09.06.	Gymnasium, Königstein	46
11.06.	Studienstiftung, Heidelberg	13
13.06.	Schülerprogramm	36
15.06.	Universität Mainz	17
15.06.	HF-Gruppe, SIN, Schweiz	10
15.06.	Fachhochschule, Darmstadt	23
20.06.	Schüler, Bad Vilbel	30
20.06.	Universität Göttingen	60
21.06.	Berufschüler, Darmstadt	29
23.06.	Universität Konstanz	38
24.06.	Leistungskurs Physik, Koblenz	6
28.06.	Biologie Workshop, Darmstadt	80
01.07.	Universität Heidelberg	54
08.07.	Treuarbeit	5
18.07.	Kurpfalz-Gymnasium, Schriesheim	21
19.07.	Nikolaus-Kistner Gymn., Mosbach	11
16.08.	Studenten- und Lehrerfortbildung	40
17.08.	Städt. Frauenklinik, Darmstadt	18
22.08.	Fünf Rotary Clubs, Frankfurt	40
24.08.	Ind. u. Handelskammer, Darmstadt	10
26.08.	Schule f. Kerntechnik, Karlsruhe	23
31.08.	Alfred Delp Gymnasium, Dieburg	26
31.08.	Abendgymnasium, Neu Isenburg	9
02.09.	Georg Büchner Schule, Darmstadt	21
11.09.	Studenten, Dänemark	22
15.09.	Inst. f. Strahlenphysik, Stuttgart	16
16.09.	Berufl. Schulen Rüsselsheim	39
21.09.	Einhardt-Gymnasium, Seligenstadt	28
23.09.	Gymnasium Hemsbach	21
27.09.	Techn. Fachhochschule Berlin	14
28.09.	Fa. BBC, Mannheim	10
05.10.	Rektoren, Schulleiter, Darmstadt	16
07.10.	Fachhochschule Rüsselsheim	21
19.10.	Lions Club, Bad Ems	20
26.10.	Arbeitsamt, Darmstadt	16
27.10.	VDE-Bezirksverein, Frankfurt	58
04.11.	Hess. Straßenbauamt, Darmstadt	20
05.11.	Rotary Club, Frankfurt	5
04.11.	Fachhochschule Rüsselsheim	14
08.11.	Bayrischer Philologenverband	48
09.11.	Universität Gießen	16
11.11.	Seniorenkreis, Bickenbach	22
15.11.	Freiherr v. Stein Schule, Frankfurt	32
18.11.	Verein Deutscher Elektr. Werke	35
23.11.	Liebig Schule, Frankfurt	26
25.11.	Laborbesichtigung, DPG	14
01.12.	Lessing Gymnasium, Frankfurt	48
06.12.	Elektrotechnik Assistentinnen, AEG	23
08.12.	VDE-Jungmitglieder	16
10.12.	Techniker, Lufthansa	11
13.12.	Werner v. Siemens Schule, Frankfurt	14
14.12.	Univ. Frankfurt, Physik Studenten	59
14.12.	Universität Marburg, Historiker	10
16.12.	Architekten	7
20.12.	TU München, Studenten	118
and 24 guided tours with alltogether		67
	totalizing	2990
		visitors

7.3 Scientific Committees, Directorate and Personnel

Scientific Council

Prof. E.W. Otten (Mainz, Chairman), Dr. G. Friedlander (Brookhaven), Dr. H.A. Grunder (Berkeley), Prof. F. Gudden (Erlangen), Prof. P. Gütlich (Mainz), Prof. P. Kienle (München), Dr. H.J. Langmann (Darmstadt), Prof. K.H. Lindenberger (Berlin), Prof. U. Mosel (Gießen), Prof. R.H. Siemssen (Groningen), Prof. V. Soergel (Hamburg),

Users Committee

Prof. H. Backe (Mainz, Chairman), Prof. P. Armbruster (GSI), Prof. R. Bock (GSI), Dr. H. Gäggeler (GSI), Prof. V. Metag (Gießen), Dr. G. Münzenberg (GSI), Prof. D. Groß (Berlin), Prof. H.R. von Gunten (Würenlingen), Prof. H. Morinaga (München), Prof. B. Müller (Frankfurt), Prof. F. Pühlhofer (Marburg), Prof. D. Schwalm (Heidelberg)

Scientific Directorate

Prof. G. zu Putlitz (Chairman, Scientific and Technical Managing Director till 31.08.1983), H.O. Schuff (Administrative Managing Director), Dr. N. Angert, Prof. P. Armbruster (Vice Chairman), Prof. W. Nörenberg

Scientific and Technical Division Leaders

Dr. N. Angert, Prof. P. Armbruster, Prof. R. Bock, Dr. D. Böhne, Prof. G. Herrmann, Prof. W. Nörenberg

Scientific Committee

Prof. E. Roeckl (Chairman), Dipl. Chem. H. Ahrens, Prof. R. Bock, Dr. D. Böhne, Dipl. Chem. H. Folger, Dr. E. Grosse, Dipl. Phys. U. Grundinger, Prof. G. Herrmann, Dr. K.D. Hildenbrand, Dr. J. Knoll, Prof. P.H. Mokler, Dr. W. Reisdorf, Dr. M. Richter, Ing. N. Schneider, Dr. R. Spohr, Dipl. Phys. R. Steiner, Dr. P. Strehl

Guest Scientists and Consultants

S. Arai (Japan), F. Azgui (Algeria), A. Balanda (Poland), D. Berdichevsky (Argentina), T. Biro (Hungary), E. Blakely (USA), N. Carjan (France), M. Chen (Peoples's Rep. China), G. Dai (People's Rep. China), A. Demin (USSR), R.D. Deslattes (USA), R. Devito (USA), K. Dietrich (FRG), J. Doernyei (Hungary), B. Eichler (DDR), A. Fässler (FRG), H. Feldmeier (FRG), G.-N. Flerov (USSR), F. Folkmann (Denmark), H. Freiesleben (FRG), L. Ge (People's Rep. China), A. Ghiorso (USA), J. Greenberg (USA), W. Greiner (FRG), G. Guarino (Italy), J. Harris (USA), M. Hass (Israel), P.O. Hess (FRG), K. Hulet (USA), S. Ito (Japan), C.-L. Jiang (People's Rep. China), R. Katz (USA), I. Kelson (Israel), M. Kleber (FRG), V.T. Koslowski (Canada), J. Kuti (Hungary), V.-B. Kutner (USSR), J. Kuzminski (Poland), P.-O. Larsson (Sweden), Y. Lazarev (USSR), M.E. Leino (Finland), B. Liu (People's Rep. China), A. Lukasiak (Poland), U. Lynen (FRG), D. Maor (Israel), D. Marinescu (Rumania), J. Maruhn (FRG), K. Moody (USA), U. Müller (FRG), A. Oskarsson (Sweden), A. Plochocki (Poland), J. Plocki (Poland), S. Polikanov (FRG), L.P. Pressniakov (USSR), K. Redlich (Poland), S. Reinsch (USA), M. Reiser (USA), F. Riess (FRG), P. Ring (FRG), B. Rydberg (Sweden), K. Rykaczewski (Poland), A. Sandoval (Mexico), Ch. Schmelzer (FRG), H.A. Schuessler (USA), V. Semiarcuk (Poland), N. Shenbar (Israel), R. Shyam (India), J.D. Silver (Great Britain), Z. Stachura (Poland), M. Stepaniak (Poland), A. Szentgali (Hungary), G. Ter-Akopian (USSR), J. Theis (FRG), J. Töke (Poland), U. Trebus (USA), L. Turko (Poland), J. Ungrin (Canada), P. Vincent (USA), V.V. Volkov (USSR), R. Wada (Japan), A. Warczak (Poland), B. Warczak (Poland), H. Wieman (USA), J. Wood (Great Britain), C. Yannouleas (Greece), J. Yu (People's Rep. China), E. Zganjar (USA), W. Zhao (People's Rep. China), I.P. Zielinski (Poland), J. Zychor (Poland), J. Zylicz (Poland)

Scientific Personnel

H. Ahrens, J. Ahrens, R. Albrecht, N. Angert, P. Armbruster, W. Becker, K. Beckert, H. Beyer, K. Blasche, R. Bock, D. Böhne, H. Bokemeyer, F. Bosch, H. Brandis, G. Breitenberger, R. Brockmann, W. Brüchle, M. Brügger, F. Busch, W. Cassing, T.E. Cowan, L. Dahl, H. D. Dohmann, H. Egger, H. Eickhoff, H. Emling, M. Emmerling, H.G. Essel, J. G. Festag, P. Finke, B. Fischer, H. A. Folger, B. Franczak, B. Franzke, P. Fuchs, H. Gäggeler, I. Giese, J. Glatz, S. Glückert, A. Gobbi, H. Göringer, P. Grimm, E. Grosse, U. Grundinger, H. H. Gutbrod, T. Györffy, E-M. Heck, G. Herrmann, F. P. Hessberger, L. Hieber, K. Hildenbrand, D.H.H. Hoffmann, J. Hoffmann, I. Hofmann, S. Hofmann, H. Hübner, H. Hultzsch, G. Hutter, W. Jacoby, K. Kaspar, H. J. Keller, R. Keller, M. M. Khaouli, R. Kirchner, J. Klabunde, O. Klepper, J. Knoll, C. Kozhuharov, G. Kraft, P. Krejcik, T. Kühl, B. Langenbeck, H. D. Liesen, J. Lowsky, H. J. Lustig, R. Mann, D. Marx, R. Meyer-Prüssner, P. H. Mokler, B. Morgenstern, G. Moritz, M. Müller, R. Müller, W.F.J. Müller, G. Münzenberg, F. Nickel, H. Nienstädt, W. Nörenberg, K. Poppensieker, H. B. Prange, H.J. Rabe, H. Rafelski, W. Reisdorf, M. Richter, C. Riedel, H. G. Ritter, E. Roeckl, H. J. Sann, M. Schädel, E. Schaffner, D. Schardt, K. H. Schmidt, W. Schneider, W-A. Schönfeldt, A. Schönlein, M. Schuber, D. Schüll, H. Schulte, R. Schulze, D. Schwalm, O. Siart, G. Siegert, R. Simon, R. Spohr, R. Steiner, H. Stelzer, R. Stock, H. Stöcker, B. Strack, P. Strehl, H. Ströbele, J. Struckmeier, K. Sümmerer, H. Trautmann, D. Vermeulen, K. Winkelmann, G. Wirth, B. Wolf, H. I. Wollersheim, V. Zelba

Technical and Administrative Staff

F. Achenbach, K. Adelberger, J. Alt, W. Amann, S. Andresen, T. Archinal, G. Augustinski, E. Babinsky, A. Bach, H. Balonier, S. Bauer, G. Baumann, E. Bayersdorf, H.-J. Beeskow, K-H. Behr, E. Benz, G. P. Benz, H. J. Benz, W. Bergsträsser, L. Bernhardt, C. Besthorn, H. Bingel, W. Bleuel, H. Blinn, F. Blumert, F. Bock, W. Bock, W. Bock, E. Bohländer, J. Bolle, P. Borisch, I. Bormet, R. Bormet, J. Bossler, W. Bourgeois, G. Braatz, W. Brenger, H. Britz, A. Brünle, S. Brür, M. Brügger, N. Brunner, C. Bruske, D. Bruske, K. Büttner, E. Burger, K. H. Burkhard, H. G. Burkhard, A. Busch, M. Cartharius, R. Christmann, J-P. Clain, H. Dächert, H. Damm, H. W. Daues, J. R. Dengler, G. Dick, I. M. Diedrich, R. Diehl, H. Döpke, R. Döring, L. Dörr, H. Dünkel, R. Dünkel, O. Eberhardt, H. Eckhardt, K. A. Ehrich, M. F. Eick, G. Eidmann, G. Eisold, E. Eitel, H. Emig, W. Enders, G. Englert, U. Ernst, F. Ertan, A. Fehres, M. Feyerabend, H. Fischer, M. Fradj, O. Frank, P. W. Frank, G. R. Freiwald, P. Freudenberger, E. Fritsch, G. Fröhlich, G. Fröse, R. Gärtner, H. Gaiser, M. Gambietz, K. D. Ganser, A. Gasper, M. Gassner, H. Gebhardt, I. Georg, E. Gerbig, O. Gerhardt, H. Gilbert, W. Gockel, M-G. Göttmann, V-G. Gomez, K. Graf, H. Grein, D. Grimm, G. Grimm, H. Grösch, J. Grösser, H. Gross, J. Gross, J.L. Gundlach, W. Gutowski, E. Häcker, B. Häfner, D. Hager, W. Hahn, P. Hahne, P. Hahnel, H. Hammal, E. Hammann, H. Hardel, O. P. Hartmann, R. Hartmann, W. Hartmann, W. Hartmann, M. Hartung, H. Heckwolf, J. Hehner, T. Heinbüchner, K. Heinz, H. Heller, H. Helms, D. Henke, H. Hewig, J. Hey, K .Hill, F. Himmelmann, C. Hoffmann, R-H. Hoffmann, N. Hofmann, G. Holzschuh, L. Horas, H. Horneff, A. Hotop, R. Hotz, W. v.d.Hoya, W. Huber, W. Hüller, G. Ickert, A. Igel, W. Ille, K. Illert, E. Jäger, H. Jakobi, S. Jansen, K. Jobb, I. Jobst, G-K. Jöst, G. Kaiser, R. Kaiser, H. J. Kalawsky, E. Kammer, W. Kappel, F. Keil, H. L. Kempf, H. R. Kiesewetter, C. P Kiesslich, N. Kischnick, A. Kissler, G. Klappich, H. Klecker, H. Klemm, J. Klemm, S. Klemm, P. Klink, R. Kluber, K-D. Knapp, U. Kniess, W. Köthe, K. Kohl, B. Kolb, U. Kopf, W. Krall, H. Kraus, K-R. Kress, W. Kreuzer, H. Krichbaum, A. Kritzer, C. Kröh, T. Kroll, L. Krüger, G. Kube, K. Kucharczky, H. Kühn, R. Kühn, J. Kühtz, K.K.B. Küper, W. Kunz, H-P. Kurz, E. Labinsky, H. Lameli G. Langer, H. Larem, G. Ledl, K-D. Leible, G. Leidel, E. Leiser, H. Leiser, W. Leiser, G. Lenz, H. Leonhardt, R. Leonhardt, H. P. Liebold, L. Liebschwager, R. Lischetzki, F. List, N. Lohneis, D. Loos, A. Lorenz, I. Lorenz, W. Losert, M. Ludwig, S. Lüdtke, S. Lüttges, H. Mader, K-H. Mader, E. Magnussen, E. Malwitz, I. Malwitz, H. G. Manns, M. Marquardt, H. G. Martens, W. Marx, R. Matheis, K-H. Matthöfer, R. Mayr, H. Meder, H. Meister, M. Melchior, K. Metz, D. Metzger, S. Metzger, W. Meufels, G. Micsa, E. Mitz, K. Möller, K. Mömerzheim, L. Molnar, A. Morhardt, T. Mrugalla, C. H. Mühle, A. Müller, B. Müller, B. Müller, G. Müller, K. Müller, W. Müller, K-H. Neff, K. Neimanns, W. Neuhäuser, A. Nicklas, G. Niemann, D. Nitsch, R. Norcia, B. Ohmstede, G. Olscha, G. Otto, G. Pabst, J. Palm, W. Panschow, F. Peldzinski, H. Penninger, K. Petrich, F. Petrone, E. Pfaff, E-L. Pfaff, K-L. Pfaff, E. Pfeng, P. Pfizenmeier, D. Pissowotzki, D. Pollet, A. Poppe, I. Poppert, M. Poth, G. Pritz, A. Przybyla, W. Quick, D. Quis, M. Rack, E. Rass, W. Rehm, J. Rempe, R. Retzlaff, M. Rhein, T. Riedel-Heine, H. Riesner, D. Rochna, C. Röder, D. Röder, H. Röder, W. Rösch, R. Rulfs, D.H. Russ, W. Salzer, V. Schaa, H. W. Schäfer, F. Schäffer, J. Schäffer, M. Scheid, H. Schiemann, G. Schill, E. Schimpf, H.J. Schlitt, A. Schlossarek, D. Schmalz, G. Schmelig, H-G. Schmidt, W. Schmidt, H. Schmiedler, L. Schmiedler, R. Schmitt K. Schneider, M. Schneider, N. Schneider, H-J. Schött, M. Schuber, P. Schue, W. Schue, H. Schütz, H.O. Schuff, P. Schulte, K. Schultze, R. Schumann, G. Schunk, W. Schuth, G. Schwarz, R. Schwarz, V. Schwarz, R. Schwedhelm, G. Schweipert, U. Seckert, S. Selent, K. Senft, R-F. Sigmund, H. Sitta, G. Sobainsky, H. Sondershaus, P. Spädtke, H. Spengler, S. Sperling, W. Spiess, H. Spika, A. Spitaler, A. Stagno, K. Stallmann, W. Stampp, E. Stenger, R. Stenner, J. Störmer, M. Stork, U. Stork, W. Stork, I. Strehl, K. Streich, G. Stubenrauch, E. Sturm, A. Suderleith, K. D. Süssbrich, D. Svrcina, W. Thalheimer, R. Thieme, H. Thomas, E. Thurau, C. Vad, H-G. Valter, E. Veith, H. Vilhjalmsson, W. Vinzenz, H. Vogel, U. Vogel, D. Vogt, D. Volz, R. Vrtal, V. Wagner, H. Wahl, K. Waitz, G. Wannemacher, K-H. Wannemacher, I-H. Warsow, R. Weber, W. Weber, E. Weigand, P. W. Weinreuter, L. Weiss, H. Weitzel, D. Wendt, E. Werkmann, H. Wesp, W. Weyrich, G. Wilde, K. Wilhelm, S. Wilhelm, D. Wilms, H. Wirth, W. Wissing, H. Wörner, C. Wolf, G. Wolf, I. Wortmann, R. Zecher, H. Ziegler, A. Ziem, E. Zilch, S. Zipprich, A. Zschau, K. Zweig,

FEDERAL REPUBLIC OF GERMANY

Hahn-Meitner-Institut, Berlin
H.G. Bohlen, A. Gamp, B. Gebauer, R. Künkel, A. Miczaika, W. von Oertzen

Siemens AG, Berlin, München
I. Beling, J. Denteler, K. Sapotta

Universität Bochum
H. Freiesleben, H. Sohlbach

Universität Bonn
G.J. Kumbartzki, K. Recker, H.J. Simonis, K.-H. Speidel

Deutsches Kunststoff Institut, Darmstadt
B. Hahn

Technische Hochschule Darmstadt
F. Beck, O. Becker, W. Bonin, C. Brendel, P. J. Brülls, P. Buck, H.-G. Clerc, M. Dahlinger, U. Gollerthan, P. Grimm, F.-J. Hambsch, U. Helm, H.P. Hollenbach, E. Kankeleit, G. Klotz, W. Knippelberg, W. Kraft-Weyrather, M. Krämer, R. Krieg, U. Meyer, H.G. Miltenburger, W. Müller, M. Mutterer, H.Oeschler, J. Pannicke, K. Pielenz, A. Richter, W. Rösch, C.-C. Sahm, P. Senger, W. Schimmerling, C. Schmitt, G. Schrieder, H. Spangenberger, J.P. Theobald, K. Weingärtner, K. Wien

Herder Gymnasium, Frankfurt
H. Dittmar

Universität Frankfurt
U. Arlt, K. Baltschukat, D. Barthel, R. Bass, H. Baumann, K. Bethge, U. Bork, G. Buchwald, J. Cieza, L.P. Csernai, H. Deitinghoff, K. Depta, R.M. Dreizler, H. Th. Elze, Th. W. Elze, E. Engel, G. Graebner, F. Granzer, W. Greiner, E.K.U. Groß, A. Gruppe, R. Herrmann, P.O. Hess, J. Idzko, W.R. Johnson, P. Junior, A.R. Kranz, Th. Kratz, S. Kelbch, H. Klein, K. Koller-Lampert, K. Langbein, P. Leipe, B. Lohmüller, U. Lynen, P. Malzacher, J.A. Maruhn, A. Mauthofer, G. Mehler, B. Müller, L. Neise, W. Neumann, H. Noll, N. Noll, H. Ower, W.T. Pinkston, G. Plunien, B. Pischel, F. Rauch, W. Reeh, J. Reinhardt, T. Rentzsch, T. de Reus, G. Riehl, A. Rosenhauer, W. Schadt, A. Schäfer, A. Schempp, P. Schlüter, H. Schmidt-Böcking, V. Schneider, M. Seiwert, M.E. Starke, K. Stelzer, K.E. Stiebing, H. Stöcker, A. Thiel, M. Uhlig, T. Ullrich, D. Vasak, C.S. Warke, K.-H. Wietschorke, X.-Z. Wu, K.H. Ziegenhain

Universität Gießen
U. Becker, G. Breitbach, P. Crombach, D.R. Dean, G. Döll, G. Fiedler, R.D. Fischer, W. Groh, N. Grün, J. Günzl, A. Höhler, E. Huttel, R. Kaps, P. Keiner, P.C. Kester, J. Kiefer, G. Koch, E. Koglin, M. Kost, W. Kühn, J. Makowka, D. Masak, V. Metag, U. Mosel, K. Mühlhans, R. Mühlhans, A. Müller, E. Müller, R. Novotny, U. Post, E. Reichwein, E. Salzborn, K.-H. Schartner, K. Schaupert, W. Scheid, E. Schneider, B. Schuch, H. Ströher, O. Tanimura, M. Tokyama, S.R. Valluri, K.J. Weber, I. Wirkner-Bott, R. Wolf, E. Wüst

Universität Göttingen
H. Dornhöfer, W. Eschner, K.-L. Gippert, E. Runte, W.-D. Schmidt-Ott, P. Tidemand-Petersson

Herfurth GmbH, Hamburg
K.H. Knobbe

Universität Hamburg
A. Knöchel, L. Rikus, H. Röhl

Max Planck Institut für Kernphysik, Heidelberg
I. Bock, H. Feldmeier, H. Gröger, H.J. Hennrich, W. Hennerici, G. Himmele, T.L. Khoo, W. Koenig, N. Kwong, U. Lynen, B. Martin, R. Repnow, J. Schirmer, J. Soltani, W. Wahl, H. Wirth, M. Zirnbauer

Universität Heidelberg
J. Aichelin, W. Ensinger, H. Ferber, G. Frech, P. Glässel, D. Habs, D. v. Harrach, U. v. Helmolt, H.W. Heyng, J. Hüfner, R. Ibarra, J. Konrad, R. Kroth, A. Meger, Ph. Munn, A. Oppenländer, D. Pelte, G. Reiss, R.E. Renfordt, D. Schall, R. Schuch, J. Schuhkraft, M. Schulz, D. Schwalm, B. Schwartz, G. Seiler-Clark, H.J. Specht, H. Ströbele, K. Tittel, N. Trautmann, B. Traving, U. Winkler, G.K. Wolf

Kernforschungsanlage Jülich
P. Kreijcik

Kernforschungszentrum Karlsruhe
H. Beer, G. Walter

Universität Karlsruhe
M. Malvetti

Gesamthochschule Kassel
B. Fricke, H. Hartung, D. Kolb, W.Schulze, W.Sengler, W.-D. Sepp, G. Torbohm

Universität Kiel
R. Beaujean, M. Berndt, W. Enge, J. Krause, G. Siegmon

Deutsche Forschungs- und Versuchsanstalt für Luft- und Raumfahrt, Köln
H. Bücker, R. Facius, G. Horneck, M. Schäfer

Universität Köln
G. Freisem-Broda, U. Saßmannshausen, K. Thiel

Universität Mainz
O. Althoff, H. Backe, M. Begemann, G. Berthes, Th. Blaich, J. Eberz, C. Frink, N. Greulich, U. Hickmann, N. Hildebrand, G. Huber, N. Kaffrell, T. Karlewski, W. Kieling, M. Klüver, J.V. Kratz, E. Kuchinka, M. Lerch, H. Lochmann, K. Lützenkirchen, R. Menges, P. Peuser, J. Stachel, H. Stuhrmann, N. Trautmann, G. Ulm, S. Zauner

Universität Marburg
D. Bangert, R. Beckmann, U. Bieschke, H.-A. Bösser, R. Brandt, G. Dersch, R. Dersch, R.A. Esterlund, E. Ganßauge, B. Grabez, B. Jäckel, H. Kallies, H.-J. Keim, E.U. Khan, F. Killinger, N. Klein, B. Kohlmeyer, R. Kretschmer, A. Laschek, B. Ludewigt, T. Lund, M. Marinescu, P. Patzelt, M. Plachky, F. Pühlhofer, W. Rauch, U. Reus, A Rox, H. Schulte, H. Stege, G. Tress, P. Vater, W. Weidner, W. Westmeier

Technische Universität München
G. Beier, E. Berdermann, K. Dietrich, H. Ernst, J. Friese, D.H. Jakubaßa-Amundsen, J. Kemmer, P. Kienle, M. Kleber, H.J. Körner, G. Korschinek, P. Kubik, W. Mayer, W.A. Mayer, H. Morinaga, L. Müller, E. Nolte, U. Ratzinger, P. Ring, H. Tsertos, A. Ulrich, W. Wagner

Universität München
Ch. Lauterbach, H. Lenske, H.H. Wolter

Fraunhofer-Institut für Toxikologie und Aerosolforschung, Münster
W. Holländer

Universität Münster
M. Doss, G. Gaul, R. Glasow, K.H. Kampert, H. Löhner, R. Santo, R. Trockel

Universität Regensburg
M. Brack, E. Werner

Universität Stuttgart
E. Nehl, K. Pöhlandt, M. Weiergräber

Universität Tübingen
W.H. Dickhoff, A. Faessler, M. Ismail, M. Rashdan, L. Satpathy, M. Trefz, W. Wadia

Fachhochschule Wiesbaden
M. Witzky

Universität Würzburg
A.M. Kellerer, M. Laßmann, H. Roos, W.-H. Thomas, A. Wenning, F. Zilker

BELGIUM
Universite de Louvain
Ch. Michel

CANADA
Chalk River Laboratories
J. Ungrin

DENMARK
University of Aarhus
N. Eisum, F. Folkmann

Niels Bohr Institute, Copenhagen
S. Bjoernhoim

Nordita, Copenhagen
P.A. Amundsen

ENGLAND
University of Manchester
I.S. Grant

University of Oxford
J.S. Brown, B.P. Duval, H.A. Klein, J. Laursen, A.F. McClelland, J.D. Silver

University of Surrey
U. Bangert

University of Sussex
D.E. Arafah

FRANCE
Centre d'Etudes Nucleaires de Bordeaux-Gradignan
N. Carjan

Universite de Caen
G. Bizard, J.L. Laville

Grand Accelerateur National des Ions Lourds, Caen
J. Peter, A.C. Mueller

Institut Laue-Langevin, Grenoble
M. Roth

Institut de Physique Nucleaire, Orsay
M. Bernas, P. Dessagne, M. Langevin

Centre National de la Recherche Scientifique, Paris
M. Maury, P. Pellas, C. Perron

Universite de Paris VI
J.P. Briand, P. Indelicato, M. Tavernier

Centre d'Etudes Nucleaires, Saclay
J. Barette, C. Gregoire, J. Julien, R. Lucas, C. Ngo, G. Pappalardo, J. Poitou, E. Tomasi

Centre de Recherche Nucleaire, Strasbourg
F.A. Beck, T. Byrski, G.J. Costa, M. Debeauvais, D. Freeman, C. Gehringer, B. Haas, F. Haas, B. Heusch, S. Jokic, J.C. Merdinger, J. Ralarosy, J. Tripier, J.P. Vivien

INDIA
Physical Research Institute, Ahmedabad
S.B. Khadkikar

Institute of Physics, Bhubaneswar
A. Ansari

Tata Institute for Fundamental Research, Bombay
Y.K. Agarwal

ISRAEL
Weizmann Institute of Science, Rehovot
C. Broude, M. Hass

ITALY
University of Bari
G. Guarino

University of Catania
R. Fonte

Instituto Nationale di Fisica Nucleare, Florence
A. Olmi

University of Florence
P. Maurenzig, A. Stefanini

University of Napoli
V.G. Vaccaro

JAPAN
Institute of Nuclear Study, Tokyo
S. Arai

MEXICO
University of Mexico, Mexico City
A. Dacal, M. Ortiz

PAKISTAN
Gomal University
E.U. Khan

Pakistan Institute of Technology, Rawalpindi
K. Jamil, H.A. Khan, N.A. Khan, M.A. Sial

People's Republic of China
Institute of Modern Physics, Lanzhou
G.X. Dai, B. Liu, T.-S. Kang, P.-J. Zhai

Nuclear Research Institute of Shanghai
M. Chen

POLAND
University of Cracow
E. Bozek, R. Kulessa, A. Warczak, B. Warczak

University of Katowice
J. Kuzminski

University of Lublin
A. Baran, A. Gozdz

University of Warsaw
W. Kurcewicz, T. Matulewicz, A. Plochocki, T. Siemiarczuk, J. Stepaniak, J. Toke, J. Zylicz

ROMANIA
Institute of Physics and Nuclear Engineering, Bucharest
M. Petrovici

SOUTH AFRICA
University of Cape Town
J. Rafelski

University of the Witwatersrand, Johannesbourgh
J. Carter

SWEDEN
Chalmers University of Technology, Göteborg
G. Nyman, A. Rosen

Studsvik Science Research Laboratory, Nyköping
K. Aleklett

University of Uppsala
B. Rydberg

SWITZERLAND
University of Bern
H.R. von Gunten

UNITED SOVIET SOCIALIST REPUBLIC
Joint Institute for Nuclear Research, Dubna
B. Eichler, V.P. Perelygin, S.G. Stetsenko

UNITED STATES OF AMERICA
Argonne National Laboratory
B.B. Back, W. Henning, R.V.F. Janssens, W. Kutschera

Lawrence Berkeley Laboratory
E.A. Blakely, H. Bowman, P. Eitner, E.M. Friedlander, A. Ghiorso, H.-A. Gustafsson, D. Lee, M. Leino, P. Mc Gaughey, K.J. Moody, G. Odyniec, A.M. Poskanzer, H.G. Pugh, J. Rasmussen, T. Renner, H. Riedesel, R. Roots, L.S. Schroeder, G.T. Seaborg, C.A. Tobias, M. Wong, J.-S. Xu, T.C. Yang

State University, Corvallis
W. Loveland

AT&T Bell Laboratories, Holmdale
D.E. Murnick

University of Tennessee, Knoxville
C.R. Bingham, M.W. Guidry

Purdue University, Lafayette
N. Porile

Lawrence Livermore Laboratory
A.D. Dougan, R.J. Dougan, E.K. Hulet, J.H. Landrum, R.W. Lougheed, J.F. Wild

Los Alamos National Laboratory
W.R. Daniels, M.M. Fowler, D.C. Hoffman, M.S. Moore, J.B. Wilhelmy

Kansas State University, Manhattan
S. Hagmann, P. Richard

University of Maryland
M. Reiser

Vanderbilt University, Nashville
U. Heinz, W.T. Pinkston

Yale University, New Haven
T. Cowan, J.S. Greenberg, J. Schweppe

Oak Ridge National Laboratory
F.E. Obenshain, G.D. O'Kelley, G.R. Young

Stanford University, Palo Alto
R. Anholt, W.E. Meyerhof, J.D. Molitoris, C. Stoller

Rutgers University
P. Vincent

University of Washington, Seattle
A. Lazzarini

State University of New York, Stony Brook
P. Braun-Munzinger, P. Paul, L. Ricken, J. Stachel, P.H. Zhang

Texas A&M University, College Station
S. Chen, H.A. Schüssler, U. Trebus, K.L. Wolf, J. Zhang

National Bureau of Standards, Washington
R.D. Deslattes, R.E. LaVilla

Agarwal, Y.K. 5, 73, 77, 79, 81
Aichelin, J. 126
Albrecht, D. 210, 211
Albrecht, R. 257, 267, 269, 270
Alekiett, K. 54
Althoff, O. 270
Amundsen, P.A. 170
Angert, N. 298
Anholt, R. 347, 348
Ansari, A. 90, 91, 92
Arafah, D.E. 214
Arai, S. 340
Arlt, U. 7
Armbruster, P. 5, 73, 77, 79, 81, 151, 210, 211
Augustinski, G. 236, 238
Azgui, F. 62, 63, 65, 66, 243, 244
Back, B.B. 11
Backe, H. 149
Baltschukat, K. 198
Bangert, D. 18, 45, 241
Bangert, U. 214
Bär, H.-J. 177
Baran, A. 95
Barette, J. 62
Barthel, D. 130, 131, 351, 352
Bass, R. 21
Baumann, H. 235
Bayerbach, S. 165
Beaujean, R. 219
Beck, F. 20, 107
Beck, F.A. 63
Becker, O. 222
Becker, U. 180
Becker, W. 163
Beckert, K. 333, 334
Beckmann, R. 42, 54
Beer, H. 75
Beeskow, H.J. 236, 238
Begemann, M. 149
Behr, K.H. 229
Beier, G. 22
Beling, I. 302
Berdermann, E. 148, 151, 248
Berdichevsky, D. 68, 87
Bernas, M. 70
Berndt, M. 219
Berthes, G. 249
Besthorn, C. 289
Bethge, K. 149, 235
Beyer, H.F. 156, 160, 349, 350
Bieschke, U. 55, 56
Bingham, C.R. 62
Biro, T. 142
Bizard, G. 44
Bjoernholm, S. 11
Blaich, Th. 33, 85
Blakely, E.A. 208
Blasche, K. 292, 295, 311, 318
Bleuel, W. 292
Bock, I. 39, 41
Bock, R. 11, 28, 29, 45
Bohlen, H.G. 19
Böhne, D. 311, 333
Bokemeyer, H. 149
Bolle, J. 340
Bonin, W. 245
Borisch, P. 305
Bork, U. 209
Bosch, F. 148, 151, 159, 248
Bösser, H.-A. 26
Bossler, J. 299
Bourgeois, W. 320, 321
Bowman, H. 347, 348
Bozek, E. 150
Bozsik, I. 335
Brack, M. 111
Brandis, H. 327
Brandt, R. 35, 36, 42, 54, 220, 221, 261, 264
Braun-Munzinger, P. 32, 43, 44
Breitbach, G. 34
Breitenberger, G. 309
Brendel, C. 20, 43, 44, 240
Briand, J.P. 160
Brockmann, R. 45, 46, 241
Broude, C. 58, 59
Brown, J.S. 161
Bräuer, H. 250
Bruske, C. 229
Brüchle, W. 78, 82, 85, 233, 246, 247, 271
Brügger, M. 72, 78, 82, 85, 246, 247
Brülls, P.J. 27
Brünle, A. 229
Buchwald, G. 129, 130, 131, 132, 140, 351, 352
Buck, P. 107
Bücker, H. 197, 198
Burkhard, K. 229
Busch, F. 274, 281, 290
Byrski, T. 63
Carjan, N. 13
Carter, J. 20
Cassing, W. 108, 112, 113, 115, 119, 120, 133, 134
Chen, M. 229
Chen, S. 163
Chytrek, H. 287
Cieza, J. 351, 352
Clerc, H.-G. 2, 3, 4, 5, 80, 254
Costa, G.J. 63
Cowan, T. 149
Crombach, P. 34
Croome, D. 281, 285
Csernai, L.P. 128

Dabrowski, H. 43, 44
Dacal, A. 241
Dahlinger, M. 245
Dai, G.X. 11, 12, 29
Daniels, W.R. 85
Daues, H.W. 236, 238, 257
Dean, D.R. 99
Debeauvais, M. 37, 53
Deitinghoff, H. 341
Dengler, J. 267
Denteler, J. 302
Depta, K. 122
Dersch, G. 54
Dersch, R. 264
Deslattes, R.D. 349, 350
Dessagne, P. 70
Dickhoff, W.H. 125
Dietrich, K. 95
Dittmar, H. 7
Döll, G. 266
Dornhöfer, H. 82, 232
Dörr, L. 25
Doss, M. 47, 257
Dougan, A.D. 15, 78, 83
Dougan, R.J. 15, 78, 83
Dreizler, R.M. 186
Duval, B.P. 161
Eberz, J. 67, 167
Eckhardt, H. 295
Egger, H. 275
Eichler, B. 232
Eickhoff, H. 312, 320, 321, 334
Eidmann, G. 267
Eisum, N. 164
Eitner, P. 241
Elze, H. Th. 144
Elze, Th. W. 64
Emig, H. 299, 338
Emling, H. 61, 62, 63, 64, 65, 66, 243, 244, 2
Emmerling, M. 322, 324, 325
Enge, W. 219
Engel, E. 186
Ensinger, W. 223
Ernst, H. 76
Ernst, U. 291
Eschner, W. 75
Essel, H.-G. 267, 274
Esterlund, R.A. 16, 17
Facius, R. 197, 198
Faessler, A. 97, 98, 125
Fehres, A. 267
Feldmeier, H. 104, 105, 107
Ferber, H. 223
Feyerabend, M. 287
Fiedler, G. 34, 211
Finke, P. 326
Fischer, B.E. 215, 216, 250
Fischer, R.D. 57
Fleischer, W. 192
Folger, H. 149, 223, 228
Folkmann, F. 164, 349
Fonte, R. 149
Fowler, M.M. 85
Franczak, B. 316
Franzke, B. 311, 313, 320, 321, 333
Frech, G. 224
Freeman, D. 6
Freiesleben, H. 14, 18, 32
Freisem-Broda, G. 213
Fricke, B. 187, 188, 189, 190
Friedlander, E.M. 54, 264
Friese, J. 22
Frink, C. 82, 84
Fuchs, P. 64
Gäggeler, H. 15, 78, 82, 83, 84, 85, 232, 233, 246
Gaiser, H. 217, 292, 295
Gamp, A. 19
Ganßauge, E. 55, 56
Gasper, A. 322
Gaul, G. 256
Gebauer, B. 19
Gehringer, C. 63
Ghiorso, A. 77, 79, 81
Giese, I. 287, 288
Gippert, K.-L. 70, 74, 75
Glasow, R. 39, 40, 41, 256, 258
Glässel, P. 8, 9, 10
Glückert, S. 275
Gobbi, A. 11, 12, 13, 24, 28, 29, 30, 31, 38, 39, 40, 41, 109, 236, 237
Gollerthan, U. 150
Göringer, H. 274, 281, 283
Gozdz, A. 111
Grabez, B. 42
Graebner, G. 129, 130, 131, 132, 143
Gralla, S. 11, 12, 28, 29, 30, 31, 236, 237
Grant, I.S. 71
Granzer, F. 265
Greenberg, J.S. 149
Gregoire, C. 24, 25
Grein, H. 61, 149, 243, 244, 272, 274
Greiner, W. 96, 103, 121, 122, 123, 124, 128, 129, 130, 131, 132, 138, 139, 140, 141, 142, 143, 144, 145, 169, 171, 172, 173, 174, 175, 176, 179, 181, 182, 183, 191
Greulich, N. 82, 84, 231, 232
Grimm, P. 239, 255
Gröger, H. 6
Groß, E.K.U. 186
Groh, W. 166
Grösch, H. 245
Grosse, E. 43, 44, 61, 62, 64, 65, 66, 239, 240, 244
Grün, N. 180

Gruppe, A. 149
Guarino, G. 28
Guidry, M.W. 62
Gunten v., H.R. 85
Günzl, J. 199
Gustafsson, H.-A. 47, 48, 49, 51, 52, 257, 258
Gutbrod, H.H. 47, 48, 49, 50, 51, 52, 257, 258
Gutowski, W. 301, 303
Haas, B. 6, 63
Haas, F. 6
Habs, D. 6, 8, 57, 58, 59, 60, 245
Haefner, B. 247
Hagmann, S. 165
Hahn, B. 215
Hambsch, F.-J. 255
Hammal, H. 267
Hardel, H. 267
Harrach v., D. 8, 9, 10
Harris, J.W. 45, 46, 241
Hartmann, V. 21, 274, 281, 284
Hartmann, W. 228, 301
Hartung, H. 188
Hass, M. 61
Heßberger, F.P. 2, 3, 4, 5, 73, 77, 79, 81
Heckwolf, H. 43, 44, 239
Heinz, U. 172, 173
Helm, U. 254
Helmolt v., U. 60
Hennerici, W. 60
Henning, W. 22, 76
Hennrich, H.J. 57, 60
Herrmann, G. 72, 82, 84, 85, 230, 231
Herrmann, N. 30, 31, 237
Herrmann, R. 122
Hess, P.O. 94, 121
Heusch, B. 14
Heyng, H.W. 60
Hickmann, U. 82, 84, 230
Hieber, L. 195, 203, 204
Hildebrand, N. 72, 82, 84
Hildenbrand, K.D. 11, 12, 28, 29, 30, 31, 38, 39, 40, 41, 236, 237
Himmele, G. 60
Hlavac, S. 6
Hoffman, D.C. 85
Hoffmann, C. 292
Hoffmann, D.H.H. 154, 156, 157, 158, 347, 348
Hoffmann, J. 267, 274
Hofmann, I. 332, 333, 335
Hofmann, N. 299
Hofmann, S. 5, 73, 77, 79, 81
Höhler, A. 270
Hollenbach, H.P. 27
Holländer, W. 220
Horneck, G. 198
Huber, G. 67, 167, 249
Hüfner, J. 126
Hulet, E.K. 15, 78, 83
Hüller, W. 229
Hultzsch, H. 275, 282
Hummel, K.-D. 216
Huttel, E. 199
Hutter, G. 298, 301, 302, 303
Ibarra, R. 126
Idzko, J. 64
Illert, K. 292
Indelicato, P. 160
Ismail, M. 97, 98
Jacoby, W. 299, 308
Jakubaßa-Amundsen, D.H. 170, 178
Jamil, K. 35
Janssens, R.V.F. 6
Johnson, W.R. 168, 185
Jokic, S. 37, 53
Jäckel, B. 16, 17
Jäger, E. 246
Julien, J. 44
Junior, P. 341
Kaffrell, N. 70, 72, 74
Kallies, H. 55, 56
Kampert, K.H. 39, 40, 41, 47, 256, 257, 258
Kang, T.-S. 259
Kankeleit, E. 150
Kaps, R. 100, 136, 137
Karlewski, T. 72
Kaspar, K. 322, 323, 324, 325
Keim, H.-J. 26
Keiner, P. 199
Kelbch, S. 162
Keller, J.G. 2, 3, 4
Keller, R. 336, 338, 339
Kellerer, A.M. 194, 263
Kemmer, J. 148, 248
Kester, P.C. 166
Khadkikar, S.B. 125
Khan, E.U. 36, 220, 264
Khan, H.A. 35, 260, 261, 262
Khan, N.A. 35, 260, 261, 262
Khaouli, M.M. 299, 300, 308
Khoo, T.L. 6
Kido, Y. 149
Kiefer, J. 199, 200, 201
Kieling, W. 84
Kienle, P. 22, 148, 151, 156, 248
Kiesewetter, H.-R. 217, 292
Killinger, F. 55, 56
Kirchner, R. 67, 69, 70, 71, 74, 75, 229
Klabunde, J. 298, 338, 343, 344, 345, 346
Kleber, M. 184
Klein, H. 341
Klein, H.A. 161

Klein, N. 55, 56
Klemm, J. 228
Klepper, O. 43, 44, 67, 69, 70, 71, 74, 75, 240
Klotz, G. 150
Klüver, M. 149
Knippelberg, W. 222
Knobbe, K.H. 302
Knoll, J. 127, 135
Knöchel, A. 234
Koch, G. 57
Koenig, W. 148, 159, 248
Koglin, E. 34
Kohlmeyer, B. 14, 18, 26, 32
Kolb, B.W. 47, 48, 49, 51, 52, 257, 258, 273
Kolb, D. 188, 189, 190
Koller-Lampert, K. 209
Konrad, J. 155
Kopf, U. 292, 340
Korschinek, G. 76
Kost, M. 199, 266
Kozhuharov, C. 148, 151, 159, 248
Kraft-Weyrather, W. 206, 207, 208
Kraft, G. 202, 203, 204, 205, 206, 207, 208
Krämer, M. 150
Kranz, A.R. 209
Kratz, J.V. 24, 25, 33, 82, 85, 233
Kratz, Th. 7
Krause, J. 219
Kreijcik, P. 339
Kretschmer, R. 55, 56
Krichbaum, H. 299
Krieg, R. 150
Kritzer, A. 326
Kroth, R. 57, 58, 59, 60
Kube, G. 301
Kubik, P. 76
Kuchinka, E. 204, 233
Kulessa, R. 61, 63, 65
Kumbartzki, G.J. 61
Kurcewicz, W. 71, 74
Kurz, H.-P. 299
Kutschera, W. 76
Kuzminski, J. 12, 29, 30, 31, 236, 237
Kwong, N. 58, 59
Kynast, W. 286, 287
Körner, H.J. 22
Kühl, T.U. 67, 167
Kühn, R. 327
Kühn, W. 6, 57
Künkel, R. 19
Laßmann, M. 194
Landrum, J.H. 15, 78, 83
Langbein, K. 341
Langenbeck, B. 314
Langevin, M. 70
Larsson, M. 195, 203
Larsson, P.O. 67, 69, 70, 71, 73, 74
Laschek, A. 55, 56
Laursen, J. 161
Lauterbach, Ch. 62
LaVilla, R.E. 349
Laville, J.L. 44
Lazzarini, A. 57, 60
Lee, D. 85
Leible, K.-D. 299, 338
Leino, M. 77, 79, 81
Leipe, P. 341
Lenske, H. 99
Lenz, G. 266
Lerch, M. 85
Liebold, H.P. 267
Liesen, D. 152, 153, 160
Liu, B. 152, 153, 160
Lochmann, H. 67, 167, 249
Lohmüller, B. 7
Löhner, H. 47, 48, 49, 50, 51, 52, 256, 257, 258
Lougheed, R.W. 15, 78, 83
Loveland, W. 54
Lowsky, J. 274, 275, 281, 282
Lucas, R. 24, 25
Ludewigt, B. 47, 48, 49, 51, 52, 257, 258
Ludwig, M. 236, 237
Lukasiak, A. 114, 115, 116, 117
Lund, T. 54
Lützenkirchen, K. 25
Lynen, U. 24, 28, 29, 38, 39, 40, 41, 238
Maier, M. 46, 241
Makowka, J. 102
Malvetti, M. 119
Malwitz, E. 292
Malzacher, P. 186
Mann, R. 159, 162, 163, 165
Marinescu, D.C. 274, 281, 282
Marinescu, M. 18, 32
Martens, H.-G. 267
Martin, B. 159
Maruhn, J.A. 94, 122, 123, 124, 128, 129, 130, 131, 132, 139, 140, 141, 143, 351, 352
Marx, D. 67, 69
Masak, D. 136, 137
Matulewicz, T. 109
Maurenzig, P. 30, 31
Maury, M. 218
Mauthofer, A. 64
Mayer, W. 22, 76
Mayer, W.A. 22
Mc Gaughey, P. 54
McClelland, A.F. 161
Meger, A. 223
Mehler, G. 169, 176, 181
Menges, R. 67, 167, 249
Merdinger, J.C. 63
Metag, V. 6, 57, 60

Meufels, W. 267
Meyer, U. 150
Meyerhof, W.E. 347, 348
Michel, Ch. 43, 44, 61, 65, 66, 239, 240, 244
Miczaika, A. 19
Miltenburger, H.G. 202, 207, 208
Mokler, P.H. 154, 155, 157, 158, 161, 164, 349
Molitoris, J.D. 347, 348
Mömerzheim, K. 267
Moody, K.J. 15, 79, 81, 82, 83, 85
Moore, M.S. 65
Morgenstern, B. 118
Morhardt, A. 301
Morinaga, H. 76
Mosel, U. 87, 88, 89, 90, 91, 93, 99, 100, 101, 102, 136, 137
Mueller, A.C. 44
Mühlhans, K. 88, 92
Mühlhans, R. 57
Müller, A. 166
Müller, B. 138, 145, 169, 171, 172, 173, 174, 175, 176, 179, 181, 182, 191
Müller, E. 89
Müller, L. 22
Müller, M. 76, 298, 299, 300, 308
Müller, R.W. 332, 333, 340, 341
Müller, U. 169, 171, 172, 173, 174, 175, 176, 179, 181
Müller, W. 40, 202, 207, 208
Müller, W.F.J. 11, 12, 28, 29, 30, 31, 38, 39, 41, 43, 44, 236, 237, 240, 274
Munn, Ph. 223
Münzenberg, G. 2, 3, 4, 5, 73, 77, 79, 81
Murnick, D.E. 156
Mutterer, M. 27, 65, 66, 255
Neise, L. 123
Neumann, W. 341
Ngo, C. 24
Nickel, F. 229
Noll, H. 21, 43, 44, 239, 240
Nolte, E. 76
Novotny, R. 57
Nyman, G. 71
Nörenberg, W. 112, 114, 115, 116, 117, 118
O'Kelley, G.D. 78
Obenshain, F.E. 44
Odyniec, G. 45, 241
Oertzen v., W. 19
Oeschler, H. 150
Olmi, A. 11, 12, 24, 28, 29, 30, 31, 41, 236, 237
Oppenländer, A. 155
Ortiz, M. 241
Oskarsson, A. 239
Ower, H. 64
Pannicke, J. 27, 255
Pappalardo, G. 44
Patzelt, P. 16, 17
Paul, P. 44
Pellas, P. 218
Pelte, D. 38, 39, 40, 41, 61
Perelygin, V.P. 218, 264
Perron, C. 218
Peter, J. 44
Petrovici, M. 28, 29, 30, 31
Peuser, P. 70, 74
Pielenz, K. 80
Pinkston, W.T. 96, 121
Pischel, B. 265
Plachky, M. 220
Plochocki, A. 71
Plunien, G. 182
Poitou, J. 24
Pollet, D. 203
Poppensieker, K. 73, 77, 79, 81, 217, 267
Porile, N. 54
Poskanzer, A.M. 47, 48, 49, 50, 51, 52, 257, 258
Post, U. 93
Prange, H. 311, 326
Przybyla, A. 267
Pugh, H.G. 45, 46, 241
Pühlhofer, F. 14, 18, 26, 32
Quick, W. 236, 237
Quis, D. 267
Rabe, H. 39, 40
Rafelski, J. 144
Ralarosy, J. 37, 53
Rashdan, M. 97
Rasmussen, J. 347, 348
Ratzinger, U. 76
Rauch, F. 235
Rauch, W. 45, 241
Recker, K. 214
Reeh, W. 235
Reichwein, E. 34
Reinhardt, J. 169, 171, 172, 173, 174, 175, 176, 179, 181
Reisdorf, W. 2, 3, 4, 5, 73, 77, 79, 81
Reiser, M. 343, 344
Reiss, G. 224
Renfordt, R.E. 45, 46, 241
Renner, T. 47, 48, 49, 50, 51, 52
Rentzsch, T. 132
Repnow, R. 6, 60
Reus de, T. 169, 171, 174, 175, 176, 179, 181
Reus, U. 17, 86
Richard, P. 162
Richter, A. 20
Richter, M. 267, 274
Ricken, L. 44
Riedel, C. 330
Riedesel, H. 47, 48, 49, 50, 51, 52
Riehl, G. 341
Rikus, L. 125
Ring, P. 95

Ritter, H.G. 47, 48, 49, 50, 51, 52, 257, 258
Roeckl, E. 69, 70, 71, 74, 75, 229
Röhl, H. 234
Roos, H. 194, 263
Roots, R. 208
Rösch, W. 43, 44, 240
Rosen, A. 187
Rosenhauer, A. 128
Roth, M. 210, 211
Rox, A. 16, 17
Rulfs, R. 299, 300
Runte, E. 70, 74, 75
Rydberg, B. 196
Rykaczewski, K. 70, 74
Saßmannshausen, U. 212, 214
Sahm, C.-C. 2, 3, 4, 5, 80, 254
Salzborn, E. 166
Sandoval, A. 45, 46, 241
Sann, H. 24, 28, 29, 30, 31, 38, 39, 40, 41, 236
Santo, R. 39, 40, 41
Sapotta, K. 7, 21
Satpathy, L. 97
Schädel, M. 15, 78, 82, 83, 85, 246, 247
Schadt, W. 155
Schäfer, A. 191
Schäfer, M. 197, 198
Schaffner, E. 327
Schall, D. 45, 46, 241, 242
Schardt, D. 67, 69, 70, 71, 74, 75, 78, 246
Schartner, K.-H. 349
Schaupert, K. 210, 211, 217
Scheid, W. 180
Schempp, A. 341
Schimmerling, W. 208
Schimpf, E. 246, 247
Schirmer, J. 58, 59
Schlüter, P. 181, 183
Schmidt-Böcking, H. 155, 162
Schmidt-Ott, W.-D. 70, 74, 75
Schmidt, H.-G. 267
Schmidt, K.-H. 2, 3, 4, 5, 77, 79, 80, 81
Schmidt, W. 292
Schmitt, C. 254
Schneider, E. 199, 200, 266
Schneider, G. 267, 274
Schneider, J.R.H. 73, 77, 79, 81
Schneider, K. 299
Schneider, N. 307
Schneider, V. 122
Schneider, W.F.W. 14, 18, 19, 26, 32, 77, 79, 81
Schönfeldt, W.A. 154, 157, 158
Schönlein, A. 345, 346
Schött, H.-J. 73
Schrieder, G. 20
Schroeder, L.S. 45, 46
Schuber, M. 205, 207
Schuch, B. 166
Schuch, R. 155
Schuette, G. 289
Schukraft, J. 8
Schüll, D. 18, 19, 20, 32, 76
Schulte, H. (GSI) 310
Schulte, H. (Univ. Marburg) 16, 17
Schulz, M. 155
Schulze, R. 267, 269, 270
Schulze, W. 189
Schüssler, H.A. 163
Schwalm, D. 57, 58, 59, 60, 61, 64, 65, 66, 149
Schwartz, B. 245
Schweppe, J. 149
Seaborg, G.T. 15, 54, 82, 83, 85
Seiler-Clark, G. 61, 62, 243
Seiwert, M. 94, 96, 131
Senft, K. 267
Senger, P. 150
Sengler, W. 190
Sepp, W.-D. 188
Shenhav, N. 253
Shyam, R. 135
Sial, M.A. 35
Siart, O. 275, 289
Siegmon, G. 219
Siemiarczuk, T. 50
Silver, J.D. 161
Simon, R.S. 6, 31, 57, 60, 65, 66, 245
Simonis, H.J. 119
Sitta, H. 243
Soff, G. 168, 169, 171, 174, 175, 176, 177, 181, 183, 185, 192
Sohlbach, H. 18, 32
Soltani, J. 159
Spangenberger, H. 104
Specht, H.J. 8, 9, 10
Speidel, K.-H. 61
Spohr, R. 210, 211, 217
Spreng, W. 62, 63, 65, 66
Spädtke, P. 336, 337, 338, 339, 340, 346
Stachel, J. 44, 62, 272
Starke, M.E. 209
Stefanini, A. 30, 31
Stege, H. 14, 26
Steiner, R. 309, 311
Stelzer, H. 2, 11, 12, 28, 29, 30, 31, 38, 39, 40, 41, 43, 44, 236, 237, 238, 240, 253, 257
Stelzer, K. 7, 21, 64
Stepaniak, J. 50
Stetsenko, S.G. 218
Stiebing, K.E. 149
Stock, R. 45, 46, 241
Stoller, C. 347, 348
Stork, M. 299
Strack, B. 110, 127
Strehl, P. 298, 304
Struckmeier, J. 343, 344, 346

Ströbele, H. 45, 46, 241, 242
Ströher, H. 57
Stuhrmann, H. 210, 211
Sturm, E. 267
Stöcker, H. 129, 130, 132, 141, 143
Sümmerer, K. 33, 78, 82, 84, 85, 246
Tanimura, O. 100, 101
Tavernier, M. 160
Thalheimer, W. 228
Theis, J. 129, 141, 142, 143
Theobald, J.P. 27, 65, 66, 255
Thiel, A. 103
Thiel, K. 212, 213, 214
Thomas, W.-H. 194
Tidemand-Petersson, P. 70, 71, 74
Tittel, K. 46, 242
Tobias, C.A. 208
Tohyama, M. 136, 137
Toke, J. 11, 12, 28, 29, 30, 31, 109, 236, 237
Tomasi, E. 24
Torbohm, G. 187
Trautmann, N. 65, 72, 82, 84, 85, 149, 230, 231
Traving, B. 225
Trebus, U. 163
Trefz, M. 125
Tress, G. 220, 221
Tripier, J. 37, 53
Trockel, R. 38, 39, 40
Tsertos, H. 148, 151, 248
Uhlig, M. 139, 140
Ullrich, T. 162
Ulm, G. 67, 68, 167, 249
Ulrich, A. 156
Ungrin, J. 342
Vaccaro, V.G. 334
Valluri, S.R. 180
Valter, H. 301
Vasak, D. 138, 139, 140, 145
Vater, P. 36, 42, 220, 221, 264
Vermeulen, D. 4, 5, 77, 79, 81
Vilhjalmsson, H. 306
Vincent, P. 149
Vinzenz, W. 301
Vivien, J.P. 63
Vogt, D. 338
Wada, R. 38, 39, 40, 238
Wadia, W. 97
Wagner, W. 22, 148, 151, 248
Wahl, W. 60
Walter, G. 75
Wang, S.J. 108, 112
Warczak, A. 152, 153, 154, 157, 158, 160
Warczak, B. 165, 206
Warke, C.S. 139
Warwick, A. 47, 48, 49, 50, 51, 52
Weber, K.J. 200
Weidner, W. 55, 56
Weik, F. 49, 50, 51, 52
Weingärtner, K. 27
Wenning, A. 194
Werner, E. 111
Westmeier, W. 16, 17, 86
Wieman, H. 47, 48, 49, 50, 51, 52, 257, 258
Wien, K. 222
Wietschorke, K.-H. 145, 181, 183
Wild, J.F. 15, 78, 83
Wilhelmy, J.B. 151
Wilms, D. 298
Winkelmann, K. 274, 281, 285
Winkler, U. 39, 41
Wirkner-Bott, I. 166
Wirth, G. 24, 25, 33, 82, 84, 85
Wirth, H. 235
Witzky, M. 306
Wolf, B. 213, 214, 338
Wolf, G.K. 223, 224, 225
Wolf, K.L. 45, 46
Wolf, R. 100, 101, 102
Wollersheim, H.J. 23, 28, 29, 61, 62, 63, 64, 65, 66, 244
Wolter, H.H. 99
Wong, M. 208
Wu, X.-Z. 122, 124
Wüst, E. 90, 91, 92, 93
Xu, J.-S. 347, 348
Yang, T.C. 208
Yannouleas, C. 106
Young, G.R. 44
Zaidman, G. 281, 284
Zauner, S. 233
Zhai, P.-J. 259
Zhang, J. 163
Zhang, P.H. 44
Ziegenhain, K.H. 122
Ziem, A. 305
Zilker, F. 194
Zirnbauer, M. 58, 59
Zylicz, J. 71, 74